THE JAHN–TELLER EFFECT

The Jahn–Teller effect is one of the most fascinating phenomena in modern physics and chemistry, providing a general approach to understanding the properties of molecules and crystals and their origins. The effect inspired one of the most important recent scientific discoveries, the concept of high-temperature superconductivity. This comprehensive volume presents the background of the theory and its main applications in physics and chemistry, along with more recent achievements. Full descriptions are presented alongside thorough references to original material. The book contains over 200 figures to aid visual explanation and avoids bulky mathematical deductions and overly technical language. It is intended for graduate students and academic researchers working in solid-state physics, theoretical, physical, and quantum chemistry, crystallography, spectroscopy, and materials science.

ISAAC B. BERSUKER is a Senior Research Scientist and Adjunct Professor of Theoretical Chemistry at the University of Texas at Austin. His main scientific interest is in the theory of vibronic interactions and Jahn–Teller Effect with applications to solid-state physics, chemistry, and biology. He is the author and co-author of 12 books, 25 major reviews, and more than 300 original publications.

THE JAHN–TELLER EFFECT

ISAAC B. BERSUKER
The University of Texas at Austin

CAMBRIDGE
UNIVERSITY PRESS

In memory of my wife Liliya Bersuker

CAMBRIDGE UNIVERSITY PRESS
Cambridge, New York, Melbourne, Madrid, Cape Town, Singapore, São Paulo

CAMBRIDGE UNIVERSITY PRESS
The Edinburgh Building, Cambridge CB2 2RU, UK

www.cambridge.org
Information on this title: www.cambridge.org/9780521822121

First published 2006

Printed in the United Kingdom at the University Press, Cambridge

A catalog record for this publication is available from the British Library

Library of Congress Cataloging in Publication data

ISBN-13 978-0-521-82212-1 hardback
ISBN-10 0-521-82212-2 hardback

Contents

Preface

The Jahn–Teller effect (JTE) is one of the most fascinating phenomena in modern physics and chemistry. It emerged in 1934 in a discussion between two famous physicists, L. Landau and E. Teller, and grew into a general tool for understanding and an approach to solving molecular and crystal problems, which is applicable to any polyatomic system. The first formulation of this effect as *instability of molecular configurations in electronically degenerate states* proved to be the beginning of a whole trend which rationalizes the origin of *all possible instabilities* of high-symmetry configurations, and the peculiar nuclear dynamics resulting from these instabilities as well as the origins of all structural symmetry breakings in molecular systems and condensed matter.

Intensive development of the JTE theory began in the late 1950s together with a wave of main applications to spectroscopy, stereochemistry, and structural phase transitions, which lasted a couple of decades. The next significant resurgence of interest in the Jahn–Teller effect is related to the late 1980s and is still continuing. It was triggered by one of the most important Nobel Prize discoveries in physics of our times inspired by the Jahn–Teller effect: the *high-temperature superconductivity*. As explained by the authors of this discovery, "*the guiding idea in developing this concept was influenced by the Jahn–Teller polaron model*" (J. G. Bednorz and K. A. Müller, in *Nobel Lectures: Physics*, Ed. G. Ekspong, World Scientific, Singapore, 1993, p. 424).

Another recent discovery in solid-state physics, the *colossal magnetoresistance*, is also explained with essential implication of the Jahn–Teller effect. With regard to recent achievements in application to molecular systems, in addition to vast numbers of solutions of *structural, spectroscopic, and magnetic problems*, the Jahn–Teller effect has been most instrumental in explaining the properties of a novel class of compounds, the fullerenes, and it is now invoked in growing applications to the origin of *reactivity and mechanisms of chemical reactions*.

This book is devoted to presenting the JTE phenomenon in its integral unity, including the background of the theory and its main applications in physics and chemistry with emphasis on more recent achievements (as explained in more detail in the introduction). The goal is also to make the JTE more accessible to a wider circle of readers, meaning more visual explanation of the origin of the effects, omitting bulk mathematical deductions, where possible, and, in view of the multidisciplinary nature of the subject, trying to avoid heavy professional language specific for narrow groups of researchers. To compensate for any possible inconvenience for some of the readers created by this style, detailed references and cross-references have been included, allowing one to reach the desired level of description. We tried to address all aspects of the JTE theory and applications to all kinds of molecular systems and crystals, *making the book almost encyclopedic* in this respect.

The presentation in this book is based on our experience in this field. I started thinking on the Jahn–Teller effect in 1959 when reading a paper on the crystal field theory and have continued to work in this field ever since, so I witnessed and participated in its main achievements. My first book on this topic in English was published in 1984 (the first book on the JTE was published by R. Englman in 1972). Another book prepared together with V. Z. Polinger for a narrower circle of theoreticians was published in English in 1989 (the Russian version of this book was published in 1983). Together with my coworkers we published in 1984 a bibliographic review of the JTE publications. The new book follows the style of presentation of my first book and it uses some materials from, and references to, the book of 1989. In essence the new book is quite novel with regard to both the content and the level of presentation: in view of the achievements of the last two decades, the previous books, mentioned above, look rather incomplete (and in some respects obsolete). However, the book of 1989 authored with V. Z. Polinger remains valid with respect to many theoretical derivations referred to in the new book.

During the preparation of this book I benefited from the cooperation with my previous and present coworkers and colleagues from the community of scientists working in this field. My thanks are due to C. A. Bates, G. Bevilacqua, G. I. Bersuker, J. E. Boggs, S. A. Borshch, L. S. Cederbaum, A. Ceulemans, L. F. Chibotaru, J. T. Devreese, J. L. Dunn, R. Englman, J. P. Fackler, Jr., P. Garcia-Fernandez, M. D. Kaplan, H. Koizumi, H. Köppel, N. N. Kristoffel, A. A. Levin, L. Yu, W. J. A. Maaskant, N. Manini, L. Martinelli, T. A. Miller, M. Moreno, K. A. Müller, I. Ya. Ogurtsov, Yu. E. Perlin, V. Z. Polinger, D. Reinen, S. S. Stavrov, E. Teller, B. S. Tsukerblat, C.-L. Wang, and Yu. V. Yablokov. I am especially thankful to V. Z. Polinger for continuing discussion of JT problems of this book, and to J. E. Boggs for support and

cooperation. I am thankful also to E. Teller for an encouraging chat on some aspects of the JTE; unfortunately, he did not survive to write the (promised) foreword to this book.

I acknowledge the cooperation of many publishers of academic journals and books for their kind permission to reprint figures, including the American Chemical Society, the American Institute of Physics, the American Physical Society, Elsevier Science Publishers, Helvetica Chimica Acta Verlag, the Institute of Physics, John Wiley & Sons, Kluwer Academic Publishers, NRC Research Press, Princeton University Press, the Royal Society London, Springer Verlag, and Taylor & Francis. I am grateful to the team of Cambridge University Press for help and cooperation in the copy-editing and production of this book.

Isaac B. Bersuker
Austin, Texas, January 2005

Abbreviations

AA – adiabatic approximation
AO – atomic orbitals
APES – adiabatic potential energy surface
BCS – Bardeen–Cooper–Schrieffer
BLYP – Becke–Lee–Yang–Parr (DFT functional)
BOD – bicyclooctadienediyl
CASSCF – complete active space SCF
CI – configuration interaction
CJTE – cooperative JTE
CNDO – complete neglect of differential overlap
COT – cyclooctatetraene
CPJTE – cooperative PJTE
DFT – density functional theory
DPH – diphenylhexatriene
EPR (ESR) – electron paramagnetic resonance (electron spin resonance)
EXAFS – extended X-ray absorption fine structure
HF – Hartree–Fock
HOMO – highest occupied MO
HTSC – high-temperature superconductivity
INDO – intermediate neglect of differential overlap
IR – infrared
JT – Jahn–Teller
JTE – Jahn–Teller effect
LSD – local spin density
LUMO – lowest unoccupied MO
MCSCF – multicenter SCF
MCZDO – multicenter zero differential overlap
MFA – mean-field approximation

MINDO – modified INDO
MO – molecular orbitals
MO LCAO – MO linear combination of AOs
MP – metal porphyrin
MPc – metal phthalocyanine
MP2 – Möller–Plesset 2 (second-order perturbation theory)
MRCI – multireference CI
MRSDCI – MRCI with single and double excitations
MV – mixed valence
NMR – nuclear magnetic resonance
NGR – nuclear gamma resonance
phen – phenanthroline
PJT – pseudo JT
PJTE – pseudo JTE
QCISD – quadratic CI with single and double excitations
QM/MM – quantum mechanics/molecular mechanics
RF – reductions factor
RMP2 – restricted MP2
ROHF – restricted open-shell HF
RT – Renner–Teller
RTE – Renner–Teller effect
SB – symmetry breaking
SCF – self-consistent field
SP – square-pyramidal
STO – Slater-type orbitals
TBP – trigonal-bipyramidal
TCNE – tetracyanoethylene
TCNQ – 7,7,8,8-tetracyano-*p*-quinodimethane
TTF – tetrathiofulvalene
UQCISD – unrestricted QCISD
ZEKE – zero electron kinetic energy

1
Introduction

This introductory chapter has two goals. The first one is usual for books of this kind and is aimed at providing the reader with a brief outline of the background history of the subject, its main content, form of presentation, and correlation with other related subjects. The second goal is to give this introduction in a way which allows the reader to get a general (although maybe rather rough and superficial) impression of the whole subject and its possibilities, a very brief insight into this trend without reading the corresponding chapters or sections. This is done keeping in mind that quite a number of physicists, chemists, and biologists, who at present are not engaged in the use of the Jahn–Teller effect, may be interested to know in general the status quo in this field and make a fast choice of the parts of it they may be interested in. In other words, the introduction is aimed at giving a very brief qualitative description of the main features of the Jahn–Teller effect theory in a way useful also for the reader who has no intention to read the whole book or its parts. The applications of the theory to chemical problems and molecular systems are given in Chapter 7, while the Jahn–Teller effect in specific solid-state problems is considered in Chapter 8.

1.1 The history and evolution of understanding of the Jahn–Teller effect

The so-called Jahn–Teller (JT) effect (JTE), which includes the proper JTE, pseudo JTE (PJTE), and Renner–Teller effect (RTE), nowadays forms a whole trend in the theory of structure and properties of molecules and crystals jointly termed *JT vibronic coupling effects*, or abbreviated JTE (this abbreviation is used throughout the whole book). In fact the JT theory is *an approach* to (*a tool* for) general understanding and solving of molecular and crystal problems, which is in principle applicable to any system with more than two atoms.

As for many other fundamental properties of matter, the JTE was first formulated in the early thirties of the twentieth century [1.1–1.4]. There were four persons who initiated this trend: L. Landau, E. Teller, H. Jahn, and R. Renner. In 1934 L. D. Landau in a discussion with E. Teller about his student's (R. Renner's) work first formulated the statement that *a molecule in an orbitally degenerate electronic state is unstable with respect to spontaneous distortion of the nuclear configuration that removes the degeneracy* (see in [1.4]). Presumably, Landau's arguments were based on ideas similar to that used in the proof of the von Neumann–Wigner theorem about crossing electronic terms [1.5]. This Landau statement was later verified by E. Teller and H. Jahn and more rigorously formulated as (what is now known as) the Jahn–Teller theorem [1.1].

The proof of this theorem (Section 2.5) is based on perturbation theory, in which the influence of the nuclear displacements (vibrations) via *electron–vibrational (vibronic) interactions* is considered as a perturbation to the degenerate states, and only linear terms of this *vibronic coupling* of the electronic states to the nuclear displacements are taken into account. Qualitatively (roughly) the origin of instability of molecules in high-symmetry configurations with orbital degeneracy can be easily understood if one takes into account that *when there are two or more electronic distributions with the same energy, they are necessarily nontotally symmetric with regard to the environment* (cf. three atomic p states, p_x, p_y, and p_z), and hence the electron on any one of them distorts the otherwise symmetrical environment, thus lowering its energy (Section 2.5).

In the linear approximation (first order in the vibronic coupling) linear geometries are exceptions from the JT theorem (Renner's molecule CO_2 was just such an exception, with regard to which, at first sight, Landau was wrong). However, linear molecules are subject to similar instabilities when the quadratic terms of vibronic coupling are taken into account [1.3], and then it is called the RTE (Section 4.4). Another exception from the JT theorem is a spin double degenerate (Kramers) term, which cannot be split by nuclear displacements (it splits under magnetic fields only).

Before World War II only one more paper was devoted to the JTE, that of Van Vleck [1.6]. In this paper the simplest JT problem of a twofold degenerate electronic term E interacting with twofold degenerate e vibrations (hereafter the vibrational modes are indicated with small letters), *the* $E \otimes e$ *problem*, was explored, and it was shown that in this case the *adiabatic potential energy surface* (APES) has the form of a "Mexican hat" (Section 3.2).

Among other things the author of this publication Van Vleck, wrote that "*it is a great merit of the JTE that it disappears when not needed*." This declaration reflects the situation when there was very poor understanding

of what observable effects should be expected as a consequence of the JT theorem. The point is that the simplified formulation of the consequences of the JT theorem as "spontaneous distortion" is incomplete and therefore inaccurate, and may lead to misunderstanding. In fact, there are several (or an infinite number of) equivalent directions of distortion (like in the three p-state directions in the example above), and the system may resonate between them (the *dynamic JTE*). In a more rigorous treatment (Chapters 3–5) the lack of minimum of the APES results in a variety of novel properties, but it does not necessarily lead to observable nuclear configuration distortion, and this explains why such distortions often cannot be observed directly (Section 7.1).

This period of "stagnation," misunderstanding of the JTE, lasted almost two decades. Even in 1960 Low in his book [1.7] stated that "*it is a property of the JTE that whenever one tries to find it, it eludes measurements*."

In 1950 Abragam and Price [1.8] first revealed the dynamic nature of the JT distortions by analyzing the temperature dependence of ESR spectra of Cu(II) compounds [1.9] (Section 6.3.1). The usually well-defined anisotropy of the ESR signal from octahedral complexes of Cu(II) disappeared at certain temperatures due to the thermal averaging over the different directions of JT distortions in the $E \otimes e$ problem (in fact the JT dynamics is more complicated, involving tunneling splitting, Sections 5.3 and 6.3.1). This was seemingly the first experimental observation of the JTE.

In 1957 Öpik and Pryce [1.10] developed a method of calculation of the possible JT distortions (Section 3.3) and revealed the number and kind of extrema points of the APES for threefold degenerate states interacting with both e and threefold degenerate t_2 vibrations, the *linear* $T \otimes (e + t_2)$ *problem* (Section 3.3), showing that in this case either tetragonal or trigonal distortions are possible. In this paper the *PJTE problem* was formulated for the first time. The idea behind the PJTE is that not only exact degeneracy (required by the JT theorem), but sufficiently close-in-energy (*pseudodegenerate*) states may produce instabilities, similar to those of the JTE (Section 4.1). The condition of the PJT instability requires that the energy gap between the mixing states is sufficiently small in comparison with other vibronic parameters of the system. The PJTE became most important later when it was shown that it is the only source of instability of high-symmetry configurations of polyatomic systems in nondegenerate states.

In 1957–58 Longuet-Higgins *et al.* [1.11] and independently Moffit and Thorson [1.12] calculated the vibronic energy levels of systems with the linear $E \otimes e$ problem, transitions to and from these states, and band shapes of optical spectra involving such degenerate states. It was the first demonstration of the

JTE in optical spectroscopy showing that it results in specific forms of the band shape (Section 6.3.1). Liehr and Ballhausen [1.13] explored the JT $E \otimes e$ problem with quadratic terms of vibronic interactions and revealed the so-called warping of the Mexican-hat-type APES. This warping results in the formation of three equivalent minima along the bottom of the trough, which correspond to three directions of tetragonal distortions of the system (Section 3.2).

An explosion of publications began at this point, from which we mention here a few main contributions, which explored in detail the origin of different kinds of JT dynamics. An account for the publications of the whole period from inception up to 1979 inclusive is given in the bibliographic review [1.14].

In 1961–63 Bersuker [1.15] first considered the splitting of the lowest vibronic energy levels due to the *tunneling* of the system between the equivalent distorted configurations (Section 5.3) and its influence on ESR spectra (Section 6.3.3). In 1964 O'Brien [1.16] calculated numerically the vibronic energy levels in the $E \otimes e$ problem with linear and quadratic terms of vibronic coupling included (Section 3.2). In 1965 Ham [1.17] generalized the idea of *vibronic reduction factors* (Section 5.6). The latter are of special interest since they allow one to calculate physical properties of electronic origin without fully solving the vibronic coupling problem.

An important development of the JTE theory began with the treatment of interactions of JT centers, especially regular JT centers in crystals, known as the *cooperative JTE* (CJTE) (Sections 8.2–8.4). Kanamori [1.18] in 1960 first explicitly explored such cooperative phenomena in JT crystals, while Elliot *et al.* [1.19] and other authors essentially advanced this important trend in application to rare-earth zircons (Section 8.2.1). In 1966 Bersuker [1.20] first suggested the vibronic theory of ferroelectricity as a *cooperative PJTE* (Section 8.3). While the idea of interactions between JT centers in crystals and the consequent ordering of JT distortions was physically transparent and quite understandable, the very possibility of the PJTE in dielectric crystal centers with relatively large band energy gaps and their interaction to lead to ferroelectric (and other) phase transitions was questionable at that time.

The book of Englman in 1972 was the first to give a comprehensive review of this field as a whole [1.21] (before that a review of this topic was published by M. D. Sturge [1.22]). With this book the first stage of the JTE theory was accomplished, resulting in a full understanding of the basics of this phenomenon: the JTE became a firmly established trend in the theory of matter. This was also marked by the beginning of separate JT symposia; the first four symposia took place in Bad Honnef (1976), Leoni (1977), Trento (1978), and Chantilly (1979).

In the 1970s most of the further efforts in this field were devoted to spectroscopic consequences of the JTE (Chapter 6), as well as to cooperative phenomena in crystals (Sections 8.2 and 8.3). During the 1980s, alongside applications of the JTE to physical and chemical phenomena, new developments of the theory emerged. First, numerical calculations of vibronic coupling effects became more widespread, allowing a more detailed insight into observable JTE (here we stop citing the names of contributors because they are many; they can be found in the books and reviews cited below, as well as in the corresponding sections with more detailed description).

Among chemical applications attention was paid to the JTE in stereochemistry and chemical activation (Section 7.1), and in mixed-valence compounds (Section 7.6.2). In the general theory more attention was also paid to the multimode problem (Section 5.4). Quite a number of papers in the 1970s and 1980s were devoted to the JTE in impurity centers in crystals (Section 8.1). At this point the geography of JT symposia became more widespread and they attracted more participants: the Vth Symposium took place in Oxford (1980), the VIth in Nijmegem (1981), the VIIth in Liblice (1983), the VIIIth in Marburg (1985), the IXth in Nottingham (1987), the Xth in Kishinev (1989), the XIth in Ovronnaz (1992), the XIIth in Tartu (1994), the XIIIth in Berlin (1996), the XIVth in Erice (1998), the XVth in Boston (2000), and the XVIth in Leuven (2002), and an international workshop was organized in Beijing (2004).

The next important achievement of the theory was made by proving that the PJTE not only explains possible structural instabilities of systems in pseudodegenerate electronic states, but also is the only possible source of instability of such systems (Section 4.1). Moreover, it was shown that any instability of high-symmetry configurations of any system is of JT (in degenerate states), PJT (in nondegenerate states), or RT (in linear systems) origin. With this result all polyatomic systems became subject to JT vibronic coupling effects, and any of their spontaneous distortions is of JT, PJT, or RT origin.

A new wave of increasing interest in the JTE emerged in the late 1980s and early 1990s following the discovery of high-temperature superconductivity, which was inspired by the JTE, and the colossal magnetoresistance, the origin of which is explained in essence by the JTE (Section 8.4). In the 1990s several other advances emerged in this field. First, the theory of the JTE was enriched by exploring its tight relation to the so-called topological phase problem (Section 5.7), with important consequences for observable properties of JT systems (Section 5.3). Also the JTE was shown to be very instrumental in explaining the properties of fullerenes, including their superconductivity (Sections 3.4, 5.6, and 7.5.3). Further achievements were reached in treating

phase transition with the CJTE (Section 8.2). Novel fields of applications emerged in reactivity and mechanisms of chemical reactions (Chapter 7).

Thus the evolution of understanding of the JTE went from the simple idea of spontaneous distortions of some very specific systems to a general method of solving molecular and crystal problems via revealing the complex JT dynamics, tunneling splitting, cooperative phenomena, and the essential role of the PJTE which includes all the polyatomic systems under the same JT vibronic coupling approach. The role and place of this approach in modern physics and chemistry is outlined in Section 1.2. Earlier stages of development of this field are presented in a series of books and reviews [1.22–1.57]; the intention of this book is to present a full account of the trend as a whole.

1.2 The role and place of the JTE in modern physics and chemistry

As mentioned in the previous section, in the evolution of understanding and development of the theory the JTE grew into a general approach to understanding and solving molecular and crystal problems. Now we intend to explain why this approach is different from other existing approaches and how they are interrelated.

First we notice that the main interaction which results in the JTE is the vibronic (electron–vibrational) coupling between electronic and nuclear motions. Vibronic interaction in molecules or electron–phonon interaction in crystals is one of the main elements of any theory of matter; it has been well studied since the very inception of quantum mechanics. So what is novel in the JT approach to the problem?

Consider polyatomic systems with discrete energy spectra. For them the essential difference between the usual approaches that include vibronic (or electron–phonon) coupling and the JT approach is in *the number of electronic states and hence the kind of vibrations* involved in this procedure. While the traditional approaches consider the coupling of phonons (vibrations) to a given (usually ground) electronic state, the JT approach requires necessarily two or more (degenerate or pseudodegenerate) electronic states that are mixed under these vibrations in a *nonadiabatic coupling*. In other words, the JTE involves *a new quality*, namely, the mixing of electronic states by vibrations, and the back influence of this mixing on the nuclear motion, resulting in special coupled electron–nuclear dynamics that influences all the properties of the polyatomic system.

Since the "one-state" coupling may be described by the diagonal matrix element of the operator of vibronic coupling, while the mixing of different electronic states is an off-diagonal (nonadiabatic) effect, the two

approaches, "usual" and JT, may be related as diagonal and off-diagonal vibronic (electron–phonon) coupling. The diagonal coupling is nonzero for totally symmetric vibrations only, and therefore they do not distort the symmetry of the system, whereas the off-diagonal elements involve low-symmetry JT distortions.

In the case of metals or semiconductors with states that are continuous or very close in energy the traditional theory includes all possible interactions with the phonons, but in a simplified manner without involving the nonadiabatic coupling between the electronic and nuclear motions. In other words the non-JT approach ignores the mixing of electronic states by nuclear displacements and the back influence of this mixing on the phonon spectrum. The JT electron–phonon coupling in metals involves many electronic states, which in our classification is a combination of JT (at the Fermi level) and PJT problems (Section 4.2). This is the so-called *band JTE* considered in Section 8.2.5.

An illustration of the JT approach to electron–phonon coupling in solids may be found in the modern attempts to explain the origin of high-temperature superconductivity (HTSC) (Section 8.4). Experimental data show that the electron–phonon interaction is essential in this phenomenon. The existing Bardeen–Cooper–Schrieffer (BCS) theory of superconductivity takes into account the electron–phonon interaction "in general" as an interaction of the electrons with the "bath of phonons" without detailed analysis of the local aspects of this interaction leading to the JTE. As shown in Section 8.2.5, for broad-band metals with widely delocalized electrons the JT electron–phonon coupling is weak and the JTE may be ignored. This is why the BCS theory explains the origin of superconductivity at low temperatures without taking into account the JTE. For narrower bands (which are characteristic of systems with HTSC) the JTE becomes significant, and the application of the achievements of the JTE theory to the HTSC problem seems to be most appropriate. This is indeed the subject of most current attempts to treat the HTSC yielding reasonable (reassuring) results (Section 8.4).

Another important point is the *universality of JT symmetry breaking*. The most widespread knowledge about the JTE is that it results in distortion of high-symmetry configurations of polyatomic systems. As mentioned above, this statement may be inaccurate, but under certain conditions the JTE does indeed trigger a breaking of the high symmetry of the system (Sections 7.1 and 8.2). Symmetry breaking is an important phenomenon employed to explain the evolution of the universe by cooling, beginning from the big bang. In condensed matter (atoms, molecules, crystals) symmetry breaking looks like a phase transition that takes place under the condition that at a

certain temperature both the symmetry and the entropy of the system become lower at lower temperatures, and this condition is satisfied in the presence of the JTE (Sections 4.5 and 8.2). Moreover, since the JTE has been shown to be the only source of spontaneous distortion of high-symmetry configurations, we come to the conclusion that *the JTE is a unique mechanism of all the symmetry breakings in condensed matter* (Section 8.2).

With regard to computational chemistry and physics another question emerges. As follows from that said above and in more detail from Section 2.5, the JTE is basically a perturbational approach in which two or more electronic states are mixed by the vibronic coupling. The main result of this perturbation is the instability of the reference configuration meaning the lack of minimum on the APES at the point of degeneracy or pseudodegeneracy. On the other hand, modern computational (numerical) methods allow one to (relatively easily) calculate the APES with its main features including the extrema points. These computationally revealed features of the APES obviously cover the predictions of the JTE with regard to instabilities. Then where is the heuristic role of the JTE in these problems?

To begin with, numerical computations of APES are (so far) limited to molecular systems and clusters of moderate size and limited numbers of vibrational degrees of freedom, and this does not allow one to consider extended systems. The JTE has no such limitations, but this is not the main point of importance of the JTE. More important is the *general relevance of the JTE*. Indeed, it is well known that the mainstream computational chemistry calculations of electronic structure at fixed nuclei that reveal the APES of specific molecular systems may be regarded as (have all the features of) *computer experiments*; the results cannot be transferred directly to other molecules. To rationalize such computer data, i.e., to explain their origin, they should be put in correspondence with more general models obtained by simplification and reasonable assumptions introduced in the first principles. *The JTE serves as an approved general model, which allows one to rationalize the results on molecular structure and properties obtained by other methods.*

Note that in the presence of degeneracy or pseudodegeneracy conventional electronic structure calculations with fixed nuclei, strictly speaking, do not predict observable properties; the calculated APES in these cases loses its physical meaning of the potential energy of the nuclei because of the strong nonadiabacity (Sections 2.1 and 2.5). The vibronic coupling theory thus remains here the only criterion of reliability of the results. To calculate observable magnitudes, the system of coupled equations (2.6) should be solved, and this contributes to a higher level of computational chemistry and physics.

1.3 Main goals of this book and means of their realization

The main goal of this book is to present a generalized picture of the status quo in the theory and applications of the JTE with a stronger emphasis on the latest achievements. Following the request of the publisher and our experience with previous books on related subjects, the presentation of the material is given in a way suitable for a wide circle of college-level physicists and chemists. This means that we avoid bulky mathematical deductions (or give them in a way that they may be skipped, if not necessary) and restrict heavy professional language, where possible. On the other hand, detailed citations and a full list of references to each chapter are included to allow the reader to go to original work for more details, if necessary. With regard to the citations (of which there are thousands) we tried to avoid listing the authors' names in the text (but they are all given in the citations!). Several names mentioned above in the brief history are exceptions made for the "founders" of this trend, meaning people who contributed essentially to the first stages of its development; without their names there is no history of this subject.

The material of this book is arranged as follows. Chapter 2 introduces the problem of vibronic coupling and the JT theorem. Chapters 3 and 4 formulate in general the JT, PJT, and RT problems and reveal their APES, while Chapter 5 discusses the solutions of the JT problems, including perturbation theory, numerical methods, tunneling splitting, the multimode problem, vibronic reduction factors, and the topological phase implications.

The theoretical background of the JTE in one of the most widely used experimental methods of investigation – spectroscopy – is given in Chapter 6. Chapter 7 (largest in volume and number of cited publications) deals with all kinds of applications of the JT theory to specific molecular formations, including molecules, radicals, and ions from different classes of compounds, plus clusters, coordination compounds, and mixed-valence systems, as well as some more general chemical problems. Chapter 8 is devoted to specific JT problems in solid-state physics, including impurity centers in crystals, the cooperative JTE in phase transitions (the largest part of the chapter), and contributions to the JTE in HTSC and colossal magnetoresistance.

The appendix, subject index and formula index are deemed to help the reader navigate through the vast material of this book with a large number of cross-references. The Formula Index is of special interest, allowing the reader to easily find the specific molecular and solid-state systems considered with regard to the JTE, thus contributing to the attempt to introduce encyclopedia features with regard to the trend under consideration. The list of abbreviations is intended to play a similar helpful role.

References

1.1. H. A. Jahn and E. Teller, *Proc. R. Soc. London A* **161**, 220 (1937).
1.2. H. A. Jahn, *Proc. R. Soc. London A* **164**, 117 (1938).
1.3. R. Renner, *Z. Phys.* **92**, 172 (1934).
1.4. E. Teller, in R. Englman, *The Jahn–Teller Effect in Molecules and Crystals*, London, Wiley, 1972 (Foreword); *Electron–Phonon Dynamics and Jahn–Teller Effects*, Eds. G. Bevilacqua, L. Martinelli, and N. Terzi, Singapore, World Scientific, 1999, p. 1; and in *Vibronic Interactions: Jahn–Teller Effect in Crystals and Molecules*, Eds. M. D. Kaplan and G. O. Zimmerman, NATO Science Series II, Vol. 39, Dordrecht, Kluwer, 2001, p. 1.
1.5. J. von Neumann and E. Wigner, *Phys. Z.* **30**, 467 (1929).
1.6. J. H. Van Vleck, *J. Chem. Phys.* **7**, 61 (1939).
1.7. W. Low, *Paramagnetic Resonance in Solids*, New York, Academic Press, 1960.
1.8. A. Abragam and M. H. L. Pryce, *Proc. R. Soc. London A* **63**, 409 (1950).
1.9. B. Bleaney and D. J. F. Ingram, *Proc. Phys. Soc. A* **63**, 408 (1950).
1.10. U. Öpik and M. H. L. Pryce, *Proc. R. Soc. London A* **238**, 425 (1957).
1.11. H. C. Longuet-Higgins, U. Öpik, M. H. L. Pryce, and R. A. Sack, *Proc. R. Soc. London A* **244**, 1 (1958).
1.12. W. Moffit and W. Thorson, *Phys. Rev.* **108**, 1251 (1957).
1.13. A. D. Liehr and C. J. Ballhausen, *Ann. Phys. (N.Y.)* **3**, 304 (1958).
1.14. *The Jahn–Teller Effect. A Bibliographic Review*, Ed. I. B. Bersuker, New York, IFI/Plenum, 1984.
1.15. I. B. Bersuker, *Opt. Spektrosk.* **11**, 319 (1961); *Zh. Eksp. Teor. Fiz.* **43**, 1315 (1962) (English transl.: *Sov. Phys. – JETP* **16**, 933 (1963)); **44**, 1238 (1963).
1.16. M. C. M. O'Brien, *Proc. R. Soc. London A* **281**, 323 (1964).
1.17. F. S. Ham, *Phys. Rev.* **138**, 1727 (1965).
1.18. J. Kanamori, *J. Appl. Phys.* **31**, 14 (1960).
1.19. R. J. Elliot, R. T. Harley, W. Hayes, and S. R. P. Smith, *Proc. R. Soc. London A* **328**, 217 (1972).
1.20. I. B. Bersuker, *Phys. Lett. A* **20**, 589 (1966).
1.21. R. Englman, *The Jahn–Teller Effect in Molecules and Crystals*, London, Wiley, 1972.
1.22. M. D. Sturge, *The Jahn–Teller Effect in Solids*, in *Solid State Physics*, Vol. 20, Eds. F. Seitz, D. Turnbull, and H. Ehrenreich, New York, Academic Press, 1967.
1.23. I. B. Bersuker, *Coord. Chem. Rev.* **14**, 357 (1975).
1.24. I. B. Bersuker, B. G. Vekhter, and I. Ya. Ogurtsov, *Uspekhi Fiz. Nauk (Sov. Phys. – Uspekhi)* **116**, 605 (1975).
1.25. J. Gazo, I. B. Bersuker, J. Garaj, M. Kabesova, J. Kohout, M. Langfelderova, M. Melnik, M. Serator, and F. Valach, *Coord. Chem. Rev.* **19**, 253 (1976).
1.26. F. S. Ham, in *Electron Paramagnetic Resonance*, Ed. S. Geschwind, New York, Plenum, 1972.
1.27. D. Reinen and C. Friebel, *Struct. Bonding* **37**, 1 (1979).
1.28. L. K. Burdett, *Molecular Shapes. Theoretical Models of Inorganic Stereochemistry*, New York, Wiley, 1980.
1.29. I. B. Bersuker and V. Z. Polinger, *Adv. Quant. Chem.* **15**, 85 (1982).
1.30. *Dynamical Jahn–Teller Effect in Localized Systems*, Eds. Yu. E. Perlin and M. Wagner, Amsterdam, Elsevier, 1984.

1.31. I. B. Bersuker, *The Jahn–Teller Effect and Vibronic Interactions in Modern Chemistry*, New York, Plenum, 1984.
1.32. G. Fischer, *Vibronic Coupling: The Interaction between the Electronic and Nuclear Motions*, London, Academic Press, 1984.
1.33. H. Köppel, W. Domcke, and L. S. Cederbaum, *Adv. Chem. Phys.* **57**, 59 (1984).
1.34. R. L. Whetten, G. S. Ezra, and E. R. Grant, *Annu. Rev. Phys. Chem.* **36**, 277 (1985).
1.35. I. B. Bersuker and I. Ya. Ogurtsov, *Adv. Quant. Chem.* **18**, 1 (1986).
1.36. G. D. Watkins, in *Deep Centers in Semiconductors*, Ed. S. T. Pantelides, New York, Gordon and Breach, 1986, p. 147.
1.37. I. B. Bersuker and S. S. Stavrov, *Coord. Chem. Rev.* **8**, 1 (1988).
1.38. A. Ceulemans and L. G. Vanquickenbourne, *Struct. Bonding* **71**, 125 (1989).
1.39. *Vibronic Processes in Inorganic Chemistry*, Ed. C. D. Flint, Dordrecht, Kluwer, 1989.
1.40. I. B. Bersuker and V. Z. Polinger, *Vibronic Interactions in Molecules and Crystals*, New York, Springer, 1989.
1.41. D. Reinen and M. Atanasov, *Magn. Reson. Rev.* **15**, 167 (1991).
1.42. I. B. Bersuker and S. A. Borshch, *Adv. Chem. Phys.* **81**, 703 (1992).
1.43. A. A. Levin, in *Soviet Science Reviews B, Chemistry Reviews*, Vol. 9, Ed. M. E. Vol'pin, New York, Harwood, 1987, p. 2791; *New J. Chem.* **17**, 31 (1993).
1.44. A. Ceulemans, *Topics Current Chem.* **171**, 27 (1994).
1.45. M. D. Kaplan and B. G. Vekhter, *Cooperative Phenomena in Jahn–Teller Crystals*, New York, Plenum Press, 1995.
1.46. I. B. Bersuker, *J. Coord. Chem.* **34**, 289 (1995).
1.47. P. V. Schastnev and L. N. Schegoleva, *Molecular Distortions in Ionic and Excited States*, New York, CRC Press, 1995.
1.48. I. B. Bersuker, *Ferroelectrics* **164**, 75 (1995).
1.49. I. B. Bersuker, *Electronic Structure and Properties of Transition Metal Compounds. Introduction to the Theory*, New York, Wiley, 1996.
1.50. C. C. Chancey and M. C. M. O'Brien, *The Jahn–Teller Effect in C_{60} and other Icosahedral Complexes*, Princeton, New Jersey, Princeton University Press, 1997.
1.51. T. A. Barckholtz and T. A. Miller, *Internat. Rev. Phys. Chem.* **17**, 435 (1998).
1.52. *Electron–Phonon Dynamics and Jahn–Teller Effects*, Eds. G. Bevilacqua, L. Martinelli, and N. Terzi, Singapore, World Scientific, 1999.
1.53. I. B. Bersuker, *Chem. Rev.* **101**, 1067 (2001).
1.54. R. Englman and A. Yahalom, in *Vibronic Interactions: Jahn–Teller Effect in Crystals and Molecules*, NATO Science Series, Vol. 39, Eds. M. D. Kaplan and G. O. Zimmerman, Dordrecht, Kluwer, 2001, p. 5.
1.55. *The Role of Degenerate States in Chemistry*; a special volume of *Adv. Chem. Phys.* **124**, Eds. M. Baer and G. D. Billing, New York, Wiley, 2002.
1.56. I. B. Bersuker, *Adv. Quant. Chem.* **44**, 1 (2003).
1.57. *Conical Intersections: Electronic Structure, Dynamics, and Spectroscopy*, Eds. W. Domcke, D. R. Yarkony, and H. Köppel, Singapore, World Scientific, 2003.

2

Vibronic interactions

In this chapter we present the basic expressions for the changes in electron–nuclear interactions due to nuclear motions (*vibronic interactions*) in degenerate and nondegenerate electronic states, which lie in the background of the JT vibronic coupling theory.

2.1 The adiabatic approximation

In molecular and solid-state theory the electron–nuclear interaction is treated quantum-mechanically, e.g., based on the Schrödinger equation:

$$(H - E)\Psi(r, Q) = 0 \tag{2.1}$$

where $\Psi(r, Q)$ is the full wavefunction, r and Q denote the whole set of coordinates of the electrons r_i, $i = 1, 2, \ldots, n$, and nuclei Q_α, $\alpha = 1, 2, \ldots, N$, respectively, H is the energy operator (Hamiltonian) of the system, and E is the total energy. The exact solution of Eq. (2.1) is extremely difficult except for very simple systems of two or three atoms. Fortunately there is a very good and widely acceptable approximation that makes the problem soluble for the majority of all small to moderate and some large to very large molecular systems and crystals, the *adiabatic approximation* (AA). Notice that the very notion of *nuclear configuration* (geometry of the nuclear framework) of polyatomic systems employs essentially the AA.

The AA is based on the fundamental inequality of the masses and velocities of electrons and nuclei. Since the nuclear mass is about 2000 times that of the electron, the velocity of the latter is much larger than that of the former. Therefore we can assume that for each instantaneous position Q of the nuclei, a stationary (relaxed) distribution of the electronic cloud $\Psi(r, Q)$ is attained, while the nuclei move in the averaged field of the electrons, which is thus a function of the nuclear coordinates Q. This assumption enables us to solve the

problem in two steps: first we solve the electronic part of the Schrödinger equation (2.1) for each of the fixed nuclear coordinates Q and then we use the obtained mean electronic energy as the potential energy for the nuclear motions.

Divide the total Hamiltonian H in Eq. (2.1) into three parts:

$$H = H_r + H_Q + V(r, Q) \tag{2.2}$$

where H_r is the electronic component which includes the kinetic energy of the electrons and the interelectronic electrostatic interaction, H_Q is the kinetic energy of the nuclei, and $V(r, Q)$ is the energy of the interaction of the electrons with the nuclei and internuclear repulsion.

In Cartesian coordinates

$$V(r, R) = \sum_{i,\alpha} h_{i,\alpha} + \sum_{\alpha,\beta} G_{\alpha,\beta} \tag{2.2a}$$

where

$$h_{i,\alpha} = -e^2 Z_\alpha / \left|\vec{r}_i - \vec{R}_\alpha\right| \tag{2.2b}$$

and

$$G_{\alpha,\beta} = e^2 Z_\alpha Z_\beta / \left|\vec{R}_\alpha - \vec{R}_\beta\right| \tag{2.2c}$$

The operator $V(r, Q)$ can be expanded as a series of small displacements of the nuclei about the point $Q_\alpha = Q_{\alpha 0} = 0$, chosen as the origin (hereafter we use symmetrized coordinates Q_α, for nuclear displacements, defined below, instead of $\vec{R}_\alpha$):

$$V(r, Q) = V(r, 0) + \sum_\alpha (\partial V / \partial Q_\alpha)_0 Q_\alpha + \frac{1}{2} \sum_{\alpha,\beta} (\partial^2 V / \partial Q_\alpha \, \partial Q_\beta)_0 Q_\alpha Q_\beta + \cdots \tag{2.3}$$

Taking only the first term of this expansion as the potential energy of the electrons in the field of nuclei fixed at $Q_\alpha = 0$, one can solve the electronic part of the Schrödinger equation

$$[H_r + V(r, 0) - \varepsilon'_k]\varphi_k(r) = 0 \tag{2.4}$$

and obtain a set of energies ε'_k and wavefunctions $\varphi_k(r)$ for the given nuclear configuration corresponding to the point $Q_{\alpha 0} = 0$.

In order to see how these solutions vary under nuclear displacements, the full Schrödinger equation (2.1) must be solved. Let us expand the total wavefunction $\Psi(r, Q)$ in terms of electronic functions $\varphi_k(r)$,

$$\Psi(r, Q) = \sum_k \chi_k(Q)\varphi_k(r) \tag{2.5}$$

where the expansion coefficients $\chi_k(Q)$ are functions of the nuclear coordinates. On substituting Eq. (2.5) into Eq. (2.4) one obtains, after some simple transformations, the following system of coupled equations for the energies and the functions $\chi_k(Q)$:

$$[H_Q + \varepsilon_k(Q) - E]\chi_k(Q) + \sum_{m \neq k} W_{km}(Q)\chi_m(Q) = 0 \tag{2.6}$$

where $W_{km}(Q)$ denotes the electronic matrix element of *vibronic interactions*, i.e., that part of the electron–nuclear interaction $V(r, Q)$ which depends on Q:

$$\begin{aligned} W(r, Q) &= V(r, Q) - V(r, 0) \\ &= \sum_\alpha (\partial V/\partial Q_\alpha)_0 Q_\alpha + \frac{1}{2}\sum_{\alpha,\beta} (\partial^2 V/\partial Q_\alpha\, \partial Q_\beta)_0 Q_\alpha Q_\beta + \cdots \end{aligned} \tag{2.7}$$

and

$$\varepsilon_k(Q) = \varepsilon'_k + W_{kk}(Q) \tag{2.8}$$

is the potential energy of the nuclei in the mean field of the electrons in the state $\varphi_k(r)$. In the absence of electronic degeneracy or pseudodegeneracy $\varepsilon(Q)$ is the potential energy of the nuclei in the field of the electrons in this state, the *adiabatic potential energy surface* (APES).

It is seen from the system of coupled equations (2.6) that if vibronic mixing of different electronic states can be ignored ($W_{km}(Q) = 0$ for $k \neq m$), coupling between these states vanishes, and the system of equations decomposes into a set of simple equations:

$$[H_Q + \varepsilon_k(Q) - E]\chi_k(Q) = 0, \qquad k = 1, 2, 3, \ldots \tag{2.9}$$

Each of these equations for given k represents the Schrödinger equation for the nuclei moving in the mean field $\varepsilon_k(Q)$ of the electrons in the state $\varphi_k(r)$.

In other words, in the case under consideration the motions of the nuclei and electrons are separated and the problem as a whole can be solved in the two stages mentioned above. In the first stage the electronic states $\varphi_k(r)$ are determined as solutions of Eq. (2.4) and used to calculate the potential energy of the nuclei $\varepsilon_k(Q)$ by means of Eq. (2.8). In the second stage, the wavefunctions $\chi_k(Q)$ and energies E of the nuclei are determined by Eq. (2.9), the total wavefunction being $\Psi(r, Q) = \varphi_k(r)\chi_k(Q)$. This is the *crude adiabatic approximation*, or the *Born–Oppenheimer approximation* [2.1, 2.2].

Thus the simple (crude) AA is valid if and only if the terms of the vibronic mixing of different electronic states in Eq. (2.6) can be ignored. It can be shown [2.3] that the perturbation of the total wavefunction by vibronic interactions is sufficiently small if

$$\hbar\omega \ll \left|\varepsilon'_m - \varepsilon'_k\right| \tag{2.10}$$

where $\hbar\omega$ is the energy quantum of vibrations in the electronic state under consideration (k or m), and ε'_m and ε'_k are the energy levels of Eq. (2.4). Equation (2.10) may be considered as the criterion of validity of the adiabatic approximation. Its deduction implies that the electronic state is stable and generates localized vibrational states. Obviously, criterion (2.10) does not hold when the two electronic states are degenerate or close in energy (pseudodegenerate).

In the *full adiabatic approximation* the electronic part of the Schrödinger equation includes the electron–nuclear interaction $V(r, Q)$ in the whole range of nuclear coordinates, making the electronic wavefunction $\varphi(r, Q)$ and energies $\varepsilon(Q)$ dependent on Q as on a parameter (cf. Eq. (2.4)):

$$[H_r + V(r, Q) - \varepsilon'_k(Q)]\varphi_k(r, Q) = 0 \tag{2.11}$$

Accordingly, the full wavefunction is taken as $\Psi(r, Q) = \varphi_k(r, Q)\chi_k(Q)$, and Eqs. (2.6) are significantly modified, mainly because of the Q derivatives (in H_Q) applied to $\varphi(r, Q)$: instead of $W_{km}(Q)$ in Eqs. (2.6) we get the *operator of nonadiabacity* $\Lambda_{km}(Q)$ [2.1–2.3] (M_α is the nuclear mass),

$$\Lambda_{km}(Q) = -\hbar^2 \sum_\alpha (1/M_\alpha)\left[A^{(\alpha)}_{km}(Q)\,\partial/\partial Q_\alpha + \frac{1}{2}B^{(\alpha)}_{km}(Q)\right] \tag{2.12}$$

with

$$A^{(\alpha)}_{km}(Q) = \int \partial\tau\, \varphi^*_k\, \partial\varphi_m/\partial Q_\alpha, \qquad B^{(\alpha)}_{km}(Q) = \int \partial\tau\, \varphi^*_k\, \partial^2\varphi_m/\partial Q^2_\alpha$$

If the electronic state is nondegenerate and the criterion (2.10) holds, the full AA is more accurate than the simple one. General estimates by orders of magnitude show (see, e.g., in [2.3]) that in the simple AA the error in energy is of the order $(m/M)^{\frac{1}{2}} \approx 2.3 \times 10^{-2}$ (m and M are the electron and proton masses, respectively), while in the full AA the error is $(m/M)^{\frac{3}{4}} \approx 3 \times 10^{-3}$. However, if the criterion (2.10) is not satisfied, as in the case of electronic degeneracy or pseudodegeneracy, none of these estimates is valid, and the problem should be solved in another way. In these cases Eqs. (2.6) (rather than the full AA with Λ_{km} instead of W_{km}) are more suitable as a starting point of the JT vibronic coupling theory.

The nonadiabatic corrections (2.12) have *diagonal* ($k = m$) and *off-diagonal* ($k \neq m$) *terms*. Both types of corrections depend on the rate of wavefunction changes with nuclear displacements, which is the strongest in the regions of the Q_α coordinates where the energies of the states under consideration are close. Therefore, in the same approximation as the AA, the vibronic coupling of the degenerate term to other terms may be neglected, provided the energy gaps between them are sufficiently large (however, see Section 4.1). Then for an f-fold degenerate term only f coupled equations remain in the system of Eqs. (2.6).

The nonadiabatic coupling between different electronic states at APES intersections described by the terms (2.12) is presently a topic of intensive study, especially as related to corresponding chemical reactions and collision scattering [2.4–2.23]. This trend was developed significantly during the last decade. It emerged in connection with special properties of systems with *conical intersections* on their APES (Section 3.2) where the nonadiabatic corrections in Eq. (2.6) produce essential singularities. A related subject, the topological (geometric) phase problem is one of the most studied too in this field (Section 5.7).

For strong vibronic coupling the electronic wavefunctions in the adiabatic approximation change rapidly with the nuclear coordinates Q and have singularities at conical intersections (similar to that of the APES). This means that the nonadiabatic corrections (2.12), as off-diagonal coupling elements, may also have singularities, which complicate the solution of Eqs. (2.6). To avoid these difficulties, it is sometimes useful to pass to *diabatic wavefunctions*, obtained approximately as an *adiabatic-to-diabatic matrix transformation*. The latter is chosen to produce wavefunctions that are smooth functions of Q with the kinetic energy as a diagonal matrix (in case of strong vibronic coupling) and the potential energy acquiring off-diagonal elements, which are also functions of Q with no singularities. In a recent application to JT systems [2.10, 2.11] the authors [2.11] extended their diabatic approach to be able to treat seams of symmetry-allowed conical intersections by means of constructing "regularized" diabatic states, in which only the singular parts of the nonadiabatic coupling elements are removed. Diabatic bases in simpler systems are discussed, e.g., in [2.8].

The treatment of nonadiabacity in the diabatic approximation led to some interesting consequences, one of which is the demonstration of the full analogy between the equations obtained in this scheme for molecular systems with vibronic coupling and the Yang–Mills equations of field theory derived to describe interactions between elementary particles (see [2.20] and references therein). For reviews and further achievements in the solution of nonadiabacity problems see [2.12–2.23].

2.2 Vibronic interactions. Vibronic coupling constants

If by solving the electronic Schrödinger equation (2.4) with nuclei fixed at the point of *reference configuration* $Q_\alpha = 0$ (see below) we get states that are degenerate or relatively close in energy, then the criterion (2.10) does not hold and the AA is invalid. To solve the problem in these cases, the system of Eqs. (2.6), which couple the several degenerate or pseudodegenerate states, should be solved.

As can be seen from Eqs. (2.6), the mixing of the states is put into effect by the matrix elements $W_{km}(Q)$ of the vibronic interaction operator (2.7) that contains linear, quadratic, cubic, etc., terms. For most cases it is enough to take into account the linear and quadratic terms in order to reveal the vibronic effects, provided the initial configuration has been chosen correctly (cubic terms may also be important, Section 3.2). In the quadratic approximation the use of *normal coordinates* essentially simplifies the investigation due to symmetry considerations and application of group theory.

Let us define the *reference configuration* which is the starting nuclear arrangement in space at $Q_\alpha = 0$. First, the reference configuration is that of high symmetry for which the electronic term is degenerate or pseudodegenerate. This definition gives no unique indication of the real geometric arrangement of the atoms because there may be different configurations that produce degenerate or pseudodegenerate states. For instance, an AX_4 system may have degenerate states in its tetrahedral, planar-quadratic, pyramidal-quadratic, and bipyramidal-triangular configurations. The JTE in these cases is significantly different, resulting in a variety of different observable properties. Therefore, in the absence of other information all these possibilities should be tried. But there is no degeneracy in any configuration intermediate to these four. The symmetries of configurations that produce degenerate terms are known from group theory (Section 2.5 and Appendix).

For pseudodegeneracy the choice of the reference configuration is more complicated since electronic states that are close in energy may be present in any nuclear configuration. However, in this case the notion of high symmetry has a very good criterion: the first derivative of the APES with respect to the distortions under consideration at the high-symmetry point should be zero. As shown below (Section 2.5), at the point of electronic degeneracy this first derivative of the APES in nonlinear systems is nonzero, but it is such because of the vibronic interactions. Without the vibronic coupling this derivative is zero too.

In other words, the reference configuration in JT vibronic coupling problems should have sufficiently high symmetry to produce either a degenerate

Table 2.1. *Classification of symmetrized displacements* Γ *for several types of molecules with N atoms (the number of normal vibrations* $3N-6$ *is indicated in parentheses)*

N	Symmetry	Example, shape	Γ
4 (6)	C_{3v}	NH_3, pyramid	A_1', A_1'', E', E''
5 (9)	T_d	MnO_4^-, tetrahedron	A_1, E, T_2', T_2''
7 (15)	O_h	CrF_6^{3-}, octahedron	$A_{1g}, E_g, T_{2g}, T_{2u}, T_{1u}', T_{1u}''$

term (in proper JT and RT systems), or states that are close in energy (pseudo-degenerate) with zero first-order derivatives of the lower branch of the APES with respect to the expected distortions.

For the high-symmetry reference configuration the normal coordinates can be related to *normal vibrations*. The latter have a real meaning only for stable configurations. In the adiabatic approximation for nondegenerate electronic states normal vibrations can be determined by Eq. (2.9) in which the APES $\varepsilon = \varepsilon_k' + W_{kk}(Q)$ is taken in the aforementioned quadratic (harmonic) approximation. With quadratic terms included $W_{kk}(Q)$ (the diagonal matrix element of a part of Eq. (2.7)),

$$W_{kk}(Q) = \sum_{\alpha} (\partial V_{kk}/\partial Q_\alpha)_0 Q_\alpha + \frac{1}{2}\sum_{\alpha\beta} (\partial^2 V_{kk}/\partial Q_\alpha\, \partial Q_\beta)_0 Q_\alpha Q_\beta \qquad (2.13)$$

can be reduced by means of normal coordinates to the canonical (diagonal) shape, in which the linear and cross-terms containing $Q_\alpha Q_\beta$ vanish (and only terms of type $\Sigma_\alpha c_\alpha Q_\alpha^2$ remain), while the kinetic energy operator maintains its additive form: $-(\hbar^2/2)\Sigma_\alpha M_\alpha^{-1}(\partial/\partial Q_\alpha)^2$.

The normal coordinates can be determined by means of *symmetrized displacements*, meaning collective (concerted) nuclear displacements which, under the symmetry operation of the molecular point group, transform according to one of its irreducible representations; they can be found by methods of group theory [2.24–2.26] and are available in tabular form. If a molecule has N atoms, then the number of vibrational degrees of freedom and hence the number of symmetrized displacements is $3N-6$ (or $3N-5$ for linear molecules). Examples of their classification by irreducible representations are shown in Table 2.1. Tables of irreducible representations of the most usable point groups are given in the appendix. The corresponding atomic displacements are illustrated in Figs. 2.1–2.4. Expressions for symmetrized displacements in terms of Cartesian coordinates (shown in Fig. 2.3(a) and 2.4(a)) are given in Table 2.2.

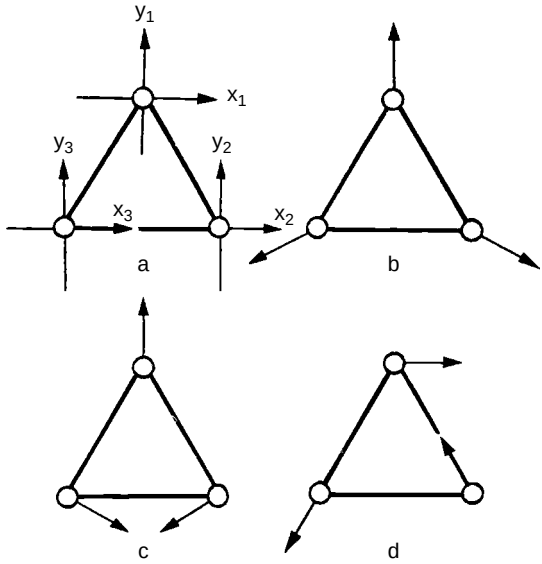

Fig. 2.1. Symmetrized displacements of atoms in a triangular molecular system: (a) labeling of Cartesian displacements; (b) totally symmetric displacements of the type A_1; (c) E'-type Q_y displacements; and (d) E'-type Q_x displacements.

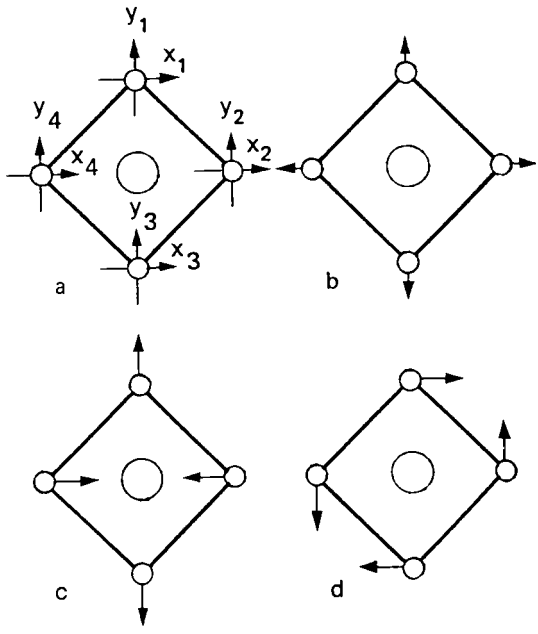

Fig. 2.2. Symmetrized displacements of atoms in a square-planar molecular system: (a) labeling of Cartesian displacements; (b) totally symmetric displacements of the type A_1; (c) B_{1g}-type Q_y displacements; and (d) B_{2g}-type displacements.

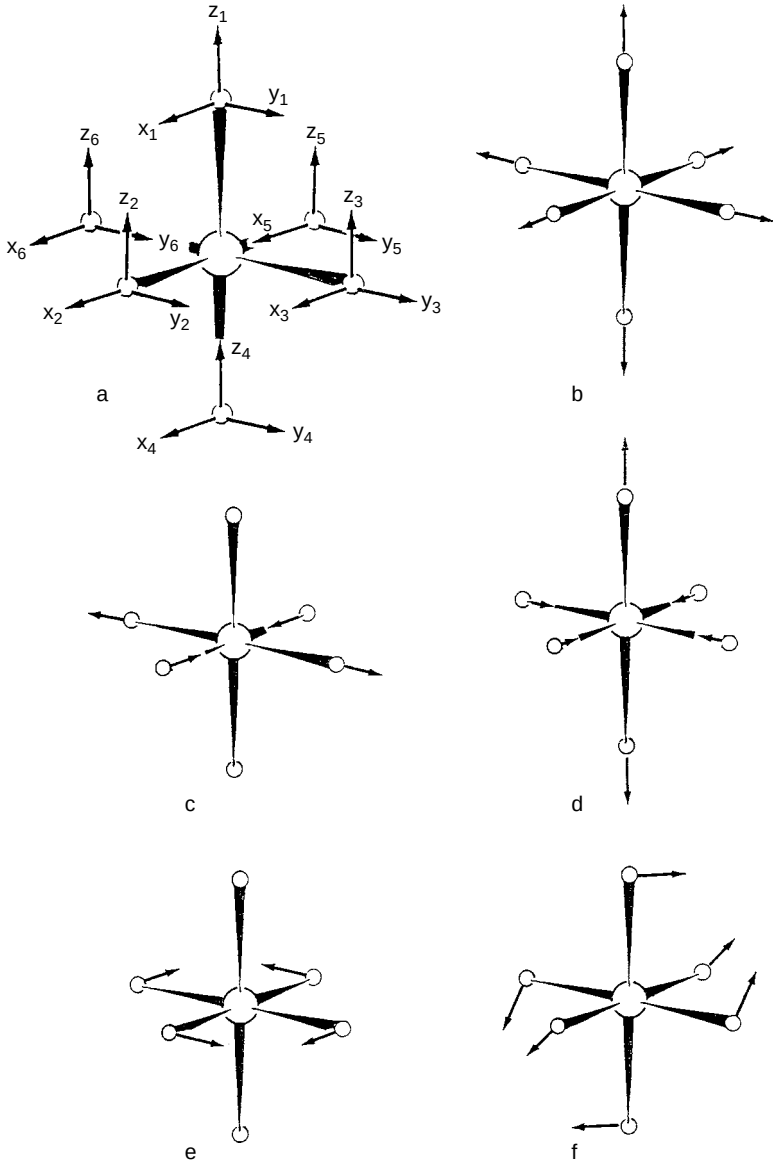

Fig. 2.3. The shapes of symmetrized displacements of atoms in an octahedral complex ML_6: numbering and orientation of Cartesian displacements (a), totally symmetric A_{1g} (b), E_g-type Q_ε (c), E_g-type Q_ϑ (d), and T_{2g}-type Q_ξ (e) displacements. For degenerate displacements, any linear combination of them can be realized, e.g., $(Q_\zeta + Q_\eta + Q_\xi)/\sqrt{3}$ for T_{2g} (f).

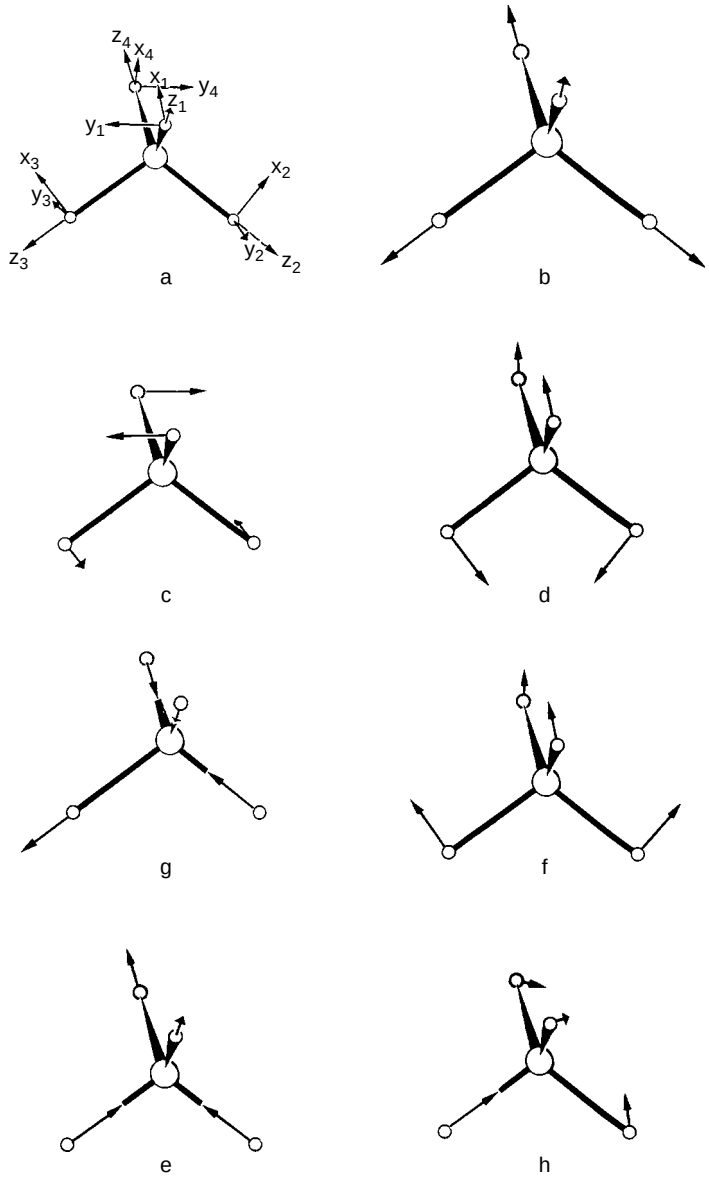

Fig. 2.4. The shapes of symmetrized displacements of atoms in a tetrahedral complex: numbering and orientation of Cartesian coordinates (a), totally symmetric A_1 (b), E-type Q_ε (c), E-type Q_ϑ (d), T_2-type Q_ξ (e), T'_2-type Q'_ξ (f) displacements. In the case of degeneracy any combination of component displacements can be realized, e.g., $(Q_\zeta + Q_\eta + Q_\xi)/\sqrt{3}$ (g) and $(Q'_\zeta + Q'_\eta + Q'_\xi)/\sqrt{3}$ (h).

Table 2.2. *Symmetrized displacements Q (normal coordinates) expressed by Cartesian coordinates for some trigonal, tetragonal, tetrahedral, and octahedral systems (Figs. 2.1–2.4) (X_0, Y_0, Z_0 are the Cartesian displacements of the central atom, S_z is an axial vector)*

Q	Symmetry type	Transformation properties	Expressions by Cartesian coordinates
Trigonal systems X_3. Symmetry D_{3h}			
$Q_x^{(t)}$	E'	x	$(X_1+X_2+X_3)/\sqrt{3}$
$Q_y^{(t)}$		y	$(Y_1+Y_2+Y_3)/\sqrt{3}$
$Q_{a_2}^{(r)}$	A_2'	S_z	$(2X_1-X_2-\sqrt{3}Y_2-X_3+\sqrt{3}Y_3)/\sqrt{12}$
Q_a	A_1'	x^2+y^2	$(2Y_1+\sqrt{3}X_2-Y_2-\sqrt{3}X_3-Y_3)/\sqrt{12}$
Q_x	E'	$2xy$	$(2X_1-X_2+\sqrt{3}Y_2-X_3-\sqrt{3}Y_3)/\sqrt{12}$
Q_y		x^2-y^2	$(2Y_1-\sqrt{3}X_2-Y_2-\sqrt{3}X_3-Y_3)/\sqrt{12}$
Square-planar systems ML_4. Symmetry D_{4h}			
Q_a	A_{1g}	x^2+y^2	$(1/2)(Y_1+X_2-Y_3-X_4)$
Q_1	B_{1g}	x^2-y^2	$(1/2)(Y_1-X_2-Y_3+X_4)$
Q_2	B_{2g}	xy	$(1/2)(X_1+Y_2-X_3-Y_4)$
Q_a'	A_{2g}	S_z	$(1/2)(X_1-Y_2-X_3+Y_4)$
Q_x	E_{1u}	x	$(1/2)(X_1+X_2+X_3+X_4)$
Q_y		y	$(1/2)(Y_1+Y_2+Y_3+Y_4)$
Q_x'	E_{1u}'	x	X_0
Q_y'		y	Y_0
Tetrahedral systems ML_4. Symmetry T_d			
Q_a	A_1	$x^2+y^2+z^2$	$(1/2)(Z_1+Z_2+Z_3+Z_4)$
Q_ϑ	E	$2z^2-x^2-y^2$	$(1/2)(X_1-X_2-X_3+X_4)$
Q_ε		$\sqrt{3}(x^2-y^2)$	$(1/2)(Y_1-Y_2-Y_3+Y_4)$
Q_ξ'	T_2'	x, yz	$(1/2)(Z_1-Z_2+Z_3-Z_4)$
Q_η'		y, xz	$(1/2)(Z_1+Z_2-Z_3-Z_4)$
Q_ζ'		z, xy	$(1/2)(Z_1-Z_2-Z_3+Z_4)$
Q_ξ''		x, yz	$(1/4)(-X_1+X_2-X_3+X_4)$ $+(\sqrt{3}/4)(-Y_1+Y_2-Y_3+Y_4)$

Table 2.2. (*cont.*)

Q	Symmetry type	Transformation properties	Expressions by Cartesian coordinates
Q''_η	T''_2	y, xz	$(1/4)(-X_1 - X_2 + X_3 + X_4)$ $+ (\sqrt{3}/4)(Y_1 + Y_2 - Y_3 - Y_4)$
Q''_ζ		z, xy	$(1/2)(X_1 + X_2 + X_3 + X_4)$
Q_x		x	X_0
Q_y	T_2	y	Y_0
Q_z		z	Z_0
Octahedral systems ML_6. Symmetry O_h			
Q_a	A_{1g}	$x^2 + y^2 + z^2$	$(X_2 - X_5 + Y_3 - Y_6 + Z_1 - Z_4)/\sqrt{6}$
Q_ϑ		$2z^2 - x^2 - y^2$	$(2Z_1 - 2Z_4 - X_2 + X_5 - Y_3 + Y_6)/2\sqrt{3}$
Q_ε	E_g	$\sqrt{3}(x^2 - Y^2)$	$(1/2)(X_2 - X_5 - Y_3 + Y_6)$
Q_ξ		yz	$(1/2)(Z_3 - Z_6 + Y_1 - Y_4)$
$Q_{\tilde{\eta}}$	T_{2g}	xz	$(1/2)(X_1 - X_4 + Z_2 - Z_5)$
$Q_{\tilde{\zeta}}$		xy	$(1/2)(Y_2 - Y_5 + X_3 - X_6)$
Q'_x		x	$(1/2)(X_1 + X_3 + X_4 + X_6)$
Q'_y	T'_{1u}	y	$(1/2)(Y_1 + Y_2 + Y_4 + Y_5)$
Q'_z		z	$(1/2)(Z_1 + Z_3 - Z_5 + X_6)$
Q''_x		x	$(X_2 + X_5)/\sqrt{2}$
Q''_y	T''_{1u}	y	$(Y_3 + Y_6)/\sqrt{2}$
Q''_z		z	$(Z_1 + Z_4)/\sqrt{2}$
Q_x		x	X_0
Q_y	T_{1u}	y	Y_0
Q_z		z	Z_0
Q'_ξ		$x(y^2 - z^2)$	$(1/2)(X_3 + X_6 - X_1 - X_4)$
Q'_η	T_{2u}	$y(z^2 - x^2)$	$(1/2)(Y_1 + Y_4 - Y_2 - Y_5)$
Q'_ζ		$z(x^2 - y^2)$	$(1/2)(Z_2 + Z_5 - Z_3 - Z_6)$

The f-fold degenerate representations (symmetry types) Γ have f lines γ (see Appendix). For instance, the twofold degenerate representation $\Gamma = E$ has two lines, $\gamma = \vartheta, \varepsilon$, while $\gamma = \xi, \eta, \zeta$ for the threefold representation $\Gamma = T$. As usual, for degenerate representations the division into components corresponding to the γ lines is rather conventional. The displacement types shown in Figs. 2.1–2.4 are commonly used. Below, the notation introduced by Mulliken will be used wherever possible: A, B for nondegenerate terms, E for twofold, T for threefold, G for fourfold, and H for fivefold degenerate representations.

The symmetrized displacements that belong to the irreducible representations, which occurs only once in the group-theoretical classification for the system under consideration (Table 2.1) are automatically normal coordinates. For repeated types of symmetrized displacements (e.g., T_2' and T_2'' in tetrahedral systems, E' and E'' in C_{3v} symmetry, etc.) the normal coordinates are linear combinations of the symmetrized ones and can be obtained by means of an additional (sometimes involved) procedure.

The operator of vibronic interactions (2.7) can be written in normal coordinates:

$$W(r,\ Q) = \sum_{\Gamma\gamma} (\partial V/\partial Q_{\Gamma\gamma})_0 Q_{\Gamma\gamma} + \frac{1}{2} \sum_{\Gamma'\gamma'\Gamma''\gamma''} (\partial^2 V/\partial Q_{\Gamma'\gamma'}\, \partial Q_{\Gamma''\gamma''})_0 Q_{\Gamma'\gamma'} Q_{\Gamma''\gamma''} + \cdots \quad (2.14)$$

Consider the coefficients of this expansion, which are derivatives of the operator of electron–nuclear interaction $V(r, Q)$. The matrix elements of these derivatives calculated with the electronic function of the degenerate term are the *constants of vibronic coupling* or *vibronic constants*. They are very important in the analysis of vibronic interaction effects: *vibronic constants characterize the measure of coupling between the electronic structure and nuclear displacements, i.e., the measure of influence of the nuclear displacements on the electron distribution and, conversely, the effect of the changes in the electron structure upon nuclear dynamics.*

Denote the electronic states by the corresponding irreducible representations Γ, Γ' of the symmetry group of the molecular system, and assume first that the states Γ and Γ' are not degenerate. The matrix element

$$F_{\overline{\Gamma}}^{(\Gamma\Gamma')} = \langle \Gamma | \left(\frac{\partial V}{\partial Q_{\overline{\Gamma}}} \right)_0 | \Gamma' \rangle \quad (2.15)$$

is called the *linear vibronic constant*. Following the rules of group theory, $F_{\overline{\Gamma}}^{(\Gamma\Gamma')}$ is nonzero if and only if $\Gamma \times \Gamma' = \overline{\Gamma}$. If Γ or Γ' or both are degenerate (in this case $\overline{\Gamma}$ may also be degenerate), a set of linear vibronic constants corresponding to all the lines γ and γ' of the two representations Γ and Γ' and their combinations $F_{\overline{\Gamma}\overline{\gamma}}^{(\Gamma\gamma\Gamma'\gamma')}$must be introduced instead of one vibronic constant (2.15). This can be easily done if one takes into account that the matrix elements within a degenerate term differ solely in numerical coefficients, their values being known. Indeed, according to the group-theory *Wigner–Eckart theorem* [2.27], for any physical operator $X_{\overline{\Gamma}\overline{\gamma}}$ which transforms according to line $\overline{\gamma}$ of representation $\overline{\Gamma}$ we have

$$\langle \Gamma\gamma | X_{\overline{\Gamma}\overline{\gamma}} | \Gamma'\gamma' \rangle = \langle \Gamma \| X_{\overline{\Gamma}} \| \Gamma' \rangle \langle \overline{\Gamma}\overline{\gamma} \Gamma'\gamma' | \Gamma\gamma \rangle \quad (2.16)$$

where $\langle \Gamma \| X_{\overline{\Gamma}} \| \Gamma' \rangle$ is the reduced matrix element (which does not depend on $\overline{\gamma}$, γ and γ') and $\langle \overline{\Gamma}\overline{\gamma}\Gamma'\gamma'|\Gamma\gamma \rangle$ are the Clebsch–Gordan coefficients available from tabular data [2.27].

Using formula (2.16) for the operator $X_{\overline{\Gamma}\overline{\gamma}} = (\partial V/\partial Q_{\overline{\Gamma}\overline{\gamma}})$ we obtain the following relation between different components of the linear vibronic constants:

$$F_{\overline{\Gamma}\overline{\gamma}}^{(\Gamma\gamma\Gamma'\gamma')} = F_{\overline{\Gamma}}^{(\Gamma\Gamma')} \langle \overline{\Gamma}\overline{\gamma}\Gamma'\gamma'|\Gamma\gamma \rangle \tag{2.17}$$

It follows that if one knows at least one vibronic constant $F_{\overline{\Gamma}\overline{\gamma}}^{(\Gamma\gamma\Gamma'\gamma')}$, all the others can be easily calculated by Eq. (2.17) using tabular data of the Clebsch–Gordan coefficients.

Some of the linear vibronic constants have a clear physical meaning. *The diagonal constant* of the linear coupling $F_{\overline{\Gamma}\overline{\gamma}}^{(\Gamma\gamma\Gamma\gamma)} \equiv F_{\overline{\Gamma}\overline{\gamma}}^{(\Gamma\gamma)}$ *has the meaning of the force with which the electrons in state* $\Gamma\gamma$ *affect the nuclei in the direction of symmetrized displacements* $Q_{\overline{\Gamma}\overline{\gamma}}$ (see also [2.28]). For instance, $E_{E\theta}^{E\varepsilon}$ denotes the force with which the electrons in the state $E\varepsilon$ distort the nuclear configuration in the direction of the Q_ϑ displacements, illustrated in Fig. 2.4.

For degenerate states Γ, according to the group-theoretical requirements, the diagonal matrix element $F_{\overline{\Gamma}}^{(\Gamma)}$ is nonzero if the symmetrical product $[\Gamma \times \Gamma]$ contains $\overline{\Gamma}$: $\overline{\Gamma} \in [\Gamma \times \Gamma]$ (compare this with the condition for off-diagonal elements: $\overline{\Gamma} \in \Gamma \times \Gamma'$). For nondegenerate states $[\Gamma \times \Gamma] = \Gamma \times \Gamma = A_1$, where A_1 is the totally symmetric representation. It follows that for nondegenerate states the symmetry of the vibronic perturbation should be $\overline{\Gamma} = A_1$, and the electrons can distort the nuclear configuration only in the direction of totally symmetric displacements, for which the symmetry of the system does not change. If the electronic state Γ is degenerate, the symmetric product $[\Gamma \times \Gamma]$ contains nontotally symmetric representations along with the symmetric one. Indeed, for cubic symmetry systems $[E \times E] \to A_1 + E$, $[T \times T] \to A_1 + E + T_1 + T_2$; for D_{4h} symmetry systems $[E \times E] \to A_1 + B_1 + B_2$, etc. In these cases $\overline{\Gamma}$ may be nontotally symmetric (degenerate E, T, or nondegenerate B_1, B_2, etc.). Hence under the influence of the electrons the nuclear configuration undergoes corresponding distortions, which are not totally symmetric. It is just these distortions that are predicted by the JT theorem (Section 2.5).

The *quadratic vibronic constants* can be introduced in principle in a fashion similar to the linear ones. However, complications arise because the diagonal matrix elements of some of the second derivative $(\partial^2 V/\partial Q_{\Gamma''\gamma'}\partial Q_{\Gamma''\gamma''})$ in Eq. (2.14) in appropriate combinations form the curvature of the APES, or the force constants (in the equilibrium position). The remaining terms and the off-diagonal matrix elements contain the quadratic vibronic constants, which should

be distinguished from the force constants. In order to investigate this question we subject the second (quadratic) term in Eq. (2.14) to further group-theoretical transformations. We introduce the tensor convolution (denoted in braces) $\{(\partial^2 V/\partial Q_{\Gamma'}\partial Q_{\Gamma''})_0\}_{\Gamma\gamma}$, which means the linear combination of second derivatives with respect to the $Q_{\Gamma'}$ and $Q_{\Gamma''}$ coordinates that transforms according to line γ of the representation $\Gamma \in \Gamma' \times \Gamma''$. This combination can be found by means of group theory and the Wigner–Eckart theorem (2.16). Similarly, the corresponding tensor convolution for the coordinates $\{Q_{\Gamma'} \times Q_{\Gamma''}\}_{\Gamma\gamma}$ may be introduced. It can be shown [2.3] that in this notation the vibronic interaction operator (2.14) takes the form

$$W(r,\ Q) = \sum_{\Gamma\gamma}\left(\frac{\partial V}{\partial Q_{\Gamma\gamma}}\right)_0 Q_{\Gamma\gamma} + \frac{1}{2}\sum_{\Gamma\gamma}\sum_{\Gamma_1\Gamma_2}\left\{\left(\frac{\partial^2 V}{\partial Q_{\Gamma_1}\partial Q_{\Gamma_2}}\right)\right\}_{\Gamma\gamma}\{Q_{\Gamma_1} \times Q_{\Gamma_2}\}_{\Gamma\gamma} + \cdots \tag{2.18}$$

In this expression all the terms are grouped such that the terms in each group transform according to a specific representation of the symmetry group of the system.

Now we introduce matrix elements of the quadratic term coefficients in Eq. (2.18):

$$G^{\Gamma\Gamma'}_{\overline{\Gamma}\overline{\gamma}}(\Gamma_1 \times \Gamma_2) = \frac{1}{2}\langle\Gamma|\left\{\left(\frac{\partial^2 V}{\partial Q_{\Gamma_1}\partial Q_{\Gamma_2}}\right)_0\right\}_{\overline{\Gamma}\overline{\gamma}}|\Gamma'\rangle \tag{2.19}$$

Similar to the linear case considered above, the representation $\overline{\Gamma} \in \Gamma_1 \times \Gamma_2$ for nondegenerate states in the diagonal matrix element $G^{\Gamma\Gamma}_{\overline{\Gamma}}$ can only be totally symmetric, $\overline{\Gamma} = A_1$, while for degenerate states it can be both totally symmetric and non-totally symmetric. It is clear that since $\overline{\Gamma} \in \Gamma_1 \times \Gamma_2$, for the totally symmetric part $\overline{\Gamma} = A_1$ we have $\Gamma_1 = \Gamma_2$ (the product of only equal irreducible representations contains A_1). In this case the totally symmetric combination of second derivatives in Eq. (2.19) is as follows:

$$\left\{\left(\frac{\partial^2 V}{\partial Q^2_\Gamma}\right)_0\right\}_{A_1} = \sum_{\bar{\gamma}}\left(\frac{\partial^2 V}{\partial Q^2_{\overline{\Gamma}\bar{\gamma}}}\right)_0 \tag{2.20}$$

For instance,

$$\left\{\left(\frac{\partial^2 V}{\partial Q^2_E}\right)_0\right\}_{A_1} = \left(\frac{\partial^2 V}{\partial Q^2_{E\theta}}\right)_0 + \left(\frac{\partial^2 V}{\partial Q^2_{E\varepsilon}}\right)_0 \tag{2.21}$$

Similarly, $\{Q^2_{\overline{\Gamma}}\}_{A_1} = \sum_{\bar{\gamma}} Q^2_{\overline{\Gamma}\bar{\gamma}}$; in particular, $\{Q^2_E\}_{A_1} = Q^2_{E\theta} + Q^2_{E\varepsilon}$.

The totally symmetric part of the diagonal matrix element in Eq. (2.19) $G^{\Gamma\Gamma}_{\overline{\Gamma}} \equiv K^{\Gamma}_{0\overline{\Gamma}}$ is an important component of the APES curvature, or *force constant* (at its minimum), discussed in Section 2.4, while the off-diagonal elements $G^{\Gamma\Gamma'}_{\overline{\Gamma}\overline{\gamma}}$ are *quadratic vibronic coupling constants*.

2.3 Orbital vibronic constants

One of the special features of the operator $V(r, Q)$ in Eq. (2.2), which includes the electron–nuclear and the nuclear–nuclear interactions (see Eqs. (2.2a)–(2.2c)) is its additive nature with respect to the electrons (the nuclear–nuclear interaction does not depend on electron coordinates). This allow us to present $V(r, Q)$ as follows:

$$\begin{aligned} V(r,\ Q) &= \sum_{i=1}^{n} V_i(r_i,\ Q) \\ V_i(r_i,\ Q) &= -\sum_{\alpha} \frac{e^2 Z_\alpha}{\left|\vec{r}_i - \vec{R}_\alpha\right|} + \frac{1}{n}\sum_{\alpha\neq\beta} \frac{e^2 Z_\alpha Z_\beta}{\left|\vec{R}_\alpha - \vec{R}_\beta\right|} \end{aligned} \tag{2.22}$$

where n is the number of electrons.

This additivity of the operator $V(r, Q)$ allows further simplification of the vibronic coupling constants (2.15) and (2.19). Indeed, assume that the wavefunction of the electronic state under consideration can be presented in a multiplicative one-determinant form:

$$|\Gamma\rangle = \det|\varphi_1(r_1)\varphi_2(r_2)\ldots\varphi_n(r_n)| \tag{2.23}$$

where $\varphi_i(r)$ are one-electron molecular orbitals (MOs) that describe the electronic state. On substituting Eqs. (2.22) and (2.23) into (2.15) and introducing *linear orbital vibronic constants* [2.29],

$$f^{(ij)}_{\overline{\Gamma}\overline{\gamma}} = \langle\varphi_i(r)|\left(\frac{\partial V_i(r,\ Q)}{\partial Q_{\overline{\Gamma}\overline{\gamma}}}\right)_0 |\varphi_j(r)\rangle \tag{2.24}$$

we find that the diagonal vibronic constant is a sum of orbital vibronic constants multiplied by the MO occupation numbers q^{Γ}_i,

$$F^{(\Gamma\Gamma)}_{\overline{\Gamma}} = \sum_i q^{\Gamma}_i f^{(ii)}_{\overline{\Gamma}} \tag{2.25}$$

For the off-diagonal vibronic constant, a simple formula can be obtained in the "frozen orbital" approximation, in which it is assumed that the one-electron excitation $\Gamma \rightarrow \Gamma'$ can be described by the change of MO occupations in the one-electron $i \rightarrow j$ transition, while the other MOs remain unchanged. In this approximation

$$F_{\overline{\Gamma}\overline{\gamma}}^{(\Gamma\Gamma')} = f_{\overline{\Gamma}\overline{\gamma}}^{(ij)} \tag{2.26}$$

or, more generally,

$$F_{\overline{\Gamma}\overline{\gamma}}^{(\Gamma\Gamma')} = (q_i - q_j) f_{\overline{\Gamma}\overline{\gamma}}^{(ij)} \tag{2.27}$$

where q_i and q_j are the occupation numbers of the ith and jth orbitals, respectively. Equation (2.27) is more useful in applications because it may be valid also for fractional q values.

In the same approximation a similar relation can be obtained for the diagonal quadratic vibronic constants:

$$G_{\overline{\Gamma}\overline{\gamma}}^{(\Gamma\Gamma)}(\Gamma_1 \times \Gamma_2) = \sum_i q_i^{\Gamma} g_{\overline{\Gamma}\overline{\gamma}}^{(ii)}(\Gamma_1 \times \Gamma_2) \tag{2.28}$$

where, similar to Eq. (2.19),

$$g_{\overline{\Gamma}\overline{\gamma}}^{(ii)}(\Gamma_1 \times \Gamma_2) = \frac{1}{2}\langle \varphi_i(r) | \left\{ \left(\frac{\partial^2 V}{\partial Q_{\Gamma_1} \partial Q_{\Gamma_2}} \right)_0 \right\}_{\overline{\Gamma}\overline{\gamma}} | \varphi_j(r) \rangle \tag{2.29}$$

is the definition of the *quadratic orbital vibronic constant* (as in (2.19), the braces mean tensor convolution that transforms as the $\overline{\gamma}$ line of the $\overline{\Gamma}$ representation).

A similar expression can be derived for the force constant $K_{0\overline{\Gamma}}^{\Gamma}$ presented as a sum of orbital contributions $k_{\overline{\Gamma}}^{i}$,

$$K_{0\overline{\Gamma}}^{\Gamma} = \sum_i q_i^{\Gamma} k_{\overline{\Gamma}}^{i} \tag{2.30}$$

but the dependence of $k_{\overline{\Gamma}}^{i}$ on the orbital vibronic constant is more complicated (Section 2.4, Eq. (2.38)).

It follows from Eq. (2.25) that the distorting influence of the electrons on the nuclear framework with a force $F_{\overline{\Gamma}}^{(\Gamma\Gamma)}$ is produced additively by all the corresponding MO single-electron contributions $f_{\overline{\Gamma}}^{(ii)}$. A clear physical meaning for the linear diagonal orbital vibronic constant follows immediately: $f_{\overline{\Gamma}\overline{\gamma}}^{(ii)}$ *equals the force with which the electron of the* ith *MO distorts the nuclear configuration in the direction of the symmetrized displacement* $Q_{\overline{\Gamma}\overline{\gamma}}$ minus the corresponding part of the internuclear repulsion in this direction (see Eq. (2.22)).

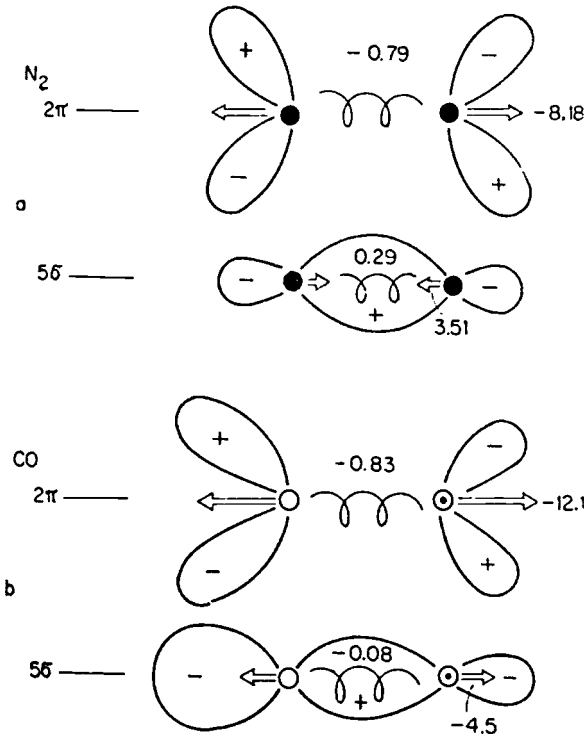

Fig. 2.5. Illustrations to the vibronic molecular-orbital description of electronic structure. In addition to the MO energies and wavefunctions the orbital vibronic constants characterize the contribution of the orbital electron to the distorting force f (shown by arrows; values are given in 10^{-4} dyn) and force-constant coefficient k (shown by springs; values are given in 10^6 dyn/cm): (a) HOMO and LUMO of the nitrogen molecule – the HOMO 5σ is bonding ($f>0$), whereas the LUMO 2π is antibonding ($f<0$); and (b) HOMO and LUMO of carbon monoxide – the HOMO is weakly antibonding, whereas the LUMO is strongly antibonding.

The orbital vibronic constants thus complement the MO description of polyatomic systems with fixed nuclei by additional parameters of back influence of the MO electrons on the nuclear configuration and dynamics. It is important that if the orbital vibronic constants are known, changes in nuclear stable configurations, force constants, and anharmonicities due to small changes in electronic structure (changes in MO occupation numbers q_i^Γ, e.g., by ionization, excitation, coordination to active centers, etc.) can be numerically predicted using Eq. (2.25) (see Chapters 7 and 8).

In Fig. 2.5 the new parameterization of the molecular structure is illustrated for the highest occupied MO (HOMO) 5σ and lowest unoccupied MO (LUMO) 2π of two molecules N_2 and CO taken as examples [2.29]. It is seen that

in addition to the MO energy value and wavefunctions (shown schematically in Fig. 2.5 by their symmetry), the electron of the HOMO in the N_2 molecule tightens the nuclei with a force $f_R^{5\sigma}(N_2) = 3.51 \times 10^{-4}$ dyn (R is the distance between the nuclei), while in the CO molecule the electron of the analogous MO pushes them away with force $f_R^{5\sigma}(CO) = -4.5 \times 10^{-4}$ dyn (more precisely, the binding of the nuclei by the electron is less than their repulsion by this amount). The electron of the LUMO 2π pushes away the nuclei in both the N_2 and CO molecules with forces $f_R^{2\pi}(N_2) = -8.18 \times 10^{-4}$ dyn and $f_R^{2\pi}(CO) = -12.1 \times 10^{-4}$ dyn, respectively. For the corresponding one-electron MO contribution to the force constant (Eq. (2.30)) shown in Fig. 2.5 by a spring, we have $k_R^{5\sigma}(N_2) = 0.29 \times 10^{-6}$ dyn/cm, $k_R^{5\sigma}(CO) = -0.08 \times 10^{-6}$ dyn/cm, $k_R^{2\pi}(N_2) = -0.79 \times 10^{-6}$ dyn/cm, and $k_R^{2\pi}(CO) = -0.83 \times 10^{-6}$ dyn/cm.

It follows from these data that the orbital 5σ is bonding in N_2 and antibonding in CO, whereas the 2π MO is antibonding in both cases. Note that when there are several orbitals of the same type, as in the cases under consideration ($5\sigma, 4\sigma, 3\sigma, \ldots$), it is difficult to reveal the bonding nature of each of them, even qualitatively, without the vibronic approach. The latter also provides *quantitative information about the degree of the bonding or antibonding nature of the MO and its contribution to the distorting force, force constants, and anharmonicity constant* (Section 2.4). As mentioned above, this information is of special importance for analysis of the influence of electronic rearrangements on the nuclear configuration behavior (Section 7.1.3).

The diatomics N_2 and CO, taken as examples, are the simplest. In polyatomic molecules the orbital vibronic constants and the orbital contributions to the force constants contain much more information than just the measure of the bonding or antibonding nature of the MO. Indeed, following the group-theory rules, the linear orbital vibronic constant (2.24) is nonzero if the direct product of the irreducible representations Γ_i and Γ_j of the i and j MOs contain the $\overline{\Gamma}$ representation of the $Q_{\overline{\Gamma}}$ displacement. Dependent on Γ_i and Γ_j, $\overline{\Gamma}$ may be of any type possible for the symmetry group of the system under consideration. For the diagonal constant $f_{\overline{\Gamma}}^{ii}$, $\overline{\Gamma}$ must be the component of the symmetrized product $[\Gamma_i \times \Gamma_j]$. Therefore (quite similar to the discussion above of the integral vibronic constant), if Γ_i and Γ_j are nondegenerate, $\overline{\Gamma}$ is totally symmetric. In other words, the electrons of nondegenerate MOs distort the nuclear configuration along Q_{A_1}, which does not change its symmetry. Dependent on the sign of $f_{\overline{\Gamma}}^{ii}$, these MO are either bonding ($f_{\overline{\Gamma}}^{ii} > 0$) or antibonding ($f_{\overline{\Gamma}}^{ii} < 0$).

For degenerate MOs the product $[\Gamma_i \times \Gamma_j]$ contains nontotally symmetric representations in addition to the A_1 one. It follow that the electrons of

degenerate MOs distort the nuclear framework, changing its symmetry in accordance with (and in directions determined by) the JTE (Section 2.5). In addition to this distortion (in limited directions), the orbital electron softens, or hardens, the nuclear framework (Section 2.4).

The idea of orbital vibronic coupling and its direct influence on a variety of molecular and crystal properties is exploited in many papers relevant to different molecular and crystal problems, from spectra in fullerenes and mixed-valence compounds to superconductivity in molecular systems and crystals (Chapters 7 and 8). As a simple tool for analyzing molecular properties it was used in combination with the extended Hückel theory to work out direct correlations between orbital occupation numbers and molecular shapes [2.30]. Some general rules controlling calculation of vibronic constants along the periodic table are discussed in [2.31].

2.4 Force constants, anharmonicity, and instability

Consider a polyatomic system in a nondegenerate state and electrostatically equilibrated reference configuration $Q_\alpha = 0$ for which, in the adiabatic approximation, the first derivative of the APES in the Q direction is zero. The configuration instability of this system with respect to $Q_{\bar{\Gamma}}$ displacements means that the curvature $K_{\bar{\Gamma}}^{\Gamma}$ of the APES in this direction ($E^{\Gamma}(Q)$ is the total energy in the state Γ),

$$K_{\bar{\Gamma}}^{\Gamma} = \frac{1}{2}\left(\frac{\partial^2 E^{\Gamma}}{\partial Q_{\bar{\Gamma}}^2}\right)_0 \tag{2.31}$$

is negative at this point, $K_{\bar{\Gamma}}^{\Gamma} < 0$. Configuration instability does not mean that the system decays; it may be stable at other configurations with $Q_\alpha \neq 0$.

Employing the equation (see (2.1))

$$E^{\Gamma}(Q) = \langle \Psi^{\Gamma} | H | \Psi^{\Gamma} \rangle \tag{2.32}$$

where Ψ^{Γ} and $H(r, Q)$ are the full wavefunction and Hamiltonian of the system, and using some obvious relations similar to the Hellman–Feynman theorem [2.32] (see also [2.33]), we get

$$K_{\bar{\Gamma}}^{\Gamma} = \left\langle \Psi_0^{\Gamma} \middle| (\partial^2 H/\partial Q_{\bar{\Gamma}}^2)_0 \middle| \Psi_0^{\Gamma} \right\rangle + 2\left\langle \Psi_0^{\Gamma} \middle| (\partial H/\partial Q_{\bar{\Gamma}})_0 \middle| (\partial \Psi^{\Gamma}/\partial Q_{\bar{\Gamma}})_0 \right\rangle \tag{2.33}$$

where Ψ_0^{Γ} and all the derivatives are taken at the reference point $Q = 0$. The derivative $\Psi_0' = (\partial \Psi/\partial Q_{\bar{\Gamma}})_0$ can be presented by the perturbation-theory first correction to Ψ. Then (primes on H denote derivatives)

$$K_{\overline{\Gamma}}^{\Gamma} = \left\langle \Psi_0^{\Gamma} \middle| H''_{Q_{\overline{\Gamma}}} \middle| \Psi_0^{\Gamma} \right\rangle - 2 \sum_{\Gamma'} \frac{\left| \left\langle \Psi_0^{\Gamma} \middle| H'_{Q_{\overline{\Gamma}}} \middle| \Psi_0^{\Gamma'} \right\rangle \right|^2}{E_0^{\Gamma'} - E_0^{\Gamma}} \tag{2.34}$$

where E_0^{Γ} is the reference-state energy, while $E_0^{\Gamma'}$ and $\Psi_0^{\Gamma'}$ are the energies and wavefunctions of the excited states (in the same configuration) that yield nonzero matrix elements $\langle \Psi_0^{\Gamma} | H'_{Q_{\overline{\Gamma}}} | \Psi_0^{\Gamma} \rangle$, i.e., for which $\Gamma \times \Gamma' \in \overline{\Gamma}$. Taking into account that $\partial H/\partial Q = \partial V/\partial Q$ and employing the definitions of the vibronic constants from Eq. (2.15) in Section 2.2, we come to the formula

$$K_{\overline{\Gamma}}^{\Gamma} = K_{0\overline{\Gamma}}^{\Gamma} - \sum_{\Gamma' \neq \Gamma} \frac{\left| F_{\overline{\Gamma}}^{(\Gamma\Gamma')} \right|^2}{\Delta_{\Gamma'\Gamma}} \tag{2.35}$$

where $\Delta_{\Gamma'\Gamma} = \frac{1}{2}(E_0^{\Gamma'} - E_0^{\Gamma})$ and

$$K_{0\overline{\Gamma}}^{\Gamma} = \left\langle \Psi_0^{\Gamma} \middle| H''_{Q_{\overline{\Gamma}}} \middle| \Psi_0^{\Gamma} \right\rangle \tag{2.36}$$

By comparison with Eq. (2.19) we see that $K_{0\overline{\Gamma}}^{\Gamma}$ is the totally symmetric part of the diagonal matrix element of the quadratic terms of the vibronic coupling. For reasons given below $K_{0\overline{\Gamma}}^{\Gamma}$ may be called the *primary (nonvibronic) contribution to the curvature*, while the second part of Eq. (2.35) denoted by $K_{v\overline{\Gamma}}^{\Gamma}$,

$$K_{v\overline{\Gamma}}^{\Gamma} = -\sum_{\Gamma' \neq \Gamma} \frac{\left| F_{\overline{\Gamma}}^{(\Gamma\Gamma')} \right|^2}{\Delta_{\Gamma'\Gamma}} \tag{2.37}$$

which essentially depends on the linear vibronic coupling of the state under consideration Γ to the excited states Γ' of appropriate symmetry is the *vibronic contribution to the curvature*. Obviously, as a second-order perturbation contribution $K_{v\overline{\Gamma}}^{\Gamma} < 0$.

It is shown in Section 4.1 that this vibronic contribution to K is just the summarized pseudo JTE of the vibronic coupling to all the excited states that destabilize or soften the ground state in the given direction $Q_{\overline{\Gamma}}$. Equation (2.35) can be applied also to excited states Γ. But for them the sum (2.37) includes terms of coupling to states that are lower in energy for which $\Delta_{\Gamma'\Gamma} < 0$, meaning that $K_{v\overline{\Gamma}}^{\Gamma}$ is not necessarily negative.

From Eq. (2.32), by direct derivation with one-determinant wavefunctions, similar to that resulting in Eqs. (2.26) and (2.27) (and in the same approximation), we get the formula (2.30) for the curvature in terms of orbital vibronic constants:

$$K_{0\overline{\Gamma}}^{\Gamma} = \sum_i q_i^{\Gamma} k_{\overline{\Gamma}}^{i} \tag{2.30}$$

where

$$k^i_{\overline{\Gamma}} = k^i_{0\overline{\Gamma}} - \sum_j \frac{f^{(ij)}_{\overline{\Gamma}}}{\Delta_{\Gamma'\Gamma}} \tag{2.38}$$

$k^i_{0\overline{\Gamma}} = g^{(ii)}_{\overline{\Gamma}}$ is the totally symmetric part of the quadratic diagonal orbital constant of Eq. (2.29) (determined similarly to $K^{\Gamma}_{0\overline{\Gamma}}$ from Eq. (2.19)), and $\Delta_{\Gamma'\Gamma}$ has the same meaning as in (2.35) with the Γ' term formed by the one-electron $i \to j$ excitation from the reference state Γ.

The presentation of the APES curvature or force constant K in Eq. (2.31) as a sum of two terms after (2.34)–(2.37),

$$K = K_0 + K_{\mathrm{v}} \tag{2.39}$$

has some interesting features which will be discussed in more detail in subsequent sections. In particular, it was shown that the primary contribution K_0 is always positive [2.34, 2.35], $K_0 > 0$. This means first of all that the system under consideration in the reference nondegenerate state may not be unstable without the vibronic contribution, and the instability ($K < 0$) occurs when $|K_{\mathrm{v}}| > K_0$. In view of the note above about the PJT origin of the vibronic term, we come to the conclusion that the PJTE is the only source of configuration instability of polyatomic systems in nondegenerate states (Section 4.1).

If $|K_{\mathrm{v}}| < K_0$, then $K > 0$ and the APES has a minimum at the reference configuration. However, the K_{v} contribution is still rather important in lowering the absolute value of K and hence the vibration frequency at the minimum point. But even more important is its *contribution to the anharmonicity* of the vibrations. As follows from Eq. (2.37), the negative contribution to the K value due to the vibronic coupling to excited states increases with the decrease of the energy gap $(E^{\Gamma'}_0 - E^{\Gamma}_0)$. In a typical situation illustrated in Fig. 2.6 it results in strong anharmonicity of the ground-state vibrations (*vibronic anharmonicity*). Distinct from the proper anharmonicity which is due to the cubic (in nuclear coordinates) and higher-order terms in the expansion (2.3), the vibronic anharmonicity may occur already in the linear and quadratic approximation of this expansion: it is not just the large amplitude of nuclear displacements themselves but the presence of appropriate low-lying excited electronic states that creates the anharmonic nuclear vibrations.

Note that the anharmonicity may produce larger errors in the AA calculations than the AA itself. Indeed, the harmonic approximation is valid if the nuclear displacements from the minimum point ΔQ are small compared with the interatomic distances d. Using the semiclassical approximation, it can be

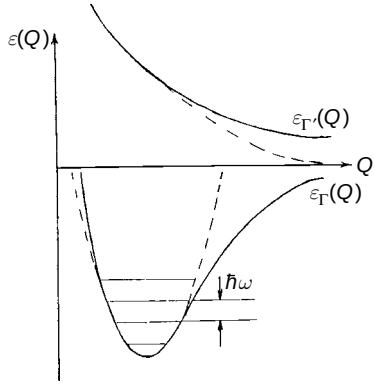

Fig. 2.6. Anharmonicity of the APES due to the vibronic mixing of the ground state with the near-lying excited state (vibronic anharmonicity). The APES of noninteracting states are shown by dashed lines.

shown [2.3] that the root-mean-square $(\overline{\Delta Q^2})^{\frac{1}{2}} \sim d(m/M)^{\frac{1}{4}}$, and hence $(\overline{\Delta Q^2})^{\frac{1}{2}}/d \sim (m/M)^{\frac{1}{4}} \approx 0.15$. On the other hand the simple AA, as mentioned above (Section 2.1), introduces an error of $(m/M)^{\frac{1}{2}} \approx 0.02$, provided the state is nondegenerate and the criterion (2.10) holds. It follows that for nondegenerate stable states anharmonicity corrections are more important than the nonadiabacity in the simple AA.

If only two electronic states participate in the vibronic mixing in the K_v term (2.37), the system may have some special features. In particular, for the two-level system we have

$$K_{\overline{\Gamma}}^{\Gamma} = K_{0\overline{\Gamma}}^{\Gamma} - \frac{\left|F_{\overline{\Gamma}}^{(\Gamma\Gamma')}\right|^2}{\Delta_{\Gamma'\Gamma}} \tag{2.40}$$

$$K_{\overline{\Gamma}}^{\Gamma'} = K_{0\overline{\Gamma}}^{\Gamma'} + \frac{\left|F_{\overline{\Gamma}}^{(\Gamma\Gamma')}\right|^2}{\Delta_{\Gamma'\Gamma}} \tag{2.41}$$

Since $K_0 > 0$, the excited state curvature $K_{\overline{\Gamma}}^{\Gamma'} > 0$. This means that in the two-level model any configuration instability of the ground state should be accompanied by a stable excited state, which causes the instability of the ground state.

If there is more than one excited state contributing to the instability of the ground state, each of them gets a positive vibronic contribution equal to its negative contribution to the ground-state value, but this does not mean that the K value for these excited states will be positive because of possible negative contributions of higher energy states of appropriate symmetry. Usually the number of excited electronic states that are vibronically considerably strong coupled to the ground state is small, and a two-level model may be valid in many cases.

2.5 The Jahn–Teller theorem

So far we have not considered possible solutions of the system of equations (2.6) in case of electronic degeneracy when the criterion (2.10) does not hold and the AA is invalid. The direct solution of these equations is discussed in Chapter 5. However, a general understanding and a variety of qualitative and semiquantitative results can be obtained based on the JT theorem [2.36], which initiated this whole trend.

The JT theorem is based on a perturbational group-theoretical analysis of the behavior of the APES of polyatomic systems near the point of electronic degeneracy. Similar to other group-theoretical statements, the JT theorem allows one to deduce a series of qualitative results without specific calculations.

Assume that by solving the electronic Schrödinger equation (2.4) for the nuclei fixed at the point $Q_{\Gamma\gamma} = Q^0_{\Gamma\gamma} = 0$ we obtain an f-fold degenerate electronic term, i.e., f states $\varphi_k(r)$, $k = 1, 2, \ldots, f$, with the same energies $\varepsilon'_k = \varepsilon_0$. How do these energy levels vary under nuclear displacements $Q_{\Gamma\gamma} \neq 0$? To answer this question the APES for arbitrary coordinates near the point of degeneracy should be determined. This can be done by estimating the effect of the vibronic interaction terms $W(r, Q)$ in Eq. (2.14) on the energy level positions ε'_k.

For sufficiently small nuclear displacements $Q_{\Gamma\gamma}$ the APES ε_k(Q) for an f-fold degenerate electronic term Γ can be obtained as solutions of the secular equation of the perturbation theory:

$$\begin{vmatrix} W_{11} - \varepsilon & W_{12} & \cdots & W_{1f} \\ W_{21} & W_{22} - \varepsilon & \cdots & W_{2f} \\ \vdots & \vdots & \vdots & \vdots \\ W_{f1} & W_{f2} & \cdots & W_{ff} - \varepsilon \end{vmatrix} = 0 \qquad (2.42)$$

where W_{ij} are the matrix elements of the operator (2.14) calculated with the wavefunctions of the degenerate term. Since the degeneracy is assumed due to the high symmetry of the system, the totally symmetric displacements Q_A do not remove the degeneracy and do not change the symmetry; they will not be considered in this section as nonessential (however, see Section 3.2). Again, second-order terms may also be omitted due to the assumed small values of $Q_{\Gamma\gamma}$. Keeping only linear terms in the vibronic corrections to the electronic energy (see below and Section 3.1), $W_{ij} = \sum_{\Gamma\gamma} \langle i|(\partial V/\partial Q_{\Gamma\gamma})_0|j\rangle Q_{\Gamma\gamma}$ and, taking into account Eq. (2.17), we have

$$W_{\Gamma\gamma\Gamma\gamma'} = \sum_{\Gamma\gamma} F^{\Gamma\gamma\Gamma\gamma'}_{\overline{\Gamma}\overline{\gamma}} Q_{\overline{\Gamma}\overline{\gamma}} = \sum_{\Gamma\gamma} F^{\Gamma\Gamma}_{\overline{\Gamma}} Q_{\overline{\Gamma}\overline{\gamma}} \langle \overline{\Gamma}\overline{\gamma}\Gamma\gamma'|\Gamma\gamma\rangle \qquad (2.43)$$

where $F_{\overline{\Gamma}}^{\Gamma\Gamma}$ are the linear vibronic constants (2.15). If at least one of them is nonzero, then at least one of the roots of Eq. (2.42) contains linear terms in the corresponding displacements $Q_{\Gamma\gamma}$, and hence the APES $\varepsilon_k(Q)$ has no minimum at the point $Q_{\Gamma\gamma}^0 = 0$ with respect to these displacements.

On the other hand, the question of whether the vibronic constant $F_{\overline{\Gamma}}^{\Gamma\Gamma} = \langle\Gamma|\left(\partial V/\partial Q_{\overline{\Gamma}}\right)_0|\Gamma\rangle$ is zero or not may be easily answered by means of the well-known group-theoretical rule: $F_{\overline{\Gamma}}^{\Gamma\Gamma}$ is nonzero if and only if the symmetric product $[\Gamma \times \Gamma]$ contains the representation of the symmetrized displacement $\overline{\Gamma}$; for instance, for a doubly degenerate E term $[E \times E] = A_1 + E$. Thus, if the system under consideration has E vibrations (see the classification of vibrations given in Table 2.1), it has no minimum at the point of degeneracy with respect to the E displacements.

Jahn and Teller [2.36] examined all types of degenerate terms of all symmetry point groups and showed that for any orbital degenerate term of any molecular system there are nontotally symmetric displacements with respect to which the APES of the electronic term (more precisely, at least one of its branches) has no minimum; molecules with linear arrangements of atoms are exceptions (see below). It was later shown by Jahn [2.37] that a similar statement is valid also in case of spin degeneracy with the exception of two-fold degeneracy for systems with total spin 1/2 (Kramers degeneracy). The statement about the absence of an extremum at the point of degeneracy is just the Jahn–Teller theorem which may be formulated more rigorously as follows: *if the APES of a nonlinear polyatomic system has several ($f > 1$) sheets coinciding at one point (f-fold degeneracy), at least one of them has no extremum at this point, the cases of Kramers degeneracies being exceptions.*

The variation of the APES in the simplest case of a doubly degenerate electronic term in the space of only one coordinate Q is shown schematically in Fig. 2.7; many other cases are considered in Chapter 3. It is seen that the two curves intersect at the point of degeneracy. Away from this point the energy term splits, and the degeneracy is removed. As a result, the energy is lowered so that the small nuclear displacements Q are of advantage. For larger values of Q the quadratic, cubic, and higher-order terms become important and further distortion of the system may be inconvenient energetically (see Chapter 3).

The exclusion of linear molecules from the JT statement needs clarification. For linear molecules the nontotally symmetric displacements are of odd type with respect to reflections in the plane containing the molecular axis, whereas the product of wavefunctions of the degenerate term is always even with respect to such reflections. This means that the corresponding vibronic constant (2.15) equals zero, and hence the APES at the point of linear configuration, as opposed to nonlinear molecules, has no linear terms, i.e., it is an

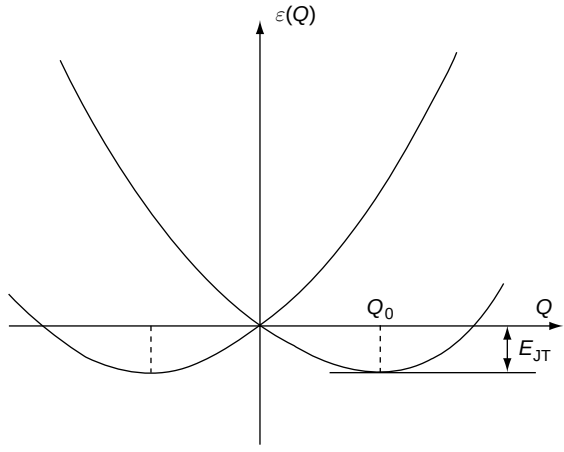

Fig. 2.7. Variation of the adiabatic potential of a molecular system in a twofold orbitally degenerate electronic state with respect to one active coordinate Q. At the point of degeneracy $Q = 0$ there is no minimum. E_{JT} is the JT stabilization energy.

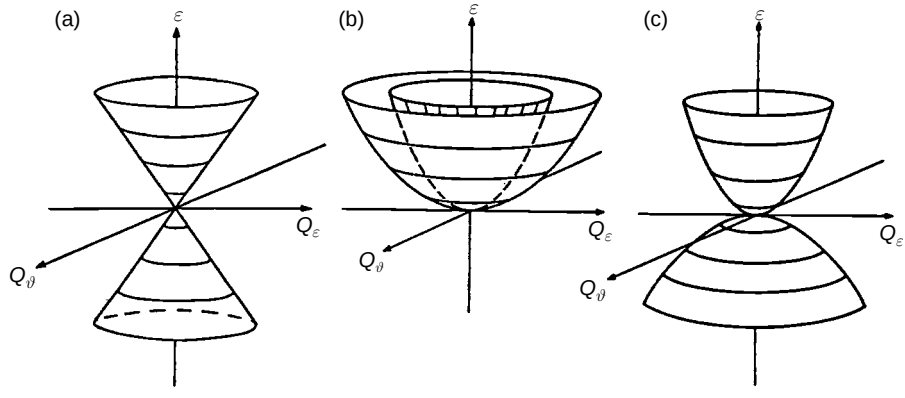

Fig. 2.8. Branching of the APES at the point of twofold degeneracy in the cases of (a) nonzero linear coupling (*conical intersection*); (b) zero linear and weak quadratic coupling; and (c) sufficiently strong quadratic coupling.

extremum. However, in these cases the effect of quadratic terms of the vibronic coupling is nonzero. Pure quadratic coupling may also lead to lack of minimum at the point of degeneracy, as illustrated in Fig. 2.8, but distinguished from the linear case the quadratic instability is possible only for sufficiently strong coupling. In case of linear molecules this instability results in the Renner–Teller effect described in Section 4.4, but it may take place also in nonlinear systems in which the linear coupling constant, although allowed to be non-zero by symmetry considerations, is in fact "accidentally" zero or negligibly small (while the quadratic coupling is significant).

The lack of a minimum of the APES at the point of electronic degeneracy is often interpreted as instability of the nuclear configuration, which leads to its real (observable) spontaneous distortion that removes the electronic degeneracy. This formulation and interpretation of the JT theorem initiated by its authors [2.36] appears in some monographs and handbooks and has found widespread use in the general treatment of experimental results. Meanwhile, as will be shown later in this book, the actual situation in systems with electron degeneracy may be much more complicated than implied by the simple statement of instability. Moreover, taken literally, this statement is not true and may lead to misunderstandings [2.38] (this misinterpretation led to a period of "stagnation" in the understanding of the consequences of the JT theorem mentioned in Chapter 1). The conclusion about the lack of a minimum of the APES $\varepsilon(Q)$ at the point of degeneracy was reached as a consequence of the solution of the electronic part of the Schrödinger equation, and therefore it cannot be attributed directly to the nuclear behavior. The latter is determined by the solution of the nuclear motion equations (2.6).

The absence of a minimum of the function $\varepsilon(Q)$ may rigorously be interpreted as instability only when there is no degeneracy. Indeed, in the absence of degeneracy (or in areas far from the point of degeneracy) the electronic and nuclear motions can be separated in the AA (Section 2.1), so that the APES $\varepsilon(Q)$ has the meaning of the potential energy of the nuclei in the mean field of the electrons, and hence the derivative $(d\varepsilon/dQ)_0$ means the force acting upon the nuclei at the point $Q_{\Gamma\gamma}=0$. Here the condition $(d\varepsilon/dQ)_0 \neq 0$ may be interpreted as a nonzero distorting force (in the Q direction) due to which the nuclear configuration becomes unstable.

However, in the presence of electronic degeneracy $\varepsilon(Q)$ loses the meaning of potential energy of the nuclei in the mean field of the electrons because the motions of the electrons and nuclei near the point of degeneracy cannot be separated. In this area the notion of APES becomes formal, without unambiguous physical meaning. Accordingly, the reasoning about distorting forces and instability is, strictly speaking, invalid here. In these cases the term "instability" should be taken formally as an indication of the lack of a minimum of the APES, but not as an observable nuclear feature. The latter, as indicated above, must be deduced from the solutions of Eqs. (2.6) for nuclear dynamics.

The nuclear distortions due to the JTE and the PJTE in the absence of low-symmetry perturbations are in general of a dynamic nature, for which the nuclear configuration (determined quantum-mechanically as the Ψ-averaged values of the nuclear coordinate operators) is not distorted [2.38] (see also Eq. (5.136) in Section 5.6). It is not simply the nuclear configuration distortion, but rather the special nuclear dynamics that is predicted by the JTE and PJTE

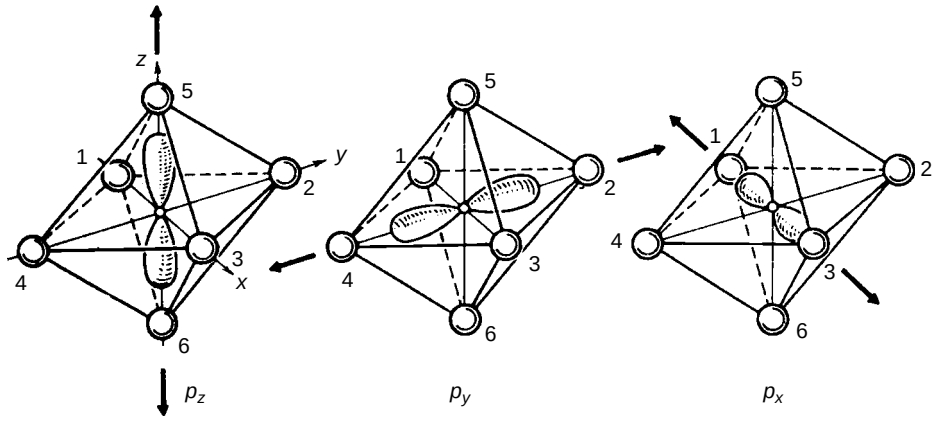

Fig. 2.9. A rough illustration of the electrostatic origin of JT distortions of the nuclear configuration of an octahedral ML_6 complex in a threefold degenerate electronic state. If the electron of the central atom falls into one of the three equivalent states, it repels (or attracts) the corresponding pair of ligands, resulting in a tetragonal distortion. The three equivalent directions of distortion are shown by arrows.

in free (unperturbed) molecular systems. In many cases the electronic degeneracy is not removed either, but it is transferred from the electronic to the vibronic degeneracy (Chapter 5). The consequences of the lack of minimum of the APES at the point of degeneracy result in a variety of most important effects that include also structural distortions of the reference configuration as a particular case in the presence of external perturbations or cooperative effects.

The specific JT behavior of the APES due to electronic degeneracy or pseudodegeneracy can be explained by simple images. Consider, for example, the case of one electron in one of three equivalent p orbitals (p_x, p_y, and p_z) of the central atom of a hexacoordinated molecular system MX_6 (term T_{1u}), the ligand X bearing negative charge (Fig. 2.9). It is clear that if the electron is on the p_x orbital, it interacts more strongly with the nearest ligands 1 and 3, pushing them away (and producing a potential well for itself). As a result the octahedral complex becomes tetragonally distorted along the Ox axis. Similarly, the electron on the p_y orbital pushes away ligands 2 and 4, distorting the complex equivalently to the previous case, but along the Oy axis; and for the electron on the p_z orbital the distortion is along Oz.

Note that in the absence of the ligands the electron has no specific location within the degenerate manifold, but in the presence of the ligands the distorted configuration with the electron in one of the three orbitals becomes preferable energetically. Since the three states in cubic fields remain equivalent, the system has three minima, corresponding to the three directions of distortions,

and no minimum in the high-symmetry octahedral configuration due to obvious electrostatic forces. The same result emerges from the MO description with the atomic p orbital taking part in the corresponding antibonding MO (for bonding orbitals the distortions are of opposite sign). Note also that in the case of the T term under consideration in this visual example alternative trigonal distortions are also possible (Section 3.3).

The proof of the JT theorem by means of an examination of all types of degenerate terms in all symmetry point groups [2.36] as illustrated above, although rigorous, cannot be considered elegant. More general proofs have been obtained in [2.39, 2.40] (see also in [2.3]). These proofs deal with molecular groups only. A proof of the JT theorem for both molecular and space groups was suggested in [2.41]; for further discussion and improvements see in [2.42–2.44].

However, the proof by examination of all possible degenerate terms [2.36] has its advantages, one of which is to reveal the *JT active modes*, i.e., the nuclear displacements $Q_{\overline{\Gamma}}$ for which the vibronic constant $F_{\overline{\Gamma}}^{\Gamma\Gamma}$ is nonzero and which remove the degeneracy of the electronic term Γ. These active modes (active vibrations) are very important basic components of the JT problem since they form the space of the nontotally symmetric nuclear displacement in which the JTE is realized.

If the types of possible vibration of the system under consideration are known (Table 2.2), the JT active nuclear displacement $Q_{\overline{\Gamma}}$ can be obtained easily. As indicated above, $F_{\overline{\Gamma}}^{\Gamma\Gamma}$ is nonzero if the symmetric product $[\Gamma \times \Gamma]$ contains the representation of the symmetrized displacement $\overline{\Gamma}$. It follows that displacements $Q_{\overline{\Gamma}}$ can be found as the irreducible parts of the reducible representation $[\Gamma \times \Gamma]$. The nontotally symmetric components of the latter are just the representation $\overline{\Gamma}$ of the active displacements $Q_{\overline{\Gamma}}$. For instance, for an E_g term in an octahedral system $[E_g \times E_g] = A_{1g} + E_g$, and hence the JT active displacements are of E_g type. Similarly, for a T term in a tetrahedral system $[T \times T] = A_1 + E + T_2$, and both the E- and T_2-type displacements are JT active. The JT-active displacements for all important point groups are given in Table 2.3.

With the JT-active coordinates Q_α known the symmetry of the JT-distorted configuration can be predicted by means of group-theoretical considerations using the *epikernel principle* [2.45]. If the symmetry group of the system in the reference configuration is G, then as a result of the Q_α distortion it reduces to S,

$$G \xrightarrow{Q_\alpha} S$$

where S is a subgroup of G in which only those symmetry operations (elements) of G that leave Q_α invariant remain. In other words, in the S subgroup Q_α is totally symmetric, whereas in the G group Q_α is nontotally symmetric (by definition) and it belongs to one of the degenerate irreducible representations Γ of the group G (e.g., in tetrahedral T_d group Q_θ belongs to the E representation).

Table 2.3. *Expansion of symmetric* $[\Gamma \times \Gamma] = [\Gamma^2]$ *and antisymmetric* $\{\Gamma \times \Gamma\} = \{\Gamma^2\}$ *products of irreducible representations of degenerate terms of systems with different symmetry groups (antisymmetric products refer to terms* Γ *classified by double groups); the nontotally symmetric representations in these expansions describe the JT-active modes (adapted from [2.3])*

Group	$[\Gamma^2]$, $\{\Gamma^2\}$
$C_{\infty,\mathrm{v}}$	$[E_k^2] = A_1 + E_{2k} \qquad (k = 1, 2, ...)$
$D_{\infty,\mathrm{h}}$	$[E_{k\mathrm{g}}^2] = [E_{k\mathrm{u}}^2] = A_{1\mathrm{g}} + E_{2k,\mathrm{g}} \qquad (k = 1, 2, ...)$
C_{2p+1}	$[E_k^2] = \begin{cases} A + E_{2k} & k \le p/2 \\ A + E_{2p+1-2k} & k > p/2 \end{cases} \quad (k = 1, 2, ..., p)$
C_{2p}	$[E_k^2] = \begin{cases} A + E_{2k} & k < p/2 \\ A + 2B & k = p/2 \\ A + E_{2p-2k} & k > p/2 \end{cases} \quad (k = 1, 2, ..., p-1)$
D_{2p+1} $C_{2p+1,\mathrm{v}}$	$[E_k^2] = \begin{cases} A_1 + E_{2k} & k \le p/2 \\ A_1 + E_{2p+1-2k} & k > p/2 \end{cases} \quad (k = 1, ..., p)$
D_{2p} $C_{2p,\mathrm{v}}$	$[E_k^2] = \begin{cases} A_1 + E_{2k} & k < p/2 \\ A_1 + B_1 + B_2 & k = p/2 \\ A_1 + E_{2p-2k} & k > p/2 \end{cases} \quad (k = 1, ..., p-1)$
$C_{2p+1,i}$	$[E_{k\mathrm{g}}^2] = [E_{k\mathrm{u}}^2] = \begin{cases} A_\mathrm{g} + E_{2k,\mathrm{g}} & k \le p/2 \\ A_\mathrm{g} + E_{2p+1-2k,\mathrm{g}} & k > p/2 \end{cases} \quad (k = 1, ..., p)$
$C_{2p,i}$	$[E_{k\mathrm{g}}^2] = [E_{k\mathrm{u}}^2] = \begin{cases} A_\mathrm{g} + E_{2k,\mathrm{g}} & k < p/2 \\ A_\mathrm{g} + 2B_\mathrm{g} & k = p/2 \\ A_\mathrm{g} + E_{2p-2k,\mathrm{g}} & k > p/2 \end{cases} \quad (k = 1, ..., p-1)$
$D_{2p+1,i}$	$[E_{k\mathrm{g}}^2] = [E_{k\mathrm{u}}^2] = \begin{cases} A_{1\mathrm{g}} + E_{2k,\mathrm{g}} & k \le p/2 \\ A_{1\mathrm{g}} + E_{2p+1-2k,\mathrm{g}} & k > p/2 \end{cases} \quad (k = 1, ..., p)$
$D_{2p,i}$	$[E_{k\mathrm{g}}^2] = [E_{k\mathrm{u}}^2] = \begin{cases} A_{1\mathrm{g}} + E_{2k,\mathrm{g}} & k < p/2 \\ A_{1\mathrm{g}} + B_{1\mathrm{g}} + B_{2\mathrm{g}} & k = p/2 \\ A_{1\mathrm{g}} + E_{2p-2k,\mathrm{g}} & k > p/2 \end{cases} \quad (k = 1, ..., p-1)$
$C_{2p+1,\mathrm{h}}$ $D_{2p+1,\mathrm{h}}$	$[E_k'^2] = [E_k''^2] \begin{cases} A' + E'_{2k} & k \le p/2 \\ A' + E'_{2p+1-2k} & k > p/2 \end{cases} \quad (k = 1, ..., p)$
S_{4p}	$[E_k^2] = \begin{cases} A + E_{2k} & k < p \\ A + 2B & k = p \\ A + E_{4p-2k} & k > p \end{cases} \quad (k = 1, ..., 2p-1)$
$S_{4p,\mathrm{v}}$	$[E_k^2] = \begin{cases} A_1 + E_{2k} & k < p \\ A_1 + B_1 + B_2 & k = p \\ A_1 + E_{4p-2k} & k > p \end{cases} \quad (k = 1, ..., 2p-1)$
T	$[E^2] = A + E$ $[T^2] = A + E + T$ $\{\Gamma_8^2\} = A + E + T$

Table 2.3. (*cont.*)

Group	$[\Gamma^2]$, $\{\Gamma^2\}$
T_d	$[E^2] = A + E$ $[T_{1,2}^2] = A + E + T_2$ $\{\Gamma_8^2\} = A_1 + E + T_2$
T_h	$[E_g^2] = [E_u^2] = A_g + E_g$ $[T_g^2] = [T_u^2] = A_g + E_g + T_g$ $\{\Gamma_{8g}^2\} = \{\Gamma_{8u}^2\} = A_g + E_g + T_g$
O_h	$[E_g^2] = [E_u^2] = A_{1g} + E_g$ $[T_{1g}^2] = [T_{1u}^2] = [T_{2g}^2] = [T_{2u}^2] = A_{1g} + E_g + T_{2g}$ $\{\Gamma_{8g}^2\} = [\Gamma_{8u}^2] = A_{1g} + E_g + T_{2g}$
I	$[T_1^2] = [T_2^2] = A + V$ $[U^2] = A + U + V$ $[V^2] = A + U + 2V$ $\{\Gamma_8^2\} = A + V$ $\{\Gamma_9^2\} = A + U + V$
I_h	$[T_{1g}^2] = [T_{1u}^2] = [T_{2g}^2] = [T_{2u}^2] = A_g + V_g$ $[U_g^2] = [U_u^2] = A_g + U_g + V_g$ $[V_g^2] = [V_u^2] = A_g + U_g + 2V_g$ $\{\Gamma_{8g}^2\} = \{\Gamma_{8u}^2\} = A_g + V_g$ $\{\Gamma_{9g}^2\} = \{\Gamma_{9u}^2\} = A_g + U_g + V_g$

The kernel of Γ in G, denoted $K(G, \Gamma)$, is the subgroup of G that includes all symmetry elements that are represented in Γ by unit matrices (see tables in the appendix). This means that in the kernel subgroup all the basis functions of Γ are totally symmetric. An *epikernel* of Γ in G, denoted $E(G, \Gamma)$ is the subgroup of G that contains all the symmetry elements for which at least one basis function of Γ remains totally symmetric. The epikernel principle can be formulated as follows [2.45]: *extrema points on a JT surface prefer epikernels; they prefer maximal epikernels to lower-ranking ones. Stable minima are to be found with the structures of maximal epikernel symmetry*.

This statement implies that, although forced to distort in order to remove the electronic degeneracy, the system prefers nuclear configurations with higher symmetry compatible with this requirement. In this formulation the epikernel principle can be related to a more general statement formulated by Pierre Curie in 1894 [2.46]: *the symmetry characteristic of a phenomenon is the maximal symmetry compatible with the existence of this phenomenon*.

The epikernels can be found directly from the character tables of the corresponding point groups: $E(T_d, E) = D_{2d}$; $E(T_d, T_2) = C_{3v}, C_{2v}, C_s$; $E(T_d, E + T_2) =$

D_{2d}, D_2, C_{3v}, C_{2v}, C_2, C_s. In the latter case it is assumed that the E and T_2 vibrations have the same frequency, forming a five-fold degenerate JT-active space. For the octahedral O_h group $E(O_h, E) = D_{4h}$, C_{4v}, $E(O_h, T_2) = D_3$, C_{3v}, and so on.

The epikernel principle is formulated for the JT distortions that are linear in the active coordinates Q_α. This means that it can be violated when higher-order vibronic interaction terms in Eq. (2.7) are taken into account.

Topological problems related to the JTE are discussed also in [2.47–2.50]. A DFT analysis is given in [2.51].

The formulation of the JT theorem given above is the basis of the JT effects, which cover a large variety of molecular and crystal properties outlined in this book. With the inclusion of the PJTE and RTE, and especially after the proof of the uniqueness of the vibronic coupling instabilities (Section 4.1), the basic theorem needs extensions and reformulation [2.52, 2.53]; they are discussed in Section 4.5.

References

2.1. M. Born and R. Oppenheimer, *Ann. Phys.* **84**, 457 (1927).
2.2. N. Born and K. Huang, *Dynamical Theory of Crystal Latices*, London, Oxford University Press, 1954, Appendix VIII.
2.3. I. B. Bersuker and V. Z. Polinger, *Vibronic Interactions in Molecules and Crystals*, New York, Springer, 1989.
2.4. W. Lichten, *Phys. Rev.* **131**, 329 (1963); **139**, 27 (1965); **164**, 131 (1967).
2.5. T. F. O'Malley, *Adv. At. Mol. Phys.* **7**, 223 (1971).
2.6. M. Baer, *Mol. Phys.* **40**, 1011 (1980); *Phys. Rep.* **358**, 75 (2002).
2.7. C. A. Mead and T. G. Truhlar, *J. Chem. Phys.* **77**, 6090 (1982).
2.8. E. S. Kryachko and D. R. Yarkony, *Internat. J. Quant. Chem.* **76**, 235 (2000); *Theor. Chem. Acc.* **100**, 154 (1998); E. S. Kryachko, *J. Phys. Chem. A* **103**, 4368 (1999).
2.9. N. Matsunaga and D. R. Yarkony, *Mol. Phys.* **93**, 79 (1998).
2.10. A. Thiel and H. Köppel, *J. Chem. Phys.* **110**, 9371 (1999).
2.11. H. Köppel, J. Gronki, and S. Mahapatra, *J. Chem. Phys.* **115**, 2377 (2001).
2.12. *Conical Intersections: Electronic Structure, Dynamics, and Spectroscopy*, Eds. W. Domcke, D. R. Yarkony, and H. Köppel, Singapore, World Scientific, 2003.
2.13. A. W. Jasper, B. K. Kendrick, C. A. Mead, and D. G. Truhlar, in *Modern Trends in Chemical Reaction Dynamics*, Eds. X. Yang and K. Liu, Singapore, World Scientific, 2003.
2.14. M. Baer, in *The Role of Degenerate States in Chemistry*; a special volume of *Adv. Chem. Phys.* **124**, Eds. M. Baer and G. D. Billing, New York, Wiley, 2002, p. 39.
2.15. R. Englman, A. Yahalom, and M. Baer, *Internat. J. Quant. Chem.* **90**, 266 (2002); A. J. C. Varandas, M. Baer and R. Englman, *Mol. Phys.* **97**, 1185 (1999); M. Baer and R. Englman, *Chem. Phys. Lett.* **265**, 105 (1997).
2.16. J. W. Zwanziger, R. L. Whetten, G. S. Ezra, and E. R. Grant, *Chem. Phys. Lett.* **120**, 106 (1985).
2.17. W. Kutzelnigg, *Mol. Phys.* **90**, 909 (1997).
2.18. S. Golden, *Mol. Phys.* **93**, 421 (1998); J. F. Ogilvie, *Chem. Phys. Lett.* **267**, 590 (1997).
2.19. R. Englman and A. Yahalom, in *Vibronic Interactions: Jahn–Teller Effect in Crystals and Molecules*, Eds. M. D. Kaplan and G. O. Zimmerman, NATO Science Series II, Vol. 39, Dordrecht, Kluwer, 2001, p. 5; and in *The Role of*

Degenerate States in Chemistry; a special volume of *Adv. Chem. Phys.* **124**, Eds. M. Baer and G. D. Billing, New York, Wiley, 2002, p. 197.
2.20. (*a*) M. Baer, A. Vibok, G. Halasz, and D. J. Kouri, *Adv. Quant. Chem.* **44**, 103 (2003); (*b*) T. Vertesi, A. Vibok, G. Halasz, and M. Baer, *J. Chem. Phys.* **121**, 4000 (2004).
2.21. F. Dufey and S. Fisher, *Phys. Rev. A* **63**, 2510 (2001).
2.22. T. Patcher, L. S. Cederbaum, and H. Köppel, *Adv. Chem. Phys.* **84**, 293 (1993).
2.23. K. Kendrick, C. A. Mead, and D. G. Truhlar, *Chem. Phys.* **277**, 31 (2002).
2.24. R. Hochstrasser, *Molecular Aspects of Symmetry*, New York, Benjamin, 1966.
2.25. L. D. Landau and E. M. Lifshitz, *Quantum Mechanics: Non-relativistic Theory*, Oxford, Pergomon Press, 1977.
2.26. B. S. Tsukerblat, *Group Theory in Chemistry and Spectroscopy. A Simple Guide to Advanced Usage*, New York, Academic Press, 1994.
2.27. J. S. Griffith, *The Irreducible Tensor Method for Molecular Symmetry Groups*, Englewood Cliffs, New Jersey, Prentice-Hall, 1962.
2.28. W. L. Clinton and B. Rice, *J. Chem. Phys.* **30**, 542 (1959).
2.29. I. B. Bersuker, *The Jahn–Teller Effect and Vibronic Interactions in Modern Chemistry*, New York, Plenum, 1984.
2.30. J. R. Letelier, *Internat. J. Mod. Phys. C* **10**, 1177 (1999); J. R. Letelier and A. Toro-Labbe, *Bol. Soc. Chil. Quim.* **44**, 87 (1999); J. R. Letelier, A. Toro-Labbe, and Y.-N. Chiu, *J. Chinese Chem. Soc.* **44**, 101 (1999); F. Eisner, M. D. Gonzales, and J. R. Letelier, *J. Chil. Chem. Soc.* **48**, 105 (2003).
2.31. W. Grochala, R. Konecny, and R. Hoffmann, *Chem. Phys.* **265**, 153 (2001); W. Grochala and R. Hoffmann, *Polish J. Chem.* **75**, 1603 (2001).
2.32. H. Hellman, *Einführung in die Quantenchemie*, Leipzig, Franz Deuticke, 1937; R. P. Feynman, *Phys. Rev.* **56**, 340 (1939).
2.33. R. F. W. Bader, *Mol. Phys.* **3**, 137 (1960); *Can. J. Chem.* **40**, 1164 (1962); R. F. W. Bader and A. D. Bandrauk, *J. Chem. Phys.* **49**, 1666 (1968).
2.34. I. B. Bersuker, *Nouv. J. Chim.* **4**, 139 (1980); *Teor. Eksp. Khim.* **16**, 291 (1980); *Pure Appl. Chem.* **60**, 1167 (1988); *Fiz. Tverd. Tela* **30**, 1738 (1988); *New J. Chem.* **17**, 3 (1993).
2.35. I. B. Bersuker, N. N. Gorinchoi, and V. Z. Polinger, *Theor. Chim. Acta* **66**, 161 (1984); I. B. Bersuker, V. Z. Polinger, and N. N. Gorinchoi, *J. Struct. Chem. (THEOCHEM)* **5**, 369 (1992).
2.36. H. A. Jahn and E. Teller, *Proc. R. Soc. London* **161**, 220 (1937).
2.37. H. A. Jahn, *Proc. R. Soc. London A* **164**, 117 (1938).
2.38. I. B. Bersuker, *Teor. Eksp. Khim.* **2**, 518 (1966).
2.39. E. Ruch and A. Schonhofer, *Theor. Chim. Acta* **3**, 291 (1965).
2.40. E. L. Blount, *J. Math. Phys. (N.Y.)* **12**, 1890 (1971).
2.41. I. V. V. Raghavacharyulu, *J. Phys. C* **6**, L455 (1973).
2.42. J. Birman, *Phys. Rev.* **125**, 1959 (1962); **127**, 1093 (1973).
2.43. R. Berenson, J. N. Kotzev, and D. B. Litvin, *Phys. Rev. B* **25**, 7523 (1982).
2.44. S. Aronowitz, *Phys. Rev. A* **14**, 1319 (1976).
2.45. A. Ceulemans and L. G. Vanquickenborne, in *Struct. Bonding* **71**, 125 (1989).
2.46. P. Curie, *Oeuvres de Pierre Curie*, Paris, Gauthiers-Villars, 1908, p. 118.
2.47. E. R. Davidson, *J. Am. Chem. Soc.* **99**, 397 (1977).
2.48. E. R. Davidson and W. T. Borden, *J. Phys. Chem.* **87**, 4783 (1983).
2.49. R. Balawender, F. de Proft, and P. Geerlings, *J. Chem. Phys.* **114**, 4441 (2001).
2.50. R. B. King, *Mol. Phys.* **100**, 1567 (2002).
2.51. N. Sukumar, *Internat. J. Quant. Chem.* **52**, 809 (1994).
2.52. I. B. Bersuker, *Adv. Quant. Chem.* **44**, 1 (2003).
2.53. I. B. Bersuker, in *Fundamental World of Quantum Chemistry*, Vol. 3, Eds. E. J. Brandas and E. S. Kryachko, Dordrecht, Kluwer, 2004.

3

Formulation of Jahn–Teller problems. Adiabatic potentials

This chapter is to formulate in general the different "traditional" situations that occur due to the lack of minimum of the APES in systems with degenerate electronic terms, as predicted by the JT theorem (Section 2.5). They are labeled as *JT problems*. Each of them is characterized by the type of degenerate electronic term Γ and the JT-active vibrational modes γ_i (denoted as the $\Gamma \otimes (\gamma_1 + \gamma_2 + \cdots)$ problem), and has a specific APES. The latter is most important to the solution of the vibronic coupling equations (2.6), which yield the energies and wavefunctions considered in Chapter 5. But the APES has also independent value, allowing qualitative and semiquantitative evaluation of important properties of the system. Other (less traditional) situations including PJT, RT, and product JT problems are formulated in Chapter 4.

3.1 Basic formulation. The simplest ($E \otimes b_1$) and $E \otimes (b_1 + b_2)$ problems

The JT problems refer to polyatomic (molecular and crystalline) systems with degenerate electronic states, for which the JT theorem is operative. As follows from group-theoretical considerations, degenerate states may occur in systems with high symmetry that have at least one rotational or rotoflection axis of the order $n > 2$. The higher the symmetry, the more and higher-order degenerate terms are possible. Systems with axial symmetry have twofold degenerate E terms, cubic systems have E and threefold degenerate T terms (with spin–orbital interaction included they may have also fourfold degenerate G terms), while icosahedral systems have E, T, G, and fivefold degenerate H terms (see the corresponding point groups in the appendix). The JT theorem reveals the symmetry of the JT-active displacements for each of these terms in the corresponding symmetry group (Table 2.3).

For each degenerate electronic term, the vibronic coupling to one or several types of JT-active nuclear displacements has its specific features forming a

separate *JT problem*. If there is more than one type of JT-active coordinates for a given term, the problem may be further divided into several sub-problems. For instance, as follows from Table 2.3, twofold degenerate E terms may have JT-active nondegenerate displacements of the type b_1 and b_2, if the system has an axis of symmetry of the order $4n$, where $n = 1, 2, \ldots$, (and then the JT problem is $E \otimes b_1$ or $E \otimes b_2$ or $E \otimes (b_1 + b_2)$), or twofold e-type degenerate vibrations in all the other cases (the $E \otimes e$ problem). Hereafter for convenience the nuclear-displacement (vibrational) symmetry representations are denoted by small letters to distinguish them from the capital letters used in general cases and for electronic terms. For T terms there may be $T \otimes e$, $T \otimes t_2$ and $T \otimes (e + t_2)$ problems, and so on. If the system has two or more or an infinite number of JT-active vibrations of the same symmetry (e.g., t_2' and t_2'' in tetrahedral systems), the JT problem is called *multimode* (Section 3.5), to distinguish it from the problems above, called *ideal*.

The special features of each JT problem can be evaluated from the solution of the vibronically coupled equations (2.6). However, some important properties can be revealed using general theoretical considerations. In what follows in this chapter the formulation of the JT problems and brief discussion of some of their general qualitative features is given. Full solutions to these problems are considered in Chapter 5.

It follows from the Jahn–Teller theorem that at the point of the nuclear configuration where the electronic state is degenerate the surface of the potential energy of the nuclei in the mean field of electrons (the APES) has no minimum. The question of whether this surface possesses any minimum, and, if so, where it is situated, then arises. A more general formulation of this problem is as follows: what is the stable configuration of the nuclei, their dynamics, and energy spectra in the presence of the JT effect? To answer this question the shape of the APES of the system $\varepsilon(Q)$ in the configurational space of all nuclear displacements Q must be determined first. For a nondegenerate electronic state the expression for $\varepsilon(Q)$ is given by Eq. (2.8). If the electronic state is f-fold degenerate, the APES has f sheets $\varepsilon_k(Q)$, $k = 1, 2, \ldots, f$, which intersect at the point of degeneracy $Q_{\Gamma\gamma} = 0$. The functions $\varepsilon_k(Q)$ are determined by the secular equation (2.42).

Before proceeding to the solution of Eq. (2.42) for specific JT problems, some general considerations may be appropriate. First we separate the totally symmetric part of the diagonal matrix elements of the quadratic vibronic interactions, which is the force constant K_Γ^Γ (Section 2.4). Then we choose the initial *reference configuration* of the system at the point $Q_{\Gamma\gamma} = 0$ and assume that the proper anharmonicity (Section 2.4) may be neglected. Under these conditions (see [3.1, 3.2] for more details) the following expressions can be

obtained (the Γ superscript denoting the electronic term symmetry is hereafter omitted where possible):

$$\varepsilon_k(Q) = \frac{1}{2}\sum_{\Gamma\gamma} K_\Gamma Q_{\Gamma\gamma}^2 + \varepsilon_k^v(Q), \qquad k = 1, 2, \ldots, f, \tag{3.1}$$

where $\varepsilon_k^v(Q)$ are the roots of the secular equation of the type (2.42) written here in a converted form:

$$\left\| W_{\gamma\gamma'}^v - \varepsilon^v I \right\| = 0, \qquad \gamma, \gamma' = 1, 2, \ldots, f. \tag{3.2}$$

Here $W_{\gamma\gamma'}^v$ is an $f \times f$ matrix in which, unlike Eq. (2.42), the diagonal matrix elements $W_{\gamma\gamma}^v$ do not contain the totally symmetric part of the quadratic terms used in formation of the force constant K_Γ^Γ, and I is a unit matrix of the same order f.

With the adiabatic potential $\varepsilon_k(Q)$ known, the vibronic system of equations (2.6), which determine the nuclear energy spectrum and dynamics, can be solved (in principle). However, the *determination of the APES is of special, independent interest*. In the region of nuclear configurations far from the point of degeneracy (especially near the minima of the APES in the case of strong vibronic coupling), the energy gap between different sheets of the APES can be sufficiently large. In this case the nuclei may be approximately treated semiclassically as moving along the APES. Knowledge of the shape of this surface makes possible qualitative analysis of the nuclear behavior, and the information thus obtained may sometimes be as important as that deduced from the numerical solution of the vibronic equations (2.6).

To calculate the matrix elements $W_{\gamma\gamma'}^v$ in Eq. (3.2) we should turn to specific JT problems. The simplest one, mentioned above, is $E \otimes (b_1 + b_2)$ or its particular case $E \otimes b_1$ (or $E \otimes b_2$). These problems are possible for systems possessing symmetry axes of fourth order or multiples of four, for which, according to group theory, $[E \times E] = A_1 + B_1 + B_2$. The full problem is thus $E \otimes (a_1 + b_1 + b_2)$, but since the totally symmetric coordinates of A_1 type do not distort the symmetry of the system, they can be neglected in the general consideration (however, they may be significant in special cases).

In the remaining $E \otimes (b_1 + b_2)$ problem the two JT-active modes $Q_{b_1} \equiv Q_1$ and $Q_{b_2} \equiv Q_2$ (Fig. 2.2), and two linear $F_{b_1} \equiv F_1$ and $F_{b_2} \equiv F_2$ vibronic constants should be introduced:

$$\begin{aligned} F_1 &= \langle B_1 | (\partial V/\partial Q_1)_0 | B_1 \rangle = -\langle B_2 | (\partial V/\partial Q_1)_0 | B_2 \rangle \\ F_2 &= \langle B_1 | (\partial V/\partial Q_2)_0 | B_2 \rangle \end{aligned} \tag{3.3}$$

where $|B_1\rangle$ and $|B_2\rangle$ are the two wavefunctions of the E term in systems with fourfold symmetry transforming as $x^2 - y^2$ and xy, respectively. The matrix W in the second-order secular equation (3.2) is thus

$$W = \begin{bmatrix} F_1Q_1 & F_2Q_2 \\ F_2Q_2 & -F_1Q_1 \end{bmatrix} \tag{3.4}$$

with the solutions for ε,

$$\varepsilon_{\pm}^{v} = \pm(F_1^2Q_1^2 + F_2^2Q_2^2)^{\frac{1}{2}}$$

Taking the two primary force constants as $K_{b_1} \equiv K_1$ and $K_{b_2} \equiv K_2$, we get the following expression for the two APES (Fig. 3.1(a)):

$$\varepsilon_{\pm}(Q_1,\ Q_2) = \tfrac{1}{2}(K_1Q_1^2 + K_2Q_2^2) \pm (F_1^2Q_1^2 + F_2^2Q_2^2)^{\frac{1}{2}} \tag{3.5}$$

Its two extrema points and JT stabilization energies are

$$Q_1^{(0)} = \pm F_1/K_1, \qquad Q_2^{(0)} = 0, \qquad E_{\mathrm{JT}}^{(1)} = F_1^2/2K_1 \tag{3.6}$$

and

$$Q_1^{(0)} = 0, \qquad Q_2^{(0)} = \pm F_2/K_2, \qquad E_{\mathrm{JT}}^{(2)} = F_2^2/2K_2 \tag{3.7}$$

For the two wavefunctions presented as $a_1|B_1\rangle + a_2|B_2\rangle$ the solution at the point (3.6) yields $a_1 = 1$, $a_2 = 0$ and $a_1 = 0$, $a_2 = 1$, while for (3.7) $a_1 = 1/\sqrt{2}$ and $a_2 = \pm 1/\sqrt{2}$, respectively.

The new curvatures K_1' and K_2', in comparison with K_{01} and K_{02} without the vibronic interaction, are given by the following relations:

$$K_1' = K_{01}, \qquad K_2' = K_{02}[1 - (E_{\mathrm{JT}}^{(2)}/E_{\mathrm{JT}}^{(1)})] \tag{3.8}$$

at the points (3.6), and

$$K_1' = K_{01}[1 - (E_{\mathrm{JT}}^{(1)}/E_{\mathrm{JT}}^{(2)})], \qquad K_2' = K_{02} \tag{3.9}$$

at the points (3.7).

It follows that if $E_{\mathrm{JT}}^{(1)} > E_{\mathrm{JT}}^{(2)}$, the points (3.6) are minima and those of (3.7) are saddle points, and if $E_{\mathrm{JT}}^{(1)} < E_{\mathrm{JT}}^{(2)}$, the opposite is true: the points (3.7) are minima and those of (3.6) are saddle points. If $E_{\mathrm{JT}}^{(1)} = E_{\mathrm{JT}}^{(2)}$, an elliptical trough of equal-energy minima is realized, and if $F_1/K_1 = F_2/K_2$, the trough is circular, similar to the $E \otimes e$ problem (Section 3.2). If the vibronic coupling with one of the JT-active modes is negligible (one of the vibronic constants is small

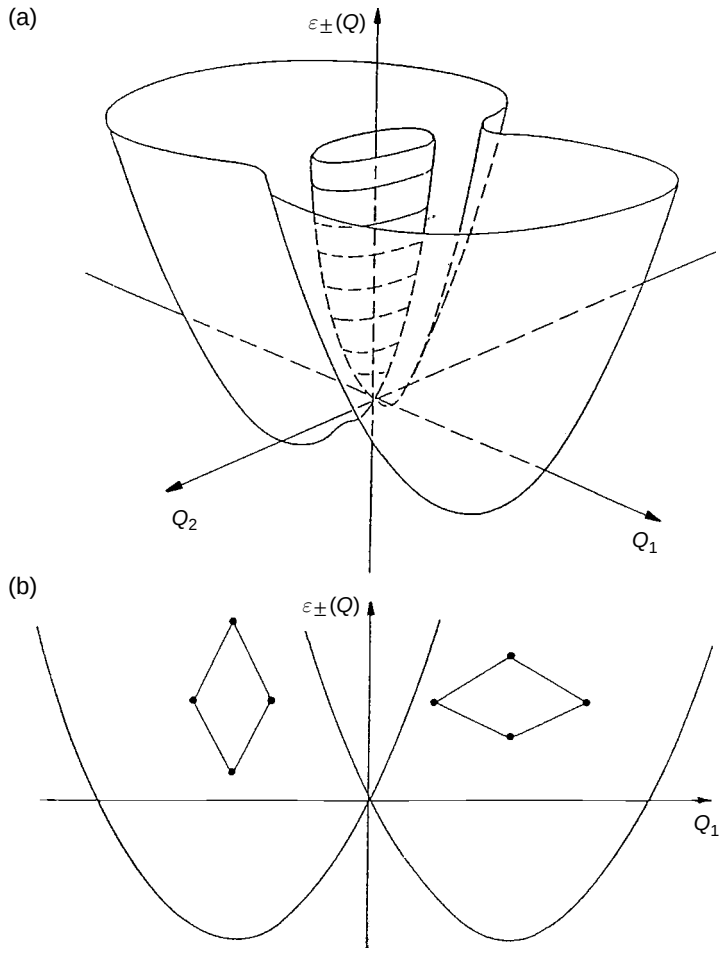

Fig. 3.1. The APES of a quadratic X_4 molecule in an E state linearly coupled to b_1 and b_2 displacement ($E \otimes (b_1 + b_2)$ problem) when $E_{JT}^{(1)} > E_{JT}^{(2)}$: (a) general view; and (b) cross-section along the Q_1 coordinate ($E \otimes b_1$ problem) with illustration of distortions of the square at the minimum points.

compared with the other), we obtain the $E \otimes b_1$ problem, its APES shape being shown in Fig. 3.1(b). In a recent work [3.3] the case of $E_{JT}^{(1)} = E_{JT}^{(2)}$ was analyzed under the condition of $K_1 \neq K_2$ that results in an APES with an elliptical trough of equivalent minima. The author [3.3] shows that under certain conditions the classical motion in such an elliptical trough may become chaotic.

Upon taking into account the quadratic terms of the vibronic interactions a coexistence of both types of minima, (3.6) and (3.7), becomes possible [3.4]. Indeed, with the quadratic terms of the vibronic coupling W of Eq. (2.18)

included the matrix elements of the secular Eq. (3.4) contain terms $Q_a Q_1$ and $Q_a Q_2$, where Q_a is the totally symmetric displacement:

$$W = \begin{bmatrix} F_1 Q_1 + G_1 Q_a Q_1 & F_2 Q_2 + G_2 Q_a Q_2 \\ F_2 Q_2 + G_2 Q_a Q_2 & -F_1 Q_1 - G_1 Q_a Q_1 \end{bmatrix} \tag{3.10}$$

Here the quadratic vibronic coupling constants $G_1 \equiv G(A \times B_1)$ and $G_2 \equiv G(A \times B_2)$ of Eq. (2.19) are introduced; for the terms Q_1^2, Q_2^2, and $Q_1 Q_2$ the quadratic vibronic coupling constants vanish.

The solution of Eq. (3.10) is straightforward. Together with the harmonic terms it yields the following two sheets of the APES in the space of the three coordinates Q_a, Q_1, and Q_2:

$$\begin{aligned} \varepsilon_{\pm}(Q_a, Q_1, Q_2) = {} & \tfrac{1}{2}(K_1 Q_1^2 + K_2 Q_2^2 + K_a Q_a^2) \\ & \pm [(F_1 + G_1 Q_a)^2 Q_1^2 + (F_2 + G_2 Q_a)^2 Q_2^2]^{\frac{1}{2}} \end{aligned} \tag{3.11}$$

As in the linear case, this APES has two kinds of stationary points:

$$\begin{aligned} Q_1^0 &= \pm \frac{F_1 K_a}{K_1 K_a - G_1^2} \\ Q_2^0 &= 0 \\ Q_a^0 &= \frac{F_1 G_1}{K_1 K_a - G_1^2} \end{aligned} \tag{3.12}$$

which feature the b_1 (rhombic) distortion, and

$$\begin{aligned} Q_1^0 &= 0 \\ Q_2^0 &= \pm \frac{F_2 K_a}{K_2 K_a - G_2^2} \\ Q_a^0 &= \frac{F_2 G_2}{K_2 K_a - G_2^2} \end{aligned} \tag{3.13}$$

for the b_2 (rectangular) distortions. The two correct first-order wavefunctions remain the same as in the linear case. The energy depths of these stationary points read off the point of degeneracy, the *JT stabilization energy*, are

$$E_{JT}^{b_1} = \frac{F_1^2 K_a}{2(K_1 K_a - G_1^2)} \tag{3.14}$$

$$E_{JT}^{b_2} = \frac{F_2^2 K_a}{2(K_2 K_a - G_2^2)} \tag{3.15}$$

The minimum conditions for the stationary points (3.12) and (3.13) show [3.4] that the b_1 points (3.12) are minima (rhombic distortions) when

$$K_1 K_a > G_1^2$$

and

$$\frac{F_1^2}{K_1} > \frac{F_2^2}{K_2}\left(1 + \frac{G_1(F_1G_2 - F_2G_1)}{K_1K_aF_2}\right)^2 \tag{3.16}$$

while the b_2 points (rectangular distortions) became minima when

$$K_2 K_a > G_2^2$$

$$\frac{F_2^2}{K_2} > \frac{F_1^2}{K_1}\left(1 + \frac{G_2(F_2G_1 - F_1G_2)}{K_1K_aF_1}\right)^2 \tag{3.17}$$

It is seen from the formulas (3.16) and (3.17) that in the linear approximation when G_1, $G_2 \to 0$ only one type of minima may exist, either b_1 or b_2, because the presence of one type of minima excludes the other type. However, if the quadratic vibronic constants G_1 and G_2 are nonzero, there are ranges of parameter values dependent on the second terms in the brackets of Eqs. (3.16) and (3.17) where the *two types of minima coexist*. The coexistence area may be reached with small G_1 and G_2 values when $F_1^2/K_1 \sim F_2^2/K_2$. Figure 3.2 illustrates the two minima in the Q_a space for the following parameter values [3.4] (F_1 and F_2 in $10^3\,\mathrm{cm}^{-1}/\text{Å}$, K and G values in $10^4\,\mathrm{cm}^{-1}/\text{Å}^2$): $F_1 = 3$, $F_2 = 1$, $K_a = 2$, $K_1 = 1.8$, $K_2 = 4$, $G_1 = 1$, and $G_2 = -0.5$. These parameters are arbitrary but reasonable. Since in this numerical example $F_1^2/K_1 = 2F_2^2/K_2$, the distortion is rhombic when the quadratic coupling is ignored, while a local minimum that is higher in energy (attainable at higher temperatures) occurs when the

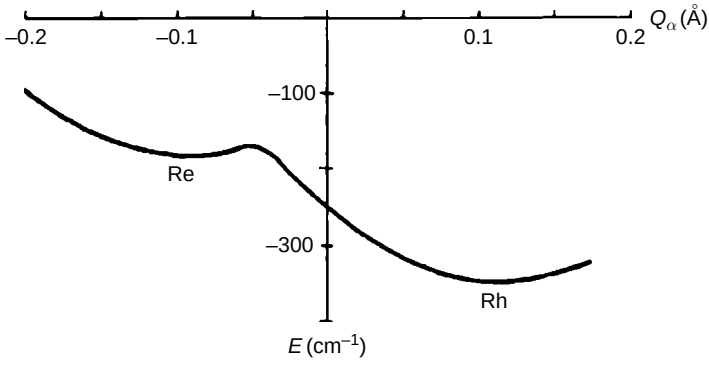

Fig. 3.2. A cross-section of the APES of the $E \otimes (a + b_1 + b_2)$ problem along the projection on the Q_a axis connecting rhombic (Rh) and rectangular (Re) minima (obtained by *ab initio* calculations with parameter values given in the text) [3.4].

quadratic coupling is included. Quadratic coupling reduces also the barrier height between the two equivalent rhombic distortions.

Coexistence of two (or several) kinds of distortions described by local (nonequivalent) minima on the APES seems to be of general importance in JT systems, and we will come back to the discussion of this phenomenon in later sections (see, e.g., Section 3.3).

3.2 The $E \otimes e$ problem

The JT problem for a molecular system in an orbital doubly degenerate electronic E state interacting with doubly degenerate e modes, *the* $E \otimes e$ *problem*, is one of the simplest and most widespread. As mentioned above, E terms are possible for molecules which possess at least one axis of symmetry of not less than third order (see the appendix). The triangular molecules of the type X_3 and triangular-pyramidal, tetrahedral, octahedral, cubic, icosahedral, pentagonal, and hexagonal molecular systems are among those having two-fold degenerate E terms in the ground or excited states that interact with e displacements shown in Figs. 2.1–2.4. In this problem $[E \times E] = A_1 + E$ and hence in addition to the e vibrations the totally symmetric vibrations a_1 may be effective, so *the problem is in fact* $E \otimes (a_1 + e)$.

Consider first the $E \otimes e$ problem. The two electronic wavefunctions of the E term may be denoted by $|\vartheta\rangle$ and $|\varepsilon\rangle$ with symmetry properties of the well-known functions $\vartheta \sim 3z^2 - r^2$ and $\varepsilon \sim x^2 - y^2$ (or $\vartheta \sim d_{z^2}$ and $\varepsilon \sim d_{x^2-y^2}$ in the transition metal d function nomenclature). The two components of the normal E-type (tetragonal) displacements Q_ϑ and Q_ε are illustrated in Fig. 2.4, while the expressions in Cartesian coordinates of the nuclei are given in Table 2.2. Accordingly, the matrix elements $W^v_{\gamma\gamma'}$ and hence $\varepsilon^v_k(Q)$ in Eq. (3.2) depend only on these two coordinates. In all the other coordinates the APES, in line with Eq. (3.1), retains a simple parabolic form:

$$\varepsilon_k(Q) = \frac{1}{2} \sum_{\Gamma\lambda, \Gamma \neq E} K_\Gamma Q^2_{\Gamma\gamma} \tag{3.18}$$

Using the definition of vibronic constants introduced above (see Eqs. (2.15) and (2.19) and the Wigner–Eckart theorem (2.16)), we can evaluate the remaining four nonzero matrix elements of the vibronic interaction W by means of one linear and one quadratic constant. Denote, respectively,

$$F_E = \langle\vartheta|\left(\frac{\partial V}{\partial Q_\vartheta}\right)_0|\vartheta\rangle, \qquad G_E = \langle\vartheta|\left(\frac{\partial^2 V}{\partial Q_\vartheta\, \partial Q_\varepsilon}\right)_0|\varepsilon\rangle \tag{3.19}$$

Then, retaining only the linear and second-order terms in Q, the explicit form of W in Eq. (3.2) for the $E \otimes e$ problem is [3.5]

$$W = \begin{vmatrix} F_E Q_\vartheta + G_E(Q_\vartheta^2 - Q_\varepsilon^2) & -F_E Q_\vartheta + 2G_E Q_\vartheta Q_\varepsilon \\ -F_E Q_\vartheta + 2G_E Q_\vartheta Q_\varepsilon & -F_E Q_\vartheta - G_E(Q_\vartheta^2 - Q_\varepsilon^2) \end{vmatrix} \tag{3.20}$$

In the matrix form it can be presented as

$$W = F_E(Q_\vartheta \hat{\sigma}_z - Q_\varepsilon \hat{\sigma}_x) + G_E[(Q_\vartheta^2 - Q_\varepsilon^2)\hat{\sigma}_z + 2Q_\vartheta Q_\varepsilon \hat{\sigma}_x] \tag{3.20'}$$

where some of the Pauli matrices,

$$\begin{aligned} \hat{\sigma}_x &= \begin{bmatrix} 0 & 1 \\ 1 & 0 \end{bmatrix} & \hat{\sigma}_y &= \begin{bmatrix} 0 & -i \\ i & 0 \end{bmatrix} \\ \hat{\sigma}_z &= \begin{bmatrix} 1 & 0 \\ 0 & -1 \end{bmatrix} & \hat{\sigma}_0 &= \begin{bmatrix} 1 & 0 \\ 0 & 1 \end{bmatrix} \end{aligned} \tag{3.20''}$$

are employed.

In polar coordinates

$$Q_\vartheta = \rho \cos\phi, \qquad Q_\varepsilon = \rho \sin\phi \tag{3.21}$$

the solution to Eq. (3.2) with the matrix W from (3.20) is

$$\varepsilon_\pm^v(\rho, \phi) = \pm\rho[F_E^2 + G_E^2\rho^2 + 2F_E G_E \rho \cos(3\phi)]^{\frac{1}{2}} \tag{3.22}$$

Substitution of these values into Eq. (3.1) yields the following expression for the APES in the space of Q_ϑ and Q_ε coordinates:

$$\varepsilon_\pm^v(\rho, \phi) = \tfrac{1}{2}K_E\rho^2 \pm \rho[F_E^2 + G_E^2\rho^2 + 2F_E G_E \rho \cos(3\phi)]^{\frac{1}{2}} \tag{3.23}$$

In particular, in the linear coupling case [3.6], i.e. neglecting quadratic terms ($G_\mathrm{E} = 0$) this surface simplifies to

$$\varepsilon_\pm^v(\rho, \phi) = \tfrac{1}{2}K_E\rho^2 \pm |F_E|\rho \tag{3.24}$$

We see that in this linear approximation the APES is independent of the angle ϕ and has the form of a surface of revolution, often called the "*Mexican hat*" (Fig. 3.3). The radius ρ_0 of the circle at the bottom of the trough and its depth, read off from the degeneracy point at $\rho = 0$, *the JT stabilization energy* E_{JT}^E, are given by the relationships

$$\rho_0 = |F_E|/K_E \tag{3.26}$$

$$E_{\mathrm{JT}}^E = F_E^2/2K_E \tag{3.27}$$

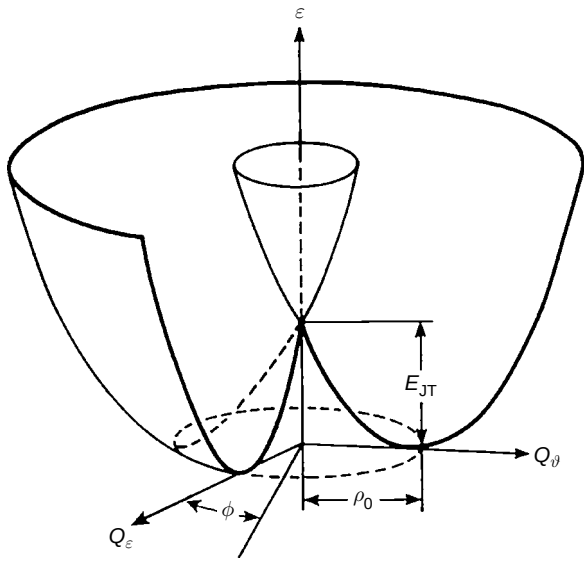

Fig. 3.3. The APES for a twofold degenerate E term interacting linearly with the twofold degenerate E-type vibrations described by Q_ϑ and Q_ε coordinates with a conical intersection at $Q_\vartheta = Q_\varepsilon = 0$ (linear $E \otimes e$ problem, the "*Mexican hat*"). E_{JT} is the JT stabilization energy, ρ_0 is the radius of the trough (reprinted with permission from [3.25]. Copyright 1996 John Wiley & Sons, Inc.).

If the quadratic terms in W are taken into account, this surface warps, and along the bottom of the trough of the "Mexican hat" three wells occur, alternating regularly with three humps (Figs. 3.4 and 3.5). The extrema points (ρ_0, ϕ_0) of the APES (3.23) are

$$\rho_0 = \frac{\pm F_E}{K_E \mp (-1)^n 2G_E}, \qquad \phi_0 = n\pi/3, \qquad n = 0, 1, \ldots, 5 \tag{3.28}$$

the upper and lower signs corresponding to cases $F_E > 0$ and $F_E < 0$, respectively. If $F_E G_E > 0$, the points with $n = 0$, 2, and 4 are minima, while those with $n = 1$, 3, and 5 are saddle points, whereas for $F_E G_E < 0$ these two types of extrema points interchange. For the JT stabilization energy we get

$$E_{\mathrm{JT}} = F_E^2/2(K_E - 2|G_E|) \tag{3.29}$$

while the minimal barrier height δ between the minima is

$$\delta = 4E_{\mathrm{JT}}|G_E|/(K_E + 2|G_E|) \tag{3.30}$$

In the linear approximation the curvature K at the bottom of the trough is the same at all points. Along the trough $K_\phi = 0$ and in the perpendicular

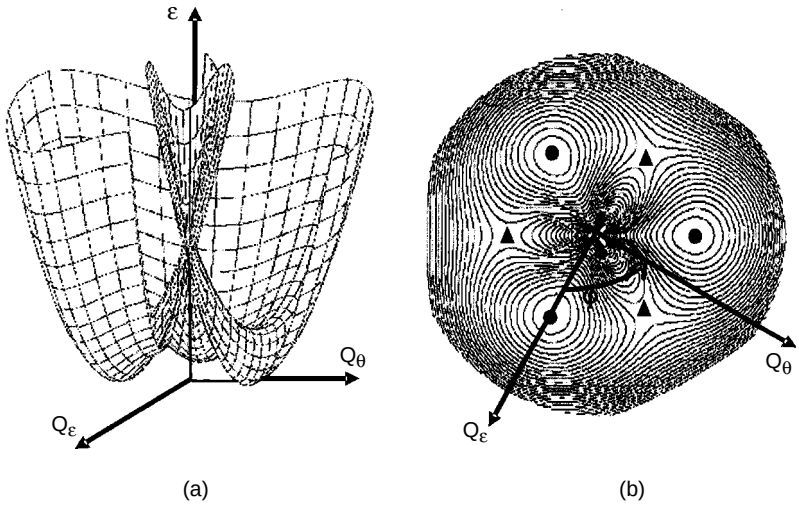

Fig. 3.4. The APES for the $E \otimes e$ problem with both the linear and quadratic terms of the vibronic interaction included: (a) general view (the "*tricorn*"); (b) equipotential sections of the lower sheet; three minima and three saddle points are indicated by black circles and triangles, respectively (courtesy of P. Garcia-Fernandez).

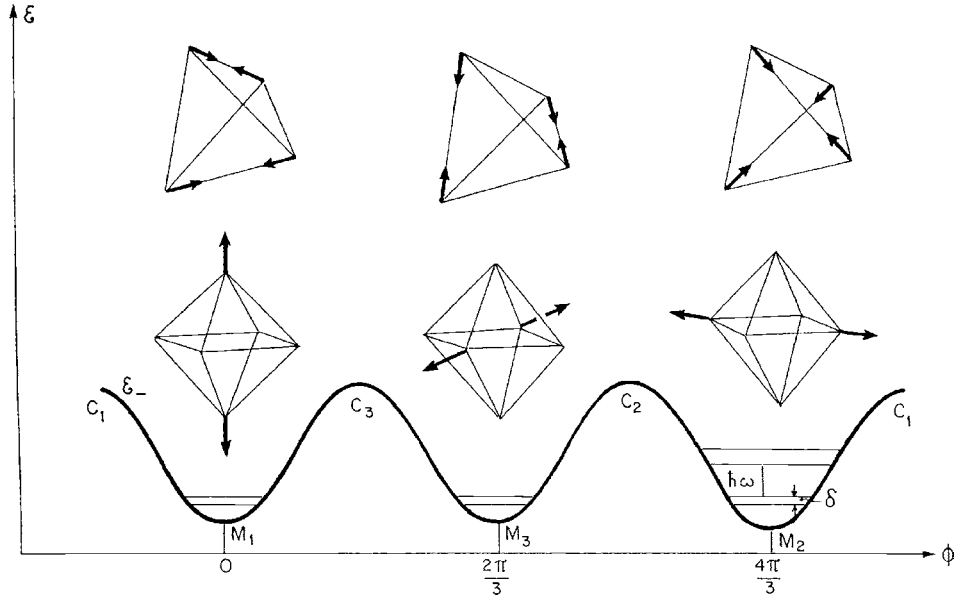

Fig. 3.5. The section of the lowest sheet ε_- of the APES of the quadratic $E \otimes e$ problem along the line of steepest slope that connects the minima and saddle points in Fig. 3.4, with illustration of the distortions of octahedral and tetrahedral systems at the points of minima.

(radial) direction $K_\rho = K_E$, while in the absence of vibronic coupling $K_\phi = K_\rho = K_E$; in the denotation of the tetragonal symmetry of the minima $K_\rho = K_A$ and $K_\phi = K_B$. Taking into account the quadratic terms, we obtain at the minima [3.1]

$$K_\rho = K_E - 2|G_E|, \qquad K_\phi = 9|G_E|(K_E - 2|G_E|)/(K_E - |G_E|) \tag{3.31}$$

It follows that if $2|G_E| > K_E$, the system under consideration has no minima at the point ρ_0 and decomposes, provided higher-order terms in Q in the vibronic coupling W, neglected above, do not make the system stable at larger distances (see in Chapter 5). At the minima points the curvature equals the force constant, which is proportional to the square of the frequency of the corresponding vibrations.

The two wavefunctions $\psi_\pm$, which are the solutions of the perturbation problem (3.20), corresponding to the two sheets (3.22) are

$$\begin{aligned} \psi_-(\rho,\phi) &= \cos(\mathbf{\Omega}/2)|\vartheta\rangle - \sin(\mathbf{\Omega}/2)|\varepsilon\rangle \\ \psi_+(\rho,\phi) &= \sin(\mathbf{\Omega}/2)|\vartheta\rangle + \cos(\mathbf{\Omega}/2)|\varepsilon\rangle \end{aligned} \tag{3.32}$$

where

$$\tan\mathbf{\Omega} = \frac{F_E \sin\phi - |G_E|\rho\sin(2\phi)}{F_E\cos\phi + |G_E|\rho\cos(2\phi)} \tag{3.33}$$

It is often assumed that $\mathbf{\Omega} = \phi$, which is true only in the absence of quadratic vibronic coupling ($G_E = 0$).

As seen from Figs. 3.3 and 3.4, the point of degeneracy on the APES is a conical intersection, which was shown to be very important in JT problems, especially in relation to the topological phase problem (Section 5.7). There may be more than one conical intersection in the $E \otimes e$ problem (see below in this section), and they affect strongly the spectroscopic properties of JT systems (Sections 5.2 and 5.3). The known shapes of the symmetrized displacements Q_ϑ and Q_ε and their values at the minima points can be used to determine the corresponding JT distortions of different types of molecules. Some distortions for tetrahedral and octahedral systems are illustrated in Fig. 3.5.

The motion of the nuclei can be investigated properly by solving Eq. (2.6) with the APES obtained above. However, some qualitative features of the nuclear behavior, as indicated earlier, can be clarified in the *semiclassical approximation* by considering the nuclei moving along the APES. This treatment has some physical basis when the energy gap between different APES sheets is sufficiently large, i.e., for strong vibronic coupling and for nuclear

configurations near the minima of the lowest (ground) sheet where in the $E \otimes e$ problem the gap equals $4E_{JT}$.

If only linear terms are considered, i.e., when the lowest sheet of the APES has the shape of a "Mexican hat," *the nuclear configuration performs free rotations in the space of Q_ϑ and Q_ε coordinates along the circle of minima in the trough*. In this case [3.7] each atom of, say, a triangular molecule X_3, describes a circle of radius $\rho_0\sqrt{3}$. The variation of the Cartesian coordinates of the atoms x_i, y_i $(i = 1, 2, 3)$ during the motion of the system along the trough is given by the following expressions:

$$\begin{aligned} x_1 &= (1/\sqrt{3})\rho\cos\phi, & y_1 &= (1/\sqrt{3})\rho\sin\phi \\ x_2 &= (1/\sqrt{3})\rho\cos[\phi - (2\pi/3)], & y_2 &= (1/\sqrt{3})\rho\sin[\phi - (2\pi/3)] \\ x_3 &= (1/\sqrt{3})\rho\cos[\phi - (4\pi/3)], & y_3 &= (1/\sqrt{3})\rho\sin[\phi - (4\pi/3)] \end{aligned} \tag{3.34}$$

It is seen that the circular motions of these atoms are correlated: the vectors of their displacements are shifted in phase through an angle of $2\pi/3$ (Fig. 3.6). At any instant of time the equilateral triangle X_3 is distorted into an isosceles triangle, and *this distortion travels as a wave around the triangle's geometric center* performing a specific internal rotation.

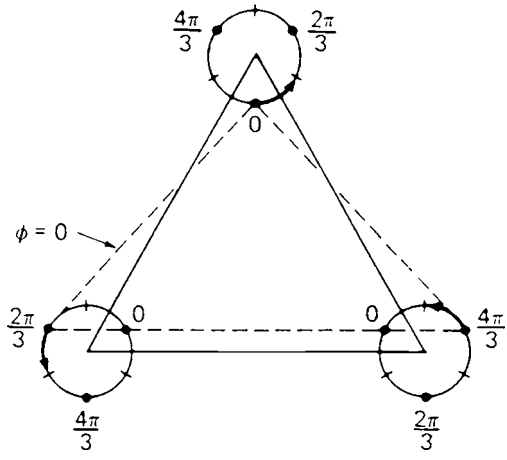

Fig. 3.6. Distortions of a triatomic molecule X_3 caused by moving along the bottom of the trough of the lowest sheet of the APES in the linear $E \otimes e$ problem. Each of the three atoms moves along a circle, their phases being concerted. The bold points indicate the minima positions when quadratic terms are taken into account. The dashed triangle corresponds to the point $\phi = 0$ in Eq. (3.23) ($Q_\varepsilon = 0$, $Q_\theta = \rho$ in Fig. 3.3), and the case of compressed triangles is shown; with the opposite sign of the vibronic coupling constant the triangles are elongated.

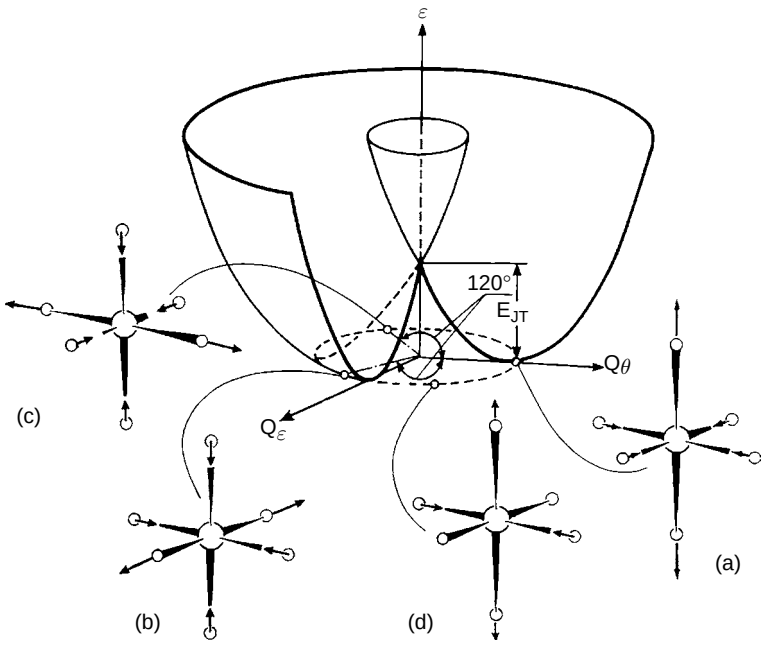

Fig. 3.7. Distortions of an octahedral system ML_6 at different points along the bottom of the trough of the "Mexican hat" in the linear $E \otimes e$ problem. At the points $\phi = 0$, $2\pi/3$, and $4\pi/3$ the octahedron is tetragonally distorted along the three fourfold axes, respectively (a)–(c). In between these points the configuration has D_{2h} symmetry (d) and varies continuously from one tetragonal configuration to another.

In the case of an octahedral molecule, which in a trigonal projection looks like two equilateral triangles, the two deformation waves traveling around each of the latter are opposite in phase. As a result the octahedron becomes elongated (or compressed) alternatively along one of the three fourfold axes and simultaneously compressed (or elongated) along the remaining two axes (Fig. 3.7). For more on trajectories in different JT problems see in [3.8].

When the quadratic terms of the vibronic interaction are taken into account, the lowest sheet of the APES has three minima, at each of which the octahedron is elongated (or compressed) along one of the three axes of order four (Fig. 3.4). *The nuclear motions along the APES surface* when allowing for quantum effects *are likewise hindered rotations and tunneling transitions between the minima*. Starting with the configuration in one of these minima, the JT dynamics in this case may be presented, by way of illustration, as *"pulse" motions*, (or "fluctuations") along the three axes, which are discussed in Chapter 5.

As indicated earlier, since $[E \times E] = A_1 + E$, the totally symmetric displacements of A_1 type are also JT active in the twofold degenerate E state (as in all

the other cases): strictly speaking, in general the $E \otimes (e + a_1)$ problem must be solved instead of the $E \otimes e$ problem considered above. However, totally symmetric displacements do not change the molecular symmetry; they change proportionally only the interatomic distances. Therefore, considering vibronic effects, it may be assumed that the reference configuration is taken at a new minimum position with regard to the A_1 coordinates, so that the interaction with the a_1 displacements, as with all other JT-inactive modes, becomes unimportant here. This cannot be done when one has to compare vibronic effects in different systems or in a series of systems, for which the a_1 displacement contributions may be different. For this and other reasons the more rigorous expressions for the APES, which include interaction with all the active modes, may be useful.

Let us denote the linear vibronic constant and the corresponding force constant for totally symmetric displacements ρ_A by F_A and K_A, respectively. Then the APES is as follows [3.5]:

$$\begin{aligned}\varepsilon(\rho_A,\ \rho,\ \phi) = {} & \tfrac{1}{2}K_A\rho_A^2 - F_A\rho_A + \tfrac{1}{2}K_E\rho^2 \\ & \pm \{F_E^2 + G_E^2\rho^2 + 2F_EG_E[\rho\cos(3\phi) - 2\sqrt{2}\rho_A] \\ & + 4G_E^2\rho_A[2\rho_A - \sqrt{2}\rho\cos(3\phi)]\}^{\frac{1}{2}}\end{aligned} \tag{3.35}$$

The extrema points for this surface are (cf. Eq. (3.28))

$$\begin{aligned}\rho_0 &= \frac{\pm(F_E + 2\sqrt{2}\beta F_A)}{K_E \mp (-1)^n 2G_E - 4\beta G_E} \\ \rho_{A0} &= F_A/K_A \pm 2\sqrt{2}\beta\rho_0 = \rho_{A0}^0 \pm 2\sqrt{2}\beta\rho_0\end{aligned} \tag{3.36}$$

where $\beta = G_E/K_E$ characterizes the role of the quadratic terms of vibronic interactions with respect to the "homogeneous hardness" of the system K_A.

In strongly coupled $E \otimes e$ problems the totally symmetric (breathing) mode alters a variety of properties, in particular, the absorption spectra (Section 6.1).

Note that Eqs. (3.28)–(3.33), as well as (3.35) and (3.36), are deduced under the assumption that $G_E < K_E$, i.e. the quadratic coupling is small. In the limit $G_E \ll K_E$ the following approximate formulas can be useful for estimation of parameters:

$$\begin{aligned}E_{\mathrm{JT}} &\approx F_E^2/2K_E \\ \rho_0 &= F_E/K_E \\ \delta &\approx 4E_{\mathrm{JT}}|G_E|/K_E\end{aligned} \tag{3.37}$$

In more widespread notations in dimensionless units with energy in $\hbar\omega$ units, time in ω^{-1}, length in $(\hbar/m\omega)^{1/2}$, and normal coordinates in mass-weighted length $(\hbar/\omega)^{1/2}$, we have $K_E = 1$, $F_E = k$, $G_E/K_E = g/2$, $D = E_{\mathrm{JT}}/\hbar\omega = k^2/2$, $\delta/\hbar\omega = k^2 g$, and Eq. (3.23) can be written in the following form:

$$\varepsilon_{\pm}(\rho,\ \phi) = \tfrac{1}{2}\rho^2 \pm \rho[k^2 + \tfrac{1}{4}g^2\rho^2 + kg\rho\cos(3\phi)]^{\frac{1}{2}} \tag{3.38}$$

If cubic terms are included in the vibronic coupling, the two branches of the APES look as follows [3.9a]:

$$\begin{aligned}\varepsilon_{\pm}(\rho,\ \phi) =& \tfrac{1}{2}\rho^2 + \gamma\rho^3\cos(3\varphi) \\ &\pm \rho\{k^2 + kg\rho\cos(3\varphi) + [2k\gamma_1 + (1/4)g^2]\rho^2 - g\gamma_1\rho^3\cos(3\varphi) + \gamma_1^2\rho^4\}^{\frac{1}{2}}\end{aligned} \tag{3.39}$$

where in addition to the constants above we introduced anharmonicity constants: γ, the totally symmetric part of the matrix elements of the cubic terms of W in Eq. (2.18), meaning the usual (nonvibronic) anharmonicity constant, and γ_1, the E-symmetry part of these cubic terms that emerge due to the electronic degeneracy. As we see from this formula, the cubic terms produce qualitatively the same APES warping (resulting in three minima) as the quadratic coupling terms, so the question of their relative contributions to this warping emerges [3.9a]. For contributions of higher order terms see [3.9(*b*)].

An important development of the $E \otimes e$ problem emerged recently when it was realized that since the linear and quadratic coupling terms of the vibronic interaction W in Eq. (2.14) are described by rather independent constants, the quadratic coupling is not necessarily small compared with the linear coupling. If the quadratic coupling is sufficiently large, the form of the APES and all the consequent properties change essentially. Indeed, as seen from Eq. (3.23) or (3.38), the two branches of the APES in this case intersect not only at $\rho = 0$ (central conical intersection), but also at

$$\rho = 2k/g, \qquad \phi = \pi/3, \pi, 5\pi/3 \tag{3.40}$$

These additional three conical intersection points are positioned along the three lines that include the central conical intersection and the three saddle points on the APES [3.10]. Figure 3.8 shows one of these points in the cross section of the APES with a plane containing the minimum M at $\phi = 0$, the saddle point at $\phi = \pi$, and two conical intersections, the central one C and the additional one in this direction. Figure 3.9 illustrates the APES with the three additional conical intersections [3.11]. Their presence was confirmed by direct

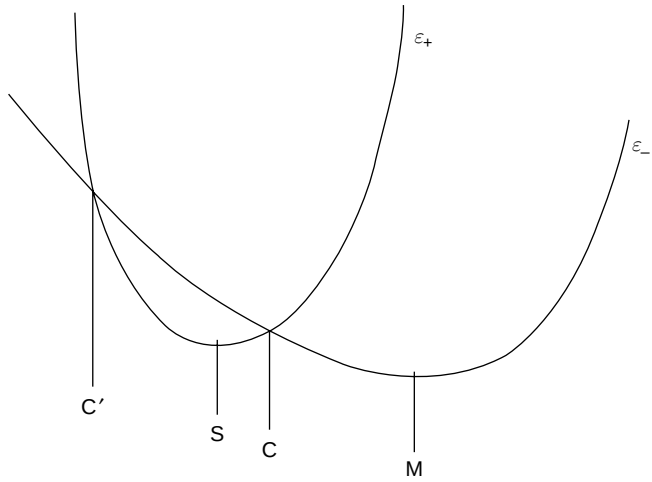

Fig. 3.8. A cross-section of the APES of an $E \otimes e$ system (with linear and quadratic terms included) with a plane containing one minimum M, the central conical intersection C, and a saddle point S. For sufficiently strong quadratic coupling an additional conical intersection C′ emerges at $\delta = 2k/g$. There are three (equivalent) such additional conical intersections on the APES (see Fig. 3.9).

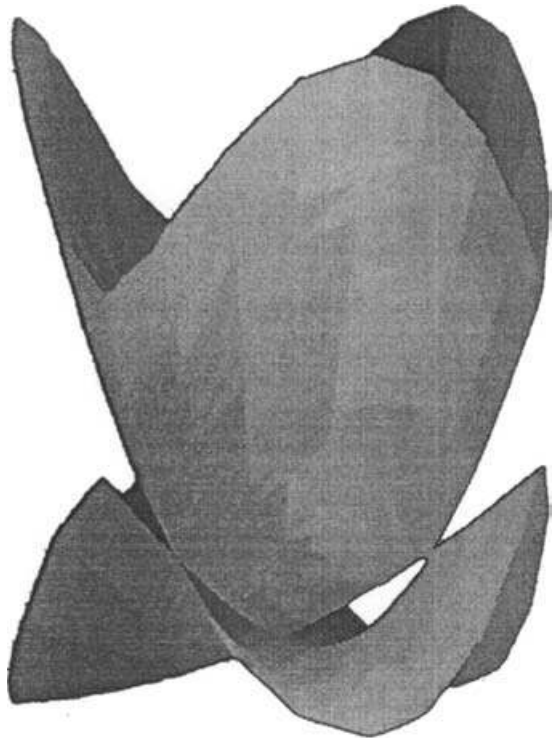

Fig. 3.9. A general view (conventional) of a part of the APES of an $E \otimes e$ system with strong quadratic coupling that produces three additional conical intersections (see Fig. 3.8) (courtesy of G. Bevilacqua).

numerical calculations for specific systems NiF_3 [3.12], Li_3 [3.13], and Na_3 [3.14], as well as in general for systems with $E \otimes e$ and $T \otimes t_2$ problems and different coupling constants [3.15, 3.16].

If g (or G_E) is small, the additional conical intersections are far away from the central conical intersections, the minima positions, and the saddle points, thus almost not affecting the main properties of the system. However, the quadratic coupling g may be sufficiently large, and then it affects dramatically the spectral properties, in particular, the tunneling splitting and our general understanding of the problem (Sections 5.2 and 5.3).

Another interesting development is related to APES of short-lived (metastable) states [3.17]. In application to linear and quadratic $E \otimes e$ problems, it was shown that by introducing an imaginary term in the equation of APES to stand for its lifetime, the JT coupling affects significantly both the form of the real APES (producing additional minima and conical intersections) and its imaginary part, the lifetime of the state under consideration. *Ab initio* calculations that allow for numerical estimations of these effects were carried out on Π-type resonance states of the tris(boramethyl)amine anion.

Further developments for the $E \otimes e$ problem are more related to the solution of the system of vibronically coupled Eqs. (2.6) than to just evaluation of the APES. Therefore they are discussed in Chapter 5.

3.3 $T \otimes e$, $T \otimes t_2$, $T \otimes (e + t_2)$, and $\Gamma_8 \otimes (e + t_2)$ problems for triplet and quadruplet terms

Threefold orbitally degenerate terms are possible for molecular systems with cubic or icosahedral symmetry point groups T, T_d, T_h, O, O_h, I, and I_h (see the appendix). There are two types of orbital triplets, T_1 and T_2. Since the vibronic effects in these two states are similar, the results obtained for one of them can be easily transferred to the other one. We consider first the term T_2. Its three functions, which transform as the coordinate products yz, xz, and xy, are denoted by $|\xi\rangle$, $|\eta\rangle$, and $|\zeta\rangle$, respectively. In the T term problem, distinct from the E case, there are five JT-active nontotally symmetric coordinates (Table 2.3): two tetragonal (E type), Q_ϑ and Q_ε, and three trigonal (T_2 type), Q_ξ, Q_η, and Q_ζ (see Fig. 2.3 and Table 2.2). For all the other (JT-inactive) coordinates the APES remains parabolic (i.e., they provide no vibronic contributions ε_k^ν in Eq. (3.1)). The JT problem is thus $T_2 \otimes (e + t_2)$.

With three electronic functions, the secular equation (3.2) that determines the vibronic contribution $\varepsilon_k^\nu(Q)$ to the APES is of third order. The matrix elements $W_{\gamma\gamma}^\nu$ contain two linear vibronic constant F_E and F_T and several

quadratic G_Γ depending on the number of nontotally symmetric tensor convolutions that can be prepared by different quadratic combinations of $Q_{E\gamma}$ and $Q_{T\gamma}$ (Section 2.4). It can be shown [3.1] that for a T term there may be four quadratic vibronic constants: $G_E(E \times E)$, $G_E(T \times T)$, $G_T(T \times T)$, and $G_T(E \times T)$.

Consider first the linear approximation for which all $G_\Gamma = 0$. Denote

$$F_E = \langle \zeta | \left(\frac{\partial V}{\partial Q_\vartheta} \right)_0 | \zeta \rangle, \qquad F_T = \langle \eta | \left(\frac{\partial V}{\partial Q_\xi} \right)_0 | \zeta \rangle \tag{3.41}$$

According to Eq. (2.16) all the matrix elements of the linear terms of the vibronic interaction can be expressed by means of these two constants, and the matrix W in the secular equation (3.2) for $\varepsilon_k^\nu(Q)$ takes the form [3.18]

$$W = \begin{bmatrix} F_E\left(\frac{1}{2}Q_\vartheta - \frac{\sqrt{3}}{2}Q_\varepsilon\right) & -F_T Q_\zeta & -F_T Q_\eta \\ -F_T Q_\zeta & F_E\left(\frac{1}{2}Q_\vartheta + \frac{\sqrt{3}}{2}Q_\varepsilon\right) & -F_T Q_\xi \\ -F_T Q_\eta & -F_T Q_\xi & -F_E Q_\vartheta \end{bmatrix} \tag{3.42}$$

The three roots of Eq. (3.2) with this matrix, $\varepsilon_k^\nu(Q)$, $k = 1, 2, 3$, are the three electronic parts of the surfaces in the five-dimensional space of the above five coordinates $Q_{\Gamma\gamma}$. Together with the elastic (nonvibronic) part in Eq. (3.1) they determine the three sheets of the APES (in the space of these coordinates), crossing at $Q_{\Gamma\gamma} = 0$:

$$\varepsilon_k(Q) = \tfrac{1}{2}K_E(Q_\vartheta^2 + Q_\varepsilon^2) + \tfrac{1}{2}K_T(Q_\xi^2 + Q_\eta^2 + Q_\zeta^2) + \varepsilon_k^\nu(Q), \qquad k = 1, 2, 3 \tag{3.43}$$

However, the analytical solution of Eq. (3.2) with W from Eq. (3.42) is difficult. In [3.18] a special procedure was worked out to determine the extrema points of the surface (3.43) without the full solution of Eq. (3.42). This procedure is based on the fact that the minimization of the expression (3.43) to find the extrema points is equivalent to solving a system of equations, which in the matrix form can be written as follows (for more details see [3.1, 3.18]). Denote (cf. Eqs. (3.1) and (3.2))

$$\hat{U} = \tfrac{1}{2}\sum_{\Gamma\lambda} K_\Gamma Q_{\Gamma\gamma}^2 I + W$$

where I is a unit matrix and W is the vibronic coupling matrix (both have the rank of the electronic degeneracy). Assume that $\hat{a}$ is the eigenvector (a column vector) of $\hat{U}$. Then we have

$$\hat{U}\hat{a} = \varepsilon\hat{a}, \qquad \hat{a}^+\hat{a} = 1, \qquad \hat{a}^+ \frac{\partial \hat{U}}{\partial Q_{\Gamma\gamma}} \hat{a} = 0 \tag{3.43$'$}$$

By solving these equations with respect to $Q_{\Gamma\gamma}$ we get the extrema points of the APES. It was also shown [3.18] how, by calculating second-order perturbation corrections to the energies at the extrema points, one can determine the kind of the latter: minimum, maximum, or saddle point.

This approach, which has widely been used to evaluate distortions in JT systems, was also extended to the so-called method of *isostationary functions* [3.19] in which the Eqs. (3.43′), which minimize the energy with respect to the nuclear coordinates, are transformed into equations for the electronic wavefunction coefficients.

To solve Eq. (3.2) using the method of [3.18], consider first the particular case when $F_T = 0$ while $F_E \neq 0$ (the $T \otimes e$ problem). In this case the matrix (3.42) is diagonal and Eq. (3.2) can be solved directly:

$$\begin{aligned} \varepsilon_1^v(Q_\vartheta,\ Q_\phi) &= -F_E Q_\vartheta \\ \varepsilon_2^v(Q_\vartheta,\ Q_\phi) &= F_E\left(\frac{1}{2}Q_\vartheta + \frac{\sqrt{3}}{2}Q_\varepsilon\right) \\ \varepsilon_2^v(Q_\vartheta,\ Q_\phi) &= F_E\left(\frac{1}{2}Q_\vartheta - \frac{\sqrt{3}}{2}Q_\varepsilon\right) \end{aligned} \tag{3.44}$$

Substitution of these solutions into Eq. (3.43) yields the APES consisting of a set of paraboloids, of which only those containing the tetragonal Q_ϑ and Q_ε coordinates have minima displaced from the origin. In these coordinates the surface has the shape of three equivalently displaced paraboloids intersecting at the point $Q_\vartheta = Q_\varepsilon = 0$ (Fig. 3.10). The positions of the three minima are given by the following coordinates:

$$(Q_0^E,\ 0), \qquad \left(\frac{1}{2}Q_0^E,\ \frac{\sqrt{3}}{2}Q_0^E\right), \qquad \left(\frac{1}{2}Q_0^E,\ -\frac{\sqrt{3}}{2}Q_0^E\right) \tag{3.45}$$

where $Q_0^E = F_E/K_E$. For the depth of the minima, the energy of JT stabilization, we have

$$E_{\mathrm{JT}}^E = F_E^2/2K_E \tag{3.46}$$

Note that the relief of the surface sheets near the point of degeneracy (Fig. 3.10) differs from that of the E term (Figs. 3.3 and 3.4): in the case of the T term there is a real intersection of the surface sheets at the point $Q_\vartheta = Q_\varepsilon = 0$, whereas for the E term a branching of the APES occurs at this point with a conical intersection. The three wavefunctions $|\xi\rangle, |\eta\rangle$, and $|\zeta\rangle$ for the three paraboloids, as distinct from the three functions in the three minima

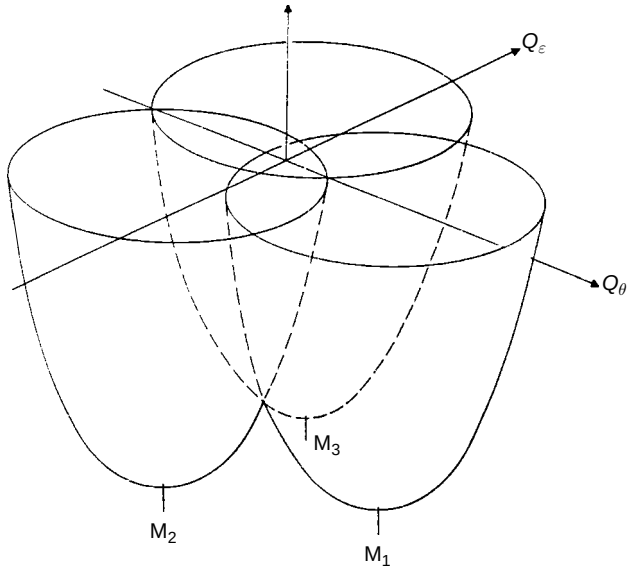

Fig. 3.10. The APES for the JT $T \otimes e$ problem: three paraboloids intersect at $Q_\theta = Q_\varepsilon = 0$; M_1, M_2, and M_3 are the three minima.

of the E-term case, are mutually orthogonal and are not mixed by the tetragonal displacements (therefore no tunneling between the minima occurs, Section 5.3).

In the other particular case when $F_E = 0$, but $F_T \neq 0$ (the $T \otimes t_2$ problem) the third-order Eq. (3.2) with the matrix W in (3.42) cannot be solved directly in simple expressions. Using the method [3.18], one can determine the extrema points of the APES by solving Eqs. (3.43′), without solving Eq. (3.2). For the case in question the surface $\varepsilon(Q_\xi, Q_\eta, Q_\zeta)$ in the space of the trigonal coordinates has four minima lying on the C_3 axis of the cubic system at the points $(m_1 Q_0^T, m_2 Q_0^T, m_3 Q_0^T)$, where the four sets of the (m_1, m_2, m_3) numbers are (1, 1, 1), (−1, 1, −1), (1, −1, −1), and (−1, −1, 1), and

$$Q_0^T = 2F_T/3K_T \tag{3.47}$$

At these minima the system is distorted along the trigonal axes. The kind of displacements of the atoms corresponding to this distortion for an octahedral system are illustrated in Fig. 3.11. The six ligands, in two sets of three ligands each, move on the circumscribed cube toward two apexes lying on the corresponding C_3 axes [3.7, 3.18]. The JT stabilization energy is

$$E_{\mathrm{JT}}^T = 2F_E^2/3K_E \tag{3.48}$$

In this case the frequency ω_T of the trigonal T_2 vibrations splits into two [3.1] (for other frequency relations, see in [3.1]):

$$\omega_A = \omega_T \qquad \text{or} \qquad K_A = K_T \qquad \text{and} \qquad \omega_E = (2/3)^{\frac{1}{2}}\omega_T$$

The electronic wavefunctions at the minima are given by the relationship

$$\psi = \frac{1}{\sqrt{3}}(m_1|\xi\rangle + m_2|\eta\rangle + m_3|\zeta\rangle \tag{3.49}$$

with the values of the sets of numbers m_i, $i = 1, 2, 3$, given above.

In the general case of the $T \otimes (e + t_2)$ problem, when simultaneous interaction with both the tetragonal ($F_E \neq 0$) and trigonal ($F_T \neq 0$) displacements is taken into account, the APES in the five-dimensional space of the five coordinates $Q_{\Gamma\gamma}$ is rather complicated, but the extrema points may be obtained using the procedure of Eqs. (3.43′) [3.18]. In general, the APES for the linear $T \otimes (e + t_2)$ problem has three types of extrema points summarized in Table 3.1. (1) Three equivalent tetragonal points, at which only tetragonal coordinates Q_ϑ and Q_ε are displaced (from the origin $Q_{\Gamma\gamma} = 0$). Here the coordinates of the minima and their depths are the same as in the linear $T \otimes e$ problem and are given by Eqs. (3.45) and (3.46). (2) Four equivalent trigonal points at which only the trigonal coordinates Q_ξ, Q_η, and Q_ζ are displaced (Fig. 3.11). The minimum coordinates coincide with those obtained in the $T \otimes t_2$ problem (see Eqs. (3.47) and Table 3.1). (3) Six equivalent orthorhombic points at each of which one trigonal and one tetragonal coordinate is displaced (Table 3.1); their depth is given by

$$E_{\mathrm{JT}}^0 = \frac{1}{2}E_{\mathrm{JT}}^E + \frac{3}{4}E_{\mathrm{JT}}^T \tag{3.50}$$

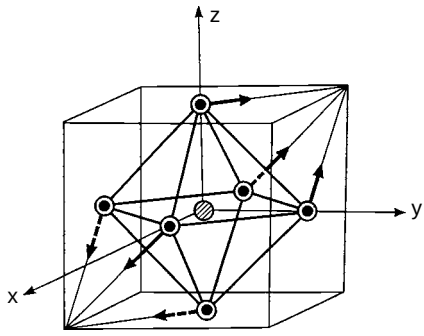

Fig. 3.11. Trigonal distortion of an octahedron in an electronic T state (cf. the $Q_\xi + Q_\eta + Q_\zeta$ displacement in Fig. 2.3).

Table 3.1. *Extrema points of the APES of an electronic T term in the linear* $T \otimes (e + t_2)$ *problem*

Number of equivalent extrema points	Nature of the extremum	Coordinates of the extremum in five-dimensional space $(Q_\vartheta, Q_\epsilon, Q_\xi, Q_\eta, Q_\zeta)$
3	Tetragonal minima or saddle points	$(F_E/K_E, 0, 0, 0, 0)$ $(-3F_E/2K_E, F_E/2K_E, 0, 0, 0)$ $(-3F_E/2K_E, -F_E/2K_E, 0, 0, 0)$
4	Trigonal minima or saddle points	$(0, 0, 2F_E/3K_T, 2F_E/3K_T, 2F_E/3K_T)$ $(0, 0, -2F_E/3K_T, -2F_E/3K_T, 2F_E/3K_T)$ $(0, 0, -2F_E/3K_T, 2F_E/3K_T, -2F_E/3K_T)$ $(0, 0, 2F_E/3K_T, -2F_E/3K_T, -2F_E/3K_T)$
6	Orthorhombic saddle points	$(-F_E/2K_E, 0, 0, 0, F_T/K_T)$ $(-F_E/2K_E, 0, 0, 0, -F_T/K_T)$ $(3F_E/4K_E, -F_E/4K_E, 0, F_T/K_T, 0)$ $(3F_E/4K_E, -F_E/4K_E, 0, -F_T/K_T, 0)$ $(3F_E/4K_E, F_E/4K_E, F_T/K_T, 0, 0)$ $(3F_E/4K_E, F_E/4K_E, -F_T/K_T, 0, 0)$

In this problem, if $E_{\mathrm{JT}}^E > E_{\mathrm{JT}}^T$, the tetragonal extrema points are deepest and hence absolute minima, while the trigonal ones are saddle points. If, however, $E_{\mathrm{JT}}^E < E_{\mathrm{JT}}^T$, the trigonal points are minima and the tetragonal ones are saddle points. The orthorhombic extrema points are always saddle points in the linear approximation.

The curvature of the APES at the extrema points can also be investigated by the method of [3.18]. In each of the three equivalent tetragonal minima the symmetry O_{h} of the system is reduced to $D_{4\mathrm{h}}$ and the irreducible representations of the JT-active displacements E_{g} and $T_{2\mathrm{g}}$ are reduced: $E_{\mathrm{g}} = A_{1\mathrm{g}} + B_{1\mathrm{g}}$ and $T_{2\mathrm{g}} = B_{2\mathrm{g}} + E_{\mathrm{g}}$. While the $A_{1\mathrm{g}}$ and $B_{1\mathrm{g}}$ vibrations remain degenerate, the $B_{2\mathrm{g}}$ and E_{g} ones split:

$$\tilde{\omega}_{A_1}^2 = \tilde{\omega}_{B_1}^2 = \omega_E^2, \qquad \tilde{\omega}_{B_2}^2 = \omega_T^2, \qquad \tilde{\omega}_E^2 = \omega_T^2(1 - \eta^{-1}),$$
$$\eta = E_{\mathrm{JT}}^E / E_{\mathrm{JT}}^T \tag{3.51}$$

Similarly, at the trigonal extrema points the JT displacements transform as E_{g} and $A_{1\mathrm{g}} + E_{\mathrm{g}}$ of the $D_{3\mathrm{d}}$ group; the transformed vibrational frequencies are $\tilde{\omega}_A = \omega_T$, while two frequencies $\tilde{\omega}_E$ are solutions that diagonalize the matrix

$$\begin{vmatrix} \omega_{\mathrm{E}}^2\left(1 - \frac{2}{3}\eta\right) & -\frac{\sqrt{2}}{3}\omega_E\omega_T\sqrt{\eta} \\ -\frac{\sqrt{2}}{3}\omega_E\omega_T\sqrt{\eta} & \frac{2}{3}\omega_T^2 \end{vmatrix} \tag{3.52}$$

This quadratic form is positive definite if the determinant of (3.52) is positive:

$$\tfrac{2}{3}\omega_E^2\omega_T^2(1-\eta) > 0 \tag{3.53}$$

meaning $\eta < 1$ ($E_{\mathrm{JT}}^E < E_{\mathrm{JT}}^T$).

At the orthorhombic extrema points the symmetry group is $D_{2\mathrm{h}}$, $E_{\mathrm{g}} = A_{1\mathrm{g}} + B_{1\mathrm{g}}$ and $T_{2\mathrm{g}} = A_{1\mathrm{g}} + B_{2\mathrm{g}} + B_{3\mathrm{g}}$, and for the five vibrational frequencies we get

$$\begin{aligned} &\tilde{\omega}_A^2 = \omega_E^2, \qquad \tilde{\omega}_{A'}^2 = \tilde{\omega}_{B_3}^2 = \omega_T^2, \\ &\tilde{\omega}_{B_1}^2 = \omega_E^2(1-\eta), \qquad \tilde{\omega}_{B_2}^2 = \omega_T^2\frac{\eta-1}{\eta+1} \end{aligned} \tag{3.54}$$

By comparing Eqs. (3.51)–(3.54) we can conclude that in the linear $T_2 \otimes (e + t_2)$ problem, depending on the value of $\eta = E_{\mathrm{JT}}^E / E_{\mathrm{JT}}^T$, either tetragonal or trigonal extrema points are absolute minima, whereas the orthorhombic points can never be absolute minima. Indeed, it follows from Eq. (3.54) that for any value of η there is at least one negative value of ω^2 meaning negative curvature ($K = M\omega^2$) in the corresponding direction. If $\eta > 1$, all the tetragonal frequencies are positive, whereas some of the trigonal ones are negative. In the opposite case of $\eta < 1$ all the trigonal frequencies are positive, while some of the tetragonal ones become negative.

In the particular case when $E_{\mathrm{JT}}^E = E_{\mathrm{JT}}^T$ all the extremum points (including the orthorhombic ones) have the same depth. It was shown [3.20] that in this case a continuum of minima is realized, forming a two-dimensional trough on the five-dimensional surface of the APES (in a sense similar to the "Mexican hat" in the $E \otimes e$ problem). If, additionally, $K_E = K_T$, the problem is of equal coupling to e and t_2 displacement (the $T \otimes d$ *problem* [3.20]). In this situation the two-dimensional trough in the five-dimensional space of $Q_\vartheta, Q_\varepsilon, Q_\xi, Q_\eta$, and Q_ζ coordinates can be conveniently described by a spherical surface. For the minima points along the bottom of the trough, using polar coordinates ϑ and ϕ, we have [3.1, 3.20]

$$\begin{aligned} &Q_\vartheta^0 = \rho^0(3\cos\vartheta - 1), \qquad Q_\varepsilon^0 = \rho^0\sqrt{3}\sin^2\vartheta\ \cos(2\phi), \\ &Q_\xi^0 = \rho^0\sqrt{3}\sin(2\vartheta)\sin\phi, \qquad Q_\eta^0 = \rho^0\sqrt{3}\sin(2\vartheta)\cos\phi, \\ &Q_\zeta^0 = \rho^0\sqrt{3}\sin^2\vartheta\ \sin(2\phi) \end{aligned} \tag{3.55}$$

with $\rho^0 = F_E/2K_E$, and the JT stabilization energy

$$E_{\mathrm{JT}} = F_E^2/2K_E \tag{3.56}$$

In this case the classical motion of an octahedron along the trough corresponds to motions of the ligands around identical spheres centered at the apexes of the octahedron [3.1]. The displacements of different ligands are correlated: at every instant their radius vectors drawn from the center of the sphere, if shifted to a common origin, form a star, the apexes of which produce a regular octahedron rotating around its geometric center (the $T \otimes d$ problem is relevant to mostly large-radius F-centers in solids, Section 8.1).

In the quadratic approximation the vibronic $T \otimes (e + t_2)$ problem is very complicated [3.21–3.24] (cubic terms have also been taken into account [3.24]). Similar to the E-term problem, the quadratic terms of the vibronic interaction W in Eq. (2.18) produce significant changes in the shape of the APES for a T term. With these terms included, the matrix (3.42) contains the previous two linear plus four quadratic vibronic constants. The latter span the following symmetries: $E \times E$, $T_2 \times T_2(E + T_2)$, and $E \times T_2$. Among them, the constant $G_E(E \times T_2)$, which mixes the E-and T_2-type displacements, seems to be most important in changing the shape of the APES. Therefore, certain qualitative and semiquantitative results can be obtained by retaining only one quadratic constant,

$$G = G_E(E + T_2) = \frac{1}{2}\langle \xi | \left(\frac{\partial^2 V}{\partial Q_\xi \, \partial Q_\eta} \right)_0 | \eta \rangle \tag{3.57}$$

and disregarding all the other vibronic constants [3.21].

In this approximation the APES contains five parameters: F_E, F_T, K_E, K_T, and G. It was shown [3.21] that only two dimensionless combinations A and B of these five parameters are necessary to describe the main features of the system:

$$A = G(K_E K_T)^{-\frac{1}{2}}, \qquad B = F_E G / F_T K_E \tag{3.58}$$

The linear vibronic coupling at $G = 0$ corresponds to the origin (0, 0) on the plane (A, B) shown in Fig. 3.12. Along the two lines $A = \pm(\sqrt{3}/2)B$, the energies at the tetragonal and trigonal extrema points are the same (the positions and depths of these points are not affected by the $E \times T_2$-type quadratic vibronic interaction). In the cross-hatched area the trigonal extremum points are deeper than the tetragonal ones, whereas in the hatched area the opposite is true. In all cases the stability of the system requires that $A < 1$, which means that $G^2 < K_E K_T$.

An account of the $E \times T_2$-type quadratic terms is most essential in determining the positions and pattern of the six equivalent orthorhombic extremum points which, in the linear approximation, are only saddle points. Their depth

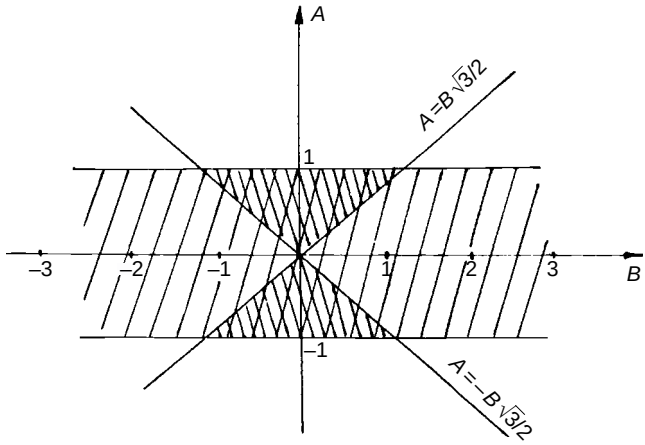

Fig. 3.12. Areas of stability in (A, B) coordinates of a molecule with a JT quadratic $T \otimes (e + t_2)$ problem. The molecule is stable when $|A| < 1$. Along the lines $A = \pm B\sqrt{3}/2$ the tetragonal and trigonal stationary points have the same energy. In the cross-hatched area the tetragonal stationary points have lower energy, whereas in the remaining area the trigonal points have lower energy [3.1].

and the coordinates of one of them are as follows (the others can be easily derived from symmetry considerations) [3.21]:

$$\begin{aligned} E_{\mathrm{JT}}^{\mathrm{O}} &= F_E^2(4A^2 - 4A^2B + B^2)/8K_EB^2(1 - A^2) \\ Q_\xi^0 &= Q_\eta^0 = Q_\varepsilon^0 = 0 \\ Q_\zeta^0 &= F_T(2 - B)/2K_T(1 - A^2) \\ Q_\vartheta^0 &= -F_E(B - 2A^2)/2K_EB(1 - A^2) \end{aligned} \tag{3.59}$$

When approaching the point $G = 0$ ($A = B = 0$) along the lines $A = \pm(\sqrt{3}/2)B$ on the plane (A, B) (Fig. 3.12), the depth of the orthorhombic extremum points in question, $E_{\mathrm{JT}}^{\mathrm{O}}$, becomes equal to that of the trigonal and tetragonal distortions ($E_{\mathrm{JT}}^{\mathrm{O}} = E_{\mathrm{JT}}^{T} = E_{\mathrm{JT}}^{E}$), resulting in the two-dimensional trough of minima on the five-dimensional APES. Away from this point $E_{\mathrm{JT}}^{\mathrm{O}} \neq E_{\mathrm{JT}}^{E,T}$, and the trough is warped; as in the E-term case, wells and humps emerge regularly, alternating along the line of the minima. It is important that for a large area of the A and B parameters shown in Fig. 3.13 the orthorhombic extremum points become absolute minima.

Beside these three types of extremum points, the quadratic terms of the vibronic interaction generate three new types with 12, 12, and 24 equivalent extremum points, respectively. Calculations carried out numerically [3.21] show that the latter type (24 points) is irrelevant since for the parameters for

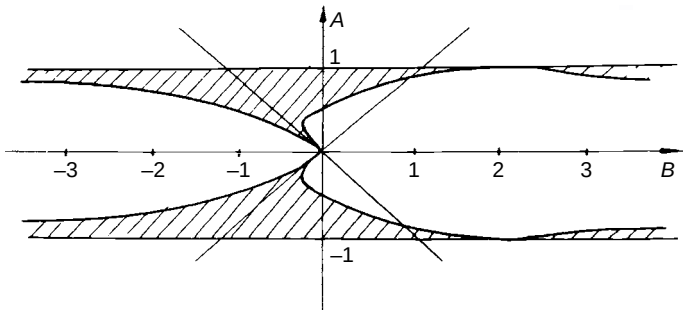

Fig. 3.13. The area of existence (hatched) of orthorhombic absolute minima of the APES for a quadratic $T \otimes (e + t_2)$ problem [3.1].

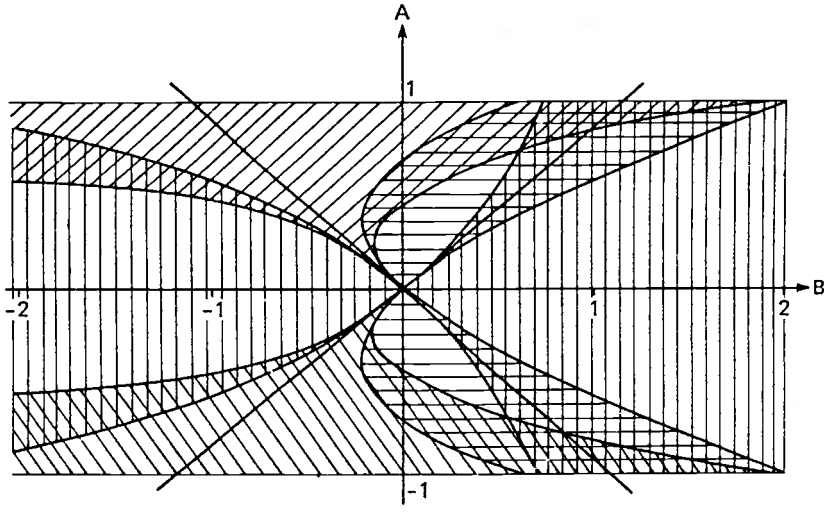

Fig. 3.14. Areas of existence and coexistence of different types of minima of the APES for the quadratic $T \otimes (e + t_2)$ problem (in A and B coordinates); vertical, horizontal, and oblique shadings correspond to areas of existence of tetragonal, trigonal, and orthorhombic minima, respectively. Overlap shading shows areas of coexistence of corresponding minima (from [3.21]).

which it might occur, the system is unstable, while the first two types (with 12 points each) never become absolute minima. A group-theoretical consideration of possible extremum points on the APES is given elsewhere [3.25]. The classical motion of atoms along the APES in this case was discussed in [3.8, 3.26].

Figure 3.14 shows the areas of A and B parameters (Eqs. (3.58)) where the three types of minima on the APES are realized. An important feature in this

graphic presentation is the areas of *coexistence of different types of minima* (cf. coexistence in the $E \otimes (b_1 + b_2)$ problem, Section 3.1). This coexistence means that for the same parameter values (more precisely for the same values of the combinations A and B of the parameters) the APES of the system has two types of coexisting minima (tetragonal and trigonal, tetragonal and orthorhombic, trigonal and orthorhombic), while for some marginal values all three types of minima coexist. However, the presence of minima on the APES is just one of the necessary conditions of possible observance of different kinds of minima, the others being relatively low energy with respect to the absolute minimum and sufficiently high barriers between them.

Another type of quadratic terms, namely $G_{T_2}(T_2 \times T_2)$, was considered for the $T \otimes t_2$ problem [3.22]. Similar to the case above, for some of the vibronic coupling parameters the orthorhombic stationary states, which are saddle points in the linear approximation, become minima in this quadratic approximation. The $G_E(E \times E)$ and $G_{T_2}(T_2 \times T_2)$ couplings in the $T \otimes (e + t_2)$ problem were taken into account in [3.23, 3.24]. In [3.24] similar cubic terms ($E \times E \times E$ and $T_2 \times T_2 \times T_2$), as well as totally symmetric a_1 displacement, were also included (see also [3.27]). The conclusions from these works are qualitatively similar to those described above in [3.21], but with rather complicated dependence on (more) coupling parameters and additional changes in the a_1 coordinates at the minima.

An important feature of orbital T terms, as distinct from E terms, is the large splitting caused by spin–orbit interaction (in first-order perturbation theory). Therefore, if the system in question has unpaired electrons or, in general, if the total spin S of the state under consideration is nonzero, we do not deal with T terms as such, but with their components which result from spin–orbital splitting. For instance, the spin doublet ^2T (one unpaired electron in an orbital T state) under spin–orbit interaction splits into two components, $\Gamma_8 + \Gamma_6$, of which the first (Γ_8) is a spin quadruplet and the second (Γ_6) is a spin doublet. The latter can be treated like the doublet E, considered above (Section 3.2), whereas the quadruplet term Γ_8 requires additional treatment.

Since $[\Gamma_8 \times \Gamma_8] = A_1 + E + T_2$ (Table 2.3), the JT-active displacements for the Γ_8 state are of E and T_2 type, so the problem is $\Gamma_8 \otimes (e + t_2)$. The solution of the secular equation (3.2) results in two sheets of the APES (two spin doublets) given by the following expression [3.7, 3.1]:

$$\varepsilon_{\pm}(\rho,\ Q) = \tfrac{1}{2}(K_E\rho^2 + K_T Q^2) \pm (F_E^2\rho^2 + F_T^2 Q^2)^{\frac{1}{2}} \tag{3.60}$$

where $\rho^2 = Q_\vartheta^2 + Q_\varepsilon^2$ and $Q^2 = Q_\xi^2 + Q_\eta^2 + Q_\zeta^2$. It is seen that the surface (3.60) depends on only two (ρ and Q) of five coordinates, being thus a surface of revolution for the remaining three (the angle ϕ in the polar coordinates $Q_\vartheta = \rho\cos\phi$ and $Q_\varepsilon = \rho\sin\phi$, and similar angles α and β in the corresponding spherical coordinates for Q_ξ, Q_η, and Q_ζ). On the other hand, expression (3.60) formally coincides with Eq. (3.5) for the APES of the $E\otimes(b_1+b_2)$ problem, which means that in (ρ, Q) space the surface (3.60) has the shape illustrated in Fig. 3.1, provided only positive values or $Q_1 = \rho$ and $Q_2 = Q$ are taken into account. It follows that, depending on the relation between the JT stabilization energies E_{JT}^E and E_{JT}^T,

$$E_{\mathrm{JT}}^E = F_E^2/2K_E, \qquad E_{\mathrm{JT}}^T = F_T^2/2K_T \tag{3.61}$$

the minimum of the surface will be either tetragonal,

$$\rho^0 = F_E/K_E, \qquad Q^0 = 0 \tag{3.62}$$

or trigonal

$$\rho^0 = 0, \qquad Q^0 = F_T/K_T \tag{3.63}$$

The first case (tetragonal distortion) occurs if $E_{\mathrm{JT}}^E > E_{\mathrm{JT}}^T$, the second case (trigonal distortion) is specific for the opposite inequality. Since the other three coordinates remain arbitrary at the minimum points, the latter produce a three-dimensional continuum, a three-dimensional trough [3.28] (formally analogous to the one-dimensional trough of displacements in the $E\otimes e$ problem, Section 3.2). If $E_{\mathrm{JT}}^E = E_{\mathrm{JT}}^T$, an additional trough in the (ρ, Q) space occurs, resulting in a four-dimensional trough in the five-dimensional space of e and t_2 coordinates.

3.4 The $T\otimes h$, $p^n\otimes h$, $G\otimes(g+h)$, and $H\otimes(g+h)$ problems for icosahedral systems

The latest achievements in preparation and studies of icosahedral systems (fullerenes) stimulated their further intensive and extensive investigation, although the first work on the JT effect in such systems [3.29] was published before the discovery of fullerenes. An essential contribution to the development of the JTE theory in application to icosahedral systems was made in a series of works [3.29–3.60], partly reviewed in [3.30].

In icosahedral systems, there are fourfold (G) and fivefold (H) orbitally degenerate electronic terms in addition to the T terms that are present also in systems with lower symmetry. The typical JT problems here are $T\otimes h$ (a T term

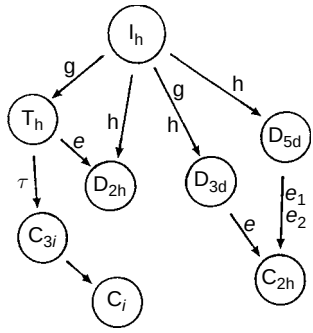

Fig. 3.15. Possible distortions (symmetry reduction) of an icosahedral system with I_h symmetry in degenerate states under g and h modes (displacements), and further distortions of the lower-symmetry configurations under e and t_2 modes; all modes are even, as required by the JT theorem; "i" means inversion (reprinted with permission from [3.2]. Copyright 1972 John Wiley & Sons, Inc.).

interacting with fivefold degenerate nuclear displacements h), $G \otimes (g + h)$ (a G term interacting with fourfold g and/or fivefold h vibrations), and $H \otimes (g + h)$ (an H term interacting with g and/or h vibrations). Because of the high symmetry of the icosahedron additional degeneracy between atomic terms (up to the angular momentum $L = 2$) may occur, producing $p^n \otimes h$ JT problems. Figure 3.15 illustrates the possible JT distortions of an icosahedron with I_h symmetry as a result of vibronic coupling to the corresponding symmetrized nuclear displacements [3.2] (see also Table 2.3).

In the formation of molecular terms in fullerene ionic states $C_{60}^{n\pm}$ special relations between interelectron Coulomb interaction (that favors the Hund's rule high-spin states) and JT coupling (that favors degenerate states) should be taken into account [3.38]. Numerical calculations show that low-spin states prevail in negative ions, whereas high-spin states dominate all positive ions.

For obvious reasons of higher complexity, the JT problems in icosahedral systems are less studied than those in the simplest systems, discussed above, although the number of publications on the JTE in fullerenes is significant and is increasing continuously.

The $T \otimes h$ problem [3.29–3.32, 3.37] is similar to the particular case of the $T \otimes (e + t_2)$ one when the vibronic coupling to the e and t_2 vibrations and their frequencies are the same (cf. the $T \otimes d$ problem, Section 3.3). The five-dimensional space of the JT effect in this case can be presented as combined from the two e coordinates, $Q_\vartheta \sim d_{z^2}$ and $Q_\varepsilon \sim d_{x^2-y^2}$, and three t_2 coordinates, $Q_\xi \sim xz$, $Q_\eta \sim yz$, and $Q_\zeta \sim xy$, of the cubic group. It is convenient to denote them by Q_i, $i = 1, 2, \ldots, 5$, and present them in "polar" coordinates with

one radial distance $0 \le Q_h < \infty$ and four angles $0 \le \alpha < \pi/3$, $0 \le \lambda < \pi$, $0 \le \vartheta < \pi/2$, and $0 \le \phi < 2\pi$:

$$
\begin{aligned}
Q_1 &= Q_h[(1/2)(3\cos^2\vartheta - 1)\cos\alpha + (\sqrt{3}/2)\sin^2\vartheta\sin\alpha\cos(2\gamma)] \\
Q_2 &= Q_h[(\sqrt{3}/2)\sin^2\vartheta\cos(2\phi)\cos\alpha + (1/2)(1+\cos^2\vartheta)\cos(2\phi) \\
&\quad \times \sin\alpha\cos(2\gamma) - \cos\vartheta\sin(2\phi)\sin\alpha\sin(2\gamma)] \\
Q_3 &= Q_h[(\sqrt{3}/2)\sin^2\vartheta\sin(2\phi)\cos\alpha + (1/2)(1+\cos^2\vartheta)\sin(2\phi) \\
&\quad \times \sin\alpha\cos(2\gamma) + \cos\vartheta\cos(2\phi)\sin\alpha\sin(2\gamma)] \\
Q_4 &= Q_h[(\sqrt{3}/2)\sin(2\vartheta)\cos\phi\cos\alpha - (1/2)\sin(2\vartheta)\cos\phi\sin\alpha\cos(2\gamma) \\
&\quad + \sin\vartheta\sin\phi\sin\alpha\sin(2\gamma)] \\
Q_5 &= Q_h[(\sqrt{3}/2)\sin(2\vartheta)\sin\phi\cos\alpha - (1/2)\sin(2\vartheta)\sin\phi\sin\alpha\cos(2\gamma) \\
&\quad - \sin\vartheta\cos\phi\sin\alpha\sin(2\gamma)]
\end{aligned}
\tag{3.64}
$$

Following the Wigner–Eckart theorem (2.16), the vibronic coupling constants $F_h^{Q_i}$ to all these displacements differ by only numerical (Clebsch-Gordan) coefficients. For the $T_1 \otimes h$ problem, which we consider first, $F_h^{Q_3} = F_h^{Q_4} = F_h^{Q_5} = \sqrt{3}F_h^{Q_i} = \sqrt{3}F_h^{Q_2}$. With this in mind the secular equation (3.2) of the vibronic coupling that determines the electronic states ε^{ν} of the threefold degenerate T_1 term as a function of the coordinates (3.64) in the linear approximation with regard to the latter is very similar to (3.42):

$$
W = \begin{bmatrix}
F_h\left(\frac{1}{2}Q_1 - \frac{\sqrt{3}}{2}Q_2\right) & -F_hQ_3 & -F_hQ_4 \\
-F_hQ_3 & F_h\left(\frac{1}{2}Q_1 + \frac{\sqrt{3}}{2}Q_2\right) & -F_hQ_5 \\
-F_hQ_4 & -F_hQ_5 & -F_hQ_1
\end{bmatrix}
\tag{3.65}
$$

This matrix is simpler than (3.42) because it contains the same constant F_h in all the matrix elements which is thus a common factor. It can be shown [3.29–3.32] that with the solutions ε_i^{ν} of Eq. (3.2) with this matrix the lowest branch of the APES (3.1) has a two-dimensional trough of minima points in the five-dimensional space, similar to the one-dimensional trough of minima on the two-dimensional APES of the $E \otimes e$ problem (Section 3.2). It means that the minima points are characterized by just three coordinates instead of five. This can be seen directly if we look into a cross-section of the five-dimensional surface, say, at $\alpha = 0$ and $\gamma = 0$, at which only the first terms in the coordinate presentation (3.64) remain (they correspond to the five coordinates of

d symmetry in the cubic group mentioned above, such as those in Eq. (3.42)). With these coordinates Eq. (3.65), distinguished from (3.42), leads to a simple solution that is independent of the polar angles ϑ and ϕ:

$$\begin{aligned} \varepsilon_1^v &= -F_h Q_h \\ \varepsilon_{2,3}^v &= \tfrac{1}{2} F_h Q_h \end{aligned} \tag{3.66}$$

which together with the elastic term in (3.1) gives for the lowest branch of the APES (K_h is the primary force constant, Section 2.2)

$$\varepsilon_1 = \tfrac{1}{2} K_h Q_h^2 - F_h Q_h \tag{3.67}$$

This curve has a minimum at

$$Q_h^0 = F_h / K_h \tag{3.68}$$

We see that neither the electronic energies ε_i^v nor the total energy ε_i as a function of the five nuclear displacements (3.64) depend on the angles ϑ and ϕ. In other words, the surface has the same minimum energy in any of these ϑ and ϕ directions, thus forming a two-dimensional trough in the five-dimensional space (3.64). For the wavefunction of the branch (3.67) in the same basis of the three T_2 term functions $|\xi\rangle$, $|\eta\rangle$, and $|\zeta\rangle$ as in Section 3.3, we have

$$|u\rangle = \sin\vartheta\cos\phi|\xi\rangle + \sin\vartheta\sin\phi|\eta\rangle + \cos\vartheta|\zeta\rangle \tag{3.69}$$

Similar to the one-dimensional trough in the $E \otimes e$ problem (Section 3.2), the presence of a two-dimensional trough on the five-dimensional APES emerges due to (is an indication of) the higher symmetry of the JT Hamiltonian in the linear (in vibronic coupling) approximation than that of the original system ($SO(3)$ instead of I_h of the icosahedron). In the $SO(3)$ symmetry (the symmetry that specifies a point on a three-dimensional unit hypersphere) the Hamiltonian contains additional symmetry elements that are not present in the icosahedral group [3.30, 3.31], and this happened because of the simplifications introduced by the linear approximation.

The $SO(3)$ symmetry of the trough allows a simple presentation of the mode of distortion of the icosahedron as a rotating distortion shown in Fig. 3.16. Denoting the two coordinates of distortion by the angles ϑ and ϕ, we can illustrate the motion along the bottom of the trough as an internal free rotation of quadrupole distortions of a sphere. Let us present the threefold degenerate electronic state by three atomic states and assume the initial state is p_z-like with the spheroidal distortion along the Z axis, $\vartheta = 0$. On moving along the trough the sphere remains quadruply distorted, but the direction of distortion is gradually

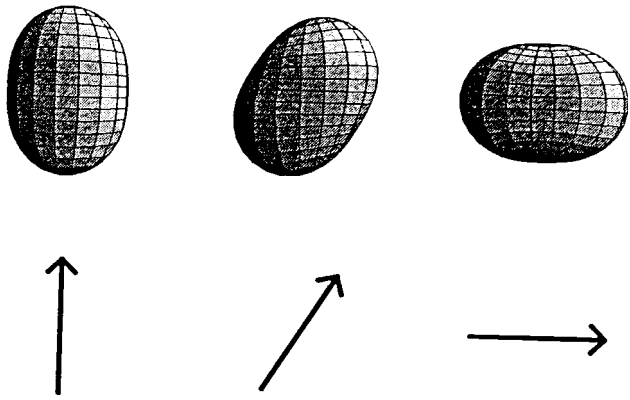

Fig. 3.16. Three orientations in the pseudorotation of a quadrupole-distorted spherical surface. The principal axis of the associated electronic p state is shown below each distortion (reprinted with permission from [3.30]. Copyright 1997 Princeton University Press).

changing along the (ϑ, ϕ) directions. Note that, as in other JT pseudorotations, an internal rotation of the distortion, not a rotation of the system as a whole, takes place. The system is thus performing free internal rotation along the bottom of the trough at which its symmetry is lower than icosahedral.

If the quadratic terms of vibronic coupling are taken into account, the initial lower (icosahedral) symmetry is restored in the Hamiltonian [3.30]. This results in warping of the trough (again, similar to the $E \otimes e$ case) with minima, maxima, and saddle points along its bottom. At each of these extremum points of the same kind, the icosahedron is distorted equivalently in different directions, the latter being complementary to each other, so that the system (dynamically) regains its icosahedral symmetry. Figure 3.17 illustrates this case [3.30]: there are six D_{5d}-type minima (maxima) on the spherical surface at the vertices of the icosahedron, ten D_{3d} maxima (minima) at the vertices of a dodecahedron, and 15 D_{2h} saddle points at the centers of the edges of either polyhedron. Figure 3.18 shows schematically one of the D_{5d} distortions. Changing the sign of quadratic coupling interchanges the minima and maxima, leaving the saddle points intact. Depending on the coupling strength, these minima may be deep enough to quasi-localize the distorted configuration. In this case the system performs hindered rotations – tunneling transitions between the minima via the lowest barriers at the saddle pints (Sections 5.3 and 7.1.1).

Calculations show [3.37] that minima of D_{5d} symmetry are realized when

$$15\sqrt{2}/8 > 3G_2/K_h > \sqrt{5}G_3/K_h > -15\sqrt{2}/8 \tag{3.70}$$

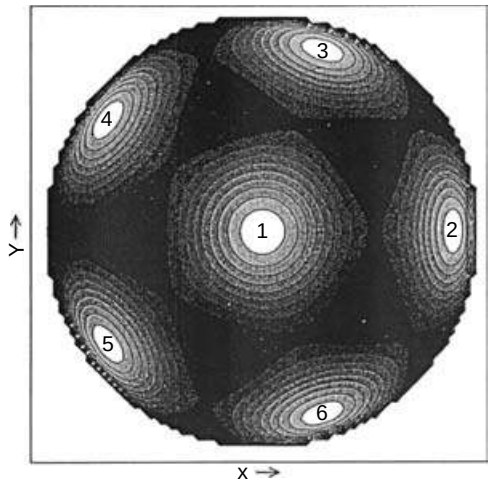

Fig. 3.17. Illustration of the D_{5d}-type minima on the spherical surface of an icosahedral system with a $T \otimes h$ problem, which occupy the vertices of the icosahedron, while the maxima are at the vertices of the dodecahedron. Changing the sign of the quadratic coupling interchanges the maxima and minima (reprinted with permission from [3.30]. Copyright 1997 Princeton University Press).

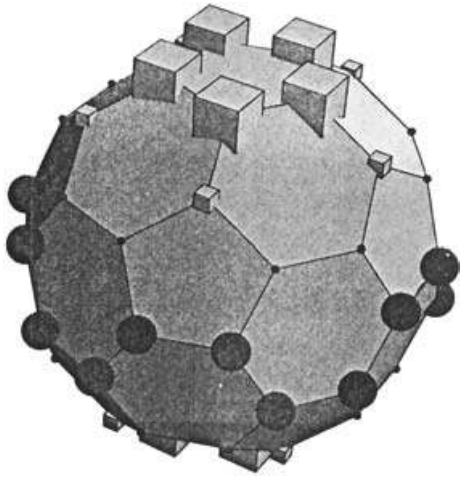

Fig. 3.18. Illustration to the D_{5d} distortion of a C_{60} cage produced by an h mode of Q_ϑ type with its axis along a fivefold axis of the octahedron. Cubes represent displacements outwards and spheres displacements inwards. The magnitude of the displacement is proportional to the cube/sphere size (reprinted with permission from [3.30]. Copyright 1997 Princeton University Press).

while minima of D_{3d} symmetry occur if

$$15\sqrt{2}/8 > \sqrt{5}G_3/K_h > 3G_2/K_h > -15\sqrt{2}/8 \tag{3.71}$$

where G_2 and G_3 are the two constants of quadratic vibronic coupling to D_{5d} and D_{3d} displacements, respectively. The JT stabilization energies are

$$\begin{aligned} E_{D_{5d}} &= 1/(5 - 4\sqrt{2}G_2/K_h) \\ E_{D_{3d}} &= 1/(5 - 4\sqrt{10}G_3/3K_h) \end{aligned} \tag{3.72}$$

If instead of the T_1 term a T_2 one is considered (the $T_2 \otimes h$ problem), the secular equation is very similar to (3.65), provided the following symmetry-controlled substitutions are made:

$$Q_1 \to Q_1; \quad Q_2 \to Q_4; \quad Q_3 \to -Q_5; \quad Q_4 \to -Q_2; \quad Q_5 \to -Q_3 \tag{3.73}$$

Obviously, a similar solution emerges with a two-dimensional trough with somewhat different distortions at the minima, and the quadratic terms of vibronic coupling produce similar warping of the trough [3.30–3.32].

The high symmetry of the icosahedron, which becomes even higher ($SO(3)$) in the linear approximation with regard to the vibronic coupling, allows further simplifications of its JT problems. First, all the angular momentum states up to $L = 2$ (S, P, and D states) remain unsplit in icosahedral symmetry. This means that all the states with the same spin formed from atomic configurations p^n can be considered as a degenerate term (d^n may have states with $L > 2$, and states with different spin are not coupled by the vibronic interaction). For instance, in p^2 and p^4 the interelectron interaction in the L–S coupling scheme produces the terms ^3P, ^1D and ^1S. While ^3P is a typical T_{1u} term and should be treated as shown above (the $^3T_{1u} \otimes h$ problem), the ^1D and ^1S terms form together a joint manifold that should be treated as six degenerate states coupled by the vibronic interaction. The S state has no diagonal matrix elements of the linear vibronic coupling, but there are nonzero elements for S–D coupling. The matrix W in the secular equations (3.2) of the linear vibronic coupling in this case looks as follows [3.30]:

$$W = \begin{vmatrix} 0 & \sqrt{2}F_hQ_1 & \sqrt{2}F_hQ_4 & \sqrt{2}F_hQ_3 & \sqrt{2}F_hQ_2 & \sqrt{2}F_hQ_5 \\ \sqrt{2}F_hQ_1 & -F_hQ_1 & -\frac{1}{2}F_hQ_4 & F_hQ_3 & F_hQ_2 & -\frac{1}{2}F_hQ_5 \\ \sqrt{2}F_hQ_4 & -\frac{1}{2}F_hQ_4 & F_h\left(-\frac{1}{2}Q_1 - \frac{\sqrt{3}}{2}Q_2\right) & -\frac{\sqrt{3}}{2}F_hQ_5 & -\frac{\sqrt{3}}{2}F_hQ_4 & -\frac{\sqrt{3}}{2}F_hQ_3 \\ \sqrt{2}F_hQ_3 & F_hQ_3 & -\frac{\sqrt{3}}{2}F_hQ_5 & F_hQ_1 & 0 & -\frac{\sqrt{3}}{2}F_hQ_4 \\ \sqrt{2}F_hQ_2 & F_hQ_2 & -\frac{\sqrt{3}}{2}F_hQ_4 & 0 & F_hQ_1 & \frac{\sqrt{3}}{2}F_hQ_5 \\ \sqrt{2}F_hQ_5 & -\frac{1}{2}F_hQ_5 & -\frac{\sqrt{3}}{2}F_hQ_3 & -\frac{\sqrt{3}}{2}F_hQ_4 & \frac{\sqrt{3}}{2}F_hQ_5 & F_h\left(-\frac{1}{2}Q_1 + \frac{\sqrt{3}}{2}Q_4\right) \end{vmatrix} \tag{3.74}$$

It can be shown that the lowest value of the lowest energy level occurs at

$$\varepsilon_1^v = -2F_hQ \tag{3.75}$$

with the wavefunction

$$\begin{aligned}|u\rangle = (1/\sqrt{3})|s\rangle + (1/2)(3\cos^2\vartheta)|D_1\rangle + (\sqrt{3}/2)\sin(2\vartheta)\cos\phi|D_2\rangle \\ + \sqrt{3}\sin^2\vartheta\cos\phi\sin\phi|D_3\rangle + (\sqrt{3}/2)\sin^2\vartheta\cos(2\phi)|D_4\rangle \\ + (\sqrt{3}/2)\sin(2\vartheta)\sin\phi|D_5\rangle\end{aligned} \tag{3.76}$$

where $|D_i\rangle$, $i = 1, 2, \ldots, 5$, are the five wavefunctions of the atomic D state.

Note that were it not for the high symmetry of the icosahedron, the $({}^1D + {}^1S) \otimes h$ problem would require two coupling constants, one for D–h and the other for the pseudo JT coupling S–D (assuming that the five frequencies of the h vibrations are the same).

For the $p^3 \otimes h$ problem, p^3 produces ${}^4S$, ${}^2D$ and ${}^2P$ terms, of which only the eight states ${}^2D + {}^2P$ are subject to vibronic coupling (S is a non-JT state) [3.30].

The $G \otimes (g + h)$ problem [3.29–3.34, 3.36, 3.42] is more complicated since it involves $4 + 5 = 9$ degrees of freedom in JT distortions with two types of constants of linear, F_g and F_h, and quadratic, G_g and G_h, vibronic coupling to g and h displacement, respectively. Similar to the $T \otimes (e + t_2)$ problem (Section 3.3), the approach to the solution is to consider first the particular cases when the coupling to one of the two types of vibrations is much stronger than to the other one. This allows one to ignore the weaker coupling in the zeroth-order approximation and to take it into account as a perturbation afterwards. Another approach can be employed when the two types of coupling are of approximately the same magnitude, which would allow one to ignore their difference in the zeroth approximation.

For *the $G \otimes g$ problem* the four coordinates of g type may be chosen with the following angular dependence (similar to the "polar" coordinates in (3.64)):

$$\begin{aligned}Q_6 &= Q_g \sin\vartheta\sin\alpha, \qquad Q_7 = Q_g \sin\vartheta\cos\alpha \\ Q_8 &= Q_g \cos\vartheta\sin\beta, \qquad Q_9 = Q_g \cos\vartheta\cos\beta\end{aligned} \tag{3.77}$$

with $0 \le Q_g < \infty$, $0 \le \vartheta < \pi/2$, $0 \le \alpha < \pi/3$, and $0 \le \beta < 2\pi$ (cf. the angles in (3.64)). In these coordinates and using electronic functions for the fourfold degenerate term G as shown in [3.30], the secular equation (3.2) of the linear vibronic coupling problem yields

$$W = \begin{vmatrix} -F_g Q_8 & -F_g Q_9 & -F_g(Q_6 - Q_8) & -F_g(Q_7 + Q_9) \\ -F_g Q_9 & F_g Q_8 & F_g(Q_7 - Q_9) & -F_g(Q_6 + Q_8) \\ -F_g(Q_6 - Q_8) & F_g(Q_7 - Q_9) & F_g Q_6 & -F_g Q_7 \\ -F_g(Q_7 + Q_9) & -F_g(Q_6 + Q_8) & -F_g Q_7 & -F_g Q_6 \end{vmatrix} \tag{3.78}$$

Direct analytical solution of Eq. (3.2) with this vibronic coupling matrix W is difficult. However, using the method [3.18] (Eqs. (3.43′)), we can determine the coordinates of the extremum points on the APES and estimate (by means of perturbation theory) whether they are minima, maxima, or saddle points. In the coordinates (3.77) one of the minima is located at the point

$$(Q_g,\ \vartheta,\ \alpha,\ \beta) = \left(Q_g,\ \frac{\pi}{4},\ \frac{3\pi}{2},\ \frac{\pi}{2}\right) \tag{3.79}$$

where with K_g as the primary force constant (Section 2.2)

$$Q_g = \frac{3F_g}{\sqrt{2}K_g} \tag{3.80}$$

and the JT stabilization energy

$$E_{\mathrm{JT}} = -\frac{9F_g^2}{4K_g} \tag{3.81}$$

At this minimum point the icosahedron is tetrahedrally distorted (T_h distortion, Fig. 3.19).

Presenting the wavefunction in terms of the four basis functions of the G term, $|G_i\rangle$, i = 1, 2, 3, 4, we get

$$|u\rangle = \sin\vartheta \sin\alpha |G_1\rangle + \sin\vartheta \cos\alpha |G_2\rangle + \cos\vartheta \sin\beta |G_3\rangle + \cos\vartheta \cos\beta |G_4\rangle \tag{3.82}$$

with the angles (ϑ, α, β) at the minimum point from Eq. (3.79). There are four more minima that are equivalent to this one and can be found by symmetry operations on the icosahedron. The coordinates of all the five minima of tetrahedral T_h symmetry are listed in Table 3.2.

It is difficult to visualize the positions of these extremum points in the five-dimensional space of the APES as a function of the four coordinates. Figure 3.20 gives some impression of the minima and saddle-point positions projected on the plane (α, β). The five minima form a square mesh, each of them having the other four as neighbors in equivalent positions, so that the five equidistant points (with the same distance from the origin) form a four-dimensional analog of a tetrahedron. There are also ten saddle points of $D_{3\mathrm{d}}$ symmetry at the midpoint

Table 3.2. *The positions* $(g, \theta, \alpha, \beta)$ *of the five minima of an icosahedron with a linear* $G \otimes g$ *JT problem;* $g_0 = (9\hbar/2\omega_g)^{1/2} k_g$, *where* k_g *is the coupling constant* (*from [3.30]*)

	g	θ	α	β
Min 1	g_0	$\pi/4$	$3\pi/2$	$\pi/2$
Min 2	g_0	$\pi/4$	$7\pi/10$	$9\pi/10$
Min 3	g_0	$\pi/4$	$3\pi/10$	$\pi/10$
Min 4	g_0	$\pi/4$	$11\pi/10$	$17\pi/10$
Min 5	g_0	$\pi/4$	$19\pi/10$	$13\pi/10$

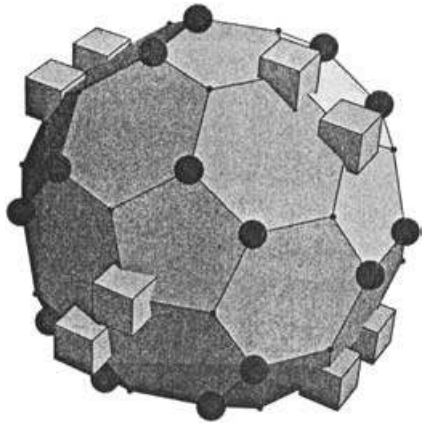

Fig. 3.19. Illustration to a T_h distortion of a C_{60} cage produced by g-type modes. Cubes represent displacements outwards and spheres displacements inwards. The magnitude of the displacement is proportional to the cube/sphere size (reprinted with permission from [3.30]. Copyright 1997 Princeton University Press).

between the minima on the (α, β) plane, but with slightly different Q_g and ϑ values. Table 3.3 lists some additional information about this APES.

The $G \otimes h$ *problem* is much similar to the $G \otimes g$ one, and it has also features that are similar to the $T \otimes h$ problem, considered above. The W matrix in the secular equation (3.2) for the four electronic energy levels in the space of the five coordinates (3.64) in the linear approximation with respect to the vibronic coupling is as follows:

$$W = \begin{vmatrix} F_h(-\sqrt{3}Q_1 + 2Q_4) & 2F_hQ_5 & F_h(Q_4 - Q_2) & F_h(Q_3 - Q_5) \\ 2F_hQ_5 & F_h(-\sqrt{3}Q_1 - 2Q_4) & F_h(-Q_3 - Q_5) & F_h(-Q_4 - Q_2) \\ F_h(Q_4 - Q_2) & F_h(-Q_3 - Q_5) & F_h(\sqrt{3}Q_1 - 2Q_2) & -2F_hQ_3 \\ F_h(Q_3 - Q_5) & F_h(-Q_4 - Q_2) & -2F_hQ_3 & F_h(\sqrt{3}Q_1 + 2Q_4) \end{vmatrix} \tag{3.83}$$

Table 3.3. *Four types of extrema points in the icosahedral JT $G \otimes g$ and $G \otimes h$ problems and their energies in the linear coupling approximation [3.30] (k_g is given in units where $\hbar\omega = 1$)*

Symmetry	$E(G \otimes g)$	$E(G \otimes h)$
D_{3d} (I)	$-(3/2)k_g^2\hbar\omega_g$	$-(3/2)k_h^2\hbar\omega_h$
D_{2h} (II)	$-(1/4)k_g^2\hbar\omega_g$	$-4k_h^2\hbar\omega_h$
D_{3d} (III)	$-(1/6)k_g^2\hbar\omega_g$	$-(25/6)k_h^2\hbar\omega_h$
T_h (IV)	$-(9/4)k_g^2\hbar\omega_g$	0

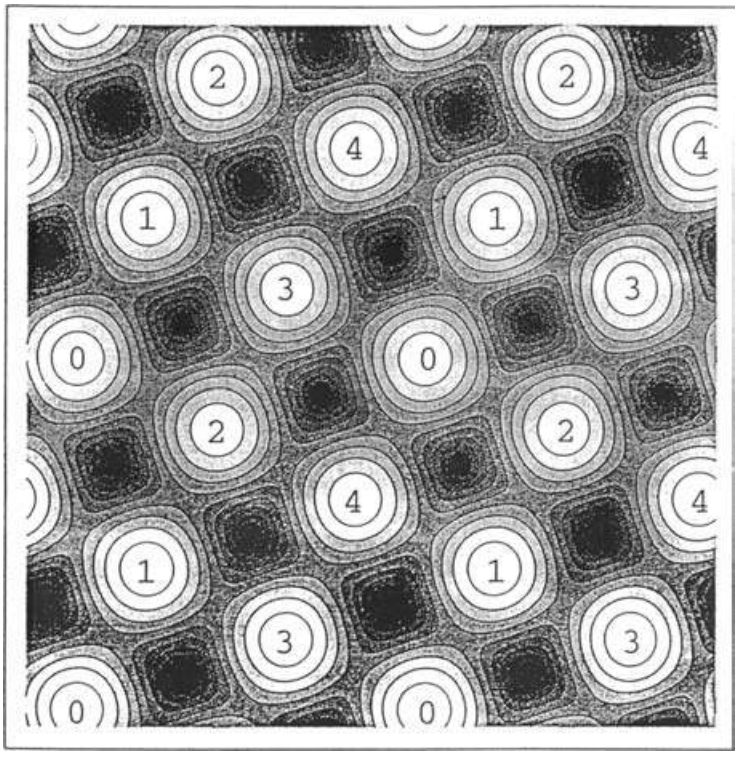

Fig. 3.20. Energy contours for the lowest APES in the $G \otimes g$ problem plotted on an (α, β) surface, with α horizontal. The range of α and β is $(0, 4\pi)$, $\theta = \pi/4$, and g is constant. The minima are numbered to show how each one recurs with a period of 2π in each direction. The projections of the saddle points onto this surface are midway between neighboring minima (reprinted with permission from [3.30]. Copyright 1997 Princeton University Press).

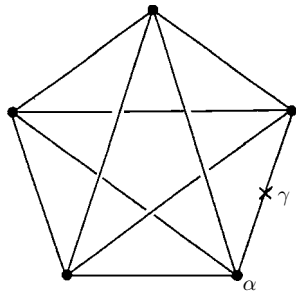

Fig. 3.21. Topology of the APES for preferential $G \otimes g$ coupling in an icosahedral system. The five vertices of the graph represent the five tetrahedral minima (α), while the ten edges refer to isomerization paths over trigonal transition states (γ) [3.32].

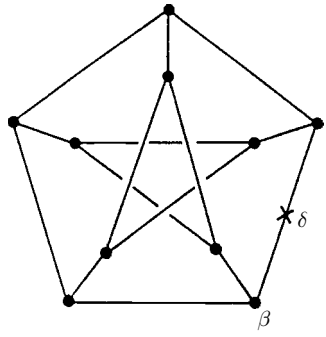

Fig. 3.22. Topology of the APES for preferential $G \otimes h$ coupling in an icosahedral system. The ten vertices of the graph represent the ten trigonal minima (β), while the 15 edges refer to isomerization paths over D_2 transition states (δ) [3.32].

As in the $G \otimes g$ case, the method [3.18] (Eqs. (3.43′)) allows an investigation of the extremum points of the APES with the ε_i^v values as solutions of Eq. (3.2) with the matrix (3.83). As a result, the APES has ten D_{5d} minima, which are also possible minima in the $T \otimes h$ problem (Fig. 3.17), but distinguished from the latter in that the six D_{5d} symmetry points are lines of degeneracy (surface intersections), not stationary points. There are also (other than in the $T \otimes h$ problem) 15 D_{2h} saddle points near the shortest path between pairs of minima which form the lowest energy barrier between the latter. Table 3.3 gives additional information, while Figs. 3.21 and 3.22 provide some illustrations to these two $G \otimes g$ and $G \otimes h$ problems [3.32].

In the *general case of the* $G \otimes (g + h)$ *problem* some complications emerge, but in the linear approximation with respect to the vibronic coupling the

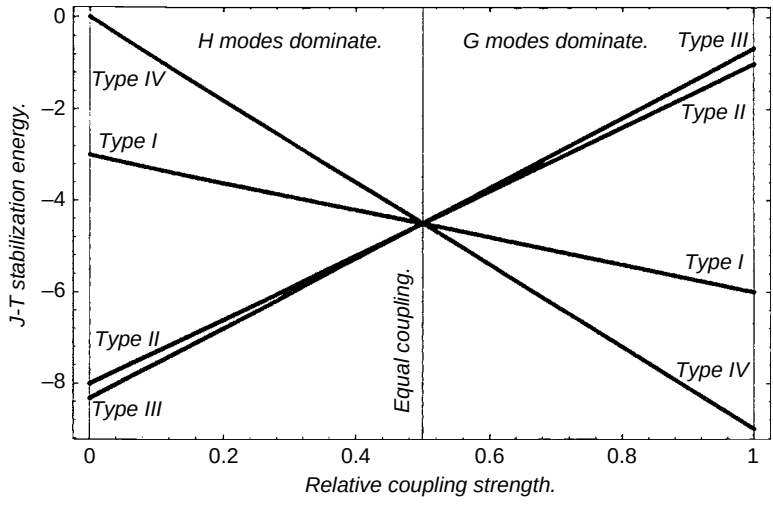

Fig. 3.23. The JT stabilization energies of the four types of minima in the linear $G \otimes (g + h)$ problem as a function of the coupling constant. If the coupling to the H-type modes dominates, the D_{3d} minima are the lowest, whereas if the G-type modes dominate, the T_h minima are lower.

solution of this problem can be essentially reduced to that obtained for the particular case of $G \otimes g$ and $G \otimes h$. Indeed, it can be shown that in this (linear) approximation the APES has the same number and kind of extremum points as in the two particular cases shown in Table 3.3. If the coupling to the g vibrations predominates, the minima are of T_h type and the path of lowest energy between them is via the D_{3d}(I) saddle points (Fig. 3.21). Conversely, if the h coupling is stronger, the minima are of D_{3d}(III) type and the intermediate saddle points are of D_{2h} symmetry (Fig. 3.22). All the above points coincide in energy when $k_g^2 \hbar\omega_g = k_h^2 \hbar\omega_h$ (the equal-coupling regime, see Table 3.3). In this case the symmetry of the Hamiltonian, $SO(4)$, is higher than the icosahedral symmetry of the system. The energy plot in Fig. 3.23 shows how the minima and saddle points of one type gradually change to that of the other type on moving from one predominant type of coupling (say, h) to the other one (g).

The linear $H \otimes (g + h)$ problem was considered in a most general way in [3.33] (see also in [3.29, 3.30]). It was shown that since $[H \times H] = A + G + 2H$, there are two types of JT-active h displacements that influence the main features of the APES (in the first work on the $H \otimes h$ problem [3.29] only one generalized type of h displacements was considered). Denote the two h distortions by h_a and h_b. Then the corresponding JT stabilization energies from interactions with g, h_a, and h_b displacements can be expressed in terms of the linear vibronic

coupling constants (F_g, F_{h_a}, and F_{h_b}, respectively) and primary force constants (K_g, K_{h_a}, and K_{h_b}, respectively) as follows:

$$\begin{aligned} E_{\mathrm{JT}}^{g} &= -\tfrac{1}{2}F_g^2/K_g \\ E_{\mathrm{JT}}^{h_a} &= -\tfrac{1}{2}F_{h_a}^2/K_{h_a} \\ E_{\mathrm{JT}}^{h_b} &= -\tfrac{1}{2}F_{h_b}^2/K_{h_b} \end{aligned} \tag{3.84}$$

The average JT stabilization energy E^{av} is

$$E^{\mathrm{av}} = (4E_{\mathrm{JT}}^{g} + 5E_{\mathrm{JT}}^{h_a} + 5E_{\mathrm{JT}}^{h_b})/14 \tag{3.85}$$

where the coefficients of the corresponding E_{JT} values stand for degeneracies. Another parameter ΔE characterizes the difference in strengths of the two h distortions:

$$\Delta E = (5/56)(4E_{\mathrm{JT}}^{g} + 5E_{\mathrm{JT}}^{h_a} - 9E_{\mathrm{JT}}^{h_b}) \tag{3.86}$$

Similar to the $G \otimes (g + h)$ problem, three types of stationary points of the APES were found in this approximation: pentagonal D_{5d}, trigonal D_{3d}, and two sets of D_{2h} points. If $\Delta E > 0$, the D_{5d} points are minima, whereas the D_{3d} points are minima in cases of $\Delta E < 0$. The D_{2h} stationary points are always saddle points in this approximation: one set yields isolated points, while the other is situated on continuous curves in the phase space. Figure 3.24 illustrates the energy-level splitting of the fivefold degenerate H term in the two types of distortions that lead to pentagonal and trigonal minima, while Fig. 3.25 gives additional insight into the D_{3d} minima positions and paths between them (Section 5.3).

Thus, in spite of their complexity, the icosahedral JT problems $G \otimes (g + h)$ and $H \otimes (g + h)$ are in fact reduced to two-mode problems when the interaction with one of the modes is independent of the interaction with the other one, and they compete just in forming the absolute minima. This situation is similar to that of the $T \otimes (e + t_2)$ problem (in the linear approximation), where either tetragonal or trigonal minima occur, depending on the predominant coupling to either e or t_2 vibrations, respectively, while the intermediate orthorhombic stationary points are always saddle points (Section 3.3).

However, as stated in Section 3.3, in the $T \otimes (e + t_2)$ problem the quadratic terms of the vibronic coupling change the APES topology essentially. In particular, with quadratic terms included the orthorhombic saddle points may become minima, and there is a variety of different types of coexisting minima [3.1, 3.21–3.24]. As far as we know, solutions of the $G \otimes (g + h)$ and $H \otimes (g + h)$ problems with quadratic vibronic coupling have not yet been

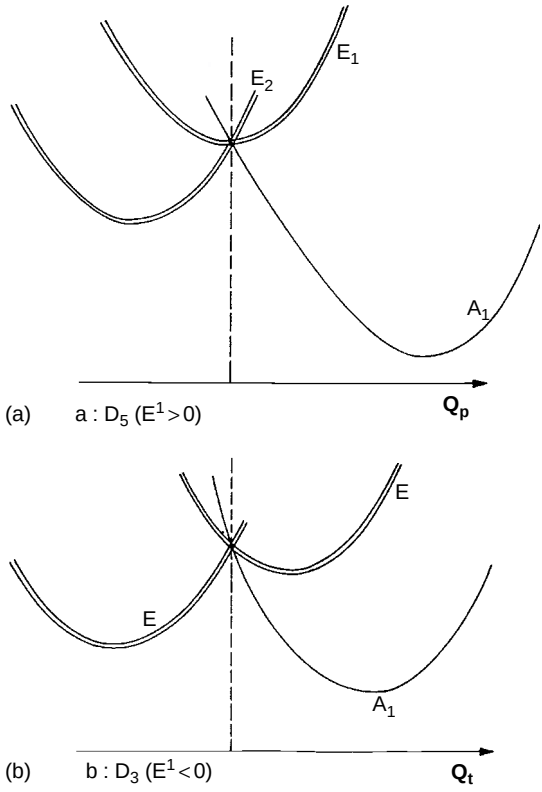

Fig. 3.24. Splitting of the electronic fivefold degenerate state under a pentagonal Q_p (a) and trigonal Q_t (b) distortion in the linear $H \otimes (g + 2h)$ problem (reprinted with permission from [3.33]. Copyright 1990 American Institute of Physics).

published. It can be expected that, similar to the $E \otimes e$, $T \otimes t_2$, $T \otimes (e + t_2)$, etc. JT problems, the quadratic terms alter significantly the topology of the APES, thus influencing essentially the tunneling splitting and other properties.

A more detailed insight into this rather complicated $H \otimes (g + h_a + h_b)$ problem, that is very rich in physical content, can be reached by considering several particular cases. In the $H \otimes g$ problem the matrix W in the secular equation of linear coupling to the four symmetrized coordinates (3.77) with an appropriate choice of the basis set of electronic wavefunctions is as follows [3.30]:

$$W = \begin{vmatrix} 0 & 2\sqrt{3}F_gQ_8 & 2\sqrt{3}F_gQ_7 & -2\sqrt{3}F_gQ_6 & 2\sqrt{3}F_gQ_9 \\ 2\sqrt{3}F_gQ_8 & -4F_gQ_6 & F_g(Q_7 - Q_9) & F_g(Q_6 - Q_8) & 4F_gQ_7 \\ 2\sqrt{3}F_gQ_7 & F_g(Q_7 - Q_9) & -4F_gQ_8 & -4F_gQ_9 & F_g(-Q_6 - Q_8) \\ -2\sqrt{3}F_gQ_6 & F_g(Q_6 - Q_8) & -4F_gQ_9 & 4F_gQ_8 & F_g(Q_7 + Q_9) \\ 2\sqrt{3}F_gQ_9 & 4F_gQ_7 & F_g(-Q_6 - Q_8) & F_g(Q_7 + Q_9) & -4F_gQ_6 \end{vmatrix} \tag{3.87}$$

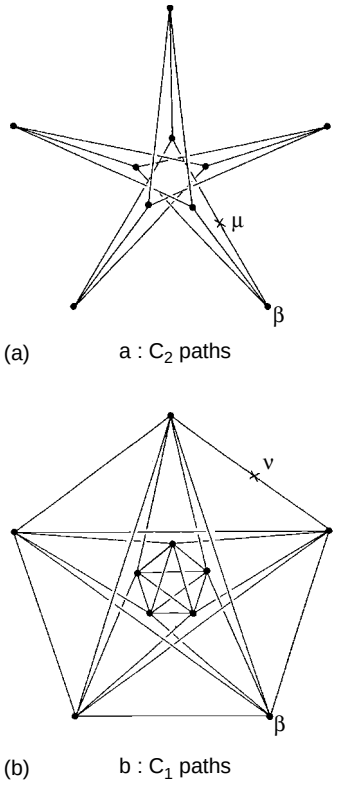

Fig. 3.25. Topology of the APES in the case of trigonal minima of the β orbit (cf. Fig. 3.22). The ten vertices of the graphs represent the ten equivalent trigonal minima. The 15 edges in (a) refer to C_2 isomerization paths over D_2 transition states belonging to orbit μ. The 30 edges in (b) refer to C_1 isomerization paths over C_2 transition states belonging to orbit ν. Each graph is complementary to the other (reprinted with permission from [3.33]. Copyright 1990 American Institute of Physics).

As in the previous cases, using the method of Eqs. (3.43′), one can reveal the stationary points of the APES, avoiding the need for a full solution of Eq. (3.2) with this matrix. Table 3.4 shows the types of stationary points obtained in this way. The lowest in energy are the ten D_{3d} minima. In the four-dimensional space of the coordinates (3.77) each minimum has six others as equidistant nearest neighbors and three at a greater distance. If plotted on the vertices of a dodecahedron, the two vertices related by inversion symmetry form one minimum, and the six nearest-neighbor minima of the $H \otimes h$ problem are not at near-neighbor vertices; there are only three of the latter and they form the three minima at larger distances in the four-dimensional space of this problem. The remaining six pairs of inversion-related vertices produce the six near-neighbor minima. As compared with Table 3.3, if only g displacements are included, the

Table 3.4. *Special points on the APES of the $H \otimes g$ problem and their energies [3.30]*

Symmetry	Type	Energy
D_{3d}	Minima	$-32F_g^2/3K_g$
T_d (I)	Degenerate	$-4F_g^2/K_g$
T_d (II)	Degenerate	$-9F_g^2/K_g$
D_{5d}	Degenerate	0

D_{2d} stationary points become T_d ones at which (as at D_{5d} points) the electronic term remains degenerate.

In the $H \otimes (h_a + h_b)$ problem the coupling to the two h-type displacements can be described by the two linear vibronic coupling constants, F_{h_a} and F_{h_b}, each of which generates its own vibronic coupling matrix W for the secular equation (3.2) that determines the electronic energy levels ε_i^v as a function of the five coordinates (3.64) [3.30]:

$$W_{h_a} = \begin{vmatrix} 0 & \sqrt{3}F_{h_a}Q_4 & -\sqrt{3}F_{h_a}Q_3 & -\sqrt{3}F_{h_a}Q_2 & \sqrt{3}F_{h_a}Q_5 \\ \sqrt{3}F_{h_a}Q_4 & F_{h_a}(\sqrt{3}Q_1+Q_2) & F_{h_a}(Q_3+Q_5) & F_{h_a}(Q_4-Q_2) & F_{h_a}Q_3 \\ \sqrt{3}F_{h_a}Q_3 & F_{h_a}(Q_3+Q_5) & F_{h_a}(-\sqrt{3}Q_1+Q_4) & F_{h_a}Q_5 & F_{h_a}(Q_4+Q_2) \\ \sqrt{3}F_{h_a}Q_2 & F_{h_a}(Q_4-Q_2) & F_{h_a}Q_5 & F_{h_a}(-\sqrt{3}Q_1-Q_4) & F_{h_a}(Q_3-Q_5) \\ \sqrt{3}F_{h_a}Q_5 & F_{h_a}Q_3 & F_{h_a}(Q_4+Q_2) & F_{h_a}(Q_3-Q_5) & F_{h_a}(-\sqrt{3}Q_1-Q_2) \end{vmatrix} \tag{3.88}$$

and

$$W_{h_b} = \begin{vmatrix} \frac{4}{\sqrt{3}}F_{h_b}Q_1 & -\frac{1}{\sqrt{3}}F_{h_b}Q_4 & -\frac{1}{\sqrt{3}}F_{h_b}Q_3 & -\frac{1}{\sqrt{3}}F_{h_b}Q_2 & -\frac{1}{\sqrt{3}}F_{h_b}Q_5 \\ -\frac{1}{\sqrt{3}}F_{h_b}Q_4 & F_{h_b}\left(-\frac{1}{\sqrt{3}}Q_1+Q_2\right) & F_{h_b}(Q_3+Q_5) & F_{h_b}(Q_4-Q_2) & F_{h_b}Q_3 \\ -\frac{1}{\sqrt{3}}F_{h_b}Q_3 & F_{h_b}(Q_3+Q_5) & F_{h_b}\left(-\frac{1}{\sqrt{3}}Q_1-Q_4\right) & -F_{h_b}Q_5 & F_{h_b}(Q_4-Q_2) \\ -\frac{1}{\sqrt{3}}F_{h_b}Q_2 & F_{h_b}(Q_4+Q_2) & -F_{h_b}Q_5 & F_{h_b}\left(-\frac{1}{\sqrt{3}}Q_1+Q_4\right) & F_{h_b}(-Q_3-Q_5) \\ -\frac{1}{\sqrt{3}}F_{h_b}Q_5 & F_{h_b}Q_3 & F_{h_b}(Q_4-Q_2) & F_{h_b}(-Q_3-Q_5) & F_{h_b}\left(-\frac{1}{\sqrt{3}}Q_1-Q_2\right) \end{vmatrix} \tag{3.89}$$

The first one, taken separately, yields D_{3d} minima with energies

$$E_{JT}^{h_a} = -\frac{8F_{h_a}^2}{3K_{h_a}} \tag{3.90}$$

while the second equation gives D_{5d} minima at

$$E_{JT}^{h_b} = -\frac{8F_{h_b}^2}{3K_{h_b}} \tag{3.91}$$

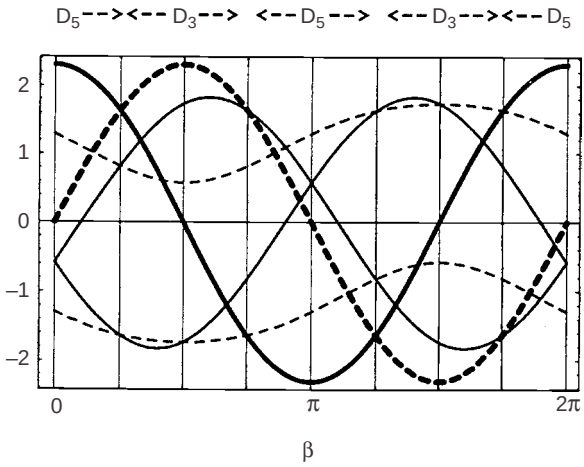

Fig. 3.26. The eigenvalues of Eq. (3.92) as a function of the parameter β. Solid and dashed lines are D_{5d} and D_{3d} eigenvalues, respectively. In both symmetries heavy lines indicate nondegenerate states, while the light lines correspond to doubly degenerate states. The ranges of appearance of the two types of minima on the lowest APES are indicated [3.30].

For the general problem $H \otimes (h_a + h_b)$ the secular equation (3.2) for ε_i^v can be presented by the following matrix equation, which is a linear combination of the above two equations:

$$[(F_h/F_{h_a}) \sin \beta] W_{h_a} + [(F_h/F_{h_b}) \cos \beta] W_{h_b} - \varepsilon^v I = 0 \qquad (3.92)$$

where the angle $0 < \beta < 2\pi$ covers all the possible combinations of the two types of coupling to the h_a and h_b displacements, and F_h is introduced for normalization. Figure 3.26 illustrates the behavior of the lowest energy level as a function of β for D_{3d} and D_{5d} distortions. We see that in the regions where the coupling to h_b is dominant (for β values near 0, π, and 2π), we get the D_{5d} distortions at lower energies (deeper minima), while in between these β values the h_a coupling is dominant and the D_{3d} minima are lower. For the application of graph theory to icosahedral problems, in particular, to the $H \otimes 2h$ problem, see in [3.45].

A more detailed consideration of the coupling to only one of the h displacements, say h_b, reveals two types of saddle points in addition to the D_{5d} minima and D_{3d} saddle points. Their relative energies are shown in Table 3.5. There are several other particular cases of the icosahedral problem considered in the literature [3.29–3.60] (see also Sections 5.4, 5.6, and 7.5.3).

Table 3.5. *Stationary (extrema) points on the APES of the $H \otimes h_b$ problem and their energies (adapted from [3.30])*

Symmetry	Type	Energy
D_{5d}	Minima	$-54F_{h_b}^2/K_{h_b}$
D_{2h} (I)	saddle points	$-40F_{h_b}^2/K_{h_b}$
D_{2h} (II)	saddle points	$-(45/2)F_{h_b}^2/K_{h_b}$
D_{3d}	saddle points	$-(50/3)F_{h_b}^2/K_{h_b}$

3.5 Adiabatic potentials in multimode problem

It is known that in a nonlinear molecular system with N atoms ($N > 2$) there are $2N-6$ degrees of freedom, which in the harmonic approximation are conveniently described by normal coordinates that transform according to corresponding irreducible representations of the symmetry point group of the system (see Section 2.2 and the appendix). If N is not very small, there may be two or more (or an infinite number for a crystal lattice) normal modes of the same symmetry, which are active in the JTE. For instance, even in a simple tetrahedral system of type MA_4, there are two types of normal coordinates of T_2 symmetry, T_2' and T_2'' (Table 2.1), both JT active. In this case the APES features must be considered in the space of not three, but six coordinates transforming as T_2' and T_2'', and the problem will be not $T \otimes (e + t_2)$, but $T \otimes (e + t_2' + t_2'')$. Such problems in which there is more than one set of JT active coordinates of given symmetry are called *multimode problems*. Unlike the latter, those with only one JT-active mode of given symmetry are called *ideal problems* [3.2].

The multimode problems are very important in the investigation of polyatomic molecules, especially crystals in which the JT center in question and its nearest neighbors cannot be isolated from the remaining lattice. The number of JT-active modes with a particular symmetry increases with the number of coordination spheres around the JT center, making the multimode problem much more complicated. For the above example of the MA_4 molecule, the number of JT active coordinates is eight, instead of five in the ideal problem.

In addition to the increasing dimensionality of the JT-active space, the number of vibronic constants is also increasing because in general the vibronic coupling to each of the modes has to be described by its own vibronic constants (however, see below). Fortunately, there is an important feature of the

multimode problem which allows some simplification, at least at the stage of qualitative consideration. With this simplification the stationary points of the multimode-problem APES are similar to those of the corresponding ideal problem. As an example we illustrate this statement for the two-mode $E \otimes (b_1' + b_1'')$ problem. The corresponding ideal problem is $E \otimes b_1$, which leads to a simple APES illustrated in Fig. 3.1(b).

Set $Q_{b_1'} = Q_1$ and $Q_{b_1''} = Q_2$ and denote the corresponding constants of linear coupling with b_1' and b_1'' displacements by F_1 and F_2, respectively. Then the vibronic coupling matrix W in the secular equation (3.2) takes the form

$$W = \begin{vmatrix} F_1 Q_1 + F_2 Q_2 & 0 \\ 0 & -F_1 Q_1 - F_2 Q_2 \end{vmatrix} \tag{3.93}$$

with roots of Eq. (3.2)

$$\varepsilon_{\pm}^{v} = \pm (F_1 Q_1 + F_2 Q_2) \tag{3.94}$$

which, upon substitution into Eq. (3.1), yield the following APES (the force constants are denoted by $K_{b_1'} = K_1$ and $K_{b_1''} = K_2$):

$$\varepsilon_{\pm}(Q_1,\ Q_2) = \tfrac{1}{2}(K_1 Q_1^2 + K_2 Q_2^2) \pm (F_1 Q_1 + F_2 Q_2) \tag{3.95}$$

with minima at the points

$$Q_1^0 = \pm (F_1/K_1), \qquad Q_2^0 = \pm (F_2/K_2) \tag{3.96}$$

at depth

$$E_{\mathrm{JT}} = \tfrac{1}{2}[(F_1^2/K_1) + (F_2^2/K_2)] \tag{3.97}$$

It is seen that in the $E \otimes (b_1' + b_1'')$ problem, as in the corresponding ideal $E \otimes b_1$ problem, there are two equivalent minima of the APES. But in the multimode case both coordinates Q_1 and Q_2 are displaced at the minima, whereas in the ideal problem only one coordinate is shifted. However, the expression (3.95) allows a linear transformation to other coordinates, in which only one mode will be displaced at the minima (as in the ideal case). These new coordinates are given by

$$\begin{aligned} q_1 &= [(F_1/K_1)Q_1 + (F_2/K_2)Q_2]/F \\ q_2 &= (-F_2 Q_1 + F_1 Q_2)/F\sqrt{K_1 K_2} \\ F &= [(F_1^2/K_1) + (F_2^2/K_2)]^{\frac{1}{2}} \end{aligned} \tag{3.98}$$

In terms of these coordinates the APES (3.95) takes the form

$$\varepsilon_{\pm}(q_1,\ q_2) = \tfrac{1}{2}(q_1^2 + q_2^2) \pm Fq_1 \tag{3.99}$$

with minima displaced only in q_1:

$$q_1^0 = \pm F, \qquad q_2^0 = 0 \tag{3.100}$$

The depth of the minima remains as in (3.97).

In other words, by means of a coordinate transformation the APES of the two-mode problem has been reduced to qualitatively the same shape as that of the ideal problem, i.e., with the same vibronic features, and the same number and types of minima in which only one coordinate, the "*interaction mode*," is displaced. This result, illustrated here by the $E \otimes (b_1' + b_1'')$ problem, is of general validity [3.1].

Note that the reduction of the multimode problem to the form in which vibronic effects are expressed by only one mode does not mean that some of the atoms of the polyatomic system are excluded from participation in the JTE. Actually, the coordinates of all the atoms are present in the interaction mode $q_{1,2}$ given by Eq. (3.98). However, the displacements of different atoms in the JT distortion are not independent, but concerted (coherent), and therefore they can be taken into account by means of an essentially smaller number of coordinates.

For instance, in case of the linear multimode $E \otimes (e_1 + e_2 + \cdots)$ problem the APES can be reduced to that of the "Mexican hat" for the ideal $E \otimes e$ problem (Fig. 3.3). When the system is moving along the trough, *the circular motions of the atoms of the first coordination sphere* (ideal system), described in Section 3.1, *involve in these motions the atoms of all the coordination spheres* through the vibronic and vibrational coupling. This produces *a wave of deformations*, which *rotates around the JT center, drawing into this rotation all the coordination spheres of atoms*, the magnitude of deformation falling with the distance from the JT center (Section 5.5).

As indicated above, the number of JT-active modes and vibronic constants increases with the number of next-neighbor coordination spheres involved in the vibronic interaction. There are cases, however, when the electronically degenerate term is strongly localized and therefore the proper vibronic coupling (of the electrons with the nuclear displacements) is negligible beyond the first, or first few coordination spheres. In this case there is no need to introduce as many vibronic constants as there are JT-active modes: the number of these constants may be greatly reduced, in many cases to one, which characterizes the vibronic interaction with the atomic displacements of the first coordination

sphere. This does not mean, however, that the problem ceases to be multimode and becomes ideal, since the displacements of the first coordination sphere enter into all the symmetrized displacements e_1, e_2, ..., etc. The coupling to even one (the first) coordination sphere involves all the modes in the JTE, but the fewer the number of nonzero vibronic constants, the easier the solution of the problem.

Consider for instance, the n-mode $E \otimes e$ problem (the $E \otimes (e_1 + e_2 + \cdots e_n)$) problem) with only one vibronic coupling constant F_E. The APES, as indicated above, can be reduced, by means of a coordinate transformation, to the shape of a trough, similar to that illustrated in Fig. 3.3. In this trough there is a free "rotation" of the system (a rotation of the wave of the JT deformation) around the JT center, and harmonic vibrations along the remaining $2n-1$ coordinates. The dimensions of the trough, its radius and depth, are determined by the contributions of all the modes e_i proportional to $F_{e_i} = F_E a_{e_i}$, where $a_{e_i} = a_i(E)$ is the coefficient with which the displacements of the first coordination sphere enter the e_i mode in question according to the general formula

$$Q_{\overline{\Gamma}} = \sum_{\kappa} a_{\kappa}(\overline{\Gamma}) q_{\kappa} \tag{3.101}$$

The numerical values of the coefficients a_{e_i} are known, provided the dynamic problem of molecular vibrations is solved: for crystals, a_{e_i} are called Van Vleck coefficients [3.61] (see also [3.1]). As a result, the JT stabilization energy equals the sum of the contributions E^i_{JT} of each JT-active mode e_i:

$$\begin{aligned} E^i_{\mathrm{JT}} &= F^2_{e_i}/2K_{e_i} = F^2_E a^2_{e_i}/2K_{e_i} \\ E_{\mathrm{JT}} &= \tfrac{1}{2} F^2_E \sum_i (a^2_{e_i}/K_{e_i}) \end{aligned} \tag{3.102}$$

Thus with known coefficients a_{e_i} and corresponding force constants $K_{e_i} = M_{e_i}\omega^2_{e_i}$ (for a crystal lattice the phonon density of states $\rho(\omega)$ is employed instead of K_{e_i}), the shape of the APES for the multimode problem can be determined. It must be emphasized, however, that the transformation (3.98), essentially simplifying the expression for the APES and allowing separation of a single active JT mode (the interaction mode), *does not simplify the multimode problem as a whole*, especially the calculations of the energy spectra and wavefunctions. In general, this transformation does not separate the variables: as a result of the APES simplification the expression for the kinetic energy will become more complicated [3.1]. But in some particular cases, especially for strong vibronic coupling, this simplification may be very useful; Section 5.5 continues the presentation of this topic.

As mentioned earlier, the JT parameters of ideal systems can be calculated numerically by means of existing methods of electronic structure calculations. This refers also to multimode problems, provided the number of JT active modes is not very large, meaning molecular systems of small to moderate size. For large systems and impurity centers in crystals, for which the number of JT modes is very large or infinite, the numerical methods cannot be applied directly. However, if the vibronic coupling is essentially localized around the JT center (the wavefunctions of the degenerate term are rather localized), the so-called *quasimolecular (cluster) models* may be useful as an approximation to the real system. In these models a cluster with a limited number of atoms around the JT center is cut off from the lattice and considered separately, and then the interaction with the lattice is taken into account using reasonable approximations.

Obviously, the JT parameters of the multimode cluster can be calculated numerically, while the influence of the rest of the crystal may be approximated by analytical potentials, the simplest being the Madelung potential. A more elaborate *ab initio* model-potential-embedding method was suggested recently [3.62] for this procedure. In this method the cluster-environment Coulomb and exchange interaction (without correlation effects) is included in the embedded cluster calculations, yielding reasonable results for the JT parameters of impurity centers in ionic crystals (Section 8.1). More on the cluster model see in Section 5.5.

Again, the APES parameters of JT systems, as outlined in Section 3.1, have limited applicability in revealing observable properties. To obtain the energy spectrum and wavefunctions, the dynamic problem formulated by the vibronic coupling equations (2.6) should be solved. The dynamic multimode problem in JT systems considered in [3.1, 3.63–3.84] is given full attention in Section 5.5.

3.6 Multicenter systems

So far we have considered molecular systems with one JT center, usually an atom or ion in a degenerate electronic state with its near-neighbor environment (pseudodegenerate states are considered in Chapter 4). However, in some cases, within the same polyatomic system there are two or more such JT centers with sufficiently strong interaction between them, which influences the energy spectrum and wavefunctions of the system as a whole. The vibronic interaction in such multicenter systems is important for two main reasons. First, they are of special interest as coordination systems, mixed-valence compounds, interacting impurity centers in crystals, and in molecular biology (Section 7.6).

Second, polynuclear clusters serve as a model system for crystals with a cooperative JT or PJT effect and structural phase transitions (Sections 8.2 and 8.3).

If there are direct chemical interactions (no intermediate binding atoms) between the JT centers, the direct exchange interaction between them is very strong, resulting in corresponding energy gaps of the order of several electronvolts in the energy spectrum. In such cases the vibronic coupling can be considered for each of the exchange terms separately, thus resulting in one of the vibronic problems discussed above, the only distinction being that the electronic state involves not one but all the JT centers participating in the direct exchange. Usually these states are coupled to a relatively large number of vibrational degrees of freedom, and hence the vibronic problem is a multimode one (Sections 3.5 and 5.5).

The situation is rather different when there are bridging atoms between the JT ions. In this case we have the so-called indirect superexchange with corresponding relatively small splittings of the order of 10–100 cm^{-1} in the energy spectrum. If the vibronic coupling at each center is sufficiently weak, the exchange interaction has to be considered first, and then the possibility of vibronic mixing of exchange-coupled terms with the same multiplicity must be included. Even when there is no orbital degeneracy at each center, such degeneracy may occur as a result of the exchange interaction of pure spin multiplets. For instance, the exchange interaction within a system of three electronic spins positioned at three corners of an equilateral triangle results in the multiplets $^4A_2$ and ^2E [3.85]. The latter corresponds to a wave of spin density propagating around the perimeter of the triangle clockwise or counterclockwise. In this case the $E \otimes e$-type JTE takes place for the exchange ^2E term, but the vibronic coupling is expected to be rather small. The vibronic mixing of such spin states in three- and four-center systems is considered in [3.86–3.88].

Below in this section the opposite limit of strong vibronic coupling on each center is considered. In this case the vibronic interaction has to be taken into account first, and then the indirect exchange coupling may be included as a small perturbation. Various many-center JT systems differ in both the number of interacting JT centers and the mode of their coordination. For instance, two octahedral complexes of the type ML_6 can form a two-center system (bioctahedron) in three different ways with the two central atoms lying on the common axes of symmetry of the fourth, third, and second order, respectively (Fig. 3.27). Quite a large number of three- and four-center JT systems are well known, some of them containing several identical metal atoms (exchange-coupled clusters) [3.89, 3.90]. Other examples are provided by crystals with two or more JT impurities occupying near-neighbor lattice cells (Section 8.1).

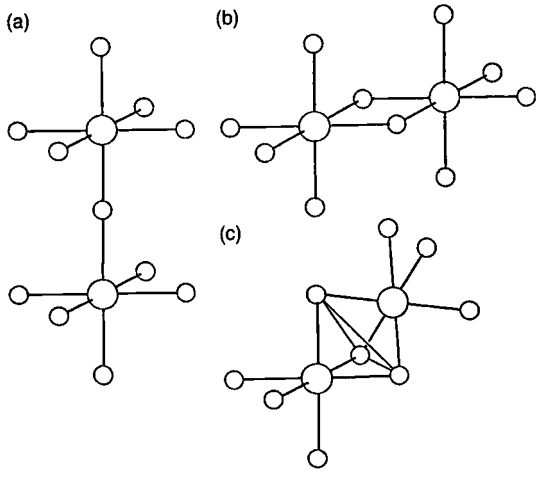

Fig. 3.27. Three types of JT two-center bioctahedral systems with a common symmetry axis of fourth (a), second (b), and third (c) order [3.1].

Among the polynuclear clusters, the bioctahedron with a common vertex (Fig. 3.27(a)) is the most studied from the point of view of vibronic coupling. The adiabatic potentials of a bioctahedron with an $E \otimes e$ JTE at each of the two centers were considered first in [3.91]. In [3.92] this problem is treated as a first step to the cooperative JTE in spinels (see also [3.93]). A different approach based on the analysis of vibrational dynamics is suggested in [3.94]. In [3.95, 3.96] the energy of the system is minimized with respect to nuclear displacements within the framework of a simple model with a Born–Mayer potential and Coulomb interaction between nearest-neighbor ions; in this way the problem is reduced to electronic interaction of the orbitally degenerate states of the centers. The molecular field approximation is employed in [3.97] in order to explain the temperature dependence of the exchange interaction. Further advance were achieved in a series of papers [3.98–3.105].

The results obtained in these studies differ in some respects. As shown below, these differences are due to different ways of accounting for the translational degrees of freedom of the octahedrons, in particular, for the differences in the masses of central atom and ligands. The problem and its possible solutions are illustrated below by considering the example of vibronic interactions in a bioctahedron based on the results of the works mentioned above, and following the presentation in [3.1].

Consider a 13-atom system of D_{4h} symmetry shown in Fig. 3.27(a). We assume first that each of the two ions in an octahedral environment has an orbital double ^2E_g state formed by a single electron (or a hole) in the highest

occupied orbital e_g. Labeling the two electronic states by ϑ and ε, the two centers by 1 and 2, and the two spin states by α and β, one can form 28 two-electron determinants describing the possible symmetrized electronic states of the two-center system. The group-theoretical classification according to the representations of the D_{4h} group and total spin $S_1 + S_2$ results in the following possible terms: $4^1A_{1g} + 2^1B_{1g} + 2^1B_{2u} + 2^1A_{2u} + 2^3B_{1g} + 2^3B_{2u} + 2^3A_{2u}$. We thus arrive at a very difficult problem of the vibronic mixing of 10 singlet and 18 triplet states by a considerable number of nuclear displacements, which it is hardly possible to solve without simplifications.

The first approximation that can be introduced is based on the fact that the interaction between the electrons is much stronger when they are localized on the center than when they are delocalized over two centers. This allows us to use the Heitler–London approach and to exclude the high-energy states, i.e. those for which both electrons are localized on one center (the vibronic coupling to these states is considered below). Then the number of mixing electronic states is reduced to 16, $2^1A_{1g} + {}^1B_{1g} + {}^1B_{2u} + 2^3A_{2u} + {}^3B_{1g} + {}^3B_{2u}$. Since the states with the same spin and spin projection quantum numbers only are mixed by the vibronic interaction, the modes of nuclear displacements mixing these states are of the types A_{1g}, A_{2u}, B_{1g}, and B_{2u}.

If the exchange interaction (and hence the overlap of the wavefunctions of different centers) is neglected, the symmetrized determinant representation may be omitted, and any linear combination of the above 16 degenerate wavefunctions can be chosen as a basis set. In particular, the multiplicative states on the centers $\psi^{(1)}_{E\gamma_1}(r_1)\sigma_1\psi^{(2)}_{E\gamma_2}(r_2)\sigma_2$, where r_1 and r_2 are the electron (hole) coordinates, and σ_1 and σ_2 are the spin states of the two centers can serve as such a set. Since different spin states are not mixed by the vibronic interaction, these 16 multiplicative states can be divided into four groups with different orbital parts only. The matrix of vibronic interaction is the same for all these groups. Thus we have reduced the problem to the investigation of the vibronic mixing of four states $\psi^{(1)}_{\vartheta}(r_1)\psi^{(2)}_{\vartheta}(r_2)$, $\psi^{(1)}_{\vartheta}(r_1)\psi^{(2)}_{\varepsilon}(r_2)$, $\psi^{(1)}_{\varepsilon}(r_1)\psi^{(2)}_{\vartheta}(r_2)$, and $\psi^{(1)}_{\varepsilon}(r_1)\psi^{(2)}_{\varepsilon}(r_2)$ by the displacement of A_{1g}, A_{2u}, B_{1g}, and B_{2u} symmetry.

The second simplification can be introduced in the vibrational subsystem. The full vibrational representation of the 13-atom molecule shown in Fig. 3.27(a) contains the following irreducible representations of the D_{4h} group: $4A_{1g} + A_{1u} + 4A_{2u} + 2B_{1g} + B_{1u} + B_{2g} + 2B_{2u} + 4E_g + 5E_u$. The number of active modes, even if the totally symmetric representation A_{1g} is excluded, is too large ($4A_{2u} + 2B_{1g} + 2B_{2u} = 8$). It could be reduced by the method described in Section 3.5 by passing to the so-called interaction modes. However, an easier

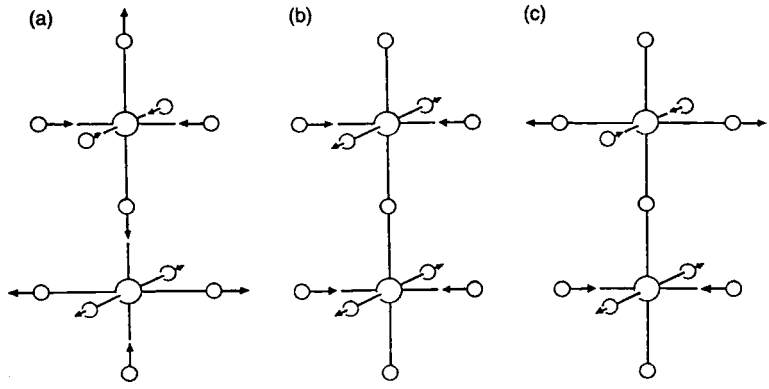

Fig. 3.28. Symmetrized atomic displacements in a bioctahedron with D_{4h} symmetry, which transform as the irreducible representations A_{2u} (a), B_{1g} (b), and B_{2u} (c) [3.1].

way is possible here. Remembering that E_g terms interact only with local e_g vibrations (Section 3.2), the elastic energy of isolated octahedra can be presented as a sum of the main contributions from e_g vibrations,

$$U_0 = \frac{1}{2}\sum_{n=1,2} K_E[Q_\vartheta^2(n) + Q_\varepsilon^2(n)] \tag{3.103}$$

where n labels the two octahedra, and K_E is the corresponding force constant for the e_g vibrations. Using the group projection operator one can form the following linear combinations of the $Q_{E\gamma}(n)$ coordinates transforming as the irreducible representations of the D_{4h} group [3.1]:

$$\begin{aligned} Q(A_{1g}) &= (1/\sqrt{2})[Q_\vartheta(1) + Q_\vartheta(2)] \\ Q(B_{1g}) &= (1/\sqrt{2})[Q_\varepsilon(1) + Q_\varepsilon(2)] \\ Q(A_{2u}) &= (1/\sqrt{2})[Q_\vartheta(1) - Q_\vartheta(2)] \\ Q(B_{2u}) &= (1/\sqrt{2})[Q_\varepsilon(1) - Q_\varepsilon(2)] \end{aligned} \tag{3.104}$$

The resulting symmetrized displacements $Q(A_{2u})$, $Q(B_{1g})$, and $Q(B_{2u})$ of the bioctahedron as a whole are illustrated in Fig. 3.28. In these coordinates the elastic energy (3.103) is

$$U_0 = \tfrac{1}{2}K_E[Q^2(A_{1g}) + Q^2(A_{2u}) + Q^2(B_{1g}) + Q^2(B_{2u})] \tag{3.105}$$

Now one has to take into account the shared (bridging) atom due to which the two octahedrons are not isolated. Its displacements introduce additional

coupling conditions, which can be evaluated in the following way. The Cartesian displacements of this atom can be expressed by the symmetrized displacements of either the first octahedron $Q_{\Gamma\gamma}(1)$, or the second $Q_{\Gamma\gamma}(2)$. By equating these two expressions for each component x, y, and z, we get three conditions of coupling. If only e_g and translational degrees of freedom are considered (the latter have no elasticity), then all the $Q_{\Gamma\gamma}(n)$ coordinates are zero except $Q_\vartheta(n)$, $Q_\varepsilon(n)$, $Q_x(n)$, $Q_y(n)$, and $Q_z(n)$. On separating the motion of the bioctahedron center of mass we find that two of three coupling relations become identities, while the third one can be reduced to

$$Q_\vartheta(1) + Q_\vartheta(2) = \left(\frac{3m}{M+6m}\right)^{\frac{1}{2}} [Q_z(1) + Q_z(2)] \tag{3.106}$$

where m is the mass of the ligand and M is the mass of the central atom, and we use mass-weighted coordinates. If the mass of the central atom is much larger than the mass of the ligands, i.e., $M \gg 6m$, then the right-hand side of (3.106) is close to zero, and to a good approximation one can assume that $Q_\vartheta(1) + Q_\vartheta(2) = 0$. This obvious result means that if $M \gg 6\,m$, then the translational motion of the octahedra can be neglected due to the high interia of the central atoms, and the axial elongation of one of the octahedra has to be accompanied by equal compression of the other. However, in general, this is not the case, since the octahedra can adjust to each other at the expense of translational degrees of freedom.

For crystals with a pair of impurity atoms the intermediate case becomes important when the translational motion of the octahedra is not completely excluded, but is not free either. Corresponding results in this case can be obtained by adding to (3.105) the term $\frac{1}{2}K_{T_{1u}}[Q_z^2(1) + Q_z^2(2)]$ which describes the elastic energy of the shift of the octahedra.

To take into account the condition (3.106), let us change to new coordinates [3.1]:

$$\begin{aligned}
q(A_{1g}) &= \frac{\lambda^2}{1+\lambda^2} Q(A_{1g}) + \frac{\lambda}{1+\lambda^2} \tilde{Q}(A_{1g}) \\
\tilde{q}(A_{1g}) &= -\frac{1}{\lambda} Q(A_{1g}) + \tilde{Q}(A_{1g}) \\
q(A_{2u}) &= Q(A_{2u}) \\
q(B_{1g}) &= Q(B_{1g}) \\
q(B_{2g}) &= Q(B_{2g})
\end{aligned} \tag{3.107}$$

where $\lambda = [3m/(M+6m)]^{\frac{1}{2}}$, and $\tilde{Q}(A_{1g}) = [Q_z(2) - Q_z(1)]/\sqrt{2}$ is the coordinate describing the relative motion of the octahedra, the other $Q(\Gamma)$ being determined by Eq. (3.104). Since $\tilde{q}(A_{1g}) = 0$ (see Eqs. (3.104) and (3.106)), the elastic energy in new coordinates acquires the form

$$U_0 = \tfrac{1}{2}K_E[q^2(A_{1g}) + q^2(A_{2u}) + q^2(B_{1g}) + q^2(B_{2u})] \tag{3.108}$$

while the reduced mass for the coordinate $q(A_{1g})$ equals $(1+\lambda^2)/\lambda^2$. In the old coordinates expression (3.108) is more complicated (see in [3.1]). It shows that as a result of coupling condition (3.106) the degeneracy of the e vibrations of the octahedra is removed; the translational motion of the octahedra in the axial direction is no longer free but elastic with an elastic constant $\lambda^2 K_E/2(1+\lambda^2)^2$, while the nuclear displacements $Q_\vartheta(n)$ and $Q_z(n)$, which belong to the same irreducible representation A_1 of the local symmetry group of the center, are no longer independent, but mixed.

With these transformations, the resulting four adiabatic potential surfaces are [3.1]

$$\varepsilon(q) = \tfrac{1}{2}K_E[q^2(A_{1g}) + q^2(A_{2u}) + q^2(B_{1g}) + q^2(B_{2u})] \pm |F_E|[\rho(1) \mp \rho(2)] \tag{3.109}$$

where, taking into account Eqs. (3.104), (3.106), and (3.107), we have

$$\begin{aligned} \rho(1) &= \{\tfrac{1}{2}[q(A_{1g}) + q(A_{2u})]^2 + \tfrac{1}{2}[q(B_{1g}) + q(B_{2u})]^2\}^{\frac{1}{2}} \\ \rho(2) &= \{\tfrac{1}{2}[q(A_{1g}) - q(A_{2u})]^2 + \tfrac{1}{2}[q(B_{1g}) - q(B_{2u})]^2\}^{\frac{1}{2}} \end{aligned} \tag{3.110}$$

The extrema points of the lowest sheet (corresponding to the lower signs in Eq. (3.109)) form a two-dimensional equipotential manifold (a trough):

$$\begin{aligned} q^{(0)}(A_{1g}) &= (1/\sqrt{2})(\cos\varphi_1 + \cos\varphi_2) \\ q^{(0)}(B_{1g}) &= (1/\sqrt{2})(\sin\varphi_1 + \sin\varphi_2) \\ q^{(0)}(A_{2u}) &= (1/\sqrt{2})(\cos\varphi_1 - \cos\varphi_2) \\ q^{(0)}(B_{2u}) &= (1/\sqrt{2})(\sin\varphi_1 - \sin\varphi_2) \end{aligned} \tag{3.111}$$

where φ_1 and φ_2 are arbitrary parameters varying between 0 and 2π, and $\rho_0 = |F_E|/K_E$. The JT stabilization energy is $E_{JT} = F_E^2/K_E$.

The physical meaning of this result can be understood if one notes that E_{JT} equals the sum of JT stabilization energies of the two isolated octahedra.

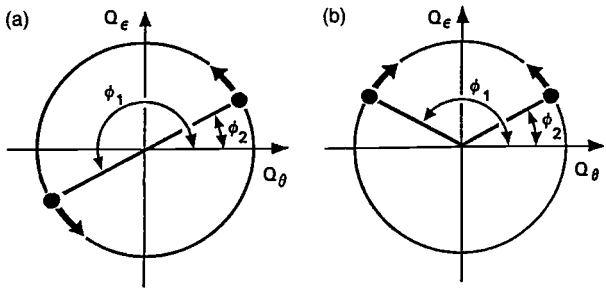

Fig. 3.29. Correlated motions of the waves of E-type deformations of each of the two octahedra in an bioctahedron with an $E \otimes e$ problem on each center: (a) in-phase motion corresponding to ferrodistortive ordering of the distortions; (b) anti-phase motion for antiferrodistortive ordering.

Taking into account Eqs. (3.104)–(3.107), the extrema point coordinates (3.111) can be written as

$$\begin{aligned} Q_\vartheta^{(0)}(1) &= \rho_0 \cos\varphi_1 \\ Q_\vartheta^{(0)}(2) &= \rho_0 \cos\varphi_2 \\ Q_\varepsilon^{(0)}(1) &= \rho_0 \sin\varphi_1 \\ Q_\varepsilon^{(0)}(2) &= \rho_0 \sin\varphi_2 \end{aligned} \tag{3.112}$$

These relations mean that in a bioctahedron with one common (bridging) atom the rotations of the waves of deformation around each JT center are not correlated, i.e., they proceed independently in each octahedron. This is due to the inclusion of the translational degrees of freedom, which remove any constraint on the packing of the two octahedra with distortions [3.86]. However, if the mass of the central atoms is much larger than the mass of the ligands ($M \gg 6m$), then $\lambda \approx 0$ and the coupling condition (3.106) imposes restrictions on the angular parameters φ_1 and φ_2, namely, $\varphi_1 \pm \varphi_2 = \pi$, i.e., one of them is no longer independent. It follows from this equation, in particular, that $\dot{\varphi}_1 \pm \dot{\varphi}_2 = 0$ (overdots denote time derivatives). This means that in the bioctahedron with one bridging atom and a heavy central atom the two waves of deformations propagate around each center not independently, but with a certain phase shift, the motions along the bottom of the trough occurring either in the same direction ($\dot{\varphi}_1 = \dot{\varphi}_2$), or in opposite directions ($\dot{\varphi}_1 = -\dot{\varphi}_2$). These two possibilities are shown schematically in Fig. 3.29.

The presence of a trough in the potential energy surface means that the symmetry of the APES is higher than that of the bioctahedron in its initial high-symmetry configuration (D_{4h}). This is due to the approximations used above: neglect of exchange interactions and tetragonal crystal fields, the

Table 3.6. *Coordinates of the nine types of extrema points on the APES of a bioctahedron with a JT $E \otimes e$ or $T \otimes e$ problem on each of the two centers (in units of ρ_0) [3.1, 3.94, 3.101]*

Symmetry	$q(A_{1g})$	$q(A_{2u})$	$q(B_{1g})$	$q(B_{2u})$	$Q_\vartheta(1)$	$Q_\varepsilon(1)$	$Q_\vartheta(2)$	$Q_\varepsilon(2)$
D_{4h}	$\sqrt{2}$	0	0	0	1	0	1	0
D_{2h}	$-\sqrt{2}/2$	0	$\sqrt{6}/2$	0	$-1/2$	$\sqrt{3}/2$	$-1/2$	$\sqrt{3}/2$
D_{2h}	$-\sqrt{2}/2$	0	$-\sqrt{6}/2$	0	$-1/2$	$-\sqrt{3}/2$	$-1/2$	$-\sqrt{3}/2$
D_{2d}	$-\sqrt{2}/2$	0	0	$\sqrt{6}/2$	$-1/2$	$\sqrt{3}/2$	$-1/2$	$-\sqrt{3}/2$
D_{2d}	$\sqrt{3}/2$	0	0	$-\sqrt{6}/2$	$-1/2$	$-\sqrt{3}/2$	$-1/2$	$\sqrt{3}/2$
C_{2v}	$\sqrt{2}/4$	$3\sqrt{2}/4$	$\sqrt{6}/4$	$-\sqrt{6}/4$	1	0	$-1/2$	$\sqrt{3}/2$
C_{2v}	$\sqrt{2}/4$	$3\sqrt{2}/4$	$-\sqrt{6}/4$	$\sqrt{6}/4$	1	0	$-1/2$	$-\sqrt{3}/2$
C_{2v}	$\sqrt{2}/4$	$-3\sqrt{2}/4$	$\sqrt{6}/4$	$\sqrt{6}/4$	$-1/2$	$\sqrt{3}/2$	1	0
C_{2v}	$\sqrt{2}/4$	$-3\sqrt{2}/4$	$-\sqrt{6}/4$	$-\sqrt{6}/4$	$-1/2$	$-\sqrt{3}/2$	1	0

limitation to one-center vibronic coupling, and the linear vibronic interaction. The removal of any one of these approximations restores the D_{4h} symmetry, resulting in the corresponding warping of the trough.

Taking into account the quadratic terms of vibronic interactions leads to a more general result [3.92, 3.93]. Indeed, on replacing in expressions (3.109) and (3.110) the square roots from Eq. (3.23), we obtain four types of extrema points with coordinates given in Table 3.6. All the coordinates are proportional to ρ_0 (cf. Eq. (3.28)),

$$\rho_0 = |F_E|/(K_E - 2|G_E|) \tag{3.113}$$

and therefore only the corresponding coefficients are given in Table 3.6. The JT stabilization energies for all nine extrema points coincide and are given by

$$E_{JT} = F_E^2/(K_E - 2|G_E|) \tag{3.114}$$

which is exactly twice the E_{JT} value for an isolated octahedron, Eq. (3.29). This allows us to give the following physical interpretation of the results [3.91]. As in cases of linear vibronic coupling at each center, the octahedron distortions are not correlated, and the resulting nuclear configuration is determined only by the packing of differently distorted octahedra; as in the linear case, this becomes possible due to inclusion of the translational degrees of freedom of the octahedra.

However, if $M \gg 6m$ ($\lambda \approx 0$) the translations become rather inertial and the condition (3.106) is reduced to the requirement $Q_\vartheta(1) = -Q_\vartheta(2)$, i.e., $q(A_{1g}) = 0$. With this condition none of the nine extrema points obtained above remains. Instead, others appear, but with the same types of symmetry, D_{2h}, D_{2d}, and C_{2v} [3.94]. At the extrema points of the type D_{2h}, $Q_\varepsilon(1) = Q_\varepsilon(2)$, while for D_{2d} type, $Q_\varepsilon(1) = -Q_\varepsilon(2)$. These two types of extrema points correspond to two special types of packing of the distorted octahedra. In the case of $Q_\varepsilon(1) = Q_\varepsilon(2)$, when $q^{(0)}(B_{1g}) \neq 0$ and $q^{(0)}(B_{2u}) = 0$, the packing is "parallel" (Fig. 3.28(b)), or of "ferro" type, and it is called ferrodistortive, whereas for $Q_\varepsilon(1) = -Q_\varepsilon(2)$, $q^{(0)}(B_{1g}) = 0$ and $q^{(0)}(B_{2u}) \neq 0$, the packing is antiferrodistortive (Fig. 3.28(c)). Such an ordering of local JT distortions in crystals with regular JT centers results in the cooperative JTE (Section 8.2).

Consider now the case when the JTE on each center of the two-center bioctahedral system has a $T \otimes e$ coupling, i.e. the electronic state of the isolated octahedron is threefold degenerate and the vibronic coupling with the t_{2g} vibrations can be neglected. In the same approximation as above, the potential energy operator can be written as in Eqs. (3.1) and (3.2) with the W matrix from Eq. (3.42) and with $F_T = 0$ for each center. In the basis of nine multiplicative states $\psi^{(1)}_{T\gamma_1}(r_1)\psi^{(2)}_{T\gamma_2}(r_2)$ we get a 9×9 diagonal matrix, and therefore the APES can be evaluated directly, quite similar to the one-center case that yields the solutions (3.44). The electronic contribution to the potential energy is linear with respect to the normal coordinates, and the adiabatic potential consists of nine intersecting paraboloids [3.101]. The minima coordinates are given in Table 3.6. Here, instead of (3.113) for the $E \otimes e$ problem, the ρ_0 value is

$$\rho_0 = |F_E|/K_E \tag{3.115}$$

In a similar way, the JTE in a bioctahedron with $T \otimes t_2$ coupling at each center can be considered. The minima configurations in this case can be presented as different possible packings of the two trigonally distorted octahedra. The bioctahedron with two edge- and face-shared octahedra is considered in [3.104].

More complicated four-center JT systems of the type $Cu_4OX_6L_4$ are considered in [3.102, 3.103]. In these systems with the initial nuclear configurations of T_d symmetry four identical transition metal ions occupy the vertices of a tetrahedron, and the configuration of the atoms nearest to the vertices has C_{3v} symmetry. The local trigonal symmetry splits the ^2D term of the JT Cu^{2+} (d^9) ion into $A_1 + E' + E$, allowing a two-fold degenerate ground state with $E \otimes e$ coupling on each center. As in the previous cases, the JTE results in the wave of deformation of the local environment of each center, and the waves of deformation of different centers, owing to intercenter interactions, are correlated in phase and magnitude. In the linear approximation of the vibronic interaction

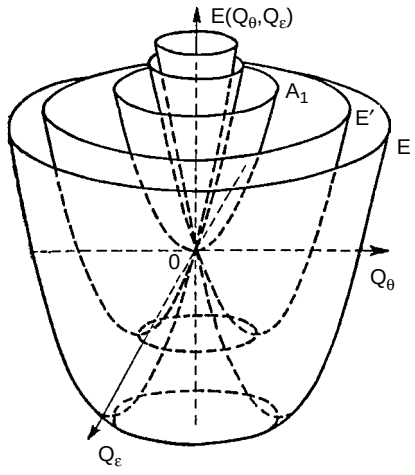

Fig. 3.30. The APES of a tetrahedral four-center system with a JT Cu^{2+} (d^9) ^2D term and trigonal symmetry on each center producing $A_1 + E + E'$ branches in the space of the interaction e mode Q_ϑ and Q_ε of the reduced multimode problem [3.102].

the lowest sheet of the adiabatic potential has a continuum of equivalent minima points in the space of e displacements (a trough).

Figure 3.30 illustrates the five-sheet APES obtained for this case in the space of two interaction modes Q_ϑ and Q_ε that reduce the multimode space to the one-mode one (Sections 3.5 and 5.5). The results obtained explain the origin of the anomalous, nonmonotonic dependence of the magnetic moment on temperature in some of these complexes [3.102]. The quadratic terms of vibronic interactions result in a warping of the trough with alternating tetragonal minima and saddle points on its bottom. The nuclear configuration at the minima is, in principle, similar to that of the one-center Jahn–Teller tetrahedral $E \otimes e$ problem in accordance with the general symmetry requirements (Section 3.2).

For arbitrary multicenter JT systems with significant elastic interaction between the centers, an effective-Hamiltonian method was suggested [3.104, 3.105], in which the extrema points of the APES can be found by analyzing an effective APES in the space of the active one-center displacements only. This method was applied to the problem of a bioctahedron with two edge- and face-shared octahedra [3.105].

Two-center, three-center, and other multicenter JT and PJT systems are widespread among exchange-interacting mixed-valence compounds. Since their treatment involves essentially the PJTE (Chapter 4), vibronic coupling in mixed-valence compounds is considered later, in Section 7.6.3.

References

3.1. I. B. Bersuker and V. Z. Polinger, *Vibronic Interactions in Molecules and Crystals*, New York, Springer, 1989.
3.2. R. Englman, *The Jahn–Teller Effect in Molecules and Crystals*, London, Wiley, 1972.
3.3. R. S. Markiewicz, *Phys. Rev. E* **64**, 6216 (2001).
3.4. M. Bacci, *Phys. Rev. B* **17**, 4495 (1978).
3.5. A. D. Liehr and C. J. Ballhausen, *Ann. Phys. (N.Y.)* **3**, 304 (1958).
3.6. J. H. Van Vleck, *J. Chem. Phys.* **7**, 61 (1939).
3.7. A. D. Liehr, *J. Phys. Chem.* **67**, 389 (1963); *Progr. Inorg. Chem.* **3**, 281 (1962); **4**, 455 (1962); **5**, 385 (1963).
3.8. B. R. Judd, *Adv. Chem. Phys.* **57**, 247 (1984).
3.9. (a) P. Garcia-Fernandez, I. B. Bersuker, J. A. Aramburu, M. T. Barriuso, and M. Moreno, *Phys. Rev.*, to be published. (b) A. Viel and W. Eisfeld, *J. Chem. Phys.* **120**, 4603 (2004).
3.10. W. Zwanziger and E. R. Grant, *J. Chem. Phys.* **87**, 2954 (1987).
3.11. G. Bevilacqua, in *Electron–Phonon Dynamics and Jahn–Teller Effects*, Eds. G. Bevilacqua, L. Martinelli, and N. Terzi, Singapore, World Scientific, 1999.
3.12. N. Balabanov, Thesis, Ivanovo State University for Chemical Sciences and Technology, Ivanovo (Russia), 1998.
3.13. G. Sadygov and D. R. Yarkony, *J. Chem. Phys.* **110**, 3639 (1999).
3.14. D. R. Yarkony, *J. Chem. Phys.* **111**, 4906 (1999).
3.15. H. Koizumi and I. B. Bersuker, *Phys. Rev. Lett.* **83**, 3009 (1999).
3.16. H. Koizumi, I. B. Bersuker, J. E. Boggs, and V. Z. Polinger, *J. Chem. Phys.* **112**, 8470 (2000).
3.17. S. Feuerbacher, L. S. Cederbaum, and T. Sommerfeld, *J. Chem. Phys.* **120**, 3201 (2004); S. Feuerbacher and L. S. Cederbaum, *J. Chem. Phys.* **121**, 5 (2004).
3.18. U. Öpik and M. H. L. Price, *Proc. R. Soc. London A* **238**, 425 (1957).
3.19. A. Ceulemans, *J. Chem. Phys.* **87**, 5374 (1987); A. Ceulemans and L. F. Chibotaru, *Theor. Chim. Acta* **94**, 205 (1996).
3.20. M. C. M. O'Brien, *Phys. Rev.* **187**, 407 (1969).
3.21. I. B. Bersuker and V. Z. Polinger, *Phys. Lett. A* **44**, 495 (1973); *Zh. Eksp. Teor. Fiz.* **66**, 2078 (1974).
3.22. S. Muramatsu and T. Iida, *J. Phys. Chem. Solids* **31**, 2209 (1970).
3.23. M. Bacci, M. P. Fontana, A. Ranfagni, and G. Viliani, *Phys. Lett. A* **50**, 405 (1975); *Phys. Rev. B* **11**, 3052 (1975).
3.24. M. Bacci, M. P. Fontana, M. Cetica, and G. Viliani, *Phys. Rev. B* **12**, 5907 (1975).
3.25. R. S. Dagis and I. B. Levinson, in *Optika i spektroskopiya*, part 3, Leningrad, Nauka, 1967.
3.26. B. R. Judd, *J. Chem. Phys.* **68**, 5643 (1978).
3.27. M. Baci, E. Mikokova, and K. Polak, *Phys. Rev. B* **55**, 14 257 (1997-I); M. Baci and S. Porcinai, in *Electron–Phonon Dynamics and Jahn–Teller Effects*, Eds. G. Bevilacqua, L. Martinelli, and N. Terzi, Singapore, World Scientific, 1999, p. 3.
3.28. B. R. Judd, *Colloques Internat. CNRS* **255**, 127 (1978).
3.29. V. P. Khlopin, V. Z. Polinger, and I. B. Bersuker, *Theor. Chim. Acta.* **48**, 87 (1978).

3.30. C. C. Chancey and M. C. M. O'Brien, *The Jahn–Teller Effect in C_{60} and Other Icosahedral Complexes*, Princeton, New Jersey, Princeton University Press, 1997.
3.31. D. R. Pooler, *J. Phys. C* **13**, 1029 (1980).
3.32. A. Ceulemans and P. W. Fowler, *Phys. Rev. A* **39**, 481 (1989).
3.33. A. Ceulemans and P. W. Fowler, *J. Chem. Phys.* **93**, 1221 (1990).
3.34. J. P. Cullerne and M. C. M. O'Brien, *J. Phys.: Condens. Matter* **6**, 9017 (1996).
3.35. A. Ceulemans and P. W. Fowler, *J. Chem. Soc. Faraday Trans.* **88**, 2797 (1992).
3.36. J. P. Cullerne, M. N. Angelova, and M. C. M. O'Brien, *J. Phys.: Condens. Matter* **7**, 3247 (1995).
3.37. J. L. Dunn and A. C. Bates, *Phys. Rev. B* **52**, 5996 (1995).
3.38. M. Lueders, N. Manini, P. Gatari, and E. Tosatti, *Eur. Phys. J. B* **35**, 57 (2003).
3.39. A. Ceulemans and L. F. Chibotaru, *Phys. Rev. B* **53**, 2460 (1996-I); **53**, 15 522 (1996-I).
3.40. M. C. P. Moate, M. C. M. O'Brien, J. L. Dunn, C. A. Bates, Y. M. Liu, and V. Z. Polinger, *Phys. Rev. Lett.* **77**, 4362 (1996).
3.41. A. Ceulemans, L. F. Chibotaru, and F. Cimpoesu, *Phys. Rev. Lett.* **78**, 3725 (1997).
3.42. A. Auerbach, N. Manini, and E. Tosatti, *Phys. Rev. B* **49**, 12 998 (1999).
3.43. A. Ceulemans, L. F. Chibotaru, and S. P. Cojocaru, *Phys. Rev B* **59**, 12 728 (1999-II).
3.44. A. L. Sobolewski, *Chem. Phys. Lett.* **267**, 452 (1997).
3.45. E. Lijnen and A. Ceulemans, *Adv. Quant. Chem.* **44**, 183 (2003).
3.46. C.-L. Wang, in *Electron–Phonon Dynamics and Jahn–Teller Effects*, Eds. G. Bevilacqua, L. Martinelli, and N. Terzi, Singapore, World Scientific, 1999, p. 280.
3.47. F. Negri and G. Orlandi, in *Electron–Phonon Dynamics and Jahn–Teller Effects*, Eds. G. Bevilacqua, L. Martinelli, and N. Terzi, Singapore, World Scientific, 1999, p. 264.
3.48. C. A. Borshch and K. Prassides, *J. Phys. Chem.* **100**, 9348 (1996).
3.49. J. L. Dunn, M. R. Eceles, C. P. Moate, Y. M. Liu, and A. C. Bates, in *Electron–Phonon Dynamics and Jahn–Teller Effects*, Eds. G. Bevilacqua, L. Martinelli, and N. Terzi, Singapore, World Scientific, 1999, p. 241; C. P. Moate, Y. M. Liu, J. L. Dunn and A. C. Bates, *ibid.*, p. 258; Q. C. Qiu, J. L. Dunn, A. C. Bates, and Y. M. Liu, *ibid.*, p. 273.
3.50. L. F. Chibotaru and A. Ceulemans, in *Electron–Phonon Dynamics and Jahn–Teller Effects*, Eds. G. Bevilacqua, L. Martinelli, and N. Terzi, Singapore, World Scientific, 1999, p. 233.
3.51. U. Rothlisberger, W. Andreoni, and P. Gianrozzi, *J. Chem Phys.* **96**, 1248 (1992).
3.52. S. Sookhum, J. L. Dunn, and C. A. Bates, *Phys. Rev. B* **68**, 235 403 (2003).
3.53. M. Lanoo, G. A. Baraft, M. Schliiter, and D. Tomanek, *Phys. Rev. B* **44**, 12 106 (1991).
3.54. V. de Coulon, J. L. Martins, and F. Reuse, *Phys. Rev. B* **45**, 13 671 (1992).
3.55. B. Gu, Z. Li, and J. Zhu, *J. Phys.: Condens. Matter* **5**, 5255 (1993).
3.56. P. B. Oliete, C. A. Bates, J. L. Dunn, and G. E. Stedman, *Phys. Rev. B* **60**, 2319 (1999-II).
3.57. Q. C. Qiu, J. L. Dunn, A. C. Bates, M. Abou-Ghantous, and V. Z. Polinger, *Phys. Rev. B* **62**, 16 155 (2000-I).
3.58. I. D. Hands, J. L. Dunn, C. A. Bates, and V. Z. Polinger, *Chem. Phys.* **278**, 41 (2002).

3.59. Y. M. Liu, J. L. Dunn, A. C. Bates, and V. Z. Polinger, *J. Phys.: Condens. Matter* **9**, 7119 (1997).
3.60. G. Colo, N. Breda, R. A. Broglia, D. Provasi, H. E. Roman, G. Onida, and E. Vigezzi, in *Electron–Phonon Dynamics and Jahn–Teller Effects*, Eds. G. Bevilacqua, L. Martinelli, and N. Terzi, Singapore, World Scientific, 1999, p. 241.
3.61. J. H. Van Vleck, *Phys. Rev.* **57**, 426 (1940).
3.62. J. L. Pascual, L. Seijo, and Z. Barandiaran, *Phys. Rev.* **53**, 1138 (1996-I).
3.63. E. Haller, L. S. Cederbaum, W. Domcke, and H. Köppel, *Chem. Phys. Lett.* **72**, 427 (1980); E. Haller, L. S. Cederbaum, and W. Domcke, *Mol. Phys.* **41**, 1291 (1980).
3.64. M. C. M. O'Brien and S. N. Evangelou, *J. Phys. C* **13**, 611 (1980).
3.65. S. N. Evangelou, M. C. M. O'Brien, and R. S. Perkins, *J. Phys. C* **13**, 4175 (1980).
3.66. J. S. Slonczewski, *Phys. Rev.* **131**, 1596 (1963).
3.67. A. V. Vaisleib, V. P. Oleinikov, and Yu. B. Rozenfeld, *Phys. Status Solidi B* **109**, K35 (1982); *Phys. Lett. A* **89**, 41 (1982); *Fiz. Tverd. Tela* **24**, 1074 (1982).
3.68. Yu. B. Rozenfeld and A. V. Vaisleib, *Zh. Eksp. Teor. Fiz.* **86**, 1059 (1984); *J. Phys. C* **19**, 1721 and 1739 (1986).
3.69. M. C. M. O'Brien, *J. Phys. C* **5**, 2045 (1972); **16**, 6345 (1983).
3.70. H. Köppel, W. Domcke, and L. S. Cederbaum, *Adv. Chem. Phys.* **57**, 59 (1984).
3.71. C. S. Sloane and R. Silbee, *J. Chem. Phys.* **56**, 6031 (1972).
3.72. V. Z. Polinger and G. I. Bersuker, *Phys. Status Solidi B* **96**, 403 (1979).
3.73. V. Z. Polinger and G. I. Bersuker, *Fiz. Tverd. Tela* **22**, 2545 (1980).
3.74. J. C. Slonczewski and W. L. Moruzzi, *Physics* **3**, 237 (1967).
3.75. Fan Li-Chin and Ou. Chin, *Kexue Tonbao* **17**, 101 (1966); *Acta Phys. Sin.* **22**, 471 (1966).
3.76. G. I. Bersuker and V. Z. Polinger, *Zh. Eksp. Teor. Fiz.* **80**, 1788 (1981); *Solid State Commun.* **38**, 795 (1981).
3.77. V. Z. Polinger, *Zh. Eksp. Teor. Fiz.* **77**, 1503 (1979).
3.78. G. I. Bersuker and V. Z. Polinger, *Phys. Status Solidi B* **125**, 401 (1984).
3.79. G. I. Bersuker and V. Z. Polinger, *Zh. Strukt. Khim.* **24**, 62 (1983).
3.80. R. Englman and B. Halperin, *Ann. Phys.* **3**, 453 (1978).
3.81. S. N. Evangelou and A. C. Hewson, *Numerical Renormalization-Group Approach for Locally-Coupled Electron–Phonon System*, Preprint Ref. 34/82, University of Oxford, 1982, p. 27.
3.82. E. Haller, H. Köppel, and L. S. Cederbaum, *Chem. Phys. Lett.* **101**, 215 (1983); *Phys. Rev. Lett.* **52**, 1665 (1984); *J. Phys. A* **17**, L831 (1984).
3.83. N. Manini and E. Tosatti, *Phys. Rev. B* **58**, 782 (1998-II).
3.84. N. Manini and E. Tosatti, in *Recent Advances in the Chemistry and Physics of Fullerenes and Related Materials*, Vol. 2, Eds. K. M. Kadish and R. S. Ruoff, Pennington, New Jersey, 1995, p. 1017.
3.85. B. S. Tsukerblat, M. I. Belinskiy, and A. V. Ablov, *Dokl. Akad. Nauk SSSR* **201**, 1409 (1971).
3.86. A. V. Vaisleib, Yu. B. Rozenfeld, and B. S. Tsukerblat, *Fiz. Tverd. Tela* **18**, 1864 (1976).
3.87. T. Murao, *Phys. Lett. A* **49**, 33 (1974).
3.88. V. Z. Polinger, L. F. Chibotaru, and I. B. Bersuker, *Phys. Status Solidi B* **129**, 615 (1985).

3.89. B. S. Tsukerblat and M. I. Belinskiy, *Magnetochemistry and Radiospectroscopy of Exchange Clusters*, Kishinev, Shtiintsa, 1983 (in Russian).
3.90. J. Catterick and P. Thornton, *Adv. Inorg. Chem. Radiochem.* **20**, 291 (1977); *Mixed-Valency Systems: Applications in Chemistry, Physics and Biology*, Ed. K. Prassides, NATO ASI Series C, Vol. 343, Dordrecht, Kluwer, 1991; J. P. Fackler Jr., in *Encyclopedia of Inorganic Chemistry*, Ed. R. B. King, New York, Wiley, 1994, p. 2270.
3.91. L. L. Lohr, *Proc. Nat. Acad. Sci. USA* **59**, 720 (1968).
3.92. R. Englman and B. Halperin, *Phys. Rev. B* **2**, 75 (1970).
3.93. A. Raisman, J. Barak, R. Englman, and J. T. Suss, *Phys. Rev. B* **24**, 6262 (1981).
3.94. I. B. Bersuker, B. G. Vekhter, and M. L. Rafalovich, *Kristallografiya* **18**, 11 (1973).
3.95. P. Novak, *J. Phys. Chem. Solids* **30**, 2357 (1969).
3.96. M. V. Eremin, Yu. V. Yablokov, T. A. Ivanova, and R. M. Gumerov, *Zh. Eksp. Teor. Fiz.* **87**, 220 (1984).
3.97. M. Kurzynski, *J. Phys. C* **8**, 2749 (1975).
3.98. P. Novak and K. W. H. Stevens, *J. Phys. C* **3**, 1703 (1970).
3.99. M. C. G. Passeggi and K. W. H. Stevens, *J. Phys. C* **6**, 98 (1973).
3.100. T. Fujiwara, *J. Phys. Soc. Japan* **34**, 36 (1973).
3.101. I. B. Bersuker, B. G. Vekhter, and M. L. Rafalovich, *Cryst. Lattice Defects* **6**, 1 (1975).
3.102. V. Z. Polinger, L. F. Chibotaru, and I. B. Bersuker, *Mol. Phys.* **52**, 1271 (1984).
3.103. V. Z. Polinger, L. F. Chibotaru, and I. B. Bersuker, *Teor. Eksp. Khim.* **20**, 1 (1984).
3.104. L. F. Chibotaru, *J. Phys. A* **27**, 6919 (1994).
3.105. L. F. Chibotaru, *Mol. Phys.* **81**, 891 (1994); **81**, 873 (1994).

4

Pseudo Jahn–Teller, product Jahn–Teller, and Renner–Teller effects

This chapter is to introduce the reader to JT problems that may be considered as "less traditional" in the sense that they do not follow exactly from the original ("classical") JT theorem. Indeed, the PJTE considered below takes place in nondegenerate states, while the RTE is relevant to linear molecules, which are exceptions in the original JT formulation. The product JTE is an approximation to both JT and PJT problems. All these effects are inalienable components of the JT trend as a whole.

4.1 Two-level and multilevel pseudo JT (PJT) problems. Uniqueness of the PJT origin of configuration instability and its bonding nature

Among the JT vibronic coupling effects the pseudo JT (PJT) effect occupies an outstanding place. Indeed, while the occurrence of the JT and RT effects is limited to polyatomic systems in degenerate electronic states, the PJT effect may take place, in principle, in any system without *a priori* limitations. This circumstance enlarges essentially the possible subjects of the JT vibronic coupling effects, transforming the JTE theory into a general tool for better understanding and solving problems of structure and properties of molecules and crystals. The waiver of the degeneracy restrictions together with the proof of the uniqueness of the PJT origin of structural instabilities of polyatomic high-symmetry configurations elevates the JT effect theory to a *general approach to molecular and crystal problems*.

The PJT effect emerges directly from the basic equations (2.6) for the vibronically coupled electronic states. If written for the *nondegenerate* ground state k, the vibronic coupling to the excited states is given by the last term on its left-hand side controlled by the matrix elements of the vibronic coupling $W_{km}(Q)$. If $W_{km}(Q)$ is sufficiently small, the system (2.6) can be decoupled and reduced to the usual equation of the adiabatic approximation for

nondegenerate states. However, in many cases the vibronic coupling between the ground and excited states (or two excited electronic states) $W_{km}(Q)$ is not small. In these cases the system of coupled equations (2.6) should include all the vibronically coupled states.

The effects originating from the vibronic mixing of two (or several) nondegenerate electronic states under nuclear displacements are called the pseudo JT effect (PJTE). This notion comes from the two-level problem, ground and excited, discussed below: sufficiently strong vibronic coupling to the excited state leads to the ground-state instability, which in many respects is similar to the JT instability. The effect as a whole can be regarded as emerging from avoided JT crossing, and it is equally applicable to any two (or several) interacting states, not just ground and excited. The PJT effect was considered first by Öpik and Price [4.1] and emerges as a natural extension of the JT effect when a small perturbation that splits the degenerate term does not remove completely the JT instability and distortion.

Note that the term "second-order JT effect" sometimes used instead of pseudo JTE may be misleading: there are no first-order (JT) and second-order (PJT) effects, the two effects are described by different and unrelated vibronic coupling constants, and involve different distortions; the PJTE may be very strong when the proper JT effect is zero and vice versa.

Consider first an easy case of two nondegenerate states Γ and Γ' separated by an energy interval of 2Δ. In order to obtain the adiabatic potential of these states the vibronic contributions ε_k^v must be calculated as solutions of secular equation (3.2). Assuming that only one coordinate $Q = Q_{\overline{\Gamma}}$, $\overline{\Gamma} = \Gamma \times \Gamma'$, mixes the two states (in principle, there may be more than one coordinate of type $\overline{\Gamma}$) and taking into account only linear terms in the vibronic interaction W in Eq. (2.14), we obtain (the energy is read off the middle of the 2Δ interval between the initial levels)

$$W = \begin{vmatrix} -\Delta & FQ \\ FQ & \Delta \end{vmatrix} \tag{4.1}$$

where

$$F = \langle \Gamma | \left(\partial V / \partial Q_{\overline{\Gamma}}\right)_0 | \Gamma' \rangle \tag{4.2}$$

is the *off-diagonal linear vibronic coupling constant*. Inserting the solutions of Eq. (3.2) with W from (4.1),

$$\varepsilon_k^v = \pm(\Delta^2 + F^2 Q^2)^{\frac{1}{2}} \tag{4.3}$$

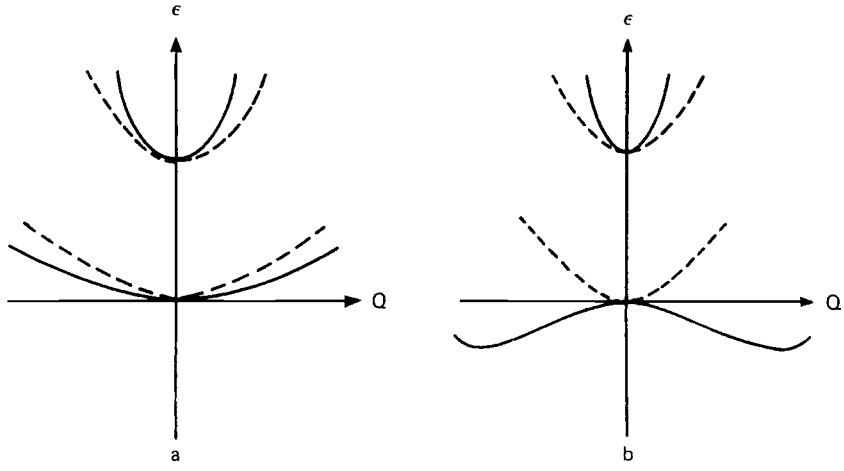

Fig. 4.1. The APES in the case of (a) weak PJTE, the ground state is softened but remains stable; and (b) strong PJTE, the ground state becomes unstable at $Q = 0$. The terms without vibronic coupling are shown by dashed lines.

into Eq. (3.1) and assuming that the primary force constant ($K_0 = M\omega^2$) is the same in both states, $K_0 = K_{0\Gamma} = K_{0\Gamma'}$, we obtain

$$\varepsilon_{\pm}(Q) = \tfrac{1}{2}K_0Q^2 \pm (\Delta^2 + F^2Q^2)^{\frac{1}{2}} \tag{4.4}$$

or, after expanding the second term in Q,

$$\varepsilon_{\pm}(Q) = \tfrac{1}{2}(K_0 \pm F^2/\Delta)Q^2 \pm \Delta \mp \tfrac{1}{4}(F^4/\Delta^3)Q^4 \pm \cdots \tag{4.5}$$

It is seen from this expression that, on taking into account the vibronic coupling, the two APES curves change in different ways: in the upper sheet the curvature (the coefficient at Q^2, the force constant) increases, whereas in the lower one it decreases. But until $\Delta > F^2/K_0$ the minima of both states correspond to the point $Q = 0$, as in the absence of vibronic mixing. This is the case of the *weak PJTE* (Fig. 4.1(a)).

However, if

$$\Delta < F^2/K_0 \tag{4.6}$$

the curvature of the lower curve of the APES becomes negative, and the system is unstable with respect to the Q displacements. This is the *strong PJTE* (Fig. 4.1(b)). The minima of the APES in this case are given by

$$\pm Q_0 = [(F^2/K_0^2) - (\Delta^2/F^2)]^{\frac{1}{2}} \tag{4.7}$$

with the JT stabilization energy

$$E_{\mathrm{JT}} = \frac{F^2}{2K_0} - \Delta\left(1 - \frac{\Delta K_0}{2F^2}\right) \tag{4.8}$$

and curvature at these minima points

$$K = K_0\left[1 - \left(\frac{\Delta K_0}{F^2}\right)^2\right] \tag{4.9}$$

For $\Delta = F^2/K_0$ the curvature is zero everywhere.

If $K_{0\Gamma} \neq K_{0\Gamma'}$, then

$$\varepsilon_-(Q) = \tfrac{1}{2}(K_{0\Gamma} - F^2/\Delta)Q^2 - \Delta + \tfrac{1}{4}(F^4/\Delta^3)Q^4 - \cdots$$

and

$$\varepsilon_+(Q) = \tfrac{1}{2}(K_{0\Gamma'} + F^2/\Delta)Q^2 + \Delta - \tfrac{1}{4}(F^4/\Delta^3)Q^4 + \cdots \tag{4.10}$$

Following these equations, the curvatures of the APES of the two states Γ and Γ' that are coupled by the PJT interaction in the $Q_{\overline{\Gamma}}$ direction,

$$K_{\overline{\Gamma}}^{\Gamma} = K_{0\overline{\Gamma}}^{\Gamma} - \left|F_{\overline{\Gamma}}^{\Gamma\Gamma'}\right|^2 \Big/ \Delta \tag{4.11}$$

and

$$K_{\overline{\Gamma}}^{\Gamma'} = K_{0\overline{\Gamma}}^{\Gamma'} + \left|F_{\overline{\Gamma}}^{\Gamma\Gamma'}\right|^2 \Big/ \Delta \tag{4.12}$$

depend on the linear vibronic coupling constant $F_{\overline{\Gamma}}^{\Gamma\Gamma'}$, which is nonzero only if the two states Γ and Γ' obey the symmetry restriction $\overline{\Gamma} \in \Gamma \times \Gamma'$. This means that only selected excited (higher in energy) states contribute to the instability of the ground (lower-energy) state in a given direction $\overline{\Gamma}$, and this contribution is the larger, the smaller Δ and the larger F.

If there is more than one excited state with required symmetry, all of them may contribute to the instability of their ground (or lower in energy) state. In the linear coupling approximation the total effect is a sum of contributions of all higher-energy states (cf. (2.35)):

$$K_{\overline{\Gamma}}^{\Gamma} = K_{0\overline{\Gamma}}^{\Gamma} - \sum_{\Gamma'} \left|F_{\overline{\Gamma}}^{\Gamma\Gamma'}\right|^2 \Big/ \Delta_{\Gamma'\Gamma} \tag{4.13}$$

and the condition of instability, instead of Eq. (4.6), becomes as follows:

$$\sum_{\Gamma'} \left|F_{\overline{\Gamma}}^{\Gamma\Gamma'}\right|^2 \Big/ \Delta_{\Gamma'\Gamma} > K_{0\overline{\Gamma}}^{\Gamma} \tag{4.14}$$

Equations (4.13) and (4.14) pertain to the *linear multilevel PJT effect*, provided no degenerate terms, ground or excited, are involved in the vibronic coupling. If at least one of the coupling terms is degenerate or the quadratic vibronic coupling terms are taken into account, the problem becomes more complicated as laid out in the next sections.

The nonadiabacity terms (2.12) ignored so far may have significant influence on the PJTE. If the diagonal matrix element of the nonadiabacity (2.12) is taken into account, the off-diagonal elements still being ignored, the system of Eqs. (2.6) is decoupled into two independent equations for the lower and upper sheets of the APES, but Eq. (4.3) changes to the following [4.2]:

$$\varepsilon_{\pm}(Q) = \tfrac{1}{2}K_0Q^2 \pm [\Delta^2 + F^2Q^2]^{\frac{1}{2}} + (\hbar\omega\Delta)^2(F^2/K_0)/8(\Delta^2 + F^2Q^2)^2 \quad (4.15)$$

The last (nonadiabacity) term decreases rapidly with increasing distance Q from the reference configuration. It changes from $(\hbar\omega)^2(F^2/K_0)/8\Delta^2$ at $Q=0$ to $(\hbar\omega\Delta)^2/(F^2/K_0)^3$ at the point Q_0 of the minimum of the APES given by Eq. (4.7). Since it is assumed that $\Delta < F^2/K_0$ (Eq. (4.6)), the nonadiabacity at the minima points (but not at the barrier top at $Q=0$) may be neglected. If in addition to Eq. (4.6) $\Delta \gg \hbar\omega$, then the diagonal nonadiabacity may be neglected everywhere.

We will show now that the PJT origin of instability is unique in the sense that the condition (4.14) is both *necessary and sufficient* for the instability to occur, and hence there are no other sources of such instability of high-symmetry configurations [4.3–4.5]. In Section 2.4 we presented the curvature K of the APES in the direction Q as a sum of two terms (for simplicity, the Γ indices are omitted):

$$K = K_0 + K_\nu \quad (4.16)$$

where (prime indicates Q derivative)

$$K_0 = \langle\psi_0|H''_Q|\psi_0\rangle \quad (4.17)$$

and

$$K_\nu = \langle\psi_0|H'_Q|\psi'_0\rangle + \langle\psi'_0|H'_Q|\psi_0\rangle \quad (4.18)$$

or

$$K_\nu = 2\sum_n \frac{\left|\langle\psi_0|H'_Q|\psi_n\rangle\right|^2}{E_0 - E_n} \quad (4.19)$$

Since for the ground state $E_n > E_0$, expression (4.19) is negative. It follows that the excited states for which $\langle\psi_0|H'_Q|\psi_n\rangle \neq 0$ destabilize the system in the ground state in the direction of the displacements Q. Expressions similar to (4.19) were used by different authors to explain the possible origin of molecular instability (see [4.6] and references therein).

On the other hand Eq. (4.19), as demonstrated above, is equivalent to the summarized PJT contributions of the corresponding excited states to the destabilization of the ground state. Since $K_\nu < 0$, the instability $K < 0$ may be due to either $K_0 > 0$ and $|K_\nu| > K_0$ or $K_0 < 0$. In general, if the inequality $K_0 < 0$ cannot be *a priori* excluded, then the system may be unstable with respect to Q displacement even without the PJT contribution K_ν, and then the PJT contribution is just one of the possible reasons for instability, as implied in [4.6] (see the discussion below in this section). However, if

$$K_0 > 0 \tag{4.20}$$

the condition (4.14) of vibronically induced instability is both necessary and sufficient, and the PJT mechanism of instability is the only possible one in polyatomic systems.

There are several particular proofs of the inequality $K_0 > 0$ for different kinds of polyatomic systems. First the formulation of the problem and a general (but not very rigorous) proof was given [4.3]. Then this proof was significantly improved and expanded [4.4], followed by more rigorous proofs for particular cases [4.5] (see also [4.2]). To illustrate the idea of these proofs (but not to repeat them), consider the expression (4.17) for K_0 in more detail. The second derivative of the Hamiltonian H''_Q equals the second derivative of the electron–nuclear and nuclear–nuclear interactions $V(r, Q)$ given by Eq. (2.3). Since the transformation from normal to Cartesian coordinates is unitary, $Q_k = \Sigma_i a_k U_k$ (U_k stands for the coordinates X_i, Y_i, and Z_i),

$$\frac{\partial^2 H}{\partial Q_k^2} = \sum_i a_{ki}^2 \frac{\partial^2 V}{\partial U_i^2} \tag{4.21}$$

For the Coulomb interaction terms V there is a general formula

$$\langle 0|\frac{\partial^2 V}{\partial X_i^2}|0\rangle = \frac{4\pi}{3} eZ_i\rho_i + eZ_i Q_{xx}^{(i)} \tag{4.22}$$

where ρ_i is the numerical value of the electron density at the ith nucleus, and $Q_{xx}^{(i)}$ is the gradient of the electric field created by the electrons and other nuclei at the given one i (not to be confused with symmetrized coordinates); the ground state is denoted by $|0\rangle$. By definition, $Q_{xx} + Q_{yy} + Q_{zz} = 0$ and $\rho_i > 0$.

Hence the first term on the right-hand side of (4.22) is always positive (eZ is the absolute value of the nuclear charge), and if the environment of the displacing nuclei under consideration is cubic, $Q_{xx} = Q_{yy} = Q_{zz} = 0$ and

$$K_0 = \langle 0| \left(\frac{\partial^2 H}{\partial Q_k^2} \right)_0 |0\rangle = 4\pi e \sum_\alpha a_{k\alpha}^2 Z_\alpha \rho_\alpha \geq 0 \tag{4.23}$$

If the environment is not cubic, the first term in 4.22 is still positive, but the second one, the gradient of the electric field at the given nucleus, is nonzero and it can be either positive or negative; but it was shown that the second term is much smaller than the first [4.2, 4.3–4.5].

A less rigorous but more general proof that the nonvibronic contribution $K_0 > 0$ is based on the representation of the electronic wavefunction of the ground state in the form of a Slater determinant in the MO LCAO approximation, $|0\rangle = \sqrt{N}\ \det|\psi_1 \psi_2 \cdots \psi_N|$, where $\psi_i = \Sigma_\mu C_{i\mu} \varphi_\mu$, $C_{i\mu}$ are the LCAO coefficients, and ϕ_μ is the appropriate atomic function [4.4]. Calculating the diagonal matrix element (4.17) with this function and making reasonable approximations, one can see that K_0 consists of two contributions: positive terms of the order of $\Sigma_\alpha q_\alpha \zeta_\alpha^3 Z_\alpha$, which are due to the interaction of the displacing nuclei with their own atom-in-molecule electronic shells with the most contribution from s electrons, and possible negative terms of the order of $\Sigma_{\alpha,\beta} Z_\alpha Z_\beta R_{\alpha\beta}^{-3}$ due to the second derivative of internuclear interactions. If the inner and valence electrons are separated, ζ_α is the parameter of the Slater ns orbital of the α atom of the first ns shell not included in the core, q_α is the electronic population of this ns orbital, and $R_{\alpha\beta}$ are interatomic distances. Since $\zeta_\alpha \sim Z_\alpha$ (this is true also when Z_α is the effective charge of the core), $R_{\alpha\beta} \approx 2$ a.u., and $q_\alpha \sim 1$, the positive term $\sim \Sigma_\alpha Z_\alpha^4$ is much larger than the possible negative ones $\sim \Sigma_{\alpha,\beta} Z_\alpha Z_\beta$ provided $Z_\alpha > 1$. Thus K_0 is also positive in the general case of arbitrary structure and symmetry, and this proves the PJT origin of the structural instability of any system, provided it exists in the high symmetry configuration.

The case $Z_\alpha = 1$ when the displacing nuclei are hydrogens requires additional consideration (in all other cases, including that of the core–valence-electron separation approximation, $Z_\alpha > 1$). For this case nonempirical calculations of K_0 were carried out together with an evaluation of the vibronic contribution to the curvature for several series of molecular systems in high-symmetry configurations that are unstable with respect to symmetrized nuclear displacements of hydrogen atoms [4.4]. In all these (and any other) cases with any Z_α K_0 calculated by Eq. (4.17) is positive.

As can be seen from the discussion above, the proof of the inequality $K_0 > 0$ is not trivial. Several authors tried to sidestep the necessity to prove it by stating implicitly (as, e.g., in [4.6(*a*)]) or explicitly (see, for example, [4.6(*b*), 4.7]) that $K_0 > 0$ because the wavefunction ψ_0 in the definition (4.17) is a solution of the Schrödinger equation which minimizes the energy $\langle \psi_0 | H | \psi_0 \rangle$. This is a typical example of wrong reasoning: the energy is minimized with respect to the variation of ψ_0, *not the nuclear coordinates* Q. Only for single atoms does a shift transformation make the two minimization procedures equivalent, but this cannot be done for molecules and crystals because of essential interatomic interactions.

With respect to *ab initio* calculations of K_0 and K_ν, which provide a further insight into the origin of PJT instability of high-symmetry configurations of polyatomic systems, a more elaborate investigation was performed recently [4.8]. The first attempts to calculate K_0 and K_ν by *ab initio* methods [4.4] encountered essential difficulties. First, although the relative values of K_ν for different distortions, as mentioned above, depend mainly on the first several excited states, the absolute values depend significantly on all other states that are higher in energy in the sum of Eq. (4.19), including the continuum spectrum (in [4.4] this difficulty was overcome by means of including derivative functions in the basis set to partially account for the floating of inner orbitals). The reason that the lowest several excited states are still sufficient for a comparable analysis of the possible distortions in spite of the much larger contribution of higher states and the continuum spectrum is due to the fact that the contribution of the latter (being mostly an intraatomic, not interatomic, feature) is approximately the same for all distortions and does not influence significantly their relative values.

Second, the K value in Eq. (4.16) is a small difference of two large terms, K_0 and K_ν, meaning that a much higher accuracy of the calculation is required for reasonably accurate results. At present accurate calculation of the K_0 values encounters essential difficulties because there are no basis sets available with sufficiently accurate behaviors of the atomic orbitals near the nuclei (due to the singularity of the potential at the nuclei). The low accuracy of existing basis sets for calculations of nuclear displacement derivatives is an essential obstacle to using Eqs. (4.16)–(4.19) for *ab initio* evaluation of instabilities.

The authors [4.8] overcome both these difficulties in *ab initio* calculations of vibronic instabilities by introducing two main innovations. First the calculation of K_ν is performed using Eq. (4.18) in which, distinct from the traditional Eq. (4.19), the infinite sum over excited states is substituted by wavefunction derivatives. Second, it is taken into account that for a free atom the curvature for any nuclear displacement is zero, $K = K_0 + K_\nu = 0$, or $K_0 = -K_\nu$, and this

relation is independent of the electronic structure of the atom, so it should be valid for each atomic orbital $\chi_{\alpha i}$ taken separately (cf. "floating orbitals"). In other words,

$$\langle\chi_{\alpha i}|h''_{X_\alpha X_\alpha}|\chi_{\alpha j}\rangle + \langle(\chi_{\alpha i})'_{X_\alpha}|h'_{X_\alpha X_\alpha}|\chi_{\alpha j}\rangle + \langle\chi_{\alpha i}|h'_{X_\alpha X_\alpha}|(\chi_{\alpha j})'\rangle = 0 \tag{4.24}$$

and this equation can be easily verified for any atomic orbitals.

Equation (4.24) allows one to exclude the diagonal in α terms that appertain to the same atom in the corresponding sums of K_0 and K_ν calculated in the MO LCAO approximation. Finally one gets [4.8] (for h see Eq. (2.2b), Section 2.1)

$$K = \tilde{K}_0 + \tilde{K}_\nu \tag{4.25}$$

$$\tilde{K}_0 = \sum_\gamma D_\gamma^2 \sum_{m=1}^{N} \sum_{\alpha i,\beta j} C^m_{\alpha i} C^m_{\beta j} \langle\chi_{\alpha i}|h''_{X_\gamma X_\gamma}|\chi_{\beta j}\rangle(1-\delta_{\alpha\beta\gamma}) + \sum_{\gamma,\zeta} D_\gamma D_\zeta G''_{X_\gamma X_\zeta} \tag{4.26}$$

$$\tilde{K}_\nu = 2\sum_{\gamma,\zeta} D_\gamma D_\zeta \sum_{m=1}^{N} \sum_{\alpha i,\beta j} \left[C^m_{\alpha i} C^m_{\beta j} \langle\chi_{\alpha i}|h'_{X_\gamma}|(\chi_{\beta j})'_{X_\zeta}\rangle(1-\delta_{\alpha\beta\gamma\zeta}) + C^m_{\alpha i}(C^m_{\beta j})'_{X\zeta}\langle\chi_{\alpha i}|h'_{X_\lambda}|\chi_{\alpha j}\rangle \right] \tag{4.27}$$

where $C^m_{\alpha i}$ are the LCAO coefficients of the MO LCAO method in the one-determinant presentation, and D_γ are the coefficients in the transformation of the Q displacements to Cartesian coordinates X_γ:

$$Q = \sum_\gamma D_\gamma X_\gamma$$

Similar formulas for a more sophisticated approximation using configuration interaction were also derived [4.8]. Illustrative results of calculation using these formulas are given in Section 7.6. Another approximation to the evaluation of the PJT instability using floating orbitals was employed in [4.9].

The proof that $K_0 > 0$ means that configuration instability with $K < 0$ is due to, and only to, the vibronic coupling to the excited states. For a two-level system, the curvatures of the adiabatic potentials of the two states at the point of instability are given by Eqs. (4.11) and (4.12). Because $K_{0\Gamma} > 0$ and $K_{0\Gamma'} > 0$, the curvature of the excited state $K_{0\Gamma'} + F^2/\Delta$ is positive while that of the ground-state $K_{0\Gamma} - F^2/\Delta$ under condition (4.6) is negative. Thus *instability of the ground-state is accompanied by a stable excited state*, coupling with which produces the instability. This result, *prediction of the existence of stable excited states in dynamically unstable ground-state configurations*, is one of the general consequences of vibronic instability, which may have interesting applications.

If more than one excited state contributes to the instability of the ground state in Eq. (4.13), the relation among the K values of all these states becomes more complicated, but the general idea is the same: the negative contribution to the curvature of the ground state, which makes the latter unstable, equals the sum of positive contributions to the excited states. *As a result of vibronic mixing, the excited states become stabilized.* If the excited state that causes the instability of the ground state is occupied by electrons, the instability disappears: Eqs. (4.11) and (4.12) show that the total change of curvature of the two interacting states equals zero. Therefore, in molecular orbital approximations vibronic coupling between fully occupied MOs does not contribute to the instability.

For a further understanding of the origin of vibronic instability, the terms in the sum (4.13) or (4.19) for K_v may be divided into two groups.

1. The basis wavefunctions $|0\rangle$ and $|i\rangle$ in the matrix element $F^{(0i)} = \langle 0|(\partial V/\partial Q)_0|i\rangle$ are mainly from the same atom. The term $-\left|F^{(0i)}\right|^2/\Delta_{i0}$ in Eq. (4.13) calculated with these functions can be interpreted as the contribution to the polarization of this atom by the displacements of other atoms. For instance, for the instability of the central position of the Ti ion in the octahedron of oxygens in the $[TiO_6]^{8-}$ cluster of $BaTiO_3$ with respect to off-center displacements, discussed in Section 4.3, the contribution to the polarization of the oxygen atom by the off-center displacement of the titanium ion is given by the mixing of the oxygen $2p$(O) and $3s$(O) atomic functions under this displacement [4.2, 4.10]:

$$K_v^{\text{pol}} = -\left|\langle 2p_{\sigma z}|(\partial V/\partial Q_z)_0|3s\rangle\right|^2/\Delta_{3s2p} \tag{4.28}$$

In the integrals $F^{(0i)} = \langle 0|(\partial V/\partial Q)_0|i\rangle$ calculated with the orthogonal (ground and excited) wavefunctions of the same atom we can transform the symmetrized coordinate Q into Cartesian coordinates. Then taking the corresponding derivative of the Coulomb potential $V = e^2\left|r - R_\beta\right|^{-1}$, we come to integrals of the type $I_x = \langle 0|(x - X_\beta)/\left|r - R_\beta\right|^3|i\rangle$, where x are the electronic coordinates of the polarized atom and X_β are the nuclear coordinates of the displacing atoms. If we assume that approximately R_β is much larger then the atomic size (which is true for the second and next coordination spheres), then $I_x \approx R_\beta^{-3}\langle 0|x|i\rangle$, and the polarization contribution is

$$K_v^{\text{pol}} \sim e^2\alpha_x R_\beta^{-6} \tag{4.29}$$

where, according to quantum mechanics,

$$\alpha_x \sim e^2\left|\langle 0|x|i\rangle\right|^2/\Delta_{i0} \tag{4.30}$$

is the part of the atomic polarizability in the x direction that is due to the contribution of the ith excited state (the summation over i gives the full atomic polarizability in this direction).

2. The two functions in $F^{(0i)}$ are mainly from two different (near-neighbor) atoms. In this case *the vibronic contribution is due to new covalency* produced by the distortion. Indeed, in the reference configuration the overlap of these two electronic states is zero (they are orthogonal), hence their vibronic mixing means that a nonzero overlap occurs under the low-symmetry displacements Q.
For the Ti ion's off-center displacements with respect to the oxygen octahedron, the covalent contribution is due to the new overlap of the ground-state t_{1u} combination of the highest occupied $2p_{\pi z}$(O) functions of the oxygen atoms with the lowest unoccupied d_{xz}(Ti) function of the titanium ion (Section 4.3):

$$K_v^{\text{cov}} \approx -\left|\langle 2p_{\pi z}(\text{O})|(\partial V/\partial Q_x)_0|3d_{xz}(\text{Ti})\rangle\right|^2/\Delta_{3d\,2p} \tag{4.31}$$

The new overlap (which is forbidden by symmetry in the reference configuration) produces new (additional) covalency. Inequality (4.6), made possible by this term, means that with the new covalency the energy is lower than that of the reference configuration, resulting in instability. Figure 4.2 illustrates this case. Another case of new covalency in MA_4 (C_{4v}) systems is illustrated in Fig. 4.3.

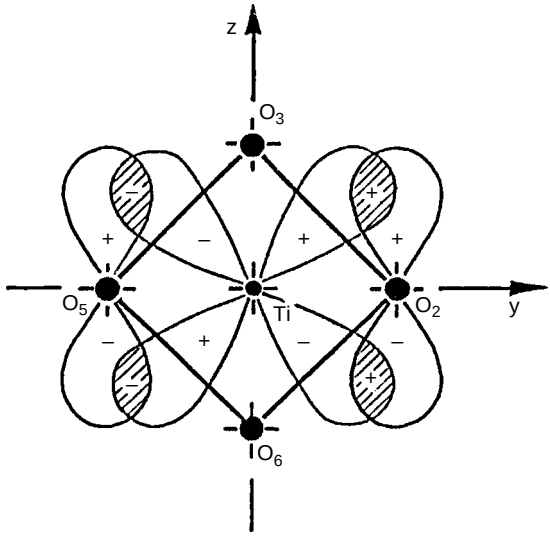

Fig. 4.2. Symmetry properties of the HOMO $|t_{1u}z\rangle$ and LUMO $|3d_{yz}\rangle$ in the octahedral cluster $[TiO_6]^{8-}$ in the yz plane (the oxygen numbering follows that of Fig. 2.3). The overlap integral between these orbitals (hatched area) is zero in the high-symmetry configuration and becomes nonzero upon displacement of the Ti^{4+} ion along the y axis.

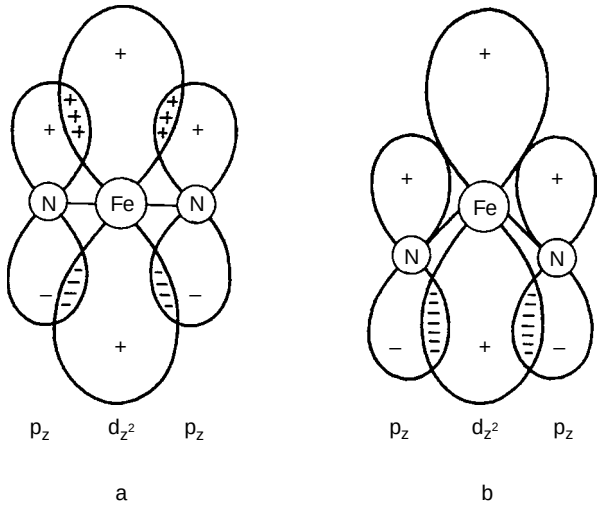

Fig. 4.3. Illustration to the visual treatment of the origin of the PJTE using the N—Fe—N fragment of the square-planar FeN_4 group as an example (cf. iron porphyrin, Section 7.6): (a) when Fe is in the N_4 plane (on the N—Fe—N line) the d_π–p_π overlap between the HOMO (nitrogen p_π) and LUMO (iron d_{z^2}) orbitals is zero; (b) the out-of-plane displacement of the Fe atom results in nonzero d_π–p_π overlap and additional bonding which lowers the curvature of the APES in the direction of such a displacement [4.20] (reprinted with permission from [4.20]. Copyright 1996 John Wiley & Sons, Inc.).

Both kinds of vibronic contribution to instability, new covalency and atomic polarization, may be significant, but the numerical calculations performed so far show that the covalency contribution is larger by an order of magnitude than the polarization. Table 4.1 shows three examples of such calculations [4.11]: the instability of NH_3 in the planar configuration with respect to out-of-plane displacements of the nitrogen atom (toward the stable C_{3v} configuration), $[CuCl_5]^{3-}$ in the trigonal-bipyramidal configuration with respect to E' displacements (toward a square pyramid), and the $[TiO_6]^{8-}$ cluster in $BaTiO_3$ with respect to T_{1u} (Ti off-center) displacements initiating the spontaneous polarization of the crystal [4.10] (see also Section 8.3). In all these examples the new covalency contribution to the instability is indeed much more significant, by at least an order of magnitude. As seen from these illustrative examples, *the PJT distortion is a (covalency) bonding effect*.

One of the fundamental consequences of the uniqueness of the vibronic instability, the existence of stable excited states that cause the instability of the ground state, has applications in various fields of physics and chemistry. In the MO presentation, considering the symmetries of the appropriate MOs, *one can control (manipulate) the geometry (configuration instability) of molecular*

Table 4.1. *New covalency K_ν^{cov} versus polarization K_ν^{pol} contributions to the instability of the high-symmetry configuration of several polyatomic systems [4.11]*

	NH_3	$CuCl_5^{3-}$	TiO_6 in $BaTiO_3$
Reference configuration	Planar D_{3h}	Trigonal bipyramidal D_{3h}	Octahedral O_h
Instability coordinate	A_2''	E'	T_{1u}
Ground state[a]	$^1A_1'[2p_z(N)]$	$^2A_1'[3d_{z^2}(Cu)]$	$^1A_{1g}[2p(O)]$
Excited state – covalent[b]	$^1A_2''$ $2p_z(N)\rightarrow 1s(H)$	$^2E'$ $3s(Cl)\rightarrow 3d(Cu)$	$^1T_{1u}$ $2p(O)\rightarrow 3d(Ti)$
K_ν^{cov}	-0.62 mdyn/Å	$-2.85\times 10^{28}s^{-2}$[c]	
Excited state – polarized[b]	$^1A_2''$ $2p_z(N)\rightarrow 3s(N)$	$^2E'$ $3d_{xy}(Cu)\rightarrow 3d_{z^2}$	$^1T_{1u}$ $2p(O)\rightarrow 3s(O)$
K_ν^{pol}	-0.06 mdyn/Å	$-0.05\times 10^{28}s^{-2}$[c]	
K_ν^{cov}/K_ν^{pol}	10.3	57	11

[a] The main contributing AOs are indicated in brackets.

[b] Corresponding one-electron excitations are shown.

[c] In mass-weighted units.

systems by means of electronic rearrangements: charge transfer, excitation, ionization, MO population changes by coordination, redox processes, and so on (Section 7.1).

In addition to instability of the high-symmetry configuration, strong vibronic mixing of the ground state with the excited states causes anharmonicity in the nuclear motions of the former (vibronic anaharmonicity, Section 2.4). In some cases the vibronic anharmonicity is more important than the proper anharmonicity caused by the higher-order terms in the expansion (2.3).

4.2 Pseudo JT $(A+E)\otimes e$, $(A+T)\otimes t$, $(T_1+T_2)\otimes e$, and combined JT and PJT problems

If the excited state that influences vibronically the nondegenerate ground state A is degenerate, the vibronic coupling problem becomes more complicated because more than two electronic states are involved in the vibronic interaction. For instance, if the excited state involved is doubly degenerate E, the

number of coupled states becomes three and the problem is $(A+E)\otimes e$; for T excited states we get four electronic states involved, the A and T states being mixed by t vibrations (the $(A+T)\otimes t$ problem). If both mixing states are degenerate, their PJT coupling involves five states in the $(E+T)\otimes(t_1+t_2)$ problem, six states in the $(T_1+T_2)\otimes(e+t_2)$ problem, and so on.

Considering just the PJT mixing of two terms in the above problems may be a rough simplification because any degenerate state is subject to the JT effect within itself, which may affect also its PJT coupling to other states. This means that if the PJT mixing involves degenerate terms, the problem in fact becomes a combined JT + PJT one. In particular, the PJT $(A+E)\otimes e$ problem is in fact a combination of the JT $E\otimes(a+e_1)$ and PJT $(A+E)\otimes e_2$ problems, resulting in $(A+E)\otimes(a+e_1+e_2)$. The two e-type couplings in the combined problem should be described by two coupling constants, one for the two E states coupled to e vibrations, the other for A–E coupling to the same e vibrations. Similarly, the PJT $(A+T)\otimes t$ problem is strictly speaking a combination of the PJT problems $(A+T)\otimes t$ and $T\otimes(a+e+t_2)$, yielding $(A+T)\otimes(a+e+t_2+t)$ with four vibronic coupling constants (t is either t_1 for $T=T_1$, or t_2 for $T=T_2$).

But the simplified $(A+E)\otimes e$, $(A+T)\otimes t$, $(T_1+T_2)\otimes e$, $(T_1+T_2)\otimes t$, etc., pure PJT problems may still be important as a first approximation to the more complex problem, especially when the PJT coupling is stronger than the JT effect within the degenerate term (note that the two kinds of couplings, JT and PJT, are controlled by different and unrelated vibronic coupling constants).

Consider first the PJT A_1+E problem (the ground state A_1 is shown first) for a *system with* C_{4v} *symmetry* [4.12]. In this case the JT problem on the E term is not $E\otimes(a_1+e)$, but $E\otimes(b_1+b_2)$ (Section 3.1), and hence the combined problem is $(A+E)\otimes(e+b_1+b_2)$. Ignoring the JTE on the excited E term (i.e. the coupling to b_1 and b_2 displacements; they do not mix the A and E terms directly, but they may affect the latter indirectly), we come to the PJT $(A+E)\otimes e$ problem. The results below are similar for the $(E+A)\otimes e$ problem, i.e., when the E term is lower than the A one. For a system with C_{4v} symmetry the two wavefunctions of the E term transform as the x and y coordinates, while the A_1 term is totally symmetric and transforms as an atomic s function. If we denote the two components of the e mode by Q_x and Q_y and the energy gap between the E and A_1 levels by 2Δ, the matrix W in the secular equation (3.2) in the linear vibronic coupling approximation takes the form

$$W=\begin{vmatrix} \Delta & 0 & FQ_x \\ 0 & \Delta & FQ_y \\ FQ_x & FQ_y & -\Delta \end{vmatrix} \tag{4.32}$$

where $F = \langle s|(\partial V/\partial Q_x)_0|x\rangle$ is the PJT linear coupling constant (Section 2.2). In polar coordinates

$$Q_x = \rho\cos\phi, \qquad Q_y = \rho\sin\phi \tag{4.33}$$

the solutions of the Eqs. (3.2) with this matrix W are

$$\varepsilon_{1,3} = \pm\sqrt{\Delta^2 + F^2\rho^2}, \qquad \varepsilon_2 = \Delta \tag{4.34}$$

which for the APES of the ground state yields

$$\varepsilon(\rho,\ \phi) = \tfrac{1}{2}K_E\rho^2 - \sqrt{\Delta^2 + F^2\rho^2} \tag{4.35}$$

It is seen that in the linear approximation the adiabatic potential is independent of the angle ϕ, it is a surface of revolution. Similar to the two-level case (Section 4.1), if $\Delta < F^2/K_E$, the surface has a maximum at the point $\rho = 0$ (dynamic instability) and a circular trough at

$$\rho = \rho_0 = \sqrt{(F^2/K_E^2) - (\Delta^2/F^2)} \tag{4.36}$$

The depth of the trough (read off the point $\varepsilon(0) = -\Delta$) is the same as in the two-level problem (4.8),

$$E_{\mathrm{PJT}} = \frac{F^2}{2K_0} - \Delta\left(1 - \frac{\Delta K_0}{2F^2}\right) \tag{4.37}$$

If quadratic terms of the vibronic interaction are taken into account, the two states of the E term become mixed by quadratic e displacements, and two quadratic constants G_1 and G_2 must be introduced.

Denote

$$G_1 = \frac{1}{2}\langle x|\left(\frac{\partial^2 V}{\partial Q_x^2}\right)_0|x\rangle, \qquad G_2 = \frac{1}{2}\langle x|\left(\frac{\partial^2 V}{\partial Q_x\,\partial Q_y}\right)_0|y\rangle \tag{4.38}$$

Then W in the secular equation (3.2) for the case in question takes the form

$$W = \begin{vmatrix} \Delta + G_1(Q_x^2 - Q_y^2) & 2G_2Q_xQ_y & FQ_x \\ 2G_2Q_xQ_y & \Delta - G_1(Q_x^2 - Q_y^2) & FQ_y \\ FQ_x & FQ_y & -\Delta \end{vmatrix} \tag{4.39}$$

Turning to polar coordinates (4.33), it can be shown that the APES corresponding to Eq. (4.39), as distinct from the linear case, is dependent on angle ϕ;

four minima regularly alternating with four saddle points occur on the APES as a function of ϕ (along the trough (4.35)), restoring the C_{4v} symmetry of the problem. At the extremum points $\phi = n\pi/4$, $n = 0, 1, 2, \ldots, 7$. If $G_1 > G_2$, the minima are given by

$$\phi_0 = n\pi/4, \qquad n = 1, 3, 5, 7 \tag{4.40}$$

and the saddle points are at $n = 0, 2, 4, 6$. In the opposite case $G_1 < G_2$, the minima and saddle points interchange, and if $G_1 = G_2$ the surface preserves the shape of the rotation body (the trough) of the linear approximation.

In *systems with trigonal symmetry* the full problem of vibronic coupling of a ground nondegenerate state A with an excited E state, as mentioned above, includes both their PJT interaction via e displacements, $(A + E) \otimes e$, and the $E \otimes (a_1 + e)$ JT effect in the E term itself (Section 3.2), resulting in the combined $(A + E) \otimes (a_1 + e_1 + e_2)$ problem. In this case the two E state functions can be taken as $|zx\rangle$ and $|zy\rangle$ with the A state function as $|s\rangle$ (as in the local Ni site in $KNiCl_3$ [4.13]), while the two e displacements are described by the coordinates Q_{zx} and $Q_{x^2-y^2}$. The two linear coupling constants to the e vibrations are thus

$$F_1 = \langle s|(\partial V/\partial Q_{zx})_0|zx\rangle \tag{4.41}$$

$$F_2 = \langle zx|(\partial V/\partial Q_{x^2-y^2})_0|zx\rangle \tag{4.42}$$

and an additional two constants should be introduced for the interaction with the totally symmetric displacement Q_s and the quadratic coupling respectively:

$$F_A = \langle zx|(\partial V/\partial Q_A)_0|zx\rangle \tag{4.43}$$

$$G = \langle zx|(\partial^2 V/\partial Q_{zx}^2 - \partial^2 V/\partial Q_{zy}^2)_0|zx\rangle \tag{4.44}$$

With these denotations the matrix W in the vibronic coupling equation (3.2) is [4.13]

$$W = \begin{vmatrix} -\Delta & F_1 Q_{zx} & F_1 Q_{zy} \\ F_1 Q_{zx} & \Delta + F_2 Q_{x^2-y^2} + G(Q_{zx}^2 - Q_{zy}^2) + F_A Q_A & -F_2 Q_{xy} + 2F_1^2 Q_{zx} Q_{zy} \\ F_1 Q_{zy} & -F_2 Q_{xy} + 2F_1^2 Q_{zx} Q_{zy} & \Delta - F_2 Q_{x^2-y^2} - G(Q_{zx}^2 - Q_{zy}^2) + F_A Q_A \end{vmatrix} \tag{4.45}$$

For discussion of the solutions of this equation, consider first the linear approximation with respect to the PJT effect ignoring the quadratic terms and the interaction with totally symmetric displacements. It can be shown [4.13]

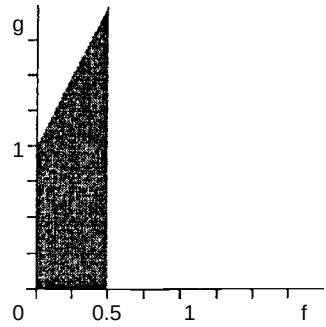

Fig. 4.4. The region of f and g parameters of Eq. (4.46) (the blank area on the (f, g) plane) for which the PJT instability takes place in the $(A+E)\otimes(a_1+e_1+e_2)$ problem. The greater f, the stronger the PJTE [4.13].

that in this case the APES has a trough of minima points that are equivalent in energy in the space of the Q_{zx} and Q_{zy} coordinates. Introducing the parameter combinations

$$f = F_1^2/K_{E_1}\Delta, \qquad g = F_2^2/K_{E_2}\Delta \tag{4.46}$$

we can derive the conditions of the PJT instability in the Q_{zx}, Q_{zy} space as follows (f and g are positive) [4.13]:

$$4f - g > 0 \qquad \text{and} \qquad 2f < g - 1 \text{ and/or } f > \tfrac{1}{2} \tag{4.47}$$

with the stabilization energy

$$E_{\mathrm{PJT}} = 2(2f-1)^2/(4f-g) \tag{4.48}$$

Figure 4.4 illustrates these conditions. We see that when $f = \frac{1}{2}$ or less $\left(F_1^2/K_{E_1} \le \frac{1}{2}\Delta\right)$ the PJT instability disappears, while for the JT stabilization within the E term there are limitations,

$$2f + 1 < g < 4f, \qquad \text{or} \qquad 2F_1^2/K_{E_1} + \Delta < F_2^2/K_{E_1} < 4F_1^2/K_{E_1} \tag{4.49}$$

As in the $E\otimes e$ JT problem (Section 3.2), the quadratic terms of the PJT coupling produce a warping resulting in three minima alternating with three saddle points when moving along the trough [4.13].

A special case of the PJTE occurs in JT systems with *spin–orbital splitting*. If the latter is of significant value compared with the JT stabilization energy, it should be taken into account simultaneously with the vibronic interaction, resulting, as shown below, in a PJT problem. Consider a spin doublet ^2E term, which is in fact a quartet. The four basis functions of the latter can be taken as $|\psi_-\rangle\cdot|\tfrac{1}{2}\rangle$, $|\psi_+\rangle\cdot|\tfrac{1}{2}\rangle$, $|\psi_-\rangle\cdot|-\tfrac{1}{2}\rangle$, and $|\psi_+\rangle\cdot|-\tfrac{1}{2}\rangle$, where ψ_- and ψ_+ are

given by Eq. (3.32), and $\left|\frac{1}{2}\right\rangle$ and $\left|-\frac{1}{2}\right\rangle$ are the two spin functions for the spins $S=\frac{1}{2}$ and $S=-\frac{1}{2}$, respectively. Under the influence of the linear vibronic coupling to the e vibrations and the spin–orbital interaction operator $\lambda(\vec{L}\vec{S})$ ($\vec{L}$ is the orbital momentum with quantum numbers ± 1 for the two E states and λ is the spin–orbital coupling constant) we get for the matrix W in Eq. (3.2):

$$W=\begin{vmatrix} -\frac{\lambda}{2} & F_E\rho & 0 & 0 \\ F_E\rho & \frac{\lambda}{2} & 0 & 0 \\ 0 & 0 & \frac{\lambda}{2} & F_E\rho \\ 0 & 0 & F_E\rho & -\frac{\lambda}{2} \end{vmatrix} \tag{4.50}$$

With this matrix Eq. (3.2) decomposes into two equivalent equations, yielding two solutions for two branches of the APES of Eq. (3.1), each being twofold degenerate:

$$\varepsilon_{i,\pm}=\frac{1}{2}K_E\rho^2 \pm \sqrt{F_E^2\rho^2+\frac{\lambda^2}{4}}, \qquad i=1,2 \tag{4.51}$$

For a given i value this expression coincides with Eq. (4.4) for a two-level PJTE with $2\Delta=\lambda$: the spin–orbital splitting transforms the JT $E\otimes e$ problem (Section 3.2) into a PJT $(\Gamma+\Gamma)\otimes e$ problem. This transformation modifies essentially the APES. Indeed, the radius ρ_0 of the two-dimensional trough on the lower sheet of the APES (instead of (3.26)) and the JT stabilization energy (instead of (3.27)) become as follows:

$$\rho_0=\sqrt{(F_E/K_E)^2-(\lambda/2F_E)^2} \tag{4.52}$$

$$E_{\mathrm{JT}}^E=\frac{F_E^2}{2K_E}-\frac{\lambda}{2}\left(1-\frac{\lambda K_E}{2F_E^2}\right) \tag{4.53}$$

As in all the other PJT problems, the energy gap λ created by the spin–orbital splitting is essential in determining the possible distortions, which decrease with increasing λ. If

$$\lambda<2F_E^2/K_E \tag{4.54}$$

there is still distortion, which disappears at the threshold value $\lambda=2F_E^2/K_E$. At $\lambda>2F_E^2/K_E$ there is no distortion. *The spin–orbital interaction diminishes the JTE and completely reduces the distortions at sufficiently large values of the*

spin–orbital coupling constant. However, the effect of vibronic coupling remains significant because it changes the curvature of the two terms as they should follow the PJT formulas (4.11) and (4.12) with $\Delta = \lambda$. A quite similar treatment of simultaneous vibronic interaction and spin–orbital coupling for the $E \otimes (b_1 + b_2)$ problem is given in [4.14].

Consider now an example of a threefold degenerate excited T state in a cubic or icosahedral system that influences vibronically a nondegenerate ground state A, the $(A + T) \otimes t$ PJT problem. Since the JT problem for the T term is $T \otimes (a + e + t_2)$ (Section 3.3), the full (combined) problem, as mentioned above, is $(A + T) \otimes (a + e + t_2 + t)$, where t has the same symmetry as T (T_1 or T_2). In particular, if the system has an inversion center with $A = A_{1g}$ and $T = T_{1u}$, the e_g and t_{2g} displacements do not couple the A_{1g} and T_{1u} terms (although they affect this coupling indirectly), and the cross-section of the APES in the T_{1u} space is given by the pure PJT $(A_{1g} + T_{1u}) \otimes t_{1u}$ problem. This particular case is especially important in applications because the t_{1u} displacements result in the formation of dipole moments, which may trigger ferroelectric phase transitions (Sections 4.3 and 8.3).

Taking the A_{1g} function as an $|s\rangle$ type, the three T_{1u} functions as $|x\rangle$, $|y\rangle$, and $|z\rangle$, and the three components of the t_{1u} displacements as Q_x, Q_y, and Q_z, respectively, we easily obtain the following matrix W in the secular equation (3.2):

$$W = \begin{vmatrix} -\Delta & FQ_x & FQ_{xy} & FQ_z \\ FQ_x & \Delta & 0 & 0 \\ FQ_y & 0 & \Delta & 0 \\ FQ_z & 0 & 0 & \Delta \end{vmatrix} \tag{4.55}$$

where 2Δ is the energy gap between the A_{1g} and T_{1u} terms and $F = \langle s|(\partial V/\partial Q_x)_0|x\rangle$ is the PJT linear vibronic coupling constant. The solution of the secular equation (3.2) with this matrix is straightforward. In polar coordinates ρ, ϑ, ϕ, $\rho^2 = Q_x^2 + Q_y^2 + Q_z^2$,

$$\begin{aligned} \varepsilon_{1,2}^v &= \pm\sqrt{\Delta^2 + F^2\rho^2} \\ \varepsilon_{3,4}^v &= \Delta \end{aligned} \tag{4.56}$$

which together with the elastic term in (3.1) yields the APES in the three-dimensional t_{1u} space with the lower sheet as

$$\varepsilon(\rho, \vartheta, \phi) = \tfrac{1}{2}K_0\rho^2 - \sqrt{\Delta^2 + F^2\rho^2} \tag{4.57}$$

This is a surface of two-dimensional revolution in the three-dimensional space. As in the two-level case (Section 4.1), if $\Delta \geq F^2/K_0$, this surface has one minimum point at $\rho = 0$. In this case the system is stable in the

high-symmetry configuration in which the T term remains threefold degenerate. But the PJT coupling is still important since it lowers the frequency of the t_{1u} vibrations in the ground state. Indeed, similar to Eq. (4.5), by expanding the square root in Eq. (4.57) with regard to small ρ displacements from the point $\rho_0 = 0$ we get

$$\varepsilon(\rho, \vartheta, \phi) = \tfrac{1}{2}[K_0 - (F^2/\Delta)]\rho^2 + \tfrac{1}{4}(F^4/\Delta^3)\rho^4 - \Delta + \cdots \tag{4.58}$$

meaning that the curvature at the minimum is

$$K = K_0 - (F^2/\Delta) \tag{4.59}$$

However, if

$$\Delta < F^2/K_0 \tag{4.60}$$

the APES has a maximum at $\rho = 0$ and a two-dimensional trough of equivalent (equipotential) minima points at

$$\rho_0 = \sqrt{(F^2/K_0^2) - (\Delta^2/F^2)} \tag{4.61}$$

and arbitrary ϑ and ϕ angles. The JT stabilization energy at these minima is quite similar to the two-level case (4.8):

$$E_{\mathrm{PJT}} = F^2/2K_0 - \Delta(1 - \Delta K_0/2F^2) \tag{4.62}$$

As in the previous JT and PJT problems, when the quadratic terms of the vibronic interaction are taken into account, the two-dimensional trough of equipotential minima points becomes warped, with regularly alternating maxima and minima along its path.

If the JT effect within the T term is also taken into account, the problem becomes $(A + T) \otimes (a + e + t_2 + t)$, where t has the same symmetry as T. Consider the $(A_{1g} + T_{1u}) \otimes (a_{1g} + e_g + t_{2g} + t_{1u})$ problem important to applications (Section 8.3). The matrix (4.55) is now complicated by the additional nonzero matrix elements for the coupling of the degenerate states to a_{1g}, e_g, and t_{2g} displacements described by means of the following vibronic coupling constants, respectively:

$$\begin{aligned} F_A &= \langle z | (\partial V/\partial Q_A)_0 | z \rangle \\ F_E &= \langle z | (\partial V/\partial Q_\vartheta)_0 | z \rangle \\ F_T &= \langle x | (\partial V/\partial Q_{xy})_0 | y \rangle \end{aligned} \tag{4.63}$$

Then we get

$$W = \begin{vmatrix} -3\Delta & FQ_x & FQ_y & FQ_z \\ FQ_x & \Delta - F_E\left(\frac{1}{2}Q_\vartheta - \frac{\sqrt{3}}{2}Q_\varepsilon\right) + F_AQ_A & F_TQ_{xy} & F_TQ_{xz} \\ FQ_y & F_TQ_{xy} & \Delta - F_E\left(\frac{1}{2}Q_\vartheta + \frac{\sqrt{3}}{2}Q_\varepsilon\right) + F_AQ_A & F_TQ_{yz} \\ FQ_z & F_TQ_{xz} & F_TQ_{yz} & \Delta + F_EQ_\vartheta + F_AQ_A \end{vmatrix} \tag{4.64}$$

where, following [4.15], we put the A_{1g} level at -3Δ and the T_{1u} level at Δ, the energy gap thus being 4Δ. Let us introduce the following combinations of constants:

$$\begin{aligned} h &= F_A^2/4K_A\Delta \\ f &= F^2/K_0\Delta \\ e &= F_E^2/4K_E\Delta \\ t &= F_T^2/3K_T\Delta \end{aligned} \tag{4.65}$$

With these constants the method of Öpik and Price [4.1] (Section 3.3) allows one to reveal three types of minima points on the APES with energies (in Δ units) (Fig. 4.5) [4.15]

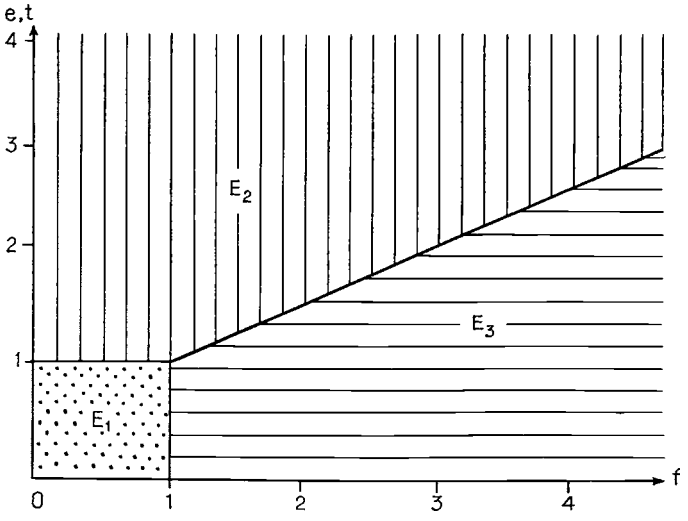

Fig. 4.5. Three domains of existence of different JT and PJT distortions in MX_6 systems with $(ns)^2$ lone pairs in each of the two *e–f* and *t–f* planes: E_1 – no distortions (inert lone pair); E_2 – combined dipolar *T* and either tetragonal E_g (in the *e–f* plane), or trigonal T_{2g} (in the *t–f* plane) distortions; E_3 – pure JT distortions, either tetragonal (in the *e–f* plane) or trigonal (in the *t–f* plane) (reprinted with permission from [4.15]. Copyright 1991 Institute of Physics).

$$\begin{aligned} E_1 &= -3 \\ E_2 &= 1 - 2g \\ E_3 &= (f + 2 - 2g)(f - 2)/2(f - g) - (f + 1) \end{aligned} \tag{4.66}$$

with

$$g = \begin{cases} e + h, \text{in the space of tetragonal distortions} \\ t + h, \text{in the space of trigonal distortions} \end{cases} \tag{4.67}$$

which can be rewritten as

$$\begin{aligned} E_2 &= E_1 - 2(g - 2) \\ E_3 &= E_1 - (f - 2)^2/2(f - g) \\ E_3 &= E_2 - (f + 2 - 2g)^2/2(f - g) \end{aligned} \tag{4.68}$$

In the region E_1 (Fig. 4.5) the system is undistorted. In E_2 the pure JT distortions described in Section 3.3 prevail, i.e. either tetragonal e type (three equivalent "tetragonal" minima), or trigonal t_2 type (four equivalent "trigonal" minima). In the E_3 area combined PJT trigonal (dipolar) t_{1u} and JT either tetragonal e, or trigonal (nonpolar) t_2, distortions take place. We see that if $g < 2$ and $f < g$, the minima are at the points with energies E_1 where no distortion takes place. At $g > 2$, $f < g$, and $f + 2 < 2g$, the E_2 points are the lowest and the system is under the pure JT effect with three tetragonal (if $e > t$) or four trigonal (for $e < t$) minima of the APES. Finally, if $f > g$, $f > 2$, and $f + 2 > 2g$, the minima of the APES at the points E_3 correspond to much lower symmetry of combined trigonal dipolar t_{1u} with JT either e (if $e > t$), or nonpolar t_2 (trigonal) (when $e < t$) distortions.

In many cases of local distortions from octahedral symmetry in coordination compounds and crystals, a PJT $(T_{1g} + T_{2g}) \otimes e_g$ problem may be important [4.16], which is a particular case of the full $(T_{1g} + T_{2g}) \otimes (\sum_i y_i)$ problem with all possible active modes y_i. It turns out that in some real systems there are grounds to ignore the JT coupling in the T_{1g} state which is weakly involved in the bonding of the central atom with the ligands (has small vibronic coupling constants), and to consider preferably tetragonal distortions of e type. This leaves us with the $(T_{1g} + T_{2g}) \otimes e_g$ PJT and $(T_{1g} + T_{2g}) \otimes (e_g + e'_g)$ combined problems.

For the $(T_{1g} + T_{2g}) \otimes e_g$ problem we denote the linear coupling constant by $F = \langle t_{1g} | (\partial V / \partial Q_\vartheta)_0 | t_{2g} \rangle$, where the e displacements are taken as Q_ϑ and Q_ε (Section 3.2), while $|t_{1g}\rangle$ and $|t_{2g}\rangle$ are wavefunction components of the two

terms T_{1g} and T_{2g}. The 6×6 matrix W in the secular Eq. (3.2) has the following nonzero matrix elements:

$$\begin{aligned} W_{ii} &= -\Delta, \qquad i = 1, 2, 3 \\ W_{ii} &= \Delta, \qquad i = 4, 5, 6 \\ W_{14} &= W_{41} = \frac{1}{\sqrt{2}} F \left(Q_\vartheta + \frac{1}{\sqrt{3}} Q_\varepsilon \right) \\ W_{25} &= W_{52} = \frac{1}{\sqrt{2}} F \left(-Q_\vartheta + \frac{1}{\sqrt{3}} Q_\varepsilon \right) \\ W_{36} &= W_{63} = -\sqrt{\frac{2}{3}} F Q_\varepsilon \end{aligned} \tag{4.69}$$

The roots of Eq. (3.2) with this matrix W can be obtained straightforwardly. In polar coordinates (4.33) we get [4.16]

$$\begin{aligned} \varepsilon^v_{1,4} &= \pm [\Delta^2 + (2/3) F^2 \rho^2 \sin^2 \phi]^{\frac{1}{2}} \\ \varepsilon^v_{2,5} &= \pm [\Delta^2 + (2/3) F^2 \rho^2 \sin^2 (\phi + \pi/3)]^{\frac{1}{2}} \\ \varepsilon^v_{3,6} &= \pm [\Delta^2 + (2/3) F^2 \rho^2 \sin^2 (\phi - \pi/3)]^{\frac{1}{2}} \end{aligned} \tag{4.70}$$

The lowest three sheets of the APES for the three negative values of the electronic energy levels ε^v_i with $i = 1, 2, 3$ are

$$\varepsilon_i(\rho, \phi) = \frac{1}{2} K_0 \rho^2 + \varepsilon^v_i(\rho, \phi), \qquad i = 1, 2, 3 \tag{4.71}$$

If $\Delta \geq (2/3) F^2 / K_0$, all the three branches of the APES have one minimum at $\rho = 0$. However, if

$$\Delta < 2F^2 / 3K_0 \tag{4.72}$$

each of the three surfaces (4.71) has a saddle point at $\rho = 0$ and two equivalent minima along one line at

$$\rho_0 = \sqrt{(2F^2 / 3K_0^2) - (3\Delta^2 / F^2)} \tag{4.73}$$

The coordinates of these minima are $(\rho_0, \pi/2)$ and $(\rho_0, 3\pi/2)$ for the ε_1 surface, $(\rho_0, \pi/6)$ and $(\rho_0, 7\pi/6)$ for ε_2, and $(\rho_0, 5\pi/6)$ and $(\rho_0, 11\pi/6)$ for ε_3. All the six minima have the same JT stabilization energy

$$E_{\mathrm{JT}} = \frac{F^2}{3K_0} - \Delta \left(1 - \frac{4K_0 \Delta}{3F^2} \right) \tag{4.74}$$

and are situated along a circle of radius ρ_0 with an interval of $\pi/3$.

However, they are only interconnected pairwise via a saddle point on the same branch of the surface, so in fact we have three equivalent pairs of minima situated on three equivalent branches of the APES with two equivalent minima in each of them. In each of these minima the octahedral symmetry O_h of the system is lowered to D_{2h} in which three diagonals of the octahedron along the fourfold axes become different in length, with one shortened and another elongated compared with the third one which remains unchanged (see the Q_ε coordinate in Fig. 2.3). In the other minimum of the pair the longer axis is interchanged with the shorter one; the three equivalent pairs are determined by the three different fourfold axes that remain unchanged (along these axes the surface has a minimum at $\rho = 0$).

The remaining three branches of the APES formed by the three positive values of ε_i^v, $i = 4, 5, 6$, in (4.70) have only one minimum at $\rho = 0$.

In the more elaborate combined problem $(T_{1g} + T_{2g}) \otimes (e_g + e'_g)$ a second vibronic coupling constant for the JT e'_g-type interaction within the T_{2g} term should be introduced:

$$F' = \langle t_{2g} | (\partial V / \partial Q_\vartheta)_0 | t_{2g} \rangle \tag{4.75}$$

This constant is nonzero only for diagonal coupling thus affecting the three diagonal matrix elements W_{44}, W_{55}, and W_{66}, which instead of (4.69) become as follows [4.16]:

$$\begin{aligned} W_{44} &= \Delta + \frac{1}{\sqrt{2}} F' \left(Q_\vartheta - \frac{1}{\sqrt{3}} Q_\varepsilon \right) \\ W_{55} &= \Delta - \frac{1}{\sqrt{2}} F' \left(Q_\vartheta + \frac{1}{\sqrt{3}} Q_\varepsilon \right) \\ W_{66} &= \Delta + \sqrt{\frac{2}{3}} F' Q_\varepsilon \end{aligned} \tag{4.76}$$

With these matrix elements the electronic energy levels (4.70) and the APES (4.71) change, resulting in the following APES of the combined problem [4.16]:

$$\begin{aligned} \varepsilon'_1(\rho, \phi) &= \frac{1}{2} K_0 \rho^2 - \left(\Delta^2 + \frac{2}{3} F^2 \rho^2 \sin^2 \phi + \frac{1}{6} F'^2 \rho^2 \cos^2 \phi + \sqrt{\frac{2}{3}} F' \rho \Delta \cos \phi \right)^{\frac{1}{2}} \\ \varepsilon'_2(\rho, \phi) &= \frac{1}{2} K_0 \rho^2 - \left[\Delta^2 + \frac{2}{3} F^2 \rho^2 \sin^2 \left(\phi + \frac{\pi}{3} \right) + \frac{1}{6} F'^2 \rho^2 \cos^2 \left(\phi + \frac{\pi}{3} \right) \right. \\ &\qquad \left. - \sqrt{\frac{2}{3}} F' \rho \Delta \cos \left(\phi + \frac{\pi}{3} \right) \right]^{\frac{1}{2}} \\ \varepsilon'_3(\rho, \phi) &= \frac{1}{2} K_0 \rho^2 - \left[\Delta^2 + \frac{2}{3} F^2 \rho^2 \sin^2 \left(\phi - \frac{\pi}{3} \right) + \frac{1}{6} F'^2 \rho^2 \cos^2 \left(\phi - \frac{\pi}{3} \right) \right. \\ &\qquad \left. - \sqrt{\frac{2}{3}} F' \rho \Delta \cos \left(\phi - \frac{\pi}{3} \right) \right]^{\frac{1}{2}} \end{aligned} \tag{4.77}$$

These three branches of the APES are significantly different from those for the pure PJT problem. Depending on the values of the two vibronic coupling constants F and F' and their relation to the energy gap Δ, the extremum points have much lower symmetry than the D_{2h} ones above. To clarify the features of these surfaces, consider the branch ε_1, for convenience presenting it as a function of the two e-type coordinates $Q_\vartheta = \rho\cos\phi$ and $Q_\varepsilon = \rho\sin\phi$,

$$\varepsilon_1'(Q_\vartheta, Q_\varepsilon) = \frac{1}{2}K_0(Q_\vartheta^2 + Q_\varepsilon^2) - \left(\Delta^2 + \frac{2}{3}F^2Q_\varepsilon^2 + \frac{1}{6}F'^2Q_\vartheta^2 + \sqrt{\frac{2}{3}}F'\Delta Q_\vartheta\right)^{\frac{1}{2}} \tag{4.78}$$

and examine this APES in cross-sections. In the cross-section $Q_\vartheta = 0$

$$\varepsilon_1'(Q_\vartheta) = \frac{1}{2}K_0Q_\varepsilon^2 - \left(\Delta^2 + \frac{2}{3}F^2Q_\varepsilon^2\right)^{\frac{1}{2}} \tag{4.79}$$

This surface has the same features as the pure PJT one (4.71): a minimum at $Q_\varepsilon = 0$ if $\Delta > (2/3)F^2/K_0$, and a maximum at this point if $\Delta < (2/3)F^2/K_0$ with two minima at

$$Q_\varepsilon^0 = \pm\sqrt{(2F^2/3K_0^2) - (3\Delta^2/2F^2)} \tag{4.80}$$

In fact this result is similar to that of a PJT T_{1g}–T_{2g} interaction with $F' = 0$, except that the direction of the axis of the distortion is rotated by $\pi/2$ as compared with the pure PJT case: the two equivalent minima in the latter case have the coordinates $(\rho_0, \pi/2)$and $(\rho_0, 3\pi/2)$ instead of $(\rho_0, 0)$ and (ρ_0, π) in the combined problem. We get thus the same Q_ε ($O_h \to D_{2h}$) distortion at the minima, but in another (perpendicular) direction.

In the other cross-section $Q_\varepsilon = 0$ (which is equivalent to the assumption that $F = 0$)

$$\varepsilon_1'(Q_\vartheta) = \frac{1}{2}K_0Q_\vartheta^2 - \left(\Delta^2 + \frac{1}{6}F'^2Q_\vartheta^2 + \sqrt{\frac{2}{3}}F'\Delta Q_\vartheta\right)^{\frac{1}{2}} \tag{4.81}$$

there is no extremum at $Q_\vartheta = 0$: the JT tetragonal distortion $O_h \to D_{2h}$ due to the $T_{2g} \otimes e$ coupling takes place for any nonzero F' value, but it is accompanied by PJT implications ($\Delta \neq 0$) which depend on the sign of F'. The other two branches of the APES, ε_2' and ε_3' in (4.77), have the same features as ε_1', but with the D_{2h} (Q_ε) axis of distortion rotated by angles $\pi/3$ and $2\pi/3$, respectively, compared with that of ε_1'. The picture as a whole emerges as a combination of the PJT D_{2h} distortion of the octahedron described above combined with

the JT D_{4h} distortion along the axis that remained intact in the D_{2h} distortion. The resulting symmetry of the system may be very low, thus violating the epikernel principle (Section 2.5). Further discussion of this superposition of distortions is given in Section 4.3 in connection with the product JT effect. The combined JT plus PJT $(T_{1u} + T_{1g}) \otimes (a_g + h_g + a_u + t_{1u} + h_u)$ problem relevant to the icosahedral system C_{60}^{-} is considered in [4.17].

4.3 Product JTE problems

The so-called "*product JT effect*" (the term was introduced in [4.18]) is an approach to some rather complicated JT and PJT problems in which there are multi-electron open-shell configurations that produce degenerate terms that are sufficiently close in energy. The traditional approach requires that one reveals first the possible terms, their wavefunctions and energies, and then, using the methods described above, considers the implications produced by vibronic coupling, the JT and PJT effects. In cases of two or many resulting degenerate terms this way may be very difficult. On the other hand, it may happen that the interelectron interaction which leads to term formation is smaller than the vibronic coupling. If this assumption holds, we can try to solve the vibronic coupling problem first, and then to introduce the interelectron repulsion. This means that the vibronic coupling problem can be considered using one-electron states (e.g. MOs) as a basis set. It simplifies essentially the treatment and allows one to get solutions in reasonable approximations.

Consider a system in which the ground and excited states are formed by two different electron configurations (two different electronic shells). For instance, assume that the excited state is produced by the HOMO $\rightarrow$ LUMO one-electron excitation in which both the HOMO and the LUMO are degenerate. Denote their symmetry representations by Γ_a and Γ_b. The usual scheme for treatment of such cases, as mentioned above, is to find all the energy terms of both electronic configurations, and then to treat the vibronic coupling within each of the terms, as well as their PJT interaction. The terms arising from the interelectron repulsion in these configurations can be found from the direct product $\Gamma_a \times \Gamma_b$ of the two representations.

However, in some special situations (especially in large polyatomic systems) the interelectron repulsion may be small, so the different terms formed by this interaction may be almost degenerate. This happens, in particular, in fullerenes C_{60}, where the additional electron in the excited state is distributed over the large icosahedral surface, thus producing very weak additional electron repulsion.

In such cases we can assume that the JT stabilization energy is larger than the term splitting within the manifold in question and consider the vibronic coupling problem in the one-electron approximation taking the product of $\Gamma_a \times \Gamma_b$ degenerate MOs as a basis set of the problem. The manifold of $\Gamma_a \times \Gamma_b$ functions acts thus as a single degenerate term, for which the JT active coordinates $Q\gamma_i$ will be those from the symmetric products $[\Gamma_a \times \Gamma_a]$ and $[\Gamma_b \times \Gamma_b]$. This model problem was called the *product* $\{\Gamma_a \otimes \Gamma_b\} \otimes \{\Sigma_i \gamma_i\}$ *JT problem* [4.18].

Consider, for example, the product $\{T_1 \otimes T_2\}$ problem [4.18]. In this case γ_i displacements are $e + t_2$ (the totally symmetric displacements are ignored; see Section 3.1), so the product problem is $\{T_1 \otimes T_2\} \otimes (e + t_2)$. Assume that the two configurations that produce this problem emerge from the one-electron excitation $t_1 \to t_2$ in a cubic (or higher-symmetry) system. Denote the three T_1 functions by x, y, z, and the three T_2 functions by ξ, η, ζ (Section 3.3). Then the $T_1 \otimes T_2$ space can be taken as the corresponding products $(x, y, z) \otimes (\xi, \eta, \zeta)$, yielding the nine functions $x\xi, x\eta, x\zeta, y\xi, y\eta, y\zeta, z\xi, z\eta, z\zeta$. There should be also four vibronic coupling constants for the coupling of the two configurations to two JT-active displacements e and t_2: $F_E^{T_1}, F_T^{T_1}, F_E^{T_2}$, and $F_T^{T_2}$ (an equivalent denotation of the problem will then be $\{T_1 \otimes T_2\} \otimes (e' + e'' + t_2' + t_2'')$). Consequently, the secular equation (3.2) will be of ninth order with respect to the five $e + t_2$ coordinates $Q_\vartheta, Q_\varepsilon, Q_\xi, Q_\eta, Q_\zeta$.

In the linear approximation with respect to these coordinates the problem is relatively simple, as its JT Hamiltonian can be presented as a sum of the coupling to, respectively, e and t_2 displacements taken separately. Similar to the pure $T_1 \otimes e$ (or $T_2 \otimes e$) problems, the $\{T_1 \otimes T_2\} \otimes e$ problem yields a diagonal matrix (3.3); it allows direct evaluation of energies ε_i^γ as functions of Q_ϑ and Q_ε coordinates, which together with the elastic energy $\frac{1}{2}K_E(Q_\vartheta^2 + Q_\varepsilon^2)$ form the APES. It has two types of minima depending on the relative sign of $F_E^{T_1}$ and $F_E^{T_2}$. If $F_E^{T_1} F_E^{T_2} > 0$, the lower part of the surface has three potential wells with absolute minima along the tetragonal directions (Fig. 3.10). The coordinates of the minima points are very similar to those obtained in the $T \otimes e$ problem (Section 3.3, Eqs. (3.45) and (3.46)), but with a different distortion in the minima that summarizes both T_1 and T_2 contributions (Table 4.2):

$$Q_0^{(1)} = (F_E^{T_1} + F_E^{T_2})/K_E \tag{4.82}$$

and

$$E_{\mathrm{JT}}^{D_{4h}} = (F_E^{T_1} + F_E^{T_2})^2/2K_E \tag{4.83}$$

Table 4.2. *Wavefunctions and coordinates of the three equivalent tetragonal D_{4h} minima in the product $\{T_1 \otimes T_2\} \otimes e$ problem with $F_E^{T_1} F_E^{T_2} > 0$ (their JT stabilization energy is given in Eq. (4.83)) (adapted from [4.18]))*

Label	Wavefunction $(x, y, z) \otimes (\xi, \eta, \zeta)$	Q_ϑ^0	Q_ε^0
$x\xi$	$(1, 0, 0) \otimes (1, 0, 0)$	$\frac{1}{2}Q_0$	$-\sqrt{3}Q_0/2$
$y\eta$	$(0, 1, 0) \otimes (0, 1, 0)$	$\frac{1}{2}Q_0$	$\sqrt{3}Q_0/2$
$z\zeta$	$(0, 0, 1) \otimes (0, 0, 1)$	Q_0	0

Table 4.3. *Wavefunctions and coordinates of the six equivalent orthorhombic D_{2h} minima in the product $\{T_1 \otimes T_2\} \otimes e$ problem with $F_E^{T_1} F_E^{T_2} < 0$ (their JT stabilization energy is given in Eq. (4.85)) (adapted from [4.18]))*

Label	Wavefunction $(x, y, z) \otimes (\xi, \eta, \zeta)$	Q_ϑ^0	Q_3^0
$x\eta$	$(1, 0, 0) \otimes (0, 1, 0)$	$(1/2)Q_0^{(1)}$	$-(1/2)Q_0^{(2)}$
$y\xi$	$(0, 1, 0) \otimes (1, 0, 0)$	$(1/2)Q_0^{(1)}$	$(1/2)Q_0^{(2)}$
$x\zeta$	$(1, 0, 0) \otimes (0, 0, 1)$	$-(1/4)Q_0^{(1)} + (\sqrt{3}/4)Q_0^{(2)}$	$-(\sqrt{3}/4)Q_0^{(1)} - (1/4)Q_0^{(2)}$
$y\zeta$	$(0, 1, 0) \otimes (0, 0, 1)$	$-(1/4)Q_0^{(1)} + (\sqrt{3}/4)Q_0^{(2)}$	$(\sqrt{3}/4)Q_0^{(1)} + (1/4)Q_0^{(2)}$
$z\xi$	$(0, 0, 1) \otimes (1, 0, 0)$	$-(1/4)Q_0^{(1)} - (\sqrt{3}/4)Q_0^{(2)}$	$-(\sqrt{3}/4)Q_0^{(1)} + (1/4)Q_0^{(2)}$
$z\eta$	$(0, 0, 1) \otimes (0, 1, 0)$	$-(1/4)Q_0^{(1)} - (\sqrt{3}/4)Q_0^{(2)}$	$(\sqrt{3}/4)Q_0^{(1)} - (1/4)Q_0^{(2)}$

More novel results emerge in cases of different signs of the two coupling constants, $F_E^{T_1} F_E^{T_2} < 0$. In this case there are six equivalent minima of orthorhombic D_{2h} symmetry situated in between the tetragonal turning points. The C_2 axis of this D_{2h} subgroup coincides with the C_4^2 elements of the cubic group, so the minimum point symmetry is $D_{2h}(C_4^2)$, in accordance with the E kernel of the epikernel principle (Section 2.5). The parameters of these six minima are given in Table 4.3 with

$$Q_0^{(2)} = \sqrt{3}(F_E^{T_1} - F_E^{T_2})/K_E \tag{4.84}$$

and

$$E_{\mathrm{JT}}^{D_{2h}} = -[(F_E^{T_1})^2 - F_E^{T_1} F_E^{T_2} + (F_E^{T_2})^2]/2K_E \tag{4.85}$$

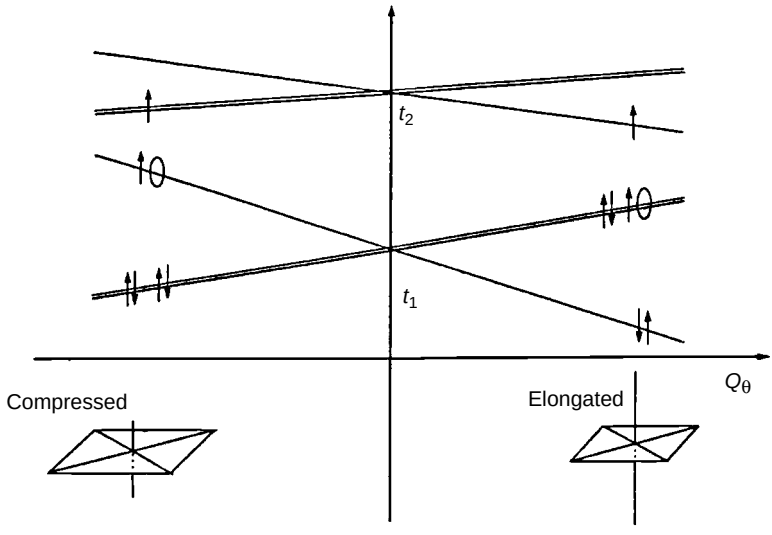

Fig. 4.6. A two-shell system of the type $t_1^5 t_2^1$. The t_1 shell induces tetragonal compression, while the t_2 shell favors tetragonal elongation (reprinted with permission from [4.18]. Copyright 2000 American Physical Society).

From these data, it follows that both the symmetry and the magnitudes of distortion and the minima depths are strongly influenced by the interference of the two contributions from the two configurations with opposite signs of vibronic coupling.

The origin of orthorhombic minima is quite unusual and needs clarification (there are no such minima in $T \otimes e$ problems). Consider, for instance, that the two configurations emerge from the six-electron system $t_1^5 t_2^1$. Figure 4.6 shows schematically the MO energy level behavior of the two configurations in the space of tetragonal e-type (Q_ϑ) distortions of an octahedron under the assumption of $F_E^{T_1} < 0$ (tetragonal compression produced by the t_1 hole) and $F_E^{T_2} > 0$ (elongation along the same axis). We see that in both cases the electronic state under these distortions remains degenerate either due to the t_2 electron in the compressed configuration, or to the t_1 hole in the elongated case. According to the JT theorem these tetragonally distorted configurations remain unstable with respect to further distortions of lower symmetry.

The outcome is that when the system is distorted, say, elongated along one of the C_4 axes due to the larger configuration contribution with $F_E^{T_2} > 0$, the second (smaller) contribution from the other configuration with $F_E^{T_1} < 0$ will produce its required tetragonal compression along another C_4 axis. As a result the system is orthorhombically distorted. Figure 4.7 illustrates this case: the vector sum of two possible distortions of opposite signs in three

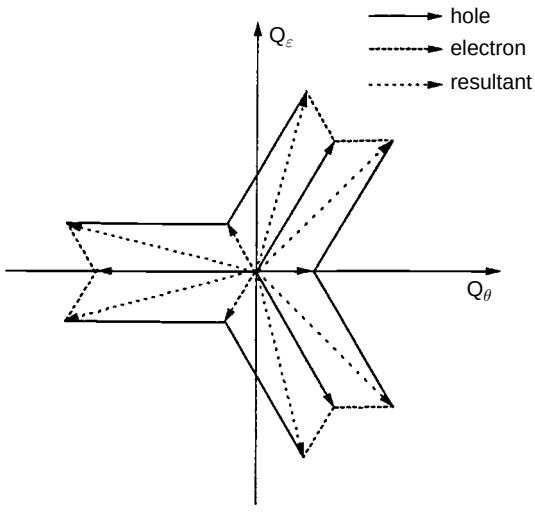

Fig. 4.7. The orthorhombic distortions in the Q_ϑ and Q_ε plane caused by dominant JT forces of the hole and particle. The resultant vectors are the sums of the hole and particle vectors that have the smallest angle between them (reprinted with permission from [4.18]. Copyright 2000 American Physical Society).

tetragonal minima of the APES leads to six orthorhombic distortions. Note that if $F_E^{T_1} = F_E^{T_2}$, distortions in all the six minima become tetragonal with three positive (elongation) and three negative (compression) signs of the deformations.

The $\{T_1 \otimes T_2\} \otimes t_2$ problem is more complicated because the vibronic coupling matrix, as in the $T \otimes t_2$ problem (Section 3.3), is not diagonal. However, using the method of Öpik and Price [4.18] (Section 3.3) the extremum points of the APES can be retrieved. If the two coupling constant $F_E^{T_1}$ and $F_E^{T_2}$ have the same sign, the APES has two types of extremum points: four trigonal D_{3d} and six orthorhombic D_{2h} (cf. the $T \otimes t_2$ problem, Section 3.3), the former being minima, while the latter are saddle points. The parameters of these two types of extremum points are given in Tables 4.4 and 4.5 with

$$Q_0^{(t)} = \sqrt{2}(F_T^{T_1} + F_T^{T_2})/K_T \tag{4.86}$$

$$E_{\mathrm{JT}}^{D_{3d}} = (F_T^{T_1} + F_T^{T_2})^2/3K_T \tag{4.87}$$

$$E_{\mathrm{JT}}^{D'_{2h}} = (F_T^{T_1} + F_T^{T_2})^2/4K_T \tag{4.88}$$

Table 4.4. *Wavefunctions and coordinates of the four equivalent trigonal D_{3d} minima in the product $\{T_1 \otimes T_2\} \otimes t_2$ problem with $F_E^{T_1} F_E^{T_2} < 0$ (their JT stabilization energy is given in Eq. (4.87)) (adapted from [4.18]))*

Label	Wavefunction ($a = 1/\sqrt{3}$) $a(x,y,z) \otimes a(\xi,\eta,\zeta)$	Q_ξ^0	Q_η^0	Q_ζ
$x\eta$	$a(1,0,0) \otimes a(0,1,0)$	$Q_0^{(t)}$	$Q_0^{(t)}$	$Q_0^{(t)}$
$y\xi$	$a(0,1,0) \otimes a(1,0,0)$	$Q_0^{(t)}$	$-Q_0^{(t)}$	$-Q_0^{(t)}$
$x\zeta$	$a(1,0,0) \otimes a(0,0,1)$	$-Q_0^{(t)}$	$Q_0^{(t)}$	$-Q_0^{(t)}$
$y\zeta$	$a(0,1,0) \otimes a(0,0,1)$	$-Q_0^{(t)}$	$-Q_0^{(t)}$	$Q_0^{(t)}$

Table 4.5. *Wavefunctions and coordinates of the six equivalent orthorhombic D'_{2h} saddle points in the product $\{T_1 \otimes T_2\} \otimes t_2$ problem with $F_E^{T_1} F_E^{T_2} > 0$ (their JT stabilization energy is given in Eq. (4.88)) (adapted from [4.18]))*

Label	Wavefunction ($a = 1/\sqrt{2}$) $a(x,y,z) \otimes a(\xi,\eta,\zeta)$	Q_ξ^0	Q_η^0	Q_ζ
xy	$a(1,1,0) \otimes a(1,1,0)$			$(3/2)Q_0^{(t)}$
$x\bar{y}$	$a(1,-1,0) \otimes a(1,-1,0)$			$-(3/2)Q_0^{(t)}$
xz	$a(1,0,1) \otimes a(1,0,1)$		$(3/2)Q_0^{(t)}$	
$x\bar{z}$	$a(1,0,-1) \otimes a(1,0,-1)$		$-(3/2)Q_0^{(t)}$	
yz	$a(0,1,1) \otimes a(0,1,1)$	$(3/2)Q_0^{(t)}$		
$y\bar{z}$	$a(0,1,-1) \otimes a(0,1,-1)$	$-(3/2)Q_0^{(t)}$		

At the D_{3d} minima the nine energy levels above split into one nondegenerate ground state A_2, two doubly degenerate E states, and an accidentally fourfold degenerate E_3 (A_1, A_2, E) state:

$$\begin{aligned} E_0(A_2) &= -(F_T^{T_1} + F_T^{T_2})^2/3K_T \\ E_1(E) &= [2(F_T^{T_1})^2 + F_T^{T_1} F_T^{T_2} - (F_T^{T_2})^2]/3K_T \\ E_2(E) &= [-(F_T^{T_1})^2 + F_T^{T_1} F_T^{T_2} + 2(F_T^{T_2})^2]/3K_T \\ E_3(A_1, A_2, E) &= -2(F_T^{T_1} + F_T^{T_2})^2/3K_T = -2E_{\mathrm{JT}}^{D_{3d}} \end{aligned} \tag{4.89}$$

If the signs of $F_E^{T_1}$ and $F_E^{T_2}$ are different, the APES becomes much more complicated [4.18], with six orthorhombic D_{2h} (C_4^2, $2C_2$) (the axes of distortion are given in parentheses) and 12 C_{2h} (C_2) extremum points with JT stabilization energies.

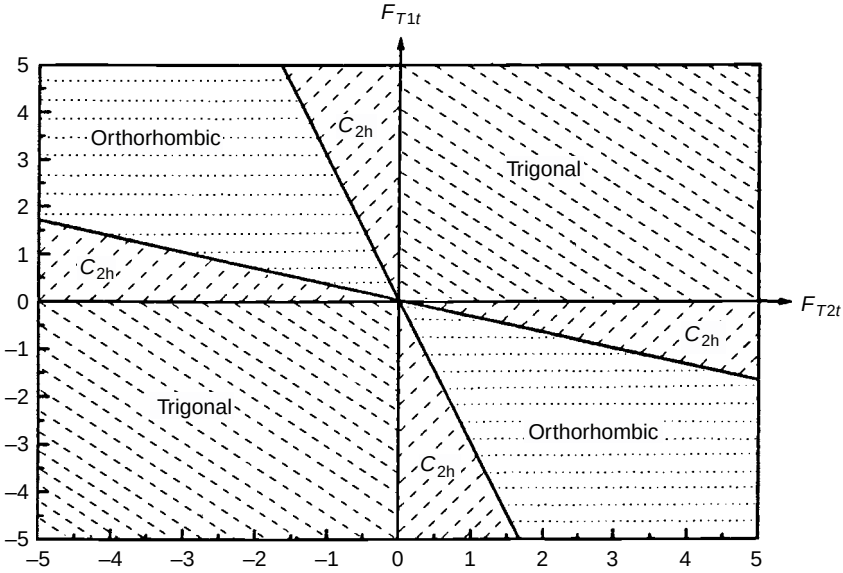

Fig. 4.8. Regions of existence of absolute minima of different symmetries for the $\{T_1 \otimes T_2\} \otimes t_2$ product JT system (reprinted with permission from [4.18]. Copyright 2000 American Physical Society).

$$E_{\mathrm{JT}}^{D'_{2h}} = (F_T^{T_1} - F_T^{T_2})^2/4K_T \tag{4.90}$$

$$E_{\mathrm{JT}}^{C_{2h}} = [(F_T^{T_1})^2 - (2/3)F_T^{T_1}F_T^{T_2} + (F_T^{T_2})^2]/3K_T \tag{4.91}$$

Depending on the vibronic-constant ratio $F_E^{T_1}/F_E^{T_2}$, either D'_{2h} or C_{2h} saddle points become absolute minima. Figure 4.8 shows the regions of existence of these two types of minima on the $F_T^{T_1}$ versus $F_T^{T_2}$ plane in the $\{T_1 \otimes T_2\} \otimes t_2$ problem. The boundaries of D_{2h} and C_{2h} phases are given by the following straight lines:

$$F_T^{T_1} = -3F_T^{T_2} \qquad \text{and} \qquad F_T^{T_1} = -(1/3)F_T^{T_2} \tag{4.92}$$

In the general case of the $\{T_1 \otimes T_2\} \otimes (e + t_2)$ problem all the four vibronic coupling constants enter the interplay yielding a variety of extremum points on the APES, including orthorhombic D_{2h} $(C_4^2, 2C_2)$, C_{2h} (C_2), and C_{2h} (C_4) points in addition to the D_{3d} and D_{4h} extremum points of the $T \otimes (e + t_2)$ problem (Section 3.3). In [4.18] all these special points of the APES are revealed and analyzed.

The most important general conclusion emerges from the fact that in the presence of two competing distortions produced by each of the two configurations the resulting symmetry of the system is lower than that produced by

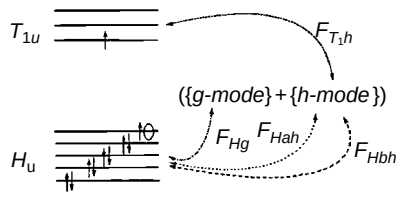

Fig. 4.9. A schematic description of the vibronic coupling of the product $\{T_1 \otimes H\} \otimes (g + 2h)$ JT system. The two electronic levels are interacting via coupling to common vibrational modes (reprinted with permission from [4.19]. Copyright 2001 American Physical Society).

each of them. If the ratio between $F_T^{T_1}$ and $F_E^{T_1}$ produces trigonal D_{3d} minima in the linear $T_1 \otimes (e + t_2)$ problem (Section 3.3), while for the $T_2 \otimes (e + t_2)$ problem the $F_T^{T_2}$ and $F_E^{T_2}$ constants are such that the tetragonal symmetry D_{4h} is lower in energy, neither D_{3d} nor D_{4h} geometry is a solution for the $\{T_1 \otimes T_2\} \otimes (e + t_2)$ problem: its APES minima are found at C_{2h} (C_2) symmetry, which is the intersection of D_{4h} and D_{3d}. If the minima on the APES are of the same symmetry in both configurations T_1 and T_2, say D_{4h}, the resulting distortion will be at still lower symmetry D_{2h} ($3C_4^2$), which is the highest common subgroup of two D_{4h} groups with different principal axes (see the discussion above and illustrations in Figs. 4.6 and 4.7).

Another example of the product JT problems emerges from a real situation in icosahedral fullerenes C_{60}, where the lowest excitation is produced by a one-electron $h_u \rightarrow t_{1u}$ transition resulting in the two-shell configuration $h_u^9 t_{1u}$, as illustrated in Fig. 4.9 [4.19]. The two open-shell configurations that contribute to the JT vibronic coupling are thus h_u^9 with the JT problem $H \otimes (g + 2h)$ (Section 3.4) and t_{1u} with the $T_1 \otimes h$ JT effect. Provided we can neglect the interelectron interaction, as outlined above, the vibronic coupling can be treated starting with the product $\{T_1 \otimes H\} \otimes (g + 2h)$ JT problem. A detailed consideration of this problem is given in [4.19].

Since the T_1 manifold is not coupled to the g vibrations, the Hamiltonian of the coupling to g remains as in the $H \otimes (g + 2h)$ problem (Section 3.4), and the two types of distortions in the two open shells may interfere only via h displacements. Therefore it is worthwhile to consider first the product $\{T_1 \otimes H\} \otimes 2h$ problem. In the linear approximation with respect to the vibronic coupling there are three independent linear vibronic coupling constants (cf. Eq. (3.70)): $F_h^{T_1}$, $F_{h_a}^H$, and $F_{h_b}^H$ (the T_1 term is coupled to only one h displacement). Depending on their values, the APES has a very rich structure with four types of extremum points of D_{5d}, D_{3d}, D_{2h}, and C_{2h} symmetry, and equipotential troughs of $SO(3)$ and $SO(5)$ symmetry in between these extremum points.

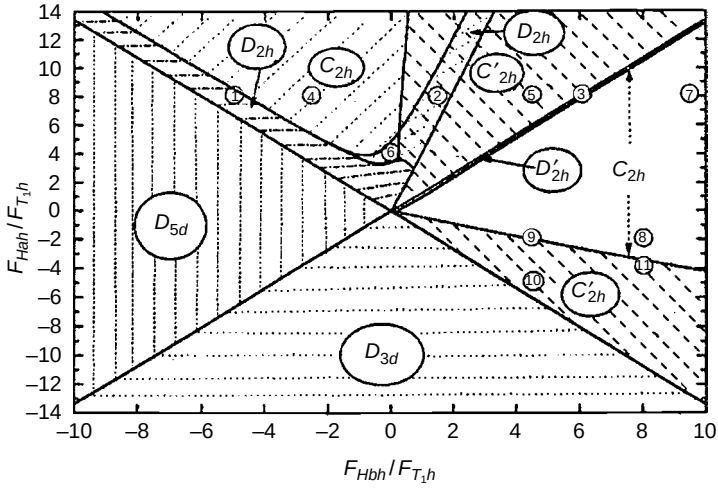

Fig. 4.10. The phase diagram for the $\{T_1 \otimes H\} \otimes 2h$ problem as a function of the vibronic coupling-constant ratios $F^H_{h_a}/F^{T_1}_h$ and $F^H_{h_b}/F^{T_1}_h$. The encircled numbers refer to the stationary points (for more details see [4.19]) (reprinted with permission from [4.19]. Copyright 2001 American Physical Society).

Figure 4.10 shows schematically the regions of occurrence of lowest-in-energy extremum points of different symmetries as a function of the vibronic coupling constant ratios $F^H_{h_a}/F^{T_1}_h$ and $F^H_{h_b}/F^{T_1}_h$. As seen from this diagram and further explanations in [4.19], the space on the $(F^H_{h_a}/F^{T_1}_h)$–$(F^H_{h_b}/F^{T_1}_h)$ plane is divided into four regions (wedges) by two diagonal lines of "equal coupling" at

$$F^H_{h_a} = \pm(3/\sqrt{5})F^H_{h_b} \tag{4.93}$$

In the left-side lower wedges we have the usual D_{5d} and D_{3d} minima separated by the line $F^H_{h_a} = (3/\sqrt{5})F^H_{h_b}$, along which the system has $SO(3)$ symmetry with an equipotential two-dimensional trough in the five-dimensional space of h displacements (Section 3.4). In these two regions the contributions of the two open-shell configurations to the distortion of the system are "in phase" and enhance each other.

The JT stabilization energy in the D_{5d} minima is given by

$$E^{D_{5d}}_{JT} = (\sqrt{2}F^H_{h_b} - F^{T_1}_h)^2/5K_h \tag{4.94}$$

while in the D_{3d} minima

$$E^{D_{3d}}_{JT} = (\sqrt{10}F^H_{h_a} - 3F^{T_1}_h)^2/45K_h \tag{4.95}$$

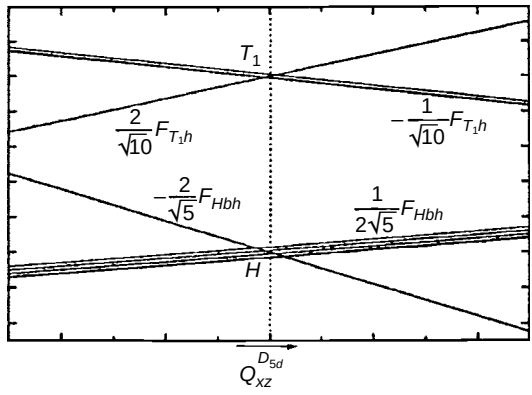

Fig. 4.11. Term splitting by pentagonal distortions along $Q_{xz}^{D_{5d}}$ in the $\{T_1 \otimes H\} \otimes 2h$ problem. The JT forces acting on the orbital singlet components of the H and T_1 terms are given by $-(2\sqrt{5})F_{h_b}^{H}$ and $(2\sqrt{10})F_{h}^{T_1}$, respectively (reprinted with permission from [4.19]. Copyright 2001 American Physical Society).

and along the trough between them

$$E_{\mathrm{JT}}^{SO(3)} = (\sqrt{2}F_{h'_b}^{H} - F_{h}^{T_1})^2/5K_h \tag{4.96}$$

where h'_b is chosen to satisfy the condition of a trough (4.93) for this case [4.19].

In the two upper and right wedges in Fig. 4.10 the two sources of distortion from the two configurations are "out of phase," resulting in lower symmetries of the system, D_{2h} and C_{2h}. Along the line dividing these two regions, $F_{h_a}^{H} = -(3/\sqrt{5})F_{h''_b}^{H}$, there is a two-dimensional trough too, while the state remains twofold degenerate (the authors [4.19] call it an "*anti-JT trough*" because the degeneracy is not lifted in this approximation). Its stabilization energy is

$$E_{\mathrm{JT}}^{SO(3)} = (\sqrt{2}F_{h''_b}^{H} + F_{h}^{T_1})^2/5K_h \tag{4.97}$$

Figures 4.11 and 4.12 provide a further insight into the energy level splitting of the two open-shell configurations under the pentagonal $Q_{D_{5d}}$ (one of them can be presented as $Q_{xz}^{D_{5d}} = (1/\sqrt{10})(\sqrt{3}Q_\vartheta - Q_\varepsilon + \sqrt{6}Q_\eta)$) and trigonal $Q_{D_{3d}}$, $Q_{xz}^{D_{3d}} = (1/\sqrt{6})(Q_\vartheta + \sqrt{3}Q_\varepsilon + \sqrt{2}Q_\eta)$, distortions of an octahedron. More results and detailed discussion of this problem are given in [4.19].

The limitation to the product JT approximation imposed by the requirement that the term splitting (including the energy gap between the ground and excited configurations) should be smaller than the JT stabilization energy does not hold in the majority of JT systems, although, as mentioned above, it may

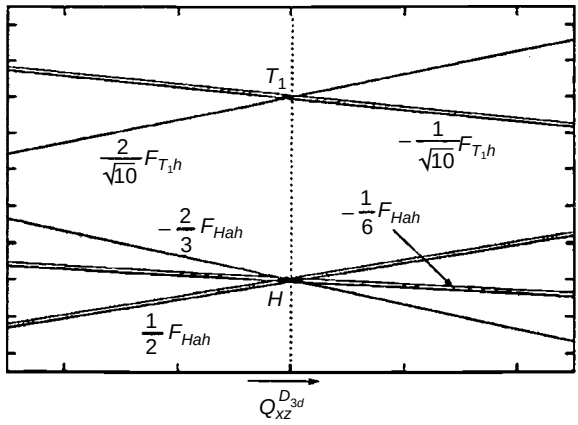

Fig. 4.12. Term splitting by trigonal distortions along $Q_{xz}^{D_{3d}}$ in the $\{T_1 \otimes H\} \otimes 2h$ problem. The JT forces acting on the orbital singlet components of the H and T_1 terms are given by $-(2/3)F_{h_a}^{H}$ and $(2\sqrt{10})F_h^{T_1}$, respectively (reprinted with permission from [4.19]. Copyright 2001 American Physical Society).

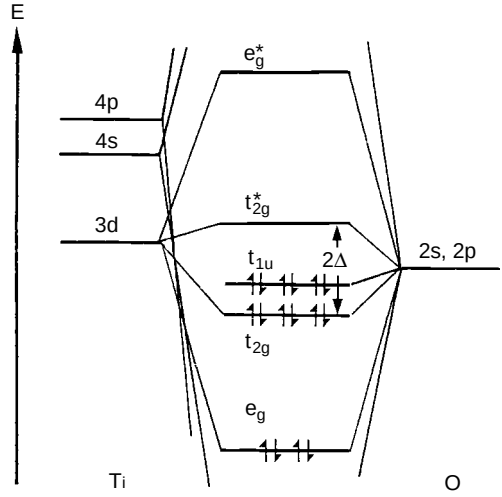

Fig. 4.13. A schematic presentation of the HOMO and LUMO for the $[TiO_6]^{8-}$ cluster in the $BaTiO_3$-type crystal [4.20].

be valid for specific problems in large polyatomic systems, such as C_{60} fullerenes, polymers, and crystals. The applicability of this approximation may be essentially enlarged if complemented with a PJT parameter Δ, the energy gap between the ground- and excited-state configurations.

Indeed, consider the usual MO LCAO scheme of an octahedral cluster in Fig. 4.13, which is qualitatively the same or similar in all octahedral transition metal systems and local sites in crystals [4.20]. Depending on the number of

d electrons of the central atom and ligand electrons on the atomic orbitals participating in the formation of MOs, the threefold degenerate t_{2g}, t_{1g}, t_{1u}, and t_{2g}^* are more or less populated, forming the HOMO and LUMO. While the t_{2g}, t_{1g}, and t_{1u} MOs formed mainly by ligand orbitals are very close in energy (and produce terms that are close in energy), the t_{2g}^* MOs (emerging mostly from the central atom) are separated by a considerable gap 2Δ. We thus have a situation with two separated open shells, for which the approximation of small interelectron interaction compared with vibronic coupling may be applied to each of the open shells, but not to their separation 2Δ. This approach was first realized in the problem of the origin of dipolar distortions and spontaneous polarization in crystals [4.10, 4.21] long before the term "product JT problem" was introduced [4.18].

Consider, for example, the possible PJT instability of a transition metal cluster of octahedral symmetry, e.g. titanium in an octahedral oxygen environment as in the cluster $[TiO_6]^{8-}$ in $BaTiO_3$, with regard to odd t_{1u} displacements that produce dipolar distortions [4.21]. The ground state of this cluster is nondegenerate (the Ti^{4+} ion has a d^0 configuration and the O^{2-} ions have closed shells too). For the approximate treatment in the sense of a product PJT effect, one may restrict the problem by considering the vibronic mixing of a group of close-in-energy electronic terms that are well separated from the other terms. A typical qualitative scheme of the MO energy levels and electron occupation numbers for this complex is shown in Fig. 4.13.

It is seen that at least the nine MOs, t_{2g}, t_{1u}, and t_{2g}^* forming the HOMO–LUMO group (occupied by 12 electrons in the $[TiO_6]^{8-}$ cluster) should be taken into account in the approximate (zeroth-order) consideration. There are also three t_{1g} orbitals in the same energy range, but they are pure ligand (nonbonding) orbitals, which do not participate in the vibronic coupling with t_{1u} displacements. With allowance of interelectron repulsion, these orbital states form the ground $^1A_{1g}$ and a variety of excited states, from which those of the same multiplicity (singlets) are $^1A_{2u}$, ^1E_u, $^1T_{1u}$, $^1T_{2u}$, $^1A_{2g}$, ^1E_g, $^1T_{1g}$, and $^1T_{2g}$. For reasons given above in the treatment of the product problem, the vibronic interactions may be considered at an earlier stage, before multi-electron term formation. As a first approximation we can also neglect the weak covalency in the π-bonding of the above-mentioned t_{2g}, t_{1u}, and t_{2g}^* orbitals (the main Ti—O bonding is formed by the inner, lower-in-energy σ-bonds of the e_g, a_{1g}, and t_{1u} orbitals, see [4.20]). In this approximation the t_{2g}^* orbital is formed by three $3d_\pi$ atomic functions of the Ti^{4+} ion (d_{xy}, d_{xz}, and d_{yz}), while the six combinations of the $2p_\pi$ atomic functions of O^{2-} ions produce the three t_{1u} and three t_{2g} MOs (see Table 5.1 in [4.20]).

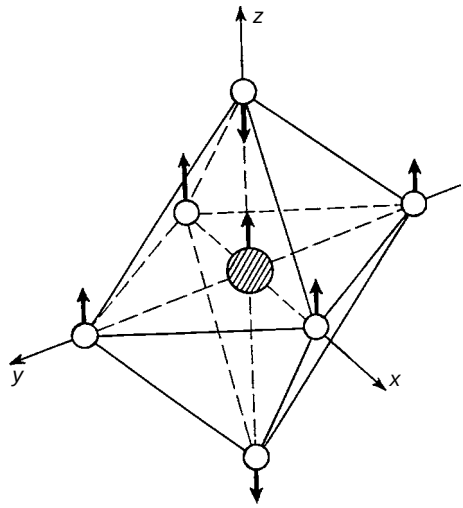

Fig. 4.14. The Z-component of the chosen T_{1u} displacement in the octahedral TiO_6 cluster [4.20].

The T_{1u} nuclear displacements form a dipole moment in this cluster, one of the components of which, Q_z, is shown schematically in Fig. 4.14. Under these T_{1u}-type displacements the t_{1u} ligand states mix with the central atom t_{2g}^* states, producing additional (π-type) covalent bonding (Section 4.2; in the regular octahedral configuration these two types of orbital are orthogonal). However, the t_{1u}–t_{2g} mixing between the pure ligand orbitals under the t_{1u} displacements, although allowed by symmetry considerations, does not affect the metal–ligand bonding (has a zero coupling constant with regard to metal–ligand displacements). The problem is thus a product $\{T_{1u} \otimes T_{2g}\} \otimes t_{1u}$ problem, which incorporates a simpler PJT $(A_{1g} + T_{1u}) \otimes t_{1u}$ problem. If we neglect the π-bonding in the reference configuration, the t_{1u} MOs are pure ligand (oxygen) orbitals, while the t_{2g} ones are of pure Ti origin. This means that the JTE in each of them, taken separately, is irrelevant to the T_{1u}-type metal–ligand displacements that produce a dipole moment (see below). In this case the product problem is reduced to a simpler PJT one: $(A_{1g} + T_{1u}) \otimes t_{1u}$.

The vibronic coupling matrix W in secular equation (3.2) with the basis set above is as follows:

$$W = \begin{vmatrix} \Delta & 0 & 0 & FQ_y & FQ_x & 0 \\ 0 & \Delta & 0 & FQ_z & 0 & FQ_x \\ 0 & 0 & \Delta & 0 & FQ_z & FQ_y \\ FQ_y & FQ_z & 0 & -\Delta & 0 & 0 \\ FQ_x & 0 & FQ_z & 0 & -\Delta & 0 \\ 0 & FQ_x & FQ_y & 0 & 0 & -\Delta \end{vmatrix} \tag{4.98}$$

where

$$F = \langle 2p_y | (\partial V/\partial Q_x)_0 | 3d_{xy} \rangle \tag{4.99}$$

and 2Δ is the energy gap between the $3d_{xy}$ and $2p_y$ atomic states of respectively the Ti^{4+} and O^{2-} ions.

There are three types of possible T_{1u}-type dipolar nuclear displacements in the octahedral cluster $[TiO_6]^{8-}$ [4.20], but the results below do not depend essentially on the choice of any of them or their linear combination. For simplicity we choose the T_{1u} coordinates as shown in Fig. 4.14 for the Q_z component, the other two components Q_x and Q_y being equivalently oriented along the x and y axes, respectively. With this choice of the t_{1u} displacements it is more convenient to involve another basis set for the problem that includes all the nine atomic functions mentioned above: three functions d_{xy}, d_{xz}, and d_{yz} of the Ti atom and six combinations of the 12 p_π functions of the oxygen atoms, which we take in the following symmetry-adapted form (see Fig. 5.1(a) in [4.20]): $\pi_{1x} - \pi_{4y}, \pi_{1y} - \pi_{4x}, \pi_{2x} - \pi_{5y}, \pi_{2y} - \pi_{5x}, \pi_{3x} - \pi_{6y}$, and $\pi_{3y} - \pi_{6x}$; with our choice of the Q displacements (Fig. 4.14) only these six combinations of the 12 p_π oxygen functions are active in the vibronic coupling.

With this basis set of nine functions the matrix W is

$$W = \begin{vmatrix} \Delta & 0 & 0 & 0 & 0 & 0 & FQ_x & FQ_y & 0 \\ 0 & \Delta & 0 & FQ_z & 0 & FQ_x & 0 & 0 & 0 \\ 0 & 0 & \Delta & 0 & FQ_z & 0 & 0 & 0 & FQ_y \\ 0 & FQ_z & 0 & -\Delta & 0 & 0 & 0 & 0 & 0 \\ 0 & 0 & FQ_z & 0 & -\Delta & 0 & 0 & 0 & 0 \\ 0 & FQ_x & 0 & 0 & 0 & -\Delta & 0 & 0 & 0 \\ FQ_x & 0 & 0 & 0 & 0 & 0 & -\Delta & 0 & 0 \\ FQ_y & 0 & 0 & 0 & 0 & 0 & 0 & -\Delta & 0 \\ 0 & 0 & FQ_y & 0 & 0 & 0 & 0 & 0 & -\Delta \end{vmatrix} \tag{4.100}$$

The solutions of Eq. (3.2) with this matrix W can be obtained straightforwardly:

$$\begin{aligned} \varepsilon^v_{1,2} &= \pm[\Delta^2 + F^2(Q_x^2 + Q_y^2)]^{\frac{1}{2}} \\ \varepsilon^v_{3,4} &= \pm[\Delta^2 + F^2(Q_y^2 + Q_z^2)]^{\frac{1}{2}} \\ \varepsilon^v_{5,6} &= \pm[\Delta^2 + F^2(Q_x^2 + Q_z^2)]^{\frac{1}{2}} \\ \varepsilon^v_{7,8,9} &= -\Delta \end{aligned} \tag{4.101}$$

Of these nine levels only the lower six are occupied in the ground state by the 12 electrons mentioned above. On substituting $\varepsilon^v_1, \varepsilon^v_3$, and ε^v_5 from Eqs. (4.101)

into Eq. (3.1) we obtain the following expression for the ground-state APES (read off from the undistorted configuration at $Q_i = 0$) [4.21]:

$$\varepsilon(Q_x, Q_y, Q_z) = \tfrac{1}{2}K_0(Q_x^2 + Q_y^2 + Q_z^2) - 2\{[\Delta^2 + F^2(Q_x^2 + Q_y^2)]^{\frac{1}{2}} + [\Delta^2 + F^2(Q_x^2 + Q_z^2)]^{\frac{1}{2}} + [\Delta^2 + F^2(Q_y^2 + Q_z^2)]^{\frac{1}{2}}\} \tag{4.102}$$

The shape of this surface depends on the relation among the constants Δ, F, and K_0. If $\Delta > 4F^2/K_0$, the surface has one minimum at the point $Q_x = Q_y = Q_z = 0$ and the system remains undistorted. This is the weak pseudo Jahn–Teller effect (Fig. 4.1). However, if (cf. Eq. (4.6))

$$\Delta < 4F^2/K_0 \tag{4.103}$$

the surface (4.102) acquires a rather complicated shape with four types of extremum points.

1. One maximum at $Q_x = Q_y = Q_z = 0$ (instability).
2. Eight minima at the points $|Q_x| = |Q_y| = |Q_z| = Q_0^{(1)}$,

$$Q_0^{(1)} = [(8F^2/K_0^2) - (\Delta^2/2F^2)]^{\frac{1}{2}} \tag{4.104}$$

with the JT stabilization energy

$$E_{\mathrm{JT}}^{(1)} = 3[(4F^2/K_0) + (\Delta^2 K_0/4F^2) - 2\Delta] \tag{4.105}$$

At these minima the Ti atom is displaced along the trigonal axes, equally close to three oxygen atoms and removed from the other three.

3. Twelve saddle points at $|Q_p| = |Q_p| \neq 0$, $p, q, r = x, y, z$, with a maximum in the section r and minima along p and q. At these points the Ti atom is displaced toward two oxygen atoms lying on the p and q axes, respectively.
4. Six saddle points at $Q_p = Q_q = 0,\ Q_r = Q_0^{(2)}$,

$$Q_0^{(2)} = [(16F^2/K_0^2) - (\Delta^2/F^2)]^{\frac{1}{2}} \tag{4.106}$$

with a depth

$$E_{\mathrm{JT}}^{(2)} = 2[(4F^2/K_0) - (\Delta^2 K_0/4F^2) - 2\Delta \tag{4.107}$$

With covalency and multi-electron term formation included, these results, especially their quantitative expression, are modified, but the main qualitative conclusions do not alter.

The origin of the instability of the position of the Ti^{4+} ion in the center of the octahedron can be given a visual treatment already mentioned in Section 4.1. When the Ti atom is in the central position exactly, the overlap of its d_{xy} atomic orbital with the appropriate (T_{1u}) combination of the oxygen p_y orbitals is zero on grounds of symmetry (positive overlaps are compensated by negative ones). However, if the Ti atom is shifted toward any of the oxygens, resulting in its off-center position (Fig. 4.14), the overlap becomes nonzero and produces additional covalent bonding that lowers the energy by such distortions (Fig. 4.2). Note also that if the number of d electrons of the central atom is nonzero, the condition of strong PTJE (4.103) required for dipole moment formation deteriorates, and if the excited t_{2g} level is fully populated by six electrons, the PJT interaction is totally vanished (Section 8.3).

The $BaTiO_3$ crystal is an example of the well-studied phenomenon of ferroelectricity, and the dipolar t_{1u} distortions in the minima of the APES of the Ti site explain the origin of spontaneous polarization (Section 8.3). In many other crystals the local distortions of the octahedral sites with nondegenerate ground states are of e_g type, i.e. tetragonal with preservation of the inversion center. Looking at the MO LCAO scheme in Fig. 4.13 for octahedral complexes, we see that the e_g-type distortion may occur as a result of the product JT plus PJT $\{T_{1g} \otimes T_{2g}\} \otimes (e_g + e'_g)$ problem [4.16]. Indeed, as in the previous example, the combination of three t_{1u}, three t_{2g}, and three t_{1g} ground and excited MOs that are most active and close in energy (Fig. 4.13) produces a bundle of degenerate terms, among which only the vibronic coupling between T_{1g} and T_{2g} or within the T_{2g} terms results in e_g distortions; the JT effect within the T_{1g} term, as noticed in Section 4.2, is usually small and may be neglected. Since the t_{1u} MOs do not participate directly in the (linear) vibronic coupling with e_g displacements, the authors [4.16] used a simpler basis set for the product problem, namely the three t_{1g} plus three t_{2g} MOs with an energy gap 2Δ between them, making the problem combined JT plus PJT $\{T_{1g} \otimes T_{2g}\} \otimes (e_g + e'_g)$.

The solution for the nonproduct $(T_{1g} + T_{2g}) \otimes (e_g + e'_g)$ problem is given in Section 4.2, Eqs. (4.77). In the product problem these solutions are just one-electron energy levels to be populated by electrons, the number of which (the number of central-atom and ligand electrons on the atomic orbitals that were used to form the t_{1g} and t_{2g} MOs) depends on the problem. In nondegenerate d^0 complexes ($[TiF_6]^{2-}$, PF_6^-, WF_6) there are six electrons, which occupy the three energy levels of Eq. (4.77), resulting in the following APES [4.16]:

$$E(\rho,\,\phi) = \frac{1}{2}K_0\rho^2 - 2\left(\Delta^2 + \frac{2}{3}F^2\rho^2\sin^2\phi + \frac{1}{6}F'^2\rho^2\cos^2\phi + \sqrt{\frac{2}{3}}F'\rho\Delta\cos\phi\right)^{\frac{1}{2}}$$
$$- 2\left[\Delta^2 + \frac{2}{3}F^2\rho^2\sin^2\left(\phi+\frac{\pi}{3}\right) + \frac{1}{6}F'^2\rho^2\cos^2\left(\phi+\frac{\pi}{3}\right) + \sqrt{\frac{2}{3}}F'\rho\Delta\cos\left(\phi+\frac{\pi}{3}\right)\right]^{\frac{1}{2}}$$
$$- 2\left[\Delta^2 + \frac{2}{3}F^2\rho^2\sin^2\left(\phi-\frac{\pi}{3}\right) + \frac{1}{6}F'^2\rho^2\cos^2\left(\phi-\frac{\pi}{3}\right) + \sqrt{\frac{2}{3}}F'\rho\Delta\cos\left(\phi-\frac{\pi}{3}\right)\right]^{\frac{1}{2}} \tag{4.108}$$

with the same two vibronic coupling constants F and F' and energy gap Δ as in the one-electron case, Eqs. (4.77).

Distinct from the one-electron case, however, the APES in this product problem is more complicated with an interference of JT distortions somewhat similar to that described above for other product problems. Although the saddle points remain at the same six positions, $\phi = 0, \pi/3, \ldots, \pi/5$, the minima positions change significantly: with the increase of the F' constant (the JT coupling within the T_{2g} term) the minima points approach pairwise the saddle point between them, forming three equivalent pairs, and simultaneously the energy of this saddle point lowers, while that of the remaining three saddle points (between the three pairs) increases. At $F' \gg F$ two minima in each pair merge, resulting in the usual three equivalent tetragonal minima of the $T \otimes e$ problem with three saddle points (Section 3.3).

4.4 The Renner–Teller effect

The RT effect refers to linear molecules, which were excluded from the formulation of the JT effect in its earlier versions. The peculiarity of the linear molecules emerges from the fact that for them the orbital angular momentum determines the parity of the wavefunctions in inversion transformations, in which $\Psi_{LM}(r)$ is multiplied by $(-1)^L$. All the wavefunctions of a degenerate state have the same quantum number L and hence they are all either odd (for odd L values), or even (for even L). Therefore any matrix element of an odd operator with the functions of a degenerate term equals zero by symmetry considerations. Since the bending distortion of the linear configuration of any linear molecule is of odd nature, the matrix element (2.15) that defines the linear vibronic coupling constant equals zero. Hence *no linear JTE is possible in linear molecules*. However, for the quadratic terms of vibronic coupling the coupling constant is nonzero, resulting in a nonzero *Renner–Teller effect* (RTE).

The RTE first suggested for triatomic molecules in [4.22] (see also [4.23]) was extended to tetraatomic systems [4.24], higher-order interactions [4.25, 4.26], and other advances (for reviews see [4.23–4.30]). In this section we consider only examples of RT APES with continuation in Chapters 5 and 7.

Consider a *linear triatomic molecule* in a doubly degenerate electronic Π state with the orbital quantum number $\Lambda = 1$ in the space of a doubly degenerate bending e vibration (formally similar to the $E \otimes e$ problem in nonlinear molecules). As stated above, no linear JTE is possible in this system, but the limitation of the JT theorem to just first-order linear displacements from the high-symmetry configuration is an unnecessary constraint. For the quadratic terms of e bending in the vibronic interactions in Eq. (2.14), which transform as $[E \times E] = A_1 + E$, the matrix element of vibronic coupling (2.19) is nonzero, resulting in the nonzero RTE under consideration.

The linear molecules in the reference configuration have cylindrical symmetry, so we can introduce the two components of the bending distortion in polar coordinates, $Q_x = \rho \cos\phi$, $Q_y = \rho \sin\phi$, with $\rho^2 = Q_x^2 + Q_y^2$. Accordingly, the quadratic terms of the vibronic coupling between the two electronic terms are equal to $\frac{1}{2}g\rho^2$ with $\frac{1}{2}g$ as the quadratic vibronic coupling constant (2.19). The vibronic coupling matrix in the secular equation (3.2) for this case is

$$W = \begin{vmatrix} 0 & \frac{1}{2}g\rho^2 \\ \frac{1}{2}g\rho^2 & 0 \end{vmatrix} \tag{4.109}$$

with the solution of Eq. (3.2),

$$\varepsilon_{\pm}^{v} = \pm\tfrac{1}{2}g\rho^2 \tag{4.110}$$

Then, by including the elasticity term of Eq. (3.1), we get

$$\varepsilon_{\pm}(\rho) = \tfrac{1}{2}(K_0 \pm g)\rho^2 \tag{4.111}$$

The two branches (4.111) of the APES are shown in Fig. 4.15(a). We see that, as far as $g < K_0$, the APES is just split into two by the bending vibrations. For larger g values the curvature of the lower surface becomes very small (and negative when $g > K_0$), so fourth-order terms may be essential in the APES behavior (third-order terms vanish for the same reason as the first-order ones). With the fourth-order terms included the APES acquires the following form (j is the fourth-order coupling constant):

$$\varepsilon_{\pm}(\rho) = \tfrac{1}{2}(K_0 \pm g)\rho^2 + j\rho^4 \tag{4.112}$$

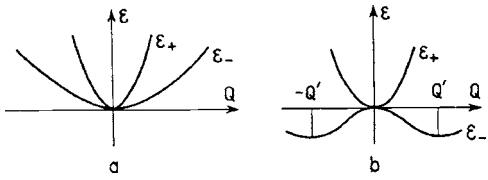

Fig. 4.15. Variation of the APES of a linear molecular system with respect to odd displacements Q in the case of the RTE: (a) weak coupling – term splitting without instability; (b) strong coupling – dynamic instability of the ground state.

At $\rho = 0$ and $g > K_0$ this surface has a maximum on the lower sheet and a minimum on the higher sheet with additional equivalent minima on the lower sheet at a distance ρ_0 from the center (Fig. 4.15(b)),

$$\rho_0 = \sqrt{(g - K_0)/4j} \tag{4.113}$$

The minima positions (4.113) do not depend on the rotational angle ϕ, meaning that the APES has a two-dimensional trough. Some results on the solution of the vibronic equations with the APES (4.112) are given in Section 5.1 and further discussed in Section 7.1.1 for specific systems.

For a Δ term with $\Lambda = 2$ the APES problem is similar to that of the Π term, but the energy levels and wavefunctions are quite different (Section 5.1).

The vibronic coupling in an accidentally fourfold degenerate ($\sigma\sigma\pi$) state of a triatomic system is considered in [4.31]. Elaborate methods of calculation of RT interaction matrices using Green's function formalisms are presented in [4.32].

The RTE is not the only source of bending of the linear configuration of molecules. Another important bending force arises from the PJT mixing of the electronic state under consideration with other states (of appropriate symmetry) under the bending distortion. Similar to other cases, bending configurations in linear molecules in nondegenerate states may occur as a result of the PJT effect. For a linear system, the bending displacements are of doubly degenerate Π symmetry. This means that if the system is in a nondegenerate Σ state, the bending may occur due to the vibronic coupling to the excited state of Π symmetry ($\Sigma \times \Pi = \Pi$), provided the coupling is strong enough and the inequality (4.6) holds. The same is true for the PJT mixing of two excited states.

Although the bending produced by the PJT Σ–Π mixing is geometrically the same as in the RTE for degenerate terms, in fact these two distortions are somewhat different in nature and this results in significant differences in the observable effects. In the PJT case there is an additional parameter Δ, the

energy gap between the mixing states, which is significant in forming the APES (involving also the totally symmetric displacements [4.2]). Most important, the PJT distortions may be linear in the bending coordinate [4.33], whereas the RT ones are always quadratic (or of even higher order). The result is that the APES in these two cases are different, the PJT one being more complicated because of anharmonicity and possible conical intersections.

If the linear system with more than two atoms has a center of inversion, the PJT vibronic mixing between electronic states of opposite parity (say, Σ_g with Σ_u) may remove the center of inversion and form a dipole moment in the minima, leaving the linear configuration intact. The RTE does not produce this kind of dipolar distortion.

The study of PJT distortions in linear systems is at its beginning, although the first investigations were carried out more than two decades ago [4.33]. In this work the authors derived the general Hamiltonian of such Σ–Π vibronic coupling in linear systems and applied it to the linear-to-bent transition in HCN and DCN to explain their photoelectron spectra. The solution of the PJT problem of vibronic coupling between the Σ and Π states with energies E_σ and E_π, respectively, including the two bending vibrations with coordinates Q_x and Q_y ($\rho^2 = Q_x^2 + Q_y^2$) and the totally symmetric one Q_g (with frequencies ω and ω_g, respectively) yields the following three branches of the APES (in conventional units [4.33]):

$$V_\pi = -E_\pi + \tfrac{1}{2}\omega\rho^2 + \tfrac{1}{2}\omega_g^2 Q_g^2 + 2^{\frac{1}{2}} k_\pi Q_g \tag{4.114}$$

$$\begin{aligned} V_\pm = {} & -\tfrac{1}{2}(E_\pi + E_\sigma) + \tfrac{1}{2}\omega\rho^2 + \tfrac{1}{2}\omega_g^2 Q_g^2 + 2^{\frac{1}{2}}(k_\pi + k_\sigma) Q_g \\ & \pm \{[\tfrac{1}{2}(E_\pi - E_\sigma) + 2^{\frac{1}{2}}(k_\pi - k_\sigma) Q_g]^2 + 2\lambda^2\rho^2\}^{\frac{1}{2}} \end{aligned} \tag{4.115}$$

where k_π and k_σ are the constants of vibronic coupling of, respectively, the Π and Σ states to the Q_g vibrations, and λ is the constant of the Σ–Π PJT coupling.

It is seen from these equations that one of the branches (V_π) is not affected by the bending, while the distortion in the other two depends on the value of Q_g. Figure 4.16 illustrates this effect for the cationic states of HCN that are most important in the photoelectron spectra. For $Q_g = 0$ (note that this read-off of the totally symmetric coordinate is conventional) and $4\lambda^2 > |E_\sigma - E_\pi|$ the lower branch of the potential V_- is unstable at the point $\rho = 0$ that corresponds to the linear configuration. It has a continuum of minima forming a circle at the bottom of a trough, at which the configuration

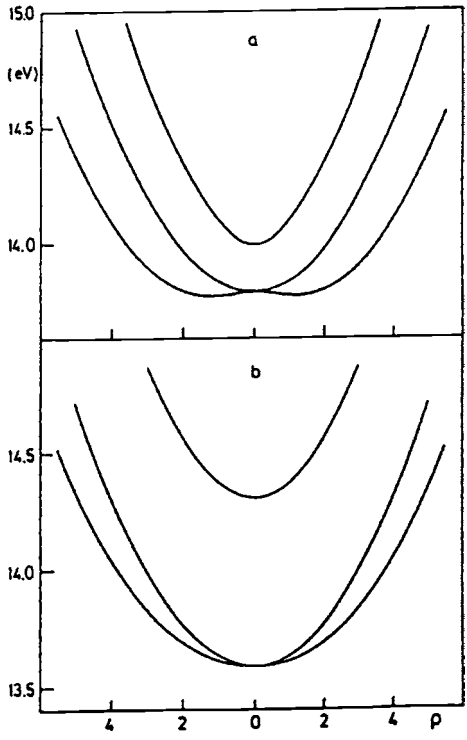

Fig. 4.16. The APES curves for the lowest cationic states of HCN as functions of the bending coordinate $\rho = (Q_x^2 + Q_y^2)^{\frac{1}{2}}$ for (a) $Q_g = 0$ and (b) $Q_g = -1.26$. The three curves represent (from top to bottom) V_+, V_π, and V_- in Eqs. (4.113) and (4.114) (reprinted with permission from [4.33]. Copyright 1979 Elsevier Science Publishers).

of the system is bent. In the linear HCN molecule the totally symmetric displacement Q_g involves H—C and C—N stretching, which thus play a significant role in the $\Sigma-\Pi$ PJT coupling and formation of the APES.

The two sets of curves in Fig. 4.16, (a) and (b), should be regarded as two cross-sections along the totally symmetric coordinate Q_g illustrating the complexity of the fully anharmonic APES in which the different kind of vibrations are nonseparable.

4.5 Reformulation of the JT theorem

The JT theorem for degenerate states as formulated by its authors [4.34] and the corrected version [4.2] are analyzed in Section 2.5. The simplest formulation of this theorem is as follows: *the nuclear configuration (geometry) of a nonlinear molecule in an orbitally degenerate electronic state (except twofold spin degeneracy) is unstable with respect to nuclear displacements that remove*

the degeneracy. As explained in Section 2.5, this statement cannot be directly applied to observable properties. Indeed, as seen from the proof of this theorem, it is related to the behavior of the APES near the point of degeneracy, which is by itself not observable. Also, because the proof [4.34] is carried out by including linear coupling terms only (Section 2.5), it excludes the RTE for molecules with linear configurations.

A more rigorous formulation of the JT theorem [4.2] given here with some further improvements is devoid of the failures noted above: *for any polyatomic system with two or more branches of the APES that intersect at the point of degeneracy or are tangential and interact sufficiently strongly at this point, there is at least one branch that has no minimum, the case of twofold spin degeneracy being an exception*. This formulation concerns the specific properties of the APES of systems with both JTE and RTE, which lead to a variety of observable effects (when solving the nuclear motion problem with this APES) but not necessarily to distortions. The lack of minimum of the APES at the point of degeneracy results, first of all, in special dynamics of the nuclear configuration, it may lead to observable distortions in particular cases in the presence of external peturbations (Sections 2.5, 7.1.1). Therefore the terms *instability* and *distortions*, which are widely in use to describe JT situations also in this book, should not be taken literally, but as an abbreviation of the *lack of minimum of the APES*, which under certain conditions may result in observable distortions.

Still this formulation of the basic theorem does not include the PJTE discussed in this chapter. Before the latest achievements on this topic, when the PJTE was considered as a case of quasidegeneracy (as a small deviation from the JTE produced by a small splitting of the degenerate term), there was no necessity to include it in the formulation of the basic theorem. As shown in Section 4.1, it follows from numerical calculations that the energy gap between the strongly mixing terms may be very large (tens of electron-volts), and anyhow it is not the crucial limiting parameter of the strong PJTE as there are other parameters, that compensate for the large energy gap. Moreover, since the PJTE is the only possible source of instability of high-symmetry configurations of polyatomic systems in nondegenerate states (Section 4.1), it expands the application of the JT vibronic coupling theory to any molecular system and to crystals, embracing all the possible structural instabilities of high-symmetry configurations. Obviously, it is desirable that the basic statement of this trend incorporates all these possibilities.

Following the discussion above, we suggest an extended and more rigorous formulation of the JT theorem as follows (see also [4.35]): *the necessary and sufficient condition of instability (lack of minimum of the APES) of the*

high-symmetry configuration of any polyatomic system is the presence of two or more electronic states that are either degenerate in this configuration, or nondegenerate but sufficiently strongly interacting under the nuclear displacements in the direction of instability, the twofold spin (Kramers) degeneracy being an exception.

In this formulation, compared with the previous one above, there are several novel aspects. First, it refers to *any polyatomic system* without exceptions. Second, it includes all the JT vibronic coupling effects, JTE, RTE, and PJTE. Third, it implies that these effects are necessary and sufficient for the instability to occur, meaning that *there are no other mechanisms* to produce structural instabilities of high-symmetry configuration. The case of twofold (Kramers) spin degeneracy remains the only exception as it cannot be removed by nuclear displacements (Kramers degeneracy can be split only by magnetic fields).

Note that the term *high-symmetry configurations* in this formulation is introduced to satisfy the condition of uniqueness of the PJT origin of instabilities of molecular systems in nondegenerate states, which requires that the first derivative of the APES in the direction of instability is zero. This does not limit the cases of JTE or RTE because electronic degeneracies are inherent in systems with no less than a threefold axis of symmetry, and for them the first derivative of the APES in the direction of instability *without vibronic coupling* is zero too.

In all the formulations of the JTE above it is implicitly assumed that the reference configuration is a bonded polyatomic system, i.e. the degenerate or pseudodegenerate electronic states are inherent to the nuclear configuration of a polyatomic system formed by a set of *bonded* atoms at (or near to) equilibrium. Meanwhile, in the proof of these statements the atoms of the reference configuration *are not required to be necessarily bonded*. The only essential requirement in the proof of the JT theorem is the presence of two or more electronic states, which become mixed under nuclear displacements from the reference configuration.

However, so far all the applications of the JT effect theory were considered only for chemically bonded systems in their high-symmetry configuration and transition states of chemical reactions. It was shown that this is an unnecessary restriction [4.35–4.37]: *the JT instabilities are inherent to all the cases of degeneracy or pseudodegeneracy, including nonbonded states in molecule formation from atoms, intermolecular interaction, and chemical reactions.*

Consider first chemical bonding, i.e. the formation of molecules from atoms. In the formation of a homonuclear molecule, the two electronic states of the two identical atoms at large interatomic distances R have the same energy, and hence they form a doubly degenerate state. Introducing for

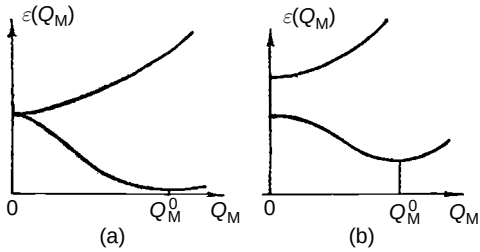

Fig. 4.17. The APES $\varepsilon(Q_M)$ of interacting atoms or groups of atoms as a function of the inverse coordinate of their approach Q_M ($Q_M = 0$ when the interatomic distance is infinite, Q_M^0 is the point of equilibrium): (a) the interacting atoms are identical, the system is degenerate at infinity – the bonding curve is similar to the JTE one; and (b) the interacting atoms (groups) are different, the bonding curve is similar to the PJTE one [4.37].

convenience the coordinate $Q_M = 1/R$, we get for the interaction between the atoms treated by perturbation theory the same secular equation as in the JT $E \otimes b_1$ problem (Section 3.1), in which $V(r, Q)$ is the operator of interatomic interaction (H is the Hamiltonian):

$$\begin{vmatrix} H_{11} - \varepsilon' & V_{12} \\ V_{12} & H_{22} - \varepsilon' \end{vmatrix} = 0 \tag{4.116}$$

with

$$\varepsilon'_{1,2} = \tfrac{1}{2}\{H_{11} + H_{22} \pm [(H_{11} - H_{22})^2 + 4|V_{12}|^2]\}^{\frac{1}{2}} \tag{4.117}$$

For degenerate states $H_{11} = H_{22}$, making one of the two states (4.117) lower and the other higher than the corresponding energies at $Q = 0$ (Fig. 4.17(a)). The lower level describes the bonding that lowers the symmetry from that of spherical atoms to the symmetry of diatomics. This reasoning can be easily expanded to the bonding of more than two identical atoms or groups of atoms and to chemical reactions. Bonding may thus formally be considered as a typical JT effect in nonbonded ($K_0 = 0$) systems.

For the bonding in heteronuclear diatomics we start from a pseudodegenerate term of the two different atoms at $Q = 0$ and get the same secular equation (4.116) with the solutions (4.117). Again, one of the solutions leads to bonding with the same decrease in symmetry as in the homonuclear case (Fig. 4.17(b)), and this picture is similar to any other cases of the PJTE (cf. the right-hand side of Fig. 4.1(b)). It can easily be extended to the bonding of several different atoms or groups of atoms.

We see that there is a full similarity between the JT (or RT) and PJT distortions of stable polyatomic systems and the formation of, respectively,

homonuclear and heteronuclear diatomics, as well as bonding in extended systems. The formation of molecules from atoms (or bonding of groups of atoms) is thus another particular case of spontaneous symmetry reductions controlled by the JT vibronic coupling effects. The differences between the particular cases of JT instability are in the details of the APES behavior at the point of degeneracy: in the proper JT case the level crossing is linear in Q (Section 2.5), whereas in the RT effect it is quadratic (Section 4.4; see also Fig. 2.8), in the PJTE it is quadratic with an energy gap between the two mixing states (Section 4.1), in homonuclear bonding it is rather exponential with $K_0 = 0$ (Fig. 4.17(a)), and in heteronuclear bonding it is exponential too with a PJT energy gap and $K_0 = 0$ (Fig. 4.17(b)). In the latter case, there is also another distinction from the general PJT case: because $K_0 = 0$ there is no limiting threshold of the type (4.6) in the formation of heteronuclear diatomics; instead the possibility of formation of bonding states gradually vanishes with increasing energy gap 2Δ.

In chemical reactions with a transition state the latter is a typical JT or (in most cases) PJT situation with the instability coordinate leading to the formation of products (Section 7.1.3). For pure Van der Waals interaction of closed-shell systems the polarization and correlation effects that lead to intermolecular bonding can in principle be described by the mixing of the ground state of one system with the excited state of the other one, which form together the pseudodegenerate situation of the PJTE.

With the chemical bonding and other interatomic and intermolecular interactions presented as a JT or PJT (or RT) effect, and taking into account the results of Sections 8.2 and 8.3, in which all first- and second-order phase transitions are shown to be triggered by the same effects, we can formulate the *uniqueness of the JT mechanism of all the symmetry breakings in molecular systems and condensed matter* [4.36, 4.37], which will be discussed in Section 8.2.5.

The broad formulation of the JT theorem given above, which is valid for any polyatomic system, including nonbonded systems, brings us back to the statement in the introduction that the JTE grew into a general approach to (tool for) understanding (rationalizing) and solving molecular and crystal problems, and to the question of the difference between this approach and other existing ones. The JTE emerges directly from the interaction of the electronic states with the nuclear displacements (vibrations), which in principle are well known as electron–vibrational interactions in molecules and electron–phonon interactions in crystals, and are included in any approaches to relevant problems. The novelty of the JT approach in this respect is that it involves more than one electronic state in the *nonadiabatic* interaction with the vibrations, and consequently there may be low-symmetry phonons that mix these states to result in

Table 4.6. *Comparison of the main features of the JT approach to solving vibronic (electron–phonon) coupling problems with other (traditional) approaches (HTSC, high-temperature superconductivity; BCS, Bardeen–Cooper–Schrieffer)*

Approaches	Electronic states involved	Active vibrations	Recent example: HTSC
Traditional approach	One state (ground)	Totally symmetric	BCS theory
JT approach	Two or more	Low symmetry (distorting)	JTE theory

what we call now the JTE. A general comparison of the JT with other (traditional) approaches to the electron–vibrational (electron–phonon) coupling problem is illustrated in Table 4.6.

As shown elsewhere in this book, in molecular systems and impurity centers and clusters in crystals the JTE may be most important. In metals there are many close-in-energy band electronic states and even degenerate states at the Fermi level which produce combined JT and PJT problems. As shown in Section 8.2.5, this results in a window of bandwidth for which the band JTE is most important. For broad bands and delocalized electronic states the JT electron–phonon interaction is weak and the JTE implications may be ignored. For narrower bands (as in the crystals with high-temperature superconductivity) the JTE becomes most important (Section 8.4). For very narrow bands the JT electron–phonon coupling is again small and the band JTE becomes negligible.

References

4.1. U. Öpik and M. H. L. Pryce, *Proc. R. Soc. London A* **238**, 425 (1957).

4.2. I. B. Bersuker and V. Z. Polinger, *Vibronic Interactions in Molecules and Crystals*, New York, Springer, 1989.

4.3. I. B. Bersuker, *Nouv. J. Chim.* **4**, 139 (1980); *Teor. Eksp. Khim.* **16**, 291 (1980).

4.4. I. B. Bersuker, N. N. Gorinchoi, V. Z. Polinger, *Theor. Chim. Acta* **66**, 161 (1984); I. B. Bersuker, V. Z. Polinger, and N. N. Gorinchoi, *J. Struct. Chem. (THEOCHEM)* **5**, 369 (1992).

4.5. I. B. Bersuker, *Pure Appl. Chem.* **60**, 1167 (1988); *Fiz. Tverd. Tela* **30**, 1738 (1988).

4.6. (*a*) R. F. W. Bader, *Mol. Phys.* **3**, 137 (1960); *Can. J. Chem.* **40**, 1164 (1962); R. F. W. Bader and A. D. Bandrauk, *J. Chem. Phys.* **49**, 1666 (1968); (*b*) R. G. Pearson, *Symmetry Rules for Chemical Reactions. Orbital Topology for Elementary Processes*, New York, Wiley,1976.

4.7. M. J. Bearpark, L. Blancafort, and M. A. Robb, *Mol. Phys.* **100**, 1735 (2002).

4.8. I. B. Bersuker, N. B. Balabanov, D. Pekker, and J. E. Boggs, *J. Chem. Phys.* **117**, 10 478 (2002).
4.9. L. F. Chibotary and F. Chimpoesu, *Internat. J. Quant. Chem.* **65**, 37 (1997); F. Chimpoesu, *Rév. Romaine Chim.* **44**, 929 (1999); F. Chimpoesu and K. Hirao, *Adv. Quant. Chem.* **44**, 369 (2003).
4.10. I. B. Bersuker, *Ferroelectrics* **164**, 75 (1995).
4.11. I. B. Bersuker, *New J. Chem.* **17**, 3 (1993).
4.12. I. B. Bersuker and S. S. Stavrov, *Coord. Chem. Rev.* **8**, 1 (1988).
4.13. Z. W. Hendrikse and W. J. A. Maaskant, *Z. Physik. Chem.* **200**, 21 (1997).
4.14. C. J. Ballhausen, *Theor. Chim. Acta* **3**, 368 (1965).
4.15. W. J. A. Massnant and I. B. Bersuker, *J. Phys.: Condens. Matter* **3**, 337 (1991).
4.16. S. A. Borshch, I. Ya. Ogurtsov, and I. B. Bersuker, *Zh. Strukt. Khim.* **23**, 7 (1982).
4.17. A. Ceulemans and L. F. Chibotary, *Phys. Rev. B* **53**, 2460 (1996-I)
4.18. A. Ceulemans and Q. C. Qiu, *Phys. Rev. B* **61**, 10 628 (2000-II).
4.19. Q. C. Qiu, L. F. Chibotary, and A Ceulemans, *Phys. Rev. B* **65**, 035104 (2001).
4.20. I. B. Bersuker, *Electronic Structure and Properties of Transition Metal Compounds. Introduction to the Theory*, New York, Wiley, 1996.
4.21. I. B. Bersuker, *Phys. Lett. A* **20**, 589 (1966).
4.22. R. Renner, *Z. Phys.* **92**, 172 (1934).
4.23. G. Gerzberg and E. Teller, *Z. Phys. Chem. B* **21**, 410 (1933).
4.24. A. V. Petelin and A. A. Kiselev, *Internat. J. Quant. Chem.* **6**, 701 (1972).
4.25. J. A. Pople and H. C. Longuet-Higgins, *Mol. Phys.* **1**, 37 (1958).
4.26. R. N. Dixon, *Mol. Phys.* **9**, 357 (1965).
4.27. H. Köppel, W. Domcke, and L. S. Cederbaum, *Adv. Chem. Phys.* **67**, 59 (1986).
4.28. J. M. Brown, in *Computational Molecular Spectroscopy*, Eds. P. Jensen and R. J. Bunker, New York, Wiley, 2000, p. 517.
4.29. M. Perić, E. Engles, and S. D. Peyerimhoff, in *Quantum Mechanical Electronic Structure Calculations with Chemical Accuracy*, Ed. S. R. Langhoff, Dordrecht, Kluwer, 1995, p. 261.
4.30. M. Perić and S. D. Peyerimhoff, *Adv. Chem. Phys.* **124**, 583 (2002).
4.31. L. V. Poluyanov and W. Domcke, *Chem. Phys.* **293**, 179 (2003); **279**, 215 (2002).
4.32. G. Bevilacqua, L. Martinelli, and G. P. Parravicini, *Adv. Quant. Chem.* **44**, 45 (2003).
4.33. H. Köppel, L. S. Cederbaum, W. Domcke, and W. Von Niessen, *Chem. Phys.* **37**, 303 (1979).
4.34. H. A. Jahn and E. Teller, *Proc. R. Soc. London A* **161**, 220 (1937).
4.35. I. B. Bersuker, in *Fundamental World of Quantum Chemistry*, Vol. 3, Eds. E. J. Brandas and E. S. Kryachko, Dordrecht, Kluwer, 2004.
4.36. I. B. Bersuker, *Adv. Quant. Chem.* **44**, 1 (2003).
4.37. I. B. Bersuker, *Chem. Rev.* **101**, 1067 (2001).

5

Solutions of vibronic equations: energy spectra and JT dynamics

The main effects of JT vibronic couplings are due to the special dynamics of the nuclear configuration that follows from the JT instability. The energy levels and wavefunctions describing these effects are solutions of the system of coupled equations (2.6) in Section 2.1. They were obtained for the most important JT problems formulated in Chapters 3 and 4, and are discussed in this chapter.

5.1 Weak vibronic coupling, perturbation theory

Calculation of the energy spectrum and wavefunctions of a JT or PJT molecule as solutions of the coupled equations (2.6) is a very complicated problem which cannot be solved in a general form, without simplifications, for arbitrary systems. However, as in similar quantum-mechanical situations, analytical solutions for some limiting cases in combination with exact numerical solutions of some particular cases yield the general trends and provide understanding of the origin and mechanism of the phenomenon as a whole.

For vibronic problems the limiting cases of weak and strong vibronic coupling with relatively small and large vibronic coupling constants, respectively, can be solved analytically. A quantitative criterion of weak and strong coupling can be defined by comparing the JT stabilization energy E_{JT}^{Γ} with the zero-point energy $n_{\overline{\Gamma}}\hbar\omega_{\overline{\Gamma}}/2$ of $n_{\overline{\Gamma}}$-fold degenerate $\overline{\Gamma}$ vibrations. Denote $\lambda_{\Gamma} = 2E_{\mathrm{JT}}^{\Gamma}/n_{\overline{\Gamma}}\hbar\omega_{\overline{\Gamma}}$. Then, if $\lambda_{\Gamma} \ll 1$ $(2E_{\mathrm{JT}}^{\Gamma} \ll n_{\overline{\Gamma}}\hbar\omega_{\overline{\Gamma}})$, the vibronic coupling will be regarded as weak, and if $\lambda_{\Gamma} \gg 1$, the coupling is strong; λ_{Γ} is the dimensionless vibronic coupling constant. Note that the vibrational frequency in the minima of the distorted configurations may be different from that in the reference configuration.

In the limiting case of weak vibronic coupling the depths of the adiabatic potential minima formed by the vibronic interactions are much smaller than the zero vibration energies, and therefore there are no local states in the minima. In the strong coupling case such local states exist. Nevertheless, in both cases the system is delocalized into all the equivalent minima, provided stationary states of the free system (and not instantaneous or specially prepared ones) are considered. However, the terms "*dynamic JTE*" and "*static JTE*" may still be meaningful if the latter is used to indicate the situation when, in the limiting case of very deep minima, the one-minimum state for the given process of measurement may be regarded as quasistationary (see the "relativity rule concerning the means of observation" in Section 7.1.1).

Consider first the solutions of the vibronic equations for weak coupling, when $\lambda \ll 1$. General considerations show (for more details see [5.1, 5.2]) that in this case the angular momenta of the electrons and nuclei are not preserved separately but as their vector sum [5.3–5.5]. Therefore, to characterize the energy levels of the system as a whole, an additional special quantum number, which comprises the quantum numbers of the projections of the angular momenta of electrons and nuclei, is required. This situation is similar to that in atomic theory where orbital L and spin S angular momenta in the weak coupling limit are summarized by the L–S coupling scheme, so we can use some results of spin–orbital coupling theory.

When $\lambda \ll 1$ the energy levels of the system with vibronic interaction can be obtained by means of perturbation theory. For the *linear $E \otimes e$ problem*, the unperturbed system is a dimeric oscillator with energies $E_n = \hbar\omega_E(n+1)$, $n = 0, 1, 2, \ldots$ Here, the angular momentum of the nuclei defined by the quantum number $l = n, n-2, \ldots, -n+2, -n$ is preserved, and therefore each energy level is $(n+1)$-fold degenerate with respect to the vibrational quantum numbers; taking into account the twofold electronic degeneracy, it results in a total $2(n+1)$-fold degeneracy.

If the vibronic interaction is sufficiently weak, the quantum number l remains "good." In addition, the total angular momentum of the electrons and nuclei defined by the quantum number $m = l \pm \frac{1}{2}$ must be preserved (the effective angular momentum of the electrons in the doubly degenerate state is defined by quantum numbers $\pm\frac{1}{2}$). As a result the following expression for the energy levels has been obtained using second-order perturbation theory with respect to linear vibronic interaction terms [5.3] (Figs. 5.1 and 5.2):

$$E_{nlm} = \hbar\omega_E[n + 1 + 2\lambda_E(l^2 - m^2 - \tfrac{3}{4})] \tag{5.1}$$

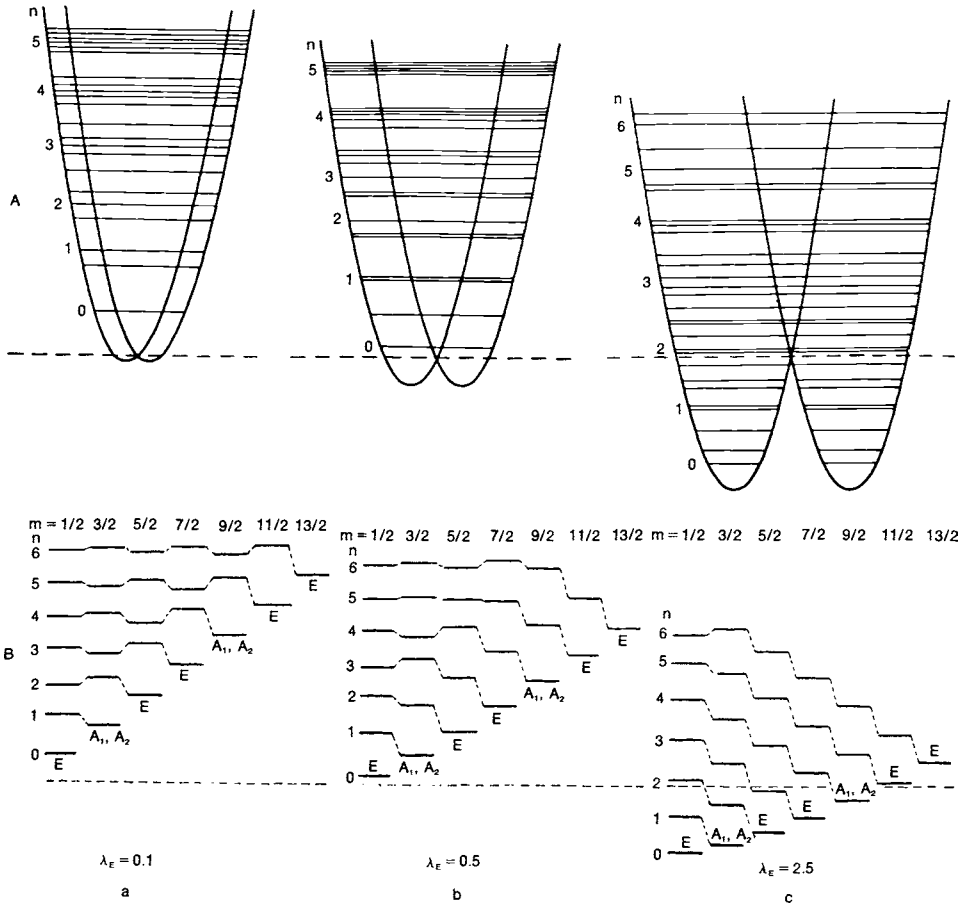

Fig. 5.1. Cross-sections of the APES and vibronic energy levels for a linear $E \otimes e$ problem (A) and the same levels with indication of the quantum numbers and symmetries (B) for three values of the dimensionless coupling constants: (a) $\lambda_E = 0.1$; (b) $\lambda_E = 0.5$; and (c) $\lambda_E = 2.5$. Energy levels with the same vibrational quantum number n are linked by dashed lines. All levels with a given m have the same symmetry indicated at the lowest level.

$$\begin{aligned} l &= n, n-2, \ldots, -n+2, -n \\ m &= \pm\tfrac{1}{2}, \pm\tfrac{3}{2}, \ldots, \pm(n+\tfrac{1}{2}) \end{aligned} \tag{5.2}$$

where $\lambda_E = E_{\mathrm{JT}}^E/\hbar\omega_E = F_E^2/2\hbar\omega_E K_E$ (see Eq. (3.27)).

Since l and m are not independent, the energy E_{nlm} depends on only two quantum numbers, say n and l, so $E_{nl} = \hbar\omega_E[n+1+2\lambda_E(\pm l-1)]$. It is seen that the $(2n+1)$-degenerate level with given n splits into $n+1$ components (since l may have $n+1$ values). Each level remains twofold degenerate because the

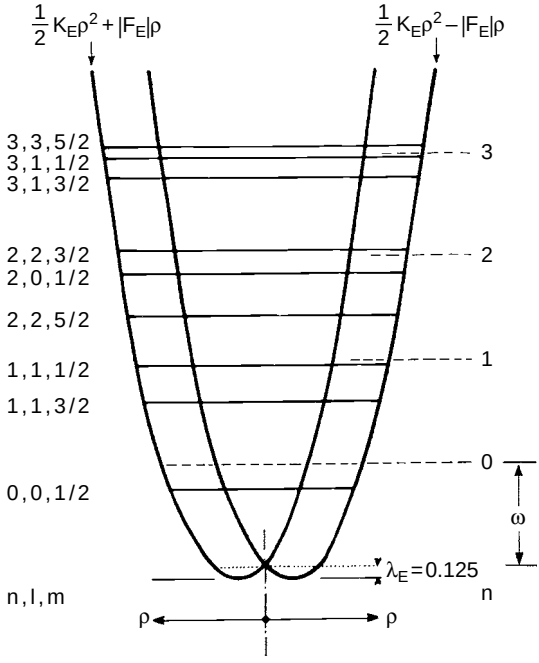

Fig. 5.2. More detailed illustration of the cross-section of the APES and vibronic energy levels for the linear $E \otimes e$ problem with weak vibronic coupling, $\lambda_E = 0.125$, with indication of quantum numbers n, l, m. The positions of vibrational levels without vibronic coupling are shown by dashed lines.

energy (5.1) does not depend on the sign of m. The ground state is also twofold degenerate:

$$E_{00\pm 1/2} = \hbar\omega_E(1 - 2\lambda_E) = \hbar\omega_E - 2E_{\mathrm{JT}}^E \tag{5.3}$$

However, some of these levels, namely, those with quantum numbers $m = \frac{3}{2}, \pm\frac{9}{2}, \pm\frac{15}{2}, \ldots$, pertain to the symmetry $A_1 + A_2$, which indicates that they are incidentally degenerate, the others being of E symmetry and therefore regularly degenerate.

The energy distance between the extreme doublets for a given value of n is $4n\hbar\omega_E\lambda_E = 4nE_{\mathrm{JT}}^E$. Hence according to the criterion of validity of the perturbation theory Eq. (5.1) is valid if and only if this value $4nE_{\mathrm{JT}}^E$ is much smaller than the distance to the next vibrational level, i.e., if $E_{\mathrm{JT}}^E \ll \hbar\omega_E/4n$.

The wavefunctions of the unperturbed two-dimensional oscillator may be written in the form

$$\Psi_{\pm n_1 n_2} = \psi_{\pm}|n_1 n_2\rangle \tag{5.4}$$

where $|n_1 n_2\rangle$ is the vibrational harmonic function, in which one of the components of the twofold degenerate e vibration (say, the e_ϑ component) is in the n_1 state, the other in the n_2 state, and the electronic functions $\psi_\pm$ are given in the general form by [5.1]

$$\begin{aligned} \psi_+ &= |\vartheta\rangle + i|\varepsilon\rangle \\ \psi_- &= |\vartheta\rangle - i|\varepsilon\rangle \end{aligned} \tag{5.5}$$

where $|\vartheta\rangle$ and $|\varepsilon\rangle$ are the two wavefunctions of the E term (Section 3.2).

Then, the perturbed functions of the ground state assume the following form [5.1]:

$$\begin{aligned} \Psi_{+00}(r, Q) &= \psi_+|00\rangle - i(2E_{\mathrm{JT}}^E/\hbar\omega_E)^{\frac{1}{2}}]\psi_-|01\rangle \\ \Psi_{-00}(r, Q) &= \psi_-|00\rangle + i(2E_{\mathrm{JT}}^E/\hbar\omega_E)^{\frac{1}{2}}]\psi_+|10\rangle \end{aligned} \tag{5.6}$$

It is seen that a weak linear vibronic coupling mixes the ground state with the first vibrational excited state.

In the $E \otimes b_1$ and $E \otimes b_2$ problems there are no nonadiabatic terms in Eq. (2.6) that couple the two electronic states of the E term, and hence all the vibrational levels are just shifted by an amount of magnitude E_{JT}, the JT stabilization energy. Similarly, for a T term coupled to only e vibrations (*the $T \otimes e$ problem*) the energy levels of the initial three-dimensional oscillator $E_n = \hbar\omega_T[n + (3/2)]$ under the influence of vibronic interaction are not split, but shifted down by an amount E_{JT}. This result has a general meaning and remains valid in the strong coupling case too [5.6].

When coupling with only trigonal t_2 vibrations is taken into account (*the $T \otimes t_2$ problem*), the initial zero-approximation system is also a three-dimensional oscillator with energy levels $E_n = \hbar\omega_T[n + (3/2)]$ but, unlike the $T \otimes e$ problem, the vibronic interaction mixes the electronic and nuclear motions. The quantum number of the vibrational angular momentum $l = n, n-2, n-4, \ldots, 1$ or 0, in case of weak coupling remains a "good" one. Besides, the energy is classified by the quantum number m of the square of the total angular momentum equal to the sum of the orbital and vibrational momenta: $m = 1, l \pm 1$ for $l \geq 1$, and $m = 1$ for $l = 0$. The resulting expression for the energy in the approximation of second-order perturbation theory is [5.5]

$$E_{nlm} = \hbar\omega_T\{n + (3/2) + (9/16)\lambda_T[m(m+1) - l(l+1) - 6]\} \tag{5.7}$$

where $\lambda_T = 2E_{\mathrm{JT}}^T/3\hbar\omega_T$. Each of these levels is $(2m+1)$-fold degenerate with respect to the quantum number of the projection of the angular momentum, which is also preserved. In particular, for the ground state $n = 0$, $l = 0$, $m = 1$, $2m + 1 = 3$, i.e., the ground state is threefold degenerate, as is the initial electronic T term.

The energy gap between the extreme components of the split level with a given value of n equals $\frac{3}{4}(2n+1)E_{\mathrm{JT}}^{T}$. Therefore, the perturbation theory formula (5.7) is valid until $E_{\mathrm{JT}}^{T} \ll 4\hbar\omega_T/3(2n+1)$.

If the coupling with both e and t_2 nuclear displacements is taken into account simultaneously (*the* $T\otimes(e+t_2)$ *problem*), the solution becomes considerably more complicated even in the limiting case of weak vibronic coupling. Analytical expressions for the splitting of several first vibronic levels in the second-order perturbation theory approximation have been obtained by means of a special functions [5.7]. If the coupling to the e vibration is stronger than to t_2, the vibrational energy levels do not split under the influence of weak vibronic coupling to t_2 vibrations, they are just shifted down by the JT stabilization energy E_{JT}^{E}, as in the $T\otimes e$ *problem*.

The $\Gamma_8\otimes e$ *problem* (Section 3.3) is quite similar to the $E\otimes e$ one [5.8], with the same vibronic splitting properties. Indeed, the Γ_8 term may be regarded as an ^2E term with nonzero spin–orbital coupling. Since the spin states are not related directly to the vibronic $E\otimes e$ problem (spin states are not mixed by vibronic interaction), the system of coupled equations (2.6) decomposes into two equivalent equations with the result that the vibrational level splitting is the same as in Eq. (5.1); the only difference is that all the levels are quadruplets instead of doublets E (since they are additionally twofold degenerate by spin), and the coincidentally degenerate doublets are $\Gamma_6+\Gamma_7$ instead of A_1+A_2 (see Fig. 5.1).

For similar reasons the $\Gamma_8\otimes t_2$ problem may be formally reduced to the $T\otimes t_2$ one with a pseudo spin $\frac{3}{2}$, for which the vibrational energy level splitting under weak vibronic coupling is given by Eq. (5.7) with $m = l\pm\frac{3}{2}$, $l\pm\frac{1}{2}$ if $l>1$, $m=\frac{3}{2}\pm 1$ if $l=1$, and $m=\frac{3}{2}$ if $l=0$ [5.9].

For weak PJT coupling of two nondegenerate states, as shown in Section 4.1, there is no instability but just a change in the curvature of the two APES given by Eqs. (4.11) and (4.12). Accordingly the vibrational frequencies in the two states of an $(A+B)\otimes b$ problem are changed, being decreased in the ground state and increased in the excited state. Assuming that the primary (nonvibronic) frequencies ω are the same in the two mixing states, we get [5.1, 5.10]

$$\omega_{\pm}^{2} = \omega^{2}\left(1 \pm \frac{F^{2}/\Delta K_0}{1-(\hbar\omega/2\Delta)^{2}}\right) \tag{5.8}$$

where 2Δ is the A–B energy gap. Accordingly, for the energy levels we get

$$E_n^{(\pm)} = \hbar\omega_{\pm}\left(n+\frac{1}{2}\right) \pm \Delta + \frac{1}{2}\left(\frac{\hbar\omega}{2\Delta}\right)^{2}\frac{F^{2}/K_0}{1-(\hbar\omega/2\Delta)^{2}} \tag{5.9}$$

Equations (5.8) and (5.9) differ from that which can be obtained directly from Eqs. (4.11) and 4.12) with $K_{0\Gamma} = K_{0\Gamma'} = K_0$ and $K_0 = M\omega^2$ because of the nonadiabacity terms in Eq. (4.15) that emerge when the operator of kinetic energy is included in Eqs. (2.6). The discrepancy disappears when $\hbar\omega \ll 2\Delta$ and the nonadiabacity can be ignored.

Obviously, the weak coupling limit and the second-order perturbation theory used to obtain Eqs. (5.8) and (5.9) imply that $\Delta > F^2/K_0$ and $2\Delta \gg \hbar\omega$. If the two levels are closer and $2\Delta \approx \hbar\omega$, another form of perturbation theory for quasidegenerate states should be applied, resulting in [5.10]

$$E_n^{(\pm)} = n\hbar\omega \pm \tfrac{1}{2}\sqrt{\delta^2 + 2n\hbar\omega F^2/K_0} \tag{5.10}$$

with $\delta = \hbar\omega - 2\Delta$.

Note that $\delta = 0$ means exact resonance between the vibrational quantum and the energy gap 2Δ between the two states A and B. Still for weak pseudo JT coupling 2Δ should be large enough, $\Delta > F^2/K_0$.

The Renner–Teller effect in linear molecules with weak vibronic coupling splits the rotational levels [5.11–5.18]. For a triatomic molecule in a doubly degenerate state Π (with the orbital quantum number $\Lambda = 1$), which in the absence of vibronic coupling is a two-dimensional oscillator in the space of the two components of bending vibrations, the energy levels under the quadratic vibronic coupling (Section 4.4) in the second-order perturbation theory are as follows [5.11, 5.18].

(a) For the rotational quantum number $K = 0$ (vibronic Σ states; do not confuse this quantum number K with the curvature K_0 or K^Γ):

$$E^{(\pm)}(n, 0) = \hbar\omega(n+1)\sqrt{1+\varepsilon}, \qquad n = 1, 3, 5 \tag{5.11}$$

(b) For $K \neq 0$ and $n = K - 1$ (lowest vibronic levels Π, Δ, ...):

$$E(n, K) = \hbar\omega[(n+1) - \tfrac{1}{8}\varepsilon^2 K(K+1)] \tag{5.12}$$

(c) For $K \neq 0$ and $n > K - 1$ (other Π, Δ, ..., levels):

$$E^{(\pm)}(n, K) = \hbar\omega(1 - \tfrac{1}{8}\varepsilon^2)(n+1) \pm \tfrac{1}{2}\hbar\omega\varepsilon\sqrt{(n+1)^2 - K^2} \tag{5.13}$$

where ω is the bending frequency and $\varepsilon = g/K_0$ is the dimensionless RT vibronic coupling constant: g is the quadratic vibronic coupling constant that mixes the two states of the Π term by bending distortions (Sections 4.4), and K_0 is the usual primary (nonvibronic) curvature (Section 2.4).

As we can see from these formulas and Fig. 5.3, the splitting of the rotational levels with quantum numbers $K < n+1$ is of the order of $\frac{1}{2}\hbar\omega\varepsilon$, while for $K=0$ the vibronic coupling does not mix the two states essentially, their vibrational frequencies being adjusted to the modified curvatures $K^{(\pm)} = K_0(1 \pm \varepsilon)$ (Section 4.4; again, don't confuse curvatures with the rotational quantum number K; the latter has neither subscripts nor superscripts). The levels with $K = n+1$ are special, they are called "unique," in the sense that for them, distinguished from other vibronic levels, the orbital momentum is not quenched and the degeneracy is not lifted, meaning they are subject to spin–orbital splitting and the Zeeman effect.

For a similar treatment of Δ states with $\Lambda = 2$ the fourth-order terms of the APES (jQ^4 in Eq. (4.14)) were involved, resulting in the following vibronic energy levels [5.15b].

(a) For $K \neq n$ or $n+2$:

$$E^{(\pm)}(n,K) = \hbar\omega(n+1) \pm 3aj\{(n^2-K^2)[(n+2)^2-K^2]\}^{\frac{1}{2}} - (a^2j^2/\hbar\omega)(n+1)[17n(n+2)+3K^2] \tag{5.14}$$

(b) For $K = n$:

$$E(n,K) = \hbar\omega(n+1) - (a^2j^2/\hbar\omega)K(K+1)(K+2)(K+35) \tag{5.15}$$

(c) For $K = n+2$:

$$E(n,K) = \hbar\omega(n+1) - (a^2j^2/\hbar\omega)K(K-1)(K+1)(K+2) \tag{5.16}$$

where $a = \hbar^2\omega^2/2K_0^2$, j is the constant of coupling with the fourth-order terms defined in Section 4.4 (Eq. (4.14)), and the levels with $K = n$ and $K = n+2$ are "unique" in the sense described above.

5.2 Strong vibronic coupling. Some simple cases

In the other limiting case of strong vibronic coupling, when $2E_{\mathrm{JT}}^{\Gamma} > n_{\overline{\Gamma}}\hbar\omega_{\overline{\Gamma}}$, some analytical solutions have been obtained too. Consider first the *linear $E \otimes e$ problem*. The corresponding APES has the shape given in Figs. 3.4 and 3.5. If the JT stabilization energy E_{JT} is sufficiently large (as assumed in the strong coupling case), the energy separation from the ground-state sheet of the APES to the upper one in regions far from the branching point is also large (near the bottom of the trough this distance equals $4E_{\mathrm{JT}}^{E}$). It follows that for the nuclear motion in these areas the vibronic equations (2.6) may be

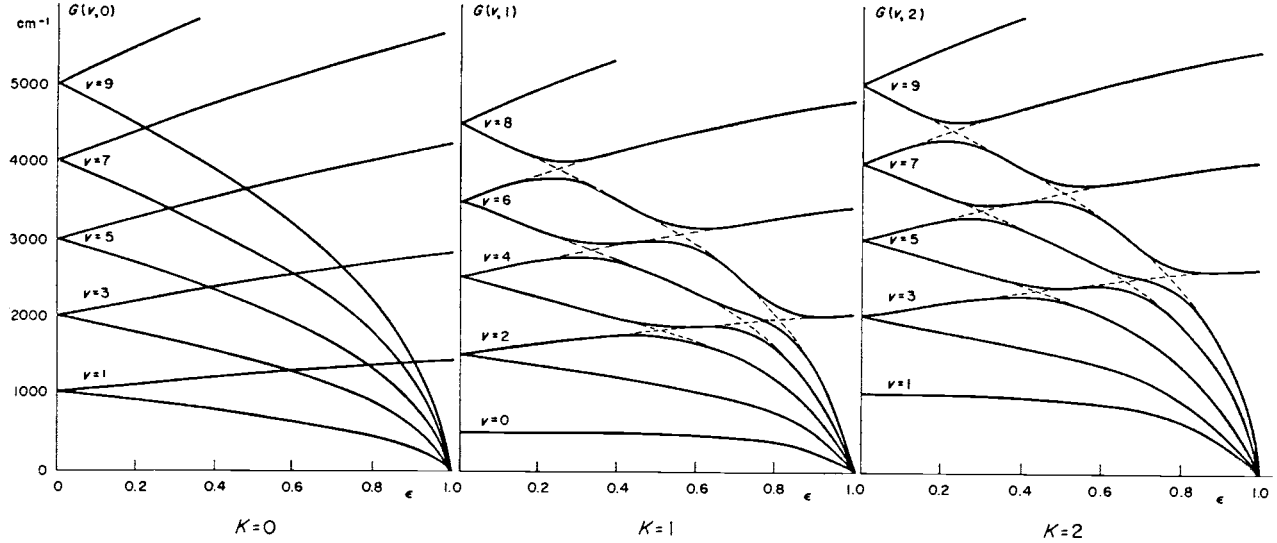

Fig. 5.3. Variation of the Σ, Π, and Δ vibronic energy levels of a Π electronic state of a linear triatomic molecule XY_2 as a function of the Renner parameter ε. The bending frequency is assumed to be $500\,\mathrm{cm}^{-1}$, so the lowest level occurs for $\varepsilon = 0$ and $K = 1$. The broken-line correlations correspond to Eqs. (5.12) and (5.13) [5.18].

approximately decoupled, and the Hamiltonian H of the lowest branch of the APES (see below) in polar coordinates takes the form [5.20]

$$H = -\frac{\hbar^2}{2M}\left[\frac{1}{\rho}\frac{\partial}{\partial\rho}\left(\rho\frac{\partial}{\partial\rho}\right) + \frac{1}{\rho^2}\frac{\partial^2}{\partial\phi^2}\right] + \frac{1}{2}K_E\rho^2 - |F_E|\rho \tag{5.17}$$

In the Schrödinger equation (2.1) with this Hamiltonian the variables ρ and ϕ separate. The motions along the trough described by the ϕ coordinate are free rotations (more precisely, pseudorotations, see below) with energies $m^2(\hbar\omega_E)^2/4E_{\mathrm{JT}}^E$ and wavefunction $(2\pi)^{\frac{1}{2}}\exp(im\phi)$, where m is the rotational quantum number, while radial motions (along ρ) are described well by harmonic vibrations with energies $\hbar\omega_E(n+\frac{1}{2})$ and oscillator wavefunctions $\chi_n(\rho-\rho_0)$. The resulting energy and wavefunction are (the factor $1/\sqrt{2\pi\rho}$ is introduced for normalization)

$$\begin{aligned}\Psi_{nm}(r,\,\rho,\,\phi) &= \psi_-(r,\,\phi)\chi_n(\rho-\rho_0)\exp(im\phi)/(2\pi\rho)^{\frac{1}{2}}\\ E_{nm} &= \hbar\omega_E(n+\tfrac{1}{2}) + m^2(\hbar\omega_E)^2/4E_{\mathrm{JT}}^E - E_{\mathrm{JT}}^E\\ n &= 0,\,1,\,2,\ldots;\; m = \pm\tfrac{1}{2},\pm\tfrac{3}{2},\pm\tfrac{5}{2},\ldots\end{aligned} \tag{5.18}$$

where $\psi_-(r,\,\phi)$ is the electronic function of the lower sheet of the APES determined by Eq. (3.32). The half-integer values of the quantum number m of the rotational motions follow from the special condition of the problem, namely from symmetry properties of the electronic function $\psi_-(r,\,\phi)$, which changes sign every 2π rotation, whereas the total wavefunction must remain unchanged. This issue is discussed in more detail in Section 5.7. The ρ_0 and E_{JT} values are given by Eqs. (3.26) and (3.27), respectively.

It is seen from Eq. (5.18) that in this limiting case of strong linear vibronic coupling, every level of radial vibration (with frequency $\hbar\omega_E$) is accompanied by a series of doublet levels of rotational motion with energy intervals $\Delta E_{\mathrm{rot}} = (3|m|+1)(\hbar\omega_E)^2/4E_{\mathrm{JT}}^E$ equal to the quantum of rotational frequencies. Since $\hbar\omega_E \ll E_{\mathrm{JT}}^E$ the usual relation between the frequencies of molecular motion is maintained: $\Delta E_{\mathrm{el}} \gg \Delta E_{\mathrm{vib}} \gg \Delta E_{\mathrm{rot}}$.

The general picture of nuclear motions described by Eq. (5.18) is as follows. At any point of the bottom of the trough the distorted (as shown in Fig. 3.7) system performs radial (E-type) vibrations with frequency ω_E while simultaneously moving over ϕ along the bottom of the trough with a rotational frequency much smaller than ω_E. Unlike the vibrations, the rotation along ϕ is not a real rotation of the system, but rather *a kind of internal rotation* often

called *pseudorotation*. In real rotations, all the atoms bend synchronously around a common axis of rotation, whereas in motion along the trough each atom bends around its individual axis, the angular motions of these axes being correlated (see Section 3.7, Fig. 3.6). As a result of this "rotation" a slow (compared with the vibrations) change of the nuclear configuration in the space of E coordinates takes place (Fig. 3.7); actually *the molecule does not rotate itself, but the direction of its E-type deformations does rotate* (see also Section 7.1.1).

The adiabatic separation of the two coupled equations (2.6) for the E term resulting in the Hamiltonian (5.17) with the solution (5.18) is made possible by neglecting the nonadiabatic term that couples the two sheets of the APES (Fig. 3.3). It can be shown [5.1] that this neglected term equals $m^2(\hbar\omega_E)^2/2K_0\rho^2$. Since it does not contain the angle ϕ, this term does not affect the rotational motions. However, it does affect the radial motions in the trough. With the nonadiabatic term included the Hamiltonian of the radial motion may be written as follows:

$$H_{\pm} = -\frac{\hbar^2}{2M}\frac{\partial^2}{\partial\rho^2} + V_{\pm}(\rho) \tag{5.19}$$

where

$$V_{\pm} = \tfrac{1}{2}K_E\rho^2 \pm |F_E|\rho + \frac{m^2(\hbar\omega_E)^2}{2K_E\rho^2} \tag{5.20}$$

is the effective potential energy for this motion. Figure 5.4 shows this potential energy behavior as a function of ρ [5.19]. Its main feature is the divergence at $\rho = 0$ due to the last term in Eq. (5.20), *the centrifugal energy*. Note that since the quantum number m is half-integer, this term never vanishes. Following Eq. (5.20), the minima points of the two sheets in Fig. 5.4 are

$$\rho_0 = \frac{|F_E|}{K_E}\left(1 + \frac{m^2(\hbar\omega_E)^2}{4E_{\mathrm{JT}}^2}\right) \tag{5.21}$$

for the lower branch of the APES, and

$$\rho_0 = \left(\frac{m^2(\hbar\omega_E)^2}{K_E|F_E|}\right)^{\frac{1}{3}}\left[1 - \frac{K_E}{3|F_E|}\left(\frac{m^2(\hbar\omega_E)^2}{K_E|F_E|}\right)^{\frac{1}{3}}\right] \tag{5.22}$$

for the upper branch.

For strong vibronic coupling the minima position of the lower sheet $\rho_0 \approx |F_E|/K_E$ coincides with that in Eq. (3.26) obtained earlier without

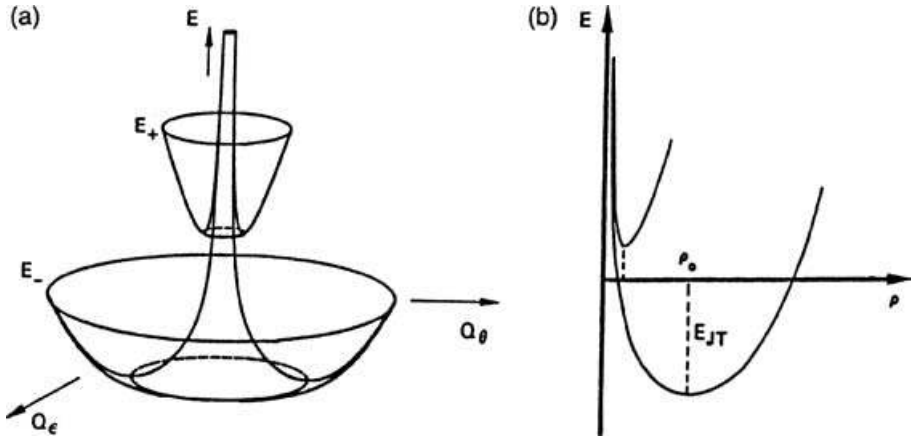

Fig. 5.4. The APES of the linear $E \otimes e$ problem including centrifugal energy: (a) a general view of E_+ (upper sheet) and E_- (Mexican-hat-type lower sheet); and (b) the two-valued APES of radial motion (radial cross-section of (a)) (reprinted with permission from [5.19]. Copyright 1984 Elsevier Science Publishers).

nonadiabacity, while for the upper sheet $\rho_0^{(+)} \approx 0$. At this point the elastic term $\frac{1}{2}K_E\rho_0^2$ in Eq. (5.20) is negligible, and the minimum (5.22) results from the compensation of the JT distortion force F_E with the centrifugal force $m^2(\hbar\omega_E)^2/2K_0\rho^2$ (*centrifugally stabilized states* [5.21]). On the contrary, at ρ_0 in the lower branch of the APES the centrifugal term is negligible, and the JT force $-|F_E|$ is compensated by the elastic term (*elastically stabilized states*). For the lowest states in this case the ρ coordinate in the small centrifugal term in (5.20) can be substituted by ρ_0, making this term constant. This allows one to solve the Schrödinger equation with the Hamiltonian H_- from (5.19) resulting in the solution (5.18).

When the quadratic and/or cubic terms of vibronic interaction are taken into account, the warping of the APES produces regularly alternating wells and humps along the bottom of the trough every 120° of the ϕ angle (Section 3.2, Eq. (3.23), Figs. 3.4 and 3.5). The bigger the quadratic barrier height δ given by Eq. (3.30), the more the motion along such a warped trough differs from free rotations.

Assume first that the values of δ are small compared with the quantum of radial vibrations ($\delta \ll \hbar\omega_E$), while the criterion of strong linear vibronic coupling $E_{\mathrm{JT}}^E \gg \hbar\omega_E$ is preserved (the case $\delta > \hbar\omega_E$ is treated below). In this limit the expansion of the APES, Eq. (3.23), with respect to the small quadratic vibronic coupling is valid, and the approximate Hamiltonian for motion near the bottom of the trough takes the form [5.20]

$$H = -\frac{\hbar^2}{2M}\left[\frac{1}{\rho}\frac{\partial}{\partial\rho}\left(\rho\frac{\partial}{\partial\rho}\right) + \frac{1}{\rho^2}\frac{\partial^2}{\partial\phi^2}\right] + \tfrac{1}{2}K_E\rho^2 - |F_E|\rho + G_E\rho^2\cos(3\phi) \quad (5.23)$$

Exact separation of the variables ρ and ϕ in Eq. (5.23) is impossible due to the additional term $G_E\rho^2\cos(3\phi)$ that is not present in Eq. (5.17). However, if this term is sufficiently small (as was actually assumed in [5.20]) and the difference in the aforementioned frequencies of the radial and rotational motion is sufficiently large, an approximate separation of these variables is possible in the adiabatic approach. Indeed, under these conditions stationary (fast) radial motions along ρ are adjusted for every instantaneous configuration of the system corresponding to a fixed angle ϕ, and hence the kinetic energy of the motions along ϕ may be neglected when considering radial motions (another way of separation of these variables is discussed in [5.22]).

Following the adiabatic approach (Section 2.1), the total wavefunction may be sought in the form $\chi'_n(\rho, \phi)\Phi(\phi)$, where $\chi'_n(\rho, \phi)$ is determined by the solution of the equation for the fast subsystem (5.23), in which the term $\partial^2/\partial\phi^2$ is neglected. If the last term of this equation, regarded as small, is also neglected, the remaining equation is independent of ϕ and yields the same solution $\chi_n(\rho-\rho_0)$ (with normalizing factor $1/\sqrt{\rho}$) as in the linear case. On substituting this solution into Eq. (5.23) and averaging over the variables ρ with the ground-state function χ_0, the following equation of motion along ϕ is derived [5.20]:

$$\left(-\alpha\frac{\partial^2}{\partial\phi^2} + \beta\cos(3\phi) - E_m\right)\Phi(\phi) = 0 \quad (5.24)$$

where $\alpha = \hbar^2/3M\rho_0^2$ and $\beta = G_E\rho_0^2$.

This equation was solved numerically by means of the expansion $\Phi = \Sigma_m C_m \exp(im\phi)$ in the free-rotation functions $\exp(im\phi)$ with the C_m coefficients calculated by a minimization procedure. The energy levels obtained as functions of β/α are illustrated in Fig. 5.5. It is seen that some of the doublet rotational levels (5.18) for $\beta = 0$, namely those transforming after the irreducible representations $A_1 + A_2$ (i.e., accidentally degenerate), become split when the quadratic vibronic coupling is taken into account, i.e., when $\beta \neq 0$.

The total wavefunction in this case is

$$\Psi(r, \rho, \phi) = (2\pi\rho)^{-\frac{1}{2}}\psi_-(r, \phi)\chi_0(\rho - \rho_0)\sum_m C_m\exp(im\phi) \quad (5.25)$$

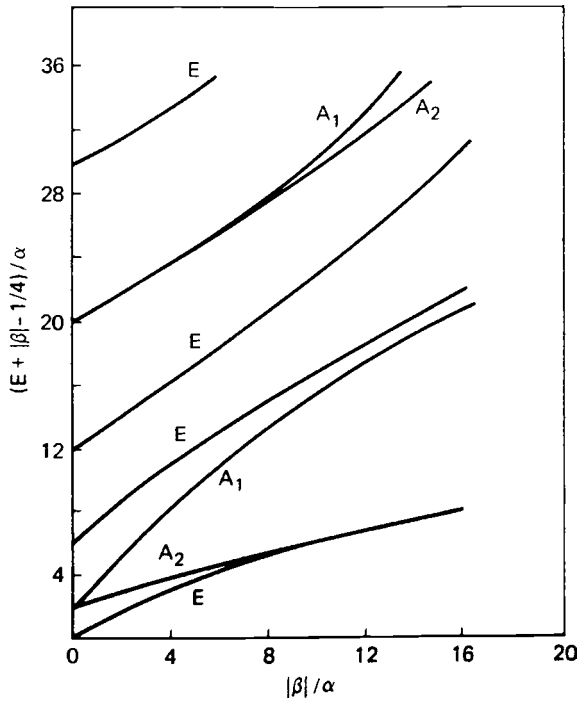

Fig. 5.5. Energy levels for the quadratic $E \otimes e$ problem – solutions of Eq. (5.24) – as functions of the ratio of the quadratic and linear vibronic constants, β/α [5.20].

where the finite number of m values, $m = \pm\frac{1}{2}, \pm\frac{3}{2}, \ldots, \pm k$ corresponds to the number of functions of free rotations in the trough chosen as a basis of the calculations, C_m are the expansion coefficients mentioned above, and the electronic function $\psi_-(r, \phi)$ is given by Eqs. (3.32) and (3.33).

In the case of small quadratic vibronic coupling under consideration the motions in the circular trough, as distinct from the linear case, cease to be free pseudorotations. At every point of the trough (as in the linear case) the distorted system performs fast radial vibrations with frequency ω_E, and the distortion of the nuclear configuration changes slowly while assuming a continuous set of geometric figures in the space of e displacements, illustrated in Fig. 3.7. However, unlike the linear case for which the "motion" of the distorted configuration along the bottom of the trough is uniform, in the case of nonzero quadratic and/or cubic vibronic coupling the above changes in nuclear configuration are hindered (or even reflected) by the quadratic barriers. As a result, the system remains longer at the minima (Fig. 3.5) than at the barrier maximum area. *The picture as a whole is that of hindered internal rotations of the JT distortions.*

Note that the solution of Eq. (5.24) in the form (5.25) shown in Fig. 5.5 is valid for sufficiently small values of the quadratic barrier presented by the β parameter. Indeed, for β values of the order of or larger than the quantum of radial vibrations $\hbar\omega_\rho$ the motion along ρ and ϕ cannot be separated and the quadratic terms cannot be considered as a perturbation to the ground vibrational state. To overcome this important limitation, a variational calculation of the lowest vibronic energy level ε_E and ε_A was suggested [5.23]. As trial wavefunctions for the ground vibronic E and first excited A_1 levels one may choose

$$\begin{aligned}\psi_E(\rho, \phi) &= N_E \left\{ \begin{matrix} \cos(\phi/2) \\ \sin(\phi/2) \end{matrix} \right\} \exp[v\cos(3\phi)] q^{\frac{1}{2}} \exp[u(q-1)^2/2] \\ \psi_A(\rho, \phi) &= N_{A_1} \cos(3\phi/2) \exp[v\cos(3\phi)] q^{\frac{1}{2}} \exp[u(q-1)^2/2]\end{aligned} \tag{5.26}$$

where $q = \rho/\rho_0$ and v and u are variational parameters.

With these functions, the numerical minimization of the total energy for the APES parameter values $\lambda = 2E_{\mathrm{JT}}^E/\hbar\omega_\rho$ and $\gamma = 2\delta/\hbar\omega_\rho$ yields the results presented in Table 5.1. We see that for small γ values (small β values) these variational results are very similar to that obtained above in the perturbational approach. However, for $\gamma > 2.6$ (not shown in Table 5.1) the energy gap $3\Gamma = E(A_1) - E(E)$ (the tunneling splitting, see the next section) becomes negative, which is essentially different from the results in Fig. 5.5. This challenging result is discussed in Section 5.3.

A somewhat similar treatment is possible for the particular case of the $T \otimes (e + t_2)$ problem with $E_{\mathrm{JT}}^E = E_{\mathrm{JT}}^T$ and $K_E = K_T$, when a two-dimensional trough in the five-dimensional space of the e and t_2 vibrations is realized (Section 3.3). It was shown that, using polar coordinates to describe the motion along the trough, the angular coordinates ϑ and ϕ can be separated from the "radial" motions [5.6, 5.21]. The free motion along the trough corresponds to the rotation of the Jahn–Teller distortion, and it can be described by spherical functions $Y_{lm}(\vartheta, \phi)$. If $E_{\mathrm{JT}}^E \neq E_{\mathrm{JT}}^T$, then additional humps and wells, corresponding to trigonal, tetragonal, and orthorhombic extremum points, occur along the bottom of the trough (Section 3.3). In other words, the two-dimensional trough is "warped," quite similarly to the quadratic $E \otimes e$ problem.

If the height of the barriers dividing the minima of the adiabatic potential is less than the magnitude of the quantum of radial vibrations, then the angular motion can be separated from the radial one by the adiabatic approximation, in the same way as in the $E \otimes e$ case. The Hamiltonian of the slow (angular) subsystem is

Table 5.1. *Lowest energy levels ε_E and ε_A, tunneling splitting 3Γ, and dimesionless variational parameters v and u in the wavefunction (5.26) for the $E \otimes e$ problem with the dimensionless linear vibronic coupling $\lambda_E = E_{\mathrm{JT}}^E/\hbar\omega_E = 2$ as functions of the height of the barrier between the minima $\gamma = \delta/\hbar\omega_E$ (at larger γ values 3Γ becomes negative) (data from [5.23])*

	E level			*A* level			Tunneling splitting
2γ	v	u	ε_E	v	u	ε_A	$3\Gamma = \varepsilon_A - \varepsilon_E$
0.0							
0.2	0.071	4.774	−2.590	0.036	4.544	−2.208	0.382
0.4	0.140	4.908	− 2.456	0.071	4.619	−2.134	0.322
0.6	0.206	5.019	−2.332	0.105	4.694	−2.062	0.270
0.8	0.269	5.104	−2.218	0.138	4.755	−1.993	0.225
1.0	0.329	5.165	−2.111	0.170	4.815	−1.926	0.185
1.2	0.385	5.219	−2.013	0.201	4.870	−1.861	0.152
1.4	0.438	5.271	−1.921	0.231	4.926	−1.799	0.122
1.6	0.489	5.298	−1.835	0.260	4.974	−1.738	0.097
1.8	0.536	5.336	−1.753	0.289	5.018	−1.679	0.075
2.0	0.581	5.356	−1.677	0.317	5.059	−1.621	0.056
2.2	0.623	5.374	−1.604	0.344	5.096	−1.565	0.039
2.4	0.663	5.400	−1.535	0.370	5.130	−1.511	0.024
2.6	0.701	5.415	−1.469	0.396	5.168	−1.457	0.012

$$H = \frac{(\hbar\omega_E)^2 K_E}{6F_E^2}\left[-\frac{1}{\sin\vartheta}\,\frac{\partial}{\partial\vartheta}\left(\sin\vartheta\,\frac{\partial}{\partial\vartheta}\right) - \frac{1}{\sin^2\vartheta}\,\frac{\partial^2}{\partial\phi^2}\right] + V(\vartheta,\,\phi) \qquad (5.27)$$

where $V(\vartheta, \phi)$ is the lowest sheet of the APES averaged over the coordinates of the fast subsystem. This function can be expanded in a series with respect to cubic harmonic functions. Cutting off this expansion after the fourth-order harmonics, one obtains (see also [5.24])

$$V(\vartheta,\,\phi) \approx -E_{\mathrm{JT}} + \Delta\left(Y_{4,0}(\vartheta,\,\phi) + \sqrt{\frac{5}{14}}[Y_{4,4}(\vartheta,\,\phi) + Y_{4,-4}(\vartheta,\,\phi)]\right) \qquad (5.28)$$

where E_{JT} is given by (3.27), while Δ is here a coefficient, independent of ϑ and ϕ.

It can easily be checked that the APES (5.28) has the same extremum points as the exact surface $V(\vartheta, \phi)$. For instance, for negative Δ values the three points with the coordinates

$$(\vartheta,\,\phi) = (0,\,0), \qquad (\pi/2,\,0), \qquad \text{and} \qquad (\pi/2,\,\pi/2) \qquad (5.29)$$

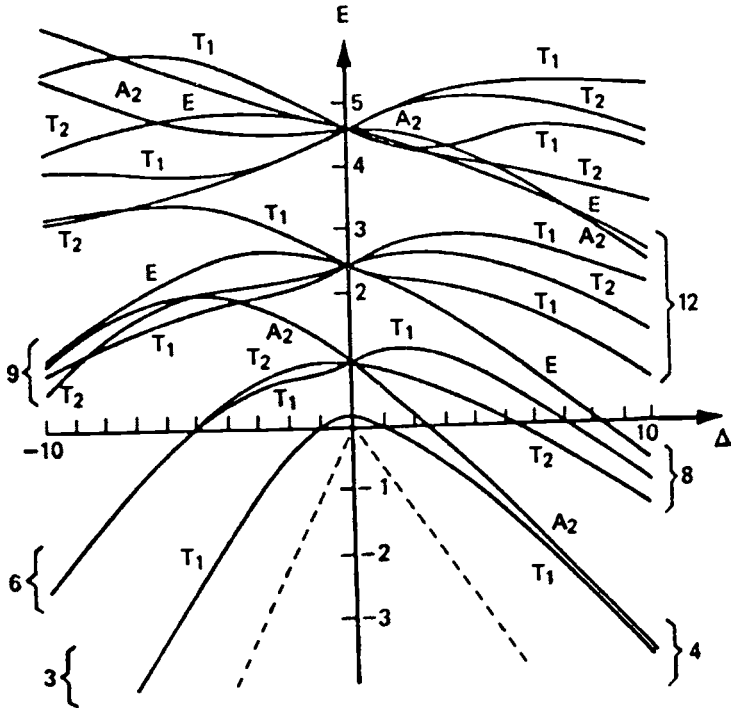

Fig. 5.6. Vibronic energy levels for the $T \otimes (e + t_2)$ problem – solutions of the Hamiltonian (5.27) – as functions of the parameter Δ of the APES (5.28), in units $(\hbar\omega_E)^2 K_E/6F_E^2$. The dashed lines show the energy at the minima of APES (reprinted with permission from [5.6]. Copyright 1969 American Physical Society).

are tetragonal minima. For positive Δ values the minima are situated at four points with the coordinates

$$(\vartheta, \phi) = (\vartheta_0, n\pi/2), \qquad n = 1, 3, 5, 7 \tag{5.30}$$

where $\cos\vartheta_0 = 1/\sqrt{3}$. These points prove to be of trigonal symmetry. At arbitrary Δ values the surface (5.27) has an additional six extremum points at

$$(\vartheta, \phi) = (\pi/4, n\pi/2), \qquad (\pi/2, \pi/4 + n\pi/2), \qquad n = 0, 1, 2, 3 \tag{5.31}$$

which have orthorhombic symmetry and are always saddle points. These results coincide qualitatively with those obtained in Section 3.3 for the linear $T \otimes (e + t_2)$ problem.

The numerical diagonalization of the Hamiltonian (5.27) was carried out in the same way as for the $E \otimes e$ problem. The rotational functions $Y_{lm}(\vartheta, \phi)$ were

taken as a basis set for the calculations, the total function being presented by the following expansion [5.6, 5.24]:

$$\Phi_{\Gamma\gamma}(\vartheta, \phi) = \sum_{lm} C_{lm}^{\Gamma\gamma} Y_{lm}(\vartheta, \phi) \tag{5.32}$$

The results obtained in [5.6] with all the terms up to $l = 13$ kept in the expansion (5.32) are illustrated in Fig. 5.6. The motion of the system in this case can be visualized as hindered rotations of the JT distortion, in much the same way as in the case of the quadratic $E \otimes e$ problem.

5.3 Tunneling in JT systems

As mentioned in the introduction, the nonzero slope of the APES predicted by the JT theorem for systems in degenerate electronic states (Section 2.5) cannot be observed directly, so the real meaning of the JTE is in the far-reaching consequences of the JT theorem. One of the first predicted observables in the JTE was the *tunneling splitting* [5.1, 5.25] (originally, it was called inversion splitting by analogy with inversion splitting in ammonia). In the majority of JT problems under certain conditions (mostly strong quadratic coupling) there are several equivalent APES minima divided by potential barriers. If the latter are sufficiently high, the phenomenon of tunneling between the equivalent minima resulting in relatively small (tunneling) splitting of the corresponding energy levels should be expected.

Consider the $E \otimes e$ problem (Section 3.2). For sufficiently large quadratic and/or cubic vibronic coupling terms when the quadratic barrier δ in Eq. (3.30) is of the order of, or greater than, the vibrational quanta $\hbar\omega_E$, the APES acquires three equivalent minima with high barriers between them (for the T, G, and H terms the minima appear already in the linear approximation, Sections 3.3 and 3.4). In the $E \otimes e$ problem with $\delta \gg \hbar\omega_E$, the separation of variables ρ and ϕ performed in Section 5.2 is not valid, so the problem must be solved by another technique. Since the minima of the APES are deep enough, local states arise at each of them, which in the limiting case of high barriers between the minima may be considered as quasistationary states. Therefore, as far as the lowest vibronic states are concerned, the local states in the three minima can be taken as a starting approximation in the calculations and then modified due to their interactions (finite barrier height δ) by means of perturbation theory [5.25]. A similar approach is applicable to all JT systems with several equivalent minima which are sufficiently deep, with high barriers between them, and with the electronic states of different minima mutually non-orthogonal (see below).

Let us assume that in the absence of tunneling the system performs small harmonic oscillations near the minimum, and for the lowest states localized in the ith well the wavefunction can be taken as

$$\Psi_n^{(i)}(r, Q) = \psi_-(r, Q)\Phi_n(Q - Q^{(i)}) \tag{5.33}$$

where $\psi_-(r, Q)$ is the electronic wavefunction for the lower sheet of the adiabatic potential, and $\Phi_n(Q - Q^{(i)})$ is the vibrational wavefunction in the ith well, $Q^{(i)}$ being the coordinate of its minimum point. In particular, for the quadratic $E \otimes e$ problem, $Q^{(i)}$ for the three minima are given in polar coordinates by Eq. (3.28), and the frequencies of the harmonic vibrations near these minima are determined by the corresponding curvatures of the adiabatic potential given by Eqs. (3.31).

For the sake of simplicity the Born–Oppenheimer functions with fixed nuclear coordinates in the electronic functions

$$\Psi_n^{(i)}(r, Q^{(i)}) = \psi_-(r, Q^{(i)})\Phi_n(Q - Q^{(i)}) \tag{5.33$'$}$$

will be used hereafter instead of the adiabatic ones given by Eq. (5.33), and we assume that $F_E > 0$ and $G_E > 0$. Then, on substituting the minima coordinates (3.28) into the expression of $\psi_-(r, Q^{(i)})$ from (3.32) and taking into account Eq. (3.33), one finds the following three functions for the ground states in the three minima:

$$\begin{aligned}
\Psi_0^{(1)} &= |\vartheta\rangle\Phi_0(Q - Q^{(0)}) \\
\Psi_0^{(2)} &= \left(\frac{\sqrt{3}}{2}|\vartheta\rangle - \frac{1}{2}|\varepsilon\rangle\right)\Phi_0(Q - Q^{(2)}) \\
\Psi_0^{(3)} &= \left(-\frac{\sqrt{3}}{2}|\vartheta\rangle - \frac{1}{2}|\varepsilon\rangle\right)\Phi_0(Q - Q^{(4)})
\end{aligned} \tag{5.34}$$

where the superscript n in $Q^{(n)}$ corresponds to the value n in (3.28).

In the absence of tunneling transitions the states (5.34) localized in the wells have the same energy and form a triply degenerate term due to the equivalency of the three minima. Assuming the tunneling to be weak (the criterion of weak tunneling is given below), one can use perturbation theory to diagonalize the full Hamiltonian (2.2) using the functions (5.34) as a basis set; the solution is sought as a linear combination of the latter:

$$\Psi = \sum_{i=1}^{3} C_i \Psi_0^{(i)}(r, Q) \tag{5.35}$$

On substituting this expression into the Schrödinger equation, multiplying it by $\Psi_0^{(k)*}$ on the left-hand side and integrating over the r and Q variables, we obtain the following system of equations for the energy E and the coefficients C_i:

$$\sum_i H_{ki}C_i = E\sum_i S_{ki}C_i \tag{5.36}$$

Here S_{ki} is the overlap integral for the basis functions (5.34) (which are not orthogonal) and H_{ki} are the Hamiltonian matrix elements. A nontrivial solution of the system (5.36) is possible if

$$\det|H_{ik} - ES_{ik}| = 0 \tag{5.37}$$

For the $E\otimes e$ problem, by using symmetry considerations, one can easily show that $H_{ik} = H_{12}$, $H_{ii} = H_{11}$, and $S_{ik} = S_{12} = S$, thereby reducing (5.37) to

$$\begin{vmatrix} H_{11}-E & H_{12}-ES & H_{12}-ES \\ H_{12}-ES & H_{11}-E & H_{12}-ES \\ H_{12}-ES & H_{12}-ES & H_{11}-E \end{vmatrix} = 0 \tag{5.38}$$

The three localized states (5.34) belong to a threefold reducible representation of the symmetry point group of the molecule, which decomposes into the irreducible representations $A_1 + E$ (if $F_E < 0$ or $G_E < 0$, it will be $A_2 + E$). Since the latter does not contain repeating representations, the symmetry-adapted wavefunctions are the correct zeroth-order functions, and they can be found directly using projection operators:

$$\begin{aligned} \Psi_A &= \frac{1}{\sqrt{3}}(\Psi_0^{(1)} + \Psi_0^{(2)} + \Psi_0^{(3)}) \\ \Psi_{E_+} &= \frac{1}{\sqrt{3}}(\Psi_0^{(1)} + e^{2\pi i/3}\Psi_0^{(2)} + e^{4\pi i/3}\Psi_0^{(3)}) \\ \Psi_{E_-} &= \frac{1}{\sqrt{3}}(\Psi_0^{(1)} + e^{-2\pi i/3}\Psi_0^{(2)} + e^{-4\pi i/3}\Psi_0^{(3)}) \end{aligned} \tag{5.39}$$

The initial triply degenerate energy level is split by tunneling into a singlet A and a doublet E,

$$E(A) = \frac{\langle\Psi_A|H|\Psi_A\rangle}{\langle\Psi_A|\Psi_A\rangle} = \frac{H_{11} + 2H_{12}}{1 + 2S} \tag{5.40}$$

$$E(E) = \frac{\langle\Psi_{E_\pm}|H|\Psi_{E_\pm}\rangle}{\langle\Psi_{E_\pm}|\Psi_{E_\pm}\rangle} = \frac{H_{11} - H_{12}}{1 - S} \tag{5.41}$$

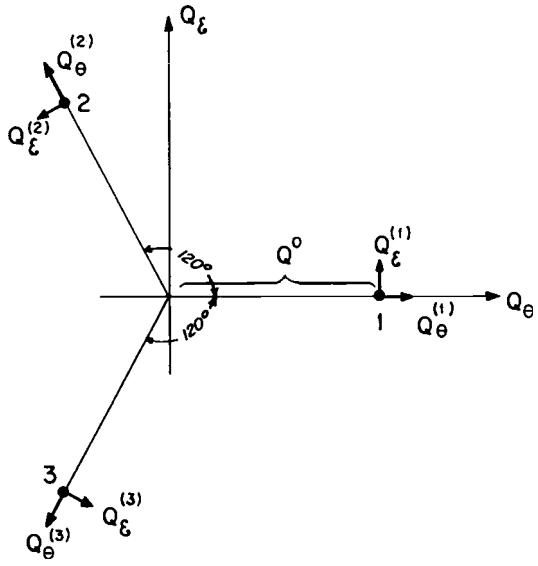

Fig. 5.7. General $(Q_\vartheta, Q_\varepsilon)$ and local $(Q_\vartheta^{(i)},\ Q_\varepsilon^{(i)})$ E-type symmetrized coordinates at the minima in the $E \otimes e$ problem.

The magnitude of the tunneling splitting of the ground state is thus

$$3\Gamma = E(A) - E(E), \qquad \Gamma = \frac{H_{12} - H_{11}S}{1 + S - 2S^2} \tag{5.42}$$

The matrix element H_{12} and the overlap integral S can be calculated as follows. Owing to the multiplicative form of the basis functions (5.34) the integration over the electronic variables can be carried out directly. For the overlap of two vibrational functions from the near-neighbor minima the meaning of the symmetrized vibrational coordinates $Q^{(n)}$ in the minima should be clarified. Figure 5.7 illustrates the following choice of the two coordinates $Q_\vartheta^{(n)}$ and $Q_\varepsilon^{(n)}$ in the three minima as functions of the Q_ϑ and Q_ε:

$$\begin{aligned}
Q_\vartheta^{(1)} &= Q_\vartheta - \rho_0, & Q_\varepsilon^{(1)} &= Q_\varepsilon \\
Q_\vartheta^{(2)} &= -\frac{1}{2}Q_\vartheta + \frac{\sqrt{3}}{2}Q_\varepsilon - \rho_0, & Q_\varepsilon^{(2)} &= -\frac{1}{2}Q_\varepsilon - \frac{\sqrt{3}}{2}Q_\vartheta \\
Q_\vartheta^{(3)} &= -\frac{1}{2}Q_\vartheta - \frac{\sqrt{3}}{2}Q_\varepsilon - \rho_0, & Q_\varepsilon^{(2)} &= -\frac{1}{2}Q_\varepsilon + \frac{\sqrt{3}}{2}Q_\vartheta
\end{aligned} \tag{5.43}$$

where ρ_0 is given by Eq. (3.28). In these coordinates the ground-state functions of the two-dimensional harmonic oscillator in the two minima, 2 and 3, respectively, are

$$\Phi_0(Q-Q^{(2)}) = N\exp\left[-\frac{M\varpi_A}{2\hbar}\left(-\frac{1}{2}Q_\vartheta+\frac{\sqrt{3}}{2}Q_\varepsilon-\rho_0\right)^2-\frac{M\varpi_B}{2\hbar}\left(\frac{\sqrt{3}}{2}Q_\vartheta+\frac{1}{2}Q_\varepsilon\right)^2\right]$$
$$\Phi_0(Q-Q^{(4)}) = N\exp\left[-\frac{M\varpi_A}{2\hbar}\left(-\frac{1}{2}Q_\vartheta-\frac{\sqrt{3}}{2}Q_\varepsilon-\rho_0\right)^2-\frac{M\varpi_B}{2\hbar}\left(\frac{\sqrt{3}}{2}Q_\vartheta-\frac{1}{2}Q_\varepsilon\right)^2\right] \tag{5.44}$$

Here M is the mass of the oscillator, ϖ_A and ϖ_B are the frequencies of the normal vibrations (in the minimum configuration) determined by Eqs. (3.31), ρ_0 is given by Eq. (3.28), and $N = M(\varpi_A\varpi_B/\pi^2\hbar^2)^{\frac{1}{2}}$ is the normalization constant (reminder: $K_n = M\omega_n^2$)

As a result of straightforward calculations, we obtain

$$S = -\frac{1}{2}\gamma, \qquad H_{ii} = -E_{\mathrm{JT}}^E + \frac{1}{2}\hbar(\varpi_A+\varpi_B) \tag{5.45}$$

$$H_{23} = H_{11}S + \frac{3E_{\mathrm{JT}}^E\gamma(9+54\lambda-6\lambda^3-\lambda^4)}{2(9-\lambda^2)(1+3\lambda)^2} \tag{5.46}$$

where $\lambda = \varpi_A/\varpi_B = [9G_E/(K_E-G_E)]^2$, E_{JT}^E is given by Eq. (3.29), and γ is the overlap integral for the vibrational functions (5.44):

$$\gamma = \left(\frac{16\lambda}{3\lambda^2+10\lambda+3}\right)^2\exp\left(-\frac{6E_{\mathrm{JT}}^E}{\hbar\varpi_A}\frac{\lambda}{1+3\lambda}\right) \tag{5.47}$$

Neglecting λ^2 compared with unity, we find [5.1, 5.25–5.27]

$$3\Gamma \cong 9\gamma E_{\mathrm{JT}}^E\frac{9+54\lambda-6\lambda^3-\lambda^4}{2(9-\lambda^2)(1+3\lambda)^2} \tag{5.48}$$

In particular, if $|G_E| \ll K_E$, i.e. when $\lambda \ll 1$, we have

$$3\Gamma \approx 18E_{\mathrm{JT}}^E\sqrt{\lambda/3}\exp\left(-\frac{6\lambda E_{\mathrm{JT}}^E}{\hbar\omega_E}\right) \tag{5.49}$$

It follows from Eqs. (5.48) and (5.49) that the criterion of validity of the perturbation theory used above requires that $E_{\mathrm{JT}}^E \geq \hbar\omega_E$, which means that there is at least one localized state in the well.

The picture of deep minima of the APES separated by relatively high barriers is typical for polyatomic systems in degenerate electronic states with strong vibronic coupling. Therefore *the tunneling phenomenon is a characteristic feature of JT systems*, and the method of calculation of the tunneling splitting given above is, in general, valid for all these cases of strong coupling.

The physical meaning of the tunneling splitting is as follows. As discussed above, if the APES has a continuum of equivalent minima (a trough), the orbital momentum (the sum of the momenta of electronic and nuclear motions) is preserved, and free rotations of JT distortions of the nuclear framework take place (Section 5.2). For a finite number of minima when the potential barriers between them are small compared with the quanta of radial vibrations, the rotations of the JT distortions are hindered.

When the barrier height becomes comparable to or larger than the quantum of radial vibrations, the angular motion cannot be separated from the radial motion, and the idea of rotation of the JT distortion loses physical sense. In this case the dynamics of the system is well described by localized vibrations at the minima accompanied by tunneling between neighboring equivalent minima. Analogously to the previous cases, this phenomenon can be visualized as *pulse motions of the JT distortion*: the distorted nuclear configuration at the minimum periodically changes its orientation ("fluctuates") in space in accordance with the symmetries of the other minima equivalent to the first one. It does this with a frequency proportional to the tunneling splitting, which is much lower than the frequency of vibrations within the well. Note that in all the cases discussed above the term "motion of JT distortions" means the concerted motions of both the nuclear framework and the electrons. Although outwardly the pulse motions look like fluctuations of the distorted configuration, in origin these two types of motion are quite different, the latter being driven by accidental, thermally controlled stochastic processes, while the pulse motions are just quantum-mechanical tunnelings that occur when the system is prepared in one of the minima.

The free and hindered rotations of JT distortions and their pulse motions form a new type of intramolecular motion (which should not be confused with the usual rotation of the molecule or its separate parts); it essentially distinguishes the JT systems from non-JT ones.

The tunneling splitting in *electronic T states* can be considered in a similar way. In the $T \otimes (e + t_2)$ problem without tunneling (Section 3.3) the ground vibronic states localized within each of the four trigonal minima of the APES form a fourfold degenerate term. In the cubic symmetry groups there are no fourfold irreducible representations, and therefore the fourfold degeneracy is accidental. The tunneling removes the degeneracy, resulting in a singlet

A_1 (or A_2) and triplet T_2 (or T_1) state, $A_1 + T_2$ (or $A_2 + T_1$). The magnitude of the tunneling splitting is (cf. Eq. (5.42))

$$4\Gamma = E(A) - E(T), \qquad \Gamma = \frac{H_{12} - H_{11}S}{1 + 2S - 3S^2} \tag{5.50}$$

For the $T \otimes t_2$ problem, if the harmonic approximation is employed for the states localized in the wells, and taking into account the redetermined frequencies of vibrations near the bottom of the wells given by Eqs. (3.50) and (3.51), we obtain [5.1, 5.26]

$$4\Gamma \approx 2E_{\mathrm{JT}}^{T} \exp\left(-1.24 \frac{E_{\mathrm{JT}}^{T}}{\hbar\omega_T}\right) \tag{5.51}$$

where the JT stabilization energy is given by Eq. (3.47). Note that here $4\Gamma > 0$, and hence the ground state is a vibronic triplet with the same symmetry properties as the initial electronic term. However, this inequality may be reversed by strong quadratic coupling (Section 5.4).

The tunneling splitting in the presence of six orthorhombic minima of the APES in the quadratic $T \otimes (e + t_2)$ problem (Section 3.3) results in two lowest vibronic triplet states T_1 and T_2 with the splitting magnitude given by [5.1, 5.27–5.30]

$$6\Gamma = \frac{3E_{\mathrm{JT}}^{\mathrm{O}}}{2} \frac{24 - 28B - 2B^2 + 9B^3}{(4 - 3B)(4 - 3B^2)} \frac{S}{1 - 4S^2} \tag{5.52}$$

where the expressions for B and the JT stabilization energy $E_{\mathrm{JT}}^{\mathrm{O}}$ are given by Eqs. (3.57) and (3.58), respectively, and

$$S = \exp\left(-\frac{3E_{\mathrm{JT}}^{\mathrm{O}}}{2\hbar\omega} \frac{12 - 20B - 11B^2}{(4 - 3B)(4 - 3B^2)}\right) \tag{5.53}$$

In this case too, the ground state is a vibronic triplet with the same transformation properties as the initial electronic T term. Table 5.2 summarizes some of these results.

The magnitude of the tunneling splitting, as shown above, is determined by the overlap S of the localized states of nearest-neighbor minima, i.e., by the behavior of the tails of the wavefunctions under the potential barriers. From this point of view the harmonic approximation used above with oscillator functions of the type (5.44) may lead to a rather crude approximation for the splitting, because these functions, although satisfactory near the minimum points, decrease too fast in the most important region under the barrier. This

Table 5.2. *Expressions for energies and wavefunction coefficients (in formulas of the type (5.35) with $H_{11}=0$ and $H_{12}=U$) for tunneling states in JT systems with three, four, and six equivalent minima*

Number of equivalent minima	Symmetry of the tunneling states	Energy	Wavefunction coefficients[a] $N_\alpha(C_{1\alpha}, C_{2\alpha}, \ldots, C_{r\alpha})$
3	E	$-\frac{U}{1-s}$	$\begin{cases}[6(1-S)]^{-\frac{1}{2}}(2,-1,-1)\\ [2(1-S)]^{-\frac{1}{2}}(0,1,-1)\end{cases}$
	A	$\frac{2U}{1+2s}$	$[3(1+2S)]^{-\frac{1}{2}}(1,1,1)$
4	T	$-\frac{3U}{1-s}$	$\begin{cases}[4(1-S)]^{-\frac{1}{2}}(1,-1,-1,1)\\ [4(1-S)]^{-\frac{1}{2}}(1,-1,1,-1)\\ [4(1-S)]^{-\frac{1}{2}}(1,1,-1,-1)\end{cases}$
	A	$\frac{U}{1+3s}$	$[4(1+3s)]^{\frac{1}{2}}(1,1,1,1)$
6	T_1	$\frac{2U}{1+2s}$	$\begin{cases}[4(1+2S)]^{-\frac{1}{2}}(1,1,1,1,0,0)\\ [4(1+2S)]^{-\frac{1}{2}}(1,0,-1,0,1,1)\\ [4(1+2S)]^{-\frac{1}{2}}(0,-1,0,1,1,-1)\end{cases}$
	T_2	$-\frac{2U}{1-2s}$	$\begin{cases}[4(1-2S)]^{-\frac{1}{2}}(1,-1,1,-1,0,0)\\ [4(1-2S)]^{-\frac{1}{2}}(-1,0,1,0,1,1)\\ [4(1-2S)]^{-\frac{1}{2}}(0,-1,0,1,-1,1)\end{cases}$

[a] N_α is a common factor.

fault is partly removed by diagonalizing the exact Hamiltonian, which involves a variational procedure. However, the basis set of (5.34) and (5.44) is very limited, and therefore the results obtained above should be considered as semiquantitative estimations of the magnitude of the tunneling splitting.

These results can be improved in two ways. First, one can increase the number of vibrational functions in the basis set and evaluate the tunneling splitting numerically with a computer program. In this way the splitting can be obtained with any desired accuracy (see in the next section). The second method is to improve the behavior of the basis functions in the barrier region. This can be done by an appropriate choice of parametrically dependent probe functions in a variational procedure [5.23] or by involving semiclassical approaches (see below).

Note also that the oscillator wavefunctions in the wells of the type (5.44) can be regarded as coherent states of harmonic oscillators [5.31] with the shift parameters determined by the minimum point coordinates. Hence the tunneling splitting can be evaluated by the method of coherent states [5.32] (similar anharmonic coherent states with Morse potentials are considered in [5.33]). These calculations in essence repeat the first paper's [5.25] approach. In these papers the splitting of the degenerate vibrational frequencies at the minimum point due to reduced symmetry is ignored. Meanwhile, the difference in frequencies of vibrations in the minima (e.g., different frequencies of radial and angular vibrations in the minima of the $E \otimes e$ problem) is very important in evaluation of the magnitude of the tunneling splitting because it changes the vibrational wavefunctions in the minima and their overlap in the region under the potential barrier. The solutions (5.48), (5.49), (5.51), and (5.52) were obtained by directly taking into account this vibrational frequency splitting by means of parameter $\lambda = \varpi_A/\varpi_B$. This anisotropy of vibrations was also taken into account in more recent works on tunneling splitting in icosahedral systems [5.34].

A more accurate behavior of the wavefunctions in the region under the barriers can also be reached within the quasi-classical approximation. In the simplest cases the multidimensional problem can be reduced to one dimension along the line of steepest slope from the barrier top to the minimum point (Fig. 3.4). Postponing the discussion of this approximation to the end of this section, we present here some results obtained by calculation of the tunneling splitting in the $E \otimes e$ and $T \otimes (e + t_2)$ problems using the so-called *Wentzel–Kramers–Brillouin* approximation [5.35].

For the three minima of the APES of the $E \otimes e$ problem the quasi-classical tunneling splitting is

$$3\Gamma = \frac{3\hbar\varpi_B}{2\pi} \exp\left(-\frac{1}{\hbar} \int_a^b \sqrt{2m[\varepsilon_-(q) - E_0]}\, dq \right) \tag{5.54}$$

Here, as above, ϖ_B is given by Eq. (3.31), a and b are the turning points at the entrance to and exit from the forbidden region under the barrier, respectively, $\varepsilon_-(q)$ is given by Eq. (3.23), E_0 is the energy of the ground state in the minimum configuration, m is the effective mass of the "particle" corresponding to the generalized coordinate q [5.35], and the integration is carried out along the line of steepest slope from the top of the barrier to the minimum (Fig. 3.4).

Equation (5.54) has a clear-cut physical meaning: it represents the probability of decay per second of the metastable state in the well. Indeed Γ is proportional to the number of "particle" collisions with the barrier wall per

second, $\varpi_B/2\pi$, and to the probability of tunneling through the barrier at each of these collisions,

$$D = \exp\left(-\frac{1}{\hbar}\int_a^b \sqrt{2m[\varepsilon_-(q) - E_0]}dq\right)$$

The factor of three in (5.54) is related to the equal probability of the "particle" occurring at any of the three minimum configurations, i.e., to the existence of three equivalent metastable states.

Evaluating the integral in Eq. (5.24) and assuming that $G_E \ll K_E$, we obtain [5.35] (cf. Eq. (5.49))

$$3\Gamma \approx 2.46\hbar\omega_E\left(\frac{\lambda^3 E_{\mathrm{JT}}^E}{\hbar\omega_E}\right)\exp\left(-\frac{16\lambda E_{\mathrm{JT}}^E}{9\hbar\omega_E}\right) \tag{5.55}$$

Analogously, for the $T\otimes t_2$ or $T\otimes(e+t_2)$ problems with four equivalent trigonal minima the tunneling splitting of the ground vibronic level is given by the expression

$$4\Gamma = \frac{2\hbar\varpi_E}{\pi}\exp\left(-\frac{1}{\hbar}\int_a^b \sqrt{2m[\varepsilon(q) - E_0]}dq\right) \tag{5.56}$$

Here $\varpi_E \approx \omega_T\sqrt{2/3}$ is the frequency of the "particle" collisions with the barrier wall, $\varepsilon(q)$ is the lower sheet of the APES, and the integral has to be taken again along the steepest slope path.

Note, however, that in this case the tunneling is in fact multidimensional [5.27]. Figure 5.8 illustrates the equipotential cross-sections of the APES for a $T\otimes t_2$ problem of a cubic system mapped onto the surface of a unit sphere $x^2+y^2+z^2=1$ (we remind you that the trigonal distortion coordinates are $Q_\xi \sim yz$, $Q_\eta \sim xz$, and $Q_\zeta \sim xy$). There are eight trigonal extrema points (four saddle points and four minima separated by six orthorhombic saddle points along x, $-x$, y, $-y$, z, and $-z$. In each of the minima wells the system has three equivalent ways to tunnel to the nearest-neighbor equivalent well via the steepest descent (shown by a broken line), which connects two near-neighbor vertexes in a cubic system, and two tetrahedral vertexes in a tetrahedral system (note that this tunneling sidesteps the orthorhombic saddle points). It was shown [5.27] that in spite of this three-dimensional nature of the tunneling, the formula (5.56) for the magnitude of the tunneling splitting obtained by approximate reduction of the problem to the one-dimensional case remains valid, owing mostly to the high symmetry of the problem.

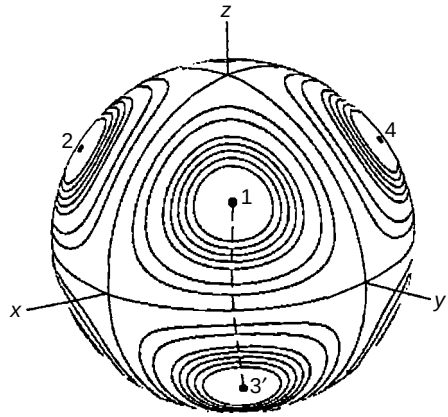

Fig. 5.8. Illustration to the multidimensional nature of the tunnelling in the $T\otimes t_2$ problem by means of equipotential cross-sections of the APES mapped onto the surface of a unit sphere $x^2+y^2+z^2=1$. The minima wells are labeled 1, 2, 3, and 4, with the corresponding antipodal doubles as $1'$, $2'$, $3'$, and $4'$. The broken line is the steepest descent between the minima 1 and $3'$ [5.27].

Numerical calculation [5.36] of 4Γ using Eq. (5.56) requires knowledge of the APES curve $\varepsilon(q)$ along the steepest descent, which is a curvilinear motion. This may involve further simplification and corrections beyond the adiabatic approximation [5.27, 5.29, 5.35], in particular, the inclusion of a centrifugal term in the equation of the APES (Section 5.2). Further discussion of this important problem is given in Section 5.4.

Some general features of the tunneling splitting can be obtained from symmetry considerations [5.27, 5.37–5.39]. If we denote the symmetry group of the system in the undistorted (reference) state by G and that in the distorted (at the minimum) state by L (which is a subgroup of G; see also Section 3.1), than the factor group $F=G/L$ ($G=F\times L$) is important to establish the possible tunneling energy levels. In particular, for sufficiently deep minima (strong enough vibronic coupling) when the overlap integral of two near-neighbor well wavefunctions Ψ_i and Ψ_j may be neglected, the tunneling splitting is determined by the resonance integrals $\langle\Psi_i|H|\Psi_j\rangle$ (cf. Eqs. (5.42) and (5.50)). The formula for the energy of any tunneling level (not to be confused with the magnitude of the tunneling splitting $n\Gamma$ in Eqs. (5.42) and (5.50)) is [5.27]

$$E_\Gamma=\sum_k m_k(\Gamma)H_{1k} \tag{5.57}$$

where H_{1k} is the resonance integral between the first and kth minima (the same for the whole group of equivalent minima labeled by k), $m_k(\Gamma)$ is the weight of

equivalent 1–k tunnelings, and the sum is taken over all the non-equivalent groups of equivalent minima. The multidimensional tunneling is thus reduced to a sum of much simpler tunnelings between the wells 1 and k that is determined by steepest descent along the APES between these minima.

On the other hand, the $m_k(\Gamma)$ values are fully determined by the symmetry of the factor group $F = G/L$. There are no general formulas for these values; they should be evaluated for each particular case [5.27]. For instance, for the icosahedral $H \otimes h$ problem the reference symmetry group is I_h, and there are ten trigonal minima on the APES with local symmetry D_{3d} (Section 3.4). Accordingly, the factor group is $I_h/D_{3d} = D_5$. The simplest system with all the elements of D_5 is a five-center regular pentagon. It has two kinds of intercenter resonance integrals: between two near-neighbor centers H_{1a} and between any center and its second neighbor H_{1b}. Hence there are two terms in the sum (5.57). Without tunneling, the ten equivalent states in the ten minima form a tenfold accidentally degenerate term, which splits into three levels, A, G, and H, with the following energies [5.40]:

$$E_A = 6H_{1a} + 3H_{1b}, \qquad E_G = H_{1a} - 2H_{1b}, \qquad E_H = -2H_{1a} + H_{1b} \quad (5.58)$$

By comparison of Eq. (5.58) with (5.57) we find that $m_a(A) = 6$, $m_b(A) = 3$, $m_a(G) = 1$, $m_b(G) = -2$, $m_a(H) = -2$, and $m_b(H) = 1$.

For a tetrahedral T_d reference group and trigonal C_3 minima the factor group $F = T_d/C_{3v} = D_2$. The simplest system with D_2 symmetry is a four-center tetrahedron, for which there is only one type of tunneling resonance integral, $H_{12} = H_{13} = H_{14}$.

As for the tunneling between two minima of the strong pseudo JT effect (Section 4.1), the problem may be reduced to conventional tunneling between two equivalent wells with a barrier between them [5.42], provided the influence of the excited state (the nonadiabacity terms in (4.15)) may be neglected.

One of the features of the solution (5.48) is that for small λ values $3\Gamma > 0$ and hence the doublet E level of the tunneling splitting is lower than the singlet A. Together with similar results for the JT T-term problems (where the vibronic T level is the lowest), this prompted generalizations that formed a stable *paradigm*: the lowest vibronic levels have the same symmetry and degeneracy as the initial electronic state. This paradigm has been broken recently when it was shown by direct calculations for large quadratic terms, and in some cases even for specific values of only linear terms, that a crossover of the ground and next excited vibronic levels takes place, making the ground-state vibronic energy level nondegenerate.

This *crossover phenomenon* follows already from the solutions obtained above in the approximation of strong vibronic coupling. As is seen from Eq. (5.48), in the JT $E \otimes e$ problem the crossover between the vibronic E and A energy levels takes place at $\lambda \geq 2.587$, where 3Γ becomes negative. Note that nondegenerate ground states were obtained already in the first calculations of the tunneling splitting [5.25] performed for the case of very large (infinite) barriers between the minima, but since this result contradicted that obtained in more accurate calculations for finite (small) barriers [5.20], and especially since it contradicted the conclusions from the Berry-phase implications (Section 5.7), it was attributed to the rough approximation used that yielded the "wrong sign" of the tunneling splitting.

An attempt to elucidate this unclear situation was made by means of numerical calculations of 3Γ in the $E \otimes e$ problem using the variational method with two parameters [5.23] described in Section 5.2. Again, for large quadratic coupling a vibronic level E–A crossover takes place, and the A level becomes the ground one (see the end of Table 5.1; the negative $3\Gamma = \varepsilon_A - \varepsilon_E$ values were not included in Table 5.1 because of their possible inaccuracy, in view of the above contradiction, but they follow directly from the calculations outlined in [5.23]).

A correct solution of this problem was given recently [5.43, 5.44], where it was shown that the crossover phenomenon emerges from direct numerical calculations of Eqs. (2.6) with the APES given by Eq. (3.38) to which a fourth-order term $f\rho^4$ is added in order to provide the necessary stability of the system as a whole (with large quadratic terms without fourth-order terms the system decomposes). For the $E \otimes e$ problem the results are illustrated in Fig. 5.9(a), where the calculated energy difference between the A and E vibronic levels as a function of the linear coupling k and quadratic coupling g is given. We see that for any g value (in the region of large enough g values) there is a k value for which the two levels intersect and the nondegenerate A level becomes the ground state.

The interpretation of this effect is that for sufficiently large g values the three additional conical intersections discussed in Section 3.2 (see Eq. (3.9) and Figs. 3.8 and 3.9), approach the central conical intersection, thus creating an alternative pass for the tunneling between the near-neighbor minima [5.43] (Fig. 5.10). This additional pass goes around all the four conical intersections, in contrast to that for small g values, which encircles only one, the central conical intersection.

In a conjecture with the Berry-phase problem (Section 5.7) this means that by encircling one conical intersection, the wavefunction changes sign, resulting in the ground state with a half-integer quantum number and double degeneracy. If the four conical intersections are encircled, the phase of the

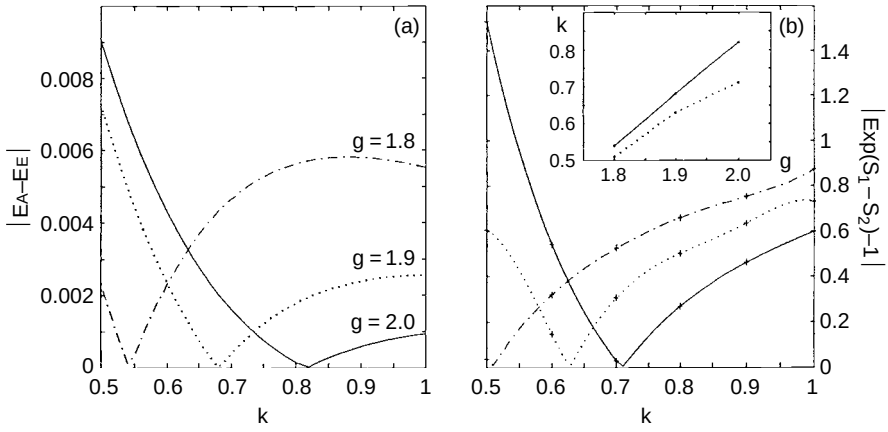

Fig. 5.9. Illustration to the vibronic energy level E–A crossover in JT $E \otimes e$ problems: the absolute values of the energy difference $|E_A - E_E|$ between the lowest A and E levels (a) and the ratios of the tunneling rates via paths P_1 and P_2 plotted as $|\exp(S_1 - S_2) - 1|$, as functions of k for $f = 0.05$ and three values of g. Calculated points are indicated by + and polynomially interpolated curves for the values $g = 2.0$, 1.9, and 1.8 are depicted by solid, dotted, and dash–dotted lines, respectively. Inset: the g versus k values at the crossing points $E_A = E_E$ (solid line) and at $S_1 = S_2$ (dotted line) (reprinted with permission from [5.43]. Copyright 1999 American Physical Society).

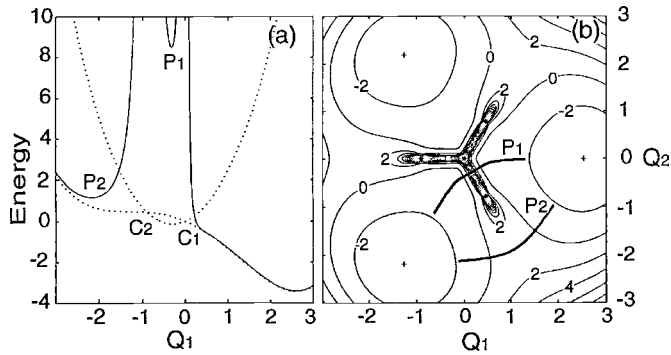

Fig. 5.10. The APES of a JT $E \otimes e$ system for parameter values $k = 0.9$, $g = 2$, and $f = 0.05$: (a) cross-sections with (solid line) and without (dotted line) the Born–Huang contributions at $Q_2 = 0$. C_1 and C_2 indicate conical intersections, while P_1 and P_2 indicate two saddle points; and (b) contour plot of the APES; $*$ and + indicate a conical intersection and a minimum, respectively. The two tunneling paths P_1 and P_2 of steepest descent are shown by thick lines (reprinted with permission from [5.43]. Copyright 1999 American Physical Society).

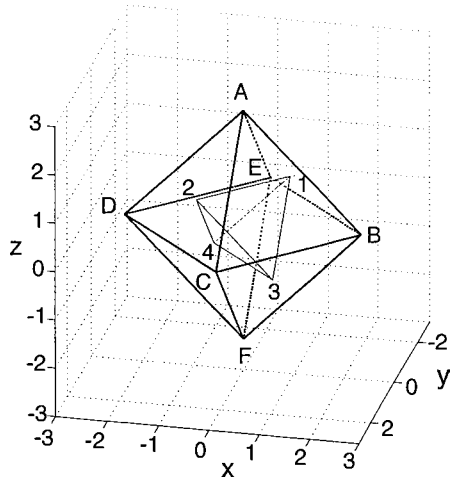

Fig. 5.11. A schematic presentation of the positions of the six orthorhombic minima A, B, C, D, E, and F, and four trigonal minima 1, 2, 3, and 4 in the space of the x, y, and z coordinates of the t_2 displacements in the $T \otimes t_2$ problem. The vibronic coupling parameters used are $k = 1$, $g = 1.6$, and $f = 0.1$ (reprinted with permission from [5.44]. Copyright 2000 American Institute of Physics).

wavefunction does not change, and a double degeneracy of the ground state is not required. The crossing of the two levels, A and E, and a nondegenerate ground state A emerges when the tunneling path around all the four conical intersections is lower in energy. Approximate calculations for the two tunneling passes illustrated in Fig. 5.9(b) and 5.10 confirm this interpretation [5.43].

For a similar (but more complicated) $T \otimes t_2$ problem with quadratic and fourth-order coupling terms included [5.44] there are four trigonal and six orthorhombic minima, conventionally shown in Fig. 5.11. They are separated by saddle points and conical intersections. Distinct from the much simpler $E \otimes e$ problem where the quadratic terms produce an additional (to the central one) three conical intersections, in the $T \otimes t_2$ problem with quadratic coupling there are four lines of conical intersections between the trigonal minima that originate from the center of the tetrahedron (1, 2, 3, and 4 in Fig. 5.11) and proceed along the four trigonal directions that cross the centers of its four faces (Fig. 5.12), plus six lines of conical intersections that connect each two of the four points 1, 2, 3, 4, as indicated in Fig. 5.12.

An easier way to visualize this rather complicated topology is to look into cross-sections. Figure 5.13 brings one such cross-section perpendicular to one of the lines of conical intersections, showing the energy contours around the three original minima, 1, 2, and 3, and three orthorhombic minima, A, B, and C,

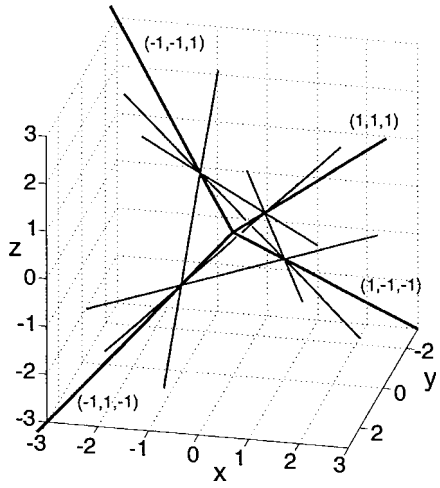

Fig. 5.12. The ten lines of conical intersection in the lowest potential-energy surface of the $T \otimes t_2$ problem. Four of them drawn by thick lines extend from (0, 0, 0) in the directions of (1, 1, 1), (1, −1, −1), (−1, 1, −1), and (−1, −1, 1). The other six lines connect two of the following four points: ($2k/3g$, $2k/3$ g, $2k/3g$), ($2k/3g$, $-2k/3g$, $-2k/3g$), ($-2k/3g$, $2k/3g$, $-2k/3g$), and ($-2k/3g$, $-2k/3g$, $2k/3g$). The vibronic coupling parameters are $k = 1$, $g = 1.6$, and $f = 0.1$ (reprinted with permission from [5.44]. Copyright 2000 American Institute of Physics).

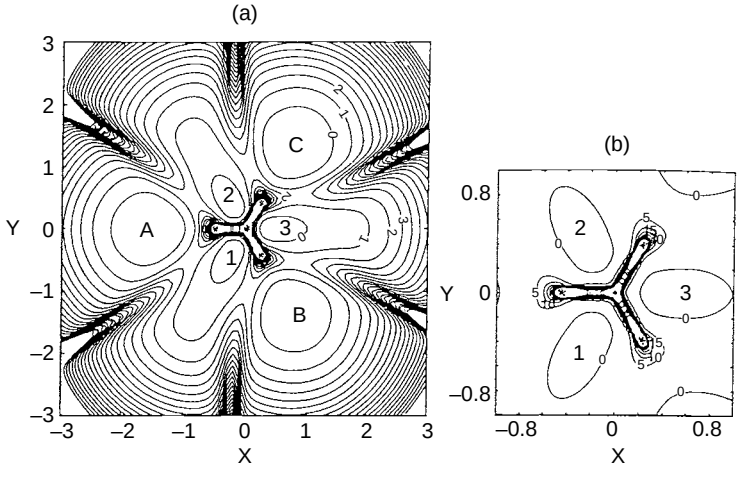

Fig. 5.13. (a) Cross-sections of the lowest APES in the X–Y plane at the trigonal minima ($Z = 0.157$) for $k = 1$, $g = 1.6$, and $f = 0.1$. The letters A, B, and C and numbers 1, 2, and 3 denote three orthorhombic and three trigonal minima, respectively. Conical intersections are located at $(X, Y) = (0, 0)$ and $-0.45[\cos(2n\pi/3), \sin(2n\pi/3)]$, $n = 0, 1, 2$. (b) The same around $(X, Y) = (0, 0)$, enlarged; * indicates the position of conical intersections (reprinted with permission from [5.44]. Copyright 2000 American Institute of Physics).

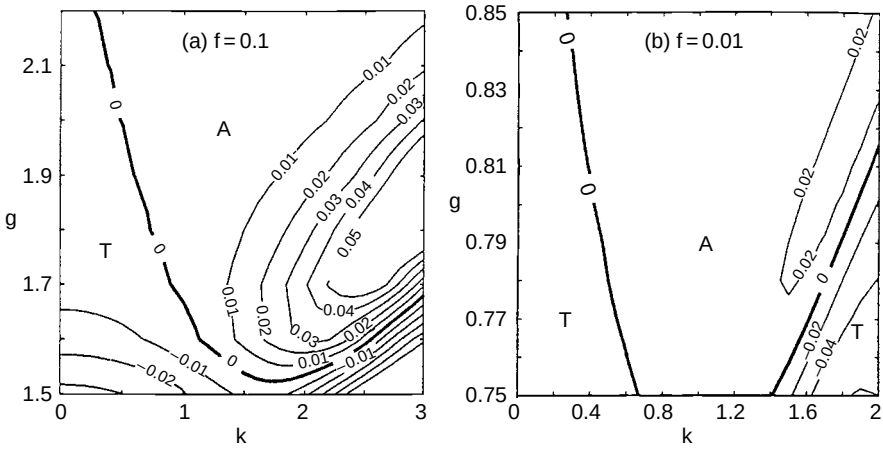

Fig. 5.14. The energy difference between the lowest T and A vibronic states for $f = 0.1$ (a) and $f = 0.01$ (b), as a function of k and g. Thick lines are zero contour lines. The letters T and A denote the regions of T and A ground states, respectively (reprinted with permission from [5.44]. Copyright 2000 American Institute of Physics).

and the central conical intersection plus three lateral conical intersections. The six additional conical intersections between the orthorhombic minima are outside the picture in the well-seen directions.

The positions of minima and conical intersections depend on the parameter values. For strong linear coupling and weak quadratic coupling only trigonal minima are important and only the four lines of intersections that originate from the center (Fig. 5.12) are significant in formation of the energy spectrum. On increasing the quadratic coupling, the orthorhombic saddle points become minima and the six additional lines of conical intersection become significantly involved. As a result, similar to the $E \otimes e$ case, a new tunneling path occurs, which encircles an even number of conical intersections. For parameter values for which this path is lower, the nondegenerate A state becomes the ground state. Figure 5.14 illustrates some of these results [5.44]. As in the $E \otimes e$ problem, the parameter f stands for the contribution of the fourth-order terms that provide the necessary chemical stability of the system.

For some problems the crossover of vibronic energy levels takes place already in the approximation of linear coupling, i.e. without quadratic and higher-order terms. This result emerged for the first time in the investigation of the icosahedral $H \otimes h$ problem [5.40] (see also [5.41]), which contributed significantly to the solution of the vibronic ground-state problem and the collapse of the paradigm that the vibronic ground-state symmetry and degeneracy should be the same as that of the initial electronic term. Figure 5.15 depicts

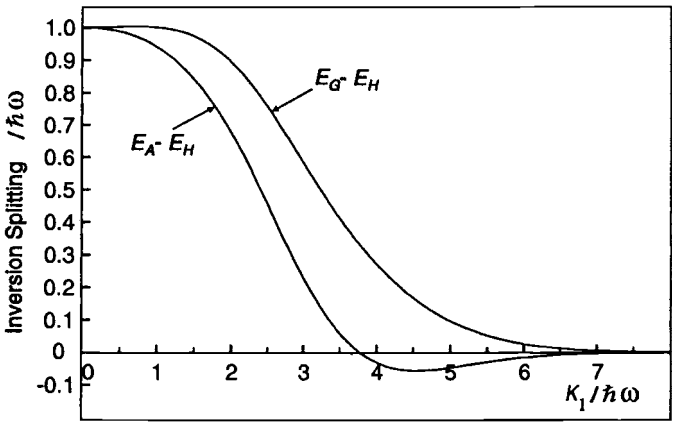

Fig. 5.15. Tunneling splitting and A–H level crossover as a function of the linear coupling constant k in the $H \otimes h$ problem with D_{3d} minima (in $\hbar\omega$ units). At certain values of k the E_A–E_H splitting becomes negative and the nondegenerate A level becomes the ground state (the E_G–E_H splitting is also shown) (reprinted with permission from [5.40]. Copyright 2000 American Institute of Physics).

the results of the calculations [5.40] that show explicitly that at a certain value of the vibronic coupling constant k the higher-in-energy A level crosses the lower one (H), thus becoming the ground state at higher values of k. The explanation of the origin of the crossover in this case is in principle similar to that for the $E \otimes e$ and $T \otimes t_2$ problems: for the $H \otimes h$ problem with ten trigonal minima there are two kinds of possible passes of tunneling between two near-neighbor wells, which are shown to generate different Berry phases, π and 0 [5.45] (see also [5.27]). If, depending on the vibronic coupling constant k, the former pass dominates, the lowest vibronic level is H (with the same symmetry and degeneracy as the reference electronic H term), while for the pass with no Berry phase that dominates at larger k values, the level order reverses and the nondegeneate A level becomes the ground state. Further developments in the solution of this problem using higher-level investigation of the APES topology are seen in [5.46].

Similar results were obtained for the $T \otimes (e + t_2)$ problem [5.47]. Numerical solutions of Eq. (2.6) for this case yield results that are partially illustrated in Fig. 5.16, from which it is seen that for relatively large coupling to the trigonal distortions, for instance, for $k_t = 5$ and a tetragonal-to-trigonal ratio of vibrational frequencies equal to 5, there is a range of constants of vibronic coupling to tetragonal displacements $k_e \sim 1.6$–2.7 for which the tunneling splitting $\varepsilon_A - \varepsilon_T$ becomes negative and the A level is the lowest, which is quite similar to the above cases of $E \otimes e$, $T \otimes t_2$, and $H \otimes h$ problems. The physical explanation

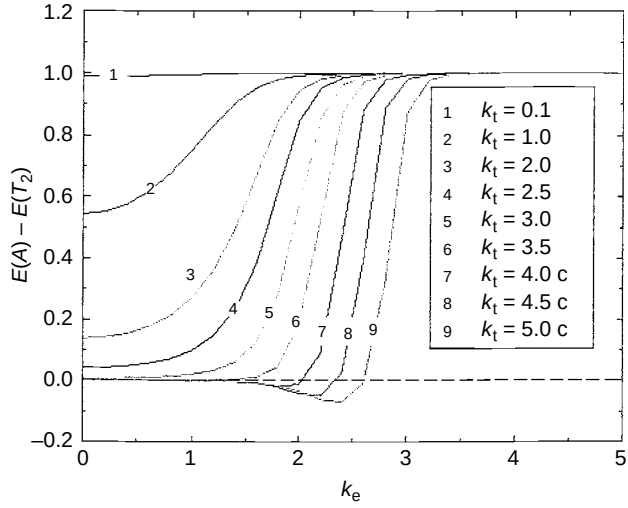

Fig. 5.16. Calculated tunneling splitting $E(A) - E(T_2)$ as a function of the k_E coupling constant in the linear $T \otimes (e + t_2)$ problem with $\hbar\omega_E/\hbar\omega_T = 5$ (in $\hbar\omega_T$ units) [5.47].

of this result is expected to be similar to the previous ones: there should be at least two different paths between the equivalent minima, which have different energy barriers and different wavefunction (Berry) phase shifts. However, so far the attempt to reveal the two competing paths (similar to the $E \otimes e$ case above [5.43]) using a simple APES with either trigonal or tetragonal minima has been unsuccessful [5.48]. This does not influence the result of the exact numerical solution [5.47]: the analytical APES used in [5.48] is far from being sufficiently accurate because it does not include the centrifugal energy (Section 5.2), which was shown to be very important in these problems [5.43, 5.44].

For the parameter values under consideration the system has four trigonal minima, plus three tetragonal and six orthorhombic saddle points (Section 3.3). The paths connecting three minima and going across the tetragonal saddle points have a trivial Berry phase π that results in a vibronic T ground-state energy level, while for passing through the orthorhombic saddle points the Berry phase is zero, leading to the nondegenerate ground-state A level. An energy analysis of these two paths shows that when the e-mode coupling is very weak, the tetragonal paths are forbidden: the only paths accessible are the orthorhombic paths as in the $T \otimes t_2$ problem. The tetragonal paths become significant when the couplings to e and t_2 displacements become comparable (and in this case the problem is similar to the $H \otimes h$ one in Section 3.4). This mechanism explains the origin of the vibronic T–A energy-level crossing at

certain values of vibronic coupling parameters and the occurrence of the nondegenerate ground state A at larger couplings found in the numerical diagonalization of the linear $T \otimes (e + t_2)$ problem [5.47].

The change of the ground-state symmetry and degeneracy is most important in the spectroscopy and low-temperature dynamics of the system (Sections 6.1.2 and 8.2). It is particularly important for the theory of first-order vibronic reduction factors, which is invalid if the symmetry of the ground vibronic energy level is different from that of the reference electronic state (Section 5.6).

A more general conclusion from the works on tunneling splitting that lead to either degenerate or nondegenerate ground states as a function of the vibronic coupling parameters, illustrated above, is that the orbital degeneracy of the ground term is not necessarily related to the global symmetry of the system, it is rather dependent on internal interactions. A somewhat similar situation emerges in the so-called *spin crossover phenomenon* in transition metal complexes in which the ground-term orbital and spin degeneracy changes from high-spin to low-spin configuration as a function of the strength of the ligand field (see, e.g., in [5.49]).

In a series of papers (see [5.48, 5.50] and references therein, as well as examples mentioned above and in Sections 5.4–5.6 and 7.5) vibronic energy levels and tunneling splitting in systems with $E \otimes e$, $T \otimes t$, $T \otimes (e + t_2)$, and icosahedral symmetry problems with strong vibronic coupling were calculated using an approach which is in essence similar to that discussed above in this section. The total wavefunction is presented as a linear combination of the wavefunctions in the equivalent minima (as in (5.39)), but the latter (e.g., (5.44)) are obtained by means of unitary transformations (Section 5.4). In the earlier works the anisotropy of vibrations in the minima, mentioned above, was ignored, but it was taken into account in more recent publications by means of a scaling transformation [5.34].

5.4 Numerical methods and general solutions

Approximate analytical solutions of the vibronic equations (2.6) are possible in limiting cases of very weak or very strong vibronic coupling and for a limited number of lowest vibronic states, as outlined in the previous three sections. A series of other analytical methods [5.51–5.54] were employed to overcome these limitations in the solution of JT (mostly $E \otimes e$) problems. However, in general cases with arbitrary vibronic coupling constants (that include the majority of JT systems) numerical solutions are unavoidable; some of them are mentioned above. The simplest approach to this problem follows well-known methods of quantum chemistry by presenting the unknown wavefunctions of the

vibronic states sought as an expansion over a finite number of zeroth-order basis functions – solutions for the reference undistorted configuration. For example, in the $T \otimes t_2$ problem the wavefunction of the undistorted configuration in the adiabatic approximation is presented as a product of the threefold degenerate electronic state $\Psi_{\Gamma\gamma}$, $\gamma = a, b, c$, and three-dimensional oscillator functions $\chi_{n_x n_y n_z}(Q) = |x, n_x\rangle \cdot |y, n_y\rangle \cdot |z, n_z\rangle$, where $|x, n_x\rangle$, $|y, n_y\rangle$, and $|z, n_z\rangle$ are the corresponding one-dimensional harmonic oscillators, n_x, n_y, and n_z being their vibrational quantum numbers. The wavefunction of the vibronic state $\Gamma'\gamma'$ is sought as the following expansion:

$$\Psi_{\Gamma'\gamma'}(r, Q) = \sum_{\gamma} \sum_{n_x, n_y, n_z} C^{(\Gamma'\gamma')}_{\gamma, n_x, n_y, n_z} \Psi_{\Gamma\gamma}(r, Q) \chi_{n_x n_y n_z}(Q) \tag{5.59}$$

where the coefficients $C^{(\Gamma'\gamma')}_{\gamma, n_x, n_y, n_z}$ should be determined from the condition of minimum energy of the Hamiltonian (2.2) with the vibronic coupling from Eq. (2.14). By diagonalizing this Hamiltonian we come to a secular equation the order of which is determined by the number of functions in the expansion (5.59), which is obviously limited by the computer time and cost. For instant, in the $T \otimes (e + t_2)$ problem, if the vibrational functions of the lowest unperturbed e and t_2 vibrations up to $n = 8$ are included in the basis of calculations, the secular equation to be solved has the order 3861×3861, and if the spin–orbit interaction is included, the matrix becomes of order $15\,444 \times 15\,444$ (the group-theoretical classification by irreducible representations of the symmetry group reduces these dimensions by a factor of 3–4). On the other hand, in order to obtain accurate results larger numbers of basis functions should be included.

Therefore this approach has important limitations. Although it fares well for weak and intermediate coupling, it is practically unacceptable for the case of strong vibronic coupling, when the vibronic states are localized in the minima where they are significantly different from the basis functions of non-displaced oscillators. It is obvious that the stronger the vibronic coupling, the more terms of the expansion (5.59) must be kept, and the greater the dimensionality of the Hamiltonian matrix. The algorithms of diagonalization of the matrix that are usually used in numerical calculations require storage of the whole matrix in the operative memory. If the dimensionality of the basis space (i.e., the number of terms in the expansion (5.59)) is N, then the number of the operative memory cells needed for computer storage is proportional to N^2. The restricted size of the operative memory of the computer thus determines the upper limit for the vibronic constant values for which the numerical diagonalization of the vibronic Hamiltonian in the above scheme gives

reasonable results. Another limitation is the fact that the finiteness of the basis set influences the accuracy of the results. The nearer the energy of the states under consideration to the upper limit of the energy spectrum of the basis states, the less accurate the results. Therefore reasonable accuracy can be obtained only for a relatively small number of the lowest vibronic states.

In order to weaken these constraints symmetry considerations are usually employed. An example of such symmetry-based simplification is considered above in Section 5.2, where in the solution of the $E \otimes e$ problem the radial and angular motions are separated, and the numerical method is applied to the angular motion only. In more rigorous solutions symmetry-adapted basis sets in (5.59) simplify the matrix Hamiltonian significantly [5.1].

The first numerical results for the vibronic energy levels and wavefunctions of the linear $E \otimes e$ problem as functions of the dimensionless vibronic constant were obtained in [5.8, 5.55]. As expected, for small values ($\lambda \leq 0.25$) of the dimensionless vibronic coupling $\lambda = E_{JT}^{E}/\hbar\omega_{\mathrm{E}}$ the positions of the vibronic levels resulting from the numerical solutions agree well with that obtained from the analytical expression (5.1) for the weak coupling case, while for large values of λ they follow expression (5.18). With the energies and wavefunctions obtained the authors calculated the probabilities of transition to these states from the vibrational states of the nondegenerate electronic A term, and vice versa ($A \rightarrow E$ and $E \rightarrow A$ transitions). The resulting spectra are discussed in Section 6.1.

The first numerical calculations for the $T \otimes t_2$ problem were carried out in [5.56]. The vibronic energy levels as functions of the ratio $E_{\mathrm{JT}}^{T}/\hbar\omega_T$, illustrated in Fig. 5.17, were obtained using expansion (5.59) simplified by symmetry considerations. It is seen that without vibronic interactions the spectrum contains equidistant levels spaced according to those of the three-dimensional oscillator $E_n = \hbar\omega_T[n + (3/2)]$. In the other limiting case of very strong vibronic coupling, all the levels are fourfold degenerate (in accordance with the four minima of the APES) and join into two groups of equidistant levels with steps $\Delta E = \hbar\omega_T = \hbar\omega_A$ and $\Delta E = \hbar\omega_T\sqrt{2/3} = \hbar\omega_E$, respectively; these two frequency distances are due to splitting of the ω_T frequency into two components: $\omega_{A_1} = \omega_T$ and $\omega_E = \sqrt{2/3}\omega_T$ in the trigonal minima (Section 3.3). In the area where $E_{\mathrm{JT}}^{T}/\hbar\omega_T \geq 2$, the levels correspond to those predicted by the theory of tunneling splitting (Section 5.3).

The same approach was used in the papers [5.57, 5.58] for numerical solution of the quadratic $E \otimes e$ and $\Gamma_8 \otimes e$ problems. The vibronic energy levels as functions of the quadratic coupling constant are similar to the approximate results given in Fig. 5.5. In the limit of strong coupling corresponding to deep

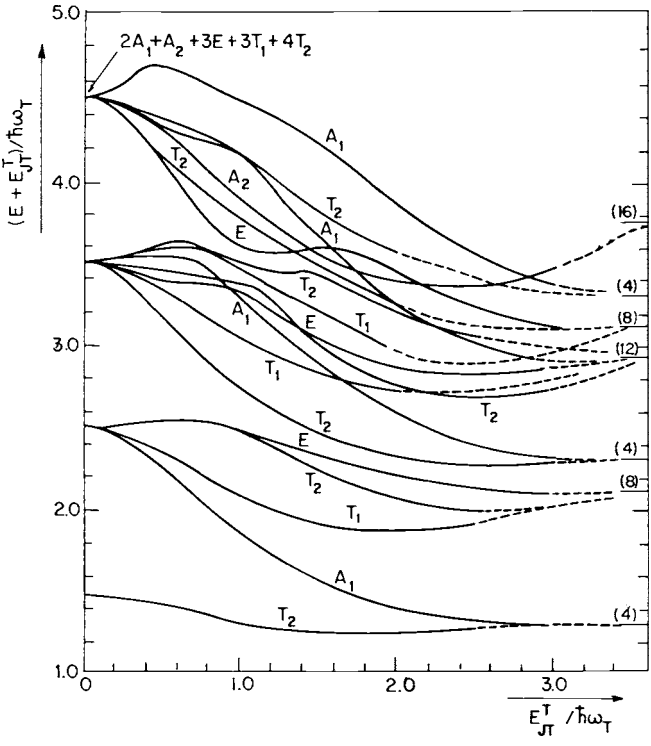

Fig. 5.17. Vibronic energy levels for the linear $T_1 \otimes t_2$ problem as a function of $E_{\mathrm{JT}}^{T}/\hbar\omega_T$ [5.56]. For the $T_2 \otimes t_2$ problem the level subscripts 1 and 2 should be interchanged.

APES minima, the lowest energy levels are grouped in tunneling multiplets, forming almost equally spaced sets that correspond to small vibrations at the bottom of the minima. However, there is no quantitative agreement between these results and those of Fig. 5.5. The differences become more important as the vibronic constant decreases; at $E_{\mathrm{JT}}^{E}/\hbar\omega_E \lesssim 2.5$ only the lowest vibronic doublet and singlet may be satisfactorily described in terms of the results of Section 5.2.

For the zero value of the linear vibronic constant the Hamiltonian of the quadratic $E \otimes e$ problem reduces to that of the RTE (Section 4.4). Figure 5.18 illustrates the vibronic energy levels for a RT system obtained in [5.58] by numerical diagonalization of the Hamiltonian. In accordance with Eq. (4.111), for the quadratic coupling constant $g = K_E$ the lowest sheet of the adiabatic potential is planar. As seen from Fig. 5.18, for this value of g the vibronic levels condense into a continuous spectrum. Similar ideas were employed for numerical solutions of the JT $(A + B) \otimes b$ [5.59] and $(A + E) \otimes e$ problems [5.60, 5.61], as well as the RT problem $(A + E) \otimes e$ [5.62].

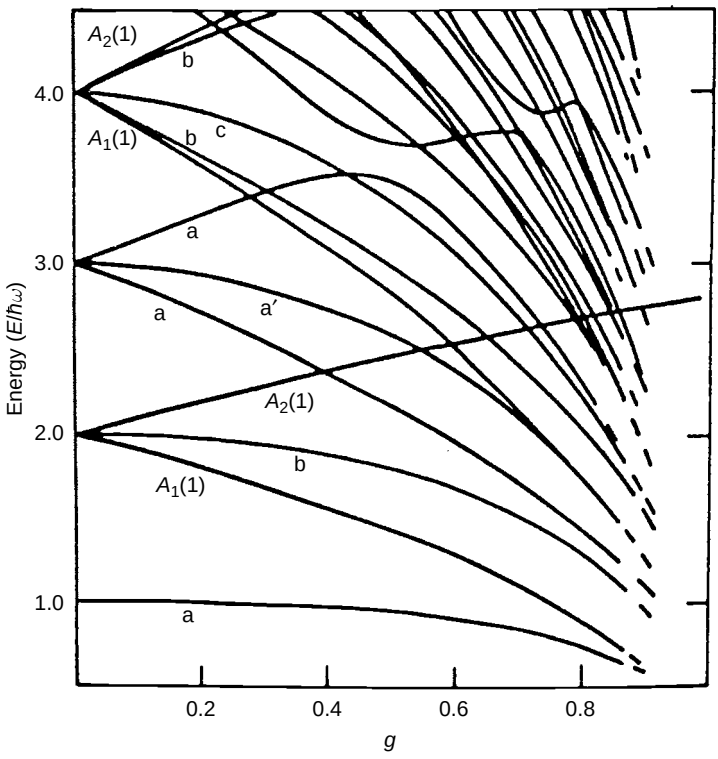

Fig. 5.18. Vibronic energy levels (in $\hbar\omega_E$ units) as a function of the quadratic vibronic coupling constant g (in K_E units) of the $E \otimes e$ problem with zero linear coupling, which is in fact a RT problem (reprinted with permission from [5.58]. Copyright 1978 Taylor & Francis).

In more complicated cases special algorithms for matrix diagonalization best suited to the JT problems under consideration, in particular, the method of minimal iterations, the Lanczos method [5.63, 5.64], proved to be most useful (see also [5.65]). This method is based on building a new basis set obtained by the action of the Hamiltonian on a given initial function $|\psi_1\rangle$:

$$
\begin{aligned}
|\psi_2\rangle &= H|\psi_1\rangle - |\psi_1\rangle \frac{\langle\psi_1|H|\psi_1\rangle}{\langle\psi_1 \mid \psi_1\rangle} \\
|\psi_3\rangle &= H|\psi_2\rangle - |\psi_1\rangle \frac{\langle\psi_1|H|\psi_1\rangle}{\langle\psi_1 \mid \psi_1\rangle} - |\psi_2\rangle \frac{\langle\psi_2|H|\psi_2\rangle}{\langle\psi_2 \mid \psi_2\rangle}
\end{aligned}
\tag{5.60}
$$

and so on. The process is continued according to the formula

$$
|\psi_{n+1}\rangle = H|\psi_n\rangle + g_{n1}|\psi_1\rangle + g_{n2}|\psi_2\rangle + \cdots + g_{nn}|\psi_n\rangle \tag{5.61}
$$

where

$$g_{ik} = \frac{\langle \psi_k | H | \psi_i \rangle}{\langle \psi_k | \psi_k \rangle} \tag{5.62}$$

until the zero vector is obtained. An interesting feature of the Lanczos method is that when choosing the initial function to belong to a certain line of an irreducible representation of the symmetry group we obtain, by means of the recurrence formulas (5.61), a new basis of states that has the same transformation properties. The recurrent process results in the zero vector when the set of states of given symmetry is exhausted, while the dimensionality of the resulting basis space of states $\psi_i^{(\Gamma\gamma)}$ is the number of repeating irreducible representations Γ in the initial basis of the weak coupling.

For non-Kramers electronic degeneracy of the initial JT term the Hamiltonian matrix in the basis of states (5.60) and (5.61) is tridiagonal [5.65]. This circumstance is very important as it provides for a significant economy of computation time and operative memory. Approved algorithms with rapid convergence are available for numerical diagonalization of tridiagonal matrices [5.66].

The Lanczos algorithm was first used in [5.67] in the numerical solution of the $E \otimes (b_1 + b_2)$ problem (Section 3.1) by means of the diagonalization of the 231×231 matrix (equivalent to mixing the first $n_1 + n_2 \leq 20$ vibrational levels of the unperturbed system). The results also include data for the linear $E \otimes e$ problem as a particular case when $K_1 = K_2$ and $F_1 = F_2$ (Fig. 5.19). An interesting feature in the behavior of the excited vibronic levels occurs for large vibronic coupling: with increasingly large vibronic coupling their energies oscillate near the mean value $\hbar\omega_E(n+1) - E_{\mathrm{JT}}^E$, and then one of these levels descends smoothly, ultimately taking its place among the levels of the rotational structure of the strongly coupled spectrum (see also Fig. 5.20).

In fact the *multiple accidental degeneracy* at the points where the levels intersect first revealed in the $\Gamma_8 \otimes t_2$ problem (see below), may be non-accidental. Analyzing the nature of the degeneracy in the $\Gamma_8 \otimes t_2$ problem, it was concluded [5.69] that a similar phenomena should take place in the linear $E \otimes e$ problem. This was observed indeed in the numerical calculations [5.67], which were obtained seemingly independently from the paper [5.69]. Some considerations about its nature are given in [5.67–5.69], but up to now no full group-theoretical analysis of the Schrödinger equation has been performed in order to reveal the internal dynamic symmetry which determines this degeneracy. Another important feature of this solution is the strong dependence of the vibronic level positions on the coupling constant even when the coupling is weak (Figs. 5.19 and 5.20), meaning that vibronic effects in the problems under consideration cannot be neglected even in the weak-coupling limit.

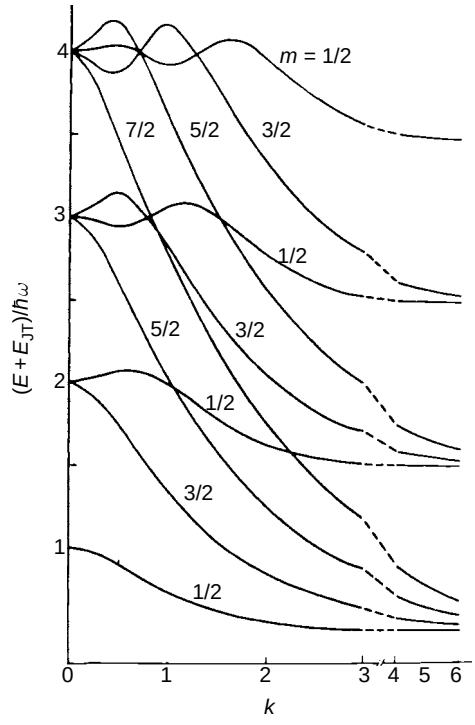

Fig. 5.19. Vibronic energy levels as a function of the dimensionless coupling parameter $k = (2E_{\mathrm{JT}}^{E}/\hbar\omega_E)^{\frac{1}{2}}$ in the linear $E \otimes e$ problem, obtained by numerical solutions without separation of the radial and angular motion [5.67].

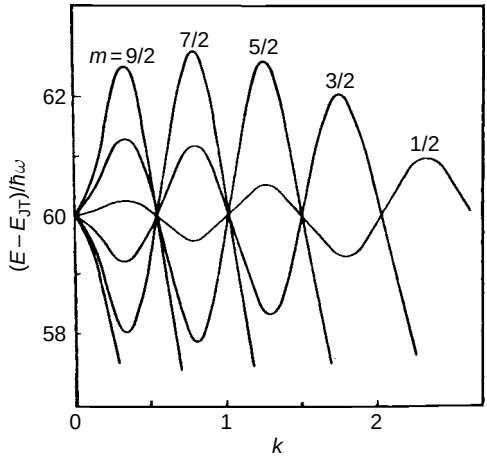

Fig. 5.20. Energy levels for highly excited states of the linear $E \otimes e$ problem (the same as for low-lying states in Fig. 5.19); m is the quantum number in Eq. (5.18). Accidental multiple degeneracy is a special feature of these states [5.67].

For further general applications of the Lanczos method, see in [5.70], as well as in the solution of the $E \otimes (e_1 + e_2)$ problem [5.71], in determination of the ground-state wavefunction [5.72], etc. (see the review paper [5.73]). The discussion of this approach and its improvements in application to JT problems are given in a series of papers [5.74–5.76]. For other numerical calculations for E terms, see in [5.77–5.79], in particular, the application of high-level *ab initio* coupled-cluster approximations [5.78].

Numerical solutions of the $E \otimes e$ problem with large quadratic coupling were obtained recently [5.43]. The results are discussed in Section 5.3 because they are most important in understanding the tunneling phenomena in JT systems, in particular, the crossover of the lowest vibronic energy levels A and E (Figs. 5.9 and 5.10) which, together with other contributions [5.41, 5.45–5.47] removed the paradigm that the ground vibronic state must be of the same symmetry and degeneracy as the initial electronic state.

On moving to higher-degeneracy problems we note that the number of mixing states which should be kept in the expansion (5.59) is determined not only by the magnitude of the constant of vibronic coupling, but also by the number of JT-active vibrational degrees of freedom. The degeneracy of the nth level of the s-dimensional isotropic oscillator is of the order of $n^{s-1}/(s-1)!$, and therefore, considering the mixing of N excited quantum states in the expansion (5.59), we must deal with a basis dimension of the order $N^s/(s-1)!$. If we take into account also the electronic quantum number, then the full dimension of the basis has to be multiplied by f_Γ, the degeneracy of the electronic term.

For instance for the $T \otimes (e + t_2)$ problem ($f_\Gamma = 3$, $s = 5$), taking into account the admixture of the vibrational states with $n_\vartheta + n_\varepsilon + n_\xi + n_\eta + n_\zeta \leq 20$, a $59\,136 \times 59\,136$ matrix should be diagonalized in the numerical solution. The classification of the states according to irreducible representations reduces the Hamiltonian matrix to a block form, the dimension of each block being less than that of the initial matrix by approximately an order of magnitude. But even after such a simplification, the diagonalization of each block requires significant computer time and cost. Again, the cutoff of the basis by vibrational state s with $N = 20$ allows one to obtain reliable results only for moderate vibronic coupling ($k \leq 4$) and only for the lowest vibronic states.

The status of calculations of the vibronic spectrum for the linear $T \otimes (e + t_2)$ problem is illustrated schematically in Fig. 5.21. As can be seen from this figure, the works [5.6, 5.8, 5.21, 5.56, 5.80–5.82] in fact cover most of the domain of possible values of vibronic constants for which the problem is solved. Of course, the borders of the regions in this figure are conventional. In some of these calculations rough approximations and models are employed.

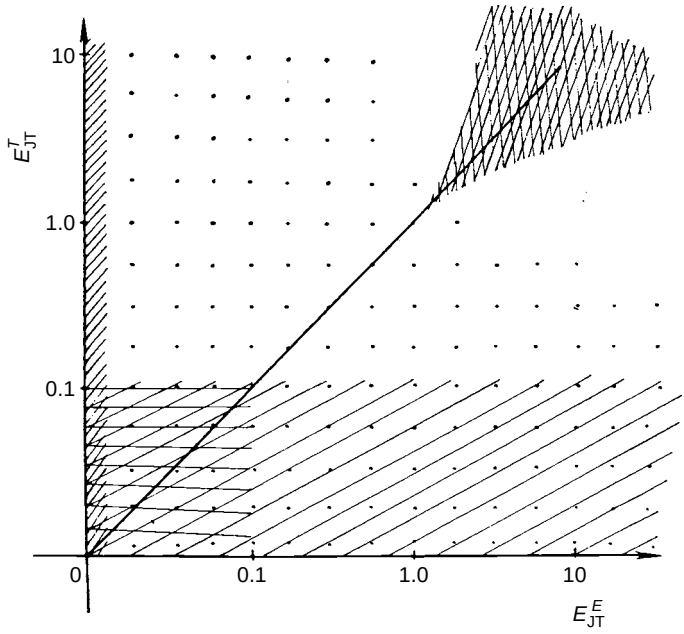

Fig. 5.21. Illustration to the results of numerical calculations for the $T \otimes (e + t_2)$ problem obtained by different methods. The dimensionless values of JT stabilization energies E_{JT}^{E} and E_{JT}^{T} in units $\hbar\omega_E = \hbar\omega_T = \hbar\omega$ are plotted on the axes with a logarithmic scale. In the area with horizontal shading the perturbation theory [5.5] is valid. The thin-spaced oblique shading shows the area of applicability of the numerical results [5.56]. The wider-spaced oblique shading corresponds to the validity of the perturbation theory [5.80]. Along the line $E_{JT}^{E} = E_{JT}^{T}$ the results of the d model [5.89] are valid. Double shading at large E_{JT}^{E} and E_{JT}^{T} values corresponds to the qualitative results [5.6, 5.21]. The area of applicability of numerical results [5.81] and [5.82] is shown by points (from [5.1]).

One of them is the so-called d-mode approximation (Section 3.3). In this model it is assumed that $E_{JT}^{E} = E_{JT}^{T}$ and $K_E = K_T$, and consequently the Hamiltonian acquires higher symmetry ($O(3)$), than the initial one (this approximation is adequate to the situation in some F-centers in crystals in which the diffuse electronic orbitals are insensitive to the cubic symmetry of the local environment in the lattice [5.83]). The same vibronic Hamiltonian is suitable for the $T \otimes h$ problem in icosahedral systems (Section 3.4). The high symmetry of the Hamiltonian allows one to use the powerful Racah method for its diagonalization [5.21, 5.84–5.86], or the symmetry advantages of the Lanczos method [5.66, 5.87].

The Lanczos method was also employed for more elaborate numerical calculations of the linear $T \otimes (e + t_2)$ problem [5.47]. In these calculation the crossover between the lowest A and T vibronic energy levels was found

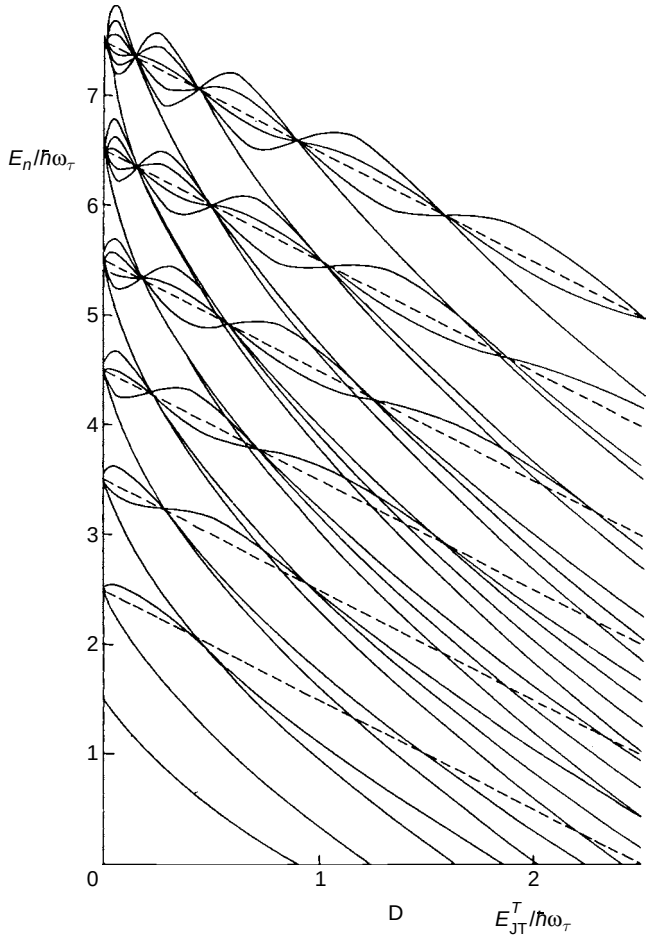

Fig. 5.22. Vibronic energy levels as a function of the dimensionless linear vibronic coupling constant $E_{\mathrm{JT}}^T/\hbar\omega_T$ for the $\Gamma_8 \otimes t_2$ problem. Dashed lines show mean values around which the excited-state energy levels oscillate (cf. Figs. 5.19 and 5.20) (reprinted with permission from [5.89]. Copyright 1977 Institute of Physics).

(Section 5.3 and Fig. 5.16), similar to the crossover in the linear $T \otimes h$ problem [5.40, 5.41]. Crossover was also found in the $T \otimes t_2$ problem with large quadratic coupling terms [5.44] (similar to the $E \otimes e$ case), discussed in Section 5.3 and illustrated in Figs. 5.11–5.14.

The solution of the $\Gamma_8 \otimes (e + t_2)$ problem is more complicated because it has a larger number of electronic states involved, but it simplifies owing to its additional integrals of motion [5.1]. The results of numerical calculations for the $\Gamma_8 \otimes t_2$ problem obtained in [5.8, 5.68, 5.88, 5.89] are given in Fig. 5.22. Excited vibronic levels of the linear $\Gamma_8 \otimes t_2$ case oscillate as a function of

the vibronic constant about the mean values $\hbar\omega_T[n+(3/2)] - E_{\mathrm{JT}}^T$, and at some vibronic coupling values they coincide, forming nodal points of accidental degenerate multiplets, similar to those in the linear $E \otimes e$ problem (cf. Fig. 5.20), mentioned above.

This accidental degeneracy was found first in [5.88], ten years before the similar degeneracy was discovered in the $E \otimes e$ problem [5.67]. In order to explain this specific behavior of the vibronic levels of the $\Gamma_8 \otimes t_2$ problem the differences between the matrix Hamiltonians for different quantum numbers m were analyzed, and it was shown that the intersections of the corresponding energy levels occur at $J_1(2k\sqrt{2n+3}) = 0$, where $J_n(z)$ is a Bessel function (which is independent of the quantum number m), and k is the coupling constant [5.69].

The numerical solution of the linear $\Gamma_8 \otimes t_2$ problem in the d-mode approximation, i.e., at $E_{\mathrm{JT}}^E = E_{\mathrm{JT}}^T$ and $K_E = K_T$, is given in [5.89]. After the separation of the cyclic variables the secular matrix W in the basis of weak coupling has the same form as in the linear $E \otimes e$ and $\Gamma_8 \otimes t_2$ cases, the only difference being that the quantum number m has to be replaced by $2\mu + (3/2)$, where μ is half-integer. In this problem, too, the excited vibronic levels oscillate about the mean values $\hbar\omega[n+(5/2)] - E_{\mathrm{JT}}$ coinciding at nodal points at specific values of the linear vibronic coupling constant.

The PJT problem with a small energy gap Δ between the electronic terms, $\Delta \ll \hbar\omega$, where $\hbar\omega$ is the quantum of JT-active vibrations, can be considered by means of perturbation theory (Section 5.1; see also the band JTE in Section 8.2.5). If $\Delta \geq \hbar\omega$, the PJT problem should be solved by a different method. The same is true when the group of neighboring electronic terms mixed by the vibrations arises because of *spin–orbital splitting* (Section 4.2). If the spin–orbital interaction results in splitting in first-order perturbation theory, then this splitting, as a rule, is not small, and it has to be taken into account along with the vibronic interaction. A simple two-level problem with spin–orbital coupling is considered in Section 4.2. Another typical example of this kind is the cubic polyatomic systems in a triply degenerate electronic state. The effective Hamiltonian of the ${}^{2S+1}T$ term including the second-order perturbation terms with respect to the spin–orbital interaction has the form

$$H_{\mathrm{SO}} = \zeta \vec{L}\vec{S} + \mu(\vec{L}\vec{S})^2 + \rho(L_x^2 S_x^2 + L_y^2 S_y^2 + L_z^2 S_z^2) \tag{5.63}$$

where L_x, L_y, and L_z are the matrices of the operator of the orbital momentum of the electrons determined in the basis of electronic states of the T term (they coincide with the matrices of the energy spin [5.1]), S_x, S_y, and S_z are the spin

matrices, and ζ, μ, and ρ are the parameters of the effective spin Hamiltonian (in the approximation of the crystal field theory the constants ζ, μ, and ρ are simple functions of the crystal field parameter Dq [5.90]). If, besides the spin–orbital interaction, the low-symmetry tetragonal or trigonal crystal field is also significant, an additional two parameters of coupling to the crystal field, ε and τ, enter the Hamiltonian (5.63).

The problem of the JTE for the ${}^{2S+1}T$ term in the presence of spin–orbital interactions and low-symmetry crystal fields is therefore one of the most complicated in the theory of vibronic interactions. The difficulties are caused by a large number of JT-active vibrational degrees of freedom ($s \geq 5$ in the $T \otimes (e + t_2)$ problem) and mixing states ($f = 3(2S + 1)$), and by the low symmetry of the problem, which prevents effective use of group-theoretical methods. The vibronic Hamiltonian in this case contains a large number of independent parameters (two frequencies ω_E and ω_T or force constants K_E and K_T, two vibronic constants F_E and F_T, three spin–orbital constants ζ, μ, and ρ, and a parameter of the low-symmetry crystal field, ε or τ), thus requiring multiple calculations of the vibronic spectrum (in contrast to, say, the linear $E \otimes e$ problem).

These difficulties can be reduced if one looks for the solution to the so-called *partial eigenvalue problem*, *i.e.*, when only one or a few of the most important eigenvalues and eigenfunctions are sought. For this partial solution of the problem some more powerful and rapidly converging methods have been worked out [5.65, 5.66], allowing significant economy of computer time and on-line storage. Most of the algorithms used in numerical methods for solution of the partial eigenvalue problem are based on the variational principle. The lowest eigenvalue corresponds to the wavefunction that minimizes the so-called Rayleigh quotient:

$$E\{\Psi\} = \frac{\langle \Psi | H | \Psi \rangle}{\langle \Psi | \Psi \rangle} \tag{5.64}$$

Here the energy depends on the probing function (5.59); in the matrix representation this quotient is a function of the coefficients of the expansion (5.59).

In [5.82], the *method of coordinate relaxation* [5.65] was used to determine the lowest vibronic eigenvalues and eigenfunctions of the JT ${}^3T \otimes (e + t_2)$ problem with spin–orbital interaction, taking into account also the influence of trigonal crystal fields. The method is based on the idea of the coordinate slope by successive minimization of the Rayleigh quotient along each of the coordinates in the multidimensional space in which the function $E\{\Psi\}$ is defined. In these calculations there is no need to keep the whole matrix (to be diagonalized) in the computer memory. The simplicity of the matrix elements of the vibronic Hamiltonian defined with vibrational oscillator

functions allows one to calculate them each time they are needed, and to use the on-line memory of the computer for storing the calculated eigenvectors only. If the dimension of the basis set is N, the volume of the computer memory used in this method is proportional to N and not to N^2, as in the case of the full solution of the eigenvalue problem. This increases the computational possibilities (see also [5.87]).

It is important that in all the iteration methods based on the variational principle, as in the Lanczos method mentioned above, the transformation properties of the probe function are preserved during the minimization. If $\Psi_{\Gamma\gamma}^{(0)}$ transforming as the γ line of the irreducible representation Γ is chosen as the trial function, the iteration process results in the exact eigenfunction $\Psi_{\Gamma\gamma}$with the same transformation properties for the lowest energy level.

Some other numerical methods for the diagonalization of the JT Hamiltonians using their specific forms of so-called block-band and sparse matrices have also been proposed [5.73, 5.89].

Multi-particle methods (mainly the *Green-function method*) that proved to be very useful in quantum theory, in general, have not found widespread application in JTE calculations. The reason lies in the difficulties that occur with direct application of these methods [5.91, 5.92], due mainly to the degeneracy of the ground state inherent to all the JT problems with not very large couplings. This difficulty may be partly overcome by introducing additional restrictions that allow one to separate one of the states in the degenerate manifold [5.93, 5.94], like applying an external field that removes the degeneracy [5.95, 5.96].

As mentioned in Chapter 2, there is a formal analogy between the JT problem and that of pion–nucleon interaction in the static model of the nucleon [5.97]. This analogy was employed [5.98] in order to use the ideas and methods of the scattering theory, developed in quantum field theory [5.99], to solve JT problems. In particular, the Green-function method was applied in this way to solve the multimode problem [5.95–5.98] (Section 5.5). The perturbation version of this approach was used to consider the $T \otimes t_2$, $T \otimes d$, and $\Gamma_8 \otimes t_2$ problems [5.98] (see also [5.100]). For more recent works on application of field theory (Yang–Mills equations) to problems with conical intersections and nonadiabacity see in [5.101].

The *method of unitary, or canonical, transformations* proved to be very useful, especially during the earlier stage of application of the multi-particle theory to JT problems (for a comprehensive review see [5.102]). This method is based on a transformation of the Schrödinger equation to a new set of coordinates, for which the operator of potential energy contains a small parameter, so that the

usual perturbation theory may be used with respect to this small parameter. In JT problems with strong vibronic coupling the nuclear motion is localized in low-symmetry minima of the APES, and the transformation to new coordinates in the minima can be reduced to a shift transformation of the type

$$\hat{U} = \exp(\lambda \hat{S})$$

where $\hat{S}$ is proportional to the vibronic coupling constant F_Γ and it is determined from the condition that in the transformed Hamiltonian the linear terms of the perturbation vanish (see in [5.1]). On applying this to the Hamiltonian $H = H_0 + W$ we get

$$\hat{U} H \hat{U}^{-1} = \tilde{H}_0 + \tilde{W}$$

where the transformed operator of vibronic interaction $\tilde{W}$ is proportional to the renormalized constant of vibronic coupling, $F_\Gamma \exp(-\alpha E_{\mathrm{JT}}^\Gamma / \hbar\omega_\Gamma)$, and α is a numerical coefficient. The parameter λ in the transformed Hamiltonian is determined from the condition of minimum ground-state energy. The renormalized coupling constant, as seen from its expression, can serve as a small parameter of the perturbation theory both for $F_\Gamma \to 0$ and for $F_\Gamma \to \infty$. Therefore it may be expected that the perturbation theory with this parameter will yield reasonable results in the region of intermediate coupling too [5.102, 5.103].

The attempts to use the ideas of *coherent states* in JT problems [5.32, 5.104] are also related to the method of canonical transformations, since the transition to coherent states is performed by a similar shift transformation. The use of the so-called *para-Bose operators* [5.105] may also be relevant.

All these methods are based on the variational principle. Therefore they are expected to give satisfactory results when applied to ground-state calculations; they become less accurate when used for excited states. Nevertheless, good agreement with exact numerical results was also obtained for some excited states [5.106]. Unitary transformations were used to analyze the full $E \otimes (e + t_2)$ problem with strong vibronic coupling, orthorhombic minima, and tunneling [5.107] and in calculations of vibronic energy levels and tunneling splitting in a series of systems including fullerenes (Sections 5.3, 5.6, and 7.5).

The principal shortcoming of the method of unitary transformations (as of other variational methods) consists in the fact that it is not so universally applicable as, for instance, the Green-function method. Another deficiency in this method (and some other approaches) emerges from neglecting the changes of the frequencies of vibrations in the minima of the adiabatic potentials compared with the initial frequencies mentioned in Section 5.3; it results in

inaccurate behavior of the "tools" of the wavefunctions and consequently inaccurate energy intervals in the spectrum. This failure was corrected by introducing an additional scale transformation to take into account the anisotropy of vibrations in the JT wells [5.34]. More difficulties follow from the fact that the transformation shifts the system towards one of the minima, thus lowering the symmetry of the Hamiltonian and complicating the calculations [5.108] (see also [5.109]).

A general treatment of an E term interacting with harmonic oscillators in the presence of external fields employing some forms of unitary transformations with applications to the cyclobutane radical cation is given in [5.110]. Canonical transformations are also used in considering the PJTE in an $E \otimes e$ problem with a small splitting of the E term [5.111]. Analytical expressions for vibronic energy levels and wavefunctions in the $(s+p) \otimes t_{1u}$ problem are obtained in [5.112].

Calculation of vibronic coupling in positive and negative fullerene ions has its specific features in the competition of interelectron interaction controlled by Hund's rule and JT stabilization that favors degenerate terms. In a series of works devoted to $C_{60}^{n\pm}$ ions [5.113] calculations reveal important details of these interactions. In particular, in negative ions low-spin states prevail, whereas in positive ions high-spin states dominate, with the exception of ions with $4 \leq n \leq 6$, for which the nonadiabatic corrections that soften the vibrations and lower the zero-point energy push the states with lower spin below that of high spin. In a series of works (see [5.114] and references therein) the so-called Bogoliubov–de Gennes formalism was used to explore the JTE in fullerenes and their ions (see also Sections 7.5.3 and 8.4). For calculations for negative fullerene ions C_{60}^{n-} with the n excessive electrons in t_{1u} orbitals and JT $p^2 \otimes h$ and $p^4 \otimes h$ problems see in [5.115]. Here it is worth noting also attempts to find exact analytical solutions for some vibronic problems [5.116].

5.5 Solutions of multimode problems

As formulated in Section 3.5, the multimode JT problem occurs when there are more than one JT-active vibrational modes of the same symmetry, distinct from the ideal problems where there is only one such mode. Qualitatively, it is clear that in general all the JT-active vibrations are involved in the JT distortions (and in the rotations of this distortion around the JT center), but the measures of their involvement may be different. If the degenerate electronic state is localized mostly on the JT center, the first coordination sphere around this center (the near-neighbor atoms) will be directly involved in the JT

distortion by the vibronic coupling, while the next and further away layers of atoms will be affected indirectly, via their vibrational interaction with the directly coordinated atoms. Obviously, the further the atomic layer from the JT center, the smaller the distortion influence. The dynamic picture is thus a wave of distortions around the JT center that, strictly speaking, covers the whole polyatomic system, but the amplitude of distortion is rapidly falling with distance from the center. In the crystal environment this looks like an electron–vibrational formation of a *polaron* type, which performs free (in case of an equipotential trough on the APES) or hindered (in the presence of potential barriers between equivalent wells) rotations or pulse motions (for high barriers and tunneling), similar to the corresponding dynamics in ideal JT systems (Sections 5.1–5.4).

Mathematically, in the multimode problem the JT-active coordinates of the same symmetry (symmetrized coordinates) are linear combinations of the displacements of all the atoms of the system, but the vibronic coupling to them is the larger, the greater the coefficient of contribution of the atoms of the first coordination sphere. By including all of them in the vibronic interaction directly we get a very difficult multidimensional problem. As shown in Section 3.5, as far as the form of the APES in this multidimensional space is concerned, the number of active modes can be reduced to one effective mode, sometimes called the interaction mode. This cannot be done for the solution of the vibronic equations.

With regard to the solution for the energy spectrum and wavefunctions there are two aspects of the multimode problem. For molecular systems and clusters with a limited number of coordination spheres around the JT center the number of vibrational modes to be included in the vibronic coupling is finite, mostly a small number, beginning with two. In many cases this problem can be solved by numerical methods, similar to the ideal problem (see below). However, if the environment of the JT center is large (like in the case of an impurity center in crystals) the number of JT-active modes becomes very large (infinite), and the solution of the problem requires other approaches.

The solution of the multimode JT problem is discussed in a series of papers (see [5.1, 5.70–5.72, 5.97–5.98, 5.117–5.131] and references therein). For the simplest linear multimode (n-mode) $E \otimes (e_1 + e_2 + \cdots + e_n)$ problem the vibronic coupling to each of these modes leads to formation of a circular trough of equipotential minima on the APES, so its lowest sheet as a function of the polar coordinates of all these modes including their interaction looks as follows [5.117]:

$$\varepsilon(\rho_i, \phi_i) = \frac{1}{2}\sum_i \omega_i^2 \rho_i^2 - \left(\sum_i k_i^2 \omega_i^2 \rho_i^2 + 2 \sum_{i>j} k_i k_j \omega_i \omega_j \rho_i \rho_j \cos(\phi_i - \phi_j) \right)^{\frac{1}{2}} \tag{5.65}$$

where, following the references above, we used here dimensionless vibronic coupling constants k_i (Section 3.2), and set $\hbar = 1$, so ω is given in units of energy and ρ is dimensionless too (ρ_i and ϕ_i in Eq. (5.65) stand for the coordinates of all the modes). The minimum of this expression is attained at

$$\rho_{i0} = k_i, \qquad \phi_{i0} = \phi_{j0} = \phi \tag{5.66}$$

meaning that the n circular troughs may have different radii, but a common rotational angle ϕ, the energy being independent of the latter. Similar to the ideal problem, the JT stabilization energy (the energy at the minima) is

$$E_{\mathrm{JT}} = \varepsilon(\rho_{i0}, \phi) = -\frac{1}{2}\sum_i k_i^2 \omega_i = -\frac{1}{2} k_{\mathrm{eff}}^2 \omega_{\mathrm{eff}} \tag{5.67}$$

Here the effective coupling constant $k_{\mathrm{eff}}^2 = \sum_i k_i^2$ and effective frequency (energy) $\omega_{\mathrm{eff}} = \sum_i k_i^2 \omega_i / k_{\mathrm{eff}}^2$ are introduced for convenience (cf. Section 3.5). For the energy levels with the potential (5.65), the dynamic problem should be solved. The energies for the ideal problem with one active vibration in the strong coupling limit are given by Eq. (5.18), which in the notations of this section are

$$E_{nm} = -\tfrac{1}{2}k^2\omega + (n - \tfrac{1}{2})\omega + \tfrac{1}{2}\omega k^{-2} m^2 + O(k^{-4}) \tag{5.68}$$

where the vibrational energy here is read off that of the doubly degenerate oscillator (at $n = 0$) and the last term stands for higher-order corrections in terms of the inverse coupling constant. In the multimode case the problem is more complicated essentially because of the shift of the vibrational frequencies ω_i due to the mode interactions via the vibronic coupling. The new modes ν_j follow the transcendental equation [5.1, 5.130]

$$\sum_j \frac{k_j^2 \omega_j^3}{\omega_j^2 - \nu^2} = \sum_i k_i^2 \omega_i \tag{5.69}$$

Graphic analysis of this equation shows that it has many solutions. For any k_i and ω_i the lowest solution is $\nu_1 = 0$. This is the "soft mode" of free rotation in the circular trough. The other solutions follow the inequalities $\omega_{j-1} \le \nu_j \le \omega_j$, the ν_j value being nearer to the mode with weaker coupling (smaller k_j; at $k_j = 0$, $\nu_j = \omega_j$). In particular, for a two-mode problem $E \otimes (e_1 + e_2)$

$$\begin{aligned} \nu_1 &= 0 \\ \nu_2 &= [\omega_1 \omega_2 (k_1^2 \omega_2 + k_2^2 \omega_1)/(k_1^2 \omega_1 + k_2^2 \omega_2)]^{\frac{1}{2}} \end{aligned} \tag{5.70}$$

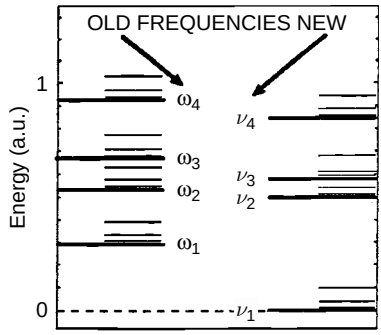

Fig. 5.23. Comparison of uncoupled (old) vibrational frequencies ω_i with the (new) frequencies ν_i coupled via vibronic interaction in a multimode JT problem with strong vibronic coupling obtained from approximate (semiclassical) solution of Eq. (5.69). The thin lines represent low-lying pseudorotational levels (reprinted with permission from [5.130]. Copyright 1998 American Institute of Physics).

Figure 5.23 shows schematically the relative positions of ν_j and ω_j in Eq. (5.69).

With the frequencies ν_j known the lowest energy levels in the multimode problem are given by the following equations [5.130]:

$$E_{0m} = -\frac{1}{2}k_{\text{eff}}^2\omega_{\text{eff}} + \frac{1}{2}\sum_j(\nu_j - \omega_j) + \frac{m^2}{2\sum_j k_j^2\omega_j^{-1}} \tag{5.71}$$

where m is the same as in Eqs. (5.18) and (5.68).

In the "effective-mode" approximation [5.117] which avoids calculation of the new (real) frequencies ν_j, an average squared frequency $\overline{\omega}^2 = \sum_i k_i^2\omega_i^2/k_{\text{eff}}^2$ is introduced (in addition to the above $\omega_{\text{eff}} = \sum_i k_i^2\omega_i/k_{\text{eff}}^2$), with which the multimode $E\otimes(e_1+e_2+\cdots+e_n)$ lowest-state energy is

$$E_{0,\pm1/2} = -\frac{1}{2}k_{\text{eff}}^2\omega_{\text{eff}} - \frac{1}{2}\omega_{\text{eff}} - \frac{1}{4}\frac{\overline{\omega}^2 - \omega_{\text{eff}}^2}{\omega_{\text{eff}}} + O(k_{\text{eff}}^{-2}) \tag{5.72}$$

with more complicated terms for higher m values.

Numerical calculations for a two-mode problem [5.130] show that the differences between this expression and the more accurate Eq. (5.71) with the frequencies ν_j from Eq. (5.70) is the larger, the greater the difference between the two frequencies ω_1 and ω_2 and reaches ~5% of ω_{eff} at $\omega_2 = 10\omega_1$.

A similar formula was derived [5.130] for the multimode problem $T\otimes(h_1+h_2+\cdots+h_n)$ for fullerene systems (Section 3.4). In particular, the ground-state energy is given by a formula similar to Eq. (5.72),

Table 5.3 *Frequencies ω_i, coupling constants k_i, energies $\frac{1}{2}k_i^2\omega_i$, and new frequencies ν_i in the eight-mode JT problem $T\otimes(h_1+h_2+\cdots+h_8)$ for C_{60}^- (from [5.130])*

i	$\omega_i\,(\mathrm{cm}^{-1})$	k_i	$\frac{1}{2}k_i^2\omega_i\,(\mathrm{cm}^{-1})$	$\nu_i\,(\mathrm{cm}^{-1})$
1	270.0	0.868	101.71	0.0
2	430.5	0.924	183.78	329.5
3	708.5	0.405	58.11	633.8
4	772.5	0.448	77.52	742.3
5	1099.0	0.325	58.04	1031.8
6	1248.0	0.000	0.00	1248.0
7	1426.0	0.368	96.56	1302.4
8	1575.0	0.368	106.65	1519.0
	$\omega_{\mathrm{eff}}=581.1$	$K_{\mathrm{eff}}=1.532$	$\sum_i \frac{1}{2}K_i^2\omega_i = 682.36$	

$$E_0 = -\frac{1}{2}K_{\mathrm{eff}}^2\omega_{\mathrm{eff}} + \sum_j (\nu_j - \omega_j) + O(K_{\mathrm{eff}}^{-2}) \tag{5.73}$$

The results of numerical calculations for an eight-mode problem $T\otimes(h_1+h_2+\cdots+h_8)$ of C_{60}^- are given in Table 5.3.

The formulas for the energy levels are simpler for systems with weak vibronic coupling taken into account by perturbation theory. It turned out (see [5.1]) that odd-order perturbation corrections to the energy vanish, so for the $E\otimes(e_1+e_2)$ problem the fourth-order correction to the ground-state energy is [5.118]

$$E_0^{(4)} = \frac{1}{2}\left(\frac{F_1^4/K_1^2}{\hbar\omega_1} + \frac{F_2^4/K_2^2}{\hbar\omega_2}\right) + 2\frac{(F_1^2/K_1)(F_2^2/K_2)}{\hbar\omega_1+\hbar\omega_2} \tag{5.74}$$

where in the notations of Section 3.2 the first term gives the sum of corrections to the JT stabilization energies of the two modes (cf. Eq. (3.96)) and the last term stands for their interaction via the vibronic coupling. In the same approximation the energy gap to the lowest excited state (which is $\hbar\omega_1$ in the unperturbed system) is [5.118]

$$\Delta E_0^{(4)} = -\frac{3}{2}\frac{F_1^4/K_1^2}{\hbar\omega_1} + 2\frac{(F_1^2/K_1)(F_2^2/K_2)}{\hbar\omega_1}\frac{3\omega_2^2-\omega_1\omega_2-\omega_1^2}{\omega_1^2-\omega_2^2} \tag{5.75}$$

The energy gap to the next excited state (equal to $\hbar\omega_2$ in the zeroth-order approximation) can be obtained by interchanging the indices 1 and 2 in (5.75). The second term diverges at $\omega_1=\omega_2$, where there is accidental degeneracy of

the two single-phonon states. In this case degenerate perturbation theory has to be employed. If $\omega_1 < \omega_2$, the second term in Eq. (5.75) is negative, which means that the mixing of the modes results in the reduction of the smaller energy gap. These results are confirmed also by numerical calculations for the $E \otimes (e_1 + e_2)$ problem [5.69–5.71, 5.117–5.119, 5.130].

The case of an infinite number of JT-active modes of the same symmetry inherent to JT impurity centers in crystals is most important in solid-state applications (Section 8.1). For so-called impurity centers of "small radius," for which the wavefunctions of the degenerate state are rather localized, the situation is somewhat similar to a finite-mode problem, but the infinite number of active modes makes it technically different. One of the approaches mentioned above is to assume that the vibronic coupling is nonzero only to the first coordination sphere, while all the other atoms in further layers are involved via their vibrational interaction with the first neighbors to the JT center. The active JT modes of the system are described by symmetrized coordinates $Q_{n\Gamma\gamma}$ that involve the normal coordinates q_k of all the (n) coordination spheres (see Eq. (3.100)):

$$Q_{n\Gamma\gamma} = \sum_k a_k(n\Gamma\gamma) q_k$$

where the coefficients $a_k(n\Gamma\gamma)$ can be evaluated for specific cases [5.132, 5.133]. In these coordinates the vibronic coupling contains phonon interaction terms including the interaction of the first coordination sphere $n = 1$ with all the others, which for the $E \otimes (e_1 + e_2 + \cdots)$ problem in polar coordinates is

$$H_{\text{int}} = \sum_n K_{n1}^{(E)} \rho_n \rho_1 \cos(\phi_n - \phi_1) \tag{5.76}$$

where

$$K_{nm}^{(\Gamma)} = \sum_k a_k(n\Gamma\gamma) a_k(m\Gamma\gamma) K_k^{(\Gamma)} \tag{5.77}$$

and $K_k^{(\Gamma)}$ is the crystal analog of the force constant ($K = M\omega^2$) for the k branch of the Γ phonons.

This interaction leads to expressions that in essence are similar to Eq. (5.65) and results in the same condition of minimum at $\phi_n = \phi_1$ which means that rotation of the distortion of the first coordination sphere involves the whole crystal forming a polaron-like formation that travels around the impurity center. This concerted rotation is stationary because the corresponding momentum is an integral of motion [5.1]. In spite of this physically visual picture of the phenomenon, its quantitative treatment is rather complicated. In the

weak-coupling limit the corrections to the energy spectrum may be obtained by second-order perturbation theory, which makes the JT contributions of different modes additive. Using the Green-function method, it was shown [5.1, 5.98, 5.100] that in the limit of weak coupling, the JTE produces some local and pseudolocal resonances. If the initial density of states in the crystal is

$$\rho_{\Gamma}^{(0)}(\omega) = \sum_{k} a_k^2(\Gamma\gamma)\delta(\omega_k^2 - \omega^2) \tag{5.78}$$

the redetermined density of states has the shape of a Lorentzian [5.1]:

$$\rho(\omega) \sim \frac{1}{\pi}\frac{\gamma_\alpha}{(\omega - \omega_\alpha)^2 + \gamma_\alpha^2} \tag{5.79}$$

where for the $E \otimes (e_1 + e_2 + \cdots)$ problem (the prime means derivative)

$$\gamma_\alpha \approx \rho_E^{(0)}(\omega_\alpha)/[r_E^{(0)}(\omega_\alpha)]' \tag{5.80}$$

and $r_E^{(0)}$ is a Gilbert transform,

$$r_E^{(0)}(\omega_\alpha) = \frac{1}{\pi}\int_0^{\omega_{\max}} \frac{z\rho_E^{(0)}(z)}{\omega_\alpha^2 - z^2}\,dz \tag{5.81}$$

Here $\omega_{\max}$ is the largest frequency of the lattice vibrations and ω_α are the roots of the transcendental equation

$$1 \pm \frac{4\pi}{\hbar\omega} r_E^{(0)}(\omega)\tilde{E}_{\mathrm{JT}}^E = 0 \tag{5.82}$$

where $\tilde{E}_{\mathrm{JT}}^E = \sum_n F_{nE}^2/K_{nE}$ is the "total" JT stabilization energy equal to the sum of all active mode contributions.

If some of the roots fall within the forbidden zone where $\rho_E^{(0)}(\omega) = 0$, $\rho(\omega)$ in Eq. (5.79) becomes a δ-function, and Eqs. (5.82) and (5.81) yield a local state. As seen from the dispersion equation (5.82), its roots depend essentially on the total JT stabilization energy $\tilde{E}_{\mathrm{JT}}^E$.

Hence even weak vibronic coupling may lead to essential redetermination of the density of states in the impurity crystal, in particular, to the formation of local (pseudolocal) states in the forbidden zone. These states can be interpreted as follows. Without the vibronic coupling the continuous spectrum of the lattice can be considered as a spectrum of free phonons. In the presence of weak vibronic coupling the wavefunction of the ground state becomes mixed with one-phonon excited states and describes finite motions of the electron–phonon system that can be considered as coupled states of the impurity center with a phonon. The weak vibronic coupling produces a low-symmetry

electron distribution that rotates around the JT impurity center involving one phonon captured in a stationary orbital.

In general such local and pseudolocal states split off from the continuous phonon bands in crystals (often called "*hybrid states*" and "*dialectric modes*") were considered in solid-state theory (see, e.g., [5.134] and the review article [5.135]). The specifics of the JT local mode is that it is created by a low-symmetry distortion that rotates around the impurity center (most studied totally symmetric polarons have no rotational properties). This is one of the essential differences between usual (traditional) and JT approaches to electron–phonon coupling mentioned in the introduction and in Section 4.5 (see also Section 8.2.5). It may result in qualitatively new properties of the system (see, e.g., superconductivity in Section 8.4).

The multimode $T \otimes (t_2^{(1)} + t_2^{(2)} + \cdots)$ and $\Gamma_8 \otimes (t_2^{(1)} + t_2^{(2)} + \cdots)$ problems in the weak-coupling limit using Green's function method were considered in [5.98].

In the other limit of the multimode JT problems with strong vibronic coupling the lowest energy states with the lowest sheet of the APES (Section 3.5) can be considered in the adiabatic approximation, similar to the ideal case. With an infinite number of JT active modes the problem has some features which are similar to that of a limited number of modes, described above. For the $E \otimes (e_1 + e_2 + \cdots)$ problem with only linear coupling the APES can be presented as follows [5.1] (cf. Section 3.2, Eq. (3.23)):

$$\varepsilon_{\pm}(Q_{n\vartheta}, Q_{n\varepsilon}) = \frac{1}{2}\sum_n K_{nE}(Q_{n\vartheta}^2 + Q_{n\varepsilon}^2) \pm \left[\left(\sum_n F_{nE}Q_{n\vartheta}\right)^2 + \left(\sum_n F_{nE}Q_{n\varepsilon}\right)^2\right]^{\frac{1}{2}} + \frac{\hbar^2 m^2}{2I} \tag{5.83}$$

where the last term is a crystal analog of the centrifugal energy of the ideal case in Eq. (5.20) (see also Fig. 5.4) with I as the moment of inertia of the concerted rotation of the distortion,

$$I = \sum_n \frac{F_{nE}^2/K_{nE}}{\omega_{nE}^2} \tag{5.84}$$

On introducing the angular velocity of this rotation $\mathbf{\Omega} = m\hbar/I$ and using the condition of minimum energy in (5.83), we get for the $\mathbf{\Omega}$ value the following equation which is similar to Eq. (5.69) [5.1]:

$$\mathbf{\Omega}\sum_n \frac{(F_{nE}^2/K_{nE})\omega_{nE}^2}{(\omega_{nE}^2 - \mathbf{\Omega}^2)^2} = m\hbar \tag{5.85}$$

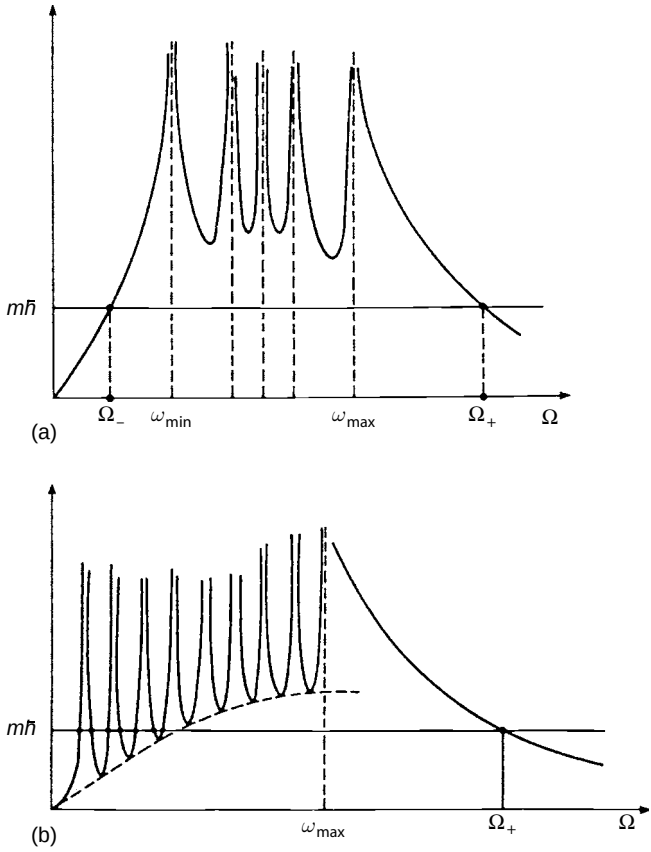

Fig. 5.24. Graphical solution of the transcendental Eq. (5.85) for the multimode JT $E \otimes (e_1 + e_2 + \cdots)$ problem with strong vibronic coupling. (a) Molecular multimode vibronic coupling with one optical vibrational mode. The dashed lines are the asymptotes of the left-hand side of the equation crossing at the points $\mathbf{\Omega} = \omega_n$. For strong vibronic coupling only two solutions, $\mathbf{\Omega}_+$ and $\mathbf{\Omega}_-$, remain. (b) A JT (impurity) center in a crystal interacting with the acoustic vibrational mode. The sloping dashed line is the envelope of the minimum points of the left-hand side of the equation for low frequencies (from [5.1]).

Figure 5.24 illustrates the graphic solution of this transcendental equation in two cases: (a) interaction with only optical vibrations of the lattice that have relatively high frequencies ω_{nE} (this case is similar to the molecular problem with a limited number of JT active modes of the same symmetry); and (b) the infinite number of acoustic modes of the lattice ω_{nE} are JT active. In the former case for sufficiently strong vibronic coupling the minima of the left-hand-side expression in Eq. (5.85) as a function of $\mathbf{\Omega}$ lie above the line $m\hbar =$ constant. Therefore there are only two roots of Eq. (5.85): $0 < \mathbf{\Omega}_- < \omega_{\min}$ and $\mathbf{\Omega}_+ > \omega_{\max}$

(Fig. 5.24(a)). Here $\omega_{\min}$ and $\omega_{\max}$ are the lower and upper limits of the optical band frequencies, and $\mathbf{\Omega}_-$ and $\mathbf{\Omega}_+$ are the JT concerted rotation frequencies in the lower and upper branches of the APES, respectively.

If the acoustic modes are involved in the JT distortions their frequencies ω_{nE} begin from $\omega_{0E}=0$, so we come to the solution of Eq. (5.85) illustrated in Fig. 5.24(b). We see that there may be an infinite number of $\mathbf{\Omega}$ values, beginning with very small ones. The envelope of the minima between the singularities $\mathbf{\Omega}=\omega_{nE}$ shown by the dashed line in Fig. 5.24(b) follows the expression $F_E^2\overline{\omega}^{-4}\mathbf{\Omega}$, where $\overline{\omega}^{-k}$ is defined quite similarly to $\overline{\omega}^{-2}$ in the text before Eq. (5.72):

$$\begin{aligned}\overline{\omega}_E^m &= \sum_n \omega_{nE}^m F_{nE}^2/F_E^2\\ F_E^2 &= \sum_n F_{nE}^2\\ \overline{K}_E^m &= \sum_n K_{nE}^m F_{nE}^2/F_E^2\end{aligned} \tag{5.86}$$

Here the definitions $\overline{K}_E = M\overline{\omega}_E^2$ and $\overline{K}_E^{-1} = M^{-1}\overline{\omega}_E^{-2}$ are implied.

For $\omega_{\min}=0$, we get $\mathbf{\Omega}\approx 0$, meaning solutions with low-to-zero concerted rotation frequencies for which the moment of inertia $I_- = m\hbar/\mathbf{\Omega}_-$ tends to infinity. For the small ω_{nE} values the force constant $K_{nE}=M\omega_{nE}$ is also very small, making the radius of the JT trough $\rho^{(0)}$ tend to infinity too ($\rho_n^{(0)} \sim F_{nE}/K_{nE}$). Hence in the radial direction the lower sheet of the APES has a "ravine" with a warped bottom going to infinity. However, this singularity does not affect very strongly the solution of the problem: the density of the limiting long-wavelength acoustic phonons is negligibly small, so the ravine contracts rapidly with the distance from the impurity center.

With infinite moment of inertia I the concerted rotation of the distortion cannot be excited. On the other hand the interaction of the first coordination sphere (which is most affected by the vibronic coupling) with the low-frequency acoustic phonons is proportional to ω^3 [5.1] and hence tends to zero, so these phonons may be neglected in the first approximation. This means that quasistationary rotations are possible, yielding *rotational resonances* in the vibronic density of states, which are subject to weak decay due to the participation of the utmost long-wavelength vibrations.

The mathematical realization of these physical ideas is not straightforward. For the linear $E\otimes(e_1+e_2+\cdots)$ problem the peaks in the density of states are located at frequencies which are the roots of the following equation [5.120(*a*)]:

$$2\pi r_E^{(0)}(\omega) + \overline{\omega}^{-2} = 0 \tag{5.87}$$

where $r_E^{(0)}$ is given by Eq. (5.81). The relaxational broadening of these rotational states is considered in [5.120(*b*)]. From the general physical point of view these rotational states of JT distortions around the impurity center may be viewed as *multiphonon electron–vibrational formations of polaron type* localized on a degenerate quasistationary orbital. The stronger the vibronic coupling, the greater the lifetime of this low-symmetry quasi-polaron and the smaller the width of the rotational resonances.

The treatment of the upper branch of the APES in the $E \otimes (e_1 + e_2 + \cdots)$ problem by means of perturbation theory considering the term H_{int} in (5.76) as a small perturbation leads to rotational resonances, sometimes called *Slonczewski resonances* [5.97, 5.121]. A similar treatment of the lower branch proved to be incorrect as a general approach, but may be satisfactory when the interaction of the first coordination sphere with the remaining lattice is sufficiently small, as in the *cluster model* [5.1]. The Green-function method was also applied to the multimode $\Gamma_8 \otimes (e + t_2)$ problem with strong vibronic coupling [5.122].

So far only linear multimode vibronic coupling has been considered. However, the quadratic and cubic terms of vibronic coupling may be significant, as discussed in more detail in the treatment of ideal problems (Chapters 3–5). In particular, for the $E \otimes e$ problem the joint contribution of quadratic, cubic, and PJT coupling results in three equivalent minima along the bottom of the trough (of the APES in the linear coupling approximation) divided by three barriers, leading to essential redetermination of the spectrum of vibronic states, including the tunneling phenomena (Section 5.3). In the multimode $E \otimes (e_1 + e_2 + \cdots)$ problem the treatment can be carried out in a similar (to the ideal problem) fashion [5.123]. In the approximation when the motion along the trough is much slower than the radial vibrations, the former obey the following equation (cf. Eq. (5.24)):

$$\left(-\alpha \frac{\partial^2}{\partial \phi^2} - \beta \cos(3\phi) - E_m\right)\Phi(\phi) = 0 \tag{5.88}$$

where

$$\alpha = \frac{\hbar^2}{2M}(F_E \overline{K}_E^{-1})^{-2}, \qquad \beta = G_E F_E^2 (\overline{K}_E^{-1})^{-2} \tag{5.89}$$

and (following Eq. (5.86))

$$\overline{K}_E^{-1} = M^{-1}\overline{\omega}_E^{-2}, \qquad G_E = \sum_n G_{nE} F_{nE}^2 / F_E^2 \tag{5.89$'$}$$

with the lattice-averaged radial distortion as $\overline{\rho} = F_E \overline{K}^{-1}$.

Equation (5.88) is formally similar to Eq. (5.24) for the ideal case, but with the constants α and β after (5.89) that includes the "averaged" multimode information, especially the phonon and vibronic coupling dispersion in Eqs. (5.86) (5.89) and (5.89′).

The solutions of Eq. (5.88) are discussed in detail in Section 5.2. They correspond to hindered rotations of the polaron-type formation with multiple over-barrier reflections. For large β values the minima of the adiabatic potential are divided by rather high barriers. In a visual interpretation, the motion of the polaron formation in this case is reduced to tunneling through the barriers: for most of the time the quasi-polaron is centered at one of the minima along the fourth-order axis of the cubic system, jumping from time to time from one axis distortion to another one with the frequency of tunneling splitting.

The energy spectrum of the system under consideration is a superposition of the continuous spectrum of the fast subsystem (vibrations at the bottom of the minimum) and the discrete spectrum of the slow subsystem (hindered rotations along the trough or tunneling between the minima). Owing to the strong vibronic coupling the positions of the rotational levels of the slow subsystem are shifted toward the region of low frequencies where the density of states of the fast subsystem is small. For this reason the nonadiabatic corrections causing the broadening of the energy levels of the discrete spectrum are expected to be very small; this broadening was estimated in [5.123]. The approximation of the adiabatic separation of the radial and angular motions resulting in Eq. (5.88) also constrains the magnitude of the constant of quadratic vibronic interaction: $G_E K_E^{-1} \ll 1$. The magnitude of the tunneling splitting can be calculated, in principle, in a manner similar to the ideal case by using the method discussed in Section 5.3, which is valid for the multimode JT systems as well.

In some JT problems tunneling between the minima of the adiabatic potential is forbidden by symmetry restrictions. A simple example of this kind is provided by the $E \otimes (b_1 + b_2)$ problem. In such cases the modification of the vibronic spectrum is caused by the change of the curvature of the minima for the lowest states, and by the vibronic anharmonicity of the adiabatic potential for higher states. Since the change of the minimum curvature is of local origin, the problem can be reduced to that of changes in the force constant and can be relatively easily solved. A similar treatment for the multimode $T \otimes (e + t_2)$ problem with predominant coupling to e vibrations (where the tunneling is forbidden) is given in [5.124].

In cases where the tunneling is not forbidden by symmetry (these cases are in the majority, see Section 5.3) the vibronic spectrum of local and pseudolocal vibrations in the minima is complicated by additional lines of tunneling

splitting, and the whole spectral picture is complicated by relaxational broadening. Indeed, the tunneling energy levels are superimposed over the continuous vibrational spectrum, and the interaction of the vibrational system with the dynamic (tunneling) subsystem (not taken into account in the above treatments) results in relaxational broadening of the discrete energy levels. The magnitude of this broadening γ is proportional to the projected density of vibrational states $\rho(\omega)$ of the dissipative subsystem at the frequency of the tunneling splitting $\delta = r\Gamma$, $r = 3, 4, 6, \ldots$ (Section 5.3). For low-frequency acoustic vibrations with a Debye dispersion law, $\rho(\omega)$ is proportional to ω^4 and hence $\gamma \sim (r\Gamma)^4$. To observe the tunneling splitting $r\Gamma$, the broadening γ should be less than $r\Gamma$. In the case of strong vibronic coupling $r\Gamma$ may be very small, and since γ has a higher order of smallness, the above requirement is satisfied. As the vibronic coupling decreases, $r\Gamma$ increases, but $\gamma \sim (r\Gamma)^4$ increases faster and the effect of tunneling splitting disappears in the relaxational broadening. Note, however, that due to the strong exponential dependence of $r\Gamma$ on E_{JT}, tunneling splitting takes place even for rather moderate intermediate vibronic couplings, and therefore the range of applicability of the tunneling-splitting theory with respect to the vibronic coupling constant is rather large.

The tunneling states occur as weakly broadened peaks (resonances) in the vibronic density of states which, as above, can be interpreted as multi-phonon formations of a polaron type coupled with the impurity, i.e., as *low-symmetry inhomogeneities of the electronic density surrounded by a phonon fur coat*.

The multimode $T \otimes (t_2^{(1)} + t_2^{(2)} + \cdots)$ problem with tunneling and relaxation was considered in [5.136] in the limit of strong coupling and localized states in the four trigonal minima taken as a starting approximation (Section 5.3). Employing phonon densities $\rho_T(\omega)$ and Green functions, an expression for the tunneling splitting was derived in terms of the JT stabilization energy E_{JT}^T and averaged frequencies

$$\langle \omega^{-m} \rangle = \int \rho_T(\omega) \omega^{-m} \, d\omega \tag{5.90}$$

In the same approximation the relaxational broadening γ was estimated as

$$\gamma \approx 0.425 E_{\mathrm{JT}}^T \left(E_{\mathrm{JT}}^T / \hbar \omega_T^2 \langle \omega^{-1} \rangle \right)^{\frac{1}{2}} \exp\left(-1.29 E_{\mathrm{JT}}^T / \hbar \omega_T^2 \langle \omega^{-1} \rangle \right) \tag{5.91}$$

where $\omega_T = \left[\langle \omega^{-2} \rangle \right]^{-\frac{1}{2}}$. For a single acoustic phonon band and the Debye model of phonon dispersion the following approximate expressions were obtained for the tunneling splitting 4Γ and relaxational broadening γ:

$$4\Gamma = 0.2 E_{\mathrm{JT}}^T \exp(-0.96 E_{\mathrm{JT}}^T / \hbar \omega_{\mathrm{m}}) \tag{5.92}$$

$$\gamma \approx 0.5E_{\mathrm{JT}}^{T}(E_{\mathrm{JT}}^{T}/\hbar\omega_{\mathrm{m}})^{\frac{1}{2}}\exp(-1.72E_{\mathrm{JT}}^{T}/\hbar\omega_{\mathrm{m}}) \tag{5.93}$$

where ω_{m} is the maximum phonon frequency in the Debye model.

Equations (5.92) and (5.93) allow an approximate estimate of the condition $\gamma < 4\Gamma$ for the tunneling splitting to be observed in spite of relaxational broadening: $E_{\mathrm{JT}}^{T} \geq 1.5\hbar\omega_{\mathrm{m}}$. In other words, as mentioned above, in the strong-coupling limit the stronger the coupling, the better the conditions of observation of the tunneling splitting, in spite of the decrease in 4Γ with the strength of coupling (the γ value decreases faster). The condition for observation of tunneling is also improved by lower values of the Debye frequency ω_{m}.

For the *intermediate coupling* neither weak- nor strong-coupling limits apply, and the problem becomes more complicated. Some progress was achieved by using the methods of quantum field theory mentioned above applied to the pion–nucleon interaction, which has some analogies with the JT vibronic coupling theory [5.1, 5.97, 5.98(*b*)]. In particular, the method of dispersion equations applied to the lowest states of the multimode JT $E \otimes (e_1 + e_2 + \cdots)$ problem for impurity centers with intermediate coupling and a continuous spectrum of JT-active lattice vibrations yields the following local resonance frequency [5.98(*b*)]:

$$\omega_{\mathrm{r}} \approx \frac{\hbar\overline{\omega}^{2}}{F_E^2\overline{K}_E(\overline{K}_E^{-2})} \tag{5.94}$$

This resonance corresponds to the transition from the ground state with $m = 1/2$ to the rotational state with $m = 3/2$ [5.125]. The broadening of this level due to the processes of direct one-phonon decay is [5.98(*b*)]

$$\gamma \sim F_E\rho_E^{(0)}(\omega_{\mathrm{r}}) \tag{5.95}$$

Again, it follows from Eq. (5.94) that the rotational frequency decreases with the increase of the average vibronic coupling constant F_E, but the density of phonons $\rho_E^{(0)}(\omega_{\mathrm{r}})$ decreases faster, thus reducing the broadening γ.

The results above obtained under the assumption of a continuous phonon spectrum can nevertheless be applied to the ideal JT problem by assuming that the phonon band is infinitely narrow and has one frequency ω_E. In so doing the following expression was obtained for the energy gap ΔE between the ground and first excited vibronic states [5.98(*b*)]:

$$\Delta E = E_{3/2} - E_{1/2} = \hbar\omega_E\left[\left(1 + \frac{q^2F_E^4}{K_E^2\hbar^2\omega_E^2}\right)^{\frac{1}{2}} - \frac{qF_E^2}{K_E\hbar\omega_E}\right] \tag{5.96}$$

where $q = K_E(E)$ is here the vibronic reduction factor for E-type operators in the $E \otimes e$ problem (Section 5.6).

Similar analysis of possible low-frequency resonances in the spectral density was carried out for the $E \otimes (b_1 + b_2)$, $T \otimes t_2$, and $T \otimes (e + t_2)$ problems [5.98(*b*)]. These resonanaces may be considered as characteristic demonstrations of the multimode JT effect.

In the theory of impurity centers in crystals significant attention is paid to the so-called *quasimolecular (cluster) model* mentioned in Section 3.5. In this model a cluster with a limited number of atoms around the impurity center is cut off the lattice and considered separately from the remaining crystal, taking into account the influence of the latter as a perturbation or by means of an additional potential (e.g., a Madelung-like potential). In the cluster part the problem can be reduced to a multimode one with a limited number of JT-active modes.

The cluster-model treatment of JT problems proved to be successful in many applications. In particular, the results obtained in evaluation of expected ESR spectra of JT defects (Section 6.3) are in good agreement with the low-temperature experimental data in spite of the ignorance of the continuous phonon spectrum (for a review see [5.137] and Section 8.1). As above in considering the relaxational broadening, the explanation of this result lies in the small density of low-frequency phonon states. Simple estimates show that the density of states below the region of $\sim 0.1\hbar\omega_D$, where ω_D is the Debye frequency, is negligibly small and does not contribute to the relaxation, whereas the phonon states above $\sim 0.1\hbar\omega_D$ are not populated at sufficiently low temperatures. The relaxation processes become important at higher temperature where the JTE implications in the EPR spectrum disappear. With the cluster problem solved, the influence of the rest of the lattice can be included in a phenomenological way [5.71(*b*), 5.117(*a*), 5.126].

Another example where the cluster model works satisfactorily is the qualitative evaluation of the impurity optical absorption band shape (Section 6.1). Indeed, as discussed in Section 3.5, the APES for the multimode problem has qualitatively the same features as for the ideal problem, and therefore the envelope of the individual absorption lines, which for sufficiently strong coupling are determined mostly by the shape of APES, can be predicted without involving the details of the phonon spectrum. The optical band shapes can be evaluated also quantitatively, provided the JT characteristics of the APES are considered as adjustable parameters (Section 6.1).

To summarize, the cluster model may be very useful in describing either properties of JT systems at sufficiently low temperatures or integral (with regard to the spectrum), "averaged" characteristics, like JT distortions, local

dynamics, optical band shapes, etc. However, the fine structure of the spectrum is not reproduced well by this model.

An improvement of the cluster model is reached in the so-called model of the *relaxing cluster*, in which the influence of the lattice on the cluster is taken into account by perturbation theory (see the review article [5.127]). Obviously, this approximation is valid only when the influence of the lattice is smaller than that of the cluster energy spacing in crystals with narrow phonon bands. An advanced method is suggested in the so-called "*embedded cluster*" model (Sections 3.5 and 8.1, [3.57]). Another idea employs renormalization-group theory [5.128]. For a review of some of the earlier works on this topic see [5.127]. In [5.129] the statistical distribution of irregular vibronic energy levels in multimode problems is considered.

5.6 Vibronic reduction factors

The reduction of ground-state physical quantities of electronic origin in JT systems is one of the important effects of vibronic coupling. It originates from the back influence of the JT nuclear dynamics on the electronic structure and related properties. As follows from the discussions in Sections 5.1–5.5 in this chapter, in the majority of JT problems, except for strong quadratic coupling in the $E \otimes e$ and $T \otimes t_2$ problems and the special relation between the vibronic coupling constants in the linear $T \otimes (e + t_2)$ and $T \otimes h$ strong-coupling problems, the ground vibronic state has the same symmetry and degeneracy as the electronic term in the reference configuration. This coincidence of important characteristics of the ground states with and without vibronic coupling is very significant and allows essential simplification of the calculations of many properties of electronic origin. Already in the first calculations of the spin–orbital splitting of the ground vibronic state [5.138] it was shown that, ignoring the mixing with other vibronic levels, this splitting is proportional not only to the spin–orbital-coupling constant, as in the usual nonvibronic cases, but to this constant multiplied by the overlap integral between the vibrational functions of different minima, equal to γ in Eq. (5.47). Since $\gamma < 1$ the vibronic coupling essentially reduces the spin–orbital splitting, sometimes by several orders of magnitude. Ham [5.139, 5.140] generalized this idea and has shown that such a reduction occurs for any physical quantity, provided its operator depends on electronic coordinates only. This reduction is often called the *Ham effect*.

A series of works contributed to the earlier development of the vibronic reduction theory [5.138–5.155]. In review of these contributions, the following theorem of vibronic reduction can be formulated [5.1]. Suppose we need to

calculate the matrix element of the physical quantity $X_{\overline{\Gamma}\overline{\gamma}}(r)$ (transforming according to the γ line of the Γ irreducible representation of the symmetry group of the system) which depends on the electronic variables only, with the functions of the ground vibronic state $\Psi_{\Gamma\gamma}(r, Q)$. We denote the corresponding wavefunctions of the initial electronic term by $\psi_{\Gamma\gamma}(r)$. The theorem of vibronic reduction states that the matrix element of the operator $X_{\overline{\Gamma}\overline{\gamma}}(r)$ (which represents the corresponding observable properties) calculated with the vibronic functions $\Psi_{\Gamma\gamma}(r, Q)$ is proportional to the matrix element of the same operator calculated with the initial electronic wavefunctions $\psi_{\Gamma\gamma}(r)$ of the reference configuration:

$$\langle \Psi_{\Gamma\gamma_1}(r, Q)|X_{\overline{\Gamma}\overline{\gamma}}(r)|\Psi_{\Gamma\gamma_2}(r, Q)\rangle = K_\Gamma(\overline{\Gamma})\langle \psi_{\Gamma\gamma_1}(r)|X_{\overline{\Gamma}\overline{\gamma}}(r)|\psi_{\Gamma\gamma_2}(r)\rangle \tag{5.97}$$

where $K_\Gamma(\overline{\Gamma})$ is a constant which depends on the JT vibronic properties of the Γ state and the symmetry $\overline{\Gamma}$ of the operator X, independent of its nature. The constant $K_\Gamma(\overline{\Gamma})$ is called the *vibronic reduction factor* (not to be confused with the curvature or force constants denoted by K_Γ). *If the vibronic reduction factors $K_\Gamma(\overline{\Gamma})$ are known, there is no necessity to solve the vibronic problem in order to obtain electronic properties of the ground state; they can be calculated from wavefunctions of the initial electronic term.* In particular, the $K_\Gamma(\overline{\Gamma})$ constants can be determined from some experimental data, and then used to predict the vibronic contribution to all the other observable properties.

In an extended definition, *off-diagonal vibronic reduction factors* $K_{\Gamma\Gamma'}(\overline{\Gamma})$ are also used to estimate the difference between off-diagonal matrix elements calculated by vibronic state wavefunctions and their pure electronic components. Such reduction factors emerge when there is an excited vibronic (tunneling) state Γ' close to the ground-state one Γ, and the matrix elements of the operator X under consideration contain off-diagonal elements. Since the electronic part in all the tunneling state wavefunctions is built up from the same electronic functions of the degenerate electronic term, the off-diagonal elements contain the same electronic reduced matrix element $\langle \psi_\Gamma||X_{\overline{\Gamma}}||\psi_\Gamma\rangle$, but with different coefficients that depend on the symmetries of the two states and the overlap integrals of the vibrational functions in two near-neighbor minima. Therefore the off-diagonal matrix element can be presented in a manner formally similar to the diagonal one by means of off-diagonal vibronic reduction factors $K_{\Gamma\Gamma'}(\overline{\Gamma})$ [5.1, 5.139]:

$$\langle \Psi_{\Gamma_1\gamma_1}(r, Q)|X_{\overline{\Gamma}\overline{\gamma}}(r)|\Psi_{\Gamma_2\gamma_2}(r, Q)\rangle = K_{\Gamma\Gamma'}(\overline{\Gamma})\langle \psi_\Gamma(r)||X_{\overline{\Gamma}}(r)||\psi_\Gamma(r)\rangle\langle \overline{\Gamma}\overline{\gamma}\Gamma_2\gamma_2|\Gamma_1\gamma_1\rangle \tag{5.97'}$$

where the tabulated Clebsch–Gordan coefficient $\langle \overline{\Gamma}\overline{\gamma}\Gamma_2\gamma_2 | \Gamma_1\gamma_1 \rangle$ satisfies the symmetry requirements. Note, however, that while $K_\Gamma(\overline{\Gamma})$ is always reducing the matrix element ($K_\Gamma(\overline{\Gamma}) \leq 1$), the off-diagonal factor $K_{\Gamma\Gamma''}(\overline{\Gamma})$ may be either reducing or enhancing, so its denotation as a reduction factor should not be taken literally. To calculate $K_\Gamma(\overline{\Gamma})$ or $K_{\Gamma\Gamma''}(\overline{\Gamma})$, Eqs. (5.97) and (5.97′) can be employed directly, provided the wavefunctions of the initial electronic and final vibronic states for the JT problem under consideration are known.

In the majority of practical cases the operator $X_{\overline{\Gamma}\overline{\gamma}}(r)$is a perturbation, and there are important cases when second-order perturbation corrections determine the property under consideration. In such cases second-order vibronic coupling constants $K_\Gamma^{(2)}(\overline{\Gamma})$ are important (see below).

Approximate analytical expressions for the vibronic reduction factors in the linear $E \otimes e$ problem $K_E(A_2)$ and $K_E(E)$, often denoted by p and q, respectively, can be derived immediately from the approximate solutions to the problem (Sections 3.2, 5.1, and 5.2) by calculating the ratio of the integrals in Eq. (5.97). It can be shown that for the ideal problem with linear coupling the following relationship is valid:

$$2q - p = 1 \tag{5.98}$$

In the case of weak vibronic coupling with $E_{\mathrm{JT}}^E \ll \hbar\omega_E$,

$$p \approx \exp(-4E_{\mathrm{JT}}^E/\hbar\omega_E) \tag{5.99}$$

For arbitrary coupling the value of p can be derived from the numerical solutions [5.55]; for $\sim 0.1 \leq E_{\mathrm{JT}}^E/\hbar\omega_E \lesssim 3.0$ they obey the function [5.142]

$$p = \exp[-1.974(E_{\mathrm{JT}}^E/\hbar\omega_E)^{0.761}] \tag{5.100}$$

These data are illustrated in Fig. 5.25. For sufficiently strong vibronic coupling $p = 0$ and $q = \frac{1}{2}$. Note that in this limit case the asymptotic behavior of p is not exponential: $p \sim (E_{\mathrm{JT}}^E/\hbar\omega_E)^{-2}$.

The relation (5.98) is, strictly speaking, invalid in the general case. In particular, it fails in the multimode problem, as well as under quadratic vibronic coupling. In general $2q - p \leq 1$, and the deviation from unity may be regarded as an indicator of quadratic and/or multimode effects. It can be shown [5.120(*a*)] that in the multimode $E \otimes e$ problem with strong vibronic coupling $p = 0$ and $q = \frac{1}{2}\exp(-M/2)$, where $M \geq 0$ and depends on the value of the dimensionless vibronic constant.

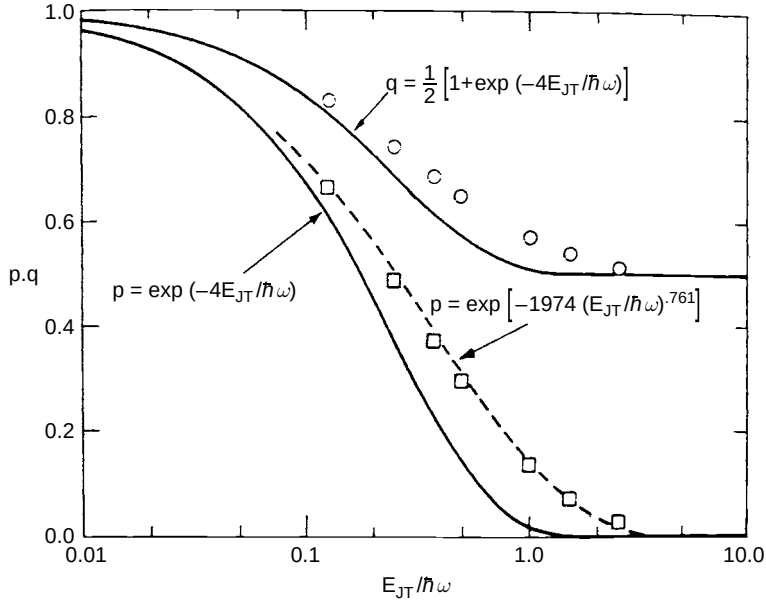

Fig. 5.25. Vibronic reduction factors $p = K_E(A_2)$ and $q = K_E(E)$ as functions of the dimensionless coupling constant $\lambda_E = E_{JT}^E/\hbar\omega_E$ for the linear $E \otimes e$ problem. Exact numerical values are shown by points; the dashed line is chosen to fit the numerical data in the region $0.1 \leq \lambda_E \leq 3.0$ [5.140].

Although in general the relationship (5.98) does not hold in multimode problems, it still holds in second-order perturbation theory in the weak-coupling case. In fourth-order perturbation theory we have [5.95, 5.147] (Section 5.5)

$$p = 1 - 2\sum_n \frac{F_{nE}^2/K_{nE}}{\hbar\omega_n} + 4\left(\sum_n \frac{F_{nE}^2/K_{nE}}{\hbar\omega_n}\right)^2$$
$$q = \frac{1}{2}(1+p) - \frac{1}{2}\sum_{n,m} \frac{F_{nE}^2/K_{nE}}{\hbar\omega_n}\frac{F_{mE}^2/K_{mE}}{\hbar\omega_m}\left(\frac{\omega_n - \omega_m}{\omega_n + \omega_m}\right)^2 \tag{5.101}$$

In the multimode $E \otimes e$ problem with strong linear vibronic coupling $p = 0$ (this is a result of the adiabatic approximation), while $q = \frac{1}{2}(1+p) = \frac{1}{2}$.

Quadratic terms of the vibronic interaction also result in violation of the relationship (5.98). In the limit of strong vibronic coupling, using the tunneling states (5.39)–(5.41) to determine q and p, we find [5.148, 5.149]

$$p = 0, \qquad q \leq \frac{1}{2} \tag{5.102}$$

Strong vibronic coupling means tunneling levels that are close in energy (Section 5.3), the mixing of which under perturbations may influence significantly the observable properties. To take into account this effect in the vibronic coupling problems the off-diagonal vibronic reduction factors mentioned above (Eq. (5.97′)) can be employed. For the $E \otimes e$ problem, there is only one such off-diagonal reduction factor for the mixing of the lowest E and A tunneling states $K_{AE}(E)$, often denoted by r. In the limit of strong coupling $r = \pm 1/\sqrt{2}$ [5.139].

Similarly, for the $T \otimes (e + t_2)$ problem in the limiting case of weak coupling we have [5.1]

$$\begin{aligned} K_T(E) &= 1 - \frac{9}{4}\frac{E_{\mathrm{JT}}^T}{\hbar\omega_T} \\ K_T(T_1) &= 1 - \frac{3}{2}\frac{E_{\mathrm{JT}}^E}{\hbar\omega_E} - \frac{9}{4}\frac{E_{\mathrm{JT}}^T}{\hbar\omega_T} \\ K_T(T_2) &= 1 - \frac{3}{2}\frac{E_{\mathrm{JT}}^E}{\hbar\omega_E} - \frac{3}{4}\frac{E_{\mathrm{JT}}^T}{\hbar\omega_T} \end{aligned} \tag{5.103}$$

In the absence of vibronic interactions with t_2 vibrations the $T \otimes e$ problem can be solved exactly. Simple calculations result in

$$K_T(E) = 1, \qquad K_T(T_1) = K_T(T_2) = \exp\left(-\frac{3}{2}\frac{E_{\mathrm{JT}}^E}{\hbar\omega_E}\right) \tag{5.104}$$

If the vibronic coupling to t_2 vibrations is stronger than the e coupling (Section 3.3), the limiting values of the vibronic reduction factors for very strong coupling are

$$K_T(E) = 0, \qquad K_T(T_1) = 0, \qquad K_T(T_2) = \tfrac{2}{3} \tag{5.105}$$

Approximate expressions for intermediate coupling were estimated by interpolation between the strong- and weak-coupling expressions [5.139] (Fig. 5.26):

$$\begin{aligned} K_T(E) \approx K_T(T_1) &= \exp\left(-\frac{9}{4}\frac{E_{\mathrm{JT}}^T}{\hbar\omega_T}\right) \\ K_T(T_2) &\approx \frac{1}{3}\left[2 + \exp\left(-\frac{9}{4}\frac{E_{\mathrm{JT}}^T}{\hbar\omega_T}\right)\right] \end{aligned} \tag{5.106}$$

The results of numerical calculations of the wavefunctions of the ground state in the $T \otimes t_2$ problem [5.56], and consequently the vibronic reduction factors (see also [5.165]), confirm approximately the validity of the formulas (5.106), but there are some remarkable discrepancies. As seen from Eqs. (5.106) and Fig. 5.26,

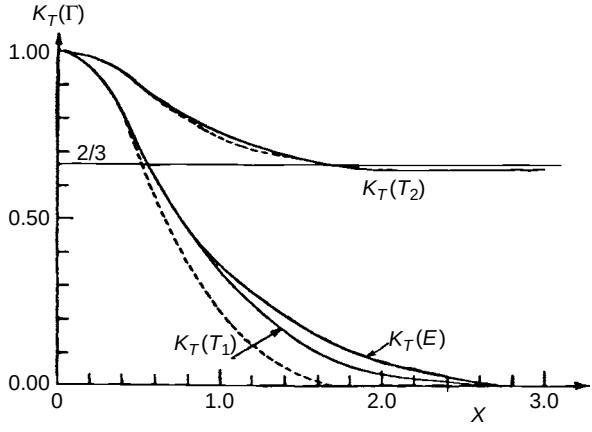

Fig. 5.26. Vibronic reduction factors for the linear $T \otimes t_2$ problem as functions of the dimensionless parameter $X = (3E_{\mathrm{JT}}^{T}/2\hbar\omega_T)^{\frac{1}{2}}$. The dashed lines correspond to the approximate expressions (5.106) [5.140].

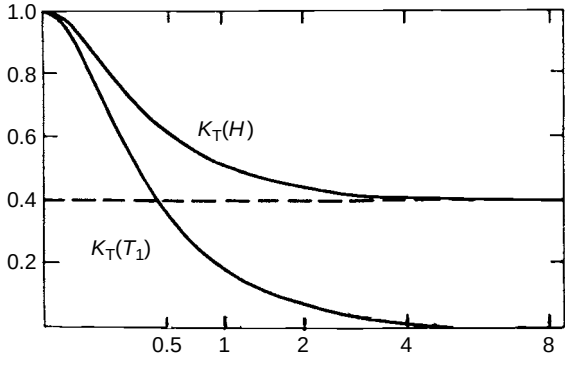

Fig. 5.27. Vibronic reduction factors for the linear $T_1 \otimes h$ problem as functions of the dimensionless vibronic coupling constant $\lambda = E_{\mathrm{JT}}^{T_1}/\hbar\omega_T$ [5.159].

$K_T(T_2)$ approaches the limit value of $\frac{2}{3}$ from above, while the numerical values [5.56, 5.67] show that at large coupling constant it becomes slightly lower than $\frac{2}{3}K_T(T_2)$ and reaches a minimum value of 0.65 [5.67]. The reason for this was shown [5.140, 5.150] to be due to the crude adiabatic approximation employed that ignores the dependence of the electronic wavefunctions on the nuclear coordinates within the minimum, which lowers the inter-minima overlap S. In the more accurate calculations the strong-coupling formulas are [5.150]

$$K_T(T_1) = 0, \qquad K_T(E) = S/(1+S), \qquad K_T(T_2) = \frac{2}{3}\left(\eta + \frac{3}{2}S\right)\Big/(1+S) \tag{5.106'}$$

where η is a parameter slightly smaller than 1. Note, however, that this correction is small.

By comparison of the reduction factors in Eqs. (5.103), (5.104), (5.105), and (5.106) one can easily see that [5.141]

$$K_T(E) + \tfrac{3}{2}[K_T(T_2) - K_T(T_1)] = 1 \tag{5.107}$$

but with the corrections above this equation is approximate too.

Numerical results for reduction factors for the $T \otimes (e + t_2)$ problem are given in [5.82] (see also [5.68, 5.81]). For reduction factors for Γ_8-term problems see in [5.156].

The strong dependence on the JT coupling taken as the dimensionless ratio $E_{\mathrm{JT}}/\hbar\omega$ is a general feature of almost all reduction factors; it may result in reducing physical quantities by several orders of magnitude. As mentioned above this was shown first in [5.138] where the vibronic reduction of the spin–orbital splitting in the ${}^2T$ term was evaluated. In [5.139, 5.140] the general nature of the reduction phenomenon was revealed and generalized in the theory of vibronic reduction of electronic operators of arbitrary symmetry.

The expressions for the vibronic reduction factors in the $T \otimes e$ and $T \otimes t_2$ problems for cubic systems (5.103)–(5.107) were modified for a practically useful case of a trigonal system regarded as a trigonally distorted tetrahedron [5.157]. It was shown that while the $T \otimes e$ factors remain the same as in the regular cubic case, the $T \otimes t_2$ reduction factors may differ significantly.

For orthorhombic minima of the APES in the quadratic $T \otimes (e + t_2)$ problem (Section 3.3) subject to equal tetragonal and trigonal vibration frequencies $\omega_E = \omega_T = \omega$, (and hence $K_E = K_T = K$, where K is here the force constant), we have [5.29]

$$\begin{aligned} K_T(E) &= (1 + 8S + 6\tilde{S})/(4 + 8S) \\ K_T(T_1) &= (3S + \tilde{S})/(1 + 2S) \\ K_T(T_2) &= (1 + 6S)/(2 + 4S) \\ S &= \tfrac{1}{2}\exp\{-K[3(Q_\vartheta^{(0)})^2 + 2(Q_\zeta^{(0)})^2]/4\hbar\omega\} \\ \tilde{S} &= \tfrac{1}{2}\exp[-K(Q_\zeta^{(0)})^2/\hbar\omega] \end{aligned} \tag{5.107$'$}$$

where the coordinates of the minimum points $Q_\gamma^{(0)}$ are given by Eq. (3.58) in Section (3.3). A quantum field approach to the calculation of reduction factors in cubic systems is discussed in. [5.158]

A general result applicable to all JT problems and physical-quantity operator symmetries was obtained for the vibronic reduction factors $K(\overline{\Gamma})$ in the limiting case of very strong coupling [5.98*b*]: $K(\overline{\Gamma}) \sim Q_0(\overline{\Gamma})$,where $Q_0(\overline{\Gamma})$ is

the distance from one of the equivalent minima of the APES to the high-symmetry point of the reference nuclear configuration in the subspace of nuclear displacements $Q_{\Gamma\gamma}$. For instance, for the $T \otimes t_2$ problem the trigonal minima of the APES are displaced from the high-symmetry reference point in the subspace of the t_2 vibrations only: $Q_0(T_2) = 2/\sqrt{2}$ (in conventional units), while $Q_0(E) = 0$. It follows that the limiting values of $K_T(T_2)$ and $K_T(E)$ in the strong-coupling case under consideration are $K_T(T_2) \neq 0$ and $K_T(E) = 0$. Similar conclusions about the magnitudes of reduction factors in the limiting case of strong vibronic coupling are summarized in [5.98(*b*)] for many JT problems. These results are also valid for the multimode problems.

For higher-symmetry (icosahedral) systems (Section 3.4) vibronic reduction factors were discussed already in the first work on the JT effect in such systems [5.159] and further advanced in [5.160–5.164, 5.166–5.175]. For the simplest $T \otimes h$ problem there are three vibronic reduction factors: $K_T(A)$, $K_T(T)$, and $K_T(H)$ ($T \times T = A + [T] + H$; $T = T_1$ or T_2, and square brackets indicate the antisymmetric part of the Kronecker product), but totally symmetric operators A are not reduced: $K(A) = 1$ for all the JT problems. The numerical values [5.159] for linear coupling illustrated in Fig. 5.27 show that $K_T(T)$ as a function of $E_{\mathrm{JT}}/\hbar\omega$ ranges from 1 for extremely weak coupling to $K_T(T) \approx 0$ at $E_{\mathrm{JT}}/\hbar\omega \gtrsim 4$, while $K_T(H)$ falls from 1 to a constant value of $K_T(H) = \frac{2}{5}$ for the same region of couplings. For arbitrary coupling these two reduction factors are related by the following equation [5.161] (cf. Eqs. (5.98) and (5.107)):

$$5K_T(H) - 3K_T(T) = 2 \tag{5.108}$$

Note that while $K_{T_1}(T_1) = K_{T_2}(T_2)$, the importance of these two reduction factors in applications is essentially different. Indeed, the angular momentum transforms as T_1, whereas T_2 is irrelevant to angular-momentum matrix elements. This means that the spin–orbital splitting, that goes to zero in icosahedral T_1 states with sufficiently strong vibronic coupling, will not be reduced at all in T_2 states.

If quadratic coupling is included, the equipotential two-dimensional trough of the linear case becomes warped, yielding either pentagonal $D_{5\mathrm{d}}$, or trigonal $D_{3\mathrm{d}}$ minima depending on the relative coupling strengths (Section 3.4). For both types of minima of the quadratic $T \otimes h$ problem with strong coupling, employing the method described in Section 5.3 [5.1, 5.25], symmetry-adapted vibronic states were constructed [5.162], and explicit expressions for the reduction factors were evaluated using Eq. (5.97) [5.163, 5.164]. For pentagonal $D_{5\mathrm{d}}$ minima

$$\begin{aligned} K_{T_1}(T_1) &= 2S_{\mathrm{p}}/(1 + S_{\mathrm{p}}) \\ K_{T_1}(H) &= 2(1 + 4S_{\mathrm{p}})/5(1 + S_{\mathrm{p}}) \\ K_{T_2}(H) &= \tfrac{2}{5} \end{aligned} \tag{5.109}$$

while for trigonal minima

$$\begin{aligned} K_{T_1}(T_1) &= 2S_t(1+4S_t)/(3+5S_t+2S_t^2) \\ K_{T_1}(H) &= 2(3+8S_t+14S_t^2)/5(3+5S_t+2S_t^2) \\ K_{T_2}(H) &= -2(3-7S_t+4S_t^2)/5(3-5S_t+2S_t^2) \\ K_G(T_1) &= -(2/3)^{\frac{1}{2}}S_t/(1+S_t) \\ K_G(H) &= (2/9)^{\frac{1}{2}}(1+S_t-2S_t^2)/(1-S_t^2) \end{aligned} \tag{5.110}$$

where the overlap integrals between, respectively, two near-neighbor pentagonal S_p and two trigonal S_t minima are quite similar to those calculated in Section 5.3 (cf. Eqs. (5.45)–(5.47)). Calculations yield

$$\begin{aligned} S_p &= \exp[-30E_{JT}^{H}(E_{JT}^{D_{5d}})^2] \\ S_t &= \exp[-(50/3)E_{JT}^{H}(E_{JT}^{D_{5d}})^2] \end{aligned} \tag{5.111}$$

Here $E_{JT}^{H} = F_H^2/5K_H\hbar\omega_H$ is the dimensionless JT stabilization energy due to linear coupling to h displacement, while $E_{JT}^{D_{5d}} = (5-4\sqrt{2}G_2/K_H)^{-1}$ and $E_{JT}^{D_{3d}} = (5-4\sqrt{10}G_3/K_H)^{-1}$ in $F_H^2/K_H\hbar\omega_H$ units are the additional stabilizations due to the formation of pentagonal D_{5d} and trigonal D_{3d} minima via corresponding quadratic couplings G_2 and G_3, respectively (Section 3.4). At $G_2 = G_3 = 0$, $E_{JT}^{D_{5d}} = E_{JT}^{D_{3d}} = \frac{1}{5}$, meaning that a two-dimensional trough of depth equal to E_{JT}^{H} is formed.

It can easily be seen that the expressions (5.109) and (5.110) obey the sum rule (5.108).

For the icoshedral G term there are four nontrivial reduction factors ($K_G(A) = 1$) that obey the sum rules [5.161]:

$$K_G(T_1) = K_G(T_2), \qquad 4K_G(G) + 5K_G(H) - 6K_G(T_1) = 3 \tag{5.112}$$

Limiting values for infinitely strong coupling when the overlap of vibrational functions of different minima is negligibly small yield the following numbers [5.167]. For the $G \otimes g$ problem with minima of T_d symmetry (Section 3.4):

$$K_G(T_1) = K_G(T_2) = K_G(H) = 0, \qquad K_G(G) = \tfrac{3}{4} \tag{5.113}$$

For the $G \otimes h$ problem with minima of D_3 symmetry:

$$K_G(T_1) = K_G(T_2) = 0, \qquad K_G(\mathrm{H}) = 5/9, \qquad K_G(\mathrm{G}) = 5/90 \tag{5.114}$$

For the general $G \otimes (g + h)$ problem with a finite vibrational overlap integral S_{AB} between two tetrahedral minima (the analog of S_{23} in Eqs. (5.45)–(5.47) in Section 5.3 and the S_p and S_t above), we have [5.161, 5.166, 5.167]

$$\begin{aligned} K_G(T_1) = K_G(T_2) = K_G(H) &= -5S_{AB}/(1 - S_{AB}) \\ K_G(G) &= (3 - 8S_{AB})/4(1 - S_{AB}) \end{aligned} \tag{5.115}$$

The S_{AB} integral was calculated [5.167] as

$$S_{AB} = -\tfrac{1}{4}\exp(-4E_{JT}^G/3) \tag{5.116}$$

where the dimensionless JT stabilization energy for these minima is $E_{JT}^G = 3F_G^2/K_G\hbar\omega_G$.

If D_3 minima dominate, there are two types of vibrational overlap integrals, S_{ab} and S_{ac} (Section 3.4), and the reduction factors are

$$\begin{aligned} K_G(T_1) = K_G(T_2) &= -5N_G^2(3S_{ab} - 42S_{ac}) \\ K_G(G) &= (N_G^2/18)(1 - 12S_{ab} + 21S_{ac}) \\ K_G(H) &= (5N_G^2/18)(2 - 6S_{ab} + 18S_{ac}) \end{aligned} \tag{5.117}$$

with $N_G^2 = (1 - 2S_{ab} + S_{ac})^{-1}$. For S_{ab} and S_{ac} we have [5.167]

$$\begin{aligned} S_{ab} &= -(2/3)\exp[-(10/81)(E_{JT}^G + 5E_{JT}^H)] \\ S_{ac} &= (1/6)\exp[-(5/81)(E_{JT}^G + 20E_{JT}^H)] \end{aligned} \tag{5.118}$$

where the dimensionless JT stabilization energies are $E_{JT}^G = 3F_G^2/8K_G\hbar\omega_G$ and $E_{JT}^H = 3F_H^2/10K_H\hbar\omega_H$. First-order vibronic reduction factors (5.117) are illustrated in Figs. 5.28 (a) and (b).

There are also off-diagonal reduction factors in this problem for matrix elements that couple the ground vibronic G level with the next A level via G perturbations, as well as the A level with an H one via H operators:

$$\begin{aligned} K_{AG}(G) &= (\sqrt{2}N_G/12)(1 + 3S_{ab} + 6S_{ac})^{\frac{1}{2}} \\ K_{AH}(H) &= (5N_G/6)(1 + 3S_{ab} + 6S_{ac})^{\frac{1}{2}} \end{aligned} \tag{5.119}$$

For extremely strong coupling $S \approx 0$ and Eqs. (5.114) and (5.117) coincide with (5.112) and (5.113), respectively.

As discussed in Section 3.4, the calculations for the fivefold degenerate H term that generates the JT $H \otimes (g + h)$ problem encounter additional difficulties because the Kronecker product $H \times H = A + T_1 + T_2 + 2G + 2H$ contains repeating irreducible representations G and H. In general this yields a 2×2

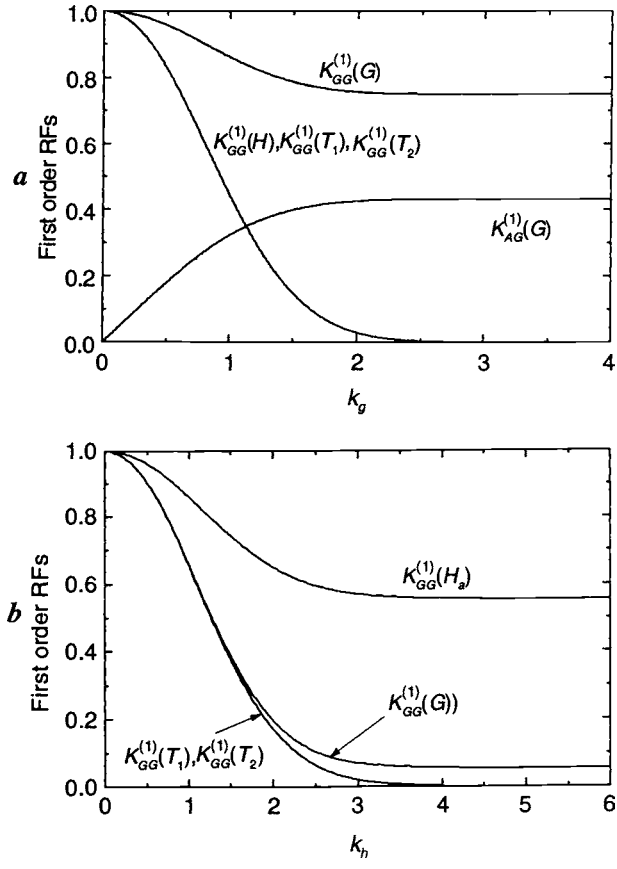

Fig. 5.28. First-order reduction factors for an icosahedral G term, $K_G(\Gamma)$, as a function of the vibronic coupling constants: (a) k_g, with wells of T symmetry (one off-diagonal constant $K_{AG}(G)$ is also shown); and (b) k_h, with wells of D_3 symmetry and $k_g = 0$ (reprinted with permission from [5.167]. Copyright 2002 Institute of Physics).

matrix for each of these two symmetries [5.168] (meaning two diagonal and two off-diagonal reduction factors), but a proper separation of the two kinds of g and h distortions eliminates the off-diagonal quantities [5.169]. Hence only two components (two symmetries) of the repeating representations G_a and G_b, and H_a and H_b, remain and hence there are six physically relevant diagonal reduction factors $K_\Gamma(\overline{\Gamma})$ for the $H \otimes (g + h)$ problem under consideration. Their calculation for D_{5d} minima yields [5.168] (Fig. 5.29)

$$\begin{aligned} &K_H(T_1) = K_H(T_2) = K_H(G_a) = K_H(G_a) = K_H(H_a) = -6S_{AB}/(1 - S_{AB}) \\ &K_H(H_b) = \tfrac{4}{5} - 2S_{AB} \end{aligned} \tag{5.120}$$

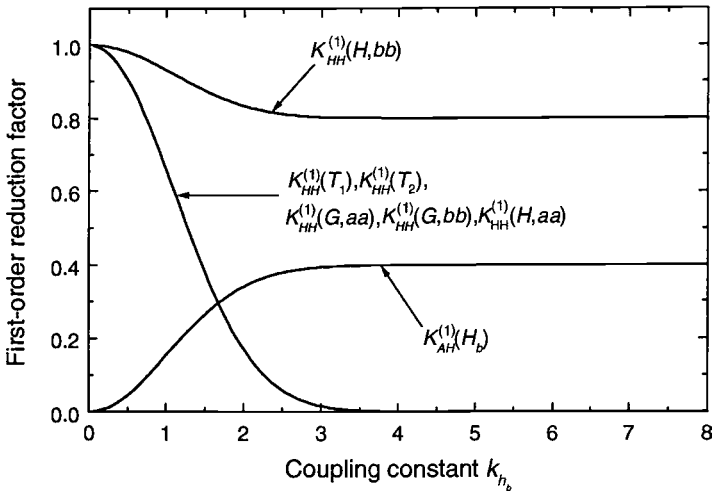

Fig. 5.29. First-order reduction factors for an icosahedral H term in the $H \otimes h$ problem with minima of D_{5d} symmetry, $K_H(\Gamma)$, as a function of the vibronic coupling constant k_{h_b}; one off-diagonal constant $K_{AH}(H_b)$ is also shown (reprinted with permission from [5.168]. Copyright 2002 Institute of Physics).

with

$$S_{AB} = -\tfrac{1}{5}\exp(-8E_{JT}^{H_b}/5) \tag{5.121}$$

and

$$E_{JT}^{H_b} = 3F_{H_b}^2/10K_{H_b}\hbar\omega_{H_b}$$

There is also one off-diagonal reduction factor $K_{AH}(H_b)$ for operators that mix the vibronic ground state H with the next tunneling state A by H_b perturbations [5.168]:

$$K_{AH}(H_b) = (\tfrac{2}{5} - 2S_{AB})/(1 - S_{AB})^{\frac{1}{2}}(1 + 5S_{AB})^{\frac{1}{2}} \tag{5.122}$$

For the other H component $K_{AH}(H_a) = 0$.

For the ten D_{3d} minima of the $H \otimes (g + h)$ problem (Section 3.4), as in the case of the $G \otimes (g + h)$ problem considered above, there are two different vibrational overlap integrals (which, however, are different from the (5.118) values):

$$\begin{aligned} S_{ab} &= -(1/3)\exp[-(40/81)(E_{JT}^{G} + 2E_{JT}^{H_a})] \\ S_{ac} &= (1/3)\exp[-(40/81)(2E_{JT}^{G} + E_{JT}^{H_a})] \end{aligned} \tag{5.123}$$

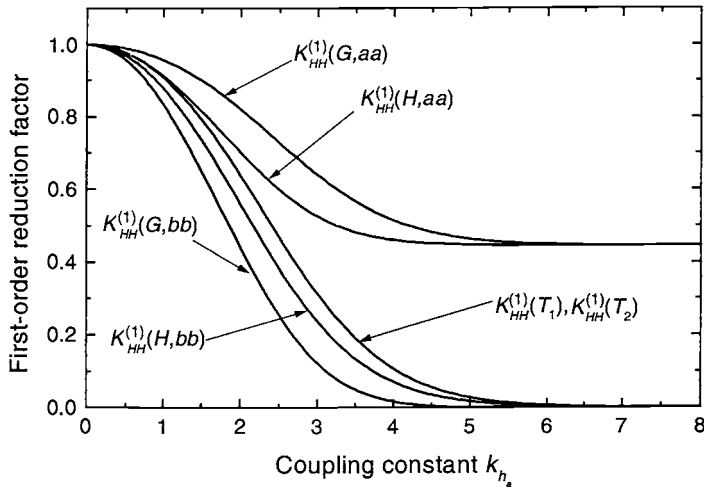

Fig. 5.30. First-order reduction factors for an icosahedral H term in the $H \otimes h$ problem with minima of D_{3d} symmetry, $K_H(\Gamma)$, as a function of the vibronic coupling constant k_{h_a} ($k_g = 0$) (reprinted with permission from [5.168]. Copyright 2002 Institute of Physics).

The $K_\Gamma(\overline{\Gamma})$ expressions as functions of these integrals are [5.168] (Fig. 5.30)

$$\begin{aligned} K_H(T_1) &= K_H(T_2) = -(2N_H^2/3)(4S_{ab} - 5S_{ac}) \\ K_H(G_a) &= (2N_H^2/9)(2 - 9S_{ab} + 12S_{ac}) \\ K_H(G_b) &= -6N_H^2 S_{ab}/(1 - 2S_{ab} + S_{ac}) \\ K_H(H_a) &= (2N_H^2/9)(2 - 18S_{ab} + 3S_{ac}) \\ K_H(H_b) &= -2N_H^2(2S_{ab} - S_{ac}) \end{aligned} \tag{5.124}$$

with $N_H^2 = (1 - 2S_{ab} + S_{ac})^{-1}$.

For the tunneling G states of the $H \otimes (g + h)$ problem with D_3 minima similar reduction-factor expressions were obtained [5.168] (Fig. 5.31):

$$\begin{aligned} K_G(T_1) &= -K_G(T_2) = -(2\sqrt{10}N_G^2/3)(S_{ab} + S_{ac}) \\ K_G(G_a) &= -(2\sqrt{2}N_G^2/9\sqrt{5})(1 - 9S_{ab} - 12S_{ac}) \\ K_G(H_a) &= (4N_G^2/9)(1 - 3S_{ac}) \end{aligned} \tag{5.125}$$

with $N_G^2 = (1 + S_{ab} - 2S_{ac})^{-1}$; several off-diagonal $K_{GH}(\overline{\Gamma})$ reduction factors are also evaluated in this paper [5.168].

In many cases physical observables are defined as second-order perturbation corrections of operators acting upon the electronic states, sometimes resulting from simultaneous action of two first-order perturbations

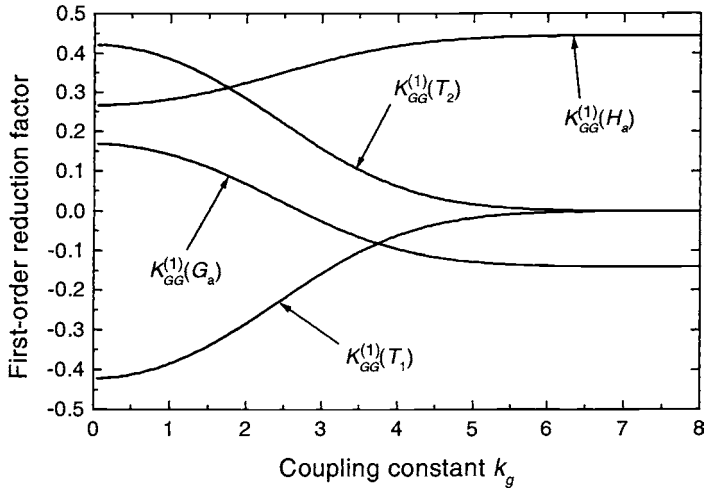

Fig. 5.31. First-order reduction factors for an icosahedral H term in the $H \otimes g$ problem, $K_H(\Gamma)$, as a function of the vibronic coupling constant k_g ($k_{h_a} = 0$) (reprinted with permission from [5.168]. Copyright 2002 Institute of Physics).

(e.g., spin–orbital coupling and an external magnetic field). As mentioned above, to take into account the effect of vibronic coupling on properties of the system determined as second-order corrections in perturbation theory, we introduce second-order vibronic reduction factors $K^{(2)}_{\Gamma}(\overline{\Gamma})$. They can be defined by inserting into Eqs. (5.97) or (5.97′), instead of the operator $X_{\overline{\Gamma}\overline{\gamma}}$, a symmetrized component $\Gamma^*\gamma^*$ of its second-order expression [5.1, 5.139]:

$$X^{(2)}_{\Gamma^*\gamma^*} = \sum_{\gamma_1,\gamma_2} X_{\overline{\Gamma}\overline{\gamma}_1} \left(\sum_{nv} \frac{|\Psi_{nv}(r, Q)\rangle\langle\Psi_{nv}(r, Q)|}{E_0 - E_{nv}} \right) X_{\overline{\Gamma}\gamma_2} \langle \overline{\Gamma}\gamma_1 \overline{\Gamma}\gamma_2 | \Gamma^*\gamma^* \rangle \qquad (5.126)$$

where $\Psi_{\mathrm{nv}}(r, Q)$ are full excited-state wavefunctions, and the Clebsch–Gordan coefficients $\langle \overline{\Gamma}\gamma_1 \overline{\Gamma}\gamma_2 | \Gamma^*\gamma^* \rangle$ are introduced to get the $\Gamma^*\gamma^*$ symmetry component from the product $\overline{\Gamma} \times \overline{\Gamma}$ of the perturbation. If the vibronic coupling is not included, as on the right-hand side of Eq. (5.97), the wavefunction $\Psi_{nv}(r, Q)$ is multiplicative with regard to the electronic and vibrational parts, and since X is a pure electronic operator, the orthonormalized vibrational functions disappear, making the expression (5.126) pure electronic. This cannot be done on the left-hand side of definition (5.97) with the operator $X^{(2)}_{\Gamma\gamma}$ because of the essential non-multiplicative wavefunctions of the vibronic coupling states. The second-order vibronic reduction factor is thus the ratio of the matrix elements of $X^{(2)}_{\Gamma\gamma}$ with and without the vibronic coupling.

Since the product $\overline{\Gamma} \times \overline{\Gamma}$, in general, contains several irreducible representations Γ^* of different symmetries, the second-order vibronic reduction factor may be different for each of them. If the second-order perturbation occurs as a product of two perturbations with different symmetries, say $X_{\overline{\Gamma}_1\overline{\gamma}_1}$ and $Y_{\overline{\Gamma}_2\overline{\gamma}_2}$, they should stay on the two sides of the infinite sum in Eq. (5.126). Therefore a more general definition of the second-order vibronic reduction factor is $K_\Gamma^{(2)}(\Gamma^*; \overline{\Gamma}_1 \times \overline{\Gamma}_2)$, where Γ is the symmetry of the initial electronic term in the JT problem. Similar to first-order off-diagonal reduction factors $K_{\Gamma\Gamma'}(\overline{\Gamma})$ there are also off-diagonal second-order reduction factors $K_{\Gamma\Gamma'}^{(2)}(\Gamma^*; \overline{\Gamma}_1 \times \overline{\Gamma}_2)$. For the most important diagonal second-order reduction factors with one kind of perturbation $\overline{\Gamma}_1 = \overline{\Gamma}_2 = \overline{\Gamma}$, we use the notation $K_\Gamma^{(2)}(\Gamma^*, \overline{\Gamma})$ or, omitting the $\overline{\Gamma}$ symbol where possible, $K_\Gamma^{(2)}(\Gamma^*)$.

Second-order reduction factors were introduced and first used to consider spin–orbital interaction in a JT system with a T term in the $T \otimes e$ problem [5.139, 5.140]. Denoting the spin–orbital operator as $\lambda(\vec{L}\vec{S})$ and taking the L_α as the operator X in the above definitions, one finds the following expression for the spin Hamiltonian of the second-order perturbation theory:

$$H_{\mathrm{SO}}^{(2)} = -(\lambda^2/\hbar\omega_E)[f_{\mathrm{a}}(\vec{L}\vec{S})^2 + (f_{\mathrm{a}} - f_{\mathrm{b}})(L_x^2 S_x^2 + L_y^2 S_y^2 + L_z^2 S_z^2) \tag{5.127}$$

where f_{a} and f_{b} serve as second-order reduction factors,

$$\begin{aligned} f_{\mathrm{a}} &= \exp(-3E_{\mathrm{JT}}^E/\hbar\omega_E) g(3E_{\mathrm{JT}}^E/2\hbar\omega_E) \\ f_{\mathrm{b}} &= \exp(-3E_{\mathrm{JT}}^E/\hbar\omega_E) g(3E_{\mathrm{JT}}^E/\hbar\omega_E) \end{aligned} \tag{5.128}$$

and

$$g(x) = \int_0^x (e^t - 1)t^{-1}dt \approx x^{-1}e^x\left(1 + \frac{1}{x} + \frac{2}{2!x^2} + \frac{2 \cdot 3^2}{3!x^3} + \cdots\right) \tag{5.129}$$

For strong vibronic coupling when $E_{\mathrm{JT}}^E \gg \hbar\omega_E$ the first term in (5.127) goes to zero, while the second yields the following asymptotic expression:

$$(\lambda^2/\hbar\omega_E)(f_{\mathrm{a}} - f_{\mathrm{b}}) \approx \lambda^2/3E_{\mathrm{JT}}^E \tag{5.130}$$

The vibronic reduction is thus $K^{(2)} \approx 1/3E_{\mathrm{JT}}^E$. Since $3E_{\mathrm{JT}}^E$ is the energy gap to the upper sheet of the APES at the point of the minimum in the tetragonal distortion (see the $T \otimes e$ problem, Section 3.3), the effect of very strong vibronic coupling is equivalent to that of a tetragonal field with only one (the lowest) excited state taken into account in the second-order perturbation. It follows that in the second-order perturbation-theory splitting given by

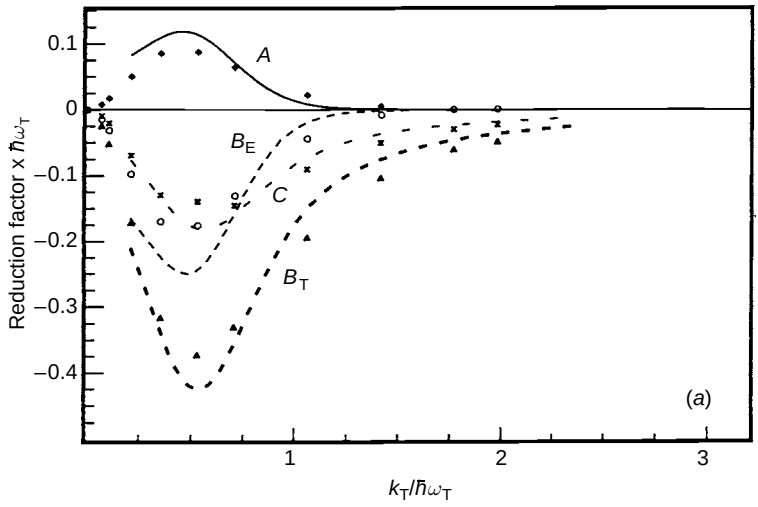

Fig. 5.32. Second-order reduction factors $A = -\frac{1}{2}K_T^{(2)}(T_1)$, $B_E = K_T^{(2)}(E)$, $B_T = K_T^{(2)}(T_2)$, and $C = \frac{1}{3}K_T^{(2)}(A_1)$ calculated including anisotropy, compared with the numerical results [5.171] denoted by ♦, ○, ▲, and ×, respectively (data from [5.172]).

Eq. (5.127) the second-order reduction factor decreases with E_{JT}^E as $(E_{\mathrm{JT}}^E)^{-1}$ and thus changes much slower than the almost exponential first-order splitting (first-order reduction factors). Therefore in this limit case the second-order reduction may be stronger than the first-order one for large values of E_{JT}.

Second-order reduction factors were calculated for quite a number of JT problems. In continuation of the first calculations [5.139, 5.140], analytical formulas for the $T\otimes t_2$ problem with trigonal distortions and the $T\otimes(e+t_2)$ problem with orthorhombic minima were obtained [5.170(*a*)]. The calculations for the $T\otimes t_2$ problem were further improved to take into account the anisotropy (splitting) of t_2 vibrations in the trigonal minima [5.170(*b*)]. Numerical calculations of second-order reduction factors were carried out for spin–orbital coupling in $T\otimes t_2$ and $T\otimes d$ problems [5.171]. Figure 5.32 (from [5.172]) illustrates the analytical results [5.170(*a*)] in comparison with the numerical values [5.171] for the $T\otimes t_2$ problem.

A general theory of second-order vibronic reduction factors based on symmetry arguments only was given in [5.173]. Using symmetry-adapted wavefunctions for the tunneling levels and basic group-theory theorems the authors derived a general formula for $K_\Gamma^{(2)}(\Gamma^*; \overline{\Gamma}_1 \times \overline{\Gamma}_2)$, which is in principle applicable to any JT problem and any second-order perturbation symmetry $\overline{\Gamma}_1 = \overline{\Gamma}_2$ or two first-order perturbations $\overline{\Gamma}_1 \neq \overline{\Gamma}_2$, as well as off-diagonal factors $K_{\Gamma\Gamma'}^{(2)}(\Gamma^*; \overline{\Gamma}_1 \times \overline{\Gamma}_2)$. Applied to the $T\otimes e$, $T\otimes t_2$, and $T\otimes(e+t_2)$ problems

[5.172], the general formulas yield in the weak-coupling limit the same results as in the earlier simpler and more straightforward evaluations [5.139, 5.140]. In particular, for the $T \otimes t_2$ system with a T_1-type perturbation, for which $\Gamma^* = T_1 \times T_1 = A_1 + E + T_1 + T_2$, one gets

$$\begin{aligned} K_T^{(2)}(A_1) &= 2K_T^{(2)}(E) = 2K_T^{(2)}(T_1) = -9E_{\mathrm{JT}}^T/2\hbar^2\omega_T^2 \\ K_T^{(2)}(T_2) &= -15E_{\mathrm{JT}}^T/4\hbar^2\omega_T^2 \end{aligned} \tag{5.131}$$

Similarly, in the weak-field limit of the $T \otimes e$ problem and T_1 perturbation [5.172]

$$\begin{aligned} K_T^{(2)}(A_1) &= K_T^{(2)}(E) = 2K_T^{(2)}(T_1) \\ K_T^{(2)}(T_1) &= 2K_T^{(2)}(T_2) = -3E_{\mathrm{JT}}^E/2\hbar^2\omega_E^2 \end{aligned} \tag{5.132}$$

In the $T \otimes (e + t_2)$ problem with weak coupling to both e and t_2 displacements the second-order reduction factors for T_1 perturbations are sums of the two reduction factors obtained above separately for the $T \otimes e$ and $T \otimes t_2$ problems:

$$\begin{aligned} K_T^{(2)}(A_1) &= -9E_{\mathrm{JT}}^T/2\hbar^2\omega_T^2 - 3E_{\mathrm{JT}}^E/\hbar^2\omega_E^2 \\ K_T^{(2)}(E) &= -9E_{\mathrm{JT}}^T/4\hbar^2\omega_T^2 - 3E_{\mathrm{JT}}^E/\hbar^2\omega_E^2 \\ K_T^{(2)}(T_1) &= -9E_{\mathrm{JT}}^T/4\hbar^2\omega_T^2 - 3E_{\mathrm{JT}}^E/2\hbar^2\omega_E^2 \\ K_T^{(2)}(T_2) &= -15E_{\mathrm{JT}}^T/4\hbar^2\omega_T^2 - 3E_{\mathrm{JT}}^E/2\hbar^2\omega_E^2 \end{aligned} \tag{5.133}$$

In the limit case of very strong vibronic coupling when the system with a T term is trapped in one of the trigonal minima of the $T \otimes t_2$ problem, it was shown that the second-order reduction factors are proportional to the first-order factors [5.172]: $K_T^{(2)}(\Gamma^*, T_1) = -(1/3E_{\mathrm{JT}}^T)K_T(\Gamma^*)$. With the values of $K_T(\Gamma^*)$ in the limit of strong coupling from (5.105) and with $K_T(A_1) = 1$, we get

$$K_T^{(2)}(A_1) = -1/3E_{\mathrm{JT}}^T, \qquad K_T^{(2)}(E) = K_T^{(2)}(T_1) = 0, \qquad K_T^{(2)}(T_2) = -2/9E_{\mathrm{JT}}^T \tag{5.134}$$

For the off-diagonal second-order reduction factor applied to matrix elements between the T_1 and A_2 tunneling states in the same approximation we have

$$K_{T_1A_2}^{(2)}(T_1) = -1/(3\sqrt{3}E_{\mathrm{JT}}^T) \tag{5.135}$$

As above (see Eq. (5.130)), $3E_{\mathrm{JT}}^T$ is the energy gap to the upper sheet of the APES at the point of the trigonal minimum (Section 3.3) and hence the inverse

proportionality of the reduction factors with $3E_{\mathrm{JT}}^{T}$ may be interpreted as the corresponding contribution of the lowest excited state to the second-order perturbation (without vibronic coupling this energy gap is zero).

Second-order reduction factors were also evaluated for JT problems in icosahedral systems [5.164, 5.167, 5.168, 5.174, 5.175]. For the $T_{1\mathrm{u}} \otimes h_{\mathrm{g}}$ problem that occurs, in particular, in the ground state of the icosahedral system C_{60}^{-}, second-order factors were calculated assuming that the excited states in the infinite sum in Eq. (5.126) are excited vibrational harmonic-oscillator states in the distorted configuration of the minimum of the APES [5.164]. The analytical results obtained for all possible kinds of second-order reduction factors for both trigonal and pentagonal minima contain the overlap integrals (5.111), as well as infinite sums emerging from harmonic-oscillator matrix elements.

The approximation of vibronic states taken as linear combinations of displaced oscillators employed in the work [5.164] is strictly speaking valid only when the JT distortions are large, with infinite barriers between the minima. Its possible validity for limited barriers remains unclear because of the problem of overfilled basis sets. Another approach to this problem was suggested [5.174], in which the Franck–Condon approximation is used to convolute the infinite sum of excited (vibrational)-state overlaps with the ground one into a delta function. In this approximation the limiting values of the second-order reduction factors are more accurate than those obtained in [5.164]. Further improvements of this method were achieved by means of introducing perturbational non-Condon corrections into the Franck–Condon approximation, which were shown to be inversely proportional to the square of the JT stabilization energy [5.175].

The same approximation of displaced-oscillator excited states was applied to evaluate analytically the second-order reduction factors in the $G \otimes (g + h)$ [5.167] and $H \otimes (g + h)$ [5.168] problems, considering the cases of $D_{5\mathrm{d}}$ and $D_{3\mathrm{d}}$ minima separately. Figures 5.33–5.36 illustrate the results obtained for the main reduction factors of these problems. Note that in the majority of cases given in Figs. 5.33–5.36 the second-order vibronic reduction factors are *negative*, meaning that if the first-order reduction factor is small the vibronic coupling described by these *second-order reduction factors results in reversal of the energy-level ordering*.

As mentioned above, the first-order reduction factors decrease with the coupling strength much faster than the second-order ones, and hence the latter may prevail over the former for some values of the strong vibronic coupling. Also, it may happen that the first-order perturbation corrections are forbidden by symmetry considerations. In all these cases the energy-level reversal is an

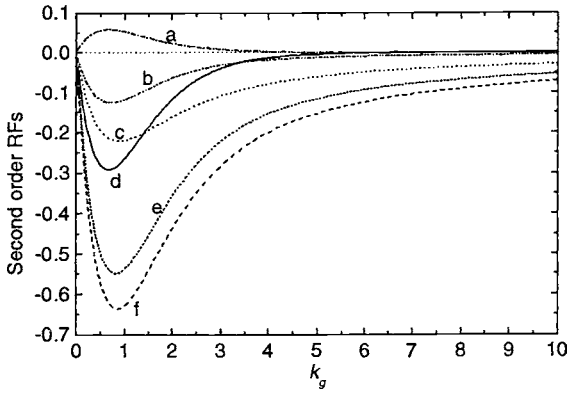

Fig. 5.33. Second-order reduction factors $K_{\Gamma}^{(2)}(\overline{\Gamma} \otimes \overline{\Gamma})$ (the symmetry of the perturbation is that contained in $\overline{\Gamma} \times \overline{\Gamma}$) for the JT $G \otimes g$ problem as a function of k_g: $a = K_{T_1}^{(2)}(G \otimes G)$, $K_{T_2}^{(2)}(G \otimes G)$, $K_{H_a}^{(2)}(G \otimes G)$; $b = K_{G_a}^{(2)}(G \otimes G)$; $c = K_{A}^{(2)}(G \otimes G)$; $d = K_{T_1}^{(2)}(T_1 \otimes T_1), K_{T_1}^{(2)}(T_2 \otimes T_2), K_{T_1}^{(2)}(H \otimes H), K_{T_2}^{(2)}(H \otimes H)$, $K_{H_a}^{(2)}(H \otimes H)$; $e = K_{G_a}^{(2)}(H \otimes H)$; $f = K_{A}^{(2)}(T_1 \otimes T_1), K_{A}^{(2)}(T_2 \otimes T_2), K_{A}^{(2)}(H \otimes H)$ (reprinted with permission from [5.167]. Copyright 2002 Institute of Physics).

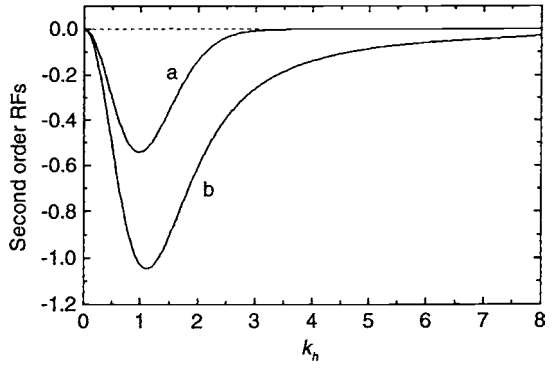

Fig. 5.34. Second-order reduction factors $K_{\Gamma}^{(2)}(\overline{\Gamma} \otimes \overline{\Gamma})$ for the JT $G \otimes h$ problem as a function of k_h: $a = K_{T_1}^{(2)}(T_1 \otimes T_1)$, $K_{T_2}^{(2)}(T_2 \otimes T_2)$, $K_{H}^{(2)}(T_1 \otimes T_1)$, $K_{H}^{(2)}(T_2 \otimes T_2)$; $b = K_{A}^{(2)}(T_1 \otimes T_1)$, $K_{A}^{(2)}(T_2 \otimes T_2)$ (reprinted with permission from [5.167]. Copyright 2002 Institute of Physics).

expected reality. To the best of our knowledge, there have been no attempts so far to reveal this effect experimentally.

Another kind of second-order vibronic reduction factors emerges when one tries to take into account the admixture of the excited electronic states of the system with the ground-state JT term in calculation of the second-order

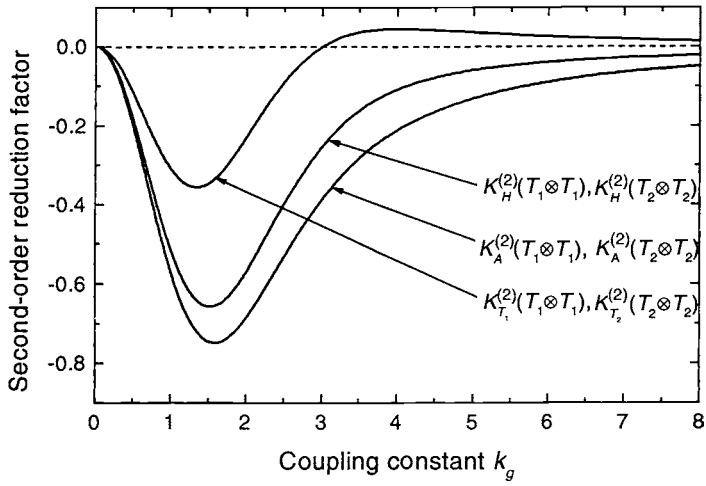

Fig. 5.35. Second-order reduction factors $K_\Gamma^{(2)}(\overline{\Gamma}\otimes\overline{\Gamma})$ for the JT $H\otimes g$ problem with perturbations of T_1 and T_2 symmetries as a function of k_g (reprinted with permission from [5.168]. Copyright 2002 Institute of Physics).

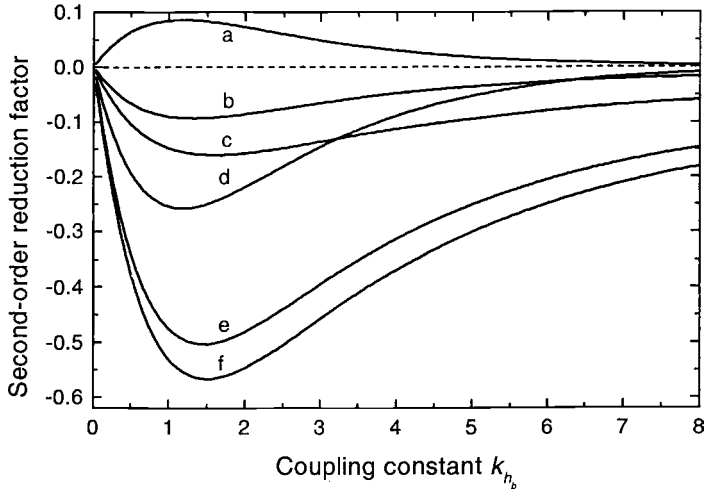

Fig. 5.36. Second-order reduction factors $K_\Gamma^{(2)}(\overline{\Gamma}\otimes\overline{\Gamma})$ for the JT $H\otimes h$ problem as a function of k_{h_b}: (a) $K_{T_1}^{(2)}(H_b\otimes H_b)$, $K_{T_2}^{(2)}(H_b\otimes H_b)$, $K_{G_a}^{(2)}(H_b\otimes H_b)$, $K_{G_b}^{(2)}(H_b\otimes H_b)$, $K_{H_a}^{(2)}(H_b\otimes H_b)$; (b) $K_{H_b}^{(2)}(H_b\otimes H_b)$; (c) $K_A^{(2)}(H_b\otimes H_b)$; (d) $K_{T_1}^{(2)}(T_1\otimes T_1)$, $K_H^{(2)}(T_1\otimes T_1)$, $K_{T_1}^{(2)}(G_a\otimes G_a)$, $K_G^{(2)}(G_a\otimes G_a)$, $K_H^{(2)}(G_a\otimes G_a)$, $K_{T_1}^{(2)}(H_a\otimes H_a)$, $K_{T_2}^{(2)}(H_a\otimes H_a)$, $K_{G_a}^{(2)}(H_a\otimes H_a)$, $K_{G_b}^{(2)}(H_a\otimes H_a)$, $K_{H_a}^{(2)}(H_a\otimes H_a)$; (e) $K_{H_b}^{(2)}(H_a\otimes H_a)$; (f) $K_A^{(2)}(T_1\otimes T_1)$, $K_A^{(2)}(G_a\otimes G_a)$, $K_A^{(2)}(H_a\otimes H_a)$ (reprinted with permission from [5.168]. Copyright 2002 Institute of Physics).

perturbations [5.154]. Such excited-state admixture changes the electronic matrix elements, and these changes may be taken into account by second-order "reduction" factors $\tilde{K}^{(2)}$ (similar to $K^{(2)}$) that depend on the spectrum of the excited electronic states. In particular, if only one excited electronic state is taken into account and the energy gap to this state Δ is much larger than the gaps between the vibronic (tunneling) energy levels, these second-order reduction factors are approximately equal to the first-order reduction factors, $\tilde{K}^{(2)}(\overline{\Gamma}) \approx K_\Gamma(\overline{\Gamma})$. But this is not true in the general case [5.154].

From the discussion above it follows that only the first-order diagonal reduction factors are positive and reduce the value of the matrix elements ($K_\Gamma(\overline{\Gamma}) \ll 1$), while the off-diagonal $K_{\Gamma\Gamma'}$ and second-order $K_\Gamma^{(2)}$ and $K_{\Gamma\Gamma'}^{(2)}$ reduction factors may be both positive and negative, and may either reduce or enhance the physical magnitudes.

On the other hand, we have considered so far only electronic perturbations. It can be shown that if the perturbation operator $X_{\overline{\Gamma}\overline{\gamma}}$ is a function of nuclear coordinates Q, the first-order effect of vibronic coupling will be enhancing, not reducing (see also Section 7.1.1). Indeed, assume that $X_{\overline{\Gamma}\overline{\gamma}}$ is first order in the JT-active nuclear coordinates $Q_{\overline{\Gamma}\overline{\gamma}}$. It can be shown that their reduced matrix elements on vibronic states are [5.1, 5.140]

$$\langle \Psi_\Gamma \| Q_{\overline{\Gamma}} \| \Psi_\Gamma \rangle = -(F_{\overline{\Gamma}}/K_{\overline{\Gamma}}) K_\Gamma(\overline{\Gamma}) \tag{5.136}$$

where $K_\Gamma(\overline{\Gamma})$ is the first-order reduction factor and $F_{\overline{\Gamma}}/K_{\overline{\Gamma}}$ is proportional to the JT distortion in the $Q_{\overline{\Gamma}\overline{\gamma}}$ direction (see Chapter 3; do not confuse the force constant $K_{\overline{\Gamma}}$ with the reduction factors $K_\Gamma(\overline{\Gamma})$), and

$$\langle \Psi_{\Gamma\gamma} | Q_{\overline{\Gamma}\overline{\gamma}} | \Psi_{\Gamma\gamma} \rangle = \langle \Psi_\Gamma \| Q_{\overline{\Gamma}} \| \Psi_\Gamma \rangle \langle \overline{\Gamma}\overline{\gamma}\Gamma\gamma | \Gamma\gamma \rangle \tag{5.136a}$$

Since in the absence of vibronic coupling $\langle \Psi_\Gamma \| Q_{\overline{\Gamma}} \| \Psi_\Gamma \rangle = 0$, the JTE results in enhancing the perturbation $Q_{\overline{\Gamma}\overline{\gamma}}$. For strong vibronic coupling to $Q_{\overline{\Gamma}}$ displacements for which $K_\Gamma(\overline{\Gamma})$ is a nonzero constant, the effect of perturbation is proportional to the JT distortion and increases with the vibronic coupling strength. For instance, in the $T \otimes t_2$ problem the limit value of $K_T(T_2)$ is $\frac{2}{3}$ (Eq. (5.105)), and for a tetrahedral system T_2 distortions are dipolar. The operator of interaction of this system with a corresponding external electric field $\vec{E}$ is proportional to EQ_{T_2} and the effect of this perturbation, which is zero without the vibronic coupling (no polarization effects are taken into account), will be proportional to $(F_T/K_T)K_T(T_2)$.

Note that without external perturbation the average distortion of the JT system *in stationary states* is also zero. Indeed, for the mean displacement

$\langle Q_{\overline{\Gamma}\overline{\gamma}}\rangle$ in the degenerate state we have to evaluate the sum of such values over all the states of the degenerate term:

$$\langle Q_{\overline{\Gamma}\overline{\gamma}}\rangle = \sum_{\gamma} \langle \Psi_{\Gamma\gamma}|Q_{\overline{\Gamma}\overline{\gamma}}|\Psi_{\Gamma\gamma}\rangle = -(F_{\overline{\Gamma}}/K_{\overline{\Gamma}})K_{\Gamma}(\overline{\Gamma}) \sum_{\gamma} \langle \overline{\Gamma}\overline{\gamma}\Gamma\gamma|\Gamma\gamma\rangle = 0 \quad (5.137)$$

The meaning of this result is that without external perturbations the JT distortions are of dynamic nature, preserving, in stationary states, the initial high symmetry of the reference configuration, but in the presence of external perturbations the behavior of the JT system is quite different from that without vibronic coupling (see also Section 7.1.1).

5.7 Conical intersections and the topological phase problem

As discussed in Section 3.2, one of the simplest JT $E\otimes e$ problems with linear vibronic coupling yields an APES in the form of a "Mexican hat" (Fig. 3.3) with a characteristic conical intersection of the two sheets in the center, at the point of twofold degeneracy. When the quadratic and/or cubic terms of vibronic coupling are included, there are three additional conical intersections placed symmetrically around the central one (Fig. 3.9). In more complicated JT problems, there are multiple conical intersections and seams of conical intersections in extended space coordinates (Section 3.3). We have also seen that these conical intersections, their number and their positions affect essentially the vibronic energy spectrum of JT systems and related properties (Sections 5.2–5.4).

For a long time, up to the last decade, not very much attention was paid to these conical intersections; rather they were viewed largely as a "theoretical curiosity." This perception changed recently in view of the latest achievements in the treatment of such systems (see [5.176–5.184] and references therein). One of these achievements is a generalization directly related to the JTE and now known as the *topological (geometric) phase*, or the *Berry-phase problem* (others are related mostly to chemical reaction dynamics).

Consider the two electronic wavefunctions in the linear JT $E\otimes e$ problem as functions of the nuclear coordinates ρ and ϕ in Eq. (3.32) with $G_E=0$. It can easily be seen that these wavefunctions are not single-valued: when moving along the bottom of the trough in Fig. 3.3, along the angle ϕ, from $\phi=0$ to $\phi=2\pi$ (i.e. coming back to the same starting point) the wavefunctions (3.32) change sign! On the other hand the total wavefunction should be single-valued. To satisfy this condition a phase factor $e^{im\phi}$ should be attached to the electronic wavefunctions (3.32) and (5.18) (or to their nuclear counterparts) with

half-integer values of m: $m = \pm(\frac{1}{2}),\ \pm(\frac{3}{2}),\ \pm(\frac{5}{2}), \ldots$ Since with these m values $e^{im(\phi+2\pi)} = -e^{im\phi}$, the additional phase is here $\phi_0 = n\pi$ with $n = 1, 3, 5, \ldots$

The energy is a function of m^2 (see (5.1) and (5.18)), and hence all the energy levels with the above quantum numbers, including the ground state, are doubly degenerate. It follows that the singularity of the conical intersection produces a very strong effect, making the ground and excited states doubly degenerate. Some of these degeneracies are removed by quadratic coupling (Section 5.2), but as was shown in [5.185], the ground state, due to the periodicity condition for the vibrational function along the trough, remains that with $m = \pm\frac{1}{2}$ (the E state) and it is not split by the quadratic terms. The first exited state with $m = \pm\frac{3}{2}$ splits into $A_1 + A_2$. Only very strong quadratic coupling that involves the additional three conical intersections makes the ground state nondegenerate (see section 5.3 and the discussion below).

The wavefunction phase problem, which is directly related to the conical intersection on the APES (the topological phase), as shown above, was first revealed from the solution of the $E \otimes e$ problem [5.55, 5.186]. Berry [5.187] generalized this result and proved that similar phase problems occur in many other situations where the physical quantity depends on a parameter adiabatically, resulting in novel observable effects (see also his precursors [5.188–5.190]).

The Berry-phase theorem [5.187] (not to be confused with Berry pseudorotation, Section 7.1) was proved for any adiabatic process when the Hamiltonian of the system $H(R)$ depends on a parameter R, or several parameters, and changes slowly (adiabatically) with the changes of these parameters. The slow changes mean that at every instant in time the Schrödinger equation for stationary states is valid:

$$H(R(t))|n(R(t))\rangle = E_n(R(t))|n(R(t))\rangle \tag{5.138}$$

The full wavefunction $\Psi(t)$ is proportional to $|n(R(t))\rangle$ with a dynamic phase factor, which in traditional quantum mechanics can be shown to be equal to $\exp[(1/i\hbar)\int E_n(R(t'))dt']$ (for fully stationary states E_n is a constant and the phase is simply $\exp(-iE_nt/\hbar)$). Berry showed that if under these conditions the system is transferred along a closed path in the parameter (R) space, an *additional geometric phase $\gamma(t)$ occurs*, the total phase being $\exp[i\gamma(t) + (1/i\hbar)\int E_n(R(t'))dt']$. The geometric phase can be easily calculated [5.187]:

$$\gamma_n(C) = i\oint_C \langle n(R)|\nabla_R n(R)\rangle dR \tag{5.139}$$

where the integral is taken along any (adiabatic) closed path C (the expression $\langle n(R)|\nabla_R n(R)\rangle$ is imaginary, so γ is real). The parameter R may represent either an external perturbation (and then it is under experimental control), or internal dynamic variables, e.g., nuclear coordinates in the adiabatic approximation, as in the JT case discussed above. In the former case a series of experimental confirmations of the significance of the geometric phase were obtained, including the Aharonov–Bohm effect [5.191] which was shown to be a particular case of the Berry phase [5.187, 5.189], rotation of the polarization vector of light propagating in optical fibers [5.192], high-field NMR experiments [5.193], the fractional quantum Hall effect [5.194], conductance in low-dimensional metals [5.195], λ doubling in diatomics [5.196], etc. The situation is more complicated when the parameter space is formed by dynamic variables, which are beyond experimental control. In these cases the Berry-phase implications result in indirect effects, like the double degeneracy of the vibronic states of the $E \otimes e$ problem mentioned above.

The wavefunction topological phase depends on just the presence of conical intersections, all the other characteristics of the APES being irrelevant, and becomes essential when some global property like transport around a finite closed circuit on the surface is considered. As a simple example of somewhat similar phase behavior, consider parallel translation of a vector on the surface of a sphere [5.197], the length of the vector and the angle it makes with the surface of the sphere being kept constant. If this vector is transported along the perimeter of a spherical triangle with all the three angles equal to 90°, the vector returns to the initial point rotated by 90° with respect to its initial orientation. This $\pi/2$ phase rotation is obviously due to the curvature of the surface. Such *holomony* occurs also in other topology conditions, including JT systems.

We see that the special phase of the wavefunction required in the presence of conical intersection is not a "pure mathematical" result: the physical consequences of the presence of the topological phase are quite real and can be observed experimentally. This circumstance may serve as an additional source of wonder about how abstract mathematical notions like complex numbers (the wavefunction phase is complex) and analyticity turn out to be astonishingly applicable to the real (natural) world [5.198, 5.199] (cited from [5.200]).

In application to JT problems, we note first that the adiabatic (slow) changes of the electronic wavefunction as a function of nuclear coordinates may be achieved only for strong vibronic coupling and low-energy states. With regard to conical intersections in JT systems the following alternative analysis is illustrative. Assume that we keep the electronic wavefunction single-valued (meaning with an attached phase factor) and consider the equation of nuclear

motions in the adiabatic approximation, i.e., when the total wavefunction can be presented as a product of the electronic and nuclear wavefunctions: $\Psi(r, Q) = \psi(r, Q)\chi(Q)$. Conventionally, a general expression for this equation for Q vibrations can be presented as follows [5.201]:

$$[\tfrac{1}{2}M(-i\,\partial/\partial Q + A_Q)^2 + \varepsilon(Q)]\chi(Q) = E\chi(Q) \tag{5.140}$$

where in addition to the usual terms of the ordinary Hamiltonian a gauge potential A_Q is added,

$$A_Q = -i\int \psi^*(r,\ Q)(\partial\psi/\partial Q)dr \tag{5.141}$$

which coincides with $\langle n(R)|\nabla_R n(R)\rangle$ in Eq. (5.139).

If the electronic functions can be chosen single-valued and real, then $A_Q = 0$ and Eq. (5.140) acquires its usual form for nuclear motions with the potential energy $\varepsilon(Q)$. However, in the presence of conical intersections, as well as under some other conditions mentioned above, the electronic function has an attached phase factor which makes it essentially not real, and $A_Q \neq 0$. With the wavefunctions (5.18) or (5.25) the integral $\oint_C A_Q\,dQ$ taken around the conical intersection equals $2\pi m$. On the other hand, the gauge potential A is nonzero in the presence of a magnetic field. Therefore, the implication of a conical intersection is equivalent to that of an additional magnetic field. *The conical intersection acts as a fictitious magnetic field that makes all the energy levels doubly degenerate*. In [5.189] this effect was called the "molecular Aharonov–Bohm effect." It follows that the electromagnetic vector-potential A has a more general physical significance than just as a tool for calculation of the influence of an electromagnetic field. For a comprehensive review of geometric phases in physics and chemistry see [5.176–5.184, 5.200, 5.202–5.204].

An important feature of the Berry-phase implications in JT problems is that the peculiar phase factor that changes the sign of the electronic wavefunctions and makes the ground vibronic state degenerate occurs only when one or an odd number of conical intersections are encircled, while it retains the same sign if an even number (including zero) are encircled. This was shown by direct calculation of the phase (5.139) in the $E \otimes e$ problem [5.205]. In fact, the phase is $\phi_0 = n\pi$, where n is the number of conical intersections encircled; for $n = 0, 2, 4, \ldots$ the sign of the wavefunction does not change. For large quadratic coupling the three marginal conical intersection of the $E \otimes e$ problem (Fig. 3.9) approach the central one, and the tunneling between the minima was shown to encircle all the four conical intersections [5.43] (Section 5.3) resulting

in $\phi_0 = 4\pi$. In this case there is no phase problem: the ground state becomes nondegenerate.

However, as shown in a more rigorous treatment [5.206],the total phase in cases of multiple conical intersections may be model-dependent, meaning that it depends on how the conical intersections are encircled, the distance, and the speed of circling. The authors [5.206] suggested an experimental situation where these phase peculiarities can be observed.

Similarly, in the $T \otimes t_2$ problem with not very large quadratic terms, the ground vibronic state is shown to be threefold degenerate T (Section 5.3) due to the Berry phase. As in the $E \otimes e$ case [5.185], the boundary conditions for the vibrational wavefunction that should change sign when encircling a conical intersection (to compensate for the sign change in the electronic wavefunction) cause the lowest nondegenerate state A to have more nodes than the lowest T state [5.207]. This in turn results in the T state being lower than the A one; without the Berry phase attached the A state would be the ground state.

The lower vibronic T state in the $T \otimes t_2$ problem with small to moderate quadratic coupling is confirmed multiply by direct numerical calculations. However, as shown recently [5.44], for larger quadratic coupling constants a crossover takes place between the A and T vibronic levels, and the A level becomes the ground-state one. The analysis of the possible tunneling paths shows that for sufficiently large quadratic coupling the tunneling goes around an alternative path that involves both types of lines of conical intersections in Fig. 5.12, for which the Berry phase is zero or 2π (Section 5.3). This explains the origin of the crossover resulting in the nondegenerate ground state A.

Further discussion of Berry-phase implications in JT problems has been given for the $T \otimes (e + t_2)$ problem [5.208], which separates into two problems, $T \otimes e$ and $T \otimes t_2$, when one of the couplings is larger than the other. The $\Gamma_8 \otimes (e + t_2)$ problem with strong vibronic coupling has two twofold degenerate terms (the Kramers degeneracy is not removed) for which the extended proof of the Berry-phase theory for degenerate states [5.196] was employed [5.209]. If the coupling to one of the two types of distortions is predominant, the problem reduces to the previously considered $E \otimes e$ or $E \otimes (e + a)$ problems. However, if the two types of couplings have the same strength, the problem becomes more complicated and the Berry phase becomes a 2×2 matrix [5.209].

A more important situation emerges when the spin–orbital interaction splits the orbital degenerate electronic term, transforming the JT problem into a PJT one (Section 4.2). In the JT $E \otimes e$ case the spin–orbital splitting of the E term (Δ) reduces the problem to the PJT effect (Section 4.1). In the adiabatic approximation with strong linear PJT coupling k and ignoring quadratic

coupling in the geometric phase γ was shown to depend on the radius R of the circle around the point of pseudodegeneracy [5.210, 5.211]:

$$\gamma_{\mathrm{JT}}(R) = -\pi[1 + \varepsilon(\Delta,\ R)] \tag{5.142}$$

$$\varepsilon(\Delta,\ R) = \frac{\Delta/k}{\sqrt{(\Delta/k)^2 + R^2}} \tag{5.143}$$

The same (in principle) dependence of the geometric phase on Δ, k, and R is expected when the splitting Δ is produced by an external magnetic field [5.212].

At first sight the dependence of the phase on the radius R of the circle around the pseudodegeneracy (highest-symmetry) point seems to be essential. In fact, however, the adiabatic approximation required for the physicality of the Berry phase is valid just at the bottom of the trough (or the minima) of the APES where $R \approx \rho_0$ (provided k is sufficiently large and $\Delta < k^2$; see Chapters 3 and 4). For the PJT case under consideration $\rho_0 = \sqrt{k^2 - (\Delta/k)^2}$ (Eq. (4.7)) and

$$\varepsilon(\Delta,\ R) = \Delta/k^2 \tag{5.144}$$

Thus the correction to the dependence of the geometric phase on the spin–orbital splitting is essential in transforming the JT problem at $\Delta = 0$ (where the phase implication is significant) into a PJT problem at larger Δ values; at $\Delta = k^2$, $\rho_0 = 0$, and the geometric-phase implications disappear (together with the PJT instability), as expected in the absence of conical intersections.

For the PJT $(E + A) \otimes e$ problem (Section 4.2), when the JTE in the E term is ignored and the E–A energy gap is taken equal to zero, the spin–orbital splitting Δ of the E term produces the following geometric phase [5.210]:

$$\gamma_{\mathrm{PJT}}(R) = 2\pi\varepsilon(\Delta,\ R) \tag{5.145}$$

For $R \approx \rho_0$, using (5.144), we have $\gamma_{\mathrm{PJT}}(R) = 2\pi\Delta/k^2$ (where k is here the constant of PJT coupling between the two split states). This means that the phase implications (which are absent at $\Delta = 0$ since the vibronic coupling in the E state is ignored) are proportional to Δ, but for large Δ values the adiabacity of the system deteriorates (and $\rho_0 = 0$ at $\Delta = k^2$). Effects of "open path phase" may occur in degenerate and nondegenerate states in conditions reflecting the situation as if the conical intersection (or the pseudodegeneracy point) is not fully encircled [5.213] with some consequences mentioned above [5.206].

For icosahedral systems, the relation of the vibronic level H–A crossover (Section 5.3) to the geometric phase in the $H \otimes h$ problem is discussed in [5.214]. The geometric phase in C_{60}^{+} and C_{60}^{2+} is considered in [5.41].

Somewhat outstanding is the Berry-phase problem for JT crystals [5.215–5.217], which was shown to be related to a variety of crystal properties (Chapter 8). It was shown [5.217] that in a crystal with JT centers that have an $E \otimes e$ coupling problem and a geometric phase as described above, the Bloch electron wavefunction acquires a geometric phase too. This crystal conduction-electron Berry phase can change drastically the expected band structure, and may lead to an orbital ordering and orbital density wave. The crystal geometric phase has a site-to-site variation within the lattice period and changes essentially with the lattice constant. It explains also the origin of the stripe structure of manganites with colossal magnetoresistance (Section 8.4).

In development of the presentation of the Berry-phase implications as a fictitious magnetic field at the conical intersection (Eqs. (5.140) and (5.141)) it was shown [5.216] that when a real electromagnetic field is added to the fictitious one, their joint effect is very peculiar because the latter counteracts the former. As a result the ground-state wavefunction is essentially unaltered by a (weak) real magnetic field showing rigidity against penetration of an external electromagnetic influence ($U(1)$ gauge symmetry breaking [5.216]). The predicted consequences of this result are most interesting (Section 8.4).

References

5.1. I. B. Bersuker and V. Z. Polinger, *Vibronic Interactions in Molecules and Crystals*, New York, Springer, 1989.
5.2. R. Englman, *The Jahn–Teller Effect in Molecules and Crystals*, London, Wiley, 1972.
5.3. H. C. Longuet-Higgins, in *Advances in Spectroscopy*, Vol. 2, New York, 1961, p. 429.
5.4. W. Moffitt and A. D. Liehr, *Phys. Rev.* **106**, 1195 (1957).
5.5. W. Moffitt and W. Thorson, *Phys. Rev.* **108**, 1251 (1957).
5.6. M. C. M. O'Brien, *Phys. Rev.* **187**, 407 (1969).
5.7. I. B. Bersuker and V. Z. Polinger, *Phys. Status Solidi B* **60**, 85 (1973).
5.8. W. Moffitt and W. Thorson, in *Calcul des fonctions d'onde moléculaire*, Ed. R. A. Daudel, Paris, CNRS, 1958, p. 141.
5.9. B. Weinstock and G. L. Goodman, *Adv. Chem. Phys.* **9**, 169 (1965).
5.10. A. Witkowski, *Rocz. Chem.* **35**, 1409 (1961).
5.11. R. Renner, *Z. Phys.* **92**, 172 (1934).
5.12. G. Gerzberg and E. Teller, *Z. Physik. Chem. B* **21**, 410 (1933).
5.13. J. A. Pople and H. C. Longuet-Higgins, *Mol. Phys.* **1**, 37 (1958).

5.14. A. V. Petelin and A. A. Kiselev, *Internat. J. Quant. Chem.* **6**, 701 (1972).
5.15. (*a*) Ch. Jungen and A. J. Merer, in *Molecular Spectroscopy: Modern Research*, Vol. 2, Ed. K. N. Rao, New York, Academic Press, 1976, p. 127; (*b*) A. J. Merer and D. N. Travis, *Can. J. Phys.* **43**, 1975 (1965).
5.16. (*a*) H. Köppel, W. Domcke, and L. S. Cederbaum, *J. Chem. Phys.* **74**, 2945 (1984); (*b*) J. M. Brown and F. Jorgensen, *Adv. Chem. Phys.* **52**, 117 (1983).
5.17. M. Perić, E. Engles and S. D. Peyerimhoff, in *Quantum Mechanical Electronic Structure Calculations with Chemical Accuracy*, Ed. S. R. Langhoff, Dordrecht, Kluwer, 1995, p. 261; M. Perić and S. D. Peyerimhoff, *Adv. Chem. Phys.* **124**, 583 (2002).
5.18. G. Herzberg, *Electronic Spectra and Electronic Structure of Polyatomic Molecules*, Toronto, Van Nostrand, 1966.
5.19. Yu. E. Perlin and M. Wagner, in *Dynamical Jahn–Teller Effect in Localized Systems*, Eds. Yu. E. Perlin, and M. Wagner, Amsterdam, Elsevier, 1984, p. 1.
5.20. M. C. M. O'Brien, *Proc. R. Soc. London A* **281**, 323 (1964).
5.21. M. C. M. O'Brien, *J. Phys. C* **4**, 2524 (1971).
5.22. L. Yin and O. Goscinski, *Chem. Phys.* **140**, 363 (1990).
5.23. I. B. Bersuker, *Coord. Chem. Rev.* **14**, 357 (1975); I. B. Bersuker, in *Physics of Impurity Centres in Crystals*, Tallinn, Academy of Sciences of the Estonian SSR, 1972, p. 479.
5.24. G. M. S. Lister and M. C. M. O'Brien, *J. Phys. C* **17**, 3975 (1984).
5.25. I. B. Bersuker, *Opt. Spektrosk.* **11**, 319 (1961); I. B. Bersuker, *Zh. Eksp. Teor. Fiz.* **43**, 1315 (1962) (English transl.: *Sov. Phys. – JETP* **16**, 933 (1963)).
5.26. I. B. Bersuker, B. G. Vekhter, and I. Ya. Ogurtsov, *Uspekhi Fiz. Nauk (Sov. Phys. – Uspekhi)* **116**, 605 (1975).
5.27. V. Z. Polinger, *Adv. Quant. Chem.* **44**, 59 (2003).
5.28. I. B. Bersuker and V. Z. Polinger, *Adv. Quant. Chem.* **15**, 85 (1982).
5.29. I. B. Bersuker and V. Z. Polinger, *Phys. Lett.* A **44**, 495 (1973); *Zh. Eksp. Teor. Fiz.* (*Sov. Phys. – JETP* **66**, 2078 (1974)).
5.30. V. Z. Polinger and S. I. Boldyrev, *J. Phys.: Condens. Matter* **2**, 595 (1990).
5.31. A. I. Baz', Ya. B. Zel'dovich, and A. M. Perelomov, *Scattering, Reactions and Decays in Non-Relativistic Quantum Mechanics*, 2nd edn., Moscow, Nauka, 1971.
5.32. B. R. Judd and E. E. Vogel, *Phys. Rev. B* **11**, 2427 (1975).
5.33. N. M. Avram, G. E. Draganescu, and C. N. Avram, *Can. J. Phys.* **80**, 563 (2002); N. M. Avram, G. E. Draganescu, and M. R. Kibler, *Internat. J. Quant. Chem.* **88**, 303 (2002).
5.34. Y. M. Liu, J. L. Dunn, C. A. Bates, and V. Z. Polinger, *Z. Physik. Chem.* **200**, 111 (1997).
5.35. V. Z. Polinger, *Fiz. Tverd. Tela* **16**, 2578 (1974).
5.36. V. Z. Polinger, P. J. Kirk, J. L. Dunn, and C. A. Bates, *J. Phys.: Condens. Matter* **5**, 2213 (1993).
5.37. R. S. Dagis and I. B. Levinson, in *Optika i spektroskopiya: sbornik statei*, part 3, Leningrad, Nauka, 1967, p. 3; B. P. Martinenas and R. S. Dagis, *Teor. Eksp. Khim.* **5**, 123 (1969).
5.38. A. Ceulemans, *J. Chem. Phys.* **87**, 5374 (1987).
5.39. A. Ceulemans and L. G. Vanquickenbourne, *Struct. Bonding*, **71**, 125 (1989).
5.40. C. P. Moate, M. C. M. O'Brien, J. L. Dunn, C. A. Bates, Y. M. Liu, and V. Z. Polinger, *Phys. Rev. Lett.* **77**, 4362 (1996); J. L. Dunn, M. R. Eccles, Y. Liu, and C. A. Bates, *Phys. Rev. B* **65**, 115107 (2002).

5.41. P. De Los Rios, N. Manini, and E. Tosatti, *Phys. Rev. B* **54**, 7157 (1996-II).
5.42. L. D. Landau and E. M. Lifshitz, *Quantum Mechanics: Non-Relativistic Theory*, Oxford, Pergamon Press, 1977.
5.43. H. Koizumi and I. B. Bersuker, *Phys. Rev. Lett.* **83**, 3009 (1999).
5.44. H. Koizumi, I. B. Bersuker, J. E. Boggs and V. Z. Polinger, *J. Chem. Phys.* **112**, 8470 (2000).
5.45. V. Polinger, R. Huang, C. A. Bates, and J. L. Dunn, in *Vibronic Interactions: Jahn–Teller Effect in Crystals and Molecules*, NATO Science Series, Vol. 39, Eds. M. D. Kaplan and G. O. Zimmerman, Dordrecht, Kluwer, 2001, p. 329.
5.46. V. Polinger, R. Huang, C. A. Bates, and J. L. Dunn, *J. Chem. Phys.* **117**, 4340 (2002).
5.47. G. Bevilacqua, I. B. Bersuker, and L. Martinelli, in *Vibronic Interactions: Jahn–Teller Effect in Crystals and Molecules*, NATO Science Series, Vol. 39, Eds. M. D. Kaplan and G. O. Zimmerman, Dordrecht, Kluwer, 2001, p. 229.
5.48. H. M. Li, V. Polinger, J. L. Dunn, and C. A. Bates, *Adv. Quant. Chem.* **44**, 89 (2003).
5.49. I. B. Bersuker, *Electronic Structure and Properties of Transition Metal Compounds. Introduction to the Theory*, Wiley, New York, 1996.
5.50. S. Sookhun, J. L. Dunn and C. A. Bates, *Phys. Rev.* B **68**, 235403 (2003); Q. C. Qiu, *Acta Phys. Sin.* **52**, 958 (2003); C. Qiu, J. L. Dunn and C. A. Bates, *Phys. Rev. B* **64**, 075102 (2001); V. Polinger, C. A. Bates, and J. L. Dunn, *Z. Physik. Chem.* **200**, 255 (1997); J. L. Dunn and C. A. Bates, *J. Phys.: Condens. Matter* **1**, 375 (1989); R. I. Badran and C. A. Bates, *J. Phys.: Condens. Matter* **3**, 632 (1961).
5.51. H. Barentzen, G. Olbrich, and M. C. M. O'Brien, *J. Phys. A* **14**, 111 (1981); J. Rorison and M. C. M. O'Brien, *J. Phys. C* **17**, 3449 (1984).
5.52. J. W. Zwanziger, E. R. Grant, and G. S. Ezra, *J. Chem. Phys.* **85**, 2089 (1986); J. W. Zwanziger and E. R. Grant, *J. Chem. Phys.* **90**, 2357 (1989).
5.53. A. Thiel and H. Köppel, *J. Chem. Phys.* **110**, 9371 (1999).
5.54. K. A. Bosnick, *Chem. Phys. Lett.* **317**, 524 (2000).
5.55. H. C. Longuet-Higgins, U. Öpik, M. H. L. Pryce, and R. A. Sack, *Proc. R. Soc. London A* **244**, 1 (1958).
5.56. M. Caner and R. Englman, *J. Chem. Phys.* **44**, 4054 (1966).
5.57. N. Sakamoto, *J. Phys. C* **15**, 6379 (1982).
5.58. E. R. Bernstein and J. D. Webb, *Mol. Phys.* **36**, 1113 (1978).
5.59. W. H. Henneker, A. P. Penner, W. Siebrand, and M. Z. Zgiersk, *J. Chem. Phys.* **69**, 1884 (1978).
5.60. R. Lacroix, J. Weber, and E. Duval, *J. Phys. C* **12**, 20 650 (1979).
5.61. M. Zgierski and M. Pawlikowski, *J. Chem. Phys.* **70**, 3444 (1979).
5.62. H. Köppel, L. S. Cederbaum, and W. Domcke, *Chem. Phys.* **69**, 175 (1982).
5.63. C. Lanczos, *J. Res. Nat. Bur. Stand. USA* **45**, 255 (1950); **49**, 33 (1952); *Applied Analysis*, Englewood Cliffs, New Jersey, Prentice-Hall, 1956.
5.64. B. N. Parlett, *The Symmetrical Eigenvalue Problem*, Englewood Cliffs, New Jersey, Prentice-Hall, 1980, Section 13.
5.65. D. K. Fadeev and V. N. Fadeeva, *Computational Method of Linear Algebra*, Moscow, Fizmatigiz, 1963; R. Haydock, V. Heine, and M. J. Kelly, *J. Phys. C* **5**, 2845 (1972); **8**, 2591 (1975); D. W. Bullet, R. Haydock, V. Heine, and M. J. Kelly, in *Solid State Physics: Advances in Research and Applications*, Vol. 35, Eds. H. Erhenreich, F. Seitz, and D. Turnbull, New York, Academic Press, 1980.

5.66. J. H. Wilkinson and C. Reinsch, *Handbook for Automatic Computation. Linear Algebra, Grundlehren der mathematischen Wissenschaften*, Band 186, Vol. 2, Berlin, Springer, 1971.
5.67. S. Muramatsu and N. Sakamoto, *J. Phys. Soc. Japan* **44**, 1640 (1978); **46**, 1273 (1979); N. Sakamoto, *J. Phys. C* **17**, 4791 (1984).
5.68. N. Sakamoto, *J. Phys. Soc. Japan* **48**, 527 (1980); **51**, 1516 (1982); N. Sakamoto, *Phys. Rev. B* **26**, 6438 (1982).
5.69. B. R. Judd, *J. Chem. Phys.* **67**, 1174 (1977).
5.70. E. Haller, L. S. Cederbaum, W. Domcke, and H. Köppel, *Chem. Phys. Lett.* **72**, 427 (1980); *Mol. Phys.* **41**, 1291 (1980).
5.71. (*a*) M. C. M. O'Brien and S. N. Evangelou, *J. Phys. C* **13**, 611 (1980); (*b*) J. R. Fletcher, M. C. M. O'Brien, and S. N. Evangelou, *J. Phys. A* **13**, 2035 (1980).
5.72. S. N. Evangelou, M. C. M. O'Brien, and R. S. Perkins, *J. Phys. C* **13**, 4175 (1980).
5.73. D. R. Pooler, in *The Dynamical Jahn–Teller Effect in Localized Systems*, Eds. Yu. E. Perlin and M. Wagner, Amsterdam, North-Holland, 1984, p. 199.
5.74. G. Grosso, L. Martinelli, and G. P. Parravicini, *Phys. Rev.* B **51**, 13033 (1995-I).
5.75. L. Martinelli and G. P. Parravicini, *Phys. Rev. B* **37**, 10 612 (1988-II); **39**, 13 343 (1989-II); **46**, 15 795 (1992-II); L. Martinelli, M. Passaro, and G. P. Parravicini, *Phys. Rev. B* **43**, 8395 (1991); **40**, 1044 (1989-II).
5.76. L. Martinelli, G. Bevilacqua, J. Rivera-Iratchet, M. A. de Orue, O. Mualin, E. E. Vogel, and J. Cartes, *Phys. Rev. B* **62**, 10 873 (2000-II).
5.77. C. W. Struck and F. Herzfeld, *J. Chem. Phys.* **44**, 464 (1966); H. Uehara, *J. Chem. Phys.* **45**, 4536 (1966).
5.78. R. F. Bishop, N. J. Davidson, R. M. Quick, and D. M. van der Walt, *J. Chem. Phys.* **113**, 4008 (2000); W. M. Wong and C. F. Lo, *Phys. Lett. A* **223**, 123 (1996).
5.79. E. Majernikova and S. Shpyrko, *J. Phys.: Condens. Matter* **15**, 2137 (2003).
5.80. I. B. Bersuker and V. Z. Polinger, *Phys. Status Solidi B* **60**, 85 (1973).
5.81. M. Sakamoto and S. Muramatsu, *Phys. Rev. B* **17**, 868 (1978).
5.82. S. I. Boldyrev, V. Z. Polinger and I. B. Bersuker, *Fiz. Tverd. Tela* **23**, 746 (1981).
5.83. M. Estribe and A. E. Hughes, *J. Phys. C* **4**, 2537 (1971).
5.84. B. R. Judd, *Can. J. Phys.* **52**, 999 (1974).
5.85. B. R. Judd, in *The Dynamical Jahn–Teller Effect in Localized Systems*, Eds. Yu. E. Perlin and M. Wagner, Amsterdam, North-Holland, 1984, p. 87.
5.86. M. C. M. O'Brien, *J. Phys. C* **9**, 3153 (1976).
5.87. M. C. M. O'Brien, *J. Phys. C* **18**, 4963 (1985).
5.88. W. Thorson and W. Moffitt, *Phys. Rev.* **168**, 362 (1968).
5.89. D. R. Pooler and M. C. M. O'Brien, *J. Phys. C* **10**, 3769 (1977).
5.90. A. Abraham and B. Bleaney, *Electron Paramagnetic Resonance of Transition Ions*, Oxford, Clarendon, 1970, Chapter 21.
5.91. A. Barchielli, E. Mulazzi, and G. Parravicini, *Phys. Rev. B* **24**, 3166 (1981)
5.92. H. A. M. Van Eekelen and K. W. H. Stevens, *Proc. Phys. Soc. London* **90**, 199 (1967).
5.93. N. N. Bogolubov; *Quasiaverages in the Problems of Statistical Mechanics*, Preprint D-781, Joint Institute for Nuclear Research, Dubna, 1961 (see also N. N. Bogolubov, *Selected Works*, Vol. 3, Kiev, Naukova Dumka, 1971, p. 174 (in Russian)).

5.94. A. A. Abrikosov, *Physics (N. Y.)* **2**, 5 (1965).
5.95. N. Gauthier and M. B. Walker, *Phys. Rev. Lett.* **31**, 1211 (1973); *Can. J. Phys.* **54**, 9 (1976).
5.96. S. N. Payne and G. E. Stedman, *J. Phys. C* **16**, 2679, 2705, and 2725 (1983).
5.97. J. S. Slonczewski, *Phys. Rev.* **131**, 1596 (1963).
5.98. (*a*) A. V. Vaisleib, V. P. Oleinikov, and Yu. B. Rozenfeld, *Phys. Status Solidi B* **109**, K35 (1982); *Phys. Lett. A* **89**, 41 (1982); *Fiz. Tverd. Tela* **24**, 1074 (1982); (*b*) Yu. B. Rozenfeld and A. V. Vaisleib, *Zh. Eksp. Teor. Phys.* **86**, 1059 (1984); *J. Phys. C* **19**, 1721 and 1739 (1986).
5.99. E. M. Henley and W. Thirring, *Elementary Quantum Field Theory*, New York, McGraw-Hill, 1962, Chapter 18.
5.100. Yu. B. Rozenfeld and V. Z. Polinger, *Zh. Eksp. Teor. Fiz.* **70**, 597 (1976).
5.101. M. Baer, A. Vibok, G. Halasz, and D. J. Kouri, *Adv. Quant. Chem.* **44**, 103 (2003); T. Vertesi, A. Vibok, G. Halasz, and M. Baer, *J. Chem. Phys.* **121**, 4000 (2004).
5.102. M. Wagner, in *The Dynamical Jahn–Teller Effect in Localized Systems*, Eds. Yu. E. Perlin and M. Wagner, Amsterdam, North-Holland, 1984, p. 155.
5.103. H. Barentzen and O. E. Polansky, *J. Chem. Phys.* **68**, 4398 (1978).
5.104. C. C. Chancey, *J. Phys. A* **17**, 3183 (1984).
5.105. M. Schmutz, *Physica A* **101**, 1 (1980).
5.106. H. Barentzen, G. Olbrich, and M. C. M. O'Brien, *J. Phys. A* **14**, 111 (1981).
5.107. C. A. Bates, J. L. Dunn, and E. Sigmund, *J. Phys. C* **20**, 1965 (1987).
5.108. J. R. Fletcher, *Solid State Commun.* **11**, 601 (1972); J. Maier and E. Sigmund, *Solid State Commun.* **51**, 961 (1984).
5.109. C. J. Ballhausen, *Chem. Phys. Lett.* **93**, 407 (1982).
5.110. R. Englman, A. Yahalom, and M. Baer, *J. Chem. Phys.* **109**, 6550 (1998); *Phys. Lett. A* **251**, 223 (1999); *Eur. Phys. J. A* **60**, 1802 (2000).
5.111. P. Huai and H. Zheng, *Phys. Lett. A* **240**, 341 (1998).
5.112. D. R. Pooler, *Phys. Rev. B* **21**, 4804 (1980).
5.113. N. Manini, A. Dal Corso, M. Fabrizio, and E. Tosatti, *Phil. Mag. B* **81**, 793 (2001); M. Lueders, A. Bordoni, N. Manini, A. Dal Corso, M. Fabrizio, and E. Tosatti, *Phil. Mag. B* **82**, 1611 (2002); M. Lueders, N. Manini, P. Gatari, and E. Tosatti, *Eur. Phys. J. B* **35**, 57 (2003); M. Lueders and N. Manini, *Adv. Quant. Chem.* **44**, 289 (2003).
5.114. Y.-S. Yi, L. Tian, C.-L. Wang, Z.-B. Su, and L. Lu, *Physica C* **282–287**, 1927 (1997); C. Wu, C.-L. Wang, and Z.-B. Su, *Internat. J. Mod. Phys. B* **13**, 1513 (1999); W.-Z. Wang, A. R. Bishop, and L. Lu, *Phys. Rev. B* **50**, 5016 (1994-I); C.-L. Wang, W.-Z. Wang, Y.-L. Liu, Z.-B. Su, and L. Lu, *Phys. Rev. B* **50**, 5676 (1994-II).
5.115. S. S. Sookhun, C. A. Bates, J. L. Dunn, and W. Diery, *Adv. Quant. Chem.* **44**, 319 (2003).
5.116. J. Singh, *Internat. J. Quant. Chem.* **19**, 859 (1981); C. C. Chancey and B. R. Judd, *J. Phys. A* **16**, 875 (1983); H. G. Reik, in *The Dynamical Jahn–Teller Effect in Localized Systems*, Eds. Yu. E. Perlin and M. Wagner, Amsterdam, North-Holland, 1984, p. 117.
5.117. (*a*) M. C. M. O'Brien, *J. Phys. C* **5**, 2045 (1972); (*b*) *J. Phys. C* **16**, 6345 (1983).
5.118. H. Köppel, W. Domcke, and L. S. Cederbaum, *Adv. Chem. Phys.* **57**, 59 (1984)
5.119. C. S. Sloane and R. Silbee, *J. Chem. Phys.* **56**, 6031 (1972).
5.120. (*a*) V. Z. Polinger and G. I. Bersuker, *Phys. Status Solidi B* **96**, 403 (1979); (*b*) *Fiz. Tverd. Tela* **22**, 2545 (1980).

5.121. J. C. Slonczewski and W. L. Moruzzi, *Physics* **3**, 237 (1967).
5.122. L.-C. Fan and O. Chin, *Kexue Tonbao* **17**, 101 (1966); *Acta Phys. Sin.* **22**, 471 (1966).
5.123. G. I. Bersuker and V. Z. Polinger, *Zh. Eksp. Teor. Fiz.* **80**, 1788 (1981); *Solid State Commun.* **38**, 795 (1981).
5.124. V. Z. Polinger, *Zh. Eksp. Teor. Fiz.* **77**, 1503 (1979).
5.125. G. I. Bersuker and V. Z. Polinger, *Phys. Status Solidi B* **125**, 401 (1984).
5.126. I. B. Bersuker and V. Z. Polinger, *Zh. Strukt. Khim.* **24**, 62 (1983).
5.127. R. Englman and B. Halperin, *Ann. Phys.* **3**, 453 (1978).
5.128. S. N. Evangelou and A. C. Hewson, *Numerical Renormalization-Group Approach for Locally-Coupled Electron–Phonon System*, Preprint Ref. 34/82, University of Oxford, 1982, p. 27.
5.129. E. Haller, H. Köppel, and L. S. Cederbaum, *Chem. Phys. Lett.* **101**, 215 (1983); *Phys. Rev. Lett.* **52**, 1665 (1984); *J. Phys. A* **17**, L831 (1984).
5.130. N. Manini and E. Tosatti, *Phys. Rev. B* **58**, 782 (1998-II).
5.131. N. Manini and E. Tosatti, in *Recent Advances in the Chemistry and Physics of Fullerenes and Related Materials*, Vol. 2, Ed. K. M. Kadish and R. S. Ruoff, Pennington, New Jersey, 1995, p. 1017.
5.132. K. W. N. Stewens, *J. Phys. C* **2**, 1934 (1969).
5.133. P. Steggels, *J. Phys. C* **10**, 2817 (1977).
5.134. B. M. Kogan and R. A. Suris, *Zh. Eksp. Teor. Fiz.* **50**, 1279 (1966); N. M. Aminov and B. I. Kochelaev, *Fiz. Tverd. Tela* **11**, 2906 (1969).
5.135. Y. B. Levinson and E. I. Rashba, *Rep. Prog. Phys.* **36**, 1499 (1973).
5.136. V. Z. Polinger, C. A. Bates, and J. L. Dunn, *Z. Physik. Chem.* **200**, 255 (1997).
5.137. H. Bill, in *The Dynamical Jahn–Teller Effect in Localized Systems*, Eds. Yu. E. Perlin and M. Wagner, Amsterdam, North-Holland, 1984, pp. 709–818.
5.138. I. B. Bersuker and B. G. Vekhter, *Fiz. Tverd. Tela* **5**, 2432 (1963) (English transl.: *Sov. Phys. – Solid State* **5**, 1772 (1964)).
5.139. F. S. Ham, *Phys. Rev. A* **138**, 1727 (1965).
5.140. F. S. Ham, in *Electron Paramagnetic Resonance*, Ed. S. Geschwind, New York, Plenum, 1972, p. 1.
5.141. C. H. Leung and W. H. Kleiner, *Phys. Rev. B* **10**, 4434 (1974).
5.142. F. S. Ham, *Phys. Rev. A* **166**, 307 (1968).
5.143. J. R. Fletcher, *J. Phys. C* **14**, L491 (1981).
5.144. R. Romestain and J. Merle d'Aubigne, *Phys. Rev. B* **4**, 4611 (1971).
5.145. J. R. Fletcher and G. E. Stedman, *J. Phys. C* **17**, 3441 (1984).
5.146. N. Sakamoto, *Phys. Rev. B* **31**, 785 (1985).
5.147. B. Halperin and R. Englman, *Phys. Rev. Lett.* **31**, 1052 (1973).
5.148. J. C. Slonczewski, *Solid State Commun.* **7**, 519 (1969).
5.149. B. Halperin and R. Englman, *Solid State Commun.* **7**, 1579 (1969).
5.150. B. G. Vekhter, *Fiz. Tverd. Tela* **25**, 1537 (1983).
5.151. M. C. M. O'Brien and D. R. Pooler, *J. Phys. C* **12**, 311 (1979).
5.152. G. G. Setser and T. L. Estle, *Phys. Rev. B* **17**, 999 (1978).
5.153. G. Davies and C. Foy, *J. Phys. C* **13**, 2203 (1980).
5.154. B. G. Vekhter, *Phys. Lett. A* **45**, 133 (1973).
5.155. F. S. Ham, in *Optical Properties of Ions and Crystals*, Eds. H. M. Crosswhite and H. M. Moos, New York, Interscience, 1967, p. 357.
5.156. (*a*) F. Ham, C. H. Leung, and W. Kleiner, *Solid State Commun.* **18**, 757 (1976); (*b*) D. R. Pooler and M. C. M. O'Brien, *J. Phys. C* **10**, 3769 (1977).

5.157. J. A. L. Simpson, C. A. Bates, and J. L. Dunn, *J. Phys.: Condens. Matter* **3**, 6845 (1991).
5.158. S. H. Payne and G. E. Stedman, *J. Phys. C* **16**, 2679, 2705, and 2725 (1983).
5.159. V. P. Khlopin, V. Z. Polinger, and I. B. Bersuker, *Theor. Chim. Acta* **48**, 87 (1978).
5.160. C. C. Chancey and M. C. M. O'Brien, *The Jahn–Teller Effect in C_{60} and other Icosahedral Complexes*, Princeton, New Jersey, Princeton University Press, 1997.
5.161. P. B. Oliete, C. A. Bates, J. L. Dunn, and G. E. Stedman, *Phys. Rev. B* **60**, 2319 (1999-I).
5.162. J. L. Dunn and A. C. Bates, *Phys. Rev. B* **52**, 5996 (1995).
5.163. Q. C. Qiu, J. L. Dunn, A. C. Bates, and Y. M. Liu, *Phys. Rev. B* **58**, 4406 (1998).
5.164. Q. C. Qiu, J. L. Dunn, A. C. Bates, M. Abou-Ghantous, and V. Z. Polinger, *Phys. Rev. B* **62**, 16155 (2000-I).
5.165. J. L. Dunn, C. A. Bates, and P. J. Kirk, *J. Phys.: Condens. Matter* **2**, 10 379 (1990).
5.166. J. P. Cullerne and M. C. M. O'Brien, *J. Phys.: Condens. Matter* **6**, 9017 (1994).
5.167. M. Abou-Ghantous, P. B. Oliete, C. A. Bates, J. L. Dunn, V. Z. Polinger, R. Huang, and S. P. Rough, *J. Phys.: Condens. Matter* **14**, 4679 (2002).
5.168. R. Huang, M. Abou-Ghantous, C. A. Bates, J. L. Dunn, V. Z. Polinger, and C. P. Moate, *J. Phys.: Condens. Matter* **14**, 1319 (2002)
5.169. P. W. Fowler and A. Ceulemans, *Mol. Phys.* **54**, 767 (1985).
5.170. (*a*) C. A. Bates and J. L. Dunn, *J. Phys.: Condens. Matter* **1**, 2605 (1989); (*b*) **1**, 2617 (1989).
5.171. M. C. M. O'Brien, *J. Phys.: Condens. Matter* **2**, 5539 (1990).
5.172. C. A. Bates and J. L. Dunn, L. D. Hallam, P. J. Kirk, and V. Z. Polinger, *J. Phys.: Condens. Matter* **3**, 3441 (1991).
5.173. V. Z. Polinger, C. A. Bates and J. L. Dunn, *J. Phys.: Condens. Matter* **3**, 513 (1991).
5.174. M. Abou-Ghantous, V. Z. Polinger, J. L. Dunn, and C. A. Bates, *J. Phys.: Condens. Matter* **14**, 3115 (2002).
5.175. C. A. Bates, M. Abou-Ghantous, J. L. Dunn, F. Al-Hazmi, V. Z. Polinger, and E. A. Moujaes, *J. Phys.: Condens. Matter* **16**, 5309 (2004); F. Al-Hazmi, V. Z. Polinger, J. L. Dunn, C. A. Bates, E. A. Moujaes, and M. Abou-Ghantous, *Adv. Quant. Chem.* **44**, 169 (2003).
5.176. *Conical Intersections: Electronic Structure, Dynamics, and Spectroscopy*, Eds. W. Domcke, D. R. Yarkony, and H. Köppel, Singapore, World Scientific, 2003.
5.177. A. W. Jasper, B. K. Kendrick, C. A. Mead, and D. G. Truhlar, in *Modern Trends in Chemical Reaction Dynamics*, Singapore, World Scientific, 2003.
5.178. D. R. Yarkony, *J. Phys. Chem. A* **105**, 6277 (2001).
5.179. *The Role of Degenerate States in Chemistry*; a special volume of *Adv. Chem. Phys.* **124**, Eds. M. Baer and G. D. Billing, New York, Wiley, 2002.
5.180. T. Pacher, L. S. Cederbaum, and H. Köppel, *Adv. Chem. Phys.* **84**, 293 (1993).
5.181. M. Baer, A. M. Mebel, and R. Englman, *Chem. Phys. Lett.* **354**, 243 (2002).
5.182. A. Bohm, A. Mostafazadeh, H. Koizumi, Q. Niu, and J. Zwanziger, *The Geometric Phase in Quantum Systems*, Berlin, Springer, 2003.
5.183. I. J. R. Aitchison, *Phys. Scripta T* **23**, 12 (1988).

5.184. *Geometric Phases in Physics*, Eds. A. Shapere and F. Wilczek, Singapore, World Scientific, 1989.
5.185. S. F. Ham, *Phys. Rev. Lett.* **58**, 725 (1987).
5.186. G. Herzberg and H. C. Longuet-Higgins, *Discuss. Faraday Soc.* **35**, 77 (1963).
5.187. M. V. Berry, *Proc. R. Soc. London A* **392**, 45 (1984).
5.188. C. A. Mead, and D. G. Truhlar, *J. Chem. Phys.* **70**, 2284 (1979).
5.189. C. A. Mead, *Chem. Phys.* **49**, 23 and 33 (1980).
5.190. B. Simon, *Phys. Rev. Lett.* **51**, 2167 (1983).
5.191. Y. Aharonov and D. Bohm, *Phys. Rev.* **115**, 485 (1959).
5.192. R. Y. Chiao and Y.-S. Wu, *Phys. Rev. Lett.* **57**, 933 (1986); R. Y. Chiao, *Phys. Rev. Lett.* **57**, 937 (1986).
5.193. P. Suter, G. Chingas, R. A. Haris, and A. Pines, unpublished, cited after [5.205].
5.194. D. J. Thouless, M. Kohmoto, M. P. Nightingale, and M. den Nijs, *Phys. Rev. Lett.* **49**, 405 (1982); J. E. Avron, R. Seiler, and B. Simon, *Phys. Rev. Lett.* **51**, 51 (1983); G. W. Semenoff and P. Sodano, *Phys. Rev. Lett.* **57**, 1195 (1986).
5.195. J. R. Schreiffer, *Mol. Cryst. Liq. Cryst.* **118**, 57 (1985).
5.196. F. Wilczek and A. Zee, *Phys. Rev. Lett.* **52**, 2111 (1984); J. Moody, A. Shapere, and F. Wilczek, *Phys. Rev. Lett.* **56**, 893 (1986); R. Jakiw, *Phys. Rev. Lett.* **56**, 2779 (1986).
5.197. V. I. Arnold, *Mathematical Methods of Classical Mechanics*, New York, Springer, 1978, Appendix 1.
5.198. E. P. Wigner, in *The Place of Consciousness in Modern Physics*, Eds. C. Muses and A. M. Young, New York, Outerbridge and Lazzard, 1972.
5.199. M. Steiner, *The Applicability of Mathematics as a Philosophical Problem*, Cambridge, Massachusetts, Harvard University Press, 1998.
5.200. R. Englman and A. Yahalom, *Adv. Chem. Phys.* **124**, 197 (2002).
5.201. N. Born and K. Huang, *Dynamical Theory of Crystal Latices*, London, Oxford University Press, 1954, Appendix VIII.
5.202. J. W. Zwanziger, M. Koenig, and A. Pines, *Ann. Rev. Phys. Chem.* **41**, 601 (1990).
5.203. A. Bohm, L. J. Boya, and B. Kendrick, *Phys. Rev. A* **43**, 1206 (1991).
5.204. C. A. Mead, *Rev. Mod. Phys.* **64**, 51 (1992).
5.205. J. W. Zwanziger and E. R. Grant, *J. Chem. Phys.* **87**, 2954 (1987).
5.206. R Englman, A. Yahalom, M. Baer, and A. M. Mebel, *Internat. J. Quant. Chem.* **92**, 135 (2003); R. Englman and A. Yahalom, *Phys. Rev. A* **67**, 054103 (2003); R. Englman and A. Yahalom, in *The Role of Degenerate States in Chemistry*; a special volume of *Adv. Chem. Phys.* **124**, Eds. M. Baer and G. D. Billing, New York, Wiley, 2002, p. 197S.
5.207. F. Ham, *J. Phys.: Condens. Matter* **2**, 1163 (1990).
5.208. C. C. Chancey and M. C. M. O'Brien, *J. Phys. A* **21**, 3347 (1988).
5.209. S. E. Apsel, C. C. Chancey, and M. C. M. O'Brien, *Phys. Rev. B* **45**, 525 (1992-II).
5.210. J. Schön and H. Köppel, *J. Chem. Phys.* **108**, 1503 (1998).
5.211. H. Koizumi and S. Sugano, *J. Chem. Phys.* **102**, 4472 (1995).
5.212. G. Bevilacqua, L. Martinelli, and G. P. Parravicini, *Phys. Rev. B* **63**, 132403 (2001).
5.213. R. Englman, A. Yahalom, and M. Baer, *Eur. Phys. J. D* **8**, 1 (2000); *Phys. Lett. A* **251**, 223 (1999); R. Englman and A. Yahalom, *Phys. Rev. A* **60**, 1802 (1999); *J. Phys.: Condens. Matter* **11**, 1059 (1999); A. J. C. Varandas, M. Baer, and R. Englman, *J. Chem. Phys.* **111**, 9493 (1999).

5.214. N. Manini and P. de Los Rios, in *Electron–Phonon Dynamics and Jahn–Teller Effects*, Eds. G. Bevilacqua, L. Martinelli, and N. Terzi, Singapore, World Scientific, 1999, p. 37.
5.215. H. Koizumi, *Phys. Rev. Lett.* **76**, 2370 (1996).
5.216. H. Koizumi, *Phys. Rev.* **59**, 8428 (1999-I).
5.217. H. Koizumi, T. Hotta, and Y. Takada, *Phys. Rev. Lett.* **80**, 4518 (1998).

6

The Jahn–Teller effect in spectroscopy: general theory

With this chapter we begin the applications of the general theory of the JTE to *all-range spectroscopy, molecular structure, and solid-state physics* (Chapters 6–8). Among them the JTE in spectral properties is the most significant due to the sensitivity of spectra to changes in electronic structure and vibronic coupling. On the other hand, the influence of vibronic coupling on spectra is very specific; it depends on both the system parameters and the spectral range under consideration. Still there are some general features common to all systems with the same JT problem.

This chapter is devoted to such a general theory of the JTE in spectroscopy. More particular problems are considered in Chapters 7 and 8, together with the corresponding specific systems, but the separation of the general theory from more system-oriented questions is to a large extent conventional. Obviously, there is also substantial overlap with calculations of vibronic states presented in Chapter 5: spectroscopy is inalienable from energies and wavefunctions of the system.

6.1 Electronic transitions

6.1.1 Optical band shapes

Optical band shapes with the JTE were subjected to multiple investigations by many authors (see the reviews [6.1–6.10] and references therein).

The term band shape means an envelope of elementary transitions between vibronic states, each of which has a specific width so that the vibronic lines merge into a continuous band. The light-absorption coefficient $K_{12}(\mathbf{\Omega})$ due to the electronic transition $1\rightarrow 2$ is determined by the relation $I = I_0 \exp[-K_{12}(\mathbf{\Omega})l]$, where I_0 and I are the intensities of the incident and transmitted light, respectively, and l is the absorption-layer thickness. $K_{12}(\mathbf{\Omega})$ has the following form [6.3, 6.11]:

$$K_{12}(\mathbf{\Omega}) = (4\pi^2 N\mathbf{\Omega}/3c)F_{12}(\mathbf{\Omega}) \tag{6.1}$$

where

$$F_{12}(\mathbf{\Omega}) = \sum_{\kappa,\kappa'} \rho_{1\kappa} \left| \langle 1\kappa | \vec{M} | 2\kappa' \rangle \right|^2 \delta(E_{2\kappa'} - E_{1\kappa} - \hbar\mathbf{\Omega}) \tag{6.2}$$

is the *shape function* of the band, N is the number of absorbing centers per unit volume, $M_{1\kappa 2\kappa'} = \langle 1\kappa | M | 2\kappa' \rangle$ is the matrix element of the transition moment, κ and κ' label the vibronic ground and excited states, respectively, $\rho_{1\kappa}$ is the probability that the ground energy state $E_{1\kappa}$ is populated according to the Boltzmann distribution,

$$\rho_{1\kappa} = \exp(-E_{1\kappa}/kT)/Z_1 \tag{6.3}$$

$Z_1 = \sum_{\kappa''} \exp(-E_{1\kappa''}/kT)$ is the *sum of states* of the ground term, and the δ-function takes into account the energy-conservation law, due to which the transition $1\kappa \rightarrow 2\kappa'$ is possible only if $\hbar\mathbf{\Omega} = E_{2\kappa'} - E_{1\kappa}$.

A simple relationship links the shape function for the emission band due to the $2 \rightarrow 1$ transtion, $F_{21}(\mathbf{\Omega})$, with the above function $F_{12}(\mathbf{\Omega})$ for the corresponding absorption [6.3]:

$$F_{12}(\mathbf{\Omega}) = (Z_2/Z_1) F_{12}(\mathbf{\Omega}) \exp(-\hbar\mathbf{\Omega}/kT) \tag{6.4}$$

where Z_2 is the sum of states of the excited term.

The main features of the shape function can be determined in the *semiclassical approximation*. In this approximation it is assumed that at not very low temperatures, $kT \gg \hbar\omega$, where ω is the vibrational frequency, during the electronic transition the nuclei remain fixed at their positions Q of the initial state (in accordance with the Franck–Condon principle), and therefore the energies $E_{1\kappa}$ and $E_{2\kappa'}$ can be taken approximately equal to the respective values of the APES at the point Q: $E_{1\kappa} = \varepsilon_1(Q)$ and $E_{2\kappa'} = \varepsilon_2(Q)$. Then, on passing from summation to integration in Eq. (6.2), we obtain

$$F_{12}(\mathbf{\Omega}) = \int \rho_1(Q) \left| \vec{M}_{12}(Q) \right|^2 \delta[\varepsilon_2(Q) - \varepsilon_1(Q) - \hbar\mathbf{\Omega}] dQ \tag{6.5}$$

where

$$\vec{M}_{12}(Q) = \int \Psi_1^*(r, Q) \vec{M} \Psi_2(r, Q) d\tau \tag{6.6}$$

If both states, ground and excited, are nondegenerate, then

$$\varepsilon_1(Q) = \tfrac{1}{2} K Q^2, \qquad \varepsilon_2(Q) = \hbar\mathbf{\Omega}_0 + \tfrac{1}{2} K (Q - Q_0)^2 \tag{6.7}$$

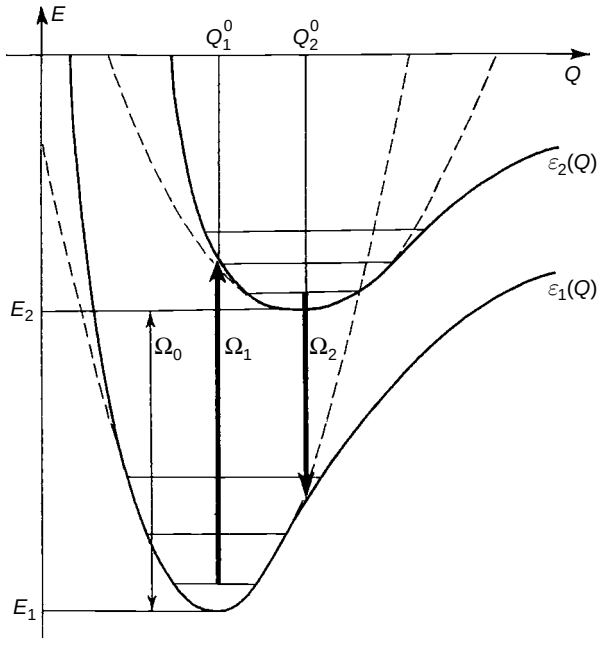

Fig. 6.1. The AP curves, vibrational states, and "vertical" transition between two electronic states. $\mathbf{\Omega}_0$, $\mathbf{\Omega}_1$, and $\mathbf{\Omega}_2$ are the pure electronic (zero-phonon), maximum absorption, and emission frequencies, respectively, while Q_1^0 and Q_2^0 are the minimum positions of the ground and excited states, respectively.

where Q is the totally symmetric coordinate, Q_0 is the shift in position of the minimum in the excited state with respect to the ground one (the other coordinates remain undisplaced), and $\mathbf{\Omega}_0$ is the frequency of the zero-phonon line (Fig. 6.1). On substituting these expressions into Eqs. (6.5) and (6.6) and neglecting the weak dependence of M_{12} on Q, we obtain

$$F_{12}(Q) = \left|\vec{M}_{12}^{(0)}\right|^2 \frac{\exp[-\hbar^2(\mathbf{\Omega} - \mathbf{\Omega}_0)^2/2kTKQ_0^2]}{(2\pi kTK)^{\frac{1}{2}}Q_0} \tag{6.8}$$

It follows that the band has a *Gaussian form*.

Assume now that the excited state is degenerate. Then, besides the totally symmetric coordinates, the nontotally symmetric JT-active coordinates are displaced. For the $A \rightarrow E$ transition in the linear vibronic coupling approximation with polar coordinates ρ and ϕ for the e_g displacements (Section 3.2), we have

$$\begin{aligned} \varepsilon_1(Q, \rho, \phi) &= \tfrac{1}{2}K_A Q^2 + \tfrac{1}{2}K_E\rho^2 \\ \varepsilon_2(Q, \rho, \phi) &= \hbar\mathbf{\Omega}_0 + \tfrac{1}{2}K_A(Q - Q_0)^2 + \tfrac{1}{2}K_E\rho^2 \pm |F_E|\rho \end{aligned} \tag{6.9}$$

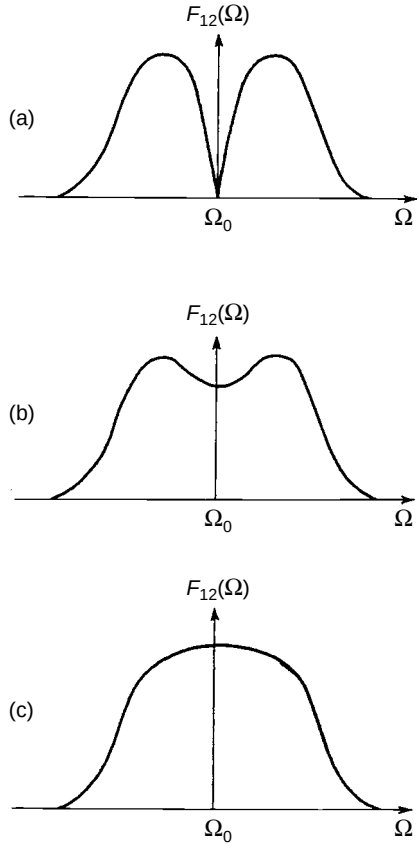

Fig. 6.2. Schematic presentation of the band shape of the $A \rightarrow E$ transition calculated in the semiclassical approximation including the linear coupling with e and a vibrations: (a) the coupling with totally symmetric vibrations a is neglected ($X_A = 0$, $X_E \neq 0$); (b) the a vibrations are included, but the coupling to e vibrations is predominant ($X_A \neq 0$, $X_E \neq 0$, but $X_E > X_A$); and (c) the coupling to a vibrations is predominant ($X_E < X_A$).

On substituting these expressions into Eq. (6.5) with $Q_0 = 0$, i.e., neglecting the contribution of the totally symmetric vibrations to the band shape, we get

$$F_{12}(Q) = \frac{\left|\vec{M}_{12}^{(0)}\right|^2 \hbar|\mathbf{\Omega} - \mathbf{\Omega}_0|}{4kTE_{\mathrm{JT}}} \exp[-\hbar^2(\mathbf{\Omega} - \mathbf{\Omega}_0)^2/2kTE_{\mathrm{JT}}] \tag{6.10}$$

The relationship (6.10) is presented graphically in Fig. 6.2(a). It has a symmetric shape with two humps and a dip at $\mathbf{\Omega} = \mathbf{\Omega}_0$. This band shape can be interpreted as being due to *JT splitting of the nonvibronic band*. The splitting (distance between the two maxima) equals $(8E_{\mathrm{JT}}kT)^{\frac{1}{2}}$. The first calculations of

the electronic absorption-band shapes of JT systems in a semiclassical approximation were performed in [6.12, 6.13], and then improved in [6.14], taking into account also the weak splitting of the E term by external fields in the $A \rightarrow E$ transition.

If the contribution of the totally symmetric vibrations is taken into account, then $Q_0 \neq 0$, and the expression (6.10) becomes more complicated. Its main feature depends on the relation between the stabilization energies $E_{\mathrm{JT}}^E = F_E^2/2K_E$ and $E_{\mathrm{JT}}^A = F_A^2/2K_A$ (Section 3.2). If the high-temperature limitation $kT \gg \hbar\omega$ is removed, then the parameters $X_E = F_E^2 \coth(\hbar\omega_E/2kT)$ and $X_A = F_A^2 \coth(\hbar\omega_E/2kT)$ should be compared. If $X_A = 0$, but $X_E \neq 0$, we get the shape function shown in Fig. 6.2(a); for $X_A \neq 0$, but $X_A < X_E$, the band shape loses its singularity at $\mathbf{\Omega} = \mathbf{\Omega}_0$, becoming as shown in Fig. 6.2(b); at $X_A > X_E$ the two-humped feature of the curve disappears and the band acquires the usual (in our case Gaussian) shape for transitions to nondegenerate terms (Fig. 6.2(c)).

For RT problems the band shapes of electronic transitions were evaluated in the semiclassical approximation in [6.15].

The semiclassical approximation yields rather rough results that nevertheless allow one to reveal the main qualitative features of the band structure of spectra of JT systems at sufficiently high temperatures. More accurate results were obtained by means of numerical calculations of the vibronic energy levels $E_{n\kappa}$ and wavefunctions $|n\kappa\rangle$ that allow direct calculation of the individual transition probabilities $M_{1\kappa 2\kappa'} = \langle 1\kappa|M|2\kappa'\rangle$ and the shape function (6.2). The first such calculations (which were also the first calculations of the optical JTE) were performed in [6.16, 6.17] for the transition between a nondegenerate A and twofold degenerate E terms.

The E-term vibronic energy levels in the linear vibronic coupling approximation are classified by the quantum number $m = \pm\frac{1}{2}, \pm\frac{3}{2}, \ldots$ (Section 5.1), while for the A term the ground vibrational state has $m = 0$ (zero quanta of e vibrations), and for dipolar transitions $\Delta m = \pm\frac{1}{2}$. Therefore in the $A \rightarrow E$ absorption at $T = 0$, transitions to vibronic levels $m = \pm\frac{1}{2}$ only are allowed. Figure 6.3 illustrates the results obtained for $A \rightarrow E$ and $E \rightarrow A$ transitions at $T = 0$ and three different values of vibronic coupling in the $E \otimes e$ problem taken in dimensionless units $\lambda = E_{\mathrm{JT}}^E/\hbar\omega$. We see that, compared with the semiclassical picture (Fig. 6.2), the two-humped band shape for the $A \rightarrow E$ transition has significant asymmetry and nonzero intensity at $\mathbf{\Omega} = \mathbf{\Omega}_0$. The asymmetry decreases with increasing vibronic coupling. The $E \rightarrow A$ transition has a bell-shaped curve in both approaches. The equidistant positions of the lines are due to the assumed equally spaced rotational energy levels.

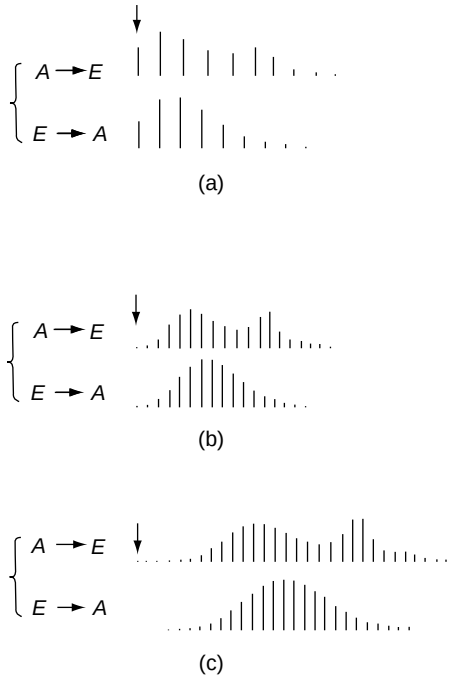

Fig. 6.3. Frequencies and relative intensities of vibronic components and the band shape (envelope) for $A \rightarrow E$ and $E \rightarrow A$ transitions calculated at $T = 0$ for the following values of the dimensionless vibronic constant: (a) $\lambda = 2.5$; (b) $\lambda = 7.5$; and (c) $\lambda = 15$. The position of the zero-phonon line is shown by an arrow (from [6.16]).

Further improvements in such calculations were achieved in several works [6.18–6.21]. In particular, for very large coupling constant ($\lambda \sim 400$) the envelope of the high-frequency wing of the spectrum has additional structure [6.18–6.20], shown in Fig. 6.4, which is sometimes called *Slonczewski resonances* [6.18, 6.20, 6.21], illustrated in Fig. 6.5. The temperature dependence of the shape function of $A \rightarrow E$ transition is demonstrated in Fig. 6.6 [6.22]. So-called continued-fraction numerical calculations for $A \rightarrow E$ transitions were performed in [6.23].

Higher-order terms of vibronic interaction and external low-symmetry fields increase the complexity of the spectrum [6.24, 6.25]. The strong anharmonicity of the APES and nonadiabacity (Sections 2.1 and 2.4) make the numerical calculations of the spectra most difficult, in particular, because of the failure of the Franck–Condon approximation in the optical transition [6.25, 6.10]. Other approaches, including the *independent-ordering approximation* [6.14, 6.26, 6.27] and the method of *canonical transformations* [6.28] (Section 5.4) were tried and compared with numerical results. Approximate

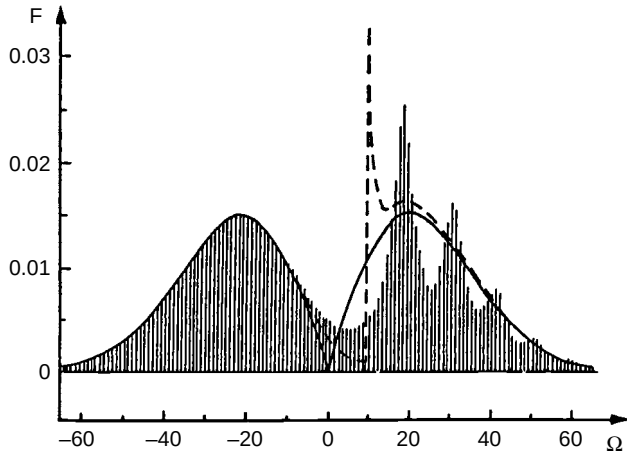

Fig. 6.4. The band shape of the $A \rightarrow E$ transition at $T = 0$ and $\lambda_E = E_{\mathrm{JT}}^E / \hbar\omega_E = 400$. Vertical lines are exact numerical solutions [6.19], while the dashed and solid curves show the semiempirical results obtained with [6.1] and without [6.14] the centrifugal interaction, respectively. $\mathbf{\Omega}$ is read off from the Franck–Condon transition frequency $\mathbf{\Omega}_{EA}$ (in ω_E units); F is the form factor (6.2).

analytical treatments were also suggested [6.29, 6.30]. The $A \rightarrow E$ transition in tetragonal systems with the JT $E \otimes (b_1 + b_2)$ problem is discussed in [6.31]. This paper considers also ${}^1A \rightarrow {}^2E$ transitions in trigonal systems including the spin–orbital coupling in the ${}^2E$ state (see below). $E \rightarrow E$ transitions treated semiclassically in the strong vibronic coupling limit yield a four-humped envelope curve for the band shape [6.14] corresponding to the transitions from the two sheets of the lower E term to the two sheets of the upper E term. ${}^2E \rightarrow {}^2T$ transitions in tetrahedral systems were also considered in a similar approximation [6.32].

For the $A \rightarrow T$ transition the first calculations of the absorption spectra were performed in [6.33] assuming that the linear coupling to the t_2 mode only is effective in the T state, the linear $T \otimes t_2$ problem (Section 3.3). The vibronic spectrum of the latter, obtained earlier [6.34] by numerical solution of the vibronic coupling equations (2.6), was used to calculate optical transitions from the ground state to individual vibronic levels of the excited state. Then, replacing each of the absorption lines by a Gaussian band, the envelope of the $A \rightarrow T$ band was revealed. The results are shown in Fig. 6.7. A special feature of these curves is their asymmetrically positioned three peaks. Qualitatively, this band shape emerges also in the semiclassical approximation based on Eq. (6.5) [6.13]. The $A \rightarrow T$ transition with the full $T \otimes (e + t_2)$ problem in the excited state was considered in [6.35]. For the $T \rightarrow A$ transition the use of the relation

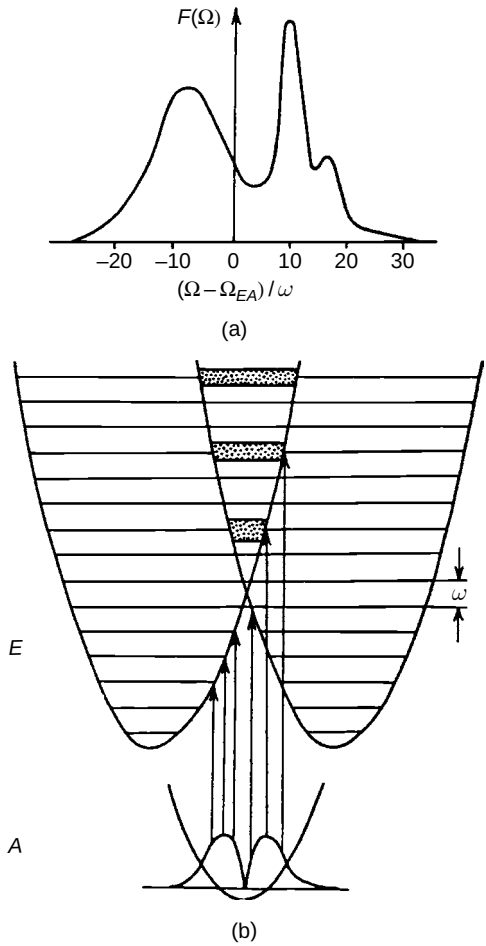

Fig. 6.5. Optical transitions $A \rightarrow E$ with strong excited-state $E \otimes e$ vibronic coupling: (a) the band shape at $\lambda_E = E_{\mathrm{JT}}^E / \hbar\omega_E = 64$; and (b) the APES cross-sections for the A and E terms with corresponding transitions shown by arrows (reprinted with permission from [6.18]. Copyright 1973 Springer-Verlag).

(6.4) is useful in establishing the band shape [6.36]; at high temperatures the more-than-one-peak structure of the band disappears because of the Boltzmann factor $\exp(-\hbar\boldsymbol{\Omega}/kT)$.

The band shape of the $A \rightarrow T$ transition was also evaluated by means of the independent-ordering approximation [6.37], and by the method of cumulant expansion [6.38]. The transition to the nearly degenerate $A_{1g} + T_{1u}$ state with an $(\mathrm{A}_{1g} + T_{1u}) \otimes (a_{1g} + e_g + t_{1u} + t_{2u})$ problem (Section 4.2) was also discussed [6.39]. Operator methods for similar problems were used in [6.40]; a bibliography of previous publications on the subject is also given in this paper.

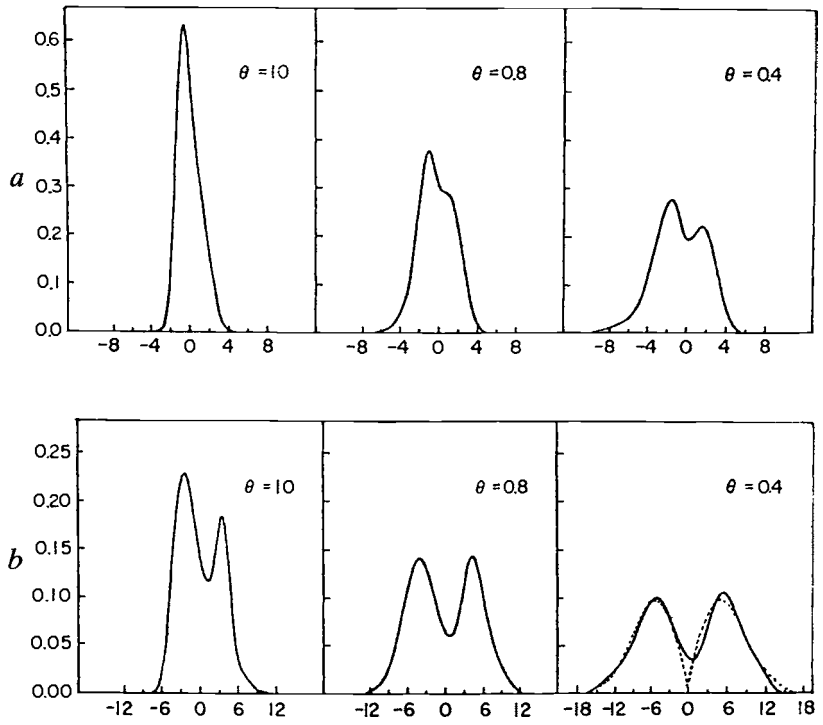

Fig. 6.6. The temperature dependence of the absorption band shape of the $A \rightarrow E$ transition obtained by numerical solution of the linear $E \otimes e$ problem including the coupling with a vibrations, $\lambda_A = 0.5$, and e vibrations, $\lambda_E = 0.5$ (a) and $\lambda_E = 5.0$ (b) [6.22]. The frequency with respect to the pure electronic transition $\mathbf{\Omega} = 0$ is given in ω_E units, and $\theta = \hbar\omega_E/KT$. For strong vibronic coupling and at high temperatures the absorption curve approaches the semiclassical limit shown by the dashed line (cf. Fig. 6.2).

The spectra of $A \rightarrow T$ transitions are often complicated by the spin–orbital splitting of the T term. For instance, as mentioned earlier, the ${}^2T_1$ term splits into a Kramers doublet Γ_6 and a quadruplet Γ_8. Although only the latter is a JT term subject to the JT $\Gamma_8 \otimes (e + t_2)$ problem (Section 3.3), the doublet Γ_6 cannot be excluded from the treatment because the vibronic coupling mixes the two terms in a PJTE. The full consideration is thus of a JT $\Gamma_8 \otimes (e + t_2)$ plus PJT $(\Gamma_6 + \Gamma_8) \otimes (e + t_2)$ problem. In [6.12(*b*)] the latter is taken into account by perturbation theory (see also [6.41]).

A similar problem emerges in the transition ${}^1A_{1g} \rightarrow ({}^1T_{1u} + {}^3T_{1u})$ for the so-called A and C absorption bands of thallium-like impurities in alkali halide crystals [6.42]. The A-band shape, taken separately and including vibronic coupling to the t_2 vibrations only, is discussed in [6.13], where the PJT (and spin–orbital) mixing of the ${}^1T_{1u}$ and ${}^3T_{1u}$ terms is also considered in the

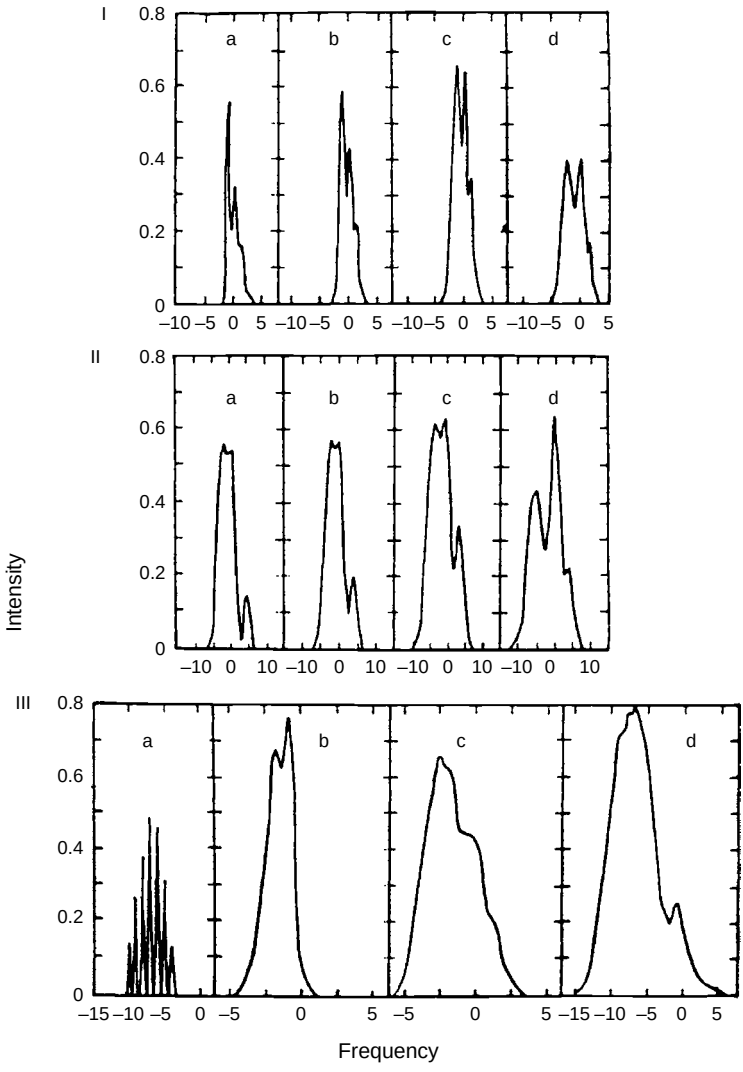

Fig. 6.7. Band shapes of the electronic $A \rightarrow T$ transitions (envelopes of elementary transitions) in absorption (**I**, **II**) and $T \rightarrow A$ transitions in emission (**III**) with a $T \otimes t_2$ problem in the T state at various temperatures: $kT/\hbar\omega_E = 0$ (a), 0.5 (b), 1.0 (**I**c, **II**c), and 4 (d), and two values of the coupling constant, $\lambda_E = E_{\mathrm{JT}}^E/\hbar\omega_E = 2/3$ (**I**, **III**b) and 3.527 (**II**, **III**a, **III**d) [6.33].

framework of perturbation theory (similarly to [6.12(*b*)].) The B-band shape of the transition ${}^1A_{1g} \rightarrow ({}^3A_{1u} + {}^3T_{1u} + {}^3E_u + {}^3T_{2u} + {}^1T_{1u})$ that includes all the vibronic mixing interactions in thallium-like centers was evaluated by means of the semiclassical approximations [6.43]. A detailed bibliography of studies of the shapes of the A, B, and C absorption bands in thallium-like centers is given in [6.8, 6.44, 6.45].

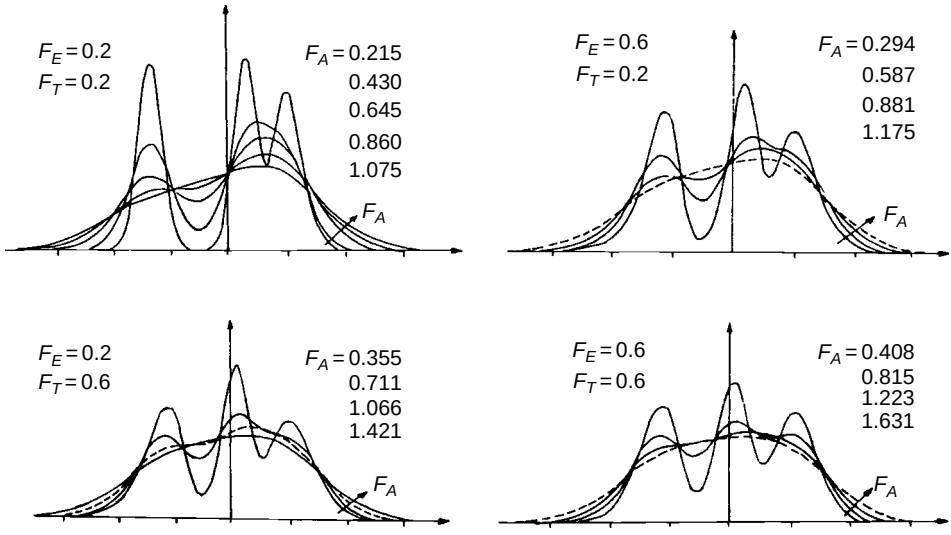

Fig. 6.8. The band shape of electronic $A \rightarrow T$ transitions with coupling to e, t_2, and a vibrations in the T state obtained in the semiclassical approximation of the $T \otimes (a + e + t_2)$ problem [6.46]. F_E, F_T, and F_A are the dimensionless vibronic coupling constants. The three-humped curve becomes essentially smoothed with the increase of totally symmetric a vibrations.

More general discussion of the band shape of the ${}^2A \rightarrow {}^2T$ transition in the semiclassical approximation taking into account the spin–orbital interaction and the coupling to the a_1, e, and t_2 vibrations is given in [6.46]. Figure 6.8 illustrates the results. The band shape is strongly dependent on the relations between the constants of vibronic coupling to the three types of active modes in the T state and the spin–orbital constant. As in the $A \rightarrow E$ transition (Figs. 6.2 and 6.3), the totally symmetric vibrations smooth out the humps of the band.

If the coupling to the e vibrations is predominant (the $T \otimes e$ problem), and the spin–orbit interaction is zero, the absorption band of the $A \rightarrow T$ transition is not split, in spite of the significant splitting of the adiabatic potential (Section 3.3). In the case of predominant coupling to the t_2 vibrations, the absorption band is split into three, and its envelope depends to a large extent on the magnitude of vibronic coupling to all the active vibrations, a_1, e, and t_2.

The special case of a T_2 term equally coupled to e and t_2 modes (the *d-mode model*, Section 3.3) with the spin–orbit interaction included was considered in [6.47–6.50]. The same d-mode approximation in numerical diagonalization of the $\Gamma_8 \otimes (e + t_2)$ problem was used to elucidate the band shape of the $\Gamma_6({}^2T_1) \rightarrow \Gamma_8({}^2T_1)$ transition [6.51]. Similarly to the $A \rightarrow E$ case (the orbital parts of Γ_6 and Γ_8 are similar to those of the A and E terms, respectively; Section 3.3), the $\Gamma_6({}^2T_1) \rightarrow \Gamma_8({}^2T_1)$ transition has a two-humped structure, and

for very strong vibronic coupling a third peak is resolved on the high-frequency wing (cf. Figs. 6.4 and 6.5), which is interpreted as a Slonczewski resonance.

The PJT mixing of one of the two combining states with a third one essentially influences the spectrum of transitions between them. Optical manifestations of this effect have received much attention ever since the foundation of the theory of vibronic interactions. First the vibronic mixing of nondegenerate electronic states was introduced in order to explain the occurrence of optically forbidden bands in the electronic absorption spectrum [6.52]. This *intensity-borrowing effect*, which is taken into account by means of a perturbation expansion of the electron wavefunctions in terms of the vibronic coupling constant, is known today as the *Herzberg–Teller effect*.

A comprehensive review of the large number of publications in this area is outside the scope of this book; we just cite some representative examples [6.51–6.56] including numerical calculations of the vibronic band structure of the optical transition $A \rightarrow (A + B) \otimes b$ [6.51], semiclassical calculations of the envelope band shape [6.54], and explanations of different spectroscopic phenomena using the one-mode PJT Hamiltonian [6.55]. In [6.56] the PJT mixing of the ground state E with the excited T_2 in tetrahedral d^1 systems was shown to influence both optical and EPR spectra. The PJTE becomes more complicated if one takes into account the additional totally symmetric vibrations that modulate the energy separation of the interacting states (Section 3.2).

In the analysis of band shapes in JT systems the *method of moments* may be useful [6.3, 6.5]. The integral

$$\langle \mathbf{\Omega}^n \rangle = \int_{-\infty}^{+\infty} \mathbf{\Omega}^n F_{12}(\mathbf{\Omega}) d\mathbf{\Omega} \tag{6.11}$$

is called the nth *moment of the optical band*. The first few moments have specific physical meaning: the zeroth moment $\langle \mathbf{\Omega}^0 \rangle$ equals the integral intensity of the band (the area limited by the band curve), the first moment $\langle \mathbf{\Omega}^1 \rangle$ gives the center of gravity of the band, the second moment $\langle \mathbf{\Omega}^2 \rangle$ is equal to the half-width of the band, the third moment $\langle \mathbf{\Omega}^3 \rangle$ characterizes the asymmetry of the band, and so on.

It appears that if the initial state of the transition is nondegenerate, the moments of the band can be calculated exactly [6.1, 6.3, 6.5, 6.57, 6.58]. Since these moments can also be determined experimentally from the band shape, some new possibilities regarding how to evaluate the system parameters arise. In particular, the vibronic constants of the excited degenerate electronic state can be estimated from the absorption band shape and its behavior under external perturbations [6.58].

Important relationships can be obtained by examining the polarization dichroism caused by the uniaxial stress. As indicated, the T term of a system with cubic symmetry under tetragonal uniaxial deformation splits into the A and E terms of the D_{4h} group. The transition from a nondegenerate A term to the A component is allowed under parallel (l) polarization and transition to the E component is allowed under perpendicular (t) polarization. The change of the first moments $\Delta\mathbf{\Omega} = \langle\mathbf{\Omega}\rangle - \langle\mathbf{\Omega}\rangle_0$ relative to the initial value $\langle\mathbf{\Omega}\rangle_0$ for the unsplit T term is

$$\Delta\langle\mathbf{\Omega}\rangle_{\mathrm{l}} = -e_\vartheta P_E/\hbar, \qquad \Delta\langle\mathbf{\Omega}\rangle_{\mathrm{t}} = -e_\vartheta P_E/2\hbar \tag{6.12}$$

where e_ϑ is the component of the strain tensor $e_{E\gamma}$, $\gamma = \vartheta$, ε, and P_E is the electron–strain coupling constant. The second moments do not change under the influence of stress:

$$\langle\mathbf{\Omega}^2\rangle_{\mathrm{l}} = \langle\mathbf{\Omega}^2\rangle_{\mathrm{t}} = \langle\mathbf{\Omega}^2\rangle_0 \tag{6.13}$$

It is important that the contributions of the totally symmetric and nontotally symmetric JT-active modes to the second moment (half-width) of the band $\sigma_2(\Gamma)$ can be separated with respect to their symmetries (A, E, and T_2 for the T term and A and E for the E term). For the term in question

$$\langle\mathbf{\Omega}^2\rangle_0 = \sigma_2(A) + \sigma_2(E) + \sigma_2(T_2) \tag{6.14}$$

where

$$\sigma_2(\Gamma) = C_\Gamma \omega_\Gamma^2 \coth(\hbar\omega_\Gamma/2kT) \tag{6.15}$$

and $C_\Gamma = F_\Gamma^2/2\hbar\omega_\Gamma K_\Gamma$ if $\Gamma = A$, E, and $C_{T_2} = F_{T_2}^2/\hbar\omega_{T_2}K_{T_2}$. In particular, at zero temperature $\sigma_2(\Gamma) = C_\Gamma\omega_\Gamma^2$.

For the third moments (η is the sign of the polarization, l or t)

$$\langle\mathbf{\Omega}^3\rangle_\eta = \langle\mathbf{\Omega}^3\rangle_0 - (3/2)\Delta\langle\mathbf{\Omega}\rangle_\eta\sigma_2(T_2)$$

or (6.16)

$$\Delta\langle\mathbf{\Omega}^3\rangle_\eta = -(3/2)\Delta\langle\mathbf{\Omega}\rangle_\eta\sigma_2(T_2)$$

Under uniaxial stress along the trigonal axis

$$\begin{aligned}\Delta\langle\mathbf{\Omega}\rangle_{\mathrm{l}} &= 2e_T P_T/\hbar\sqrt{3}\\ \Delta\langle\mathbf{\Omega}\rangle_{\mathrm{t}} &= -\Delta\langle\mathbf{\Omega}\rangle_{\mathrm{l}}/2\end{aligned} \tag{6.17}$$

For the second moments, the same relationships (6.14) and (6.15) as for tetragonal stress are valid, while for the third moments

$$\Delta\langle\mathbf{\Omega}^3\rangle_\eta = -(1/2)\Delta\langle\mathbf{\Omega}\rangle_\eta[3\sigma_2(E) + \sigma_2(T_2)] \tag{6.18}$$

The general group-theory formula [6.59, 6.60] for the change of the moments of the $A \rightarrow \Gamma$ transition under external influence is

$$\begin{aligned} \Delta\langle \boldsymbol{\Omega}^3 \rangle_\eta &= \Delta\langle \boldsymbol{\Omega} \rangle_\eta \sum_{\overline{\Gamma}} \alpha(\overline{\Gamma}) \sigma_2(\overline{\Gamma}) \\ \langle \boldsymbol{\Omega}^2 \rangle &= \sum_{\overline{\Gamma}} \sigma_2(\overline{\Gamma}) \\ \alpha(\overline{\Gamma}) &= [\overline{\Gamma}](-1)^{J(\overline{\Gamma})+J(\tilde{\Gamma})} \begin{Bmatrix} \Gamma & \Gamma & \tilde{\Gamma} \\ \Gamma & \Gamma & \overline{\Gamma} \end{Bmatrix} - 1 \end{aligned} \tag{6.19}$$

where $\overline{\Gamma}$ is the representation of the JT active modes, $[\overline{\Gamma}]$ is its dimension, $\tilde{\Gamma}$ is the representation of the external influence, $J(\Gamma)$ is the quasi-moment of the Γ representation, and the braces denote the 6Γ symbol [6.61].

From (6.18) and (6.19) it can be found that

$$\begin{aligned} -(3/2)\sigma_2(T_2) &= \Delta\langle \boldsymbol{\Omega}^3 \rangle_\eta^{\text{tetr}} / \Delta\langle \boldsymbol{\Omega} \rangle_\eta^{\text{tetr}} \\ -(3/2)\sigma_2(E) - (1/2)\sigma_2(T_2) &= \Delta\langle \boldsymbol{\Omega}^3 \rangle_\eta^{\text{trig}} / \Delta\langle \boldsymbol{\Omega} \rangle_\eta^{\text{trig}} \end{aligned} \tag{6.20}$$

It follows that if the changes of the first and third moments of the band under induced polarization dichroism can be estimated from the experimental absorption curves, the contributions of vibrations of $\sigma_2(\Gamma)$ of different symmetries and the corresponding vibronic parameters can be obtained from Eq. (6.15). Since the above relationships are precise, the accuracy of the vibronic constant determined in this way depends only on the precision of the experimental determination of the band shape and its first and third moments.

By way of example, we illustrate the evaluation of the numerical values of $\sigma_2(\Gamma)$ from the optical absorption band shape of the F center in $SrCl_2$ ($A_1 \rightarrow T_2$ transition) by means of the method of moments [6.60]. In this case a complication arises due to the presence of the term A_1, which mixes strongly with the excited T_2 term by t_2 vibrations. Therefore, besides the T_2 term JTE, the PJTE caused by mixing the pair of terms A_1 and T_2 contributes to the band shape. As a result the second moment contains not three terms as in Eq. (6.14), but four terms: $\langle \boldsymbol{\Omega}^2 \rangle_0 = \sigma_2(A_1) + \sigma_2(E) + \sigma_2(T_2) + \sigma_2(T_2')$, the last term taking into account the A_1–T_2 mixing contribution. By means of trigonal and tetragonal stress dichroism and magnetic circular dichroism, the following equations can be derived:

$$\begin{aligned} 2\Delta\langle \boldsymbol{\Omega}^3 \rangle_\eta^{\text{tetr}} &= \Delta\langle \boldsymbol{\Omega} \rangle_\eta^{\text{tetr}} [3\sigma_2(T_2) + 2\sigma_2(T_2')] \\ 2\Delta\langle \boldsymbol{\Omega}^3 \rangle_\eta^{\text{trig}} &= \Delta\langle \boldsymbol{\Omega} \rangle_\eta^{\text{trig}} [\sigma_2(T_2) + 3\sigma_2(E) + 2\sigma_2(T_2')] \\ 2\Delta\langle \boldsymbol{\Omega}^3 \rangle_\pm &= \Delta\langle \boldsymbol{\Omega} \rangle_\pm [3\sigma_2(T_2) + 3\sigma_2(E) + 2\sigma_2(T_2')] \end{aligned} \tag{6.21}$$

Now, using the empirical data for the band moment changes, one obtains (in units of the second moment $\langle \mathbf{\Omega}^2 \rangle$) $\sigma_2(A_1) = 0.025$, $\sigma_2(E) = 0.159$, $\sigma_2(T_2) = 0.36$ and $\sigma_2(T_2') = 0.456$. It is seen that in this case the main contributions to the second moment of the band are from the JTE and the PJTE. The contribution of the totally symmetric vibrations A_1 is unimportant.

If spin–orbital splitting is taken into account, additional parameters appear in Eqs. (6.20) and (6.21). However, the number of equations can also be increased by introducing additional perturbations, that induce polarization dichroisn, as in the above example [6.60]. Spin-forbidden transitions are treated using the method of moments in [6.62].

The method of moments has been developed mainly for application to optical properties of impurity centers in crystals and to exciton absorption. The application of this effective method to molecular spectroscopy, to spectroscopy of transition metal and rare-earth coordination compounds, etc., seems to be very useful.

So far we have considered ideal systems only. In the multimode JT problems (Sections 3.5 and 5.5) the evaluation of the optical band shapes is significantly more complicated. However, if the conditions of the semiclassical approximation are satisfied, the differences between the ideal and multimode problem are essentially diminished. Indeed, as shown in Section 3.5, the APES of the JT multimode problem can be reduced to that of a corresponding one-mode (ideal) problem by means of an appropriate choice of the parameters of the generalized interaction mode. In general this leads to more complicated expressions for the kinetic energy, but in the semiclassical approximation quantum effects in the nuclear motions are ignored; the nuclei are considered moving classically along the APES and hence the latter only determines the band shape (see Eq. (6.5)).

Using the method of moments outlined above one can obtain the multimode expressions for the momenta of the band shape as a sum of each mode's contribution and, by comparison with the experimental data, extract the corresponding parameter values of the vibronic interaction. For instance, for the A→E transition, the second moment (characterizing the half-width of the band) is

$$\langle \mathbf{\Omega}^2 \rangle = \sigma_2(E) = \sum_n (2E_{\mathrm{JT}}^{E,n}\, \omega_n/\hbar) \coth(\hbar\omega_n/2kT) \tag{6.22}$$

where $E_{\mathrm{JT}}^{E,n} = F_{E,n}^2/2K_{E,n}$ is the n-mode JT stabilization energy, while the third moment is

$$\langle \mathbf{\Omega}^3 \rangle = \sum_n 2E_{\mathrm{JT}}^{E,n}\omega_n^2/\hbar \tag{6.23}$$

In comparison with the expressions for the ideal case (6.15) at $T=0$, we see that the effective one-mode values for the multimode problem are (cf. (5.86)) [6.63, 6.64]

$$E_{\mathrm{JT}}^{E}=\sum_{n}E_{\mathrm{JT}}^{E,n},\qquad \omega_{\mathrm{eff}}=\sum_{n}E_{\mathrm{JT}}^{E,n}\omega_{n}^{2}\Big/\sum_{n}E_{\mathrm{JT}}^{E,n}\omega_{n} \tag{6.24}$$

For a continuous spectrum of JT-active vibrations of the same symmetry in the multimode problem of an impurity center in crystals Eq. (3.101) may be involved. This leads to a modification of Eq. (6.22):

$$\sigma_{2}(E)=\sum_{n}\frac{F_{\Gamma}^{2}a_{n}^{2}(\Gamma)}{2\hbar K_{\Gamma,n}}\omega_{n} \tag{6.25}$$

where the Van Fleck coefficients $a_n(\Gamma)$ [6.65] characterize the participation of the displacements of the first coordination sphere (that is coupled to the electronic state via the common coupling constant F_Γ) in the nth Γ-type mode [6.3, 6.5].

The semiclassical approximation and the method of moments work better for strong vibronic coupling when the separation of different APES sheets is sufficiently large. In cases of weak coupling and a finite number of discrete modes in the multimode coupling problem the more accurate Eq. (6.2) should be employed. Although, in general, individual mode contributions are interrelated via the vibronic coupling to the same electronic state, in the weak-coupling limit these contributions can be estimated as additive second-order perturbation corrections. Under these conditions the shape function (6.2) can be presented as a convolution of the partial contributions of each mode (the convolution approximation [6.66]). Examples with this approach are considered in Section 6.2.

6.1.2 Vibronic fine structure, zero-phonon lines, and tunneling splitting

In this section we discuss the general features of fine structure of JT spectra when individual spectral lines can be observed. The fine structure of the spectrum carries more information about the electronic structure and JT vibronic coupling effects than the band shape, but the two aspects of the electronic light absorption are in fact complementary, and their separation is conventional.

The fine structure of the spectrum can be observed when the individual transitions between the vibronic states of the two electronic terms are resolved. From the theoretical point of view this means that the vibronic energy levels and wavefunctions are calculated for the two combining electronic terms and

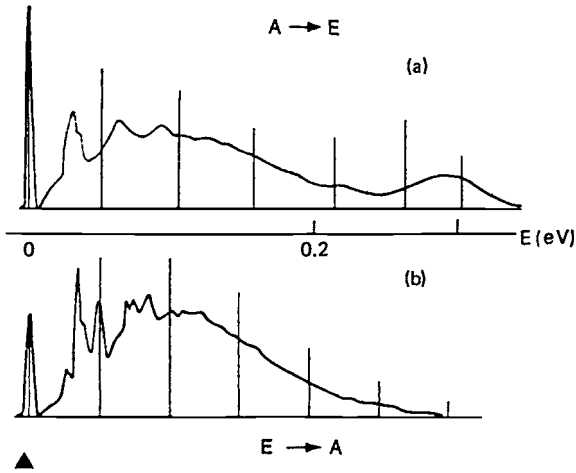

Fig. 6.9. The R′ band in KCl: comparison of the experimental spectrum (continuous curve) with the numerical solution of the $E \otimes e$ problem (vertical lines) in absorption $A \rightarrow E$ (a) and luminescence $E \rightarrow A$ (b). The best agreement is obtained for $E_{\mathrm{JT}}^{E}/\hbar\omega_E = 2.5$, $\hbar\omega_E = 395\ \mathrm{cm}^{-1}$. The zero-phonon line indicated by the sign ▲ occupies the same position in both spectra [6.82].

the probabilities of transition between them are evaluated. Methods of calculation of vibronic states are given in Chapter 5, while calculations of spectra for specific systems are discussed in Chapters 7 and 8.

Some general features of the expected vibronic spectra were already described in the first publications on numerical calculation of transitions between the vibronic states in the A→E and E→A [6.16, 6.17] and A→T and T→A spectra [6.33] discussed in the previous section. A series of works devoted to the vibronic spectra in relatively small organic and some other molecules with detailed discussion of the numerical procedures and results gives a real impression of the significance of the vibronic coupling [6.6, 6.10, 6.25, 6.69–6.77]. Some results for specific molecules obtained in these papers are discussed in Chapter 7.

For impurity centers in crystals, in addition to the influence on the optical band shapes, the JT vibronic coupling produces *local and pseudolocal resonances* and affects the *zero-phonon line* (Section 5.5). The local resonances occur as a result of the multimode JTE [6.78–6.81, 6.59], and are in a way similar to the low-frequency JT transitions in ideal systems (e.g., tunneling splitting, Section 5.3), broadened by the influence of other vibrations of the continuum phonon spectrum. They determine the fine structure of the optical absorption band at low temperatures. Figure 6.9 shows an illustrative example [6.82] of both the band shape (envelope curve) and the low-frequency structure

of the R' band in KCl with the zero-phonon line in both absorption and luminescence.

The vibronic implications in the *zero-phono-line problem* need some more detailed attention. It is obvious that if the adiabatic potentials ε_1 (Q) and ε_2 (Q) of the two combining terms (Fig. 6.1) have the same curvature, the energies of the transitions $0\rightarrow0$, $1\rightarrow1$, $2\rightarrow2$, ... coincide, the corresponding lines in the spectrum of optical absorption are superimposed, and at this frequency only a single line is observed. These are the *zero-phonon transitions*, and the corresponding line in the optical spectrum is called the *zero-phonon line*. A distinguishing feature of this line is that its position coincides in absorption and luminescence (Fig. 6.9). The idea that many zero-phonon transitions can add up to contribute to one narrow spectral line remains valid also for multimode systems, in particular, for crystals, where the zero-phonon line is a sharp intense peak on the background of the continuous multi-phonon absorption.

The difference between the curvatures of the APES ε_1(Q) and ε_2(Q), and hence between the frequencies of vibrations ω_1 and ω_2, produces differences in the energies of the zero-phonon transitions $0\rightarrow0$, $1\rightarrow1$, $2\rightarrow2$, ... As a result, the zero-phonon line is slightly split into many lines, which in multimode systems merge into one broadened zero-phonon line. The influence of this so-called frequency effect (sometimes called the *Dushinski effect*) on the width of the zero-phonon line of optical transitions between nondegenerate states is well studied [6.3, 6.5]. The anharmonicity of the potential curves ε_1(Q) and ε_2(Q) is another cause of broadening and shifts of the zero-phonon line.

The generalization of the theory of zero-phonon lines (which has been developed for polyatomic systems with nondegenerate electronic states) to include the vibronic coupling in cases of degenerate and pseudodegenerate terms is not trivial, even when the JTE occurs in only one of the combining electronic terms. First, with the vibronic interaction included the oscillator occupation numbers of the JT-active normal vibrations cease to be good quantum numbers, and the vibronic states of the JT systems are no longer characterized by the phonon numbers. From this point of view, the "zero-phonon transitions," for which the "vibrational state" of the Jahn–Teller system does not change, have no physical meaning. Second, the vibronic energy levels are distinctly not equally spaced (see, e.g., Fig. 5.19 in Section 5.4), and therefore the coincidence of the energies of the allowed transitions, and hence the corresponding superposition of the spectral lines, is extremely improbable.

Nevertheless, the experimentally observed optical bands of absorption and luminescence of JT systems at low temperatures in some cases display a sharp peak: the zero-phonon line. At $T=0\,\mathrm{K}$ it is the lowest-frequency line of the

absorption spectra, i.e., it is located at the low-frequency edge of the band. With increasing temperature the zero-phonon line of JT systems rapidly broadens, its intensities decreasing, and at higher temperatures it ceases to be seen against the background of the multi-phonon band.

In JT systems at $T = 0\,\mathrm{K}$ only the ground vibronic state of the term (from which the optical transition starts) is populated, and therefore the lowest-frequency line seen in the absorption spectrum corresponds to the $0 \rightarrow 0$ transition, i.e., to the transition between the lowest vibronic states of the combining terms. (Note that the zeros in the expression "$0 \rightarrow 0$ transition" are no longer the vibration occupation numbers as in the case of transitions between non-degenerate states). In molecular systems and clusters with a discrete vibronic spectrum, the $0 \rightarrow 0$ transition line is similar to other δ-type spectral lines. The situation is different in multimode vibronic systems with continuous vibrational spectra, in particular, in crystals with JT impurity centers. As mentioned above and in Section 5.5, the vibronic interaction in the localized JT center affects the electron–vibrational energy spectrum of the system as a whole, resulting in the occurrence of local and pseudolocal vibronic states (resonances). For weak-to-intermediate vibronic coupling (for which the zero-phonon line can be expected, in general) these changes take place only in separate discrete regions of the spectrum; in other respects the density of states remains the same as without the impurity JTE. If the vibronic resonances are neglected, the properties of the zero-phonon line of the system are in many ways similar to its properties in transitions between nondegenerate states. In particular, the density of vibrational states near the ground state is very small. Therefore at $T = 0\,\mathrm{K}$ there is a gap in the optical absorption band on the right-hand side of the $0 \rightarrow 0$ transition line, and this gap allows the separation of the zero-phonon line (Fig. 6.9).

Since the vibronic interaction is localized at the JT impurity center, the vibronic coupling of the electron and nuclear motions takes place only for several collectivized degrees of freedom localized near this center (Section 5.5). For most long-wave vibrations for which $\omega_\kappa \rightarrow 0$ the impurity JTE hardly changes the oscillator nature of their motion. In this sense, one can view the system approximately as a set of vibronic states for the JT degrees of freedom of the impurity center plus oscillator vibrational states for most lattice modes. Therefore, as in the non-JT case, the zero-phonon line can be considered as resulting from electron transitions that do not change the vibrational quantum numbers of these lattice modes, while the one-phonon, two-phonon, etc. side bands result from transitions involving one, two, etc. phonons.

The one-phonon transitions, comparable in their integral intensities to the zero-phonon transition, have frequencies distributed over a spectral interval of

the order of the width of the band of vibrations, whereas the zero-phonon transitions are concentrated in one narrow line (for this reason the zero-phonon line is considerably more intense than the one-phonon satellite). If the vibronic couplings in the initial and final electronic terms (between which the optical transition takes place) are significantly different, their APES minima are displaced and the overlap integral of the wavefunctions of the lowest vibronic states of these two terms (and hence the integral intensity of the zero-phonon line) will be small. In this case, in spite of its otherwise higher intensity, the zero-phonon line will not be seen against the background of the broad multi-phonon band.

The separation of the zero-phonon line has physical meaning only for rather weak vibronic coupling in both combining electronic terms, when the Debye–Waller factor determining the integral intensity of this line is not very small and it can be experimentally observed. The region of intermediate vibronic coupling constants, for which the zero-phonon line is still observable, is superimposed on the region of large vibronic constants, for which the formulas of strong coupling become approximately valid (Section 5.2). This allows us to investigate the properties of the zero-phonon line using also the analytical results of Chapter 5.

Consider first the case of weak coupling. Assume that for both electronic terms taking part in the optical transition the vibronic interaction is a small perturbation that slightly splits the equally spaced levels of the zero Hamiltonian (Section 5.1). In this case the oscillator occupation numbers may still be considered approximately as "good" quantum numbers, so that one can characterize the vibronic states of the JT system with phonon numbers. It is obvious that the optical transitions $0\rightarrow0$, $1\rightarrow1$, $2\rightarrow2$, ..., for which the "vibrational state" does not change, result in spectral lines occupying a narrow frequency interval with a small spread caused by the weak splitting of the excited oscillator levels (Section 5.1).

Recall that the ground vibronic level of the system for both electronic terms is not split by the vibronic interaction in any order of the perturbation theory (we do not consider here the ground vibronic level crossover due to large quadratic coupling, see Section 5.3). Therefore at $T=0\,\mathrm{K}$ when the population of the excited vibronic states of the initial electronic term vanishes, the vibronic structure and the width of the zero-phonon line are frozen out, and in the optical spectrum only the unsplit narrow peak of the zero-phonon transition $0\rightarrow0$ remains. Some attempts [6.83, 6.84] to obtain the splitting of the zero-phonon line at $T=0\,\mathrm{K}$ without considering low-symmetry crystal fields seem to be ungrounded.

As the temperature increases, the excited vibronic states of the initial electronic term become populated, and the lines of the transition $1\rightarrow1$, $2\rightarrow2$, etc.,

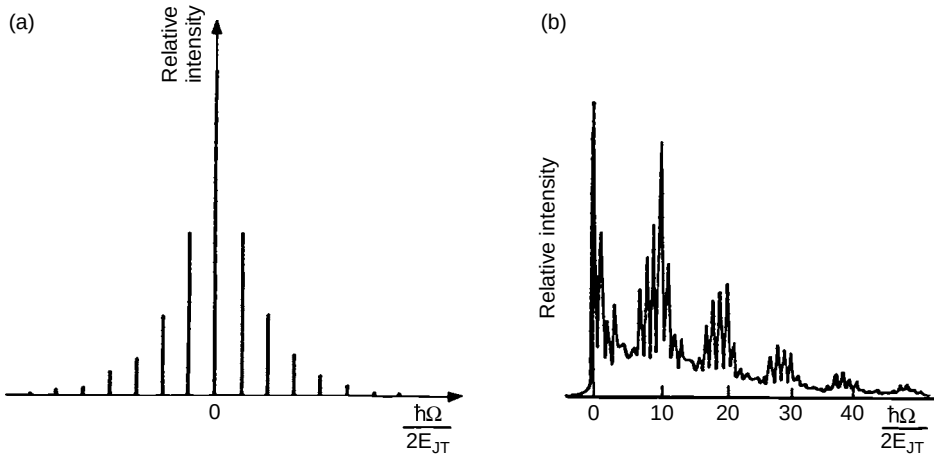

Fig. 6.10. Vibronic structure of the zero-phonon line of the optical $A \rightarrow E$ transition without (a) and with (b) a strong frequency effect [6.86].

at frequencies slightly different from that of the $0 \rightarrow 0$ transition, are added to the latter. This may lead to the temperature-dependent changes in structure of the zero-phonon line.

Consider as an example the zero-phonon line of the optical transition A→E with weak linear vibronic coupling of the E term with e vibrations. On substituting the equally spaced energy values of the e vibrations for the non-JT A term, $E_{m_1,m_2} = \hbar\omega(m_1 + m_2 + 1)$, and for the E term from Section 5.1 (Eq. (5.1)) into Eq. (6.2), one gets the following expression for the shape function (6.2) for the zero-phonon line of this transition [6.86]:

$$F(x) = \tanh(\beta_E/2)\exp(\beta_E|x|/2\lambda_E)\sum_{n=-\infty}^{\infty}\delta(x - 2n\lambda_E), \qquad n = 0, 1, 2, \ldots \tag{6.26}$$

where $\beta_E = \hbar\omega_E/\mathrm{kT}$, $x = [\hbar\mathbf{\Omega} - (E_E - E_A - 2E_{\mathrm{JT}}^E)/\hbar\omega_E]$, and $\lambda_E = E_{\mathrm{JT}}^E/\hbar\omega_E$. From this equation we see that the single intense line of vibrationless transitions between the A and E terms (at $x = 0$ and $\lambda_E = 0$) is split by the weak vibronic coupling into many lines (at $x = 2\lambda_E$) with different frequencies spaced at $\Delta\mathbf{\Omega} = 2E_{\mathrm{JT}}^E/\hbar$. The intensities of these lines are determined by the Boltzmann exponents. The structure of the zero-phonon line described by Eq. (6.26) is illustrated in Fig. 6.10(a).

If the influence of the frequency effect (different vibrational frequencies in the two electronic states) is taken into account [6.86], the frequencies of the e vibrations in the electronic states of the A and E terms do not coincide: $\Delta\omega = \omega_E(\mathrm{A}) - \omega_E(\mathrm{E}) \neq 0$, and the fine structure of the zero-phonon line of

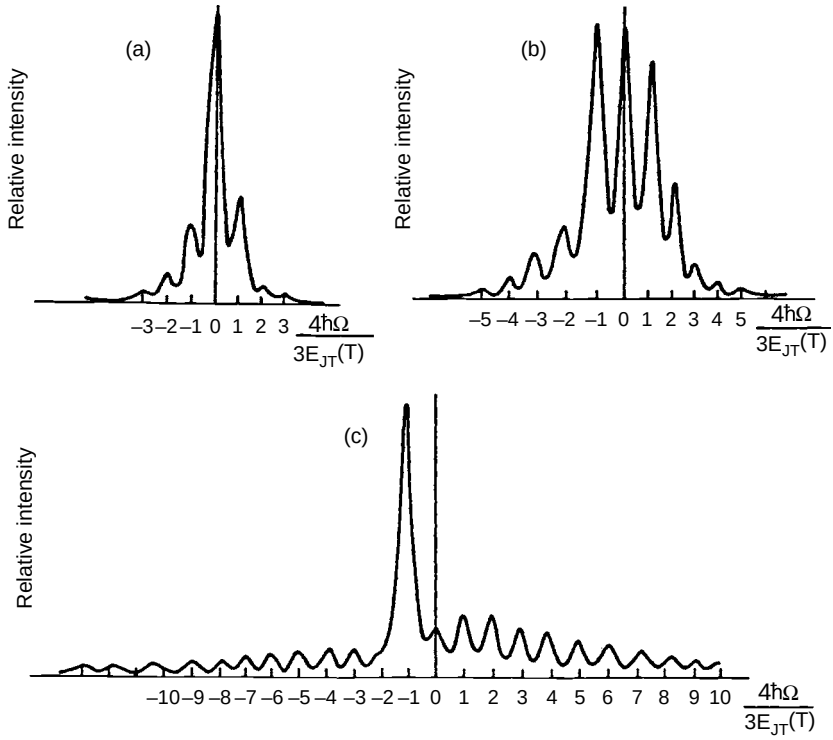

Fig. 6.11. Vibronic structure of the zero-phonon line of the optical $A \rightarrow T$ transition at three temperatures: $\hbar\omega_T/kT = 2.74$ (a), 1.45 (b), and 0.37 (c) [6.1].

the A→E transition becomes asymmetric and further structured. Figure 6.10(b) shows the zero-phonon line of the A→E transition with a strong frequency effect and weak vibronic coupling: $\Delta\omega/\omega_E(E) = -0.98 \times 10^{-2}$, $\lambda_E = 0.25 \times 10^{-2}$, and $\beta_E = 0.26$. An anomalous temperature dependence of the homogeneous width of the zero-phonon line (T^3 instead of the usual T^7) was shown to result from the JTE in the $E \otimes e$ problem of the excited state [6.85]. The theory was applied to the nitrogen N-V center in diamond.

If the electronic T term is coupled to both e and t_2 vibrations with the latter predominant, the e vibrations cause just a shift of all the vibronic energy levels, so the zero-phonon line structure is determined by the coupling to t_2 vibrations in the $T \otimes t_2$ problem (Section 3.3). Figure 6.11 shows the vibronic structure of the zero-phonon line of the A→T transition for three different temperatures, $\beta_T = \hbar\omega_T/kT = 2.74$, 1.45, and 0.37, obtained by means of summing up the zero-phonon contributions in Eq. (6.5). As seen from this figure, three qualitatively different types of zero-phonon line of the A→T transition are possible: at low temperatures (Fig. 6.11(a) the intensity of the line of the 0→0 transition

is predominant; at intermediate temperatures (Fig. 6.11(b) the intensity of the line of the 0→0 transition and the intensities of components of the fine structure nearest to it are comparable; and at high temperatures (Fig. 6.11(c)) the line shifted from the 0→0 one towards the low-frequency region by $\Delta\mathbf{\Omega} = \frac{3}{4}E_{\mathrm{JT}}^{T}/\hbar$ is predominant. It is noteworthy that in this case the fine structure of the zero-phonon line is also equally spaced with intervals $\Delta\mathbf{\Omega} = \frac{3}{4}E_{\mathrm{JT}}^{T}/\hbar$.

At higher temperatures the width of the wings of the zero-phonon line increases as kT, while their intensity decreases. As a result the zero-phonon line again becomes narrow, its position being shifted by $\Delta\mathbf{\Omega} = \frac{3}{4}E_{\mathrm{JT}}^{T}/\hbar$ in the long-wavelength region with respect to the 0→0 transition. The frequency effect $\omega_T(A) \neq \omega_T(T)$ causes its further broadening and asymmetry. The rather complicated problem of the influence of the multimode (continuous phonon spectrum) problem on the zero-phonon line is discussed in [6.3, 6.5, 6.86–6.89].

For intermediate and strong vibronic coupling $E_{\mathrm{JT}} \gtrsim \hbar\omega$, even a small increase of temperature from $T = 0$ results in significant broadening of the zero-phonon line, and the latter becomes invisible against the background of the wide band of the multi-phonon absorption or luminescence.

For vibronic coupling constants for which the ground vibronic state of a JT system has the same transformation properties as its electronic term (Section 5.6), the splitting of the 0→0 transition line is possible under the influence of low-symmetry perturbations that remove the degeneracy of the ground vibronic state. If this perturbation is described by an electronic operator, i.e., it is independent of nuclear coordinates, the magnitude of the observed splitting is reduced compared with the primary (nonvibronic) splitting due to the vibronic reduction factors (Section 5.6). However, for vibronic coupling constants at which the ground-state vibronic energy-level crossover takes place (Section 5.3), both crossing levels may be seen in the zero-phonon line as a corresponding splitting without any external influence. So far this issue has not been considered in detail.

In transitions from nondegenerate to degenerate states the primary splitting of the zero-phonon line under perturbations can be extracted from the change of the first moment of the band (the centroid of the spectrum) under the influence of the strain perturbation (Section 6.1.1). For instance, for the $A \rightarrow T$ transition under the influence of tetragonal strain the T term is split into the terms E and A of the group $D_{4\mathrm{h}}$. In the parallel polarization the transition is allowed only to the electronic singlet term, whereas in the perpendicular polarization it is allowed to the E term. The change of the first moment of the band (normalized with respect to the oscillator

strength) is given in Eq. (6.12), from which we find the primary electronic splitting

$$\Delta\mathbf{\Omega}_E = \left|\Delta\langle\mathbf{\Omega}\rangle_1 - \Delta\langle\mathbf{\Omega}\rangle_t\right| = (3/2\hbar)|P_E\varepsilon_\vartheta| \tag{6.27}$$

The observable zero-phonon-line splitting due to the above tetragonal deformation equals $\Delta\mathbf{\Omega}_E K_T(E)$, where $K_T(E)$ is the vibronic reduction factor. Similarly, in the case of trigonal deformation we find from Eq. (6.17)

$$\Delta\mathbf{\Omega}_T = \left|\Delta\langle\mathbf{\Omega}\rangle_1 - \Delta\langle\mathbf{\Omega}\rangle_t\right| = (\sqrt{3}/\hbar)|P_T\varepsilon_T| \tag{6.28}$$

and the experimentally observed splitting should be $\Delta\mathbf{\Omega}_T K_T(T_2)$. The ratios of the corresponding experimental splitting of the zero-phonon line to the $\Delta\mathbf{\Omega}_E$ and $\Delta\mathbf{\Omega}_T$ values allow one to estimate the vibronic reduction factors $K_T(E)$ and $K_T(T_2)$, respectively.

In this way experiments on polarization dichroism of $A\rightarrow\Gamma$ ($\Gamma = E$, T, etc.) optical transition bands and their zero-phonon lines allow direct observation of the effect of vibronic reduction unambiguously determined by the JTE.

An experimental example of the effect of vibronic reduction of the zero-phonon line splitting in the ${}^4A_2\rightarrow{}^4T_2$ impurity absorption in $V^{2+}:KMgF_3$ taken from [6.90] is shown in Fig. 6.12. It is seen that the calculated spectrum with unreduced spin–orbital interaction does not correspond to the experimental zero-phonon line. The observable splitting of the latter is less than half the unquenched value of the splitting. Its interpretation in terms of the vibronic reduction shown in Fig. 6.12(b) looks quite satisfactory. For other examples see in [6.3, 6.9, 6.90–6.92] and in Section 8.1.

As mentioned above, at $T = 0$ K the line of the $0\rightarrow0$ transition is positioned at the low-frequency edge of the absorption band. On the high-frequency side of this line there are the lines of the allowed transitions $0\rightarrow m$ from the ground vibronic state of the lower electronic term to the vibronic states of the upper electronic term. Among the latter there may also be excited components of the tunneling sublevels (Section 5.3), provided the corresponding transitions are allowed. If the vibronic coupling is sufficiently strong and hence the magnitude of tunneling splitting is relatively small, the spectral lines of the transition to a group of tunneling levels of similar energy are observed as one zero-phonon line split by the tunneling. Thus the effect of *tunneling splitting can be observed in the splitting of the zero-phonon line*.

Although the transition to some of the tunneling sublevels is often forbidden, there are always some low-symmetry perturbations, which remove (partly or completely) this restriction. For impurity absorption in crystals these transitions can be allowed due to random strain and inhomogeneities of the

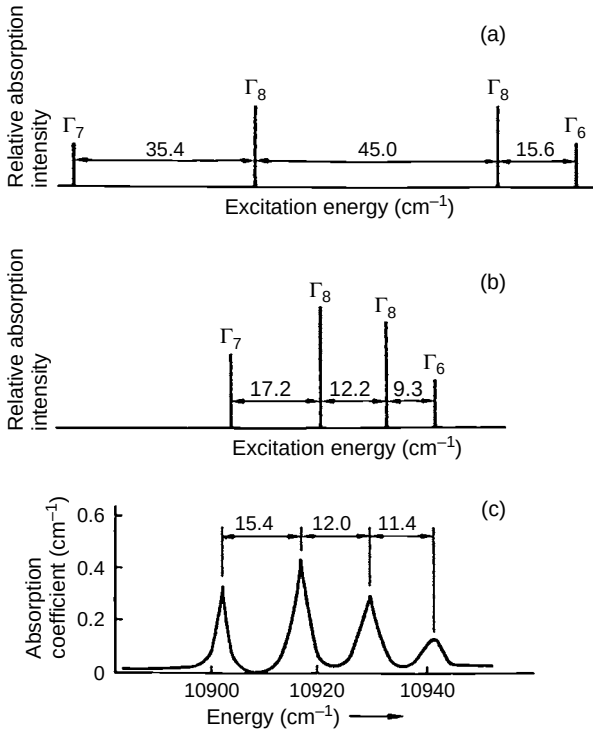

Fig. 6.12. Vibronic reduction of the spin–orbital splitting of the zero-phonon line of the ${}^4A_2 \rightarrow {}^4T_2$ transition in the optical absorption spectrum of V^{2+}: $KMgF_3$: (a) the expected line positions without the JTE in the ${}^4T_2$ state; (b) the same with the vibronic reduction due to the JTE; and (c) the experimental spectrum (reprinted with permission from [6.90]. Copyright 1970 American Physical Society).

crystal structure, clustering of the impurities, and the presence of other nearby defects, e.g., dislocations. External low-symmetry perturbations, e.g., uniaxial stress, can be even more efficient.

Consider a cubic E term with a quadratic JT $E \otimes e$ problem under tetragonal stress. The three lowest vibronic (tunneling) states of the tunneling splitting $3\Gamma = E_A - E_E$ (Section 5.3) can be labeled $|a\rangle$, $|\vartheta\rangle$, and $|\varepsilon\rangle$, with which the strain perturbation matrix W in the secular equation of the type (3.2) is [6.1]

$$W = \begin{vmatrix} E_A & rP_E e_\vartheta & 0 \\ rP_E e_\vartheta & E_E - qP_E e_\vartheta & 0 \\ 0 & 0 & E_E + qP_E e_\vartheta \end{vmatrix} \tag{6.29}$$

where $q = K_E(E)$ and $r = K_E(A|E|E)$ are the diagonal and off-diagonal vibronic reduction factors, respectively, and, as in Section 6.1.1, P_E is the electron-strain coupling constant and ε_ϑ is the component of the strain tensor.

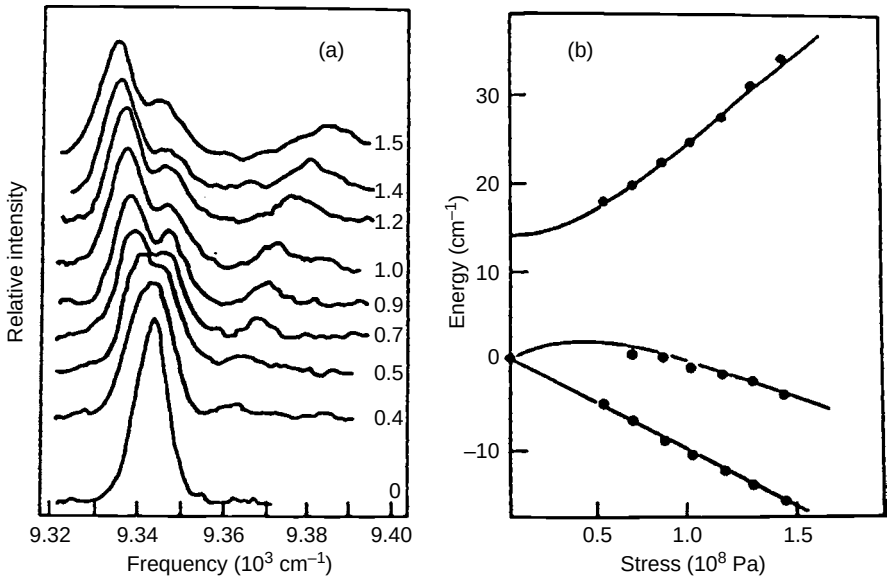

Fig. 6.13. Splitting of the zero-phonon line of the optical ${}^5T_2 \rightarrow {}^5E$ transition in the impurity center Fe^{2+}: MgO under uniaxial stress along the [001] axis: (a) the line shape at $T = 1.5$ K and different stress values shown at the right in 10^8 Pa; and (b) observed (dots) and theoretical predicted (solid lines) absorption maximum positions (reprinted with permission from [6.93]. Copyright 1977 American Physical Society).

The solution of the secular equation (3.2) with the matrix (6.29) yields

$$E_1 = E_A + qP_E e_\vartheta$$
$$E_{2,3} = \frac{1}{2}(E_A + E_E - qP_E e_\vartheta) \pm \sqrt{(E_A - E_E + qP_E e_\vartheta)^2 + (2rP_E \varepsilon_\vartheta)^2} \quad (6.30)$$

In Fig. 6.13 the splitting of the zero-phonon line of the magnetic-dipole transition ${}^5T_{2g} \rightarrow {}^5E_g$ in a cubic impurity system Fe^{2+}: MgO observed at T = 1.5 K under uniaxial stress along the direction [001] is illustrated [6.93]. It is seen that on increasing the stress the forbidden line of the transition to the vibronic singlet emerges on the high-frequency side of the split line of the $0 \rightarrow 0$ transition. In Fig. 6.13(b) the full line shows the energy levels versus the stress described by Eq (6.30); the points in this figure correspond to the experimental results and demonstrate excellent agreement with the predictions of the theory. It follows from this experiment that for the ${}^5E$ term of Fe^{2+}: MgO the magnitude of the tunneling splitting $3\Gamma \approx 14\,\text{cm}^{-1}$, $qP_E \approx 21 \times 10^3\,\text{cm}^{-1}$, $|r/q| \approx \frac{1}{2}$.

The first experiments in which the tunneling splitting of the zero-phonon line of the A→E transition was observed by the piezospectroscopic method were performed in 1965 and reported in [6.94, 6.95]. For Eu^{2+} impurity centers in CaF_2 and SrF_2 crystals, the values $3\Gamma \approx 15.3\,cm^{-1}$ and $3\Gamma \approx 6.5\,cm^{-1}$, respectively, were obtained, and for Sm^{2+} impurities in CaF_2 and SrF_2 the magnitudes of 27 and $26\,cm^{-1}$ were evaluated. The interpretation of these experiments in terms of tunneling splitting was given in [6.96]. For other examples see in Section 8.1.

6.1.3 The JTE in excited-state decay

If the excited state is subject to the JT and/or PJT effects, its lifetime and hence the emission spectrum (luminescence and phosphorescence) are essentially influenced by the multi-minimum and anharmonic form of its APES. Let us begin with the temperature dependence of the polarization of luminescence.

The polarization of the incident light can be chosen in such a way that the optical transition to one of the minima of the adiabatic potential of the excited term takes place. The tunneling relaxation of the excitation equalizes the population of equivalent minima, resulting in a depolarization of the luminescence. At low temperatures, if the radiative lifetime is much shorter than the time of the tunneling relaxation, the polarization of the incident light is predominant in the emission spectrum. An increase of the temperature leads consequently to:

(a) population of the excited states in the minima for which the potential barrier is lower and hence the tunneling rate is higher;
(b) temperature-induced jumps of the system to other minima through excited vibronic states of the lower sheet of the APES of the excited state which are higher in energy than the saddle points of the potential barriers; and
(c) population of states of the higher sheets of this APES.

All these processes lead to depolarization of the emission. They take place at rather strong vibronic coupling when the nuclear motions corresponding to different sheets of the APES are less interrelated. For weak and intermediate coupling the depolarization of the luminescence can be explained by dynamic and stochastic mechanisms of relaxation [6.97]. Experimental investigations of the polarized luminescence in alkali halide crystals activated by T1-like ions were reported in [6.98].

The dependence of the polarization of luminescence on the polarization of the incident light provides the opportunity to evaluate the symmetry of the JT minima of the excited state [6.99, 6.100]. Consider, for example, allowed

magnetic-dipole transitions in a cubic center with O_h symmetry. If in the minima of the APES the cubic system is tetragonally distorted, the polarized absorption with the magnetic field vector of the incident light $\vec{H} \parallel C_4$ results in polarized luminescence with the same polarization, while the polarization of the absorbed light $\vec{H} \parallel C_3$ gives completely depolarized luminescence. For trigonal distortions in the minima the luminescence is partly polarized for $\vec{H} \parallel C_3$ and depolarized for $\vec{H} \parallel C_4$ in the absorption light. These results are based on the assumption that after absorption the system has time to relax to the minima states before emission.

The dependence of the degree of polarization of luminescence light on the frequency of the exciting light can also be a characteristic feature of the JTE [6.99]. If the absorption center is selectively excited to the vibrational states near the bottom of the minimum of the APES, the polarization of luminescence should be maximal, and the depolarization increases with increasing frequency of excitation. The influence of the vibrational relaxation on the process of depolarization is discussed in [6.101]. Another interesting topic is the JTE in nonradiative decay of excited states [6.102, 6.103]. An approach to the problem based on quasi-classical treatment of the nuclear motion on separate sheets of the APES was proposed in a series of papers [6.104–6.106] (see the review article [6.107]). Note also some archetypal cases in [6.108]. The influence of the PJTE on nonradiative decay may be most significant. Numerical calculation of the occupation probability of the upper electronic state $^2B_{2g}$ of the ethylene cation $C_4H_4^+$, due to the PJT $(^2B_{2u} + {}^2B_{2g}) \otimes (a_g + a_u)$ coupling [6.109] (see also [6.10]), shows that the calculated ultrafast decay may explain the absence of emission from the $\tilde{A}^2B_{2g}$ state in this molecule. More generally, it was proposed [6.10] that the absence of detectable fluorescence may be expected whenever there exists a conical intersection close to the minimum of the corresponding APES.

Another interesting effect confirmed by numerical calculations is the quenching of radiative decay rates for systems in individual vibronic states [6.10]. The fluorescence decay rate of any vibronic state written in the form of Eq. (2.5), $\Psi(r, Q) = \sum_k \chi_k(Q)\varphi_k(r)$, can be shown to gain contributions from the mixed electronic states [6.10]:

$$\Gamma = \sum_{k=1}^{f} \gamma_k \langle \chi_k \,|\, \chi_k \rangle \tag{6.30'}$$

where γ_k are the decay rates of the individual electronic states and χ_k satisfy the normalization condition $\sum_{k=1}^{f} \langle \chi_k | \chi_k \rangle = 1$. The value of Γ is smaller than the largest of the decay rates γ_k. Therefore the lifetime of the corresponding vibronic level, defined as the inverse decay rate Γ^{-1}, in the presence of vibronic

coupling must always be longer than the shortest lifetime of the mixed electronic states. The first suggestion that the anomalously long radiative lifetimes observed for some molecules arise due to the mixing of different electronic states was given in [6.110]. Equation (6.30′) thus provides a quantitative description of this effect.

This result explains, for instance, the situation in the NO_2 molecule where the radiative decay rate of the excited electronic term $^2B_2$ was found to be one or two orders of magnitude smaller than expected from the integrated absorption coefficient [6.111]. Theoretical calculations [6.112] (see also [6.10]) confirm the assumption that the anomalously small fluorescence decay rates of the excited B_2 vibronic states of the NO_2 molecule are caused by the strong PJT interaction between the $^2A_1$ and $^2B_2$ electronic states ($^2A_1$ has zero decay rate).

In a recent work [6.113] mentioned also in Section 3.2 the linear and quadratic $E \otimes e$ problems were considered for *short-lived (metastable) excited states*. It was shown that by introducing an imaginary term into the equation for the APES to stand for its lifetime, the JT coupling affects significantly both the form of the real APES (producing additional minima and conical intersections) and its imaginary part, the lifetime of the state under consideration. *Ab initio* calculations that allow numerical estimations of these effects were carried out on Π-type resonance states of the tris(boramethyl)amine anion.

6.2 Vibronic infrared and Raman spectra

6.2.1 Vibronic infrared absorption

The separation in electronic, vibrational, and rotational spectra based on frequency differences may be invalid in JT systems for two reasons. First, due to the complicated and essentially anharmonic APES (Chapter 3) the vibrational frequencies of the free and hindered internal pseudorotations (Chapter 5) fall within the region of non-JT pure rotational frequencies. Second, the frequencies of electronic transitions between different sheets of the APES (with the energy gap $\sim E_{\mathrm{JT}}$) fall within the region of infrared (IR) absorption. Therefore the term "*vibronic infrared spectra*" instead of "vibrational spectra" seems to be appropriate.

The operator of the electric-dipole transition is $\vec{e}\vec{D}$, where $\vec{e}$ is a unit vector of the electromagnetic wave polarization and

$$\vec{D} = \vec{D}_e(r) + \vec{D}_n(Q) \tag{6.31}$$

is the vector of the dipole moment of the electrons and nuclei of the polyatomic system.

The dipole moment of the nuclear framework $\vec{D}_n(Q)$ can be expressed as

$$\vec{D}_n(Q) = \vec{D}_n^{(0)} + \sum_{\Gamma\gamma} Z_{\overline{\Gamma}} Q_{\overline{\Gamma}\overline{\gamma}} \vec{n}_{\overline{\Gamma}\overline{\gamma}} \tag{6.32}$$

where the summation is performed over the irreducible representation $\overline{\Gamma}$ to which the components of the vector belong; $\vec{n}_{\overline{\Gamma}\overline{\gamma}}$ are the symmetrized combinations of the unit vectors of the coordinate system related to the high-symmetry reference configuration Q_0 of the polyatomic system (Section 2.2); $Z_{\overline{\Gamma}}$ is the effective charge of the polar vibrational mode that produces a dipole moment (for nonpolar displacements $Z_{\overline{\Gamma}} = 0$), and $\vec{D}_n^{(0)}$ is the dipole moment of the nuclei fixed at the initial nuclear configuration Q_0. The operator $\vec{D}_n^{(0)}$ obviously causes only pure rotational transitions between the states of a rigid top. Molecules for which $\vec{D}_n^{(0)} \neq 0$ are called rigid-dipole molecules. For simplicity we restrict our consideration to high-symmetry molecules for which $\vec{D}_n^{(0)} = 0$.

The scalar product $\vec{e}\vec{D}_n$ can be written then in the form of a convolution of irreducible tensor operators:

$$\vec{e}\vec{D}_n = \sum_{\Gamma\gamma} Z_{\overline{\Gamma}} Q_{\overline{\Gamma}\overline{\gamma}} e_{\overline{\Gamma}\overline{\gamma}} \tag{6.33}$$

Vibronic effects in the IR spectra occur only when the electromagnetic radiation interacts with the JT or PJT degrees of freedom of the polyatomic system. If one assumes that the electronic dipole moment $\vec{D}_e(r) = 0$ and the total interaction of the radiation with the molecule is described by Eq. (6.32), then vibronic IR spectra are possible only for molecules for which the JT-active normal vibrations are also dipole active. In other words vibronic effects are possible in the IR spectra only for *dipolar-unstable systems* (Sections 4.1 and 4.4).

However, in the presence of both dipolar and non-dipolar JT-active coordinates, they are indirectly coupled via the same electronic state, with which they interact. Therefore the electromagnetic irradiation, which interacts only with dipole-active vibrations, causes a response of the whole JT system, including those JT vibrations which are not dipole active. In particular, weak JT interaction allows IR absorption in the region of non-dipolar JT vibrations, which is forbidden in non-JT systems. This circumstance was first noted in [6.114].

Another important issue emerges from the fact that in nondegenerate molecules in the harmonic approximation the operator (6.33) is subject to selection rules $n_{\Gamma\gamma} \rightarrow n_{\Gamma\gamma} + 1$, where $n_{\Gamma\gamma}$ is the vibrational quantum number of the oscillator $Q_{\Gamma\gamma}$. Because of the equal spacing of the energy spectrum of the

normal vibrations, all the transitions $n_{\Gamma\gamma} \rightarrow n_{\Gamma\gamma} + 1$ correspond to the absorption at the same frequency $\mathbf{\Omega} = \omega_\Gamma$. Therefore the temperature population of the excited levels does not cause new lines in the IR absorption; the probabilities of allowed transitions are redistributed among the partial contributions to each line of the fundamental tone, the total intensity remaining unchanged. It follows that in the harmonic approximation the IR spectra of molecules in nondegenerate states are independent of temperature. Small anaharmonicity results in a temperature transfer of the intensity from the lines of the fundamental tone to that of the overtones, but this effect is usually negligible.

In contrast to this, the energy spectrum in the presence of the JTE is strongly unequally spaced (Chapter 5) and the population of excited states at $T \neq 0$ results in the *formation of new spectral lines*. This is manifested as a strong temperature dependence of the vibronic IR spectra.

Consider now the effects caused by the interaction of electromagnetic radiation with the dipole moment of the electrons. As in Eq. (6.33), the scalar product $\vec{e}\vec{D}_e(r)$ can be written in the form of a tensor convolution,

$$\vec{e}\vec{D}_e(r) = \sum_{\overline{\Gamma}\overline{\gamma}} e_{\overline{\Gamma}\overline{\gamma}} D_{\overline{\Gamma}\overline{\gamma}}(r) \tag{6.34}$$

where the summation is performed over the irreducible representations $\overline{\Gamma}$ of the vector representation. The matrix elements of the operator $D_{\overline{\Gamma}\overline{\gamma}}(r)$ calculated with the JT states of the electronic term Γ are nonzero if $\overline{\Gamma} \in [\Gamma^2]$. Therefore the interaction of the radiation with the dipole moment of the electrons causes a response of the JT system only in cases when the symmetrized square of $[\Gamma^2]$ contains dipole-active representations. Since, on the other hand, the irreducible representations contained in $[\Gamma^2]$, except the trivial one A_1, determine the JT-active normal vibrations (Section 2.5), we come to the condition formulated above: *the vibronic effects in the IR spectra occur only for dipolar-unstable polyatomic systems*, i.e. for systems for which the JT-active displacements produce a dipole moment.

As mentioned in Section. 4.1, the occurrence of a dipolar instability is also possible due to the vibronic mixing of a given term Γ with another one Γ', i.e., due to the PJTE on dipole-active vibrations, provided the product $\Gamma \times \Gamma'$ contains dipole-active representations. This case is more general and can be realized for both degenerate and nondegenerate electronic states.

The coefficient of electric-dipole IR absorption is described by the expressions (6.1) and (6.2), where $M = \vec{e}\vec{D}$ with the operator $\vec{D}$ from Eq. (6.32) and both indices 1κ and 2κ correspond to the ground electronic term. In trigonal systems (e.g., in the triatomic molecule X_3) with a linear JT effect for the

E term the actual symmetry is axial (Section 3.2), and it is convenient to write Eqs. (6.33) and (6.34) in the form

$$\vec{e}\vec{D}(r) = e_z D_z(r) + e_- D_+(r) + e_+ D_-(r) \tag{6.35}$$

and

$$\vec{e}\vec{D}_n = Z_E(e_- Q_+ + e_+ Q_-) \tag{6.36}$$

where

$$\begin{aligned} e_\pm &= (e_x + ie_y)/\sqrt{2}, \qquad D_\pm = (D_x + iD_y)/\sqrt{2} \\ Q_\pm &= (Q_\vartheta \pm iQ_\varepsilon)/\sqrt{2} = \rho\exp(\pm i\phi) \end{aligned} \tag{6.37}$$

have the transformation properties of the momentum $J_z = \pm 1$ (the contribution of the D_z component vanishes in systems with axial symmetry). This allows one to deduce simple selection rules for the quantum number m of the operator $\hat{J}_z$ for the IR transition in the linear $E \otimes e$ system: $m = m \pm 1$ (Section 5.1). In particular, at $T = 0$, if only the ground vibronic state $\left|0, \pm\frac{1}{2}\right\rangle$ is populated (Sections 5.1 and 5.2), the following changes of m are allowed in transition: $-\frac{1}{2} \to +\frac{1}{2}$; $-\frac{1}{2} \to -\frac{3}{2}$; $\frac{1}{2} \to \frac{3}{2}$; and $\frac{1}{2} \to -\frac{1}{2}$.

The frequency structure is the same for electronic and vibrational dipole transitions because they have the same selection rules. The relative intensities of the spectral lines are determined by the effective charge Z_E and the reduced matrix element M for each specific system (see Eq. (6.2)). Unlike the non-degenerate case where the contributions of the electric dipole moment and nuclear dipole moment in the IR absorption can be separated because they have different frequency ranges, in the JT case they fall within the same frequency range, and in general they cannot be separated from one another. Nevertheless, in some special cases these contributions can be separated if the sums (6.33) and (6.34) contain terms that have significantly different values of the reduced parameters Z_Γ and M_Γ for given Γ. The separation can be realized by considering the IR absorption of polarized light taking into account the corresponding selection rules.

The vibronic IR spectrum for arbitrary values of the vibronic coupling constant can be obtained from Eq. (6.2) using the results of numerical solution of the vibronic equations (Chapter 5). Figure 6.14 illustrates the vibronic structure of the IR absorption spectra for a linear $E \otimes e$ problem obtained by means of numerical calculations [6.115]. The set of lines corresponding to transitions to the vibronic states with the same m value forms an almost equally spaced paling; the lines above and below the abscissa correspond to

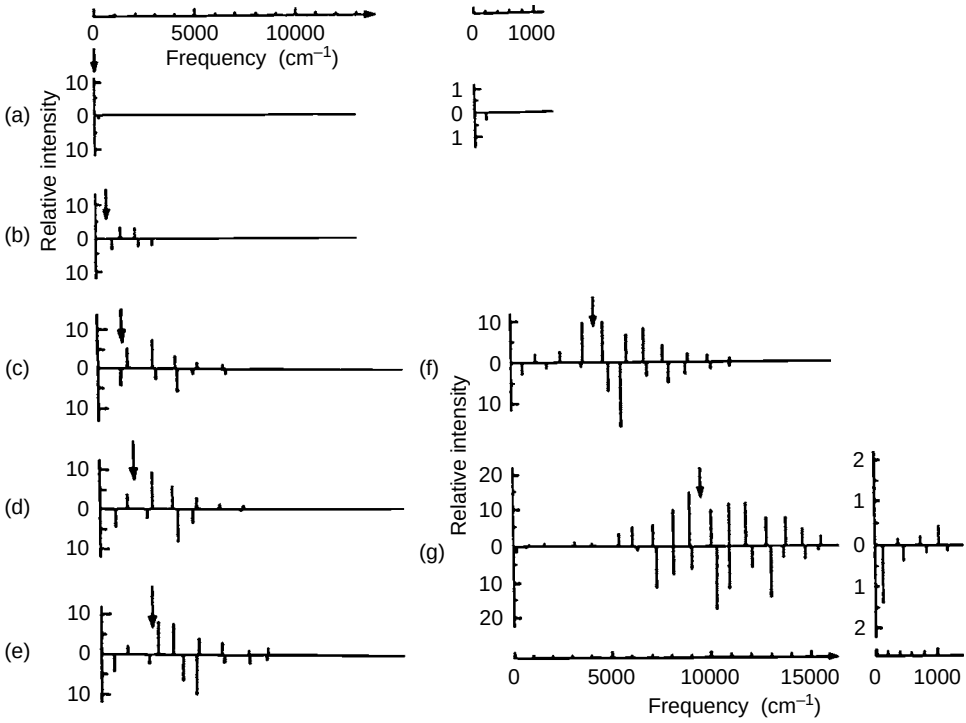

Fig. 6.14. Intensities of the vibronic components of the IR spectrum of a linear $E \otimes e$ system obtained by numerical calculations for $E_{\mathrm{JT}}^{E}/\hbar\omega_E = 0$ (a), 0.125 (b), 0.25 (c), 0.375 (d), 0.5 (e), 1.0 (f), and 2.5 (g) (note the different scales). The lines above and below the abscissa correspond to transitions $|m| = \frac{1}{2} \rightarrow |m| = \frac{1}{2}$ and $|m| = \frac{1}{2} \rightarrow |m| = \frac{3}{2}$, respectively. The lowest frequency of intersheet transition is shown by an arrow (reprinted with permission from [6.115]. Copyright 1962 Institute of Physics)

the values $|m| = \frac{1}{2}$ and $|m| = \frac{3}{2}$, respectively. The nature of the accidentally equal spacing of the lines is discussed in Sections 5.2 and 5.4.

The numerical results in Fig. 6.14 can be explained by means of the approximate solutions of the vibronic equations obtained in Chapter 5. In the case of weak vibronic coupling of the wavefunctions obtained from perturbation theory, the correct (symmetry-adapted) zeroth-order functions $|nlm\rangle$ can be used as a starting point for the solution of the problem. In this approximation the vibrational quantum number n is still a good quantum number. The matrix elements of the operators $Q_{\pm}$ are nonzero when n changes by a unit, i.e., for transitions from the ground vibronic state (at $T = 0\,\mathrm{K}$) to only the first excited vibrational level weakly split into two sublevels by the vibronic interaction (Section 5.1). The matrix elements of these transition are [6.115]

$$\langle 0,\ 0,\ \pm\tfrac{1}{2}|Q_{\pm}|1,\ 1,\ \pm\tfrac{3}{2}\rangle = \langle 0,\ 0,\ \pm\tfrac{1}{2}|Q_{\pm}|1,\ 1,\ \mp\tfrac{1}{2}\rangle = \sqrt{\hbar\omega_E/2K_E} \quad (6.38)$$

Accordingly, the fundamental line of the e vibrations in the IR spectrum is slightly split by $\Delta\mathbf{\Omega} = 2E_{\mathrm{JT}}^E/\hbar$ (Fig. 6.14(b)).

The electronic dipole moment does not change the vibrational quantum number, and at $T = 0$ K it just causes transitions between the degenerate states $\pm\frac{1}{2} \to \mp\frac{1}{2}$ of the ground vibronic term. These transitions cannot be observed directly since the IR frequency is $\mathbf{\Omega} = 0$. However, they determine the intensity of the transitions between the rotational states of the free molecule related to the ground vibronic level (see below).

If the vibronic coupling is sufficiently strong, the energies and wavefunctions of the vibronic states are those of Eq. (5.18). All the IR transitions in this case can be divided into intrasheet transitions between the vibronic states of the same lower sheet of the adiabatic potential, and intersheet transitions between the states of different sheets. At $T = 0$ K the lowest-frequency line of the intersheet transitions corresponds to the energy gap $\hbar\mathbf{\Omega}_0 \approx \varepsilon_+(\rho_0^{(+)}) - \varepsilon_-(\rho_0)$ that connects the minima of the upper and lower sheets of the adiabatic potential (Sections 3.2 and 5.2). Intrasheet transitions correspond to frequencies $\mathbf{\Omega} < \mathbf{\Omega}_0$.

It can be seen that $Q_{\pm}$ causes only intrasheet transition $|\pm, n, m\rangle \to |\pm, n', m \pm 1\rangle$. If we take $\rho = \rho_0 + r$, then after Eq. (6.36)

$$Q_{\pm} = (1/\sqrt{2})\rho_0 e^{\pm i\phi} + (1/\sqrt{2})re^{\pm i\phi} \quad (6.39)$$

In the harmonic approximation the first term causes transitions with $n' = n$, while the second term causes transitions with $n' = n \pm 1$. At $T = 0$ K only transitions from the ground vibronic state remain, with matrix elements [6.115]

$$\left\langle -,\ 0,\ \pm\frac{1}{2}|Q_{\pm}|-,\ 0,\ \mp\frac{1}{2}\right\rangle = \left\langle -,\ 0,\ \pm\frac{3}{2}|Q_{\pm}|-,\ 0,\ \pm\frac{1}{2}\right\rangle = F_E/K_E\sqrt{2} \quad (6.40)$$

$$\left\langle -,\ 0,\ \pm\frac{1}{2}|Q_{\pm}|-,\ 1,\ \mp\frac{1}{2}\right\rangle = \left\langle -,\ 0,\ \pm\frac{3}{2}|Q_{\pm}|-,\ 1,\ \pm\frac{1}{2}\right\rangle = \sqrt{\hbar\omega_E/4K_E} \quad (6.41)$$

The transitions (6.40) correspond to two intense lines at the frequencies $\mathbf{\Omega} = 0$ and $\mathbf{\Omega} = \hbar/\rho_0^2$. Of course, the line $\mathbf{\Omega} = 0$ cannot be observed directly but, as already mentioned, it is related to the transitions between the rotational states of a free molecule (see below).

The transitions (6.41) correspond to two weak lines at $\mathbf{\Omega} = \omega_E$ and $\mathbf{\Omega} = \omega_E + \hbar/\rho_0^2$, their intensities being $2E_{\mathrm{JT}}^E/\hbar\omega_E$ times weaker than those of the lines (6.40). The anharmonicity of the potential surface $\varepsilon_-(\rho)$ allows also

overtones with $n' > n+1$. In the region of weak anharmonicity (small n) their intensities decrease with n and then, when passing to the region of strong anharmonicity (large n), they begin to increase (Fig. 6.14).

The electronic operators cause both intrasheet $|\pm,\ n,\ m\rangle \to |\pm,\ n,\ m \pm 1\rangle$ and the intersheet $|\pm,\ n,\ m\rangle \to |\mp,\ n',\ m \pm 1\rangle$ transitions. The intensity of the latter is determined by the Franck–Condon overlap integrals $\left\langle \chi_n(\rho - \rho_0) \middle| \chi_{n'}^{(+)}(\rho - \rho_0^{(+)}) \right\rangle$. In this sense the intersheet transition is reduced to the usual electronic transition between electron–vibrational states of two singlet electronic terms with significantly anharmonic APES.

At $T = 0\,\mathrm{K}$ when only the ground vibronic state is populated the following two types of intersheet transitions are possible: $\left|-,\ 0,\ \pm\tfrac{1}{2}\right\rangle \to \left|+,\ n,\ \mp\tfrac{1}{2}\right\rangle$ and $\left|-,\ 0,\ \pm\tfrac{1}{2}\right\rangle \to \left|+,\ n,\ \pm\tfrac{3}{2}\right\rangle$. As mentioned in Sections 5.2 and 5.4, the energy spectrum of vibronic states of the linear $E \otimes e$ system with fixed m values is almost equally spaced and therefore each of the above two types of transition results in an almost equally spaced series of spectral lines with a bell-shaped envelope. The frequency of the envelope maximum is that of the Franck–Condon transition between the sheets (Fig. 6.14):

$$\hbar\omega_{\max} = \varepsilon_+(\rho_0) - \varepsilon_-(\rho_0) = 4E_{\mathrm{JT}}^E \tag{6.42}$$

Vibronic effects in the IR absorption in multimode JT systems can be described in the framework of the same approximations of weak and strong coupling. As mentioned above, in the case of weak vibronic coupling, the transitions caused by the electronic dipole moment cannot be observed directly, and therefore one can assume that the $\vec{e}\vec{D}$ magnitude is determined by the nuclear term (6.33). In particular, for an uncharged impurity in a homopolar crystal with a trigonal E term in the ground state, the operator $\vec{e}\vec{D}$ acquires the form (6.36), where $Q_\pm$ are the symmetrized displacements of the atoms of the nearest coordination sphere. By substituting (6.36) into Eq. (6.2), it can be shown [6.1, 6.79] that the IR spectrum of the multimode JT system reproduces the density of vibrational states substantially renormalized by the vibronic coupling. In particular, it contains JT local and pseudo-local resonances (Section 5.5).

In the multimode system, as in the ideal case considered above, the approach based on separation of the sheets of the adiabatic potential is applicable for strong vibronic coupling. The broad band of the IR absorption is composed of intrasheet and intersheet transitions. The latter are due to the operator of the electronic dipole moment and differ slightly from multi-phonon bands of electronic transitions between nondegenerate terms. The zero-phonon line of the above band is positioned at the frequency $\boldsymbol{\Omega}_0 \approx E_{\mathrm{JT}}^E$. The main

contribution to the intrasheet transitions comes from $d = \vec{e}\vec{D}_n$, the operator of the interaction of light with the dipole moment of the nuclei, which, considering Eq. (6.39), can be written in the form $d = d_0 + d_1$, where

$$d_0 = Z_E \rho_0 (e_+ e^{-i\phi} + e_- e^{i\phi})/\sqrt{2}, \qquad d_1 = Z_E r (e_+ e^{-i\phi} + e_- e^{i\phi})/\sqrt{2} \quad (6.43)$$

For strong vibronic coupling the contribution of d_0 is obviously predominant because $\rho_0 \sim F_E$. The operator d_0 causes transitions between rotational states of the system with $m' = m \pm 1$. Since the states with different m values correspond to different equilibrium coordinates of the trough (see Eq. (5.21)), this transition is accompanied by a pulse of radial vibrations of the nuclei. In a sense this phenomenon is analogous to the Mössbauer effect, with the distinction that in the case under consideration the momentum is transferred, rather than the photon impulse. As in the Mössbauer effect, the IR absorption spectrum contains an intense line at the frequency $\mathbf{\Omega}_0$, which corresponds to the process "without recoil," and weak phonon satellites reproducing the modified density of radial vibrations [6.116].

If the quadratic terms of the vibronic interaction are included in the strong-vibronic-coupling problem, three deep minima occur at the bottom of the trough of the lowest sheet of the adiabatic potential (Section 3.2) and the nuclear motion is localized at the bottom of these minima (Section 5.3). If we neglect the tunneling between the minima, the system (once prepared) remains in the distorted configuration of the minima for an infinitely long time (at low temperatures). For instance, in the minima configurations the molecule X_3 has the form of an isosceles triangle (symmetry C_{2v}), octahedral molecules ML_6 acquire the symmetry D_{4h}, etc., and the degeneracy of the e vibrations at the minimum point is removed due to the lower symmetry (Section 3.2). Therefore when tunneling is neglected the IR spectra of JT systems coincide with the usual IR spectra of normal molecules in the configuration of the lower symmetry at the minima [6.115]. Here the lines of the fundamental tone are split in accordance with the splitting of the frequencies in the minima (Section 3.2).

Allowing for tunneling, the spectral lines of the IR absorption are split and the possible transitions are determined by the usual selection rules. For instance, for a D_{3h} system with a quadratic $E \otimes e$ problem and a doublet ground vibronic level, in the dipole approximation, the IR transitions from the ground vibronic E state to all excited states are allowed (because $E \times E = A_1 + A_2 + E$). In particular, an intense line corresponding to the transition between the tunneling sublevels of the ground state can be expected at the frequency $\mathbf{\Omega} = 3\Gamma/\hbar$ (in the microwave range) [6.117].

The special JT features of the vibronic IR spectra described above are general for all JT systems. Anomalous IR spectra for molecular systems with $E \otimes (b_1 + b_2)$, $T \otimes (e + t_2)$, and $\Gamma_8 \otimes (e + t_2)$ type effects and weak vibronic coupling are considered in [6.118]. Strong vibronic coupling with one of the two types of vibrations in the $\Gamma_8 \otimes (e + t_2)$ system and weak coupling with the other one is discussed in [6.119]. Detailed tables of optically active vibrations for molecular systems with different symmetries are given in [6.115, 6.119].

Vibronic IR spectra of systems with intermediate vibronic coupling can be obtained from numerical solutions of the vibronic equations (Section 5.4) in a way similar to that used to determine the spectral lines given in Fig. 6.14. IR spectra of molecular systems with a ^3T term including the spin–orbital and linear vibronic interactions with e and t_2 vibrations were obtained by numerical calculations [6.120]. A simple case of the PJTE for two close-in-energy nondegenerate electronic terms mixed by one vibration (Section 4.1) was considered in [6.121, 6.122]. As in the usual JT case, the IR spectra of such systems have a complicated unequally spaced structure with a complicated temperature and polarization dependence.

The discussion of the IR spectra of free molecules cannot be complete without considering transitions between the rotational levels. Consider first a simple JT system, the X_3 molecule. It is well known that any molecule with D_{3h} symmetry in a nondegenerate electronic state has no dipole moment (i.e., it is not a rigid-dipolar molecule), and therefore it does not display a purely rotational absorption of electromagnetic radiation. However, in degenerate electronic states such a molecule may have a (linear in the electric field) dipole moment (a linear Stark effect), since the external electric field removes the electronic degeneracy. The Hamiltonian of the Stark interaction has the form of Eq. (6.35). This operator may cause purely rotational transitions [6.115]. On the other hand, in the absence of vibronic coupling the electric dipole interaction with the nuclei (6.36) does not lead to purely rotational transitions since its matrix elements are nonzero only when $n' = n \pm 1$. The vibronic interaction removes this restriction on n and allows purely rotational electric-dipole absorption with $n' = n$ based on the nuclear dipole moment.

This conclusion has a clear-cut physical sense. In systems without an inversion center, including the molecule X_3 under consideration, the dipole moment in the minima of the adiabatic potential can occur due to the JTE on dipole-active vibrations. The contribution of the nuclear dipole moment to the electric-dipole rotational IR spectra is the larger, the greater the magnitude of this moment in the minima of the APES, i.e., the stronger the vibronic interaction. In the case of strong vibronic coupling the contribution of the nuclear dipole moment to the purely rotational transitions can be dominant.

The JTE influences both the intensities and the positions of the spectral lines of the rotational IR absorption. As follows from Section 3.2 (and as mentioned above), the JT internal rotation moment J^{int} equals the sum of the electronic and vibrational momenta (see [6.1]). Taking into account this total momentum of the internal rotation in the Coriolis interaction, the Hamiltonian of the rotational motion of a symmetric-top-type molecule can be written in the form (see [6.123], Section 104)

$$\hat{H}_{\text{rot}} = B(J - J^{\text{int}})^2 + (A - B)(J_z - J_z^{\text{int}}) \tag{6.44}$$

where A and B are the rotational constants and J is the preserved total momentum of the top (for the sake of simplicity we neglect the dependence of the molecule's moment of inertia on nuclear displacements; additional effects related to this dependence are considered in [6.124]). If the vibronic–rotational interaction is neglected, the total wavefunction of the molecule can be written in the form of a product of the vibronic function $|nm\rangle$ (n is the quantum number of the radial motion and $m = \pm\frac{1}{2}, \pm\frac{3}{2}, \ldots$ is the quantum number of the electron–vibrational momentum in the linear $E \otimes e$ system; see Sections 5.1 and 5.2) and the rotational wavefunction of a symmetric top $|JKM\rangle$:

$$|nmJKM\rangle = |nm\rangle|JKM\rangle \tag{6.45}$$

The Hamiltonian H_{rot} from (6.44) averaged over the states (6.45) yields the rotational energy E_{rot}. Omitting the constants that are independent of the rotational quantum numbers, we have [6.115, 6.124, 6.125]

$$E_{\text{rot}} = BJ(J + 1) + (A - B)K^2 - 2AK\zeta \tag{6.46}$$

where the constant

$$\zeta = \langle nm|J^{\text{int}}|nm\rangle = (\zeta_{\text{e}} - \tfrac{1}{2})\langle nm|\hat{\sigma}_z|nm\rangle + m \tag{6.47}$$

is the Coriolis interaction, and ζ_{e} is its electronic contribution (σ_z is the Pauli matrix (3.20″)).

For the rotational levels accompanying the ground vibronic term ($n = 0$, $m = \pm\frac{1}{2}$) the matrix element $\langle nm|\hat{\sigma}_z|nm\rangle$ is expressed by the vibronic reduction factor p (Section 5.6), and therefore

$$\zeta = p(\zeta_{\text{e}} - \tfrac{1}{2})\,\text{sign}(m) + m \tag{6.48}$$

In particular, for strong vibronic coupling when $p \approx 0$, $\zeta \approx m$. Thus the expression (6.46) for the energy of the rotational levels agrees with the usual

results for nondegenerate molecules, but the constant of the Coriolis interaction changes significantly from one vibronic level to another [6.124].

The selection rule for rotational transitions $\Delta K = \pm 1$ follows from the transformation properties of the operators (6.37). For instance, for the Q-type transitions ($J = J'$) (do not confuse with the Q coordinate) we obtain from (6.46) a set of lines with frequencies corresponding to the energy gaps [6.115]

$$\Delta E_K = [A(1 + 2\zeta) - B](2K + 1) \tag{6.49}$$

With the wavefunctions (6.45) known, one can determine the intensities of the lines of induced dipole transitions caused by the operators (6.35) and (6.36). As mentioned above, in the case of strong vibronic coupling the contribution of the operator (6.36) is dominant, and therefore the probability of rotational transitions between the states that accompany the ground vibronic doublet is determined by the matrix element (6.40).

All the foregoing means that due to the dipolar instability the JT systems which have no nuclear dipole moment show the properties of rigid-dipole systems with a dipole moment corresponding to a distorted molecule in the minimum of the adiabatic potential. It follows that the division of all the molecules into those having a proper dipole moment (rigid-dipole molecules) and those without is to a large degree conventional. This conclusion was first drawn in [6.126] on the basis of the temperature dependence of the averaged dipole moment of freely orienting JT molecules with dipolar instability.

The difference between rigid-dipole and symmetric molecules depends on temperature [6.127]. The corresponding dependence of the averaged dipole moment on temperature is given by $\bar{D} \sim \tanh(r\Gamma/KT)$, where $r\Gamma$ ($r = 3, 4, 6, \ldots$) is the magnitude of the tunneling splitting (Section 5.3). In the limit of high temperature $r\Gamma \ll kT$ we get $\bar{D} \sim T^{-1}$, i.e., the classical result for rigid-dipole molecules. In the other limiting case of low temperature $\bar{D}$ becomes a constant, independent of temperature, which is characteristic of symmetric molecules that have no proper dipole moment.

The rotational IR spectra of JT spherical-top molecules that have dipolar instability (symmetry group T_d, $T \otimes t_2$ problem) were considered in [6.128]. Figure. 6.15 gives an approximate scheme of the rotational energy levels which (in the absence of a rotational–vibronic interaction) adjoin the vibronic levels T_2 and A_1 of a tetrahedral molecule with tunneling splitting due to strong vibronic coupling (Section 5.3):

$$E_{T_2 J} = BJ(J + 1), \quad E_{A_1 J} = 4\Gamma + BJ(J + 1) \tag{6.50}$$

Here B is the rotational constant and 4Γ is the magnitude of the tunneling splitting determined by Eq. (5.50).

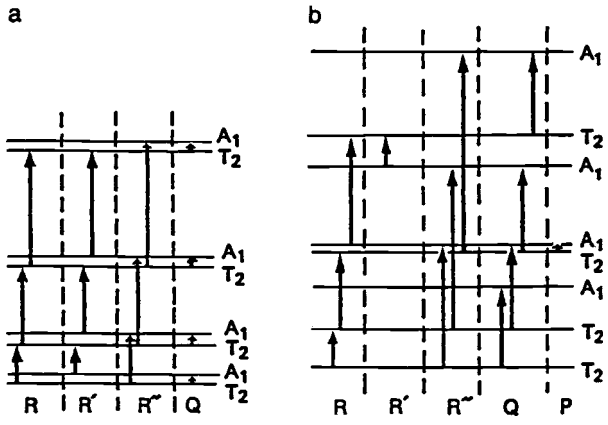

Fig. 6.15. Tunneling–rotational energy levels and allowed transitions for a spherical-top molecule with dipolar instability (T_d symmetry and $T \otimes t_2$ JT problem) with $4\Gamma < 2B$ (a) and $4\Gamma > 2B$ (b). The transitions related to different branches are divided by dashed lines [6.128].

For each rotational level the wavefunction can be written in the form of a product of the vibronic function $|\Gamma\gamma\rangle$ and the rotational function of a spherical top $|JKM\rangle$ (cf. Eq. (6.45)):

$$|\Gamma\gamma JKM\rangle = |\Gamma\gamma\rangle|JKM\rangle \tag{6.51}$$

With these wavefunctions one can determine the probabilities of transitions and the intensities of the induced dipole transitions $\Gamma J \rightarrow \Gamma' J'$ per unit of radiation density [6.128, 6.129],

$$W_{\Gamma J \rightarrow \Gamma' J'} = \frac{8\pi^3 M_0^2 N}{9\hbar^2 c^2 Z}(E_{\Gamma' J'} - E_{\Gamma J})[\exp(-E_{\Gamma J}/kT) - \exp(-E_{\Gamma' J'}/kT)]C_{JJ'} g_{\Gamma J}(I) \tag{6.52}$$

where Z is the statistical sum of tunneling–rotational levels (6.50),

$$C_{JJ'} = \begin{cases} 2J+1)(2J+3), & J' = J+1 \\ (2J+1)^2, & J' = J \\ (2J+1)(2J-1), & J' = J-1 \end{cases} \tag{6.53}$$

$g_{\Gamma J}(I)$ is the statistical weight that depends on the nuclear spin I, M_0 is the modulus of the nuclear dipole-moment vector of the system in the trigonal minimum, and N is the number of absorbing centers per unit volume.

From the expression (6.52) it can be seen that three types of transitions with $J' = J+1$ (R transitions) are possible: $T_2 J \rightarrow T_2(J+1)$ labeled R, $A_1 J \rightarrow A_1$ $(J+1)$ labeled R′, and $T_2 J \rightarrow A_1$ $(J+1)$ labeled R″, while the Q transition with $J = J'$ is allowed as $T_2\ J \rightarrow A_1 J$, and the P transition is $T_2\ J \rightarrow A_1$ $(J-1)$.

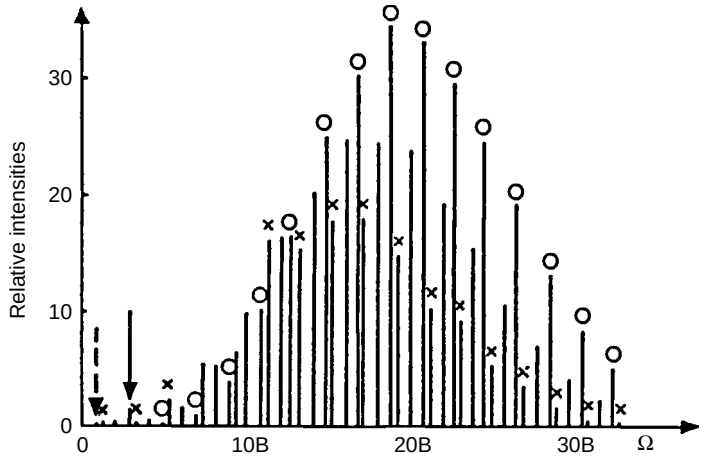

Fig. 6.16. Calculated line positions and intensities of the rotational IR spectrum of a system with dipolar instability (T_d symmetry and $T \otimes t_2$ JT problem) with $4\Gamma = 15\,\mathrm{cm}^{-1}$, $B = 5.24\,\mathrm{cm}^{-1}$, $kT = 200\,\mathrm{cm}^{-1}$ [6.128]. The R″, R′, and R branches are labeled by rings, crosses, and no symbols, respectively. The Q and P transitions are shown by an arrow and a dashed arrow, respectively.

If $4\Gamma = 0$ (more exactly $4\Gamma \ll B$), the transition frequencies in the three R-type bands coincide and the resulting spectrum consists of lines with a constant spacing of $2B$, without the P and Q branches. As 4Γ increases, each of these lines splits and the Q transition occurs at the frequency 4Γ, its intensity being small because the two tunneling levels have almost the same population.

If $4\Gamma > B$, the picture of the spectrum changes significantly (Fig. 6.16). Besides the increase of the frequency separation of the lines of the three branches, their intensities also change, increasing for the $T_2 \rightarrow A_1$ transitions and decreasing for the $A_1 \rightarrow T_2$ ones. Simultaneously the Q transition becomes stronger and the lines of the P transition emerge. The number and the intensity of the latter increase as the inequality $4\Gamma > B$ strengthens. Note that in the usual purely rotational spectra only the R-type transitions are possible, whereas all the branches of R, P, and Q transitions can be observed simultaneously in the rotational structure of the vibrational band [6.130]. In the predicted vibronic spectrum all the branches can be observed in the region of purely rotational transitions, with the distinction that there will be three R branches, while the P and Q branches occur only for large tunneling splitting.

At lower temperatures the intensity of the Q transition increases more rapidly than that of the other lines, and hence at some specific temperature the Q line becomes distinct from the background of the band (Fig. 6.17). This line corresponds to the transition with no change of the rotational quantum

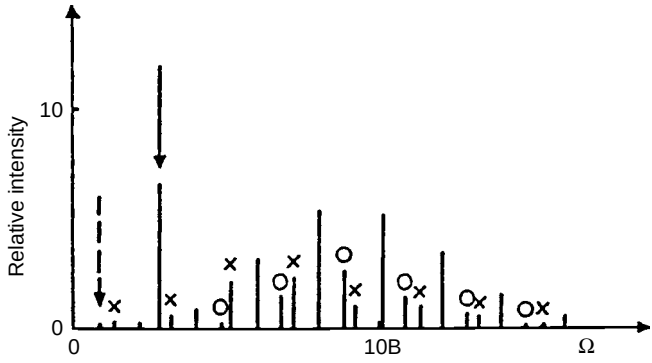

Fig. 6.17. The same as in Fig. 6.16 for $kT = 50\,\mathrm{cm}^{-1}$, the intensity scale being reduced by a factor of 100 [6.128].

number, and in terms of its shape and temperature features it is quite analogous to the zero-phonon line in the optical spectra (Section 6.1.2). Therefore it can be called the "zero-rotational" line. This line has been mentioned above as a transition between the tunneling states [6.117].

Unlike in systems with dipolar instability, the spherical-top molecules for which the dipole-active vibrations are not simultaneously JT active have no pure rotational spectra. Examples of this kind can be found, in particular, among tetrahedral molecules with a JT E term in the ground state. For twofold degenerate electronic states of spherical-top molecules there is no rotational fine structure in the excited vibronic state as well. Indeed, as shown in Chapter 5, in this case all the JT states transform as the representations E, A_1, and A_2, the squares of which do not contain the triplet representation of the operator of the dipole moment that induces the transition.

Nevertheless, as shown in [6.131], the spin–orbital interaction, by mixing in the excited T term (in the approximation of the second-order perturbation theory), removes this prohibition, allowing the rotational structure in the infrared (microwave) spectrum of the ground E term. For instance, under the influence of the spin–orbital interaction the electronic ^2E term of a tetrahedral molecule becomes a cubic Kramers quadruplet Γ_8, its symmetrized square containing the T_2 representation of the dipole moment. This explains the origin of the expected new type of rotational spectrum.

The spin–vibronic–rotational interaction for a C_{3v} molecule in an electronic ^2E state and the hyperfine Hamiltonian for the corresponding nuclear-spin–electron-spin interaction is investigated in [6.125].

The existence of rigid-dipole properties in some JT molecules that have no proper dipole moment can be manifested also in the collision-induced absorption of light by spherical-top molecules in degenerate orbital states [6.132]. The

collision of two molecules induces a dipole moment, which interacts with the electromagnetic wave, resulting in its absorption [6.133]. In the absence of electronic degeneracy the first nonzero multipole moments of spherical-top molecules determining their interaction at large distances are the octapole and hexadecapole (O_h symmetry) moments. But if the ground electronic term of the molecule is degenerate, then the first nonzero multipole moment is quadrupole or even dipole (in cases of dipolar instability). The estimates given in [6.132] show that the effective quadrupole moments under consideration may reach magnitudes comparable to the quadrupole moments of symmetric-top molecules.

Vibronic effects in infrared spectra of linear molecules were considered in terms of the RTE by various authors (Sections 4.4 and 5.1). Several reviews [6.134–6.138] provide details of expected energy spectra and wavefunctions for spectroscopic properties, similar to that considered above for E- and T-term JT systems. Further discussion involving specific molecules with the RTE is given in Chapter 7.

6.2.2 Raman spectra and birefringence

As stated above, vibronic effects in the IR spectra take place only for Jahn–Teller systems with dipolar instability. Similar spectra for systems without dipolar instability can be obtained by means of Raman light scattering. Raman spectra are determined by other selection rules, and they are in a sense complementary to the IR spectra.

The shape function of the Raman spectrum accompanied by a transition of the Jahn–Teller system from the vibronic state Ψ_n (Γ_1) to the state Ψ_m (Γ_1) is determined by Eq. (6.2) with 1κ and $2\kappa'$ from the same term and $\mathbf{\Omega} = \mathbf{\Omega}_s - \mathbf{\Omega}_i$ as the frequency difference between the incident $\mathbf{\Omega}_i$ and scattered $\mathbf{\Omega}_s$ light, while d is the two-photon transition operator determined by the tensor of electronic polarizability $P_{\alpha\beta}$ [6.139]:

$$d = \sum_{\alpha,\beta} n_{i\alpha} n_{s\beta} P_{\alpha\beta}(r, Q), \qquad \alpha,\ \beta = x,\ y,\ z \tag{6.54}$$

Here n_i and n_s are the unit vectors of polarization of the incident and scattered light, respectively.

The scalar convolution (6.54) can be written in the form of a convolution of irreducible tensor operators,

$$d = \sum_{\Gamma\gamma} N_{\Gamma\gamma} P_{\Gamma\gamma}(r, Q) \tag{6.55}$$

where Γ are the irreducible representations (of the symmetry group of the system) contained in the square of the vector representation, and $N_{\Gamma\gamma}$ and $P_{\Gamma\gamma}$ are linear combinations of the components of the second-rank tensors $n_{i\alpha}$, $n_{s\beta}$ and $P_{\alpha\beta}$, respectively, which have the transformation properties of $\Gamma\gamma$. For example, for a cubic system of O_h symmetry vectors transform as T_{1u}, and therefore $\Gamma = T_{1u} \times T_{1u} = A_{1g} + E_g + T_{1g} + T_{2g}$,

$$N_{\Gamma\gamma} = \sum_{\alpha,\beta} n_{i\alpha} n_{s\beta} \langle T_{1u}\alpha T_{1u}\beta | \Gamma\gamma \rangle, \qquad P_{\Gamma\gamma} = \sum_{\alpha,\beta} P_{\alpha\beta} \langle T_{1u}\alpha T_{1u}\beta | \Gamma\gamma \rangle \quad (6.56)$$

and $\langle T_{1u}\alpha T_{1u}\beta | \Gamma\gamma \rangle$ are Clebsch–Gordan coefficients.

Thus by choosing different polarizations for the incident and the scattered light one can separate the scattering effects determined by polarizabilities of different symmetry. For instance, for the O_h group one can distinguish A_{1g} scattering, E_g scattering, etc. We can also separate symmetric and antisymmetric representations, i.e., those contained in, respectively, the symmetric and antisymmetric squares of the vector representation. This is important because the selection rules for the symmetric scattering are the same as for the electric quadrupole moment, and therefore the spectral features and the temperature dependence of the corresponding components of scattering are the same as those for the quadrupole IR absorption. For the antisymmetric scattering the selection rules are the same as those for the operator of the magnetic dipole moment, and therefore the spectra and temperature dependence of the antisymmetric components of scattering are the same as for magnetic-dipole IR absorption.

All the results obtained for the vibronic effects in the IR absorption are equally valid for Raman spectra, with the distinction that instead of the frequency $\mathbf{\Omega}$ of the absorbed IR irradiation we deal here with the frequency shift of the scattered light. In particular, for systems without a center of inversion, among the irreducible representations Γ in the sum (6.55), there are representations to which the components of a vector belong. The corresponding components of the tensor $P_{\Gamma\gamma}$ cause the same transitions as the components of the dipole-moment vector do in IR absorption. The remaining components of the tensor $P_{\Gamma\gamma}$ produce transitions which do not appear in the IR spectra. Therefore the Raman spectra have a richer vibronic structure. For instance, the rotational spectra of free JT spherical-top molecules contain O and S branches for which $\Delta J = \pm 2$ in addition to the P, Q, and R lines in the IR spectra, discussed above [6.140].

Now we take into account that in non-resonant Raman scattering the dependence of the polarizability operator $P_{\Gamma\gamma}$ (r, Q) on the nuclear coordinates

Q is weak [6.141]. This dependence originates from the vibronic JT or PJT interactions in the excited electronic states, which serve as the intermediates in the two-photon Raman process. We can expand this operator in a power series:

$$P_{\Gamma\gamma}(r, Q) = P^{(0)}_{\Gamma\gamma}(r) + \sum_{\Gamma_1\gamma_1} P^{(1)}_{\Gamma\gamma\Gamma_1\gamma_1}(r) Q_{\Gamma_1\gamma_1} + \cdots \tag{6.57}$$

where

$$P^{(1)}_{\Gamma\gamma\Gamma_1\gamma_1}(r) = \left.\frac{\partial P_{\Gamma\gamma}(r,\ Q)}{\partial Q_{\Gamma_1\gamma_1}}\right|_{Q=Q_0} \tag{6.58}$$

The first term in Eq. (6.57) is the electronic polarizability of the system in the reference nuclear configuration Q_0. This operator is similar to the operator of the electronic quadrupole or magnetic dipole moment (in the sense mentioned above). For systems without a center of inversion there are some components of this operator which have the transformation properties of a vector, and therefore in the limited basis of the electronic states of the JT term Γ_1 they are represented by the same matrix elements as the operator of the electronic dipole moment (6.35). It follows that the Raman transitions caused by the terms containing $P^{(0)}_E$ do not differ from the IR transitions caused by the operator (6.35).

It is important that in the absence of degeneracy the term $P^{(0)}_{\Gamma\gamma}(r)$ produces Rayleigh scattering only, and hence the Raman scattering caused by this operator is an essential feature of JT systems.

The second term in Eq. (6.57) describes what is known as Raman scattering of the first order. As mentioned above, its contribution is weak compared with the zeroth-order Raman scattering. It is estimated [6.115] to be of the order of $P^{(1)} \sim F_E/(\omega_{\rm eg} - \mathbf{\Omega}_{\rm i})$, where F_E is the vibronic coupling constant in the excited electronic states (that serves as an intermediate), $\omega_{\rm eg} = (E_{\rm e} - E_{\rm g})/\hbar$ is the Bohr frequency of the dipole transition from the ground state to the excited intermediate one with the energies $E_{\rm g}$ and $E_{\rm e}$, respectively, and $\mathbf{\Omega}_{\rm i}$ is the frequency of the incident light. In non-resonant Raman scattering this parameter is relatively small, $P^{(1)} \lesssim 0.1$ (see, however, [6.142]).

The second term of Eq. (6.57) has the same transformation properties $\Gamma\gamma$ as the zeroth-order terms $P^{(0)}_{\Gamma\gamma}(r)$, and therefore it is subject to the same selection rules. Accordingly, the first-order Raman scattering contains the same allowed transitions as the Raman scattering caused by the zeroth-order terms. Therefore the separation of its contribution to the Raman scattering spectra is, in general, impossible. However, this can be done in limiting cases of weak

and strong vibronic coupling. For instance, in the case of weak coupling when the vibrational occupation numbers $n_{\Gamma\gamma}$ are still good quantum numbers, the term linear in $Q_{\Gamma\gamma}$ causes the Raman transitions $n_{\Gamma\gamma} \to n_{\Gamma\gamma} \pm 1$. This means that the corresponding spectral lines at $T = 0\,\mathrm{K}$ are at the frequencies $\mathbf{\Omega} \approx \omega_\Gamma$. On the other hand, the pure rotational Raman spectra related to the ground vibronic state are caused only by the operator $P^{(0)}_{\Gamma\gamma}(r)$ and are positioned in the immediate neighborhood of the Rayleigh line, i.e., they lie in a different range of frequencies.

If the vibronic coupling is strong, the low-energy vibronic states can be approximately considered as localized in the minima of the APES (Chapter 5). For this reason the coordinates $Q_{\Gamma\gamma}$ in Eq. (6.57) can be replaced by $Q^{(0)}_{\Gamma\gamma} + q_{\Gamma\gamma}$, where $Q^{(0)}_{\Gamma\gamma}$ are the minima coordinates and $q_{\Gamma\gamma}$ are small displacements from these minima. The terms containing $Q^{(0)}_{\Gamma\gamma}$ merge with $P^{(0)}_{\Gamma\gamma}(r)$, while the terms linear in $q_{\Gamma\gamma}$ lead to the first-order Raman scattering modified by the vibronic interaction. Since the occupation numbers at the bottom of the minimum are good quantum numbers, the operators $q_{\Gamma\gamma}$ at $T = 0\,\mathrm{K}$ cause Raman scattering at the frequencies $\mathbf{\Omega} \approx \tilde{\omega}_\Gamma$, where $\tilde{\omega}_\Gamma$ are the modified frequencies of normal vibration at the bottom of the minimum (Chapter 3). The remaining terms of the polarizability operator result in Raman transitions at frequencies $|\mathbf{\Omega}| \lesssim \hbar\omega_\Gamma^2 K_\Gamma / F_\Gamma^2$ between the rotational vibronic states (Section 5.2), and between the tunneling states for stronger coupling (Section 5.3). In multimode JT systems the first-order Raman scattering reproduces the vibrational density of states modified by the vibronic interaction (Section 5.5).

If the distance from resonance $\left|\omega_{\mathrm{eg}} - \mathbf{\Omega}_{\mathrm{i}}\right|$ in the non-resonant Raman scattering is sufficiently large, the first-order scattering is negligible and the main contribution originates from the first term in Eq. (6.57). The intensity of the Rayleigh line is determined in this case by the square of the matrix element of the electronic polarizability operator $P^{(0)}_{\Gamma\gamma}(r)$ calculated with the vibronic wavefunctions of the ground state. This matrix element is obviously proportional to the square of the corresponding vibronic reduction factor (Section 5.6), provided the polarizations of the incident and the scattered light are chosen to separate out the contribution of the polarizability component that belongs to a given irreducible representation Γ. The total intensity is equal to the zeroth-order moment of the Raman band (Section 6.1.1). It follows that it is possible to estimate the values of the vibronic reduction factors from the Raman scattering experiments with an appropriate choice of polarizations of the incident and the scattered light [6.143, 6.144].

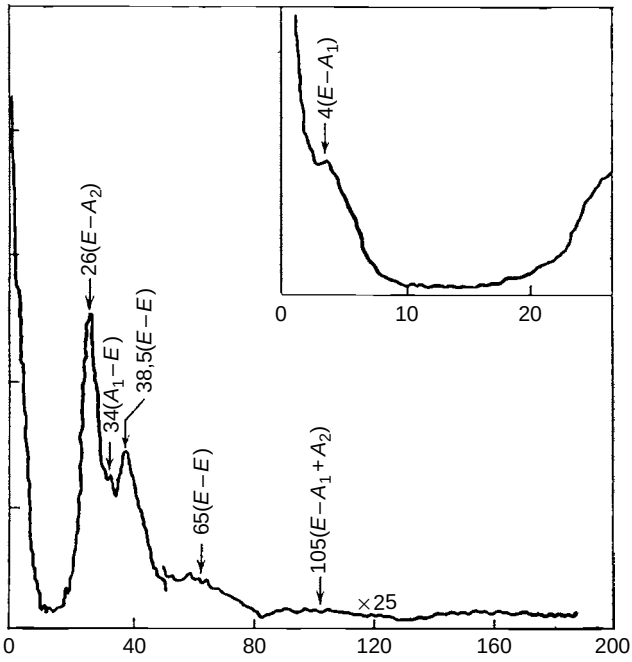

Fig. 6.18. The vibronic Raman spectrum of Cu^{2+}:CaO at $T=4.2$ K. The inset shows the part of the spectrun containing the $E\rightarrow A$ transition between the tunneling levels at a frequency of 4 cm^{-1} (Reprinted with permission from [6.141]. Copyright 1975 American Physical Society.)

The vibronic spectrum of the Raman scattering of Cu^{2+} impurity centers in CaO crystals observed at $T=4.2$ K [6.141, 6.145] is given in Fig. 6.18 as an illustrative example. In the upper right-hand corner the low-frequency part of the spectrum containing the line at the frequency $\hbar\boldsymbol{\Omega} \approx 4$ cm^{-1} is shown on a larger scale. This line is interpreted as the $E\rightarrow A$ transition between the tunneling states of the ground electronic E term of the Cu^{2+} ion.

It can be shown (see in [6.1]) that by substituting Eq. (6.55) into Eq. (6.2) we get for the intensity of the Raman scattering the following expression:

$$I(\boldsymbol{\Omega}) \sim \sum_{\Gamma} G_{\Gamma}(\boldsymbol{\Omega})(1/f_{\Gamma}) \sum_{\gamma} |N^2_{\Gamma\gamma}| \tag{6.59}$$

where f_{Γ} is the dimensionality of the representation Γ and G_{Γ} $(\boldsymbol{\Omega})$ is the contribution of the component of Γ symmetry. Since the magnitudes $|N^2_{\Gamma\gamma}|$ are composed of the components of the vectors of the incident and scattered light polarizations with respect to the symmetry axes of the scattering system, this formula determines explicitly the angular dependence and polarization properties of the scattered light.

For randomly oriented systems (molecules in gas phase and solutions, polycrystals, and so on) the magnitudes $|N^2_{\Gamma\gamma}|$ should be averaged over the orientations of the scattering systems. Direct calculation shows that the orientational averages $|N^2_{\Gamma\gamma}||/f_\Gamma$ are the same for different irreducible representations $\Gamma_s \neq A_1$ contained in the symmetric square of the vector representation (i.e., for symmetric scattering) and separately for the representations Γ_a contained in the antisymmetric square (i.e., for antisymmetric scattering, see in [6.146], Section 2).

On introducing

$$G_s = \sum_{\Gamma_s \neq A_1} G_{\Gamma_s}, \qquad G_a = \sum_{\Gamma_a} G_{\Gamma_a} \tag{6.60}$$

we obtain from Eq. (6.59) (see also [6.139], Section 61)

$$I(\mathbf{\Omega}) \sim [G_{A_1}(\mathbf{\Omega})\left|\vec{n}_s^* \vec{n}_i\right|^2 + (1/10)G_s(\mathbf{\Omega})(1 + \left|\vec{n}_s \vec{n}_i\right|^2 - (2/3)\left|\vec{n}_s^* \vec{n}_i\right|^2) + (1/6)G_a(\mathbf{\Omega})(1 - \left|\vec{n}_s \vec{n}_i\right|^2)] \tag{6.61}$$

Denote the angle between the direction of the scattering $\vec{k}_s$ and the direction of the polarization of the incident light $\vec{n}_i$ by ϑ. The scattered light contains two independent components: one polarized in the plane $(\vec{k}_s, \vec{n}_i)$ (intensity I_1) and one perpendicular to the plane (intensity I_2). The ratio $\rho_1 = I_2/I_1$ is called the *depolarization ratio*. For the scattering of linear polarized light we obtain from Eq. (6.61)

$$\rho_1 = \frac{3G_s(\mathbf{\Omega}) + 5G_a(\mathbf{\Omega})}{30G_{A_1}(\mathbf{\Omega}) + G_s(\mathbf{\Omega})(3 + \sin^2\vartheta) + 5G_a(\mathbf{\Omega})\cos^2\vartheta} \tag{6.62}$$

Specifically, at $\vartheta = \pi/2$ we have

$$\rho_1 = \frac{3G_s(\mathbf{\Omega}) + 5G_a(\mathbf{\Omega})}{30G_{A_1}(\mathbf{\Omega}) + 4G_s(\mathbf{\Omega})} \tag{6.63}$$

If the incident light is natural (nonpolarized), the expression (6.61) should be averaged over the directions of polarizations $\vec{n}_i$ for a given direction of the incident light $\vec{k}_s$. In the case of scattering to an angle of $\pi/2$ the expression for the depolarization ratio is related to ρ_1 by the simple formula

$$\rho_n(\mathbf{\Omega}) = \frac{2\rho_1(\mathbf{\Omega})}{1 + \rho_1(\mathbf{\Omega})} = \frac{6G_s(\mathbf{\Omega}) + 10G_a(\mathbf{\Omega})}{30G_{A_1}(\mathbf{\Omega}) + 7G_s(\mathbf{\Omega}) + 5G_a(\mathbf{\Omega})} \tag{6.64}$$

An important feature of molecules in nondegenerate electronic states is that the tensor of polarizability $P_{\alpha\beta}$ is real and symmetric (see [6.139], Section 62). It follows that there is no antisymmetric scattering in such molecules,

i.e., $G_a = 0$. From Eq. (6.64) we obtain in this case $\rho_n \leq 6/7$, and from Eq. (6.63) we obtain $\rho_1 \leq 3/4$. An essential feature of JT molecules is thus the possibility of antisymmetric scattering with $\rho_n > 6/7$ and $\rho_1 \leq 3/4$ [6.115]. The first calculations for Raman scattering in JT systems were obtained [6.115] for the $E \otimes e$ problem in an X_3 molecule by means of direct substitution of the vibronic energy levels and wavefunctions obtained by numerical computation (Section 5.4) into Eq. (6.2).

Further discussion of the problem is given in a series of works in which approximate weak- and strong-coupling results, as well as the intermediate-coupling case in the multimode JTE, were explored [6.79, 6.116, 6.143, 6.147–6.150]. Selection rules for first-order Raman scattering in JT systems were obtained in [6.151]. Rotational Raman spectra of free spherical-top molecules near the Rayleigh line for E and T terms were considered in [6.140].

The tensor of Rayleigh scattering of light by molecules is closely related to their polarizability in the ground state [6.139]. The traditional description of the electric properties of a molecule is based on the assumption that the charge distribution (either classical or quantum-theoretical) is totally symmetric with respect to the equilibrium nuclear configuration. It follows that, for instance, for a spherical-top molecule in a nondegenerate state only the scalar apart of the polarizability is nonzero.

In degenerate states the situation is significantly different. Using the group-theoretical selection rules for the matrix elements of the polarizability operator, it can easily be seen that there may also be nonzero matrix elements for components of the irreducible tensor operators of the polarizability and multipole moments, which are not totally symmetric. If the vibronic ground state transforms as the irreducible representation Γ, then the nonzero contribution to the polarizability arises from the components of the operator of polarizability transforming as the irreducible representations in the symmetric square $[\Gamma^2]$, or the antisymmetric square $\{\Gamma^2\}$ if Γ is a two-valued representation of a double group. It means that *in degenerate states the point symmetry of the charge distribution may be lower than in the nondegenerate case*.

In nondegenerate states the diagonal matrix element of an operator is the same as the mean value of the corresponding quantity (polarizability, multipole moments, etc.), whereas in the case of degeneracy there is no such direct relation between the matrix elements and observable properties. Indeed, in the basis of the degenerate states each physical quantity corresponds not to a matrix element but to a matrix. Therefore the correlation between the matrix elements and the observable properties has to be carried out for each distinct experimental situation separately.

Such an analysis of birefringence in gases of spherical-top molecules, in particular the Kerr and Cotton–Mouton effects, is performed below. The depolarization of light in Rayleigh, hyper-Rayleigh, and purely rotational Raman scattering by degenerate molecules is considered in [6.152]. A similar investigation of the temperature-dependent optical activity of symmetric JT and PJT systems in a magnetic field is presented in [6.153]. All these problems, as well as some other manifestations of the anomalous electric properties of molecular systems with the JTE and PJTE, are reviewed in [6.129].

So far we have discussed non-resonant Raman scattering for which the spectral density is determined by the vibronic properties of the ground electronic term only and does not depend on the properties of the virtual excited states through which the non-elastic scattering of light takes place. The situation is different in resonant Raman scattering when the frequency of the incident light $\mathbf{\Omega}_i$ lies within the absorption band of the JT system. In this case the operator $P_{\alpha\beta}$ in Eq. (6.54) that causes the two-photon transition cannot be reduced to the electronic polarizability; it depends strongly on the nuclear coordinates [6.154]:

$$P_{\alpha\beta}(r,Q)=\sum_k D_\alpha(r)\frac{\left|\Psi_k^{(\bar\Gamma)}(r,Q)\right\rangle\left\langle\Psi_k^{(\bar\Gamma)}(r,Q)\right|}{\omega_{kn}-\mathbf{\Omega}_i-i\gamma_k}D_\beta(r) \tag{6.65}$$

Here $D_\alpha(r)$ are the Cartesian components of the vector of the dipole moment of the electrons, $\bar\Gamma$ is the index of the excited electronic term (or of a group of terms that are close in energy) which is in resonance with the scattered light, $\omega_{kn}=(E_{\bar\Gamma k}-E_{\Gamma_1 n})/\hbar$ is the Bohr frequency of the transition, and γ_k is the natural line width. In Eq. (6.65), as usual, the terms containing non-resonant denominators are omitted.

As seen from this equation, the intensity of the scattered light in resonant Raman spectra depends strongly on the properties of the excited states through which the scattering takes place. In the simplest situation when both the initial and final states are from the nondegenerate electronic term $\Gamma_1=A_1$, the spectrum of the shifted scattering reproduces the equally spaced vibrational energy spectrum of the A_1 term, while the intensity of the lines depends on the frequency $\mathbf{\Omega}_i$ that determines the resonant excited state.

Of special interest is the case when the excited states are JT states. Figure 6.19 shows the dependence of the intensity of the resonant Raman scattering on the frequency of the incident light $\mathbf{\Omega}_i$ when the scattering takes place through the excited E term with an $E\otimes e$ Jahn–Teller problem, while the ground term is A_1. This result is obtained [6.155] by means of numerical calculations of the vibronic states of the linear and quadratic $E\otimes e$ problem

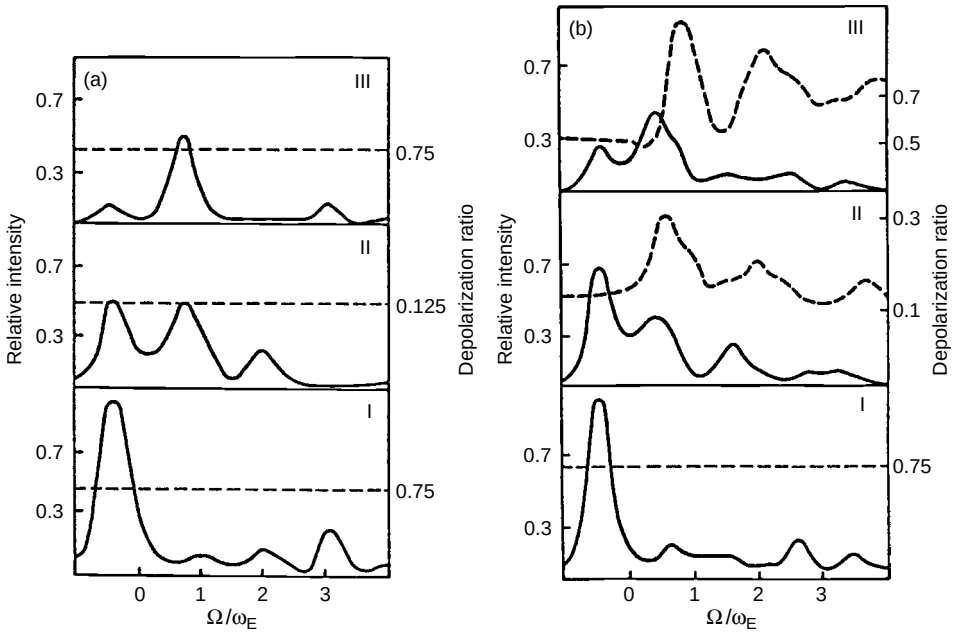

Fig. 6.19. Excitation profiles (solid lines) and depolarization ratios (dashed lines) for the resonance Raman scattering via the excited E term at $E_{JT}^{E}/\hbar\omega_E = 1$ as a function of the incident light frequency $\mathbf{\Omega}$ in ω_E units (the zero energy corresponds to the position of the degenerate E term) for $G_E = 0$ (a) and $G_E = 0.1K_E$ (b). **I**: fundamental tone; **II**: first overtone; **III**: second overtone. (Reprinted with permission from [6.155]. Copyright 1977 Elsevier Science Publishers.)

and substitution of the results into Eq. (6.65). The dashed line in Fig. 6.19 shows the dispersion of the depolarization ratio of natural light. It is seen that the depolarization ratio of the overtones depends on the frequency of the incident light $\mathbf{\Omega}_i$, this dependence being stronger for larger values of the quadratic vibronic coupling constant G_E, and this result can be used for experimental estimation of G_E. Similar results were obtained [6.156] for the excited resonance T term with a $T \otimes t_2$ problem. The multimode aspects of resonant Raman scattering in JT systems are discussed in [6.157, 6.158]. The semiclassical approach in the limiting case of strong vibronic coupling [6.158] gives satisfactory agreement with numerical quantum-mechanical calculations.

Another phenomenon in which JT spherical-top molecules manifest anisotropic properties is the *birefringence in external electric fields*, the electro-optical Kerr effect. The origin of this phenomenon in polar liquids and gases containing rigid-dipole molecules can be explained by the Langevin–Born mechanism. In accordance with this theory the random orientation of the

rigid-dipole molecules in space results in the macroscopic isotropy of the matter. Under the influence of an external electric field the molecules tend to orient along the field, causing the optical anisotropy of the medium, and hence the birefringence. A wave of light in this medium splits into two components with mutually perpendicular planes of polarization. One of these components, the ordinary ray, has the plane of polarization perpendicular to the external electric field, whereas the other one, the extraordinary ray, is polarized along the electric field.

The difference in the path lengths of the two rays in units of the wavelength is $Bl\mathcal{E}^2$, where l is the path length of the light ray as a whole in the medium, $\mathcal{E}$ is the intensity of the electric field, and B is the Kerr constant characterizing the difference between the refractive indices of the ordinary and extraordinary rays. The orientation of the molecules along the external electric field is hindered by their thermal motions, and therefore B is inversely proportional to the square of the temperature [6.159]. In addition, the Kerr constant depends on the magnitude of the dipole moment of the molecule and the wavelength of the light.

Besides the orientational Langevin–Born mechanism, the anisotropy of the medium may be caused by the deformation of the molecular electronic shell induced by the electric field, i.e. by the anisotropy of the *hyperpolarizability* (the Voight mechanism). The contribution of this effect to the Kerr constant is relatively small and independent of temperature. At first sight it seems that for spherical-top molecules, which have no anisotropy in the absence of external fields, the birefringence may occur as a result of the Voight mechanism only.

However, this conclusion implies that the ground state of the molecule is nondegenerate and transforms according to the totally symmetric representation. As mentioned above, the molecules with dipolar instability that have no proper dipole moment manifest rigid-dipole properties due to the JTE or PJTE. For these molecules birefringence of the Langevin–Born orientational mechanism should occur. The temperature dependence of its Kerr constant may be different from that indicated above because the dipole moment itself depends on temperature. It emerges from the theory given below that even in the absence of dipolar instability (say, when the vibronic coupling constant is negligibly small) the presence of electronic degeneracy determines the anisotropy of electronic polarizability, causing birefringence in external electric fields of the Langevin–Born type [6.160, 6.161].

Consider, for instance, a molecule with T_d or O_h symmetry in a twofold degenerate ground-state E term. Neglecting rotational quantization, the molar Kerr constant ${}_mB$ is related to the components of the tensor of

polarizability of the molecule in a constant homogeneous electric field $\mathcal{E}$ parallel to the z axis as follows [6.162]:

$$ {}_{\mathrm{m}}B = 2\pi N_{\mathrm{A}} \left\{ \mathcal{E}^{-2} [\langle P_{zz}(\mathbf{\Omega}_{\mathrm{i}}, \mathcal{E}) \rangle - \langle P_{xx}(\mathbf{\Omega}_{\mathrm{i}}, \mathcal{E}) \rangle] \right\}_{\mathcal{E} \to 0} \tag{6.66} $$

where N_{A} is the Avogadro number, $P_{\alpha\beta}$ is the operator of electric polarizability determined by Eq. (6.65), and $\mathbf{\Omega}_{\mathrm{i}}$ is the frequency of incident light propagating in the direction perpendicular to the electric field. All the states $\Psi_k^{(\bar{\Gamma})}$ and corresponding transition frequencies ω_{kn} in Eq. (6.65) and hence the components of the tensor of polarizability in Eq. (6.66) depend on the intensity $\mathcal{E}$. The angular brackets in this equation mean the average over all the vibronic states of the ground E term, and over all the orientations of the molecules. The calculations were performed in a series of works including [6.160, 6.161] (see the review [6.129] and references therein, as well as in [6.1]). The results are briefly as follows.

In the absence of vibronic coupling we have for the orientational contribution to the Kerr constant [6.160]

$$ {}_{\mathrm{m}}B^{(\mathrm{or})} = (6\pi N_{\mathrm{A}}/5kT) P_E^{(0)}(0) P_E^{(0)}(\mathbf{\Omega}_{\mathrm{i}}) \tag{6.67} $$

where $P_E^{(0)}(0)$ and $P_E^{(0)}(\mathbf{\Omega}_{\mathrm{i}})$ are the static and dynamic electronic polarizabilities, respectively. Thus, even without taking into account the vibronic coupling, the electronic degeneracy of the ground state results in an anomalous Kerr effect in spherical-top molecules with the Kerr constant proportional to T^{-1}. The estimates in [6.160] show that the corresponding contribution to ${}_{\mathrm{m}}B$ is comparable to the Kerr constant of anisotropically polarizable molecules. When we include the vibronic coupling, the expression (6.66) changes. These changes can be taken into account by a special factor $Q_T(E)$ [6.161]:

$$ {}_{\mathrm{m}}B^{(\mathrm{or})} = (6\pi N_{\mathrm{A}}/5kT) P_E^{(0)}(0) P_E^{(0)}(\mathbf{\Omega}_{\mathrm{i}}) Q_T(E) \tag{6.68} $$

The factor $Q_T(E)$ depends on temperature and it is similar to the vibronic reduction factors (Section 5.6). Therefore $Q_T(E)$ may be called the *temperature-dependent vibronic reduction factor* in the Kerr effect. The letter E in parentheses indicates that the operator containing the E components of the polarizability is reduced. In the absence of vibronic coupling $Q_T(E) = 1$. In the limiting case of low temperatures when only the ground vibronic state is populated $Q_T(E) = K_T^2(E)$, where $K_T(E)$ is the usual vibronic reduction factor introduced in Section 5.6. As the constant of vibronic coupling increases from zero to infinity, $K_T(E)$ lowers from 1 to $\frac{1}{2}$, and hence $Q_T(E)$ changes from 1 to $\frac{1}{4}$.

At sufficiently high temperatures $Q_T(E)$ can be represented by the first terms of the expansion in $\beta = 1/KT$:

$$Q_T(E) \approx 1 - (2E_{\mathrm{JT}}/3kT) \tag{6.69}$$

On substituting this expression into (6.68) we come to an interesting result:

$$\begin{aligned} {}_{\mathrm{m}}B^{(\mathrm{or})} &\approx \frac{A}{kT} + \frac{B}{(kT)^2} \\ A &= (6\pi N_{\mathrm{A}}/5) P_E^{(0)}(0) P_E^{(0)}(\boldsymbol{\Omega}_{\mathrm{i}}) \\ B &= -\tfrac{2}{3} A E_{\mathrm{JT}}^E \end{aligned} \tag{6.70}$$

Thus, in addition to the dependence on T^{-1}, a term $\sim T^{-2}$ characteristic of rigid-dipole molecules is present. In accordance with the estimates in [6.161] the corresponding contribution to the Kerr constant at room temperature may be more than 20% of the pure electronic value.

In [6.161] the electro-optical Kerr effect for the electronic Γ_8 term in cubic molecules of O_{h} symmetry is also discussed. The contribution to the Kerr constant in this case is given by the electronic polarizability of the e_{g} and $t_{2\mathrm{g}}$ components. If the vibronic coupling is taken into account, both these contributions are reduced by $Q_T(E)$ and $Q_T(T_2)$, respectively, for which approximate expressions are found in the limiting cases of high and low temperatures, respectively.

As mentioned in Section 6.2.1, spherical-top molecules with a degenerate ground state possess a quadrupole moment (or even a dipole moment, in cases with dipolar instability). It is clear that such quadrupole molecules should orient themselves in inhomogeneous external electric fields, resulting in optical anisotropy of the medium and birefringence. The additional contribution to the difference between the refractive indices of the ordinary and extraordinary rays $\Delta n^{(\mathrm{or})}$ due to the orienting action of the gradient of the electric field on molecules of cubic symmetry in degenerate electronic states (in the absence of dipolar instability) is considered in [6.163]. It emerges that $\Delta n^{(\mathrm{or})}$ is proportional to the absolute value of the gradient of the electric field, and in the case of the ground E term it is described by an expression similar to Eq. (6.68), with the distinction that instead of $P_E^{(0)}(0)$ (the static polarizability) the reduced matrix element of the operator of the quadrupole moment is introduced. The temperature dependence of $\Delta n^{(\mathrm{or})}$ is determined by a term proportional to T^{-1} and by the factor $Q_T(E)$.

Similar to the Stark splitting of the vibronic and rotational energy levels, which determines the Kerr effect, the Zeeman splitting of these levels in an

external magnetic field also results in optical anisotropy and birefringence. This is known as the Cotton–Mouton effect, the theory of this effect is similar to that of the Kerr effect. The difference in the path length of the ordinary and extraordinary rays is $Cl\mathcal{H}^2$, where l is the optical path length of the ray of light in the medium, and $\mathcal{H}$ is the intensity of the magnetic field, C being the Cotton–Mouton constant, which depends on the composition of the matter, the wavelength of light, and temperature. According to widespread opinion, spherical-top molecules do not orient under the external magnetic field, and hence the only reason for their optical anisotropy is the influence of the magnetic field on the molecular electronic shell, which gives no temperature dependence to the Cotton–Mouton constant. As shown in [6.164], this conclusion is based on the implicit assumption of the absence of electronic degeneracy, and it is invalid in the presence of degeneracy. Neglecting rotational quantization, the molar Cotton–Mouton constant is given by the following expression, similar to (6.66):

$$ {}_{\mathrm{m}}C = 2\pi N_{\mathrm{A}}\{\mathcal{H}^{-2}[\langle P_{zz}(\mathbf{\Omega}_{\mathrm{i}},\ \mathcal{H})\rangle - \langle P_{xx}(\mathbf{\Omega}_{\mathrm{i}},\ \mathcal{H})\rangle]_{\mathcal{H}\to 0} \qquad (6.71) $$

where $P_{\alpha\alpha}(\mathbf{\Omega}_{\mathrm{i}}, \mathcal{H})$ is the polarizability of the system in the magnetic field $\mathcal{H}$ parallel to the z axis, other notation being the same as in Eq. (6.66). By means of arguments similar to those employed above, one can separate the orientational contribution to the Cotton–Mouton constant. The theory [6.164] shows that the latter has three components. In the absence of vibronic coupling the first contribution is quadratic in T^{-1}. The second and third contributions are linear in T^{-1}. Usually, for paramagnetic molecules the first contribution is dominant, and the temperature dependence as a whole is ${}_{\mathrm{m}}C \sim T^{-2}$. For diamagnetic molecules the first and the third contributions are zero and hence ${}_{\mathrm{m}}C \sim T^{-1}$.

If the vibronic coupling is taken into account, all three contributions are reduced by temperature-dependent reduction factors, similar to the above $Q_T(\Gamma)$. Therefore the resulting temperature dependence of the Cotton–Mouton constant is rather complicated. Nevertheless, in the limiting case of very low temperatures when the population of excited vibronic states may be neglected, the temperature-dependent reduction factors transform into a combination of the usual vibronic reduction factors of electronic operators that are independent of temperature. In this case the temperature dependence is qualitatively the same as without the vibronic coupling. At higher temperature, the temperature dependence becomes more complicated, and drawing unambiguous conclusions about the paramagnetic properties of molecules from the dependence of ${}_{\mathrm{m}}C$ on T is rather difficult.

In [6.164] the general theory of the anomalous Cotton–Mouton effect for JT molecules, including the analysis of the temperature behavior of the vibronic reduction factors at high and low temperatures, is given and examples of birefringence by cubic molecules in the Γ_8 ground state are shown.

The problems considered in this section are also related to the optical activity of JT molecules in Rayleigh and hyper-Rayleigh light scattering induced by external magnetic fields. This topic is discussed in [6.165].

6.3 Magnetic resonance and related spectra

6.3.1 The JTE in electron paramagnetic resonance spectra

The method of electron paramagnetic resonance (EPR) (or electron spin resonance, ESR) has played a most important role in the development of research on the JTE and vibronic interaction in the post-war years. In the early fifties Bleaney and coworkers [6.166, 6.167] discovered unusual magnetic resonance properties of divalent copper compounds, in particular, a distinctive temperature dependence of the fine and hyperfine structure of the spectrum. A qualitatively correct interpretation of the high-temperature component of these spectra as due to the JT dynamics of the nuclear configuration was first given in [6.168]. Subsequently, the origin of the main features of the more complicated low-temperature spectrum was clarified on the basis of the theory of tunneling splitting [6.169]. These and other related results had a strong impact on the development of the trend as a whole.

EPR theory, which takes into account the vibronic JTE and PJTE, comprises a large proportion of the work on, and applications of, the EPR method, often occupying whole chapters in relevant monographs and textbooks [6.1, 6.2, 6.170, 6.171]. The achievements in this area are well presented also in reviews [6.172–6.176] (see also the bibliographic review [6.177]). In this section, applications of the vibronic interaction theory to EPR and related techniques, as well as some recent achievements, are presented.

It is known that EPR spectra may be described satisfactorily by means of the spin Hamiltonian H; its matrix elements determine the positions and intensities of the absorption lines in the radio-frequency range of electromagnetic radiation. The electronic ($\vec{S}$) and nuclear ($\vec{I}$) spin and the external magnetic field intensity $\Re$ (and their combinations) in the spin Hamiltonian are operators with coefficients depending on the structure and properties of the system. It is convenient to group the terms of the spin Hamiltonian in such a way that they pertain to (transform as) the irreducible representations of the point-group symmetry of the problem. This allows us to obtain the selection rules for

the matrix elements directly. For instance, in a system within cubic symmetry (tetrahedral, octahedral, cubic) the corresponding symmetry-adapted parts of the spin Hamiltonian are [6.1, 6.170]

$$H_{A_1} = g_1\beta(\Re,\ \vec{S}) + \tilde{A}_1(\vec{I},\ \vec{S}) + g_{\mathrm{N}_1}(\Re,\ \vec{I}) \tag{6.72}$$

$$H_{E\vartheta} = \tfrac{1}{2}g_2\beta[3\Re_z S_z - (\Re,\ \vec{S})] + \tfrac{1}{2}\tilde{A}_2[3I_zS_z - (\vec{I},\ \vec{S})] + \tfrac{1}{2}g_{\mathrm{N}_2}\beta_{\mathrm{N}}[3\Re_z I_z - (\Re,\ \vec{I})] + \tfrac{1}{2}P_2(3I_z^2 - I^2) \tag{6.73}$$

(and a similar component $H_{E\varepsilon}$);

$$H_{T_2\xi} = g_3\beta(\Re_y S_z - \Re_z S_y) + \tilde{A}_3(I_yS_z + I_zS_y) + g_{\mathrm{N}_3}\beta_{\mathrm{N}}(\Re_y I_z + \Re_z I_y) + P_3(I_yI_z + I_zI_y) \tag{6.74}$$

(and similar components $H_{T_2\eta}$ and $H_{T_2\zeta}$);

$$H_{T_1x} = g_L\beta\Re_x + \lambda S_x + aI_x \tag{6.75}$$

(and similar components H_{T_1y} and H_{T_1z}).

In these expressions g_i is the electronic g-factor, g_L is its pure orbital part, g_{N_1} is the nuclear g-factor, β and β_{N} are the electronic and nuclear Bohr magnetons, respectively, $\tilde{A}_i$ is the hyperfine structure constant, P_i is the quadrupole interaction constant, λ is the electronic spin–orbital interaction parameter, and a is a constant determining the magnitude of the interaction of the nuclear magnetic moment with the magnetic field of the electrons.

The physical meaning of each component of the spin Hamiltonian, describing the corresponding magnetic interaction within the system and with the external field, is well known [6.170]. As a result of averaging with electronic functions, there are no electronic coordinates in Eqs. (6.71)–(6.74). The matrix elements – parameters of the spin Hamiltonian – can be calculated approximately. For example, in the E state formed by d electrons in cubic-symmetry systems in the crystal-field-theory approximation of second-order perturbation theory,

$$\begin{aligned} g_1 &= g_{\mathrm{s}} - (4\lambda/\Delta E) \\ g_2 &= -(4\lambda/\Delta E) \\ \tilde{A}_1 &= -P[\kappa - (4\lambda/\Delta E)] \\ \tilde{A}_2 &= -P[6\xi + (4\lambda/\Delta E) - (4\xi\lambda/\Delta E)] \end{aligned} \tag{6.76}$$

where $\Delta E = 10Dq$ is the parameter of the splitting of the d states in cubic crystal fields, $g_{\mathrm{s}} = 2.0023$ is the pure spin g-factor, $P = 2g_{\mathrm{N}}\beta\ {}_{\mathrm{N}}\langle r^{-3}\rangle$, $\langle r^{-3}\rangle$ is

the averaged value of r^{-3}, κ is the constant of the contact Fermi interaction of the electronic shell with the nucleus, and ξ is a numerical factor (for the ^2D term $\xi = 2/21$).

If the energy levels and wavefunctions of the system are known, Eqs. (6.71)–(6.75) can be used to estimate the perturbation of the states by the magnetic field (the Zeeman effect), transitions between Zeeman levels, and resonance absorption of electromagnetic radiation in the radio-frequency range which, together with relaxations and other temperature effects, determine the EPR spectrum.

The parameters (6.76) are calculated on the assumption that the nuclei are fixed, and hence the vibronic effects in the EPR spectrum in this approach are ignored completely. If vibronic effects are taken into account, the solution of the problem becomes complicated and the resulting EPR spectrum changes significantly. In isolated systems *the main JTE in EPR is vibronic reduction and tunneling splitting*. In actual situations these effects are modified by relaxations and small random deformations. We consider each of these effects in turn.

In accord with the results obtained in Section 5.6, the matrix elements of physical properties, which depend only on electronic coordinates in the ground state Γ, as a result of vibronic coupling are multiplied by the vibronic reduction factor $K_\Gamma(\overline{\Gamma})$, where $\overline{\Gamma}$ is the irreducible representation to which the physical quantity in question corresponds. Therefore, if the ESR spectrum is determined only by the ground vibronic state, the influence of the vibronic interaction can be evaluated immediately by means of direct multiplication of the matrix elements – the parameters of the spin Hamiltonian – by the respective reduction factor $K_\Gamma(\overline{\Gamma})$. Since the totally symmetric operators are not reduced, $K_\Gamma(A_1) = 1$ (provided second-order vibronic reduction factors may be neglected; see Section 5.6), all the parameters of the spin Hamiltonian H_{A_1} remain unchanged. However, the parameters of H_E, H_{T_2}, and so on (see Eqs. (6.71–6.74)), become multiplied by $K_\Gamma(E)$, $K_\Gamma(T_2)$, etc., respectively. The resulting reduced parameters of EPR spectra in the case under consideration are

$$\begin{aligned} \tilde{g}_1 &= g_1, & A_1' &= \tilde{A}_1 \\ \tilde{g}_2 &= K_\Gamma(E) g_2, & A_2' &= K_\Gamma(E)\tilde{A}_2 \\ \tilde{g}_3 &= K_\Gamma(T_2) g_3, & A_3' &= K_\Gamma(T_2)\tilde{A}_3 \\ \tilde{g}_L &= K_\Gamma(T_1) g_L, \end{aligned} \tag{6.77}$$

Taking into account vibronic parameters, the frequencies of the two EPR transitions between the components of the two Kramers doublets of the

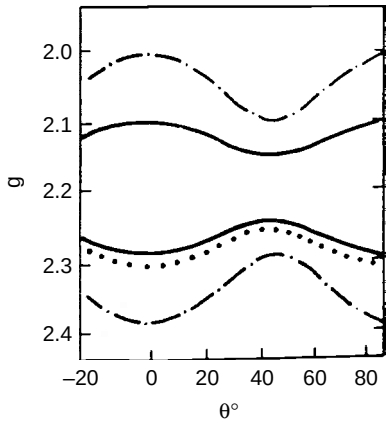

Fig. 6.20. Two limiting cases of angular dependence of the g-factor for the JT linear $E \otimes e$ problem with strong ($q = \frac{1}{2}$, solid line) and no ($q = 1$, dashed line) vibronic coupling. Experimental data [6.178, 6.179] are shown by points.

ground vibronic ^2E level in the $E \otimes e$ problem for a system of cubic symmetry (O_h, O, T_d, T) are

$$\begin{aligned} \hbar\boldsymbol{\Omega}_{\pm} &= (g_1\beta\Re + \tilde{A}_1\nu_I) \pm q(g_2\beta\Re + \tilde{A}_2\nu_I)f \\ f &= [1 - 3(l^2m^2 + l^2n^2 + m^2n^2)]^{\frac{1}{2}} \end{aligned} \tag{6.78}$$

where $q = K_E(E)$, ν_I is the quantum number of the hyperfine interaction (I is the nuclear spin) and l, m, and n are direction cosines of the magnetic field vector $\Re$. In particular, for the angular dependence of the corresponding two g-factors, we have

$$g_{1,2} = g_s - g_2 \pm qg_2 f \tag{6.79}$$

Note that without vibronic interaction, $q = 1$ (Section 5.6), whereas in the limiting case of strong vibronic coupling $q = \frac{1}{2}$. These two limiting cases of angular dependence of the ESR lines are presented in Fig. 6.20 together with experimental data for Cu^{2+}: MgO obtained at temperature $T = 1.2$ K [6.178, 6.974]. It is seen that the experimental measurements clearly confirm the results of vibronic theory with a reduction factor $q \approx \frac{1}{2}$. At present there are quite a number of such clear experimental illustrations of the essential influence of the JTE on the ESR spectra of systems with degenerate E terms (see Section 8.1, reviews [6.172–6.176], and the bibliographic review [6.177]).

The behavior of the threefold orbitally degenerate T term differs from the E-term case in cubic systems by (1) a strong spin–orbital splitting in first-order

perturbation theory (in trigonal systems the E term is also split in the first order), and (2) a larger orbital contribution to the Zeeman energy. As a result, the ground vibronic level ^{2S+1}T of the ^{2S+1}T electronic state is split by the spin–orbital interaction. If allowance is made for Zeeman interaction, the spin Hamiltonian for this ground vibronic level in first-order perturbation theory yields [6.170]

$$H = K_T(T_1)g_L\beta(\Re,\ \vec{L}) + g_s\beta(\Re,\ \vec{S}) + \lambda K_T(T_1)(\vec{L},\ \vec{S}) \tag{6.80}$$

where $K_T(T_1)$ is the vibronic reduction factor which, according to Eq. (5.106), varies from zero in the limiting case of very strong vibronic coupling to unity in the limiting case of very weak coupling (Section 5.6, Fig. 5.26).

Assuming that Zeeman splitting is smaller than reduced spin–orbit and tunneling splitting, one obtains the following expression for the g-factor of the ground state in the crystal-field approximation (the Landé formula with vibronic reduction):

$$g(J) = \{\alpha K_T(T_1)g_L[J(J+1) + 2 - S(S+1)] + g_s[J(J+1) - 2 + S(S+1)]\}/2J(J+1) \tag{6.81}$$

where J is the quantum number of the total angular momentum, which assumes all values between $|S-1|$ and $S+1$ via unity, and α is a known numerical factor.

For example, for the $^5T_2(3d^6)$ term $S=2$, $J=1$, $\alpha=-1$, and $g=\frac{1}{2}[3g_s + K_{T_2}(T_1)g_L]$, while for the $^4T_1(3d^7)$ term $S=\frac{3}{2}$, $J=\frac{1}{2}$, $\alpha=-\frac{3}{2}$, $g=\frac{5}{3}g_s + K_{T_1}(T_1)g_L$. Comparison of these results with experimental data in Section 8.1 shows that, say, for Fe^{2+} : CaO (the $^5T_2(3d^6)$ term) the experimental value is $g=3.30$, and hence the nonvibronic value $g_L=1$ is reduced by $K_{T_2}(T_1)=0.6$ (a part of this reduction may be due to covalency). For another case, Cr : Si with the same term, $g=2.97$ and hence $K_{T_2}(T_1)\approx 0$. This complete reduction of the orbital contribution is due to the presence of strong vibronic coupling (see Eq. (5.106) and Fig. 5.26). Similarly, complete reduction of the orbital contribution takes place in the case of Mn : Si (term $^4T_1(3d^7)$), while for the same term in Fe^+ : MnO, $K_{T_1}(T_1)=0.2$. Other examples are given in Section 8.1.

The angular dependence of the EPR spectrum can be used to reveal the nature of the T-term APES minima. In particular, if the vibronic constants for coupling with E and T_2 displacements are of the same order of magnitude, orthorhombic minima may occur, as shown in Section 3.3. The observed angular spectra for Ni^- : Ge, Pd^- : Si, and Pt^- : Si [6.180] may be attributed to orthorhombic minima.

For strong spin–orbital splitting of the T term, the vibronic effect in the Γ_8 state should be considered (Section 3.3). It occurs commonly from the ${}^2T_2(3d^1)$ term, which is split into Γ_8 and Γ_6. It can be shown that without vibronic interactions, the Γ_8 term is nonmagnetic, i.e., it does not split under the influence of the external magnetic field, its g-factor vanishing due to complete compensation of the orbital and spin contributions of opposite sign [6.170]. When vibronic interactions are taken into account, the orbital contribution to the g-factor becomes reduced, but the spin contribution does not: the Γ_8 term becomes magnetic [6.181]. The resulting g-factor is given by the expression $g = \frac{2}{3}[1 - K_{\Gamma_8}(T_1)]$, and it is seen that $g = 0$ only when the vibronic reduction is neglected, in which case $K_{\Gamma_8}(T_1) = 1$.

A full consideration of the magnetic properties of a ${}^2T_2$ term of d^1 and d^5 configurations in cubic environment taking into account the JT and PJT coupling, spin–orbital interaction, covalence-reduction factors, and low-symmetry crystal fields is given in [6.182]. A giant second-order Zeeman effect was observed in d^1 systems in cubic environment ($[\mathrm{Ti}(\mathrm{H_2O})_6]^{3+}$ in titanium-doped cesium gallium alum), and it was attributed to a strong JTE with close vibronic energy levels that are mixed by the magnetic field [6.183]. Other examples see in Chapters 7 and 8.

For strong vibronic coupling, when the conditions of the tunneling splitting approximation are valid, there is a low-lying excited vibronic level, which influences the ground-state properties (Sections 5.2 and 5.3). In this case, the concept of vibronic reduction of the corresponding orbital contribution to the g-factor is insufficient because the two vibronic levels mix under the magnetic field. For the ${}^2E$ term, Zeeman mixing of the tunneling ground ${}^2E$ and excited ${}^2A$ levels can be determined by perturbation theory. Taking into account that the two spin states with $S_z = \pm\frac{1}{2}$ are independent of the orbital state, the corresponding sixth-order secular equation (3.2) may be reduced to two equations of third order with the matrix W as follows [6.169]:

$$W = \begin{vmatrix} 3\Gamma \pm \frac{1}{2}g_1\beta\Re & \pm\frac{1}{4}rg_2\beta\Re(3n^2-1) & \pm\frac{\sqrt{3}}{4}rg_2\beta\Re(l^2-m^2) \\ \pm\frac{1}{4}rg_2\beta\Re(3n^2-1) & \pm\frac{1}{2}\beta\Re\left(g_1 - \frac{1}{2}qg_2(3n^2-1)\right) & \pm\frac{\sqrt{3}}{4}qg_2\beta\Re(l^2-m^2) \\ \pm\frac{\sqrt{3}}{4}rg_2\beta\Re(l^2-m^2) & \pm\frac{\sqrt{3}}{4}qg_2\beta\Re(l^2-m^2) & \pm\frac{1}{2}\beta\Re\left(g_1 + \frac{1}{2}qg_2(3n^2-1)\right) \end{vmatrix} \tag{6.82}$$

Here 3Γ is the tunneling splitting and r is the second-order vibronic reduction factor, $r = K_E(A_1|E|E)$; for strong vibronic coupling $r = -q\sqrt{2} = -1/\sqrt{2}$ (see Section 5.6).

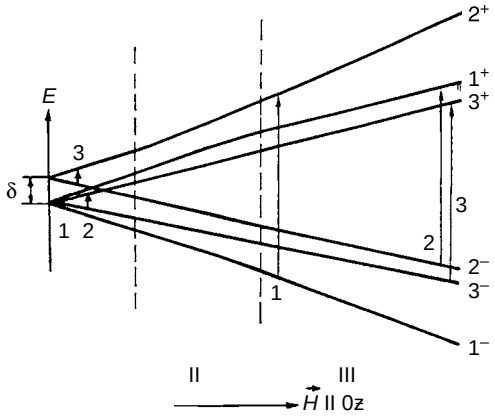

Fig. 6.21. Lowest vibronic energy levels of a system with $E \otimes e$ coupling and tunneling splitting $\delta = 3\Gamma$ in magnetic fields $\vec{H} \parallel Oz$. Magnetic-dipole-allowed transitions in regions I and III are shown by arrows [6.169].

For the magnetic field along the Oz axis (the fourfold axis of the octahedron) $l = 1$, $m = n = 0$, Eq. (6.82) is simplified, and its roots can be derived directly:

$$\begin{aligned}
\varepsilon_1^{\pm} &= \tfrac{1}{2}\{3\Gamma \pm \beta\mathfrak{H}(g_1 - qg_2) + [(3\Gamma \pm \tfrac{1}{2}qg_2\beta\mathfrak{H})^2 + r^2 g_2^2 \beta^2 \mathfrak{H}^2]^{\frac{1}{2}}\} \\
\varepsilon_2^{\pm} &= \tfrac{1}{2}\{3\Gamma \pm \beta\mathfrak{H}(g_1 - qg_2) - [(3\Gamma \pm \tfrac{1}{2}qg_2\beta\mathfrak{H})^2 + r^2 g_2^2 \beta^2 \mathfrak{H}^2]^{\frac{1}{2}}\} \\
\varepsilon_3^{\pm} &= \tfrac{1}{2}\beta\mathfrak{H}(g_1 + qg_2)
\end{aligned} \tag{6.83}$$

The behavior of these levels with respect to the magnetic-field intensity is shown in Fig. 6.21; the arrows indicate the allowed ESR transitions as determined by the wavefunctions of the states (6.83), solutions of Eq. (6.82). In order to analyze the expected ESR spectrum, it is convenient to distinguish three ranges, depending on the relation between the magnitude of the tunneling splitting 3Γ and the anisotropic part of the Zeeman interaction $g_2\beta\mathfrak{H}$: the low-frequency range I where $g_2\beta\mathfrak{H} \ll 3\Gamma$, the intermediate range II, and the high-frequency range III, where $g_2\beta\mathfrak{H} \gg 3\Gamma$. In range I where mixing of the ground vibronic state with the excited one is relatively weak, the ESR spectrum consists of three lines, two of which have the g-factor (6.79) of the isolated ground orbital doublet. The third line arises from the excited non-degenerate state and is isotropic with $g = g_1$. The intensity of this line is proportional to the population of the excited level, which is zero at $T = 0\,\mathrm{K}$ and increases with temperature.

In the high-frequency range III another three transitions are allowed, with g-factors which, in the limiting case of strong vibronic coupling when $q = \frac{1}{2}$ and

$3\Gamma \approx 0$, are $g_{\|} = g_1 + g_2$ and $g_{\perp} = g_1 - \frac{1}{2}g_2$ if the excited tunneling level is A_2, and $g_{\|} = g_1 - g_2$ and $g_{\perp} = g_1 + \frac{1}{2}g_2$ if this level is A_1. Similar relationships for the constants of the hyperfine structure are $\tilde{A}_{\|} = \tilde{A}_1 + \tilde{A}_2$ and $\tilde{A}_{\perp} = \tilde{A}_1 - \frac{1}{2}\tilde{A}_2$ if A_2 is the nearest excited level, and $\tilde{A}_{\|} = \tilde{A}_1 - \tilde{A}_2$ and $\tilde{A}_{\perp} = \tilde{A}_1 + \frac{1}{2}\tilde{A}_2$ if A_1 is the nearest level. In the intermediate range II the two spectra coexist, the low-frequency spectrum fading slowly and the high-frequency spectrum growing uniformly on moving from range I to range III.

The spectrum in range III is seen to be that of the statically distorted system frozen at the APES minimum, whereas the spectrum in range I corresponds to its free or hindered rotations (Sections 5.1–5.3). Therefore, the transition from the spectrum in range III to the spectrum in range I is often called the *transition from the static to the dynamic JTE*. Taking into account the relativity rule concerning the means of observation (Section 7.1.1), the static JTE in the EPR spectra of real systems (for which $3\Gamma \neq 0$) can be observed if the lifetime τ of the distorted configuration in the pulsating (fluctuating) motion (Section 5.2) is larger than the characteristic time of measurement interaction τ'. In the case under consideration τ' is determined by the anisotropic part of the Zeeman interaction $g_2\beta\Re$. For typical situations this means that the tunneling (pulsation) frequency is slower than $10^9\,s^{-1}$. In the above case of $\Re \parallel Oz$ the *strong external field in range III depresses the pulsations, locking the system in the minimum along the Oz* axis.

When the direction of the magnetic field $\Re$ does not coincide with Oz (with the tetragonal axes of an octahedron), the energy levels (6.83) approach each other, and the differences between the g-factors of different lines decrease. Along the trigonal axes of a cubic system all the g-factors become identically equal to g_1.

6.3.2 Random strain and relaxation in EPR

The vibronic EPR spectrum described above relates to "ideal" systems with electron degeneracy or pseudodegeneracy, when each molecule may be regarded as isolated, unaffected by the environment. In real systems, as mentioned above, there are two main effects which influence the spectra in question: random strain and relaxations. The latter are inherent in any system with energy dissipation, whereas random strain has special importance for JT systems. This is due to the fact that, since either Zeeman or tunneling splitting is relatively small, even small external perturbations split the degenerate ground vibronic state, and this splitting may suffice to cause changes in the expected EPR spectra.

If the low-symmetry perturbation is "regular," i.e., it is the same for all paramagnetic centers, it does not affect very strongly the resulting spectrum because the system, in principle, remains "ideal." Such is the case of a polyatomic molecule or a crystal, in which the paramagnetic center is weakly affected by the second coordination sphere that has lower symmetry than the first coordination sphere. However, there are cases when these low-symmetry perturbations are of random magnitude and direction. For instance, if in the above example the molecules or paramagnetic centers in crystals are arbitrarily oriented with respect to the magnetic field, the changes in the ESR spectrum (compared with that for the unperturbed system) will be as if the perturbation distortions are random.

Paramagnetic centers in crystals, for which the most precise ESR measurements are performed, are of special interest. Here random distortions occur due to imperfections of the host crystal lattice, i.e., due to small local distortions of the regular symmetry caused by dislocations, mosaic structure, impurities, locally uncompensated charges, and other defects.

Qualitatively, the role of random strain is obvious. For example, in the $E \otimes e$ problem with three equivalent APES minima, external distortions, if strong enough, make these minima nonequivalent. As a result the pulsating motion and tunneling cease, and the system is locked in one (the deepest) minimum (similar to the above case when the system is locked in the minimum by the magnetic field). The random nature of the direction of distortion determines only at which of the three equivalent minima the system is locked. Comparing this result with the above transition from the dynamic to the static JTE, we conclude that random deformations promote a transition to the static JTE.

Quantitatively, the influence of random strain is determined by the magnitude of the vibronic energy-level splitting Δ produced by this strain. In general, the expected EPR spectrum depends on the relationship among the mean value of the strain effect $\bar{\Delta}$, the tunneling splitting $r\Gamma$, and the anisotropic part of the Zeeman interaction $g_2\beta\Re$. Note that the stronger the vibronic coupling, the larger the effect of the strain influence. Indeed, the external distorting influence displaces the nuclear coordinates and the latter influence the electronic states through vibronic coupling, resulting in a corresponding energy-level splitting. Therefore the random strain is most important in cases of strong vibronic coupling.

The effect of random strain on the vibronic EPR spectra is best studied for the $E \otimes e$ problem. Consider first the isolated ground vibronic doublet ^2E when the first excited vibronic singlet ^2A is well removed, $3\Gamma \gg g_2\beta\Re$ [6.171]. In order to describe the low-symmetry strain perturbation $\tilde{W}$, we introduce the strain tensor and the electron–strain interaction constants in the form of

respective components $e_{\Gamma\gamma}$ and P_Γ, which transform according to the corresponding irreducible representation, $\tilde{W} \sim \sum_{\Gamma\gamma} C_{\Gamma\gamma} e_{\Gamma\gamma} P_\Gamma$ (cf. Section 6.1). Only one constant P_E and two components $e_{E\vartheta} = e_\vartheta$ and $e_{E\varepsilon} = e_\varepsilon$ are essential to the E-term splitting. Instead of these two components, their modulus e and orientation ϕ given by

$$e = (e_\vartheta^2 + e_\varepsilon^2)^{\frac{1}{2}}, \qquad \tan\phi = e_\vartheta / e_\varepsilon \tag{6.84}$$

are more convenient for practical use. Under this strain the E level splits in two:

$$\begin{aligned} E_1 &= qeP_E, & \psi_1 &= (1/\sqrt{2})[(1-\cos\phi)^{\frac{1}{2}}|\vartheta\rangle + (1+\cos\phi)^{\frac{1}{2}}|\varepsilon\rangle \\ E_2 &= -qeP_E, & \psi_1 &= (1/\sqrt{2})[-(1+\cos\phi)^{\frac{1}{2}}|\vartheta\rangle + (1-\cos\phi)^{\frac{1}{2}}|\varepsilon\rangle \end{aligned} \tag{6.85}$$

It follows that the orientation ϕ of the strain (in the $(Q_\vartheta, Q_\varepsilon)$ plane) does not affect the splitting, but considerably influences the wavefunctions.

The energy levels (6.85) are Kramers spin doublets. If the strain splitting $\Delta = 2qeP_E$ is large compared with the Zeeman interaction, but still small compared with the tunneling splitting, $3\Gamma \gg g_2\beta\mathfrak{H}$, the splitting of each of the levels (6.85) in the magnetic field may be treated independently by means of perturbation theory. Then (Fig. 6.22)

$$E_1^{\pm} = qeP_E \pm \tfrac{1}{2}[g_1 + qg_2\cos(\phi-\alpha)f]\beta\mathfrak{H} \tag{6.86}$$

$$E_2^{\pm} = -qeP_E \pm \tfrac{1}{2}[g_1 - qg_2\cos(\phi-\alpha)f]\beta\mathfrak{H} \tag{6.87}$$

where the angular direction α of the magnetic field satisfies the equation

$$\tan\alpha = \sqrt{3}(l^2 - m^2)/(2n^2 - l^2 - m^2) \tag{6.88}$$

The two pairs of levels (6.86) and (6.87) give rise to two allowed EPR transitions with the following frequencies (the expressions in brackets equal the g-factors):

$$\hbar\boldsymbol{\Omega}_{1,2} = [g_1 \pm qg_2\cos(\phi-\alpha)f]\beta\mathfrak{H} \tag{6.89}$$

Thus, with the strong influence of strain in question, the frequencies of the EPR transitions at a given paramagnetic center depend on the angle $\phi - \alpha$ of the orientation of the strain with respect to the direction of the magnetic field. In particular, for $\phi - \alpha = \pm\pi/2$ the EPR spectrum is isotropic with $g = g_1$, and for $\phi - \alpha = 0$ or π the spectrum is the same as in the absence of strain.

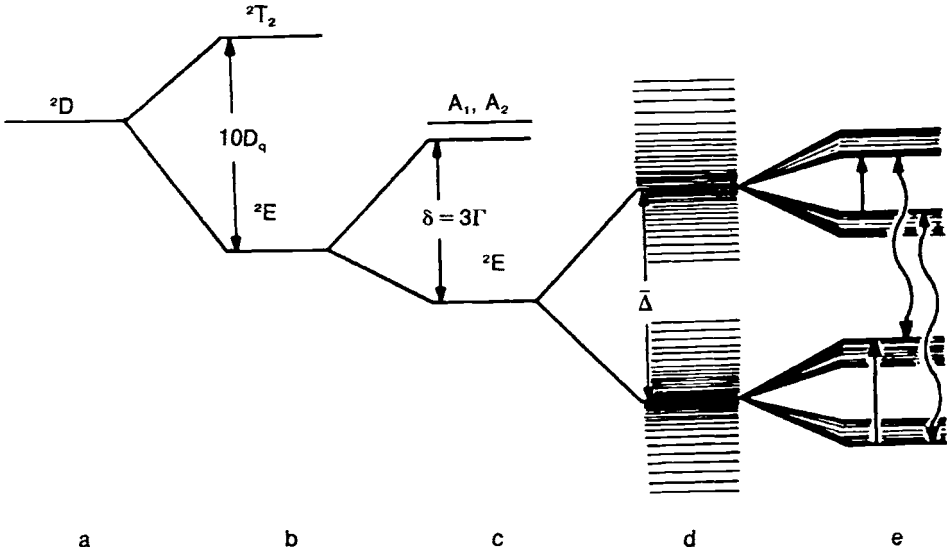

Fig. 6.22. The lowest-energy-level scheme for an octahedral system in the ^2E state: (a) free-ion term; (b) crystal-field splitting; (c) tunneling splitting; (d) splitting of the ground vibronic ^2E level into two Kramers doublets by random strain; and (e) Zeeman splitting by the magnetic field. Allowed transitions in the radio-frequency region are shown by straight arrows, whereas relaxation transitions without spin reversal are demonstrated by wavy arrows. (Reprinted with permission from [6.189]. Copyright 1975 American Physical Society.)

With intermediate values of $\phi - \alpha$ (between 0 and $\pi/2$) the anisotropic part of the g-factor varies from 0 to $\pm qg_2 f$. It can be shown that the transition probabilities (intensities) at frequencies given by Eq. (6.89) are independent of the strain and magnetic-field directions.

Therefore in the presence of strain with random orientations with respect to the direction of the magnetic field $\Re$ (originating both from random orientations of the strain with regard to different paramagnetic centers, and from constant orientation of the strain with regard to the centers but random orientation of the centers with respect to the magnetic field), the EPR frequencies (or the corresponding resonance values of $\Re$) vary from one center to another within $\pm qg_2 f$, which is equivalent to inhomogeneous broadening of the EPR lines. Assuming that the EPR line of each paramagnetic center has a δ character ($\delta(x) = 0$ if $x \neq 0$, and $\delta(x) = \infty$ if $x = 0$) and averaging over the random strain orientations ϕ, one can derive the absorption coefficient K as a function of the resonance magnetic-field intensity in the form [6.1, 6.171]

$$K(\Re) = (\pi^2 Z)^{-\frac{1}{2}} \Theta(Z), \qquad Z = (qg_2 f \beta \Re)^2 - (\hbar \mathbf{\Omega} - g_1 \beta \Re)^2 \tag{6.90}$$

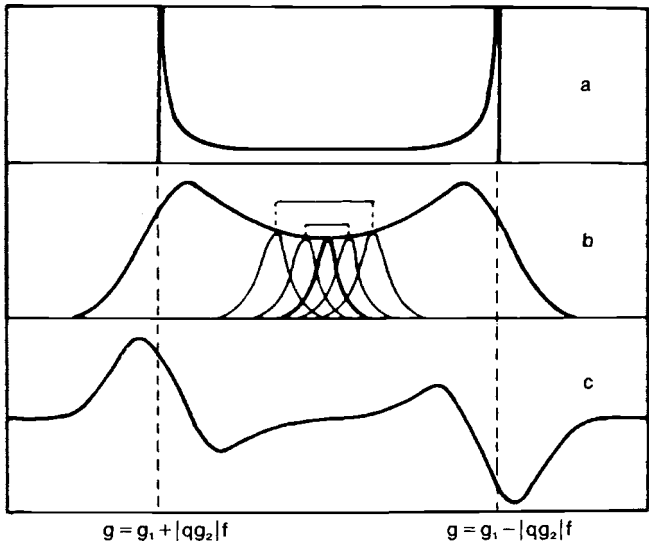

Fig. 6.23. The ESR line shape for a ground state ^2E under averaged random strain assuming that the individual transitions are δ-functions (a), or that they are Gaussian bands with a half-width equal to $0.2\mathbf{\Omega}$ (b). The first derivative of the latter is shown in (c).

where $\mathbf{\Omega}$ is the radio frequency and $\Theta(Z)$ is a step function: $\Theta(Z) = 1$ if $Z > 0$, and $\Theta(Z) = 0$ if $Z < 0$.

The line shape determined by Eq. (6.90) is illustrated in Fig. 6.23(a). Its unusual, abrupt form is due to the assumed δ character of the absorption at each center. If a Gaussian form for this absorption (with a certain half-width) is assumed instead of the δ one, the line shape becomes more natural (Fig. 6.23(b)). Another feature of the line shape (6.90) is its independence of temperature, in spite of the Boltzmann temperature population of the strain-split levels assumed when deriving Eq. (6.90). This is a consequence of averaging over random orientations of the strain.

With hyperfine splitting, each of the lines (7.89) contains $2I + 1$ components that have the following frequencies:

$$\hbar\mathbf{\Omega}_{1,2}(\nu_1) = (g_1\beta\Re + \tilde{A}_1\nu_1) \pm \tfrac{1}{2}q(g_2\beta\Re + \tilde{A}_2\nu_1)\cos(\phi - \alpha)f \tag{6.91}$$

(ν_1 is the corresponding quantum number, introduced above.)

The coefficient of absorption (line shape) is

$$K(\Re) = (\pi^2 Z)^{-\frac{1}{2}}\Theta(Z), \qquad Z = (qg_2 f\beta\Re + \tilde{A}_1 v_1)^2 f^2 - (\hbar\mathbf{\Omega} - g_1\beta\Re - \tilde{A}_2 v_1{}^2) \tag{6.92}$$

The above picture of the ESR spectrum cannot be regarded as complete, since the influence of the dissipative subsystem (lattice vibrations, collisions, etc.) has been disregarded. Under the influence of the dissipative subsystems (thermostat) there are continuous transitions between the energy levels split by the strain. These transitions lower the lifetime of the corresponding states and broaden their energy levels (Fig. 6.22). The usual ESR relaxation transitions take place between the energy levels of Kramers doublets (split in the magnetic field) that lead to spin reversal; they are affected by the thermostat indirectly through rather small spin–orbit interaction, being thus much less probable than direct non-spin transitions.

Denote by W the probability of relaxation transition without spin reversal. The general theory of relaxation [6.184] yields, instead of Eq. (6.90), the following expression for the line shape [6.185]:

$$K(\Re) \sim \frac{2W\gamma^2}{(E^2 - \gamma^2 + 4E^2W)} \tag{6.93}$$

where $E(\Re) = \hbar\mathbf{\Omega} - g_1\beta\Re$ and

$$\gamma(\Re) = qg_2\beta\Re\cos(\phi - \alpha)f \tag{6.94}$$

The relaxation probability depends strongly on temperature. For low temperatures $W \ll \gamma$, and Eq. (6.93) describes two Lorentzian lines (with centers at frequencies given by Eq. (6.89)):

$$K(\Re) \sim \frac{W}{(E-\gamma)^2 + W} + \frac{W}{(E+\gamma)^2 + W} \tag{6.95}$$

For high temperatures $W \gg \gamma$, and Eq. (6.93) describes one Lorentzian line centered at frequency $\hbar\mathbf{\Omega} = g_1\beta\Re$:

$$K(\Re) \sim \frac{W_{\text{eff}}^2}{E^2 + W_{\text{eff}}^2}, \qquad W_{\text{eff}} = \gamma^2/W \tag{6.96}$$

As a result the vibronic EPR spectrum, which at low temperatures has a well-resolved doublet structure, narrows and transforms into one isotropic line when the temperature increases. Visually, this result is due to the fact that at low temperatures relaxation transitions seldom occur, and the lifetime of the energy-level states is larger than the characteristic time of the act of measurement, so that the latter finds the system in one of the two Kramers doublets given by Eq. (6.86). In this case two lines are seen in the EPR spectrum at the same frequencies $\mathbf{\Omega}_1$ and $\mathbf{\Omega}_2$, as in the absence of relaxation. At high temperatures the relaxation is so fast that during the measurement the system performs

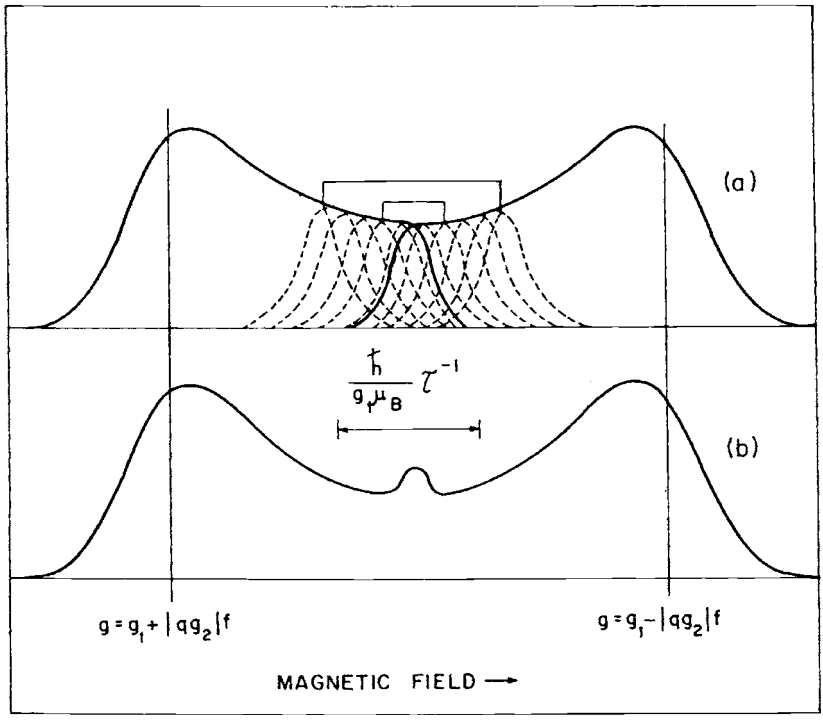

Fig. 6.24. The influence of relaxation without spin reversal on the ESR line shape (temperature narrowing): (a) at low temperatures the number of pairs with narrowing relaxation is small; and (b) at higher temperatures the narrowing produces an isotropic line in the center of the band at the expense of the intensity of the wings.

multiple transitions from one state to another, resulting in an averaged isotropic line at the mean frequency $\mathbf{\Omega}_1 + \mathbf{\Omega}_2/2$. Such a temperature narrowing of the EPR band is, in principle, similar to the well-known exchange narrowing in concentrated magnetic systems, and to motional narrowing in liquids [6.184]. Similar temperature effects are observed in the hyperfine structure of Mössbauer spectra (see below).

The anisotropic part of the Zeeman interaction $\gamma(\Re) = qg_2\beta\Re\cos(\phi - \alpha)f$ in (6.94) and hence the line $K(\Re)$ depend on the angle ϕ of strain orientation. If the latter has a random character, averaging should be performed. At low temperatures, for most orientations ϕ the inequality $W \ll \gamma$ is valid, and the vibronic EPR spectrum has the form illustrated in Fig. 6.24(a). Compared with the above spectrum without relaxation (Fig. 6.23(b)), the edges here are smoother due to relaxation broadening. A small absorption in the central range at $\hbar\mathbf{\Omega} = g_1\beta\Re$ is due to the presence of paramagnetic centers, for which $\phi - \alpha \approx \pm\pi/2$ and the inequality $W \ll \gamma$ is invalid. This absorption is

in contrast to the edges of the band, for which the angular dependence of the absorption follows the function f in Eq. (6.88).

With increasing temperature, the number of centers for which $W \gg \gamma$ increases, and the corresponding pairs of lines converge into one averaged isotropic line at $\hbar\mathbf{\Omega} = g_1\beta\Re$ (Fig. 6.24(b)). This leads to an enlarged isotropic band in the center of the spectrum at the expense of the intensity of the anisoptropic wings. The temperature dependence of this spectrum, as seen from Eqs. (6.82)–(6.84), is determined by the temperature dependence of the relaxation probabilities W, their calculation being a complicated task based on the solutions of the multimode JT problem [6.185–6.187].

The above vibronic EPR spectrum becomes more complicated when the vibronic singlet (Kramers doublet) ^2A ($^2A_1$ or $^2A_2$) approaches the ground state ^2E and the tunneling splitting 3Γ in the $E \otimes e$ problem becomes comparable to Zeeman or strain splitting [6.188–6.190]. Consider first the case when 3Γ is still large, approaching the $\bar{\Delta}$ value, and $\bar{\Delta} \gg g_2\beta\Re$. In this case, the mixing of the vibronic levels A_1 and E under the magnetic field can be neglected, while their mixing by the strain $e_\vartheta P_E$ may be taken into account by means of perturbation theory. In the zeroth approximation the spectrum is as that obtained above in the absence of the A level; at low temperatures it has the form given in Fig. 6.25 for small $\bar{\Delta}/3\Gamma$ values. Assume that the magnetic field lies in the plane (110), i.e., $l = m$. Then $\alpha = 0$ (see Eq. (6.88)) and for the perturbation of the two peaks for which $\phi - \alpha = 0$ or π we have $\phi = 0$ or π. On substituting these values into Eq. (6.84) we obtain $e_\varepsilon = 0$, i.e., the peaks of the spectrum are due to the e_ϑ component of the strain tensor. The resulting g-factors corresponding to the two peaks of the spectrum perturbed by the approaching A_1 level are [6.191]

$$\begin{aligned} g_\vartheta &= g_1 - \tfrac{1}{2}[q + (2r^2 e_\vartheta P_E/3\Gamma)]g_2(3n^2 - 1) \\ g_\varepsilon &= g_1 + \tfrac{1}{2}qg_2(3n^2 - 1) \end{aligned} \tag{6.97}$$

It follows that only one of the two peaks of the spectrum is shifted; which of them and in what direction depends on the signs of e_ϑ, g_2, and $3n^2 - 1$. For example, if $e_\vartheta > 0$, $g_2 > 0$, and $3n^2 - 1 > 0$, the right-hand-side peak corresponding to larger resonance fields $\Re$ is shifted to the right. If instead of the vibronic A_1 level the A_2 level approaches the ground E state, the sign of the effect changes, and the left-hand-side peak is shifted to the left. All these possible cases are summarized in Table 6.1. Also, with the dispersion of the absolute values of the strain, the perturbed peak is not only shifted, but in addition becomes somewhat flattened (i.e., wider and lower in its intensity).

Table 6.1. *The shift of one of the two peaks (right and left) in the vibronic ESR spectrum of the* ^2E *level under the influence of the mixing with the* ^2A *level (*$\Re \parallel [110]$, $l = m$, $3n^2 > 1$, *and* $\Re$ *increases from left to right; for* $3n^2 < 1$ *all the results change to the opposite)*

Sign of g_2	Nearest excited orbital singlet A	Shifted peak	Direction of shift
Ground Kramers doublet ^2E			
+	A_1	Right	Right
+	A_2	Left	Left
−	A_1	Left	Left
−	A_2	Right	Right
Excited Kramers doublet ^2E			
+	A_1	Right	Left
+	A_2	Left	Right
−	A_1	Left	Right
−	A_2	Right	Left

When tunneling splitting becomes comparable to strain splitting $\bar{\Delta} \approx 3\Gamma$, perturbation theory becomes invalid, and the problem must be solved by numerical solution of the sixth-order secular equation, in which splitting of the three vibronic doublets by the magnetic field and their mixing by random strain are taken into account simultaneously. The results obtained [6.188–6.190] are illustrated in Figs. 6.25–6.29.

The dependence of the spectrum on the ration $\bar{\Delta}/3\Gamma$ is illustrated in Fig. 6.25 for low temperatures, when only the lowest Kramers doublet is populated. It is seen that a small broadening begins even at $\bar{\Delta}/3\Gamma = 0.01$ and rapidly increases, simultaneously shifting to the left when the $\bar{\Delta}/3\Gamma$ value increases. At $\bar{\Delta}/3\Gamma = 1$ the rate of shifting decreases, and at $\bar{\Delta}/3\Gamma = 5$ the extreme value of the static JTE corresponding to $\beta\Re = \hbar\boldsymbol{\Omega}/(g_1 + 2qg_2)$ is attained. As the temperature increases, first the next Kramers doublet becomes populated (Fig. 6.26), and then the third one, resulting in a complicated spectrum (Fig. 6.27).

In Fig. 6.28 the angular dependence of the spectrum is presented with respect to the magnetic field $\Re$ lying in the plane $(1\bar{1}0)$ (containing the main directions of $\Re$ parallel to [001], [110], and [111]) at low temperatures, when only the lowest Kramers doublet is populated. At $\bar{\Delta}/3\Gamma = 0.01$ the angular dependence is symmetric with respect to $\Re$ parallel to the [111] direction of the magnetic field for which, according to Eq. (6.89) with $\cos(\phi - \alpha) = 1$, the two

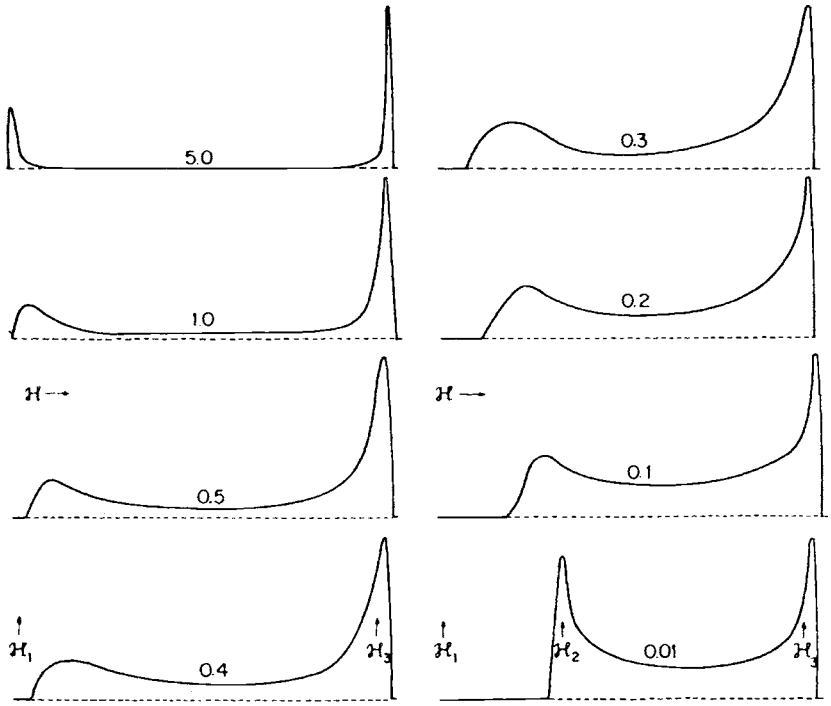

Fig. 6.25. ESR line shapes calculated for a system with an $E \otimes e$ problem at low temperatures and magnetic field $\Re \parallel [001]$ with different values of $\bar{\Delta}/3\Gamma$ indicated on the curves. The lowest nondegenerate vibronic level is assumed to be A_2 with $g_1 = 2.0$, $qg_2 = 0.05$, $q = \frac{1}{2}$, $r = -\sqrt{2q}$, $\nu_E = \boldsymbol{\Omega}/2\pi = 9\,\mathrm{GHz}$, $\beta\Re_1 = \hbar\boldsymbol{\Omega}/(g_1 + 2qg_2)$, $\beta\Re_2 = \hbar\boldsymbol{\Omega}/(g_1 + qg_2)$, and $\beta\Re_3 = \hbar\boldsymbol{\Omega}/(g_1 - qg_2)$. (Reprinted with permission from [6.189]. Copyright 1975 American Physical Society.)

peaks coincide. When $\bar{\Delta}/3\Gamma$ increases, the anisotropy of the perturbed peak increases (Table 6.1), and at $\bar{\Delta}/3\Gamma \geq 5$ the angular dependence corresponds to that of an axially symmetric spectrum of the type [001], [010], and [100] of the static JTE.

The ratio $\bar{\Delta}/3\Gamma$ can be derived from the ESR spectrum using the data of Fig. 6.28. For this purpose the angular dependence of the unperturbed peak of the observed spectrum must first be matched with the single curve in Fig. 6.28 and the values of g_1 and qg_2 (as well as the hyperfine constants $\tilde{A}_1$ and $\tilde{A}_2$) should be estimated. Then, by matching the angular dependence of the perturbed peak with one of the curves in the figure, we get the $\bar{\Delta}/3\Gamma$ value indicated on the left- and right-hand sides of this curve. Similar considerations can be applied to the case of angular dependence of the spectrum when rotating the magnetic field in the plane (001) (Fig. 6.29).

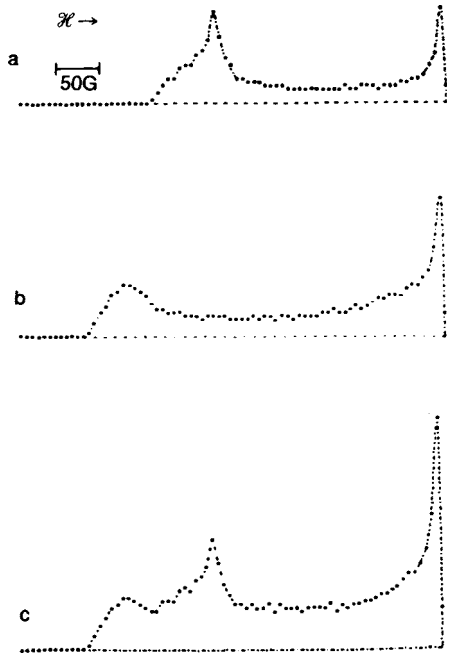

Fig. 6.26. The change in the ESR spectrum due to population of the first excited Kramers doublet in the $E \otimes e$ problem with random strain: line shapes of the excited (a) and ground (b) doublets and the summarized line (c) at $T = 1.5$ K, $\bar{\Delta}/3\Gamma = 0.13, \Gamma = 1.0, qg_2 = 0.1$, and other data as in Fig. 6.25. (Reprinted with permission from [6.189]. Copyright 1975 American Physical Society.)

The two cases of $\Re$ rotating in the planes (110) and (001) cover the main resonances of the spectrum but, in principle, there may be more complicated spectra in other directions considered in [6.189]. In the low-temperature spectra of systems with the ^2E terms under the magnetic field $\Re$ in the (100) plane at an angle of 30° to the [001] axis, besides the usual dynamic and static JTE spectra at $\bar{\Delta}/3\Gamma = 0.0033$ and at $\bar{\Delta}/3\Gamma = 5$, respectively, there is a rather complicated spectrum at intermediate values of $\bar{\Delta}/3\Gamma$. Also complicated is the spectrum with $\Re$ parallel to [111] and intermediate JT effects; in the limit cases of dynamic and static JTE it converts into a single line with g-factors

$$\begin{aligned} g_{\text{dyn}} &= [g_1^2 + \tfrac{1}{2}(qg_2)^2]^{\frac{1}{2}} \\ g_{\text{stat}} &= [g_1^2 + 2(qg_2)^2]^{\frac{1}{2}} \end{aligned} \tag{6.98}$$

respectively.

Comparison of the spectra described above with experimental spectra allows one to determine the vibronic parameters of the system. Such a

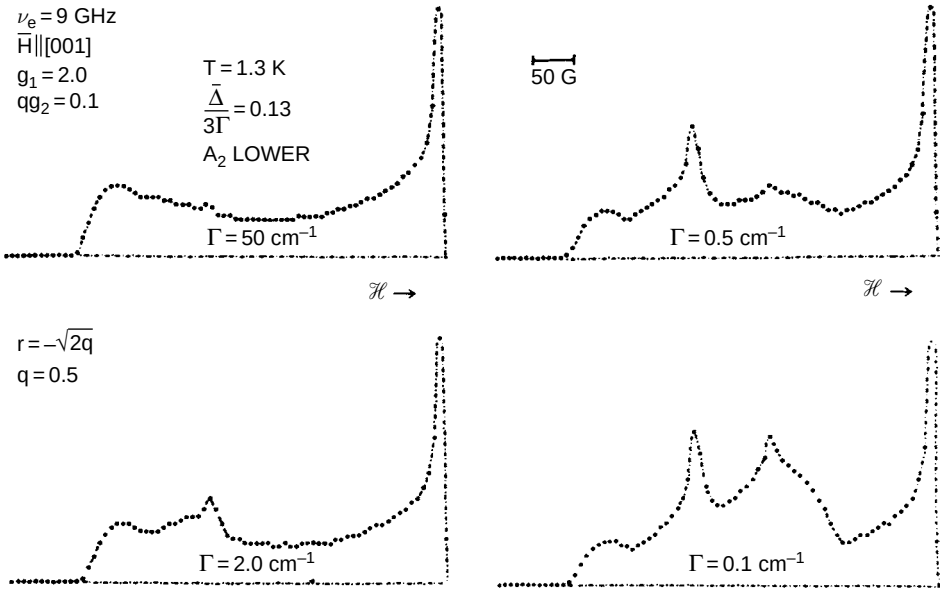

Fig. 6.27. The ESR line shape with the contribution of all three Kramers doublets at $T = 1.3$ K and different values of the tunneling splitting 3Γ; other data are as in Fig. 6.26. (Reprinted with permission from [6.189]. Copyright 1975 American Physical Society.)

comparison is illustrated in Fig. 6.30 for the Cu^{2+} ion in the CaO lattice [6.188]. Since in the above expressions the orders of magnitude are estimated with respect to the radio-frequency quantum $\hbar\boldsymbol{\Omega} = g_1\beta\Re$ of the EPR measuring instrument, by changing this $\hbar\boldsymbol{\Omega}$ value we can obtain different spectra for the same specimen (cf. the relativity rule concerning means of observation, Section 7.1). Therefore, as mentioned earlier, at small $\hbar\boldsymbol{\Omega}$ the case $|g_2\beta\Re| \ll \bar{\Delta}$ is realized, for which the value of $\bar{\Delta}/3\Gamma$ can be derived from comparison of experimental and theoretical spectra. At sufficiently large values of $\hbar\boldsymbol{\Omega}$ the ratio $g_2\beta\Re/3\Gamma$ can be determined in much the same way. The values of $\bar{\Delta}$ and 3Γ can be estimated by combining the data obtained via these two methods of measurements (by means of low and high frequencies). Some of these data are listed in Tables 8.2–8.7 of Section 8.1.

With increasing temperature the vibronic EPR spectrum changes for two reasons: relaxation broadening and population of higher Kramers doublets. Relaxation transitions in the static JTE, similar to the dynamic JTE discussed above, result in the occurrence of a single isotropic line at the average frequency

$$\overline{(\hbar\boldsymbol{\Omega})} = (\tfrac{1}{3}g_l + \tfrac{2}{3}g_t)\beta\Re + (\tfrac{1}{3}\tilde{A}_l + \tfrac{2}{3}\tilde{A}_t)\nu_1 = g_1\beta\Re + \tilde{A}_1\nu_1 \qquad (6.99)$$

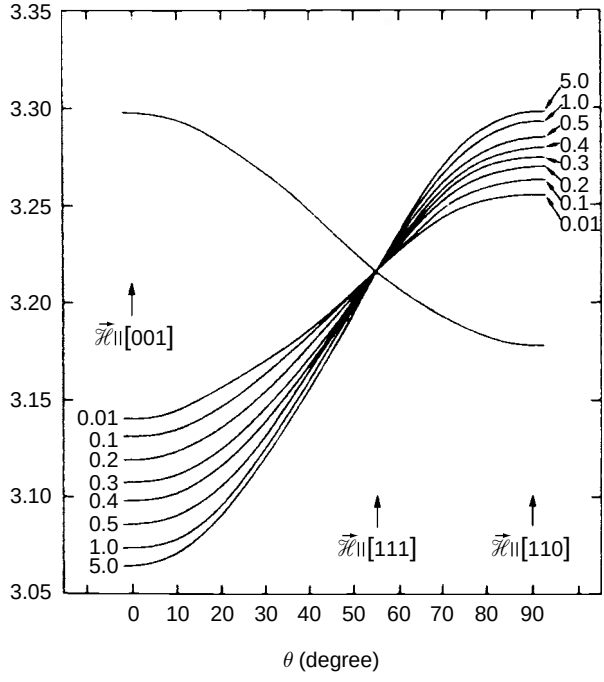

Fig. 6.28. The angular dependence of the low-temperature ESR spectrum of a system with a JT $E \otimes e$ problem shown by rotating the magnetic field $\Re$ in the plane $(1\bar{1}0)$. The absolute values of $\Re$ in kG are plotted on the ordinate. The lowest nondegenerate vibronic level is A_2. In the case of A_1 the picture should be reflected about the axis $g - g_1 = 0$. The $\bar{\Delta}/3\Gamma$ values are shown on the left- and right-hand sides of the curves. (Reprinted with permission from [6.189]. Copyright 1975 American Physical Society.)

On the other hand, the same isotropic line may occur as a result of the population of the Kramers doublet originating from the nearest vibronic singlet (A_1 or A_2). Therefore, it is often impossible to distinguish between these two reasons for the origin of the averaged spectrum.

There may be a third reason for the temperature dependence of the EPR spectrum, and that is the strong temperature dependence of the tunneling splitting itself caused by the temperature dependence of the barrier height between the minima of the APES which, in turn, is due to the temperature dependence of the population numbers for the vibrational modes in the multimode problem (Section 5.5). Visually, with an increase in temperature the frequency of pulsations increases due to the decrease of the "viscosity" of the environment [6.169]. More rigorously, the temperature dependence of the tunneling splitting 3Γ emerges from the solution of the multimode problem when taking into account anharmonicity. Some discussion of this problem is given in Section 5.5.

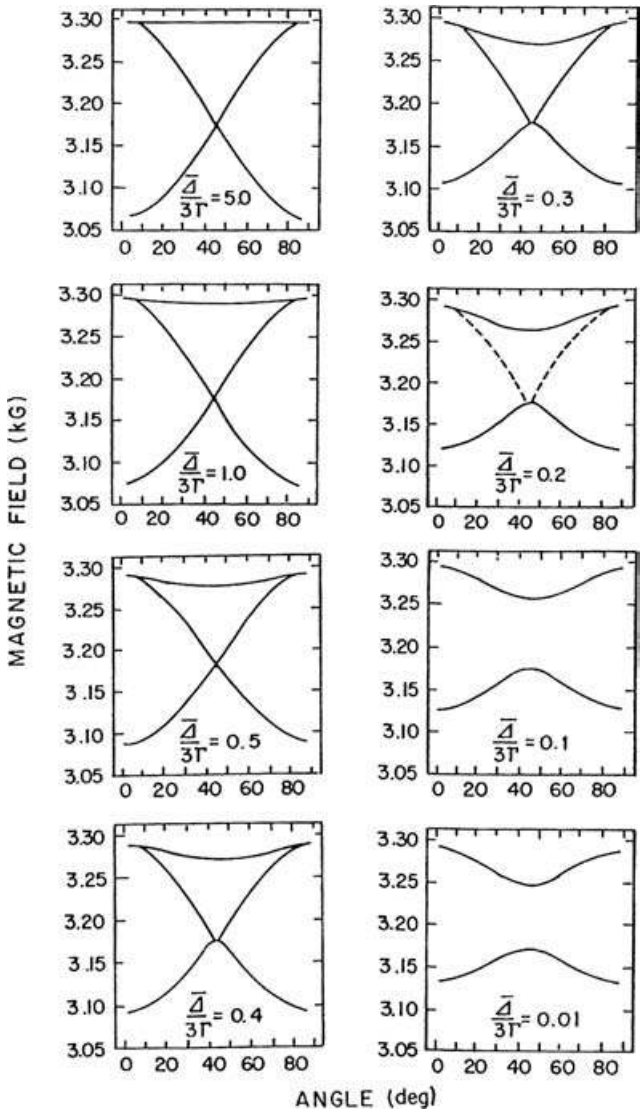

Fig. 6.29. The angular dependence of the low-temperature ESR spectrum of a system with a JT $E \otimes e$ problem shown by rotating the magnetic field $\Re$ in the plane (001) for different values of $\bar{\Delta}/3\Gamma$ (other data are as in Figs. 6.25–6.28). Angles 0, 45°, and 90° correspond to the magnetic field along [100], [110], and [010], respectively. At values $\bar{\Delta}/3\Gamma \gtrsim 0.2$ a third line appears in the spectrum, while at $\bar{\Delta}/3\Gamma \sim 5.0$ one of the lines becomes isotropic. (Reprinted with permission from [6.189]. Copyright 1975 American Physical Society.)

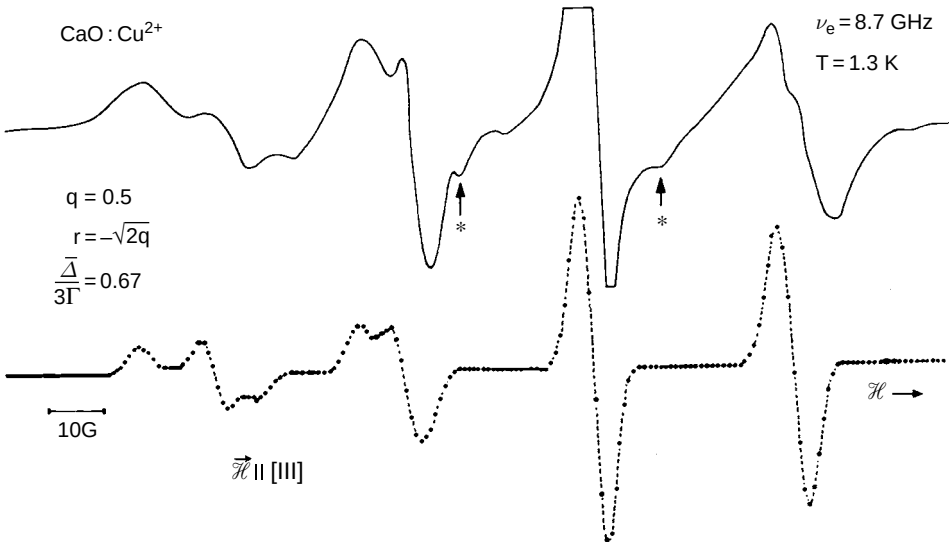

Fig. 6.30. Experimental (upper) and calculated (lower) ESR spectra of Cu^{2+}: CaO with a JT $E \otimes e$ problem at $T = 1.3\,K$ and $\nu_E = \boldsymbol{\Omega}/2\pi = 8.7\,GHz$. Vibronic parameters obtained by comparing experimental and theoretical angular dependences in the plane (110) using Fig. 6.28 are given on the left. Arrows indicate forbidden transitions induced by quadrupole interactions [6.188].

Taking into account the temperature dependence of the tunneling splitting 3Γ, both the static JTE at low temperatures when 3Γ is small (but $\bar{\Delta}/3\Gamma$ and $g_2\beta\Re/3\Gamma$ are large) and the dynamic JTE at higher temperatures can be obtained for the same values of $\bar{\Delta}$ and $g_2\beta\Re$. All the above temperature effects may be present in combined form in experimentally observed temperature transitions from one EPR spectrum to another, as illustrated in Table 8.1 of Section 8.1.

A low-symmetry environment, cooperative phenomena, and structural phase transitions (Section 8.2), which stabilize the low-symmetry configurations of the JT system, influence the expected EPR spectra [6.192–6.196].

Let us summarize briefly the above results obtained for the vibronic EPR spectra in JT systems with the $E \otimes e$ problem and cubic symmetry. The dynamic JTE spectrum is observed at low temperatures with $g_2\beta\Re/3\Gamma < 0.1$ and $\bar{\Delta}/3\Gamma < 0.1$. When $g_2\beta\Re/3\Gamma \geq 5$ or $\bar{\Delta}/3\Gamma \geq 5$ the spectrum becomes that of the static JTE. In the intermediate range, when $0.1 < g_2\beta\Re/3\Gamma \leq 5$ or $0.1 < \bar{\Delta}/3\Gamma \leq 5$, the following special features of the spectrum are expected: (1) selective broadening and shifting of one of the two peaks of the dynamic spectrum; (2) a special angular dependence

of the spectrum different from both the dynamic and static JTE; and (3) complicated fine structure of the spectrum for arbitrary orientations of the magnetic field.

With a rise in temperature, larger 3Γ values shift the spectrum from static to dynamic, while the population of the excited tunneling energy level and the relaxation gradually reduce the whole complicated spectrum to one isotropic line.

6.3.3 Nuclear γ-resonance, microwave absorption, and ultrasonic attenuation

Similar to EPR, vibronic effects should be inherent in nuclear magnetic resonance spectra, nuclear quadrupole resonance, and nuclear γ-resonance (NGR) (Mössbauer) spectra. By way of illustration consider the hyperfine structure of the Mössbauer NGR spectrum for an $E \otimes e$ system with strong vibronic coupling. The Mössbauer nucleus is assumed to be at the center of a high-symmetry coordination system which gives no quadrupole splitting if vibronic interactions are disregarded. Using the wavefunctions of the tunneling energy levels given by Eq. (5.18), it was shown [6.197] that for the nuclear transition $(I = \frac{1}{2}) \rightarrow (I = \frac{3}{2})$ (e.g., for the iron nucleus), taking into account vibronic interactions, six lines should be observed, their frequencies (read off the undisplaced line) and intensity rations being given by the following relations:

$$\begin{aligned} \hbar\mathbf{\Omega}_{1,4} &= -(3\Gamma/2)[1 \pm (1+x)^{\frac{1}{2}}] \\ \hbar\mathbf{\Omega}_{2,5} &= \mp 2qa \\ \hbar\mathbf{\Omega}_{3,6} &= (3\Gamma/2)[1 \mp (1+x)^{\frac{1}{2}}] \end{aligned} \tag{6.100}$$

$$I_{1,6} : I_{2,5} : I_{3,4} = \frac{2x}{x + [1 + (1+x)^{\frac{1}{2}}]^2} : 1 : \frac{2[1 + (1+x)^{\frac{1}{2}}]^2}{x + [1 + (1+x)^{\frac{1}{2}}]^2} \tag{6.101}$$

Here a is the usual constant of quadrupole coupling of the electrons with the nucleus, $q = K_E(E)$ is the vibronic reduction factor (Section 5.6), $x = 2(B/3\Gamma)^2$, $\mathrm{B} = bqa$, b is a numerical factor of the order of unity depending on the height of the quadratic barrier, and 3Γ is the tunneling splitting, as above. It is seen that in this case, for arbitrary values of 3Γ, the NGR spectrum has six lines, which are symmetric in positions and intensities (Fig. 6.31).

In the limiting case of very deep minima when $3\Gamma \ll a$, the six lines are arranged in two groups of three lines positioned at $\pm a$ with similar values of

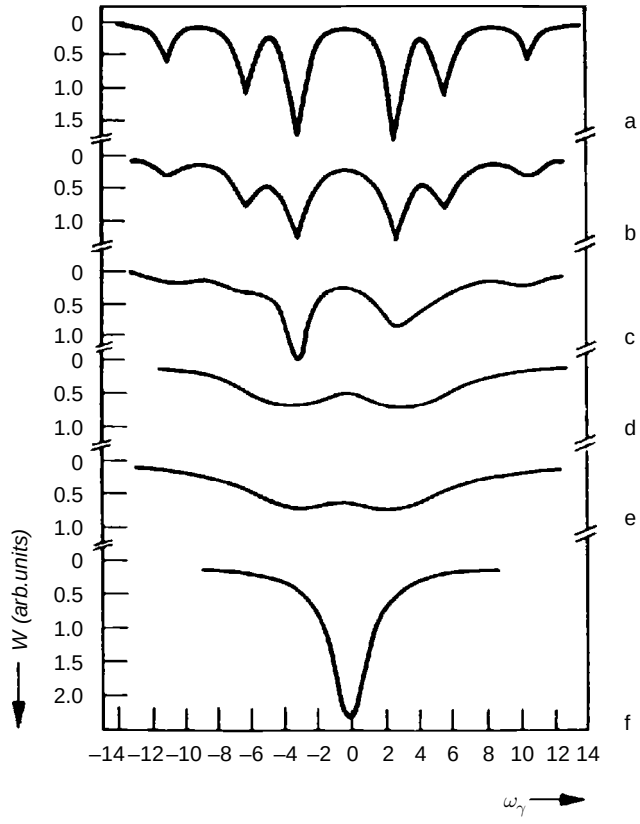

Fig. 6.31. Mössbauer absorption line shapes for a JT system with an $E \otimes e$ problem calculated including both vibronic coupling and relaxation effects with $qa = 3$, $b = 4$, $3\Gamma = 8$, and (a) $\lambda_1 = \lambda_2 = 0$; (b) $\lambda_1 = \lambda_2 = 0.1$; (c) $\lambda_1 = 1.0$, $\lambda_2 = 0.01$; (d) $\lambda_1 = 0.01$, $\lambda_2 = 1$; (e) $\lambda_1 = \lambda_2 = 1.0$; and (f) $\lambda_1 = \lambda_2 = 10$ (all in units of line width) [6.197].

frequencies and intensities, the spectrum as a whole being similar to that expected for a statically distorted system, but with a quadrupole splitting reduced by one half ($q = \frac{1}{2}$, static JTE). For larger 3Γ, two lines from each of the two groups of three lines split off, one shifting toward the center of the spectrum and increasing its intensity, the other shifting in the opposite direction and lowering its intensity. If the resulting spectrum is, as usual, not well resolved, it appears as if the quadrupole splitting should decrease when 3Γ is increased. Taking into account the above statement about the growth of the tunneling splitting 3Γ with temperature, we come to the general qualitative conclusion that, in the JT system under consideration, a reduction of quadrupole splitting should be observed as the temperature increases. Such a temperature reduction of quadrupole splitting in the NGR spectra has been

observed experimentally in many cases (e.g., see the spectra of $[FeCl_4]^{2-}$ [6.198] and $FeCr_2O_4$ [6.199]).

As for EPR, relaxation processes are of great importance here. In the $E \otimes e$ problem under consideration, with the lowest E and A tunneling energy levels, one may introduce two relaxation transition probabilities, for the transitions within the two E states (λ_1) and between the E and A states (λ_2). Then, the influence of relaxation transitions on the NGR spectrum can be taken into account by means of the stochastic approach [6.197]. The results for some of the important values of the relaxation constants λ_1 and λ_2 are given in Fig. 6.31. With increasing values of the constants λ_1 and λ_2 (for a given system – with increase in temperature) the six-line spectrum changes first to a doublet and then to the usual singlet inherent to an undistorted system, the two constants λ_1 and λ_2 affecting these changes differently.

The T-term problem may be even more important in the NGR spectra, since the most studied high-spin Fe^{2+} and low-spin Fe^{3+} octahedral complexes pertain to this case. The problem has been considered with allowance for magnetic hyperfine interaction with the electron spins 0, $\frac{1}{2}$, and 2, but disregarding relaxation [6.200, 6.201].

In particular, for the term $5T_2$ (e.g., the Fe^{2+} ion in the high-spin state of a cubic-type environment) with strong vibronic coupling and trigonal minima of the APES (Section 3.3) the spin–orbital interaction together with the tunneling splitting produce the following lowest vibronic energy levels [6.201]:

$$\begin{aligned}
\varepsilon(\Gamma_6) &= 2E_{\mathrm{JT}}^T\gamma \\
\varepsilon(\Gamma_1) &= \varepsilon(\Gamma_4') = \varepsilon(\Gamma_5') = -\tfrac{2}{3}(E_{\mathrm{JT}}^T + 4\lambda)\gamma \\
\varepsilon(\Gamma_3) &= \varepsilon(\Gamma_4) = -\tfrac{2}{3}(E_{\mathrm{JT}}^T - 2\lambda)\gamma \\
\varepsilon(\Gamma_5) &= -\tfrac{2}{3}(E_{\mathrm{JT}}^T - 6\lambda)\gamma
\end{aligned} \tag{6.102}$$

where E_{JT}^T is the usual JT stabilization energy (Section 3.3), λ is the constant of spin–orbital coupling, and γ is the overlap integral between the equivalent minima of the APES (Section 5.3; cf. Eq. (5.47) for the γ value in the $E \otimes e$ problem). The hyperfine interaction with the nuclear spin I is of the order of $10^{-3}\,\mathrm{cm}^{-1}$ and, in general, may mix the levels (6.102). But already for $\gamma \geq 10^{-3}$ this mixing may be neglected, and the influence of the nuclear spin on each of these levels may be considered separately by perturbation theory. For $\lambda > 0$ the coinciding levels Γ_1, Γ_4', and Γ_5' are the lowest, while for $\lambda < 0$ the lowest is the Γ_5 level. In the latter case the NGR spectrum is determined by the splitting of this level due to the interaction with the nuclear spin states $I = \frac{3}{2}$ and $I = \frac{1}{2}$

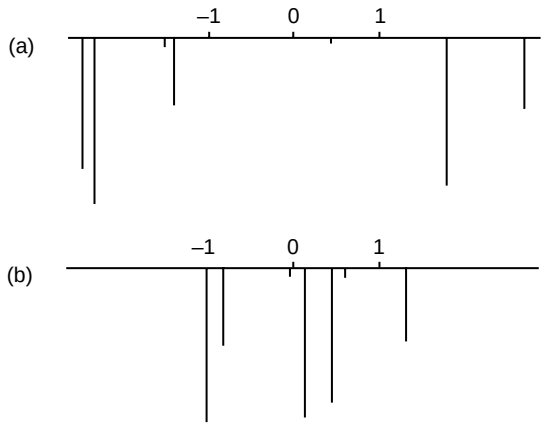

Fig. 6.32. Hyperfine splitting of the Mössbauer spectrum for a system in a ${}^5T_2$ state with strong vibronic coupling at low temperatures (in units of $\langle a_0^3/Z^3\rangle \times 10^{-2}$ cm/s, where a_0 is the quadrupole coupling constant): (a) $\gamma = 0.001$; and (b) $\gamma = 0.1$ [6.201].

and transitions between the latter. Presenting this interaction in dipole–dipole and quadrupole terms, one gets four levels (Γ_6, Γ_7, $2\Gamma_8$) for $I = \frac{3}{2}$ and two levels (Γ_7, Γ_8,) for $I = \frac{1}{2}$ with seven allowed transitions between them; their positions and intensities are strongly dependent on the γ value (in addition to the nuclear quadrupole moment).

Figure 6.32 illustrates these spectral line positions and intensities for two values: $\gamma = 0.001$ and $\gamma = 0.1$. We see that at small γ values (strong vibronic coupling, deep equivalent minima) the lines are well separated, and they converge with increasing γ, approximately coalescing at $\gamma \sim 0.15$ when the nonzero band width is taken into account. If we assume that γ is temperature dependent, the NGR spectrum looks like having quadrupole splitting at low temperatures, which decreases and finally disappears with increasing temperature. Random strain may modify this picture [6.202].

Vibronic effects in ultrasonic and electromagnetic microwave (nonmagnetic) absorption are closely related to the effects in EPR and NGR spectra discussed above. To begin with, resonance absorption of microwaves due to direct transitions between the tunneling energy levels can be anticipated [6.117]. Transitions between the lowest vibronic levels, which in general are allowed only as magnetic dipolar transitions, may be allowed also as electric dipolar transitions in the absence of an inversion center. Taking into account relaxations and crystal imperfections, which are especially important in the cases under consideration when tunneling splitting is small, the expected absorption lines may be rather broad and sometimes unresolved.

Experimentally observed [6.203] additional microwave loss due to Mn^{3+} ions in yttrium–iron garnets (E term) seems to be of the tunneling origin under consideration. Indeed, this absorption has a clear-cut frequency dependence with a temperature-dependent maximum position ($\nu_{max} = 15$ kMc at 37 K and $\nu_{max} = 56$ kMc at 58 K) in accord with the strong dependence of tunneling splitting on crystal temperature, as described above.

Similarly, transitions between tunneling levels under acoustic perturbations which lead to ultrasonic absorption can be considered [6.204, 6.205]. As distinct from acoustic spin resonance which is due to acoustic transitions between spin levels in magnetic fields, tunneling transitions are much more intense, since they are not limited by the low-probability processes of spin reversal mentioned earlier. For the $E \rightarrow A$ transition between the vibronic (tunneling) levels of the $E \otimes e$ problem for systems with a cubic-type symmetry under the assumption that $\hbar\boldsymbol{\Omega} \ll kT$, we obtain the following expression for the sound absorption coefficient as a function of frequency $\boldsymbol{\Omega}$ [6.204]:

$$\sigma_{E\rightarrow A} = \frac{\pi}{3}\frac{NR^2F_E\boldsymbol{\Omega}^2}{kT\nu^3 d}g(\boldsymbol{\Omega})L \tag{6.103}$$

where N is the number of absorption JT centers per unit volume in the crystal, R is the minimal metal–ligand distance, F_E is the linear vibronic constant, v is the velocity of sound, $g(\boldsymbol{\Omega})$ is the shape factor of the line determining its shape dependence on the relaxation processes in the crystal,

$$\int_0^\infty g(\boldsymbol{\Omega})\, d\boldsymbol{\Omega} = 1 \tag{6.104}$$

and L is the factor which takes into account the sound-propagation direction n and polarization m

$$L = \sum_i m_i^2 n_i^2 - \frac{1}{2}\sum_{i\neq j} m_i n_i m_j n_j, \quad i, j = x, y, z \tag{6.105}$$

and m_i and n_i are the direction cosines.

Estimates for hydrated copper complexes, taking $F_E = 2.5 \times 10^{-4}$ dyn, give $\sigma \approx 3.5 \times 10^{-11}\boldsymbol{\Omega}^2(4\pi T)^{-1}L$ (in cgs units), which (neglecting random strain, see below) is several orders of magnitude greater than the magnetic acoustic resonance absorption. Note that under the same conditions the probability P of relaxation due to direct transitions under thermal vibrations is given by [6.206] $P \approx 4 \times 10^{-13}\boldsymbol{\Omega}^2 T/4\pi^2$. It follows that, at least for low temperature, the width of the tunneling levels is small compared with the transition frequency. The absorption frequency can be regulated by means of magnetic fields [6.205].

Introducing the relaxation time $\tau \sim P^{-1}$, the absorption line shape can be expressed as

$$g(\mathbf{\Omega}) = \frac{2}{\pi} \frac{\tau}{1 + (\mathbf{\Omega} - \mathbf{\Omega}_0)^2 \tau^2} \tag{6.106}$$

where $\hbar\mathbf{\Omega}_0 = 3\Gamma$ is the tunneling splitting. As τ is strongly temperature dependent, $g(\mathbf{\Omega})$ has a maximum as a function of temperature, which can be derived from the expression $(\mathbf{\Omega} - \mathbf{\Omega}_0)\tau(T_{\max}) = 1$, provided the temperature dependence of 3Γ is neglected.

Acoustic loss due to the JTE was observed experimentally in $Ni^{3+}:Al_2O_3$ [6.207] (see also [6.208]). However, the authors [6.207] claim that this loss is due to relaxation processes involving tunneling effects, not to resonance transitions between tunneling levels, the motivation being that the random strain causes much greater splitting ($\bar{\Delta} \sim 2\ \mathrm{cm}^{-1}$) than the tunneling (estimated as $3\Gamma \sim 10^{-1}\,\mathrm{cm}^{-1}$). These objections are unconvincing since it can be shown [6.172] that the intensity of sound absorption depends strongly on the influence of the strain and decreases with increasing strain as the ratio $(3\Gamma)^2/[(3\Gamma)^2 + \Delta]$ (for a two-minimum system). It follows that the centers which are strongly affected by random strain do not actually absorb the sound, and only those centers which are not affected (or are only slightly affected) by the strain absorb the sound. The number of resonance-absorbing centers, and hence the total absorption intensity, is thereby strongly decreased by random strain. However, this has little influence on the possibility of experimental observation of the sound absorption since, as shown above, the effect itself is very strong. A more complete treatment of the influence of random strain on sound absorption has yet to be carried out.

Acoustic paramagnetic resonance in JT systems was considered elsewhere [6.174, 6.209–6.211]. Experimental data allow one to estimate the tunneling splitting 3Γ which, for $Cr^{2+}:MgO$ and $Cr^{2+}:KMgF_3$, lies in the range $7.6–32\,\mathrm{cm}^{-1}$ (see also Section 8.1).

References

6.1. I. B. Bersuker and V. Z. Polinger, *Vibronic Interactions in Molecules and Crystals*, New York, Springer, 1989.

6.2. R. Englman, *The Jahn–Teller Effect in Molecules and Crystals*, London, Wiley, 1972.

6.3. Yu. E. Perlin and B. S. Tsukerblat, *Effects of Electron–Vibrational Interaction in Optical Spectra of Paramagnetic Impurity Ions*, Kishinev, Shtiintsa, 1974 (in Russian).

6.4. M. C. M. O'Brien, in *Vibrational Spectra and Structure: A Series of Advances*, Ed. Yu. E. Durig, Vol. 10, Amsterdam, Elsevier, 1981, p. 321.

6.5. Yu. E. Perlin, B. S. Tsukerblat, in *The Dynamical Jahn–Teller Effect in Localized Systems*, Eds. Yu. E. Perlin and M. Wagner, Amsterdam, North-Holland, 1984, p. 251.
6.6. T. A. Barckholtz and T. A. Miller, *Internat. Rev. Phys. Chem.* **17**, 435 (1998).
6.7. A. L. Natadze, A. I. Ryskin, and B. G. Vekhter, in *The Dynamical Jahn–Teller Effect in Localized Systems*, Eds. Yu. E. Perlin and M. Wagner, Amsterdam, North-Holland, 1984, p. 347.
6.8. V. V. Hizhnyakov and N. N. Kristoffel, in *The Dynamical Jahn–Teller Effect in Localized Systems*, Eds. Yu. E. Perlin and M. Wagner, Amsterdam, North-Holland, 1984, p. 383.
6.9. W. Ulrici, in *The Dynamical Jahn–Teller Effect in Localized Systems*, Eds. Yu. E. Perlin and M. Wagner, Amsterdam, North-Holland, 1984, p. 439.
6.10. H. Köppel, W. Domcke, and L. S. Cederbaum, *Adv. Chem. Phys.* **57**, 59 (1984).
6.11. S. Sugano, Y. Tanabe, and H. Kamimura, *Multiplets of Transition Metal Ions in Crystals*, New York, Academic Press, 1970.
6.12. (*a*) M. C. M. O'Brien, *Proc. Phys. Soc. London* **86**, 847 (1965); (*b*) P. R. Moran, *Phys. Rev. A* **137**, 1016 (1965).
6.13. Y. Toyozawa and M. Inoue, *J. Phys. Soc. Japan* **20**, 1289 (1965); **21**, 1663 (1966).
6.14. B. G. Vekhter, Yu. E. Perlin, V. Z. Polinger, Yu. B. Rosenfeld, and B. S. Tsukerblat, *Cryst. Lattice Defects* **3**, 61, 69 (1972).
6.15. V. P. Khlopin, B. S. Tsukerblat, Yu. B. Rosenfeld, and I. B. Bersuker, *Fiz. Tverd. Tela* **14**, 1060 (1972); *Phys. Status Solidi B* **53**, K73 (1972); *Phys. Lett. A* **38**, 437 (1972).
6.16. H. C. Longuet-Higgins, U. Öpik, M. H. L. Pryce, and R. A. Sack, *Proc. R. Soc. London A* **244**, 1 (1958).
6.17. W. Moffitt and W. Thornson, in *Calcul des fonctions d'onde moléculaire*, Ed. R. A. Daudel, Paris, CNRS, 1958, p. 141.
6.18. P. Habitz and W. H. E. Schwarz, *Theor. Chim. Acta* **28**, 267 (1973).
6.19. V. Loorits, *Izv. Akad. Nauk Est. SSR, Fiz.-Mat.* **29**, 208 (1980).
6.20. H. Köppel, E. Haller, L. S. Cederbaum, and W. Domcke, *Mol. Phys.* **41**, 699 (1980).
6.21. M. C. M. O'Brien, *Solid State Commun.* **36**, 29 (1980).
6.22. S. Muramatsu and N. Sakamoto, *J. Phys. Soc. Japan* **36**, 839 (1974).
6.23. C. L. Martinelli, M. Passaro, and G. P. Parravicini, *Phys. Rev. B* **43**, 8395 (1991).
6.24. N. Sakamoto, *J. Phys. C* **15**, 6379 (1982).
6.25. W. Domcke, H. Köppel, and L. S. Cederbaum, *Mol. Phys.* **43**, 851 (1981).
6.26. S. Muramatsu and K. Nasu, *Phys. Status Solidi B* **68**, 761 (1975).
6.27. E. Mulazzi, *Phys. Rev. B* **18**, 7109 (1978).
6.28. M. Rueff and E. Sigmund, *Phys. Status Solidi B* **80**, 215 (1977).
6.29. H. Barentzen, G. Olbrich, and M. C. M. O'Brien, *J. Phys. A* **14**, 111 (1981).
6.30. A. Barchielli, *Physica A* **110**, 451 (1982).
6.31. F. T. Chau and L. Karlsson, *Phys. Sci.* **16**, 248 (1977).
6.32. A. Agresti, J. H. Ammeter, and M. Bacci, *J. Chem. Phys.* **84**, 1861 (1984).
6.33. R. Englman, M. Caner, and S. Toaff, *J. Phys. Soc. Japan* **29**, 306 (1970).
6.34. M. Caner and R. Englman, *J. Chem. Phys.* **44**, 4054 (1966).
6.35. N. Sakamoto, *J. Phys. Soc. Japan* **48**, 527 (1980).
6.36. M. Bacci, B. D. Bhattacharyya, A. Ranfagni, and G. Viliani, *Phys. Lett. A* **55**, 489 (1976).

6.37. K. Nasu and T. Kojima, *Prog. Theor. Phys.* **51**, 26 (1974).
6.38. K. Nasu, *Z. Naturforsch.* **30**, 1060 (1975).
6.39. S. N. Evangelou, *J. Phys. C* **14**, 2117 (1981); Y. Kayanuma and T. Kojima, *J. Phys. Soc. Japan.* **48**, 1990 (1980).
6.40. M. J. Schultz and R. Silbey, *J. Chem. Phys.* **65**, 4375 (1976).
6.41. C. M. Weinert, F. Forstmann, R. Grinter, and D. M. Kolb, *Chem. Phys.* **80**, 95 (1983).
6.42. A. J. Honma, *Sci. Light (Tokyo)* **18**, 33 (1969).
6.43. A. Matsushima and A. Fukuda, *Phys. Rev. B* **14**, 3664 (1976).
6.44. Y. Farge and M. P. Fontana, *Electronic and Vibrational Properties of Point Defects in Ionic Crystals*, Amsterdam, North-Holland, 1979, Chapters 3 and 4.
6.45. A. Ranfagni, D. Mugnai, M. Bacci, G. Villiani, and M. P. Fontana, *Adv. Phys.* **32**, 823 (1983).
6.46. K. Cho, *J. Phys. Soc. Japan* **25**, 1372 (1968).
6.47. M. C. M. O'Brien, *J. Phys. C* **9**, 3153 (1976).
6.48. M. C. M. O'Brien, *J. Phys. C* **4**, 2524 (1971).
6.49. M. C. M. O'Brien and S. N. Evangelou, *J. Phys. C* **13**, 611 (1980).
6.50. M. C. M. O'Brien, *J. Phys. C* **18**, 4963 (1985).
6.51. D. R. Pooler and M. C. M. O'Brien, *J. Phys. C* **10**, 3769 (1977).
6.52. G. Herzberg and E. Teller, *Z. Physik. Chem. B* **21**, 410 (1933).
6.53. J. Brickmann, *Mol. Phys.* **35**, 155 (1978).
6.54. B. G. Vekhter, B. S. Tsukerblat, and Yu. B. Rosenfeld, *Theor. Chim. Acta* **27**, 49 (1972).
6.55. W. H. Henneker, A. P. Penner, W. Siebrand, and M. Z. Zgierski, *J. Chem. Phys.* **69**, 1884 (1978); M. Garsia Sucre, F. Gény, and R. Lefebore, *J. Chem. Phys.* **49**, 458 (1968); G. Fisher and G. J. Small, *J. Chem. Phys.* **56**, 5934 (1972); R. J. Shaw, J. E. Kent, and M. F. O'Dwyer, *J. Mol. Spectrosc.* **82**, 1026 (1980); M. V. Priyutov, *Opt. Spektrosk.* **51**, 90 (1981); H. Köppel, L. S. Cederbaum, and W. Domcke, *J. Chem. Phys.* **77**, 2014 (1982).
6.56. A. Agresti, J. H. Ammeter, and M. Bacci, *J. Chem. Phys.* **81**, 1861 (1984).
6.57. A. Abragam, *The Principles of Nuclear Magnetism*, Oxford, Clarendon Press, 1961.
6.58. C. H. Henry, S. E. Schnatterly, and C. P. Slichter, *Phys. Rev.* **137**, 583 (1965).
6.59. Yu. E. Perlin and B. S. Tsukerblat, in *Crystal Spectroscopy*, Moscow, Nauka, 1975, p. 61 (in Russian).
6.60. L. M. Kushkuley, Yu. E. Perlin, B. S. Tsukerblat, and G. R. Engelgardt, *Zh. Eksp. Teor. Fiz.* **70**, 2226 (1976).
6.61. J. S. Griffith, *The Irreducible Tensor Method for Molecular Symmetry Groups*, Englewood Cliffs, New Jersey, Prentice-Hall, 1962.
6.62. L. M. Kushkuley, Yu. E. Perlin, and B. S. Tsukerblat, *Fiz. Tverd. Tela* **19**, 2178 (1977).
6.63. J. R. Fletcher, M. C. M. O'Brien, and S. N. Evangelou, *J. Phys. A* **13**, 2035 (1980).
6.64. L. S. Cederbaum, E. Haller, and W. Domcke, *Solid State Commun.* **35**, 879 (1980).
6.65. J. H. Van Vleck, *Phys. Rev.* **57**, 426 (1940).
6.66. E. Haller, L. S. Cederbaum, and W. Domcke, *Mol. Phys.* **41**, 1291 (1980).
6.67. L. S. Cederbaum, W. Domcke, and H. Köppel, *Chem. Phys.* **33**, 319 (1978).
6.68. E. Haller, H. Köppel, L. S. Cederbaum, G. Bieri, and W. von Niessen, *Chem. Phys. Lett.* **85**, 12 (1982).

6.69. E. Haller, H. Koppel, and L. S. Cederbaum, *J. Chem. Phys.* **78**, 1359 (1983).
6.70. W. Duch and G. A. Segal, *J. Chem. Phys.* **79**, 2951 (1983).
6.71. L. S. Cederbaum, W. Domcke, H. Köppel, and W. von Niessen, *Chem. Phys.* **26**, 169 (1977).
6.72. H. Köppel, L. S. Cederbaum, W. Domcke, and S. S. Shaik, *Angew. Chem., Int. Edn. Engl.* **22**, 210 (1983).
6.73. L. S. Cederbaum, W. Domcke, J. Schirmer, and H. Köppel, *J. Chem. Phys.* **72**, 1348 (1980).
6.74. T. A. Barckholtz and T. A. Miller, in *Computational Molecular Spectroscopy*, Eds. P. Buenker and P. Jensen, New York, Wiley, 2000, p. 539.
6.75. V. Boudon, F. Michelot, and J. Moret-Bailly, *J. Mol. Spectrosc.* **166**, 449 (1994); V. Boudon, M. Rotger, and D. Avignant, *J. Mol. Spectrosc.* **175**, 327 (1996).
6.76. H. Köppel, L. S. Cederbaum, W. Domcke, and W. von Niessen, *Chem. Phys.* **37**, 303 (1979).
6.77. H. Köppel, W. Domcke, and L. S. Cederbaum, *J. Chem. Phys.* **74**, 2945 (1981).
6.78. E. Mulazzi and A. A. Maradudin, *Solid State Commun.* **41**, 487 (1982).
6.79. Yu. B. Rosenfeld and V. Z. Polinger, *Zh. Eksp. Teor. Fiz.* **70**, 597 (1976).
6.80. Yu. B. Rosenfeld and A. V. Vaisleib, *Zh. Eksp. Teor. Fiz.* **86**, 1059 (1984).
6.81. Yu. B. Rosenfeld and A. V. Vaisleib, *J. Phys. C* **19**, 1721 and 1739 (1986).
6.82. J. A. Davis, *'R' Center in Lithium Fluoride: An Optical Study of Jahn–Teller Distorted System*, Ph.D. Thesis, Cornell University (1970).
6.83. R. Barrie and R. G. Rystephanick, *Can. J. Phys.* **44**, 109 (1966); K. V. Korsak and M. A. Krivoglaz, *Ukr. Fiz. Zh.* **14**, 2019 (1969).
6.84. E. Mulazzi and A. A. Maradudin, *J. Phys. Colloq.* **37**, 114 (1976).
6.85. V. Hizhnyakov, V. Boltrushko, H. Kaasik, and I. Sildos, *J. Luminesc.* **107**, 351 (2004).
6.86. B. S. Tsukerblat, Yu. B. Rosenfeld, V. Z. Polinger, and B. G. Vekhter, *Zh. Eksp. Teor. Fiz.* **68**, 1117 (1975).
6.87. M. A. Krivoglaz, *Zh. Eksp. Teor. Fiz.* **48**, 310 (1965).
6.88. R. H. Silsbee, *Phys. Rev.* **128**, 1726 (1962).
6.89. B. Scharf, *Chem. Phys. Lett.* **98**, 81 (1983).
6.90. M. D. Sturge, *Phys. Rev. B* **1**, 1005 (1970).
6.91. A. S. Abhvani, C. A. Bates, B. Clerjaud, and D. R. Pooler, *J. Phys. C* **15**, 1345 (1982).
6.92. M. J. Ponnambalam and J. J. Markham, *Solid State Commun.* **43**, 555 (1982).
6.93. A. Hjortsberg, B. Nygrén, J. Vallin, and F. S. Ham, *Phys. Rev. Lett.* **39**, 1233 (1977).
6.94. A. A. Kaplyanskiy and A. K. Przevuskii, *Opt. Spektrosk.* **19**, 597 (1966).
6.95. A. A. Kaplyanskiy and A. K. Przevuskii, *Opt. Spektrosk.* **20**, 1045 (1966).
6.96. L. L. Chase, *Phys. Rev. Lett.* **23**, 275 (1969); *Phys. Rev. B* **2**, 2308 (1070).
6.97. K. Nasu, *Prog. Theor. Phys.* **57**, 361 (1977).
6.98. S. G. Zazubovich, V. P. Nagirnyi, and T. A. Soovik, *Opt. Spektrosk.* **57**, 952 (1984).
6.99. B. G. Vekhter and B. S. Tsukerblat, *Fiz. Tverd. Tela* **10**, 1574 (1968).
6.100. B. S. Tsukerblat, B. G. Vekhter, I. B. Bersuker, and A. V. Albov, *Zh. Strukt. Khim.* **11**, 102 (1970).
6.101. G. S. Zavt, V. S. Plekhanov, V. V. Hizhnyakov, and V. V. Shepelev, *J. Phys. C* **17**, 2839 (1984).
6.102. Yu. E. Perlin and V. M. Polyanovskii, *Fiz. Tverd. Tela* **26**, 3325 (1984).

6.103. R. Englman, *Non-Radiative Decay of Ions and Molecules in Solids*, Amsterdam, North-Holland, 1979.
6.104. R. Englman and A. Ranfagni, *Physica B + C* **98**, 151 and 161 (1980).
6.105. D. Mugnai and A. Ranfagni, *Physica B + C* **98**, 282 (1980); *Phys. Rev. B* **25**, 4284 (1982).
6.106. R. Englman, A. Ranfagni, A. Agresti, and D. Mugnai, *Phys. Rev. B* **31**, 6766 (1985).
6.107. A. Ranfagni, D. Mugnai, and R. Englman, *Phys. Rep.* **108**, 165 (1984).
6.108. M. Wagner, *Phys. Status Solidi B* **115**, 427 (1983).
6.109. H. Köppel, *Chem. Phys.* **77**, 359 (1983).
6.110. A. E. Douglas, *J. Chem. Phys.* **45**, 1007 (1966).
6.111. V. M. Donnelly and F. Kaufman, *J. Chem. Phys.* **66**, 4100 (1977).
6.112. E. Haller, H. Köppel, and L. S. Cederbaum, *J. Mol. Spectrosc.* **111**, 377 (1985).
6.113. S. Feuerbacher and L. S. Cederbaum, and T. Sommerfield, *J. Chem. Phys.* **120**, 3201 (2004).
6.114. W. R. Thorson, *J. Chem. Phys.* **29**, 938 (1958).
6.115. M. S. Child and H. C. Longuet-Higgins, *Phil. Trans. R. Soc. London A* **254**, 259 (1962).
6.116. V. Z. Polinger and G. I. Bersuker, *Phys. Status Solidi B* **96**, 153 (1979).
6.117. I. B. Bersuker and B. G. Vekhter, in *Transactions of the Spectroscopy Commission of the Academy of Sciences of the USSR*, first issue, Proceedings of the 15th Conference on Spectroscopy, Minsk, 1963, Vol. 3, Moscow, Nauka, 1965, p. 520 (in Russian).
6.118. M. S. Child, *J. Mol. Spectrosc.* **10**, 357 (1963).
6.119. M. S. Child, *Phil. Trans. R. Soc. London A* **255**, 31 (1963).
6.120. S. I. Boldyrev, V. Z. Polinger, and I. B. Bersuker, *Fiz. Tverd. Tela* **23**, 746 (1981).
6.121. R. L. Fulton and M. Gouterman, *J. Chem. Phys.* **41**, 2280 (1964).
6.122. V. Loorits, *J. Phys. C* **16**, L711 (1983).
6.123. L. D. Landau and E. M. Lifshitz, *Quantum Mechanics: Non-Relativistic Theory*, 3rd edn. Course of Theoretical Physics, Vol. 3, Oxford, Pergamon, 1977.
6.124. M. S. Child, *Mol. Phys.* **5**, 391 (1962).
6.125. J. T. Hougen, *J. Mol. Spectrosc.* **81**, 73 (1980).
6.126. I. B. Bersuker, *Teor. Eksp. Khim.* **5**, 293 (1969).
6.127. I. B. Bersuker, I. Ya. Ogurtsov, and Yu. V. Shaparev, *Teor. Eksp. Khim.* **9**, 451 (1973).
6.128. I. B. Bersuker, I. Ya. Ogurtsov, and Yu. V. Shaparev, *Opt. Spektrosk.* **36**, 315 (1974).
6.129. I. B. Bersuker and I. Ya. Ogurtsov, *Adv. Quant. Chem.* **18**, 1 (1986).
6.130. G. Herzberg, *Molecular Spectra and Molecular Structure, Vol. 2, Infrared and Raman Spectra*, Princeton, New Jersey, Van Nostrand, 1945.
6.131. I. Ya. Ogurtsov, *Opt. Spektrosk.* **56**, 60 (1984).
6.132. I. Ya. Ogurtsov, *Opt. Spektrosk.* **58**, 799 (1985).
6.133. C. G. Gray, *J. Phys. B* **4**, 1661 (1971).
6.134. H. Köppel, W. Domcke, and L. S. Cederbaum, *Adv. Chem. Phys.* **67**, 59 (1986).
6.135. J. M. Brown, in *Computational Molecular Spectroscopy*, Eds. P. Jensen and R. J. Bunker, New York, Wiley, 2000, p. 517.

6.136. J. M. Brown and F. Jorgensen, *Adv. Chem. Phys.* **52**, 117 (1983).
6.137. M. Perić, E. Engles, and S. D. Peyerimhoff, in *Quantum Mechanical Electronic Structure Calculations with Chemical Accuracy*, Ed. S. R. Langhoff, Dordrecht, Kluwer, 1995, p. 261.
6.138. M. Perić and S. D. Peyerimhoff, *Adv. Chem. Phys.* **124**, 583 (2002).
6.139. V. B. Berestetskiy, E. M. Lifshitz, and L. P. Pitaevskiy, *Relativistic Quantum Theory*, part 1, Moscow, Nauka, 1968, Section 60.
6.140. I. Ya. Ogurtsov, Yu. V. Shaparev, and I. B. Bersuker, *Opt. Spektrosk.* **45**, 672 (1978).
6.141. S. Guha and L. L. Chase, *Phys. Rev. B* **12**, 1658 (1975).
6.142. B. Scharf and Y. B. Band, *J. Chem. Phys.* **79**, 3175 (1983).
6.143. Yu. B. Rosenfeld and A. V. Vaisleib, *J. Phys. C* **19**, 1721 and 1739 (1986).
6.144. A. V. Vaisleib, V. P. Oleinikov, and Yu. B. Rosenfeld, *Fiz. Tverd. Tela* **23**, 3486 (1981).
6.145. S. Guha and L. L. Chase, *Phys. Rev. Lett.* **32**, 869 (1974).
6.146. M. M. Sushchinskiy, *Raman Spectra of Molecules and Crystals*, Moscow, Nauka, 1969 (in Russian).
6.147. A. V. Vaisleib, V. P. Oleinikov, and Yu. B. Rosenfeld, *Phys. Status Solidi B* **109**, K35 (1982).
6.148. A. V. Vaisleib, Yu. B. Rosenfeld, and V. P. Oleinikov, *Phys. Lett. A* **89**, 41 (1982).
6.149. A. V. Vaisleib, V. P. Oleinikov, and Yu. B. Rosenfeld, *Fiz. Tverd. Tela* **24**, 1074 (1982).
6.150. Yu. B. Rosenfeld and A. V. Vaisleib, *Zh. Eksp. Teor. Fiz.* **86**, 1059 (1984).
6.151. E. Mulazzi and N. Terzi, *Solid State Commun.* 18, 721 (1976); *Phys. Rev. B* **19**, 2331 (1979).
6.152. V. L. Ostrovski, I. Ya Ogurtsov, and I. B. Bersuker, *Mol. Phys.* **48**, 13 (1983).
6.153. V. L. Ostrovski, I. Ya. Ogurtsov, and I. B. Bersuker, *Mol. Phys.* **51**, 1205 (1984).
6.154. Y. Fujumura and S. N. Lin, *J. Chem. Phys.* **70**, 247 (1979).
6.155. M. Pawlikowski and M. Z. Zgierski, *Chem. Phys. Lett.* **48**, 201 (1977).
6.156. M. Pawlikowski and M. Z. Zgierski, *J. Raman Spectrosc.* **7**, 106 (1978).
6.157. S. Muramatsu, K. Nasu, M. Takahashi, and K. Kaya, *Chem. Phys. Lett.* **50**, 284 (1977).
6.158. S. Muramatsu and K. Nasu, *J. Phys. Soc. Japan.* **46**, 189 (1979).
6.159. I. L. Fabelinskii, *Molecular Scattering of Light*, Moscow, Nauka, 1966 (in Russian).
6.160. I. Ya. Ogurtsov, V. L. Ostrovski, and I. B. Bersuker, *Opt. Spektrosk.* **53**, 356 (1982).
6.161. I. Ya. Ogurtsov, V. L. Ostrovski, and I. B. Bersuker, *Khim. Fiz.* **5**, 579 (1983).
6.162. A. D. Buchingham and B. J. Orr, *Trans. Faraday Soc.* **65**, 673 (1969).
6.163. I. Ya. Ogurtsov and V. L. Ostrovski, *Mol. Phys.* **54**, 119 (1985).
6.164. I. Ya. Ogurtsov, V. L. Ostrovski, and I. B. Bersuker, *Mol. Phys.* **50**, 315 (1983).
6.165. V. L. Ostrovski, I. Ya. Ogurtsov, and I. B. Bersuker, *Mol. Phys.* **51**, 1205 (1984).
6.166. B. Bleaney and D. J. E. Ingram, *Proc. Phys. Soc. London A* **63**, 408 (1950).
6.167. B. Bleaney and K. D. Bowers, *Proc. Phys. Soc. London A* **65**, 667 (1952).
6.168. A. Abraham and M. H. L. Pryce, *Proc. Phys. Soc. London A* **63**, 409 (1950).
6.169. I. B. Bersuker, *Zh. Eksp. Teor. Fiz.* **44**, 1239 (1963).

6.170. A. Abraham and B. Bleaney, *Electron Paramagnetic Resonance of Transition Ions*, Oxford, Clarendon, 1970, Chapter 21.
6.171. F. S. Ham, in *Electron Paramagnetic Resonance*, Ed. S. Geschwind, New York, Plenum, 1972, p. 1.
6.172. I. B. Bersuker, B. G. Vekhter, and I. Ya. Ogurtsov, *Uspekhi Fiz. Nauk* **116**, 605 (1975).
6.173. H. Bill, in *The Dynamical Jahn–Teller Effect in Localized Systems*, Eds. Yu. E. Perlin and M. Wagner, Amsterdam, North-Holland, 1984, p. 709.
6.174. C. A. Bates, *Phys. Rep.* **35**, 187 (1978).
6.175. K. A. Müller, in *Magnetic Resonance and Relaxation. Proc. XIV Colloque Ampère, Ljubljana, 1966*, Ed. R. Blinc, Amsterdam, North-Holland, 1967, p. 192.
6.176. I. B. Bersuker, B. G. Vekhter, and V. Z. Polinger, in *Problemy magnitnogo rezonansa*, Moscow, Nauka, 1978, p. 31.
6.177. *The Jahn–Teller Effect. A Bibliographic Review*, Ed. I. B. Bersuker, New York, IFI/Plenum, 1984.
6.178. R. E. Coffman, *J. Chem. Phys.* **48**, 609 (1968).
6.179. R. E. Coffman, *Phys. Lett.* **21**, 381 (1966).
6.180. G. W. Ludwig and H. H. Woodbury, *Phys. Rev.* **113**, 1014 (1959); *Solid State Phys.* **13**, 1 (1962); H. H. Woodbury and G. W. Ludwig, *Phys. Rev.* **126**, 466 (1962).
6.181. I. B. Bersuker and V. Z. Polinger, *Phys. Lett. A* **44**, 495 (1973); *Zh. Eksp. Teor. Fiz.* **66**, 2078 (1974).
6.182. K. R. Dunbar, E. J. Shelter, B. S. Tsukerblat, S. M. Ostrovsky, V. Y. Mirovitsky, and A. V. Palii, *Polyhedron* **22**, 2545 (2003); K. R. Dunbar, E. J. Shelter, B. S. Tsukerblat, A. V. Palii, S. M. Ostrovsky, and V. Y. Mirovitsky, *Adv. Quant. Chem.* **44**, 413 (2003).
6.183. P. L. W. Tregenna-Piggott, M. C. M. O'Brien, H. Weihe and H. U. Güdel, *J. Chem. Phys.* **109**, 2967 (1998).
6.184. A. Abragam, *The Principles of Nuclear Magnetism*, Oxford, Clarendon, 1961.
6.185. N. Gauthier and M. B. Walker, *Can. J. Phys.* **54**, 9 (1976).
6.186. V. Z. Polinger and G. I. Bersuker, *Fiz. Tverd. Tela* **22**, 2445 (1980); G. I. Bersuker and V. Z. Polinger, *Solid State Commun.* **38**, 795 (1981); G. I. Bersuker and V. Z. Polinger, *Zh. Eksp. Teor. Fiz.* **80**, 1788 (1981).
6.187. C. A. Bates and P. Steggles, *J. Phys. C* **8**, 2283 (1975).
6.188. R. W. Reynolds, L. A. Boatner, M. M. Abraham, and Y. Chen, *Phys. Rev. B* **10**, 3802 (1974).
6.189. R. W. Reynolds and L. A. Boatner, *Phys. Rev. B* **12**, 4735 (1975).
6.190. L. A. Boatner, R. W. Reynolds, Y. Chen, and M. M. Abraham, *Phys. Rev. B* **16**, 86 (1977).
6.191. L. L. Chase, *Phys. Rev. Lett.* **23**, 275 (1969).
6.192. A. M. Ziatdinov, M. M. Zaripov, Yu. V. Yablokov, and R. L. Davidovich, *Phys. Status Solidi B* **88**, 439 (1978).
6.193. V. E. Petrashen, Yu. V. Yablokov, and R. L. Davidovich, *Phys. Status Solidi B* **88**, 439 (1978).
6.194. J. H. Ammeter and J. D. Swalen, *J. Chem. Phys.* **57**, 678 (1972).
6.195. J. H. Ammeter, *J. Magn. Res.* **30**, 299 (1978).
6.196. J. H. Ammeter, H. B. Bürgi, E. Camp, V. Meyer-Sandrin, and W. P. Jensen, *Inorg. Chem.* **18**, 733 (1979).
6.197. I. B. Bersuker, S. A. Borshch, and I. Ya. Ogurtsov, *Phys. Status Solidi B* **59**, 707 (1973).

6.198. T. C. Gibb and N. H. Greenwood, *Tech. Rept. I.A.E.A.* **50**, 143 (1966).
6.199. M. Tanaka, T. Tokoro, and Y. Aijama, *J. Phys. Soc. Japan* **21**, 262 (1966).
6.200. I. B. Bersuker and I. Ya. Ogurtsov, *Fiz. Tverd. Tela* **10**, 3651 (1968); and in *XXII IUPAC Congress*, Abstracts, Sidney, IUPAC, 1969, p. 92.
6.201. I. B. Bersuker, I. Ya. Ogurtsov, and E. I. Polinkovskii, *Izv. Akad. Nauk Mold. SSR* **4**, 70 (1969).
6.202. F. S. Ham, *Phys. Rev.* **160**, 328 (1967); F. S. Ham, W. H. Schwarz, and M. C. M. O'Brien, *Phys. Rev.* **185**, 548 (1969).
6.203. E. M. Gyorgy, R. C. LeCraw, and M. D. Struge, *J. Appl. Phys.* **37**, 1303 (1966).
6.204. I. B. Bersuker, *Zh. Eksp. Teor. Fiz.* **44**, 1577 (1963).
6.205. I. B. Bersuker, *Fiz. Tverd. Tela* **6**, 436 (1964).
6.206. S. A. Altshuller, V. I. Kochelaev, and A. M. Leushin, *Uspekhi Fiz. Nauk* **75**, 459 (1961).
6.207. M. D. Sturge, J. T. Krause, E. M. Gyorgy, R. C. LeCraw, and F. R. Merritt, *Phys. Rev.* **155**, 218 (1967).
6.208. M. D. Sturge, *Solid State Phys.* **20**, 91 (1967).
6.209. J. P. Fletcher and K. W. H. Stevens, *J. Phys. C* **2**, 444 (1969).
6.210. M. Abou-Ghantous, C. A. Bates, J. P. Fletcher, and P. C. Jaussand, *J. Phys. C* **8**, 3641 (1975).
6.211. J. Lange, *Phys. Rev. B* **14**, 4791 (1976); S. Guha and J. Lange, *Phys. Rev. B* **15**, 4157 (1977).

7

Geometry, spectra, and reactivity of molecular systems

7.1 General: JT vibronic coupling effects in geometry and reactivity

This chapter is devoted to applications of the JTE, PJTE, and RTE theory to solve the problems of origin of geometry and spectra, as well as other properties of molecular systems. With regard to geometry, as mentioned in the introduction, increased computer power allows sufficiently accurate calculations of APES of small to moderate-sized molecular systems to determine their absolute minima, which are assumed to define the molecular geometry. In many cases and for many electronic states, ground and excited, the APES are rather complicated: there may be several equivalent minima which do not correspond to the high-symmetry configuration that one may expect from a general, classical point of view. Instead, complicated dynamics due to the multi-minimum APES, anharmonicity, conical intersections, and lines of conical intersections may occur. Obviously, molecular properties other than geometry, including spectra and reactivity, are strongly dependent on the APES too.

On the other hand, as follows from the previous chapters, the JT vibronic effects are the only sources of instability of high-symmetry configurations. Therefore the vibronic effects may serve as a fundamental basis for understanding (rationalizing) the results of quantum-chemical computations (as well as results obtained by other methods). In addition, for large systems *ab initio* calculations with geometry optimization are impossible or impractical, leaving the perturbational vibronic approach as the only source of information on bulk and local instabilities.

Where they have been possible, *ab initio* calculations of systems with JT and RT degeneracies confirm the general predictions of the theory and extend them to larger distortions for which the perturbation theory is not that accurate. The PJT situation is more complicated because until recently there

was no proof that the distortions of high-symmetry configurations in non-degenerate states are due to, and only to, their PJT mixing with electronic states that are higher in energy. The proof of this statement (Section 4.1) allows one to classify all (calculated and/or observed) nuclear configuration instabilities as due to JT or PJT effects.

For the purpose of investigation of JT vibronic coupling effects it is convenient to group the molecular systems with respect to their reference high-symmetry configuration (Section 2.2), i.e. the configuration from which the JT, PJT, and RT distortions start. We emphasize that without a reference configuration there is no way to formulate the JT problems. In this respect it is important to follow the terminology below: electronic ground state in the high-symmetry configuration means the *calculated* ground state of the system when it is *fixed* in this configuration. If this state is degenerate, the nuclear configuration is unstable and the ground state of the stable (APES minimum) configuration may differ from the ground state of the reference configuration.

Obviously, in some cases the choice of reference configuration may be somewhat ambiguous. For instance, a strongly distorted flattened tetrahedron may be regarded also as a distorted square-planar configuration. The choice of the reference configuration in such cases is conventional, but all possibilities should be tried.

In this and the next few sections we discuss many examples that illustrate these statements, as well as experimental confirmation of various vibronic effects. Citing numerical data from different papers, we try to keep the form of presentation and units of the original work, where possible. The variety of the applications presented below in this and the next chapters confirms that the JTE is now a general approach to understanding (rationalizing) and solving molecular and solid-state problems.

7.1.1 Dynamic molecular shapes of JT systems

Molecular geometry, or stereochemistry, underlies chemical intelligence: without assumptions of molecular shapes there is no way to rationalize molecular structure and chemical transformations. On the other hand, the definition of molecular shape is not always straightforward. The widespread idea is to identify the molecular geometry with its configuration at the absolute minimum of the APES. But if there are other close-in-energy minima on the APES or they are equivalent, as in the JT situations, the configuration at the minimum under consideration may be unobservable. To observe a molecular system in a given configuration, it should have a "*lifetime*" τ that

is larger than the characteristic "*time of measurement*" τ' determined by the means of observation:

$$\tau > \tau' \tag{7.1}$$

The lifetime of a given molecular configuration is directly related to the presence of other minima and the energy barriers δ between them. The quantum-mechanical necessary condition of an observable configuration is the presence of localized vibrational states in the minimum, which is possible when at least

$$\delta > \hbar\omega \tag{7.2}$$

where ω is the vibrational frequency in the minimum (cf. the condition of strong vibronic coupling, Section 5.1).

Obviously, to observe these vibrational states the inequality $\tau' > 2\pi/\omega$ should hold. On the other hand, in JT systems with several minima under the condition (7.2), there is tunneling splitting, $r\Gamma$, $r = 3, 4, 6, \ldots$ ($r\Gamma < \hbar\omega$) (Section 5.3), so the lifetime in the minimum is $\tau \sim 2\pi\hbar/r\Gamma$. According to Eq. (7.1), to observe the configuration at the minimum, the inequality $\tau' < 2\pi\hbar/r\Gamma$ should hold. It follows that the JT-distorted configuration can be observed if and only if

$$2\pi\hbar/r\Gamma > \tau' > 2\pi/\omega \tag{7.3}$$

Since the time τ' is dependent on the method of measurement (usually the higher the frequency in resonance methods, the lower τ'), we come to the conclusion that *in JT systems the observable nuclear configurations depend on the means of observation and may vary with the method of measurement* [7.1] (see also [7.2, 7.3]). In particular, we can observe the distorted configuration of the APES minima, say, in optical experiments and the undistorted (averaged over all the equivalent minima) geometry of the same system at the same temperature in EPR spectra, but not vice versa.

In the case of "full dynamics" or free pseudorotations, as, e.g., in the JT linear $E \otimes e$ problem (Section 3.2, Figs. 3.3 and 3.4), there are no localized states for instant distorted configurations ($\tau = 0$), and hence no distorted configurations can be observed experimentally. As shown in Section 5.6 (Eq. (5.136)), in a stationary state of any JT system the averaged configuration corresponds to the initial undistorted (reference) configuration. However, this free JT pseudorotation can be easily violated (stopped) by small external perturbations that depend on nuclear coordinates Q. In the first order such perturbations are enhanced by the vibronic coupling (see Eqs. (5.135)

and (5.135′)), in contrast to electronic perturbations, which are reduced. Here we bring a simple and rather visual description of this effect.

Consider a system with a linear $E \otimes e$ problem and a Mexican-hat-type APES (Section 3.2). Under the influence of a small distorting perturbation, say, elongation in the Q_ϑ direction, the circular trough becomes distorted, namely, an additional potential well appears in the Q_ϑ direction at the point (ρ_0, ϕ_0) (and a hump in the opposite $-Q_\vartheta$ direction). If the depth of the well is greater than the kinetic energy of the circular motion in the trough E_k (which in the $E \otimes e$ problem equals $\hbar^2/8M\rho_0^2$), then at sufficiently low temperatures the nuclear motions are localized in this well and the corresponding distorted nuclear configuration near the point point (ρ_0, ϕ_0) can be observed in the experiments.

Low-symmetry perturbations distort the system anyway, but in the presence of the JTE, as mentioned above, *the distortion is essentially amplified* (Section 5.6). In the absence of vibronic coupling the magnitude Q_0 of distortion can be found from the fact that the perturbation energy W transforms into strain energy: $W = \frac{1}{2}K_E Q_0^2$, where K_E is the force constant for the E distortions under consideration (Section 3.2); hence $Q_0 = (2W/K_E)^{\frac{1}{2}}$. If the vibronic effects are taken into account, $Q_0^{\mathrm{JT}} = \rho_0 + Q_0$, where ρ_0 is the radius of the trough (Eq. (3.26)), and the amplification coefficient, equal to the ratio of the corresponding distortions, is [7.1]

$$P_{\mathrm{a}} = Q_0^{\mathrm{JT}}/Q_0 = 1 + (E_{\mathrm{JT}}/W)^{\frac{1}{2}} \tag{7.4}$$

Here the relationship $\rho_0 = (2E_{\mathrm{JT}}/K_E)^{\frac{1}{2}}$ is employed (see Eqs. (3.26) and (3.27)). The maximum amplification is attained when $W = E_k$:

$$P_{\mathrm{a}}^{\max} = 1 + 4(E_{\mathrm{JT}}/\hbar\omega_E) = 1 + 4\lambda_E \tag{7.5}$$

It follows that the vibronic amplification may be very large since the λ_E value may be substantial. For example, if we assume that λ_E is about 5–10 (as expected in many cases, e.g. for octahedral clusters of Cu(II), Mn(III), Cr(II), etc.), then $P_{\mathrm{a}}^{\max} \sim 20$–$40$. Similarly, the system may be "locked" in one of its equivalent minima in the JT problems with several minima on the APES.

Temperature effects were omitted in the above consideration. It can be shown [7.4] that for a Jahn–Teller system with a threefold degenerate T term interacting with t_2 nuclear distortions (the $T \otimes t_2$ problem, Section 3.4) at not very low temperatures (and with a sufficiently strong external electric field as a perturbation), the approximate temperature dependence of the vibronic amplification of external distortions P_{a} is

$$P_{\mathrm{a}} \approx E_{\mathrm{JT}}^T/kT \tag{7.6}$$

where E_{JT}^{T} is the Jahn–Teller stabilization energy. For instance, if $E_{\mathrm{JT}}^{T} \sim 10^3\,\mathrm{cm}^{-1}$, then $P_{\mathrm{a}} \sim 10$ even at room temperatures.

The rough estimates (7.1)–(7.6) are aimed at qualitative general assessment of the possible observation of molecular shapes of JT systems. The main conclusion is that, strictly speaking, in the absence of external perturbations JT distortions are of dynamic nature and are not manifested in an absolute way in molecular shapes (stereochemistry), but relatively small perturbations may lock the system in the distorted configuration predicted by the JTE. Hence in multiminima systems the means of observation that obey inequality (7.3) show the distorted configuration in the minima.

As stated in Chapters 3–5, the internal dynamics in JT systems may be presented as *free (pseudo) rotations* (in linear $E \otimes e$ and other similar problems), *hindered rotations* (when there are small barriers between the APES minima), and *pulsating (fluctuating) motions* (in cases of sufficiently deep minima and high barriers between them). These internal motions can be called *pseudorotations*, although pulsating motions are more similar to *large-amplitude (slow) vibrations*. They can be observed experimentally in the NMR spectra, isotopic substitution experiments, central-atom nuclear quadrupole resonance spectra, tunneling splitting (Section 5.3), and other spectroscopic measurements.

Pseudorotations in molecular systems, in general, were known for a long time but their JT and/or PJT origin was revealed just recently. Berry [7.5] assumed that the APES of such systems has several equivalent minima (without specifying their origin) with small energy barriers between them, and the observed pseudorotations are due to the transitions between the minima. For instance, the pseudorotation molecule PF_5 is assumed to have an energy minimum in the trigonal-bipyramidal (TBP) configuration, and as a result of the combined E-type displacements transforms into the (higher in energy) square-pyramidal (SP) configuration, which by further transformation converts again into the TBP configuration, but with other F atoms on the threefold axis.

Another example is the SF_4 molecule with minima at $C_{2\mathrm{v}}$ symmetry, which can be considered as either a strongly distorted tetrahedron or a less distorted square-planar configuration with two angles F—S—F of 183° and 104°. Here the Berry rotation consists of transitions between two equivalent distorted configurations via the intermediate unstable square-planar geometry; this mechanism of interconversion in SF_4 is confirmed by dynamic NMR experiments [7.6] and by direct electronic structure calculations [7.7].

In both examples the intermediate configuration has a maximum of the APES of the nondegenerate ground state with respect to a specific symmetrized direction of distortion. According to the conclusions of the vibronic theory, the instability of the high-symmetry intermediate configuration is due

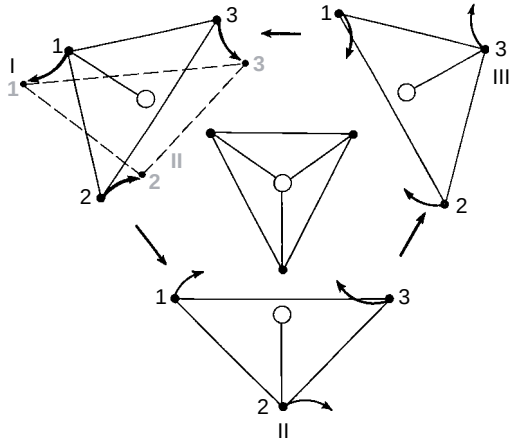

Fig. 7.1. Pseudorotation in the $[CuCl_5]^{3+}$-type system with the $E \otimes e$ JT problem and three equivalent equilibrium configurations of square-pyramidal (SP) (or near-SP) symmetry (top view); the interconversion between them goes beyond the trigonal-bipyramidal (TBP) configuration. The arrows show (schematically) the displacements of the equatorial ligands transforming one configuration into another (the axial ligand displacements are not shown).

to the vibronic mixing of its electronic ground state with some excited states of required symmetry determined by the nonzero vibronic constant. The Berry rotations under consideration are thus pseudorotations caused by a strong PJTE resulting in a corresponding APES.

It is important that *the pseudorotations of Jahn–Teller distortions in orbitally degenerate ground states do not follow Berry rotations*. Indeed, consider an MX_5 system in the TBP configuration outwardly similar to the PF_5 molecule, but with a doubly degenerate electronic E term (examples of such systems, are mentioned in Section 7.6.1). According to the general solution of the $E \otimes e$ problem (Section 3.2), in a D_{3h} system there are three minima of the adiabatic potential in the space of two E-type displacements (Fig. 3.4). In the case under consideration these minima correspond to three SP (or near to SP) configurations shown in Fig. 7.1.

The pseudorotations here are just interconversions between the three SP configurations. Direct examination of the APES in the $E \otimes e$ problems (Figs. 3.4 and 3.7) shows that the lowest pathway to overcome the barriers between the minima never goes through the high-symmetry TBP configuration D_{3h}, and hence the latter is not involved in the pseudorotation; the coordinates of interconversion do not include the point $Q_\vartheta = Q_\varepsilon = 0$. Thus the JT pseudorotation cannot be reduced to the direct TBP $\longleftrightarrow$ SP interconversions, as in the Berry mechanism, which is based on the PJTE.

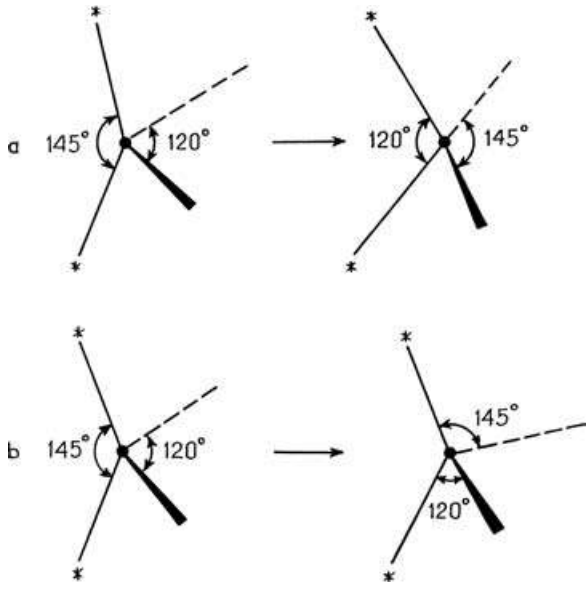

Fig. 7.2. Pseudorotation in the $Fe(CO)_4$ system. The interconversion between two distorted C_{2v} configurations: (a) predicted by the Berry mechanism; and (b) observed experimentally. The two ligands bearing isotopes ^{13}C and ^{18}O are marked by stars (the complex studied experimentally is $Fe(CO)_2(^{13}C^{18}O)_2$ [7.8]).

The situation for tetrahedral systems is similar: the pseudorotation of the JT distortions is different from that predicted by the Berry mechanism. Indeed, in the $Fe(CO)_4$ complex taken as an example [7.8, 7.9], the ground-state electronic term T is threefold degenerate and the JT problem is $T \otimes (e + t_2)$. As mentioned above, if both types of displacements, e and t_2, are active (this is determined by the corresponding vibronic constants), the epikernel of the problem is C_{2v} (Section 2.5), and this is the symmetry of the six minima for the distorted tetrahedron. The experimental data confirm these distortions: the configuration of the $Fe(CO)_4$ complex is similar to SF_4 with the two angles C—Fe—C at $\sim 145^\circ$ and $\sim 120^\circ$, respectively (Fig. 7.2).

In the Berry rotation scheme the interconversion between two C_{2v} configurations goes via the high-symmetry square-planar D_{4h} configuration or tetrahedral T_d intermediates. The latter seem to be more appropriate for $Fe(CO)_4$ in view of the relatively large angles between the bonds (compared with those of SF_4). However, the experimental data do not confirm such a pathway in the mechanism of interconversion of equivalent distorted configurations in $Fe(CO)_4$.

The pseudorotation in this system was studied experimentally by means of ligands marked by ^{13}C and ^{18}O isotopes [7.8]. If in the system $Fe(CO)_2(^{13}C^{18}O)_2$

an isomerization is induced by means of an infrared laser which excites the C—O bond, the expected Berry interconversion is that shown in Fig. 7.2(a). The observed interconversion is illustrated in Fig. 7.2(b); it does not reduce to the Berry rotations. Meanwhile, if one examines the APES of the $T \otimes (e + t_2)$ problem (Section 3.3), one can see that the isomerization observed experimentally (Fig. 7.2(b)) corresponds directly to the pathway via the lowest energy barrier between two nearest-neighbor minima of C_{2v} symmetry. As in the JT $E \otimes e$ problem for MX_5 complexes, considered above, *the pathway of the transition between two equivalent minima via the lowest energy barrier does not cross the configuration of highest symmetry*.

The difference between the PJT (Berry) and JT (non-Berry) mechanisms of pseudorotation has an even more important reason than that of energy barriers. To make this statement clear, consider the simple case of the $E \otimes b_1$ JT problem (Section 3.1). The twofold degenerate electronic E term, for instance, in square-planar systems, interacts with one JT-active coordinate $Q(b_{1g})$, resulting in two minima, at $+Q_0$ and $-Q_0$, as shown in Fig. 3.1. It is important that the electronic functions of these two minima configurations are mutually orthogonal, and therefore in the absence of additional perturbations *no transitions between these two configurations are possible*; they are strictly forbidden. If additional interactions are nonzero (e.g., the interaction with b_{2g} coordinates in the above $E \otimes b_{1g}$ problem that makes it $E \otimes (b_{1g} + b_{2g})$), then there is a nonzero probability of transitions between the two configurations via b_{2g} coordinates, but not directly along b_{1g}.

In the above-discussed JT systems the situation is much the same as in the $E \otimes b_1$ problem. Indeed, the Berry rotation in Fig. 7.2(a) is a transition between two C_{2v} minima of the adiabatic potential of the tetrahedral $T \otimes (e + t_2)$ problem. The configurations in these minima can be regarded as tetrahedra distorted, respectively, to $+Q_{0\zeta}$ and $-Q_{0\zeta}$ from the regular configuration. As in the $E \otimes b_1$ problem, the electronic wavefunctions of these two configurations are orthogonal to each other, and hence the direct transition between them is forbidden. However, *the transitions via other coordinates are not forbidden*.

In the PF_5 and SF_4 systems, discussed above, the ground state is nondegenerate and hence the electronic states in the minima are not orthogonal. If the excited state producing the instability of the ground state is also nondegenerate, there is only one coordinate of inter-minimum conversion, namely the coordinate which mixes the two states. Here the Berry mechanism is the only possible one. If the excited state is degenerate, there may be more than one coordinate of interconversion of the minima configurations, and hence both the Berry and the non-Berry mechanisms of pseudorotation are possible.

Quite a few studied cases of JT and PJT pseudorotations are discussed below in several subsections. In coordination compounds pseudorotations are sometimes called "*flexional behavior*" [7.10]. As seen from the examples considered above, in many cases the JT and PJT dynamics can be interpreted visually as a continuously changing "flexional" configuration. One of the first observations of such a behavior relates to Cu(II) compounds [7.10(*b*)]. Another kind of flexionality takes place in coordination compounds with the so-called *alterdentate ligands*; they offer to the metal ion two or more equivalent coordination sites, and hence under certain conditions the metal can resonate between them (e.g., in the alloxan radical anion [7.10(*c*)]).

With regard to experimental observation of pseudorotation, modern laser systems are able to produce pulses of a few femtoseconds in temporal width, and on this timescale nuclear motion is effectively frozen. Multiple-pulse techniques (so-called "pump–probe" experiments) utilize carefully controlled time-delays, which may be used to take snap-shots that permit one to follow nuclear dynamics. Such techniques have already been shown to be capable of detecting pseudorotation of molecules in real-time. For example, time-resolved two-photon ionization experiments indicate that in its excited B state Na_3 pseudorotates with a period of $\sim$3 ps [7.11].

An important aspect of such ultrafast dynamics experiments as applied to JT systems is that they offer direct access to pseudorotation rates. Such experiments should permit elucidation of the vibronic coupling parameters in circumstances where this is not otherwise possible. An interesting example of this may be found in the negative ions of C_{60}. As proposed in [7.12], rotational reorientation measurements involving C_{60}^{n-} ions generated electrochemically in solution should permit direct measurement of pseudorotation in these ions. The temperature dependence of these rates allows one to separate the contributions of quadratic coupling terms from linear contributions.

7.1.2 Types of JT and PJT distortions. The lone-pair effect

In the JT effect the distorted configurations are determined by the JT-active coordinates (Section 2.5). Since the JT theorem is based on perturbation theory, only relatively small deviations from the reference configuration can be predicted by these coordinates. The final symmetry of the JT-distorted system can be predicted in a general way by means of group-theoretical considerations using the *epikernel principle* [7.13] discussed in Section 2.5: *extrema points on a Jahn–Teller APES prefer epikernels; they prefer maximal epikernels to lower-ranking ones. Stable minima are to be found with the structures of maximal epikernel symmetry*.

This statement implies that, although forced to distort in order to remove the electronic degeneracy, the system prefers nuclear configurations with higher symmetry compatible with this requirement. As mentioned in Section 2.5, in this formulation the epikernel principle is related to the more general statement of Pierre Curie given in 1894 [7.14]: *the symmetry characteristic of a phenomenon is the maximal symmetry compatible with the existence of this phenomenon.* Remarkably, the JTE is the only general quantum-mechanical mechanism of breaking the (expected in classical physics) structural symmetry of molecular systems and crystals (Section 8.2.5).

If the conditions of the epikernal principle are obeyed (see below), one can predict the possible distorted configurations of the system in a given degenerate state, and vice versa, to explore the origin of the observed distorted configuration by tracing it back to the degenerate term of the reference configuration. For a system with a point-group symmetry G in the reference configuration and JT-active coordinates Γ (Table 2.3) the epikernels $E(G, \Gamma)$ can easily be found directly from the character tables of the corresponding point groups (see the Appendix). For a system with T_d symmetry and an E or T term coupled to e vibrations (the $E \otimes e$ or $T \otimes e$ problem) the epikernel is D_{2d}: $E(T_d, e) = D_{2d}$. Similarly $E(T_d, t_2) = C_{3v}, C_{2v}, C_s$; $E(T_d, e + t_2) = D_{2d}, D_2, C_{3v}, C_{2v}, C_2, C_s$. In the last case it is assumed that the e and t_2 vibrations have the same frequency, forming a fivefold degenerate JT-active space (Section 3.2). For the octahedral O_h group $E(O_h, e) = D_{4h}, C_{4v}$, $E(O_h, t_2) = D_3, C_{3v}$, and so on. These distortions are well known from the general formulation of the JT problems in Sections 3.1–3.4.

As illustrations of the epikernel principle, some specific examples may be mentioned: Ni^{2+} (d^8) and Cu^{2+} (d^9) four-coordinated complexes usually have the D_{2d} structure compatible with an electronic T term and e distortions of a tetrahedron (similar Zn^{2+} complexes have undistorted tetrahedra, but some of them may be subject to PJT distortions); $Fe(CO)_4$ exhibits C_{2v} distortions, as if resulting from a $T \otimes (e + t_2)$ problem (see the discussion below), while the $Co(CO)_4$ fragment shows trigonal geometry [7.13, 7.15].

However, in general, it is not excluded that the epikernel principle can be violated. In particular, this can take place when higher-order vibronic interaction terms in Eq. (2.7) are taken into account. But the greatest concern about the applicability of the epikernel principle arises when one tries to use it to reveal the origin of observed or numerically calculated distorted configurations when the deviation from the reference configuration is large. Indeed, in these situations the distortion may include a large amount of PJT contributions. The bottom line is that molecular configurations at the minimum of the APES may result from combined JT and PJT effects (Section 4.3) to which the

epikernel principle is not applicable. Neglecting the possible PJT contributions may lead to controversies and useless discussions [7.16, 7.17].

The PJTE is important and may contribute to solving many stereochemical problems. Consider, for example, MX_n systems, where M is a transition element. In a planar MX_4 system the typical electronic configuration of MOs is

$$\cdots (a_{1g})^2(b_{1g})^2(e_u)^4\{(b_{2g})(e_g)(2a_{1g})(2b_{1g})\}(a_{2u})^0(3a_{1g})^0 \qquad (7.7)$$

where the MOs in braces should be populated by the *d* electrons. If the ground electronic state is nondegenerate, the distortion of the square towards D_{2d} and tetrahedral T_d symmetry requires strong mixing of the ground state with the excited state by B_{2u}-type nuclear displacements. This excited state can be obtained by one of the following one-electron transitions: $e_u \rightarrow e_g$, $b_{1g} \rightarrow a_{2u}$, or $b_{2u} \rightarrow 2a_{1g}$ (b_{2u} is an inner MO). Therefore, if the e_g and $2a_{1g}$ MOs are fully occupied by *d* electrons, but the $2b_{1g}$ MO is unoccupied, the square-planar configuration is stable. In other words, low-spin MX_4 (d^8) complexes of Ni(II), Pd(II), and Pt(II) are expected to be square planar. On the contrary, high-spin d^5 and d^{10} complexes with an occupied $2b_{1g}$ MO may be unstable in the planar configuration due to the strong mixing with the low-lying $B_{2u}(2b_{1g} \rightarrow a_{2u})$ term.

Passing on to octahedral MX_6 systems, let us consider the example of XeF_6. Non-empirical calculations of the electronic structure of this molecule [7.18] show that the outer MOs are arranged in the following sequence: $(t_{2g})^6(t_{2u})^6(t_{1u})^6(t_{1g})^6(e_g)^4(a_{1g})^2(2t_{1u})^0$, with an energy gap of about 3.7 eV between the a_{1g} and t_{1u} MOs. This results in instability of the system with respect to T_{1u}-type displacements. For comparison, the calculations [7.19] performed for a similar system SF_6 yield the following sequence of MOs: $(t_{2g})^6(e_g)^4(t_{1u})^6(t_{2u})^6(t_{1g})^6(a_{1g})^0(2t_{1u})^0$. Since the energy gap between the highest occupied t_{1g} and unoccupied t_{1u} MOs, as distinct from XeF_6, is sufficiently large, the O_h symmetry configuration of SF_6 is stable with respect to odd (dipolar) displacements.

By comparison one can see that the pair of electrons in the a_{1g} MO in XeF_6 (absent in SF_6) is subject to the PJTE that produces the distortion. Since the a_{1g} MO is formed from the $(5s)^2$ electrons of the Xe atom, the distortion is called a "*lone-pair effect*" (see below). A series of investigations of the XeF_6 system, including electronographic and spectral measurements and MO LCAO calculations (see in [7.20]), confirm the PJT origin of the instability with respect to the odd T_{1u} displacements (dipolar instability). For recent more elaborate calculations of the electronic structure of this system see [7.21]. The PJT origin of the distortions in this and other systems was subjected to special investigation (Section 4.1) [7.22].

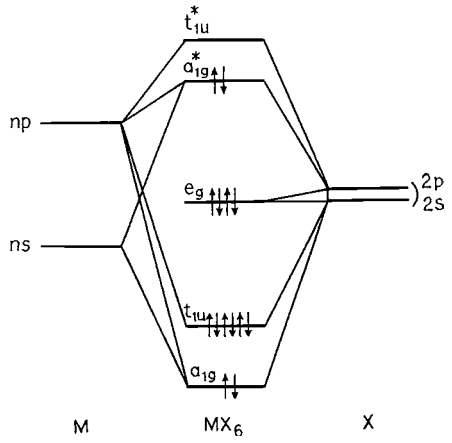

Fig. 7.3. The MO LCAO energy-level scheme for an MX_6 system with an $(ns)^2$ configuration above the closed shells of M and X. Six ligand $\sigma(sp)$ AOs together with the central atom *ns* and *np* AOs form the bonding a_{1g} and t_{1u} MOs and the non-bonding e_g MOs occupied by 12 electrons, while the antibonding MO a^*_{1g} is occupied by the two $(ns)^2$ electrons (π MOs and ligand non-bonding MOs are not indicated).

The lone-pair effect is of general importance in stereochemistry and deserves a more general treatment in view of its PJT origin. In the semiclassical approach (see [7.3], Chapter 9) the lone pairs are considered as repulsion units alongside the bond pairs, and as such they occupy a coordination place distorting the otherwise symmetric coordination polyhedron. However, in some systems the polyhedron is not distorted, in spite of the presence of a lone pair, and in these cases the latter is called an inactive or "*inert lone pair*."

Very often the lone pair originates from the $(ns)^2$ configuration, with $n = 4$, 5, 6; the post-transition elements In(I), Tl(I), Pb(II), Sb(III), Te(IV), Xe(VI), and so on are of this type. In $[SbBr_6]^{3-}$ and $[TeCl_6]^{2-}$, for example, the $(ns)^2$ lone pair is stereochemically inert (the octahedron is not distorted), whereas in XeF_6, $[InCl_6]^{5-}$, ..., the octahedron is distorted. The $(ns)^2$ pair itself is spherically symmetric and it does not cause distortions. Hence to explain the origin of distortion one has to assume that there is a strong hybridization of the *ns* states with the *np* ones, resulting in a directed lone pair [7.23, 7.24].

A more rigorous and full explanation of the origin of the lone-pair effect can be achieved based on the PJTE [7.25]. Consider the general MO LCAO scheme for an undistorted octahedral system MX_6 (Fig. 7.3) which, in the representation of local M—X bonds, has an $(ns)^2$ electron pair above the six bonding pairs. In this scheme the two *ns* electrons occupy the antibonding MO a_{1g} (π MOs and ligand non-bonding MOs are not indicated in Fig. 7.3). The ground state of the

system as a whole, A_{1g}, is nondegenerate, but the excited T_{1u} states formed by one-electron excitations $a_{1g} \rightarrow t_{1u}$ are relatively close in energy. The pseudo Jahn–Teller mixing of the ground $^1A_{1g}$ state with the excited $^1T_{1u}$ by T_{1u}-type nuclear displacements results in the instability of the ground state with respect to t_{1u} distortions (Section 4.3), provided the condition of instability (4.6) is satisfied.

This distortion is somewhat similar to the dipolar instability produced by the same A_{1g}–T_{1u} mixing in the $[TiO_6]^{8-}$ octahedron (Section 4.4), but the change from *d* electrons in Ti to *sp* electrons in the MX_6 systems under study in this section introduces significant alterations. It can be shown that in the linear approximation with respect to the vibronic coupling terms in the Hamiltonian the *s*–*p* (A_{1g}–T_{1u}) vibronic mixing ($(A_{1g} + T_{1u}) \otimes t_{1u}$ JT problem) results in a trough of minima in the space of t_{1u} distortions (Section 4.3), and only the second-order terms make the eight trigonal directions preferable.

However, this problem may be complicated by the fact that the excited T_{1u} term is degenerate and hence it is subject to the JT $T_{1u} \otimes (e_g + t_{2g})$ coupling. If the latter is taken into account, the vibronic problem as a whole is a combined PJT and JT problem $(A_{1g} + T_{1u}) \otimes (t_{1u} + e_g + t_{2g})$, meaning that there may be distortions of three types: t_{1u}, e_g, and t_{2g}. The solutions obtained in the linear approximation with respect to the vibronic coupling in Section 4.2, Eqs. (4.63)–(4.68), show that, depending on the vibronic coupling constants and the energy gap 4Δ between the ground A_{1g} and excited T_{1u} states, several possibilities arise. Assume that F_A, F, F_E, and F_T are the coupling constants to the a_{1g}, t_{1u}, e, and t_{2g} displacements, K_A, K_0, K_0^E, and K_0^T are the respective primary force constants, and the energies of the two mixing terms are $E(^1A_{1g}) = -3\Delta$, $E(^1T_{1u}) = \Delta$. Then the corresponding JT stabilization energies in units of Δ can be presented as in Eqs. (4.65):

$$h = F_A^2/4K_0\Delta \tag{7.8}$$

$$f = F^2/K_0\Delta \tag{7.9}$$

$$e = F_E^2/4K_E\Delta \tag{7.10}$$

$$t = F_T^2/3K_T\Delta \tag{7.11}$$

With these constants and the additional relation (4.67),

$$g = \begin{cases} e + h, \text{ in the space of tetragonal distortions} \\ \\ t + h, \text{ in the space of trigonal distortions} \end{cases} \tag{7.12}$$

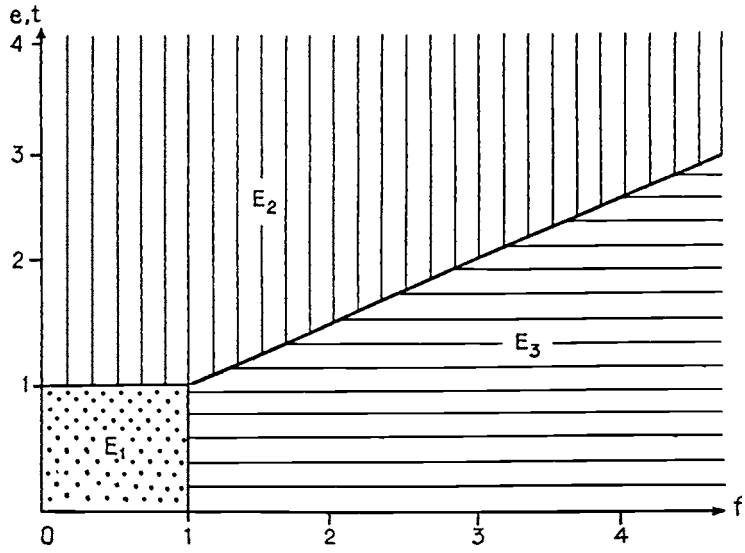

Fig. 7.4. Three domains of existence of different JT and PJT distortions in MX_6 systems with $(ns)^2$ lone pairs in each of the two e–f and t–f planes: E_1 – no distortions (inert lone pair); E_2 – combined dipolar T and either tetragonal E_g (in the e–f plane), or trigonal T_{2g} (in the t–f plane) distortions; E_3 – pure JT, either tetragonal (in the e–f plane) or trigonal (in the t–f plane) distortions.

we get the following results presented schematically in Fig. 7.4. In the region E_1 the system is undistorted. In E_2 the pure JT distortions described in Section 3.3 prevail, i.e. either tetragonal e type (three equivalent "tetragonal" minima), or trigonal t_2 type (four equivalent "trigonal" minima). In the E_3 area combined PJT trigonal (dipolar) t_{1u} and JT either tetragonal e, or trigonal (nonpolar) t_2 distortions take place. We see that if $g < 2$ and $f < g$, the minima are at the points with energies E_1 where no distortion takes place. At $g > 2$, $f < g$, and $f + 2 < 2g$, the E_2 points are the lowest and the system is under the pure JT effect with three tetragonal (if $e > t$) or four trigonal (for $e < t$) minima of the APES. Finally, if $f > g$, $f > 2$, and $f + 2 > 2g$, the minima of the APES at the points E_3 correspond to much lower symmetry of combined trigonal dipolar t_{1u} with JT either e (if $e >$ t), or nonpolar t_2 (trigonal) (when $e < t$) distortions.

All these distorted configurations of MX_6 systems with $(ns)^2$ lone-pair configurations are found in different systems (see in Section 7.6). Moreover, the combined distortions, described above, explain the origin of complicated (helicoidal) crystal structures (Section 8.2.4). In particular, in the InCl crystal ($InCl_6^{5-}$ units) both types of distortions in the E_2 area of Fig. 7.4, trigonal t_{2g} plus dipolar t_{1u}, and tetragonal e_g plus dipolar t_{1u}, are observed in two phases of the crystal, yellow and red, respectively [7.26].

The vibronic origin of the lone-pair effect in a variety of molecular systems was also confirmed by *ab initio* (DFT) calculations using a method that allows one to separate different contributions to the geometry formation and discriminate the lone-pair effect [7.27, 7.28].

Lone-pair distortions, discussed above, are dipolar-type distortions, in the sense that they lead to the formation of a dipole moment in nonpolar molecules. But dipolar distortions are not necessarily related to lone pairs: the PJT mixing of any pair of electronic states of different parities in systems with an inversion center results in softening or instability of the system with regard to odd displacements of dipolar type. In systems without an inversion center the mixing states producing dipolar distortions are easily found from symmetry considerations.

In molecular systems or local formations in crystals dipolar distortions are often produced by out-of-center displacements of the central atom, as, e.g., in $[TiO_6]^{8-}$ (Sections 4.3 and 8.3), off-center impurities in crystals (Section 8.1), out-of-plane displacement of the iron atom in hemoproteins (Section 7.6), etc.

7.1.3 JT-induced reactivity and chemical activation

The possibility to use JT distortions in prediction of specific reactivity was suggested first for octahedral complexes of Cu(II) and other similar MX_6 systems with a JT $E \otimes e$ problem and an elongated octahedron at the APES minima [7.29]. In such systems the two axial ligands are less bonded and/or more vulnerable to substitution, favoring the formation of *trans*-substituted not *cis*-substituted, CuX_4Y_2 complexes. This conclusion is fully confirmed by a lot of experimental data. There are now many known examples of JT-driven chemical transformations, some of which are cited below in this chapter.

It is obvious that the JT and PJT distortions create distinguished directions along which the molecular system is most vulnerable for transformations, thus essentially influencing the mechanisms of elementary chemical reactions. In some cases this may lead to unimolecular reactions, e.g., dissociation in the direction of the JT distortion; in other cases it just lowers the energy barrier of interaction with other molecular systems in this direction [7.2, 7.3].

In general the reaction curve in the direction of the reaction path Q is a cross-section of the APES in this direction. In the absence of vibronic coupling it can be presented as (Fig 7.5)

$$\varepsilon_0(Q) = \tfrac{1}{2}K_0Q^2 - \gamma_0 Q^3 \tag{7.13}$$

where K_0 is the force constant and γ_0 is the cubic anharmonicity constant.

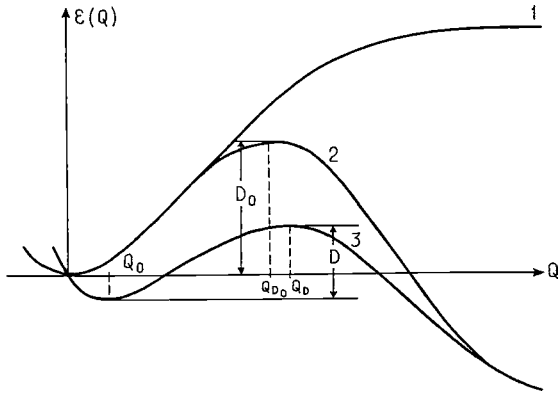

Fig. 7.5. A section of the APES of a molecular system in the direction of the reaction path Q: (1) the free molecule (*dissociation curve*); (2) the influence of another reactant (*reaction curve*); and (3) the influence of the catalyst (*activation curve*).

By differentiating, one can easily make sure that the barrier height D_0 and the coordinate of the maximum of the energy barrier Q_{0D} are

$$D_0 = K_0^3/54\gamma_0^2 \tag{7.14}$$

$$Q_{0D} = K_0/3\gamma_0 = (6D_0/K_0)^{\frac{1}{2}} \tag{7.15}$$

and it is implied that $Q = 0$ is the equilibrium position of the system.

With the vibronic coupling included a nonzero force F (the JT distorting force equal to the linear vibronic constant) occurs, and the other constants of the curve may also change: and $K = K_0 + \Delta K$ and $\gamma = \gamma_0 + \Delta\gamma$. Then

$$\varepsilon(Q) = FQ + \tfrac{1}{2}KQ^2 - \gamma Q^3 \tag{7.16}$$

with

$$D = (K - 6\gamma Q_0)^3/54\gamma^2 \tag{7.17}$$

where Q_0 is the new equilibrium position of the reactants:

$$Q_0 = (K/6\gamma)[1 - (1 + 12\gamma F/K^2)^{\frac{1}{2}}] \tag{7.18}$$

The new position of the maximum of the energy barriers is

$$Q_D = K/3\gamma - Q_0 \tag{7.19}$$

Compared with the non-perturbed values, we have

$$D/D_0 = (K - 6\gamma Q_0)^3 \gamma_0^2 / K_0^3 \gamma^2 \tag{7.20}$$

All the parameters on the right-hand side of (7.20) can, in principle, be estimated from empirical data. K and K_0 are directly related to IR spectra: $K_0 = M\omega_0^2$, and $K = M\omega^2$, where ω_0 and ω are the corresponding vibrational frequencies in the initial and vibronically rearranged states, respectively, Q_0 is the new equilibrium position (JT distortion). The coefficients in the cubic terms γ_0 and γ can be expressed by the spectroscopic anharmonicity correction ωx [7.30]: $\gamma_0/\gamma = \beta^{\frac{1}{2}}(K_0/K)^{\frac{3}{2}}(\hbar\omega/\hbar\omega_0) = \beta^{\frac{1}{2}}K_0/K$, where $\beta = \omega_0 x_0/\omega x$ is the ratio of the anharmonicity corrections in the initial and rearranged systems, respectively (usually, for small rearrangements β does not differ very much from unity).

For the change $-\Delta D$ of the activation energy due to the vibronic coupling we have

$$-\Delta D = D - D_0 = D_0[1 - (K/K_0)^3(\gamma/\gamma_0)^2] + K^2 Q_0/3\gamma - 2KQ_0^2 + 4\gamma Q_0^3 \tag{7.21}$$

The last term proportional to Q_0^3 is very small (Q_0 is of the order of 10^{-1} Å) and can be neglected. The remaining expression can be presented as two terms:

$$-\Delta D = D_0[1 - \beta(K/K_0)] + KQ_0(Q_D - Q_0) \tag{7.22}$$

where $Q_D - Q_0 = Q'_D$ is the coordinate distance between the minimum R and maximum M in the rearranged system (Fig. 7.5), and in the same notations $Q_D = (6\beta D_0/K_0)^{\frac{1}{2}} - Q_0$. The following formula may be convenient:

$$D/D_0 = (K/\beta^{\frac{1}{2}}K_0)(Q'_D/Q_{0D})^3 \tag{7.23}$$

If the quadratic vibronic interaction terms are neglected, then $K = K_0$, $\gamma = \gamma_0$, and the expression (7.25) is simplified:

$$-\Delta D = (12 D_0 E_{\mathrm{JT}})^{\frac{1}{2}} - 4E_{\mathrm{JT}} \tag{7.24}$$

where E_{JT} is the JT stabilization energy. For instance, for a system with a doubly degenerate electronic E term $E_{\mathrm{JT}} = F^2/2K_0$ (Section 3.2), and

$$-\Delta D = F(6D_0/K_0)^{\frac{1}{2}} - 2F^2/K_0 \tag{7.25}$$

The calculation of the chemical activation $-\Delta D$ for a PJT system becomes more complicated since an additional important parameter emerges: the energy gap 2Δ between the ground state and the excited states whose admixing

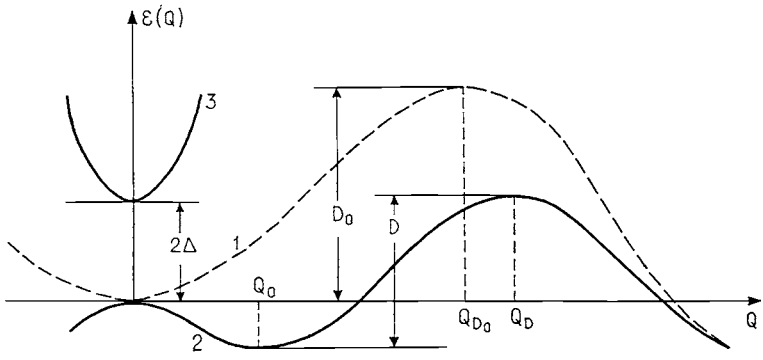

Fig. 7.6. The adiabatic potential curves along the reaction path Q without (1) and with (2) the strong PJTE that mixes the states 1 and 3. (Reprinted with permission from [7.3]. Copyright 1996 John Wiley & Sons, Inc.)

produces the instability of the ground state of the reactants. Figure 7.6 shows the two reaction curves without and with the PJTE in the direction of the reaction path Q.

If the condition of strong PJTE $K_0 < F^2/\Delta$ (Eq. (4.6)) holds, the ground state is unstable at $Q = 0$ and the adiabatic potential curve (4.4) has two minima at the points (4.7) with the curvature at the minima points given by Eq. (4.9). Taking into account the anharmonicity produced by the interacting reactants, we can present the reaction curve by adding a negative cubic anharmonicity term to Eq. (4.4) or (4.5) which, unlike (7.13) or (7.16), should be of sixth order to preserve the symmetry conditions:

$$\varepsilon(Q) = \tfrac{1}{2}K_0Q^2 - (\Delta^2 + F^2Q^2)^{\frac{1}{2}} - \gamma Q^6 \tag{7.26}$$

This curve has not been studied in detail as yet. Approximately, by expansion of the square root, we get

$$\varepsilon(Q) = \tfrac{1}{2}KQ^2 + (F^4/4\Delta^3)Q^4 - \gamma Q^6 \tag{7.27}$$

with $K = K_0 - F^2/\Delta$, and for the points of the minimum Q_0 (stable system), and maximum Q_D (activated complex) we have

$$Q_{0,D} = \{(F^4/12\Delta^3\gamma)[1 \pm (1 + 24\gamma K\Delta^6/F^8)^{\frac{1}{2}}]\}^{\frac{1}{2}} \tag{7.28}$$

with the minus sign for Q_0 and plus sign for Q_D. Note that, due to Eq. (4.6), $K < 0$, and hence for real roots of Eq. (7.28) the condition $|24\gamma K| < F^8/\Delta^6$ must be obeyed. If this inequality is sufficiently strong, we have approximately

$$Q_0 \approx (\Delta/F)[1 - K_0\Delta/F^2]^{\frac{1}{2}} \tag{7.29}$$

$$Q_0 \approx [(F^8 + 6\Delta^6 K\gamma)/6\gamma\Delta^3 F^4]^{\frac{1}{2}} \tag{7.30}$$

By substituting the parameters (7.28) or (7.29) and (7.30) into (7.26), one can estimate the activation energy modified by the PJTE:

$$D = \varepsilon(Q_D) - \varepsilon(Q_0) \tag{7.31}$$

and the chemical activation $-\Delta D = D_0 - D$ (with D_0 according to (7.14)).

Both the JT and PJT-induced activation are due to the instability of the reference configuration with respect to distortions in the direction of the active coordinate Q. In the JT systems the latter are the JT-active coordinates determined by the degeneracy of the electronic state and the vibronic coupling constants, while in the PJTE Q may be of any symmetry, depending on the excited states that contribute to the PJT distortion.

Similar chemical activation may take place in molecular systems subjected to relatively small (perturbational) electronic rearrangements. The latter include (but are not limited to) excitation, ionization, oxidation, reduction, and any other change of MO population numbers due to coordination to (interaction with) other molecular systems, e.g., in catalysis. According to the adiabatic approximation, any changes in the electronic structure of the system produces corresponding changes in the APES via the vibronic coupling, and these changes proved to be similar to that produced by the JT and/or PJT distortions shown in Figs. 7.5 and 7.6. To explore this kind of influence of vibronic coupling, the orbital vibronic constants introduced in Section 2.3 are of indispensable value [7.2, 7.31–7.34].

According to the definition (2.25), the diagonal linear orbital vibronic constant $f^i_{\Gamma^*}$ equals the force with which the electron of the ith MO distorts the nuclear framework in the direction of the symmetrized displacements Q_{Γ^*} minus the proportion of the nuclear repulsion force in this direction per electron. Consequently, the total force distorting the molecule in this direction (the integral vibronic constant $F^\Gamma_{\Gamma^*}$) is given by Eq. (2.26): $F^\Gamma_{\Gamma^*} = \sum_i q^\Gamma_i f^i_{\Gamma^*}$; q^Γ_i is the electron occupation number for the ith MO in the electronic state Γ under consideration. If the system is (statically) stable with respect to the Q_{Γ^*} displacement, then

$$F^\Gamma_{\Gamma^*} = \sum_i q^\Gamma_i f^{\,i}_{\Gamma^*} = 0 \tag{7.32}$$

The orbital vibronic constants are different for different orbitals: the nuclear repulsion per electron is independent of the MO, whereas the electron distribution changes considerably from one MO to another. In particular, in

diatomics the bonding influence of the electron of the bonding MO is stronger than the nuclear repulsion per electron, $f_R^i > 0$ (R is the interatomic distance), whereas for the antibonding orbitals the opposite is true: $f_R^i < 0$. The orbital vibronic constants are thus a measure of the MO bonding. At the point of stability these different values of orbital vibronic constants compensate each other exactly and Eq. (7.32) holds. Similarly, according to Eqs. (2.30) and (2.38) the curvature of the reaction curve in a given direction $K_{\Gamma^*}^{\Gamma}$ equals the sum of orbital contributions $k_{\Gamma^*}^i$. However, unlike the orbital vibronic constants, the orbital coefficient $k_{\Gamma^*}^i$ is determined not only by the ith MO, but also by the contribution of the vibronic mixing with other MOs. From the latter, only the free and not fully occupied MOs should be taken into account: the contributions of the mixing of any two fully occupied MOs vanish because they enter the sum for $K_{\Gamma^*}^{\Gamma}$ twice with opposite signs (see also Eq. (2.27)).

Electronic rearrangements that change the occupation numbers $q_i \to q_i + \Delta q_i$ obviously violate the condition (7.32), as well as Eqs. (2.30) and (2.38). Assuming that the rearrangement is a small perturbation, we may ignore its influence on orbital vibronic constants (as a second-order correction). If the initial system is stable, $F_{\Gamma^*} = 0$ and $K_{\Gamma^*} > 0$ (the superscript Γ of the electronic state of the system as a whole is omitted), the substitution $q_\mathrm{i} \to q_\mathrm{i} + \Delta q_\mathrm{i}$ in Eqs. (7.32), (2.30), (2.38), and (7.27) leads to the following relationships (as above, q_i and q_j are orbital occupation numbers, cf. Eq. (2.27)):

$$F_{\Gamma^*} = \sum_i \Delta q_i f_{\Gamma^*}^i \tag{7.33}$$

$$\Delta K_{\Gamma^*} = K'_{\Gamma^*} - K_{\Gamma^*} = \sum_i \Delta q_i \left(k_{\Gamma^*}^i + \sum_{j \neq i} (q_i - q_j) \left| f_{\Gamma^*}^{(ij)} \right|^2 \Big/ \Delta ji \right) \tag{7.34}$$

Hence the electronic rearrangement taken into account by the changes in orbital occupancies Δq_i results in a nonzero distorting force $F_{\Gamma^*} \neq 0$ and a change of the force constant ΔK_{Γ^*} in the direction Q_{Γ^*}, for which $f_{\Gamma^*}^i \neq 0$ (i is the index of the MO for which $\Delta q_i \neq 0$). The direction of the distorting force Q_{Γ^*} depends on the symmetry Γ_i of the ith MO: $f_{\Gamma^*}^i$ is nonzero if the symmetric product $[\Gamma_i \times \Gamma_i]$ contains Γ^*. If Γ_i is nondegenerate, $\Gamma = A_1$ is totally symmetric: electrons of nondegenerate MOs distort the molecule in the direction of totally symmetric displacements A_1, which do not change the symmetry of the system. If Γ_i is degenerate, Γ^* can be nontotally symmetric, but it should be JT active.

As for the change of the force constant ΔK_{Γ^*}, Γ^* can be of any symmetry allowed in the appropriate point group. This is seen directly from the second term in Eq. (2.38), in which $f_{\Gamma^*}^{(ij)}$ is nonzero if $\Gamma^* = \Gamma_i \times \Gamma_j$, while Γ_i and Γ_j for the ground and excited states, respectively, may belong to any symmetry representations. Similar expressions can be obtained for the change of the anharmonicity constants $\Delta\gamma$.

The occurrence of distorting forces and changes in the force constants and anharmonicities induced by electronic rearrangements via vibronic coupling directly explain the change in the reactivity of the molecule – its chemical activation. With the new constants of the rearranged electronic structure F, $K = K_0 + \Delta K$, and $\gamma = \gamma_0 + \Delta\gamma$, the rising portion of the reaction curve becomes as given in Eq. (7.16) and Fig. 7.5 with all the consequent formulas (7.17)–(7.34) for the change in activation energy of chemical reactions given above. More details with semiempirical applications of this approach are given in [7.2] and [7.3]. Examples of JT-induced reactivity in specific systems are discussed in Sections 7.3–7.6.

7.1.4 Mutual influence of ligands

There is a large amount of experimental and correlation data on the mutual influence of ligands in coordination compounds and similar effects in other molecular systems. The trend began in the mid-1920s with the works of Chernyaev [7.35], who demonstrated convincingly that in the substitution reactions with square-planar Pt(II) complexes $\mathrm{PtXYZV} + \mathrm{U} \rightarrow \mathrm{PtXYZU} + \mathrm{V}$, the ligand V to be substituted first is determined by the properties of that located in the *trans* position to V (trans-*influence*), and all the ligands can be arranged in a series of their *trans*-influence power. Later it was established that not only a *trans*-effect, but also a *cis*-effect, as well as other mutual influence of ligands is manifest in many properties of transition metal compounds, including stereochemistry and reaction kinetics.

For a review of the mutual influence of ligands in coordination compounds and its interpretation the reader is referred to Chapter 9 of [7.3]. Here we present just a brief account of the vibronic origin of this phenomenon. Indeed, the substitution of one ligand in the complex by another can be regarded as a change in the electronic structure, which produces changes in the nuclear configuration via vibronic coupling. In the previous Section 7.1.3 we discussed vibronic changes in geometry and reactivity produced by electronic rearrangement. A somewhat similar idea is used here in this section to consider the mutual influence of ligands or, more precisely, the change in mutual influence brought about by changing ligands [7.36–7.38].

Consider a homo-ligand coordination system of the type MX_n with a non-degenerate electronic ground state. Its Hamiltonian can be presented as

$$H = H_{el} + W \tag{7.35}$$

where H_{el} is the electronic part of the Hamiltonian for fixed nuclei and W is the vibronic coupling (2.14). In the stable configuration $Q_\alpha = 0$, $\alpha = 1, 2, \ldots, N$, the APES $\varepsilon(Q_\alpha)$ has a minimum with respect to all symmetrized coordinates Q_α, and in the harmonic approximation $\varepsilon(Q_\alpha)$ has the usual quadratic form (3.1).

Upon substitution of the ligand X by Y, the change of the Hamiltonian (7.35) can be presented just by adding the so-called substitution Hamiltonian H_S equal to the difference between the Hamiltonians of the $MX_{n-1}Y$ and MX_n systems:

$$H = H_{el} + W + H_s \tag{7.36}$$

Now we assume that H_S can be considered as a perturbation. This implies that changes in energy states induced by H_S are small. Then, to obtain the APES of the system, one has to consider two perturbations, H_S and W, instead of W only in the MX_n system. With the two perturbations the adiabatic potential $\varepsilon'(Q_\alpha)$ is [7.36]

$$\varepsilon'(Q_\alpha) = \varepsilon(Q_\alpha) + h_{00} - \sum_j h_{0j}^2/\Delta_{j0} - 2\sum_{\alpha,j} h_{0j} F_\alpha^{(0j)} Q_\alpha/\Delta_{j0} \tag{7.37}$$

where we denoted

$$h_{0j} = \langle 0 | H_s | j \rangle \tag{7.38}$$

and $F_\alpha^{(0j)} = \langle 0 | (\partial H/\partial Q_\alpha)_0 | j \rangle$ are the vibronic coupling constants (2.15), Δ_{ij} being the energy gaps. From Eq. (7.37) one can see that in addition to the constant terms h_{00} and $-\sum_j h_{0j}^2/\Delta_{j0}$ which shift the energy levels, there is a term which is linear in Q_α. Added to the quadratic terms in $\varepsilon(Q_\alpha)$ this linear term displaces the minimum position in the Q_α (or $-Q_\alpha$) directions, the sign of this displacement being determined by the sign of the product $h_{0j}F_\alpha^{(0j)}$. The new equilibrium positions are

$$Q_\alpha^0 = 2\sum_j h_{0j} F_\alpha^{(0j)}/\Delta_{j0} K_{\alpha 0} \tag{7.39}$$

where $K_{\alpha 0}$ is given by Eq. (2.36).

Thus the idea of vibronic mutual influence of ligands is that if one substitutes one of the ligands, the changes in the electronic structure are no longer

Table 7.1. *The parameters characterizing the distortions in σ-bonded complexes of transition and non-transition elements produced by the substitutions $MX_6 \rightarrow MX_5Y$ in octahedral and $MX_4 \rightarrow MX_3Y$ in square-planar complexes (adapted from [7.36, 7.37]; CA stands for central atom)*

Type of Complex	HOMO	LUMO	Distortion mode with $F_\alpha \neq 0$	AOs of CA with $h \neq 0$	Distortion coordinate Q_α
Octahedral					
(i)	t_{1u}	e_g^*	T_{1u}, T_{2u}	p_z, d_{z^2}	$Q_z'' = (Z_1 + Z_4)/\sqrt{2}$
(ii)	a_{1g}^*	t_{1u}^*	T_{1u}	s, p_z	$Q_z'' = (Z_1 + Z_4)/\sqrt{2}$
(iii)	e_g	a_{1g}^*	E_g	d_{z^2}, s	$Q_\vartheta'' = (2Z_1 - 2Z_4 - X_2 + X_5 - Y_3 + Y_6)/2\sqrt{3}$
Square-Planar					
(i)	e_u	b_{1g}^*	E_u	p_z, $d_{x^2-y^2}$	$Q_x = (X_2 + X_4)/\sqrt{2}$
(ii)	a_{1g}^*	e_u^*	E_u	s, p_x	$Q_x = (X_2 + X_4)/\sqrt{2}$

consistent with the previous geometry, and other ligands relax to new equilibrium positions (new minima of the APES). To find them, the matrix elements of the vibronic coupling (the vibronic constants $F_\alpha^{(0j)}$) and the substitution operator h_{0j} should be analyzed. This can be done by a model description for more specific types of systems.

Consider, for example, the MO LCAO model for octahedral σ-bonded complexes MX_6 of the following three basic types.

(i) M is a transition element, and there are 12 electrons in the valence σ MOs.
(ii) M is a non-transition element in a low oxidation state, and there are 14 electrons in the σ MOs (i.e., there is an electron lone pair).
(iii) M is a non-transition element in a higher oxidation state.

The typical MO energy-level schemes for these systems are illustrated in Fig. 7.7. By populating the one-electron MOs with the number of valence electrons available, we easily find the HOMO and LUMO. For the group (*i*) the HOMO is t_{1u}, while the LUMO is e_g^*, for (*ii*) the HOMO and LUMO are a_{1g}^* and t_{1u}^*, respectively, and so on (Table 7.1).

The next step of simplification is to restrict the treatment by considering the HOMO and LUMO only. With this constraint there is only one off-diagonal matrix element (7.38), $h_{01} = h$, only one vibronic constant $F^{(01)} = F$, and one energy gap $\Delta_{10} = \Delta$, and Eq. (7.39) simplifies significantly:

$$Q_\alpha = 2hF_\alpha/\Delta K_\alpha \tag{7.40}$$

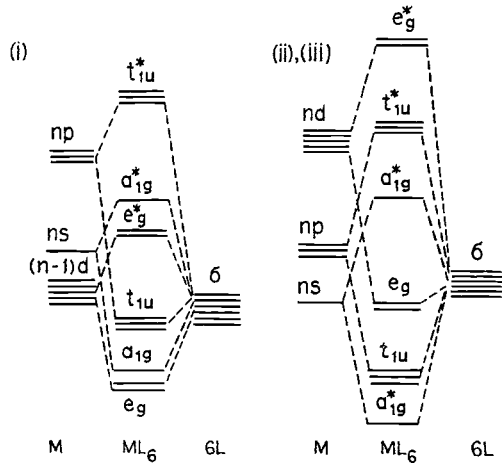

Fig. 7.7. Typical σ MO energy-level schemes for octahedral MX_6 complexes of transition (i) and non-transition (ii, iii) elements. The HOMOs are (i) t_{1u}, (ii) a^*_{1g}, and (iii) e_g (for the denotations (i), (ii), and (iii) see the text).

Thus only one type of symmetrized coordinates is nonzero, and this is determined by the selection rules. Indeed, the vibronic constant is nonzero if the product of the irreducible representations of the ground $|0\rangle$ and excited $|1\rangle$ states contains the irreducible representation of the derivative of the Hamiltonian over Q_α (Section 2.2). The representation of this derivative coincides with that of Q_α. Hence, for nonzero F_α, it is required that $\Gamma_0 \times \Gamma_1$ contains Γ_α. For instance, for complexes of the type (i), $|0\rangle$ and $|1\rangle$ are the HOMO and LUMO t_{1u} and e^*_g, respectively, and since $T_{1u} \times E_g = T_{1u} + T_{2u}$, only $Q(T_{1u})$ and/or $Q(T_{2u})$ distortions can, in principle, occur as a result of the above substitution $MX_6 \rightarrow MX_5Y$.

On the other hand, the nonzero distortion after (7.39) also requires that $h = \langle 0|H_s|1\rangle$ should be nonzero, which means that the HOMO and LUMO should contain the atomic orbital of the substituted atom. To obey this condition, if Y is on the z axis, the t_{1u} and e^*_g MOs should contain the p_z and d_z^2 orbitals of the central atom, respectively. With these orbitals F is nonzero for $Q(T_{1u})$ only, namely for its Q''_z component: $Q''_z = (Z_1 + Z_4)/\sqrt{2}$ [7.3]. This distortion displaces the two ligands in the *trans* positions 1 and 4 along the z axis (both in the same direction) with respect to the plane of the central atom and the other four ligands. In the same manner the distortion coordinates Q_α that are active in the mutual influence of ligands were obtained for other types of coordination systems as shown in Table 7.1.

Thus within the limits of the HOMO–LUMO approximation, the coordinates of mutual influence of ligands can be revealed directly without detailed

calculations. As seen from Table 7.1, the distortions induced by ligand substitution are indeed directed, and for the most part these directions are along the *trans*-coordinate (*trans*-influence), except the case (*iii*) in octahedral σ-bonded complexes of non-transition elements in high oxidation states, in which the active Q' coordinate yields both *trans* and *cis* displacements with opposite signs, the *cis*-influence being weaker by a factor of two than the *trans*-influence.

However, the picture as a whole remains incomplete, even qualitatively, without knowledge of the sign of Q_α. Following (7.40), the sign of Q_α is determined by the sign of the product hF_α, so we should analyze the signs of h and F_α in Eqs. (7.38) and (2.15), respectively. This can be done by an approximate model description of the donor properties produced by the $X \rightarrow Y$ substitution [7.36]. By applying this approach to different specific situations the authors [7.36–7.38] got a reasonable qualitative description of the origin of mutual influence of ligands in coordination compounds, including the most widespread *trans*- and *cis*-influence (see also [7.3]). For a review of further details and applications of this approach see in the book [7.37].

7.2 Linear configurations of simple molecular systems

In this section we consider molecular systems that are linear or "quasilinear" (see below) in the high-symmetry configuration, but may be unstable with regard to RT and PJT distortions.

7.2.1 Linear triatomic and tetraatomic systems

The configurations of presumably linear triatomics have been of special attention to researchers ever since the dawn of quantum mechanics (see [7.39–7.48] and references therein). According to the RTE theory (Section 4.4) the linear configuration of any molecular system is unstable with respect to bending if its electronic state is degenerate and the vibronic coupling is sufficiently large. This explains directly why the NH_2 radical is bent in the ground state H—N—H configuration (one unpaired π electron forms a doubly degenerate Π term in the linear configuration) and linear in the excited nondegenerate state. Similarly AlH_2, BH_2, HCO, H_2O^+, NO_2, etc., are bent in the ground state and linear in the lowest excited state [7.44, 7.49]. In contrast, CO_2 is linear in the ground nondegenerate state and bent in the excited state [7.39, 7.50]. A direct probe of both linear and RT (static) bent configurations of this molecule was achieved recently by means of the triple-ion-coincidence momentum technique [7.51]. The radical CH_2^+ is bent in the ground state and becomes linear upon absorption of light [7.52–7.54].

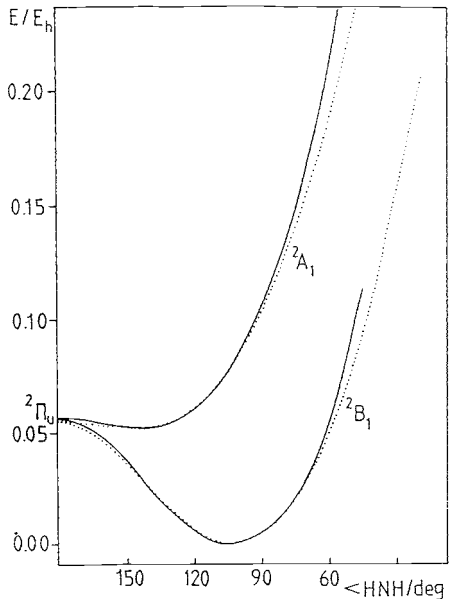

Fig. 7.8. Comparison of *ab initio* calculated effective bending potential curves for the $^2B_1$ and $^2A_1$ states of NH_2 (full lines) [7.55] with the counterparts derived by fitting experimentally observed vibronic band positions (dotted lines) [7.56]. (Reprinted with permission from [7.47]. Copyright 1995 Kluwer Academic Publishers.)

More recent numerical calculations [7.47] confirm the earlier qualitative assignments and allow one to predict the distortions quantitatively in agreement with experimental data. *Ab initio* calculations of the NH_2 radical [7.55] yield the unstable linear configuration in the degenerate $^2\Pi_u$ ground state, and the bent configuration with the ground $^2B_1$ and excited $^2A_1$ states (with H—N—H angles of 103° and 143°, respectively) in the minimum APES configurations. Figure 7.8 illustrates the calculated bending potentials of these two states in comparison with that derived from spectroscopic data [7.56].

For BH_2 the $^2\Pi_u$ state of the reference linear configuration is unstable too; the stable ground state $^2A_1$ is bent with an H—B—H angle of 129°, while the excited state $^2B_1$ is linear [7.57]. Several examples of *ab initio* calculation are given in Table 7.2. The C_3, NCO, and BO_2 molecules seem to be linear in the degenerate ground state, which may be explained by very weak RT coupling (Section 4.4). Calculations of vibronic coupling constants have not been reported.

An interesting APES with a conical intersection in the excited state was obtained by electronic-structure calculations of the HCO molecule [7.81]. Figure 7.9 illustrates a part of the complicated APES of this molecule. It confirms that conical intersections with consequent vibronic coupling effects

Table 7.2. *Calculated* ab initio *Renner–Teller distortions of linear configurations of triatomic molecules ABA and ABC (adapted from [7.47])*

System	Linear ground state	Stable state	∠A—B—A or A—B—C (degrees)	Reference	See also references
BH_2	$^2\Pi_u$	$^2A_1$ $^2B_1$	129 180	[7.57]	[7.64, 775, 7.76, 7.79]
CH_2^+	$^2\Pi_u$	$^2A_1$ $^2B_1$	141 180	[7.53, 7.54]	[7.71, 7.72]
CH_2	$^1\Delta_g$	$^1A_1$ $^1B_1$	103 137	[7.58]	[7.71, 7.72]
NH_2^+	$^1\Delta_g$	$^1A_1$ $^1B_1$	108 155	[7.59]	
NH_2	$^2\Pi_u$	$^2B_1$ $^2A_1$	103 143	[7.55]	[7.73, 7.74]
OH_2^+	$^2\Pi_u$	$^2B_1$ $^2A_1$	109 180	[7.60]	[7.73]
AlH_2	$^2\Pi_u$	$^2A_1$ $^2B_1$	118 180	[7.61]	
SiH_2^+	$^2\Pi_u$	$^2A_1$ $^2B_1$	119 180	[7.62]	
PH_2	$^2\Pi_u$	$^2B_1$ $^2A_1$	91 122	[7.63]	
SH_2^+	$^2\Pi_u$	$^2B_1$ $^2A_1$	93 128	[7.65]	
HNO^+	$^2\Pi$	$^2A'$	125	[7.66]	
HNF	$^2\Pi$	$^2A''$ $^2A'$	101 123	[7.67]	
C_3	$^1\Pi_u$	$^1B_1$, $^1A_1$	180	[7.68]	[7.77]
NCO	$^2\Pi$	$^2A'$	180	[7.69]	
BO_2	$^2\Pi_g$	$^2B_2$, $^2A_2$	180	[7.70]	
CCN	$^2\Delta$			[7.78]	
NCN	$^3\Pi_u$			[7.80]	

take place more often than it would seem at first sight. By means of numerical calculations carried out for the four lowest electronic states of HCO the authors [7.81] explained the origin of several important features of this molecule. In particular, it was shown that the *A* bands in the hydrocarbon flame are due to electronic transitions from the strongly bent configuration of the $\tilde{B}\,^2A'$ state to the ground state $X\,^2A'$.

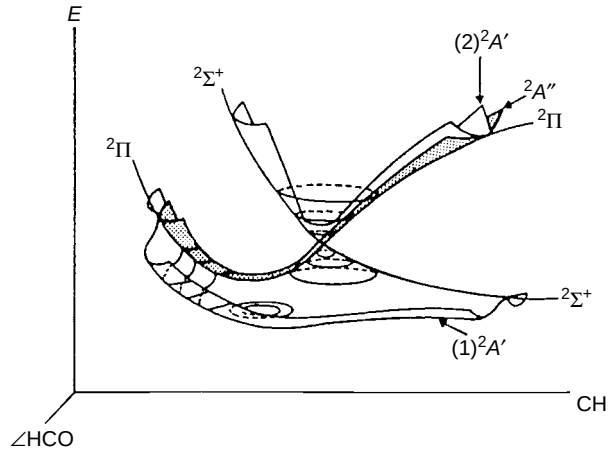

Fig. 7.9. A schematic presentation of the APES of the lowest three states of the HCO molecule; the CO bond length is kept fixed. (Reprinted with permission from [7.81]. Copyright 1979 American Institute of Physics.)

Further work on HCO may be found in [7.47, 7.82–7.84]. *Ab initio* calculations of ground and excited states confirm the presence of several conical intersections and avoided (PJT) crossings with bent configurations in the excited states due to the RTE and PJTE coupling. A full interpretation of the spectroscopic data for this system seems to remain a difficult task.

For the somewhat similar systems HNO^+ and HON^+ the RT geometry and energy levels were calculated in *ab initio* CASSCF–MRCI approximation [7.84]. In both systems the $^2\Pi$ electronic state in the linear configuration reduces to the two states X $^2A'$ and A $^2A''$ in the RT minima, in which the molecule is bent. A conical intersection arises at the crossing of the first excited $^2\Sigma^+$ state with the X $^2\Pi$ one along the collinear dissociation path $NO^+(X\ ^1\Sigma^+) + H(^2S)$. The RT and dissociation barriers are illustrated in Figs. 7.10 and 7.11. Rovibronic and rovibrational levels are also calculated in this work.

The RTE splits the APES into two branches and influences very strongly the expected spectral properties. Even for weak RT coupling when the molecule remains linear in both branches of the APES, the rotational levels split, as follows from Eqs. (5.11)–(5.16) in Section 5.1. For stronger coupling with bending instability the influence of the RTE on the spectra is much stronger. Figures 7.12 and 7.13, respectively, illustrate how the energy levels are changed by the RTE in the $^2\Pi_u$ state of BH_2 (split into X $^2A_1$ and A $^2B_1$ in the bent configuration at the minima) [7.79], and in a similar state of NH_2 [7.73]. Other studies of the RTE in triatomics were performed for CCH [7.85], HCN^+ [7.86], SO_2 [7.87], O_3 [7.88], O_3^+ [7.89], NO_2 [7.90], H_2S [7.91], Cl_2O and Cl_2O^+ [7.92].

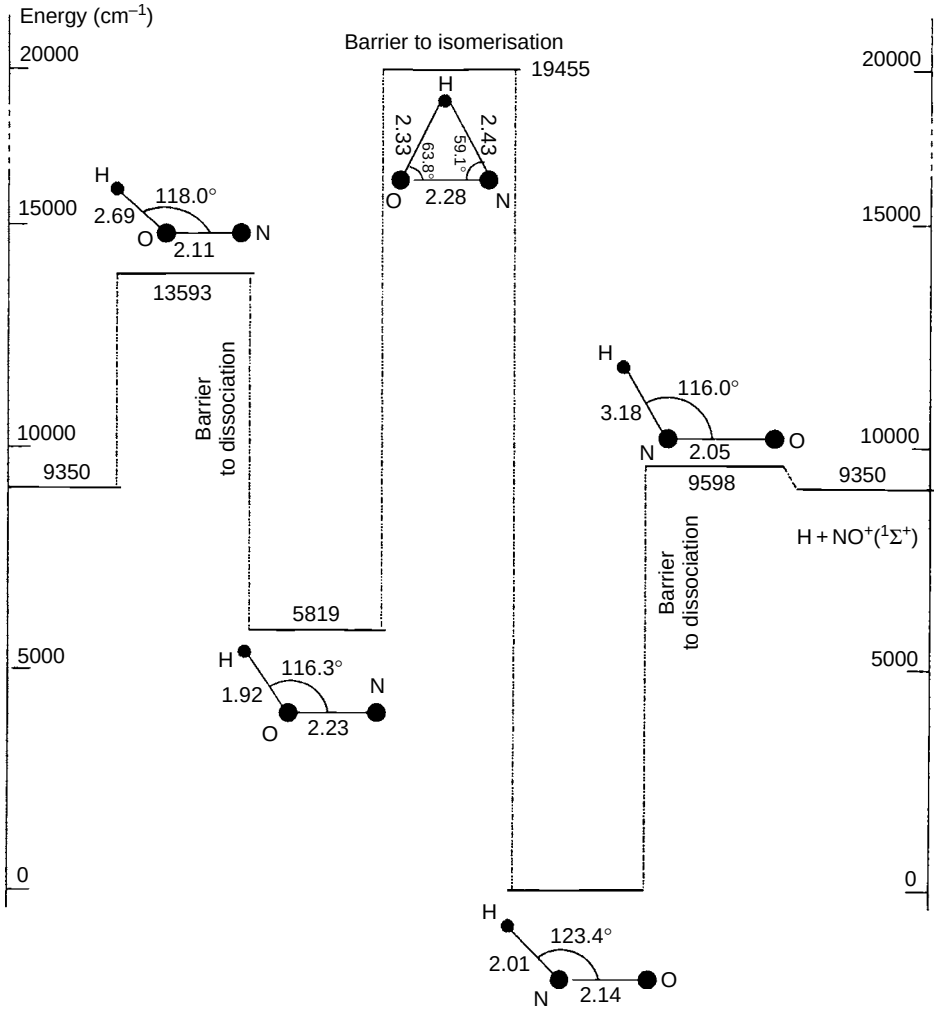

Fig. 7.10. Energy profile of the X^2A' ground state of the complex [H^+, NO]. Calculated bond lengths are shown in Bohr units with angles in degrees. (Reprinted with permission from [7.84]. Copyright 2001 Elsevier Science Publishers.)

As mentioned in Section 4.4, the RTE is not the only source of bending of the linear configuration of molecules. Another important bending force arises from the PJT mixing of the electronic state under consideration with other states of appropriate symmetry under the bending distortion. If the system is in a nondegenerate Σ state, the bending may occur due to the mixing with the excited state of Π symmetry ($\Sigma \times \Pi = \Pi$), provided the coupling is sufficiently strong and the inequality (4.6) holds. The same is true for the PJT mixing of two excited states.

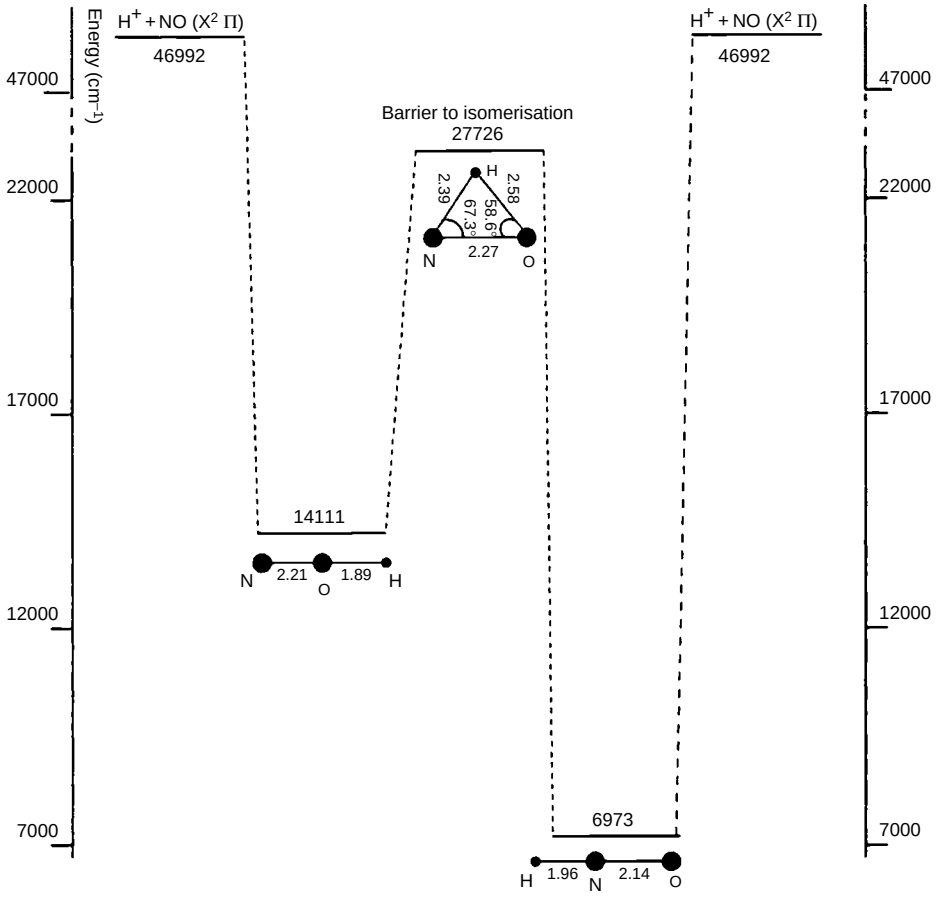

Fig. 7.11. The energy profile of the $^2A''$ state of the complex [H^+, NO]. Calculated bond lengths are shown in Bohr units with angles in degrees. (Reprinted with permission from [7.84]. Copyright 2001 Elsevier Science Publishers.)

The first investigation of such Σ–Π vibronic coupling in linear systems [7.93] was applied to the linear-to-bent transition in HCN and DCN to explain their photoelectron spectra. The solution of the PJT problem of vibronic coupling between the Σ and Π states with energies E_σ and E_π, respectively, including the two bending coordinates Q_x and Q_y ($\rho^2 = Q_x^2 + Q_y^2$) and one totally symmetric coordinate Q_g with frequencies ω and ω_g, respectively, yields the three branches of the APES given in Eqs. (4.113) and (4.114), and illustrated in Fig. 4.16 (Section 4.4) for cationic states of HCN that are most important in the photoelectron spectra. For $Q_g = 0$ and $4\lambda^2 > |E_\sigma - E_\pi|$ the lower branch of the APES is unstable in the linear configuration and has a continuum of minima forming a circle at the bottom of a trough, at which the configuration of the system is bent. In the linear HCN molecule the totally symmetric

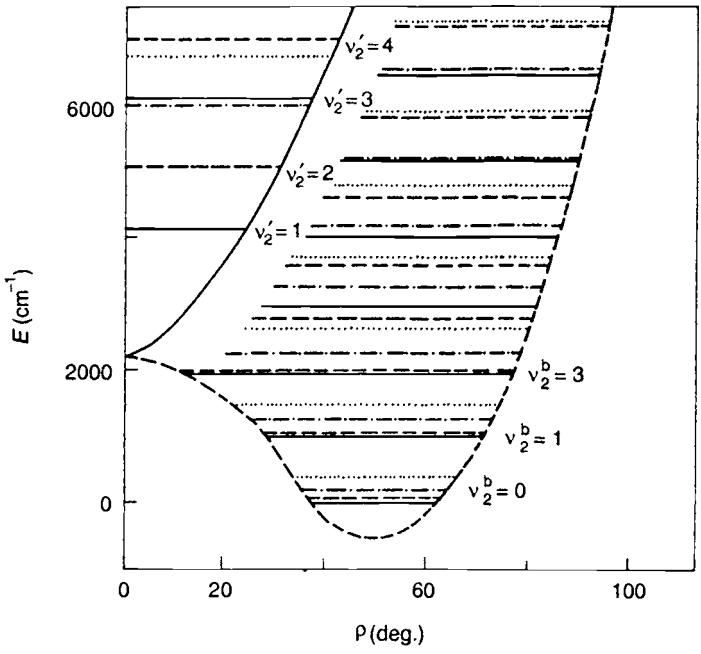

Fig. 7.12. Bending AP curves for the X $^2A_1$ and A $^2B_1$ electronic terms of the BH_2 molecule. Full horizontal lines correspond to vibronic levels with $K=0$; dashed, dashed–dotted, and dotted lines correspond to $K=1$, $K=2$, and $K=3$, respectively. Vibronic levels in the minimum are assigned in "bent" notations, while those in the upper states are labeled with the notation of the "linear" molecule. (Reprinted with permission from [7.79]. Copyright 1981 NRC Research Press.)

displacement Q_g involves H—C and C—N stretching, which play thus a significant role in the PJT coupling Σ–Π and formation of the APES.

By means of numerical calculations taking into account this complex APES, the authors [7.93] succeeded in explaining the origin and vibronic structure of the first photoelectron band at 14 eV and the excitation band at ~9 eV. The RTE in the excited (cationic) Π state is also important, but by itself it cannot explain the origin of the vibronic structure of the spectra.

For the main APES features that determine the geometry, qualitative results can be obtained with much less effort than in the above-mentioned investigations. The following example, the series of six molecular systems, two triatomics Ag_3 and I_3 and their positive (Ag_3^+, I_3^+) and negative (Ag_3^-, I_3^-) ions, is given here in somewhat more detail in order to show some of the intimate electronic transformations that accompany JT vibronic coupling effects [7.94]. There are several works devoted to these systems in which theoretical calculations [7.95–7.98] combined with femtosecond spectroscopy [7.99, 7.100] and

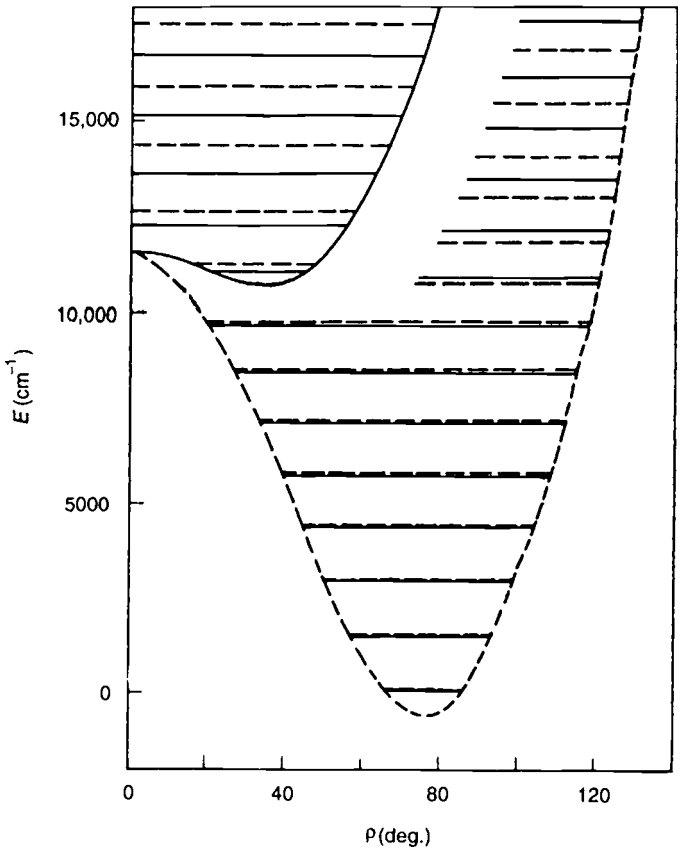

Fig. 7.13. Bending AP curves for the X $^2A_1$ and A $^2B_1$ electronic terms of the NH_2 molecule. Full horizontal lines and dashed lines correspond to vibronic levels with $K=0$ and $K=1$, respectively. (Reprinted with permission from [7.73]. Copyright 1980 Taylor & Francis Publishers.)

X-ray measurements [7.101] allow one to conclude that Ag_3^- and I_3^- are linear, while the neutral molecules and their positive ions are bent and have the configuration of mostly an isosceles triangle; Ag_3^+ is an equilateral triangle, while Ag_3 is not equilateral because of its degenerate electronic ground state resulting in the JTE (Fig. 7.14; see also Section 7.3.1).

Starting with the high-symmetry linear configuration, one can determine approximately its electronic structure and estimate the numerical values of the PJTE parameters and the curvature of the adiabatic potential with respect to the PJT-active displacements. The electronic structure of the linear configuration of all the six systems under consideration was calculated [7.94] by means of the semiempirical extended-Hückel method including self-consistency with respect to the atomic charges and electron configurations and the

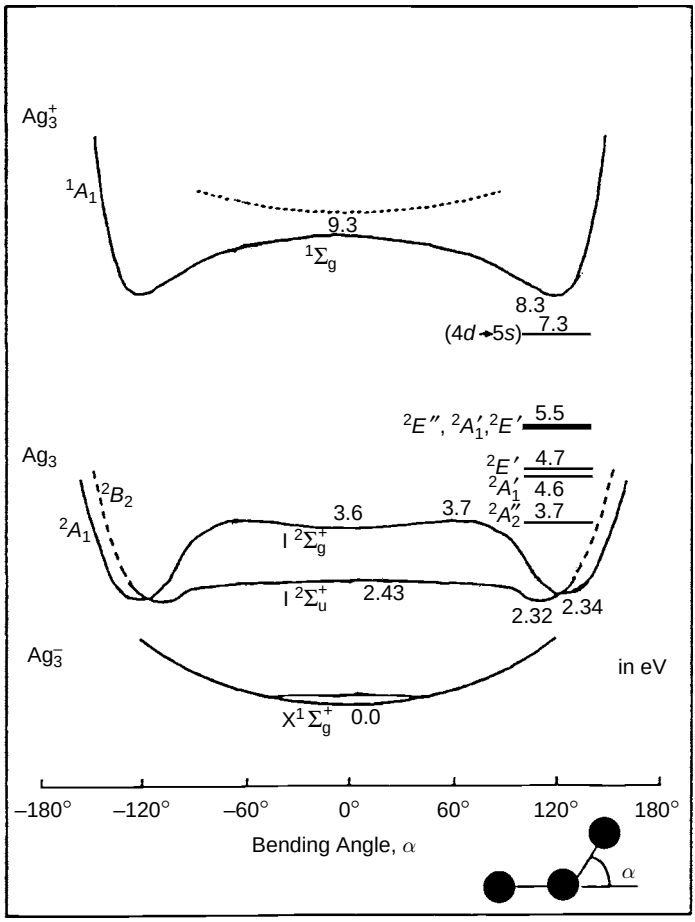

Fig. 7.14. Schematic APES cross-sections for Ag_3^-, Ag_3, and Ag_3^+ along the bending coordinate. The energies indicated are drawn from a multiplicity of sources and represent the best present knowledge of this system. (Reprinted with permission from [7.100]. Copyright 1997 American Chemical Society.)

intramolecular electrostatic effects. The method itself is not very reliable for getting exact numbers to be compared with experimental data. However, in the case under consideration the question is about large effects of orders of magnitude, which provide a general understanding of the problem and allow one to make qualitative and semiquantitative predictions, especially when series of related systems are considered in comparison to each other.

With the calculated MOs and taking the excited states as one-electron excitations $i \rightarrow \alpha$ from the occupied MO to the virtual one, the authors [7.94] estimated the constants of RT vibronic coupling $F_Q^{(ij)}$ from Eq. (4.2) (where Q is the bending coordinate and $|i\rangle$ and $|j\rangle$ are the ground and excited states), the

Table 7.3. *Contributions of the PJT coupling to the excited states* Π_u *(formed by one-electron excitation* $i \rightarrow \alpha$*) to the ground-state force constant for* Ag_3^n *systems (*$n = -1, 0, +1$*); all values are in mdyn/Å [7.94]*

$i \rightarrow \alpha$	Ag_3^-	Ag_3	Ag_3^+
$3\alpha_g \rightarrow 2\pi_u$	−7.56	−6.87	−5.08
$2\sigma_u \rightarrow 3\pi_g$	−4.43	−1.44	–
$1\pi_g \rightarrow 2\sigma_u$	–	−1.13	−1.72
$2\pi_g \rightarrow 2\sigma_u$	–	−0.42	−0.79
$K^{(v)} = \sum_i K_i^{(v)}$	−11.99	−9.86	−7.59
$K = K^{(0)} + K^{(v)}$	1.55	−0.47	−2.17

Table 7.4. *Contributions of the PJT coupling to the excited states* Π_u *(formed by one-electron excitation* $i \rightarrow \alpha$*) to the ground-state (*A_g*) force constant for* I_3^n *systems (*$n = -1, 0, +1$*); all values are in mdyn/Å [7.94]*

$i \rightarrow \alpha$	I_3^-	I_3	I_3^+
$1\pi_g \rightarrow 3\sigma_u$	−0.44	−0.38	−0.38
$1\pi_u \rightarrow 3\sigma_g$	–	−2.62	−4.96
$2\pi_u \rightarrow 3\sigma_g$	–	−0.58	−0.89
$K^{(v)} = \sum_i K_i^{(v)}$	−0.44	−3.58	−6.23
$K = K^{(0)} + K^{(v)}$	3.13	−2.71	−7.90

primary force constant $K^{(0)}$ from Eq. (4.17), the vibronic contribution to the curvature of the adiabatic potential energy from Eq. (4.13), and the full curvature with respect to Q displacements (bending distortions). Some results are shown in Tables 7.3 and 7.4.

From Table 7.3 it can be seen that all the excited states that contribute to the bending of the linear configuration are of $\sigma \Leftrightarrow \pi$ type, which confirms the general explanation of the origin of the PJT instability [7.2, 7.3] (Section 4.1): in the linear configuration the overlap of σ and π orbitals is zero, while in the bent geometry this overlap becomes nonzero, thus producing additional covalent bonding. The two main vibronic contributions arising from the PJT mixing of the ground state with two low-lying excited states Π_u formed by one-electron excitations $3\sigma_g \rightarrow 2\pi_u^*$ and $2\sigma_u \rightarrow 3\pi_g$ decrease on passing along the

series Ag_3^-, Ag_3 and Ag_3^+. The decrease of the former contribution is due to some increase of the energy gap between the ground and excited states, while for the latter it is due to the decrease of the occupation number of the $2\sigma_u$ MO (2 in Ag_3^-, 1 in Ag_3 and 0 in Ag_3^+).

Note that these two main contributions come from the excited states associated with a transfer of electron density from occupied σ to the vacant π orbital. For Ag_3 and Ag_3^+, significant contributions come also from the vibronic mixing to the two Π_u excited states formed by one-electron excitations from the occupied *d* shell to the $2\sigma_u$ MO ($1\pi_g \rightarrow 2\sigma_u$ and $2\pi_g \rightarrow 2\sigma_u$ excited states), which is partly occupied in Ag_3 and unoccupied in Ag_3^+. As a whole, the resulting negative vibronic contribution K_v decreases on going from Ag_3^- to Ag_3^+, but more slowly than the decrease of the positive K_0 values.

As a result the value of the curvature of the ground-state adiabatic potential with respect to the bending displacements is positive for Ag_3^- and negative for Ag_3 and Ag_3^+, and the increase of instability along this series will be stronger when the contribution of the 5*s* electron density (which is omitted in the estimation of K_0) is taken into account. The not very large value of K for Ag_3 is in agreement with *ab initio* calculations of its APES, which yield the $^2B_2$ ground state and bent nuclear configuration in the minima [7.95]. The excited $^2\Sigma_u^+$ state with linear geometry is close in energy to the $^2B_2$ state, and the bent $^2B_2$ state minima were found to be shallow.

For I_3, in contrast to the silver series, the negative vibronic contribution to the curvature increases in absolute value on going from I_3^- to I_3 and I_3^+ (Table 7.4). This is due to the fact that in I_3 and I_3^+ there are two new (as compared with I_3^-) excited π_u states for which the vibronic mixing to the ground state gives significant contribution to the K value. These excited states are formed by one-electron excitations from the occupied $|\pi_u\rangle$ and $|2\pi_u\rangle$ MOs to the $|3\sigma_g\rangle$ MO, which is singly occupied in I_3 and unoccupied in I_3^+.

The vibronic mixing to the excited Π_u state formed by the one-electron excitation $1\pi_g \rightarrow 3\sigma_u$, which exists in all three iodine systems, gives a relatively small contribution to the K value. Since, moreover, the positive nonvibronic contribution decreases in this series, the whole value of curvature K decreases essentially on passing from I_3^- (for which it is positive) to I_3 and to I_3^+ (for which it is negative). The contribution of the 5*s* electron density at the nuclei omitted in the estimation of K_0 just increases all these values by approximately the same amount. All the excited states of π_u symmetry active in the PJTE are associated with a transfer of electron density from occupied π to the not fully occupied σ bonds, which explains the new covalent bonding created by distortion [7.2, 7.3] (Section 4.1).

Linear tetraatomic systems were considered mainly in the theoretical treatment of the RTE [7.43]. For acetylene, the high-resolution absorption spectrum in the region of 1205–1255 Å [7.102], as well as the highly excited (Rydberg) states [7.103, 7.104], and the ground state of $C_2H_2^+$ [7.104–7.106] were analysed in this way. Further investigation of $C_2H_2^+$ and $C_2D_2^+$ in the $\tilde{X}\ ^2\Pi_u$ and $\tilde{A}\ ^2\Sigma_g^+$ states using *ab initio* CASSCF/CASPT2 electronic structure and quantum wave-packet calculations reveals a conical intersection of the $^2\Sigma_g^+$ and $^2\Pi_u$ states that explains the extremely short lifetime of the $^2\Sigma_g^+$ state with respect to fast internal conversion [7.107]. Quantum-dynamic examination of the vibronic singlet and triplet spectra in this molecule is reported in [7.108].

The RTE was also employed to analyze the ground state of tetraatomics HCCS [7.109], to predict the spectra of B_2H_2 (electronic I $^1\Delta_g$ term) [7.110, 7.111], $B_2H_2^+$ (X $^2\Pi_u$ term) [7.112–7.114], and to interpret the spectra of HCCO [7.115, 7.116] and HCCS [7.117, 7.118]. Further details on these and other RT systems can be found in [7.44–7.47, 7.118].

7.2.2 "Quasilinear" molecules

We call the system quasilinear if it has a linear framework in the high-symmetry configuration with additional hydrogen atoms that make it nonlinear. This definition is conventional, suited here for JT vibronic coupling problems, and it may differ from other definitions.

An interesting example of combined JT and PJT effects in a simple seven-atom quasilinear system is the allene radical cation $C_3H_4^+$, the final state of the photoelectron spectrum of allene. This system was investigated in a series of papers [7.119–7.124]. In its high-symmetry D_{2d} geometry $C_3H_4^+$ has a twofold degenerate ground-state ^2E term, the next term being $^2B_2$. The system has a total of 15 vibrational modes, of which 11 modes, $3A_1 + B_1 + 3B_2 + 4E$, are JT and PJT active. Since $[E \times E] = A_1 + B_1 + B_2$, three totally symmetric A_1 plus four B type, $B_1 + 3B_2$, are JT active in the distortion of this system in its electronic ^2E state. The vibronic mixing of the latter with the first excited $^2B_2$ state takes place under E vibrations ($E \times B = E$). The authors [7.119] calculated the APES using a polarized valence triple-ζ basis set with MP2 perturbation theory for correlation effects, and determined the linear vibronic coupling constants.

The numerical data for the constants of coupling to all the 11 types of vibrational modes and their vibrational frequencies are given in Table 7.5. It is seen that, as expected, the ^2E term is coupled to all the three A_1 and four B-type modes, while the four degenerate E modes participate in the PJT mixing

Table 7.5. *Constants of linear vibronic coupling of the* ^2E *and* $^2B_2$ *states to* A_1 *displacements (*$k_A(^2E)$ *and* $k_A(^2B)$*, respectively) and of the* ^2E *state to B-type displacements (*$k_B(^2E)$*, the* $^2E \otimes {}^2B_2$ *mixing (*$k(^2E \otimes {}^2B_2)$*), and the harmonic vibrational frequencies* ω *in the ground state* $^1A_1$ *for the 11 JT and PJT active modes* ν_i*,* $i = 1, 2, \ldots, 11$*, in* $C_3H_4^+$ *(all quantities in eV) [7.119]*

	$\nu_1(A_1)$	$\nu_2(A_1)$	$\nu_3(A_1)$	$\nu_4(B_1)$	$\nu_5(B_2)$	$\nu_6(B_2)$	$\nu_7(B_2)$	$\nu_8(E)$	$\nu_9(E)$	$\nu_{10}(E)$	$\nu_{11}(E)$
$k_A(^2E)$	0.321	0.294	0.180								
$k_B(^2E)$				0.103	0.308	0.114	0.371				
$k_A(^2B_2)$	−0.165	−0.445	−0.005								
$k(E \otimes B_2)$								0.245	0.237	0.133	0.044
ω	0.3945	0.1846	0.1359	0.1110	0.2944	0.2529	0.1782	0.4055	0.136	0.1069	0.0446

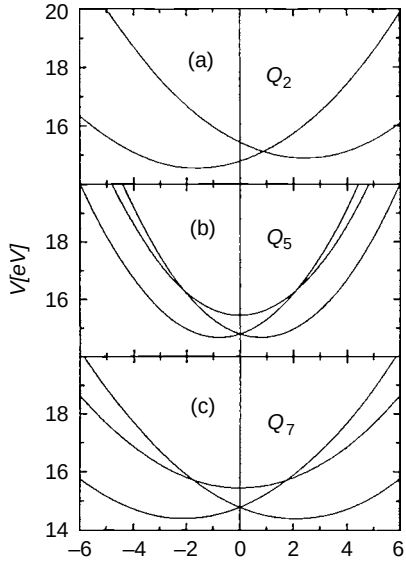

Fig. 7.15. The cross-sections of the APES for the A ^2E and $\tilde{\text{B}}$ $^2B_2$ electronic states of the allene radical cation ($C_3H_4^+$) along the dimensionless normal coordinates (a) Q_2 (A_1 symmetry), (b) Q_5 (B_2 symmetry), and (c) Q_7 (B_2 symmetry). The equilibrium geometry of allene in its electronic ground state ($^1A_1$) corresponds to $Q = 0$. (Reprinted with permission from [7.119]. Copyright 1999 American Institute of Physics.)

of the ^2E and ^2B states. The JT distortions with regard to A_1 and B_2 displacements are illustrated in Fig. 7.15. These results are essential for interpretation of the photoelectron spectra [7.119, 7.120] and provide a nice demonstration of the importance of the PJTE in the spectra of even relatively small molecules such as allene.

Note that the $C_3H_4^+$ molecule has D_{2d} symmetry in its ground state, in contrast to cumulenes with an even number of carbons, which belong to the D_{2h} symmetry. This seemingly small difference in symmetry is very important from the point of view of the JT and PJT effects: the D_{2d} molecules possess twofold degenerate electronic E states and e vibrations, whereas D_{2h} symmetry has no degenerate representations. But the E states of the D_{2d} molecules do not interact with the e vibrations. Similar to D_{4h}, D_{4d}, D_{8h},... groups, the JT-active coordinates here are b_1 and b_2 ($[E \times E] = A_1 + B_1 + B_2$) instead of e in trigonal and cubic groups (Section 3.2), so the JT problem is $E \otimes (b_1 + b_2)$ instead of $E \otimes e$. However, the degenerate e vibrations may be very significant in PJT mixing of E terms with nondegenerate A or B states.

The final states in the photoelectron spectrum of allene are those of $C_3H_4^+$, which in the D_{2d} configuration has the ground term $\tilde{\text{X}}$ ^2E followed by the terms

$\tilde{A}\,^2E$ and $\tilde{B}\,^2B_2$ (formed by one-electron excitation from the $2e$, $1e$, and $3b_2$ valence orbitals, respectively), the latter two being rather close in energy. The photoelectron band of transitions to the $\tilde{X}\,^2E$ state (around 10 eV) was shown to be JT active with respect to the b_1 vibrations ($E \otimes b_1$ problem) [7.123], but a more elaborate theoretical consideration [7.121, 7.122] shows that one of the (three) b_2 vibrations is also involved significantly.

The spectrum produced by transitions to the $\tilde{A}\,^2E$ and $\tilde{B}\,^2B_2$ terms (the $\tilde{A}\,^2E$ / $\tilde{B}\,^2B_2$ system) is more complicated. First, a small peak between the $\tilde{X}\,^2E$ band and the $\tilde{A}\,^2E$ /$\tilde{B}\,^2B_2$ system at 12.7 eV, initially considered as a correlation peak, was reconsidered [7.120] and shown to be (possibly) due to a non-Franck–Condon transition to the mixed state formed by the strong vibronic coupling between two excited states, namely, the higher component of the JT-split $\tilde{X}\,^2E$ state and the lower component of the $\tilde{A}\,^2E$ state that intersect at the dihedral angle of 144°.

The $\tilde{A}\,^2E$ /$\tilde{B}\,^2B_2$ system was subjected to a much more elaborate investigation [7.119]. In a three-state vibronic Hamiltonian, using the *ab initio*-determined vibronic coupling parameters mentioned above and numerical calculations of the vibronic energy levels and transition probabilities, they took into account both the JTE in the $\tilde{A}\,^2E$ state and the PJT coupling between this state and the $\tilde{B}\,^2B_2$ one by the degenerate e-type vibrations. The multimode (15-mode) problem was simplified by introducing effective interaction modes (Section 3.5). The results explain well this part of the photoelectron spectrum and show that, while the lower-energy part of it follows relatively well the yield of earlier calculations of the $\tilde{A}\,^2E$ band as due to the JT $E \otimes b$ coupling, the higher-energy part of the spectrum is essentially determined by the PJT coupling between the $\tilde{A}\,^2E$ and $\tilde{B}\,^2B_2$ states which affects significantly both the vibronic energy-level positions and the intensities of transitions. This part of the spectrum cannot be understood, even roughly, without involving the PJTE.

Further work on this $\tilde{A}\,^2E/\tilde{B}\,^2B_2$ system in $C_3H_4^+$ including all the 15 vibrational modes and quadratic vibronic coupling [7.124] allowed the authors to significantly improve the assignment of the observed spectral lines to the corresponding vibrational modes. Vibronic coupling was also used to explain dynamic processes in polyenes at an ultrafast timescale [7.125].

Another example with another kind of PJT treatment is provided by formaldehyde in excited states. Formaldehyde, H_2CO, is planar in the ground state, but it is nonplanar in the two lowest excited states $^1A_2$ and $^3A_2$, and has an elongated C—O bond (1.32 Å instead of 1.2 Å in the ground state) with an angle between the C—O bond and the H—C—H plane of 20° in the $^1A_2$ state

and 35° in the $^3A_2$ state [7.126]. The PJTE explains qualitatively and semiquantitatively the origin of these peculiar geometries [7.127].

According to the theory (Section 4.1) the planar configuration of H_2CO in a given electronic state may become unstable with respect to the out-of-plane bending of the C—O bond if, and only if, there are such excited (higher in energy than that under consideration) states, the vibronic coupling to which is strong enough to produce the inequality (4.6). To compare the instabilities of two excited states, singlet and triplet, a more detailed consideration of the interelectron interaction as it affects the parameters in (4.6) is given, employing the single-transition approximation (STA), as well as configuration interaction (CI) with single and double excitations [7.127].

The calculation of the excited singlet and triplet states of H_2CO for the planar configuration was performed with a simple basis set, STO-6G, which proved to be satisfactory for this problem. In the ground state the molecule is planar with C_{2v} symmetry and the following interatomic distances: R(C—O) = 1.216 Å, R(H–H) = 1.8497 Å, R(C—H) = 1.093 Å, and R(O–H) = 2.0308 Å. With this symmetry, the numerical data for the one-electron MO energy levels and wavefunctions were obtained.

The CI included all the configurations produced by single and double excitations form the HOMO $2b_2$ to the lower four MOs $2b_1(\pi_2^*)$, $6a_1(\sigma_2^*)$, $3b_2$, and $7a_1$ that remain unoccupied in the ground state; higher MOs are neglected. The energies and wavefunctions of the excited singlet and triplet states obtained in the STA and CI approximations show that the lowest excited singlet $^1A_2$ and triplet $^3A_2$ states are mainly formed by the electron excitation from the HOMO $2b_2(n_{2p}O)$ to the LUMO $2b_1(\pi_2^*)$, while the next excited states may be more implicated in the CI approximation. With these data, the ratio $K_{B1}(^3A_2)/K_{B1}(^1A_2)$ of the PJT contributions to the instability of the planar configuration (b_1 distortions) in the exited states $^1A_2$ and $^3A_2$ was estimated by Eq. (4.13) as approximately equal to 1.20 in the STA approximation and 1.31 in the CI approximation.

Thus the essentially nonplanar geometry of the formaldehyde molecule in two excited states, singlet $^1A_2$ and triplet $^3A_2$, as compared with the planar configuration in the ground state, was attributed to the vibronic PJT mixing of these states with higher excited states of appropriate symmetry: $^1B_2(2b_2 \rightarrow 6a_1)$ and $^1B_2(2b_2 \rightarrow 7a_1)$, and $^3B_2(2b_2 \rightarrow 6a_1)$ and $^3B_2(2b_2 \rightarrow 7a_1)$, respectively [7.127]. This vibronic coupling produces the b_1 distortion of the planar configuration as predicted by the general theory. It is shown also that the elongation of the C—O bond in the excited A_2 states as compared with the ground state is due to the change of the corresponding diagonal orbital vibronic constants (see Eqs. (2.24) and (2.25)) produced by the above one-electron excitation [7.127].

7.3 Trigonal molecular systems

7.3.1 Triangular triatomics X_3

Equilateral triangular triatomics X_3 are the simplest systems with a threefold axis of symmetry that allow for twofold degenerate E terms, ground or excited. In these states, if only the linear coupling is taken into account, the JT distortions result in the "*Mexican-hat*"-type APES with a conical intersection in the center (Section 3.2, Fig. 3.3). With the quadratic coupling terms included the APES acquires three equivalent minima, becoming a "*tricorn*" (Section 3.2, Figs. 3.4 and 3.5); at each of these minima the equilateral triangle is distorted to an isosceles one.

For triangular H_3 the topography of the APES was shown [7.128] to have these "tricorn" features with instability and dissociation to $H_2 + H$ along the three minima (see also [7.129–7.136] and references therein). The presence of the upper branch of the Mexican hat and the topological phase factor (Section 5.7) influence essentially the reactive scattering process of this system and its isotopomers [7.137–7.139]. Since triangular H_3 is stable in some excited states, most important are the implications of this topography in the emission spectra. The optical emission spectra of Rydberg-excited ($n = 3$) H_3 and D_3 was calculated taking into account the JTE in the ground state $(2p)1E'$. In the excited-state components $(3d)1E''$ and $(3d)3E'$ (separated by about 200 cm^{-1}), which give the most contribution to the spectrum, the JTE is very weak and hence the emission band shape is expected to be "two-humped" due to the JT APES in the ground state (Section 6.1.1). Using the time-dependent wave-packet method and the vibronic coupling theory the authors [7.137] calculated the expected emission spectra in good agreement with the experimental data. For the JTE in the H_3^+ ion see [7.134, 7.136].

The alkali trimers Li_3, Na_3, and K_3 are stable, and they possess an electronic ground-state E term in the regular triangular configuration. Quite a few papers are devoted to the JTE in these systems (see [7.140–7.161] and references therein). The first calculations of their APES beyond the HF approximation were carried out in the DFT approach (LSD approximation) using pseudo-potentials for the contribution of core electrons [7.140] (see references in [7.140] for earlier attempts). In all the three cases the equilateral triangular D_{3h} configuration is unstable, with a conical intersection at this point (as in Figs. 3.3 and 3.4 in Section 3.2) and extrema points at the three obtuse (isosceles with the apex angle larger than 60°) and three acute triangles.

In Li_3 all these extrema points have approximately the same energy, so there is a trough along which the system performs free rotations (more precisely,

Table 7.6. *Some numerical data for Li_3, Na_3, and K_3 in their minima (obtuse triangular) and saddle-point (acute triangular) configurations; R is the smallest interatomic distance, D_e is the dissociation energy, and θ is the apex angle*

Extrema points	Parameters and units	Li_3	Na_3	K_3
Minima	D_e (eV)	0.64	0.38	0.38
	R (a.u.)	5.3	6.0	7.5
	θ (degrees)	73	80	77
Saddle points	D_e (eV)	0.64	0.35	0.36
	R (a.u.)	5.1	5.8	7.2
	θ (degrees)	52	50	41

pseudorotations) as illustrated in Fig. 3.5 (Section 3.2). This means that the quadratic coupling and cubic anharmonicity is very weak to negligible (at least in this approximation of the calculations). For Na_3 the obtuse configurations are minima, while the acute ones are saddle points that form a potential barrier between the minima of about 1 kcal/mol. The K_3 system APES is qualitatively the same as in Na_3 with some different interatomic distances and angles in the distorted triangle. The ionized systems, the cations Li_3^+, Na_3^+, and K_3^+, are regular triangles in the ground state, as expected for the nondegenerate electronic states without PJT implications.

Some numerical data for alkali X_3 geometry are given in Table 7.6. Vibronic coupling constants and other JT parameters estimated based on the APES geometry and spectroscopic data are given in Table 7.7 for several of the systems with a threefold axis of symmetry and an electronic degenerate E state discussed below in this and the next sections. They include the dimensionless JT stabilization energy $D = E_{JT}/\hbar\omega_E$, the vibronic coupling constants k and g (Section 3.2, Eqs. (3.38)), as well as the JT-active ω_E and totally symmetric ω_A vibrational frequencies, where available. Because of complicated topology with conical intersections, minima, and saddle points, and approximations used in their evaluation, not all the data in this table seem to be sufficiently reliable.

Among the triangular JT X_3 systems Na_3 and Li_3 are the most studied both theoretically and experimentally. The reason is their relatively simple electronic structure and existence in the vapor phase that allows one to use jet-cooled supersonic beam expansion and optical–optical double resonance with high-resolution resonant two-photon ionization techniques [7.143]. The molecule Na_3 may be regarded as a probe system serving to provide better

Table 7.7. *Dimensionless JT stabilization energies $D = E_{JT}/\hbar\omega_E$, linear k and quadratic g vibronic coupling constants, and frequencies of E-type and totally symmetric A-type vibrations for the JT $E \otimes e$ problem in some small molecules with a threefold axis of symmetry*

System	$D = E_{JT}/\hbar\omega_E$	k	g	$\omega_E(\mathrm{cm}^{-1})$	$\omega_A(\mathrm{cm}^{-1})$	Reference
Li_3	1.92	1.96 ± 0.33	0.22 ± 0.07	278 ± 61		[7.59]
Li_3	2.53	2.25 ± 0.24	0.14 ± 0.06	250 ± 41		[7.140]
Na_3	4.50	3.00 ± 0.08	0.20 ± 0.03	97 ± 5		[7.142]
Na_3	7.56	3.89 ± 0.22	0.21 ± 0.06	98 ± 9		[7.140]
K_3	21.98	6.63 ± 2.48	0.44 ± 0.53	34 ± 11		[7.140]
$Cu_3(^2E')$	2.27	1.86	0.223	137	269.5	[7.167]
$Cu_3(^2E')$	2.48	2.23	0.154	224		[7.162]
$Cu_3(X\ ^2E')$	11.99	4.90 ± 1.41	0.35 ± 0.19	94 ± 27		[7.164]
$Cu_3(X\ ^2E')$	1.22	1.56	0.274	132	270	[7.141]
$Cu_3(^2E'')$	0.04	0.273	0.127	138.7		[7.141]
$Ag_3(^2E')$	1.86	1.93	0.25	99	121	[7.173]
$Ag_3(^2E')$	3.72	2.73		134		[7.163]
$Ag_3(^2E'')$	0.02	0.19	0.02	96	158.2	[7.173]
$Ag_3(A^4E')$	0.29	0.757	3.86	61.9	179.7	[7.176]
VF_3	0.306	0.78	0.044	784	692	[7.183]
$C_3H_3^-$	2.10	2.04 ± 0.04	0.02 ± 0.02	1410 ± 51		[7.211]
$C_3(CH_2)_3$	3.79	2.75 ± 0.03	0.04 ± 0.01	701 ± 13		[7.227]
MnF_3	3.10	2.490	0.896	810	758	[7.184]

understanding of the implications of the JT and PJT effects which can be used as a base for the treatment of more complicated systems.

To explain the high-resolution two-photon ionization spectrum of Na_3 the authors [7.143] attributed the so-called *B* band (600–625 nm) to transitions to the excited electronic state, which is an *E* state too. Figure 7.16 illustrates their identification of the spectral lines. From the experimental spectrum we see, first, a long progression composed of nearly equally spaced doublet lines at $\omega_\rho \approx 128\,\mathrm{cm}^{-1}$ which can be attributed to the higher-frequency radial vibrations in the trough along the ρ coordinate (Section 3.2, Figs. 3.3 and 3.4, Eq. (3.31)), plus a series of more closely spaced lines that represent the pseudorotation energy levels for the motions along ϕ. A series of weaker lines was attributed to the totally symmetric harmonic vibrations with $\omega_a = 137\,\mathrm{cm}^{-1}$. Ignoring the latter and considering the pseudorotations to be free rotations (i.e. neglecting the energy barrier between the minima along

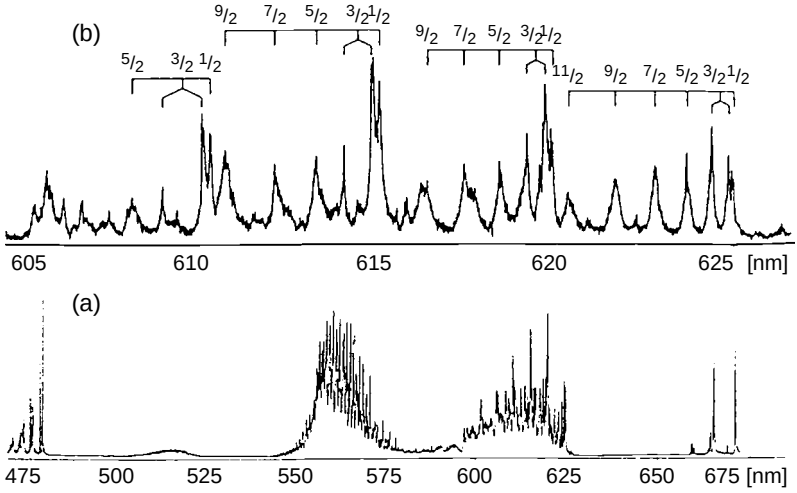

Fig. 7.16. (a) The resonant two-photon ionization spectrum of Na_3 in the visible region. Spectra in different regions are not rigorously normalized with respect to variation in dye-laser parameters. (b) Expanded spectrum of the region 600–625 nm. State labels correspond to the assignment given in [7.143]. (Reprinted with permission from [7.143]. Copyright 1986 American Physical Society.)

the ϕ coordinate), these energy levels may be approximated by the following equation:

$$E_{n,j} = (n + \tfrac{1}{2})\omega_\rho + Am^2 \tag{7.41}$$

where n is the quantum number of the high-frequency ω_ρ vibrations, $A = \hbar^2/2I$ is the constant of internal rotations with the moment of inertia $I = M\rho_0^2$, M is the reduced mass of Na_3, ρ_0 is the distortion amplitude (Eq. (3.37)), and m is the half-integer quantum number that emerges from theoretical treatment (Eq. (5.18)).

By fitting the experimental line positions with this formula and with the constants of the Hamiltonian, Eq. (3.38), the authors [7.143] got a reasonable estimation of the constants of the JT linear coupling, $k = 4.04$, and quadratic coupling, $g = 0.012$, the JT stabilization energy $E_{JT} = 1050\,cm^{-1}$, the barrier between the minima $\delta = 26\,cm^{-1}$, and the tunneling splitting $3\Gamma \approx 3$–$5\,cm^{-1}$. The authors claim that these results are the first manifestation of the half-integer quantum numbers for the pseudorotation in the exited state of Na_3 predicted by the theory (Section 3.2, Eq. (5.18)).

However, this identification of the B band in the Na_3 spectrum has been contested in a series of consequent papers [7.141, 7.151, 7.152]. First, *ab initio* calculations by the GVB CI method [7.144] revealed that the linear vibronic

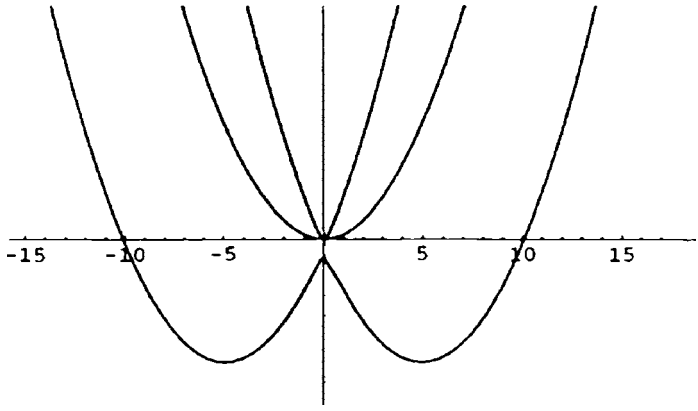

Fig. 7.17. A schematic presentation of the cross-section of the APES in the case of an $(E+A)\otimes e$ PJTE along one of the E-type coordinates (quadratic terms are neglected). The whole APES is cylindrically symmetric and allows free pseudorotation of the distorted configuration.

coupling in the excited $^2E'$ state is weak, but there is an $^2A_1$ state very close in energy above the $^2E'$ state which affects essentially the electronic transition to the latter (the E–A energy gap $\Delta \leq 100\,\mathrm{cm}^{-1}$). The pseudo JT ^2E–$^2A_1$ mixing of these two states (Section 4.2) was fully considered in [7.151], with the result that the origin of the individual transitions in the B series should be reconsidered. The authors [7.151] solved the combined problem for two models: (1) a JT model in which the PJT E–A coupling constants, linear λ and quadratic f, are neglected; and (2) a PJT model in which the JT coupling is neglected ($k=g=0$) (in both cases the E–A energy separation is neglected, $\Delta=0$). By fitting the first 19 energy levels to those observed experimentally, it was shown that the PJT model with $\lambda/\omega=3.07$ and $f/\omega=0.0045$ ($\omega=127\,\mathrm{cm}^{-1}$) is considerably better than the JT model (the root-mean-square error in the former is $1.7\,\mathrm{cm}^{-1}$ as compared with $2.3\,\mathrm{cm}^{-1}$ in the latter).

The lowest branch of the APES in this PJT system in the space of the two E-type vibrations is a trough, similar to the JT $E\otimes e$ problem one, but with a different behavior at the intersection (Fig. 7.17). Hence there are pseudorotations along the bottom of the trough. If we neglect the rather weak quadratic PJT coupling ($f=0$), the energy levels follow the equation [7.151]

$$E_{n,j} = (n+\tfrac{1}{2})\omega_\rho - (\lambda^2\omega) + (\omega^3/4\lambda^2)m^2 \tag{7.42}$$

where λ, as above, is the PJT linear coupling constant, and $m=0, 1, 2, \ldots$ is the quantum number of the free pseudorotation which, distinct from the JT case, is an integer: in the PJTE there is no wavefunction sign-change upon encircling

the origin (Section 5.7), and no superimposed condition of half-integer m values (no fractional quantization).

The PJT model was confirmed by more elaborate calculations of the relative intensities of the individual lines in comparison with the experimental values. To get the vibronic states, the E' data for the ground electronic state were re-estimated for the best fit to the APES and then refined for the PJT spectrum. The obtained parameter values are $k = 5.350$, $g = 0.076$, $\omega_\rho = 82.2\,\mathrm{cm}^{-1}$, $\omega_\phi = 49.7\,\mathrm{cm}^{-1}$ and, $\delta = 199\,\mathrm{cm}^{-1}$. The comparison of intensities obtained in the JT and PJT models confirms, again, that the latter fits the experimental data better.

An even more unambiguous experimental confirmation of integer (not fractional) quantization of the vibronic energy levels in the excited state of the B site of the Na_3 spectrum was obtained from the analysis of the rotational structure of, and Coriolis interaction in, the spectral bands [7.147]. For a triangular X_3 (symmetric-top) molecule the rotational energy is given by the following approximate expression [7.48] (see Eq. (6.46)):

$$E = BJ(J+1) - (B-C)K_c^2 \pm 2C\zeta K_c \tag{7.43}$$

where B and C are the rotational constants (the C axis is perpendicular to the X_3 plane), J and K_c are the rotational quantum numbers of a symmetric top, and the last term describes the Coriolis interactions with the Coriolis constant ζ. For a strong JTE or PJTE the effective Coriolis constant can be taken equal to the quantum number of pseudorotation m [7.48] (see also Eq. (6.48) with $p = 0$).

It emerges from Eq. (7.43) that the Coriolis splittings for different K_c values and integer m values will differ essentially from those for half-integer m. Moreover, the ground vibronic state with $m = 0$ should not be split by the Coriolis interaction, whereas it should be split in the state with fractional quantization where $m = \frac{1}{2}$. The analysis of the high-resolution rotational structure of the optical transitions [7.147] confirms the integer-quantization model. For $m = 0$ only one P and one R branch of unsplit lines are observed, while for nonzero m values both the P and R lines are split, the splitting being approximately equal to $4CK_cm$. A total of 106 transitions for $n = 1$, 2 and $m = 0$, 1, 2, 3, 4, 5 were assigned in this way. This assignment based on rotation and pseudorotation interaction (*rovibronic coupling*) was further refined taking into account more sophisticated theoretical consideration [7.152] and the influence of quadratic coupling which makes the pseudorotation not free, but hindered.

With these works the spectrum of the Na_3 system has been given one of the most detailed interpretations known so far for JT and PJT systems.

Another detailed interpretation of high-resolution spectra with essential JT implications has been performed on Li_3 [7.154–7.157]. This molecule is similar to Na_3, but has fewer electrons (meaning advantages in *ab initio* calculations) and a smaller mass (meaning a larger rotational constant that allows better resolution of the rovibronic-transition single lines). The authors used two-photon ionization of $^{21}Li_3$ with continuous-wave lasers and mass-selective detection of Li_3^+ to record rotationally resolved spectra of the electronic $A\,^2E'' \leftarrow X\,^2E'$ transition. The spectra were analyzed by optical double-resonance techniques in combination with accurate *ab initio* calculations of the APES and rovibronic energy levels of both electronic states. The APES of the E state was shown [7.155] to have the JT stabilization energy $E_{JT} = 502\,cm^{-1}$ and the barrier between the minima $\delta = 72\,cm^{-1}$ in the $\tilde{X}(1^2E')$ electronic state, yielding a ground-state tunneling splitting of $3\Gamma = 36\,cm^{-1}$, while in the $\tilde{A}(1^2E'')$ state $E_{JT} = 787\,cm^{-1}$, $\delta = 156\,cm^{-1}$, and $3\Gamma = 5\,cm^{-1}$ (for Na_3 the tunneling splittings for these two states are $0.003\,cm^{-1}$ and $0.017\,cm^{-1}$, respectively [7.154, 7.160]). The 3Γ values give the splitting between the lowest E and next A pseudorotation states.

Using an effective rovibronic Hamiltonian [7.161] the authors [7.155] analyzed the rotational structure of the rovibronic spectra and, after a series of corrections, reached an accuracy of $0.001\,cm^{-1}$. The results confirm that the ground vibronic state is E, in accordance with the Berry-phase requirement for this case of rather weak quadratic coupling (Section 5.3), and the rovibronic energy levels are described well by an effective pseudorotation Hamiltonian with five parameters: three rotational constants for the system in the minimum C_{2v} configuration plus the vibronic and Coriolis coupling constants.

Further understanding of Li_3 was achieved by investigating the origin of the hyperfine structure of the $A\,^2E'' \leftarrow X\,^2E'$ transition [7.156]. The authors calculated the vibronic density matrices that generate nonsymmetrical effective spin densities at the nuclei of the JT-distorted system, and showed how they give rise to a large variety of observed hyperfine patterns in the transition lines.

For Cu_3 calculations [7.141, 7.162–7.166] yield a Mexican-hat-type APES in the ground state with three minima and three saddle points, in accordance with general theory (Section 3.2). At the minima, the configuration Cu1–Cu2–Cu3, similar to the alkali metals, is an obtuse isosceles triangle: $R(1\text{–}2) = R(1\text{–}3) = 4.474$ a.u., $R(2\text{–}3) = 5.035$ a.u. At the saddle points the triangle is acute: $R(1\text{–}2) = R(1\text{–}3) = 4.753$ a.u., $R\ (2\text{–}3) = 4.383$ a.u. [7.162, 7.163]. The JT stabilization energy is estimated as $E_{JT} = 555\,cm^{-1}$ with a barrier between the minima $\delta = 171\,cm^{-1}$. In another estimation [7.165] $E_{JT} = 280\,cm^{-1}$ and $\delta = 59\,cm^{-1}$.

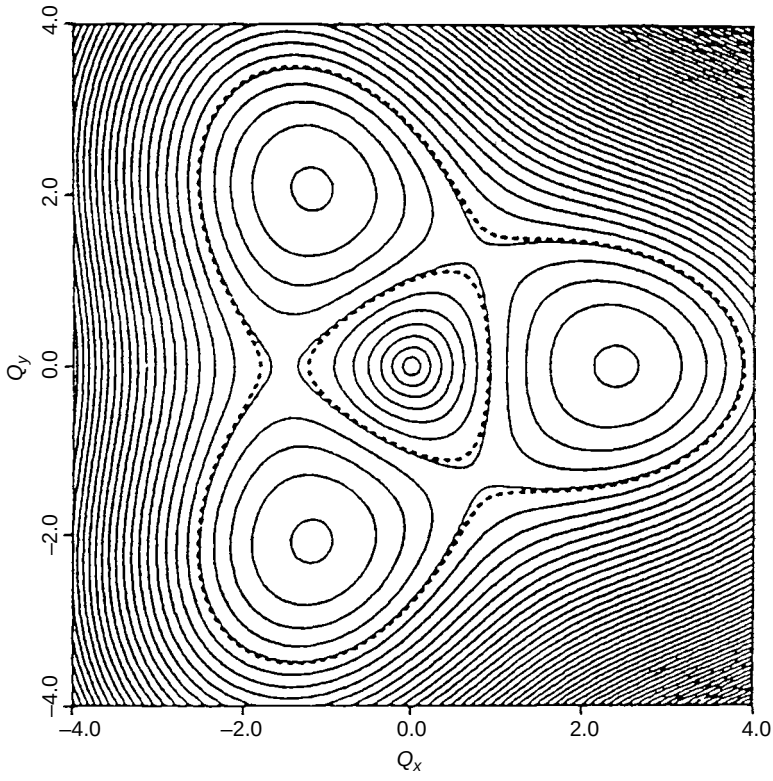

Fig. 7.18. The lower APES for the $^2E'$ state of Cu_3 obtained from the experimental spectra [7.167]. The contour spacing equals $27.4\,cm^{-1}$. Dashed contours correspond to the classical turning points of the zero-point level. (Reprinted with permission from [7.167]. Copyright 1986 American Chemical Society.)

The parameters of the APES can also be determined from comparison of the vibronic energy-level positions with those extracted from absorption, emission, two-photon ionization, and photoelectron spectra [7.141, 7.162, 7.167, 7.168]. In particular, by fitting the calculated energy levels obtained from numerical diagonalization of the Hamiltonian (3.38), the authors [7.167] obtained the APES shown in Fig. 7.18 with the numerical values of the vibronic coupling constant $k = 1.86$, $g = 0.223$, and $\omega_E = 137\,cm^{-1}$ in the D_{3h} configuration (the totally symmetric vibration frequency is estimated as $\omega_A = 269.5\,cm^{-1}$). They estimated the JT stabilization energy $E_{JT} = 305\,cm^{-1}$ and the barrier between the minima $\delta = 111\,cm^{-1}$. With the zero-point vibrations at $118\,cm^{-1}$ (higher than the barrier δ), the authors [7.167] concluded that there are no localized states in the minima in this system and the JT distortions perform hindered pseudorotations along the bottom of the trough of the Mexican hat (Section 3.2).

The JT distortions in the ground state $^2E'$ of the copper trimer Cu_3 (Fig. 7.18) and its obtuse triangular configurations in the C_{2v} minima were confirmed by ESR measurements of copper isolated in an adamantane matrix [7.169]. The spin density was found to be localized mainly on the two terminal atoms. However, the interpretation of the nature of the excited state that participates in the electronic transition observed at 5397 Å in two-photon ionization and fluorescence [7.170, 7.171] was a subject of controversial discussion [7.168]. The first assignments of this spectrum as due to $^2E'' \leftarrow\rightarrow {}^2E'$ transitions was questioned [7.168] based on a more detailed comparison with the $^2A_1' \leftarrow {}^2E'$ transition in the fluorescence spectrum, especially on the selection rules for vibronic transitions from the vibrationally excited $^2A_1'$ levels. More work on intensities may be useful to further elucidate this problem.

The APES of Ag_3 in the ground state is similar to that of Cu_3. *Ab initio* calculations [7.163] (see also [7.172, 7.173]) show that at the minima the regular triangle configuration is distorted to an obtuse isosceles triangle, $R(1\text{–}2) = R(1\text{–}3) = 5.119$ a.u. and $R(2\text{–}3) = 5.810$ a.u., while at the saddle points the triangle is acute: $R(1\text{–}2) = R(1\text{–}3) = 5.452$ a.u. and $R(2\text{–}3) = 5.054$ a.u., with $E_{JT} = 498\,cm^{-1}$, $\delta = 108\,cm^{-1}$, and $\omega_E = 134\,cm^{-1}$. The corresponding vibronic constants together with data obtained by other authors are listed in Table 7.7.

The absorption spectrum of Ag_3 was interpreted [7.174] as due to the electronic transitions $^2E'' \leftarrow {}^2E'$ with a strong JTE in the ground state $^2E'$ ($k = 1.93$, $g = 0.25$) and a much weaker JTE in the excited state $^2E''$ ($k = 0.19$, $g = 0.02$). These parameters give a good fit of the calculated vibronic level positions with those observed experimentally in the lower range of vibrational energies. However, at higher energies the calculations predict fewer bands than observed. The authors [7.174] assume that inclusion of spin–orbital interactions quenched by vibronic reduction factors (Section 5.6) may resolve the problem. No full calculations of this kind have been performed so far.

In the series Ag_3^-, Ag_3, Ag_3^+ discussed above (Section 7.2.1), the first system, Ag_3^-, is linear, Ag_3 is a JT-distorted triangle, and Ag_3^+ is a regular triangle (Fig. 7.14). This sequence of configurations was confirmed by experimental studies of ultrafast dynamics using a charge-reversal technique based on femtosecond spectroscopy [7.100]. It can be understood qualitatively by means of JTE-based argumentation: Ag_3^+ has a nondegenerate ground state and remains in a regular triangle configuration, whereas in Ag_3 the additional electron occupies the twofold degenerate $^2E'$ state in the triangular configuration, resulting in the JT distortion with an obtuse triangle and the electronic state $^2B_2$ at the APES minimum. The next electron in Ag_3^-, if occupying the

same E' orbital, enhances the distortion of the triangle, resulting in a more stable linear configuration in the state $^1\Sigma_g'$.

For Au_3 [7.163, 7.172, 7.173, 7.175–7.177] in the ground state $^2E'$ the APES is qualitatively similar to Cu_3 and Ag_3, but the quadratic coupling is very weak [7.175], $E_{JT} = 561\,cm^{-1}$ and $\delta = 45\,cm^{-1}$, so the system is assumed to perform almost free pseudorotations. The distortions at the minima are $R(1–2) = R(1–3) = 5.021$ a.u., and $R(2–3) = 5.469$ a.u., while at the saddle points $R(1–2) = R(1–3) = 5.287$ a.u. and $R(2–3) = 4.932$ a.u. Recent relativistic coupled-cluster calculations [7.177] confirmed the low energy barrier between the minima.

The complicated vibronic spectrum of the so-called $\tilde{A} \leftarrow \tilde{X}$ system (13,300–14,000 cm^{-1}) observed in Au_3 by means of resonant two-photon ionization technique [7.176] is assigned to a spin-forbidden doublet ($S = \frac{1}{2}$)-to-quartet ($S = \frac{3}{2}$) transition, $\tilde{A}\,^4E' \leftarrow \tilde{X}\,^2E'$, in which both states are JT active. The assignment is based on fitting 25 vibronic levels of the excited $\tilde{A}$ state taking into account the linear JT coupling plus spin–orbital interaction and significant anharmonicity. The combined effect of spin–orbit coupling and anharmonicity in the JT problem is considered seemingly for the first time in this paper [7.176]. More elaborate calculations [7.178] show that the spin–orbital splitting of the order of ~0.2 eV quenches the JT distortion in the ground E state of Au_3, so the system in this state retains the D_{3h} symmetry (Section 4.2). Similar calculations for Pb_3 and Pb_3^+ [7.179] show that while in Pb_3^+ the JT distortion is quenched by the spin–orbital interaction, it is not completely removed in the neutral Pb_3 system, the latter thus being subject to the JTE with a tri-minimum APES of the $E \otimes e$ problem. Regarding calculations for Al_3, see in [7.180].

7.3.2 *Trigonal tetraatomic AB_3 systems*

First consider the JT MX_3 systems with M as a transition metal and X as a halogen or hydrogen (see [7.181–7.197] and references therein). CuF_3 is one of many examples. In the ground singlet state ^1E of the planar D_{3h} configuration this system has the outer electron configuration $(e'')^4(a_1')^2(e')^2$ (note that only one of the twofold degenerate e orbitals is occupied by two electrons). At the minima of the JT $E \otimes e$ APES within the planar configuration, CuF_3 is almost T-shaped with C_{2v} symmetry and the following interatomic distances [7.181]: R_1(Cu—F1) = 1.7305 Å, R_2(Cu—F2) = R_3(Cu—F3) = 1.7148 Å, and ∠F1—Cu—F2 = ∠F1—Cu—F3 = 95.4°. The E_{JT} value and saddle-point positions are not reported. The lowest triplet excited state $^3A_2'$ has undistorted D_{3h} symmetry.

VF_3 has a $^3E''$ ground state in the D_{3h} configuration [7.182] and three equivalent C_{2v} minima on the APES, one of them at $R_1(V—F1) = 1.768$ Å, $R_2(V—F2) = R_3(V—F3) = 1.748$ Å and $\angle F2—V—F3 = 129°$. At one of the saddle points these parameters are 1.744 Å, 1.761 Å, and 112°, respectively. The JT stabilization energy is estimated as $E_{JT} = 270\,cm^{-1}$ with the barrier between the minima $\delta = 24\,cm^{-1}$.

Similar to CuF_3, the MnF_3 molecule has a strong JTE in the ground $^5E'$ state of the planar D_{3h} symmetry (for which the Mn—F distance is $R = 1.754$ Å) [7.183]. At the minima of the APES the molecule remains planar with a nearly T-shaped C_{2v} symmetry: $R(Mn—F1) = 1.735$ Å, $R(Mn—F2) = R(Mn—F3) = 1.753$ Å, and $\angle F2—Mn—F3 = 145.2°$. At the saddle point these parameters are 1.777 Å, 1.734 Å, and 105.2°, respectively. The JT stabilization energy is rather large, $E_{JT} = 2515\,cm^{-1}$, with $\delta = 726\,cm^{-1}$.

In another work on MnF_3 [7.184], similar data obtained by both gas-phase electron diffraction and quantum-chemical calculations are reported. The system has three equivalent C_{2v} minima with a distorted planar configuration and $R(Mn—F1) = 1.728 \pm 0.014$ Å, $R(Mn—F2) = R(Mn—F3) = 1.754 \pm 0.008$ Å, and $\angle F2—Mn—F3 = 143.3 \pm 2.0°$. The JT stabilization energy is calculated as 25 kJ/mol on the CASPT2 level with the barrier between the minima $\delta = 6.4$ kJ/mol. Similarly, three minima with equivalent T-shaped configurations and an energy barrier of 3.6 kcal/mol between them were found in AuF_3 by means of electron diffraction and electronic-structure calculations [7.185]. However, correctly attributing the distortions to the JTE, the authors [7.185] did not reveal the degenerate E state of the D_{3h} configuration that causes this effect: they refer to the states $^3A'$ at 46 kcal/mol (above the bottom of the minimum) and $^1A'$ at 13 kcal/mol higher, both nondegenerate; these states do not produce the JTE. Note that similar MX_3 systems in nondegenerate states (e.g., CrF_3 [7.195], FeF_3 [7.196], etc.) have regular undistorted D_{3h} symmetry (see also [7.197, 198] and Section 7.6.1).

Relativistic calculations for AuH_3, AuF_3, and $AuCl_3$ are reported in [7.186]. Other MF_3 and MH_3 systems with M = N, P, As, Sb, and Bi were studied with regard to the barrier to inversion, slightly involving the JTE and PJTE in the interpretation of the results [7.187, 7.188]. Recent relativistic calculations of EF_3 with E = I, At, and the element 117 show that sufficiently strong relativistic interactions quench the JT instability [7.189].

Several series of trihydrides MH_3 with M = Sc, Ti, V, Fe [7.190], M = Cr, Mo, W [7.191], M = Cu, Ag, Au [7.192], and M = Mn [7.193] were calculated using high-level *ab initio* methods. In the first of these series only TiH_3 and VH_3 have low-lying excited degenerate E states with small JT distortions [7.190]. In the second series all the trihydrides, CrH_3, MoH_3, and WH_3, were

found to be pyramidal with large energy barriers to inversion [7.191]. This geometry is a consequence of the PJT instability of the planar configuration with respect to A_2'' type out-of-plane displacement of the central atom due to the vibronic mixing to the excited A_2'' state, quite similar to the NH_3 molecule (see below and Section 4.1).

In the first excited state $^4E'$ of CrH_3 the JT distortion of the planar configuration is strong: R_1(Cr—H1) = 1.563 Å, R_2(Cr—H2) = R_3(Cr—H3) = 1.681 Å, and ∠H2—Cr—H3 = 167.7° in the minima (in the $^4B_2$ state), while $R_1 = 1.733$ Å, $R_2 = R_3 = 1.592$ Å, and ∠H2—Cr—H3 = 83.8° at the saddle points (in the $^4A_1$ state). The JT stabilization energy is $E_{JT} = 5246\,cm^{-1}$. In MoH_3 and WH_3 the lowest excited state is $^2E_1''$, for which the JTE is expected to be much weaker [7.191]. In the CuH_3, AgH_3, and AuH_3 series [7.192] (see also [7.186, 7.194]) the ground state in the planar configuration D_{3h} is degenerate,$^1E'$, and undergoes a relatively strong JT distortion. In the lowest excited triplet state $^3A_2'$ the planar configuration is unstable due to the PJTE; the two equivalent minima of the APES correspond to pyramidal structures, similar to those discussed for the CrH_3, MoH_3, and WH_3 series.

MnH_3 in its ground state $^5E'$ of D_{3h} symmetry is unstable subject to a strong JTE [7.193]. In the APES minima R_1(Mn—H1) = 1.6831 Å, R_2(Mn—H2) = R_3(Mn—H3) = 1.6488 Å, and ∠H2—Mn—H3 = 44.6° and $E_{JT} = 7647\,cm^{-1}$. At the saddle points $R_1 = 1.5973$ Å, $R_2 = R_3 = 1.6602$ Å, and ∠H2—Cr—H3 = 91.2°. The energy barrier between the minima is relatively high, $\delta = 1829\,cm^{-1}$, meaning that there should be localized states in the minima and tunneling splitting of their vibrational levels (Section 5.3).

Other similar series of tetraatomics studied with regard to the JTE include AH_3 and AX_3 systems with A = N, P, As, Sb, Bi; X = F, Cl, Br, I [7.27, 7.28, 7.200, 7.201]. The authors present the PJT vibronic coupling of the ground state (*s*-type state of the atom A) with the excited one (that includes *p* type of A) as an $(ns)^2$ lone-pair effect, discussed in more detail in Section 7.1.2, which is in fact an $(A + T_{1u}) \otimes t_{1u}$ PJT problem (Section 4.2). Using the DFT method of electronic-structure calculations they succeeded at separating the contribution of vibronic coupling to the optimized geometry and showed that the distortions from high-symmetry configurations are due to the PJTE (see also [7.22, 7.202]). The $E \otimes e$ problem for the NO_3 molecule was considered with a sixth-order Hamiltonian derived in a diabatic presentation (Section 2.1) [7.203].

Al_3O is an $E \otimes e$ JT system in the ground state [7.204–7.208]. High-level UB3LYP/6-31 + G* calculations [7.208] yield the following interatomic distances in the base triangle with the oxygen atom in the center: R(1—2) = 1.992 Å and R(1—3) = R(2—3) = 1.835 Å with the obtuse angle

$\phi = 163^\circ$ at the minima, and $R(1—2) = 1.780$ Å, $R(1—3) = R(2—3) = 1.950$ Å with $\phi = 91.9^\circ$ at the saddle points, the energy barrier between them being $\delta = 2.71$ kcal/mol. Note that different methods of calculation yield significantly different numerical values of these parameters [7.204–7.207]. A rather large value of the JT stabilization energy $E_{JT} = 26.4$ kcal/mol is reported in MP2/6-31G *ab initio* calculations [7.204], but the authors are not sure of this number. For Al_3O^- in the same approximation as for Al_3O [7.208] the above parameters for the ^1A state in the minimum are $R(1—2) = 2.012$ Å, $R(1—3) = R(2—3) = 1.835$ Å, and $R(1—2) = 1.735$ Å, $R(1—3) = R(2—3) = 1.987$ Å at the saddle points [7.208]. It is noticeable that in this system the lowest term in D_{3h} symmetry is nondegenerate and stable with regard to distortions (provided the PJTE is weak), but the next closest in energy is a JT ^1E term that by distortions reduces to ^1A states (in the minima), which are lower in energy than the D_{3h} states.

For JT distortions in H_3O see [7.205], while the treatment of the JTE in the hydronium ion H_3O^+ is given in [7.209].

An example of how the origin of observed geometry of small molecular systems can be explained as due to the PJT distortion of high-symmetry configurations is provided by the calculations for molecular ammonia NH_3 [7.199]. In a recent publication [7.210] a rather full vibronic-coupling investigation of the combined JTE in the $\tilde{A}\,^2E$ state and its PJT mixing with the $\tilde{X}\,^2A_1$ state is performed in order to explain the origin of photoelectron transitions to these states and the radiationless decay of the $\tilde{A}\,^2E$ state. The authors calculated the JT and PJT vibronic coupling parameters and Franck–Condon factors using high-level *ab initio* calculations, while the photoelectron band shapes were obtained with all the six vibrational degrees of freedom included. A conical intersection on the APES occurs due to the JT splitting of the $\tilde{A}\,^2E$ state; combined with the $\tilde{X}-\tilde{A}$ PJT interaction it causes a rather fast decay of this state. The PJTE seems to be most important in the origin of the photoelectron spectrum of NH_3.

The JTE in the $2E'$ state of SO_3^+ was analyzed in a model of linear coupling to two e modes, ω_3 and ω_4 [7.153]. By fitting the corresponding calculated frequencies and intensities of the electronic transitions to the experimentally determined band shapes of the photoelectron spectrum of SO_3 the authors determined that the JT stabilization energies for each of the two modes are $D_3 = E'_{JT}/\hbar\omega_3 = 0.06$, $D_4 = E''_{JT}/\hbar\omega_4 = 0.35$, the total being thus $E_{JT} = E'_{JT} + E''_{JT} = 230.4\,cm^{-1}$ ($\omega_3 = 1390\,cm^{-1}$ and $\omega_4 = 420\,cm^{-1}$).

Vibronic coupling in the radiationless decay of the $^2E'$ state of NO_3 is considered in [7.211]. The APES in Al_3H was explored in [7.180]. Distorted configurations were found in geometry optimization of Si_3C, Si_3C^+, and

Table 7.8. *Geometry parameters of CH_3O in the undistorted high-symmetry C_{3v} configuration and in the JT-distorted minima and saddle points of the APES (from [7.254])*

CH_3O	R(C—O) (Å)	R^*(C—H_b) (Å)	R(C—H_a) (Å)	∠H_b—C—O (degrees)	∠H_a—C—O (degrees)	∠H_a—C—H_b (degrees)
Undistorted, C_{3v}	1.3934	1.0892	1.0892	109.975	109.975	109.975
Distorted, C_s minimum	1.3934	1.0923	1.0876	105.3	112.3	107.9
Distorted, C_s saddle point	1.3934	1.0867	1.0904	113.4	108.3	110.3

Si_3C^-, as well as in Si_3O, Si_3O^+, and Si_3O^- [7.212], but the authors do not discuss their origin in terms of the JTE.

7.3.3 Other systems with a threefold symmetry axis

Systems with a threefold axis of symmetry which have more than four atoms possess the same E terms and $E \otimes e$ JT problems as X_3 and MX_3, but their quantitative consideration is complicated by the presence of more vibrational modes and more than one e-type vibration. The rigorous treatment of such JT systems should involve *the multimode JT problem* (Sections 3.5 and 5.5). However, in some cases the motions of the atoms outside the main triangular framework can be considered as separated from (or, alternatively, completely incorporated in) the latter, thus not participating essentially (individually) in the JT vibronic coupling (see Sections 3.5 and 5.5 for possible reduction of the multimode problem to an ideal one-mode one).

We begin with pentaatomic systems. A full theoretical investigation of the JTE in the methoxy radical CH_3O was carried out using high-level *ab initio* (CASSCF + MRCI) calculations including all the three active e-type JT modes and three totally symmetric (from a total of nine) vibrations and anharmonicities [7.213] (for earlier calculations see the references in [7.214–7.218]). This is seemingly the first multimode JT problem solved in full by *ab initio* calculations with some simplifications but without adjustable parameters. Tables 7.8–7.12 list some of the results on vibrational frequencies without and with the vibronic coupling included (both at the minima and at saddle points), the geometry parameters, the vibronic coupling constants, and anharmonicity.

Table 7.9. *Vibrational harmonic frequencies (in cm^{-1}) of A (ω_1, ω_2, ω_3) and twofold degenerate E (ω_4, ω_5, ω_6) symmetry in the undistorted configuration and at the JT minima and saddle points of CH_3O (under the distortion the e vibration splits into a′ and a″, but ω_4 does not split; the imaginary $\omega_6(a'')$ indicates the saddle point) (from [7.213])*

CH_3O	ω_1	ω_2	ω_3	$\omega_4(a')$	$\omega_4(a'')$	$\omega_5(a')$	$\omega_5(a'')$	$\omega_6(a')$	$\omega_6(a'')$
Undistorted C_{3v}	3065	1470	1070	3153	3153	1509	1509	1116	1116
JT-distorted C_s minimum	3065	1470	1070	3145	3147	1544	1512	1003	896
JT-distorted C_s saddle point	3065	1470	1070	3144	3144	1482	1542	1180	799*i*

Table 7.10. *Linear (k_i, $i=4, 5, 6$) and quadratic (g_{ii} and g_{ij}) vibronic coupling constants and anharmonicity constants (f_i) for CH_3O (in cm^{-1}) (from [7.213])*

	i						*ij*		
	1	2	3	4	5	6	45	46	56
k_i				−55.4	−216.6	−617.0			
g_{ii}				8.0	27.2	−80.3			
g_{ij}							5.4	−16.9	40.9
f_i	178	141	569						

Table 7.11. *Bilinear constants b_{ij} that couple different displacements in the quadratic approximation of the JT $E \otimes e$ problem in CH_3O (in cm^{-1}) (from [7.213])*

b_{14}	b_{24}	b_{34}	b_{15}	b_{25}	b_{35}	b_{16}	b_{26}	b_{36}
−8.1	−26.7	3.7	−15.3	106.5	−54.1	31.1	−35.5	−128.5

Table 7.12. *Dimensionless JT stabilization energies D_i and inter-minima barriers δ_i in CH_3O for three JT-active displacements $i=4, 5, 6$ (from [7.213])*

D_4	D_5	D_6	δ_4	δ_5	δ_6
0.000 16	0.010 63	0.157 16	0.005 14	0.035 89	0.145 79

In this calculation of the JT pentaatomic system there are nine vibrational frequencies, three linear coupling constants k_i, $i=4, 5, 6$, to the three JT-active e coordinates, six quadratic constants, three diagonal g_{ii}, $i=4, 5, 6$, for coupling to the three e coordinates, and three off-diagonal g_{ij}, $ij=45, 46, 56$, that represent mixed e coordinates, nine bilinear constants that stand for the terms of mixed a and e coordinates (three a coordinates mix with three e coordinates; see Eq. (3.35) for the $E\otimes(e+a)$ problem in Section 3.2), and three anharmonicity constants f_i, $i=1, 2, 3$, for the totally symmetric vibrations. It emerges from the JT stabilization energies that the mode ω_6 is most involved in the JTE, the other two e modes being less effective. In this calculation the authors reached an agreement with the experimental data within 10 percent for some vibronic energy levels.

This work on CH_3O was extended to include bilinear coupling between a_1 and e vibrational modes and analyze its influence on the spin–orbital splitting in the photoelectron spectra of CH_3O^- and CD_3O^- [7.219]. This is seemingly the first attempt to solve a quadratic PJTE problem. The most important influence of the additional terms was shown up in photoelectron spectral intensities that explain the relatively strong excitation of the JT active modes ν_5 and ν_6 and almost complete absence of the totally symmetric modes ν_2 and ν_3 (in both CH_3O and CD_3O). For a recent similar work on CH_3F see [7.217].

The methoxy radical can be regarded as a representative example of a series of CX_3Y pentaatomic systems considered with respect to the JTE in spectroscopy [7.213–7.224]. They include the methoxy family CH_3O, CH_3S, CF_3O, and CF_3S, and organometallic monomethyl radicals $MgCH_3$, $CaCH_3$, $ZnCH_3$, and $CdCH_3$. All these systems have E terms, ground or excited, $\tilde{X}\,^2E$ in the ground state of the methoxy family and $\tilde{A}\,^2E$ in the excited state of the organometallics, with three totally symmetric a_1 and three doubly degenerate e vibrations. In the organometallic series only one of the latter, ν_6, seems to be significant in the JTE, while the spin–orbital coupling is rather weak, except for $CdCH_3$. In the methoxy family the JTE is much stronger, as shown above for the methoxy radical. Table 7.13 provides some of the parameters obtained from fitting the spectroscopic data. Recently [7.224] rather full high-level *ab initio* calculations of the CH_3S molecule were performed, and it was shown that, in contrast to the CH_3O system, the spin–orbital interaction almost completely quenches the JT distortion. For more details on the JTE in this series see the review [7.218], as well as [7.213–7.224] and references therein.

Among hexaatomic systems we note first the triangular $C_3H_3^-$ [7.225] and isoelectronic $N_3H_3^{2+}$ [7.226] systems. The calculations of the latter reveal several interesting features that emerge due to the JTE in the ground $^1E'$ state of the D_{3h} configuration and the PJT vibronic coupling of this state to

Table 7.13. *JT stabilization energy E_{JT} and E-type vibration frequencies in molecular XCH_3, XCD_3, and XCF_3 systems with a JT $E \otimes e$ problem (see Tables 7.8–7.12 for more details on OCH_3)*

System	E_{JT} (cm^{-1})	ω_E (cm^{-1})	Reference
OCH_3	255.6	1065	[7.218]
OCD_3	165	825	[7.218]
SCH_3	41.1	913	[7.218]
OCF_3	20.9	465	[7.218, 7.280]
SCF_3	76.8	320	[7.218, 7.280]
$MgCH_3$	17.9	633	[7.218]
$CaCH_3$	15.3	767	[7.218, 7.221, 7.223]
$ZnCH_3$	37.5	749	[7.218, 7.221]
$CdCH_3$	14.2	710	[7.218, 7.222]

the excited $^1A_1'$ state. Both the JT $E \otimes e$ and PJT $(E' + A_1') \otimes e$ vibronic couplings contribute to the E-type distortions that make the initial equilateral triangle isosceles.

Ab initio calculations of the APES of $N_3H_3^{2+}$ with σ–π CI and a basis set of double-ζ quality including polarization functions yield $R(N_1—N_2) = R(N_1—N_3) = 1.622$ Å for the long and $R(N_2—N_3) = 1.279$ Å for the short sides of the triangle. The authors [7.226] explored also the out-of-plane bending of the hydrogen atoms (pyramidalization of the nitrogen atom). The strongest pyramidalization takes place at the distinct nitrogen N_1 with the angle $\phi_1 \approx 75^\circ$ between the N_1—H bond and the $N_1N_2N_3$ plane, the pyramidalization of the two other nitrogens being much weaker ($\phi_2 \approx -3^\circ$). The nonplanarity was attributed to the PJT π–σ mixing of the ground and corresponding excited states. This work was one of the first to explicitly involve the PJTE for the explanation of the origin of the puckering distortions in small molecules. Similar PJT explanation of out-of-plane distortions in organic compounds is given in different subsections of this section (see, e.g., puckering in Section 7.5.2).

At the saddle points the triangle is obtuse with $R(N_1—N_2) = 1.375$ Å and $R(N_2—N_3) = 1.675$ Å, and angles of pyramidalization $\phi_1 = 3.6^\circ$ and $\phi_2 = -51^\circ$. The energy barrier between the minima is rather high, $\delta = 8165\,cm^{-1}$, which means very strong quadratic coupling with all the consequences (not explored so far) for the vibronic energy spectra discussed in Sections 5.1–5.4, especially JT tunneling (Section 5.3). The JT stabilization energy is $E_{JT} \approx 20{,}390\,cm^{-1}$, seemingly the highest reported so far for JT systems. Together with the large δ value, this makes the $(NH)_3^{2+}$ system one of the most strongly influenced by

the JT $E \otimes e$-type distortions. Similar strong vibronic coupling has been found in the isoelectronic $C_3H_3^-$ [7.225]. It could be very exciting to confirm these outstanding values of JT parameters by independent calculations with the most accurate methods available now.

The two-photon absorption spectra of cyclopropane-h_6 (I) and cyclopropane-d_6 (II) were interpreted as due to electronic transitions to the JT $3s\ E'$ state [7.227]. The JTE in the latter was considered in a model with linear coupling to two active e modes, ν_{10} for the carbon-ring deformation and ν_{11} for the methylene wag mode. The linear coupling constants that fit the spectra are $k_{10} = 1.38$ and $k_{11} = 2.45$ for I, and $k_{10} = 1.48$ and $k_{11} = 2.59$ for II, the corresponding frequencies of the two modes being, respectively, $\omega_{10} = 436\,\text{cm}^{-1}$ and $\omega_{11} = 690\,\text{cm}^{-1}$ for I, and $\omega_{10} = 415\,\text{cm}^{-1}$ and $\omega_{11} = 610\,\text{cm}^{-1}$ for II. Thus the JT distortions in the excited E' state are significant, while there is no energy barrier to the pseudorotation (in this model). However, the two kinds of pseudorotations (corresponding to the two e modes) seem to be correlated. Recently [7.228] a rather full theoretical investigation of the JT interactions in the ground state $\tilde{X}\,E'$ of the cyclopropane radical cation was performed in the *ab initio* quantum-dynamic approach. The calculated photoelectron spectrum pertinent to the ionization to this state is in good agreement with the experimental data. The analysis of the results reveals a series of interesting details concerning both the JT dynamics in this system and vibronic structure of the spectrum.

In the cyclic configuration of a regular triangle of C_3H_3 (I), $C_3(CH_2)_3$ (II), and $C_3(C_3H_5)_3$ (III) the ground state $^1A_1'$ is nondegenerate, while the ionized ground state is doubly degenerate $^2E''$ followed by excited states $^2E'$ and $^2A_2''$. According to the JTE theory (Section 6.1.1), the band for the $A \rightarrow E$ transition in the photoelectron spectrum in general should be double-humped. The JT-split two-humped bands for $^1A_1' \rightarrow {}^2E''(\pi)$ and $^1A_1' \rightarrow {}^2E'(\sigma)$ were observed in the photoelectron spectrum [7.229]. Figure 7.19 shows the second band $^1A_1' \rightarrow {}^2E'(\sigma)$ for all the three compounds mentioned above. This assignment is confirmed by MINDO/3 calculations. Three equivalent JT minima were obtained in an earlier work [7.230] on the somewhat similar system $Au(CH_3)_3$ by means of extended Hückel calculations.

7.4 Distorted tetrahedral and square-planar systems

7.4.1 Tetraatomic X_4 and pentaatomic MX_4 systems

The simplest tetraatomic (X_4) JT system H_4^+ was shown by calculations [7.231–7.233] to be unstable in both high-symmetry configurations, tetrahedral

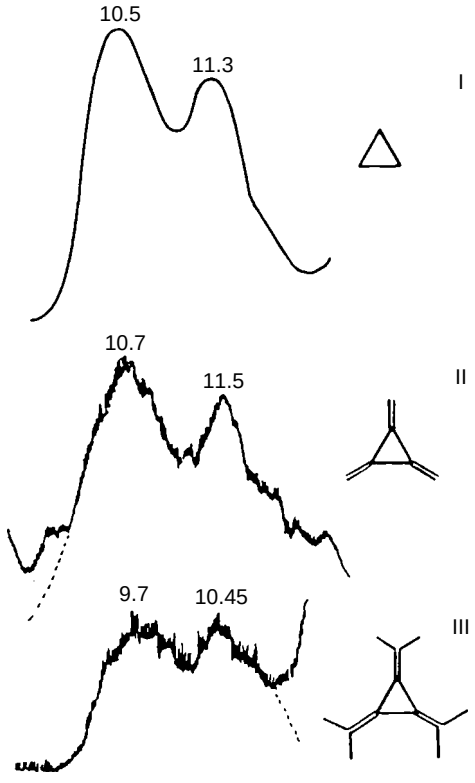

Fig. 7.19. The JT splitting of the $^1A_1' \rightarrow {}^2E'(\sigma)$ band in the photoelectron spectra of C_3H_3 (I), $C_3(CH_2)_3$ (II), and $C_3(C_3H_5)_3$ (III) (numbers are in eV). (Reprinted with permission from [7.229]. Copyright 1978 Verlag Helvetica Chimica Acta AG.)

T_d and planar D_{4h}, in accordance with the JTE for their ground T_2 and E states, respectively. *Ab initio* QCISD calculations with a 6-211G** basis set yield a planar C_{2v} ground state like $H_3^+ + H$ [7.233] (H_3^+ is an isosceles triangle).

Three tetrahedral systems, P_4, As_4, and Sb_4, have a doubly degenerate ^2E term in the final ionized states P_4^+, As_4^+, and Sb_4^+ of the photoelectron spectra. The ionized systems are thus JT unstable and subject to the $E \otimes e$ problem [7.234–7.238]. By solving the vibronic coupled equations (2.6) by means of direct diagonalization of the Hamiltonian with a two-dimensional oscillator basis set, the authors [7.234] revealed the parameters of vibronic coupling for P_4^+ by fitting the results of expected photoelectron transitions to this state with the experimental data. In this way they obtained (in eV) $E_{JT} = 0.65$, $k = 0.22$, $g = 0.0004$. For As_4^+ and Sb_4^+ in the linear coupling approximation the JT stabilization energies are 0.84 eV and 1.4 eV, respectively.

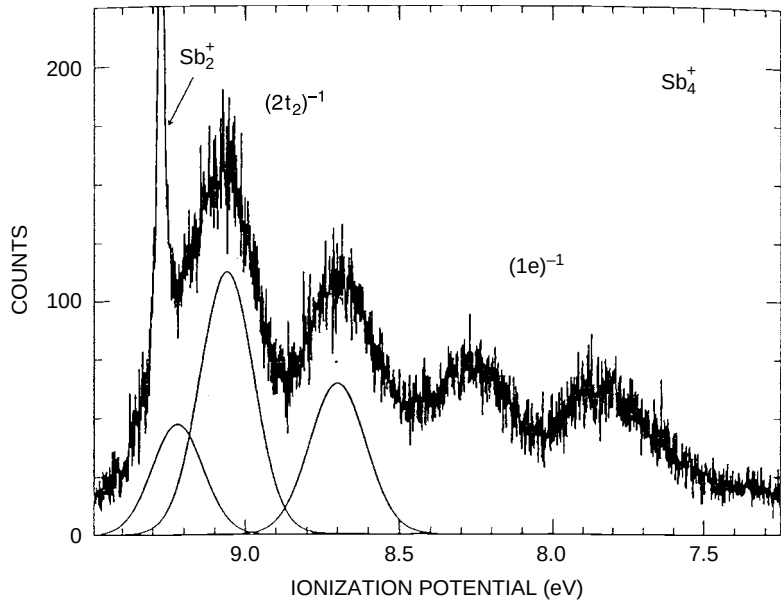

Fig. 7.20. The $(1e)^{-1}$ and $(2t_2)^{-1}$ bands of the P_4^+ photoelectron spectrum. Three component functions are drawn to show the three components in the $(2t_2)^{-1}$ bands. (Reprinted with permission from [7.235]. Copyright 1990 American Institute of Physics.)

Alongside the ^2E ground state the next one $^2T_2$ (formed by ionization of the $2t_2$ orbital) is important in the photoelectron spectrum of these X_4^+ systems [7.235]. Figure 7.20 shows the general band system in the region of transitions from the nondegenerate $^1A_1$ state of neutral P_4 to the ground state $^2E\,(1e^{-1})$ of P_4^+ and to its excited state $^2T_2(2t_2^{-1})$. The band shapes directly follow the predictions of the JTE theory (Section 6.1.1): the band of the $A_1 \rightarrow E$ transition is two-humped, while that of the $A \rightarrow T$ transition has three humps. The separations between the component bands are directly related to the strengths of the JT coupling.

Much fuller information is contained in the high-resolution spectrum [7.235]. For the ^2T state, as distinguished from the E state, the spin–orbital interaction may be important. It was shown [7.235] that, as expected, the spin–orbital interaction is most significant in Sb_4^+ and less effective in P_4^+. Note that the JTE reduces the spin–orbital interaction by the vibronic reduction factors (Section 5.6). However, there is no full treatment of the combined JT and spin–orbital interaction in these systems as yet.

The P_4^+ system was reconsidered [7.236] taking into account that the excited $^2T_2$ state in the tetrahedral configuration is close in energy to the ground ^2E state and contributes significantly to the distortion of the system in the ground

state via the PJTE. *Ab initio* SCF calculations performed on this system [7.236] reveal a rather complicated APES with a variety of conical intersections. The P_4^+ ^2E-term JT parameters from Eq. (3.38) are (in eV) $k = 0.24$, $g = -6.6 \times 10^{-3}$ and $\omega_E = 0.045$ (the latter is taken from experimental data). For the $^2T_2$ term ($T \otimes (e + t_2)$ problem) the linear vibronic coupling constants to e and t_2 vibrations are $\mu_e = 0.005$ and $\mu_r = 0.14$, respectively, with $\omega_t = 0.0577$ eV. The authors [7.236] included also the coupling to the totally symmetric vibrations (Section 3.2) that yields the coupling constants $k_g^E = -0.09$ and $k_g^t = -0.05$. The pseudo JT ^2E–$^2T_2$ mixing between the two JT terms (making the overall problem $(E + T) \otimes (a + e + t_2)$) emerged with the vibronic coupling constant $\nu = 0.12$ which is of the same order of magnitude as the JT coupling with the e and t_2 manifolds separately. It was shown [7.236, 7.237] that with these parameters, dynamic calculations using a large basis set of harmonic oscillator states explain well the observed photoelectron spectra of P_4. While the gross features of the band shape can be revealed in the simpler model of the JT coupling considered above [7.234, 7.235], the PJT vibronic mixing of the ^2E and ^2T electronic states contributes substantially to the fine structure of the spectrum.

In spite of strong JT coupling in the $E \otimes e$ problem of the P_4^+, As_4^+, and Sb_4^+ ions, high-energy peaks (Slonczewski resonances, Section 5.2) are not seen in the high-resolution photoelectron spectrum. The reason for this fact was the subject of a special investigation [7.238], and it was shown that these resonances are quenched by the breathing mode, the coupling to the totally symmetric vibrations that produce the $E \otimes (e + a_1)$ problem instead of $E \otimes e$ (Section 3.2). Recently [7.240] the reduced forms P_4^- and P_4^{2-} were also considered, and it was shown that the degeneracy produced by the excess electrons results in strong activation of the P—P bond with respect to cleavage.

Pu_4 was shown [7.239] to be unstable in the tetrahedral T_d configuration; its most stable state is ^2A_g (C_{2h}) with rhombic symmetry, which may be regarded as the state in one of the minima of the distorted D_{4h} configuration of the system in a degenerate E state. A similar rhombic D_{2h} geometry is predicted for B_4^+ [7.16], which is JT unstable in both T_d and D_{4h} symmetry. The discussion [7.17] about the JT origin of the distortion and the electronic state in the minimum of the APES in this system, on whether it emerges from the distorted tetrahedron or from the square-planar configuration seems to be pointless. Indeed, the JTE predicts possible small distortions from configurations with degenerate terms but, strictly speaking, in general there is no direct reversal of this statement: in many cases distortions (especially large distortions) cannot be unambiguously attributed to *just one* type of JTE from a given configuration, mainly because of a possible PJTE. Large deviations from a given

configuration may involve combined JT and PJT effects, sometimes in a multilevel problem, which should be taken into account when considering the origin of distortions. Many calculations reviewed in this book confirm this statement.

The methane radical cation CH_4^+ is another example of the simplest JT systems. The ground state of this cation is triply degenerate in the regular tetrahedron configuration, leading to the $T \otimes (e + t_2)$ JT problem (Section 3.4). In this case, if only linear terms of vibronic coupling are significant, the theory predicts either tetragonal or trigonal minima with orthorhombic saddle points. If the quadratic coupling is sufficiently strong, the orthorhombic saddle points become minima too, and there is a range of parameters within which different kinds of minima coexist (Section 3.4).

There are many works reported aimed at calculating the APES of this system (see in [7.241–7.253]). *Ab initio* calculations in the MRSDCI (multireference singles and doubles configuration interaction) approximation with a 6-31G** basis set [7.241] show that the six equivalent global minima are at C_{2v} symmetry with two C—H distances at $R_1 = 1.155$ Å and an angle between them of $\phi_1 = 53°$, and the other two C—H distances at $R_2 = 1.075$ Å with $\phi_2 = 127°$, the remaining four angles H—C—H being the same and equal to $\phi_3 = 113°$ (Fig. 7.21). The saddle points between these minima are 3.1 kcal/mol higher and have the C_s symmetry with the four C—H distances, respectively (in Å), 1.147, 1.100, 1.117, and 1.117, and angles $\phi_1 = 140.8°$, $\phi_2 = 142.3°$, $\phi_3 = \phi_4 = 104.8°$, and $\phi_5 = \phi_6 = 85.8°$. The C_{2v} ground-state symmetry in the minima is seemingly consistent with experimental ESR data [7.254]. In relation to the general theory, the C_{2v} minima are "orthorhombic" (the term comes from octahedron distortions) in which one E-type vibration (leading to D_{2d} symmetry) and one T_2-type (leading to C_{3v} symmetry) vibration are displaced (Section 3.4). This means that the quadratic coupling is sufficiently strong. In view of the novel achievements in tunneling-splitting theory (Section 5.3) this system may be an interesting test example.

As mentioned above, the JT distortions in molecular systems are definitively important in chemical reactions (Section 7.1.3). Some examples of JT-driven transformations are mentioned below in Section 7.5. Reactions with participation of CH_4 may serve as further examples. The abstraction of hydrogen from CH_4 (or CD_4) by oxygen in its triplet state $O(^3P)$ was shown [7.255] to involve an intermediate system OCH_4 in a doubly degenerate ^3E state, the JT distortion of which influences the consequent transformations. In another process [7.256] the impact of a proton on CH_4 abstracts an electron, resulting in the ^2T state of CH_4^+ discussed above. This determines the energy-transfer and charge-transfer reaction mechanisms. For DFT calculations of the JTE in CCl_4^+ see [7.257].

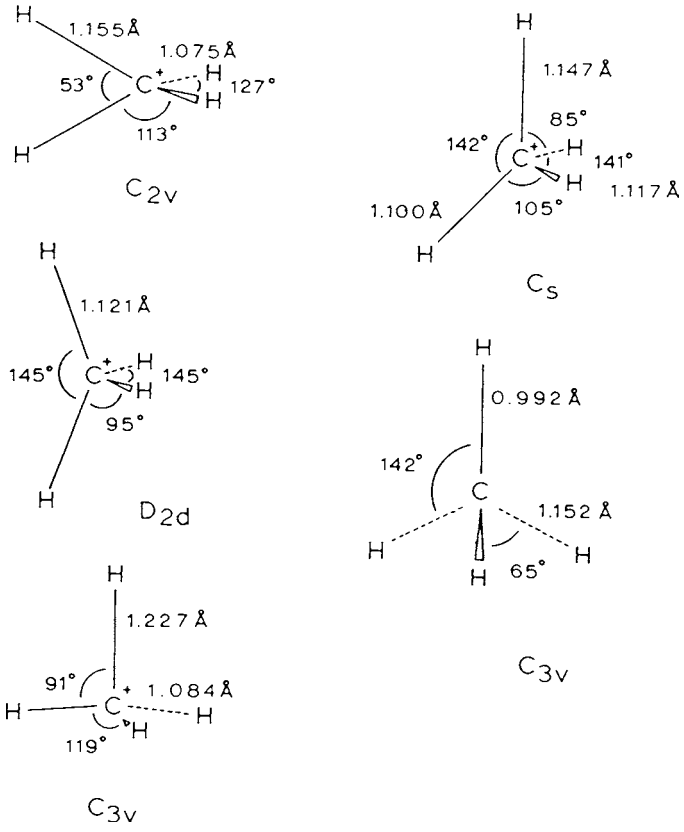

Fig. 7.21. Geometry of CH_4^+ at different symmetry points. The energy minimum is at C_{2v} with the C_s saddle points between them. The C_{3v} configuration has a nondegenerate ground electronic state, whereas at C'_{3v} the ground state is degenerate. (Reprinted with permission from [7.241]. Copyright 1988 American Institute of Physics.)

The results of computations for SiH_4^+ [7.258–7.263] are less illustrative with regard to the JTE. Different authors give different ground-state symmetries in the minima from C_{3v} to C_{2v} to C_s. The latest more elaborate calculations [7.258, 7.262] seem to indicate that the configuration that is lowest in energy corresponds to C_s symmetry with the geometry of a van der Waals-like complex $SiH_2^+ + H_2$ and with $R_1 = R_2 = 1.4590$ Å, $R_3 = 1.9730$ Å, $R_4 = 1.9240$ Å, $\phi_1 = 120.2°$, $\phi_2 = 22.1°$, $\phi_3 = \phi_5 = 33.405°$, and $\phi_4 = 99.292°$. This geometry can be considered as emerging from the C_{2v} symmetry of the $T_2 \otimes (e + t_2)$ JT effect plus a PJT influence of the corresponding excited state. However, such a possibility has not been explored as yet. Calculations for XH_4 systems with X = C, Si, Ge, Sn, Pb are presented in [7.263].

Ab initio CASSCF level calculations of the APES of the ground ^2E and first excited $^2T_2$ states of tetrahedral VF_4, NbF_4, and TaF_4 revealed their JT distortions toward D_{2d} configurations in the minima of both states (*e*-mode distortions) [7.264]. The JT stabilization energy was estimated (in cm^{-1}) as, respectively, 412, 1856, and 5970 in the ^2E state, and 3584, 6259, and 6611 in the $^2T_2$ state.

In the tetrahedral VCl_4 the APES for the ground state ^2E was calculated using DFT methods [7.265] (for earlier attempts see references in this paper). The JT distortion is rather small, $E_{JT} = 52\,cm^{-1}$ and $\delta = 12\,cm^{-1}$, which corresponds to the following constants in Eq. (5.38): $F_E = 1311 \pm 6\,cm^{-1}\,Å^{-1}$, $G_E = 1260 \pm 50\,cm^{-1}\,Å^{-2}$, $K_E = 19084 \pm 100\,cm^{-1}\,Å^{-2}$ and $\rho \cong F_E/K_E = 0.068\,Å$. For the excited state $^2T_2$ the JTE was shown to result in the distorted D_{2d} configuration with the stabilization energy $E_{JT} = 264\,cm^{-1}$ which explains the absorption spectrum [7.266].

Similarly, the JTE in tetrahedral CuX_4^{2-} yields three minima with *E*-type distortions at which the system has D_{2d} symmetry (see [7.267, 7.268] and references therein). For instance, the tetrahedron cluster of $CuCl_4^{2-}$ in Cs_2CuCl_4 is considerably flattened, $\phi_1 = \phi_2 = 129^\circ$ with $F_E = 4500\,cm^{-1}\,Å^{-1}$ [7.269, 7.270]. This system is an example of an MX_4 cluster in the crystalline state. There are many such systems; they are discussed in more detail in Section 7.6.

7.4.2 Cyclobutadiene, cyclobutane and tetrahedrane radical cations

The cyclobutadiene radical cation $C_4H_4^+$ is one of the simplest systems with a square-planar D_{4h} geometry in the high-symmetry configuration and a doubly degenerate ^2E_g term resulting in a JT $E \otimes (b_1 + b_2)$ problem (Section 3.1). Geometry optimization of this system has been reported in several papers [7.271–7.276]. Qualitatively, the possible JT and PJT distortions of this system are shown in Fig. 7.22 [7.272].

According to the general theory (Section 3.1), JT-active coordinates are of either b_{1g} or b_{2g} symmetry, resulting in D_{2h} configurations of a rhombus or rectangle, respectively. These configurations are not final because the PJTE may produce further distortions. In particular, if there is a sufficiently strong (in the sense of inequality (4.6)) vibronic coupling of the ground state $^2B_{3g}$ of the rectangular configuration to the excited $^2B_{3u}$ state, an A_u-type distortion (puckering, Section 7.5.2) of this configuration takes place ($B_{3g} \times B_{3u} = A_u$). Similar puckering of the rhombus (b_{1u} distortion) is produced by strong pseudo JT coupling to its $^2A_{2u}$ excited state. However, if in the rectangle the PJT coupling to the other $^2A_{1u}$ state is strong, the distortion b_{3u} leads to a trapezium configuration, which may also be subject to further puckering due

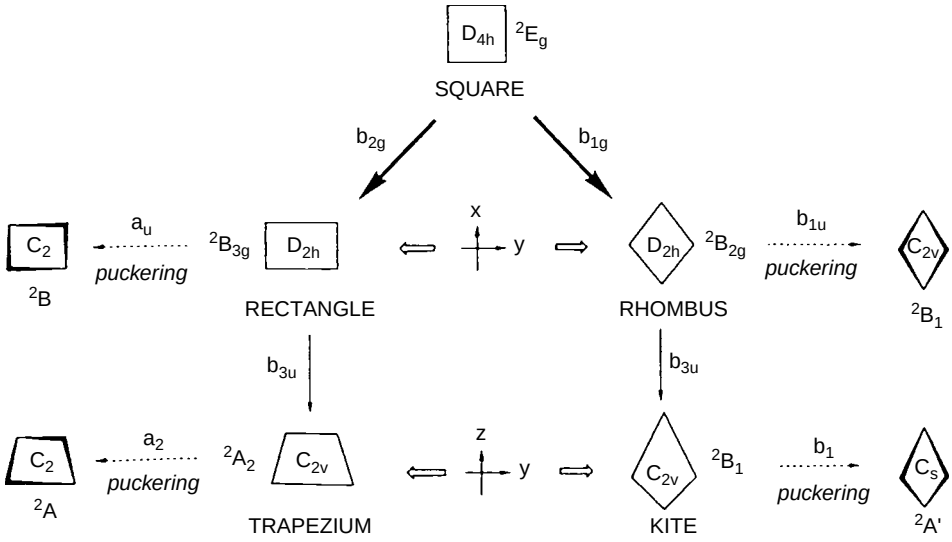

Fig. 7.22. Possible JT and PJT distortions of a square-planar configuration in an electronic E state. (Reprinted with permission from [7.272]. Copyright 1995 Elsevier Science Publishers.)

to the influence of an excited $^2A_1$ state. The rhombus can also be distorted to a kite (b_{3u} distortions) and the latter may be puckered by the PJT $B_1 \times A_1$ vibronic coupling. Quadratic coupling terms may also be important.

The energy differences between these configurations may be small. Therefore only a very high level of correlated *ab initio* calculation may be able to reveal the real minima and saddle points. Figure 7.23 illustrates the optimized geometries obtained [7.272] in the RMP2/6-31G(2*d*, *p)* level of *ab initio* calculations (RMP2/6-31G* for the puckered parallelogram). The energy differences between those configurations are given in Fig. 7.24 together with the results obtained with other methods. The best results show that the puckered rhombus gives the absolute minimum energy (Fig. 7.23), while the planar rectangle is also a minimum, which is 2.5 kcal/mol higher in energy than the puckered rhombus. The puckered parallelogram is a transition state (saddle point) between these two minima at an energy 4.6 kcal/mol higher than the absolute minimum.

From symmetry considerations, there are two planar-rectangle minima (two directions along which to elongate the square into a rectangle). The calculations show that they are $E_{\mathrm{JT}}^{B_{2g}} = 5.9$ kcal/mol lower in energy than the square-planar geometry; the energy barrier between them is $\delta = 4.2$ kcal/mol. The system is a planar rhombus at the saddle point (at the top of the barrier). For these parameters, similar values of $E_{\mathrm{JT}} = 7.0$ kcal/mol and $\delta = 1.0$ kcal/mol

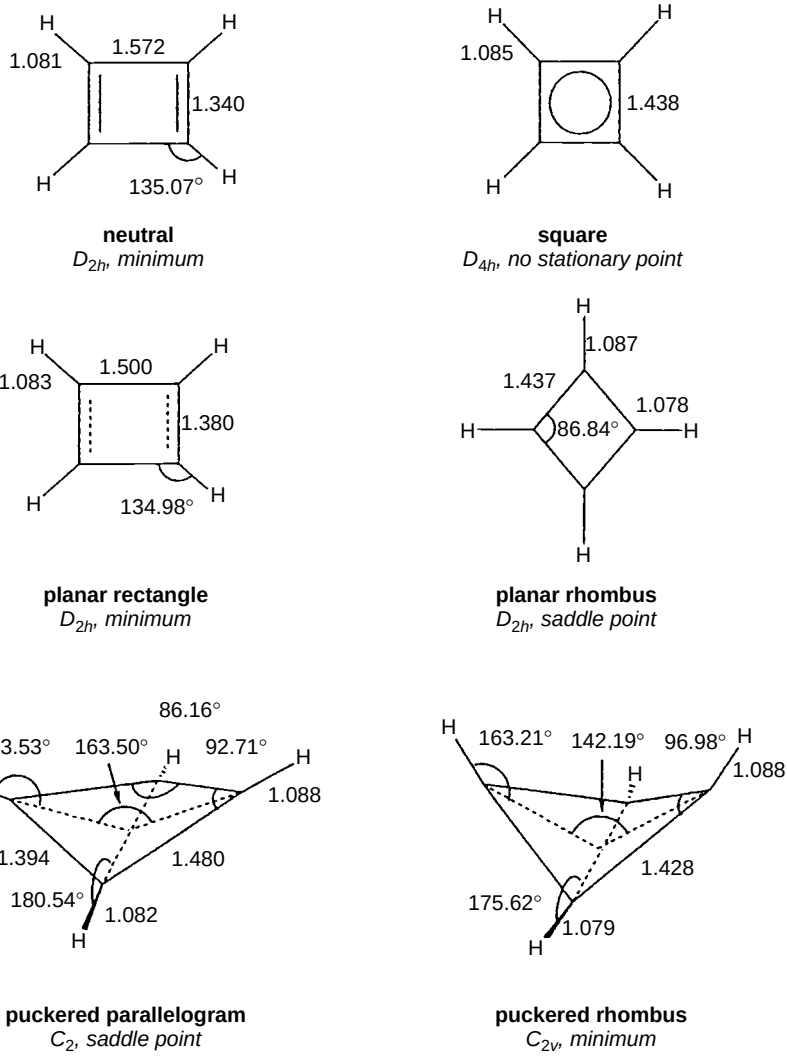

Fig. 7.23. *Ab initio* calculated geometry of neutral cyclobutadiene and its radical cations. (Reprinted with permission from [7.272]. Copyright 1995 Elsevier Science Publishers.)

were obtained in a simpler calculation at the CI/STO-3G level [7.271]. Further distortion shown in the last row of Fig. 7.22 did not emerge from these calculations.

By comparison of these results with those expected from the JTE theory, one gets an understanding of the origin of the calculated geometries. In particular, we see that the linear vibronic coupling to B_{2g}-type nuclear displacements is significant in distorting the square-planar $C_4H_4^+$ system to a planar rectangle with a

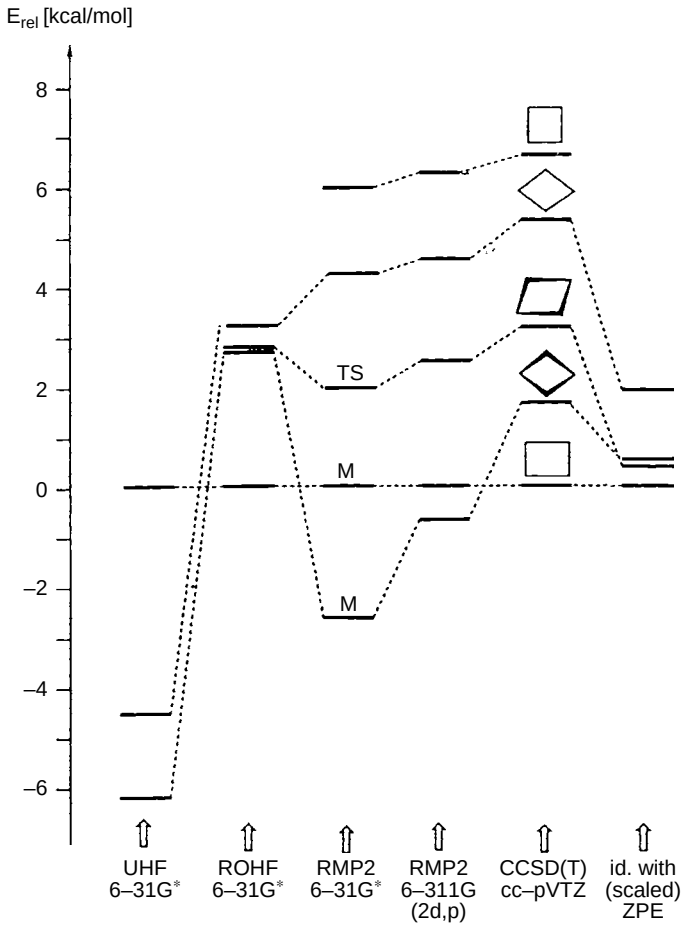

Fig. 7.24. Relative energies of the cyclobutadiene radical in different geometries calculated by the *ab initio* methods indicated. M and TS denote minima and transition state, respectively. (Reprinted with permission from [7.272]. Copyright 1995 Elsevier Science Publishers.)

stabilization energy of about 6 kcal/mol ($\sim$2100 cm^{-1}). The coupling to the B_{1g} displacements is weaker, making the planar rhombus geometry a saddle point of the APES, in full accord with the theory (in cases of strong quadratic coupling the rhombic saddle points become minima too [7.277], Section 3.1). Thus the JTE alone does not explain the origin of the calculated absolute minima.

By including the pseudo JT coupling of the ground state $^2B_{2g}$ of the planar rhombus to the $^2B_{2u}$ excited state via b_{1u} displacement, we get a puckering distortion, which makes this geometry the absolute minimum. There is no pseudo JT energy gain in puckering of the planar rectangle configuration, but the latter serves as the lowest transition state from the planar rectangle to the

puckered rhombic minima. Unfortunately, the authors [7.272] have not calculated the excited states, which would allow them to estimate vibronic coupling constants and the direction of expected PJT distortions.

As already emphasized earlier, APES cannot be observed directly. With the complicated APES obtained by numerical calculations the nuclear dynamics should be evaluated by solving the system of coupled equations (2.6). In this way the true energy spectrum and observables can be predicted. However, as mentioned above, the APES allow one to make reasonable qualitative predictions for many such observables. The authors [7.272] estimated the scaled SCF zero-point energies, which reduce the effective energy difference between the minima and saddle points to about 0.54 kcal/mol, making the APES almost flat to the corresponding pseudorotations.

Directly related to the cyclobutadiene radical cation is its isomer, the tetrahedrane (TH) cation $C_4H_4^+$ with an initial (reference) tetrahedral symmetry. It is distinguished from the cyclobutadiene (CB) cation in that the doubly degenerate electronic state of TH^+ in the configuration of a regular tetrahedron leads to a JT $E \otimes e$ problem (instead of $E \otimes (b_1 + b_2)$ in CB^+). Numerical calculation [7.278] allowed the authors to reveal the stationary points of the APES illustrated in Fig. 7.25. By comparison with analytical formulas, Eqs. (3.26)–(3.30) in the general theory of the JT effect (Section 3.2), they estimated the JT stabilization energy E_{JT} and the linear F_E and quadratic G_E vibronic coupling constants, as well as the primary force constant K_E and the barrier between the minima δ. At the UQCISD/6-31G* level $E_{JT} = 25.07\,\text{kcal mol}^{-1}$, $\delta = 5.62\,\text{kcal mol}^{-1}$, $K_E = 5.04 \times 10^2\,\text{kcal mol}^{-1}\,\text{Å}^{-2}$, $F_E = 1.45 \times 10^2\,\text{kcal mol}^{-1}\,\text{Å}^{-1}$, $G_E = 0.32\,\text{kcal mol}^{-1}\,\text{Å}^{-2}$.

The authors [7.278] calculated also the transition steps from the less stable JT minimum TH1 (Fig. 7.25) of the tetrahedron to the more stable minimum of the rectangular cyclobutadiene cation CB^+ (Fig. 7.23), which show that this isomer-interconversion reaction is driven by the JT distortion of the TH^+ configuration (see JT-induced reactivity in Section 7.1.3). Such JT-driven (triggered) reactions take place rather often. Other examples of PJT-driven transformation are given in Sections 7.5 and 7.6.

Similar numerical calculations of the APES and analysis of the JT and PJT distortions were performed on the cyclobutane radical cation $C_4H_8^+$ [7.279–7.284]. The results obtained depend significantly on the level of calculations involved. The ESR spectra for this system are consistent with a puckered rhomboidal structure [7.285] (Fig. 7.22). This corresponds to the absolute minimum found by means of the most accurate (so far) account for correlation effects in *ab initio* calculations on the QCISD(T)/6-31G*//UMP2/6-31G* level of theory [7.279]. In the majority of other works on this system that employ a

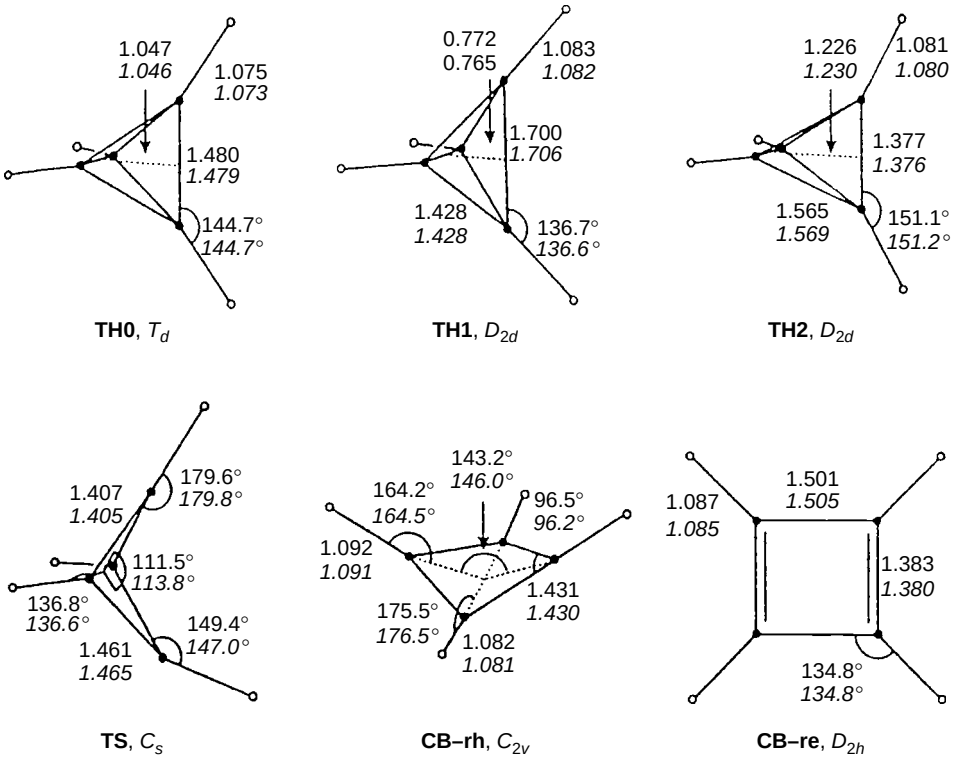

Fig. 7.25. Geometry of $C_4H_4^+$ at stationary points calculated by *ab initio* QCISD (indicated by normal font) and B3LYP methods (italic). TH and CB denote tetrahedrane and cyclobutadiene radical cations, respectively. THO is neutral TH. TH2 and TS are saddle points; all other structures are energy minima. (Reprinted with permission from [7.278]. Copyright 1997 American Chemical Society.)

lower level of calculations [7.281] the planar trapezoidal geometry was found as the global minimum, and it was suggested that the rhomboidal structure observed by ESR might be reinterpreted in terms of rapidly interconverting equivalent trapezoidal structures.

As mentioned above, observable properties cannot be obtained directly from the APES, although some specific features of the later may be very useful as qualitative indications of possible properties. With regard to ESR spectra a special theory of what can be expected as a result of vibronic coupling and multi-minima APES has been developed (Section 6.3). In particular, if as a result of the solution of the system of Eqs. (2.6) the ground vibronic state has the same degeneracy and symmetry as the initial electronic state at the point of degeneracy (see, however, Sections 5.3 and 5.4), the vibronic reduction factors allow reliable and reasonable prediction of the ESR spectra. There is not

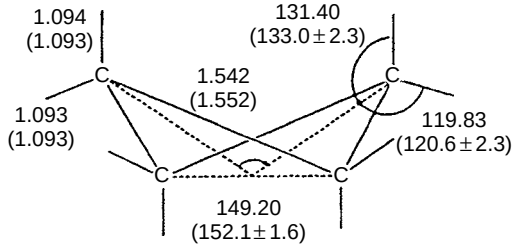

Fig. 7.26. An *ab initio* (MP2/6-31G*) optimized structure of cyclobutane [7.279]. Values in parentheses are from the electron-diffraction study [7.286]. (Reprinted with permission from [7.279]. Copyright 1993 American Chemical Society.)

enough physical meaning in comparison of the observed spectra with the calculated minima positions on the APES without involving the theory of ESR with vibronic coupling (Section 6.3).

Note that the neutral cyclobutane system C_4H_8 is not planar either (Fig. 7.26), its nonplanarity being confirmed by both electron-diffraction experiments [7.286] and *ab initio* calculation [7.279]. The out-of-plane distortion of the reference square-planar configuration is a good example of the PJT effect, the proof of which requires knowledge of the B_{1u}-type excited states.

In the cyclic system $C_4(CH_2)_4$ with D_{4h} symmetry the transition from the nondegenerate ground state $^1A_{1g}$ to the ionized ground state ^2E_g in the photoelectron spectrum is not split by the JTE in the ^2E_g state because in this case, as in the square-planar system $C_4H_4^+$, the JT problem for an ^2E_g term is $^2E_g \otimes (b_{1g} + b_{2g})$ (not $^2E_g \otimes e$), with two different coupling constants to the b_{1g} and b_{2g} displacements toward a rhombus and rectangle, respectively (Section 3.1). If the coupling to one of them is much stronger than that to the other one, the problem is reduced to $E_g \otimes b_{1g}$ or $E_g \otimes b_{2g}$. For any of them the band of $A \rightarrow E$ transition is singly peaked (Section 6.1). Equal coupling to both kinds of vibrations (provided their frequencies are equal too) would convert the problem to $E \otimes e$ with a two-humped band of the $A \rightarrow E$ transition. The calculations in the MINDO/3 approximation [7.287] allowed the authors to estimate the JT stabilization energies for the two kinds of distortions as 7.5 kcal/mol and 20.1 kcal/mol, respectively.

7.5 The benzene and cyclopentane families and some larger systems

7.5.1 The benzene-family molecular and radical cation and anion systems

The JT study of benzene-like systems and their derivatives has a long history (see [7.273, 7.288–7.333] and references therein). Neutral benzene, C_6H_6, has

D_{6h} symmetry and excited E terms. The JTE in these states was confirmed by spectroscopic data and vibronic-coupling calculations [7.312–7.313].

The JTE in *the benzene cation* $C_6H_6^+$ was subjected to multiple investigations [7.237, 7.273, 7.291, 7.297–7.311, 7.328, 7.331]. Using high-resolution threshold photoionization spectra of benzene in combination with the theoretical predictions for the JT $E\otimes e$ problem (Section 3.2), the structure of the ground E state of this system was shown [7.303] to follow the APES of the "Mexican hat" (Fig. 3.3) along the E-type C—C—C in-plane bending vibration ($\omega_6 = 536\,\mathrm{cm}^{-1}$) with $\rho_0 = 0.12$ Å and $E_{JT} = 208\,\mathrm{cm}^{-1}$. At the minimum, the C—C—C angle is 118.1°. The vibronic constants, according to Eq. (3.38), are $k = 0.88$ and $g = 0.02$, which give an estimate of the barrier between the minima $\delta = 8.32\,\mathrm{cm}^{-1}$. This δ value was confirmed [7.304] in *ab initio* calculations (BLYP with a 6-311G* basis set) and ZEKE (zero electron kinetic energy) photoelectron spectra. Compared with the zero-point energy this small barrier δ means almost free rotations.

JT coupling parameters derived from DFT-calculated APES of the lowest three electronic states $\tilde{X}\,^2E_{1g}$, $\tilde{B}\,^2E_{2g}$, and $\tilde{D}\,^2E_{1u}$ of $C_6H_6^+$ were obtained recently [7.331]. These data do not include the PJTE contributions. However, the PJT coupling plays an essential role in the structure and spectra of all benzenoid cations. The excited state $\tilde{B}\,^2E_{2g}$ of $C_6H_6^+$ is close to the $\tilde{C}\,^2A_{2u}$ electronic state with an energy separation of 0.31 eV [7.298]. The calculations [7.298, 7.302] show that there is a rather strong PJTE and an inter-state conical intersection between these two electronic states via two e_{2u} vibrational modes ν_{16} and ν_{17}. Together with the JTE on the $\tilde{B}\,^2E_{2g}$ state, which involves the e_{2g} modes ν_6 and ν_8, this explains the origin of the photoelectron band profile of the two overlapping states and the diffuse appearance of the $\tilde{C}$ state in the band. The same PJT coupling in $C_6H_6^+$ and $C_6D_6^+$ between the two states, $\tilde{B}$ and $\tilde{C}$, was taken into account [7.306] to interpret the vibrationally resolved photoinduced Rydberg ionization spectra of the dipole-forbidden $\tilde{B}\,^2E_{2g} \leftarrow \tilde{X}\,^2E_{2g}$ transition. For the calculations, the authors [7.306] employed a two-mode PJT model [7.316]. The JT coupling parameters used to fit the calculated spectral lines to the observed ones are given in Table 7.14

For higher excited states $\tilde{D}\,^2E_{1u}$ and $\tilde{E}\,^2B_{2u}$ of $C_6H_6^+$, multiple surface intersections and strong PJT coupling between them was revealed [7.305]. Using Green's function calculations (with correlation effects included), the coupling constants for the JTE in the E_{1u} state and the PJT mixing of the E_{1u} and B_{2u} states were estimated (Table 7.15). Note that both the JTE and the PJTE are triggered by the same four e_{2g} modes, ν_{15}, ν_{16}, ν_{17}, and ν_{18}.

Table 7.14. *Vibronic coupling parameters for the JTE in the ground* $\tilde{X}^2E_{1g}$ *state (via the* ν_6 *(*e_{2g}*) mode) and PJT mixing between the excited* $\tilde{B}^2E_{2g}$ *and* $\tilde{C}^2A_{2u}$ *states via the* ν_{16} *(*e_{2u}*) and* ν_{17} *(*e_{2u}*) modes in* $C_6H_6^+$ *and* $C_6D_6^+$ *(from [7.306])*

System	Vibrational mode	ω_E (cm^{-1})	$D_{JT} = E_{JT}/\hbar\omega_E$	$G = \delta/2E_{JT}$	$D_{PJT} = E_{PJT}/\hbar\omega_E$
$C_6H_6^+$	ν_6 (e_{2g})	540	0.377	0.020	
	ν_{16} (e_{2u})	333			0.44
	ν_{17} (e_{2u})	673			0.17
$C_6D_6^+$	ν_6 (e_{2g})	506	0.345	0.024	
	ν_{16} (e_{2u})	259			0.75
	ν_{17} (e_{2u})	642			0.18

Table 7.15. *Vibronic coupling constants for the JTE in the excited* $\tilde{D}^2E_{1u}$ *state and PJT mixing between this state and the* $\tilde{E}^2B_{2u}$ *state in* $C_6H_6^+$ *(in eV) (from [7.305])*

b_{2g} Mode	ω	JT linear coupling	PJT coupling
ν_{15}	0.4048	0.0971	0.0664
ν_{16}	0.2055	0.1032	0.1701
ν_{17}	0.1497	0.0579	0.1288
ν_{18}	0.0757	0.1755	0.0417

The calculated envelope of the corresponding transitions explains well the origin of the observed diffuse photoelectron band. The authors [7.305] performed also wave-packet dynamic simulations and showed that the $\tilde{E}\rightarrow\tilde{D}$ internal conversion process is very fast, occurring within several fs. This result is important for the explanation of the mechanism of fragmentation dynamics of $C_6H_6^+$ in the electronically excited state as a stepwise $\tilde{E}\rightarrow\tilde{D}\rightarrow\tilde{C}\rightarrow\tilde{B}\rightarrow\tilde{X}$ internal conversion (nonradiative) process. The $\tilde{C}\,^2A_{2u}\rightarrow\tilde{B}\,^2E_{2g}\rightarrow\tilde{X}\,^2E_{2g}$ fast nonradiative decay ($\sim$250 fs) was studied earlier [7.297] in a manner based on the investigation of the conical intersections, JTE and PJTE, and wave-packet dynamic calculations of this process.

Significant advances in the treatment of the JT and PJT effects in $C_6H_6^+$ were achieved recently [7.300]. The authors considered combined vibronic coupling within (JTE) and between (PJTE) its following five electronic

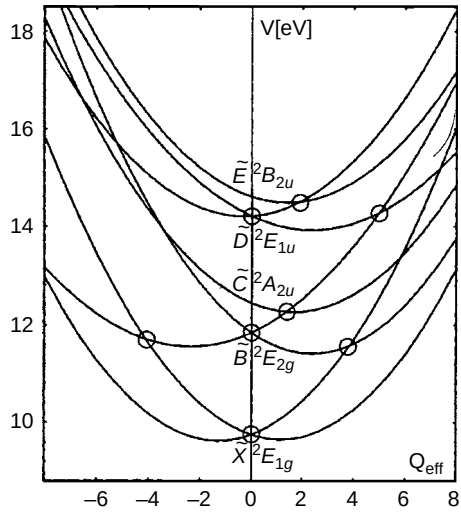

Fig. 7.27. A cross-section of the APES of the benzene cation displaying the most important conical intersections highlighted by open circles. (Reprinted with permission from [7.300]. Copyright 2002 American Institute of Physics.)

terms (vertical ionization potentials are shown in parentheses in eV): $\tilde{\mathrm{X}}\,^2E_{1\mathrm{g}}$ (9.27), $\tilde{\mathrm{B}}\,^2E_{2\mathrm{g}}$ (12.15), $\tilde{\mathrm{C}}\,^2A_{2\mathrm{u}}$ (12.61), $\tilde{\mathrm{D}}\,^2E_{1\mathrm{u}}$ (14.43), and $\tilde{\mathrm{E}}\,^2B_{2\mathrm{g}}$ (14.88). This amounts to eight electronic states interacting with 28 of the 30 nuclear degrees of freedom that results in an 8×8 matrix Hamiltonian of the vibronic coupling problem of Eq. (3.2). High-level *ab initio* calculations with only linear coupling constants taken into account show that only 14 vibrational modes contribute significantly to the vibronic coupling.

One of the main results of this work [7.300] is the finding of a whole sequence of low-energy conical intersections (Sections 3.2 and 5.7) between the eight branches of the APES of the five terms. Figure 7.27 illustrates the positions of the most important of them. In addition to the three conical intersections of the APES of the three degenerate E states in the $D_{6\mathrm{h}}$ configuration, there are another five at lower-symmetry geometries. Wave-packet dynamic simulations for these coupled APES branches were performed for the $\tilde{\mathrm{X}}-\tilde{\mathrm{B}}-\tilde{\mathrm{C}}$ and $\tilde{\mathrm{B}}-\tilde{\mathrm{D}}-\tilde{\mathrm{E}}$ manifolds, directly demonstrating the importance of nonadiabatic interactions at the conical intersections, which produce a stepwise population transfer on a timescale of 10–100 fs. Vibronic line spectra were also calculated and compared with previous results. The papers [7.300] seem to be the first quantum-dynamic study with more than three coupled APES branches.

In *benzene derivatives* not all substitutions remove the orbital E degeneracy of the electronic states. Even in disubstituted benzenes the double degeneracy of the π levels remains if the two substitution groups are, respectively, a donor

and acceptor of the same strength and they occupy *para* positions (antisymmetric substitution) [7.320]. If the strengths of the donor and acceptor groups are different, the E term splits accordingly. In *tri-substituted benzenes* with symmetric substitution the threefold axis of symmetry and hence the possibility of E terms is preserved with all the consequences for the JTE. In the earlier works the JT parameters of the ground ^2E state of *sym*-$C_6F_3H_3^+$, *sym*-$C_6F_3D_3^+$, and *sym*-$C_6Cl_3H_3^+$ were estimated from emission spectra [7.288–7.290, 7.294]. In these papers the multimode nature of the JTE is ignored. For later works and reviews on these and related systems see [7.218, 7.294, 7.318, 7.328].

For a similar system, the *sym*-triazine cation $H_3C_3N_3^+$, the authors [7.295, 7.314] calculated the vibronic energy spectrum in the ground E state linearly and quadratically coupled to a single active ring-distortion e mode ν_6. The calculated energy levels and transition intensities were compared with those observed in the two-photon absorption spectrum of the $3s^1$ E' Rydberg state, and good agreement between them was obtained for the JT parameters $k = 2.14$ and $g = 0.046$. This gives us $D = E_{JT}/\hbar\omega_E = 2.29$ and $\delta' = \delta/\hbar\omega_E = 0.21$; with $\omega_E = 661\,\mathrm{cm}^{-1}$, $E_{JT} = 1514\,\mathrm{cm}^{-1}$ and $\delta = 139\,\mathrm{cm}^{-1}$, which means hindered pseudorotation in the ground vibronic state [7.295]. Exceptions from the so-called maximum *hardness principle* (see, e.g., in [7.3]) observed in nitrogen heterocycles are explained by the PJTE [7.299].

The pseudorotation with a frequency of $\omega_\phi = 150\,\mathrm{cm}^{-1}$ in the excited E state of cyclohexane was revealed [7.296] based on the analysis of the ultraviolet spectrum of the two-photon transition from the lowest excited $^1A_{1g}$ state to the $3s^1$ E_g Rydberg state. The $E \otimes e$ problem in this system is a multimode one [7.313]; the major contribution to the linear JT distortion comes from five E-type modes with a total of $E_{JT} = 2550\,\mathrm{cm}^{-1}$. The barrier to pseudorotations is $\delta \approx 140\,\mathrm{cm}^{-1}$.

Benzene negative ions have distorted geometries due to PJT interactions [7.319]. The PJTE was shown to cause the ultrafast radiationless decay of the high-energy Rydberg states in toluene [7.315]. Vibronic coupling is taken into account to explain the origin of the absorption singlet–singlet and singlet–triplet bands in pyridazine [7.329]. $B_3N_3H_6$, which is isoelectronic to benzene, is considered in [7.334].

In $C_6F_6^+$, as in $C_6H_6^+$, all the four e_{2g} modes ν_{14}, ν_{16}, ν_{17} and ν_{18} are active in the JTE in the ground state $\tilde{X}\,^2E_{1g}$ [7.290, 7.291, 7.294, 7.328]. Table 7.16 lists the contribution of each of these modes to the JT distortions. The total JT stabilization energy equals $831\,\mathrm{cm}^{-1}$. The quadratic coupling is shown to be negligible, except for ν_{17} where it is small, $g = 0.006$. For more details on the JTE in these systems see in [7.328].

Table 7.16. *JT parameters for the ground state* $\tilde{X}\,^2E_{1g}$ *of* $C_6F_6^+$ *[7.294]*

	ν_{15}	ν_{16}	ν_{17}	ν_{18}
E_{JT} (cm^{-1})	370	61	289	101
k	0.68	0.32	1.17	0.87
g	~0	~0	0.006	~0
ω_E (cm^{-1})	1609	1220	247	116
δ (cm^{-1})	~0	~0	3.5	~0

The JTE and PJTE in substituted benzene radical anions have been studied (see [7.321–7.327, 7.332, 7.333] and references therein). Using *ab initio* ROHF approximation with a 6-31G* basis set plus MP2-level correlation calculations at the extrema points of the APES, the authors [7.324] obtained a detailed structure of this surface produced by the JTE and PJTE in $C_6F_6^-$. In the planar configuration D_{6h} the ground state is $^2A_{1g}$ with low-lying excited states $^2E_{2u}$ at 15.3 kcal/mol and $^2E_{1u}$ at 24.2 kcal/mol. The small separation of these states allows their vibronic mixing under the appropriate nuclear displacements. The JTE on the $^2E_{2u}$ term produces e_{2g} distortions within the planar configuration with three D_{2h} minima and three saddle points corresponding to electronic states $^2B_{1u}$ and ^2A_u, respectively. The PJT $^2A_{1g}$–$^2E_{2u}$ mixing under the out-of-plane e_{2u} distortions further reduces the symmetry at each minimum, forming two mirror-symmetry C_{2v} structures, while at the saddle points two D_2 structures are formed. As a result, the system has the six minima and six saddle points illustrated in Fig. 7.28. The JT stabilization energy at the minima is estimated as 16.9 kcal/mol. In comparison with neutral C_6F_6 it is seen that the electron affinity of this system is due to combined JT and PJT effects. Several substituted benzene radical anions of the type $C_6F_nH_m^-$ are considered from this point of view [7.332].

7.5.2 The cyclopentadienyl radical and cyclopentane: puckering

The JTE in the cyclopentadienyl (Cp) radical C_5H_5 and its ionic, deuterated, and substituted states were considered in a series of papers (see [7.273, 7.330, 7.335–7.346] and references therein) beginning with the earliest publications on the JTE [7.335]. In more recent calculations [7.336, 7.337] the ground E term of planar C_5H_5 in D_{5h} symmetry is shown to have distorted C_{2v} configuration at the minima due to the JTE. In a relatively simple *ab initio* UHF/STO-3G approximation [7.336] the JT stabilization energy $E_{JT} = 14.5$ kcal/mol with a barrier between the minima $\delta = 3.5$ kcal/mol and contraction of the

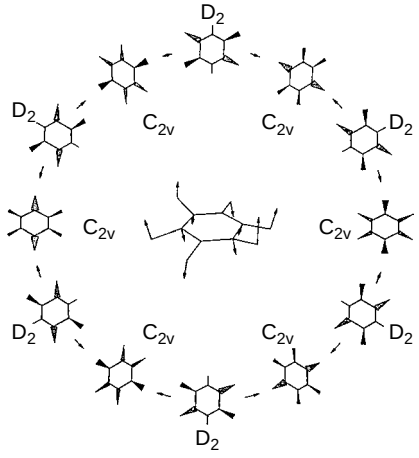

Fig. 7.28. Combined JT plus PJT pseudorotation in $C_6F_6^-$. $C_{2v(z)}$ and D_2 structures correspond to the APES minima and saddle points, respectively. Equivalent structures are congruent upon the S_6 symmetry operation. The pseudorotation coordinate $Q(b_1)$ is shown in the center. (Reprinted with permission from [7.324]. Copyright 1999 Elsevier Science Publishers.)

most distorted C—C bond $\Delta R_{CC} = 70$ mÅ. In a more elaborate calculation that includes also CI in the π space [7.337] $E_{JT} = 7.1$ kcal/mol and $\delta \approx 0$, which means free pseudorotation of the distortion. In distorted-configuration $^2A_2$ and $^2B_1$ states, the interatomic distances (in parentheses for the $^2B_1$ state) are (in Å): $R(C_1—C_2) = 1.407\,(1.457)$, $R(C_2—C_3) = 1.496\,(1.371)$, and $R(C_3—C_4) = 1.360\,(1.509)$, with almost unchanged angles of the pentagon. The authors [7.337] calculated also the APES of the cyclopentadienyl cation $C_5H_5^+$ taking into account the PJT mixing of the ground state $^1A_1'$ with the lowest excited $^1E_2'$ state (at 23 kcal/mol) by e_2' distortions, which produces deeper minima at $E_{JT} = 13.4$ kcal/mol, but without a considerable barrier between the minima (meaning free pseudorotation). Note that in both cases, C_5H_5 and $C_5H_5^+$, the distortion coordinate E allows pseudorotation that avoids the high-symmetry D_{5h} configuration. Figure 7.29 illustrates the pseudorotation pattern for $C_5H_5^+$.

In the papers [7.340–7.342] the rotationally resolved laser-induced fluorescence spectra of the $\tilde{A}^2A_2'' \leftrightarrow \tilde{X}^2E_1''$ transition in C_5H_5, C_5D_5, C_5H_4D, and C_5HD_4 are analyzed in detail in view of the JTE implications. While the authors found clear evidence of the JT pseudorotation in the ground state, the parameter values of the JT distortions that emerge from the spectral data are significantly smaller than those in the *ab initio* calculations discussed above. The low barrier between the APES minima in C_5H_5 and C_5D_5 was

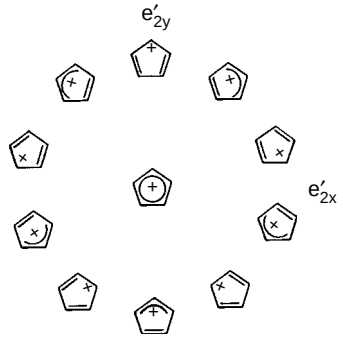

Fig. 7.29. Pseudorotation in the lowest singlet state of the cyclopentadienyl cation, distorted in an e_2' mode. (Reprinted with permission from [7.337]. Copyright 1979 American Chemical Society.)

confirmed by recent *ab initio* calculations [7.343] aimed at interpretation of the spectroscopic data on the $\tilde{A}^2A_2'' \rightarrow \tilde{X}^2E_1''$ transition. The authors calculated a variety of parameters of molecular structure and vibronic coupling in the $\tilde{X}$ and $\tilde{A}$ states. In particular, they obtained a JT stabilization energy of $E_{JT} = 2147\,cm^{-1}$ with the barrier to pseudorotation $\delta = 3.6\,cm^{-1}$. Of the four JT-active e modes ν_9, ν_{10}, ν_{11}, and ν_{12}, only three, ν_{10}, ν_{11}, ν_{12}, contribute significantly to the distortion, the mode ν_{10} being most active. The vibrational frequencies and distortions produced by each of these modes were evaluated. These and other estimated JT parameters are used to predict the $\tilde{X} - \tilde{A}$ electronic spectra of C_5H_5 and C_5D_5.

An original (non-perturbational) treatment of the ground states of C_5H_5 and $C_5H_5^+$ based on a valence-bond analysis and the so-called method of Longuet–Higgins loops was suggested in [7.345].

The APES of fluorinated cyclopentadienyl cations, $C_5H_4F^+$, and $C_5H_4CH_3^+$ in singlet states were studied by MNDO and *ab initio* MP2/6-31G* methods [7.338]. The results are related to the pseudorotation surface of $C_5H_5^+$. Vibronic effects in excited states of furan are considered in [7.346], while the vibronic structure of the π-photoelectron bands in furan, pyrrole, and thiophene is investigated in [7.347].

Cyclopentane, C_5H_{10}, in contrast to C_5H_5, has no degenerate ground state, but like $C_5H_5^+$ above it may have PJT distortions due to the vibronic mixing to the excited states. On the other hand, C_5H_{10} is a good example to illustrate the phenomenon of puckering.

In any system with more than three atoms and a reference planar configuration some atoms or atomic groups may undergo out-of-plane displacements resulting in the so-called puckering. Several examples mentioned in the

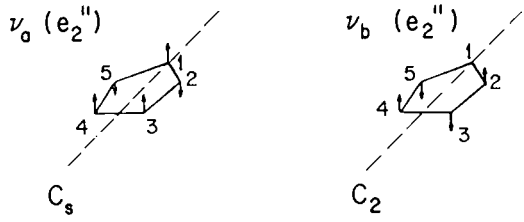

Fig. 7.30. Two components of the e''-type displacements (puckering) in a five-membered ring with D_{5h} symmetry. (Reprinted with permission from [7.348]. Copyright 1975 American Chemical Society.)

subsections above illustrate such distortions. The out-of-plane bending of the C—O bond in H_2CO [7.127] considered in Section 7.2.2 may also be regarded as an element of puckering.

Puckering is shown mostly as an effect of nonplanarity of organic ring structures. In the saturated five-member ring of cyclopentane C_5H_{10} the reference planar configuration has D_{5d} symmetry, and the puckering distortion has e'' symmetry. Figure 7.30 shows the two components of the e'' displacements of the atoms in the five-member ring. The Z-displacements of the individual carbon atoms along the fivefold axis in this symmetrized "concerted" e'' displacement are given by the following equation [7.348]:

$$Z_i = (2/5)^{\frac{1}{2}} q \cos[\phi + (4\pi/5)(i-1)], \qquad i = 1, 2, \ldots, 5 \tag{7.44}$$

where q is the amplitude of distortion and ϕ is the phase angle: on changing ϕ from 0 to 2π the structure goes from one component of displacement (at $\phi = 0$, 36, 72, ..., 324°) to the other one (at $\phi = 18$, 54, ..., 342°). This kind of typical puckering was revealed first from thermodynamic data [7.349] and then confirmed multiply by various experimental techniques (see [7.350] and references therein). Calculations of APES [7.348] confirm that in cyclopentane the planar configuration is unstable: the puckered configuration is lower in energy by ~4.2 kcal/mol (the experimental value is 5.2 kcal/mol), and the motion of the puckering distortion along the ring is rather a free internal rotation (pseudorotation).

The planar configuration of cyclopentane has a closed-shell A_1 electronic ground state and a variety of excited states, among which there are those belonging to the E'' type. Obviously, the vibronic mixing of the ground state A_1 with the excited E'' under e'' vibrations ($A_1 \times E'' = E''$) softens the former with respect to e'' displacements. If this softening is strong enough (the vibronic coupling is strong and the inequality (4.6) holds), the ground state becomes unstable with regard to these displacements.

To the best of our knowledge, the PJT origin of this puckering has not been explored so far. The numerical data show as a fact that the system is distorted, giving no information concerning its origin as due to the implication of the E'' excited electronic state that causes the instability of the ground state with respect to e'' displacements. The authors [7.348] explain the puckering as determined by the balance between the increased strain produced by the decrease in the bond angle (which is smaller in the puckered configuration) and decreased torsion strain (which is the greatest in the planar configuration). The PJT explanation is much more general and straightforward: the puckering distortion, by mixing the A_1 and E'' electronic states, *provides additional covalent bonding* that lowers the energy of the system, quite similar to many other cases considered above. As mentioned in Section 4.1, in the general formulation employed in this trend, the PJT implication of the excited electronic states is the only possible source of instability of the ground state in the high-symmetry configuration. Several other puckering situations are mentioned in this chapter.

7.5.3 Larger organic systems

Similar to C_5H_5, cycloheptatrienyl C_7H_7 has an $E \otimes e$ trough (Section 3.2) with $E_{JT} = 0.859$ kcal/mol [7.273]. In triphenylene and coronene negative ions $E_{JT} = 0.385$ kcal/mol and 0.299 kcal/mol, respectively [7.273]. Note that these numerical data were obtained by semiempirical calculations. More recent *ab initio* calculations [7.351], aimed at guiding the assignment of the $A^2E_3'' \leftarrow X^2E_2''$ transition in the two-photon ionization spectra of C_7H_7 and C_7D_7, were performed for the ground E_2'' and excited E_3'' states in the distorted C_{2v} configurations. On the CASCF and B3LYP levels of computation the JT stabilization energy E_{JT} in the ground state of the $E \otimes e$ problem in C_7H_7 was found to be 0.213 eV and 0.149 eV, respectively, while the energy barrier between the minima is very small (0.020 eV and 0.065 eV, respectively), meaning almost free pseudorotation of the distortions along the ring. In the excited state $E_{JT} = 0.365$ eV.

Distortions in cyclooctatetraene were considered recently [7.352], but the interpretation that only some of them are due to the PJTE, the others not, is based on a misinterpretation of this phenomenon: as shown in Chapter 4, any distortion of high-symmetry configurations of molecular systems in non-degenerate states is of PJT origin, its magnitude and symmetry being dependent on the excited state that causes the distortion via the PJT coupling.

An interesting mechanism of photorearrangement of the cyclooctatetraene radical cation $C_8H_8^+$ (COT^+) into the radical cation of bicyclooctadienediyl (BOD^+) was suggested to proceed by virtue of JT distortion of the excited

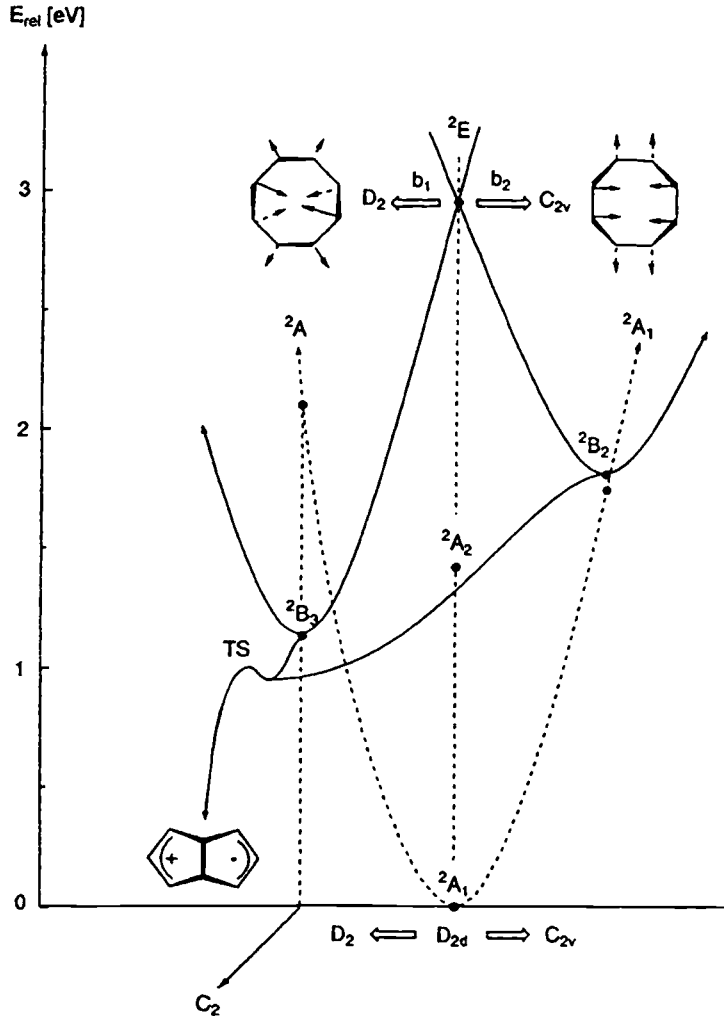

Fig. 7.31. APES cross-sections illustrating the JTE and PJTE driving the phototransformation of the cyclooctatetraene radical cation (COT^+) in oxidized bicyclooctadiene (BOD^+). The excited ^2E state is subject to a JT $E \otimes (b_1 + b_2)$ coupling, while the transition state TS is formed due to the PJT distortion in the C_2 direction. (Reprinted with permission from [7.353]. Copyright 1995 American Chemical Society.)

^2E state of COT^+ [7.353]. Figure 7.31 shows schematically the main elements of the calculated APES obtained on the RMP2/6-31G*//ROHF/6-31G* level of computation. The BOD^+ system emerges as due to a strong JTE in the second π-excited ^2E state followed by the PJTE in the $^2B_3$ minimum (which is lower than the first excited state $^2A_2$ of COT^+). Similarly, it was shown that the rearrangement products of the syn-tricyclooctadiene radical cation are

determined by the PJT distortions [7.354]. Several analogous examples including ring-opening rearrangements in oxirane and bicyclopentane radical cations have been shown to take place along the coordinate predicted by the PJTE [7.355].

MCSCF calculations for a series of seven- and eight-member unsaturated heterocycles with eight π electrons were performed with the goal of elucidating the PJT distortions from planarity [7.356]. From the author's conclusions, "the monocyclic systems examined were found to show a variety of structural changes. Azepine and oxepin undergo the pseudo JT distortion from a planar C_{2v} to a boat C_s conformation. In 1,5-diazocine, the pseudo JT distortion takes place in two stages, the initial step being from a symmetric planar D_{2h} to a skew C_{2h} structure and the subsequent step from a skew C_{2h} to a tub C_2 structure. The 1,3,5,7-tetrazocine molecule undergoes pseudo JT distortions from a symmetric planar D_{4h} to skew C_{4h} and crown-like D_{2d} structure through the respective in-plane and out-of-plane nuclear deformations. Moreover, the C_{4h} and D_{2d} structures are distorted into the same tub-shaped S_4 conformation" [7.356].

A series of papers is devoted to the JTE in acenes, fluoroacenes, phenanthrene, cubanes, and related systems [7.357–7.369]. The special feature of these works is that they handle the vibronic coupling in terms of orbital vibronic constants (Section 2.3) and aim at revealing possible superconductivity (however, it is unclear how the authors of some of the above papers handle the multimode problem). Orbital vibronic constants (Section 2.3) were calculated for anthracene, tetracene, penthacene, and their full deuterides, and used to explain the origin of the inverse isotope effects in superconductivity of such systems as due to the increase of the vibronic coupling in the C—C stretching mode by H/D substitution [7.357(*a*)]. Similar calculations were performed for benzene, naphthalene, anthracene, tetracene, penthacene, and hexacene monocations and monoanions [7.357(*b*)], for which the superconductivity transition temperatures were also estimated; they are much lower in monocations than in monoanions. Monoanions of polycyanodienes are treated in a similar way in [7.358]. For negatively charged B, N-substituted acenes the vibronic coupling constants are much lower than in corresponding acene anions [7.359].

By means of calculating the orbital vibronic coupling constants for the HOMO and LUMO of $(CH)_8$ and $(SH)_8$ and their cations and anions, the authors [7.360–7.362] estimate the vibronic contributions to a variety of their properties. In particular, they analyze the electron transition band (based on the one-electron transition $t_{2g}(\text{HOMO}) \rightarrow t_{1u}(\text{LUMO})$), investigate the precondition of high-temperature superconductivity under the assumption that the vibronic coupling between the LUMO and intramolecular vibrations plays an essential role, reveal the role of hydrogen atoms in this vibronic coupling, and investigate the isotope effect. A similar investigation was performed on

fluoroacenes [7.363(*a*)] and phenanthrene [7.363(*b*)]. Orbital vibronic constants were also used recently to assign the photoelectron spectrum and explain other properties of naphthalene [7.364].

The vibronic coupling in a series of related organic systems including [18]annulene, [30]annulene, triphenylene, coronene, and corannulene was considered recently [7.365–7.369] (see also [7.273]). In particular, in the ground E state of the anions and cations of coronene, the largest contribution of the JT $D_{6h}\rightarrow D_{2h}$ distortion (in the minima of the APES) comes from the e_g vibration at 1668 cm^{-1} that includes the C—C stretching; the C—H stretching mode of 3177 cm^{-1} is also important, more so in coronene than in deuterocoronene [7.365]. Possible superconductivity in monoanions of coronene and corannulene is considered based on calculation of the vibronic coupling constants [7.369] (Section 8.4).

The ESR spectra of the corannulene monoanion $C_{20}H_{10}^{-}$ were interpreted in terms of pseudorotation about the C_{5v} JT crossing [7.367]. The barrier between the (five) equivalent minima was estimated as $\sim 2.2\times 10^{-3}$ eV. The JTE in monoanions and trianions of {6}- (I) and {18}-hetero(A,B)annulenes (II) was discussed in [7.366]. These systems have a threefold axis of symmetry and a degenerate E term, thus being subject to the JT $E\otimes e$ problem. On the B3LYP/6-31G* level of computation the authors calculated orbital (Section 2.3) and integral vibronic coupling constants, which are shown to be most significant for the modes at 1500 cm^{-1} in I and <500 cm^{-1} in II.

The JTE in larger systems with trigonal symmetry, triptycene [7.370] (9,10-dihydro-9,10 [1′2″] benzenoanthracene) (I) and 9-fluorotripticene [7.371] (II), was investigated to explain the origin of the vibronic structure of their resolved $S_1(E)\leftarrow S_0(A_1)$ two-photon ionization spectrum. For (I), a single-mode $E\otimes e$ problem with $k=1.65$, $g=0.426$, and excited state frequency $\omega_E=47.83$ cm^{-1} accounts for ~98% of the observed absorption band intensities in the 0–350 cm^{-1} region (the a_2 mode appears through nonzero momentum coupling). For (II), three models were considered: $E\otimes e$, $(A+E)\otimes e$, and $(A+E)\otimes(e+a_2)$. The $E\otimes e$ interpretation yields essentially correct frequencies, while the coupling to the $^1A_1$ state improves the intensities. In the $(A+E)\otimes e$ model $k=1.145$, $g=0.152$, and $\omega_E=61.4$ cm^{-1}. The tunneling splitting A_2–E due to pseudorotation and quadratic barriers is 1.5 cm^{-1} (see also [7.372]).

Orbital vibronic-constant calculations are also used to discuss cubane–cyclooctatetraene conversion, as well as correlations between orbital occupation numbers and molecular properties [7.373].

The PJTE in the excited state of a relatively large molecule, diphenylhexatriene (DPH), is described in [7.374]. DPH is planar and has C_{2h} symmetry in the ground state A_{1g} with lowest excited states ^2A_g and ^1B_u related to the Raman spectra. The observed spectral properties are explained on the basis of

significant vibronic mixing of the ^2A_g and ^1B_u states by a b_u-type vibrational mode (Q_2) near 40 cm^{-1} involving also the totally symmetric A_g type vibrational mode (Q_1) at 1700 cm^{-1}. A three-level problem in which the ground state A_{1g} is coupled to Q_1 only (with a coupling constant of 1.65 eV $Å^{-1}$ $amu^{-1/2}$), while the two excited states are mixed by Q_2 only (with a coupling constant of 0.2 eV $Å^{-1}amu^{-1/2}$), yields the APES illustrated in Fig. 7.32. The results explain the origin of the observed two bands and the broadening in the Raman spectra.

The twisted configuration of ionized bicyclo[2.2.2]oct-2-ene was shown to be stabilized by the PJT coupling to the corresponding excited state [7.375].

Fullerenes constitute a special group of large organic systems with the highest possible symmetry for localized systems. Theoretical problems for fullerenes and their properties are reviewed in Section 3.4. Here we mention several examples of further application of the JTE theory to these systems, especially to their charged and/or substituted forms [7.376–7.396]. For fullerene anions C_{60}^{n-} with the electronic configuration t_{1u}^n, using a simple "quasi-atomic" model, it was shown [7.377] that the vibronic coupling of the t_{1u} electron to the h_g mode results in combined JT $\Gamma \otimes h_g$ and PJT $(\Gamma_1 + \Gamma_2) \otimes h_g$ problems (Section 4.2).

The ground state of C_{60}^{3-} with the three excess electrons in the three orbital t_{1u} states is nondegenerate. This conclusion is in contradiction with the superconductivity of A_3C_{60} (A = K, Rb, Cs) and insulator properties of A_4C_{60}. The problem was treated in several papers [7.378, 7.379, 7.392, 7.393] (see also Section 8.4). In particular, it was shown [7.392, 7.393] that the joint interelectron interaction and JT distortion under certain conditions results in disproportionation of the three t_{1u} orbital occupancies: $t_{1u}^2(x)t_{1u}^1(y)t_{1u}^0(z)$ instead of the usually assumed $t_{1u}^1(x)t_{1u}^1(y)t_{1u}^1(z)$. Similarly, the insulator properties of A_4C_{60} are explained [7.378] as due to a JT-induced transition from a Mott–Hubbard to a band insulator state.

A detailed study of the photoelectron spectrum of gaseous C_{60} revealed three tunneling states (Section 5.3) attributed to the tunneling between the D_{3d} minima of the JT-distorted cation C_{60}^+ [7.380(*a*)]. However, this interpretation of the spectrum was questioned in [7.380(*b*)]. For fullerene anion systems with the $T_{1u} \otimes h_g$ JT problem anisotropic phenomena in the D_{5d} and D_{3d} minima and tunneling between the latter are further explored [7.381]. By analyzing experimental data on the shift in infrared and Raman scattering spectra due to doping in fullerene compounds and separating charge-transfer effects the authors [7.382] (among other things) succeeded in extracting the values of the vibronic coupling constant of the $T_{1u} \otimes h_g$ problem in C_{60}^- in good agreement with those obtained from photoemission spectroscopy data. Coupling constants were also obtained by solving the multimode (eight-mode) problem (Section 5.5) for C_{60}^- [7.383].

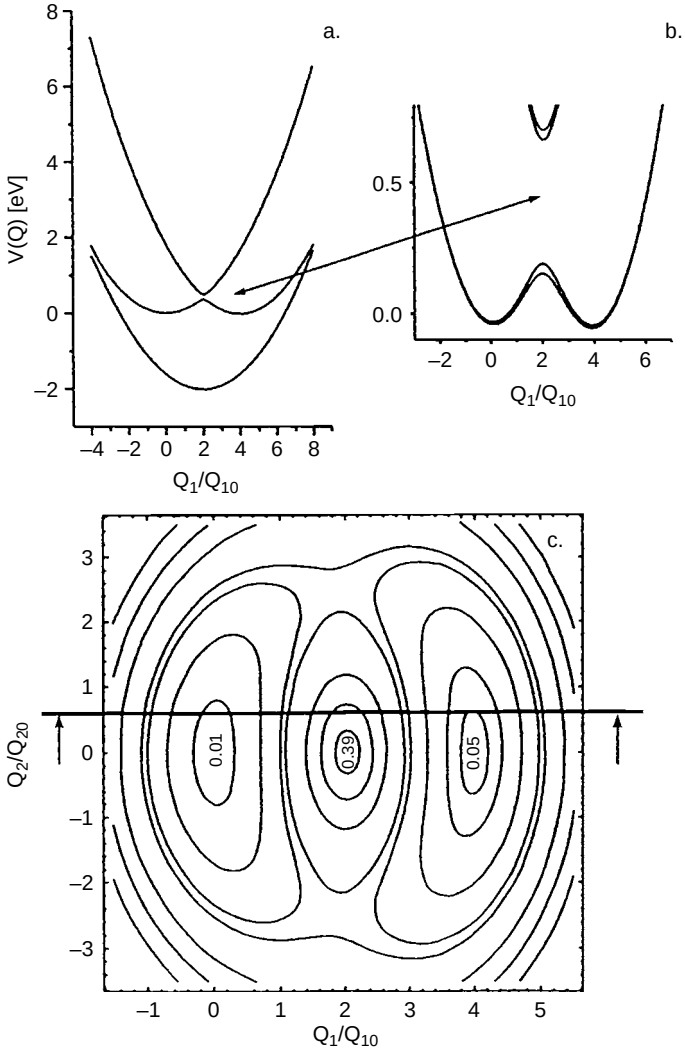

Fig. 7.32. (a) Effective potentials for the totally symmetric C=C stretching coordinate around 1700 cm^{-1} in the three vibronically coupled states of diphenylhexatriene (DPH). In the ^2A_g state the PJTE leads to a double-well potential (abscissa values of elongation are normalized with respect to the zero-point oscillation for this mode Q_{10}). (b) An enlarged segment of the range of avoided level crossing between the ^1B_u and ^2A_g singlet states; potential curves are given for two different vibronic coupling constants. (c) A contour diagram of the effective two-dimensional vibrational potential for the first excited singlet state of DPH resulting from strong vibronic coupling; the cut at $Q_2 = Q_{20}/2$ represents the lower potential in (b). (Reprinted with permission from [7.374]. Copyright 1998 Elsevier Science Publishers.)

The out-of-center position of the Li^+ ion in $Li : C_{60}$, called in [7.385] "degeneracy loss," is in fact an obvious PJTE (the authors do not refer to the JT vibronic coupling effects). Off-center positions of Li^+ ions in other molecular systems and as impurities in crystals were considered multiply (Section 8.1.1).

The cluster Ti_8C_{12} regarded as a substituted C_{20} dodecahedron is considered with respect to its two possible structures, T_h and D_{3d}, and it is shown that in combination with the JTE the zero-spin state occurs for the D_{3d} configuration [7.386]. The symmetry implications of JT distortions of charged fullerenes in entropy estimations are discussed in [7.387].

Magnetic succeptibilities and g-factors for C_{60}^- were calculated taking into account the JTE and spin–orbital coupling [7.389]. The latter is strongly reduced compared with that of the carbon atom (Section 6.3), so are the effective weak-field g-factors of low-lying states; for the ground-state doublet the g-factor is predicted to be negative: $g \sim -0.1$. High-resolution far-infrared transmission spectra of C_{60}-tetraphenylphosphoniumiodide show a doublet splitting in the two t_{1u} modes in accordance with the JT D_{5d} and D_{3d} distorted ball, as well as interband electron–phonon coupling modes [7.388]. The $E \otimes e$ problem in C_{70}^{3-} is considered in [7.390].

For the JTE in infrared absorption of charged C_{60} see in [7.391(*a*)]. JT excitons in resonant Raman spectra of C_{60} were studied [7.391(*b*)], and it was shown that the tunneling splitting ${}^3T_{3g} - {}^3T_{1g}$ explains the experimental triplet-state data. The depolarization ratio was also calculated. D_{2h} distortion in the C_{60}^- ion fixed by the crystal-field influence in single crystals of $[A^+(C_6H_5)_4]_2C_{60}^-B^-$ was observed by means of ESR spectra [7.394].

The $C_{60} \rightarrow C_{60}^+$ photoemission spectrum is calculated using the Lanczos method for the diagonalization of the vibronic Hamiltonian (Section 5.4) with all the JT-active vibrations included, and it is shown that the separation ($\sim$230 meV) of the first shoulder from the main peak is due to the h_u vibronic excitation [7.395].

Orbital vibronic constants (Section 2.3) were employed in a simple scheme to estimate the vibronic coupling in C_{60} relevant to resistivity [7.396(*a*)], while in [7.396(*b*)] a full *ab initio* calculation of the electron–phonon coupling via orbital vibronic constants was performed, with a brief discussion of its relevance to superconductivity.

7.6 Clusters, coordination, and mixed-valence systems

Applications of the JT and PJT effect to metal clusters and coordination compounds are vast, especially during the last two decades (for an account

of older publications through 1979 see [7.15]). They overlap essentially with solid-state problems, for which local properties and lattice defects are often considered in cluster presentation, at least as a first approximation to the problem. Therefore the separation of the JT problems in this section from many of those in Chapter 8 is rather conventional. Nevertheless, we made this distinction by including here clusters and coordination compounds that may exist outside a crystal lattice, or considering mostly molecular properties of JT clusters, leaving the problems of crystal interactions to the next chapter.

On the other hand, there are very vague distinctions between clusters and coordination compounds (for the definition of the latter see [7.3]). For example, $[Cu(H_2O)_6](BrO_3)_2$ is a coordination system in which the main JTE takes place in the cluster $[Cu(H_2O)_6]^{2+}$. But there are free multicenter systems like $Cu_4O_{12}H_8$, which are often called clusters too, and there are just pure metallic clusters like Ni_5 and Pb_6. Taking all this into account, there is no sense in fully separating clusters from coordination systems when discussing the JTE. Mixed-valence systems stay separate by definition although they have many features in common with coordination compounds.

7.6.1 JT clusters and coordination systems

The number of coordination systems and clusters studied with respect to their JT vibronic coupling effects is innumerable. In addition to some more recent works outlined in this section we refer the reader to several reviews [7.1–7.3, 7.15, 7.267, 7.268, 7.397–7.404] and to the overlapping topics in Sections 7.6.3 and 8.1.

Among JT systems Cu(II) coordination systems and clusters with the electronic configuration of the central atom (CA) $3d^9$ are most studied. The reason is that Cu ions are among the strongest JT centers; in fact they served as the first experimentally observed confirmations of the JTE in EPR [7.405]. Divalent Cu^{2+} ($3d^9$) systems in ligand environments with at least one threefold symmetry axis have doubly degenerate electronic ^2E terms. The simplest of these studied are trigonal bipyramidal (TBP) complexes of the CuX_5 type with nondegenerate ground state and excited E terms. X-ray analysis in combination with EPR and calculations [7.406–7.410] shows that the TBP cluster $[CuCl_5]^{3-}$ in the crystal $[Co(NH_3)_6][CuCl_5]$ is unstable with regard to e displacements toward a square-pyramidal (SP) configuration; in fact it performs pseudorotation between the three equivalent SP configurations demonstrated in Fig. 7.1 (Section 7.1.1). Since the ground state of this cluster in the TBP configuration A_1' is nondegenerate, its distortion and pseudorotation should be driven by the PJT mixing of the ground state with the excited E' states that produce the observed TBP→SP e displacements. Semiempirical calculation of

the PJT contribution of several excited E states to the instability confirmed this picture and allowed one to better understand the origin of the distortions as due to the formation of new covalence between the valence orbitals of Cu and charge-transfer states on the ligands [7.411].

This investigation enabled one to solve another related problem. The cluster $[ZnCl_5]^{3-}$ in the very similar crystal $[Co(NH_3)_6][ZnCl_5]$ exists under the same conditions as the $[CuCl_5]^{3-}$ cluster above, with the distinction of there being just one d electron more in the Zn^{2+} (d^{10}) configuration instead of Cu^{2+} ($3d^9$), but its distortion from the TBP configuration is of A_2'' type (not E' type), resulting in a distorted tetrahedron plus one ion on (almost) the trigonal axis: $[ZnCl_5]^{3-}(TBP) \rightarrow [ZnCl_4]^{2-}(tetrahedron) + Cl^-$. Calculations [7.412] quite similar to those performed on $[CuCl_5]^{3-}$ explain directly the origin of the differences between these two clusters: while there are E' and A_2'' excited electronic states (and they produce, respectively, e' and a_2'' PJT distortions) in both clusters, the MO energy positions and vibronic coupling constants in these two systems are different. As a result the e' distortions are stronger than the a_2'' ones in $[CuCl_5]^{3-}$, whereas the opposite situation is realized in $[ZnCl_5]^{3-}$.

The $MoCl_5$ complex in the TBP configuration has the ground electronic E term. The fact of pseudorotation in this complex emerges from its electron-diffraction spectra [7.413]. The authors interpreted the experimental data as compatible with a picture in which about 56% of the molecules have the SP configuration C_{4v}, while the remaining molecules have D_{3h} (TBP) symmetry with large amplitudes of the corresponding vibrations (if normal vibrations are assumed, 18% of the molecules need be considered as dimers). This explanation ignores the vibronic effects and consequent pseudorotation. The experimental results [7.413] are well understood as pseudorotations based on the vibronic coupling scheme discussed above and illustrated in Fig. 7.1; the percentages of different configurations extracted from the experimental data may even allow one to estimate the barrier height between the distorted configurations.

Experimental data and calculation for PF_5 (see [7.414, 7.415] and references therein) show that this system has equivalent TBP configurations with a barrier of about 0.17 eV between them at the C_{4v} symmetry and performs Berry pseudorotations. The latter is qualitatively different from the pseudorotations in the JT systems as discussed in Section 7.1.1.

In a series of papers the specific geometry of the expected tetragonally distorted octahedral complexes of Cu(II), namely whether they are elongated or compressed octahedra, was discussed in detail using both theoretical and experimental evidence [7.416–7.418]. While the JTE theory allows for either elongated or compressed octahedra, depending on the sign of the vibronic coupling constants, it was shown [7.416] (see also [7.419]) that configuration

interaction of the electronic $3d^9$ configuration of Cu^{2+} with the higher-in-energy $4s^2$ configuration, as well as anharmonicity, makes the elongated configuration more favorable.

Nevertheless ESR and X-ray data on some of the crystals with octahedral Cu(II) sites were first interpreted as due to compressed octahedra. Octahedral Cu(II) units in K_2CuF_4, Ba_2CuF_6, γ-$Cs_2PbCu(NO_2)_6$, (3-chloroanilinium)$_8$ $[CuCl_6]Cl_4$, etc., were originally misinterpreted as compressed by the JTE, while a more elaborate investigation including EXAFS measurements (see [7.417, 7.418] and references therein) shows that in fact the local octahedra are elongated, but their positions in the crystal are either randomly oriented (disordered) or antiferrodistortively ordered (Section 8.2), giving the average picture of compressed octahedra instead of elongated ones.

In a similar problem EXAFS investigations of the intraatomic distances in the crystals $[Cu(H_2O)_6](BrO_3)_2$, $[Cu(H_2O)_6]SiF_6$, and $[Cu(ONC_5H_5)_6](ClO_4)_2$ show that the CuA_6 octahedra are tetragonally elongated in full accordance with the JTE [7.420]. This result is in contradiction with the previous conclusion based on crystallographic studies that these octahedra are regular, serving as just another example of the relativity of the means of observation of JT molecular shapes (Section 7.1.1). Compressed tetragonal $[CuF_6]^{4-}$ clusters were observed in $KAlCuF_6$ [7.421], but in this case the octahedral units are strongly interlinked in chains via the axial fluoride ligands, forming a super-exchange system. A strong off-center JT distortion was found by ESR in the $[CuF_8]^{6-}$ cluster as a doped impurity in SrF_2 [7.422].

Among other papers devoted to the JTE in octahedral hexacoordinated transition metal clusters see, e.g., [7.423–7.437]. *Ab initio* SCF and correlated pair-functional (CPF) calculations [7.423(*a*)] of the APES of the octahedral systems of $[Cu(H_2O)_6]^{2+}$, $[Cr(H_2O)_6]^{2+}$ and $[Mn(H_2O)_6]^{2+}$ in their ground E state (JT $E \otimes e$ problem) show that they are tetragonally distorted at the minima with the ratios of, respectively, axial to equatorial $(Cu—O_{ax})/(Cu—O_{eq})$ distances (in Å) of 2.25/2.05, 2.36/2.15, and 2.15/1.99, JT stabilization energy E_{JT} $(cm^{-1}) = 930$, 749, and 1170, and energy barriers between the minima δ $(cm^{-1}) = 136$, 256, and 193. These energy values are much lower than those observed experimentally. For $[M(H_2O)_6]^{3+}$ with M = Zn, Cd, and Hg, where the ground state is nondegenerate, a PJT coupling to the excited state was revealed using Hartree–Fock and effective-core-potential calculations [7.423(*b*)]. The results show a rather flat potential in these systems that explains the softness of, e.g., the Hg—O bonds and a large spread in their mean values (see also the *plasticity effect* in Section 8.1). The JTE in hydrated transition metal ions definitely influences the water-exchange reactions [7.424], as well as in the presence of heteroligand [7.425].

A strong JTE in tris-chelate octahedral complexes formed in the solution of Cu^{2+} ions in ethylene glycol was revealed by means of isotopic substitutions in time-of-flight neutron diffraction [7.427]. In explanation of the pressure-induced change from fluorescence ${}^4A_{2g} \leftarrow {}^4T_{2g}$ to phosphorescence spin-forbidden ${}^4A_{2g} \leftarrow {}^2E_g$ transitions in the octahedral $[CrF_6]^{3-}$ complex of $(NH_4)_3[CrF_6]$ the authors [7.428] involved the PJT mixing of the ${}^4A_{2g}$ and ${}^2E_g$ terms which approach each other under pressure. This suggestion seems to be invalid because the vibronic coupling does not contain spin operators and hence it does not mix terms with different spin multiplicities. However, in principle, this mixing may take place if there is a strong spin–orbital coupling. For $[CrCl_6]^{3-}$ clusters as a doped impurity in $Cs_2NaScCl_6$ the JTE in the infrared luminescence was revealed [7.429(*a*)], and the influence of pressure on the excited ${}^4T_{2g}$ state of this system was analyzed [7.429(*b*)].

For some gas-phase octahedral systems the discussion of the JT origin of their properties is continuing. A sound example is XeF_6 and isoelectronic systems. There is a rather long history of electronic-structure investigation of these systems (see [7.21, 7.22, 7.430–7.435] and references therein). As shown in Section 7.1.2, the PJT mixing of the ground nondegenerate A_{1g} state (formed by the two *ns* electrons that occupy the antibonding MO) with the low-lying excited T_{1u} states (formed by the $a_{1g} \rightarrow t_{1u}$ excitation to the t_{1u} MO that originates from the *np* states) may lead to the trigonal t_{1u}-type distortion of the octahedron, provided the inequality (4.6) holds [7.3, 7.25]. This PJT distortion may be complicated by the proper JTE in the degenerate T_{1u} state. Depending on relations between the coupling parameters, the resulting distortion of the octahedral configuration is (Fig. 7.4) (a) combined PJT dipolar t_{1u} with either tetragonal e_g or trigonal t_{2g} JT distortions; this is the so-called stereochemically active *lone-pair effect;* (b) pure JT either tetragonal or trigonal distortions (when the JTE on the excited T_{1u} term dominates over the PJTE); or (c) no distortions (regular octahedra) when neither the PJTE nor the excited state JTE are sufficiently strong (inert lone pairs) (Section 7.1.2).

Ab initio and other calculations [7.21, 7.22, 7.430–7.435] and experimental data confirm these qualitative predictions: XeF_6, SeF_6^{2-}, and IF_6^- are trigonally distorted, ClF_6^-, BrF_6^-, and $BiCl_6^{3-}$ seem to be regular octahedra (in the condensed phase), while $SeCl_6^{2-}$, $SeBr_6^{2-}$, $TeCl_6^{2-}$, and TeI_6^{2-} may be either distorted or regular octahedra, depending on the counter ions (the environment may quench the pseudorotations).

Recent more elaborate calculations of the electronic structures of some of the above systems [7.21] show that correlation and relativistic effects diminish the PJT distortions, stabilizing undistorted octahedral configurations (for this

reason RuF_6, AtF_6^-, and PoF_6^{2-} emerge as regular octahedra). This result seems to be quite reasonable: higher symmetry favors better correlated electron distribution (and this will be reflected directly in the vibronic coupling constants of the PJTE), while the relativistic contraction of the *ns* electrons increases the A_{1g}–T_{1u} energy gap Δ; both these factors decrease the PJTE contribution to the softening of the system with respect to distortions, as well as the possible contribution of the JTE in the excited T_{1u} state (Section 7.1.2).

The authors [7.21] claim that "none of the available simple models . . . is able to predict or rationalize all these structures." This statement is to say the least ungrounded: the PJTE contains the necessary tool that explains qualitatively all these structural observations. The authors [7.21] just did not try this possibility, for which the estimation of the excited states and vibronic coupling constants would be required. A method of *ab initio* calculations that allows one to analyze the PJT origin of molecular geometries was worked out recently [7.22] and applied to several series of compounds chosen as examples. In particular, it was shown that in the three isoelectronic systems considered in [7.21], TeF_6^{3-}, IF_6^-, and XeF_6, the latter only is subject to PJT instability. In a series of octahedral hydrides MH_6 with $M = Sc^{3-}$, Ti^{2-}, V^-, Cr, and Mn^+ the PJT softening of the ground state increases from left to right, making only the last two of them unstable [7.22].

The mixed PJT (dipolar) and JT distortions mentioned above are most important in explaining the origin of complicated (helicoidal) crystal structures and chirality [7.436, 7.437]. In particular, in the InCl crystal ($[InCl_6]^{5-}$ clusters) both types of combined dipolar distortions, dipolar t_{1u} plus trigonal t_{2g}, and dipolar t_{1u} plus tetragonal e_g, are observed in two phases of the crystal, yellow and red, respectively (see also Section 8.2). Vibronic energy levels of IrF_6 were considered in [7.438]. For the vibronic origin of the lone-pair effect in a series of other systems revealed by means of DFT calculations see in [7.27, 7.28].

The geometry, energy, vibrational frequencies and EPR parameters of $V(CO)_6$ in O_h, D_{3d}, D_{4h}, and D_{2h} symmetries were computed using DFT and high-level *ab initio* methods [7.439]. The lowest configurations are of D_{3d} symmetry in accordance with the JTE in the T_{2g} term of the regular octahedron (Section 3.3) with the JT stabilization energy $E_{JT}^T = 731\,cm^{-1}$. The barrier height between the D_{3d} minima $\delta = 210\,cm^{-1}$ at a D_{2h} saddle point. This structure agrees well with a variety of experimental data including EPR, IR, and Raman spectra.

Coordination systems of gold are mentioned in Section 7.3.2. The CASSCF method was applied to calculations for a series of $AuCl_n$ systems [7.440]. It was shown that in accordance with the JTE $AuCl_3$ has three equivalent minima with C_{2v} symmetry 29 kcal/mol lower in energy than the D_{3h} configuration and

with barriers of ~6 kcal/mol between the minima. This distortion is smaller than in AuF_3. The tetrahedral $AuCl_4^-$ is also subject to JT distortions.

Coordination systems with T terms are less studied than E-term systems, except for a series of works reported recently on T-term and partly E-term JTE in octahedral aquo-complexes of transition metals [7.441–7.453]. In a comprehensive study of mostly magnetic measurements in combination with Raman spectra, neutron diffraction, and numerical calculations the authors revealed the main features of the JTE in $[Ti(H_2O)_6]^{3+}$, $[V(H_2O)_6]^{3+}$, $[Mn(H_2O)_6]^{3+}$, $[Cr(H_2O)_6]^{2+}$, and $[Ru(H_2O)_6]^{3+}$ in different crystal environments, including also cooperative phenomena and phase transitions. In particular, the cubic-to-orthorhombic phase transition at ~12 K in $CsTi(SO_4)_2 \cdot 12H_2O$ observed by EPR and neutron scattering is interpreted as triggered by local JT distortions in the $[Ti(H_2O)_6]^{3+}$ complexes. In the high-temperature phase this distortion splits the t_{2g} (O_h) orbital, leaving the e_g orbital lower in energy, while the JT $E_g \otimes e_g$ problem with cooperative interaction between the centers results in the orthorhombic phase [7.441, 7.448]. This explains the anomalous ground-state g factors, $g_{\|} = 1.25$ and $g_{\perp} = 1.14$, as due to the low-symmetry distortion (in previous interpretations the phase transition was not taken into account). The same model explains also the ground-state magnetic susceptibilities of the system [7.442, 7.448]. By numerical diagonalization of the vibronic Hamiltonian including spin–orbital interaction and vibronic coupling to the water environment of the titanium ion (involving also librational modes for the sulfate group) the authors achieved a very good fit to the magnetic measurement data and Raman spectra for the $[Ti(H_2O)_6]^{3+}$ cluster in the β-alum lattice.

The anomalous magnetic behavior of titanium(III)-doped cesium gallium alum with the magnetization strongly dependent on the strength of the magnetic field is explained as due to the second-order (giant) Zeeman effect produced by the mixing of low-lying vibronic states by the magnetic field [7.443].

The EPR spectrum of Ti(III) in $CsAl(SO_4)_2 \cdot 12H_2O$ was carefully reexamined by novel techniques and fully interpreted as due to the dynamic JT coupling and the influence of low-symmetry strain (Section 6.3.2) [7.446, 7.448]. The splitting (~2720 cm^{-1}) of the T_{1g} ground state of the octahedral $[V(H_2O)_6]^{3+}$ cluster in $[Rb(H_2O)_6][V(H_2O)_6](SO_4)_2$ due to the trigonal distortion in the minima was observed in Raman scattering, and the band shape was well reproduced based on the $({}^3A + {}^3E) \otimes e$ combined JT plus PJT vibronic-coupling model (Section 4.2) [7.447].

For the $[Cr(OD_2)_6]^{2+}$ cluster in Tutton salt $(ND_4)_2Cr(OD_2)_6(SO_4)_2$ inelastic temperature-dependent neutron-scattering data are consistent with the JT ${}^5E \otimes e$ problem perturbed by low-symmetry strain [7.453].

With the aim of explaining spectroscopic properties of impurity centers in crystals (Section 8.1) the JTE in ground and excited orbital triplet T states of the $[MnF_6]^{4-}$ (I) and $[CrF_6]^{4-}$ (II) clusters were analyzed [7.454]. For the $^4T_{1g}(G)$, $^4T_{2g}(G)$, $^4T_{2g}(D)$, and $^4T_{1g}(D)$ states of (I) and the $^4T_{2g}$ state of (II) the authors calculated values of the constants F_E of vibronic coupling to e distortions in the crystal-field approximation in reasonable agreement with some spectroscopic Huang–Rhys factors.

Monatomic clusters Ni_6 [7.455], Pb_6, $[Pb_6]^+$, and $[Pb_6]^-$ [7.456] were also considered with respect to the possible JT distortions of the reference octahedral configuration. In Ni_6 the authors [7.455] found two distorted configurations of C_{2v} (most stable) symmetry in the ^9B_g electronic state, and D_{2h} in the state $^9B_{3g}$. In the lead complexes [7.456] the JT distortions are almost completely quenched by the spin–orbital interaction (Section 4.2).

Multicenter JT problems (Section 3.6) serve as a bridge between monocenter systems and JT poly-center formations in crystals. Four-center systems of the type $Cu_4OX_6L_4$ are mentioned in Section 3.6 where they serve as a prototype for the solution of the four-center JT problem [7.457–7.460]. Following the solution of Section 3.6 in the strong-coupling limit, the APES was evaluated and, using the Heisenberg spin Hamiltonian for exchange interactions, the temperature dependence of the effective magnetic moment $\mu_{eff}(T)$ was calculated in good agreement with experimental data for $L = OP(C_6H_5)_3$ and $X = Cl$, Br; $L = (C_6H_5N)$ and $X = Br$; and $L = (tmn)$ and $X = Cl$. In particular, the origin of the unusual non-monotonic dependence of $\mu_{eff}(T)$ for some clusters was explained. The role of spin–orbital interaction was also considered.

Four-center clusters $Cu_4O_{12}H_8$ as local formations in superconducting copper oxide compounds were considered from the point of view of vibronic coupling presented as a sum of orbital vibronic contributions (Section 2.3) [7.461]. The role of HOMO and LUMO versus the most active modes in this coupling is discussed. The JTE in six-center transition metal clusters was considered recently [7.462, 7.463]. Using DFT electronic-structure calculations with geometry optimization it was shown that $[Re_6S_8Cl_6]^{3-}$ has a ground E term with three minima of D_{4h} symmetry on the APES (as expected from the $E \otimes e$ problem), in which the reference configuration O_h is compressed. The JT stabilization energy is $E_{JT}^E \sim 0.06$ eV with a small barrier between the minima of $\delta \sim 0.005$ eV. These distortions were observed experimentally in $(n\text{-}Bu_4N)_3[Re_6S_8Cl_6]$ at 100 K.

In the somewhat similar system $[W_6Cl_{14}]^-$ the ground state in the O_h configuration is T_{2u}, which is known to produce much smaller distortions then the E term. The calculations [7.462] yield shallow ($\sim$0.001 eV) D_{4h} minima,

Table 7.17. *Bond angles and bond lenths for MX_4 polyhedra in cat[MX_4], where cat is* p-*xylylene bis(triphenylphosphonium)$^{2+}$ [7.410]*

	$[Co(NCS)_4]^{2-}$	$[Ni(NCS)_4]^{2-}$	$[Cu(NCS)_4]^{2-}$	$[CuBr_4]^{2-}$
ϕ_1 (degrees)	113.9	115.6	135.0	134.5
ϕ_2 (degrees)	116.1	126.3	139.5	136.9
$\phi_3 = \phi_4 = \phi_5 = \phi_6$ (degrees)	106 ± 1	103 ± 2	97 ± 1	98 ± 2
R(M—X) (Å)	1.96	1.93	1.92	2.39

meaning that the JT $T \otimes e$ problem is realized, the coupling to t_{2g} displacements being less important (Section 3.3). The so-called *continuous symmetry-measure* methodology was applied to explore JT distortions in Cu(II) complexes quantitatively [7.464].

Examples of distortions for several tetrahedral MX_4 systems with an electronically threefold degenerate T ground state are given in Table 7.17 in terms of tetrahedral angles ϕ. There are many other examples of this kind in the review articles mentioned at the beginning of this section. The D_{2d} distortions ($\phi \approx 85^\circ$) of the NiX_4 cluster in $Ni(NMTP)_4[BF_4]_2$, where NMTP = *N*-methyl-2-thiooxopyrrolidine, allowed the authors [7.465] to estimate the vibronic coupling constants $F_E = 3250\,\text{cm}^{-1}\,\text{Å}^{-1}$, $G_E \approx 0$, and $E_{JT} = 1595\,\text{cm}^{-1}$. In the analogous cluster with Zn (instead of Ni), which has a nondegenerate ground state, there are practically no distortions except those that can be attributed to crystal packing.

The photochromic effect in sodium nitroprusside, $Na_2[Fe(CN)_5(NO)]\cdot 2H_2O$ was explained based on a PJT model [7.466] that involves in the vibronic coupling the following three electronic states of mainly the Fe—N—O triangle: $^1A_1[Fe^{2+}(\alpha_1^2\beta_1^2\alpha_2)]$, $^1B_2[Fe^{3+}(\alpha_1^2\beta_1^2\alpha_2)\beta_1(\pi_x^*\text{NO})]$, and $^1A_2[Fe^{3+}(\alpha_1^2\beta_1^2\alpha_2)\alpha_1(\pi_y\text{NO})]$, where α_1, α_2, and β_1 are the MOs belonging to the corresponding irreducible representations A_1, A_2, and B_2 of the C_{2v} group, respectively. These states are mixed by a_1 and b_1 displacements, resulting in the PJT problem $(A_1 + A_2 + B_2) \otimes (a_1 + b_1)$. A model solution of this problem allowed the authors [7.466] to obtain the APES illustrated in Fig. 7.33. It shows the ground-state (GS) minimum with two excited (metastable) minima (MS1 and MS2), at which in the distorted triangle the angle Fe—N—O is 146°, 74.8°, and 0.1°, respectively, in good agreement with the experimental data (176°, 82°, and 3°, respectively). The three minima are thus separated by relatively large barriers of conversion from the Fe—N bond in the GS to the Fe—O bond in MS2 via the intermediate side-on coordination in MS1, and this explains the long lifetime of the excited metastable states.

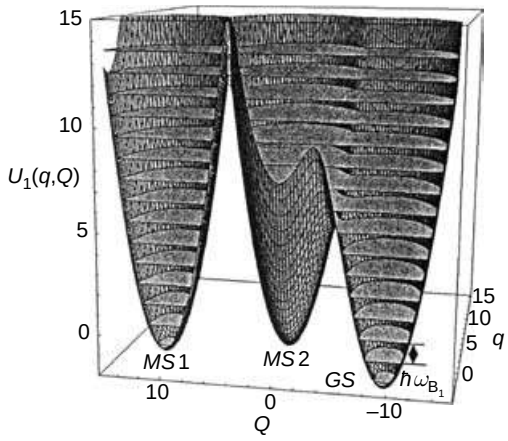

Fig. 7.33. The APES of sodium nitroprusside (obtained in a PJT model), showing the ground-state minimum GS and two excited (metastable) minima MS1 and MS2 (Reprinted with permission from [7.466]. Copyright 2003 Elsevier Science Publishers.)

The crystal stereochemistry of a series of coordination systems $[Cu(phen)_2Br][Y]$ with $Y = Br^- \cdot H_2O$, ClO_4^-, $NO_3^- \cdot H_2O$, PF_6^-, and BPh_4^- was qualitatively explained based on the JTE and especially PJTE in the basic cluster CuN_4Br [7.467].

Combined quantum-mechanical/molecular-mechanics (QM/MM) and molecular-dynamics (MD) simulations were used to study hydrated Cu^{2+} ions in water and ammonia solutions [7.468, 7.469]. The radial distributions of Cu—O and Cu—N distances were calculated in four different models of a hydrated ion with one and two heteroligands (NH_3) in *cis* and *trans* positions. The results confirm the dynamic JT distortions in the octahedral $[Cu(H_2O)_6]^{2+}$ cluster and a characteristic time of <200 fs for the inversion of the JT distortions (meaning rather large tunneling splitting). Another conclusion is the strong and position-dependent weakening influence of the heteroligands on the Cu—O bond: the acceleration of water exchange by a factor of ~ 2 for one ligand NH_3, ~ 3 in the case of two NH_3 molecules in *cis* position, and ~ 6.5 for two NH_3 molecules in *trans* position (cf. mutual influence of ligands in Section 7.1.4).

JT-induced preorganization in copper complexes important to their reactivity is considered in [7.470]. ESR spectra of $[Cu(en)_2H_2O]SO_4$ at low temperatures and high frequencies (73 GHz) were interpreted as due to two nonequivalent JT centers in the unit cell with coupled dynamic distortions [7.471]. The C_{3v} symmetry of the reference configuration of $[(\eta^6\text{-benzene})Nb(CO)_3]^+$ with consequent low-energy singlet and triplet E terms allows one to apply the JTE to evaluate the observed geometries of this and related

systems [7.472]. In particular, it was shown that there are two JT-active e modes related to bending and inversion of the metal-carbonyl moiety.

Unusually large Stokes' shifts in the phosphorescence of AuL_3, L = phosphine, were explained by the JT distortions in the excited triplet state $^3E''$ explored by means of hybrid quantum-mechanical/molecular-mechanics calculations with quantum mechanics applied to the $[Au(PH_3)_3]^+$ complexes [7.473]. DFT calculations of the JT distortions and stabilization energies in $[Cu(en)_3]^{2+}$ are used as a model to understand the properties of macrobicyclic cage complexes of Cu(II) studied by ESR [7.474]. Similar JT systems of Ag(II) studied by ESR are considered in [7.475] (see also [7.476]).

Moving to two-center and multicenter coordination systems, we note first that mixed-valence systems are considered in the next Section 7.6.3. In an edge-sharing bioctahedral structure with two octahedral Mo centers, *cis*-$Mo_2(\mu_2\text{-}O_2CCH_3)_2(\mu_2\text{-}DX_yIF^{2,6})_2$, where $DX_yIF^{2,6}$ is the anion of *N*,*N*′-di-(2,6-xylyl-formamidine), the $Mo_2(\mu_2\text{-}O)$ ring distortion is attributed to the PJTE [7.477]

An interesting example of a polyatomic T_d structure with a JTE in the excited $^1T_2$ state is presented by $Sn_6(\mu_5\text{-}O)_4(\mu_3\text{-}OH)_4$ [7.478]. By means of *ab initio* calculations with geometry optimization, it was shown that the system in the $^1T_2$ state undergoes a JT distortion from T_d to C_{2v} (as predicted by the theory), which is 23.7 kcal/mol lower in energy. This explains the observed spectral properties, which were earlier interpreted as being due to the formation of Sn—Sn bonds (the authors [7.478] show that no such bonding takes place).

The JTE was shown to be important in formation of multi-ion complexes in heteropolytungstates [7.479].

Coordination centers play important roles in biological systems, especially in metalloenzymes and other metallobiochemical formations, where the JT vibronic coupling effects are of significant importance. The general understanding here is that the transition-metal center in these systems provides the necessary degenerate or close-in-energy orbital states, while the large organic environment creates a series of soft modes, both (degenerate states and soft modes) favoring JT and PJT distortions [7.3] (cf. the Δ and K_0 values in the inequality (4.6)). A large class of such systems is formed by hemoproteins, the active site of which can be modeled by metalloporphyrins; many of their properties can be explained by the PJTE [7.400, 7.480–7.485].

With the metal atom in the center of the cavity of a planar porphyrin ring, out-of-plane displacements of the iron atom were shown to play an essential role in the functioning of hemoglobin (Hb) and other hemoproteins, providing the trigger mechanism of oxygenation [7.486]. It was shown that the out-of-plane displacement of the iron atom in iron porphyrin is a PJTE and its return to in-plane position upon oxygenation in Hb is due to the electron rearrangement

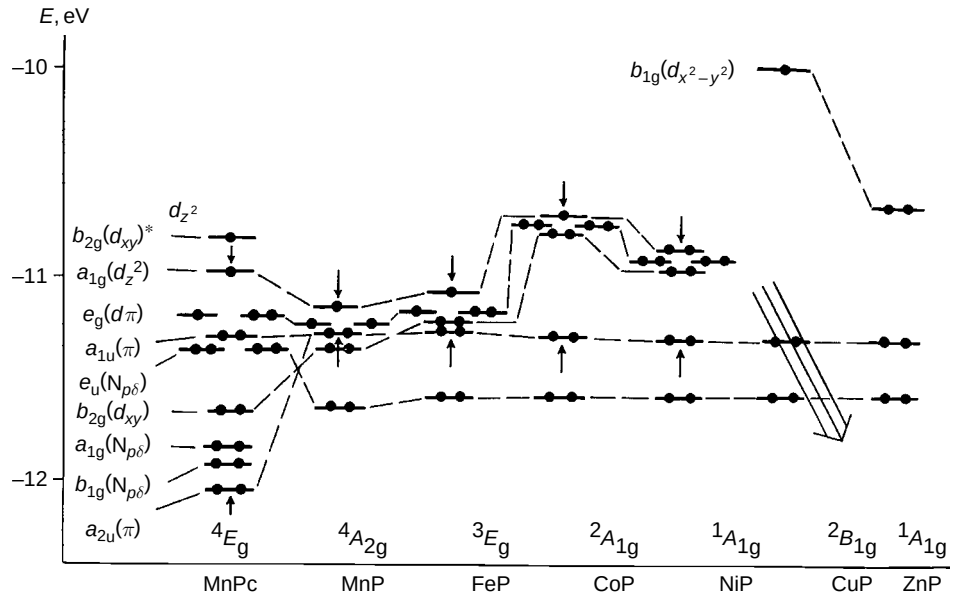

Fig. 7.34. HOMO and LUMO energy levels for some metal porphyrins (MP) and manganese phthallocyanine (MnPc) with indication of the ground state for the in-plane position of the metal. The two MOs forming the energy gap 2Δ between the ground and excited states that mix under the A_{2u} displacement are shown by dark arrows [7.487].

that quenches the PJTE (destroys the inequality (4.6)) [7.400]. In the C_{4v} symmetry of the nearest environment in the metal porphyrin (MP) center the out-of-plane displacement of the metal is an a_{2u} mode, for which the nonzero PJT coupling requires appropriate symmetries of the mixing orbital states that produce the instability. Figure 7.34 illustrates the HOMO–LUMO energy-level positions [7.486, 7.487] for several MPs, with M = Mn, Fe, Co, Ni, and Cu, and manganese phthallocyanine (MnPc). It is seen that the small energy gap Δ between the a_{1g} and a_{2u} MOs required to satisfy inequality (4.6) in order to get PJT a_{2u} displacement is satisfied for MnP and FeP, whereas other transition metals might not be appropriate for this distortion, and this conclusion is in accordance with experimental evidence (see in [7.400]).

In MnPc the energy gap Δ is large too, and its configuration is planar. This particular case shows that the previous explanation of the out-of-plane displacements as due to the non-fit of the ionic radius with the cavity dimensions does not work: the cavity is smaller in phthalocyanine than in porphyrin, but MnPc is planar, while MnP is not. Again, a series of MPs with ionic radii of M larger than Fe(II) (e.g., Sn(IV) and Mo(IV)) are planar. The PJTE explains all these stereochemical facts in a unique fashion.

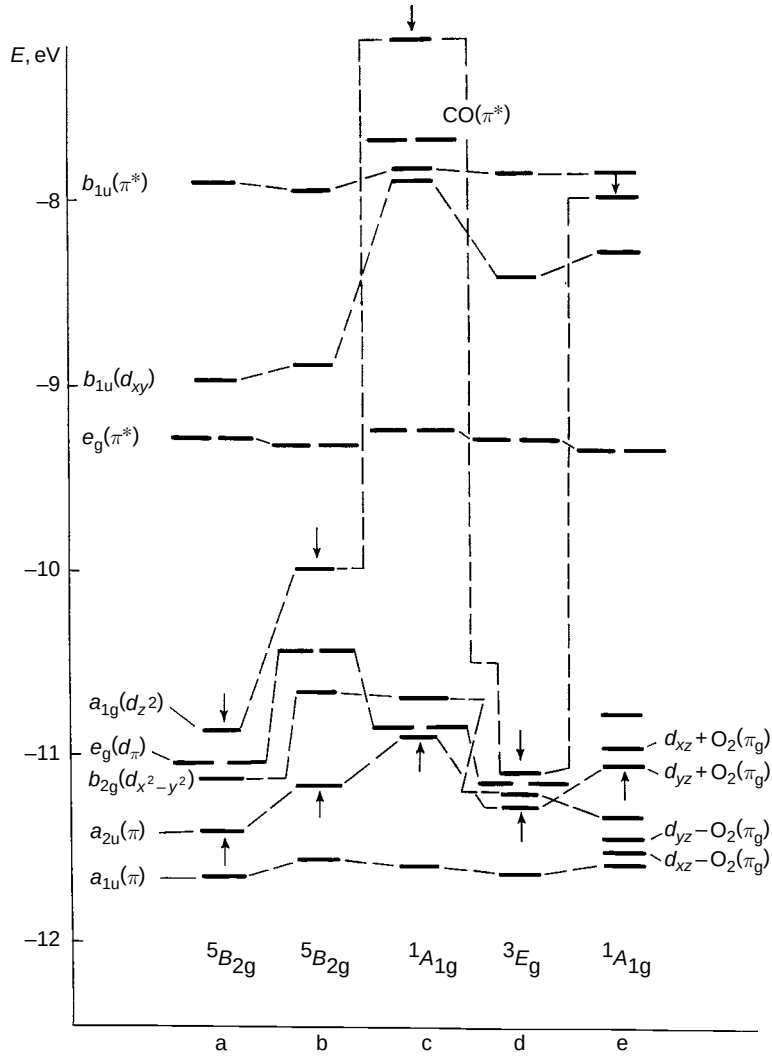

Fig. 7.35. The MO energy levels for several HOMOs and LUMOs of iron porphyrin with indication of the ground term: (a) the out-of-plane displacement of the iron atom is $\Delta R = 0.49$ Å; (b) the deoxy form of hemoglobin (Hb), $\Delta R = 0.62$ Å; (c) Hb—CO; (d) planar iron porphyrin $\Delta R = 0$; (e) Hb—O_2. The energy gap 2Δ between the two states that mix under the out-of-plane displacement of the iron atom are shown by arrows.

For the out-of-plane position of the iron ion in FeP (or in Hb) its return to in-plane position upon oxygenation is shown to be due to the increase of the energy gap Δ between the ground and excited states active in the PJTE that invalidates the inequality (4.6). Figure 7.35 illustrates this statement.

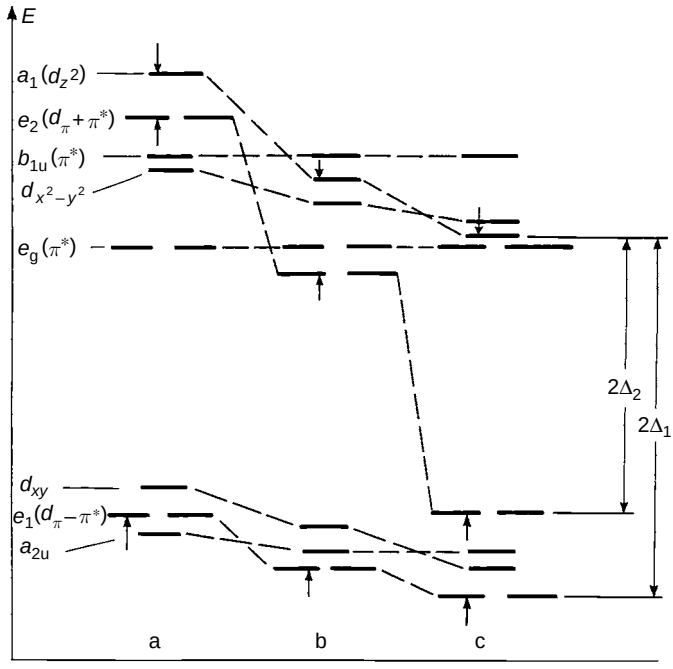

Fig. 7.36. MO energy-level diagrams for linear end-on coordination of diatomics to metalloporphyrins: (a) CO, (b) NO, and (c) O_2. The arrows indicate the energy gaps $2\Delta_1$ and $2\Delta_2$ between the e and a_1 MOs that mix under the bending (E-type) displacement of the ligand.

Another important feature of many metalloenzymes that can be explained by means of the PJTE is the geometry of coordination of small ligands (O_2, CO, CN, NO) to the metal center, which influences their reactivity and dissociation. Again, the PJT mixing of ground and excited states of the reference high-symmetry configuration with the ligand in linear end-on coordination to MP was shown to explain the origin of the E-type bending distortions for some ligands, resulting in their different geometries of coordination [7.400, 7.481, 7.482]. Figure 7.36 illustrates some of these results.

There are two main PJT mixings that contribute to the E-type bending of the ligand. Following Eq. (4.14), one can evaluate the resulting condition of end-on configuration instability, which in our case of one-electron MO presentation yields

$$\frac{(q_1 - q_3)F_1^2}{\Delta_1} + \frac{(q_2 - q_3)F_2^2}{\Delta_2} > K_E \tag{7.45}$$

where in addition to the energy gaps $2\Delta_1$ and $2\Delta_2$ and corresponding vibronic coupling constants F_1 and F_2 the populations q_1, q_2, and q_3 of the three active

MOs (e_1, e_2, and a_1, respectively) are introduced. In the case of the MP—CO bonding only the lowest e_1 level is populated, meaning that $q_2 - q_3 = 0$, and since $2\Delta_1$ is too large, no PJT bending occurs: CO is expected to be coordinated linearly end on. For MP—NO coordination the e_2 MO becomes occupied when the number n of d electrons of the metal plus the antibonding π^* electron of NO exceeds six, $n + 1 > 6$, for which case both terms in Eq. (7.45) contribute to the instability, resulting in a bent configuration. This happens when $n > 5$. Thus the PJTE for metals with $n \leq 5$ the linear end-on coordination of the NO molecule is stable, while for $n > 5$ it is unstable, in full agreement with experimental data (note that the variations of the energy gaps $2\Delta_1$ and $2\Delta_2$ and vibronic constants F_1 and F_2 for different metals and ligands are small). For MP—O_2 bonding the two contributions in Eq. (7.45) are of the same order of magnitude, resulting in instability of the end-on configuration; in fact the coordination of O_2 is side on.

One of the consequences of different geometries of ligand coordination is manifest in their dissociation features, especially in flash-photolysis [7.400, 7.482]. Indeed, due to the strong dependence of the geometry of coordination on the population of the corresponding MOs (Eq. (7.45)), some optical excitations result in essential changes of this geometry. Obviously, if the vertical excitation from a stable ground state (as, e.g., in the MP—CO linear end-on coordination) falls into the point of instability of the excited state (in the case of MP—CO this may happen by excitation to the e_2 MO), the quantum yield of photodissociation will be maximal. Different possibilities based on the PJTE picture given above were considered [7.400, 7.482]. Recent experimental data confirm these predictions [7.488].

The problem of proton dynamics in the porphyrin ring was investigated involving the PJTE [7.489]. In the reference D_{4h} configuration with two protons, one above and one below the plane of the porphine ring, the ground A_{1g} and excited E_g terms mix under the PJT e_g nuclear displacements, making this configuration unstable. The resulting APES has four minima with the protons localized near opposite nitrogen atoms accompanied by the corresponding e_g type out-of-plane distortion of the macrocycle. At low temperatures the system is localized near one of the minima. As the temperature increases transitions between the minima (correlated jumping of the protons to another pair of nitrogens) occur more often. The temperature dependence of the probability of these transitions was calculated considering the thermal interaction of the minima states with the out-of-plane vibrations of the porphine skeleton and its environment. The results obtained agree well with the experimental data on NMR measurements of proton migration in tetraphenylporphyrin.

The PJTE was also shown to be instrumental in explaining enzymatic catalysis in Cu systems, like $CuL_3 + X_2 \rightarrow CuL_3X + X$ [7.490], their mechanism

being similar to the JT- and PJT-induced chemical activation discussed in Section 7.1.3. Regarding activation of small molecules by their coordination to transition metal clusters see also in [7.491].

7.6.2 Vibronic coupling in mixed-valence systems

Mixed-valence (MV) compounds can be defined as systems with one or two excess electrons to occupy two or more equivalent centers with energy barriers between them. Depending on the magnitude of these barriers, the excess electrons may be either asymmetrically localized on some of the centers or delocalized over some or all centers. Roughly speaking, the localization–delocalization alternative is the main problem of MV compounds. MV systems proved to be important to many areas of physics, chemistry, and biology, including, for instance, redox catalytic action, metalloenzyme functioning, molecular electronics, and superconductivity (see [7.398, 7.492–7.498] and references therein).

On the other hand any full treatment of MV systems is impossible without involving vibronic coupling. Indeed, the excess electron localization is inevitably accompanied by the nuclear relaxation to the new equilibrium positions, which are determined by the vibronic coupling constants. The vibronic theory of MV systems began with the Piepho–Krausz–Schatz model [7.495, 7.496] in which it is assumed that there is one excess electron in a dimer with two equivalent closed-shell centers, 1 and 2, and the one-electron states at each center, φ_1 and φ_2, are nondegenerate. This means that when the excess electron is localized at one of the centers, it distorts its near-neighbor environment along the totally symmetric coordinate. The corresponding local distortion (breathing) coordinates can be denoted by Q_1 and Q_2, respectively. The coupling of the electronic state to these distortions is described by the vibronic constant F (Section 2.2):

$$F = \langle \varphi_1 | (\partial H/\partial Q_1)_0 | \varphi_2 \rangle = \langle \varphi_2 | (\partial H/\partial Q_2)_0 | \varphi_2 \rangle \tag{7.46}$$

where H is the Hamiltonian.

For the system as a whole the presentations of the wavefunctions,

$$\Phi_\pm = \sqrt{1/2}(\varphi_1 \pm \varphi_2) \tag{7.47}$$

and coordinates,

$$Q_\pm = \sqrt{1/2}(Q_1 \pm Q_2) \tag{7.48}$$

are more convenient. Q_+ is a totally symmetric coordinate of the system describing the simultaneous (synchronous) breathing distortion of both centers, while Q_- gives the asymmetric distortion of the anti-phase breathing of the two centers corresponding to the electron localization.

If there is an overlap between the two states φ_1 and φ_2, they form bonding Φ_+ and antibonding Φ_- states with an energy gap $2w$, where w is the resonance integral:

$$w = \langle \varphi_1 | H | \varphi_2 \rangle \tag{7.49}$$

This parameter is most important for the MV theory characterizing the strength of the intercenter interaction and hence the electron-transfer rate.

With the notations (7.46) through (7.49), the problem of the excess electron in the MV dimer under consideration can be formulated as a vibronic problem. Indeed, the two states $\Phi_\pm$ at $Q_1 = Q_2 = 0$ ($Q_\pm = 0$) mix under the nuclear displacements Q_- and shift under Q_+. For the problems considered in this section the shift Q_+ is not important and can be excluded by an appropriate choice of the energy read off. The mixing of the two electronic states by the nuclear displacements Q_- taken as a perturbation results in the PJT problem (Section 4.1) with the APES (4.4) as the solution (K_0 is the force constant of the Q_1 or Q_2 distortions):

$$\varepsilon_\pm(Q_-) = \tfrac{1}{2}K_0 Q_-^2 \pm \left(w^2 + F^2 Q_-^2\right)^{\frac{1}{2}} \tag{7.50}$$

These two curves are analyzed in Section 4.1. For $|w| > F^2/K_0$ both have a minimum at $Q_- = 0$. However, if (cf. (4.6))

$$|w| < F^2/K_0 \tag{7.51}$$

the lowest curve has a maximum at $Q_- = 0$ and two minima at $\pm Q^0$,

$$Q_-^0 = [(F^2/K_0^2) - (w^2/F^2)]^{\frac{1}{2}} \tag{7.52}$$

The curve $\varepsilon_-(Q)$ for this case is illustrated in Fig. 4.1 of the PJTE. It is seen that if the condition (7.51) is obeyed, that is, if the contribution to the energy due to the localization distortion Q_- is larger than that of the electron transfer w, the minimum energy (and the wavefunction) corresponds to the localization of the excess electron at one of the two centers. In the opposite case when $|w| > F^2/K_0$, $Q_- = 0$, and there are no localization minima, the electron is uniformly delocalized over the two centers. Thus for MV dimers the inequality (7.51) serves as the condition of localization of the excess electron.

One of the observable properties in MV systems is the *intervalence transition (IT) band of light absorption* produced by the transition from the minimum

(localized) ground state to the excited (delocalized) state. Both the frequency and the probability (band shape) of the IT are dependent on the parameters of electron transfer w and vibronic coupling F. To calculate the band shape more accurately, one has to compute the vibronic states of the system with the potential (7.50), individual transitions between them, and the envelope band shape as described in Section 6.1.1. If there is a sufficiently strong PJTE on each center, the picture of electron localization is more complicated, in particular, because the two centers are nonequivalent [7.499].

The simplest model of the MV dimer, discussed above, may be insufficient for describing real systems. The main complications may be caused by (1) the existence of more than two equivalent centers (polynuclear clusters), (2) the presence of more than one electronic state on each center that can be occupied by the excess electron; (3) the influence of low-symmetry crystal fields and spin–orbital interactions; and (4) the occurrence of open-shell (nonzero-spin) cores, resulting in magnetic exchange coupling between the centers (double exchange interaction). These and other related questions (including important implications of magnetic interactions) are considered in a series of papers outlined in the review article [7.398] and in several examples below.

One of them is related to MV trimers [7.398, 7.500]. Regular three-center triangular clusters are most widespread, the series of carboxylates $[M_3O(RCOO)_6]L_3$ being a well-known example; in Fig. 7.37 the one with $M = Fe$, $R = CF_3$, and $L = H_2O$ is illustrated.

Consider a trimeric MV cluster and assume (as in the case of a simple dimer) that there is only one excess electron over the three metal centers with closed shells and only one nondegenerate state on each center φ_i, $i = 1, 2, 3$, to be occupied by the excess electron. In the triangular symmetry C_{3v} the three one-electron states ϕ_i form three MOs of A and E symmetry (cf. Section 5.3):

$$\begin{aligned} \Psi_A &= (1/\sqrt{3})(\varphi_1 + \varphi_2 + \varphi_3) \\ \Psi_{E\theta} &= (1/\sqrt{6})(2\varphi_1 - \varphi_2 - \varphi_3) \\ \Psi_{E\varepsilon} &= (1/\sqrt{2})(\varphi_2 - \varphi_3) \end{aligned} \tag{7.53}$$

Denoting, as above, the intercenter resonance integral (the electron-transfer parameter) by w (cf. (7.49)), we find easily that the splitting $\varepsilon(A) - \varepsilon(E) = 3w$.

As in the case of a dimer the excess electron, when localized at the center, distorts its environment, thus violating the C_{3v} symmetry of the system, and this distortion is very important for the electron-transfer phenomenon. Since the φ_i states are nondegenerate, the totally symmetric local distortions Q_i ($i = 1, 2, 3$) only are affected by the excess electron. Similar to the wavefunctions (7.53), it is

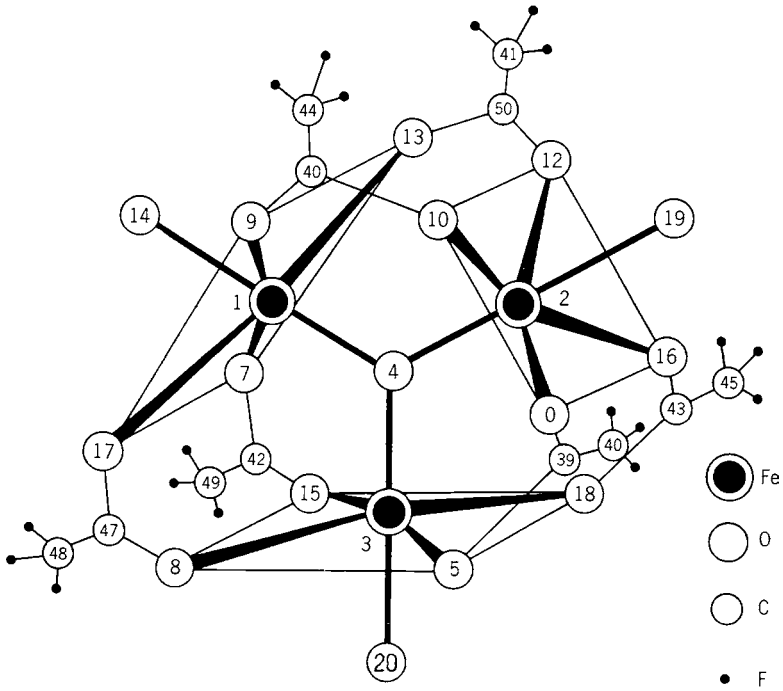

Fig. 7.37. The structure of the MV trimer $M_3O(RCOO)_6L_3$ with M = Fe, R = CF_3, and three ligands L = H_2O marked by 14, 19, and 20, respectively.

more convenient to take these three local coordinates Q_1, Q_2, and Q_3 in symmetrized combinations for the system as a whole (Section 7.1):

$$\begin{aligned} Q_A &= (1/\sqrt{3})(Q_1 + Q_2 + Q_3) \\ Q_\theta &= (1/\sqrt{6})(2Q_1 - Q_2 - Q_3) \\ Q_\varepsilon &= (1/\sqrt{2})(Q_2 - Q_3) \end{aligned} \tag{7.54}$$

While Q_A is totally symmetric in the C_{3v} configuration, Q_θ and Q_ε form two components of the twofold degenerate E displacement. The totally symmetric coordinate Q_A, similar to the dimer, can be separated by an appropriate choice of the energy read off.

With these denotations, the electronic energy levels $\varepsilon_0(Q)$ as functions of the coordinates Q_θ and Q_ε can be found by solving the corresponding secular equation of the type (3.2) which in polar coordinates $Q_\theta = \rho\cos\varphi$, $Q_\varepsilon = \rho\sin\varphi$ is [7.500]

$$\varepsilon_0^3 - (F^2\rho/2 + 3w^2)\varepsilon_0 - 2w^3 - (2/3)^{\frac{1}{2}}F^3\rho^3\cos(3\varphi) = 0 \tag{7.55}$$

where F is the constant of vibronic coupling with the Q_i displacements (7.46). The three roots of Eq. (7.55) ε_0^i $(i = 1, 2, 3)$ together with the strain (deformation) energy $\frac{1}{2}K\rho^2$ form three sheets of the adiabatic potential surface:

$$\varepsilon_i(\rho, \varphi) = \tfrac{1}{2}K\rho^2 + \varepsilon_0^i \tag{7.56}$$

For simplicity, we assume that the K values are the same for the two oxidation states of the center and, as above, we use dimensionless units for Q, F, and w.

It can be shown that the solutions of Eq. (7.55) ε_i are periodic functions of φ with a period of $2\pi/3$. The extremal points of the APES (7.56) are at $\varphi = \pi n/3$, $n = 0, 1, \ldots, 5$. If $F < 0$, then for the lowest sheet the even values of n correspond to maxima along φ (and saddle points if other coordinates are included, see below), while the odd values give minima, and vice versa for $F < 0$.

Consider the radial dependence of the adiabatic potential in the extremal cross-section $\varphi = 0$ (or, equivalently, $Q_\varepsilon = 0$). The solutions of Eq. (7.55) in this case are

$$\begin{aligned} \varepsilon_1 &= -F\rho/\sqrt{6} - w \\ \varepsilon_{2,3} &= \tfrac{1}{2}[w - F\rho/\sqrt{6} \pm 3(F^2\rho^2/6 - 2w\rho/3\sqrt{6} + w^2)^{\frac{1}{2}}] \end{aligned} \tag{7.57}$$

Further investigation of this expression requires knowledge of the sign of the parameter of intercenter electron transfer w. While for dimers the sign of w is not important, for the trimers it is essential. If $w > 0$, the electronic doublet is lowest. Its adiabatic potential shape is then similar to that in the JT $E \otimes e$ problem with the quadratic terms of the vibronic interaction included (Section 3.2).

In the case at hand the warped APES (7.57) results from simultaneous JT and PJT distortions in the linear approximation with respect to the vibronic interaction terms. The three minima of the APES describe the three possibilities of localization of the excess electron at each of the three centers. Since there is no minimum at $Q_\theta = 0$ (where the three centers are equivalent), it follows that *in trimer MV compounds with* $w > 0$ *fully delocalized electron distributions are not possible*.

The systems with $w < 0$ seem to be more interesting. Indeed, they have singlet ground electronic terms, and the APES shape, as in the dimer, is completely determined by the parameter $|w|/F^2$. On substituting

$$\rho = (2/3)^{\frac{1}{2}}(|w|/F)(2\sqrt{2}\sinh t - 1) \tag{7.58}$$

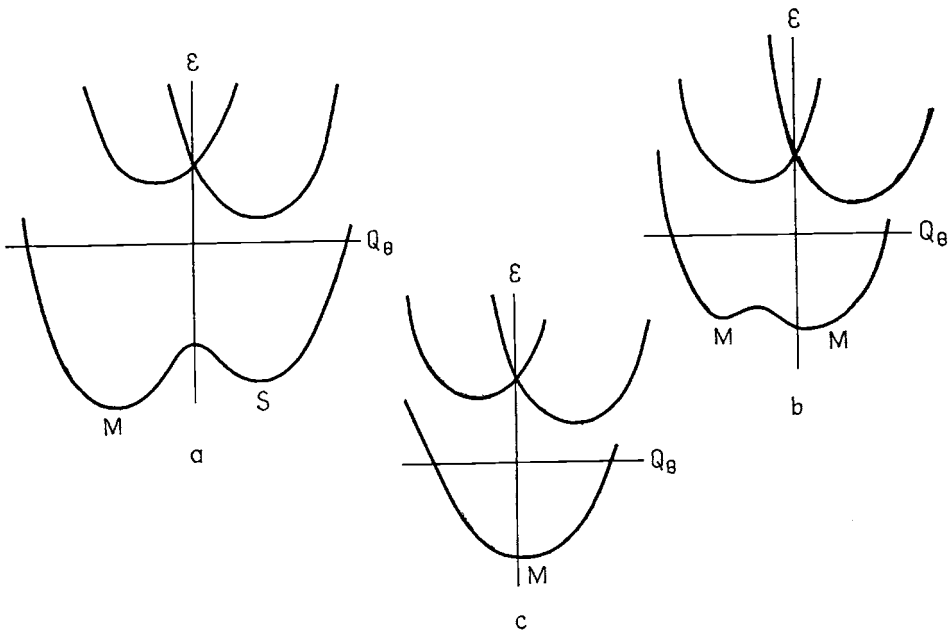

Fig. 7.38. Cross-sections $\phi = 0$ of the APES of a MV trimer as a function of $|w|/F^2$: (a) $|w|/F^2 < 2/9$, (b) $2/9 < |w|/F^2 < 0.255$, and (c) $|w|/F^2 > 0.255$. M are minima, S is a saddle point [7.398].

into Eq. (7.57), we obtain the following transcendent equation for the extrema points of the adiabatic potential:

$$4\sqrt{2}\sinh(2t) + [1 - (|w|/F^2)]\cosh t - 3\sinh t = 0 \tag{7.59}$$

Figure 7.38 illustrates the calculated shapes of the extremal cross-sections of the APES at $\phi = 0$ for different $|w|/F^2$ values. Its behavior at $\rho = 0$ can be investigated by means of the expansion of the potential function into a power series of ρ keeping the terms up to ρ^2. If $|W|/F^2 < \frac{2}{9}$ (Fig. 7.38a), the point $\rho = 0$ is a local maximum, and the potential has three absolute minima M at $\rho \neq 0$. One more minimum at $\rho \neq 0$ in Fig. 7.38(a) at the point S and two other equivalent minima at $\varphi = 2\pi/3$ and $4\pi/3$ are in fact saddle points. If $|w|/F^2 > \frac{2}{9}$, a minimum occurs at $\rho = 0$, but this is not necessarily accompanied by the disappearance of the minima at $\rho \neq 0$. In the interval $\frac{2}{9} < |w|/F^2 < 0.255$ these two types of minima coexist. Finally, when $|w|F^2 > 0.255$ the only minimum exists at $\rho = 0$.

The minimum at $\rho = 0$ describes the state of the excess electron uniformly delocalized over the three-centers, whereas the minima at $\rho \neq 0$ correspond to electron localized (at one of the three centers) states. Thus we come to the

conclusion that for three-center MV compounds in a certain interval of parameter values a *coexistence of localized and delocalized electron distributions is possible* [7.398, 7.500] (see also [7.498] and JT minima coexistence in Section 3.3). The region of parameter values required for this coexistence of two alternative electron distributions is relatively small. This region is expected to increase when the difference between the frequencies of the local one-center totally symmetric vibration in the two valence states is taken into account.

The coexistence of localized and delocalized electron distributions was observed first in a series of compounds of the type $[Fe(II)Fe_2(III)(CH_3COO)_6L_3]$ (see [7.501] and references therein). In these works it is shown that the Mössbauer spectra, besides the lines corresponding to the Fe(II) and Fe(III) ions with the intensity ratio 1:2, also contain quadrupole doublets that are characteristic of iron ions in the intermediate oxidation state.

The electronic structure with geometry optimization of a trinuclear copper (II, II, III) MV system $[Cu_3O_2L_3]^{3+}$ (I) with L = *N*-permethylated(1R,2R-cyclohexanediamine), which in its active form $[Cu_3O_2(NH_3)_6]^{3+}$ (II) can serve as a model for several biochemical systems (such as H_2O-lactase, ceruloplasmin, and ascorbate oxidase), was determined on a QM/MM level with the QM site (II) calculated by means of DFT [7.502]. In the D_{3h} configuration the active site (II) has a doubly degenerate ^3E ground state that produces three equivalent minima on the APES of the $E \otimes e$ problem (Section 3.2) with a JT stabilization energy $E_{JT}^E \cong 0.2$ eV. The minima correspond to the localized Cu(II)Cu(II)Cu(III) structure. A delocalized structure with three equivalent Cu atoms was found to be higher in energy. For the localized state further calculations of spectra and spin-manifold splitting were performed. The authors [7.502] indicate that DFT proved to be instrumental in describing the APES along the localization–delocalization path.

The MV systems under consideration form, as a rule, molecular crystals in which the interaction between the molecules depends on the intramolecular electron distribution and nuclear configuration distortions. It follows that the cooperative properties of MV compounds in the crystal state depend on their electron localization or delocalization state. APES curves of the type considered above were used to analyze possible types of *phase transitions in crystals of MV trimers* [7.503] (Section 8.2).

The above results are based on the assumption that there is only one excess electron above the three zero-spin cores of the three centers, and the validity of these results for clusters containing Fe(II), Fe(III), ... in the high-spin state (where for each value of the total spin there are several A and E energy levels) may be questioned. However, if one takes into account the exchange anisotropy (i.e., the difference between the exchange parameters in the pairs

Fe(II)–Fe(III) and Fe(III)–Fe(III)), then these levels are relatively displaced from each other, and it may be possible to consider each set of pairs of A and E levels separately, as was done above.

For a more detailed evaluation of the trimer properties the vibronic energy levels and wavefunctions of the MV system with the APES (7.56) should be computed. Such computations have been performed for different values of the parameters F and w, and the results were used to evaluate the band shapes of the IT spectra [7.504, 7.505]. For further developments in the theory of tricenter MV systems see in [7.506].

Most significant to the properties of MV systems are the magnetic implications, which, similar to the IT spectra, are strongly influenced by the vibronic coupling. If the cores of the equivalent centers of the MV system contain nonzero spins, they interact with each other via the excess electron (*double-exchange interaction*) resulting in an effective ferromagnetic coupling (see [7.398, 7.507–7.511] and references therein, as well as further examples below). The combination of double exchange with vibronic coupling, the so-called *spin-dependent electron delocalization* proved to be most important in optical and magnetic properties of polynuclear MV systems. For the tricenter $[Fe_3S_4]^0$ cluster [7.508, 7.509], which is present in many proteins and their synthetic models, the analysis of the APES formed by the combined action of the excess-electron transfer (which produces double-exchange coupling of the paramagnetic Fe(III) cores), vibronic coupling (trapping the excess electron at the centers), and the usual antiferromagnetic exchange interaction was performed on a model with a d^1–d^1–d^2 electronic configuration on the three centers.

The distribution of the excess electron was shown to depend on the ratio $\gamma = w/(F^2/2K)$, where w is the electron-transfer integral (7.52), while $F^2/2K$ is the vibronic stabilization (trapping) energy. For small γ values the electron is trapped at one center. If $\gamma \geq 1$ and the electronic manifold contains degenerate states $(A + E)$ in the C_{3v} group, the excess electron is trapped in a pair-delocalized state on two sites of the trinuclear system. For the tri-iron d^5–d^5–d^6 system the strongest vibronic stabilization on two sites is realized for the spin state $S = 2$ [7.508, 7.509], in full agreement with experimentally observed properties of these systems. In a similar study of four-center $[Fe_4S_4]^{3+}$ clusters [7.510] analogous pair-delocalized states were formed for $S = \frac{1}{2}$ in agreement with the spectroscopic data for high-potential iron proteins. These effects are also important in conductivity in metals and intermolecular electron transfer [7.512, 7.513].

When there are two excess electrons and three centers in the MV system the delocalization may stabilize spin-singlet ground states instead of the usually expected triplet states [7.514]. Similarly, localized electronic pairs may be

formed when there are two excess electrons in dodecanuclear (or other polynuclear) MV polyoxometalates [7.515, 7.524]. The problem for this system was solved by evaluating the electronic singlet and triplet states formed in the double-transfer process, and their vibronic coupling leading to combined JT and PJT $({}^3T_1 + {}^3T_2) \otimes (e + t_2)$ and $({}^1A_1 + {}^1E + {}^1T_2) \otimes (e + t_2)$ problems (Section 4.2). The APES in the one-mode space (one vibronic constant) reveals a rich variety of charge distributions and localizations. In particular, partial *e*-mode delocalization over four sites of the T_d structure with a partial delocalization over only two of the three metal octahedra of each of the M_3O_{12} triads was found in the case of weak coupling, and partial *e*-mode delocalization over two sites of the T_d structure was found in the case of strong coupling.

For multilevel vibronic-coupling problems in MV systems, a good example is provided by the calculations for the dimeric Creutz–Taube ion, $[(NH_3)_5 Ru(pyz)Ru(NH_3)_5]^{5+}$, where pyz is pyrazine [7.516–7.518].

The coupling of the excess electron to intercenter (multicenter) vibrations (in addition to the local on-center vibrations) was suggested to be significant in MV systems: while the coupling to local vibrations traps the electron at the center, the intercenter vibrations promote its delocalization [7.519, 7.520]. The author [7.519] was the first to show that the localization–delocalization problem in a dimeric MV system is exactly equivalent to a PJTE, and the orbital vibronic coupling constants (Section 2.3) can be used to parameterize the dominant features of this effect. Combined local (breathing) and intercenter vibrations together with the double-exchange interaction were used to reveal the hyperfine-interaction spectra in dimeric MV clusters [7.520].

From more recent developments, a simple MO LCAO treatment (on the extended Hückel level) of tricenter MV systems with three octahedral iron–oxygen units (Fe_3O_{16} and Fe_3O_{12} clusters) shows that more than one parameter is needed to describe the intercenter interaction (instead of w in the one-electron models above). In general each MO involved in this process should be represented by its own orbital vibronic coupling constant [7.521]. The localization–delocalization alternative for the excess electron becomes multi-featured too.

Vibronic reduction effects (Section 5.6) were taken into account in a variety of electron-transfer processes between MV centers [7.522]. Using the vibronic theory of MV systems it was shown [7.454, 7.523] that in the decatungstate anion $[W_{10}O_{32}]^{4-}$ there is a partially delocalized electron distribution of the excess electrons which coexists with the localized state at a tungsten site. This result explains the mechanism of the photocatalytic reaction, in which the intermediate (transient) form can be assigned to the partly delocalized distribution attained from the (initially localized) photoexcited state.

Bielectron transfer via the central atom in trimers was considered in [7.525]. For further developments and applications of the vibronic MV theory see in [7.526, 7.527].

From MV clusters there is a direct way to consider infinite MV chains [7.528–7.530]. Obviously, vibronic local distortions transform into Peierls transitions of the chain structure (Section 8.2.5).

References

7.1. I. B. Bersuker, *Coord. Chem. Rev*. **14**, 357 (1975).
7.2. I. B. Bersuker, *The Jahn–Teller Effect and Vibronic Interactions in Modern Chemistry*, New York, Plenum, 1984.
7.3. I. B. Bersuker, *Electronic Structure and Properties of Transition Metal Compounds. Introduction to the Theory*, New York, Wiley, 1996.
7.4. I. B. Bersuker and B. G. Vekhter, in *Proc. II Seminar on Crystal Chemistry of Coordination Compounds*, Bratislava, 1973, p. 132.
7.5. R. S. Berry, *J. Chem. Phys*. **32**, 933 (1960).
7.6. W. G. Klemperer, D. D. Traficante, and G. M. Whitesides, *J. Am. Chem. Soc*., **97**, 7023 (1975)
7.7. M. M. L. Chen and R. Hoffmann, *J. Am. Chem. Soc*. **98**, 1651 (1976).
7.8. B. Daines, A. McNeish, M. Poliakoff, and J. J. Turner, *J. Am. Chem. Soc*. **99**, 7573 (1977).
7.9. M. Poliakoff and A. Ceulemans, *J. Am. Chem. Soc*. **106**, 50 (1984).
7.10. (*a*) B. J. Hathaway, *Struct. Bonding* **57**, 55 (1984); (*b*) J. Pradilla-Sorzano and J. P. Fackler, *Inorg. Chem*. **12**, 1182 (1973); (*c*) A. von Zelewsky, *Inorg. Chem*. **20**, 4448 (1981).
7.11. J. Gaus, K. Kobe, V. Bonačić-Koutecký, H. Kühling, J. Manz, B. Reischl, S. Rutz, E. Schreiber, and L. Wöste, *J. Phys. Chem*. **97**, 12 509 (1993); B. Reischl, R. de Vivie-Riedle, S. Rutz, and E. Schreiber, *J. Chem. Phys*. **104**, 8857 (1996).
7.12. I. D. Hands, J. L. Dunn, and C. A. Bates, *to be published.*
7.13. A. Ceulemans and L. G. Vanquickenborne, *Struct. Bonding* **71**, 125 (1989).
7.14. P. Curie, *Oeuvres de Pierre Curie*, Paris, Gauthiers-Villars, 1908, p. 118.
7.15. *The Jahn–Teller Effect. A Bibliographic Review*, Ed. I. B. Bersuker, New York, IFI/Plenum, 1984.
7.16. C. L. Yang, Z. H. Zhang, T. Q. Ren, R. Wang, and Z. H. Zhu, *J. Mol. Struct. (THEOCHEM)* **583**, 63 (2002).
7.17. M. Breza, *J. Mol. Struct. (THEOCHEM)* **618**, 165 (2002); **618**, 171 (2002).
7.18. H. Bash, J. W. Moskowitz, C. Holister, and D. Hankin, *J. Chem. Phys*. **55**, 1922 (1971).
7.19. F. A. Gianturco, C. Quidotti, and U. Lamanna, *J. Chem. Phys*. **57**, 840 (1972).
7.20. L. S. Bartell, *J. Chem. Phys*. **73**, 375 (1981).
7.21. M. Kaupp, Ch. van Willen, R. Franke, F. Schmitz, and W. Kutzelnigg, *J. Am. Chem. Soc*. **118**, 11 939 (1996).
7.22. I. B. Bersuker, N. B. Balabanov, D. Pekker, and J. E. Boggs, *J. Chem. Phys*. **117**, 10 478 (2002).
7.23. L. E. Orgel, *J. Chem. Educ*. 3815 (1959).

7.24. S. Y. Wang and L. L. Lohr Jr., *J. Chem. Phys.* **60**, 3901 (1974); **61**, 4110 (1974).
7.25. W. J. A. Maaskant and I. B. Bersuker, *J. Phys.: Condens. Matter* **3**, 37 (1991).
7.26. W. J. A. Maaskant, *New J. Chem.* **17**, 97 (1993).
7.27. M. Atanasov and D. Reinen, *J. Phys. Chem. A* **105**, 5450 (2001).
7.28. M. Atanasov and D. Reinen, *Inorg. Chem.* **43**, 1998 (2004).
7.29. I. B. Bersuker, *Teor. Eksp. Khim.* **1**, 5 (1965).
7.30. L. D. Landau and E. M. Lifshitz, *Quantum Mechanics. Non-Relativistic Theory*, Moscow, Nauka, 1974.
7.31. I. B. Bersuker, *Kinetika i Kataliz.* **18**, 1268 (1977).
7.32. I. B. Bersuker, *Chem. Phys.* **31**, 85 (1978).
7.33. I. B. Bersuker, *(IUPAC) Coordination Chemistry – 20*, Ed. D. Banerjea, Oxford, Pergamon Press, 1980, p. 201.
7.34. I. B. Bersuker and S. S. Budnikov, in *Fundamental Research in Homogeneous Catalysis*, Vol. 2, Ed. A. E. Shilov, London, Gordon and Breach, 1986, p. 557.
7.35. I. I. Chernyaev, in *Selected Works: Complex Compounds of Platinum*, Moscow, Nauka, 1973 (in Russian).
7.36. A. A. Levin, *Sov. Sci. Rev. B, Chem. Rev.* **9**, 279 (1987).
7.37. A. A. Levin and P. N. Dyachkov, *Heteroligand Molecular Systems. Bonding, Shapes, and Isomer Stability*, New York, Taylor & Francis, 2002.
7.38. A. A. Levin, *New J. Chem.* **17**, 31 (1993).
7.39. R. Renner, *Z. Phys.* **92**, 172 (1934).
7.40. G. Gerzberg and E. Teller, *Z. Physik. Chem. B* **21**, 410 (1933).
7.41. J. A. Pople and H. C. Longuet-Higgins, *Mol. Phys.* **1**, 37 (1958).
7.42. R. N. Dixon, *Mol. Phys.* **9**, 357 (1965).
7.43. A. V. Petelin and A. A. Kiselev, *Internat. J. Quant. Chem.* **6**, 701 (1972).
7.44. Ch. Jungen and A. J. Merer, in *Molecular Spectroscopy: Modern Research*, Vol. 2, Ed. K. N. Rao, New York, Academic Press, 1976, p. 127.
7.45. H. Köppel, W. Domcke, and L. S. Cederbaum, *J. Chem. Phys.* **74**, 2945 (1981).
7.46. J. M. Brown and F. Jorgensen, *Adv. Chem. Phys.* **52**, 117 (1983).
7.47. M. Perić, E. Engles and S. D. Peyerimhoff, in *Quantum Mechanical Electronic Structure Calculations with Chemical Accuracy*, Ed. S. R. Langhoff, Dordrecht, Kluwer, 1995, p. 261; M. Perić and S. D. Peyerimhoff, *Adv. Chem. Phys.* **124**, 583 (2002).
7.48. G. Herzberg, *Electronic Spectra and Electronic Structure of Polyatomic Molecules*, Toronto, Van Nostrand, 1966.
7.49. P. C. H. Jordan and H. C. Longuet-Higgins, *Mol. Phys.* **5**, 121 (1962); D. A. Ramsey, *Discuss. Faraday Soc.* **35**, 90 (1963).
7.50. S. D. Peyerimhoff, R. J. Buenker, and J. L. Whitten, *J. Chem. Phys.* **46**, 1707 (1967).
7.51. Y. Muramatsu, K. Ueda, N. Saito, H. Chiba, M. Lavollee, A. Czasch, T. Weber, O. Jagudzki, H. Schmoidt-Bocking, R. Moshammer, U. Becker, K. Kubozuka, and I. Koyano, *Phys. Rev. Lett.* **88**, 133002 (2002).
7.52. G. Herzberg and J. W. C. Johns, *Proc. R. Soc. London A* **295**, 107 (1966).
7.53. W. Reuter and S. D. Peyerimhoff, *Chem. Phys.* **160**, 11 (1992).
7.54. B. Engels and M. Perić, *J. Chem. Phys.* **97**, 7129 (1992).
7.55. R. J. Buenker, M. Perić, S. D. Peyerimhoff, and R. Marian, *Mol. Phys.* **43**, 987 (1981).
7.56. C. H. Jungen, K.-E. Hallin, and A. J. Merer, *Mol. Phys.* **40**, 25 (1980).
7.57. M. Perić, S. D. Peyerimhoff, and R. J. Buenker, *Can. J. Chem.* **59**, 1318 (1981).

7.58. M. Perić, S. D. Peyerimhoff, and R. J. Buenker, *Chem. Phys. Lett.* **105**, 44 (1984).
7.59. M. Perić, R. J. Buenker, and S. D. Peyerimhoff, *Astrophys. Lett.* **24**, 69 (1984).
7.60. W. Reuter, M. Perić, and S. D. Peyerimhoff, *Mol. Phys.* **79**, 569 (1991).
7.61. B. Nestmann and M. Perić, *Chem. Phys.* **89**, 257 (1984).
7.62. P. J. Bruna, unpublished (cited in Ref. [7.47] as a personal communication).
7.63. M. Perić, R. J. Buenker, and S. D. Peyerimhoff, *Can. J. Chem.* **57**, 2491 (1979); M. Perić, *Chem. Phys. Lett.* **76**, 573 (1980).
7.64. M. Perić and M. Krmar, *Bull. Soc. Chim. Beograd.* **47**, 43 (1982).
7.65. P. J. Bruna, G. Hirsch, M. Perić, S. D. Peyerimhoff, and R. J. Buenker, *Mol. Phys.* **40**, 521 (1980).
7.66. P. J. Bruna and C. M. Marian, *Chem. Phys.* **37**, 425 (1979).
7.67. M. Perić, S. D. Peyerimhoff, and R. J. Buenker, *Can. J. Chem.* **61**, 2500 (1983).
7.68. M. Perić and J. Radić-Perić, *Chem. Phys. Lett.* **67**, 138 (1979).
7.69. M. Perić, B. A. Hess, and R. J. Buenker, *Mol. Phys.* **58**, 1001 (1986).
7.70. M. Perić, K. Phanuprakash, and R. J. Buenker, *Mol. Phys.* **65**, 403 (1988).
7.71. P. Jensen, M. Brumm, W. P. Kraemer, and P. R. Bunker, *J. Mol. Spectrosc.* **171**, 31 (1995).
7.72. G. Osmann, P. R. Bunker, P. Jensen, and W. P. Kraemer, *Chem. Phys. Lett.* **171**, 31 (1995); **172**, 194 (1995).
7.73. Ch. Jungen, K.-E. J. Hallin, and A. J. Merer, *Mol. Phys.* **40**, 25, 65 (1980).
7.74. W. Gabriel, G. Chambaund, P. Rosmus, S. Carter, and N. C. Handy, *Mol. Phys.* **81**, 1445 (1994).
7.75. M. Kolbuszewski, P. R. Bunker, W. P. Kraemer, G. Osmann, and P. Jensen, *Mol. Phys.* **88**, 105 (1996).
7.76. M. Brommer, R. Rosmus, S. Carter, and N. C. Handy, *Mol. Phys.* **77**, 549 (1992).
7.77. Ch. Jungen and A. J. Merer, *Mol. Phys.* **40**, 95 (1980).
7.78. A. J. Merer and D. N. Travis, *Can. J. Phys.* **43**, 1795 (1965); **24**, 177 (1992).
7.79. M. Perić, S. D. Peyerimhoff, and R. J. Buenker, *Can. J. Chem.* **59**, 1318 (1981).
7.80. M. Perić, M. Krmar, J. Radić-Perić, and L. J. Stevanović, *J. Mol. Spectrosc.* **208**, 271 (2001).
7.81. K. Tanaka and E. R. Davidson, *J. Chem. Phys.* **70**, 29 (1979).
7.82. H. Lorenzen-Schmidt, M. Perić, and S. D. Peyerimhoff, *J. Chem. Phys.* **98**, 525 (1993).
7.83. M. Perić and S. D. Peyerimhoff, *J. Chem. Phys.* **98**, 3587 (1993); *J. Mol. Struct.* **297**, 347 (1993).
7.84. A. Ben Houria, H. Gritli, N. Jaidane, Z. Ben Lakdhar, G. Chambaud, and P. Rosmus, *Chem. Phys.* **274**, 71 (2001).
7.85. M. Perić, S. D. Peyerimhoff, and R. J. Buenker, *Z. Phys. D* **24**, 177 (1992).
7.86. U. Manthe, H. Köppel, and L. S. Cederbaum, *J. Chem. Phys.* **95**, 1708 (1991).
7.87. H. Müller and H. Köppel, *Chem. Phys.* **183**, 107 (1994).
7.88. C. Woywod, M. Stengle, W. Domcke, H. Floethmann, and R. Schinke, *J. Chem. Phys.* **107**, 7282 (1997).
7.89. H. Müller, H. Köppel, and L. S. Cederbaum, *J. Chem. Phys.* **101**, 10 263 (1994).
7.90. E. Leonardi, C. Petrongolo, G. Hirsch, and R. J. Buenker, *J. Chem. Phys.* **105**, 9051 (1996).
7.91. B. Heumann, K. Weide, R. Düren, and R. Schinke, *J. Chem. Phys.* **98**, 5508 (1993).
7.92. S. Mahapatra, *J. Chem. Phys.* **116**, 8817 (2002).

7.93. H. Köppel, L. S. Cederbaum, W. Domcke, and W. Von Niessen, *Chem. Phys.* **37**, 303 (1979).
7.94. N. N. Gorinchoi, F. Chimpoesu, and I. B. Bersuker, *J. Mol. Struct. (THEOCHEM)* **530**, 281 (2000).
7.95. K. Balasubramanian and M. Z. Liao, *Chem. Phys.* **127**, 313 (1988).
7.96. V. Bonačić-Koutecký, L. Cespiva, P. Fantucci, P. Pittner, and J. Koutecký, *J. Chem. Phys.* **98**, 7981 (1993); **100**, 490 (1994).
7.97. H. Patridge, C. W. Bauschlicher Jr., and S. R. Landhoff, *Chem. Phys. Lett.* **175**, 531 (1990).
7.98. H. O. Jeschke, M. E. Garcia, and K. H. Bennemann, *Phys. Rev.* **54**, R4601 (1996).
7.99. S. Wolf, G. Sommerer, S. Rutz, E. Schreiber, T. Leisner, L. Wöste, and R. S. Berry, *Phys. Rev. Lett.* **74**, 4177 (1955).
7.100. D. W. Boo, Y. Ozaki, L. H. Andersen, and W. C. Lineberger, *J. Phys. Chem. A* **101**, 6688 (1997).
7.101. J. Passmore, G. Shuterland, and P. S. White, *Inorg. Chem.* **20**, 2169 (1981).
7.102. R. Colin, M. Hermann, and I. Kopp, *Mol. Phys.* **37**, 1397 (1979).
7.103. M. Takahashi, M. Fujii, and M. Ito, *J. Chem. Phys.* **96**, 6486 (1992).
7.104. Y. F. Zhu, R. Shehadeh, and E. R. Grant, *J. Chem. Phys.* **99**, 5723 (1993).
7.105. E. Reutt, L. S. Wang, J. E. Polland, D. J. Trevor, Y. T. Lee, and D. A. Shirley, *J. Chem. Phys.* **84**, 3022 (1986); S. T. Pratt and P. M. Dehmer, *J. Chem. Phys.* **95**, 6238 (1991).
7.106. M. Perić, H. Thümmel, C. M. Marian, and S. D. Peyerimhoff, *J. Chem. Phys.* **102**, 7142 (1995).
7.107. R. C. Gallen, B. Ostojić, and W. Domcke, *Chem. Phys.* **272**, 1 (2001).
7.108. K. Malsch, G. Hohlneicker, R. Shork, and H. Köppel, *Phys. Chem. Chem. Phys.* **3**, 5393 (2001).
7.109. J. Tang and S. Satio, *J. Chem. Phys.* **105**, 8020 (1996).
7.110. M. Perić, C. M. Marian, and B. Engels, *Mol. Phys.* **97**, 731 (1966).
7.111. M. Perić and B. Ostojić, *Mol. Phys.* **97**, 743 (1966).
7.112. M. Perić, B. Engels, and S. D. Peyerimhoff, *J. Mol. Spectrosc.* **171**, 494 (1995).
7.113. M. Perić and B. Engels, *J. Mol. Spectrosc.* **174**, 334 (1995).
7.114. M. Perić, B. Ostojić, B. Schäfer, and B. Engels, *Chem. Phys.* **225**, 63 (1997).
7.115. B. Schäfer, M. Perić, and B. Engels, *J. Chem. Phys.* **110**, 7802 (1999).
7.116. B. Schäfer-Bung, B. Engels, T. R. Taylor, D. M. Neumark, P. Botschwina, and M. Perić, *J. Chem. Phys.* **115**, 1777 (2001).
7.117. M. Perić, C. M. Marian, and S. D. Peyerimhoff, *J. Chem. Phys.* **114**, 6086 (1999).
7.118. M. Perić and S. D. Peyerimhoff, *Adv. Chem. Phys.* **124**, 583 (2002).
7.119. S. Mahapatra, L. S. Cederbaum, and H. Köppel, *J. Chem Phys.* **111**, 10 452 (1999).
7.120. C. Woywod and W. Domcke, *Chem. Phys.* **162**, 349 (1992).
7.121. A. D. O. Bawagan, T. K. Cheanty, E. R. Davidson, and K. H. Tan, *Chem. Phys. Lett.* **287**, 61 (1998).
7.122. L. S. Cederbaum, W. Domcke, and H. Köppel, *Chem. Phys.* **33**, 319 (1978).
7.123. R. K. Thomas and H. W. Thompson, *Proc. R. Soc. London A* **339**, 29 (1974).
7.124. S. Mahapatra, G. A. Worth, H.-Ď. Meyer, L. S. Cederbaum, and H. Köppel, *J. Chem. Phys. A* **105**, 5567 (2001).
7.125. L. Arrachea, A. A. Aligia, and G. E. Santero, *Phys. Rev. B* **67**, 134307 (2003).
7.126. D. J. Clouthier, D. A. Ramsay, *Annu. Rev. Phys. Chem.* **34**, 31 (1983).

7.127. I. Ya. Ogurtsov, G. Munteany, I. B. Bersuker, and L. Bantush, *J. Mol. Struct. (THEOCHEM)* **541**,141 (2001).
7.128. R. N. Porter, R. M. Stevens, and M. Karplus, *J. Chem. Phys.* **49**, 5163 (1968).
7.129. H. F. King and K. Morokuma, *J. Chem. Phys.* **71**, 3213 (1979).
7.130. S. Raynor and D. R. Herschback, *J. Phys. Chem.* **86**, 3592 (1982).
7.131. I. D. Petsalakis, G. Theodorakopoulos, and J. S. Wright, *J. Chem. Phys.* **89**, 6850 (1988).
7.132. W. H. Miller, *Annu. Rev. Phys. Chem.* **41**, 245 (1990).
7.133. J. L. Krause, K. C. Kulander, J. C. Light, and A. E. Orel, *J. Chem. Phys.* **96**, 4283 (1992).
7.134. F. Hagelberg, *Internat. J. Quant. Chem.* **75**, 367 (1999).
7.135. F. Hagelberg, *J. Mol. Struct. (THEOCHEM)* **487**, 151 (1999).
7.136. F. Hagelberg, *Internat. J. Quant. Chem.* **85**, 72 (2001).
7.137. S. Mahapatra and H. Köppel, *Phys. Rev. Lett.* **81**, 3116 (1998).
7.138. S. Mahapatra and H. Köppel, *J. Chem. Phys.* **109**, 1721 (1998).
7.139. H. Köppel, S. Mahapatra, and A. Thiel, in *Electron–Phonon Dynamics and Jahn–Teller Effects*, Eds. G. Bevilacqua, L. Martinelli, and N. Terzi, Singapore, World Scientific, 1999, p. 327.
7.140. J. L. Martins, R. Car, and J. Buttet, *J. Chem. Phys.* **78**, 5646 (1983).
7.141. T. C. Thompson, D. G. Truhlar, and C. A. Mead, *J. Chem. Phys.* **82**, 2392 (1985).
7.142. R. L. Martin and E. R. Davidson, *Mol. Phys.* **35**, 1713 (1978).
7.143. G. Delacretaz, E. R. Grant, R. L. Whetten, L. Wöste, and J. W. Zwanziger, *Phys. Rev. Lett.* **56**, 2598 (1986).
7.144. L. Cocchini, T. H. Upton, and W. Andreoni, *J. Chem. Phys.* **88**, 6068 (1988).
7.145. V. Bonačić-Koutecký, P. Fantucci, and J. Koutecký, *Phys. Rev. B* **37**, 4369 (1988).
7.146. Ph. Dugourd, J. Chevaleyre, R. Antoine, M. Broyer, J. P. Wolf, and L. Wöste, *Chem. Phys. Lett.* **225**, 28 (1994).
7.147. W. E. Ernst and S. Rakowsky, *Phys. Rev. Lett.* **74**, 58 (1995); *Ber. Bunsenges. Phys. Chem.* **99**, *441* (1995); *Can. J. Phys.* **72**, 135 (1994).
7.148. J. Higgins, W. E. Ernst, C. Callegari, J. Reho, K. K. Lehmann, G. Scoles, and M. Cutowski, *Phys. Rev. Lett.* **77**, 4532 (1996).
7.149. N. Ohashi, M. Tsuura, J. T. Hougen, W. E. Ernst, and S. Rakowsky, *J. Mol. Spectrosc.* **184**, 22 (1997).
7.150. D. T. Vituccio, O. Golonzka, and W. E. Ernest, *J. Mol. Spectrosc.* **184**, 237 (1997).
7.151. R. Meiswinkel and H. Köppel, *Chem. Phys.* **144**, 117 (1990).
7.152. M. Mayer, L. S. Cederbaum, and H. Köppel, *J. Chem. Phys.* **104**, 8932 (1996).
7.153. F. T. Chau and L. Karlsson, *Phys. Scripta* **16**, 248 (1977).
7.154. H. Von Busch, M. Keil, H.-G. Kramer, and W. Demtroder, in *Proc. XIV Internat. Symp. Electron–Phonon Dynamics and Jahn–Teller Effect*, Eds. G. Bevilacqua, L. Martinelli, N. Terzi, World Scientific, Singapore, 1999 p. 311.
7.155. H.-G. Kramer, M. Keil, C. B. Suarez, W. Demtroder, and W. Meyer, *Chem. Phys. Lett.* **299**, 212 (1999).
7.156. W. Meyer, M. Keil, A. Kudell, M. A. Baig, J. Zhu, and W. Demtroder, *J. Chem. Phys.* **115**, 2590 (2001).
7.157. R. G. Sadygov and D. R. Yarkony, *J. Chem. Phys.* **110**, 3639 (1999).
7.158. A. J. Dobbyn and J. M. Hutson, *J. Phys. Chem.* **98**, 11 428 (1994).

7.159. W. H. Gerber, *Ph.D. Thesis*, Universität Bern, 1980.
7.160. H. Von Bush, V. Dev, N. A. Eckel, S. Kasahara, J. Wang, W. Demtroder, P. Sebald, and W. Meyer, *Phys. Rev. Lett.* **81**, 4584 (1998).
7.161. S. Carter and W. Meyer, *J. Chem. Phys.* **93**, 8902 (1990).
7.162. S. P. Walch and B. C. Laskowski, *J. Chem. Phys.* **84**, 273 (1986).
7.163. S. P. Walch, C. W. Bauschlicher Jr., and S. R. Langhoff. *J. Chem. Phys.* **85**, 5900 (1986).
7.164. E. Miyoshi, H. Tatewaki, and T. Nakamura, *J. Chem. Phys.* **78**, 815 (1983).
7.165. S. R. Langhoff, C. W. Bauschlicher Jr., S. P. Walch, and B. C. Laskowski, *J. Chem. Phys.* **85**, 7211 (1986).
7.166. S. C. Richtsmeier, J. L. Gole, and D. A. Dixon, *Proc. Nat. Acad. Sci. USA* **77**, 5611 (1980).
7.167. J. W. Zwanziger, R. L. Whetten, and E. R. Grant, *J. Phys. Chem.* **90**, 3298 (1986).
7.168. M. D. Morse, *Chem. Phys. Lett.* **133**, 8 (1987).
7.169. J. S. Howard, K. F. Preston, R. Sutcliffe, and B. Mile, *J. Phys. Chem.* **87** (1983).
7.170. M. D. Morse, J. B. Hopkins, P. R. R. Langridge-Smith, and R. E. Smalley, *J. Chem. Phys.* **79**, 5316 (1983).
7.171. E. A. Rohlfing and J. J. Valentini, *Chem. Phys. Lett.* **126**, 113 (1986).
7.172. K. Balasubramanian and M. Z. Liao, *Chem. Phys.* **127**, 313 (1988).
7.173. K. Balasubramanian and K. K. Das, *Chem. Phys. Lett.* **186**, 577 (1991).
7.174. E. E. Wedum, E. R. Grant, P. Y. Cheng, K. F. Wiley, and M. A. Duncan, *J. Chem. Phys.* **100**, 631 (1994).
7.175. C. W. Bauschlicher, *Chem. Phys. Lett.* **156**, 91 (1989).
7.176. G. A. Bishea and M. D. Morse, *J. Chem. Phys.* **95**, 8779 (1991).
7.177. R. Wesendrup, T. Hunt, and P. J. Schwerdtfeger, *Chem. Phys.* **112**, 9356 (2000).
7.178. R. Guo, K. Balasubramanian, X. F. Wang, and L. Andrews, *J. Chem. Phys.* **117**, 1614 (2002).
7.179. K. Balasubramanian and D. Majumdar, *J. Chem. Phys.* **115**, 8795 (2001).
7.180. N. Gonzalez and J. Simons, *J. Chem. Phys.* **101**, 1074 (1994).
7.181. V. G. Solomonik, J. E. Boggs, and J. F. Stanton, *J. Mol. Struct. (THEOCHEM)* **469**, 213 (2000).
7.182. V. G. Solomonik, J. E. Boggs, and J. F. Stanton, *J. Phys. Chem. A* **103**, 838 (1999).
7.183. V. G. Solomonik, V. V. Sliznev, and N. B. Balalbanov, *Z. Physik. Chem.* **200**, 77 (1997); *Zh. Neorg. Khim (Russ. J. Inorg. Chem)* **43**, 1172 (1998).
7.184. M. Hargittai, B. Reffy, M. Kolonits, C. J. Marsden, and J.-L. Heully, *J. Am. Chem. Soc.* **119**, 9042 (1997).
7.185. B. Reffy, M. Kolonits, A. Schulz, T. M. Klapotke, and M. Hargittai, *J. Am. Chem. Soc.* **122**, 3127 (2000).
7.186. P. Schverdtfeger, P. D. V. Boyd, S. Brienne, and A. K. Burrell, *Inorg. Chem.* **31**, 3411 (1992).
7.187. P. Schverdtfeger, P. D. V. Boyd, T. Fisher, P. Hunt, and M. Liddell, *J. Am. Chem. Soc.* **116**, 9620 (1994).
7.188. P. Schverdtfeger, L. J. Laakonen, and P. Pyykko, *J. Chem. Phys.* **96**, 6807 (1992).
7.189. C. Bac, Y. K. Ham, Y. S. Lee, *J. Phys. Chem. A* **107**, 852 (2003).
7.190. N. B. Balabanov and J. E. Boggs, *J. Phys. Chem. A* **104**, 1597 (2000).

7.191. N. B. Balabanov and J. E. Boggs, *J. Phys. Chem. A* **104**, 7370 (2000).
7.192. N. B. Balabanov and J. E. Boggs, *J. Phys. Chem. A* **105**, 5906 (2001).
7.193. N. B. Balabanov and J. E. Boggs, *J. Phys. Chem. A* **106**, 6839 (2002).
7.194. C. A. Bayse and M. B. Hall, *J. Am. Chem. Soc.* **121**, 1348 (1999).
7.195. E. Z. Zasorin, A. A. Ivanov, L. L. Ermolaeva, and V. P. Spiridonov, *Zh. Fiz. Khim.* **63**, 669 (1989).
7.196. M. Hargittai, M. Kolonits, J. Tremmel, F.-L. Fourquet, and G. Ferey, *Struct. Chem.* **1**, 75 (1990).
7.197. M. Hargittai, *Chem. Rev.* **100**, 2233 (2000).
7.198. M. Hargittai, A. Schulz, B. Reffy, and M. Kolonits, *J. Amer. Chem. Soc.* **123**, 1449 (2001); A. Schulz and M. Hargittai, *Chem. Eur. J.* **7**, 3657 (2001).
7.199. I. B. Bersuker, N. N. Gorinchoi, and V. Z. Polinger, *Theor. Chim. Acta* **66**, 161 (1984).
7.200. M. A. Atanasov and D. Reinen, *J. Am. Chem. Soc.* **124**, 6693 (2002).
7.201. M. A. Atanasov and D. Reinen, *Adv. Quant. Chem.* **44**, 355 (2003).
7.202. W. J. A. Masskant and I. B. Bersuker, *J. Phys.: Condens. Matter* **3**, 337 (1991).
7.203. A. Viel and W. Eisfield, *J. Chem. Phys.* **120**, 4603 (2004).
7.204. A. I. Boldyrev and P. von R. Schleyer, *J. Am. Chem. Soc.* **113**, 9045 (1991).
7.205. A. I. Boldyrev, I. L. Shamovsky, and P. von R. Schleyer, *J. Am. Chem. Soc.* **114**, 6469 (1992).
7.206. V. G. Zakrzewski, W. von Niessen, A. I. Boldyrev, and P. von R. Schleyer, *Chem. Phys.* **174**, (1993).
7.207. P. von R. Schleyer and J. Kapp, *Chem. Phys. Lett.* **255**, 363 (1996).
7.208. T. K. Ghanty and E. R. Davidson, *J. Phys. Chem.* **103**, 2867 (1999).
7.209. F. F. Muguet, *Internat. J. Chem.* **1**, 25 (1998); **2**, 25 (1999).
7.210. C. Woywod, S. Scharfe, R. Krawczyk, W. Domcke, and H. Köppel, *J. Chem. Phys.* **118**, 5880 (2003).
7.211. L. Valachovic, C. Riehn, K. Mikhaylichenko, and C. Wittig, *Chem. Phys. Lett.* **258**, 644 (1996).
7.212. A. I. Boldyrev, J. Simons, V. A. Zakrzewski, and W. von Niessen, *J. Phys. Chem.* **98**, 1427 (1994).
7.213. U. Hoper, P. Botschwina, and H. Köppel, *J. Chem. Phys.* **112**, 4132 (2000).
7.214. C. Foster and T. A. Miller, *J. Phys. Chem.* **93**, 5986 (1989); T. A. Barckholtz and T. A. Miller, *J. Phys. Chem.* **103**, 2321 (1999).
7.215. D. R. Yarkony, H. F. Schaefer III, and S. J. Rothenberg, *Am. Chem. Soc.* **96**, 656 (1974).
7.216. J. T. Carter and D. B. Cook, *J. Mol. Struct. (THEOCHEM)* **251**, 111 (1991).
7.217. S. Mahapatra, V. Vallet, C. Woywod, H. Köppel, and W. Domcke, *Chem. Phys.* **304**, 17 (2004).
7.218. T. A. Barckholtz and T. A. Miller, in *Computational Molecular Spectroscopy*, Eds. P. Bunker and P. Jensen, New York, Wiley, 2000, p. 539; T. A. Barckholtz and T. A. Miller, *Internat. Rev. Phys. Chem.* **17**, 435 (1998).
7.219. J. Schmidt-Klügmann, H. Köppel, S. Schmatz, and P. Botschwina, *Chem. Phys. Lett.* **369**, 21 (2003).
7.220. T. A. Barckholtz, M.-C. Yang, and T. A. Miller, *Mol. Phys.* **97**, 239 (1999).
7.221. T. A. Barckholtz, P. E. Powers, T. A. Miller, and B. E. Bursten, *J. Am. Chem. Soc.* **121**, 2576 (1999); M. Pushkarsky, T. A. Barckholtz, and T. A. Miller, *J. Chem. Phys.* **110**, 2016 (1999).
7.222. A. J. Marr, F. Grieman, and T. C. Steimle, *J. Chem. Phys.* **105**, 3930 (1996).

7.223. R. Rubino, J. M. Williamson, and T. A. Miller, *J. Chem. Phys.* **103**, 5964 (1995).
7.224. A. Marenich and J. E. Boggs, *J. Phys. Chem.* A **108**, 10 594 (2004).
7.225. E. R. Davidson and W. T. Borden, *J. Chem. Phys.* **67**, 219 (1977).
7.226. W. T. Borden, E. R. Davidson, and D. Feller, *J. Am. Chem. Soc.* **102**, 5302 (1980).
7.227. J. W. Zwanziger, A. Chelichkhani, and E. R. Grant, *J. Chem. Phys.* **89**, 4012 (1988).
7.228. T. S. Venkatesan, S. Mahapatra, L. S. Cederbaum, and H. Köppel, *J. Phys. Chem. A* **108**, 2256 (2004).
7.229. T. Bally and E. Haselbach, *Helv. Chim. Acta.* **58**, 311 (1975); **61**, 754 (1978).
7.230. S. Komiya, T. A. Abbright, R. Hoffmann, and J. K. Kochi, *J. Am. Chem. Soc.* **98**, 7255 (1976).
7.231. L. R. Wright and R. F. Borkman, *J. Chem. Phys.* **77**, 1938 (1982).
7.232. T. Jungwirth, P. Carsky, and T. Bally, *Chem. Phys. Lett.* **195**, 371 (1992).
7.233. G. Jiang, H. Y. Wang, and Z. H. Zhu, *Chem. Phys. Lett.* **284**, 267 (1998).
7.234. L.-S. Wang, B. Niu, Y. T. Lee, D. A. Shirley, E. Ghelichkhani, and E. R. Grant, *J. Chem. Phys.* **93**, 6318 (1990).
7.235. L.-S. Wang, B. Niu, Y. T. Lee, D. A. Shirley, E. Ghelichkhani, and E. R. Grant, *J. Chem. Phys.* **93**, 6327 (1990).
7.236. R. Meiswinkel and M. Köppel, *Chem. Phys. Lett.* **201**, 449 (1993).
7.237. H. Köppel, *Z. Physik. Chem.* **200**, 3 (1997).
7.238. G. Bevilacqua, L. Martinelli, and G. P. Parravicini, *J. Phys.: Condens. Matter* **10**, 10 347 (1998).
7.239. D. Q. Meng, Z. H. Zhu, and G. Jiang, *J. Mol. Struct.* **610**, 241 (2002).
7.240. I. Ya. Ogurtsov and V. Mirzac, *Adv. Quant. Chem.* **44**, 401 (2003).
7.241. R. F. Frey and E. R. Davidson, *J. Chem. Phys.* **88**, 1775 (1988).
7.242. M. S. Reeves and E. R. Davidson, *J. Chem. Phys.* **95**, 6551 (1991).
7.243. J. Katriel and E. R. Davidson, *Chem. Phys. Lett.* **76**, 259 (1980).
7.244. C. A. Coulson and H. L. Strauss, *Proc. R. Soc. London A* **269**, 442 (1962).
7.245. J. Arents and L. C. Allen, *J. Chem. Phys.* **53**, 73 (1970).
7.246. R. N. Dixon, *Mol. Phys.* **20**, 113 (1971).
7.247. W. Meyer, *J. Chem. Phys.* **58**, 1017 (1973).
7.248. J. M. Garcia de la Vega, J. F. Rico, M. Paniagua, and J. I. Fernandez-Alonso, *J. Mol. Struct.* **105**, 31 (1983).
7.249. J. H. Garcia de la Vega, A. Segovia, J. F. Rico, and J. I. Fernandez-Alonso, *J. Mol. Struct. (THEOCHEM)* **123**, 203 (1985).
7.250. M. N. Paddon-Row, D. J. Fox, J. A. Pople, K. N. Houk, and D. W. Pratt, *J. Am. Chem. Soc.* **107**, 7696 (1985).
7.251. K. J. Takeshita, *Chem. Phys.* **86**, 329 (1987).
7.252. F. Marinelli and M. Roche, *Chem. Phys.* **146**, 219 (1990).
7.253. F. F. Van Dishoeck, W. J. Van Der Hast, and M. Van Hemert, *Chem. Phys.* **50**, 45 (1980).
7.254. L. B. Knight Jr., J. Steadman, D. Feller, and E. R. Davidson, *J. Am. Chem. Soc.* **106**, 3700 (1984).
7.255. J. C. Corchado, J. Espinosa-Garcia, O. Roberto-Neto, Y.-Y. Chuang, and D. G. Truhlar, *J. Phys. Chem.* **102**, 4899 (1998); J. Espinosa-Garcia and J. C. Garcia-Bernaldez, *Phys. Chem. Chem. Phys.* **2**, 2345 (2000).
7.256. Y.-N. Chiu, *J. Phys. Chem.* **92**, 4352 (1988).
7.257. J. M. Garcia de la Vega, B. Miguel, and San E. Fabian, *Internat. J. Quant. Chem.* **61**, 533 (1997).

7.258. R. F. Frey and E. R. Davidson, *J. Chem. Phys.* **89**, 4227 (1988).
7.259. M. S. Gordon, *Chem. Phys. Lett.* **59**, 410 (1978).
7.260. D. Power, P. Brint, and T. Spalding, *J. Mol. Struct.* **108**, 81 (1984).
7.261. R. Caballol, J. A. Catala, and J. M. Problet, *Chem. Phys. Lett.* **130**, 278 (1986); T. Kudo and S. Naguse, *Chem. Phys.* **122**, 233 (1988).
7.262. J. A. Pople and L. A. Curtiss, *J. Phys. Chem.* **91**, 155 (1987); L. A. Curtis and J. A. Pople, *Chem. Phys. Lett.* **144**, 38 (1988).
7.263. D. Balamurugan, M. K. Harbola, and R. Prasad, *Phys. Rev.* A **69**, 033201 (2004).
7.264. V. G. Solomonik and T. P. Pogrebnaya, *Russ. J. Inorg. Chem.* **46**, 1851 (2001).
7.265. R. Bruyndonckx, C. Daul, and P. T. Manoharan, *Inorg. Chem.* **36**, 4251 (1997).
7.266. K. K. Stavrev and M. C. Zerner, *Chem. Phys. Lett.* **263**, 667 (1996).
7.267. D. Reinen and C. Friebel, *Struct. Bonding* **37**, 1 (1979).
7.268. D. Reinen and M. Atanasov, *Magn. Reson. Rev.* **15**, 167 (1991).
7.269. J. Ferguson, *J. Chem. Phys.* **40**, 3406 (1964).
7.270. R. J. Deeth, M. A. Hitchman, G. Lehmann, and H. Sachs, *Inorg. Chem.* **23**, 1310 (1984).
7.271. W. T. Borden, E. R. Davidson, and D. Feller, *J. Am. Chem. Soc.* **103**, 5725 (1981).
7.272. M. Roeselova, T. Bally, P. Jungwirth, and P. Carsky, *Chem. Phys. Lett.* **234**, 3957 (1995).
7.273. W. D. Hobey and A. D. McLachlan, *J. Chem. Phys.* **33**, 1695 (1960).
7.274. H. Bock, B. Roth, and G. Maier, *Chem. Ber.* **117**, 172 (1984).
7.275. M. Shiotani, K. Ohta, Y. Nagata, and J. Sohma, *J. Am. Chem. Soc.* **107**, 2562 (1985); H. Tachikawa, M. Shiotani, and K. Ohta, *J. Phys. Chem.* **96**, 164 (1992).
7.276. A. Metropoulos and Y.-N. Chiu, *J. Mol. Struct. (THEOCHEM)* **365**, 119 (1996); **417**, 95 (1997).
7.277. M. Bacci, *Phys. Rev. B* **17**, 4495 (1978).
7.278. V. Hrouda, T. Bally, P. Carsky, and P. Jungwirth, *J. Phys. Chem.* **101**, 3918 (1997).
7.279. P. Jungwirth, P. Carsky, and T. Bally, *J. Am. Chem. Soc.* **115**, 5776 (1993).
7.280. T.-S Lee, M. H. Lien, S.-F. Jen, M.-C. Ou, H.-F.Wu, Y.-F. Gau, and T.-Y. Chang, *J. Mol. Struct. (THEOCHEM)* **170**, 121 (1998).
7.281. M. S. Dewar and K. M. Merz, *J. Mol. Struct. (THEOCHEM)* **122**, 59 (1985).
7.282. R. A. Pabon and N. L. Bauld, *J. Am. Chem. Soc.* **106**, 1145 (1984); N. L. Bauld, D. J. Bellville, R. A. Pabon, R. Chelsky, and G. Green, *J. Am. Chem. Soc.* **105**, 2378 (1983); D. J. Bellville and N. L. Bauld, *J. Am. Chem. Soc.* **104**, 5700 (1982).
7.283. K. Ohta, H. Nakatsuji, H. Kubodera, and T. Shida, *Chem. Phys.* **76**, 271 (1983).
7.284. W. J. Bouma, D. Poppinger, and L. Radom, *J. Mol. Struct. (THEOCHEM)* **103**, 205 (1983); *Israel J. Chem.* **23**, 21 (1983).
7.285. K. Ushida, T. Shida, M. Iwasaki, K. Toriama, and K. Nunome, *J. Am. Chem. Soc.* **105**, 5496 (1983).
7.286. T. Egawa, T. Fukuyama, S. Yamamoto, F. Takabayashi, H. Kambara, T. Ueda, and K. Kuchitsu, *J. Chem. Phys.* **86**, 6018 (1987).
7.287. T. Bally, U. Buser, and E. Haselbach, *Helv. Chim. Acta.* **61**, 38 (1978).

7.288. T. J. Sears, T. A. Miller, and V. E. Bondybey, *J. Chem. Phys.* **72**, 6070 (1980); **74**, 3240 (1981).
7.289. V. E. Bondybey, T. A. Miller, and J. H. English, *Phys. Rev. Lett.* **44**, 1344 (1980).
7.290. T. A. Miller and V. E. Bondybey, *Appl. Spectrosc. Rev.* **18**, 105 (1982).
7.291. K. Raghavachari, R. C. Haddon, T. A. Miller, and V. E. Bondybey, *J. Chem. Phys.* **79**, 1387 (1983).
7.292. C. Cossart-Magos, D. Cossart, and S. Leach, *J. Chem. Phys.* **69**, 4313 (1978); *Mol. Phys.* **37**, 793 (1979); *Chem. Phys.* **41**, 345 and 363 (1979); **48**, 329 and 349 (1980).
7.293. C. Cossart-Magos, D. Cossart, S. Leach, J. P. Maier, and L. Miser, *J. Chem. Phys.* **78**, 3673 (1983).
7.294. T. A. Miller, *Annu. Rev. Phys. Chem.* **33**, 257 (1982).
7.295. R. L. Whetten, K. S. Haber, and E. R. Grant, *J. Chem. Phys.* **84**, 1270 (1986).
7.296. R. L. Whetten and E. R. Grant, *J. Chem. Phys.* **80**, 1711 (1984).
7.297. H. Köppel. *Chem. Phys. Lett.* **205**, 361 (1993).
7.298. W. von Niessen, L. S. Cederbaum, and W. P. Kraemer, *J. Chem. Phys.* **65**, 1378 (1976).
7.299. L. Blancafort, M. Torent-Succarat, J. M. Luis, M. Duran, and M. Sola, *J. Phys. Chem. A* **107**, 7337 (2003).
7.300. (*a*) H. Köppel, M. Doscher, I. Baldea, H. D. Meyer, and P. G. Szalay, *J. Chem. Phys.* **117**, 2657 (2002); (*b*) M. Doscher, H. Köppel, and P. G. Szalay, *J. Chem. Phys.* **117**, 2645 (2002).
7.301. M. Ford, R. Lindner, and K. Muller-Dethlefs, *Mol. Phys.* **101**, 705 (2003).
7.302. H. Köppel, L. S. Cederbaum, and W. Domcke, *J. Chem. Phys.* **89**, 2023 (1988).
7.303. R. Lindner, K. Muller-Dethlefs, C. Wedum, K. Haber, and E. R. Grant, *Science* **271**, 1698 (1996).
7.304. L. Muller-Dethlefs and J. B. Peel, *J. Chem. Phys.* **111**, 10 550 (1999).
7.305. M. Doscher and H. Köppel, *Chem. Phys.* **225**, 93 (1997).
7.306. J. G. Goode, J. D. Hofstein, and P. M. Johnson, *J. Chem. Phys.* **107**, 1703 (1997).
7.307. M. Kato, K. Hirao, and M. Sano, *J. Mol. Struct.* **104**, 489 (1983).
7.308. M. Huang and S. Lunell, *J. Chem. Phys.* **92**, 6081 (1990).
7.309. K. J. Takeshita, *Chem. Phys.* **101**, 2192 (1994).
7.310. J. Eiding, R. Schneider, W. Domcke, H. Köppel, and W. von Niesen, *Chem. Phys. Lett.* **177**, 345 (1992).
7.311. J. Eiding and W. Domcke, *Chem. Phys.* **163**, 133 (1992).
7.312. R. L. Whetten, S. G. Grubb, C. E. Otis, A. C. Albrecht, and E. R. Grant, *J. Chem. Phys.* **82**, 115 (1985); S. G. Grubb, C. E. Otis, R. L. Whetten, E. R. Grant, and A. C. Albrecht, *J. Chem. Phys.* **82**, 1135 (1985).
7.313. R. L. Whetten and E. R. Grant, *J. Chem. Phys.* **84**, 654 (1986); R. L. Whetten and E. R. Grant, *J. Chem. Phys.* **80**, 5999 (1984).
7.314. R. L. Whetten and E. R. Grant, *J. Chem. Phys.* **80**, 691 (1984).
7.315. R. L. Whetten, K.-Y. Fu, and E. R. Grant, *Chem. Phys.* **90**, 155 (1984).
7.316. J. H. van der Waals, A. M. D. Berghuis, and M. S. de Groot, *Mol. Phys.* **13**, 301 (1967); **31**, 497 (1971); J. van Egmond and J. H. van der Waals, *Mol. Phys.* **28**, 457 (1974).
7.317. P. Pulay, G. Fogarasi, and J. E. Boggs, *J. Chem. Phys.* **74**, 3999 (1981).
7.318. B. E. Applegate, T. A. Barkholtz, and T. A. Miller, *Chem. Soc. Rev.* **32**, 38 (2003).

7.319. J. J Nash and R. R. Squires, *J. Am. Chem. Soc.* **118**, 11 872 (1996).
7.320. J.-M. André, J. L. Bredas, V. Coropceanu, and R. J. Silley, *Internat. J. Quant. Chem.* **90**, 1428 (2002).
7.321. L. N. Shchegoleva, I. I. Bilkis, and P. V. Schastnev, *Chem. Phys.* **82**, 343 (1983).
7.322. L. N. Shchegoleva and P. V. Schastnev, *Chem. Phys.* **130**, 115 (1989).
7.323. K. Miraoka, S. Mizume, and S. Yambe, *J. Phys. Chem.* **94**, 3689 (1990).
7.324. L. N. Shchegoleva, I. I. Beregovaya, and P. V. Schastnev, *Chem. Phys. Lett.* **312**, 325 (1999).
7.325. V. V. Konovalov, S. S. Laev, I. V. Beregovaya, L. N. Shchegoleva, V. D. Shteingarts, D. Yu. Tsvetkov, and I. I. Bilkis, *J. Phys. Chem. A* **104**, 152 (2000).
7.326. I. V. Beregovaya and L. N. Shchegoleva, *Chem. Phys. Lett.* **348**, 501 (2001).
7.327. V. F. Starichenko, L. A. Shundrin, L. N. Shchegoleva, and V. D. Shteingarts, *Zh. Strukt. Khim.* **41**, 778 (2000).
7.328. B. E. Applegate and T. A. Miller, *J. Chem. Phys.* **117**, 1065 (2002).
7.329. G. Fisher and P. Wormell, *Chem. Phys.* **257**, 1 (2000).
7.330. L. C. Snyder, *J. Chem. Phys.* **33**, 619 (1960).
7.331. P. M. Johnson, *J. Chem. Phys.* **117**, 9991 (2002).
7.332. I. V. Beregovaya and L. V. Shechegoleva, *Internat. J. Quant. Chem.* **88**, 481 (2002).
7.333. K. Yoshizawa, T. Kato, and T. Yamabe, *J. Chem. Phys.* **108**, 7637 (1998).
7.334. T. Kato and T. Yamabe, *J. Chem. Phys.* **118**, 3804 (2003).
7.335. A. D. Liehr, *Z. Physik. Chem.* **9**, 338 (1956).
7.336. R. Meyer, F. Grof, T.-K. Ha, and H. H. Gunthard, *Chem. Phys. Lett.* **66**, 65 (1979).
7.337. W. T. Borden and E. R. Davidson, *J. Am. Chem. Soc.* **101**, 3771 (1979).
7.338. L. N. Shchegoleva, V. M. Karpov, and V. E. Platonov, *Zh. Strukt. Khim.* **37**, 1023 (1996).
7.339. L. N. Schchegoleva, V. M. Karpov, and V. E. Platonov, *Zh. Strukt. Khim.* **40**, 184 (1999).
7.340. L. Yu, S. C. Foster, J. M. Williamson, M. C. Heaven, and T. A. Miller, *J. Phys. Chem.* **92**, 4263 (1988).
7.341. L. Yu, J. M. Williamson, and T. A. Miller, *Chem. Phys. Lett.* **162**, 431 (1989).
7.342. L. Yu, D. W. Cullin, J. M. Williamson, and T. A. Miller, *J. Chem. Phys.* **98**, 2682 (1993).
7.343. B. E. Applegate, T. A. Miller, and T. A. Barckholtz, *J. Chem. Phys.* **114**, 4855 (2001); B. E. Applegate, A. J. Bezant, and T. A. Miller, *J. Chem. Phys.* **114**, 4869 (2001).
7.344. M. J. Bearpark, M. A. Robb, and Y. Yamamoto, *Spectrochim. Acta A* **55**, 639 (1999).
7.345. S. Zolberh and Y. Haas, *J. Am. Chem. Soc.* **124**, 10683 (2002).
7.346. E. V. Granov, A. B. Trofimov, N. M. Witkovskaya, J. Shirmer, and H. Köppel, *J. Chem. Phys.* **119**, 737 (2003); E. V. Granov, A. B. Trofimov, N. M. Witkovskaya, H. Köppel, J. Shirmer, H. D. Meyer, and L. S. Cederbaum, *J. Chem. Phys.* **121**, 4585, (2004).
7.347. A. B. Trofimov, H. Köppel, and J. Shirmer, *J. Chem. Phys.* **109**, 1025 (1998)
7.348. D. Cremer and J. A. Pople, *J. Am. Chem. Soc.* **97**, 1358 (1975).
7.349. J. E. Kilpatrick, K. S. Pitzer, and R. Pitzer, *J. Am. Chem. Soc.* **69**, 2483 (1947); K. S. Pitzer and W. E. Donath, *J. Am. Chem. Soc.* **81**, 3213 (1959).

7.350. L. A. Carreira, G. J. Jiang, W. B. Person, and J. N. Willis Jr., *J. Chem. Phys.* **56**, 1440 (1972).
7.351. T. Pino, F. Güthe, H. Ding, and J. P. Maier, *J. Phys. Chem. A* **106**, 10 022 (2002).
7.352. M. J. Bearpark, L. Blancafort, and M. A. Robb, *Mol. Phys.* **100**, 1735 (2002).
7.353. T. Bally, L. Truttmann, S. Dai and F. Williams, *J. Am. Chem. Soc.* **117**, 7916 (1995).
7.354. T. Bally, S. Bernhard, S. Matzinger, J.-L. Roulin, G. N. Sastry, L. Truttmann, Z. Zhu, A. Marcinek, J. Adamus, R. Kaminski, J. Gebicki, F. Williams, G. F. Chen, and M. R. Fulscher, *Chem. Eur. J.* **6**, 858 (2000).
7.355. F. Williams, *Radiation Phys. Chem.* **67**, 211 (2003).
7.356. A. Toyota, S. Koseki, H. Umeda, M. Suzuki, and K. Fujimoto, *J. Phys. Chem. A* **107**, 2749 (2003).
7.357. (*a*) T. Kato, K. Yoshizawa, and T. Yamabe, *Chem. Phys. Lett.* **345**, 125 (2001); (*b*) T. Kato and T. Yamabe, *J. Chem. Phys.* **115**, 8592 (2001).
7.358. T. Kato and T. Yamabe, *J. Phys. Chem. A* **108**, 11 223 (2004).
7.359. T. Kato, K. Yoshizawa, and K. Hirao, *J. Chem. Phys.* **116**, 3420 (2002).
7.360. T. Kato and K. Yoshizawa, *J. Chem. Phys.* **113**, 2188 (2000).
7.361. T. Kato and T. Yamabe, *J. Chem. Phys.* **118**, 3300 (2003).
7.362. T. Kato and T. Yamabe, *J. Chem. Phys.* **118**, 10073 (2003); **119**, 5680 (2003); *Recent Res. Develop. Quant. Chem.* **4**, 11 (2004).
7.363. (*a*) T. Kato and T. Yamabe, *J. Chem. Phys.* **119**, 11 318 (2003); *J. Chem. Phys.* **120**, 7659 (2004); *J. Chem. Phys.* **120**, 1006 (2004); (*b*) T. Kato and T. Yamabe, *J. Chem. Phys.* **120**, 3311 (2004).
7.364. D. A. da Silva Filho, R. Frielein, V. Coropceanu, G. Ohrwal, W. Osikovicz, C. Suess, S. L. Sorensen, S. Svensson, W. R. Salaneck, and J.-L. Bredas, *Chem. Commun.* 1702 (2004).
7.365. T. Kato, K. Yoshizawa, and T. Yamabe, *J. Chem. Phys.* **110**, 249 (1999).
7.366. M. Tachibana and K. Yoshizawa, *Chem. Phys.* **260**, 303 (2000).
7.367. T. Sato, A. Yamamoto, and H. Tanaka, *Chem. Phys. Lett.* **326**, 573 (2000).
7.368. T. Kato, K. Yoshizawa, and T. Yamabe, *Synthetic Metals* **119**, 217 (2001).
7.369. T. Kato and T. Yamabe, *J. Chem. Phys.* **117**, 2324 (2002).
7.370. A. Furlan, M. J. Riley, and S. Leutwyler, *J. Chem. Phys.* **96**, 7306 (1992).
7.371. A. Furlan, S. Leutwyler, M. J. Riley, and W. Adcock, *J. Chem. Phys.* **99**, 4932 (1993).
7.372. M. J. Riley, A. Furlan, H. U. Gudel, and S. Leutwyler, *J. Chem. Phys.* **98**, 3803 (1993).
7.373. J. R. Letelier, *Internat. J. Mod. Phys. C* **10**, 1177 (1999); J. R. Letelier and A. Toro-Labbe, *Bol. Soc. Chil. Quim.* **44**, 87 (1999); J. R. Letelier, A. Toro-Labbe, and Y.-N. Chiu, *J. Chinese Chem. Soc.* **44**, 101 (1999).
7.374. M. Pfeiffer, W. Werncke, S. Hogin, A. Kummrow, and A. Lau, *Chem. Phys. Lett.* **295**, 56 (1998).
7.375. S. F. Nelsen, L. A. Reinhardt, H. Q. Tran, T. Clark, G.-F. Chen, R. S. Pappas, and F. Williams, *Chem. Eur. J.* **8**, 1074 (2002).
7.376. C. C. Chancey and M. C. M. O'Brien, *The Jahn–Teller Effect in C_{60} and Other Icosahedral Complexes*, Princeton, New Jersey, Princeton University Press, 1997.
7.377. S. A. Borshch and K. Prassides, *J. Phys. Chem.* **100**, 9348 (1996).
7.378. L. F. Chibotaru, A. Ceulemans, and S. P. Cojocaru, *Phys. Rev. B* **59**, 12 728 (1999-II).

7.379. M. Lannoo, G. A. Baraff, and M. Schluter, *Phys. Rev. B* **44**, 12106 (1991-I).
7.380. (*a*) S. E. Canton, A. J. Yencha, E. Kukk, J. D. Bozek, M. C. A. Lopes, G. Snell, and N. Berrah, *Phys. Rev. Lett.* **89**, 045502 (2002); (*b*) N. Manini and E. Tosatti, *Phys. Rev. Lett.* **90**, 249601 (2003); **53**, 2292 (2004).
7.381. Q. C. Qiu, *Acta Phys. Sinica* **52**, 958 (2002).
7.382. I. D. Hands, J. L. Dunn, and C. A. Bates, *Phys. Rev. B* **63**, 245414 (2001); *Adv. Quant. Chem.* **44**, 335 (2003).
7.383. N. Manini and E. Tosatti, *Phys. Rev. B* **58**, 782 (1998-II).
7.384. C. A. Bates and J. L. Dunn, *Appl. Magn. Reson.* **18**, 29 (2000).
7.385. A. D. Buckingham and J. P. Read, *Chem. Phys. Lett.* **253**, 414 (1996).
7.386. A. Ceulemans and P. W. Fowler, *J. Chem. Soc. Faraday Trans.* **88**, 2797 (1992).
7.387. Z. Slanina, F. Uhlik, and O. V. Boltalina, *Phys. Solid State* **44**, 548 (2002).
7.388. V. C. Long, J. L. Musfeldt, and K. Kamaras, *Phys. Rev. B* **58**, 14 338 (1998).
7.389. E. Tosatti, N. Manini, and O. Gunnarson, *Phys. Rev. B* **54**, 17 184 (1996).
7.390. L. Tian, Y.-S. Yi, C. L. Wang, and Z. B. Su, *Internat. J. Mod. Phys. B* **11**, 1969 (1997).
7.391. (*a*) W. Z. Wang, A. R. Bishop, and L. Yu, *Phys. Rev. B* **50**, 5016 (1994-I); (*b*) W. Z. Wang, C. L. Wang, A. R. Bishop, L. Yu, and Z. B. Su, *Phys. Rev. B* **51**, 10 209 (1995).
7.392. L. F. Chibotaru and A. Ceulemans, *Phys. Rev. B* **53**, 15 522 (1996); A. Ceulemans, L. F. Chihotaru, and F. Cimpoesu, *Phys. Rev. Lett.* **78**, 3725 (1997).
7.393. A. Auerbach, N. Manini, and E. Tosatti, *Phys. Rev. B* **49**, 12 998 (1999).
7.394. W. Bietch, J. Bao, J. Ludecke, and S. van Smaalen, *Chem. Phys. Lett.* **324**, 37 (2000).
7.395. N. Manini, P. Gattari, and E. Tosatti, *Phys. Rev. Lett.* **91**, 196402 (2003)
7.396. (*a*) T.-X. Lu, *Chem. Phys. Lett.* **194**, 67 (1992); (*b*) J. C. R. Faulhaber, D. Y. K. Ko, and P. R. Briddon, *Phys Rev. B* **48**, 661 (1993-I).
7.397. *Vibronic Processes in Inorganic Chemistry*, Ed. C. D. Flint, Dordrecht, Kluwer, 1989.
7.398. I. B. Bersuker and S. A. Borshch, *Adv. Chem. Phys.* **81**, 703 (1992).
7.399. J. K. Burdett, *Molecular Shapes. Theoretical Models of Inorganic Stereochemistry*, New York, Wiley, 1980.
7.400. I. B. Bersuker and S. S. Stavrov, *Coord. Chem. Rev.* **88**, 1 (1988).
7.401. A. A. Levin, *Sov. Sci. Rev. B, Chem. Rev.* **9**, 2791 (1987); *New. J. Chem.* **17**, 31 (1993).
7.402. J. Gazo, I. B. Bersuker, J. Garaj, M. Kabesova, J. Kohout, M. Langfelderova, M. Melnik, M. Serator, and F. Valach, *Coord. Chem. Rev.* **19**, 253 (1976).
7.403. I. B. Bersuker, *J. Coord. Chem.* **34**, 289 (1995).
7.404. L. R. Falvello, *J. Chem. Soc. Dalton Trans.* 4463 (1997).
7.405. B. Bleaney and D. J. E. Ingram, *Proc. Phys. Soc. London A* **63**, 408 (1950); A. Abraham and M. H. L. Pryce, *Proc. Phys. Soc. London A* **63**, 409 (1950); B. Bleaney and K. D. Bowers, *Proc. Phys Soc. London A* **65**, 667 (1952).
7.406. D. Reinen and C. Friebel, *Inorg. Chem.* **23**, 792 (1984).
7.407. D. Reinen and M. Atanasov, *Chem. Phys.* **136**, 27 (1989); D. Reinen and M. Atanasov, *Chem. Phys.* **155**, 157 (1991).
7.408. M. Atanasov, W. Koenig, M. Craupner, and D. Reinen, *New J. Chem.* **17**, 115 (1993).
7.409. D. W. Meek and J. A. Ibers, *Inorg. Chem.* **9**, 405 (1970).

7.410. D. Reinen and M. Atanasov, *Magn. Reson. Rev.* **15**, 167 (1991).
7.411. V. Z. Polinger, N. N. Gorinchoy, and I. B. Bersuker, *Chem. Phys.* **159**, 75 (1992).
7.412. N. N. Gorinchoy, I. B. Bersuker, and V. Z. Polinger, *New. Chem.* **17**, 125 (1993).
7.413. J. Brunvoll, A. A. Ischenko, V. P. Spiridonov, and T. G. Strand, *Acta Chem. Scand. A* **38**, 115 (1984).
7.414. H. Wasad and K. Hirao, *J. Am. Chem. Soc.* **114**, 16 (1992).
7.415. C. Daul, M. Frioud, O. Shafer, and A. Selloni, *Chem. Phys. Lett.* **262**, 74 (1996).
7.416. H. Yamatera, *Act. Chem. Scand. A* **33**, 107 (1979).
7.417. H. Stratemeier, B. Wagner, E. R. Krausz, R. Linder, H.-H. Schmidtke, J. Pebler, W. E. Hatfield, L. ter Haar, D. Reinen, and M. A. Hitchman, *Inorg. Chem.* **33**, 2320 (1994); P. J. Ellis, H. C. Freeman, M. A. Hitchman, D. Reinen, and B. Wagner, *Inorg. Chem.* **33**, 1249 (1994).
7.418. D. Reinen and M. A. Hitchman, *Z. Physik. Chem.* **200**, 11 (1997).
7.419. R. J. Deeth and M. A. Hitchman, *Inorg. Chem.* **25**, 1225 (1986).
7.420. I. Persson, P. Persson, M. Sandström, and A.-S. Ullström, *J. Chem. Soc. Dalton Trans.* **7**, 1256 (2002).
7.421. B. Montbaraki, D. Reinen, and H. Stratemeier, *Inorg. Chem.* **32**, 3397 (1993).
7.422. V. A. Ulanov, M. Krupski, S. K. Hoffman, and M. M. Zaripov, *J. Phys.: Condens. Matter* **15**, 1081 (2003).
7.423. (*a*) R. Akesson, L. G. M. Petterson, M. Sandström, and U. Wahlgrén, *J. Phys. Chem.* **96**, 150 (1992); (*b*) D. Stromberg, M. Sandström, and U. Wahlgrén, *Chem. Phys. Lett.* **172**, 49 (1990).
7.424. R. Akesson, M. Pettersson, M. Sandström, E. M. Siegbahn, and W. Wahlgrén, *J. Phys. Chem.* **97**, 3765 (1993).
7.425. F. Schwenk and B. M. Rode, *Chem. Commun.* 1286 (2003).
7.426. M. J. Riley, *Topics Curr. Chem.* **214**, 57 (2001).
7.427. S. E. Okan and P. S. Salmon, *Mol. Phys.* **85**, 981 (1995).
7.428. J. W. Kenney III, W. Clymire, and S. F. Agnew, *J. Am. Chem. Soc.* **117**, 1645 (1995).
7.429. (*a*) O. S. Wenger and H. U. Güdel, *J. Chem. Phys.* **114**, 5832 (2001); (*b*) O. S. Wenger, R. Valiente, and H. U. Güdel, *J. Chem. Phys.* **115**, 3819 (2001).
7.430. H. Bash, J. W. Moskowitz, C. Holister, and D. J. Hankin, *Chem. Phys.* **55**, 1922 (1971).
7.431. M. J. Rothmann, L. S. Bartell, C. S. Ewig, and J. R. van Wazer, *J. Chem. Phys.* **73**, 375 (1988).
7.432. M. Klobukowski, S. Huzinaga, L. Seijo, and Z. Barandiaran, *Theor. Chim. Acta* **71**, 237 (1987).
7.433. M. Klobukowski, *Can. J. Chem.* **71**, 141 (1993); *J. Comput. Chem.* **14**, 1234 (1993).
7.434. W. Kutzelnigg and F. Schmitz, in *Unkoventionelle Wechselwirkungen in der Chemie metallischer Elemente*, Ed. B. Krebs, Weinhein, Verlag Chemie,1992, p. 17.
7.435. R. A. Wheeler, P. N. Kumar, and V. Pavan, *J. Am. Chem. Soc.* **114**, 4776 (1992).
7.436. W. J. A. Maaskant, *New J. Chem.* **17**, 97 (1993).
7.437. W. J. A. Maaskant, *J. Alloys Compounds* **281**, 211 (1998).
7.438. V. Boudon, F. Michelot, and J. Moret-Bailly, *J. Mol. Spetrosc.* **166**, 449 (1994).

7.439. E. Bernhardt, H. Willner, A. Kornath, J. Breidung, M. Buhl, V. Jonas, and W. Thiel, *J. Phys. Chem. A* **107**, 859 (2003).
7.440. M. Hargittai, A. Schultz, B. Peffy, and M. Kolonits, *J. Am. Chem. Soc.* **123**, 1449 (2001).
7.441. P. L. W. Tregenna-Piggott, S. P. Best, M. C. M. O'Brien, K. S. Knight, J. B. Forsyth, and J. R. Pilbrow, *J. Am. Chem. Soc.* **119**, 3324 (1997).
7.442. P. L. W. Tregenna-Piggott, M. C. M. O'Brien, J. R. Pilbrow, H. U. Güdel, S. P. Best, and C. Noble, *J. Chem. Phys.* **107**, 8275 (1997).
7.443. P. L. W. Tregenna-Piggott, M. C. M. O'Brien, H. Weihe, and H. U. Güdel, *J. Chem. Phys.* **109**, 2967 (1998).
7.444. P. L. W. Tregenna-Piggott, S. P. Best, H. U. Güdel, H. Weihe, and C. C. Wilson, *J. Solid State Chem.* **145**, 460 (1999).
7.445. P. L. W. Tregenna-Piggott, H. Weihe, J. Bendix, A. L. Barra, and H. U. Güdel, *Inorg. Chem.* **38**, 5928 (1999).
7.446. P. L. W. Tregenna-Piggott, C. Noble, and J. R. Pilbrow, *J. Chem. Phys.* **113**, 3289 (2000).
7.447. D. Spichiger, G. Garver, C. Dobe, J. Bendix, P. L. W. Tregenna-Piggott, R. Meier, and G. Zahn, *Chem. Phys. Lett.* **337**, 391 (2001).
7.448. P. L. W. Tregenna-Piggott and H. U. Güdel, *Inorg. Chem.* **40**, 5497 (2001).
7.449. G. Garver, J. Bendix, and P. L. W. Tregenna-Piggott, *Chem. Phys.* **282**, 245 (2002).
7.450. S. Dolder, D. Spichiger, and P. L. W. Tregenna-Piggott, *Inorg. Chem.* **42**, 1343 (2003).
7.451. P. L. W. Tregenna-Piggott, H.-P. Anders, G. McIntyre, S. P. Best, C. C. Wilson, and J. A. Cowan, *Inorg. Chem.* **42**, 1360 (2003).
7.452. R. Basler, P. L. W. Tregenna-Piggott, H.-P. Andres, C. Dobe, H. U. Güdel, S. Janssen, and G. McIntyre, *J. Am. Chem. Soc.* **123**, 3387 (2001).
7.453. C. Dobe, H.-P. Andres, P. L. W. Tregenna-Piggott, S. Mossin, H. Weihe, and S. Janssen, *Chem. Phys. Lett.* **362**, 387 (2002).
7.454. M. T. Barriuso, J. A. Aramburu, and M. Moreno, *Phys. Status Solidi B* **196**, 193 (1996).
7.455. M. C. Michelini, R. P. Diez, and A. H. Jubert, *J. Mol. Struct. (THEOCHEM)* **490**, 181 (1999).
7.456. C. Y. Zhao and K. Balasubramanian, *J. Chem. Phys.* **116**, 10 287 (2002).
7.457. I. B. Bersuker, V. Z. Polinger, and L. F. Chibotaru, *Mol. Phys.* **52**, 1271 (1984).
7.458. I. B. Bersuker, V. Z. Polinger, and L. F. Chibotary, *Teor. Eksp. Khim.* **20**, 1 (1984).
7.459. V. Z. Polinger, L. F. Chibotary, and I. B. Bersuker, *Fiz. Tverd. Tela* **26**, 571 (1984).
7.460. I. B. Bersuker, V. Z. Polinger, and L. F. Chibotary, *Phys. Status Solidi* **129**, 615 (1985).
7.461. T. Kato, M. Kondo, M. Tashibana, T. Yamabe, and K. Yoshizawa, *Chem. Phys.* **271**, 31 (2001).
7.462. C. A. Borshch, *Adv. Quant. Chem.* **44**, 389 (2003).
7.463. A. Deluzet, H. Duclusaud, P. Sautet, and S. A. Borshch, *Inorg. Chem.* **41**, 2537 (2002).
7.464. S. Keinan and D. Avnir, *J. Chem. Soc. Dalton Trans.* **6**, 941 (2001).
7.465. A. Wilk, A. Hitchman, W. Massa, and D. Reinen, *Inorg. Chem.* **32**, 2483 (1993).

7.466. E. Coronado, S. Klokishner, O. Reu, and B. Tsukerblat, *Adv. Quant. Chem.* **44**, 429 (2003); *Polyhedron* **22**, 2527 (2003).
7.467. G. Murphy, C. O'Sullivan, B. Murphy, and B. Hathaway, *Inorg. Chem.* **37**, 240 (1998).
7.468. C. F. Schwenk and B. M. Rode, *Chem. Commun.* **11**, 1286 (2003).
7.469. C. F. Schwenk and B. M. Rode, *J. Chem. Phys.* **119**, 9523 (2003); *Chem. Phys. Chem.* **4**, 931 (2003).
7.470. P. Comba and A. Lienke, *Inorg. Chem.* **40**, 5206 (2001).
7.471. A. G. Anders, A. I. Kaplienko, O. V. Kravdina, V. S. Bondarenko, A. Feher, M. Orendac, A. Orendacova, M. Kajnakova, and J. Cernak, *Low Temp. Phys.* **28**, 642 (2002).
7.472. F. Abu-Hasanyan, P. H.-Y. Cheong, and M. Oliff, *Angew. Chem. Int. Ed. Engl.* **41**, 2120 (2002).
7.473. K. A. Barakat, T. R. Cundari, and M. A. Omary, *J. Am. Chem. Soc.* **125**, 14228 (2003).
7.474. T. K. Kundu and P. T. Manoharan, *Mol. Phys.* **97**, 709 (1999); T. K. Kundu, R. Bruyndonckx, C. Daul, and P. T. Manoharan, *Inorg. Chem.* (1999), **38**, 3931 (1999).
7.475. T. K. Kundu and P. T. Manoharan, *Chem. Phys. Lett.* **264**, 338 (1997).
7.476. T. K. Kundu and P. T. Manoharan, *Mol. Phys.* **98**, 2007 (2000).
7.477. F. A. Cotton, L. M. Daniels, C. A. Murillo, and J. G. Slaton, *J. Am. Chem. Soc.* **124**, 2878 (2002).
7.478. F. P. Arnold, J. K. Burdett, and L. R. Sita, *J. Am. Chem. Soc.* **120**, 1637 (1998).
7.479. T. M. Anderson, X. Zhang, K. I. Hardcastle, and C. L. Hill, *Inorg. Chem.* **41**, 2477 (2002).
7.480. I. B. Bersuker, S. S. Stavrov, and B. G. Vekhter, *Biofizika* **24**, 413 (1979).
7.481. I. B. Bersuker and S. S. Stavrov, *Chem. Phys.* **54**, 33 (1981).
7.482. I. B. Bersuker, S. S. Stavrov, and B. G. Vekhter, *Chem. Phys.* **69**, 165 (1982).
7.483. I. B. Bersuker and S. S. Stavrov, *Inorg. Chim. Acta* **79**, 177 (1983).
7.484. S. S. Stavrov and I. B. Bersuker, *Inorg. Chim. Acta* **79**, 176 (1983).
7.485. S. S. Stavrov, *Chem. Phys.* **271**, 145 (2001).
7.486. M. F. Perutz, *Br. Med. Bull.* **32**, 195 (1976).
7.487. M. Zerner and M. Gouterman, *Theor. Chim. Acta* **4**, 44 (1966); M. Gouterman, in *The Porphyrins*, Vol.3, Ed. D. Dolphin, New York, Academic Press, 1978, p. 1.
7.488. X. Ye, A. Demidov, and P. M. Champion, *J. Am. Chem. Soc.* **124**, 5914 (2002).
7.489. G. I. Bersuker and V. Z. Polinger, *Chem. Phys.* **86**, 57 (1984).
7.490. M. Bacci, *New J. Chem.* **17**, 67 (1993).
7.491. D. V. Korol'kov, *Russ. J. Gen. Chem.* **72**, 523 (2002).
7.492. *Mixed-Valency Systems: Applications in Chemistry, Physics and Biology*, Ed. K. Prassides, NATO ASI Series C, Vol. 343, Dordrecht, Kluwer, 1991.
7.493. *Mixed-Valence Compounds*, Ed. D. B. Brown, Dordrecht, Reidel, 1980.
7.494. J. P. Fackler Jr., in *Encyclopedia of Inorganic Chemistry*, Ed. R. B. King, New York, Wiley, 1994, p. 2270.
7.495. S. B. Piepho, E. R. Krausz, and P. N. Schatz, *J. Am. Chem. Soc.* **100**, 2996 (1978).
7.496. K. Y. Wong and P. N. Schatz, *Progr. Inorg. Chem.* **28**, 369 (1981).
7.497. N. S. Hush, *Progr. Inorg. Chem.* **8**, 391 (1967); *Coord. Chem. Rev.* **64**, 135 (1985).

7.498. M. Riley, H. U. Güdel, and A. H. Norton, *Chem. Phys.* **166**, 19 (1992).
7.499. S. A. Borshch, *Zh. Strukt. Khim.* **28**, 36 (1987).
7.500. S. A. Borshch, I. V. Kotov, and I. B. Bersuker, *Chem. Phys. Lett.* **89**, 381 (1982).
7.501. H. G. Jang, S. J. Geib, Y. Kaneko, M. Nakano, M. Sorai, A. L. Pheingold, B. Monter, and D. V. Hendrickson, *J. Am. Chem. Soc.* **111**, 173 (1989).
7.502. C. Daul, S. Fernandez-Ceballos, I. Ciofini, C. Ranzy, and C.-W. Schläpfer, *Chem. Eur. J.* **8**, 4392 (2002).
7.503. T. Cambara, D. N. Hendrickson, M. Sorai, and S. Oh, *J. Chem. Phys.* **85**, 2895 (1986); R. M. Stratt and S. H. Adachi, *J. Chem. Phys.* **86**, 7156 (1987).
7.504. R. D. Cannon and R. P. White, *Progr. Inorg. Chem.* **36**, 195 (1988).
7.505. V. Coropceanu, M. Malagoli, J. M. André, and J. L. Bradas, *J. Am. Chem. Soc.* **124**, 10 519 (2002); *J. Chem. Phys.* **115**, 10 409 (2001).
7.506. V. Ya. Gamurar, S. I. Boldirev, A. V. Palii, and B. S. Tsukerblat, *Zh. Struct. Khim.* **34**, 20 (1993); J. J. Borras-Almenar, E. Coronado, and B. S. Tsukerblat, *Chem. Phys.* **177**, 1 (1993); S. I. Boldirev, V. Ya. Gamurar, B. S. Tsukerblat, and A. V. Palii, *Mol. Phys.* **81**, 621 (1994).
7.507. S. A. Borshch, I. V. Kotov, and I. B. Bersuker, *Chem. Phys. Lett.* **111**, 264 (1984); *Khim. Fiz.* **3**, 1009 (1985).
7.508. S. A. Borshch and L. F. Chibotaru, *Chem. Phys.* **135**, 375 (1989).
7.509. S. A. Borshch, E. L. Bominaar, G. Blondin, and J.-J. Girerd, *J. Am. Chem. Soc.* **115**, 5155 (1993).
7.510. E. L. Bominaar, S. A. Borshch, and J.-J. Girerd, *J. Am. Chem. Soc.* **116**, 5362 (1994); E. L. Bominar, Z. Hu, E. Münck, J.-J. Girerd, and S. A. Borshch, *J. Am. Chem. Soc.* **117**, 6976 (1995).
7.511. G. Blondin, E. L. Bominaar, J.-J. Girerd, and S. A. Borshch, in *Nuclear Magnetic Resonance of Paramagnetic Macromolecules*, Ed. G. La Mar, Dordrecht, Kluwer, 1994, p. 369.
7.512. E. L. Bominar, C. Achim, S. A. Borshch, J.-J. Girerd, and E. Münck, *Inorg. Chem.* **36**, 3689 (1997).
7.513. E. L. Bominar, S. A. Borshch, and C. Achim, *J. Chem. Phys.* **110**, 11 411 (1999).
7.514. S. A. Borshch, *J. Mol. Struct. (THEOCHEM)* **330**, 139 (1995).
7.515. J. J. Borras-Almenar, J. M. Clemente, E. Coronado, B. S. Tsukerblat, and A. V. Palii, *Z. Physik. Chem.* **201**, 189 (1997); J. J. Borras-Almenar, J. M. Clemente-Juan, E. Coronado, and B. S. Tsukerblat, *Chem. Phys.* **195**, 29 (1995).
7.516. S. A. Borshch and I. N. Kotov, *Zh. Strukt. Khim.* **32**, 44 (1991); and in *Mixed-Valency Systems: Applications in Chemistry, Physics and Biology*, Ed. K. Prassides, NATO ASI Series C, Vol. 343, Dordrecht, Kluwer, 1991, p. 347.
7.517. K. Neuenschwander, S. Piepho, and P. N. Schatz, *J. Am. Chem. Soc.* **107**, 7862 (1985).
7.518. S. B. Piepho, *J. Am. Chem. Soc.* **112**, 4197 (1990).
7.519. S. B. Piepho, *J. Am. Chem. Soc.* **110**, 6319 (1988); and in *Mixed-Valency Systems: Applications in Chemistry, Physics and Biology*, Ed. K. Prassides, Dordrecht, Kluwer, 1991, p. 329.
7.520. A. V. Palii, M. I. Belinsky, and B. S. Tsukerblat, *Chem. Phys.* **255**, 51 (2000); J. J. Borras-Almenar, E. Coronado, S. M. Ostrovsky, A. V. Palii, and B. S. Tsukerblat, in *Proc. XIV International Symposium on Electron–Phonon Dynamics and Jahn–Teller Effect*, Eds. G. Bevilacqua, L. Martinelli, N. Terzi, Singapore, World Scientific, 1999, p. 293.

7.521. V. Robert, S. A. Borshch, and B. Bigot, *J. Phys. Chem.* **100**, 580 (1996).
7.522. S. A. Borshch and J.-J. Girerd, *Chem. Phys.* **181**, 1 (1994)
7.523. H. Duclusaud and S. A. Borshch, *Chem. Phys. Lett.* **290**, 526 (1998).
7.524. J. J. Borras-Almenar, J. M. Clemente-Juan, E. Coronado, A. V. Palii, and B. S. Tsukerblat, in *Magnetoscience – From Molecules to Materials*, Eds. J. Miller and M. Drillon, Weinheim, Wiley-VCH, 2001, p. 155.
7.525. Ya. Ogurtsov, K. I. Turta, R. D. Cannon, and V. Vrajmasu, *Ann. West Univ. Timişoara, Ser. Chem.* **8**, 1 (1999).
7.526. J. J. Borras-Almenar, J. M. Clemente, E. Coronado, S. M. Ostrovsky, A. V. Palii, and B. S. Tsukerblat, in *Proc. XIV International Symposium on Electron–Phonon Dynamics and Jahn–Teller Effect*, Eds. G. Bevilacqua, L. Martinelli, and N. Terzi, Singapore, World Scientific, 1999, p. 302.
7.527. J. J. Borras-Almenar, J. M. Clemente-Juan, E. Coronado V. Yu. Mirovitskii, A. V. Palii, and B. S. Tsukerblat, in *Vibronic Interactions: Jahn–Teller Effect in Crystals and Molecules*, Eds. M. Kaplan and G. Zimmerman, NATO Science Series II, Vol. 39, Dordrecht, Kluwer, 2001, p. 111.
7.528. V. Robert, S. A. Borshch, and B. Bigot, *Inorg. Chem.* **35**, 3913 (1996).
7.529. S. A. Borshch, K. Prasides, V. Robert, and A. O. Solonenko, *J. Chem. Phys.* **109**, 4562 (1998).
7.530. V. Robert, S. Petit, and S. A. Borshch, *Inorg. Chem.* **38**, 1573 (1999).

8

Solid-state problems: local properties and cooperative phenomena

8.1 The JTE in local properties of solids

Local properties in crystals are strongly affected by JT vibronic coupling phenomena, quite similar to molecular systems discussed in the previous chapter. There is no sharp border between clusters and coordination systems, considered in Sections 7.6.1 and 7.6.2, and local formations in crystals (which are often modeled by clusters). Differences occur for impurity centers for which the JT problem is in fact a multimode one (Sections 3.5 and 5.5) with a very large (infinite) number of JT active modes that are significantly involved in the vibronic coupling. Another important crystal problem emerges when there are multiple JT impurity centers at sufficiently small intercenter distances with sufficiently strong interaction between them. In the limit of an infinite number of such JT centers that occupy regular positions in the lattice we come to the cooperative JTE (CJTE) considered in Sections 8.2 and 8.3. The JTE in superconductivity and colossal magnetoresistance is discussed in Section 8.4.

8.1.1 Impurity centers in crystals

We start with a single JT center in a regular crystal in the form of an impurity center or a lattice defect that has localized electronic states. The latter may be either orbitally degenerate and subject to the JTE (when the crystal field of the environment has at least one axis of symmetry of third or higher order), or pseudodegenerate with a PJTE (for which there are no symmetry restrictions, but the ground state should be force-equilibrated in the reference configuration, Section 4.1). Crystal lattices overwhelmingly have sufficiently high local symmetry, and with the PJTE included, similarly to molecular systems, *there are no impurity centers that can be a priori exempt from JT vibronic coupling effects.*

We emphasize again that the JT problem for an impurity in a regular crystal lattice is essentially a multimode one, as discussed in general in Sections 3.5 and 5.5. As shown in Section 5.5, the multimode solutions are rather complicated and require knowledge of the phonon spectrum of the host crystal. Often a simple solution based on a cluster-like presentation of the impurity system at low temperatures is possible. The success of such a relatively rough approach that ignores the detailed phonon spectrum is due to the small density of low-frequency phonon states, while those with higher frequencies are not populated at low temperatures (see the discussion at the end of Section 5.5). However, this low-temperature region may be too low for many problems.

Passing to the JTE in specific crystals with impurity centers, we note first that the number of publications on this subject, as for molecular systems, is innumerable. Earlier works are well presented in a series of books and reviews [8.1–8.14], more specifically on EPR measurements [8.3, 8.10], optical spectra of impurities in II–VI and III–V crystals [8.11], mercury-like impurities [8.12], transition metal impurities [8.13], and phonon spectroscopy [8.14], as well as in the general bibliographic review [8.1] that cites all the publications on the JTE up to 1979 inclusive. These references contain most interesting examples of manifestation of the JTE in impurity systems, which, however, will not be repeated here in detail. Instead we present an overview of those results in the form of Tables 8.1–8.6 with a variety of impurity systems and their JT parameters. An outline of examples of more recent work will follow to demonstrate the applications of the latest achievements in this field and provide references as a tool for further investigations.

EPR spectra of Cu^{2+} impurity ions in zinc fluorosilicate crystals provided the first experimental confirmation of the JTE [8.15–8.17] (Section 6.3.1). Further investigations of similar Cu^{2+} systems were carried out afterwards (see [8.1–8.3, 8.10, 8.18] and references therein). As shown in Section 6.3.1, the transition from dynamic to static JT EPR spectra takes place within a temperature interval which is characteristic of the magnitude of the JT coupling. Table 8.1 shows some examples with the range of transition temperatures. In a variety of metalloorganic complexes with octahedral Cu^{2+} impurities the JT parameters are rather similar in value, which allowed the authors [8.38, 8.39] to suggest useful averages. For CuN_6 and CuO_6 units with an $E \otimes e$ problem (Section 3.2) the averaged JT parameters from 12 and 15 complexes, respectively, are ρ_0 (Å) = 0.304(42) and 0.330(70), E_{JT}^{E} ($10^3\,\mathrm{cm}^{-1}$) = 2.01(21) and 1.81(0.19), $\hbar\omega_E\,(\mathrm{cm}^{-1}) = 319(41)$ and 254(27), and $K_E\,(\mathrm{mdyn/Å}) = 0.85(0.24)$ and 0.62(13).

With regard to other JT data in Tables 8.2–8.6, we note that they were obtained mainly during the seventies and eighties, and in the overwhelming majority are based on models which neglect the multimode nature of the

Table 8.1. *Examples of JT-induced temperature transition in ESR spectra (term ^2E)*

Ion	Host	Range of transition temperature (K)	References
Cu^{2+} ($3d^9$)	$ZnSiF_6{\cdot}6H_2O$	12–50	[8.15, 8.16. 8.19]
	$Zn(BrO_3)_2{\cdot}6H_2O$	7–35	[8.15, 8.16. 8.19]
	$La_2Mg_3(NO_3)_{12}{\cdot}24H_2O$	42–44	[8.15, 8.16. 8.19]
	$Bi_2Mg_3(NO_3)_{12}{\cdot}24H_2O$	>20–<90	[8.15, 8.16. 8.19]
	$Cu_3La_2(NO_3)_{12}{\cdot}24H_2O$	170–270	[8.15, 8.16. 8.19]
	AgCl	90–300	[8.20]
	MgO	>1.2–<77	[8.21]
	CaO	>1.2–<77	[8.22]
	$Zn(pyNO)_6(BF_4)_2$	47–56	[8.23]
	$(NH_4)_2Cu(H_2O)_6(SO_4)_2$	<30–>77	[8.24]
	$LiKSO_4$	≤247	[8.25]
	$LiNH_4SO_4$	≤247	[8.25]
	$LiNaSO_4$	≤247	[8.25]
$[CuCl_6]^{4-}$	CsCdCl3	90–140	[8.26]
Ag^{2+} ($4d^9$)	LiCl	40–316	[8.27]
	NaCl	95–348	[8.27]
	KCl	160–373	[8.28]
Rh^{2+} ($4d^7$)	AgBr	35–77	[8.29]
Ni^{+} ($3d^9$)	NaF	130–230	[8.30]
Y^{2+} ($4d^1$)	CaF_2	4–10	[8.31]
La^{2+} ($5d^1$)	CaF_2	10–12	[8.32]
Sc^{2+} ($3d^1$)	CaF_2	>1.5–<10	[8.33, 8.34]
	SrF_2	>1.5–<10	[8.33, 8.34]
Ni^{3+} ($3d^7$)	CaO	62–68	[8.35, 8.36]
Pt^{3+} ($5d^7$)	Al_2O_3	>4.2–<79	[8.37]

impurity problem (Sections 3.5 and 5.5). Therefore these parameters should be regarded as approximate estimations that may serve as a starting point for further improvements. In particular, the frequencies of the JT-active vibrations ω_Γ (Tables 8.2 and 8.5) should be taken as some effective (or averaged) phonon frequencies. In spite of this shortcoming, the data in Tables 8.1–8.6 give a fairly adequate qualitative and semiquantitative picture of the JT effect in a large variety of impurity systems.

Table 8.2. *JT stabilization energy E_{JT}, energy barrier between the minima δ, vibrational frequency of the JT active mode $\hbar\omega_\Gamma$, tunneling splitting $r\Gamma$, and the vibronic coupling constant F for impurity centers in crystals, obtained from EPR and optical spectra (asterisk indicates excited state)*

System	JT problem	E_{JT} (cm^{-1})	δ (cm^{-1})	$\hbar\omega_\Gamma$ (cm^{-1})	$r\Gamma$ (cm^{-1})	F (eV/Å)	References
$Cu^{2+}:CaO$	$E\otimes e$	4300	−45	300	4	−2.4	[8.40]
$Cu^{2+}:CaO$	$E\otimes e$	1600		93		0.67	[8.41]
$Ni^{3+}:Al_2O_3$	$E\otimes e$	1100	120	465	60		[8.42, 8.43]
$Mn^{3+}:Al_2O_3$	$E\otimes e$				52		[8.44]
$Cr^{2+}:AgCl$	$E\otimes e$	1425		195		1.33	[8.45, 8.46]
$Cr^{2+}:AgBr$	$E\otimes e$	1275		155		1.50	[8.45, 8.46]
$Fe^{2+}:CdTe$	$E\otimes e$	4.2		38			[8.47]
$Cr^{2+}:ZnS$	$T\otimes e$	300		90		0.27	[8.48]
$Cr^{2+}:ZnSe$	$T\otimes e$	340		70		0.35	[8.48]
$Cr^{2+}:ZnTe$	$T\otimes e$	320		50		0.31	8.48]
$Cr^{2+}:CdTe$	$T\otimes e$	370		35		0.23	[8.48]
$Cr^{2+}:GaAs$	$T\otimes e$	660		70			[8.49, 8.50]
$Ni^{2+}:CdF_2$	$T\otimes t_2$	1730	$\leq$430			0.80	[8.51]
$Ni^{2+}:CaF_2$	$T\otimes t_2$	1600	$\leq$400			0.77	[8.51]
$Fe^{2+}:MgO^*$	Excited $E\otimes e$, transition $^5T_{2g}$–^5E_g	1600		270	14	1.31	[8.52]
$Fe^{2+}:AgCl^*$	The same	2040		195		1.59	[8.45, 8.53]
$Fe^{2+}:AgBr^*$	The same	1610		155		1.68	[8.45, 8.53]
$Fe^{2+}:KMgF_3{}^*$	The same	1750		260		1.44	[8.54]
$Fe^{2+}:CdCl_2{}^*$	The same	1550		93		0.66	[8.55]
$Fe^{2+}:CdBr_2{}^*$	The same	1160		66		0.61	[8.55]
$Ti^{3+}:AgCl^*$	Excited $E\otimes e$, transition $^2T_{2g}$–^2E_g	1040		250		1.45	[8.45, 8.46]
$Ti^{3+}:AgBr^*$	The same	1130		150		1.37	[8.45, 8.46]
$Ti^{3+}:Al_2O_3{}^*$	The same	3010		515		3.42	[8.56]
$Eu^{2+}:SrF_2{}^*$	Excited $E\otimes e$	$\sim 10^3$			6.5		[8.57, 8.58]

Table 8.2. (*cont.*)

System	JT problem	E_{JT} (cm^{-1})	δ (cm^{-1})	$\hbar\omega_\Gamma$ (cm^{-1})	$r\Gamma$ (cm^{-1})	F (eV/Å)	References
$Eu^{2+}:CaF_2^*$	The same	$\sim 10^3$			15		[8.57, 8.58]
$Sm^{2+}:SrF_2^*$	The same				26		[8.57, 8.58]
$Sm^{2+}:CaF_2^*$	The same				27		[8.57, 8.58]
$Ti^{2+}:CdS^*$	Excited $T\otimes t_2$,						
	${}^3A_2$–${}^3T_1$(F),	1050		78		0.38	[8.59]
	${}^3A_2$–${}^3T_1$(P),					0.13	[8.59]
$Ti^{2+}:CdSe^*$	The same	700					[8.60]
$Ti^{2+}:CdTe^*$	The same	520					[8.61]
$Fe^{2+}:CdF_2^*$	Excited $T\otimes t_2$, ${}^5E_g$–${}^5T_{2g}$	3750		110		0.77	[8.62]
$Co^{2+}:CdF_2^*$	Excited $T\otimes t_2$,						
	${}^4A_{2g}$–${}^4T_{1g}$(F),	2100		210		1.12	[8.62. 8.63]
	${}^4A_{2g}$–${}^4T_{1g}$(P),	1900		170		0.85	[8.62. 8.63]
	${}^4A_{2g}$–${}^4T_{1g}$(P),	1900		160		0.81	[8.62. 8.63]
$Mn^{2+}:ZnS^*$	Excited $T\otimes e$, ${}^6A_1$–${}^4T_{1g}({}^4G)$,	>180		90			[8.64, 8.65]
$Mn^{2+}:ZnSe^*$	The same	>140		70			[8.64, 8.65]

Table 8.3. *JT parameters for impurity centers in crystals with an $E\otimes e$ problem obtained from ESR measurements at low (T_1) and high (T_2) temperatures ($q = K_E(E)$ is the reduction factor, 3Γ is the tunneling splitting, and $\bar{\delta}/3\Gamma$ is the ratio of averaged strain influence to the tunneling splitting (Section 3.6))*

System	T_1 (K)	T_2 (K)	q	3Γ (cm^{-1})	$\bar{\delta}/3\Gamma$	References
$Cu^{2+}:CaO$	1.3	77		$\cong 3$	0.67	[8.66]
$Ag^{2+}:MgO$	1.3		0.577	4.8	0.13	[8.66]
$Ag^{2+}:CaO$	1.3	77	0.610	3.9	1.2	[8.66]
$Ag^{2+}:SrO$	4.2	223	0.682			[8.66]
$Ni^{+}:MgO$	4.2		$\cong 0.6$			[8.67]
$Ni^{3+}:MgO$	4.2		0.67			[8.67]
$Rh^{2+}:MgO$	4.2	77	0.64			[8.68]
$Pt^{3+}:MgO$	4.2	77			>56	[8.69]

Table 8.4. *JT parameters for some d^1 ions in alkaline-earth halides*

System	$E_{JT}/\hbar\omega$	q	References
$Sc^{2+}:CaF_2$	0.4	0.69	[8.3, 8.70, 8.71]
$Sc^{2+}:SrF_2$	0.5	0.63	[8.70]
$Sc^{2+}:BaF_2$	0.5	0.66	[8.70]
$Sc^{2+}:SrCl_2$	0.1	0.86	[8.70]
$Sc^{2+}:ZnS$		0.51	[8.72]
$Y^{2+}:SrCl_2$	0.5	0.65	[8.70]
$La^{2+}:CaF_2$		$\sim$0.5	[8.71]
$La^{2+}:SrF_2$	1	0.57	[8.71]

Table 8.5. *JT parameters for impurity centers in crystals with a $T\otimes e$ problem obtained from optical and phonon spectra ($K_T(E)$ is the vibronic reduction factor, F_E is the linear vibronic coupling constant, and R is the mean cation–anion distance (adapted from [8.14]))*

System	E_{JT}^E (cm^{-1})	ω_E (cm^{-1})	$K_T(E)$	$F_E R$ (cm^{-1})	References
$Ti^{3+}:Al_2O_3$	200	200	0.21		[8.73, 8.74]
				$\geq 7000 \pm 3500$	[8.74, 8.75]
				>6000	[8.76]
$V^{4+}:Al_2O_3$	320	200	0.09	$15\,000 \pm 4000$	[8.73, 8.42]
				9000 ± 1000	[8.76]
$Cr^{5+}:Al_2O_3$			0.025		[8.77]
$V^{3+}:MgO$	135	450	0.64	1600	[8.78]
$Ti^{2+}:CaO$	350	350	0.2	$\sim$2600	[8.79]
$V^{3+}:CaO$	1600	350	$\sim 10^{-3}$	$\sim$8500	[8.80]

In general, as in the molecular case, Cu^{2+} impurity centers in cubic-symmetry environments are among the strongest JTE systems with an $E\otimes e$ problem, and hence most studied. A series of more recent works [8.92–8.104] deals with a variety of JT properties of Cu impurities. One- and two-phonon spectroscopy was used to study $d^{10}\rightarrow d^9 s$ transitions in $Cu^+:NaF$ with degenerate excited states in the $d^9 s$ configuration [8.92]. Some of the band splittings were attributed to the JTE (Section 6.1), but the overall JT interpretation of the spectrum seems to need further investigation.

Table 8.6. *JT parameters for impurity centers in crystals with a* $T \otimes (e + t_2)$ *problem obtained from phonon spectroscopy* (*denotations and units as in Table 8.5*) (*adapted from* [8.14])

System	E_{JT}^{E}	E_{JT}^{E}	$K_T(E)$	$K_T(T)$	$F_E R$	$F_T R$	References
$V^{3+}:Al_2O_3$			0.037		56 350	4 575	[8.81]
$Cr^{4+}:Al_2O_3$			0.036		14 850	6 630	[8.82]
$Fe^{2+}:MgO$	110	83	0.09	0.09	6 300	5 300	[8.83, 8.84] [8.85]
$Fe^{2+}:KMgF_3$			0.058	0.10	15 000	12 700	[8.86] [8.87]
$Fe^{2+}:CaO$			1	0.15			[8.86]
$Fe^{2+}:Al_2O_3$*			1	0.19*	~20 000		[8.88]
$Cr^{3+}:GaAs$	2800		1/4	1/2	25 000	−17 000	[8.89]
$Cr^{2+}:GaAs$	1720		1	10^{-14}	$-16\,700 \pm 1\,700$		[8.90]
	480		1	$\sim 10^{-4}$			[8.91]

DFT calculations were employed to reveal off-center z-displacements of the Cu^{2+} ion as a substitute in CaF_2, SrF_2, and $SrCl_2$ crystals [8.93]. The values of, respectively, $z_0 = 0$, 0.3, and 1.1 Å, and PJT stabilization energies of 0, 0.12, and 0.29 eV explain well the experimental EPR data. The $Cu^{2+}:CaF_2$ system undergoes an orthorhombic distortion of the cubic environment of Cu^{2+}. This correlates with EPR experiments for Cu^{2+} in CaF_2 under uniaxial stress [8.94], which show that the JT ion in the cubic eightfold-coordinated environment occupies six equivalent D_{2h} positions, and at 4.2 K reorients between them in accordance with the $T_2 \otimes (e + t_2)$ JT problem. Similar JT eightfold-coordinated Cu^{2+} centers were studied in copper-doped fluorite-type crystals $Sr_{1-x}Ba_xF_2$ and $Ca_xSr_{1-x}F_2$ by means of EPR at frequencies 9.3 and 37 GHz in the range of 4.2–250 K [8.101]. The orthorhombic JT distortions attributed to the $T_2 \otimes (e + t_2)$ problem have a stabilization energy of $E_{\mathrm{JT}} = 1200$–$1600\,\mathrm{cm}^{-1}$ and a small tunneling splitting, $<0.5\,\mathrm{cm}^{-1}$. The latter is assumed to occur as a spin-flip tunneling, which is possible when one takes into account the spin–orbital interaction in the T state.

EPR measurements at ~9.5 GHz in the temperature interval 4.2–393 K were performed on a single crystal of potassium oxalate monohydrate ($K_2C_2O_4 \cdot H_2O$) doped with Cu^{2+} ions [8.95]. The latter occupy four magnetically nonequivalent (two pairs of physically equivalent) sites, of which two are JT active with a static spectrum below 172 K and a dynamic spectrum above

this point (Section 6.3.1). The low-temperature spectrum shows that there is a basic $E \otimes e$ JTE of the Cu^{2+} ion in an octahedral environment with an admixture of a PJTE that results in orthorhombic distortions. The tetragonally compressed octahedral environment of the Cu^{2+} ions in perovskites, $Cu^{2+}:K_2MgF_4$, is explained by the lattice influence which overcomes the local tendency toward elongated octahedra [8.96].

DFT cluster calculations [8.97(*a*)] of the $Cu^{2+}:MgO$ system reveal a weak $E \otimes e$ JTE with the dimensionless coupling constant $\lambda_E = E_{JT}^E/\hbar\omega_E = 0.65$ (Section 3.2) consistent with the observed isotropic (cubic) EPR spectrum. For $Cu^{2+}:SrO$ λ is three times larger, explaining the origin of the low-temperature static JT spectrum (Section 6.3.3). The APES of $Cu^{2+}:MgO$ was also calculated *ab initio* using the embedded-cluster model (Section 5.5) with the goal of explaining electronic absorption spectra [8.97(*b*)]. The results for $Cu^{2+}:MgO$ in [8.97(*a*)] are implicitly questioned in [8.98] in an attempt to explain the EPR and Raman spectra. The author [8.98] considered in more detail the "classical" system $Cu^{2+}:CaO$, for which the tunneling splitting $3\Gamma = 4\,cm^{-1}$ was revealed from the Raman spectra [8.40] (see Section 6.2.2, Fig. 6.18) with the other parameters given in Table 8.2. In a better fit to the EPR and Raman spectra he obtained $E_{JT}^E \simeq 1730\,cm^{-1}$ and $\hbar\omega_E \simeq 216\,cm^{-1}$. Vibronic EPR parameters for $Cu^{2+}:CaO$ obtained by comparison of the experimental spectrum with the calculated one including the JTE and random strain (Section 6.3.2) are given in Fig. 6.30 and in Table 8.3.

Cu^{2+} ions in spinels $Cu_xZn_{1-x}Cr_2O_4$ and $Cu_{1-x}Ni_xCr_2O_4$ [8.99] occupy JT-distorted tetrahedral positions with a $T \otimes e$ problem and JT stabilization energy that increases with the concentration x due to cooperative effects via elastic interactions (Section 8.2). EPR, optical, and magnetic-susceptibility studies of $[Cu\{(NH_3)_2sar\}](NO_3)_4 \cdot H_2O$, where the Cu^{2+} ion is in a macrobicyclic cage with six nitrogen atoms in the nearest octahedral environment [8.100], show that there is a dynamic $E \otimes e$-type JTE above 290 K, a situation intermediate between dynamic and static in the range of 290–122 K, and a static JTE below 122 K (Section 6.3.1). The JT stabilization energy $E_{JT}^E = 2125\,cm^{-1}$, while the radius of the distortion $\rho_0 = 0.195$ Å (Section 3.2).

Spin–lattice relaxation measurements in the temperature range of 10–50 K show that the JT dynamics in $Cu(H_2O)_6$ complexes of $Cu^{2+}:Cs_2Zn(SO_4)_2 \cdot 6H_2O$ is too slow to dominate the EPR spectra [8.102].

Cu^{2+} ions in two-dimensional perovskite layers in $Cu^{2+}:(CH_3NH_3)_2CdCl_4$ and $(CH_3NH_3)_2CuCl_4$ [8.103], and $Cu^{2+}:(C_3H_7NH_3)_2CdCl_4$ [8.104] were studied by EPR in the range of 10–300 K both in powder and single crystals. The Cd^{2+} compressed D_{4h} sites become elongated when replaced by Cu^{2+},

with the elongated axis lying within the two-dimensional layer. The dynamic features of the spectrum are associated with a two-minimum well reflecting the two-dimensional host lattice.

Ag^{2+} impurities are similar to Cu^{2+} in many respects, but the ionic radius of the former is larger, with important consequences for the magnitude of the JT distortions. Indeed, the size of impurity ion influences directly the overlap of its wavefunctions with those of the environment atoms that determines the primary (nonvibronic) force constant K_0 in the formulas of JT distortions in all the JT (Chapter 3) and PJT (Chapter 4) problems. In particular $Ag^{2+}:CaF_2$ and $Ag^{2+}:SrF_2$ exhibit trigonal distortions of an intermediate-to-strong $T_2 \otimes t_2$ JTE [8.105, 8.106]. Similarly, trigonal distortions are formed in $Ag^{2+}:Ca_xSr_{1-x}F_2$ and $Ag^{2+}:Sr_{1-x}Ba_xF_2$ with a stabilization energy $E_{JT} = 2000$–$2500\,cm^{-1}$ [8.101]. The authors explored also the influence of strain and tunneling in these systems. For $Ag^{2+}:NaF$ the EPR spectrum is tetragonal at 4.2 K and becomes dynamically averaged above ~40 K, in full agreement with that expected in the $E \otimes e$ JT problem (Section 6.3.1) [8.107]. For earlier work on $Ag^{2+}:CaO$ and $Ag^{2+}:MgO$ see in Table 8.3.

Ni^+ (d^9) centers are electronically similar to Cu^{2+}, and hence may exhibit a similar JTE. The latter was found by means of an EPR study in $Ni^+:CsCaF_3$ [8.108], where some of the centers have an octahedral environment with an $E \otimes e$ problem. For Ni^{2+} in tetrahedral sites in $Ni_xZn_{1-x}Cr_2O_4$ and $Cu_{1-x}Ni_xCr_2O_4$ the ground state $^3T_1$ is orbitally similar to the $^3T_2$ state of Cu^{2+} and results in a similar $T \otimes e$ JT problem [8.99]. Ni^{3+} in nickelates $LaSrNiO_{4\pm\delta}$ and $LaSrAl_{1-x}Ni_xO_{4\pm\delta}$ forms NiO_6 centers with a JTE of $E \otimes e$ type observable by EPR [8.109].

In a series of works on Fe^{2+} impurities ($Fe^{2+}:CdTe$ [8.111], $Fe^{2+}:ZnS$ [8.112, 8.113], Fe^{2+} in a series of cubic II–VI and III–V semiconductors [8.114]) the authors employed numerical methods to calculate vibronic energy levels in the ground ^5E and excited $^5T_2$ states and intensities of transitions between them corresponding to infrared absorption. In so doing, a variety of improvements on the Lanczos and Glauber methods were introduced (Section 5.4), in particular, by using the recursion method with modifications that allow one to create the chain of states "dipole-free" (i.e., not dipole coupled to a given initial state). In this case the transition intensity is determined by the initial state only [8.111]. Good agreement with experimental data was achieved for the first five lines of $Fe^{2+}:CdTe$ with the following parameters: spin–orbital coupling $\lambda_{SO} = -100\,cm^{-1}$, averaged JT-active mode $\hbar\omega_E = 36\,cm^{-1}$, crystal-field splitting $D_q = 256.5\,cm^{-1}$, and JT stabilization energy $E_{JT}^E = 232\,cm^{-1}$ [8.111(*a*)] (a vibronic matrix of the order 37 500 was solved in this paper).

Table 8.7. *Averaged accoustical $\hbar\omega_E$(ac) and optical $\hbar\omega_E$(opt) JT modes and corresponding stabilization energies $E^E_{\rm JT}$ (ac) and $E^E_{\rm JT}$ (opt), and their ratios $S = E^E_{\rm JT}/\hbar\omega_E$ for Fe^{2+} impurities in a series of hosts, with energy in units of cm^{-1} (adapted from [8.115])*

	Host						
	CdTe	ZnTe	ZnSe	ZnS	GaAs	InP	GaP
$\hbar\omega_E$(ac)	35	50	70	100	85	75	105
$E^E_{\rm JT}$(ac)	210	220	210	190	160	170	180
S(ac) $= E^E_{\rm JT}/\hbar\omega_E$	6.0	4.20	3.00	1.90	1.88	2.27	1.71
$\hbar\omega_E$(opt)	150	180	250	340	260	320	350
$E^E_{\rm JT}$(opt)	30	30	40	55	40	60	50
S(opt) $= E^E_{\rm JT}/\hbar\omega_E$	0.20	0.17	0.16	0.16	0.15	0.19	0.14

For Fe^{2+} : ZnS a multimode version of the calculations was suggested [8.112], in which, instead of just the one averaged JT-active mode used in the previous case of Fe^{2+} : CdTe, the range of Γ_3 (e-type) frequencies in the multimode $T_2 \otimes e$ problem is divided into three with averaged frequencies (in cm^{-1}) $\hbar\omega_E = 25$, 125, and 300, respectively. The corresponding JT stabilization energies for these three regions were estimated as (in cm^{-1}) $E^E_{\rm JT} = 50$, 130, and 70, respectively. For improved calculations for this system using a modified Lanczos-type algorithms see in [8.113].

Similar numerical methods were employed to interpret zero-phonon lines in extended absorption of Fe^{2+} impurities in ZnS, GaAs, InP, and GaP, taking into account the JT vibronic coupling in a two-mode (one acoustical and one optical) scheme [8.114]. Table 8.7 shows the estimated JT parameter values for the averaged acoustical $\hbar\omega_E$(ac), $E^E_{\rm JT}$(ac) and optical $\hbar\omega_E$(opt), $E^E_{\rm JT}$(opt) JT-active vibrational frequencies and stabilization energies, respectively ($s = E^E_{\rm JT}/\hbar\omega_E$ is the dimensionless coupling constant), that allow one to explain the origin of several main lines in the high-energy spectrum. The JTE in the far-infrared spectrum of Fe^{2+} : ZnSe was analyzed in [8.115]. The JTE with spin–orbital coupling in this system was also considered in [8.116].

A comparison of optical crystal-field and charge-transfer excitations of Fe^{6+} impurities in Fe : K_2XO_4, X = S, Se, Cr, with those of Cr^{4+} in oxides was carried out by means of DFT calculation of tetrahedral $[FeO_4]^{2-}$ and $[CrO_4]^{4-}$ clusters, respectively, taking into account the JTE in the excited states [8.117]. For earlier work on Fe^{2+} impurities in crystals see in Tables 8.2 and 8.3.

Chromium impurity ions in a variety of lattices are studied widely, mostly as laser materials. The JTE parameters of a series of systems, including $Cr^{2+}:MgO$, $Cr^{2+}:CaO$, $Cr^{2+}:SrO$, and $Cr^{2+}:KMgF_3$, were obtained by means of *ab initio* calculations within the framework of the model-potential-embedding method (Section 5.5) [8.118]. For the two lowest electronic states ${}^5E_g$ and ${}^5T_{2g}$ of the low-spin configuration of the Cr^{2+} (d^7) ion in an octahedral environment ($[CrO_6]^{10-}$ and $[CrF_6]^{4-}$ clusters) *ab initio* CASSCF and ACPF (averaged coupled-pair-functional) calculations including cluster-environment Coulomb and exchange interactions were performed to obtain the APES in the space of e_g displacements ($E_g \otimes e_g$ and $T_{2g} \otimes e_g$ problems). The JT parameters for E_g states of the four systems above are, respectively (in cm^{-1}), $\nu_{e_g} = 520$, 345, 280, and 540; $E_{JT}^E = 480$, 605, 565, and 365; $\delta = E(\text{compressed}) - E(\text{elongated}) = -5$, 20, 75, and 5. For the T_{2g} state, respectively, $\nu_{e_g} = 520$, 340, 270, and 550, while $E_{JT}^E = 100$, 155, 170, and 40. The local configuration at the minimum of the APES is thus an elongated octahedron in $Cr^{2+}:MgO$ and a compressed octahedron in the other three systems, with rather small barriers between the minima and strongest linear coupling (E_{JT}^E/ν_{e_g}) for $Cr^{2+}:CaO$ and $Cr^{2+}:SrO$.

Cr^{2+} ions in eightfold coordination of the crystal lattice in SrF_2 and CaF_2 in the ground state ${}^5T_{2g}$ with the $T_{2g} \otimes (e_g + t_{2g})$ quadratic JT problem resulting in six orthorhombic minima (Section 3.4) were considered in [8.119]. The authors employed a theoretical model with a spin Hamiltonian that includes random strain (Section 6.3.2) in order to explain EPR spectra [8.120], and the parameters that fit the spectra well were evaluated. Orthorhombic distortions were also confirmed by EPR spectra of Cr^{2+} in CdF_2 and CaF_2 [8.121]. The Cr^{2+} ion in $Cr^{2+}:ZnSe$ and $Cr^{2+}:ZnS$ with the ${}^5T_2 \otimes (e + t_2)$ ground-state problem shows relatively strong vibronic coupling, mostly to the t_2 mode [8.122(*a*)]. This was demonstrated by computation of the vibronic energy levels and spectra in the emission and absorption (from and to the lowest excited state ${}^5E$), with a variety of details revealed and discussed. A similar calculation was employed to study the JTE in the luminescence spectra of V^{2+} in $V^{2+}:ZnSe$ and $V^{2+}:ZnS$ [8.122(*b*)].

Cr^{3+} is one of the impurity ions that have been most studied by optical spectroscopy, in view of its applications in laser materials. For Cr^{3+} ions in fluorides that form octahedral $[CrF_6]^{3-}$ clusters, the vibronic coupling constants $F_{A_{1g}}$ and F_{E_g} in the first excited state ${}^4T_{2g}$ (in contrast to oxide host, where it is ${}^2E_g$) were estimated using multiple-scattering X_α and self-consistent-charge extended Hückel methods of electronic-structure calculations [8.123]. They found (in cm^{-1}/pm units) $F_{A_{1g}} = -182$ and $F_{E_g} = -130$. For the Cr^{3+} ion in $Cs_2NaScCl_6$ the $T \otimes e$ JT problem for the ${}^4T_{2g}$ state was

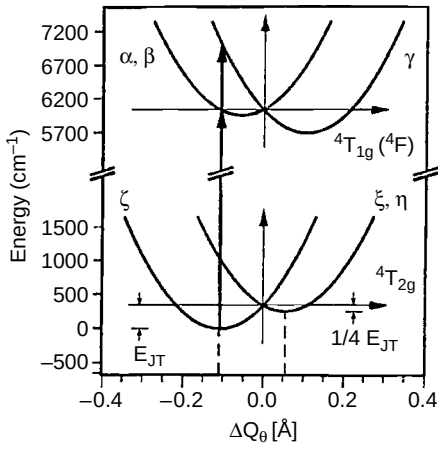

Fig. 8.1. A cross-section of the APES of the first ($^4T_{2g}$) and next ($^4T_{1g}(^4F)$) excited states in the impurity system $Cr^{3+}:Cs_2NaScCl_6$ along the Q_ϑ coordinate of the e_g displacements. The $T\otimes e$ JT coupling is assumed to be dominant in both states with the three electronic T-term functions as ξ, η, ζ and α, β, γ, respectively. The thick vertical arrow shows the expected electronic transition from the minimum of the lower state in the excited-state absorption. (Reprinted with permission from [8.124(b)]. Copyright 2002 American Institute of Physics.)

studied in [8.124(*a*)], while in [8.124(*b*)] the more complicated excited-state absorptions $^4T_{2g}\rightarrow{}^4T_{1g}(^4F)$ and $^4T_{2g}\rightarrow{}^4T_{1g}(^4P)$ where analyzed taking into account the JTE with the same $T\otimes e$ scheme in both states. Figure 8.1 shows the cross-section of the APES of the $^4T_{2g}$ and $^4T_{1g}(F)$ excited states in the plane of one of the E_g displacements, which clarifies the origin of the JT implications in the above transitions (Section 6.1.1).

To explain the origin of the $Cr^{3+}:CdIn_2S_4$ luminescence spectrum, the PJT coupling in the excited manifold of the ^2E and $^4T_2$ terms of the Cr^{3+} ($3d^3$) ion was considered [8.125]. The mixing of the three Γ_8 levels that emerge from the spin–orbital interaction by totally symmetric a vibrations was accounted for in a PJT $(\Gamma_8+\Gamma_8'+\Gamma_8'')\otimes a_1$ problem, which allowed the authors to fully explain the temperature dependence of the luminescence kinetics and intensity of the emission U-band, as well as the spectral shape of this band.

For another laser material, $Co^{2+}:KZnF_3$, the $[CoF_6]^{4-}$ cluster was studied using an *ab initio* model-potential method that includes correlation and embedding effects to take into account the influence of the lattice [8.126] (Section 5.5). The estimated JT parameters (Section 3.3) for the ground $a\,^4T_{1g}$ and excited $^4T_{2g}$ and $b\,^4T_{1g}$ states in the $T\otimes e$ coupling scheme are, respectively (in cm^{-1}), $E_{JT}^E=8$, 120, and 545; $\delta=8$, 93, and 415; $\nu_{e_g}=402$, 399, and 419; and $\nu_{a_{1g}}=502$, 518, and 516. At the minima the distorted ground $a\,^4T_{1g}$ and first excited

$^4T_{2g}$ state geometries are elongated octahedra, while the excited $b\,^4T_{1g}$ state produces a compressed octahedron. For Co^{2+} substituting Sr^{2+} in $SrLaGa_3O_7$ the authors [8.127] found a $T \otimes t_2$ coupling with $E_{JT}^T = 507\,cm^{-1}$.

There is spectroscopic evidence of distortion of the $[CrO_4]^{3-}$ tetrahedron and splitting of the ^2E ground state in Cr^{5+}-doped spodiosites $Sr_2(VO_4)Cl$ [8.128].

The JTE in Ti^{3+} impurity centers in cesium gallium alum (I) [8.129(*a*)] and cesium aluminum alum (II) [8.129(*b*)] were studied by low-temperature magnetization and EPR. In I, the JT coupling results in the formation of low-lying vibronic states that mix under the magnetic field, producing a strong dependence of the magnetization on the magnetic field. This allows measurements of the Zeeman coefficients up to the third order. In II, the measured $g_\parallel$ and $g_\perp$ factors could be modeled only under the assumption of a combined influence of the JT coupling and low-symmetry strain (Section 6.3.2).

JT broadening of emission and absorption bands (Section 6.1.1) in Ti^{3+}- and Mn^{3+}-doped $Be_3Al_2(SiO_3)_6$ was suggested to explain the origin of superbroad bands of stimulated emission [8.130]. The excited state $a\,^4T_1$ in Mn^{2+} : ZnS was studied by INDO calculations of the MnS_4 cluster with point-charge influence of the next coordination sphere [8.131]. The JT $T \otimes e$ coupling in this state was shown to have a stabilization energy of $E_{JT}^T = 650\,cm^{-1}$, with the t_2 mode influencing (reducing) the barrier height between the minima.

The JT center Rh^{2+} : NaCl was studied by DFT cluster calculations of the $[RhCl_6]^{4-}$ center plus several coordination spheres with up to 87 Na and Cl atoms (JT distortions were optimized within a 39-atom cluster, $RhCl_6Na_{12}Cl_8Na_6Cl_6$) [8.132]. The $E \otimes e$ coupling problem was confirmed, with $E_{JT}^T = 1200\,cm^{-1}$, $F_E = 90\,cm^{-1}/pm$, $\hbar\omega_E = 165\,cm^{-1}$, and $\delta = 213\,cm^{-1}$, meaning that there is a strong linear effect ($E_{JT}^T/\hbar\omega_E \approx 7.5$) and possible localized states in the three minima of elongated octahedra ($R_{ax} = 270.7\,pm$, $R_{eq} = 2.44.5\,pm$).

For the emission spectrum of Pb : CsCl [8.133], similar to Tl : CsI [8.134], a model is suggested in which two bands at 4.1–3.9 eV and 3.55 eV are attributed to transitions from, respectively, the coexisting trigonal and tetragonal minima (Section 3.3) of the relaxed excited T state of the Pb^{2+} ion, the whole spectrum being described as due to the coexistence of this state with an exciton localized near the impurity ion.

Pr^{4+} in PrO_2 was shown by neutron-spectroscopic measurements of magnetic excitations to have localized $4f^1$ states with a dynamic JTE on the Γ_8 ground electronic state described in a $\Gamma_8 \otimes t_2$ coupling model [8.135] (Section 3.3). The JTE in this state is confirmed also by the observed ordered momentum-reduction factor $\sim$0.5 (Section 5.6) [8.136]. For the calculation of

the cross-section of neutron diffraction the vibronic energy levels of the Pr^{4+} ion in the PrO_2 crystal environment were calculated by the Lanczos method (Section 5.4), taking into account the vibronic coupling to one or two e or t_2 modes and it was shown that the t_2 two-mode problem explains well the neutron-spectroscopy measurements [8.137].

In a system with a molecular impurity $[ReO_4]^{2-}$ replacing the Cl^- ion in KCl there is a tetrahedral d^1 configuration with an $E \otimes e$ problem; calculations for the free impurity reveal a relatively strong JT distortion, $E_{JT} = 762\,cm^{-1}$, which is enhanced in the crystal to $E_{JT} = 932\,cm^{-1}$ [8.138].

Among nonmetallic JT impurity centers and defects in crystals we mention here the relaxed F center in KCl (see [8.139, 8.140] and references therein), the arsenic "anti-site" defect in GaAs [8.141] in which the JTE in the $A_1 \rightarrow T_2$ transition ($T \otimes t_2$ coupling) was studied by recursion-method calculations (Section 5.4) and under uniaxial stress, and the O^- center in CaF_2, for which the $[OF_6]^{7-}$ cluster was shown by multiple-scattering X_α calculations to have a strong JT tetragonal distortion [8.142]. ESR spectra of Ga^+ : KBr showing the coexistence of tetragonal and trigonal JT minima (Section 3.3) were obtained in [8.143].

For two equivalent holes in a series of double acceptors (Zn and Be in Ge, bound excitons at the pair of acceptors Al, Ga, and In in Si, as well as Sn in GaAs) an inverted level ordering with the level $J = 0$ below the ones with $J = 2$ (the latter is required to be lower by Hund's rule) was shown to be due to the PJT stabilization of the $J = 0$ state (vibronically coupled to the two $J = 2$ states), which is larger than the spin-pairing energy [8.144]. For the JTE in In, Ga, and Te impurities in $A^{IV}B^{VI}$ semiconductors see [8.145].

An unusual temperature dependence (T^3 instead of T^7) of the zero-phonon line width (Section 6.1.2) and red shift (T^2 instead of T^4) was shown to be induced by the JTE with the linear $E \otimes e$ coupling [8.146]. The theory was applied to nitrogen N-V centers in diamond.

The evolution of applications of the PJTE theory to off-center impurities in crystals is similar to that of its application in other fields: there was a long-lasting paradigm that the PJTE requires very small energy gaps Δ between the mixing ground and excited electronic states, which limits essentially its application to real systems. This paradigm disappeared when it was shown that the magnitude of Δ should not necessarily be small, as it may be compensated by other parameters in the inequality (4.6) of the strong PJTE (Section 4.1). Moreover, if there are low-symmetry dipolar (off-center) distortions of high-symmetry configurations, they are due to, and only to, the PJTE. The paradigm above explains why the many earlier works on off-center impurities in crystals did not make use of such a powerful tool as the PJTE, which explains in a natural way the origin of the distortion and consequent properties.

Off-center distortions in crystals were first considered as being due to the PJTE for the Ti^{4+} ion in $BaTiO_3$ [8.147] in order to explain the origin of local dipole-moment formation and the cooperative interaction of dipoles to produce a ferroelectric phase transition [8.147–8.149] (see Section 8.3 for more details). Many examples of such distortions in impurity crystals are given above. In their majority they were considered in cluster models which ignore the multimode problem (Section 5.5). Below are several examples in which the multimode problem is taken into account.

An estimate of the PJT instability criterion (4.6) for the Li^+ ion in Li : KCl was given in [8.150], but more elaborate consideration of the problem was published in a series of works on the multimode PJTE in off-center systems [8.151, 8.152].

For the system Cu^{2+} : SrO the off-center position of the copper ion, the multi-minimum APES, possible tunneling, and relaxation processes were investigated by solving a multimode combined JT plus PJT problem $(E_g + T_{1u}) \otimes (e_g + t_{1u})$ (Section 4.2) in its multimode presentation (Section 5.5) [8.151]. It was shown that in each of the three minima of the starting multimode $E \otimes e$ problem the JT admixing of the excited T_{1u} state via multimode t_{1u} off-center distortions results in an additional eight minima of C_s symmetry (four in each direction of the tetragonal axis), in which the system has a dipole moment (the JTE in the excited T_{1u} state is ignored). The positions of the minima are obtained as functions of the multimode parameters of the crystal (Section 5.5) and the possible transitions between them are evaluated. In a rough estimation the results are in qualitative agreement with the experimental data on EPR spectra of this system in the temperature interval 1.6–78 K [8.153].

A general theory of the PJT origin of off-center positions of impurities with a nondegenerate ground state in a cubic environment is presented by solving the combined multimode $(A_{1g} + T_{1u}) \otimes (t_{1u} + e_g + t_{2g})$ problem, which takes into account the PJT $(A_{1g} + T_{1u}) \otimes t_{1u}$ plus JT $T_{1g} \otimes (e_g + t_{2g})$ couplings [8.152, 8.154, 8.155]. In application to Li^+ : KCl the eight equivalent off-center displacements toward the chlorines on the diagonals of the cubic coordination environment in the minima of the APES are further investigated and the transitions between them evaluated. With some reasonable phonon-spectra parameters of the lattice the estimated transition probability has the same order of magnitude as the experimental value.

The interaction between PJT off-center impurities in crystals is considered in [8.154, 8.155]. For strong PJT off-center displacements in the minima, like in $Li^+ : KTaO_3$, the tunneling between the minima on each center is negligible, but the Li^+ ions can still overcome the barrier between the minima if assisted

by the crystal phonons, provided the maximum frequency of the latter is large enough, $\hbar\omega_{\max} \gtrsim \Delta$, where Δ is the energy gap between the state in the minimum and the lowest excited state that is delocalized over all the minima [8.154, 8.155]. The local dipole-moment reorientation is thus temperature dependent with an Arrhenius-type behavior (Δ being the activation energy); it freezes at temperatures for which $\hbar\omega_{\max} < \Delta$.

The phonon-excited Li^+ ion may relax in another equivalent minimum by emitting a phonon which excites the near-neighbor Li^+ center, the two centers becoming thus coupled via phonons. Calculations of this phonon-mediated intercenter interaction between the two PJT centers show that it increases the activation energy Δ, thus increasing the temperature of the phase transition T_c to the freezing state, where the Li^+ ions rest in one minimum. Obviously Δ and T_c are dependent on the concentration x of Li^+ ions. Calculations reveal good qualitative agreement between calculated and experimentally observed T_c values in $Li^+ : KTaO_3$.

The dynamics of the Li^+ ions in $Li^+ : KCl$ was further evaluated using Mathieu's equation to solve for the motion along the ground-state APES [8.156]. Cation off-centricity in the IV–VI rocksalt chalcogenides of divalent Ge, Sn, and Pb is attributed to PJT lone-pair activity on the basis of DFT calculations, in which the mixing states were shown to include the p states of the anion [8.157].

A big off-center displacement of the Ni^+ ion in $Ni^+ : CaF_2$ was found by means of DFT calculations performed on the cluster $[NiF_8Ca_{12}]^{17+}$ in the presence of an electrostatic potential to account for the influence of the rest of the lattice [8.97, 8.110]. With the unpaired electron located on the $b_2 \sim xy$ orbital, the system is strongly distorted along the fourfold axis with the Ni^+ ion at $z_0 = 1.07$ Å in the APES minimum, in qualitative agreement with ESR data. The computational details show that this off-centricity is due to a balance between the new (additional) covalent bonding to four (of the eight) ligands acquired by the tetragonal off-center distortion and electrostatic repulsion that prevents further distortion, in accordance with the general theory (Section 4.1). For Cu^{2+} and Ag^{2+} ions in a similar environment in CaF_2 there are no off-center PJT distortions because of the predominant repulsion (the inequality (4.6) is not realized because of the large K_0 value), but in this case there are JT distortions, as mentioned above [8.97]. For the same ions in SrF_2 there are PJT off-center distortions [8.158, 8.159].

The discussion on whether off-center distortions of impurity centers in crystals are of PJT origin or occur due to "chemical rebonding" [8.160] from our point of view (presented in this book) has no sense because, as shown in Section 4.1, starting from the high-symmetry on-center configuration, all the

off-center distortions are due to, and only to, the PJTE. The latter includes the "chemical rebonding" phenomenon (plus a minor polarization contribution), so there are no two distinct mechanisms of distortion, it is one bonding mechanism fully presented by the general theory of the PJTE.

For two JT centers sharing a common axis of symmetry of third order (but not common near-neighbor atoms) with an $E \otimes e$ problem on each of them, taking into account their interaction via the crystal phonons, the solutions for the APES in the space of local e vibrations are of two kinds: a circular trough for free in-phase rotations of the e-type distortion of the two centers in the same direction and a hindered counter-phase rotation of the two waves of e distortions in opposite directions (cf. the similar pseudorotations in a two-center bioctahedron, Section 3.6). The rotation is free for zero intercenter coupling, and located at the minima in cases of strong coupling [8.161(*a*)]. Applied to EPR transitions, this interaction reduces the spectrum to one isotropic resonance line [8.161(*b*)]. Interacting JT $E \otimes e$ impurity centers also reduce the elasticity modulus of the crystal lattice [8.162]. The PJTE in impurity centers was employed recently to predict novel materials with high dielectric constants for modern electronics [8.163].

A novel field of application of the JTE and PJTE was explored recently in the theory of semiconductor *quantum dots* (see [8.164] and references therein). The theory was developed for spherical dots, for which the electronic energy levels are degenerate or quasidegenerate, and for non-spherical dots, for which the degeneracy is removed, but the PJTE is significant. For the phonon system the authors [8.164] involve the so-called multimode dielectric model, in which a finite number of phonon degrees of freedom is taken into account. It was shown that both the JT and PJT couplings are most important in the spectroscopic properties of quantum dots. The theory has been applied to ensembles of spherical (CdSe, $Cd_xSe_{1-x}S_x$, and PbS), self-assembled (InAs/GaAs and CdSe/Zn/Se), brick-shaped (InAs/GaAs) quantum dots, as well as CdS/HgS/CdS quantum-dot heterostructures.

8.1.2 The local JTE in formation of special crystal structures

The cooperative interaction of JT and PJT distortions of regular centers of the crystal that lead to the formation of special lattice properties and structural phase transitions is known as the cooperative JTE (CJTE), as mentioned above and discussed below in Sections 8.2 and 8.3. However, there are some special cases of JT- and PJT-induced crystal structures that are not described exactly by the mainstream CJTE theory. In this subsection we consider briefly three examples of such specific lattice effects: the *plasticity effect*, *distortion isomers*, and *temperature-dependent solid-state conformers*.

As stated earlier, the JT- and PJT-induced distortions in free molecular systems are dynamic in nature; they were classified in Section 5.2 as free rotations, hindered rotations, and pulsating ("fluctuating") motions. In Section 7.1.1 we discussed the role of small external perturbations that quench the dynamics of the distortions and make them static, so that a very small perturbation may result in strong distortion (vibronic amplification of external perturbations). The symmetry of this static distortion corresponds to that of the external influence, provided that it is uniaxial in the direction of one of the JT-active coordinates. It follows that among the many possible equivalent distortions of a coordination system predicted by the JTE theory (Chapters 3 and 4), the only ones realized in the crystal state are those that correspond to the symmetry of the environment, and in a measure allowed by this environment. Hence *the same coordination polyhedron may have significantly different shapes in different crystals*. This phenomenon looks as if the coordination polyhedron has a soft (plastic) coordination sphere, which in the crystal state takes the form of the crystal environment; it is called the *plasticity effect* [8.165, 8.166] (see also "flexional behavior" [8.167, 8.168]). The first observation of such effect is mentioned in [8.169].

Note that the plasticity effect is essentially local: the dynamic distortion is made static by the local low-symmetry environment, distinct from the CJTE where the static distortion is created by the interaction between the JT-distorted regular centers of the lattice.

The best examples to illustrate the plasticity effect are octahedral coordination compounds with a twofold degenerate E term [Cu(II), high-spin Mn(III) and Cr(II), low-spin (Co(II), etc.]. For them the APES in the case of weak quadratic terms (small G_E constants; Section 3.2) has the form of a Mexican hat, which allows for any distortion of the coordination sphere along the symmetrized Q_ϑ and Q_ε displacements within the limits $Q_\vartheta^2 + Q_\varepsilon^2 = \text{constant}$ (Figs. 3.3 and 3.7). If the quadratic and/or cubic vibronic coupling terms are significant, only three directions of tetragonal distortions along the fourth-order axes remain equally probable (Fig. 3.4). In other systems with other degenerate terms, distortions with three tetragonal, six orthorhombic, and so on, equivalent directions, as well as continuous sets of distortions (a trough), are possible (Chapters 3 and 4).

These predictions of the theory are confirmed by a large amount of experimental data. X-ray analysis shows that the hexacoordinated polyhedron about the metals with E_g terms is not a regular octahedron even when all the ligands are identical, and in the majority of known cases the octahedron is tetragonally distorted. In Table 8.8 the crystallographic distance to the two axial (R_L) and four equatorial (R_S) ligands in series of CuO_6 and CuN_6 polyhedra, as well as

Table 8.8. *Examples of equatorial R_S and axial R_L interatomic distances M—X in compounds containing MX_6 clusters, M = Cu, Mn; X = O, N* (*adapted from* [*8.18*])

Compound	R_S (Å)	R_L (Å)
$Cu(acac)_2$	1.92	3.08
$Ca(Cu,Zn)_4(OH)_6(SO_4)_2{\cdot}3H_2O$	1.96	2.43
$Cu_6(Si_6O_{19}){\cdot}6H_2O$	1.97	2.68
$(C_{14}H_{19}N_2)Cu(hfacac)_3$	2.02	2.18
$CdCu_3(OH)_6(NO_3)_2{\cdot}H_2O$	2.03	2.43
$K_2BaCu(NO_2)_6$	2.04	2.29
$Cu_4(NO_3)_2(OH)_6$	2.04	2.34
$Ca(Cu,Zn)_4(OH)_6(SO_4)_2{\cdot}3H_2O$	2.06	2.23
$Cu(OMPA)_3(ClO_4)_2$	2.07	2.07
$Cu(H_2O)_6SiF_6$	2.07	2.07
$Cu(IPCP)_3(ClO_4)_2$	2.07	2.11
$Ca(Cu,Zn)_4(OH)_6(SO_4)_2{\cdot}3H_2O$	2.11	2.11
$Cu(ClO_4)_2{\cdot}6H_2O$	2.13	2.28
$(NH_4)_2Cu(SO_4)_2{\cdot}6H_2O$	2.15	1.97
$Cu(phen)_3(ClO_4)_2$	2.05	2.33
$Cu(l\text{-}pn)_3Br_2{\cdot}2H_2O$	2.09	2.31
$K_2PbCu(NO_2)_6$	2.11	2.11
$Cu(en)_3SO_4$	2.15	2.15
$\gamma\text{-}K_2PbCu(NO_2)_6$	2.23	2.05
$Mn(trop)_3$	1,94	2.13
$Mn(acac)_3$	2.00	1.95
$Mn(Et_2dtc)_3$	2.38–2.43	2.55

Abbreviations: acac, acetoacetate; OMPA, octamethylpyrophosphoramide; hfacac, hexafluoracetylacetonate; IPCP, tetraisopropylmethylene-diphosphonate; PCP, octamethylmethylene-diphosphonic diamide; phen, *o*-phenanthroline; en, ethylenediamine; pn, 1,2-propanediamine; dien, diethylenetriamine; and Et_2dtc, diethyldithiocarbamate.

in similar octahedral Mn(III) systems in different compounds, are given [8.166, 8.170–8.172] (see also [8.18]).

It follows from this table and references above that the six-atom polyhedra around the Cu(II), Mn(III), and Cr(II) centers in different crystals are mainly elongated octahedra, $R_L > R_S$, with two ligands on the long axis and four on the short axes. Although for some of the tabulated compounds the atoms from

the second and next coordination spheres are different (and in the crystal state the interatomic distances also depend on the packing of the molecules in the lattice), the large number of these compounds confirms statistically that the deformation of the coordination sphere around Cu(II), Mn(III), and Cr(II) is due to internal forces, i.e. the JTE. The relations between R_L and R_S in the Cu—O and Cu—N distances within the corresponding octahedra follow the rules of Q_ϑ distortion, thus allowing estimation of the vibronic coupling constants [8.18, 8.166].

In the diversity of crystal environments, there may be cases when not one, but two or several configurations of the coordination sphere are stabilized. If these configurations are sufficiently close in energy, but differ in the magnitude and direction of distortion, they may be observed as different crystal isomers. The so-called *distortion isomers* of Cu(II) originally synthesized and studied in [8.166, 8.172] may serve as an example of this kind. These isomers have the same total composition and the same Cu(II) ligand environment, but differ in the interatomic metal–ligand distances in the distorted coordination centers. Distortion isomers also differ in their properties, such as color, appearance, crystal form, chemical behavior, solubility, and spectroscopic data. They pass from one to another under the influence of pressure, heating, or long-term storage. In some cases, besides the two principal isomers (usually called α and β), intermediate species have been obtained.

One of the simplest compounds that has distortion isomers is $Cu(NH_3)_2X_2$, where X = Cl, Br. The local PJTE on the Cu centers accompanied by the stabilizing influence of the crystal lattice provides quite a natural explanation of the origin of distortion isomers. The $Cu(NH_3)_2X_2$ crystal contains mutually parallel chains, each of which is arranged as illustrated in Fig. 8.2(a), where all the X atoms occupy equivalent bridge positions. There is a strong interaction between the Cu(II) centers via these bridging atoms inside the chain, while the van der Waals interactions and/or hydrogen bonds between the chains are weak.

If we assume that the X atoms in the plane form a regular square with two NH_3 groups in the axial *trans* positions, the polyhedron $Cu(NH_3)_2X_4$ is a tetragonally distorted octahedron that belongs to D_{4h} symmetry, the degeneracy of the ground Cu(II) state in the octahedron is removed, and the ^2E_g term is split into $^2A_{1g}$ and $^2B_{1g}$. Denote the splitting by 2Δ. The two-level PJTE on the A_{1g} and B_{1g} terms is considered in Section 4.1, so the results obtained there may be applied directly. In particular, the normal coordinate Q, which mixes the states A_{1g} and B_{1g}, transforms according to B_{1g} ($A_{1g} \times B_{1g} = B_{1g}$) and the corresponding B_{1g} displacements in the D_{4h} group coincide with the Q_ε displacement of the O_h group given in Fig. 2.3 and Table 2.1. The vibronic constant of the mixing of the two electronic states is $F = \langle A_{1g}|(\partial H/\partial Q)_0|B_{1g}\rangle$,

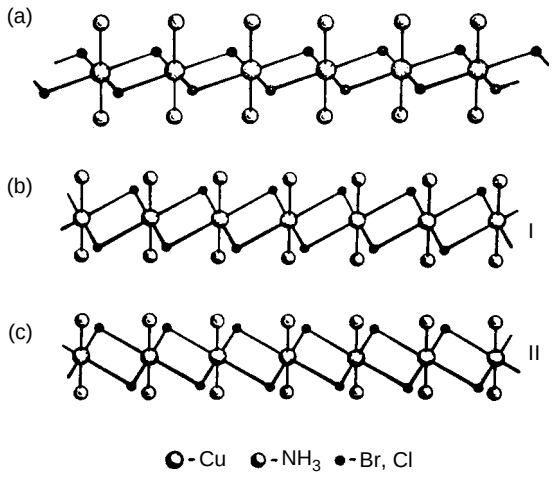

Fig. 8.2. The chain structure of the crystal $Cu(NH_3)_2X_2$ in the cubic undistorted unstable β isomer (a), and in two equivalent configurations of the α isomer, I and II, (b) and (c), resulting from the in-chain cooperative PJTE. (Reprinted with permission from [8.166]. Copyright 1976 Elsevier Science Publishers.)

and the APES in the space of the Q coordinate has the form given by Eq. (4.4). If the instability condition (4.6), $\Delta < F^2/K_0$, is satisfied, we obtain two minima on the lower sheet of the adiabatic potential at $\pm Q_0$, determined by Eq. (4.7).

Thus the PJTE at each center distorts the bipyramidal environment: the equatorial square with four X atoms at the apexes transforms into a rhombus with the major diagonal along Q_x, corresponding to the minimum I in Fig. 8.3, or along Q_y (minimum II).

Owing to the strong interaction between the distortions of neighboring centers in the chain through the ligands X in common, a ferrodistortive ordering of these distortions along the chain takes place (Section 8.2), and this ordering remains unchanged up to high temperatures. As a result of this ordering, it can be assumed that each of the chains has two stable configurations, I and II of Figs. 8.2(b) and 8.2(c), respectively, that correspond to the two minima in Fig. 8.3 (I and II, respectively).

Another important factor is the interaction between the chains in the crystal lattice. The analysis of the structure of the crystal composed by parallel chains indicates that the intermolecular interaction between the chains is optimal when the chains are not distorted and the entire crystal is cubic. In this cubic state the intermolecular distances (between two most strongly interacting atoms of different chains) are minimal, and they increase with intrachain distortions toward configuration I or II. The authors [8.165, 8.166] assumed that the interchain interaction in the crystal has a minimum at $Q = 0$ (Fig. 8.3),

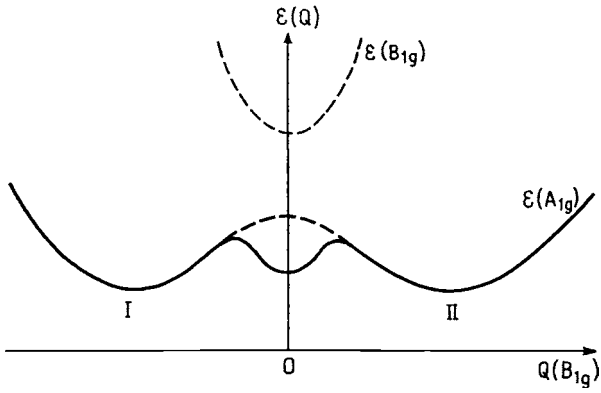

Fig. 8.3. The potential-energy curve for the $Cu(NH_3)_2X_2$ crystal as a function of the cooperative ferrodistortive intrachain distortion which is of B_{1g} symmetry on each center. I and II correspond to the PJT minima, while the additional minimum at $Q(B_{1g}) = 0$ corresponds to the best-fit interchain interactions of undistorted chains (dashed lines) [8.165].

where Q is the coordinate of the cooperative intrachain distortion corresponding to the B_{1g} distortion at each center. Hence the total energy of the crystal shown schematically in Fig. 8.3 has three minima: besides the two equivalent minima I and II for the stable distorted configurations of the chains, there is a third minimum for the undistorted (cubic) crystal, and it is also assumed that the interchain interaction is of the same order of magnitude as the intrachain PJT one.

This explains qualitatively the origin of all the main features of the distortion isomers in $Cu(NH_3)_2X_2$: the α isomer corresponds to the deepest minimum of the APES (I or II) with the structure illustrated in Fig. 8.2(b) or 8.2(c), the unstable β isomer with the cubic structure corresponds to the shallower minimum at $Q = 0$, and the observed intermediate preparations with non-cubic structures correspond to the additional relative minima for the uncorrelated chain distortions. This interpretation also agrees well with the experimental features of the isomers, including their behavior under stress and temperature, the dependence on conditions of their preparation, spectral properties, and transitions from one isomer to another [8.166, 8.172].

Approximate estimates of the PJT distortions of the $Cu(NH_3)_2X_4$ polyhedron were obtained by means of the angular-overlap model using empirical data for the value K_0 [8.173]. At the minima $Q_{B_{1g}}$ (calculated) ≈ 0.5 Å, while $Q_{B_{1g}}$(experimental) ≈ 0.4 Å.

Under the influence of the crystal environment the dynamic JT and PJT distortions may be reduced to static distortions in different ways, resulting

in a variety of possible configurations, including temperature-dependent configurations that are not related to phase transitions. One type of them is called *temperature-dependent solid-state conformers* [9.174]. They occur when there are two or several rapidly converting distorted configurations, which are slightly nonequivalent due to the crystal influence, and the observed averaged configuration is thus temperature dependent.

Consider the system $[Cu(bpy)_2(ONO)]NO_3$ (bpy is bipyridine) with the copper polyhedron *cis*-CuN_4O_2. In the high-symmetry configuration of $[Cu(bpy)_3]^{2+}$ the system has D_3 symmetry with a twofold-degenerate ^2E ground state. The substitution of one of the bpy groups by ONO reduces the symmetry to C_2 and splits the ^2E term into ^2A and ^2B. Similar to the distortion isomers discussed above, there is the possibility of a PJTE and consequent instability of the ground state ^2A with respect to B-type displacements ($A \times B = B$), provided that the vibronic coupling constant $\langle A|\partial H/\partial Q_B|B\rangle$ is sufficiently large and the inequality (4.6) holds. The B displacements emerge from Q_ε (Fig. 2.3 and Table 2.1) and have the same geometry.

Assuming that the inequality (4.6) is satisfied, we get for the APES curve as a function of the coordinate Q_B the picture shown in Fig. 4.1(b) and reproduced here on Fig. 8.4 together with the indication of the modes of distortion of the CuN_4O_2 polyhedron in the minima. The value of the distortion coordinate (the coordinate $Q_\varepsilon = \frac{1}{2}(X_2 - X_2 - Y_3 + Y_6)$; see Table 2.1) in our denotation in the *cis*-CuN_4O_2 polyhedron is

$$Q = \tfrac{1}{2}[\Delta R(\text{Cu—N}_1) + \Delta R(\text{Cu—O}_1) - \Delta R(\text{Cu—N}_2) - \Delta R(\text{Cu—O}_2)] \quad (8.1)$$

where N_1, N_2, O_1, and O_2 are the two nitrogen and two oxygen atoms in the plane containing the C_2 axis (Fig. 8.4) and ΔR denotes the elongation of the bond with respect to that in the high-symmetry configuration. It can easily be shown that for linear distortions (R(X) indicates the bond length Cu—X)

$$Q = \tfrac{1}{2}[R(N_1) - R(N_2) + R(O_1) - R(O_2)] \quad (8.2)$$

In the unstable high-symmetry configuration $Q = 0$, while in the two minima $Q = \pm Q_0 \neq 0$. If the energy barrier between the minima (i.e., the PJT stabilization energy) is not very large, the system converts rapidly between the minima configurations, and in some experimental measurements (say, by X-ray diffraction methods) the average undistorted configuration will be observed (if the minima are shallow and have no localized states, the average configuration will be observed with all the methods, Section 7.1).

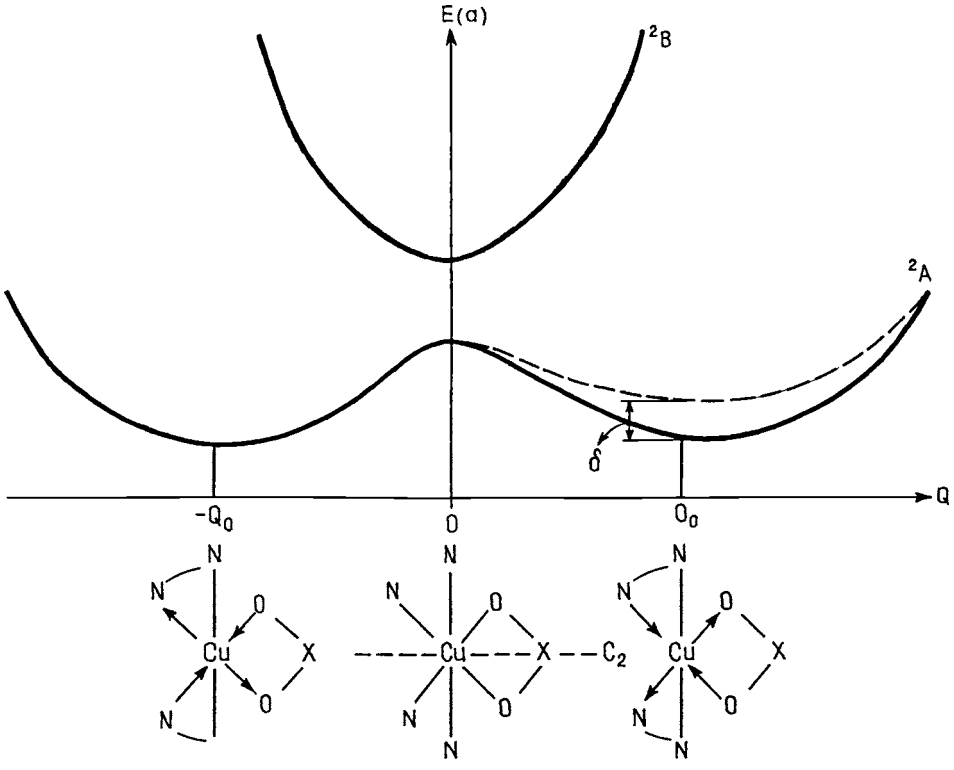

Fig. 8.4. Two minima of the adiabatic potential in the $[Cu(bpy)_2(ONO)]NO_3$ crystal with a strong PJTE on each center and slightly different minima depths ($\sim\delta$) due to the crystal environment (the influence of the next coordination sphere).

The situation changes when, due to the crystal environment, the two minima become slightly nonequivalent, as shown in Fig. 8.4 by the dashed line, but the energy difference δ between the minima is smaller than the barrier height (otherwise, the second minimum disappears). In this case there is no complete averaging over the two configurations because the two minima are not equally populated. Denote the relative populations of the two configurations by n_1 and n_2, respectively. According to Boltzmann's thermal populations, $n_2 = n_1 \exp(-\delta/kT)$ with the normalization $n_1 + n_2 = 1$. Then the observed thermal averaged distortion is $Q_{av} = (n_1 - n_2)Q_0$ or

$$Q_{av} = Q_0[1 - \exp(-\delta/kT)]/[1 + \exp(-\delta/kT)] \tag{8.3}$$

Thus the observable averaged distortion Q_{av} is temperature dependent, its absolute value being determined by both Q_0 and δ.

Table 8.9. *Bond lengths* $R(X) = R(M—X)$ *(in Å) and distortion coordinate values* Q_{av} *in the* MN_4O_2 *polyhedra of* $[M(bpy)_2(ONO)]NO_3$ *with* $M = Cu$ *at different temperatures, and for* $M = Zn$

	M = Cu				M = Zn
	20 K	100 K	165 K	296 K	295 K
$R(N_1)$	2.142(2)	2.110(2)	2.098(2)	2.085(2)	2.085(2)
$R(N_2)$	2.028(2)	2.060(2)	2.071(2)	2.074(4)	2.082(3)
$R(O_1)$	2.536(2)	2.414(2)	2.351(3)	2.320(5)	2.204(3)
$R(O_2)$	2.051(2)	2.155(2)	2.204(3)	2.230(5)	2.223(3)
Q_{av}	0.299	0.155	0.087	0.050	0.008

These distorted configurations of the same compound which change gradually with temperature can be called *temperature-dependent solid-state conformers*. At high temperature when $kT \gg \delta$, in the first order with respect to δ/kT, $\exp(-\delta/kT) \approx 1 - \delta/kT$, and

$$Q_{av} = Q_0\delta/2kT \tag{8.5}$$

In the opposite limit case when $kT \ll \delta$, $\exp(-\delta/kT) \approx 0$ and $Q_{av} = Q_0$.

The observed distortions in $[Cu(bpy)_2(ONO)]NO_3$ and similar systems [8.174, 8.175] follow these rules rather well. The atomic structure of this compound has been determined in four temperature regions of 20, 100, 165, and 296 K. Table 8.9 shows the corresponding interatomic distances and the values calculated after Eq. (8.2) for different temperatures, as well as the same data for $[Zn(bpy)_2(ONO)]NO_3$ at 295 K, for comparison. In the Zn compound there is no PJTE of the type present in $[Cu(bpy)_2(ONO)]NO_3$ and hence no temperature-dependent conformers.

The data in Table 8.9 are very illustrative for temperature-dependent solid-state conformers; the temperature dependence of Q_{av} closely follows Eq. (8.4). In particular, if we assume that at $T = 20$ K, $Q_0 = Q_{av} = 0.3$, while at $T = 296$ K Eq. (8.5) holds, we obtain directly $\delta = (Q_0/Q_{av})2kT \approx 69\,cm^{-1}$. The author [8.174] performed a more exact estimation, giving $\delta = 74\,cm^{-1}$. Note that in the Zn(II) compound Q_{av}, as expected, is small to zero, and the absence of conformers in the Zn(II) compound is also seen from the temperature factors in X-ray experiments [8.174, 8.175]. A somewhat similar but more elaborate effort to explain the temperature dependence of the crystal structure and EPR spectrum of bis(1,3,5-trihydroxycyclohexane)copper(II) tosylate is given in [8.176].

The solid-state conformers under consideration differ from each other by having different interatomic distances, and in this sense they are similar to the distortion isomers discussed above. However, the latter coexist at the same temperature, whereas different conformers are observed at different temperatures, and the larger the temperature difference, the larger the structural differences of the conformers. Also important is the fact that the structural changes with temperature in conformers take place gradually, in contrast to structural phase transitions, which take place abruptly, at a certain temperature.

The idea of JT-induced plasticity, distortion isomers, and temperature-dependent solid-state conformers was applied and further developed in different ways in order to explain the origin of a huge variety of crystal structures. For example, the plastic deformation of the complex $[Cu(H_2O)_6]^{2+}$ in $Cs_2Zn_{1-x}Cu_x(ZrF_6)\cdot 6H_2O$, with $x = 0.01$, 0.6, 0.8, and 1.0, was observed by EPR spectra in the range 4.2–330 K and X-ray analysis in the range 150–327 K (for $x = 1.0$), as well as under pressure, and explained as due to the combined influence of small lattice strains at higher T and ferroelastic strain below the phase transition [8.177–8.179].

Two nonequivalent JT CuN_6 centers were observed in $Cu(mtz)_6(BF_4)_2$, where mtz is 1-methyltetrazole, with different kinds of JT behavior induced by the local environment [8.180]. In one of them the system is trapped in one of the three JT minima of the $E \otimes e$ coupling (Section 3.2) with a glassy distribution of the distorted octahedra at low temperatures, while in the other center the system performs temperature-dependent pulsating motions (Section 5.3). The picture as a whole is produced from EPR and X-ray measurements at 293, 123, and 93 K.

For other examples of plasticity investigation see in [8.181–8.186] (the number of references to the papers [8.165, 8.166], in which the plasticity phenomenon was explored, is over 400). For instance, in [8.181] the plasticity effect is used to explain the nonplanarity of amino acid complexes in the crystalline state, in which three types of polyhedra are observed. Distortion (and related) isomerism is discussed also in [8.187–8.190].

8.2 Cooperative phenomena

8.2.1 Ordering of JT distortions and structural phase transitions

Consider a crystal in which some of the regular (translational) centers are in degenerate (or pseudodegenerate) states (JT or PJT centers, respectively) as described by means of local APES given in Chapter 3 and 4. Without

interaction between these centers, the motion of each is determined by its own APES and does not depend on the motions of other centers, and the dynamic distortions around different centers are not mutually correlated. When the interaction between the centers is taken into account, the mean "*molecular field*" produced by the environment and influencing each center is not isotropic at any given instant. Therefore, equivalent distortions in free centers become nonequivalent when the interaction is nonzero. When this happens the minimum of the free energy corresponds to the crystal state in which each JT or PJT center is statically distorted and the distortions at different centers are correlated. The structure of such a crystal may be essentially different form that expected without vibronic interaction.

Let us illustrate this process by considering a simple case when the JT centers in the crystal possess a twofold orbitally degenerate E term vibronically coupled to the b_1 vibrations (for the $E \otimes b_1$ problem, Section 3.1; the $E \otimes b_2$ problem is similar). Such a situation may occur, for example, when the crystal E-term centers in question possess local D_{4h} symmetry. For simplicity assume that the JT centers are square planar. The APES with two equivalent minima and the rhombic distortions (b_{1g} displacements) of the square at each of the minima are illustrated in Fig. 8.5 (cf. Fig. 3.1). In the absence of interaction between the centers, the two configurations (hereafter denoted by (+) and (−), respectively) are equally probable and the JTE has the above-discussed dynamic nature (the mean distortion equals zero and the initial symmetry is preserved).

The resulting picture changes when interactions between centers are taken into account. For two interacting centers at each of which the $E \otimes b_1$ problem is realized, under the assumption of parallel orientation of their squares, there

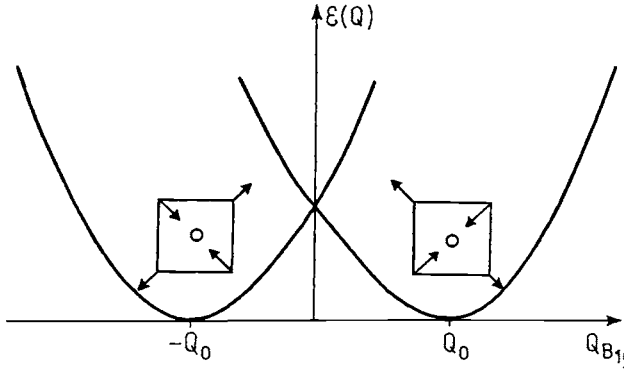

Fig. 8.5. A cross-section of the APES of a system with a JT $E \otimes b_{1g}$ problem along the b_{1g} displacements $Q_{B_{1g}}$ showing the two equivalent minima with the distortions of a square-planar (D_{4h}) system in each of them (Section 3.1).

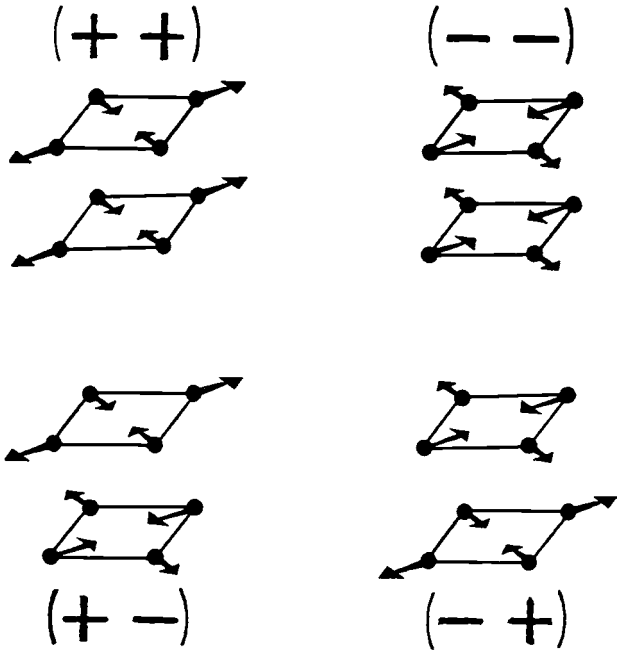

Fig. 8.6. Four types of possible packing of two interacting JT centers. For each of them the $E \otimes b_{1g}$ problem of a square-planar system with b_{1g} distortions (Fig. 8.5) is realized.

may be four configurations in which the one-center distortions are correlated: $(++)$, $(--)$, $(+-)$, and $(-+)$ (Fig. 8.6). It is clear that if the attractive interaction is stronger with parallel orientation of the distortions (*ferrodistortive* interactions), the energy of the configurations $(++)$ and $(--)$ is lower than that of the $(+-)$ and $(-+)$ cases. On the other hand, if the configurations $(+-)$ and $(-+)$ possess lower energy, the distortions directed antiparallel to each other are preferred (*antiferrodistortive* interactions). In both cases the two configurations of each center are no longer equivalent, since the interaction energy depends on the kind of distortion at the other center. This conclusion can be generalized to many interaction centers and, in the limit, to the whole crystal.

It is evident that at suitably low temperatures, the configuration of minimum free energy is realized, in which the crystal has statically distorted and distortion-correlated centers. In the case of ferrodistortive interactions, such an ordering of local distortions (*ferrodistortive ordering*) leads to a macrodeformation of the crystal as a whole. New properties of the crystal arising from the correlation (ordering) of the JT (PJT) center distortions, including the formation of new crystal structures and structural phase transitions, are called cooperative JTE (CJTE) and cooperative PJTE (CPJTE), respectively.

As in any other phase transition, the CJTE or (CPJTE), described above, results in *symmetry breaking* (Section 4.5) because the symmetry of the crystal with correlated distortions is lower than its initial symmetry. In fact the solution of the problem with thermodynamic features included, at sufficiently low temperatures yields correlated configurations, e.g., $(++)$ and $(--)$, which are equivalent and, in principle, the pair of correlated centers may resonate between the $(++)$ and $(--)$ states, dynamically preserving the initial symmetry. However, in the case of a large number of centers of the macroscopic crystal the barrier between the equivalently distorted configurations of the entire crystal $(+++\cdots)$ and $(---\cdots)$ becomes so high that spontaneous transitions between them are practically impossible (improbable), and the crystal remains in one of them. The situation here is quite similar to that found in ferromagnetics, in which there are also different equivalent directions of magnetization but no spontaneous inversion of the magnetic moment.

In these cases, as distinct from the one-center problem, the symmetry of the ground-state configuration of the crystal is lower than that of the Hamiltonian, resulting in the effect of "*broken symmetry*" (Sections 4.5 and 8.2.5). Strictly speaking, such a crystal state is not stationary, but due to the infinitely large energy barrier it may remain there for an infinitely long time.

It is clear that lattice vibrations and temperature fluctuations tend to destroy the correlation between JT distortions. Therefore, in principle, for any given energy of distortion interactions, there is a certain temperature above which the distortion ordering becomes destroyed. The lattice acquires another, more symmetric structure with an independent dynamic JTE at each center (provided the crystal does not melt). This temperature-dependent breakdown of the JT center distortion correlations (disordering) is nothing else than a *structural phase transition*. The stronger the JTE at each center and the energy of distortion interactions, the higher the temperature of the phase transition to the disordered state.

At the temperature of phase transition T_c the free energies of the two phases should be equal:

$$U_1 - T_c S_1 = U_2 - T_c S_2 \tag{8.5}$$

where U_1 and U_2 are the internal energies and S_1 and S_2 are the entropies. Hence

$$T_c = (U_1 - U_2)/(S_1 - S_2) \tag{8.6}$$

Since the entropy of the higher-temperature (disordered) phase is higher than that of the lower-temperature phase, $S_1 > S_2$, for $T_c > 0$ the internal

energy of the latter should be lower than that of the former, $U_2 < U_1$; the lower energy of the ordered phase is provided by the interaction between the JT-distorted centers.

Equation (8.6) is valid also for any other structural phase transition from higher to lower symmetry: the higher-symmetry phase has higher entropy, $S_1 > S_2$, and hence the condition for $T_c > 0$ is again $U_2 < U_1$. Here too lower energy U for lower symmetry is provided by the JTE.

The structural phase transition to the crystal state with ordered JT or PJT local distortions is one of the most important features of the CJTE or CPJTE.

The first studies of the CJTE appeared in the late fifties and early sixties [8.191–8.194]. Cooperative PJT ordering leading to spontaneous polarization and ferroelectric phase transitions has been established independently using another approach (Section 8.3). Rapid development of the CJT trend began in the seventies, when the JT origin of structural phase transitions was confirmed experimentally in a series of rare-earth orthovanadates (Section 8.2.2). The results obtained are summarized in a series of reviews [8.1, 8.195–8.200]. Below in this section we discuss the main features of this phenomenon with illustrative examples omitting bulky mathematical proof, where possible.

From the theoretical point of view the most difficult problem is to calculate the interaction between the JT centers and its dependence on the orientation of the local distortions. This interaction takes place via the phonon field (in the pseudo JT case there may be dipolar distortions and dipole–dipole interactions between the centers).

The general form of the Hamiltonian of the JT crystal can be written as follows (see also [8.196]):

$$H = \sum_{n} H_{\mathrm{JT}}(\vec{n}) + \frac{1}{2}\sum_{n,m} Q^{+}(\vec{n})K(\vec{n}-\vec{m})Q(\vec{m}) \tag{8.7}$$

where $\vec{n} = (n_1, n_2, n_3)$ and $\vec{m} = (m_1, m_2, m_3)$ label the elementary cells of the crystal, $H_{\mathrm{JT}}(\vec{n})$ is the vibronic Hamiltonian of the elementary cell, its electronic matrices being determined in the space of localized site states, while the last term in (8.7) describes the commonly used form of bilinear interactions between the atomic displacements of different elementary cells in lattice dynamics. Here the vector notation is used: $Q(\vec{m})$ is a column vector that has $3s$ components of $Q_{\Gamma\gamma}(\vec{m})$, where s is the number of atoms in the elementary cell and $Q_{\Gamma\gamma}(\vec{m})$ are the symmetrized coordinates (Section 2.2). Accordingly, $K(\vec{n}-\vec{m})$ is a $3s \times 3s$ matrix with $K_{\Gamma_1\gamma_1\Gamma_2\gamma_2}(\vec{n}-\vec{m})$ elements that describe the constants of intercell interaction. The terms with $n = m$ describe the elastic properties of isolated elementary cells, and therefore they are separated from the double sum in (8.7) and included in $H_{\mathrm{JT}}(\vec{n})$.

For simplicity, it is assumed that there are no atoms on the borders between the elementary cells. The complication of the theory, which arises due to the non-orthogonality of some of the $Q_{\Gamma\gamma}(\vec{m})$ coordinates for neighboring values of n (in cases when there are border atoms belonging simultaneously to two elementary cells), is considered in [8.201].

Another approximation used in Eq. (8.7) is that the vibronic coupling of the electrons of the JT center to the atomic displacements of the nearest-neighbor coordination spheres of the same elementary cell only is taken into account. In some works, using the Hamiltonian (8.7) as a starting point, additional approximations are introduced. In particular, the displacements $Q_{\Gamma\gamma}$ that are inactive in the JTE in the isolated elementary cell are excluded from the calculations (see, e.g., the review [8.197]). As in the one-center JT systems, this simplifies the solution significantly.

Finally it is assumed here that the inter-site resonance interaction of localized electronic states that form the energy bands is negligibly small. In most JT crystals the width of the electronic bands formed by atomic d and f orbitals is much smaller than the characteristic phonon quantum, and this justifies the above approximation. Additional effects related to the finite width of the electronic band are considered in [8.202]. For band JTE see Section 8.2.5.

There are two approaches in the theory of the CJTE due to the existence of two classes of JT polyatomic systems, with or without significant nonadiabaticity (Section 2.1 and Chapter 3). The first group is inherent in systems with $E \otimes e, T \otimes t_2$, etc. problems where there is a branching of the APES at the point of degeneracy, while the second one corresponds to the $E \otimes b_1$, $T \otimes e$, etc., and similar systems where there is a real intersection of different branches of the APES at this point (Section 3.1). In the latter case there is no overlap between the wavefunctions of the states in the near-neighbor minima and hence no tunneling between them; this allows one to present each of the distorted configurations of the JT center with its own wavefunction and consider their reorientation and intercenter interaction by *the method of pseudospin*. It cannot be done in the former case, in general, except for very deep minima and negligible tunneling.

The intercenter interaction between the local JT distortions on each center takes place via the phonon field of the crystal (via the displacements of the intermediate atoms produced by the distortions), and as such it is a function of the wave vectors of the phonons, i.e., the phase of the overlapping displacements from neighboring JT centers. The minimization of this function allows one to evaluate the wave vector $\vec{q}_0$ at which the free energy of the crystal in the two phases, ordered and disordered, coincides, thus determining the temperature of the phase transition in Eq. (8.6).

On the other hand $\vec{q}_0$ determines also the type of ordering in the low-symmetry phase. If $\vec{q}_0 = 0$, the JT distortions are uniformly ordered, all of them being frozen in-phase ("parallel"), and the size of the unit cell a (the lattice period) remains unchanged. This is the *ferrodistortive ordering*, an example of which we consider below for the $E \otimes b_1$ problem on each center (Section 8.2.2). If $q_0 = (\pi/a, \pi/a, \pi/a)$, *antiferrodistortive ordering* takes place with "anti-parallel" ordered distortions and a doubled lattice period in all the three directions. In principle, there may be intermediate extremal values of $\vec{q}_0$, for which *gelicoidal* or even *incommensurate phases* are formed (Section 8.2.4). "Parallel" and "anti-parallel" orientation of the distortions is a valid description when there are only two minima on each JT center and two directions of distortion. The situation becomes more complicated in cases of three or more minima on each center (Section 8.2.3).

For quantitative evaluation of the intercenter interaction, further simplifications of the Hamiltonian (8.7) can be achieved assuming (as is usually done for description of phase transitions in solid states) that each elementary cell in the low-temperature phase is actually affected by a low-symmetry field created by all the other elementary cells. This field lowers the symmetry of the cell under consideration, which thus becomes a source of the low-symmetry field for other cells contributing to the resulting overall low-symmetry crystal field. Owing to the thermal motion of the cell atoms the low-symmetry crystal field fluctuates. The approximation which neglects these fluctuations and takes into account only the averaged self-consistent crystal field is called the *mean-field approximation* (MFA).

As mentioned above (Section 5.5), in the absence of vibronic interactions the electronic density in degenerate electronic states rotates around the JT center and can freely orient along the external field. These properties of degenerate electronic states can be described by means of the operators of energy spin (*pseudospin*) mentioned above. The low-symmetry distribution of the electronic density creates an anisotropic electric field. For instance, the p orbitals have a dipole moment, the d orbitals have a quadrupole moment, etc. The appropriate dipole–dipole, quadrupole–quadrupole, and similar interactions of the electronic states of the centers may lead to an ordering in the electronic subsystem. The electric fields of separate cells in this case are summed to an averaged electric field.

A similar ordering in the electronic subsystem results from the non-Coulomb (exchange, superexchange, and so on) interactions of the electronic states. In the absence of vibronic coupling this ordering will not influence the nuclear behavior, i.e., it will not result in a structural phase transition. By neglecting the intercenter interaction of the electronic states we exclude the

possibility of an ordering in the electronic subsystem without the participation of the vibrational degrees of freedom of the lattice. Such effects of pure orbital ordering were considered elsewhere [8.203, 8.204].

In principle, the ordering of local distortions may take place without the participation of the electronic subsystem. The mechanism of such phase transitions is assumed to be due to the proper anharmonicity of the lattice [8.205]. However, as shown in Section 2.4, for small nuclear displacements the main part of the anharmonicity comes from the PJT mixing of the ground state with the corresponding excited states. The Hamiltonian (8.7) does not take into account the proper lattice anharmonicity; the PJT mechanism of structural ordering is considered in Section 8.3.

In the MFA the Hamiltonian of the crystal is reduced to a sum of commutative terms, each of which describes an isolated elementary cell in the external mean field (see e.g. in [8.196]):

$$H_{\mathrm{MFA}} = \sum_{\vec{n}} H(\vec{n}), \qquad H(\vec{n}) = H_{\mathrm{JT}}(\vec{n}) + \sum_{\Gamma\gamma} f_{\Gamma\gamma}(\vec{n}) Q_{\Gamma\gamma}(\vec{n}) \tag{8.8}$$

where

$$f(\vec{n}) = \sum_{\vec{m}\neq\vec{n}} K(\vec{n}-\vec{m}) \langle Q(\vec{m}) \rangle \tag{8.9}$$

and $\langle Q(\vec{m}) \rangle$ is the averaged value of the coordinate. The density matrix of the crystal described by the Hamiltonian H_{MFA} from (8.8) is factored into a product of density matrices of separate cells, and the latter is factored into a product of density matrices of separated degrees of freedom. Note that $f(\vec{n})$ has the physical meaning of the force with which the molecular field acts upon the cell $\vec{n}$. The solution with this Hamiltonian depends on the specific JT problem on each center. Related cooperative phenomena in mixed-valence compounds (Section 7.6.2) are discussed in [8.206, 8.207], while phase transitions in the JT impurity subsystem of crystals are considered in [8.208].

8.2.2 The simplest cooperative JT $E \otimes b_1$ problem: rare-earth zircons

As mentioned above, the simplest JT $E \otimes b_1$ problem is realized on centers with tetragonal symmetry (Section 3.1). Tetragonal rare-earth zircons of general formula RXO_4, where R is a rare-earth element and X = V, As, P, which include the orthovanadates, are very convenient examples for illustration of the CJTE. In these crystals the JT ion is in an environment of tetragonal symmetry, in which a twofold degenerate E term is coupled to nondegenerate

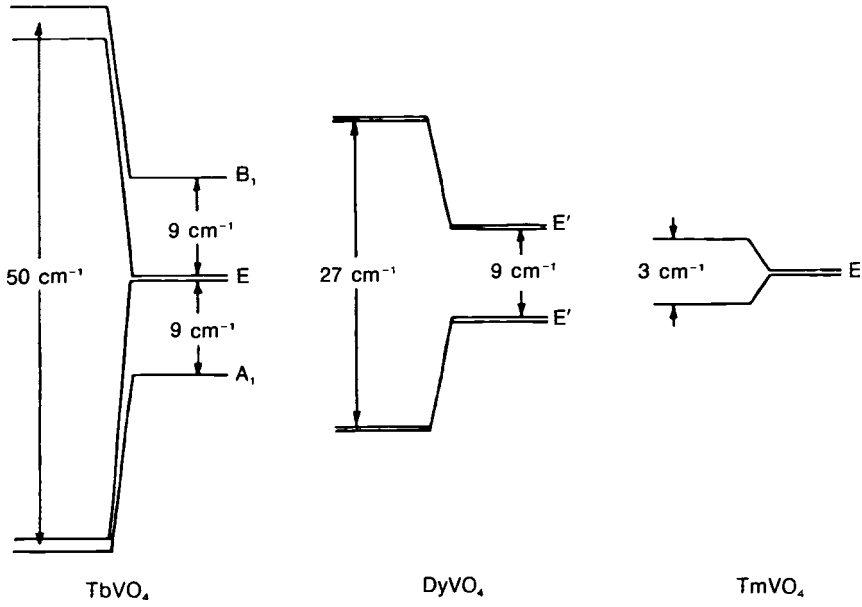

Fig. 8.7. Energy levels of the lowest vibronic states of the rare-earth ions in the crystals $TbVO_4$, $DyVO_4$, and $TmVO_4$ with (left) and without (right) the CJTE.

vibrations b_1, resulting in the simplest vibronic $E \otimes b_1$ problem. From the viewpoint of possible experimental evaluation of JTE parameters, zircons have certain comparative advantages. First, they are transparent and hence allow a series of convenient optical and spectroscopic methods of investigation to be used in order to determine the positions of the energy levels and their shifts. Second, the expected CJT structural phase transition occurs at low temperatures ($\sim$10 K), at which the measurements are not masked by thermal effects. Third, phase transitions at low temperatures mean that the corresponding JT energy-level splitting is small (see below) and can be easily changed by external perturbations.

The JT ion in rare-earth zircons is the rare-earth element. Figure 8.7 shows the energy levels of the ground and first excited states in three orthovanadates, $TmVO_4$, $DyVO_4$, and $TbVO_4$. The Tm^{3+} ion has a ground state $^3H_6$ (electron configuration $4f^{12}$), which in the tetragonal D_{4h} field of the VO_4^{3-} ions in $TmVO_4$ reduces to an orbital doublet E. The latter is coupled predominantly to the b_{1g} vibrations, which distort the square of ligands into a rhombus and split the E term into two nondegenerate terms, as shown in Figure 8.7. The Dy^{3+} ion in the same environment has a ground, orbitally nondegenerate Kramers doublet E' and another close excited state E'' at an energy interval of $\sim 9\,cm^{-1}$. The two Kramers doublets E' and E'' mix strongly under the

b_{2g} displacement, resulting in PJT instability and B_{2g}-type distortion. This increases the E'–E'' splitting. For the Tb^{3+} ion in $TbVO_4$ there are four such nearby energy levels, which mix under b_{1g} displacements.

Consider first the simplest case of $TmVO_4$. The APES of the $E \otimes b_1$ problem in question consists of two intersecting parabolas with two minima corresponding to the possible directions of distortion of a square into a rhombus (two signs in the minima of Figs. 8.5 and 8.6). The fact that the b_{1g} vibration is nondegenerate and the states (+) and (−) are described by orthogonal electronic wavefunctions (there is no continuous transition from one minimum to another along the b_{1g} coordinate, see Fig. 8.5) essentially simplifies the problem of the JT distortion correlations in the crystals. The two APES minimum states are formally similar to two possible spin states for systems with $S = \frac{1}{2}$, which can be described in the pseudospin method by means of the Pauli matrix $\hat{\sigma}_z$ (Eq. (3.20″)) that has two eigenvalues $\sigma_z = \pm 1$. In this case the averaged distortion coordinate $\langle Q(\vec{m}) \rangle$ in Eq. (8.9) can be presented by the ordering parameter $\langle \hat{\sigma}_z \rangle = \sigma$ with $\sigma = 0$ in the disordered phase and $\sigma = 1$ in the fully ferrodistortive ordered lattice.

The ordering lowers the symmetry of the molecular field, which splits the degenerate E level by an amount ΔE proportional to σ. It can be shown (see in [8.200]) that with the Hamiltonian (8.8) only one parameter λ is needed to describe the ferrodistortive interaction between the centers, but the splitting ΔE depends also on the homogeneous deformation of the lattice as a whole, which accompanies the ferrodistortive phase transition. Denoting the electron–deformation coupling parameter by μ, and introducing a total parameter of correlation of JT distortions $\gamma = \lambda + \mu$, we get [8.200]

$$\Delta E = 2\gamma\sigma \tag{8.10}$$

$$\sigma = \tanh(\Delta E / 2kT) \tag{8.11}$$

Herefrom we get the phase-transition temperature T_c for which the ordering parameter σ falls to zero,

$$kT_c = \gamma \tag{8.12}$$

The temperature dependence of the E-term splitting has been determined experimentally from the position of the line of optical transition to the lowest excited singlet level $^1G_4$ ($\hbar\Omega = 20\,940\,\mathrm{cm}^{-1}$) [8.209], as well as by magnetic measurements [8.210] (see below). The results are shown in Fig. 8.8. It is seen that, at $T = 0$, $\Delta E = 2\gamma = 3\,\mathrm{cm}^{-1}$ and hence $\gamma = \lambda + \mu = 1.5\,\mathrm{cm}^{-1}$. At $T_c = 2.1\,\mathrm{K}$ the splitting ΔE becomes zero. At this temperature a structural

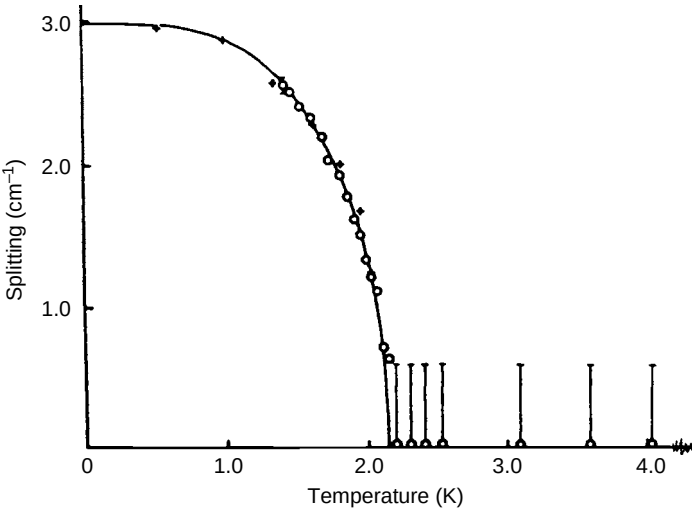

Fig. 8.8. Splitting of the ground vibronic E level of the Tm^{3+} ion in $TmVO_4$ as a function of temperature obtained from the positions of the line of optical transition to the excited $^1G_4$ level (shown by circles) and magnetic measurements (crosses). Vertical lines at $T > T_0 = 2.14\,K$ show the experimental error due to crystal imperfections. (Reprinted with permission from [8.200]. Copyright 1975 Institute of Physics.)

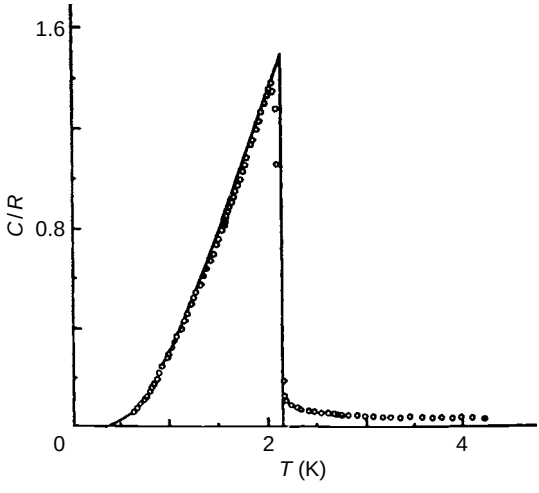

Fig. 8.9. The temperature dependence of the heat capacity of the $TmVO_4$ crystal near the phase transition due to the CJTE.

phase transition from the rhombic to the tetragonal phase is observed. Figure. 8.9 illustrates the phase transition by showing the temperature dependence of the heat capacity [8.211]. This value of T_c coincides with that predicted by the theory, Eq. (8.12).

The values of λ and μ can be obtained separately by piezospectroscopic measurements. Under external pressure P, the E-term splitting is [8.212] $\Delta E = 2(\lambda + \mu)\sigma + \alpha P$, where α is proportional to μ. Therefore, by measuring the splitting ΔE as a function of P at $T = T_c$ [8.213], one obtains $\lambda = -0.75\,\mathrm{cm}^{-1}$ and $\mu = 2.25\,\mathrm{cm}^{-1}$.

The orbital doublet E also splits under the influence of a magnetic field $\Re_z$, in the presence of which expressions (8.11) take the form

$$\begin{aligned} \Delta E &= 2\gamma \tanh(\Delta E/2kT) \\ \Delta E &= [4\gamma^2\sigma_\kappa^2 + g^2 K_E^2(T)\beta^2\Re^2]^{\frac{1}{2}} \end{aligned} \tag{8.13}$$

where $\sigma_\kappa = \langle \sigma_z^{(\kappa)} \rangle$ is the ordering parameter in the magnetic field and, besides the g-factor, the influence of the magnetic field is reduced by the vibronic reduction factor $K_E(T)$ (Section 5.6; here T indicates the symmetry of the magnetic field, not temperature!). It follows that the phase-transition temperature T_c at which σ_κ decreases to zero depends on the magnetic field:

$$\begin{aligned} kT_c &= \tfrac{1}{2}\Delta v/\mathrm{arctanh}(\Delta\nu/2\gamma) \\ \Delta v &= gK_E(T)\beta\Re_z \end{aligned} \tag{8.14}$$

Hence T_c decreases with increasing magnetic-field intensity $\Re_z$. At $\Re_z > \Re_{cr}$, where the critical value $\Re_{cr} = 2\gamma/K_E(T)\beta$, no phase transitions can occur at real temperatures. The magnetic field also reduces the ordering parameter $\sigma_\kappa = \sigma - g^2 K_E^2(T)\beta^2\Re^2/4\gamma^2$. Substitution of this expression into Eq. (8.13) yields that for $\Re_z < \Re_{cr}$ the E-term splitting ΔE does not depend on $\Re_z$. If $\Re_z > \Re_{cr}$, $\sigma_\kappa = 0$ and ΔE increases linearly with $\Re_z$. This result is in complete agreement with experimental data on optical absorption in magnetic fields [8.210] presented in Fig. 8.10 (see also [8.214]).

Thus for the $TmVO_4$ crystal under consideration, comprehensive qualitative and quantitative experimental (optical, magnetic, piezospectroscopic) confirmation of the JT nature of the low-temperature structural phase transition has been obtained. These results are also confirmed by Raman spectra, neutron scattering, ultrasound absorption, X-ray analysis, heat conductivity, and so on.

A similar explanation of the JT origin of structural phase transitions in other rare-earth zircons can be given. In $DyVO_4$, as distinct from $TmVO_4$, the PJTE is realized in the Dy^{3+} ion centers (Fig. 8.6), and as a result of their ferrodistortive interaction and cooperative structural phase transition, the splitting of the energy levels is given by (cf. Eq. (4.3))

$$\Delta E = (\gamma^2\sigma^2 + \Delta^2)^{\frac{1}{2}} \tag{8.15}$$

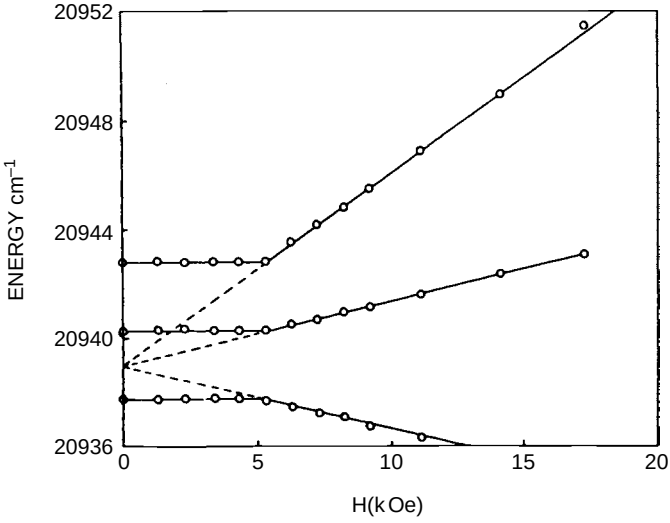

Fig. 8.10. The splitting ΔE of the Tm^{3+} ion ground state in $TmVO_4$ in magnetic fields H. At $H \leq H_{cr} = 5.4$ kOe and $T = 1.4$ K, ΔE is independent of H. (Reprinted with permission from [8.200]. Copyright 1975 Institute of Physics.)

where 2Δ is the splitting in the high-symmetry phase, for which $\sigma = 0$. On the other hand, as in the case of $TmVO_4$, the condition of ordering in a two-level system gives

$$\Delta E = 2\gamma \tanh(\Delta E/2kT) \tag{8.16}$$

and the phase-transition temperature T_c is determined by

$$\Delta = \gamma \tanh(\Delta/kT_c) \tag{8.17}$$

It follows from this equation that if $\Delta > \gamma$, there is no phase transition.

An important consequence of the structural phase transition of ferrodistortive type is the aforementioned homogeneous deformation of the crystal as a whole, due to which the elasticity constants C become temperature dependent near the phase transition. The effect was first observed in $DyVO_4$, for which the cooperative JT structural phase transition takes place at $T_c = 14$ K. Figure 8.11 presents the observed temperature dependence $C(T)/C_0$ for this crystal as determined by sound-velocity measurements [8.215] and calculated by the formula

$$C(T)/C_0 = [\Delta - (\lambda + \mu)\tanh(\Delta/kT)]/[\Delta - \lambda \tanh(\Delta/kT)] \tag{8.18}$$

with $\lambda = -3.6\,\text{cm}^{-1}$ and $\mu = 14.7\,\text{cm}^{-1}$ ($C_0 = 0.63 \times 10^{11}\,\text{dyn cm}^{-2}$ is the elasticity constant in the region far from the phase transition). These results are

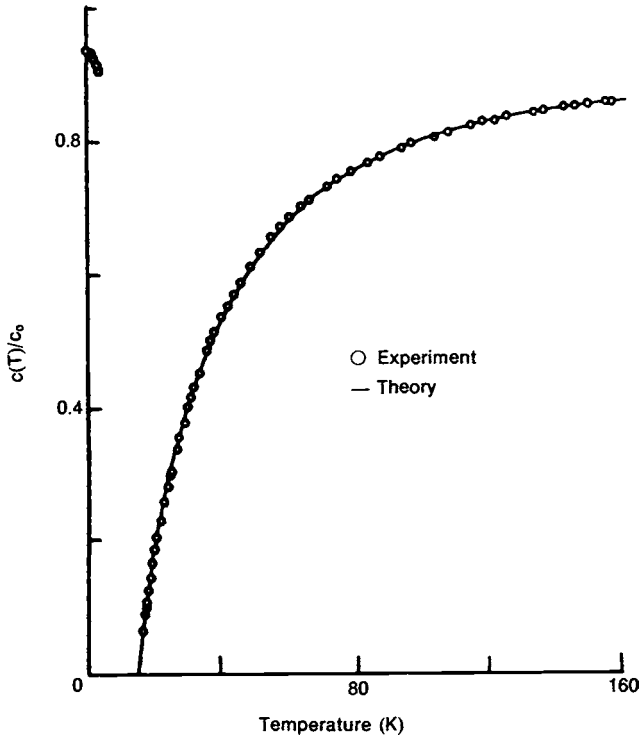

Fig. 8.11. The temperature dependence of the elasticity modulus $C(T)$ (in C_0 units) of the $DyVO_4$ crystal near the phase transition (at 14 K) induced by the CJTE. (Reprinted with permission from [8.215]. Copyright 1972 American Physical Society.)

also confirmed by other experiments, in particular, by piezospectroscopic measurements [8.216]. Relationships between elastic and dielectric parameters of this crystal can be found elsewhere [8.217].

In $TbVO_4$ the local vibronic problem for the Tb^{3+} center is a four-level one (Fig. 8.7). The A_1–B_1 splitting due to the CJTE with b_{1g} distortions is similar to the E'–E'' one, Eq. (8.15):

$$\Delta E_1 = 2(\gamma^2\sigma^2 + \Delta^2)^{\frac{1}{2}} \tag{8.19}$$

where 2Δ is the initial energy gap. The splitting of the doublet E is

$$\Delta E_2 = 2\gamma\sigma \tag{8.20}$$

It follows that the phase-transition temperature T_c obeys the equation [8.219]

$$(\gamma/\Delta) + (\gamma/\Delta)\sinh(\Delta/kT_c) = 1 + \cosh(\Delta/kT_c) \tag{8.21}$$

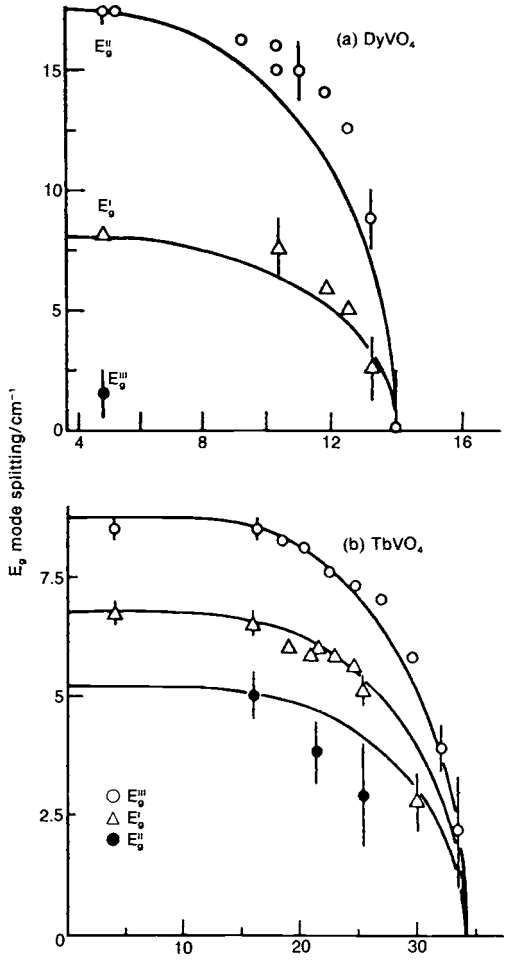

Fig. 8.12. Temperature dependences of the phonon *e*-mode splitting near the phase transition induced by the CJTE in $DyVO_4$ (a) and $TbVO_4$ (b) crystals. The points indicate experimental data obtained from Raman scattering, while the solid lines follow theoretical results obtained in the mean-field approximation. (Reprinted with permission from [8.197]. Copyright 1972 Royal Society London.)

The phase transition in $TbVO_4$ has been observed at $T_c = 33\,K$. The temperature dependence of the splitting of the phonon E mode in this crystal, determined experimentally by Raman spectra and calculated in the MFA, is illustrated in Fig. 8.12. Good agreement between theory and experiment confirms the JT origin of this phase transition.

Similar conclusions have been drawn for other rare-earth zircons mentioned above, including $TbAsO_4$ (27.7 K), $DyAsO_4$ (11.2 K), $TmAsO_4$ (6.1 K), and $TbPO_4$ (3.5 K), where the CJTE or CPJTE phase-transition

temperatures are given in parentheses. Some other classes of rare-earth compounds, such as pictides with general formula RX (X = N, P, As, and Sb), sulfides, and others of type TmCd and $PrAlO_3$, have a similar CJTE (or CPJTE). For example, DySb has a structural phase transition at $T_c = 9.5\,K$, its JT nature being confirmed by experiments on magnetic susceptibility, neutron scattering, electric conductivity, etc. [8.200]. For other examples see in [8.195].

More recent results on the CJTE obtained for such systems with a simple $E \otimes b_1$ problem on each JT center are published in a series of papers (see [8.218, 8.219] and references therein), in which the sensitivity of these crystals to external perturbations shown above is further exploited. First we note the theory of JT structural phase transitions induced by external magnetic fields and applied to crystals of the type $TmPO_4$ and $Tb_xY_{1-x}VO_4$ [8.218]. Distinct from the influence of magnetic fields on existing phase transitions mentioned in different parts of this and the next sections, the phase transitions considered in [8.218] take place at temperatures where there are no transitions in the absence of the magnetic field, *reentrant structural phase transitions*. They were shown to influence a variety of optical, magnetic, and elastic properties of these crystals, some of which were confirmed experimentally in giant magnetostriction [8.218(*b*)] and Raman scattering [8.218(*a*)].

In other cases the magnetic field "reverses" the elastic domain of the crystal, producing *reorientation phase transitions* that influence thermodynamic, elastic, and magnetic properties [8.219(*a*)]. The theory was applied to such crystals as $TmAsO_4$ and $DyVO_4$.

Among other effects revealed in such JT crystals we mention here the coexistence of spontaneous deformations of different symmetries in crystals of the type $Dy_xTb_{1-x}VO_4$ [8.219(*b*)], and the JT-induced negative Poisson's ratio (when uniaxial distortion (e.g., elongation) produces the same kind of distortion (elongation) in the perpendicular direction) in crystals of $DyVO_4$ type [8.219(*b*)].

8.2.3 Ordering of JT tri-minima distortions

If there are three equivalent minima of the local APES on each JT center of the lattice, as in the $E \otimes e$, $T \otimes e$, etc. problems (Sections 3.2–3.4), the local distortions may have three directions. In the $T \otimes e$ case the three distorted configurations are described by three independent (non-overlapping) wavefunctions that can be presented by three spin orientations in the method of pseudospin used above. In the $E \otimes e$ case this can be done only for sufficiently deep minima

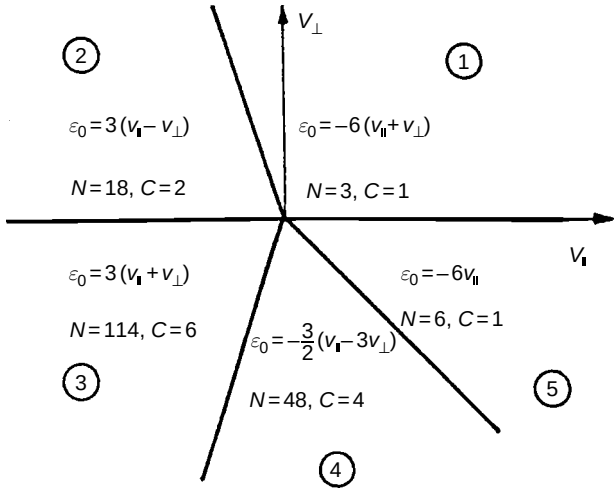

Fig. 8.13. Division of the nearest-neighbour interactions in a cubic eight-center cluster (see the text) into five groups with different energies ε_0, on the $(v_\perp, v_\parallel)$-parameter plane. The number of classes C and ground-state configurations N is also shown. (Reprinted with permission from [8.220]. Copyright 1978 Springer-Verlag.)

when the tunneling can be neglected. Assume for the sake of definiteness that eight octahedral JT centers occupy the apexes of a cube in a cubic crystal and the three directions of local tetragonal distortions of the octahedron in the $T \otimes e$ or $E \otimes e$ problems coincide with the three axes X, Y, and Z. Then the interaction of the distortions of two near-neighbor centers can formally be described by two constants $v_\parallel$ and $v_\perp$ which include, respectively, the interactions between corresponding Q_ϑ and Q_ε displacements (Fig. 2.3 and Table 2.1) on the two centers [8.220].

The total number of possible mutual orientations of the eight-center three-direction distortions is 3^8, and calculations of their energies ε_0 as a function of $v_\parallel$ and $v_\perp$ yield that many of them are degenerate. Figure 8.13 shows their mutual positions divided into five groups with different ε_0 values, each of them having N structures divided into C symmetry-equivalent classes. The orientations of the distortions of the eight octahedra in each of these classes are shown in Table 8.10 with the numeration of the eight octahedra indicated in Fig. 8.14. Restricting further discussion to only regions 1 and 3 and only to structures which can be described in terms of two sublattices, we see first that in the region 1 with $\varepsilon_0 = -6(v_\parallel + v_\perp)$ the ordering is perfectly ferrodistortive with all the local JT tetragonal distortions parallel to each other. In region 3 both interactions are antiferrodistortive. Neglecting the classes 5 and 6 (they have elevated energies due to the

Table 8.10. *Orientations* (*along X, Y, Z*) *of the distortions of the eight octahedra in each of the classes of the five regions in Fig. 8.13* (*the numeration of these octahedra is shown in Fig. 8.14* (*adapted from [8.220]*))

		Configurations							
Regions	Classes	1	2	3	4	5	6	7	8
I	1	*Z*	*Z*	*Z*	*Z*	*Z*	*Z*	*Z*	*Z*
II	1	*X*	*Y*	*X*	*Y*	*X*	*Y*	*X*	*Y*
	2	*X*	*Y*	*X*	*Y*	*Z*	*Z*	*Z*	*Z*
III	1	*X*	*Y*	*X*	*Y*	*Y*	*X*	*Y*	*X*
	2	*X*	*Y*	*X*	*Y*	*Y*	*X*	*Z*	*X*
	3	*X*	*Y*	*X*	*Z*	*Z*	*X*	*Y*	*X*
	4	*X*	*Z*	*X*	*Y*	*Z*	*X*	*Y*	*X*
	5	*X*	*Y*	*Z*	*Y*	*Y*	*X*	*Z*	*X*
	6	*X*	*Z*	*Y*	*Z*	*Y*	*X*	*Z*	*X*
IV	1	*Z*	*Y*	*Z*	*X*	*Z*	*X*	*Z*	*Y*
	2	*Z*	*X*	*Z*	*Y*	*Z*	*Y*	*Y*	*X*
	3	*Z*	*Y*	*Z*	*X*	*Z*	*X*	*Y*	*Y*
	4	*Z*	*Y*	*Z*	*Y*	*Z*	*X*	*Z*	*X*
V	1	*Y*	*Y*	*Y*	*Y*	*X*	*X*	*X*	*X*

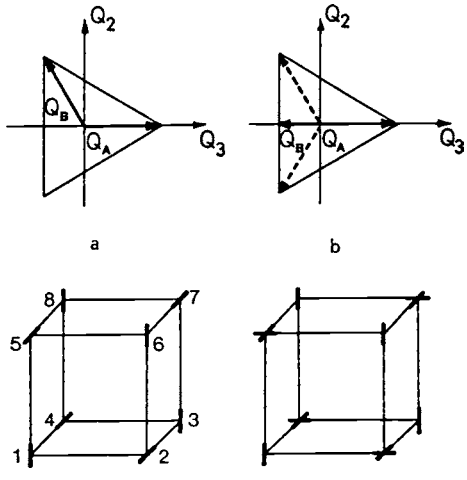

Fig. 8.14. Ground-state configurations in the antiferrodistortive ordering in region 3 of Fig. 8.13: (a) Q_2 structure; and (b) Q_3 structure [8.220].

strong interaction with the elastic strain field), we come to three possible structures [8.220]:

(a) Q_2 ordering, where all the octahedra of the sublattice A are distorted along Z (octahedra 1, 3, 6, and 8 in Fig. 8.14(a)), while in the other sublattice B they (octahedra 2, 4, 5, and 7) are distorted along X (or Y); this is a perfect antiferrodistortive ordering with the lattice space group $P4_2mc(C_{4v}^7)$;
(b) Q_3 ordering (Fig. 8.14(b)), in which the sublattice A is the same as in the Q_ε structure, while in the B sublattice the distortions are distributed randomly along X and Y with equal weight; the space group is $Pnbm(D_{4h}^3)$; and
(c) intermediate ordering, which is basically similar to the case (*b*), but with different statistical weights of octahedra distorted along X and Y; the lattice space group is $Fmm2(C_{2v}^{18})$.

The zero-point entropies of these three structures are different. Since they are degenerate with the same ε_0 value at $T=0$, the highest-entropy (less ordered) case (*b*) will be realized at $T>0$. On the other hand, the antiferrodistortive structure (*a*) is preferred when the interaction with the uniform strain is taken into account. Figure 8.15 shows the phase diagram for the antiferrodistortive interaction under consideration, taking into account the coupling to the strain g and the entropy (c in the ordinate expression g^2/cV_R is the value of the E_g component of the bare elastic tensor and V_R is the parameter of the intercenter interaction of the distortions). In a certain (small) region between T_{c2} and T_{c3} the intermediate structure (*c*) is preferred.

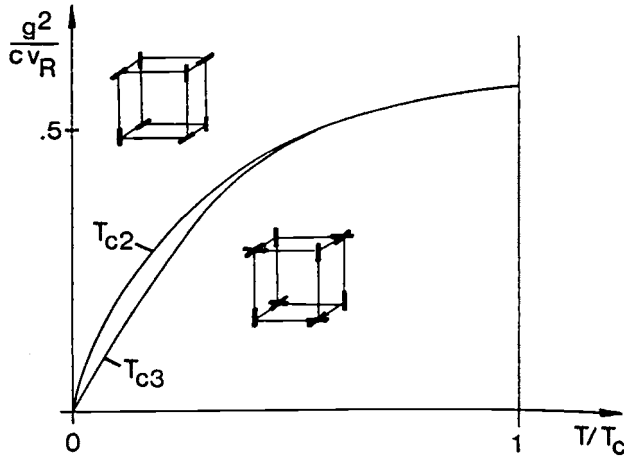

Fig. 8.15. The phase diagram for the antiferrodistortive ordered configurations of region 3 in Fig. 8.13 taking into account their coupling to elastic strain. In the area between T_{c2} and T_{c3} the intermediate structure (c) is realized. (Reprinted with permission from [8.220]. Copyright 1978 Springer-Verlag.)

Note that the high degeneracy of the possible structures is mainly accidental and will be lifted when the lower-symmetry field of the next-nearest neighbors to the eight octahedra under consideration is taken into account. In this respect only the full "molecular field" of the crystal may determine the real ground-state ordering.

If the dynamics of the JT distortions on each center is taken into account, the problem becomes more complicated. Consider the case of an $E \otimes e$ problem in cubic systems with strong vibronic coupling, $E_{\mathrm{JT}}^{E} \gg \hbar\omega_E$ at each JT center. When the quadratic and/or cubic terms of vibronic interaction are taken into account, the local APES has three minima, which in the space of polar coordinates ρ and ϕ of the $(Q_\vartheta, Q_\varepsilon)$ plane form a regular triangle with coordinates $(\rho_0, 0)$, $(\rho_0, 2\pi/3)$ and $(\rho_0, 4\pi/3)$ (Section 3.2). In the absence of external low-symmetry perturbation and for high inter-minimum barriers, the system performs local pulsating motions, i.e., tunneling transitions between the minima. If the lowest tunneling levels are E (ground) and A_1 (or A_2) and the tunneling splitting 3Γ is much smaller than the vibrational quantum $\hbar\omega_E$, the problem may be reduced to a three-level one, or to a pseudospin problem with the spin $S = 1$, $2S + 1 = 3$.

Under the influence of the anisotropic "molecular field" of the adjacent center distortions, the three minima become nonequivalent, the vibronic E and A_1 levels being displaced. The calculated dependence of the tunneling levels on the external tetragonal field f_ϑ of Eq. (8.9) in the Q_ϑ direction, together with the relative probabilities that the system is at each of the three nonequivalent minima, is shown schematically in Fig. 8.16 [8.198, 8.221]. When $f_\vartheta > 0$, the system in its ground state is in the main minimum $(\rho_0, 0)$ situated along the Q_ϑ axis, which is the deepest. When $f_\vartheta < 0$, the other two minima, $(\rho_0, 2\pi/3)$ and $(\rho_0, 4\pi/3)$, are deeper in the ground state, and the system occupies them both with equal probability. At $T = 0$ the lowest energy corresponds to the stabilization of the system in the distorted configurations. When $T > 0$, all three vibronic levels become populated after Boltzmann, and the mean value $\langle Q_\vartheta \rangle$, which characterizes the distortion of a given center in the Q_ϑ direction, becomes temperature dependent.

A simple result can be obtained in the case of ferrodistortive tetragonal interactions between the centers in the limiting case of very strong vibronic coupling, when $3\Gamma \approx 0$. In this case, for the ordering parameter $\sigma = \langle Q_\vartheta \rangle / \rho_0$ (cf. Section 8.2.2), we have [8.222]

$$\sigma = (e^{u} - e^{-2u})/(2e^{u} + e^{-2u}) \tag{8.22}$$

where $u = \gamma\sigma/2kT$. Assuming that at the phase-transition temperature the free energies in the ordered and disordered phases are identical, $E(\sigma) = E(0)$, and

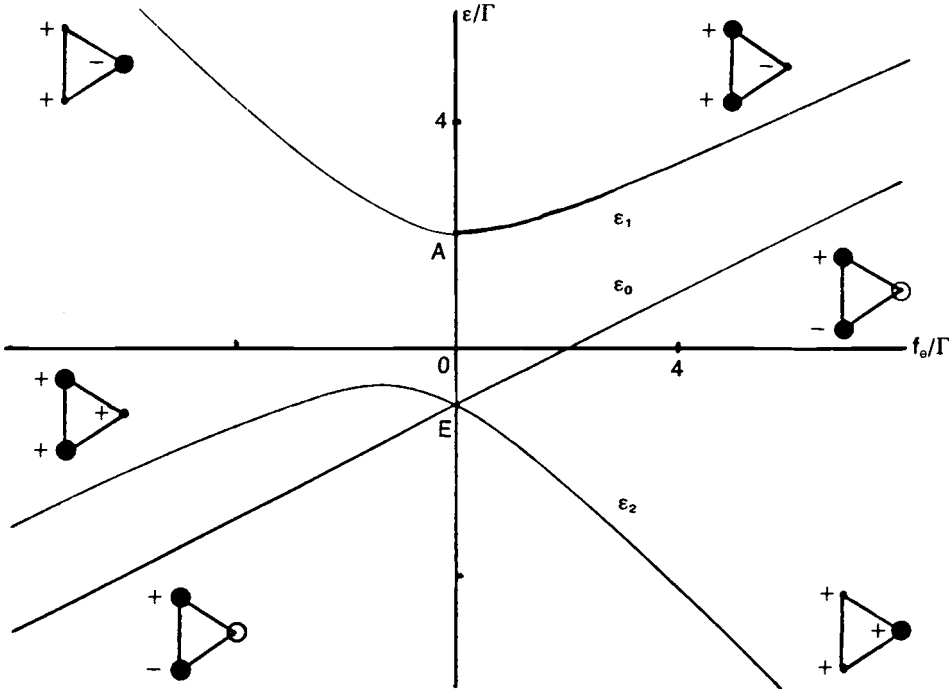

Fig. 8.16. Tunneling energy levels in systems with the JT $E \otimes e$ problem in tetragonal molecular fields f_ϑ that make the three minima nonequivalent; the size of the black circles indicates the relative distortions in the latter (zero distortion is shown by open circles). The signs + and − indicate the respective phase of the wavefunction [8.198].

taking into account the equivalency of all the centers in the crystal, the following expression can be obtained:

$$u\sigma = 2\ln[(e^u + 2e^{-u/2})/3] \tag{8.23}$$

Equations (8.22) and (8.23) can be solved together to obtain the structural phase transition temperature:

$$kT_c = 3\gamma/16\ln 2, \qquad \sigma = \tfrac{1}{2} \tag{8.24}$$

Antiferrodistortive ordering in the CJTE of the $E \otimes e$ problem in the strong-coupling case and three-level approximation under consideration results in two low-symmetry phases depending on the mode of correlation between the JT centers (much similar to the two phases (*a*) and (*b*) obtained above in the eight-center cluster). In one of them the tetragonal distortions of the sublattices Q_A and Q_B are the same, but they are oriented along different axes,

resulting in a structure similar to that of multiaxial spin ordering. In the other phase, distortions in the two sublattices differ according to the different signs of the tetragonal molecular field. For one of the sublattices we have $f_\vartheta > 0$, and in accord with the foregoing the $(\rho_0, 0)$ minimum along the Q_ϑ axis is stabilized. For the other sublattice the inequality $f_\vartheta < 0$ is valid, and the states of the other two minima (ρ_0, $2\pi/3$) and (ρ_0, $4\pi/3$), are stabilized, the dynamics between them being preserved since they remain equivalent ($\langle Q_\vartheta \rangle = \rho_0/2, \langle Q_\varepsilon \rangle = 0$). The resulting structure is a ferridistortive one, due to incomplete compensation of oppositely directed distortions.

Table 8.11 lists some examples of JT crystals with ferrodistortive and antiferrodistortive ordering. For other examples see in [8.222–8.228].

If the JT coupling on each center is not strong enough, the possible ordering is more complicated. In the general case the type of ordering and structural phase transition depends on the relative values of linear and quadratic vibronic coupling at each center and the kind of interaction between the latter. Qualitatively different results may be expected for strong, intermediate, and weak vibronic coupling (characterized by the dimensionless vibronic coupling constant $\lambda_\Gamma = E_{\mathrm{JT}}^\Gamma / n_\Gamma \hbar\omega_\Gamma$, Chapter 3) in all possible combinations of strong, moderate, and weak correlations between the centers (characterized by the parameter γ) [8.196, 8.198, 8.222, 8.229–8.236]. Structural phase transitions in fullerene anions induced by the CJTE are considered in [8.237].

The results above refer mainly to crystals with cubic symmetry. Similar situations in other crystal structures lead to quite different effects. For example, in a trigonal crystal the case illustrated in Fig. 8.14(a) corresponds to a noncollinear weak ferrodistortive ordering.

In the more complicated versions of the $E \otimes e$ problem, as well as in the more complicated $T \otimes (e + t_2), \Gamma_8 \otimes (e + t_2)$, etc., problems, the solution cannot be obtained using the simple model with only several low-lying tunneling levels. More vibronic levels of the JT center can be obtained by numerical solution and included in the molecular field of the crystal [8.221, 8.222]. However, even in simple cases more complicated types of ordering may be expected, some of which are discussed below.

8.2.4 Helicoidal structures, incommensurate phases, and structural-magnetic orderings

Besides the ferrodistortive and antiferrodistortive orderings considered above, the CJTE and CPJTE may lead to phase transitions to more complicated crystal structures. Suppose that in the above three-level $E \otimes e$ problem, owing to special distortion correlation interactions, the resulting molecular

Table 8.11. *Examples of crystals with CJT ferrodistortive and antiferrodistortive ordering (adapted from [8.195])*

Compound	Crystal structure	Symmetry change during transition	Critical temperature
(a) Ferrodistortive ordering			
$CuFe_2O_4$	Spinel	$O_h \Leftrightarrow D_{4h}$	360 °C
Mn_3O_4	Ditto	Ditto	1170 °C
$NiCr_2O_4$	Ditto	Ditto	300 K
$TmVO_4$	Zircon	$D_{4h} \Leftrightarrow D_{2h}$	2.1 K
$DyVO_4$	Ditto	Ditto	15 K
$TbVO_4$	Ditto	Ditto	34 K
$TbAsO_4$	Ditto	Ditto	27.7 K
$TmAsO_4$	Ditto	Ditto	6.1 K
$TbPO_4$	Ditto	$D_{4h} \Leftrightarrow C_2/m$	2.12 K
DySb	Pnictide	$O_h \Leftrightarrow D_{4h}$	9.5 K
$Ba_2Zn_{1-x}Cu_xWO_6$	Elpasolite	Ditto	250–1000 K
(b) Antiferrodistortive ordering			
$K_2PbCu(NO_2)_6$	Elpasolite	$T_h \Leftrightarrow D_{2h}$	7 °C
$Rb_2PbCu(NO_2)_6$	Ditto	Ditto	40 °C
$Tl_2PbCu(NO_2)_6$	Ditto	Ditto	120 °C
$Cs_2PbCu(NO_2)_6$	Ditto	Ditto	33 °C
$KDy(MoO_4)_2$	Sheelyte	$D_{2h}^{14} \Leftrightarrow C2/m(?)$	14 K
$CsDy(MoO_4)_2$	Ditto	Ditto	38 K
$RbDy(MoO_4)_2$	Ditto	Ditto	19 K
La_2CuO_4	K_2NiF_4	$D_{4h} \Leftrightarrow D_{2h}$	525 K
Rb_2NaHoF_6	Elpasolite	$T_h \Leftrightarrow D_{2h}$	170 ± 2 K
Rb_2NaTmF_6	Elpasolite	Ditto	130 ± 2 K

field is negative and directed at an angle $\alpha < \pi/2$ to the Q_ϑ axis ($f_\vartheta < 0$, $f_\varepsilon \neq 0$), and that this angle, and hence the f_ε component, vary smoothly along the crystal, assuming periodically all values between given positive and negative numbers including zero. In this case, the two minima (ρ_0, $2\pi/3$) and (ρ_0, $4\pi/3$) at each center are no longer equivalent ($\langle Q_\vartheta \rangle \neq 0$) and the degree of non-equivalency (the $\langle Q_\vartheta \rangle$ value) changes from one center to another, repeating the periodicity of the f_ε component of the molecular field.

In terms of pseudospin terminology, the three equivalent minima of the $E \otimes e$ problem can be presented by three directions of the pseudospin $S = 1$ at angles 0, $2\pi/3$, and $4\pi/3$. Then, the case $f_\vartheta < 0$, $f_\varepsilon = 0$ corresponds to the

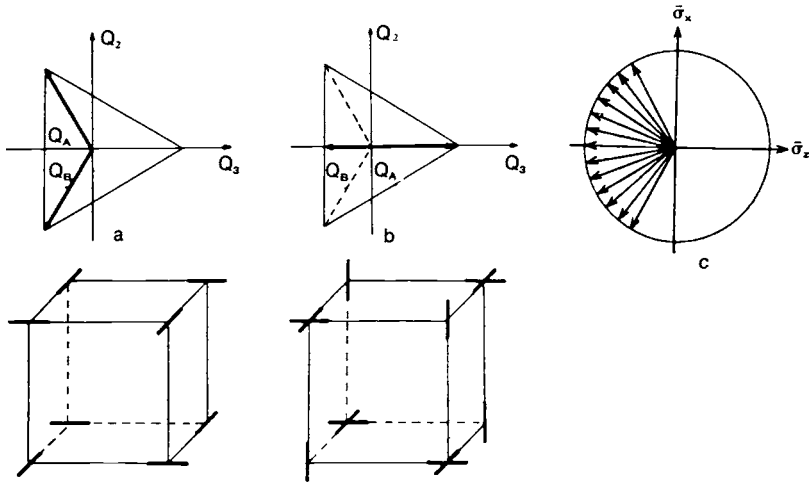

Fig. 8.17. The dependence of the type of ordering of the JT distortions on the molecular field f_γ in the CJTE with an $E \otimes e$ problem on each center: (a) $f_\vartheta \leq 0$, $f_\varepsilon = 0$; (b) $f_\vartheta > 0$, $f_\varepsilon = 0$; and (c) $f_\vartheta \leq 0$, while $f_\varepsilon \neq 0$ and varies smoothly from center to center assuming periodically all the values between some limits $\pm f_\varepsilon^{\,0}$. The directions of expected distortions on the centers in a perovskite structure in the cases (a) and (b) are also shown (cf. Fig. 8.14 for an eight-center system) [8.196].

equivalent minima with pseudospin directed at angles $2\pi/3$ and $4\pi/3$, respectively (Fig. 8.17(a)), its averaged value being oriented along the Q_ϑ axis (in the negative direction). When $f_\varepsilon \neq 0$ the averaged value of the pseudospin acquires a nonzero ε component. In this case the pseudospin behavior can be presented in terms of changes in its direction from one center to another, depending on the absolute value of f_ε. As a result, under the above conditions the pseudospin rotates from one center to another, forming fan-shaped *helicoidal structures* shown in Fig. 8.17(c) (similar to known helical structures of real spin in the theory of magnetism). In such a crystal, in which the structure is changed due to the CJTE, the lattice period increases. If the period of f_ε is a multiple of the initial lattice period of the high-symmetry phase, a *superstructure* is formed. In particular, antiferrodistortive ordering results in a superstructure with a double lattice period.

Interesting examples of helicoidal ordering of local JT distortions are presented by the chain-like hexagonal perovskite structure of the type ABX_3, where A is a monopositive ion, B is a bivalent metal, and $X = Cl^-$, Br^-, and I^- [8.238–8.244]. Consider the crystal $CsCuCl_3$. Its parallel chains in the lattice contain octahedral $CuCl_6$ polyhedra which are interlinked by triple bridges produced by three chlorine atoms, the latter thus forming a common triangular face for two nearest-neighbor polyhedra (Fig. 8.18). Each Cu(II) center,

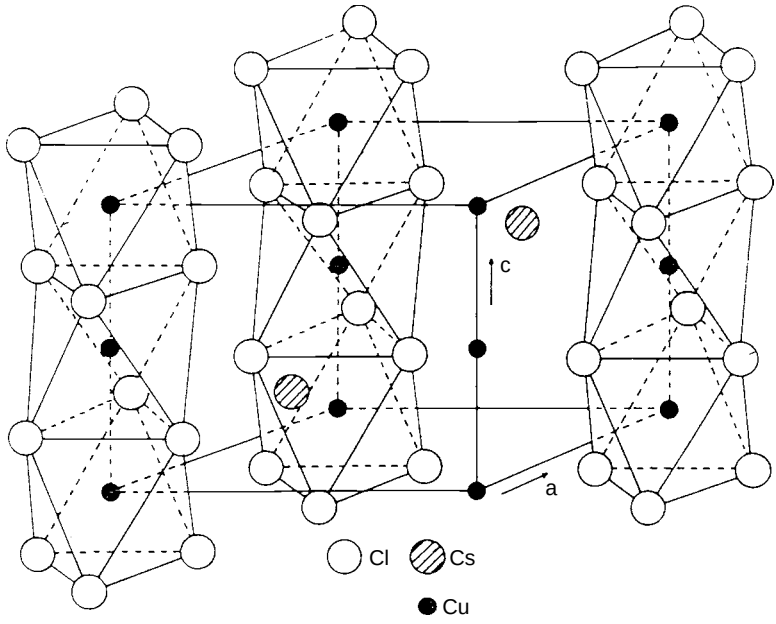

Fig. 8.18. The crystal structure of $CsCuCl_3$.

due to the JTE, requires a tetragonally distorted octahedron of six chlorine atoms, and there are three equivalent directions of distortions corresponding to three fourfold axes. However, because of the common ligands the distortions of the nearest-neighbor octahedra in the ordered phase are correlated. In particular, if the direction of distortion for the given polyhedron is, say, along the z axis, its neighbor should distort along either the x or the y axis. Figure 8.19 illustrates this situation. From the point of view of the trigonal axis along which the Cu atoms are located in the chain, the directions of the distortions of the two neighboring octahedra in this case are rotated by an angle $\phi = 60^\circ$ (from one apex of the interfacing triangle to the next). This is shown schematically in Fig. 8.20(a). As one can see, the period of the lattice in the distorted helicoidal screw-like configuration in $CsCuCl_3$ is six times larger than that of the latice in the undistorted (reference) configuration [8.238].

However, the tilts of the triangles in the AX_3 layers depend on the size of the A ion. In particular, in the case of β-$RbCuCl_3$ the angle between them is not 60° as in $CsCuCl_3$, but 180° (Fig. 8.21). For this reason β-$RbCuCl_3$ retains the inversion center at the Cu ions and the ordering of the JT distortions is just antiferrodistortive [8.241]. In Fig. 8.20 the helicoidal structure of the crystal $(CH_3)_4NCuCl_3$ and that of the undistorted high-temperature crystal $(CH_3)_2CHNH_3CuCl_3$ are illustrated. In the formation of these and other similar structures magnetic exchange interaction in addition to the CJTE

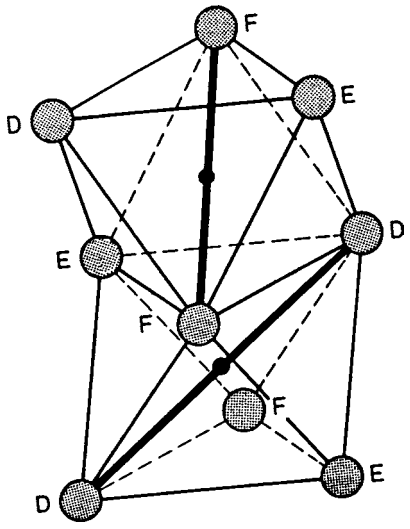

Fig. 8.19. Illustration of the formation of a helicoidal structure in the $CsCuCl_3$ crystal. Owing to the common shared octahedral face with three Cl ligands on the apexes of a regular triangle the JT-elongated axes of the two octahedra (shown by thicker lines) are rotated in phase by $\varphi = 60°$. (Reprinted with permission from [8.238]. Copyright 1986 Institute of Physics.)

may be important [8.241]. An effective Hamiltonian to handle these cases was suggested recently [8.245].

Another interesting crystal with complicated helicoidal JT distortions is the yellow InCl (see [8.246–8.248] and references therein). Its structure looks like a distorted rocksalt type, but no phase transition to the latter was observed: at 390 K it transforms into red InCl with another structure. On the other hand, there is no simple description of the deviations from the rocksalt structure, but since we know that all distortions of high-symmetry reference configurations are of JT type (Section 4.1), one can try to describe the origin of the observed structure of InCl as resulting from appropriate vibronic coupling.

First we notice that in the cubic environment of Cl^- ions in the reference rocksalt structure the In^+ ion has a lone pair $(5s)^2$ which in the cluster $InCl_6$ produces an A_{1g} ground term followed by a T_{1u} term at an energy gap 2Δ. This situation is considered in Sections 4.2 and 7.1.2 as a combination of the PJTE $(A_{1g} + T_{1u}) \otimes t_{1u}$ with the JTE in the excited state $T_{1u} \otimes (e_g + t_{2g})$ resulting in the problem $(A_{1g} + T_{1u}) \otimes (a_{1g} + t_{1u} + e_g + t_{2g})$ [8.249]. As shown in Section 4.2, it may lead to a polar distortion t_{1u} accompanied by either tetragonal e_g or trigonal t_{2g} displacements. All in all, in the two phases of InCl (yellow and red) five differently distorted $InCl_6$ octahedral are found, which are classified as trigonal (three types), digonal, and tetragonal.

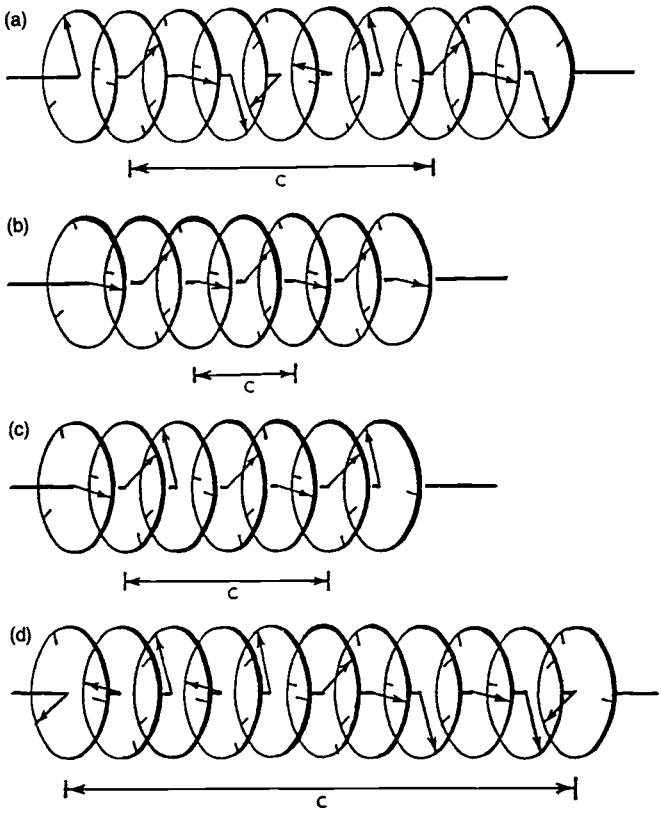

Fig. 8.20. Illustration of the formation of helicoidal structures as a superstructure of JT distortions on each center (schematically shown by arrows) in chain-like crystals with common triatomic faces between its octahedra: (a) β-$CsCuCl_3$; the JT tetragonal distortions of the near-neighbour polyhedra in the chain are shifted in phase by $\varphi = 60^\circ$ and the lattice period along the chain is six times larger than in the undistorted crystal; (b) $(CH_3)_2CHNH_3CuCl_3$ in the high-temperature phase; (c) β-$RbCuCl_3$; and (d) $(CH_3)_4NCuCl_3$. (Reprinted with permission from [8.238]. Copyright 1986 Institute of Physics.)

The digonal distortion is unusual (not predicted by the theory [8.249]), as it contains a strong t_{2u} component assumed to be due to the PJT $(A_{1g} + T_{1u}) \otimes (t_{1u} + t_{2g} + t_{2u})$ problem [8.246]. In the cubic cell of yellow InCl there are 20 trigonally and 12 digonally distorted octahedra. In the cooperative picture the yellow InCl structure is a subgroup of NaCl and can be presented as a rocksalt structure distorted by three equally strong lattice modes [8.247, 8.248]. Their combination leads to ferrodistortive chirality, tetrahedron formation, and antiferrodistortive spiral formation. Figure 8.22 illustrates the helix formation from a combination of polar (t_{1u}) and circular (t_{2u}) displacement vectors.

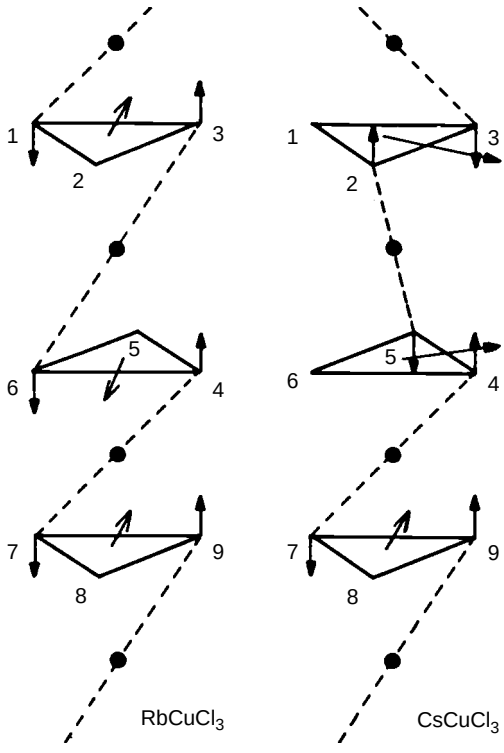

Fig. 8.21. Comparison of shifts in phase of the JT-elongated axes of the octahedra around the Cu^{2+} ions (and hence the triangles of Cl^- ions) due to the different sizes of the A atoms in β-$CsCuCl_3$ ($\varphi = 60°$, cf. Fig. 8.19) and β-$RbCuCl_3$ ($\varphi = 180°$): while the former is a helix, the latter preserves the inversion center with antiferrodistortive ordering of the distortions. (Reprinted with permission from [8.241]. Copyright 1995 Springer-Verlag.)

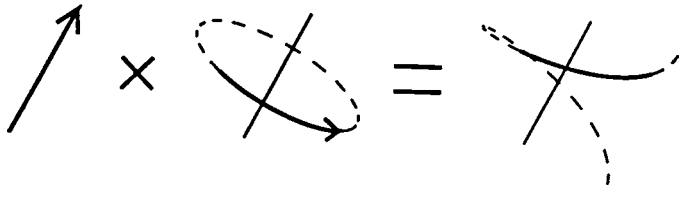

Fig. 8.22. A schematic illustration of the formation of a helix from the combination of a t_{1u} polar vector with a t_{2u} circular (axial) vector [8.247, 8.248].

In some cases, the periodicity of the f_ε component of the molecular field might not be a multiple of the lattice period. The "superstructure" is then called incommensurate: distortions of the crystal centers are frozen with a wave vector which is incommensurate with its limiting values. By taking into account the details of the JT center interactions, in particular, the interaction

of each center with its second-nearest neighbors [8.250], the helical structure becomes one of the stable phases of the CJTE, and a structural phase transition to the incommensurate phase may take place. The crystal $K_2PbCu(NO_2)_6$ appears to be an interesting example of this kind.

$K_2PbCu(NO_2)_6$ is a representative of the family of $A_2BCu(NO_2)_6$ crystals in which the CJTE takes place. In these crystals the $[Cu(NO_2)_6]^{4-}$ octahedra have an environment of cubic symmetry, which at high temperatures does not remove the pulsating (fluctuating) transitions between the three equivalent minima of the $E \otimes e$ problem with strong vibronic coupling (Section 3.2). Owing to the CJTE, a structural phase transition to the ordered state may be expected at lower temperatures.

Two phase transitions are observed in $K_2PbCu(NO_2)_6$. At room temperature the crystal is cubic (the α phase). At 280 K, a phase transition to the pseudotetragonal structure (the β phase) is observed, and at 273 K transition to a structure with symmetry lower than orthorhombic (the γ phase) takes place [8.251, 8.252]. JT distortions around the Cu^{2+} centers are also confirmed by ESR measurements [8.252, 8.253].

The nature of the low-temperature β and γ phases has been subject to discussion in the literature (the discussion is, however, not concerned with the general JT origin of these phases, which is beyond doubt). X-ray investigation shows that in the low-symmetry phases, the elementary cell is pseudotetragonal, $c/a < 1$. Therefore, it was assumed [8.251, 8.254] that at low temperatures the crystal consists of compressed octahedra, which are ferrodistortively ordered due to the CJTE. This point of view was disputed [8.255, 8.256] (see also the review article [8.199]) by showing that the observed crystal structure of the γ phase fits the description of antiferrodistortive ordering of elongated octahedra. As a result of such ordering the mean value of the observed Cu—N distances will appear as if the octahedra are compressed but packed in "parallel" (cf. Fig. 8.14).

This description is confirmed by direct and indirect data, including a detailed analysis of the ESR spectra of this and related crystals (as well as other copper compounds with a CJTE) and comparison of the thermal ellipsoids in X-ray analysis of nitrogen and oxygen atoms in the NO_2 groups. In the β phase the same JT distortions (elongated octahedra) are assumed but, as opposed to the γ phase, the dynamics of the distortions in the plane is supposed to be preserved, cooperative ordering being present only along one direction. In the high-temperature phase (above 280 K) complete dynamics of these elongated octahedra (with no ordering) is attained (cf. similar partial ordering in different phases of $BaTiO_3$, Section 8.3).

The structural phase transitions in question were studied by means of X-ray- and neutron-scattering techniques [8.257, 8.258]. Using diffuse X-ray

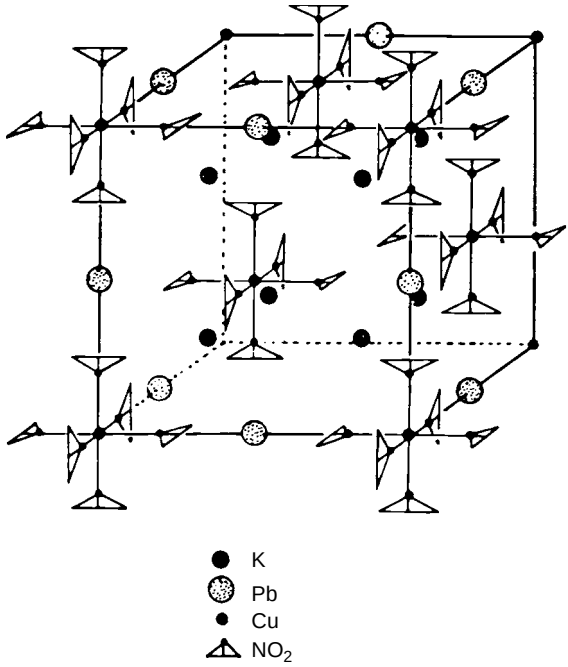

Fig. 8.23. The crystal structure of $K_2PbCu(NO_2)_6$ in the reference high-symmetry configuration.

scattering the authors succeeded in observing and studying in detail the superstructure of the two low-temperature phases. It was shown that the $[Cu(NO_2)_6]^{4-}$ octahedra of the crystal under consideration are elongated, and the interaction between them is of antiferrodistortive nature. In the high-temperature phase the three elongated configurations are equivalent; pulsations between them take place at each center independently. In the low-temperature γ phase (below 273 K), a typical antiferrodistortive structure with alternating parallel and perpendicular packing of the elongated octahedra is realized (cf. Fig. 8.14(a)).

In the intermediate β phase (at temperatures from 280 K to 273 K), an incommensurate helical structure discussed above (Fig. 8.17(c)) is formed. The structure of the crystal in the cubic phase is given in Fig. 8.23 (JT dynamics being disregarded), while observed displacements of NO_2 groups (and Pb atoms) in the β (incommensurate) and γ (antiferrodistoritive) phases are shown (in projection) in Fig. 8.24. In the γ phase the displacements corresponding to the elongation of the octahedra and their antiferrodistortive packing in the crystal produce a crystal mode with the wave vector $q_0 = (\frac{1}{2}, \frac{1}{2}, \frac{1}{2})$ conforming with the border of the vibrational band. These displacements, as mentioned above, correspond to the formation of a

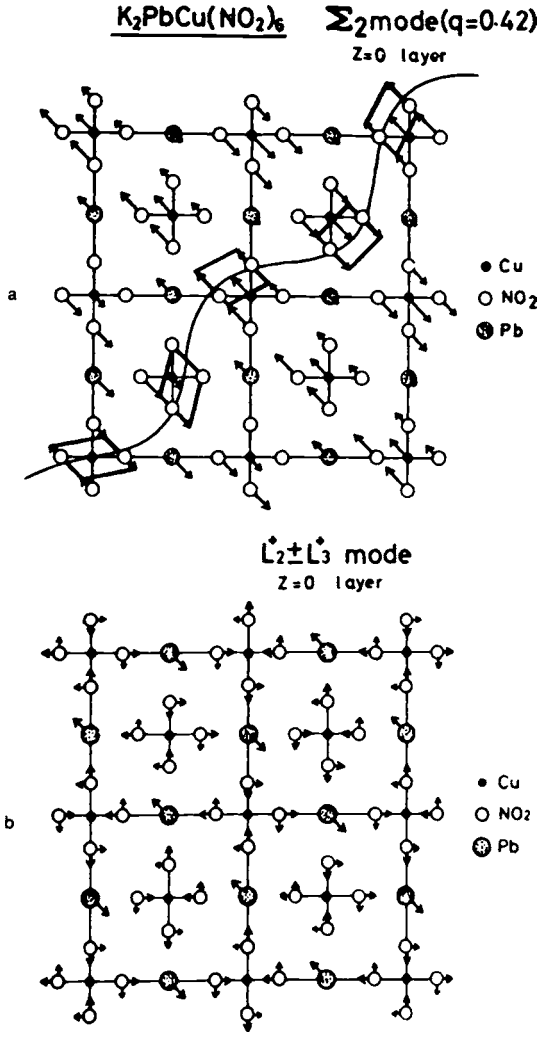

Fig. 8.24. Atomic displacements in the $Z = 0$ layer of the $K_2PbCu(NO_2)_6$ crystal in the incommensurate phase β (a) and antiferrodistortive phase γ (b) [8.258].

superstructure with a doubled period of the lattice. However, in the β phase the corresponding displacements change from one cell to another not quite "regularly," but forming a wave along the crystal with a period which is incommensurate with (not a multiple of) the period of the initial lattice. The wave vector of these displacements is shown to be (0.425, 0.425, 0). This result confirms the theoretical prediction [8.221] of possible stabilization of incommensurate phases in these crystals due to the CJTE.

Within the described series of hexanitrocomplexes of general formula $A_2BCu(NO_2)_6$, only in the case B = Pb is the above antiferrodistortive ordering

observed. The reasons are discussed elsewhere [8.199] and explained mainly by the presence of the additional unshared pair of electrons on the Pb^{2+} ion mentioned above. MO LCAO calculations of the APES of the octahedra of the hexanitrocomplexes of Co(II) and Cu(II) have been carried out in [8.249].

Another JT situation emerges when the JT centers in the crystal have unpaired electrons. In this case the CJTE structural phase transition strongly affects the possible electron orbital momentum and spin orderings leading to *structural–magnetic phase transitions*. Consider a crystal with cubic symmetry and octahedral JT centers in a ground E_g state corresponding to transition metals with electronic configuration d^9 (e.g., Cu^{2+}, Ni^{+}, Ag^{2+}), d^4 (Mn^{3+}, Cr^{2+}), and low-spin d^7 (Co^{2+}, Ni^{3+}). In these cases the E_g term is formed by the contribution of two d functions, d_{z^2} and $d_{x^2-y^2}$. Depending on the nature of the distortion, the unpaired electron of the E_g term falls either in the d_{z^2} state (producing a compressed octahedron for d^9 and an elongated one for d^4 and d^7) or in the $d_{x^2-y^2}$ state (forming an elongated octahedron for d^9 and a compressed one for d^4 and d^7).

Consider the K_2CuF_4 crystal with a perovskite structure. The lattice has a layered structure formed by the CuF_6 octahedra, which are interlinked in the (001) plane by common fluorine atoms. If the octahedra are elongated in the ordered phase, the unpaired electron at each center is in the $d_{x^2-y^2}$ orbital, whereas the d_{z^2} orbital is occupied by two electrons. If the ordering of the JT distortions is ferrodistortive, the respective orbital and spin ordering corresponds to that shown schematically in Fig. 8.25(a). It follows that planar antiferromagnetic ordering of the spins should be expected as a result of superexchange interaction through the common fluorine atoms.

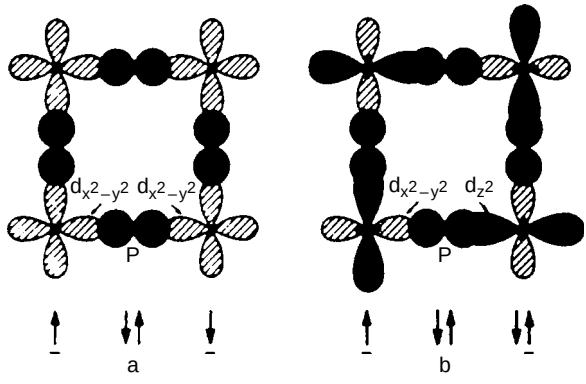

Fig. 8.25. An orbital- and spin-ordering scheme for crystals containing corner-connected octahedral $Cu^{2+}X_6$ clusters in the (001) plane in the cases of their ferrodistortive (a) and antiferrodistortive (b) orderings in the crystal [8.199].

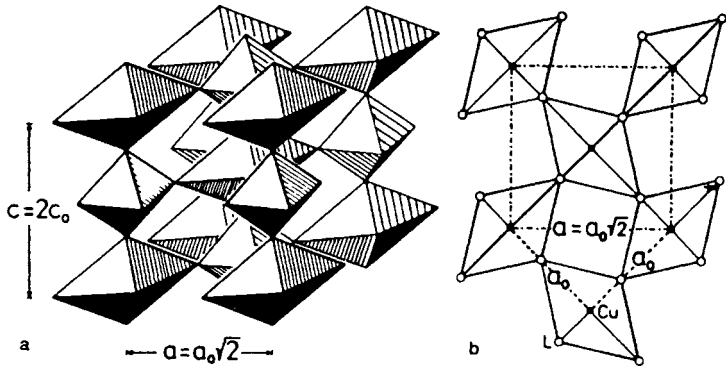

Fig. 8.26. Antiferrodistortive ordering of elongated octahedra in perovskites ABX_3: (a) a three-dimensional sketch; and (b) projection into the (001) plane [8.199].

In fact, planar ferromagnetism is observed [8.260]. Therefore, it was assumed [8.261] that in K_2CuF_4 antiferrodistortive ordering of the Cu^{2+} orbitals (and hence of the elongated CuF_6 octahedra) takes place in the (001) plane. The orientations of the orbitals and spins in line with this ordering lead to ferromagnetic interaction of the spins of the occupied d_{z^2} orbital and half-filled $d_{x^2-y^2}$ orbital (Fig. 8.25(b)). In this case planar ferromagnetism of Heisenberg type is realized. This assumption has been confirmed by ESR [8.262(*a*)] and direct X-ray [8.262(*b*)] measurements.

Passing to the $KCuF_3$ crystal, one can see that (as distinct from K_2CuF_4) the CuF_6 octahedra are linked by fluorine atoms in common not only within the (001) plane, but also along the [001] direction (Figs. 8.26 and 8.27). Here, the antiferromagnetic exchange interaction along the [001] direction between the unpaired spins of the $d_{x^2-y^2}$ orbitals is much ($\sim 10^3$ times) stronger than the ferromagnetic interaction between the occupied d_{z^2} and half-filled $d_{x^2-y^2}$ orbitals within the (001) plane. Therefore resulting linear antiferromagnetism is expected, in accordance with the experimental data [8.260] (see also [8.263]).

These ideas also explain the origin of the magnetic structure of other types of Cu(II) compounds in which the CJTE takes place [8.199, 8.264]. In particular, the compounds $Cu(ONC_5H_6)_6X_2$, $X = BF_4^-$ (I) and $X = ClO_4^-$ (II) were considered [8.264], in which, unlike in the crystals $KCuF_3$ and K_2CuF_4 where JT octahedra are strongly coupled by ligands in common, the $[Cu(ONC_5H_6)_6]^{2+}$ octahedra have no ligands in common and occupy the apexes of a slightly trigonally distorted cube [8.265]. The magnetic properties of the two crystals, I and II, are different: at low temperature, $\lesssim 1$ K, the crystal I is planar antiferromagnetic, whereas crystal II is one-dimensionally

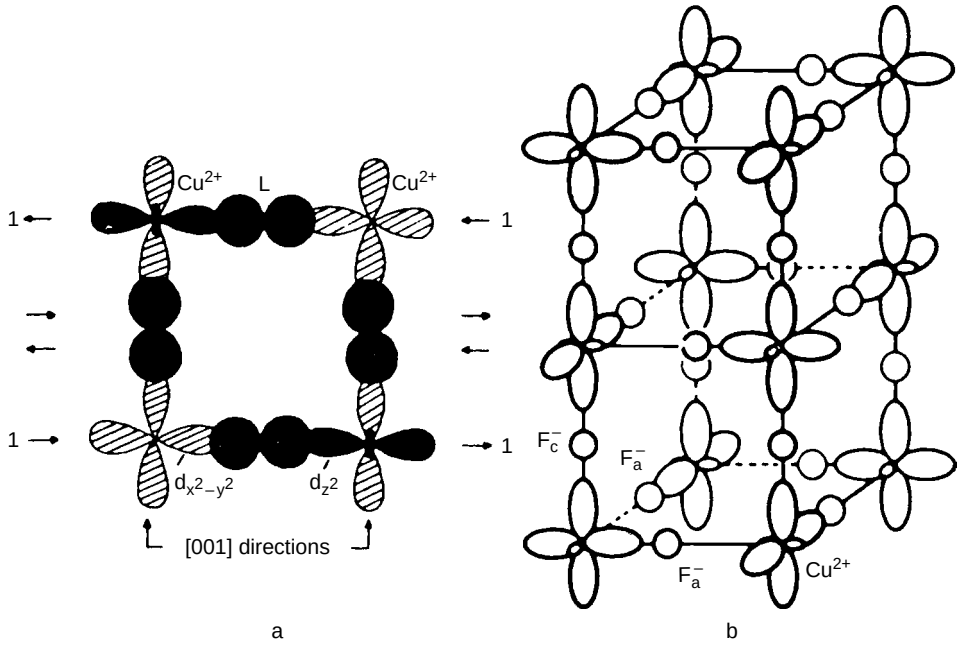

Fig. 8.27. Antiferromagnetic ordering of orbitals and spin in $KCuF_3$: (a) the ordering scheme along the [001] direction; and (b) three-dimensional orbital location [8.199].

ferromagnetic. The superexchange schemes in Fig. 8.25 can be used to assume that for elongated octahedra, as a result of the CJTE, ferrodistortive ordering takes place in the fluoroborate I, whereas antiferrodistortive ordering is realized in the perchlorate II. A study of ESR and electronic absorption spectra at different temperatures confirms these assumptions. At room temperature the distortions of the $[Cu(ONC_5H_6)_6]^{2+}$ octahedra are of dynamic nature, as confirmed by the magnitude and shape of the temperature ellipsoids in X-ray analysis [8.265]. The distortions can be evaluated from the temperature-ellipsoid dimensions using the technique given in [8.266]. In the cases under consideration the distortions are $\rho_0 \approx 0.37$ Å for I and $\rho_0 \approx 0.35$ Å for II; these values agree with the spectroscopic absorption-band splitting.

Phase transitions in these crystals take place at lower temperatures (at 90 K in I and 77 K in II). ESR data imply that low-temperature phases correspond to ferrodistortively ordered elongated octahedra in I and antiferrodistortively ordered elongated octahedra in II (compressed octahedra are unacceptable). The difference in the nature of JT center distortion interactions in the two crystals is apparently due to the different orientations of the BF_4^- and ClO_4^- groups in the lattice. The $Cu(ONC_5H_6)_6(NO_3)_2$ crystal remains ordered up to a temperature of 298 K.

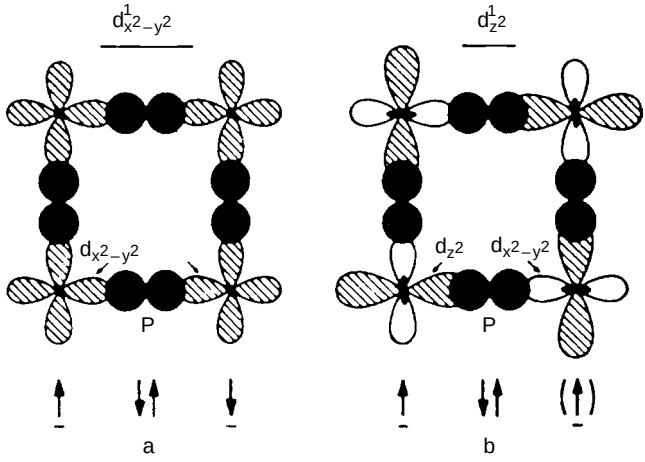

Fig. 8.28. Orbital and spin ordering of corner-connected MX_6 clusters, where M is a d^4 transition ion, in the (001) plane: (a) ferrodistortive ordering of compressed octahedra; and (b) antiferrodistortive ordering of elongated octahedra [8.199].

Analogous results in magnetic-structure investigations have also been obtained for Mn(III) and Cr(II) compounds with the d^4 electronic configuration [8.199, 8.267]. For example, a series of compounds A_2CrCl_4, where A = Cs, Pb, NH_4, and K, crystallizes in the same structure as K_2CuF_4, and similar to the latter exhibits ferromagnetic properties. The scheme of superexchange interaction, analogous to the octahedral compounds of Cu(II), is shown in Fig. 8.28 (cf. Fig. 8.25). It is seen that for the plane layers, ferromagnetism occurs only if an antiferrodistortive ordering of elongated octahedra takes place, whereas ferrodistortive ordering leads to an antiferromagnetic structure. Similar properties were observed in $AMnF_4$ with A = Cs, Pb, NH_4, and K.

In the above examples, ordering of the JT distortions in the crystal due to the CJTE leads to some orientation of the orbitals of the unpaired electrons which, in turn, determines the nature of the exchange interaction between the spins, and hence the spin ordering. The structural and magnetic phase-transition temperatures are not necessarily the same, since they are determined by different correlation constants (though there may be conditions under which the two temperatures coincide).

On stabilizing the distorted configuration of each center, cases in which structural ordering changes its orbital and spin ground state arise. Consider crystal centers with an orbitally nondegenerate ground state of type $^6A_2$ and a close orbitally degenerate excited state of another spin multiplicity, say $^2T_2$. Such a situation with two close terms of different multiplicities is in fact often

realized, for example, in a series of iron (as well as other transition metal) compounds. In particular, it is found in H[Fe(5-Clthsa)$_2$], where thsa is thiosemicarbazon. Another situation of this kind, with $^1A_{1g}$ and $^5T_{2g}$ terms instead of $^6A_2$ and $^2T_2$, is observed in Fe(III) compounds such as $[Fe(phen)_2(NCX)_2]^+$, X = S, Se. In these compounds the "crossover" phenomenon takes place for which, at certain temperatures, the magnetic moment (magnetic susceptibility) changes such that the $^2T_2$ term becomes the ground one instead of $^6A_2$ (or $^5T_{2g}$ instead of $^1A_{1g}$) or vice versa (see the review [8.268]). In many cases, this transition from one magnetic state to another is of a magnetic phase-transition nature accompanied by a structural phase transition [8.269]. Spin-crossover phase transitions in combination with the JT $E \otimes e$ problem explain the variable-temperature Raman spectra of Mn(III) complexes with large organic ligands [8.270] (see also [8.271]).

8.2.5 The band JTE, Peierls distortions, and first-order phase transitions. A general view on symmetry breaking

In the above consideration of JT crystals with orbitally degenerate centers a simplifying assumption was made, namely that the resonance interactions between the electronic states, which broaden the electronic terms into bands, may be neglected. This assumption allows one to reduce the problem to the interactions of a separate elementary cell with the molecular field of the environment, and to include the translational symmetry of the crystal at a later stage.

In the general case of broad bands and weakly coupled (almost free) electrons the translational symmetry has to be taken into account from the very beginning. The appropriate group-theoretical analysis of the matrix elements of the operator of vibronic coupling for space groups was performed and the consequent conclusion about the possible CJTE in crystals with *degenerate electronic bands* was drawn in [8.272–8.274] (see also in [8.275]). The mixing of electronic states with the same wave vector is produced by the boundary vibrations ($\vec{q} = 0$) (corresponding to a relative shift of the crystal sublattices), which, in some cases, in its final stage can be reduced to the local JTE in a separate elementary cell [8.274]. In general, however, the possibility of localizing the vibronic interaction is more relevant to some dielectric crystals.

In this section we consider crystals with partly occupied and relatively broad energy bands. The system is thus a metal; it has electrical conductivity. In systems with delocalized metallic bonds the JT vibronic coupling involves phonons with nonzero wave vectors producing corresponding (sometimes non-traditional) structural instability of the lattice. In systems with broad

bands the conduction electrons are weakly bonded and delocalized, meaning that the electron–phonon coupling is weak and in many cases the JTE implications may be neglected (see below).

Consider first the simplest example – a linear monatomic chain with one electron in the valence *s* orbital at each atom [8.196]. The Hamiltonian of the system, in contrast to the three-dimensional case, has only one acoustic branch of vibrations and its wave vector $\vec{q}$ is a scalar (wavenumber), $-\pi/a \leq q \leq \pi/a$ (a is the lattice constant). If only the nearest-neighbor atoms interact,

$$\omega(q) = 2\sqrt{A/M}\,\sin(|q|a/2) \tag{8.25}$$

where A is the constant of elastic coupling between the neighbors and M is the nuclear mass. If the energy read off is taken as the electronic energy level of the atom and the resonance interactions of only nearest-neighbor atoms are taken into account, then the energy levels may be taken as

$$\varepsilon(k) = -2h_0\cos(ka) \tag{8.26}$$

where h_0 is the corresponding resonance integral. All the energy levels (8.26) are doubly degenerate with respect to the direction of the electron momentum, $\varepsilon(k) = \varepsilon(-k)$.

Since the number of states in the band is $2N$, while the number of electrons is N, the band is half filled and the Fermi surface is at the middle of the band. As first shown in [8.276] and [8.277] (see also [8.278]), in this case the crystal is unstable with respect to spontaneous deformation of the lattice towards a doubling of its period (*Peierls distortion*) (Fig. 8.29(a)). Under this antiferrodistortive ordering of distortions the conduction band splits into two bands. The lowest band is fully occupied and goes down in energy, whereas the upper one is empty and goes up in energy; the total energy is thus lowered, and this explains the origin of the distortion under consideration.

The doubling of the lattice period – the alternation of the bond lengths (Fig. 8.29) – can be described by the nuclear displacement $Q_n = (-1)^n Q = Q\exp(\pm i\pi n)$, which after a Fourier transformation to the chain coordinates yields [8.196]

$$Q(q) = \sqrt{N}Q\delta_{q,\pm q_0} \tag{8.27}$$

where $q_0 = 2k_F = \pi/a$; k_F is the Fermi momentum of the electrons. Then by taking into account only one mode Q that doubles the lattice period, and introducing the local (elementary-cell) vibronic coupling constant F for this active mode, we can present the vibronic coupling operator as $H_{\text{int}} \sim FQ$; it

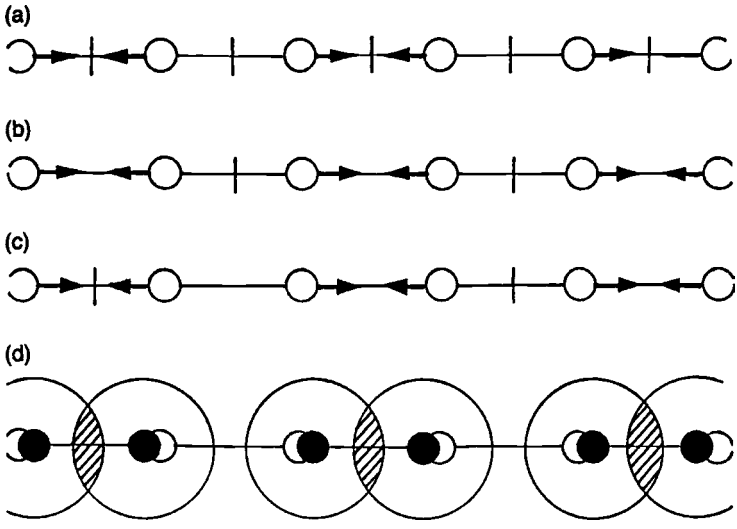

Fig. 8.29. A sketch illustration of a Peierls transition in a one-dimensional lattice with a half-filled band presented as an antiferrodistortive ordering with a doubling of the lattice period: (a) ferrodistortive distortion of a lattice with a doubled period; and (b) odd antiferrodistortive distortion of a lattice with a tripled period (vertical lines separate elementary cells). The areas of increased overlap of the nearest-neighbor atomic s orbitals resulting in additional covalency (PJTE) are shown by hatching (d) [8.196].

mixes the state of a given value of the wavenumber k with another electronic state from the first Brillouin zone with the wavenumber $k+\pi/a$ or $k-\pi/a$. The corresponding vibronic coupling matrix

$$H_{\mathrm{e}}+H_{\mathrm{int}}=\begin{vmatrix}\varepsilon(k) & FQ\\ FQ & \varepsilon(k+2k_{\mathrm{F}})\end{vmatrix} \tag{8.28}$$

has a characteristic form inherent to systems with the PJTE (Section 4.1).

Thus the electron–phonon interaction in a linear chain with a half-filled electronic band, taking account of one active vibrational mode with the wavenumber $\pm 2k_{\mathrm{F}}$, is reduced to the PJTE for different pairs of one-electron states mixed by one nondegenerate vibration. The energy gap between these states is $4h_0|\cos(ka)|$. There are two mixing states with a zero energy gap, and for them the mixing is equivalent to the JTE. There are also quite a few pairs of mixing states near the Fermi surface with a very small energy gap between them.

The eigenvalues of the matrix (8.28), the one-electron contributions to the APES, are

$$\varepsilon_{\pm}(k)=\tfrac{1}{2}[\varepsilon(k)+\varepsilon(k+2k_{\mathrm{F}})]\pm\sqrt{\tfrac{1}{4}[\varepsilon(k)-\varepsilon(k+2k_{\mathrm{F}})]^2+F^2Q^2} \tag{8.29}$$

Considering the symmetry of the electronic band with respect to the Fermi surface ε_F, $\varepsilon(k+2k_F) - \varepsilon_F = -[\varepsilon(k) - \varepsilon_F]$, the expression (8.29) can be reduced to a simpler one:

$$\varepsilon_{\pm}(k) = \varepsilon_F \pm \sqrt{[\varepsilon_F - \varepsilon(k)]^2 + F^2 Q^2} \tag{8.30}$$

By comparison with Eq. (4.3) we see that the depth of the occupied energy level under the Fermi surface is half the energy gap between the mixing states in the PJTE.

Neglecting the Coulomb and exchange corrections for the sake of simplicity, we present the APES of the ground state of the crystal $\varepsilon_0(Q)$ as a sum of the one-electron energies of the occupied states and the elastic energy of the active mode (cf. Eq. (3.1)):

$$\varepsilon_0(Q) = (N/2)M\omega_0^2 Q^2 + 2N \sum_{k=-k_F}^{k_F} \varepsilon_-(k) \tag{8.31}$$

where $\omega_0 = \sqrt{2}\omega(2k_F)$. On substituting here the expression for $\varepsilon_-(k)$ from (8.29), introducing the density of one-electron states in the band $\rho_{el}^{(0)}(\varepsilon_k)$, and performing a series of other transformations [8.196], we come to the following expression for the APES:

$$\varepsilon_0(Q) = (N/2)M\omega_0^2 Q^2 - (N/\pi)\sqrt{4h_0^2 + F^2 Q^2}\, E(z)$$
$$z = 2h_0 \Big/ \sqrt{4h_0^2 + F^2 Q^2} \tag{8.32}$$

where $E(z)$ is a full second-order elliptical integral,

$$E(z) = \int_0^{\pi/2} \sqrt{1 - z^2 \sin\varphi}\, d\varphi$$

Using its expansion near the point $z = 1$, $E(z) \approx 1 + \frac{1}{2}[\ln(4/z') - \frac{1}{2}]z'^2$, where $z' = \sqrt{1-z}$, we obtain for the function $\varepsilon_0(Q)$ near the point $Q = 0$ (corresponding to the high-symmetry nuclear configuration) [8.196]

$$\varepsilon_0(Q) = E_0 + (N/2)(M\omega_0^2 - F^2/\Delta_{eff})Q^2 + (2Nh_0/\pi)(FQ/2h_0)^2 \ln|FQ/2h_0| \tag{8.33}$$

Here $E_0 = -4Nh_0/\pi$ is the electronic energy in the undistorted lattice, and $\Delta_{eff} \approx 1.6656h_0$.

The analysis of the expression (8.33) shows that for arbitrary values of the vibronic constant the branches of the curve $\varepsilon_0(Q)$ in the close vicinity of the point $Q = 0$ are turned down, while the derivative of $\varepsilon_0(Q)$ at this point is zero. At $F^2 \geq M\omega_0^2\Delta_{eff}$ an additional instability determined by the first terms of

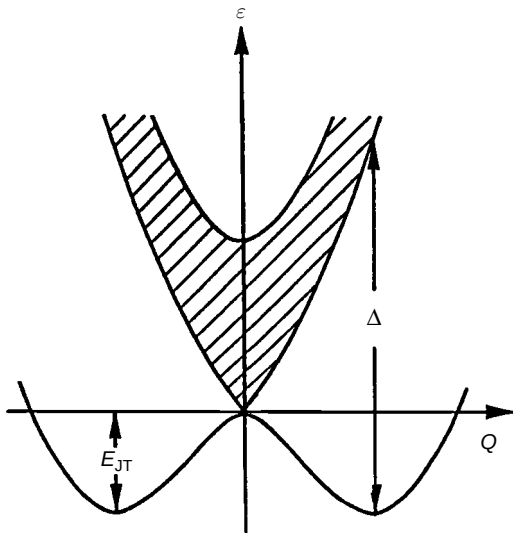

Fig. 8.30. The APES of a monatomic linear chain with a half-filled electronic band as a function of the coordinate of nuclear displacements that double the lattice period. The conduction band (empty at $T=0$) is shown by hatching [8.196].

(8.33) occurs. Nevertheless, at large values of Q the logarithmic term in (8.33) becomes dominant, and the wings of the curve $\varepsilon_0(Q)$ turn up. Although similar in shape to the lowest sheet of the APES for systems with the PJTE (Fig. 4.1), the curve $\varepsilon_0(Q)$ obtained here is free from the restriction of the inequality (4.6) required for the instability of the high-symmetry configuration in the usual molecular case. This result (the instability at $Q=0$ for arbitrary values of the vibronic constant and other lattice parameters) is a characteristic feature of the JTE, and arises here due to the significant contribution of the mixing of states with energies at or near the Fermi surface.

The shape of the curve $\varepsilon_0(Q)$ corresponding to the definition (8.31) is shown schematically in Fig. 8.30. The adiabatic potential of the ground state has a symmetric double-well shape characteristic of JT systems. As in the usual JT cases, the distortion of the lattice at the minima $\pm Q_0$ and the JT stabilization energy E_{JT} increase with the vibronic constant F. However, in the case under consideration this dependence on F is more complex. In particular, the most important contribution to the instability at $Q=0$ determined by the degenerate and quasidegenerate states with $\varepsilon \approx \varepsilon_F$ depends on the density of states at the Fermi level $\rho_{el}^{(0)}(\varepsilon_F)$. Since the free energy of the crystal at $T=0$ coincides with $\varepsilon_0(Q)$, the double-well adiabatic potential means that the low-temperature phase corresponds to a distorted lattice with a doubled period (Fig. 8.29). Thus *the band JTE in a linear monatomic lattice with a half-filled electronic*

band results in structural instability with respect to distortions with the wavenumber $q_0 = 2k_F$. This conclusion coincides with the *Peierls–Frohlich statement* mentioned above [8.276, 8.277], and the corresponding structural phase transition is the *Peierls transition*.

We neglect here the role of fluctuations, which are known to quench phase transitions in one-dimensional systems. However, real systems are never ideally one-dimensional. A weak interaction between the chains or any spatial complication of the chain itself usually remove the fluctuation restriction.

Note that the resonance integral h_0 is proportional to the overlap integral S of the atomic orbitals of the nearest-neighbor lattice sites that form the conduction band, $h_0 \sim S$, while the vibronic coupling constant F is proportional to the derivative of S with respect to the interatomic distance, $F \sim S'$ (see the expression for F in Section 2.2, Eq. (2.15) that characterizes the rate of changes in interatomic coupling with the interatomic distance; there is an erroneous statement in [8.196] that $F \sim S$). For large S values (broad bands), meaning rather full overlap between atomic orbitals of the conduction band, S' is small (the overlap integral has a maximum and falls exponentially with the interatomic distance), and the JTE is small. With the band narrowing S' and F increase and hence the band JTE increases. For very narrow bands the S' and F values (at the tool of the exponent) become again very small and the JTE vanishes. Hence *the band JTE requires a delicate balance between not very broad and not very narrow conduction bands*. This conclusion about the "window of opportunity" in the conduction bandwidth with regard to the possible JTE is important, in particular, in considering its implications in superconductivity (Section 8.4).

Similar to other cases of the PJTE discussed above, the gain of energy in the Peierls transition is due to the formation of new covalent bonds by distortion (by the pairing of the atoms in the linear chain, Fig. 8.29(d)). The diagonalization of the matrix (8.28) leads to the formation of bonding and antibonding orbitals $\psi_{\pm}(k) = (\psi_k \pm \psi_{k-q_0})/\sqrt{2}$. Transformed back to localized orbitals, they result in bonding "molecular" orbitals of pairs of atoms, shown in Fig. 8.29(d). Here, as in Section 8.3, while the cooperative properties of the chain are very important for the phase transition, they alone cannot produce the distortions: the instability of the high-symmetry configuration is triggered not by cooperative, but by short-range local forces of chemical bonding. Obviously, the bond alternation in corresponding long-chain and conjugated molecules [8.279, 8.280] is of the same origin as the Peierls distortion and period doubling.

The change of the electronic structure of the crystal due to the Peierls transition can be interpreted as the formation of a standing longitudinal wave of electron density with wavenumber $q_0 = 2k_F$ in the low-symmetry phase. Simultaneously, in the electronic spectrum a forbidden band of width

$\Delta \gtrsim E_{JT}$ arises (Fig. 8.30). At $T = 0$ K, when only the ground state is occupied, the crystal becomes dielectric. Therefore the Peierls transition is also a metal–dielectric or a metal–semiconductor transition, depending on the size of the energy gap Δ.

In the treatment of the Peierls transition with a doubling of the lattice period one can start with the extended elementary cell containing two atoms (Fig. 8.29(b)). In this case the transition is equivalent to a ferrodistortive ordering of local totally symmetric distortions of the cells, i.e., the transition is isostructural. However, the PJTE origin of the Peierls instability is more obvious when one starts with the elementary cell containing three atoms (Fig. 8.29(c)). In each elementary cell of three atoms one can form three molecular orbitals, two even and one odd. They mix under the symmetrized odd displacements (shown in Fig. 8.29(c)), realizing the PJTE in a linear triatomic system of the type BAB for three states mixed by one odd vibration, quite similar to the two-level case considered in Section 4.1 (see also Section 4.4). If the vibronic constant is sufficiently large, the PJTE is strong and the high-symmetry configuration in the elementary cell becomes unstable with respect to the odd distortion under consideration. By interaction through the phonon field the local distortions form an antiferrodistortive ordering (Fig. 8.29(c)). The active mode here is the odd optical vibration with the wavenumber $q = 0$. In this sense the Peierls transition with a doubling of the lattice period is similar to the antiferroelectric ordering considered in Section 8.3. The analogy between the Peierls transformation and antiferroelectric phase transitions was noted in [8.281].

The arguments resulting in the Peierls instability are applicable also to one-dimensional metals with the conduction band other than half occupied. In this case the distortion of the lattice with the change of the lattice period results in a band splitting such that its occupied part goes down in energy, leading to an energy gain. For instance, if the electronic band is filled up to the states with the Fermi momentum $k_F = \pi/6a$, the active mode (in the sense discussed above) is a normal vibration with the wavenumber $q_0 = \pm 2k_F$, which triples the lattice period. For other electronic band occupancies there may be transformations into structures with periods that are incommensurate with the initial one.

Following [8.276], one can assume that a *similar instability of vibronic origin may be present in two- and three-dimensional metallic systems*, but so far there is no full exploration of the band JTE for such systems similar to that illustrated above for linear chain systems [8.196]. The non-coincidence of the shape of the Wigner–Seitz cell and the Fermi surface in combination with a sufficiently strong vibronic coupling and great density of states at the Fermi surface may be the reason for the rather complicated crystal structures often observed in metals of

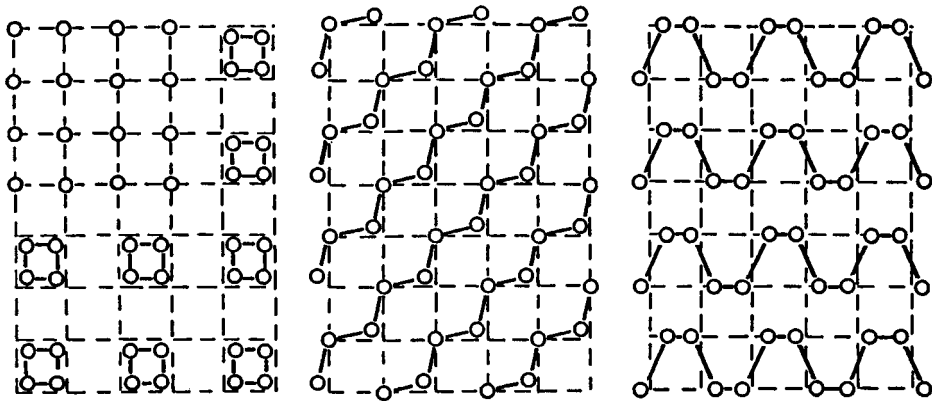

Fig. 8.31. Three examples of alternating bond lengths in a monatomic square-planar lattice. (Reprinted with permission from [8.286]. Copyright 1977 Elsevier Science Publishers.)

relatively simple composition (see, e.g., [8.282]). Some details of what can actually happen in these cases are discussed in [8.283]. Usually the observed structure is a result of one of several ways of stabilizing the initial (reference) unstable structure by deformations. Some special cases of layered crystals of the type PbFCl, ZrSiS, BiOCl, Co_2Sb, Fe_2As, were investigated in [8.284, 8.285]. Three possible ways to stabilize a square lattice, suggested in [8.286], are presented in Fig. 8.31. A monatomic cubic lattice was shown to have no less than 36 different means of stabilization by lattice distortion [8.287]. Two of these, shown in Fig. 8.32, correspond to black phosphorus and arsenic structures.

The deformation pulls down some of the states from the Fermi-level region. But because the shape of the Wigner–Seitz cell does not coincide with the Fermi surface, it might not be possible to remove all the states from the Fermi-level region. Some of the electrons remain in the conductive band and some of the holes remain in the valence band. Therefore the material may still be a conductor (see also [8.288(*a*)]). The JTE and PJTE in quasi-one-dimensional systems of the type SbSI were considered recently [8.288(*b*)].

The one-electron treatment above does not take into account the effects of electron correlation. The latter, by means of coupling the orbital and spin states of different lattice sites, may lead to an ordering in the electronic subsystem accompanied by a wave of charge density [8.289]. The Mott transitions (the transition of a metal to a dielectric), as well as bond alternation in conjugated hydrocarbons, are examples of this kind of phenomenon. Also related to these phenomena is the antiferromagnetic instability resulting in giant spin waves in crystals [8.290]. The relation of the band JTE to superconductivity is discussed in Section 8.4.

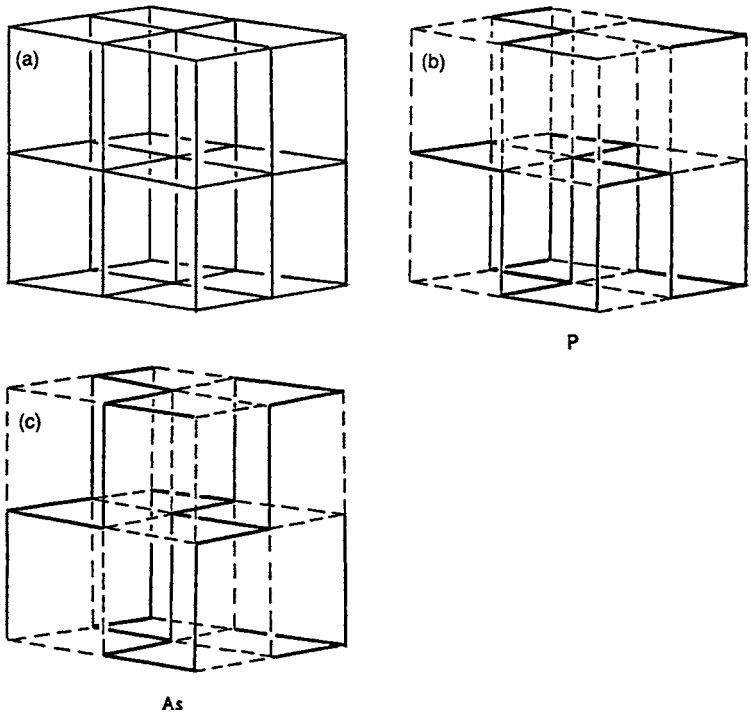

Fig. 8.32. Two examples of Peierls ordering of local distortions in a monatomic cubic lattice: (a) the reference high-symmetry (cubic) lattice; (b) the low-symmetry structure of black phosphorus; and (c) the low-symmetry structure of crystalline arsenic. (Reprinted with permission from [8.287]. Copyright 1981 American Institute of Physics.)

In all these cases the phase transition in the electronic subsystem is accompanied by the formation of an energy gap in the electronic spectrum that may strongly influence the vibronic interactions. For instance, the Mott transition, transforming a metal into a dielectric, removes the degeneracy of the one-electron states at the Fermi surface and hence the special combination of the JT and PJT effects mentioned above. The joint consideration of both the vibronic interaction and electronic correlation effects is a complex problem. Variational calculations, (e.g., in [8.291]) show that the Peierls instability and electronic correlations are not always competing effects, and sometimes the correlations may even enhance the transition to the Peierls state. This conclusion is also confirmed by perturbation theory with respect to the mean field [8.292] and to the constant of electron–electron interaction [8.293], as well as by Monte Carlo calculations [8.294] and exact computations for finite systems [8.295].

On the other hand, the electron–phonon interaction may be excluded, for instance, in second-order perturbation theory, to result in an effective

electron–electron interaction. Therefore the Peierls instability causes also instability in the electronic subsystem. For example, it was shown in [8.289] that the Peierls instability is always accompanied by BCS instability, i.e., by the occurrence of Cooper pairs. But without taking account of vibronic interaction the phase transition in the nuclear subsystem (the structural phase transition) cannot take place.

The investigation of one-dimensional structures has grown into a wide-ranging branch of scientific activity, mostly due to the hypothesis about the possibility of high-temperature superconductivity in some one-dimensional system [8.296]. For a long time the efforts of researchers were directed to quasi-one-dimensional compounds like V_3Si with an A-15 structure, as well as to organic compounds, like TTF-TCNQ (TTF is tetrathiofulvalene, $[(C_3S_2)HCH_3]_2$, and TCNQ is tetracyanoquinonedimethane, $(CN)_2C(C_6H_6)C(CN)_2)$), which exhibit structural phase transitions and anomalies in the temperature dependences of their electrical properties. Different models developed for the description of the structural transformations in these compounds [8.297–8.299] employ, in one form or another, the above ideas based on the vibronic nature of the Peierls instability. In particular, they link the spontaneous deformation of the lattice with the high density of states at the Fermi surface.

An interesting example of a quasi-one-dimensional conducting system which undergoes a Peierls transition into a dielectric phase is the *trans* modification of the polyacetylene polymer $(CH)_x$. There are two theoretical models describing the properties of this polymer [8.300]. Both are based on the vibronic mechanism of the structural instability of the chain *trans*-$(CH)_x$.

Linear chain compounds with Peierls and Peierls-like phase transitions are widely considered also as mixed-valence systems. For examples and as a source of further references see [8.301–8.308]. For instance, in [8.305, 8.306] dimeric MMX chains were considered (M is a metal and X is a halogen), and it was shown that the Peierls transition results in torsion distortion inside the dimer MM, instead of the off-center displacement of the halogen in the more often discussed monomeric MX chains. Mixed-valence compounds are discussed in more detail in Section 7.6.2.

So far in this and the next section we consider the ordering of JT units and structural phase transitions in solid-state or chain structures which can be classified as second-order phase transitions. However, nowhere in these treatments have we used any limitations on the behavior of the JT units near the phase transition. The only limitation employed together with Eq. (8.6) is that the lower-temperature phase has lower symmetry and lower internal energy, both provided by the JTE or PJTE. This means

that the same ideas of ordering and phase transitions can be applied to first-order transitions.

The liquid-crystal phase transition (crystallization) as triggered by the JT effect was considered first in [8.309]. The authors start with the idea that, in accordance with literature data, the instant local ordering in, for instance, monatomic liquids is of high (isocahedral) symmetry [8.310]. Recently this assumption was additionally confirmed experimentally [8.311]. High symmetry results in high electronic degeneracy or pseudodegeneracy, and hence in JT vibronic instability with several equivalent minima of lower (e.g., cubic) symmetry of the APES. At high temperatures the local order in the liquid state is short-lived and the distorted configurations at the minima are oriented arbitrarily with a complicated dynamics of transition between them. At the critical temperature T_c an ordering of these distortions takes place, and the system transforms into a crystal with the symmetry determined by the local distorted configurations and their interaction, quite similar to phase transitions in crystals. Another possibility is that the liquid state transforms into an amorphous state if, depending on the interaction between the centers, the freezing of the randomly oriented distortions takes place before their ordering [8.309].

The parameters of the JT distortions were calculated by the X_α method for a series of crystals and found to be in good agreement with experimental melting temperatures [8.309]. The details of the theory and specific calculations seemingly require additional refinements, but the main idea of the JT origin of the liquid-crystal phase transition seems to be quite reasonable. This work thus makes an important next step toward a better understanding of the relation between the macroscopic property of phase transitions and the microscopic electronic structure, the JTE parameters.

In the paper [8.309] the possibility of a similar gas–liquid transition is also mentioned. For a simple system of a monatomic gas [8.312], assume first that the atoms are at sufficiently large interatomic distances that their interaction can be neglected. The symmetry of such a system is very high, its Longuet–Higgins symmetry group being $G = R(3)\pi(N)C_i$, where $R(3)$ is the group of rotations of the free atom, $\pi(N)$ is the group of permutations of N identical atoms, and C_i is the group of inversion. The high symmetry determines the high degeneracy of the electronic states: all the independent combinations of N atomic functions correspond to different states with the same energy.

On approaching each other, the atoms begin to interact, the symmetry lowers, and the degeneracy is removed (completely or partly). This behavior is quite similar to the JT one, provided the splitting of the electronic states results in lowering the ground-state energy due to either chemical bonding or Van der Waals interaction [8.312].

Consider an illustrative example. Assume that $N = 13$ and choose the coordinate of mutual approach of atoms Q_L that leads to the formation of an icosahedron deemed (as above) to be the instantaneous local order in the monatomic liquid. Take the scale of Q_L such that $Q_L = 0$ at large distances and $Q_L = Q_L^{(0)}$ for the icosahedron configuration. For simplicity assume also that each atom has one electron above the closed shell which occupies a nondegenerate *ns* orbital (an alkali-metal-like atom).

At the starting point $Q_L = 0$ with the symmetry $G = R(3)\pi(13)C_i$ the electronic state is 13-fold degenerate, and hence it splits under the icosahedral distortion Q_L (the maximum allowed degeneracy in icosahedral symmetry is fivefold). Since the number of electrons (13) is smaller than the number of states (26), the icosahedral configuration at $Q_L = Q_L^{(0)}$ in the ground state has lower energy than at the point of degeneracy $Q_L = 0$. The picture as a whole is similar to the above JT description of bonding in homonuclear diatomics (Section 4.5). If all the active atomic states are fully occupied by electrons (as in inert-gas atoms), there is still an interaction that results in a Van der Waals minimum; as shown in [8.312], it can be presented as a kind of PJTE.

This explains the instant local order formation required for the transition to the liquid phase. Similar reasoning is valid for molecular interactions that result in the transition of separate gas molecules to local formations in liquids that represent their instant local ordering. Thus the necessary condition of gas–liquid phase transition, the spontaneous decrease in energy and symmetry by formation of instant local order in liquids from the gas units, may also be presented qualitatively as initiated by the JT or PJT effect.

Treatment of the first-order phase transition in UO_2 was reported recently [8.313]. In this case the $5f^2$–$5f^2$ superexchange between the U^{4+} ions is the major driving force causing magnetic and orbital ordering and suppressing the CJTE.

An interesting example of JT-like cooperative effects is presented by enantiomer formation. It was shown in [8.314] that enantiomers can be regarded as the low-symmetry, PJT-distorted configurations of a hypothetical high-symmetry structure, and as such their interaction in the liquid phase via collisions under special conditions may lead to some kind of "cooperativity" and "phase transition" resulting in a single-enantiomer broken-symmetry phase. Another peculiar mechanism of chirality generation via cooperative action of polarized light and vibronic coupling is discussed in [8.315].

With the first-order and second-order structural phase transitions shown to be due to the JT or PJT coupling, we can try to formulate a general view on structural *symmetry breaking* (SB) in nature [8.312]. The phenomenon of SB

(roughly meaning the lower symmetry of the objects in the world compared with the high symmetry of the Hamiltonian of the particles from which they are formed) is very important as it describes the consecutive transformations of matter in the Universe brought about by cooling, beginning with the Big Bang.

In particle physics the concept of SB is associated with degeneracy [8.316]. In condensed matter too the SBs are triggered by degeneracy or pseudodegeneracy via the JTE [8.312]. As shown in Section 4.5, atom–atom interactions to form molecular systems, as well as intermolecular interactions in chemical transformations, can be regarded as due to the JT, PJT, or RT effects. Looking at SB as a kind of phase transition, we can involve Eq. (8.6) that relates the SB to the JT stabilization energy by lowering the symmetry, and to a similar decrease in entropy. This allows us to present all the structural SBs in a unique picture shown in Fig. 8.33.

In this figure, at $T \sim 10^4$ K the ensemble of free atoms, as mentioned above, has very high symmetry and hence degenerate and/or pseudodegenerate states. According to the JTE theory and Eq. (8.6) this system under certain conditions is subject to JT instability, and by cooling at a certain temperature undergoes a SB to a gas of corresponding molecules. The latter still has very high symmetry and electronic degeneracy or pseudodegeneracy that causes the next phase transition to the liquid state at lower temperatures, as discussed above in this section. Then follows, at lower temperatures, liquid–solid and solid–solid phase transitions, which bring us to the real world. Together with the concept of SB in particle physics being associated with degeneracy, mentioned above [8.316], we can speculate about a general picture of consecutive transformations of matter via degeneracy-based SBs that are similar in nature, beginning with the Big Bang [8.312].

8.3 The cooperative PJTE. Ferroelectric phase transitions

Except for very small energy gaps between the mixing electronic states (as in the case of $DyVO_4$ discussed in Section 8.2.2), the cooperative PJTE (CPJTE) stays apart from all the other cooperative phenomena in JT crystals for two reasons. First, the role of the large-gap PJTE in configurational instabilities was recognized much later than in the JT case. Second, more importantly, PJT distortions on each center of a dielectric, in general, cannot be presented as orientational units that can be ordered in the lattice by means of a pseudospin-like approach, because of the very strong overlap of the wavefunctions of the PJT APES minima.

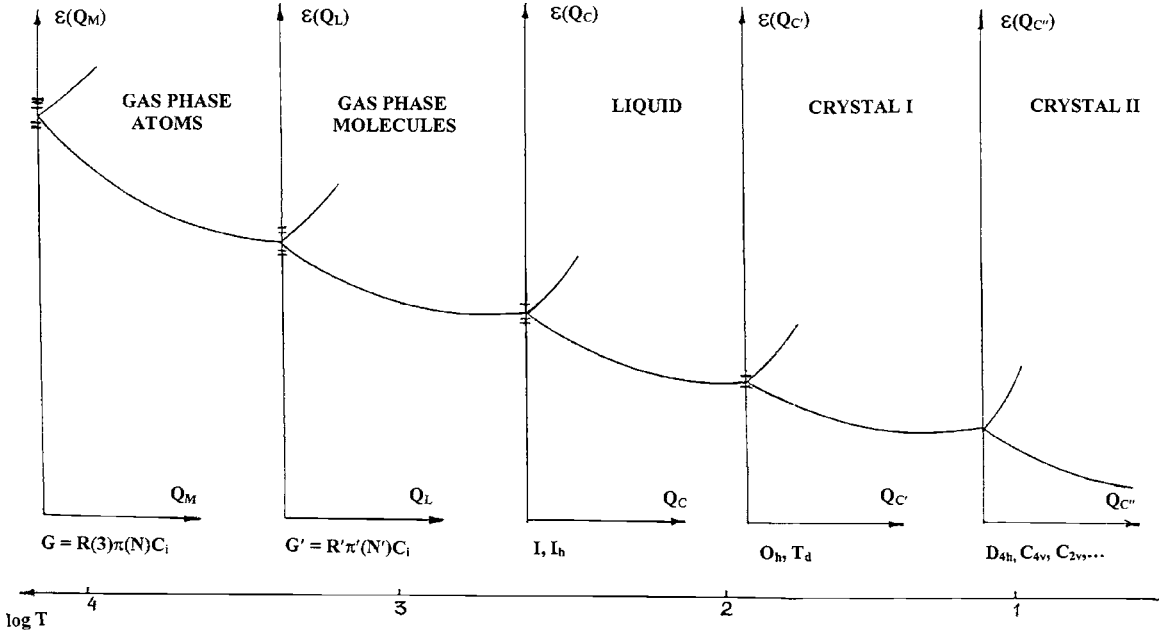

Fig. 8.33. The conventional scheme of consequent temperature-dependent symmetry breakings triggered by JT or pseudo JT effects. $G = R(3)\pi(N)C_i$ is the symmetry of an atomic gas, where $R(3)$ is the group of rotations of the free atom, $\pi(N)$ is the group of permutation, and C_i is inversion; the primed values have the same meaning for the gas of molecules. Crystal I and crystal II denote two crystal phases with decreasing symmetry, respectively. Q_M, Q_L, Q_C, $Q_{C'}$, and $Q_{C''}$ are the separate and independent JT coordinates of symmetry breaking, while the temperature scale is in common.

On the other hand, PJT distortion may lead to dipole-moment formation and hence the CPJTE may result in spontaneous polarization of the crystal (ferroelectricity). This possibility for perovskites (e.g., $BaTiO_3$) was suggested first in 1966 [8.317]. At that time this suggestion was rather bold since it implies that dipolar distortions are of local (not cooperative) PJT origin (meaning that they should be present in all the phases), and they are partly (or fully) ordered in the lower-temperature phases. No experimental data were available at that time to support this point of view. On the contrary, the dominant Cochran [8.318], Anderson [8.319], and Ginzburg [8.320] theory for displacive phase transitions excluded such polar distortion of local origin.

Nowadays the predictions of the PJT vibronic theory of ferroelectricity are fully confirmed by various experimental techniques (see the review [8.149]). In view of the uniqueness of the PJT origin of instabilities in nondegenerate states (Section 4.1), this theory may serve as a model for all the structural phase transitions in dielectric crystals.

Consider the perovskite structure and specifically $BaTiO_3$ as a model for discussing the PJT local dipolar distortions and their cooperative interaction in the crystal [8.317]. We begin with the local off-center displacements of the Ti ion. Assume that the titanium ion can be regarded as a single impurity in the lattice. Using some cluster-model molecular-orbital (MO) description of the electronic structure of the $[TiO_6]^{8-}$ cluster and the Madelung potential of the remaining crystal lattice (enlarging the cluster size doesn't change the qualitative results obtained below), we get the qualitative MO energy-level scheme shown in Fig. 4.13; it is a typical MO LCAO scheme for octahedral transition metal d^0 systems [8.321]. The ground state of the system A_{1g} is formed by the occupied 12 oxygen $2p_\pi$ orbitals of t_{1u}, t_{2g}, t_{1g}, and t_{2u} symmetry (t_{1g} and t_{2u} are not shown in Fig. 4.13 since they are inessential in this treatment), while the lowest unoccupied MO consists of the three d_π (t_{2g}) orbitals (d_{xy}, d_{xz}, and d_{yz}) of Ti^{4+}. The t_{2g} orbitals of Ti and O form π-bonds which are weak compared with the main σ-bonds.

The PJTE in such a cluster is considered in Section 4.3. The off-center displacements of titanium with respect to the oxygen octahedron and the remaining crystal are of the threefold degenerate $T_{1u}(Q_x, Q_y, Q_z)$ type (Fig. 4.14). Under these displacements, only the t_{1u} and t_{2g} states become mixed. Neglecting the weak π-bonding and considering the linear terms of the vibronic coupling as a perturbation, the secular equation for the electronic energies as a function of these nuclear displacements $\varepsilon(Q_\alpha)$ is of the ninth order (Section 4.3). Its roots can be determined directly [8.196, 8.317]; they are given in Eqs. (4.101). The six electrons of the oxygens occupy the lowest three

orbitals, yielding the following adiabatic potential $\varepsilon(Q_\alpha)$ for this site in the space of the T_{1u} displacements, which includes also the harmonic term of core interactions (Eqs. (4.102)):

$$\varepsilon(Q_x,\ Q_y,\ Q_z) = \tfrac{1}{2}K_0(Q_x^2 + Q_y^2 + Q_z^2) - 2\{[\Delta^2 + F^2(Q_x^2 + Q_y^2]^{\frac{1}{2}} + [\Delta^2 + F^2(Q_x^2 + Q_z^2]^{\frac{1}{2}} + [\Delta^2 + F^2(Q_y^2 + Q_z^2]^{\frac{1}{2}}\} - 6\Delta \tag{8.37}$$

where 2Δ is the energy gap between the $2p_\pi$(O) and d_π(Ti) states, $K_0 = M\omega_0^2$ is the bare force constant for the T_{1u} displacements determined by Eq. (2.35), and F is the vibronic coupling constant (section 2.2),

$$F = \langle 2p_\pi^z(\mathrm{O})\big|(\partial H/\partial Q_x)_0|3d_{xz}(\mathrm{Ti})\rangle \tag{8.38}$$

The adiabatic potential surface (8.37) has very interesting features discussed in Section 4.3. If $K_0 > 4F^2/\Delta$ the surface has one minimum at $Q_x = Q_y = Q_z$ with the titanium ion at the center of the octahedron. But if

$$4F^2/\Delta > K_0 \tag{8.39}$$

the point $Q_x = Q_y = Q_z = 0$ is a maximum (meaning instability), and there are eight minima at

$$|Q_x| = \big|Q_y\big| = |Q_z| = [(8F^2/K_0) - (\Delta^2/2F^2)]^{\frac{1}{2}} \tag{8.40}$$

at a depth

$$E^{(1)} = \delta = 3\Delta(Y + Y^{-1} - 2), \qquad Y = 4F^2/K_0\Delta \tag{8.41}$$

twelve saddle points at $\big|Q_p\big| = \big|Q_q\big| \neq 0$, $Q_r = 0$ ($p, q, r = x, y, z$) with a depth that lies between $E^{(1)}$ and $E^{(3)}$ (the latter is given below), and six saddle points at $\big|Q_p\big| = \big|Q_q\big| = 0$, $Q_r = [(16F^2/K_0) - (\Delta^2/F^2)]^{\frac{1}{2}}$ with a depth $E^{(3)} = \frac{2}{3}E^{(1)}$.

Since the Δ value is relatively large in this case ($\sim$2–3 eV in the $BaTiO_3$ crystal) the realization of inequality (8.39) was doubted for a long time, until it was confirmed by direct numerical calculations on this (see below) and other similar PJT systems [8.322, 8.323]. Since it has been proved that the PJTE is the only possible source of such instability, there is no ground to doubt the inequality (8.39) if the instability exists.

The cooperative interaction of these local distortions, as mentioned above, cannot be handled similarly to the CJTE because they are strongly interdependent, and the PJT electronic states form a significant bandwidth. In this case it seems more appropriate to handle the ferroelectric (antiferroelectric) distortion of the lattice as a whole. In the band-structure formulation of the

crystal as a whole [8.148, 8.324, 8.325] Q_x, Q_y, and Q_z are the optical phonon coordinates with the wave vector $\vec{q} = 0$, which describe the mutual displacements of the titanium and oxygen sublattices. Approximately, the adiabatic potential surface is qualitatively (in the sense of the relative positions of minima and saddle points) the same as in the local (titanium-site) presentation given above [8.324]. With a simple dispersion law for the band states and without dispersion of the vibronic coupling constant (see below) the authors obtained the following conditions of ferroelectric and antiferroelectric instability of a rocksalt-type diatomic lattice with valence p electrons (GeTe type) [8.148, 8.325].

For ferroelectric instability,

$$M\omega_{0\mathrm{f}}^2 < \sum_k F^2 A^{-1} \sin^2(k_x a) \tag{8.42}$$

For antiferroelectric instability,

$$M\omega_{0\mathrm{a}}^2 < \frac{1}{2}\sum_k F^2 \sin^2(k_x a)\{[\cos(k_x a) - \sin(k_x a)][\cos(k_x a) + \sin(k_x a)]^{-1} \times (A^{-1} - B^{-1}) + A^{-1} + B^{-1}\} \tag{8.43}$$

where

$$\begin{aligned} A^{-2} &= \Delta^2 + h^2 \cos^2(k_x a) \\ B^{-2} &= \Delta^2 + h^2 \sin^2(k_x a) \end{aligned} \tag{8.44}$$

and $\omega_{0\mathrm{f}}$ and $\omega_{0\mathrm{a}}$ are the bare frequencies (calculated without the vibronic coupling) of the ferroelectric and antiferroelectric displacements, respectively (analogs to the ω_0 value for the local $T_{1\mathrm{u}}$ displacements), M is the reduced mass of the elementary cell, and h is the resonance integral determining the bandwidth when an orthogonal basis is used (for a non-orthogonal basis $h' = h - S\Delta$, where S is the overlap integral).

Simplifications of the conditions (8.42) and (8.43) are possible by means of approximate summation over the k values. For $BaTiO_3$ this results in the following condition of ferroelectric instability [8.324]:

$$M\omega_{0\mathrm{f}}^2 < (2F^2/\Delta)[1 - h(h - S\Delta)/2\Delta^2] \tag{8.45}$$

or

$$M\omega_{0\mathrm{f}}^2 < 2F^2/\Delta_{\mathrm{eff}} \tag{8.46}$$

where

$$\Delta_{\mathrm{eff}} = \Delta[1 - h(h - S\Delta)/2\Delta^2]^{-1} \tag{8.47}$$

This expression is formally similar to Eq. (8.39) but with different parameters (a factor of $\frac{1}{2}$ on the right-hand side of (8.46) as compared with (8.39) emerges from the summation over k of a function of the type $\sin^2(ka)$; note that the M value on the left-hand side is also smaller than the cluster value M_0). The most important difference between (8.39) and (8.46) is in the phonon frequency ω_0 which, due to the long-range attraction forces mentioned above, is obviously lower for the coherent (ordered) displacements of all the Ti atoms with respect to the oxygen sublattice than for the displacement of one atom only. Together with the full qualitative similarity of the adiabatic potentials, this conclusion means that, as far as the internal energy only is concerned (the entropy term is ignored), the ordered distortion of the crystal as a whole is preferable (however, see the discussion below).

Numerical estimates [8.325] based on Eqs. (8.45) and (8.47) show that for reasonable values of the lattice parameters and vibronic coupling constants the lattice may become unstable with respect to ferroelectric or antiferroelectric distortion, and it has the specific features of the PJT APES described above. Figures 8.34 and 8.35 provide some illustrations for the order of magnitude of the parameters used and distortions obtained. In particular, it is seen that the calculated displacements in the minima are quite reasonable ($\sim 10^{-1}$ Å) for the parameters used, and under the condition that $\omega_{0f} = \omega_{0a}$ ferroelectric distortions are preferable rather than antiferroelectric ones. An important point here is that the increase of the bandwidth h makes the condition of both ferroelectric and antiferroelectric distortions deteriorate, and for any combination of $K_0 = M\omega_0^2$ and F there is an upper limit value of $\beta = h/\Delta$ for which the distortions disappear (Fig. 8.35). This critical value of $\beta = h/\Delta$, *ceteris paribus*, is much larger for ferroelectric distortions than it is for antiferroelectric ones.

An attempt to estimate numerical values of the parameters to check directly the condition of instability of ferroelectric crystals was made in [8.326]. For two series of perovskites, titanates $ATiO_3$ with A = Ca, Sr, Ba, and $BaMO_3$, with M = Ti, Zr, Hf, band-structure calculations were performed in the semiempirical MO LCAO extended Hückel (Hoffmann) approximation for crystal structures. The wavefunction is taken in the following form:

$$\varphi_{ik} = \sum_m C_{mi}(k) N^{-\frac{1}{2}} \sum_q b_m(\vec{r} - \vec{R}_q - \vec{R}_m) \exp[ik(\vec{R}_q + \vec{R}_m)] \tag{8.48}$$

where $b_m(\vec{r} - \vec{R}_q - \vec{R}_m)$ is the AO localized on the mth nucleus of the qth cell and C_{mi} are the LCAO coefficients. With these functions and corresponding energy gaps $\varepsilon_{pk} - \varepsilon_{ik}$ the orbital vibronic constants $\langle ik|(\partial H/\partial Q)_0|pk\rangle$ were estimated, Q being the Γ_{15} (t_{1u}-type) phonon at $q = 0$. Then the nonvibronic

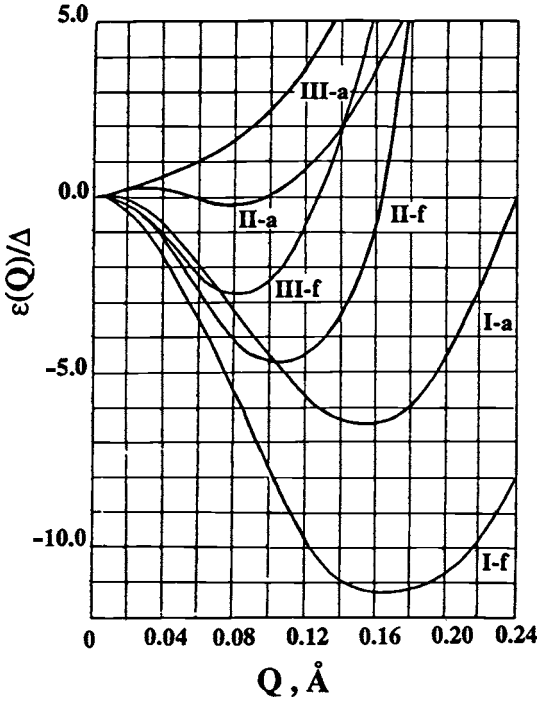

Fig. 8.34. Numerical calculations of the cross-section of the APES of a rocksalt-type crystal along the [111] direction Q for the following parameter values (in Δ units): band width $\beta = h/\Delta = 4.5$, vibronic coupling constant $F/\Delta = 3.3 \times 10^{-2}$ dyn/eV, and three values of bare force constant $M\omega_0^2/\Delta$ (in 10^6 dyn/cm eV): 5.0 (I), 7.5 (II), and 9.0(III); **f** and **a** denote ferroelectric and antiferroelectric ordering, respectively, for the same parameter values, in particular, $\omega_{0f} = \omega_{0a}$ [8.325].

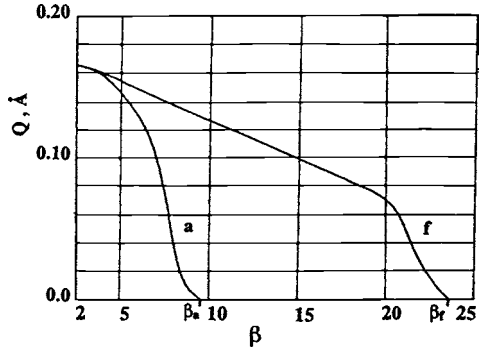

Fig. 8.35. Equilibrium ferroelectric Q_{0f} (f) and antiferroelectric Q_{0a} (a) lattice distortions as a function of the bandwidth parameter $\beta = h/\Delta$ for the same parameter values, in particular, $\omega_{0f} = \omega_{0a}$. β_f and β_a are the upper limits of bandwidth for which, respectively, ferroelectric and antiferroelectric distortions are possible [8.325].

Table 8.12. *PJT contributions of excited band states to the instability of the lattice with respect to* Γ_{15} (t_{1u})*phonon displacements at* $q = 0$ *in a series of perovskites* (*one-electron excitations are shown as* $\Gamma_i \rightarrow \Gamma_p$) *[8.326]*

$i \rightarrow p$	$CaTiO_3$	$SrTiO_3$	$BaTiO_3$	$BaZrO_3$	$BaHfO_3$
$1\Gamma_{15} \rightarrow \Gamma_{25'}$	−0.52	−0.43	−0.33	−0.08	−0.07
$1\Gamma_{15} \rightarrow \Gamma_{25'}$	−0.16	−0.14	−0.11	−0.06	−0.05
$2\Gamma_{15} \rightarrow 2\Gamma_2$	−0.24	−0.20	−0.16	−0.02	−0.02
$1\Gamma_{15} \rightarrow 2\Gamma_{12}$	−0.14	−0.13	−0.11	0.0	0.0
$2\Gamma_{15} \rightarrow 2\Gamma_{12}$	−0.35	−0.35	−0.34	−0.01	−0.01
$\sum$	−1.51	−1.33	−1.15	−0.20	−0.17
K_0	1.41	1.23	0.98	0.83	0.86
K	−0.10	−0.10	−0.17	0.63	0.69

(bare) force constant can be calculated as follows (Ω is the volume of the Brillouin zone):

$$K_0 = \boldsymbol{\Omega}^{-1} 2 \sum_{i,k} \langle ik | (\partial^2 H / \partial Q^2)_0 | pk \rangle \tag{8.49}$$

while the vibronic contribution is

$$K_v = -\boldsymbol{\Omega}^{-1} \sum_k \sum_{i,p} \left| \langle ik | (\partial H / \partial Q)_0 | pk \rangle \right|^2 \Big/ (\varepsilon_{pk} - \varepsilon_{ik}) \tag{8.50}$$

Some results obtained in this way for the above five crystals under the additional assumption that the electronic participation of the A^{2+} ion may be ignored are illustrated in Table 8.12. The calculations were carried for the interatomic distances $R(\text{Ti—O}) = 1.91$ Å, 1.95 Å, and 2.0 Å for A = Ca, Sr, and Ba, respectively, $R(\text{Zr—O}) = 2.095$ Å, and $R(\text{Hf—O}) = 2.086$ Å. The corresponding forbidden bandwidths obtained from these calculations are (in eV) 3.6 (Ca), 3.5 (Sr), and 2.9 (Ba), respectively, for the first series (the experimental values lie in the interval 1.9–3.4 eV), and much less satisfactory results for $BaZrO_3$ and $BaHfO_3$ (10.0 and 12.5 eV, while the experimental values are about 5 and 6 eV, respectively).

Concerning absolute values, the results of Table 8.12 cannot be considered sufficiently reliable, especially for K_0. Indeed, K_0 depends critically on the values of the atomic wavefunction at the nuclei (to which *ns* functions only contribute), where they are not well defined in the semiempirical method used in the calculations (see also [8.327] and the discussion in Section 4.1). Therefore the values of K_0 in Table 8.12 are rather approximate. However, the relative values of K along the series of the very similar perovskites under

consideration seem to be reasonable. They show that the instability does indeed increase toward $BaTiO_3$, with the longest Ti—O distance in the series of titanates in agreement with its best ferroelectric properties, while in the second series of perovskites $BaMO_3$ with M = Ti, Zr, and Hf, the instability decreases due to the increasing overlap of the metal valence 3*d*, 4*d*, and 5*d* orbitals, respectively, with the corresponding oxygen orbitals in the cubic configuration and decreasing vibronic coupling constant in this series (Section 8.2.5). Improvements of these calculations, including a better estimation of K_0, based on the novel contributions to the methods of calculation of PJT parameters can be obtained [8.328].

Band-structure calculations for vibronic ferroelectrics using different techniques and including also dispersion of vibronic constants have been performed multiply by different authors (see [8.148, 8.149, 8.321–8.334] and references therein).

The change of the band structure under the influence of the PJT distortions may strongly influence all the properties of the crystal that depend on the band structure. This is seen from the interaction of one-electron states $\varepsilon_1(k)$ and $\varepsilon_2(k)$ from the two mixing bands under the distortion Q,

$$\langle \varepsilon_{\pm}(k) \rangle = \tfrac{1}{2}[\varepsilon_1(k) + \varepsilon_2(k)] \pm \sqrt{\tfrac{1}{4}[\varepsilon_1(k) - \varepsilon_2(k)]^2 + \Gamma_0^2 \langle Q \rangle^2} \tag{8.51}$$

obtained also in a more rigorous self-consistent treatment [8.335], where Γ_0 is the $q = 0$ vibronic coupling constant. The temperature dependence of the order parameter $\langle Q \rangle$ determines the characteristic temperature dependence of the band structure and, in particular, the effective mass of the charge carriers [8.336]. The change of temperature may lead to essential modification of the electronic bands that changes the number of extrema of the APES and their symmetry. In its turn this influences the Van Hove singularities in the density of states. The latter should be manifested in the interband absorption, which can serve an exact method of investigation of the dispersion in vibronic problems. The anomalies of the temperature and frequency dependences of the coefficient of interband light absorption are investigated in [8.336, 8.337]. In [8.338] spontaneous birefringence in a vibronic ferroelectric was investigated. For this purpose the contribution to the optical dielectric susceptibility, renormalized by the vibronic interaction of the active bands, was calculated. Using the tetragonal phase of $BaTiO_3$ it was shown that the main aspects of spontaneous birefringence can be thought of as a natural consequence of the vibronic theory. In particular, the temperature dependence of the difference between the refractive indices is determined by the square of the order parameter in accordance with the well-known phenomenological theory.

These conclusions are essentially based on the vibronic mixing of the electronic bands and cannot be obtained from the one-band model with lattice anharmonicity. Together with other experimental data (see below) they can serve as experimental confirmation of the PJT origin of ferroelectricity.

Another example of this kind is the influence of the magnetic field on the ferroelectric phase transition. In the model of lattice anharmonicity, the magnetic field, which directly influences only the electronic subsystem, should not influence the phase transition. The influence of the magnetic field on the ferroelectric properties of the crystal is thus a direct indication of the vibronic nature of ferroelectricity.

The influence of the magnetic field on the soft-mode frequency in ferroelectrics was investigated by the method of Green's functions [8.334]. Since the quantizing magnetic field contracts the band states into Landau levels, the influence of the magnetic field on the spontaneous polarization and Curie temperature is essentially determined by the dispersion of the vibronic constant $\Gamma_q(\vec{k})$. If the vibronic constant does not increase with k, then the contraction of the band states leads to an effective increase in the energy gap between the bands, and this decreases the softening vibronic contribution to the soft-mode frequency. The resulting increase of the latter (and hence of the Curie temperature T_c) has an oscillating behavior because of the ejection of the Landau levels from the band. A strong effect should be expected for relatively large-gap vibronic ferroelectrics in which the phase transition is determined by the PJTE. The magnetic-field corrections near the point of the phase transition and the corrections to T_c are significant. Estimates made for an activated $SrTiO_3$ crystal show that the correction to the T_c value, even for magnetic fields of the order of 10^5 Oe, is important. The change of the ferroelectric properties under the influence of external magnetic fields is confirmed experimentally [8.340].

The vibronic theory was also confirmed in a set of experimental observations including the changes of the band structure of ferroelectrics at the phase transition, as well as in photoinduced effects in ferroelectrics, in particular, in the shift of the Curie temperature under irradiation [8.336, 8.341]. Other experimental evidence in support of the vibronic theory of ferroelectricity includes the interband photogalvanic effect, polar thermo-EMF and thermal conductivity, magnetization by illumination, and other effects produced by intensive electromagnetic irradiation [8.342, 8.343]. Impurity properties of the vibronic ferroelectrics are discussed in [8.343–8.345]. Note also the attempt in [8.346] to describe the domain structure of the crystal in terms of tunneling between the equivalent minima. Ferroelectricity in non-centrosymmetric crystals explained by the cooperative JTE is considered in [8.347].

A distinguishing feature of the results outlined above is that they allow, in principle, for a novel explanation of the origin of ferroelectric and other structural phase transitions. Assume first that the condition of local instability (8.39) is fulfilled. In this case the position of the Ti ion in the center of the oxygen octahedron in $BaTiO_3$, as shown above, is unstable with respect to T_{1u} distortions due to local interactions only, and they occur without any long-range forces and cooperative effects. In contrast to the theories of displacive origin of the distortions where the dipolar displacements and ferroelectricity are due to cooperative interactions only, the vibronic approach predicts for this case local distortions that exist without cooperativity and may be, or may be not ordered at higher temperatures.

If the condition (8.39) is not satisfied, the local position of the titanium ion has a minimum at the center of the octahedron and there are no local off-center displacements of each Ti ion independent of the molecular field of other ions. However, even in this case, as a result of the vibronic coupling the position of the Ti ion is softened. The softening of the Ti position with respect to the T_{1u} displacements can be easily demonstrated by means of expanding the potential (8.37) with respect to small Q_α displacements (similar to Eq. (4.58)): for nonzero vibronic coupling F the force constant in the T_{1u} direction is $K_0 - 4F^2/\Delta$ (instead of K_0), i.e., it is lowered by $4F^2/\Delta$. With the local position of the titanium atom softened but not unstable, the condition of instability of the lattice as a whole may still hold because of the above-mentioned lower value of the crystal $M\omega_0^2$ compared with the local one (see below).

The special form of the APES which emerges from the vibronic coupling with the inequality (8.39) allows a direct qualitative interpretation of all the phases observed in $BaTiO_3$ and similar systems. The main prediction of the vibronic theory concerning these phases is that only the low-temperature rhombohedral one is fully ordered, the other two ferroelectric phases being, respectively, one-dimensionally and two-dimensionally disordered, and the paraphase is three-dimensionally disordered. Table 8.13 summaries these results.

For the crystal as a whole the qualitative picture has been considered in a simple semiclassical model [8.149, 8.348] in which the phase transition is considered as occurring at high temperatures when the amplitude of vibrations in the minima of the adiabatic potential becomes sufficiently large to transfer the system from one minima to another. Obviously, by heating the system, first the lowest barrier between two nearest-neighbor minima is overcome via the orthorhombic saddle points, resulting in an average orthorhombic polarization of the crystal. At higher temperatures the next barrier at the tetragonal saddle points is surmounted, yielding an average (over four minima) tetragonal polarization. Finally, the last (highest in temperature) phase transition

Table 8.13. *Phases, phase transitions, and disorder dimensionality in $BaTiO_3$- and $KNbO_3$-type crystals predicted by the vibronic theory of ferroelectricity [8.149]*

	Phase			
	Rhombohedral	Orthorhombic	Tetragonal	Cubic
Direction of polarization	[111]	[011]	[001]	—
Dimensionality of disorder	0	1	2	3
Number of minima involved in disorder		Two, [111] and $[\bar{1}11]$	Four	Eight
Temperature of phase transition		T_c (I) <	T_c (II) <	T_c (III)

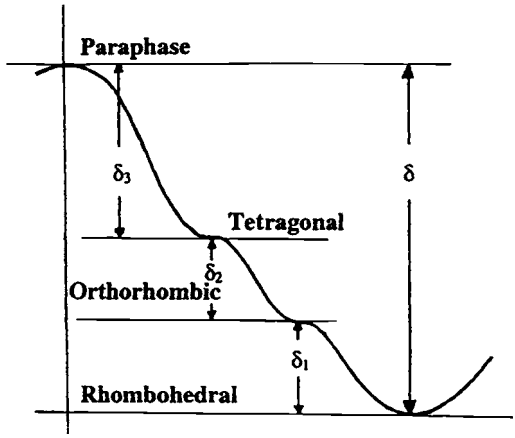

Fig. 8.36. A schematic illustration of the order–disorder phase transition in ferroelectrics. Depending on the relative positions of the saddle points (Eqs. (4.105)–(4.108)) (i.e., on the relationship among the δ_1, δ_2, and δ_3 values), some of the phases may be smeared out by vibrations [8.149].

takes place when the motion of the crystal involves all the eight minima and the lattice, on average, is in the cubic paraphase (Table 8.13).

In this treatment, also an estimation of the Curie temperature T_c is possible. It obviously depends on the parameters that determine the instability: the minima depth δ, given by Eq. (8.41), and the positions of the corresponding saddle points. Figure 8.36 illustrates this situation in a rather conventional manner (in fact the whole APES picture requires four-dimensional space). Depending on the mutual positions of the extrema points, some phases might

not be observed. This happens when the lower barriers are too small and there are no local crystal vibrations below the corresponding saddle points.

A simple modeling procedure in which the main JT features of the APES are presented by two generalized parameters [8.348] allows one to make some estimations of T_c. Using the experimental T_c values for two phase transitions in $BaTiO_3$, $T_1 = 393\,K$ and $T_2 = 278\,K$, the authors estimated the two parameters of the model and then, using the values of these parameters, they evaluated the third value $T_3 = 201\,K$, while the experimental one is $T_3 = 183\,K$. This result shows that the parameters involved and approximation made are at least not unreasonable.

Further qualitative estimates based on the strong dependence of the vibronic parameters on the interatomic distances are possible [8.149]. They explain the changes in ferroelectric properties along the series of titanates of Ca, Sr, and Ba in which the Ti—O distance R increases from left to right: $CaTiO_3$ is not ferroelectric, $SrTiO_3$ is a virtual ferroelectric (it becomes ferroelectric at very low temperatures, under pressure, or with appropriate impurities), while $BaTiO_3$ is ferroelectric at room temperature. A similar effect can be seen along the series of perovskites $BaMO_3$ with M = Ti, Zr, and Hf, in which the active orbital of the metal (which produces the vibronic contribution) changes from $3d$ to $4d$ and to $5d$, respectively, and the atomic radius of the metal increases. In effect this is similar to a decrease of the metal–oxygen distance, which decreases the Curie temperature and hence makes the ferroelectric properties deteriorate from left to right in this series.

The next step in the vibronic theory was reached in more recent times when it was shown that the instability of the high-symmetry configuration produced by the vibronic coupling to excited electronic states is the only possible source of instability of any polyatomic system (Section 4.1) [8.196, 8.322, 8.349]. In other words, if the configuration of the system is unstable, it is due to, and only to, the corresponding vibronic coupling. The proof of this statement is discussed in Section 4.1. As shown there, the local PJT instability occurs due to the nonzero overlap between the $3d_\pi$ orbital of the Ti ion and an appropriate combination of the $2p_\pi$ orbitals of the oxygen atoms produced by the Ti off-center displacement. It creates additional covalent bonding (Eq. (4.31)), which is the main effect, and a much smaller contribution of the polarization of the oxygen atoms produced by the displacement of the Ti ion (Eq. (4.29)). For $BaTiO_3$ the polarization is an order of magnitude smaller than the covalency contribution (see Table 4.1).

Even more important is the fact that both types of vibronic contribution to the lattice instability, new covalency (4.31) and atomic polarization (4.29), are due to local interactions. It follows that all the long-range interactions in the

lattice are included in the nonvibronic part K_0 of Eq. (4.17). Together with the conclusion of $K_0 > 0$ and $K_v < 0$ we come to the statement that lattice instability is triggered by, and only by, local (mainly covalent) interactions. No distortion of the lattice and hence no displacive phase transitions can occur as a result of just the long-range attractive forces without the local PJTE instability that leads to sufficient additional covalent bonding. This local aspect of the lattice instability explains also the origin of the order–disorder nature of the so-called "displacive" phase transition [8.350].

However, the cooperativity is still very important because it determines the value of K_0 or $M\omega_0^2$ (cf. Eq. (8.45)), where ω_0 is the optical primary (bare) phonon frequency, which may be much lower than that of the local t_{1u} vibration, thus facilitating the instability condition (8.39) or (8.46). But ω_0^2 cannot become negative without the vibronic coupling. There may be a situation when for a single center the K_0 value is too large and condition (8.39) does not hold, while for a larger number of ordered cells it does hold [8.350]. If condition (8.46) holds for the crystal as a whole, it explains the origin of the lowest fully ordered rhombohedral phase, but then the partially and fully disordered phases cannot be explained as due to the averaging over near-neighbor minima (the energy barrier of the crystal as a whole is too high). The intermediate condition when the instability holds for clusters with a limited number of ordered cells was assumed for $BaTiO_3$ to explain the observed entropy changes at the phase transition [8.351, 8.352]. Figure 8.37 illustrates the formation of the orthorhombic phase from the JT T_{1u} distortions which are ordered in clusters [8.351].

The qualitative aspect of the above description of the origin of ferroelectricity and phase transition in $BaTiO_3$-type crystals was given already in the first publication on this subject in 1966 [8.317] when it was in complete contradiction to the dominating (at that time) theories of displacive phase transitions. Remarkably, in 1968 the predictions of the PJTE theory were qualitatively confirmed by X-ray diffuse scattering [8.351] (the authors [8.351] claim that they did not know the works [8.317] and [8.324] published, respectively, two years and one year before their paper). Nowadays many results from experimental works performed by different methods in total undoubtedly confirm all the main predictions of the PJT vibronic theory: some of these works [8.351–8.361] are listed in Table 8.14. Further developments, improvements, and extensions of the theory of ferroelectric phase transitions based on the CPJTE were given in a variety of more rigorous theoretical investigations and numerical calculations (in addition to the references above see, e.g., [8.362–8.369] and references therein).

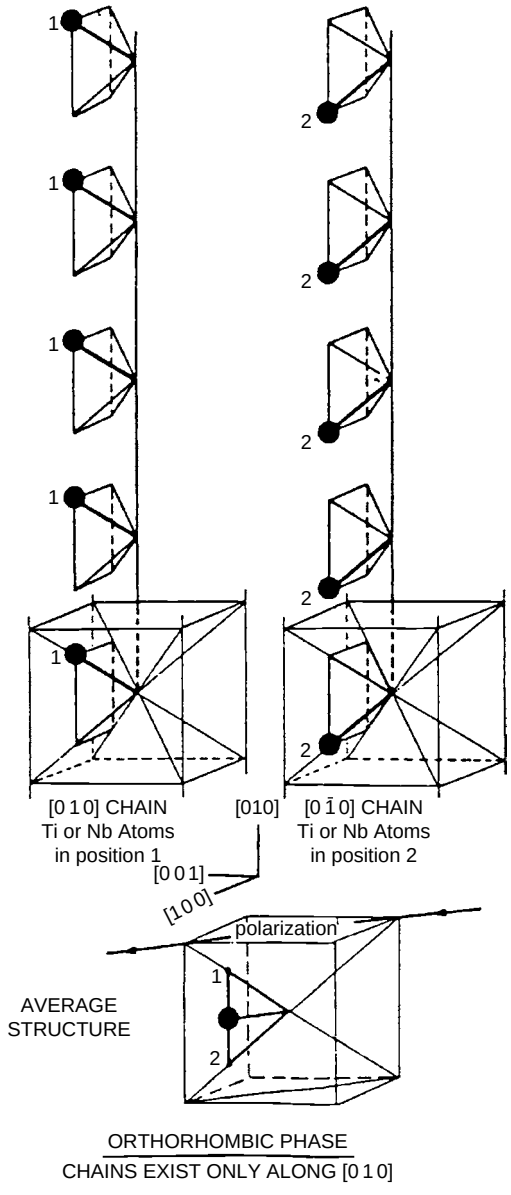

Fig. 8.37. An illustration of the formation of the orthorombic phase in $BaTiO_3$- or $KNbO_3$-like perovskite crystals. Two fragments (clusters) of the crystal with the C_2 axis of polarization (orthorhombic phase) and the ordered off-center displacements of the Ti or Nb ions toward the JT near-neighbouring minima along $[0\bar{1}0]$ and $[0\bar{1}0]$, respectively, are shown. The averaged structure, or local fast transitions between the two distorted configurations, make the crystal structure disordered along the direction $[0\bar{1}0]$ perpendicular to C_2. [351]

Table 8.14. *Experimental evidence of the local origin of distortions and order–disorder nature of phase transitions in "displacive" ferroelectrics (from [8.350])*

Authors, year	Method, system	Main result
Comes, Lambert, and Guinier [8.351], 1968	X-ray diffuse scattering, $BaTiO_3$	Qualitative confirmation of all the main predictions of the vibronic theory for BaTiO3
Quittet *et al.* [8.353], 1973	Raman spectra, $BaTiO_3$, $KNbO_3$	Polar distortions in the cubic paraphase
Burns and Dacol [8.354], 1981	Optical refractive index, $BaTiO_3$	Nonvanishing component $\langle P^2 \rangle$ in the cubic phase
Gervais [8.355], 1984	Infrared reflectivity, $BaTiO_3$	Qualitatively the same
Ehses *et al.* [8.356], 1981	X-ray, $BaTiO_3$	Strong order–disorder component in the cubic phase
Ito *et al.* [8.357], 1985	X-ray, $BaTiO_3$	[111] Displacement of Ti in the paraphase at up to 180 K above T_c
Muller *et al.* [8.358], 1986	ESR with probing ions, $BaTiO_3$, $KNbO_3$	[111] Displacements in the rhombohedral phase and reorientations in the orthorhombic phase, $10^{-10}\,s < \tau < 10^{-9}\,s$
Hanske-Petitpierre *et al.* [8.359], 1991	XAFS, $KNb_xTa_{1-x}O_3$	[111] Displacements in all the three phases for any $x > 0.08$; mean-square displacements much smaller due to dynamics
Dougherty *et al.* [8.360], 1992	Femtosecond resolution of light scattering, $BaTiO_3$, $KNbO_3$	No relaxational modes which might exclude the local distortion model
Sicron *at al.* [8.361], 1994	XAFS, $PbTiO_3$	Ti and Pb ions are displaced in the paraphase up to 200 K above T_c

8.4 The JTE in high-temperature superconductivity and colossal magnetoresistance

The origin of observable properties of solid-state systems cannot be revealed without involving their basic features, in particular, the electron–phonon coupling. At first sight this statement looks trivial. Indeed, the interaction between the electrons and phonons was taken into account beginning with

the very onset of the solid-state theory. In application to metals this electron–phonon coupling was literally understood as a rather weak interaction of the band electrons with an averaged "bath of phonons," and the electric resistance was presented as due to the scattering of the conduction electrons on these phonons. Applied to superconductivity (SC) in the *Bardeen–Cooper–Schrieffer (BCS) theory*, this approach explained well the experimental data on low-temperature SC as originating from the cooperative interaction of *Cooper pairs* of electrons formed by such electron–phonon coupling [8.370].

From the modern point of view, after the discovery of high-temperature SC (HTSC) the BCS theory may be considered as approximately correct in narrow limits of its application, but not sufficiently accurate beyond these limits. The inaccuracy is due to the neglect of the JTE, meaning ignoring the details of the electron–phonon interaction, in particular, the nonadiabatic influence of the electronic states on the lattice structure and low-symmetry phonons and the back influence of the modified lattice and phonons on the electronic states. Indeed, as shown above in Section 8.2.5, the PJT interaction between the close-in-energy occupied and unoccupied band states that is induced by low-symmetry phonons in combination with the JT coupling between such degenerate and almost degenerate states at the Fermi level under certain conditions distorts the reference lattice configuration by means of a rebounding process (Section 4.1). This leads also to significant changes in the electronic energy spectrum.

As shown in Section 8.2.5, the band JTE, as in all the other cases of the JTE, is essentially dependent on the magnitude of the JT electron–phonon coupling constant. For metals with broad bands and almost completely delocalized electronic states the JT electron–phonon coupling constant is small and the JTE implications can be ignored. This explains the success of the BCS theory (which does not take into account the JTE) for broad-band metals and low temperatures. Moving to crystals with narrower bands and more localized electronic states, we come to stronger JT electron–phonon coupling with implication of the JTE, which involves essentially low-symmetry phonons.

The narrower the conduction band (up to a certain limit), the stronger the electron–phonon coupling, leading to a stronger JTE. For narrower bands the JT electron–phonon coupling constant and the JTE again become small; narrow bands limit also the mobility of the carriers. This window in conduction bandwidth that facilitates the band JTE may be expected to be most important in HTSC. A direct exploration of this issue, to the best of our knowledge, has not yet been performed.

In general, the JTE and PJTE are most important when there are degenerate and/or relatively close-in-energy electronic states, which are sufficiently strongly mixed by corresponding phonons. Transition metal (and other

similar) compounds with open shells and/or low-lying excited states, and with sufficiently narrow (but not very narrow) bands in the crystal state are among the primary targets of strong band JTE and PJTE. If we assume that HTSC is strongly related to electron–phonon coupling, then it should be found among the properties most influenced by the JTE. In view of the basic features of the JTE and experience with their applications, it would be a puzzling surprise to find out that the JTE is not significant in this phenomenon. On the contrary, the known attempts to apply the JT approach to SC, especially to HTSC, seem to be very promising. Earlier attempts to consider the JTE implications in traditional SC can be found in [8.371, 8.372].

To the best of our knowledge, so far there is no comprehensive theory of HTSC to explain all its features from a unique point of view. However, there are many publications devoted to important particular aspects of the problem, and in many of them the JTE plays the leading role. First we refer to the authors of the discovery of HTSC [8.373], whose leading idea in search of novel superconductors with high transition temperatures was the JT polaron. The authors refer to the work [8.374], which provides a better understanding of the conditions for much stronger electron–phonon coupling than in the BCS theory. Considering a linear chain of JT centers, it was shown [8.374] that the behavior of the conducting electron depends on the balance between the JT stabilization energy E_{JT} on each center, which tends to localize the electron, and the delocalizing intercenter tunneling that forms the band width t. If $E_{\mathrm{JT}} \ll t$, the JT distortions only slightly influence the conductivity. In the opposite case $E_{\mathrm{JT}} > t$ the electron becomes coupled with the JT distortion, and they move together along the system as a JT polaron with an increased effective mass.

The relation of this result to superconductivity lies in the fact that the JT stabilization energy may reach several thousand cm^{-1}, which is two orders of magnitude larger than that produced by the non-JT ("classical") electron–phonon coupling with the bath of phonons in broad-band nonpolar systems. On the other hand, the effective electron–electron attraction (Fröhlich pairing) that leads to the formation of Cooper pairs can be obtained by extracting the JT modes of the electron–phonon coupling in the second-order perturbation theory [8.375]. Therefore the strong electron–phonon coupling in the JT polaron can be considered as an important factor in HTSC. This stimulated further exploration of JT polarons and excitons [8.376–8.380].

However, the electron–phonon coupling is not the only factor that influences the superconductivity, and it does not determine the SC transition temperature directly. The path from local JT distortions to formation of polarons via lattice dynamics, to formation of Cooper pairs, their density, stability, and mobility, temperature dependence, to perfect diamagnetism, to

structural phase transition, and finally to SC, is very long and thorny, and therefore a comprehensive JT theory of this important phenomenon has not yet been accomplished. There are hundreds of publications on this subject, and there is no way (and necessity) to cite them all here. The references [8.371–8.421] are a part of them reflecting the up-to-date picture. Below is a brief outline of the content of several works as examples of the JTE in superconductivity, which, however, does not pretend to be the best choice of such works; neither do they fully embrace the topic as a whole (publications on this subject continue to appear regularly).

The next step after the formation of JT polarons, outlined above, is the interaction between them resulting in Cooper pairs, the carriers in both low- and high-temperature SC (see, e.g., [8.422] for a review of experimental data on this question). In the overwhelming majority of the papers the authors consider cuprates with a perovskite structure of the type $La_{2-x}Sr_xCuO_4$ and $YBa_2Cu_3O_7$ with Cu ions in tetragonally distorted octahedra of oxygens. The octahedra are strongly elongated, so the picture is as if the Cu ions occupy the centers of squares in CuO_2 layers that are parallel in the crystal and separated by layers of the other ions.

The one-electron states at the Fermi level ε_F include the atomic Cu^{2+} states with the wavefunctions d_{z^2} (d_ϑ) and $d_{x^2-y^2}$ (d_ε) hybridized with oxygen p functions, which in the regular octahedron form the degenerate E term. The distorted octahedron emerges as a result of the JT $E \otimes e$ problem on each center (Section 3.2) and their cooperative ordering in the crystal (Section 8.2). Assuming that in spite of the energy gap between these states in the elongated octahedron they still may coincide in some regions of the Brillouin zone, the authors [8.381] calculated the aforementioned second-order (Fröhlich) pairing interaction energy of the electrons in these two states via the JT distortions. Since the d_ϑ state is coupled to the Q_ϑ distortion coordinate, while the d_ε state distorts the system in the Q_ε direction, and the change of the Cu—O distance in these two coordinations has opposite signs, the pairing interaction emerges with a negative sign relative to the classical Cooper pairing that ignores the JTE. However, for non-cubic symmetry this results in an attractive pairing interaction and the pairs have a spin of zero. Numerical calculations of the pairing energy and the superconducting gap parameter for some simplified conditions show that pairs are of short range and relatively stable against lattice distortions [8.381] (see also [8.382]).

The results of attempts to calculate the pairing energy of two hole carriers that form two JT polarons, taking into account their multimode nature in the crystal (Section 5.3), are given in [8.383]. In addition to the JTE in the octahedral CuO_6 site of the La_2CuO_4 lattice that leads to strong Q_ϑ elongation and formation of

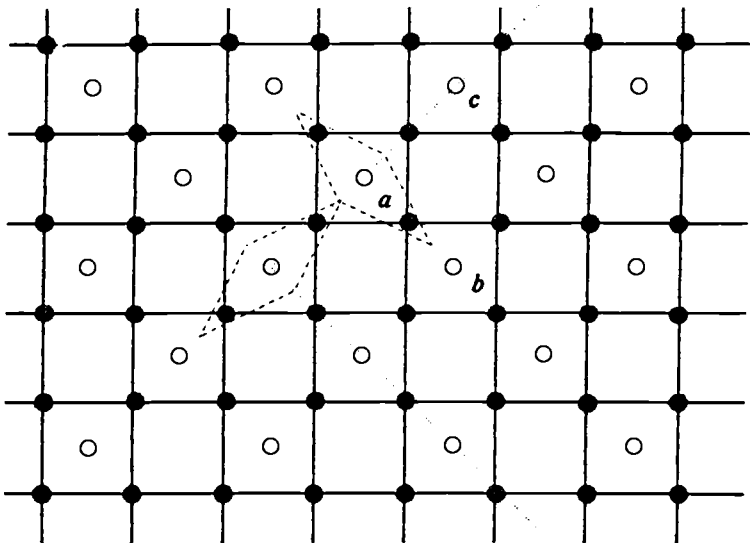

Fig. 8.38. b_{1g}-Type distortions around the copper centers with localized carriers in the conducting CuO_2 plane shown by a dashed line; a, b, and c indicate three versions of possible localization of the second carrier [8.383].

the CuO_2 layers, the authors [8.383] take into account the PJTE in the square-planar CuO_4 clusters in which the two electronic states ${}^1A_{1g}(d_\vartheta)$ and ${}^1B_{1g}(d_\varepsilon)$ mix under $Q_\varepsilon(b_{1g})$ displacements. Figure 8.38 illustrates the distorted rhombic centers and their antiferrodistortive arrangement due to their interaction. The additional hole formed by doping changes the overall electronic distribution with the result that the CuO_6 and CuO_4 clusters relax to new interatomic positions which can be taken into account by two additional constants of coupling to the totally symmetric displacements, a_{1g} and a'_{1g}, respectively. The vibronic problem thus becomes $({}^1A_{1g} + {}^1B_{1g}) \otimes (a_{1g} + a'_{1g} + b_{1g})$.

The interaction with the continuum of the three active modes in the crystal was taken into account as described in the multimode problem in Sections 3.5 and 5.5 [8.423]. Using the results described in Section 5.5 and presenting the pairing energy as $E_{\text{pairing}} = E_{\text{int}} - 2E_0$, where E_{int} is the energy of two interacting multimode JT polarons and E_0 is the energy of a single polaron in the crystal, the authors [8.383] got the following expression:

$$E_{\text{pairing}} = -\frac{1}{2}\sum_{\Gamma,\Gamma'} F_\Gamma F_{\Gamma'} \sum_{j,i\neq j} \omega_{ij}^{-2}(\Gamma,\,\Gamma') - \frac{1}{8}\frac{\Delta^2}{F_{B_{1g}}}\Bigg[\sum_i \Bigg(\sum_{j,\Gamma} F_\Gamma \omega_{ij}^{-2}(B_{1g},\,\Gamma)\Bigg)^{-1} - 2[F_{1g}\omega_{ij}^{-2}(B_{1g},\,B_{1g})]^{-1}\Bigg] \tag{8.52}$$

Here, in addition to the three vibronic coupling constants F_Γ for $\Gamma, \Gamma' = a_{1g}, a'_{1g}, b_{1g}$ (it is assumed that they are approximately the same in the electronic A_{1g} and B_{1g} states, as confirmed by numerical calculations, see below) and the energy gap Δ between A_{1g} and B_{1g} states, the crystalline multimode average frequencies ω_{ij}^{-2} of the type (5.86) are employed, but for two interacting centers instead of one in Eq. (5.86) (for one center ω_{11}^{-2} is the inverse force constant):

$$\omega_{ij}^{-2}(\Gamma, \Gamma') = \sum_\kappa a_\kappa(i, \Gamma) a_\kappa(i, \Gamma') \omega_\kappa^{-2} \tag{8.53}$$

where $a_\kappa(i, \Gamma)$ is the Van Vleck coefficient in the expansion (3.100) of the local symmetrized coordinates over the crystalline coordinates q_κ (Section 3.5),

$$Q_\Gamma = \sum_\kappa a_\kappa(\Gamma) q_\kappa \tag{8.54}$$

and ω_κ are the phonon frequencies.

Equation (8.52) is obtained as an expansion with respect to $\frac{1}{8}(\Delta/F_{B_{1g}})^2$ (note the mass-weighted units for which $F^2\omega^{-2}$ is energy). It is seen that the pairing energy increases with increasing PJT coupling constant $F_{B_{1g}}$.

Estimating the a_κ coefficients in the approximation of a monatomic lattice [8.424], using the Debye model of lattice vibrations, and performing numerical calculations of the electronic structure and vibronic coupling constants, the authors [8.383] estimated the pairing energy (calculations for clusters in the $La_{2-x}Sr_xCuO_4$ system were carried out in the semiempirical extended Hückel approximation with self-consistency for charges and electronic configuration). For the second hole in the positions a and c with respect to the first one in Fig. 8.38, $E_{\text{pairing}} \sim -10^2\,\text{cm}^{-1}$, while for the second hole in the position b $E_{\text{pairing}} \sim 10^{-2}\,\text{cm}^{-1}$ (meaning weak repulsion).

These estimates were used afterwards in a more elaborate model of the JTE in cuprate HTSC [8.384]. This model is based on the assumption that the oxidation of the parent-phase antiferromagnetic $(CuO_2)^{2-}$ units in $La_{2-x}Sr_xCuO_4$ creates δ holes $(CuO_2)^{-(2-\delta)}$ which, involving the PJTE of the type $(A_{1g} + B_{1g}) \otimes b_{1g}$, stabilize large PJT polarons containing $n = 5$–7 Cu centers. Since the hole produced by the dopant may spread over more than one center, the difference in occupation numbers of the mixing orbitals a_{1g} and b_{1g} influences directly the vibronic coupling on each center (Eq. (2.27)). Using orbital vibronic constants (Section 2.3) one can express the total vibronic coupling constant for each center $F_{B_{1g}}$ as proportional to its corresponding orbital occupancy, $F'_{B_{1g}} \approx F_{B_{1g}}/n$. With this estimate and using equations of the type (8.52)–(8.54) the authors [8.384] calculated the energy E_n of an

n-center PJT polaron presented as a sum of the contributions of individual centers E_0 and their interaction E_{int} (cf. the one-center one-mode expression (4.62); some indices are omitted):

$$E_n = E_0 + E_{\text{int}} \approx n\left[-\frac{1}{2}\sum_{\Gamma=A_{1g},B_{1g}}\left(\frac{F_\Gamma}{n}\right)^2\omega_{11}^{-2}(\Gamma) - \frac{1}{8}n^2\left(\frac{\Delta}{F_{B_{1g}}}\right)^2\frac{1}{\omega_{11}^{-2}(B_{1g})}\right] + n(n-1)\left[-\frac{1}{2}\sum_{\Gamma=A_{1g},B_{1g}}\left(\frac{F_\Gamma}{n}\right)^2\omega_{\alpha\beta}^{-2}(\Gamma) - \frac{1}{8}n^2\left(\frac{\Delta}{F_{B_{1g}}}\right)^2\frac{1}{\omega_{\alpha\beta}^{-2}(B_{1g})}\right] \tag{8.55}$$

where $\omega_{ij}^{-2}(\Gamma) = \omega_{\alpha\beta}^{-2}(\Gamma)$ is taken the same for all the pairs of centers α and β in the polaron and $\Delta/F_{B_{1g}}^2\omega_{11}^{-2}(B_{1g})$ is assumed to be small. It is seen that an increase of the polaron size (the number of centers n in the polaron) reduces the first terms in the two brackets of Eq. (8.55), and increases the smaller second terms. Therefore the inequality $E_n - E_1 < 0$ determines the lower limit $n = n_{\min}$ for the polaron size. On the other hand, the PJTE criterion (4.6) limits the upper size of such a polaron since the vibronic constant $F'_{B_{1g}} = F_{B_{1g}}/n$ should satisfy the condition $F_{B_{1g}}^2/n^2\omega_{11}^{-2}(B_{1g}) > \Delta$. Using numerical estimates for La_2CuO_4 from [8.383], the authors [8.384] found that the two inequalities above are satisfied for $6.7 > n > 5.6$. This correlates well with the experimentally measured mean size of $n = 5.3$ copper centers per carrier [8.425] (see also [8.426, 8.427]). Figure 8.39 illustrates such an antiferrodistortive ordered PJT polaron with $n = 6$. The estimations yield $T_p \approx 850$ K for the critical temperature of its stability [8.384].

The effective mass of this polaron is relatively large, raising the question of its mobility. However, the assumption in [8.384] is that in the conductivity under consideration the polaron is not moving as a whole, but performing some "crawling" motions by means of successive small steps of tunneling between different Cu—O bond lengths. At the polaron border the Cu—O bond is longer than the next one in the non-polaron neighborhood, and there is a barrier to inclusion of the next cell into the cooperative distortion. But by distorting one next bond in the front of the polaron in the direction of motion and relieving a similar distorted bond in the back of the polaron, the latter moves without changing all the other distorted bonds inside the polaron. This means that the PJT large polaron can move in piece-wise tunnelings of a fraction of itself in which its effective mass is much smaller than when the JT polaron is moving as a whole. Calculations of the bond tunneling using this scheme [8.384] yield for the mobility of the carriers a value of 1–10 $\text{cm}^2/\text{V s}$,

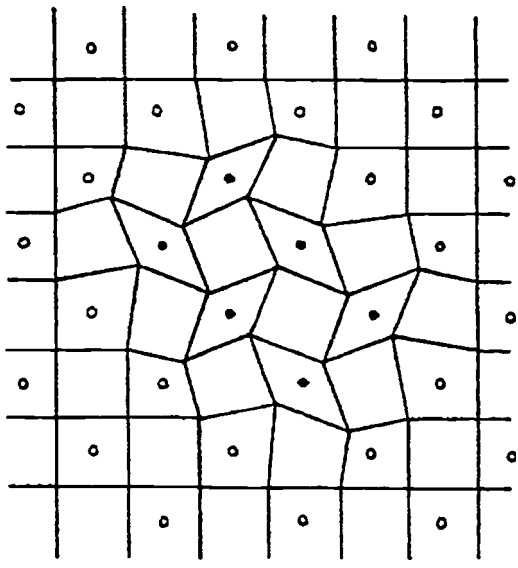

Fig. 8.39. A large six-copper polaron formed by b_{1g} distortions in the CuO_2 layer. Filled circles represent the six copper atoms that share a hole; open circles correspond to regular Cu atoms. (Reprinted with permission from [8.384]. Copyright 1997 Elsevier Science Publishers.)

which is in accord with experimental data. This explains also the linear increase of resistance with temperature at $T > T_p$.

Finally the most important problem of inter-polaron interaction at higher concentrations resulting in Cooper pairing and superconductivity was also considered in this paper in detail [8.384]. There is an attractive force between the polarons due to their cooperative interaction tending to form a unique antiferrodistortive ordered lattice (and in this way gaining elastic energy) and a repulsive force at the border between the polarons emerging from the overall shortening of the Cu—O bonds (a_{1g} distortion) due to the hole formation. It was shown that these two counteracting tendencies can be satisfied simultaneously at a certain concentration and temperature $T_d \geq T_c$ by formation of *polaronic stripes*. They consist of pairs of polarons ordered alternately along the [100] and [010] axes and forming zigzag chains parallel to a $\langle 110 \rangle$ axis of a CuO_2 plane with parent-phase stripes between the polaronic stripes (Fig. 8.40).

These stripes form an ideal superstructure for superconductivity. Indeed, with the two polarons in the unit cell the superconductive current consists of pairs of charge carriers which below T_d move freely along the stripes: the creation of an ideal superstructure with renormalized charge carriers together with the PJT vibronic coupling eliminates any possibility of scattering (in conventional superconductors simple Cooper pairing eliminates the scattering

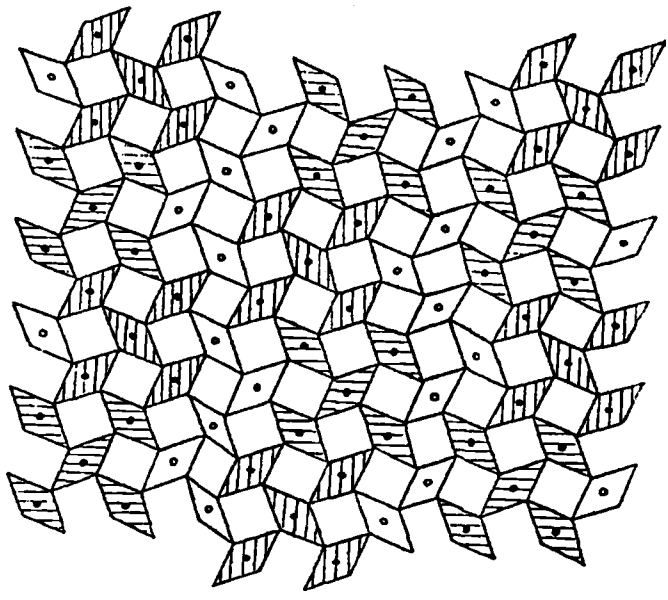

Fig. 8.40. The stripe formation from five-copper polarons resulting in a superstructure in the CuO_2 plane produced by the phase transition below T_d. Near-neighbor polarons are shadowed differently to make them visibly distinguishable. (Reprinted with permission from [8.384]. Copyright 1997 Elsevier Science Publishers.)

from existing lattice imperfections). The formation of stripes is supported experimentally (see [8.428] and references therein). For JT induced stripes formation see also [8.385].

The operation of PJT in-plane distortions as a driving force in the HTSC of single-layered SC of the type $La_{2-x}Sr_xCuO_4$ was recently confirmed in neutron-spectroscopic measurements [8.386]: in $La_{1.81}Ho_{0.04}$ $Sr_{0.15}CuO_4$ there is an oxygen $^{16}O \rightarrow {}^{18}O$ isotope shift of the pseudo-gap-formation temperature $\Delta T_O^* \approx 10$ K, whereas no shift was observed in $^{63}Cu \rightarrow {}^{65}Cu$ substitution, $\Delta T_{Cu}^* \approx 0$ K. This shows explicitly that the in-plane distortion due to the oxygen (not Cu) displacements are responsible for the pseudo-gap formation in these systems. In the two-layered superconductor $HoBa_2Cu_4O_8$ $\Delta T_O^* \approx 50$ K and $\Delta T_{Cu}^* \approx 25$ K, meaning that the other JT modes are also involved in the HTSC in this crystal (see also [8.429] for comparison). The case of isotope effects in superconductivity being due to nonadiabacity is considered in [8.387].

The local structural distortions in HTSC cuprates are assumed to be accompanied by dynamic charge-density waves (or fluxes), which were shown [8.388] to be associated with the $E \otimes e$ JT problem in the electronic subsystem. The authors relate this effect to the Berry-phase problem in the solid state (Section 5.7). In combination with the Cu—O breathing and other modes this

leads to some relations of the charge-density waves with stripe formation and the superconducting gap.

An important phenomenon that accompanies the HTSC is the tetragonal-to-orthorhombic ($T \rightarrow O$) phase transition. As shown in Sections 8.2 and 8.3, structural phase transitions in crystals are of vibronic nature. The vibronic origin of the T–O transition was subjected to several investigations [8.389–8.393]. In their majority these works attribute the phase transition to the PJTE on the two HOMO–LUMO states (or bands) emerging from the Cu^{2+} atomic d_ε and d_ϑ states that mix under b_{1g} distortions, processing this basic idea by different approaches. As shown in Sections 8.2 and 8.3, the temperature of phase transition depends on the PJT energy gap and coupling constants, as well as on the cooperative interaction. Since the occupation of these Fermi-level orbitals depends on the holes formed by doping, the latter influences the phase transition essentially. In particular, it was shown [8.390] that the reentrant $O \rightarrow T$ phase transition observed at lower temperatures in La–Ba–Cu–O superconductors can be explained in this way (see also Section 8.2.3). Indeed, the hole decreases the population of the JT-active energy levels that produce the PJTE, and at a large enough doping concentration may quench the $T \rightarrow O$ phase transition at lower temperature, resulting in a reentrant $O \rightarrow T$ structural phase transition [8.390]. Such a reentrant $O \rightarrow T$ transition was indeed observed experimentally in $La_{1.90}Ba_{0.10}Cu_2O_4$ [8.430].

In almost all the above references there are attempts to link the $T \rightarrow O$ structural phase transition to the superconductivity, as well as to find similarities between superconductivity and ferroelectricity (Section 8.3), in particular, involving the two-band theory in a way similar to the vibronic theory of ferroelectricity [8.391–8.394]. While there are some interesting relations between HTSC and $T \rightarrow O$ transition, no direct correlation between them has been revealed so far, since they take place at different temperatures. This is of no surprise because, although both these phenomena are triggered locally by the same electronic structure and PJT vibronic coupling, the cooperative interactions between the local distortions that lead to HTSC and $T \rightarrow O$ transitions are different. The phase transition from a symmetric superconducting order parameter to a broken-symmetry one in thin mesoscopic superconductors has been shown to follow a PJT-like mechanism [8.393]. For more discussion of JT topics in superconductivity see in [8.394].

An alternative approach to the HTSC problem is suggested [8.395, 8.396], in which instead of BCS electron pairing, or JT polaron pairing, two-electron bonding–antibonding geminals with lattice Bloch sums are introduced. Their RT (and other vibronic) coupling to the corresponding phonons is explored, and it is shown that under cyclic boundary conditions of the finite crystal it

produces electron–hole pairs with vibronic zero pseudo-angular momentum as possible HTSC carriers (instead of the free-electron zero space momentum in the Cooper pairing).

There is a series of works devoted to detailed theoretical and experimental investigation of JT-driven local structural peculiarities in HTSC crystals and their possible relation to the superconductivity [8.397–8.402]. In $LaCoO_3$, using neutron-scattering measurements, it was shown that the spin state changes with temperature, increasing the occupancy of the intermediate spin state that is JT active in e_g coupling. In $La_{1-x}Sr_xCoO_3$ the lattice dynamics changes with doping in accordance with local JT distortion of the intermediate spin state [8.397, 8.398]. For DFT calculations of JT distortions in CuO_6 clusters of La–Ba–Cu–O superconductors see in [8.400]. Using XAFS experiments on $La_{2-x}Sr_xCuO_4$ it was shown [8.401] that the apical oxygens near the Sr atom have a double-well potential formed by two coexisting spin-differentiated (singlet and triplet) JT distortions of Sr octahedra. Depending on the hole orbital residence, the octahedron is either longer or shorter than that of the undoped crystal.

Electronic structure and orbital vibronic coupling (Section 2.3) were analyzed for the cluster $Cu_4O_{12}H_8$ in copper oxides [8.402]. Combined structural and spectroscopic investigation of $La_{1+x}Sr_{1-x}Ga_{1-x}Cu_xO_4$ and K_2NiF_4-type perovskites [8.403] revealed a series of JT features possibly related to superconductivity.

In alkali-metal-doped fullerides of the type A_xC_{60} ($A = K$, Rb, Cs), some of which show relatively high-temperature SC ($T_c \sim 30$–$40\,K$ in A_3C_{60}), the excess electrons in C_{60}^{n-} occupy the degenerate t_{1u} orbitals. As mentioned in Section 7.5.3, the ground state of C_{60}^{3-} is nondegenerate, so at first sight only the PJTE is operative. The resulting distortions are determined by the interplay of vibronic coupling and interelectron repulsion. To attribute the superconductivity of A_3C_{60} to the JT effect on the t_{1u} states, the JT distortions as a function of the t_{1u} occupancy and some other parameter relations were estimated [8.404]. A more elaborate consideration [8.405, 8.406] shows that in this system the electron correlation effects are most essential, producing (in combination with the vibronic coupling) disproportionation of the electronic occupancy of the LUMO band structure (Section 7.5.3). The latter splits into three similar subbands with local occupations of the three t_{1u} orbitals equal to 2, 1, and 0, respectively (instead of the (1, 1, 1) occupation that results in a nondegenerate state); it takes place because in the former case each two-electron repulsion is 12/15 times smaller than in the latter. This disproportionation results in nonzero JTE, producing local distortions on each site, inhomogeneous charge distribution among the carbon atoms, and low-frequency reorientation modes, with corresponding consequences for the superconductivity.

The joint effect of correlation and vibronic interaction was also considered in [8.407] to explain the insulator properties of A_4C_{60}, which are in contrast with the superconductor A_3C_{60}. By calculating the structure of the lowest unoccupied band including all essential interactions the authors showed that there is a JT-induced transition from a Mott–Hubbard to a band insulator state.

In another investigation of the role of the JTE in the superconductivity of the systems A_xC_{60} [8.408] calculations were carried out in which the interaction between the electrons and the JT phonons is taken into account simultaneously "on an equal footing," in fact without their adiabatic separation. Since the electronic bandwidth W in these systems is of the same order as the phonon frequencies, the Eliashberg theory [8.375] does not work well, meaning that lower values of T_c of superconductivity should be expected. In the authors' calculations [8.408] the electron–phonon interaction is not separated from the Coulomb interaction, so the T_c is not expected to be lower than in the Eliashberg theory. It is shown that the JT phonons induce a local intramolecular pairing, while the requirement of coherence throughout the solid yields a very strong doping dependence of T_c (see also [8.409]).

For MgB_2, in which anomalous two-gap superconductivity was observed, the $E \otimes e$ JTE produced by the coupling of two degenerate p_σ orbitals of the two-dimensional graphite-type B layer to the doubly degenerate e_{2g} vibrations was considered in the pseudospin model [8.410], and it was shown that the hopping motions of the holes in the p_σ states, constrained by the accompanying phonons, result in a nontrivial superconducting state with multiple order parameters.

Papers [8.411] are devoted to the origin of superconductivity in a series of planar polyacenes (naphthalene, anthracene, tetracene, pentacene, etc.), in which the superconductivity is assumed to take place in their anion or cation state, and in B,N-substituted acenes. The authors involve the orbital vibronic coupling theory (Section 2.3), calculate numerically the orbital and total electron–phonon coupling constants, and estimate the expected T_c using modified Eliashberg formulas. For more on earlier and further contributions to the JTE in problems related to superconductivity see in [8.412–8.421].

The *colossal magnetoresistance* of a series of manganite perovskites of the type ABO_3 (see [8.431–8.435]) is yet another recent discovery which is explained by involving the JTE. There are quite a few publications that use the JTE theory to reveal the origin and some detailed structural, electronic, and spectroscopic properties of such materials (see [8.436–8.472] and references therein).

The colossal magnetoresistance was observed first [8.431, 8.432] as a strong variation of the electrical resistance with the magnetic-field intensity (see, e.g., Fig. 8.41 for illustration of this effect in $La_{0.75}Ca_{0.25}MnO_3$ [8.459]). In the materials with the general formula $R_{1-x}A_xMnO_3$, where R is a rare-earth element

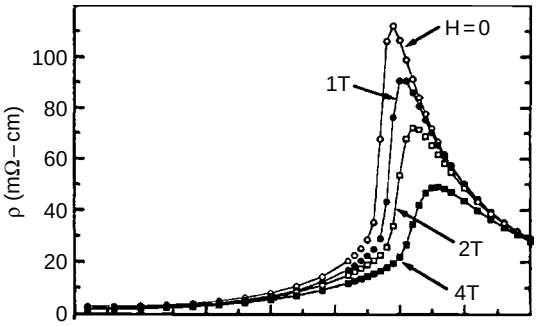

Fig. 8.41. The resistivity of $La_{0.75}Ca_{0.25}MnO_3$ (in mΩ cm) as a function of the magnetic-field intensity (in Tesla) near the temperature of the ferromagnet–paramagnet phase transition. (Reprinted with permission from [8.459]. Copyright 1995 American Physical Society.)

(La, Nd) and A is a divalent alkali-metal atom (Ca, Sr), at $x = 0$ we get a perfect perovskite which is a paramagnetic insulator. With $x > 0$ a variety of temperature and x-dependent phases with different structural, magnetic, transport, and charge-ordering properties occur. At $x \sim 0.2$ the ground state becomes a ferromagnetic metal, and at $x \geq 0.5$ it transforms into an antiferromagnetic insulator accompanied by charge ordering. In the range $0.2 < x < 0.5$ there is a temperature-dependent ferromagnet–paramagnet transition at $T_c(x) \approx 200$–500 K. The very large magnetoresistance near this phase transition at $T \approx T_c(x)$ (Fig. 8.41) is not surprising since ferromagnetic transitions are very sensitive to applied magnetic fields, which facilitate the ordered spin-parallel orientations along the field. In general, such a transition may be simultaneously a metal–insulator transition.

However, in the manganites with colossal magnetoresistance it is difficult to understand why the paramagnetic phase is insulating. Indeed, the Mn^{3+} ion in the octahedral environment of six oxygen atoms has a high-spin d^4 configuration with three electrons having parallel spins in the t_{2g} states and $1-x$ electrons in the e_g state. The latter electrons may move along the crystal subject to double-exchange limitations [8.460] (Section 7.6.2). In the low-temperature ferromagnetic phase the spins are ordered and don't scatter conduction electrons, whereas in the high-temperature paramagnetic phase the spins are disordered and scatter electrons, thus increasing the resistance. However, this increase is small to negligible [8.460, 8.461] and cannot explain the origin of the insulating behavior of the system.

The direct explanation of the crystal resistance is based on the JTE [8.436–8.438] (see also [8.439]). In the manganese e_g state a strong $E \otimes e$ JT coupling takes place, trapping the conducting electron in the tetragonally distorted octahedral cluster MnO_6 and producing a small-radius polaron. This self-trapping competes with the delocalizing tendency of band formation, which, in turn, depends on superexchange and double-exchange conditions.

The delocalization can be characterized by an effective parameter t_{eff}, e.g., the kinetic energy of the band electron in the absence of the JTE. Then the ratio $\lambda = E_{\text{JT}}/t_{\text{eff}}$, where E_{JT} is the JT stabilization energy, may serve as an indicator of possible conductivity. Calculations [8.437, 8.462–8.464] show that λ depends essentially on the material, doping, magnetic field, and temperature. In the high-temperature state with $0.2 < x < 0.5$, t_{eff} is sufficiently small, while E_{JT} is large, so λ is large and the e_g electron is localized in one of the minima of the Mn site. With the decrease of the temperature to $T_c(x)$, t_{eff} increases due to the growing ferromagnetic order. This decreases λ, turning off the localization and facilitating the occurrence of metallic behavior. Obviously the magnetic field acts in the same direction. This very brief qualitative description of the role of the JTE in the magnetoresistance phenomenon has a variety of important details that were studied in a series of papers [8.436–8.472].

First we notice a series of works on $La_{1-x}Sr_xMnO_3$ [8.451], $La_{7/8}Sr_{1/8}MnO_3$ [8.467], $L_{0.5}A_{0.5}MnO_3$ with L = Pr, $Pr_{1-y}Y_y$, Sm, and $A = Ca_{1-x}Sr_x$, Sr, and fixed ratio Mn(III)/Mn(IV) = 1 [8.453], and with L = La, Pr, Nd, Y, Eu, Sm, and A = Ca, Sr [8.468], $LaMnO_3$, $CaMnO_3$, and $YCrO_3$ [8.455], $LaMn_{1-x}Ga_xO_3$ [8.452, 8.456, 8.466], $RMnO_3$ with R = La, Pr, Nd [8.452], $RNiO_3$ with R = lanthanide [8.454], and Fe-doped $La_{1-x}Ca_xMnO_3$ [8.457], in which a variety of properties like phase formation and phase transition, orbital ordering, chemical bonding, exchange interaction, magnetic ordering, etc., are investigated. They are all directly related to the magnetoresistance, including interplay among charge, orbital, and magnetic ordering in $La_{1-x}Sr_xMnO_3$ [8.451], JT distortions and thermal conductivity [8.451], phase competition in perovskites [8.453], orbital order–disorder transition [8.452], vibronic superexchange interaction in Mn(III)—O—Mn(III) groups [8.466], spin-glass-to-ferromagnet transition [8.456], transition from Curie–Weiss to Pauli paramagnetism in $RNiO_3$ [8.454], pressure-induced transition to band antiferromagnetism [8.455], JT distortions observed by means of the Mössbauer effect [8.457]. All these papers are based on a bundle of experimental work that uses a variety of techniques, and the interpretation of the results is based essentially on the JTE involved as an inevitable basic element of the Mn site. Obviously, the JTE interacts strongly with other effects, first of all with double exchange and superexchange.

Local lattice distortions in $La_{1.4}Sr_{1.6}Mn_2O_7$ [8.448], $La_{1-x}Sr_xMnO_3$ [8.449], $LaMnO_{3+\delta}$ and $La_{0.96}Sr_{0.04}MnO_{3+\delta}$ [8.450] were studied by means of neutron scattering. The JT distortions were shown to be locally present even when they are not seen in the crystallographic structure of $La_{1-x}Sr_xMnO_3$, and they are observed also in the metallic phase up to $x = 0.35$. On the other hand excess oxygen reduces the magnitude of the JT distortions in contrast to divalent cation doping [8.450].

Direct *ab initio* numerical calculations of $[MnO_6]^{9-}$ (I) and $[MnO_6]^{8-}$ (II) complexes embedded in the corresponding sites of the lattice of $La_{2-2x}Sr_{1+2x}Mn_2O_7$ at $x = 0.40$ confirm the existence of JT distortions in these clusters related to the $E \otimes e$ and $E \otimes (b_1 + b_2)$ problems in I and II, respectively [8.444(*a*)]. Two types of $(Mn_2O_{11})^{15-}$ were also explored recently in the same manner [8.444(*b*)].

Double exchange in combination with the cooperative JTE is applied to doped manganites $A_{1-x}B_xMnO_3$ using a two-band model [8.445–8.447]. For $x = 0$ the strong intraatomic *Hund* coupling and the double exchange produces antiferromagnetic ordering along the cubic axes, which is further stabilized by the CJTE. This makes the $LaMnO_3$ crystal a band insulator with two-dimensional ferromagnetic layers. The onset of the metallic behavior at $x \gtrsim 0.16$ at low temperatures is treated by a percolation approach. For $x > 0.5$ the canted antiferromagneic A-phase occurs, for which the magnetoconductivity was considered in detail. As a result, the authors (as they state briefly in the conclusion) determined the electronic spectrum and calculated both the conductivity and the magnetoconductivity (in the ground state), which correlate with the number of carriers. Defects are described in terms of random JT centers and the magnetoresistivity is expressed in terms of magnetization. In the transition to the A-phase the JT cooperative ordering plays a leading role.

An interesting feature of stripe formation in manganites of $La_{1-x}Ca_xMnO_3$ type with $x = \frac{1}{2}$ and $x = \frac{2}{3}$ (somewhat similar to the stripes in cuprates, Fig. 8.39) was explained as due to a special cooperativity of the JT-distortions [8.442, 8.443, 8.469]. Calculations [8.469] show that at $x = \frac{1}{2}$ the interference of the totally symmetric and JT-distorted centers results in a superstructure in which a tricenter interaction stabilizes the nearest neighbor Mn^{3+}–Mn^{4+}–Mn^{3+} ions forming the structural unit of the stripe. A somewhat different ("topological") approach to stripe formation is suggested in [8.442, 8.443]. In this approach the explicit wavefunctions of the e_g electron are involved to calculate the lowest-energy one-dimensional zigzag path in an antiferromagnetic environment of the core t_{2g} spins, which is subject to Berry-phase limitations (Section 5.7). The so-called "winding number" W is introduced, and it is shown that for the observed "bi-stripe" structure the required integer W_{BS} is equal to the ratio of the numbers of Mn^{4+} and Mn^{3+} ions:

$$W_{BS} = \frac{N(Mn^{4+})}{N(Mn^{3+})} = \frac{x}{1-x} \tag{8.56}$$

This means that nontrivial charge and orbital arrangements should take place at $x = \frac{1}{2}, \frac{2}{3}, \frac{3}{4}$, etc.

An alternative approach to the problem of doped manganites "beyond the conventional double-exchange model" is suggested in [8.470], in which electronic charge-transfer states, charge disproportionation in MnO_6 octahedra, and PJT coupling are involved.

JT distortions in $LaTiO_3$ at the antiferromagnetic transition were observed using a variety of experimental techniques [8.458].

Magnetoelasticity and magnetic-field-induced structural phase transitions in low-doped $La_{1-x}Sr(Ba)_xMnO_3$ are explained by the CJTE involving an excited triplet state located relatively close to the ground state of Mn^{3+} [8.471]. This orbital doublet–triplet model also explains well the observed first-order phase transition under uniaxial and hydrostatic pressure [8.472].

References

8.1. *The Jahn–Teller Effect. A Bibliographic Review*, Ed. I. B. Bersuker, New York, IFI/Plenum, 1984.

8.2. *Dynamical Jahn–Teller Effect in Localized Systems*, Eds. Yu. E. Perlin and M. Wagner, Amsterdam, Elsevier, 1984.

8.3. F. S. Ham, in *Electron Paramagnetic Resonance*, Ed. S. Geschwind, New York, Plenum, 1972, p. 1.

8.4. M. D. Sturge, The Jahn–Teller effect in solids, in *Solid State Physics*, Vol. 20, Eds. F. Seitz, D. Turnbull, and H. Ehrenreich, New York, Academic Press, 1967.

8.5. D. Reinen and C. Friebel, *Struct. Bonding*, **37**, 1 (1979).

8.6. D. Reinen and M. Atanasov, *Magn. Reson. Rev.*, **15**, 167 (1991).

8.7. *Electron–Phonon Dynamics and Jahn–Teller Effects*, Eds. G. Bevilacqua, L. Martinelli, and N. Terzi, Singapore, World Scientific, 1999.

8.8. G. D. Watkins, in *Deep Centers in Semiconductors*, Ed. S. T. Pantelides, New York, Gordon and Breach, 1986, p. 147.

8.9. *Vibronic Interactions: Jahn–Teller Effect in Crystals and Molecules*, Eds. M. D. Kaplan and G. O. Zimmerman, NATO Science Series II, Vol. 39, Dordrecht, Kluwer, 2001.

8.10. H. Bill, in *The Dynamical Jahn–Teller Effect in Localized Systems*, Eds. Yu. E. Perlin and M. Wagner, Amsterdam, North-Holland, 1984, p. 709.

8.11. A. L. Natadze, A. I. Ryskin, and B. G. Vekhter, in *The Dynamical Jahn–Teller Effect in Localized Systems*, Eds. Yu. E. Perlin and M. Wagner, Amsterdam, North-Holland, 1984, p. 347.

8.12. V. V. Hizhnyakov, N. N. Kristoffel, in *The Dynamical Jahn–Teller Effect in Localized Systems*, Eds. Yu. E. Perlin and M. Wagner, Amsterdam, North-Holland, 1984, p. 383.

8.13. W. Ulrici, in *The Dynamical Jahn–Teller Effect in Localized Systems*, Eds. Yu. E. Perlin and M. Wagner, Amsterdam, North-Holland, 1984, p. 439.

8.14. L. J. Challis and A. M. de Goer, in *The Dynamical Jahn–Teller Effect in Localized Systems*, Eds. Yu. E. Perlin and M. Wagner, Amsterdam, North-Holland, 1984, p. 533.

8.15. B. Bleaney and D. J. F. Ingram, *Proc. Phys. Soc. London A* **63**, 408 (1950).

8.16. B. Bleaney and K. D. Bowers, *Proc. Phys. Soc. London A* **65**, 667 (1952).
8.17. A. Abragam and M. H. L. Pryce, *Proc. Phys. Soc. London* **63**, 409 (1950).
8.18. I. B. Bersuker, *The Jahn–Teller Effect and Vibronic Interactions in Modern Chemistry*, New York, Plenum, 1984.
8.19. B. Bleaney, K. D. Bowers, and R. S. Trenam, *Proc. R. Soc. London A* **228**, 157 (1955); D. Bigl and A. C. Roje-Innes, *Proc. Phys. Soc. London A* **66**, 954 (1953).
8.20. R. T. Tucker, *Phys. Rev.* **112**, 725 (1958); D. C. Burnham, *Bull. Am. Phys. Soc.* **11**, 186 (1966).
8.21. R. E. Coffman, *Phys. Lett.* **21**, 381 (1966).
8.22. R. E. Coffman, D. L. Lyle, and D. R. Mattison, *J. Phys. Chem.* **72**, 1392 (1968).
8.23. J. S. Wood, C. P. Keizers, E. de Boer, and A. Buttafava, *Inorg. Chem.* **19**, 2213 (1980).
8.24. V. E. Petrashen, Yu. V. Yablokov, and R. L. Davidovich, *Phys. Status Solidi B* **88**, 439 (1978); **101**, 117 (1980).
8.25. K. Murthy, G. Dhanaraj, H. L. Bhat, and S. V. Bhat, *Mol. Phys.* **65**, 181 (1988).
8.26. S. O. Graham and R. L. White, *Phys. Rev. B* **10**, 4505 (1974).
8.27. J. Sierro, *J. Phys. Chem. Solids* **28**, 417 (1967).
8.28. C. J. Delbecq, W. Hayes, M. C. M. O'Brien, and P. H. Yuster, *Proc. R. Soc. London A* **271**, 343 (1963).
8.29. R. S. Eachus and R. E. Graves, *J. Chem. Phys.* **59**, 2160 (1973).
8.30. W. Hayes and J. Wilkens, *Proc. R. Soc. London A* **281**, 340 (1964).
8.31. J. R. O'Connor and J. H. Chen, *Appl. Phys. Lett.* **5**, 100 (1964).
8.32. W. Hayes and J. R. Twidell, *Proc. Phys. Soc. London* **82**, 330 (1963).
8.33. Y. T. Hohli, *Phys. Rev.* **162**, 262 (1967).
8.34. Y. T. Hohli and T. L. Estle, *Phys. Rev. Lett.* **18**, 128 (1967).
8.35. W. Low and J. T. Suss, *Phys. Lett.* **7**, 310 (1963).
8.36. Y. T. Hohli, K. A. Müller, and P. Wysling, *Phys. Lett.* **15**, 5 (1965).
8.37. S. Geshwind and J. R. Remeika, *J. Appl. Phys.* **33**, 370 (1962).
8.38. J. H. Ammeter, H. B. Buergi, E. Camp, V. Meyer-Sandrin, and W. P. Jensen, *Inorg. Chem.* **18**, 733 (1979).
8.39. J. H. Ammeter, L. Zoler, J. Bachmann, P. Baltzer, E. Camp, R. Bucher, and E. Deiss, *Helv. Chim. Acta* **64**, 1063 (1981).
8.40. S. Guha and L. L. Chase, *Phys. Rev. B* **12**, 1658 (1975).
8.41. K. Kanno, S. Mukai, and Y. Nakai, *J. Phys. Soc. Japan* **36**, 1192 (1974).
8.42. M. Abou-Guantous, C. A. Bates, J. R. Fletcher, and P. C. Jaussaud, *J. Phys. C* **8**, 3641 (1975).
8.43. L. L. Chase and C. H. Hao, *Phys. Rev. B* **12**, 5990 (1975).
8.44. L. L. Chase, W. Hayes, and A. J. Rushwirth, *J. Phys. C* **10**, L575 (1977).
8.45. H. D. Koswig, U. Retter, and W. Ulrici, *Phys. Status Solidi B* **24**, 605 (1967).
8.46. H. D. Koswig, U. Retter, and W. Ulrici, *Phys. Status Solidi B* **51**, 123 (1972).
8.47. G. A. Slack, S. Roberts, and J. T. Vallin, *Phys. Rev.* **187**, 511 (1969).
8.48. J. T. Vallin and G. D. Watkins, *Phys. Rev. B* **9**, 2051 (1974).
8.49. R. J. Wagner and M. M. White, *Solid State Commun.* **32**, 399 (1979).
8.50. A. S. Abhvani, C. A. Bates, B. Clerjaud, and D. R. Pooler, *J. Phys. C* **15**, 1345 (1982); A. S. Abhvani, S. P. Austen, C. A. Bates, L. W. Parker, and D. R. Pooler, *J. Phys. C* **15**, 2217 (1982).
8.51. W. Gehlhoff and W. Ulrici, *Phys. Status Solidi B* **65**, K93 (1974); **102**, 11 (1980).
8.52. A. Hjörtsberg, B. Nygrén, J. T. Vallin, and F. S. Ham, *Phys. Rev. Lett.* **39**, 1233 (1977).

8.53. W. Ulrici, *Phys. Status Solidi B* **51**, 129 (1972).
8.54. G. D. Jones, *Phys. Rev.* **155**, 259 (1967).
8.55. T. E. Freeman and G. D. Jones, *Phys. Rev.* **182**, 411 (1969).
8.56. B. F. Gächter and J. A. Koningstein, *J. Chem. Phys.* **60**, 2003 (1974).
8.57. A. Kaplyanskii and A. K. Przewuskii, *Opt. Spektrosk.* **19**, 587 (1965); **20**, 1045 (1966).
8.58. L. L. Chase, *Phys. Rev. Lett.* **23**, 275 (1969); *Phys. Rev. B* **2**, 2308 (1970).
8.59. G. Ruszcynski and R. Boyn, *Phys. Status Solidi B* **76**, 427 (1976).
8.60. A. Rosenfeld, R. Boyn, and G. Ruszcynski, *Phys. Status Solidi B* **70**, 601 (1975).
8.61. J. Gardavsky, I. Barvik, and M. Zvara, *Phys. Status Solidi B* **84**, 691 (1977).
8.62. W. Ulrici, *Phys. Status Solidi B* **62**, 431 (1974).
8.63. G. Schwotzer and W. Ulrici, *Phys. Status Solidi B* **64**, K115 (1974).
8.64. P. Koidl, *Phys. Status Solidi B* **74**, 477 (1976).
8.65. R. Parrot, C. Naud, C. Porte, D. Fournier, A. C. Boccara, and J. C. Rivoal, *Phys. Rev. B* **17**, 1057 (1978).
8.66. W. Reynolds and L. A. Boatner, *Phys. Rev. B* **12**, 4735 (1975); L. A. Boatner, R. W. Reynolds, Y. Chen, and M. M. Abraham, *Phys. Rev. B* **16**, 86 (1977).
8.67. A. Schoeberg, J. T. Suss, Z. Luz, and W. Low, *Phys. Rev. B* **9**, 2047 (1974).
8.68. Z. Luz, A. Raizman, and J. T. Suss, *Solid State Commun.* **71**, 849 (1977).
8.69. A. Raizman, A. Schoeberg, and J. T. Suss, *Phys. Rev. B* **20**, 1863 (1979).
8.70. J. R. Herrington, L. A. Boatner, T. J. Aton, and T. L. Estle, *Phys. Rev. B* **10**, 833 (1974).
8.71. J. R. Herrington, T. L. Estle, and L. A. Boatner, *Phys. Rev. B* **3**, 2933 (1971).
8.72. A. O. Barksdale and T. L. Estle, *Phys. Lett. A* **42**, 426 (1973).
8.73. R. M. Macfarlane, J. Y. Wong, and M. D. Sturge, *Phys. Rev.* **166**, 250 (1968).
8.74. C. A. Bates and J. P. Bentley, *J. Phys. C* **2**, 1947 (1969).
8.75. A. Johnson, *Ph.D. Thesis*, University of Nottingham, 1967.
8.76. N. Devismes and A. M. de Goer, in *Proceedings of the 2nd International Conference on Phonon Scattering in Solids*, Eds. L. J. Challis, V. W. Rampton, and A. F. G. Wyat, New York, Plenum, 1976, p. 208.
8.77. M. Abou-Guantous, I. A. Clark, and W. S. Moore, *J. Phys. C* **9**, 1965 (1976).
8.78. R. Buisson and A. Nahmani, *Phys. Rev. B* **6**, 2648 (1972).
8.79. A. Nahmani and R. Buisson, *Solid State Commun.* **18**, 297 (1976).
8.80. A. Nahmani and R. Buisson, *J. Physique* **41**, 59 (1980).
8.81. M. Abou-Guantous and C. A. Bates, *J. Physique Lett.* **41**, L263 (1980).
8.82. M. Abou-Guantous, C. A. Bates, and L. C. Goodfellow, *J. Phys. Chem. Solids* **37**, 1059 (1976).
8.83. F. S. Ham, W. M. Schwartz, and M. C. M. O'Brien, *Phys. Rev.* **185**, 548 (1969).
8.84. A. Hjörtsberg, B. Nygrén, and J. T. Vallin, *Solid State Commun.* **16**, 105 (1975).
8.85. M. F. Lewis and A. M. Stoneham, *Phys. Rev.* **164**, 271 (1967).
8.86. R. Reghard and T. Ray, *Phys. Rev. B* **14**, 1805 (1976).
8.87. J. C. Combaz, *Thèse de troisième cycle*, Université de Grenoble, 1976.
8.88. C. A. Bates and P. Steggles, *J. Phys. C* **8**, 2283 (1975).
8.89. J. J. Krebs and G. H. Stauss, *Phys. Rev. B* **15**, 17 (1977); G. H. Stauss and J. J. Krebs, *Phys. Rev. B* **22**, 2050 (1980).
8.90. J. J. Krebs and G. H. Stauss, *Phys. Rev. B* **20**, 795 (1979).
8.91. A. S. Abhvani, C. A. Bates, P. Burj, P. J. King, P. R. Pooler, V. W. Rampton, and P. C. Wiscombe, *J. Phys. C* **16**, 6573 (1983).

8.92. B. Goldberg, S. A. Payne, and D. S. McClure, *J. Chem. Phys.* **81**, 1523 (1984); S. A. Payne, A. B. Goldberg, and D. S. McClure, *J. Chem. Phys.* **81**, 1529 (1984); J. M. Berg, R.-L. Chien, and D. S. McClure, *J. Chem. Phys.* **87**, 7 (1987); J. M. Berg and D. S. McClure, *J. Chem. Phys.* **90**, 3915 (1989).
8.93. P. Garcia-Fernandez, J. A. Aramburu, M. T. Barriuso, and M. Moreno, *Phys. Rev. B* **69**, 17 410 (2004).
8.94. V. Lefevre, A. Monnier, M. Schnieper, D. Lov, and M. Bill, *Z. Physik. Chem.* **200**, 265 (1997).
8.95. S. K. Misra, X. Li, and C. Wang, *J. Phys.: Condens. Matter* **3**, 847 (1991); S. K. Misra and C. Wang, *Magn. Reson. Rev.* **14**, 157 (1990).
8.96. J. M. Garcia-Lastra, J. A. Aramburu, M. T. Barriuso, and M. Moreno, *Chem. Phys. Lett.* **385**, 286 (2004).
8.97. (*a*) J. A. Aramburu, M. T. Barriuso, P. Garcia Fernandez, and M. Moreno, *Adv. Quant. Chem.* **44**, 445 (2003); (*b*) J. L. Pascual, B. Savoini, and R. Gonzalez, *Phys. Rev. B* **70**, 045109 (2004).
8.98. P. L. W. Tregenna-Piggott, *Adv. Quant. Chem.* **44**, 461 (2003).
8.99. M. Atanasov, U. Kesper, B. L. Ramakrishna, and D. Reinen, *J. Solid. State Chem.* **105**, 1 (1993).
8.100. T. K. Kundu and P. T. Manoharan, *Mol. Phys.* **97**, 709 (1999).
8.101. V. A. Ulanov, M. M. Zaripov, and E. P. Zheglov, *Phys. Solid State* **44**, 1471 (2002).
8.102. S. K. Hoffmann, J. Goslar, W. Hilczer, R. Kaszynski, and M. A. Augustyniak-Yablokow, *Solid State Commun.* **117**, 333 (2001).
8.103. R. Valiente, L. M. Lezama, F. Rodrigues, and M. Moreno, *Mater. Sci. Forum* **239–241**, 729 (1997).
8.104. R. Valiente, F. Rodrigues, M. Moreno, and L. M. Lezama, in *Vibronic Interactions: Jahn–Teller Effect in Crystals and Molecules*, Eds. M. D. Kaplan and G. O. Zimmerman, NATO Science Series II, Vol. 39, Dordrecht, Kluwer, 2001, p. 221.
8.105. M. Zaripov, V. A. Ulanov, and M. L. Falin, *Sov. Phys. Solid State* **29**, 1264 (1987).
8.106. H. Bill, D. Lovy, and H. Hagemann, *Solid. State Commun.* **70**, 511 (1989).
8.107. A. Monnier, A. Gerber, and H. Bill, *J. Chem. Phys.* **94**, 5891 (1991).
8.108. V. Villacampa, R. Alcalá, P. J. Alonso, M. Moreno, M. T. Barriuso, and J. A. Aramburu, *Phys. Rev. B* **49**, 1039 (1994-II).
8.109. Yu. V. Yablokov and T. A. Ivanova, *Coord. Chem. Rev.* **190–192**, 1255 (1999); T. A. Ivanova, I. Jacyna-Onyszkiewicz, J. Mrozinski, Yu. V. Yablokov, and V. V. Zelentsov, in *Vibronic Interactions: Jahn–Teller Effect in Crystals and Molecules*, Eds. M. D. Kaplan and G. O. Zimmerman, NATO Science Series II, Vol. 39, Dordrecht, Kluwer, 2001, p. 323.
8.110. J. A. Aramburu, P. Garcia-Fernandez, M. T. Barriuso, and M. Moreno, *Phys. Rev. B* **67**, 020101 (2003).
8.111. (*a*) L. Martinelli, M. Passaro, and G. P. Parravicini, *Phys. Rev. B* **39**, 13 343 (1989-II); (*b*) G. Bevilacqua, L. Martinelli, M. A. De Orue, J. Rivera-Iratchet, and E. E. Vogel, in *Electron–Phonon Dynamics and Jahn–Teller Effects*, Eds. G. Bevilacqua, L. Martinelli, and N. Terzi, Singapore, World Scientific, 1999, p. 178.
8.112. L. Martinelli, M. Passaro, and G. P. Parravicini, *Phys. Rev. B* **40**, 10 443 (1989-II).
8.113. G. Bevilacqua, L. Martinelli, and G. P. Parravicini, *Phys. Rev. B* **54**, 7626 (1996-I).

8.114. O. Mualin, E. E. Vogel, M. A. de Orue, L. Martinelli, G. Bevilacqua, and H. J. Schulz, *Phys. Rev. B* **65**, 035211 (2001); O. Mualin, E. E. Vogel, G. Bevilacqua, and L. Martinelli, *Rev. Méxicana Fis.* **48**, 54 (2002).
8.115. G. Bevilacqua, L. Martinelli, G. Russo, G. P. Paravicini, O. Mualin, E. E. Vogel, M. A. de Orue, and J. Rivera-Iratchet, in *Vibronic Interactions: Jahn–Teller Effect in Crystals and Molecules*, Eds. M. D. Kaplan and G. O. Zimmerman, NATO Science Series II, Vol. 39, Dordrecht, Kluwer, 2001, p. 367.
8.116. Y. Y. Zhou, *Chinese J. Chem. Phys.* **15**, 401 (2002).
8.117. K. Wissing, M. T. Barriuso, J. A. Aramburu, and M. Moreno, *J. Chem. Phys.* **111**, 10 217 (1999).
8.118. J. L. Pascual, L. Seijo, and Z. Barandiaran, *Phys. Rev. B* **53**, 1138 (1996-I).
8.119. P. B. Oliete, C. A. Bates, and J. L. Dunn, *J. Phys.: Condens. Matter* **11**, 2579 (1999).
8.120. M. M. Zaripov, V. F. Tarasov, V. A. Ulanov, G. S. Shajkurov, and M. L. Popov, *Phys. Solid State* **37**, 437 (1995); B. Oliete, V. M. Orera, and P. J. Alonso, *Phys. Rev. B* **53**, 3047 (1995).
8.121. M. M. Zaripov, V. F. Tarasov, V. A. Ulanov, and G. S. Shajkurov, *Phys. Solid State* **44**, 2050 (2002).
8.122. (*a*) G. Bevilacqua, L. Martinelli, E. E. Vogel, and O. Mualin, *Phys. Rev. B* **70**, 075206 (2004); (*b*) *Phys. Rev. B* **66**, 155338 (2002).
8.123. M. Moreno, J. A. Aramburu, and M. T. Barriuso, *Phys. Rev. B* **56**, 14423 (1997-II).
8.124. (*a*) Wenger and H. U. Güdel, *J. Chem. Phys.* **115**, 3819 (2001); (*b*) **117**, 909 (2002).
8.125. L. L. Kulyuk, S. M. Ostrovsky, A. V. Palii, S. M. Popov, and B. S. Tsukerblat, *Z. Physik. Chem.* **201**, 45 (1997).
8.126. J. L. Pascual, *Phys. Rev. B* **67**, 115112 (2003).
8.127. M. Grinberg, S. M. Kaczmarek, M. Berkowski, and T. Tsuba, *J. Phys.: Condens. Matter* **13**, 743 (2001).
8.128. D. Reinen, C. Albrecht, and U. Kaschuba, *Z. Anorg. Allgem. Chem.* **584**, 71 (1990); C. Albrecht, S. Cohen, I. Mayer, and D. Reinen, *J. Solid. State Chem.* **107**, 218 (1993).
8.129. (*a*) P. L. W. Tregenna-Piggott, M. C. M. O'Brien, H. Weihe, and H. U. Güdel, *J. Chem. Phys.* **109**, 2967 (1998); (*b*) P. L. W. Tregenna-Piggott, C. J. Noble, and J. L. Pilbrow, *J. Chem. Phys.* **113**, 3289 (2000).
8.130. E. V. Pestryakov, V. V. Petrov, V. I. Trunov, A. V. Kirpichnikov, A. G. Volkov, A. I. Alinipiev, and A. J. Rodionov, *Laser Phys.* **11**, 1138 (2001).
8.131. K. Stavrev and M. C. Zerner, *J. Chem. Phys.* **102**, 34 (1995).
8.132. M. T. Bariuso, P. Garcia-Fernandez, J. A. Aramburu, and M. Moreno, *Solid State Commun.* **120**, 1 (2001).
8.133. R. Aceves, V. Babin, M. B. Barboza Flores, P. Fabeni, E. Mihokova, V. Nagirnyi, M. Nikl, K. Nitsch, G. P. Pazzi, R. Perez Salas, and S. Zazubovich, *J. Phys.: Condens. Matter* **10**, 5449 (1998).
8.134. V. Nagirnyi, S. Zazubovich, V. Zepelin, M. Nikl, and G. P. Pazzi, *Chem. Phys. Lett.* **277**, 533 (1994).
8.135. A. T. Boothroyd, C. H. Gardiner, S. J. S. Lister, P. Santini, B. D. Rainford, L. D. Noaolles, D. B. Currie, R. S. Ecclester, and R. I. Bewley, *Phys. Rev. Lett.* **86**, 2082 (2001).

8.136. S. Kern, C.-K. Loong, J. Faber Jr., and G. H. Lander, *Solid State Commun.* **49**, 295 (1984).
8.137. G. Bevilacqua, D. Ippolito, and L. Martinelli, *Phys. Rev. B* **69**, 155208 (2004).
8.138. I. Vieito, M. Inglesias, J. M. Garcia-Lastra, J. A. Aramburu, and M. Moreno, *Internat. J. Quant. Chem.* **101**, 802 (2005).
8.139. L. Martinelli, G. P. Parravicini, and P. L. Soriani, *Phys. Rev.* **32**, 4106 (1985).
8.140. F. S. Ham and U. Grevsmühl, *Phys. Rev. B* **8**, 2945 (1973); Y. Kayamuna and Y. Kondo, *Solid. State Commun.* **24**, 442 (1977); K. Iwahana, T. Iida, and H. Ohkura, *J. Phys. Soc. Japan* **47**, 599 (1979).
8.141. L. Martinelli and G. P. Parravicini, *Phys. Rev. B* **46**, 15795 (1992-II).
8.142. J. Weber and H. Bill, *Chem. Phys. Lett.* **52**, 562 (1977).
8.143. L. S. Dang, R. Romestein, and Y. Merle d'Aubigne, *Phys. Rev. Lett.* **38**, 1539 (1977).
8.144. F. S. Ham and C.-H. Leung, *Phys. Rev. Lett.* **71**, 3186 (1993); *Solid State Commun.* **93**, 375 (1995).
8.145. Z. Dashevsky and I. Chaikovsky, in *Vibronic Interactions: Jahn–Teller Effect in Crystals and Molecules*, Eds. M. D. Kaplan and G. O. Zimmerman, NATO Science Series II, Vol. 39, Dordrecht, Kluwer, 2001, p. 197.
8.146. V. Hizhnyakov, V. Boltrushko, H. Kaasik, and I. Sildos, *J. Chem. Phys.* **119**, 6290 (2003); *J. Luminesc.* **107**, 351 (2004).
8.147. I. B. Bersuker, *Phys. Lett.* **20**, 589 (1966).
8.148. I. B. Bersuker and B. G. Vekhter, *Ferroelectrics* **19**, 137 (1978).
8.149. I. B. Bersuker, *Ferroelectrics* **164**, 75 (1995).
8.150. M. Glinchuk, M. Deigen, and A. Karamzin, *Fiz. Tverd. Tela* **15**, 2048 (1974).
8.151. G. I. Bersuker, V. Z. Polinger, and V. P. Khlopin, *Fiz. Tverd. Tela* **24**, 2471 (1982).
8.152. G. I. Bersuker and V. Z. Polinger, *Phys. Status Solidi B* **128**, 401 (1984).
8.153. V. S. Vikhnin, L. S. Sochava, and Yu. N. Tolparov, *Fiz. Tverd. Tela* **20**, 2412 (1978).
8.154. G. I. Bersuker, *Fiz. Tverd. Tela* **28**, 3716 (1986).
8.155. G. I. Bersuker, *Phys. Status Solidi B* **148**, 243 (1988).
8.156. M. Georgiev, M. Mladenova, V. Krastev, and A. Andreev, *Eur. Phys. J. B* **29**, 271 (2002).
8.157. U. V. Waghmare, N. A. Spaldin, H. C. Kandpal, and R. Seshadri, *Phys. Rev. B* **67**, 125111 (2003).
8.158. H. Bill, *Phys. Lett. A* **44**, 101 (1973).
8.159. M. Moreno, *Ann. Fiz.* **70**, 261 (1974).
8.160. G. G. Deleo, G. D. Watkins, and W. B. Fowler, *Phys. Rev. B* **37**, 1013 (1988-I); S. I. Pantelides, W. A. Harrison, and F. Yndurain, *Phys. Rev. B* **37**, 1016 (1988-I).
8.161. (*a*) G. I. Bersuker, L. F. Chibotaru, V. Z. Polinger, and A. V. Solonenko, *Mol. Phys.* **70**, 1031 (1990); (*b*) **70**, 1045 (1990).
8.162. G. I. Bersuker and A. V. Solonenko, *J. Phys.: Condens. Matter* **3**, 631 (1991).
8.163. G. Bersuker, P. Zeitzoff, G. Brown, and H. R. Huff, in *Materials Today*, January 2004, p. 26.
8.164. V. M. Fomin, V. N. Gladilin, J. T. Devreese, E. P. Pokatilov, S. N. Balaban, and S. N. Klimin, *Phys. Rev. B* **57**, 2415 (1998-II); V. M. Fomin, E. P. Pokatilov, J. T. Devreese, S. N. Klimin, V. N. Gladilin, and S. N. Balaban, *Solid State Electron.* **42**, 1309 (1998); J. T. Devreese, V. M. Fomin, and S. N. Klimin, *Internat. J. Mod. Phys.* **15**, 3579 (2001); E. P. Pokatilov, S. N. Klimin,

V. M. Fomin, J. T. Devreese, and F. W. Wise, *Phys. Rev. B* **65**, 075316 (2002); J. T. Devreese, V. M. Fomin, V. N. Gladilin, E. P. Pokatilov, and S. N. Klimin, *Nanotechnology* **13**, 163 (2002).
8.165. I. B. Bersuker, *J. Struct. Chem. (Russ.)* **16**, 935 (1975).
8.166. J. Gazo, I. B. Bersuker, J. Garaj, M. Kabesova, J. Kohout, H. Langfelderova, M. Melnik, M. Serator, and F. Valach, *Coord. Chem. Rev.* **19**, 253 (1976).
8.167. B. J. Hathaway, *Struct. Bonding* **57**, 55 (1984).
8.168. B. Hattaway, M. Duggan, M. Murphy, J. Mullane, C. Power, A. Walsh, and B. Walsh, *Coord. Chem. Rev.* **175**, 17 (1998).
8.169. J. Pradilla-Sorzano and J. P. Fackler, *Inorg. Chem.* **12**, 1182 (1973).
8.170. J. P. Fackler and A. Avdeev, *Inorg. Chem.* **13**, 1864 (1974).
8.171. J. P. Fackler and A. Avdeev, in *Proc. XIX ICCC, Prague*, 1978, Czechoslovak Academy of Sciences, p. 148.
8.172. J. Gazo, *Pure Appl. Chem.* **38**, 279 (1974).
8.173. T. Obert and I. B. Bersuker, *Proc. XIX ICCC*, Prague, 1978, Czechoslovak Academy of Sciences Vol. 2, p. 94; *Czechosl. J. Phys. B* **33**, 568 (1983).
8.174. Ch. J. Simmons, *New. J. Chem.* **17**, 77 (1993).
8.175. Ch. J. Simmons, *Struct. Chem.* **3**, 37 (1992).
8.176. Bebendorf, H.-B. Bürgi, E. Gamp, M. A. Hitchman, A. Murphy, D. Reinen, M. J. Riley, and H. Stratemeier, *Inorg. Chem.* **35**, 7419 (1996).
8.177. M. A. Augustiniak-Jablokow, Y. V. Yablokov, K. Lukaszewicz, A. Pietraszko, V. E. Petrashen, and V. A. Ulanov, *Chem. Phys. Lett.* **344**, 345 (2001).
8.178. M. A. Augustiniak-Jablokow, K. Lukaszewicz, A. Pietraszko, V. E. Petreshen, and Y. V. Yablokov, *Phys. Solid State* **44**, 1480 (2002).
8.179. M. A. Augustiniak-Jablokow and A. Krupska, *Chem. Phys. Lett.* **377**, 137 (2003).
8.180. E. M. Wijnands, J. S. Wood, J. Reedijk, and W. J. A. Maaskant, *Inorg. Chem.* **35**, 1214 (1996).
8.181. J. Sabolovic and K. R. Liedl, *Inorg. Chem.* **38**, 2764 (1999).
8.182. M. R. Sundberg, T. Laitalainen, J. Bergman, R. Uggla, J. Matikainen, and S. Kaltia, *Inorg. Chem.* **37**, 2786 (1998).
8.183. M. E. Quiros-Castro, I. Mutikainen, U. Turpeinen, and J. Reedijk, *Inorg. Chim. Acta* **297**, 129 (2000).
8.184. J. D. Crane, O. D. Fox, and E. Sinn, *J. Chem. Soc. Dalton* **9**, 1461 (1999).
8.185. P. Dera, A. Jayaraman, C. T. Prewitt, and S. A. Gramsch, *Phys. Rev. B* **65**, 134105 (2002).
8.186. P. Comba, P. Jurisic, J. D. Lampeka, A. Peters, A. I. Prikhod'ko, and H. Pritzkow, *Inorg. Chim. Acta* **324**, 99 (2001).
8.187. R. Uggla, M. Melnik, J. Valo, A. Pajunen, and M. R. Sundberg, *Acta Chem. Scand.* **49**, 585 (1995).
8.188. R. Stief and W. Massa, *Z. Anorg. Allgem. Chem.* **628**, 1685 (2002).
8.189. M. Melnik, M. Kabesova, M. Dunaj-Jurco, and C. E. Holloway, *J. Coord. Chem.* **41**, 35 (1997).
8.190. M. Hvastijova, J. Kohout, J. W. Budiler, R. Boca, J. Kozisek, and L. Jager, *Coord. Chem. Rev.* **175**, 17 (1998).
8.191. J. D. Dunitz and L. E. Orgel, *J. Phys. Chem. Solids* **3**, 20 (1957).
8.192. D. S. McClure, *J. Phys. Chem. Solids* **3**, 311 (1957).
8.193. P. J. Wojtowitz, *Phys. Rev.* **116**, 32 (1959).
8.194. J. Kanamori, *J. Appl. Phys.* **31**, 14 (1960).
8.195. M. D. Kaplan and B. G. Vekhter, *Cooperative Phenomena in Jahn–Teller Systems*, New York, Plenum, 1995.

8.196. I. B. Bersuker and V. Z. Polinger, *Vibronic Interactions in Molecules and Crystals*, Berlin, Springer, 1989.
8.197. R. J. Elliot, R. T. Harley, W. Hayes, and S. R. P. Smith, *Proc. R. Soc. London A* **328**, 217 (1972).
8.198. H. Thomas, in *Electron–Phonon Interactions and Phase Transitions*, Ed. T. Riste, New York, Plenum, 1977, p. 245.
8.199. D. Reinen and C. Friebel, *Struct. Bonding* **37**, 1 (1979).
8.200. G. A. Gehring and K. A. Gehring, *Rep. Prog. Phys.* **38**, 1 (1975).
8.201. J. C. M. Tindemans van Eijndhoven and C. J. Kroese, *J. Phys. C* **8**, 3963 (1975).
8.202. L. N. Bulaevsky, *Usp. Fiz. Nauk* **115**, 263 (1973)
8.203. K. I. Kugel and D. I. Khomskii, *Zh. Eksp. Teor. Fiz.* **64**, 1429 (1973); *Fiz. Tverd. Tela* **17**, 454 (1975).
8.204. K. I. Kugel and D. I. Khomskii, *Sov. Fiz. Usp.* **136**, 231 (1982).
8.205. M. E. Lines and A. M. Glass, *Principles and Applications of Ferroelectrics and Related Materials*, Oxford, Clarendon Press, 1977.
8.206. M. F. Moore, S. R. Wilson, M. J. Cohn, T.-Y. Dong, U. T. Mueller-Westerhoff, and D. N. Hendrickson, *Inorg. Chem.* **24**, 4559 (1985).
8.207. B. S. Tsukerblat, S. I. Klokishner, and M. I. Belinskii, *Mater. Sci.* **17**, 69 (1992); S. I. Klokishner and B. S. Tsukerblat, *Chem. Phys.* **125**, 11 (1988); S. I. Klokishner, B. S. Tsukerblat, and B. L. Kushkuley, *Phys. Lett. A* **179**, 429 (1993).
8.208. G. I. Bersuker, *Ferroelectrics* **123**, 11 (1991); *J. Phys.: Condens. Matter* **13**, 1079 (2001).
8.209. P. J. Becker, M. J. M. Leask, and R. N. Tyte, *J. Phys. C* **5**, 2027 (1972).
8.210. P. J. Becker, M. J. M. Leask, K. J. Maxwell, and R. N. Tyte, *Phys. Lett. A* **41**, 205 (1972).
8.211. A. H. Cooke, S. J. Swithenby, and M. R. Wells, *Solid State Commun.* **10**, 265 (1972).
8.212. B. G. Vekhter and M. D. Kaplan, *Fiz. Tverd. Tela* **15**, 2013 (1973).
8.213. J. E. Battison, A. Kasten, M. J. M. Leask, J. B. Lowry, and K. J. Maxwell, *J. Phys. C* **9**, 1345 (1976).
8.214. A. A. Loginov, *Low Temp. Phys.* **28**, 755, (2002).
8.215. R. L. Melcher and D. A. Scott, *Phys. Rev. Lett.* **28**, 607 (1972).
8.216. G. A. Gehburg, A. P. Malozemoff, W. Staube, and R. N. Tyte, *J. Phys. Chem. Solids* **33**, 1487 (1972).
8.217. B. G. Vekhter and M. D. Kaplan, *Zh. Eksp. Teor. Fiz.* **78**, 1781 (1980).
8.218. (*a*) M. D. Kaplan and G. O. Zimmerman, *Phys. Rev. B* **56**, 5193 (1997-I); **52**, 1 (1995); M. D. Kaplan and A. V. Vasiliyev, *Physica B* **179**, 65 (1992); (*b*) B. G. Vekhter, Z. A. Kazey, M. D. Kaplan, and Yu. F. Popov, *JETP Lett.* **54**, 578 (1992); (*c*) M. D. Kaplan, C. H. Perry, D. Cardarelly, and G. O. Zimmerman, *Physica B* **194–196**, 453 (1994).
8.219. (*a*) M. D. Kaplan, *Sov. J. Low Temp. Phys.* **14**, 33 (1988); (*b*) V. Sokolov, M. D. Kaplan, Z. A. Kazey, A. V. Vasiliev, and A. E. Dvornikova, *J. Phys. Chem. Solids* **53**, 737 (1992); (*c*) M. D. Kaplan, *Bull. Am. Phys. Soc.* **48**, 925 (2003).
8.220. H. Hock, G. Schröder, and H. Thomas, *Z. Phys. B* **30**, 403 (1978).
8.221. G. Schröder and H. Thomas, *Z. Phys. B* **25**, 369 (1976).
8.222. R. Englman and B. Halperin, *Phys. Rev. B* **2**, 75 (1970).
8.223. S. Abou-Warda, W. Pietzuch, G. Berghöfer, U. Kesper, W. Massa, and D. Reinen, *J. Solid State Chem.* **138**, 18 (1998).

8.224. M. A. Ivanov, V. L. Lisin, N. K. Tkachev, A. Y. Fishman, and K. Y. Shunyaev, *Russ. J. Phys. Chem.* **76**, 627 (2002).
8.225. S. P. Gabuda and S. G. Kozlova, *J. Struct. Chem.* **44**, 193 (2003).
8.226. A. L. Sobolewski, *Chem. Phys. Lett.* **267**, 452 (1997).
8.227. M. A. Hitchman, W. Maaskant, J. van der Plas, Ch. Simmons, and H. Stratemeier, *J. Am. Chem. Soc.* **121**, 1488 (1999).
8.228. M. de Dempallo, C. A. Marianetti, A. van der Ven, and G. Ceder, *Phys. Rev. B* **63**, 4107 (2001); C. A. Marianetti, D. Morgan, and G. Ceder, *Phys. Rev. B* **63**, 4304 (2001).
8.229. B. Halperin and R. Englman, *Phys. Rev. B* **43**, 1698 (1971).
8.230. B. G. Vekhter and M. D. Kaplan, *Phys. Lett. A* **43**, 389 (1973).
8.231. R. Brout, K. A. Müller, and H. Thomas, *Solid State Commun.* **4**, 507 (1966).
8.232. F. W. Sheard and G. A. Toombs, *J. Phys. C* **4**, 313 (1971); F. W. Sheard and G. A. Toombs, *Solid State Commun.* **12**, 713 (1973).
8.233. K. M. Leung and D. L. Huber, *Phys. Rev. B* **19**, 5483 (1979).
8.234. A. P. Young, *J. Phys. C* **8**, 3158 (1975).
8.235. J. Feder and E. Pytte, *Phys. Rev. B* **8**, 3978 (1973).
8.236. B. S. Lee, *J. Phys. C* **13**, 2651 (1980).
8.237. J. L. Dunn, *Phys. Rev. B* **69**, 064303 (2004).
8.238. J. A. Maaskant and W. G. Haije, *J. Phys. C* **19**, 5295 (1986).
8.239. W. G. Haije, J. A. L. Dobbelaar, M. N. Welter, and W. A. Maaskant, *J. Chem. Phys.* **116**, 159 (1987).
8.240. W. G. Haije and W. A. Maaskant, *J. Phys. C* **19**, 6943 (1986); **20**, 2089 (1987).
8.241. W. J. A. Maaskant, *Struct. Bonding* **83**, 55 (1995); *Proc. Estonian Acad. Sci. Phys. Math.* **44**, 153 (1995).
8.242. Z. W. Hendrikse and W. J. A. Maaskant, *Z. Physik. Chem.* **200**, 21 (1997).
8.243. Z. W. Hendrikse and W. J. A. Maaskant, *Physica B* **233**, 139 (1997).
8.244. T. Ogihara, *J. Phys. Soc. Japan* **64**, 4221 (1995).
8.245. L. F. Chibotaru, *Adv. Quant. Chem.* **44**, 649 (2003).
8.246. W. J. A. Maaskant, *New J. Chem.* **17**, 97 (1993).
8.247. W. J. A. Maaskant, *J. Phys.: Condens. Matter* **9**, 9759 (1997).
8.248. W. J. A. Maaskant, *J. Alloys Compounds* **281**, 211 (1998).
8.249. W. J. A. Maaskant and I. B. Bersuker, *J. Phys.: Condens. Matter* **3**, 37 (1991).
8.250. S. Kashida, *J. Phys. Soc. Japan* **45**, 414 (1978).
8.251. B. V. Harrowfield and R. Weber, *Phys. Lett. A* **38**, 27 (1972).
8.252. B. V. Harrowfield, A. J. Dempster, T. E. Freeman, and J. R. Riebrow, *J. Phys. C* **6**, 2058 (1973).
8.253. C. Fribel, *Z. Anorg. Allgem. Chem.* **417**, 197 (1975).
8.254. B. V. Harrowfield, *Solid State Commun.* **19**, 983 (1976).
8.255. D. Mullen, G. Heyer, and D. Reinen, *Solid State Commun.* **17**, 1249 (1975).
8.256. D. Reinen, *Solid State Commun.* **21**, 137 (1977).
8.257. Y. Noda, M. Mori, and Y. Yamada, *Solid State Commun.* **19**, 1071 (1976); **23**, 247 (1977); *J. Phys. Soc. Japan* **45**, 954 (1978).
8.258. Y. Yamada, in *Electron–Phonon Interaction and Phase Transitions*, Ed. T. Riste, New York, Plenum Press, 1977, p. 370.
8.259. D. W. Clack and D. Reinen, *Solid State Commun.* **34**, 395 (1980).
8.260. L. J. De Jongh and A. R. Miedema, *Experiments on Simple Magnetic Model Systems*, London, Taylor and Francis, 1974.
8.261. D. I. Khomskii and K. I. Kugel, *Solid State Commun.* **13**, 763 (1973); *Zh. Eksp. Teor. Fiz.* **79**, 987 (1980).

8.262. (*a*) C. Fribel and D. Reinen, *Z. Anorg. Allgem. Chem.* **407**, 193 (1974); (*b*) R. Haldele and D. Babel, *Z. Anorg. Allgem. Chem.* **409**, 11 (1974).
8.263. M. Towler, R. Divesi, and V. R. Saunders, *Science* **255**, 1490 (1992).
8.264. D. Reinen and S. Krause, *Solid State Commun.* **29**, 691 (1979).
8.265. C. J. O'Connor, E. Sinn, and R. L. Carlin, *Inorg. Chem.* **16**, 3314 (1977).
8.266. J. H. Ammeter, H. B. Bürgi, E. Gamp, V. Meyer-Sandrin, and W. P. Jensen, *Inorg. Chem.* **18**, 733 (1979).
8.267. W. J. Crama, W. J. A. Maaskant, and G. C. Verschoor, *Acta Crystallogr. B* **34**, 1973 (1978).
8.268. H. A. Goodwin, *Coord. Chem. Rev.* **18**, 293 (1976).
8.269. T. Kambara, *J. Chem. Phys.* **70**, 4199 (1979).
8.270. M. Nakano, G. Matsubayashi, and T. Matsuo, *Adv. Quant. Chem.* **44**, 617 (2003); *Phys. Rev. B* **66**, 212412 (2002).
8.271. K. Ji and H. Zheng, *J. Phys.: Condens. Matter* **13**, 1079 (2001).
8.272. J. Birman, *Phys. Rev.* **125**, 1959 (1962); **127**, 1093 (1962).
8.273. R. Berenson, J. N. Kotzev, and D. B. Litvin, *Phys. Rev. B* **25**, 7523 (1982).
8.274. N. N. Kristoffel, *Fiz. Tverd. Tela* **6**, 3266 (1964).
8.275. R. Englman, *The Jahn–Teller Effect in Molecules and Crystals*, London, Wiley, 1972.
8.276. R. E. Peierls, *Quantum Theory of Solids*, Oxford, Clarendon, 1955, p. 108.
8.277. H. Fröhlich, *Proc. R. Soc. London A* **233**, 296 (1954).
8.278. A. M. Afanasjev and Yu. Kagan, *Zh. Eksp. Teor. Fiz.* **43**, 1456 (1962).
8.279. H. Kuhn, *J. Chem. Phys.* **16**, 840 (1948).
8.280. L. Salem and H. C. Longuet-Higgins, *Proc. R. Soc. London A* **255**, 435 (1960).
8.281. P. W. Anderson and E. I. Blount, *Phys. Rev. Lett.* **14**, 217 (1956).
8.282. J. Friedel, in *Electron–Phonon Interaction and Phase Transitions*, Ed. T. Riste, New York, Plenum, 1977, p. 1.
8.283. R. Hoffman, *Solids and Surfaces: A Chemist's View of Bonding in Extended Structures*, Weinheim, VCH, 1988.
8.284. D. Keszler and R. Hoffmann, *J. Am. Chem. Soc.* **109**, 118 (1987).
8.285. W. Tremel and R. Hoffmann, *J. Am. Chem. Soc.* **109**, 124 (1987); *Inorg. Chem.* **26**, 118 (1987).
8.286. F. Hulliger, R. Schmelczer, and D. Schwarzenbach, *J. Solid State Chem.* **21**, 374 (1977).
8.287. J. K. Burdett and T. J. McLarnan, *J. Chem. Phys.* **75**, 5764 (1981); J. K. Burdett, P. Haaland, and T. J. McLarnan, *J. Chem. Phys.* **75**, 5774 (1981).
8.288. (*a*) N. Malkova, S. Kim, and V. Gopalin, *Phys. Rev. B* **68**, 045105 (2003); (*b*) A Audzijonis, V. Lazauskas, G. Gaigalas, I. Zigas, J. Narusis, and A. Pauliukas, *Physica B – Condens, Matter* **351**, 27 (2004).
8.289. Yu. A. Bychkov, L. P. Gor'kov, and I. E. Dzyaloshinskii, *Zh. Eksp. Teor. Fiz.* **50**, 738 (1966); I. E. Dzyaloshinskii and A. I. Larkin, *Zh. Eksp. Teor. Fiz.* **61**, 791 (1971).
8.290. A. W. Overhauser, *Phys. Rev. Lett.* **4**, 462 (1960).
8.291. D. Baeriswyl and K. Maki, *Phys. Rev. B* **31**, 6633 (1985).
8.292. S. Kivelson and D. E. Heim, *Phys. Rev. B* **26**, 4278 (1982).
8.293. V. Ya. Krivnov and A. A. Ovchinnikov, *Zh. Eksp. Teor. Fiz.* **90**, 709 (1986)
8.294. J. E. Hirsh, *Phys. Rev. Lett.* **51**, 296 (1983).
8.295. S. Mazumdar and S. N. Dixit, *Phys. Rev. Lett.* **51**, 292 (1983).
8.296. W. A. Little, *Phys. Rev. A* **134**, 1416 (1966).

8.297. J. Labbé and J. Friedel, *J. Physique* **27**, 153, 303, and 708 (1966); J. Labbé, *Phys. Rev.* **158**, 647 (1967); *J. Physique* **29**, 195 (1968).
8.298. S. Barišić, *Phys. Lett. A* **34**, 188 (1971); S. Barišić and S. Marcelja, *Solid State Commun.* **7**, 1395 (1969); J. Labbé, S. Barišić, and J. Friedel, *Phys. Rev. Lett.* **19**, 1039 (1967).
8.299. L. P. Gor'kov, *Pis'ma Zh. Eksp. Teor. Fiz.* **17**, 525 (1973); L. P. Gor'kov, *Zh. Eksp. Teor. Fiz.* **65**, 1658 (1973); L. P. Gor'kov and O. N. Dorokhov, *J. Low Temp. Phys.* **22**, 1 (1976).
8.300. W. P. Su, J. R. Schrieffer, and A. J. Heeger, *Phys. Rev. B* **22**, 2099 (1980); S. A. Brazovskii, *Zh. Eksp. Teor. Fiz.* **78**, 677 (1980); H. Takayama, Y. R. Lin-Liu, and K. Maki, *Phys. Rev. B* **22**, 2388 (1980).
8.301. M.-H. Whangbo and M. J. Foshee, *Inorg. Chem.* **20**, 113 (1981).
8.302. M. Alouani, J. W. Wilkins, R. C. Albers, and J. M. Wills, *Phys. Rev. Lett.* **71**, 1415 (1993).
8.303. J. Takeda, M. Okada, S. Kurita, K. Tanara, and T. Suemoto, *Phys. Rev. B* **52**, 14 441 (1995).
8.304. V. Robert, S. A. Borshch, and B. Bigot, *Inorg. Chem.* **35**, 3913 (1996).
8.305. A. Borshch, K. Prassides, V. Robert, and A. O. Solonenko, *J. Chem. Phys.* **109**, 4562 (1998).
8.306. V. Robert, S. Petit, and A. Borshch, *Inorg. Chem.* **38**, 1573 (1999).
8.307. A.-H. Whangbo, in *Crystal Chemistry and Properties of Materials with Quasi-One-Dimensional Structures: A Chemical and Physical Synthetic Approach*, Ed. J. Rouxel, Berlin, Springer, 1986, p. 27.
8.308. M. Kertész, *Adv. Quant. Chem.* **15**, 161 (1982).
8.309. M. E. Eberhart, K. H. Johnson, D. Adler, and R. C. O'Handley, *J. Non-Cryst. Solids* **83**, 12 (1986).
8.310. J. F. Sadoc, *J. Non-Cryst. Solids* **44**, 1 (1981); P. J. Steinhardt, D. R. Nelson, and M. Renchetti, *Phys. Rev. Lett.* **47**, 1297 (1981).
8.311. K. F. Kelton, G. W. Lee, A. K. Gandopadhyay, R. W. Hyers, T. J. Rathz, J. R. Rogers, M. B. Robinson, and D. S. Robinson, *Phys. Rev. Lett.* **20**, 195504 (2003).
8.312. I. B. Bersuker, *Adv. Quant. Chem.* **44**, 1 (2003).
8.313. V. S. Mironov, L. F. Chibotaru, and A. Ceulemans, *Adv. Quant. Chem.* **44**, 599 (2003).
8.314. G. Bersuker, *J. Chem. Phys.* **110**, 10907 (1999); G. Bersuker and M. Pekker, *J. Chem. Phys.* **110**, 10923 (1999).
8.315. Y.-N. Chiu, *J. Phys. Chem.* **88**, 5820 (1984).
8.316. S. Weinberg, *Quantum Theory of Fields*, Cambridge, Cambridge University Press, 1995, Chapter 11.
8.317. I. B. Bersuker, *Phys. Lett.* **20**, 586 (1966).
8.318. W. Cochran, *Phys. Rev. Lett.* **3**, 412 (1959); *Adv. Phys.* **10**, 40 (1961).
8.319. P. W. Anderson, in *Fizika dielektrikov*, Moscow, AN SSSR, 1959, p. 290.
8.320. V. L. Ginsburg, *Fiz. Tverd. Tela* **2**, 2031 (1960).
8.321. I. B. Bersuker, *Electronic Structure and Properties of Transition Metal Compounds. Introduction to the Theory*, New York, Wiley, 1996.
8.322. I. B. Bersuker, N. N. Gorinchoi, and V. Z. Polinger, *Theor. Chim. Acta* **66**, 161 (1984).
8.323. I. B. Bersuker, V. Z. Polinger, and N. N. Gorinchoi, *J. Mol. Struct. (THEOCHEM)* **270**, 369 (1992).
8.324. I. B. Bersuker and B. G. Vekhter, *Fiz. Tverd. Tela* **9**, 2432 (1963).

8.325. I. B. Bersuker, B. G. Vekhter, and A. A. Muzalewskii, *Ferroelectrics* **6**, 197 (1974).
8.326. I. B. Bersuker, N. N. Gorinchoy, and T. A. Fedorko, *Ferroelectrics* **153**, 1 (1994).
8.327. N. N. Gorinchoy, I. B. Bersuker, and V. Z. Polinger, *New J. Chem.* **17**, 125 (1993).
8.328. I. B. Bersuker, N. B. Balabanov, D. Pekker, and J. E. Boggs, *J. Chem. Phys.* **117**, 10478 (2002).
8.329. N. N. Kristoffel and P. I. Konsin, in *Titanat baria*, Moscow, Nauka, 1973, p. 11; *Ferroelectrics* **6**, 3 (1973).
8.330. P. I. Konsin and N. N. Kristofel, in *Interband Model of Ferroelectricity*, Ed. E. Bursian, Leningrad, Leningrad State Pedagogical Institute, 1987, p. 32.
8.331. Ya. G. Girshberg and V. I. Tamarchenko, *Fiz. Tverd. Tela* **18**, 1066, 3340 (1976); Ya. G. Girshberg, R. Kh. Kalimulin, V. A. Egorov, and E. V. Bursian, *Solid State Commun.* **53**, 633 (1985).
8.332. N. M. Plakida and G. L. Mailyan, *Fiz. Tverd. Tela* **19**, 121 (1977); G. L. Mailyan and N. M. Plakida, *Phys. Status Solidi B* **80**, 543 (1977).
8.333. E. V. Bursian, in *Interband Model of Ferroelectrics*, Ed. E. V. Bursian, Leningrad, Leningrad State Pedagogical Institute, 1987, p. 88.
8.334. B. G. Vekhter, V. P. Zenchenko, and I. B. Bersuker, *Fiz. Tverd. Tela* **18**, 2325 (1976); V. P. Zenchenko, B. G. Vekhter, and I. B. Bersuker, *Zh. Eksp. Teor. Fiz.* **82**, 1628 (1982).
8.335. Z. K. Petru and G. L. Maillyan, *Teor. Fiz.* **27**, 233 (1976).
8.336. B. G. Vekhter and I. B. Bersuker, *Ferroelectrics* **6**, 13 (1973).
8.337. B. G. Vekhter, V. P. Zenchenko, and I. B. Bersuker, *Ferroelectrics* **25**, 443 (1980).
8.338. V. P. Zenchenko, *Fiz. Tverd. Tela* **19**, 3345 (1977).
8.339. N. N. Kristoffel and A. V. Gulbis, *Fiz. Tverd. Tela* **19**, 3071 (1977).
8.340. K. Takaoka and K. Murase, *Phys. Rev. B* **20**, 2823 (1979); D. Wagner and D. Bäuerle, *Phys. Lett. A* **83**, 347 (1981).
8.341. V. M. Fridkin, *Pis'ma Zh. Eksp. Teor. Fiz.* **3**, 252 (1966); *Photoferroelectrics*, Berlin, Springer, 1979.
8.342. Ya. G. Girshberg, N. N. Trunov, and E. V. Bursian, *Izv. Akad. Nauk SSSR, Ser. Fiz.* **47**, 541 (1983); N. N. Kristoffel, *Preprint F-21*, Tartu, Academy of Science of the Estonian SSR, 1984, p. 15; Ya. G. Girshberg, R. Kh. Kalmullin, V. A. Egorov, and E. V. Bursian, *Solid State Commun.* **53**, 633 (1985); V. M. Fridkin, V. G. Lazarev, and A. L. Shlenskii, in *Interband Model of Ferroelectrics*, Ed. E. V. Bursian, Leningrad, Leningrad State Pedagogical Institute, 1987, p. 68.
8.343. N. N. Kristoffel and P. A. Konsin, *Fiz. Tverd. Tela* **13**, 2513 and 3513 (1971).
8.344. G. Chanussot, *Ferroelectrics* **8**, 671 (1974).
8.345. I. B. Bersuker, B. G. Vekhter, and M. L. Rafalovich, *Fiz. Tverd. Tela* **15**, 946 (1973).
8.346. N. N. Kristoffel, *Fiz. Tverd. Tela* **19**, 775 (1977); *Ferroelectrics* **199**, 41 (1997).
8.347. B. G. Vekhter, *Fiz. Tverd. Tela* **15**, 509 (1973); B. G. Vekhter and M. D. Kaplan, *Fiz. Tverd. Tela* **18**, 784 (1976).
8.348. I. B. Bersuker and B. G. Vekhter, *Izvestiya AN SSSR, Ser. Fiz.* **33**, 199 (1969).
8.349. I. B. Bersuker, *Nouv. J. Chim.* **4**, 139 (1980); *Teor. Eksp. Khim.* **16**, 291 (1980); *Fiz. Tverd. Tela* **30**, 1738 (1988).

8.350. I. B. Bersuker, in *Electron–Phonon Dynamics and Jahn–Teller Effects*, Eds. G. Bevilacqua, L. Martinelli, and N. Terzi, Singapore, World Scientific, 1999, p. 63.
8.351. R. Comes, M. Lambert, and A. Guinner, *Solid State Commun.* **6**, 715 (1968).
8.352. M. Lambert and R. Comes, *Solid State Commun.* **7**, 305 (1969).
8.353. A. M. Quitet, M. Lambert, and A. Guinier, *Solid State Commun.* **12**, 1053 (1973); R. Comes, R. Currat, F. Denoyer, M. Lambert, and M. Quittet, *Ferroelectrics* **12**, 3 (1976).
8.354. G. Burns and F. Dacol, *Ferroelectrics* **37**, 661 (1981).
8.355. F. Gervais, *Ferroelectrics* **53**, 91 (1984).
8.356. K. H. Ehses, H. Bock, and K. Fischer, *Ferroelectrics* **37**, 507 (1981).
8.357. K. Itoh, L. Z. Zeng, E. Nakamura, and N. Mishima, *Ferroelectrics* **63**, 29 (1985).
8.358. K. A. Müller, *Helv. Phys. Acta* **59**, 874 (1986); and in *Nonlinearity in Condensed Matter*, Ed. A. R. Bishop, Heidelberg, Springer, 1986, p. 234.
8.359. O. Hanske-Petitpierre, Y. Yacoby, J. Mustre de Leon, E. A. Stern, and J. J. Rehr, *Phys. Rev. B* **44**, 6700 (1992).
8.360. T. P. Dougherty, G. P. Wiederrecht, K. A. Nelson, M. H. Garrett, H. P. Jensen, and C. Warde, *Science* **258**, 770 (1992).
8.361. N. Sicron, B. Ravel, Y. Yacoby, E. A. Stern, F. Dogan, and J. J. Rehr, *Phys. Rev. B* **50**, 13 168 (1994-II).
8.362. Ya. G. Girshberg and Y. Yacoby, *Solid State Commun.* **103**, 425 (1997); *J. Supercond.* **12**, 217 (1999); *J. Phys.: Condens. Matter* **11**, 9807 (1999).
8.363. Ya. G. Girshberg and Y. Yacoby, *J. Phys.: Condens. Matter* **13**, 8817 (2001).
8.364. P. Konsin and N. Kristoffel, *Ferroelectrics* **226**, 95 (1999).
8.365. N. Kristoffel and P. Rubin, *Ferroelectrics Lett.* **26**, 29 (1999)
8.366. Z. X. Chen, Y. Chen, and Y. S. Jiang, *J. Phys. Chem.* **106**, 9986 (2002).
8.367. K. Tkacz-Smiech, A. Kolezynski, and W. S. Ptak, *Solid State Commun.* **127**, 557 (2003).
8.368. P. Konsin and S. Sorkin, *Ferroelectrics* **283**, 23 (2003).
8.369. N. A. Hill, *Annu. Rev. Mater. Res.* **32**, 1 (2002).
8.370. J. R. Schrieffer, *Theory of Superconductivity*, Reading, Massachusetts, Addison-Wesley, 1964.
8.371. R. K. Nesbet, *Phys. Rev.* **126**, 2014 (1962); K. H. Johnson and R. P. Messmer, *Synth. Metals* **5**, 193 (1983); K. H. Johnson, D. P. Clougherty, and M. E. McHenry, *Mod. Phys. Lett. B* **3**, 1367 (1989).
8.372. L. P. Gor'kov and A. V. Sokol, *Pis'ma ZhETF (JETP Lett.)* **16**, 333 (1987); H. Kamimura, *Japan. J. Phys.* **26**, 2 (1987).
8.373. J. G. Bednorz and K. A. Müller, *Rev. Mod. Phys.* **60**, 585 (1988).
8.374. K.-H. Höck, H. Nickisch, and H. Thomas, *Helv. Phys. Acta* **56**, 237 (1983).
8.375. G. M. Eliashberg, *Sov. Phys. JETP* **7**, 696 (1960); see also D. J. Scalapino, in *Superconductivity*, Vol. 1, Ed. R. D. Parks, New York, Dekker, 1969, p. 449.
8.376. S. Kohne, O. F. Schirmer, H. Hesse, T. W. Kool, and V. Vikhnin, *J. Superconduct.* **12**, 193 (1999).
8.377. (*a*) S. G. Andreev, M. D. Ivanovich, and M. Georgiev, *Internat. J. Quant. Chem.* **89**, 405 (2002); (*b*) M. Georgiev and L. Mihailov, *Pure Appl. Chem.* **67**, 447 (1995).
8.378. H. Barentzen, *J. Superconduct.* **15**, 457 (2002).
8.379. S. Fl. Shawish, J. Bonca, L. C. Ku, and S. A. Trugman, *Phys. Rev. B* **67**, 014301 (2003); S. A. Trugman, L. C. Ku, and J. Bonca, *J. Superconduct.* **17**, 193 (2004).

8.380. V. A. Ivanshin, M. V. Eremin, N. van Krug, J. Deisenhofen, and A. Loidl, in *Vibronic Interactions: Jahn–Teller Effect in Crystals and Molecules*, Eds. M. D. Kaplan and G. O. Zimmerman, NATO Science Series II, Vol. 39, Dordrecht, Kluwer, 2001, p. 317.
8.381. R. Englman, B. Halperin, and M. Weger, *Physica C* **169**, 314 (1990).
8.382. R. D. Tscheuschner and J. Appel, *Phys. Rev. B* **42**, 223 (1990); A. Heinz and R. D. Tscheuschner, *Phys. Rev. B* **43**, 5601 (1991).
8.383. G. I. Bersuker, N. N. Gorinchoy, V. Z. Polinger, and A. O. Solonenko, *Superconductivity (Russ.)* **5**, 1003 (1992).
8.384. G. I. Bersuker and J. B. Goodenough, *Physica C* **274**, 267 (1997).
8.385. D. Mihailović and V. V. Kabanov, *Phys. Rev. B* **63**, 054505 (2001); S. Shelkan, V. Hizhnyakov, G. Seibold, and E. Sigmund, in *Vibronic Interactions: Jahn–Teller Effect in Crystals and Molecules*, Eds. M. D. Kaplan and G. O. Zimmerman, NATO Science Series II, Vol. 39, Dordrecht, Kluwer, 2001, p. 349.
8.386. D. R. Temprano, K. Conder, A. Furrer, H. Mutka, V. Trounov, and K. A. Müller, *Phys. Rev. B* **66**, 184506 (2002).
8.387. V. Z. Kresin and S. A. Wolf, *Phys. Rev. B* **49**, 3652 (1994-I); A. Bill and V. Z. Kresin, *Z. Physik. Chem.* **201**, 271 (1997).
8.388. R. S. Markiewicz and C. Kusko, *Phys. Rev. B* **66**, 024506 (2002); R. S. Markiewicz, in *Electron–Phonon Dynamics and Jahn–Teller Effects*, Eds. G. Bevilacqua, L. Martinelli, and N. Terzi, Singapore, World Scientific, 1999, p. 273.
8.389. M. D. Kaplan and D. I. Khomskii, *JETP Lett.* **47**, 730 (1988).
8.390. M. D. Kaplan, *Physica C* **180**, 351 (1991); *Mater. Res. Soc. Symp. Proc.* **291**, 223 (1993); M. D. Kaplan and G. O. Zimmerman, *J. Phys. Chem. Solids* **59**, 1831 (1998).
8.391. N. Kristoffel, *Phys. Stat. Sol. (b)* **160**, K93 (1990); *Ferroelectrics* **130**, 137 (1992); N. Kristoffel, *Physica C* **250**, 361 (1995); *Physica C* **274**, 94 (1997); In *Vibronic Interactions: Jahn–Teller Effect in Crystals and molecules*, Eds. M. D. Kaplan and G. O. Zimmerman, NATO Science Series II, Vol. 39, Kluwer, Dordrecht, 2001, p. 337; N. Kristoffel, *Ferroelectrics Lett.* **24**, 33 (1998).
8.392. N. Kristoffel, *Physica C* **377**, 277 (2002); N. Kristoffel and P. Rubin, *Eur. Phys. J. B* **30**, 495 (2002).
8.393. L. F. Chibotaru, G. Teniers, A. Ceulemans, and V. V. Moshchalkov, *Phys. Rev. B* **70**, 094505 (2004).
8.394. G. G. Sergeeva and A. A. Soroka, *Low Temp. Phys.* **30**, 667 (2004). N. Kristoffel, *Physica C* **377**, 277 (2002).
8.395. Y.-N. Chiu, *Phys. Rev. B* **55**, 6022 (1997-I); *Acta Phys. Hung.* **74**, 427 (1994).
8.396. Y.-N. Chiu, S. H. Brown, N. Sondergaard, and F. E. Wang, *Theor. Chim. Acta* **90**, 205 (1995); P. Palting, J. R. Letelier, and Y.-N. Chiu, *Internat. J. Quant. Chem.* **96**, 56 (2004).
8.397. D. Louca, in *Vibronic Interactions: Jahn–Teller Effect in Crystals and Molecules*, Eds. M. D. Kaplan and G. O. Zimmerman, NATO Science Series II, Vol. 39, Dordrecht, Kluwer, 2001, p. 141; D. Louca, J. L. Sarrao, J. D. Thompson, H. Röder, and G. H. Kwei, *Phys. Rev. B* **60**, 10378 (1999-II).
8.398. D. Louca, *J. Superconduct* **15**, 591 (2002); *Z. Kristallogr.* **219**, 148 (2004).
8.399. A. S. Moskvin, in *Electron–Phonon Dynamics and Jahn–Teller Effects*, Eds. G. Bevilacqua, L. Martinelli, and N. Terzi, Singapore, World Scientific, 1999, p. 342; A. S. Moskvin and Y. D. Panov, *ibid.*, p. 351.

8.400. J. R. Soto, J. J. Castro, E. Yepez, and A. Calles, *Internat. J. Mod. Phys. B* **18**, 1937 (2004).
8.401. V. Polinger, D. Haskel, and E. A. Stern, in *Vibronic Interactions: Jahn–Teller Effect in Crystals and Molecules*, Eds. M. D. Kaplan and G. O. Zimmerman, NATO Science Series II, Vol. 39, Dordrecht, Kluwer, 2001, p. 215.
8.402. T. Kato, M. Kondo, M. Tachibana, T. Yamabe, and K. Yoshizawa, *Chem. Phys.* **271**, 31 (2001).
8.403. D. Reinen and J. Wegwerth, *Physica C* **183**, 261 (1991); D. Reinen, U. Kesper, and D. Belder, *J. Solid State Chem.* **116**, 355 (1995).
8.404. M. Lannoo, G. A. Baraff, and M. Schluter, *Phys. Rev. B* **44**, 12106 (1991-I).
8.405. L. F. Chibotaru and A. Ceulemans, *Phys. Rev. B* **53**, 15 522 (1996-I).
8.406. A. Ceulemans, L. F. Chibotaru, and F. Cimpoesu, *Phys. Rev. Lett.* **78**, 3725 (1997).
8.407. L. F. Chibotaru, A. Ceulemans, and S. P. Cojocaru, *Phys. Rev. B* **59**, 12 728 (1999-II).
8.408. J. E. Han, O. Gunnarsson, and V. H. Crespi, *Phys. Rev. Lett.* **90**, 167006-I (2003).
8.409. S. Suzuki, S. Okada, and K. Nakao, *AIP Conf. Proc.* **590 (I)**, 333 (2001).
8.410. J. Yu, Y. W. Son, and J. Ilm, *Physica C* **388**, 135 (2003).
8.411. T. Kato and T. Yamabe, *J. Chem. Phys.* **115**, 8592 (2001); **118**, 3804 (2003).
8.412. H. Aoki and H. Kamimura, *Solid State Commun.* **63**, 665 (1987).
8.413. W. Weber, A. L. Shelankov, and X. Zotos, *Physica C* **162–164**, 307 (1987).
8.414. D. V. Fil, O. Tokar, A. L. Shelankov, and W. Weber, *Phys. Rev. B* **45**, 5633 (1992-II).
8.415. B. S. Lee, *Physica C* **157**, 7282 (1989).
8.416. M. Georgiev and M. Borisov, *Phys. Rev. B* **39**, 11 624 (1989).
8.417. J. K. Burdett, *New J. Chem.* **17**, 107 (1993).
8.418. D. Emin, in *Vibronic Interactions: Jahn–Teller Effect in Crystals and Molecules*, Eds. M. D. Kaplan and G. O. Zimmerman, NATO Science Series II, Vol. 39, Dordrecht, Kluwer, 2001, p. 123.
8.419. W. M. You, C. L. Wang, F. C. Zhang, and Z. B. Su, *Phys. Rev. B* **47**, 4765 (1993); W. Z. Wang, C. L. Wang, Z. B. Su, and L. Yu, *Phys. Rev. Lett.* **72**, 3550 (1994); C. L. Wang, W. Z. Wang, Y. L. Liu, Z. B. Su, and L. Yu, *Phys. Rev. B* **50**, 5676 (1994).
8.420. J. B. Goodenough, *J. Phys.: Condens. Matter* **15**, 12 (2003).
8.421. N. Kristoffel, *Adv. Quant. Chem.* **44**, 555 (2003).
8.422. W. A. Little, *Science* **242**, 1390 (1988).
8.423. G. I. Bersuker and V. Z. Polinger, *Zh. Eksp. Teor. Fiz.* **80**, 1798 (1981).
8.424. Yu. E. Perlin and B. S. Tsukerblat, *Effects of Electron–Vibrational Interaction in Optical Spectra of Paramagnetic Impurity Ions*, Kishinev, Shtiintsa, 1974 (in Russian).
8.425. J.-S. Zhou, G. I. Bersuker, and J. B. Goodenough, *J. Superconduct.* **8**, 541 (1995).
8.426. A. S. Moskvin, E. N. Kondrashov, and V. I. Cherepanov, *Physica B* **311**, 200 (2002).
8.427. Yu. V. Yablokov and T. A. Ivanova, in *Electron–Phonon Dynamics and Jahn–Teller Effects*, Eds. G. Bevilacqua, L. Martinelli, and N. Terzi, Singapore, World Scientific, 1999, p. 357.

8.428. A. Bianconi, N. L. Saimi, T. Rossetti, A. Lanzera, A. Perali, M. Missori, H. Oyangi, H. Yamaguchi, Y. Nichibara, and D. H. Ha, *Phys. Rev. B* **54**, 12 018 (1996-I).
8.429. G.-H. Gweon, T. Sasagawa, S. Y. Zhou, J. Graf, H. Takagi, D.-H. Lee, and A. Lanzara, *Nature* **430**, 187 (2004).
8.430. J. D. Axe, D. E. Cox, K. Mohanty, H. Moudden, A. R. Moodenbaugh, Y. W. Xu, and T. R. Thurston, *IBM J. Res. Develop.* **33**, 382 (1989).
8.431. M. von Helmholt, J. Wecker, R. Holzapfel, L. Schultz, and K. Summer, *Phys. Rev. Lett.* **71**, 2331 (1993).
8.432. S. Jin, T. H. Tiefel, M. McCormeck, R. A. Fastnacht, R. Ramesh, and L. H. Chen, *Science* **264**, 413 (1994).
8.433. *Colossal Magnetoresistance, Charge Ordering, and Related Properties of Manganese Oxides*, Eds. C. N. R. Rao and B. Raveau, Singapore, World Scientific, 1998.
8.434. J. B. Goodenough, in *Handbook on the Physics and Chemistry of Rare Earth Elements*, Vol. 33, Eds. K. A. Gschneidner Jr., J.-C. G. Bünzli, and V. K. Pecharsky, Amsterdam, Elsevier, 2003, Chapter 214, p. 249.
8.435. J. B. Goodenough and J.-S. Zhou, *Struct. Bonding* **98**, 17 (2001).
8.436. A. J. Millis, P. B. Littlewood, and B. I. Shraiman, *Phys. Rev. Lett.* **74**, 5144 (1995).
8.437. A. J. Millis, B. I. Shraiman, and R. Mueller, *Phys. Rev. Lett.* **77**, 175 (1996).
8.438. A. J. Millis, *Phys. Rev. B* **53**, 8434 (1996); A. J. Millis: *Nature* **392**, 147 (1998).
8.439. H. Meskine, T. Saha-Dasgupta, and S. Satpathy, *Phys. Rev. Lett.* **92**, 056401-I (2004).
8.440. N. Mattur and P. Littlewood, *Phys. Today* **56**, No. 1, 25 (2003).
8.441. *Colossal Magnetoresistive Manganites*, Ed. T. Chatterje, Dordrecht, Kluwer, 2004.
8.442. T. Notta, Y. Takada, and H. Koizumi, *Internat. J. Mod. Phys. B* **12**, 3437 (1999).
8.443. T. Notta, Y. Takada, H. Koizumi, and E. Dagotto, *Phys. Rev. Lett.* **84**, 2477 (2000).
8.444. (*a*) H. Koizumi, S. Miyaki, and K. Makoshi, *Chem. Phys. Lett.* **358**, 29 (2002); (*b*) S. Miyaki, S. Uzuhara, K. Terada, S. Uzuhara, and K. Makoshi, *Phys. Rev. B* **71**, 085117 (2005).
8.445. L. P. Gor'kov and V. Z. Kresin, *JETP Lett.* **67**, 985 (1998).
8.446. M. O. Dzero, L. P. Gor'kov, and V. Z. Kresin, *Eur. Phys. J. B* **14**, 459 (2000); *Internat. J. Mod. Phys. B* **17**, 2095 (2003).
8.447. L. P. Gor'kov and V. Z. Kresin, *Phys. Rep.* **400**, 149 (2004).
8.448. D. Louca, G. H. Kwei, and J. F. Mitchell, *Phys. Rev. Lett.* **80**, 3811 (1998).
8.449. D. Louca and T. Egami, *Phys. Rev. B* **59**, 6193 (1991-I).
8.450. D. Louca, E. L. Brode, and T. Egami, *Phys. Rev. B* **61**, 1351 (2000-II).
8.451. J.-S. Zhou and J. B. Goodenough, *Phys. Rev. B* **64**, 024421 (2001); 144414 (2001).
8.452. J.-S. Zhou and J. B. Goodenough, *Phys. Rev. B.* **68**, 144406 (2003).
8.453. F. Rivadulla, E. Winkler, J.-S. Zhou, and J. B. Goodenough, *Phys. Rev. B* **66**, 174432 (2002).
8.454. J.-S. Zhou and J. B. Goodenough, *Phys. Rev.* **67**, 020404 (R) (2003).
8.455. J.-S. Zhou and J. B. Goodenough, *Phys. Rev. Lett.* **89**, 087201 (2002).
8.456. J. B. Goodenough, R. I. Dass, and J.-S. Zhou, *Solid State Sci.* **4**, 297 (2002).

8.457. Z.-L. Cheng, Z.-L. Wang, N.-L. Di, Z.-Q. Kou, G.-J. Wang, R.-W. Li, Y. Li, Q.-A. Li, and B.-G. Chen, *Appl. Phys. Lett.* **83**, 1587 (2003).
8.458. J. Hemberger, H.-A. K. von Nidda, V. Fritsch, J. Deisenhofer, S. Lobina, R. Rudolf, P. Lunkenheimer, F. Lichtenberg, A. Loidl, D. Bruns, and B. Buchner, *Phys. Rev. Lett.* **91**, 066403 (2003).
8.459. P. Schiffler, A. P. Ramirez, W. Bao, and S.-W. Cheong, *Phys. Rev. Lett.* **75**, 3336 (1995).
8.460. K. Kubo and A. Ohata, *J. Phys. Soc. Japan* **33**, 21 (1972).
8.461. Q. Li, J. Zang, A. R. Bishop, and C. M. Soukoulis, *Phys. Rev. B* **56**, 4541 (1997).
8.462. H. Rader, J. Zang, and A. R. Bishop, *Phys. Rev. Lett.* **76**, 1356 (1996).
8.463. J. Zang, A. R. Bishop, and H. Rader, *Phys. Rev. B* **53**, 8840 (1996).
8.464. A. J. Millis, R. Mueller, and B. I. Shraiman, *Phys. Rev. B* **54**, 5405 (1996).
8.465. A. E. Nikiforov and S. E. Popov, *Adv. Quant. Chem.* **44**, 587 (2003); *Phys. Solid State* **43**, 1132 (2001).
8.466. J.-S. Zhou, H. Q. Yin, and J. B. Goodenough, *Phys. Rev. B* **63**, 184423 (2001).
8.467. I. Gordon, P. Wagner, V. V. Moshchalkov, Y. Bruynseraede, L. Pinsard, and A. Revcolevschi, *Adv. Quant. Chem.* **44**, 563 (2003).
8.468. L. E. Gontchar, A. E. Nikiforov, and S. E. Popov, in *Vibronic Interactions: Jahn–Teller Effect in Crystals and Molecules*, Eds. M. D. Kaplan and G. O. Zimmerman, NATO Science Series II, Vol. 39, Dordrecht, Kluwer, 2001, p. 307.
8.469. M. D. Kaplan and G. O. Zimmerman, in *Vibronic Interactions: Jahn–Teller Effect in Crystals and Molecules*, Eds. M. D. Kaplan and G. O. Zimmerman, NATO Science Series II, Vol. 39, Dordrecht, Kluwer, 2001, p. 227.
8.470. A. S. Moskvin and I. L. Avvakumov, *Physica B* **322**, 374 (2002).
8.471. M. D. Kaplan, B. Vekhter, and G. O. Zimmerman, in *Vibronic Interactions: Jahn–Teller Effect in Crystals and Molecules*, Eds. M. D. Kaplan and G. O. Zimmerman, NATO Science Series II, Vol. 39, Dordrecht, Kluwer, 2001, p. 153.
8.472. M. D. Kaplan, G. O. Zimmerman, in *Solid State Chemistry of Inorganic Materials IV, MRS Symposium Proceedings*, Vol. 755, Eds. M. A Alario-Franko, M. Greenblatt, G. Rohrer, and M. S. Wittingham, 2003, p. 31.

Appendix. Tables of characters of irreducible representations of most usable symmetry point groups and direct products of some representations

The Cartesian coordinates x, y, and z and some of their combinations, as well as rotations around the axes R_x, R_y, and R_z, which belong to the corresponding representation are also indicated; for degenerate representations the corresponding degenerate combinations are shown in parenthesis.

Table A1. *Point groups* C_s, C_2, *and* C_i

C_i						E	I
		C_2				E	C_{2z}
				C_s		E	σ_z
A_g	R_x, R_y, R_z, x^2, y^2, z^2, xy, xz, yz	A	z, R_z, x^2, y^2, z^2 xy	A'	x, y, R_Z, z^2, xy	1	1
A_u	x, y, z	B	x, y, R_x, R_y, xz, yz	A''	z, R_x, R_y,	1	−1

Table A2. *Point groups* C_{2h} *and* C_{2v}

C_{2h}				E	C_2	σ_h	I
		C_{2v}		E	C_2	σ_v	σ_v'
A_g	R_z, x^2, y^2, z^2, xy	A_1	z, x^2, y^2, z^2	1	1	1	1
B_g	R_x, R_y, xz, yz	B_2	y, R_x, yz	1	−1	−1	1
A_u	z	A_2	R_z, xy	1	1	−1	−1
B_u	x, y	B_1	x, R_y, xz	1	−1	1	−1

Table A3. *Point groups C_{3v} and D_3*

C_{3v}				E	$2C_3$	$3\sigma_u$
		D_3		E	$2C_3$	$3C_2$
A_1	z, x^2+y^2, z^2	A_1	x^2+y^2, z^2	1	1	1
A_2	R_z	A_2	z, R_z	1	1	−1
E	$(x, y), (R_x, R_y),$ (x^2-y^2, xy) (xz, yz)	E	$(x, y), (R_x, R_y)$	2	−1	0

Table A4. *Point group D_{3d}*

D_{3d}		E	$2C_3$	$3C_2$	I	$2S_6$	$3\sigma_d$
A_{1g}	x^2+y^2, z^2	1	1	1	1	1	1
A_{1u}		1	1	1	−1	−1	−1
A_{2g}	R_z	1	1	−1	1	1	−1
A_{2u}	z	1	1	−1	−1	−1	1
E_g	(R_x, R_y)	2	−1	0	2	−1	0
E_u	(x, y)	2	−1	0	−2	1	0

Table A5. *Point groups C_{6v} and D_{3h}*

C_{3v}				E	C_2	$2C_3$	$2C_6$	$3\sigma_v$	$3\sigma'_v$
		D_{3h}		E	σ_h	$2C_3$	$2S_3$	$3C_2$	$3\sigma_v$
A_1	z, x^2+y^2, z^2	A'_1	x^2+y^2, z^2	1	1	1	1	1	1
A_2	R_z	A'_2	R_z	1	1	1	1	1	1
B_2		A''_2		1	−1	1	−1	1	−1
B_1		A''_2	z	1	−1	1	−1	−1	1
E_2	(x^2-y^2, xy)	E'	$(x, y), (x^2-y^2, xy)$	2	2	−1	−1	0	0
E_1	$(x, y), (R_\alpha, R_y),$ (xz, yz)	E''	$(R_x, R_y), (xz, yz)$	2	−2	−1	1	0	0

Table A6. *Point group* D_{2h}

D_{2h}		E	C_{2z}	C_{2y}	C_{2x}	I	σ_z	σ_y	σ_x
A_g	x^2, y^2, z^2	1	1	1	1	1	1	1	1
A_u	xyz	1	1	1	1	−1	−1	−1	−1
B_{1g}	R_z, xy	1	1	−1	−1	1	1	−1	−1
B_{1u}	z	1	1	−1	−1	−1	−1	1	1
B_{2g}	R_y, xz	1	−1	1	−1	1	−1	1	−1
B_{2u}	y	1	−1	1	−1	−1	1	−1	1
B_{3g}	R_x, yz	1	−1	−1	1	1	−1	−1	1
B_{3u}	x	1	−1	−1	1	−1	1	1	−1

Table A7. *Point groups* C_{4v} *and* D_{2d}

C_{4v}			E	C_2	$2C_4$	$2\sigma_v$	$2\sigma_v'$
	D_{2d}		E	C_2	$2S_4$	$2C_2'$	$2\sigma_d$
A_1	z, x^2+y^2, z^2	A_1 x^2+y^2, z^2	1	1	1	1	1
A_2	R_z	A_2 R_z	1	1	1	−1	−1
B_1	x^2-y^2	B_1 x^2-y^2	1	1	−1	1	−1
B_2	xy	B_2 z, xy	1	1	−1	−1	1
E	$(x, y), (R_x, R_y), (xz, yz)$	E $(x, y), (R_x, R_y), (xz, yz)$	2	−2	0	0	0

Table A8. *Point group* D_{4h}

D_{4h}		E	$2C_4$	C_2	$2C_2'$	$2C_2''$	I	$2S_4$	σ_Z	$2\sigma_v$	$2\sigma_d$
A_{1g}	x^2+y^2, z^2	1	1	1	1	1	1	1	1	1	1
A_{1u}		1	1	1	1	1	−1	−1	−1	−1	−1
A_{2g}	R_z	1	1	1	−1	−1	1	1	1	−1	−1
A_{2u}	z	1	1	1	−1	−1	−1	−1	−1	1	1
B_{1g}	x^2-y^2	1	−1	1	1	−1	1	−1	1	1	−1
B_{1u}		1	−1	1	1	−1	−1	1	−1	−1	1
B_{2g}	xy	1	−1	1	−1	1	1	−1	1	−1	1
B_{2u}		1	−1	1	−1	1	−1	1	−1	1	−1
E_g	$(R_x, R_y), (xz, yz)$	2	0	−2	0	0	2	0	−2	0	0
E_u	(x, y)	2	0	−2	0	0	−2	0	2	0	0

Table A9. *Point group $C_{\infty v}$ (φ is the angle of rotation around the axis of symmetry of infinite order)*

$C_{\infty v}$		E	$2C_\infty(\varphi)$	$\cdots$	$\infty\sigma_v$
$A_1 \equiv \Sigma^+$	z, x^2+y^2, z^2	1	1	$\cdots$	1
$A_2 \equiv \Sigma^-$	R_z	1	1	$\cdots$	-1
$E_1 = \Pi$	$(x, y), (R_x, R_y), (xz, yz)$	2	$2\cos(\varphi)$	$\cdots$	0
$E_2 = \Delta$	(x^2-y^2, xy)	2	$2\cos(2\varphi)$	$\cdots$	0
$E_3 = \Phi$		2	$2\cos(3\varphi)$	$\cdots$	0
$\cdots$		$\cdots$	$\cdots$	$\cdots$	$\cdots$

Table A10. *Tetrahedral point group T_d*

T_d		E	$8C_3$	$3C_2$	$6S_4$	$6\sigma_d$
A_1	x^2+y^2+z	1	1	1	1	1
A_2		1	1	1	-1	-1
E	$(2z^2-x^2-y^2, x^2-y^2)$	2	-1	2	0	0
T_1	(R_x, R_y, R_z)	3	0	-1	1	-1
T_2	$(x, y, z), (xy, xz, yz)$	3	0	-1	-1	1

Table A11. *Octahedral point group O_h*

O_h		E	$8C_3$	$3C_2\ (=C_4^2)$	$6C_4$	$6C_2$	I	$8S_6$	$3\sigma_h$	$6S_4$	$6\sigma_d$
A_{1g}	$x^2+y^2+z^2$	1	1	1	1	1	1	1	1	1	1
A_{1u}		1	1	1	1	1	-1	-1	-1	-1	-1
A_{2g}		1	1	1	-1	-1	1	1	1	-1	-1
A_{2u}		1	1	1	-1	-1	-1	-1	-1	1	1
E_g	$(2z^2-x^2-y^2, x^2-y^2)$	2	-1	2	0	0	2	-1	2	0	0
E_u		2	-1	2	0	0	-2	1	-2	0	0
T_{1g}	(R_x, R_y, R_z)	3	0	-1	1	-1	3	0	-1	1	-1
T_{1u}	(x, y, z)	3	0	-1	1	-1	-3	0	1	-1	1
T_{2g}	(xy, xz, yz)	3	0	-1	-1	1	3	0	-1	-1	1
T_{2u}		3	0	-1	-1	1	-3	0	1	1	-1

Table A12. *Icosahedral group* I_h

I_h	E	$12C_5$	$12C_5^2$	$20C_3$	$15C_2$	I	$12S_{10}$	$12S_{10}^3$	$20S_6$	15σ
A_g $x^2+y^2+z^2$	1	1	1	1	1	1	1	1	1	1
A_u	1	1	1	1	1	−1	−1	−1	−1	−1
T_{1g} (R_x, R_y, R_z)	3	$(1+\sqrt{5})/2$	$(1-\sqrt{5})/2$	0	−1	3	$(1-\sqrt{5})/2$	$(1+\sqrt{5})/2$	0	−1
T_{1u} (x, y, z)	3	$(1+\sqrt{5})/2$	$(1-\sqrt{5})/2$	0	−1	−3	$-(1-\sqrt{5})/2$	$-(1+\sqrt{5})/2$	0	1
T_{2g}	3	$(1-\sqrt{5})/2$	$(1+\sqrt{5})/2$	0	−1	3	$(1+\sqrt{5})/2$	$(1-\sqrt{5})/2$	0	−1
T_{2u}	3	$(1-\sqrt{5})/2$	$(1+\sqrt{5})/2$	0	−1	−3	$-(1+\sqrt{5})/2$	$-(1-\sqrt{5})/2$	0	1
G_g	4	−1	−1	1	0	4	−1	−1	1	0
G_u	4	−1	−1	1	0	−4	1	1	−1	0
H_g $(2z^2-x^2-y^2, x^2-y^2, xy, xz, yz)$	5	0	0	−1	1	5	0	0	−1	1
H_u	5	0	0	−1	1	−5	0	0	1	−1

Table A13. *Point group O′ (octahedral double group)*

Mulliken notations	Bethe notations	E	Q	$4C_3$ $4C_3^2Q$	$4C_3^2$ $4C_3Q$	$3C_4^2$ $3C_4^2Q$	$3C_4$ $3C_4^3Q$	$3C_4^3$ $3C_4Q$	$6C_2$ $6C_2Q$
A_1'	Γ_1	1	1	1	1	1	1	1	1
A_2'	Γ_2	1	1	1	1	1	−1	−1	−1
E'	Γ_3	2	2	−1	−1	2	0	0	0
T_1'	Γ_4	3	3	0	0	−1	1	1	−1
T_2'	Γ_5	3	3	0	0	−1	−1	−1	−1
E_2'	Γ_6	2	−2	1	−1	0	$\sqrt{2}$	$-\sqrt{2}$	0
E_3'	Γ_7	2	−2	1	−1	0	$-\sqrt{2}$	$\sqrt{2}$	0
G'	Γ_8	4	−4	−1	1	0	0	0	0

Table A14. *Direct products of irreducible representations of simple groups $\Gamma_i \times \Gamma_j$ (I), simple with double groups $\Gamma_i \times \Gamma_\alpha$ (II), and double with double groups $\Gamma_\alpha \times \Gamma_\beta$ (III) presented as a sum of Γ_i*

I. $\Gamma_i \times \Gamma_j$

$\Gamma_1 \times \Gamma_i = \Gamma_i$, $\Gamma_2 \times \Gamma_2 = \Gamma_1$
$\Gamma_2 \times \Gamma_3 = \Gamma_3$, $\Gamma_2 \times \Gamma_4 = \Gamma_5$
$\Gamma_2 \times \Gamma_5 = \Gamma_4$, $\Gamma_3 \times \Gamma_3 = \Gamma_1 + \Gamma_2 + \Gamma_3$
$\Gamma_3 \times \Gamma_4 = \Gamma_4 + \Gamma_5$, $\Gamma_3 \times \Gamma_5 = \Gamma_4 + \Gamma_5$
$\Gamma_4 \times \Gamma_4 = \Gamma_1 + \Gamma_3 + \Gamma_4 + \Gamma_5$
$\Gamma_4 \times \Gamma_5 = \Gamma_2 + \Gamma_3 + \Gamma_4 + \Gamma_5$
$\Gamma_5 \times \Gamma_5 = \Gamma_1 + \Gamma_3 + \Gamma_4 + \Gamma_5$

II. $\Gamma_i \times \Gamma_\alpha$

$\Gamma_1 \times \Gamma_6 = \Gamma_2 \times \Gamma_7 = \Gamma_6$, $\Gamma_2 \times \Gamma_6 = \Gamma_1 \times \Gamma_7 = \Gamma_7$
$\Gamma_3 \times \Gamma_6 = \Gamma_3 \times \Gamma_7 = \Gamma_8$, $\Gamma_3 \times \Gamma_8 = \Gamma_6 + \Gamma_7 + \Gamma_8$
$\Gamma_4 \times \Gamma_6 = \Gamma_5 \times \Gamma_7 = \Gamma_6 + \Gamma_8$
$\Gamma_5 \times \Gamma_6 = \Gamma_4 \times \Gamma_7 = \Gamma_7 + \Gamma_8$
$\Gamma_4 \times \Gamma_8 = \Gamma_5 \times \Gamma_8 = \Gamma_6 + \Gamma_7 + 2\Gamma_8$

III. $\Gamma_\alpha \times \Gamma_\beta$

$\Gamma_6 \times \Gamma_6 = \Gamma_7 \times \Gamma_7 = \Gamma_1 + \Gamma_4$
$\Gamma_6 \times \Gamma_7 = \Gamma_2 + \Gamma_5$
$\Gamma_6 \times \Gamma_8 = \Gamma_7 \times \Gamma_8 = \Gamma_3 + \Gamma_4 + \Gamma_5$
$\Gamma_8 \times \Gamma_8 = \Gamma_1 + \Gamma_2 + \Gamma_3 + 2\Gamma_4 + 2\Gamma_5$

Subject index

The *Section number*, given where appropriate, is shown in italic; *Table numbers* are indicated in italic and preceded by a letter *T*. Specific polyatomic systems and classes of compounds are listed in the *Formula index*.

Formula index

Classes of compounds are arranged alphabetically at the beginning of this list. *Chemical formulas* of specific JT systems are arranged along the Periodic Table of elements by their assumed JT atoms or (conventionally) JT centers, and are listed for each element by the increasing number of such atoms in the formula and increasing environment. *Section numbers*, given where appropriate, are indicated in italic; *Table numbers* are indicated in italic and preceded by a letter *T*.